NIST SPECIAL PUBLICATION 813

ICLASS–91

Proceedings
of the
Fifth International Conference on Liquid Atomization and Spray Systems

July 15–18, 1991
National Institute of Standards and Technology
Gaithersburg, MD U.S.A.

ICLASS-91

Proceedings of the Fifth International Conference on Liquid Atomization and Spray Systems

Organized by:

Institute for Liquid Atomization and Spray Systems
(ILASS-Americas)
and
National Institute of Standards and Technology

Hratch G. Semerjian, Editor

July 15-18, 1991
National Institute of Standards and Technology
Gaithersburg, MD, U.S.A.

U.S. Department of Commerce
Robert A. Mosbacher, Secretary

National Institute of Standards and Technology
John W. Lyons, Director

National Institute of Standards
and Technology
Special Publication 813
Natl. Inst. Stand. Technol.
Spec. Publ. 813
869 pages (July 1991)
CODEN: NSPUE2

U.S. Government Printing Office
Washington: 1991

For sale by the Superintendent
of Documents
U.S. Government Printing Office
Washington, DC 20402

FOREWORD

The Fifth International Conference on Liquid Atomization and Spray Systems, ICLASS-91, is hosted by the Institute for Liquid Atomization and Spray Systems (ILASS-Americas) and the National Institute of Standards and Technology. Previous international ICLASS conferences were held in Tokyo, Japan (1978), Madison, WI, USA (1982), London, UK (1985), and Sendai, Japan (1988). Regional ILASS meetings are held annually in the USA, Japan, and Europe. Proceedings have been published of papers presented at all ICLASS conferences. There has been considerable growth in interest in the subject of Atomization and Sprays as seen in the increased membership of ILASS world wide, and the considerable increase in the number of papers presented at mechanical, chemical, aeronautical and aerosol engineering societies. A new journal, Atomization and Sprays, the journal of the International Institutes for Liquid Atomization and Spray Systems, was founded in 1991. It publishes papers of specialist interest, with a wide range of applications, in an archival journal with easy access for librarians.

The papers presented at ICLASS-91 have been classified into areas of fundamental interest involving hydrodynamic instability, wave mechanics, and liquid disintegration as part of the process of atomization. New insights and information are leading to an improved understanding of the interactions between fluid dynamics and aerodynamics in two-phase flow. An important step forward in the characterization of sprays has been made by measurements with laser-based instruments; these instruments allow measurement of drop size, velocity, number density and liquid flux. Laser-based particle diagnostic techniques are being used in hundreds of laboratories worldwide, and a significant fraction of the papers presented at ICLASS-91 report on measurements made with such systems.

Important developments are being made in theoretical analyses and computations. Classical theories on wave mechanics, instability, and amplitude growth are being used to analyze liquid disintegration. Theories have been developed, based on particle-fluid mechanic interactions, to explain dispersion, collision, coalescence and evaporation of drops in sprays. Following the general trend in engineering science of rapid growth in computational fluid dynamics (CFD), there is a significant increase in the number of papers presented at ICLASS-91 on numerical analyses, computations, predictions and modeling using complex codes that account for two-phase, turbulent, three-dimensional interactions between particles and gas under conditions of heat, mass and momentum transfer. The use of supercomputers is providing closer agreement between predictions and experimental measurements.

Applications research has, in the past, been dominated by liquid fuels and combustion. The influence of sprays on combustion and emissions will become of much greater importance in the design of the next generation of aircraft engine combustors. Research on diesel engine sprays has flourished with the realization of the strong influence of atomization and mixing in the cylinder on emission of soot. The largest number of papers presented at ICLASS-91 falls into the category of internal combustion engines. Liquid metal spraying for coating, powder metallurgy and manufacturing of tools is a fast growing field in the aerospace industry. The fundamental processes of atomization in liquid metal sprays are not so different from those in spray combustion. Rapid solidification processes, which result in three-phase flows, provide improved material properties. Impingement of drops on a substrate is critical for the ultimate

strength and metallurgical properties of the end product. Many millions of gallons of paint are sprayed onto automobiles and many other commercial products. Forty percent of the spray misses its target. Blistering and nonuniform film thickness are major problems in the industry. ICLASS-91 shows how scientific analysis and detailed instrumentation can lead to important improvements for an industry that is huge and very old. Agricultural spraying is resulting in large scale pollution of the environment. Society could benefit greatly from utilization of knowledge acquired in other applications. Agricultural industry is poorly represented at ICLASS-91.

Summarizing the state of the art as represented by the 100 papers presented at ICLASS-91 and printed in these proceedings, we see significant advancements in elevating atomization and sprays to a significant specialty in the field of science. The increased use of theory and computational fluid mechanics is providing a framework for generalization and prediction which should ultimately lead to more accurate computations and fewer measurements. Atomization, a subject declared by many experts, in the past, to be too complex for study, is being tackled by theoreticians, computationalists and experimentalists using novel techniques to measure wavelength, frequency, amplitude growth rate, and wave propagation speeds on liquid surfaces. This research is showing that atomization is a highly non-linear process with steady input of liquid to the nozzle resulting in highly unsteady, pulsating flow in the spray. As a result of very detailed measurements in sprays, providing information of distributions of drop size, velocity, number density and liquid flux distributions, designers of nozzles, guns, spray chambers, combustion chambers, and chemical processing plants are beginning to realize that a scientific approach can lead to a more effective solution of design and practical problems than the traditional trial and error methods which are currently used in most industries. All of these changes are reported in the wealth of information contained in the papers published in these proceedings.

Norman Chigier
Conference Chairman, ICLASS-91

NOTE:

Opinions expressed at the Conference, or published in the Conference Proceedings, are those of the authors and contributors, and do not necessarily represent the views of the Organizing Committees. Certain commercial equipment, instruments, or materials are identified in the papers in order to adequately specify experimental procedures. Such identification does not imply recommendation or endorsement by ILASS-Americas or the National Institute of Standards and Technology, nor does it imply that the materials or equipment identified are necessarily the best available for the purpose.

ICLASS-91

Fifth International Conference on Liquid Atomization and Spray Systems

ORGANIZING COMMITTEES

Conference Committee

Norman A. Chigier - Conference Chairman (ILASS-Americas)
Hratch G. Semerjian - Conference Co-Chairman (NIST)
Arthur H. Lefebvre - Chairman, Papers Committee
Harold C. Simmons - Treasurer
G. Scott Samuelsen - Advisor

Publication Committee

Hratch G. Semerjian (Chairman)
Ashwani K. Gupta
Deborah J. Musumeci
Cary Presser
James R. Zurlo

TABLE OF CONTENTS

Session B-8 *AIRBREATHING AND ROCKET ENGINES*

Plenary Lecture

THE PHYSICS OF ATOMIZATION

N.A. Chigier

Department of Mechanical Engineering
Carnegie Mellon University
Pittsburgh, PA, U.S.A.

ABSTRACT

The fundamental physical processes of atomization of liquid sheets and jets are examined. Disturbances are generated inside nozzles in both liquid and gaseous flows due to turbulence, boundary layer growth, asymmetries, sharp bends, cavitation, pulsations in the flow, and vibrations of the nozzle. When the liquid emerges from the nozzle, the initial disturbances grow as a function of time and distance from the nozzle. Wave amplitudes grow until the liquid sheet erupts to produce a shower of drops. Pulses of liquid form clusters of drops with the same frequencies as those of the waves on the liquid surface. Growth of the waves on the free liquid surface is augmented by 1) pressure variation and shear generated by relative velocity at the gas/liquid interface 2) turbulence intensity and scale in the gas and liquid streams and 3) relaxation of the velocity profile in the liquid stream as it adjusts from the no-slip boundary condition at the nozzle wall to the equilibrium condition at the gas/liquid interface. New information has been obtained on frequency, wave length, and wave amplitude measured along the length of liquid jets and sheets for a wide range of liquid and gas velocities.

Large scale structures in the air flow generate large, ordered cell structures within the liquid sheet. These structures are bounded by large diameter ligaments with thin membranes stretched between them. The larger diameter ligaments are the origin of the large drops in the spray, and the stretched membranes are the origin of the smaller droplets. Co-axial round liquid jets, surrounded by axisymmetric air streams form flat curling liquid sheets with subsequent breakup into droplet clouds. Intact lengths were found to be strongly dependent on Reynolds and Weber numbers. Final breakup mechanisms of flat sheets, round jets, and large drops are shown to be remarkably similar.

INTRODUCTION

Even though atomization has been used very extensively in a wide variety of applications, the fundamental physical mechanisms of liquid breakup into drops have not yet been established. When the word atomization was coined in the 19th century, there was a belief that 5 μm was the smallest possible diameter of droplets that could be physically atomized. Today, there are a number of atomizers that generate much smaller droplets of submicron size. Theoretical analyses based on wave theory have postulated wave growth along surfaces but until recently there was little experimental evidence on generation and growth of waves. The influence of the fluid properties,

viscosity, surface tension, and density have always been considered important though there is conflicting evidence as to the quantitative significance of these properties. For two-fluid atomizers, it has long been established that increasing the relative velocity between the air and liquid flow streams has a very powerful and dominant influence on atomization. Fluid dynamic effects of turbulence in the liquid and air streams, boundary layer growth, flow separation at sharp bends and corners, cavitation, and pulsations in the supply lines all contribute to the generation of disturbances. After emerging from the nozzle, wave amplitudes grow under the influence of relative velocity between the air and liquid flows. Shear develops in the liquid and air flows resulting in turbulence generation with changing intensity and scale. Velocity profiles in the liquid flow relax from the no-slip wall condition inside the nozzle to the equilibrium condition at the liquid-air interface.

Several mechanisms have been postulated for the origin of disturbances. Turbulence generated inside the nozzle is the most likely source. Turbulence inside the nozzle can be generated by flow separation at sharp corners, wall roughness, boundary layers, and shear flow. The radial transverse component of the fluctuating velocity is directed towards the liquid surface and can be expected to initiate instabilities by formation of protuberances on the liquid surface. Boundary layer instability along the inner walls of the nozzle, cavitation inside the nozzle, sudden pressure drop at the nozzle exit, sudden velocity redistribution as the velocity profile relaxes on emergence from the nozzle and interfacial hydrodynamic instability are all additional sources for disturbance initiation. Lin and Woods, based on their experiments, conclude that interfacial instability is the real origin of atomization. Atomization usually produces a wide size distribution. A narrow size distribution can be achieved by controlling the external excitation at a precisely fixed frequency.

Knowledge of the physics of the atomization process will lead to improvements in atomizer design. The major objective in the design of atomizers is to generate a specified size, velocity and number density distribution of drops resulting in sprays with specified angles and liquid mass flux distributions. Sprays with radial and circumferential symmetry are generally required.

In the past, Sauter Mean Diameter has been used as a measure of atomization quality. Sprays with large differences in size distribution can yield the same global SMD so that the global SMD is an insufficient indicator of atomization quality. There has been very little information on drop velocities in sprays. The performance and effectiveness of a spray is dependent on individual drop momentum which determines individual drop trajectories. Knowledge is, therefore, required of both size and velocity of individual drops in the spray. Many processes will prescribe an upper limit of droplet size so as to prevent deposition on chamber walls. Other processes, such as agricultural spraying, will prescribe a lower limit on droplet size to avoid drift and carry over of small droplets by wind and cross currents of air flow. For processes such as coating of surfaces or powder metallurgy, uniform drop size may be required. The ultimate objective is to have sufficient control of drop size, velocity, spacing and angle of flight. In order to obtain control of the spray, all the factors that affect the atomization process must be controlled throughout the spraying process.

In addition to the fluid dynamic processes, external vibration, acoustic, electrical and magnetic forces can amplify or damp disturbances. Piezoelectric transducers generate monosize drop streams. Ultrasonic atomization produces clouds of drops at the nozzle exit. Electric fields are used to deflect drop trajectories. Loudspeakers generate acoustic fields which interact with waves on liquid surfaces to cause damping or enhanced atomization. Coupling of these external fields with the fluid dynamic fields can lead to far greater control of atomization than has been achieved up to now.

Special attention needs to be addressed to the problem of pulsations. Most studies in the past have concentrated on the long-time averaged properties of the spray. More recent studies, using high speed movies and submicrosecond high speed flash and laser photography, have revealed the

presence of pulsations which are present even under conditions where liquid and air flows supplied to the atomizer are free of pulsations. The disturbances and waves that propagate along liquid surfaces have specific frequencies. When the liquid sheets erupt, droplets are ejected in pulses with the same frequencies as the waves on the surface. These pulsations seem to be present in all sprays. The clustering of drops has important adverse effects resulting in 1) hot streaks impacting on combustion chamber walls, 2) reduced evaporation of drops within clouds where vapor becomes saturated, 3) increased emission of pollutants, 4) incomplete heat and mass transfer, 5) reduced combustion efficiency, 6) combustion instability, and 7) patchiness and non-uniformities in coatings. Since these pulsations are inherent in the break-up process, it will be very difficult to eradicate this phenomenon. Application of external acoustic and electrical fields will be needed to reduce the impact of these pulsations and clusters.

CLASSICAL BREAKUP REGIMES

The Rayleigh regime appears at low velocity when the growth of axisymmetric waves causes the detachment of drops whose size is larger than the jet diameter.

The First Wind Regime is characterized by the inception of aerodynamic interaction between the surrounding stationary gas and the liquid jet. The pressure force, induced by the aerodynamic interaction is added to the surface tension resulting in an increase in the growth of axial symmetric waves. Non-axisymmetric surface disturbances and helical deformation of the jet axis are also present.

The Second Wind Regime appears at higher jet velocities. Small asymmetric unstable waves form on the liquid surface resulting in the formation of droplets of much smaller size than the jet diameter. Droplet detachment from the surface begins far from the nozzle exit. The length of the cylindrical or undisturbed zone decreases when the jet velocity increases.

The Atomization Regime is characterized by droplet detachment close to the orifice exit. The vertex of the spray angle is near the center of the nozzle exit section. Droplet sizes are much smaller than the orifice diameter.

Ranz assumed that the diameters of droplets formed from ligaments are proportional to the wavelength of superficial unstable disturbances. Schweitzer suggested that turbulence was responsible for the production of superficial disturbances which are broken by the action of aerodynamic forces. Bergwerk made the hypothesis that the disturbances in the liquid jet are due to cavitation inside the orifice. Rupe stressed the role played by the rearrangement of the velocity profile on the jet stability. A laminar flow inside the nozzle is more unstable than a turbulent flow because the laminar profile requires a more drastic rearrangement after it leaves the nozzle than a turbulent profile.

Reitz and Bracco suggested that the outer surface of the liquid is disrupted by the interaction with the ambient gas which leads to the rapid and selective growth of surface waves whose initial amplitudes are controlled by cavitation and the rearrangement of the velocity profile.

Lane concluded that there are 3 stages of disintegration:
1) Initiation of small disturbances on the liquid surface in the form of ripples or protuberances.
2) Action of air pressure and tangential forces on these disturbances, forming ligaments which may breakup into drops.
3) Breakup of drops into smaller drops.

Aerodynamic forces have a major effect on fineness of atomization. The aerodynamic interaction between the liquid jet and the surrounding gas increases the instability resulting in shorter breakup lengths and smaller drops.

De Juhasz and Schweitzer concluded from their experiments that turbulence in the liquid flow was the main influencing factor in atomization. Mehlig stated that the radial components of velocity in the turbulent liquid flow are the predominant cause of atomization. Wave growth theory has been used with Rayleigh's instability analysis by Chuech and Krulle to calculate jet disintegration.

Strazhewski, Scheubel and Weber concluded that primary disturbances and wave growth are relatively unimportant compared to the dominant effects of air resistance and gas-liquid relative velocities. Previous reviews of atomization by Giffen and Chigier have provided no clear and distinct explanation of the dominant cause of liquid disintegration.

ANALYSES OF WAVE GROWTH

In 1878, Lord Rayleigh produced the first mathematical analysis of the break down of a simple liquid jet by surface tension. Squire carried out an analysis of wave growth on a thin inviscid liquid sheet. The analysis indicated the basic principles by which the surrounding atmosphere interacts with the sheet and predicted the existence of an optimum frequency at which a wave would grow most rapidly.

Dombrowski set up a simple model of the break-up process of a spray sheet. He assumed that the sheet breaks at the crests and troughs of the waves. Each half-wave-length contracts under surface tension to form a cylindrical thread which then breaks down to produce a string of droplets. This physical model greatly oversimplifies the real process but nevertheless provides general indications of the characteristics of sprays generated by a number of types of atomizers. The model assumes that the sheet thickness remains constant as the wave amplitude increases so that the point where the sheet breaks cannot be calculated. Also, the predicted wave frequencies are at variance with the dominant frequencies found in practice. A more rigorous analysis of wave growth included a mechanism by which the sheet thickness decreases as the wave amplitude increases. Trains of ripples on the sheet surface cause localized thinning of the sheet which cause it to break down earlier than sheets without ripples.

In swirl spray pressure nozzles which form hollow conical sheets, mean drop size decreases with increase of liquid pressure and increases with increase in viscosity. However, when mean drop size is plotted as a function of sheet velocity, which is a more fundamental parameter, then drop size is found to be independent of viscosity. This is a surprising result since it can be expected that atomization processes would be hindered by viscous forces as is found in some other forms of atomizers. High speed movie films taken of the flow pattern within an atomizer constructed of transparent material showed that high viscosity liquids produced the most disturbed air core. Dombrowski provides the following explanation. Disturbances created in the nozzle will tend to be damped by surface tension at the air core, but this action will be opposed by viscous forces. Since the surface tension of oil is relatively low, viscous drag predominates and disturbances propagate through the sheet where they offset the natural tendency of the viscous sheet to oppose breakdown.

Even though there is a general recognition that atomizers should be rigidly supported, there is a question as to whether mechanical vibrations can be imparted to the nozzle and thereby affect the wave initiation and disintegration processes. Dombrowski carried out an experiment to detect these vibrations by mounting an accelerometer to a fan spray nozzle with the output fed to a spectrum analyzer. A number of frequencies were found which were of the same order as those present on the sheets. These frequencies were traced to resonance of the brass tube on which the nozzle was located, to resonance of the experimental rig, and to disturbances arising from within the building. It has even been suggested that if the nozzle could be isolated from all external disturbances, aerodynamic disintegration would not take place. Mean drop size was found to diminish with

increase of frequency until a critical value is reached. It then increases to an effectively constant value. Small upstream disturbances initiate the disintegration process, but the final stages of breakup are effectively controlled by the interaction of the liquid and the surrounding gas. In the presence of hot gas, small wave-like disturbances grow in amplitude rapidly leading to break down of the liquid sheet close to the nozzle. Sheet perforations give rise to a network of threads. Threads tend to break down in a similar manner to a single column of liquid. Pulsing the liquid along the plane of the sheet produces symmetric waves.

Previous classifications of the modes of atomization developed by Ohnesorge, Miesse, and Reitz have shown that modes of atomization are a function of the Reynolds and Ohnesorge numbers without including the gas-liquid relative velocity. Wolfe and Buschulte used the aerodynamic Weber number as the single variable for atomization. The breakup of spherical water drops in an air stream was found by Kennedy to be a function of the air velocity and $We_a/Re_w^{0.5}$. Farago has shown that liquid jet disintegration modes are a function of only two parameters Re_ℓ and We_a.

Liquid jet disintegration can be divided into three categories:

- Rayleigh breakup: Mean drop diameter is of the order of the jet diameter. Maximum drop diameter is twice the jet diameter. There is no ligament formation. The flow may be i) axisymmetric or ii) non-axisymmetric.
- Formation of membrane ligaments: Round jets develop into thin liquid membranes. Kelvin Helmholtz waves develop along the membranes. Drop diameters are considerably smaller than the jet diameter.
- Fibers are formed on the liquid surfaces. Fibers are peeled off the liquid surface and break into drops via the Rayleigh mechanism. Drop diameters are an order of magnitude smaller than the jet diameter.

Pulsations usually develop during the process of atomization. The frequency of release of pulses of drops is close to the frequency of wave disturbances on the liquid surface. Clusters of drops are formed which move downstream into the spray.

In recent years, a series of experiments have been conducted at Carnegie Mellon University by Chigier, Farago, Mansour, and Eroglu with the specific objective of identifying the basic mechanisms that influence and determine liquid disintegration. Extensive studies have been made of liquid sheets with co-flowing air jets as well as cylindrical liquid jets with coaxial co-flowing air jets. Air and liquid velocities were varied to provide aerodynamic Weber number variations over a range of six orders of magnitude and Reynolds numbers of two orders of magnitude.

TWO DIMENSIONAL LIQUID SHEET AIRBLAST ATOMIZER

The two dimensional liquid sheet airblast atomizer, designed by Parker Hannifin, used at Carnegie Mellon University, is shown in Fig. 1. A liquid sheet emerges from a central slit. High velocity air impinges, at an angle, on both sides of the sheet at the nozzle exit. Liquid and air gap sizes and flow rates can be varied. A two dimensional liquid sheet provides an initially flat, large surface area for study of wave growth and frequency of disturbances travelling along the liquid surface. It allows direct comparison of measurements with predictions from linear theories of wave development.

A series of photographs were made of the sheet surface with progressive increases in liquid flow rate and air supply pressure. With no air flow, the liquid sheet emerges from the slit and converges under the influence of surface tension. Waves move along the length of the sheet but also emanate from the rims on either side of the sheet to form criss-cross patterns. Waves from

each rim interfere with each other resulting in increases in amplitude when the waves are in phase. These capillary waves are driven by surface tension. When the liquid flow rate is increased, small distortions appear on the sheet surface indicating a transition from laminar to turbulent flow at Reynolds numbers, based on nozzle exit conditions, around 1470.

With air flow, we can distinguish two modes of breakup: a "mechanical" effect due to the action of liquid pressure inside the nozzle and an aerodynamic effect due to the action of air friction. Large drops are formed from the rims of the sheet where the aerodynamic forces are much smaller than the surface tension and inertia forces (Fig. 2). The rims behave like columns of liquid that breakup by the Rayleigh mechanism to produce a line of drops whose diameter is slightly larger than the liquid column diameter. When the liquid flow rate (and hence the liquid velocity) is doubled, regularly ordered, organized cell structures are formed across the sheet. Each cell structure is bounded by large diameter rims with thin membranes of liquid stretched across each cell. As the sheet breaks up, the larger diameter rims generate the larger drops while the membranes generate the smaller droplets.

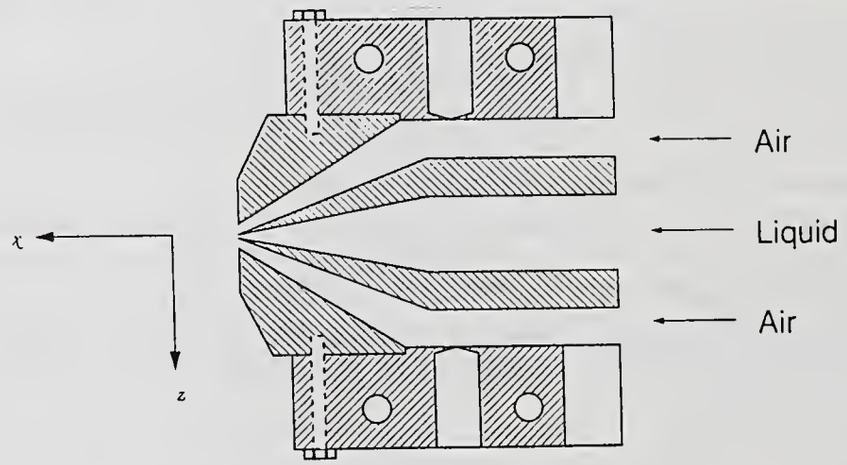

Fig. 1 Two dimensional variable geometry air blast research atomizer

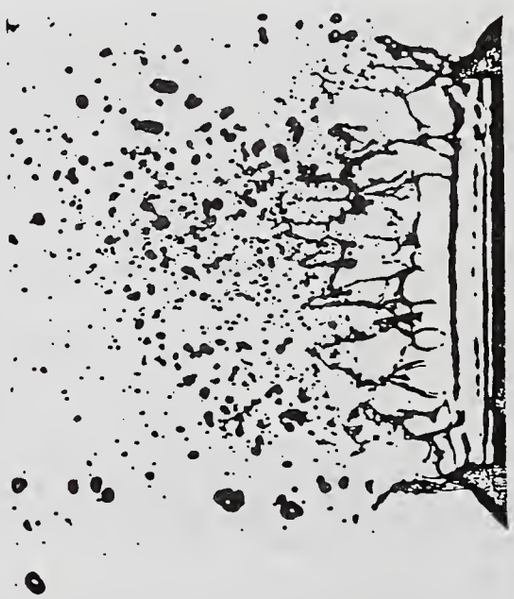

Fig. 2 Two modes of sheet breakup exist: A "mechanical" mode due to the action of liquid pressure inside the nozzle and an aerodynamic mode due to the effect of air friction (P_0 = 0.1 psig [102.015 kPa]; m_{liquid} = 11.34 g/s)

When the liquid flow rate is increased further, the intact length is increased (Fig. 3). Waves, increasing in amplitude, accompanied by formation of several ordered cell structures, can be seen to clearly develop along the length of the sheet. The cells are stretched and appear to blow up in a manner similar to the bagging of large single drops during breakup. In Fig. 3, both the mass flow rate of the liquid and the supply air pressure to the nozzle have been increased. The effects of increased turbulence in the liquid and air streams are clearly evident. The initial sheet region is more disturbed with higher frequency and short wavelength waves. Cells have smaller dimensions and are less ordered. Membrane shattering precedes cell rim breakup. Just before final breakup, the leading edge of the sheet is anchored to the remaining liquid only through the cell frames. The high shear causes slight variations in the liquid sheet thickness to develop into major disturbances resulting in holes being blown through the sheet.

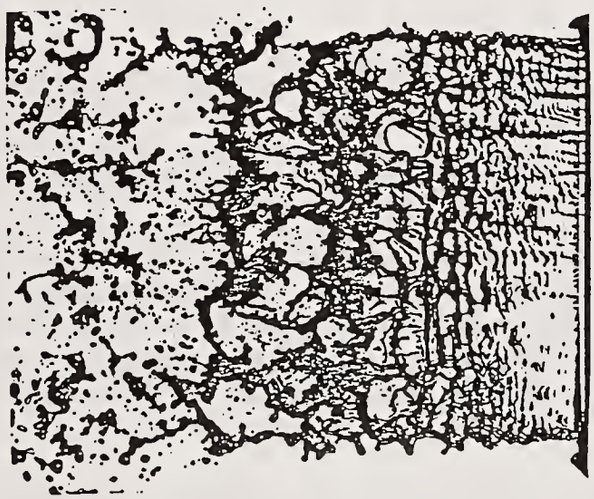

Fig.3 Small incoherent "cell" structures appear inside the larger coherent ones on the liquid sheet surface
(P_0 = 0.2 psig [102.704 kPa]; m_{liquid} = 45.42 g/s

Side views of the edge of the sheet are shown in Figs. 4 and 5. The growth in thickness of the sheet and the development of waves as the result of "flapping in the wind" are clearly seen. Wave amplitudes grow until critical conditions are reached where the liquid bursts into a shower of droplets. It appears as though some internal force exceeds the external restraining surface tension force resulting in a bursting explosion or eruption. The condition shown in Fig. 4 looks like a blown up balloon with almost the whole sheet stretched as a thin membrane, held by a larger diameter rim. A perforation is seen to form in the membrane resulting in bursting and formation of a shower of drops. The internal forces within the liquid are associated with shear and turbulence. If these forces can be shown to grow with distance from the nozzle, then this could provide an explanation for the conditions for bursting. In Fig. 5, both the liquid and the air flow rates have been increased. The initially full sinusoidal wave becomes distorted to yield two half waves that are very similar in form. The stretching of the half waves increases the free surface energy of the already distorted sheet. At the point where the two half waves are joined, localized high tensile forces pull the half waves in opposite directions and ultimately result in the thinning of the junction point. When the local thickness of the sheet falls below a critical value, perforations start to develop in the sheet which ultimately leads to separation of the half waves.

Fig. 4 Perforations which expand under the action of surface tension occur in the sheet
(Same experimental conditions as in Fig. 3)

Fig. 5 The distortion of a sinusoidal wave yields two half waves that are very similar in form
(P_0 = .2 psig [102.704 kPa]; m_{liquid} = 63.09 g/s)

These results show that when the sheet leaves the nozzle it is already perturbed by disturbances which were initiated within the nozzle. These perturbations appear as deformations of the liquid-air interface. Initial instabilities are driven by the high velocity air streams causing rapid growth of the waves. Disintegration occurs when the amplitude of these waves exceeds a critical value and half waves are torn off the sheet. The half waves break down into ligaments which in turn break down into drops.

Lines drawn along the crests of major perturbations describe the angle of spread of the perturbations which may be considered as the initial spray angle. Figure 6 shows the effect of increasing the liquid flow rate on spray angle for two different air supply pressures. The spray angle decreases progressively with increase in liquid flow rate. This can be explained by the reduction in specific energy of air per unit volume of liquid leaving the nozzle. Moreover, increasing the liquid flow rate results in decreased air/liquid relative velocities. This decrease in relative velocity reduces the amplitude of oscillations resulting in a corresponding decrease in spray angle.

Increasing the air velocity increases the specific energy of air per unit volume of liquid and this results in a substantial increase in the amplitude of oscillations of the liquid sheet. This is shown as an increase in spray angle with increase in air supply pressure, in Fig. 6. Intact length (axial length from nozzle exit to the location where liquid remains intact) increases with liquid sheet velocity and decreases with air velocity, as shown in Fig. 7. At higher air velocities, the influence of liquid sheet velocity on the intact length is less pronounced. The increase of intact length with liquid sheet velocity and its decrease with increase in air velocity are consistent with the variation of spray angle with these velocities. Higher liquid flow rates result in higher momentum for the liquid in the axial direction. The liquid remains intact over longer distances and the spray angle decreases as liquid flow rate, liquid velocity, and liquid momentum increase.

The spray is formed as a result of the breakup of the sheet. We have seen evidence that the final breakup has the appearance of an explosion producing a shower of droplets. We need to find the connection between the sheet that is in the final stages of breaking up and the subsequent formation of the spray.

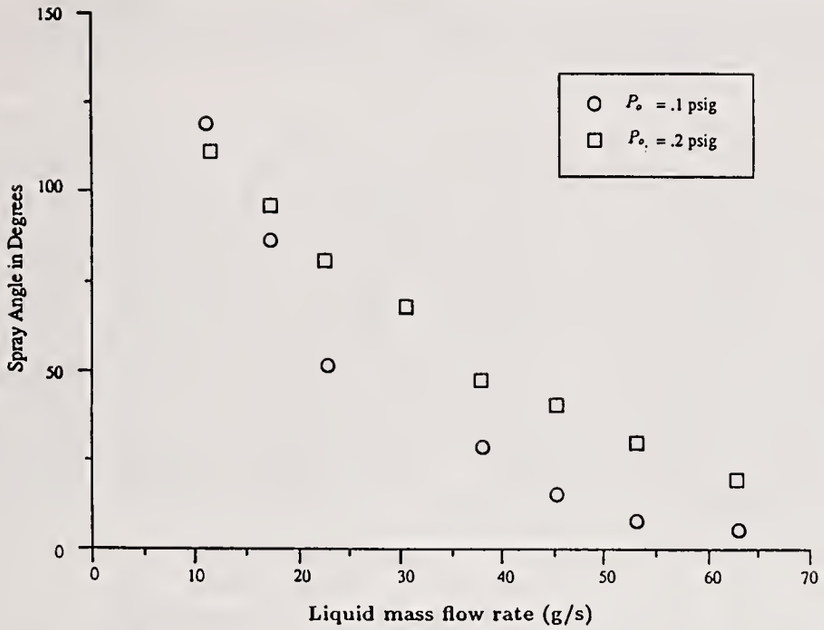

Fig. 6 Effect of air pressure and liquid flow rate on the spray angle (liquid sheet)

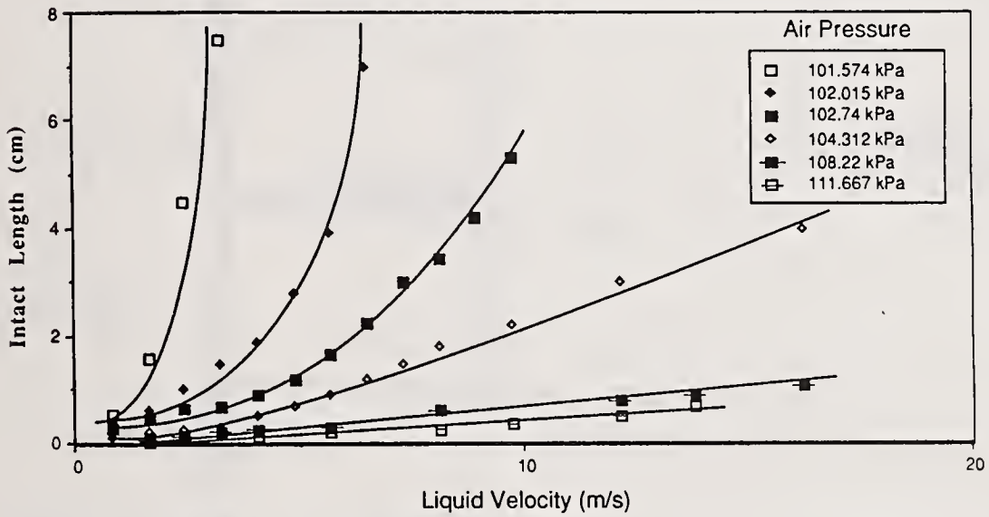

Fig. 7 Variation of liquid sheet intact length with liquid velocity for different air pressures

As soon as drops are released from the liquid sheet, they are accelerated by the air stream. The time taken for droplet velocities to reach equilibrium with the air stream depends on the drag/momentum ratio which in turn depends on the drop diameter and relative velocity between each drop and the local air velocity. Droplets are dispersed in the air flow according to their size class. Large drops subjected to shear will undergo secondary breakup while collisions of drops can lead to coalescence resulting in increase in drop size.

ROUND LIQUID JETS IN CO-AXIAL AIR STREAMS

For fundamental theoretical and experimental studies, the cylindrical liquid jet with a co-annular, co-axial, co-flowing air jet provides a base-line for determining the physics of atomization. Of particular interest is the comparison of the cylindrical jet with the flat sheet which, in theory, is a cylindrical jet with infinite diameter. We examine the generation of disturbances in the nozzle and the development of waves along the air/liquid interface. Transition from laminar to

turbulent flow occurs in the Reynolds number (based on nozzle exit conditions) range 6000 < Re < 10,000 when the inlet flow to the nozzle is uniform, oscillation free , and there is no vibration in the experimental system.

Axisymmetric Rayleigh breakup was studied for a series of horizontal liquid jets (with no air flow) with liquid velocity progressively increasing from 0.246 m/s to 18.2 m/s corresponding to an increase of Re_W from 240 to 17,650. The Ohnesorge number for this series was 0.0037. When the jet velocity was very low, less than 1 m/s, the horizontal liquid jet bends downwards under the influence of gravity. At higher liquid velocities, the jet has sufficient momentum to remain horizontal. The intact length increases progressively with increase in liquid velocity. Drop diameters are similar to those of the jet and do not change with increase in liquid velocity. Small satellite drops are formed. Introduction of a co-axial air stream is shown in Fig. 8. The air stream maintains the liquid jet horizontal except for the lowest velocity, $u_W = 0.246$ m/s. The liquid jets remain axisymmetric with a slight tendency, at higher velocities, to form a helix. The drops also tend to remain symmetric about the jet axis. Intact lengths increase with increase in liquid velocities. The length of undisturbed liquid decreases as the air velocity increases beyond 25 m/s.

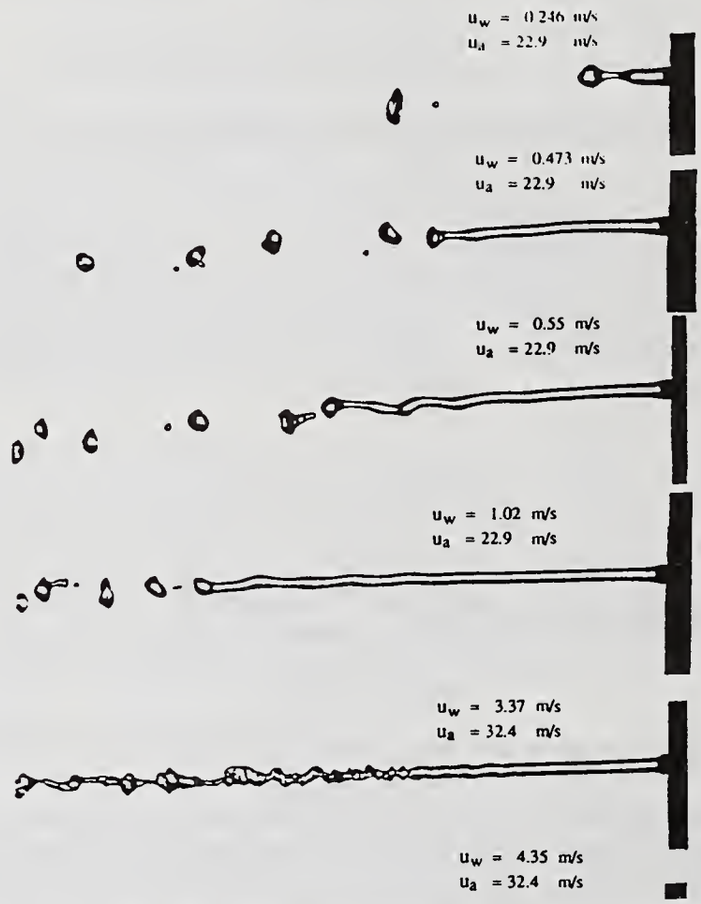

Fig. 8 Axisymmetric Rayleigh disintegration of water jet in a coaxial air stream (Jet Diameter = 1 mm)

For cases where the air velocity is one or two orders of magnitude greater than the liquid velocity, the liquid jet first accelerates rapidly in the high speed air stream with a resulting reduction in the liquid jet diameter. Organized structures in the turbulent air flow penetrate through the liquid jet. A series of photographs at short time intervals of a liquid jet with a velocity of 1.1 m/s and an annular air jet velocity of 45.8 m/s shows that the cylindrical liquid jet is distorted and stretched by the large eddy structures in the air stream to curl up in the shape of a "ladle". The liquid forms a membrane stretched between rims which provides a supporting frame. The stretched membrane

breaks up into a shower of small drops while the rims breakup into larger drops. Despite the very considerable differences in initial geometry, there is a remarkable similarity between the final breakup mechanism of 1) flat sheets 2) cylindrical jets and 3) large drops. The same phenomena can be detected even for cases of liquid velocity of 1.5 m/s and air velocity of 130 m/s.

Detailed photographs of the disintegration of cylindrical liquid jets are shown in Fig. 9 for a liquid velocity of 1.1 m/s and an air velocity of 45.8 m/s. The photographs show a time sequence of events. The cylindrical liquid jets are transformed into thin membranes which curl up to form semi-circular cups. These large scale deformations of the liquid jet are most probably caused by large eddy structures in the air. They cannot be due to instability growth in the liquid. Once the deformation has taken place, the aerodynamic pressure forces change in the shape, very similar to the "bagging" phenomenon of breakup of large drops. Impingement of air on the concave upstream surfaces and wake effects on the downstream surface accelerate the stretching of the membrane and the breakup into drops. The sheets set up a flapping motion. Detailed measurements of size distributions in the sprays show direct connections between the thick rims which form large drops and the thin membranes which form small droplets. Under the influence of surface tension forces, thick rims are formed at the edges of the membranes. The thickness of these rims is larger than the thickness of the membrane but is significantly smaller than the initial diameter of the liquid jet. The largest drops formed have the same diameter as the rim thickness while the smallest drops have the same diameters as the membrane thickness. Final breakup appears to be by the Rayleigh mechanism and can be classified as non-axisymmetric Rayleigh

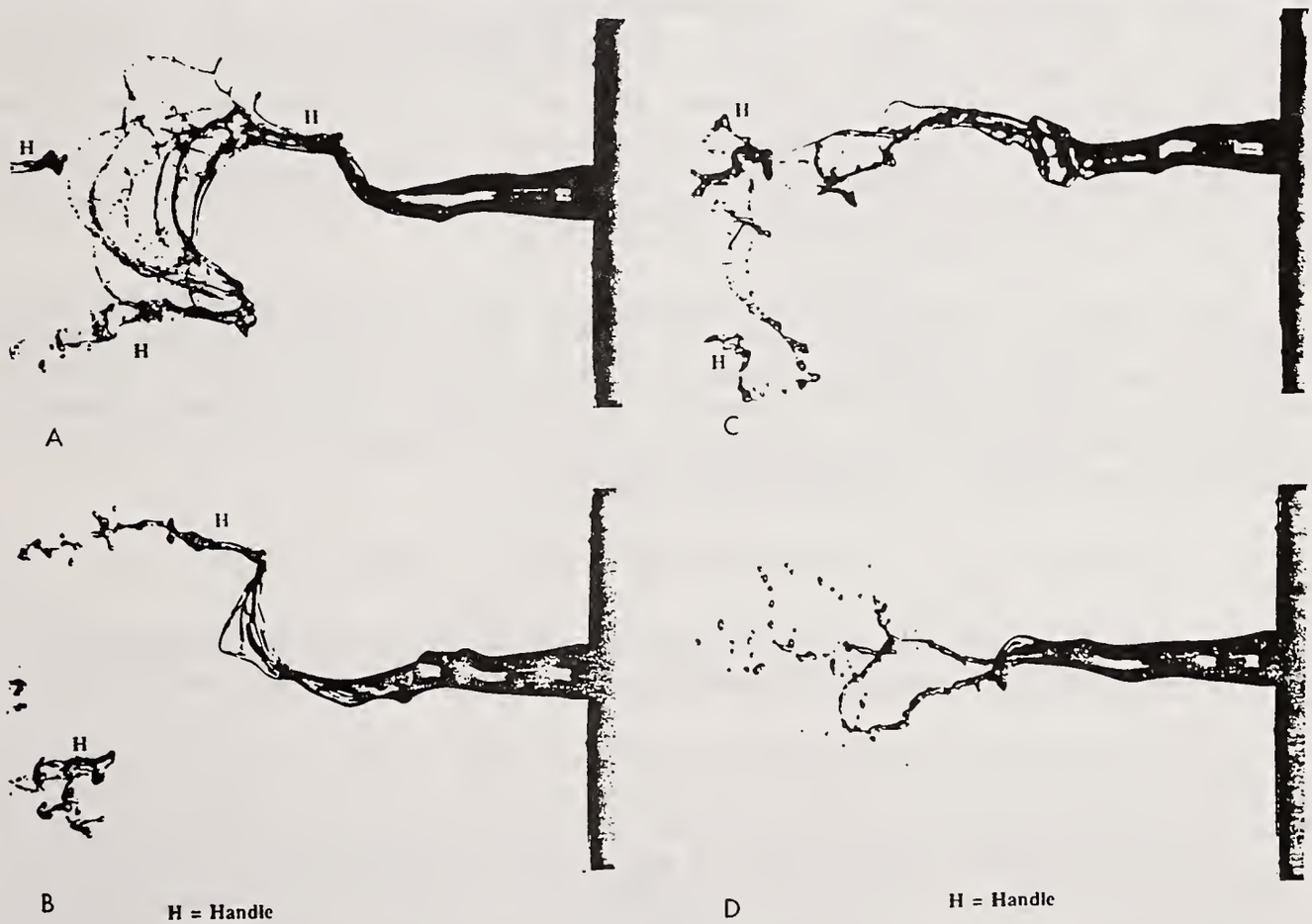

Fig. 9 Disintegration of coaxial liquid jets
(P_w = 0.7 psig [4.826 kPa]; p_{air} = 0.0433 psig [1.493 kPa])

breakup. This membrane type of disintegration of round jets is very similar to that of thin liquid sheets as described by Dombrowski. It is also very similar to the disintegration of spherical liquid drops in an air stream as reported by Lane, Wolfe, and Kennedy.

It is quite remarkable that despite the important differences in geometry between cylindrical jets, thin sheets and large spherical drops, in each case thin membranes are formed with surrounding rims leading to the formation of large and small drops. In each case, it is the penetration of large eddy structures from the turbulent air flow that distorts the liquid and stretches it into thin membranes. The thin membranes and the spray of drops provide a visualization of the organized large structures in the air.

Under conditions of high liquid velocity and high air velocity, the liquid jets maintain their symmetry about the jet axis. The liquid core remains intact while fibers are formed on the liquid surface. These fibers point in the direction of higher velocity. The diameter of the fibers is several orders of magnitude smaller than the diameter of the liquid jet. The fibers break into drops according to the Rayleigh mechanism. Disturbances develop in the liquid core which lead to breakup with the formation of ligaments with lengths of the order of 5 times the initial jet diameter. Fibers are formed on the ligaments which peel off and then break into drops. This process leads to the formation of a train of clusters of drops. When the momentum of the liquid flow is high enough, penetration by the large organized structures of the air flow is prevented.

For high speed annular air jets with a velocity of 183 m/s and liquid jets of 1 m/s, the liquid jet is broken up into very fine droplets within the short distance of two jet diameters. As the liquid velocity is increased, the liquid core is extended and the number density of drops increases because of the increased mass flow rate of liquid. Bursts of liquid can be clearly identified. The size of the bursts and the liquid concentration inside each burst increases as liquid flow rate is increased. The high speed annular air jet confines the spray so that it remains symmetric about the jet axis. These jets have been classified as super-pulsating. Organized structures from the air flow enter the liquid flow but do not penetrate fully in the case of high liquid flow rate.

Intact length (L) is a measure of the axial distance from the nozzle exit to liquid breakup on the liquid jet axis. Figure 10 shows the variation of L/d with Weber and Reynolds numbers based on nozzle exit conditions. The reduction in intact length with increase in Weber number is ascribed to the increase in relative velocity. The increase in intact length with increase in Reynolds number is due to the increased liquid velocity and flow rate which, in this Reynolds number range, increases the length of the liquid jet. The derived empirical equation is:

$$L/d = 0.5\ We_R^{-0.4}\ Re_\ell^{0.6} \qquad (1)$$

The variation of intact length with Reynolds number was found to be the same for both flat sheets and round jets. The subscripts R refer to relative velocity, ℓ to liquid and a to air.

The modes of liquid jet disintegration are shown in Fig. 11 where each jet is plotted as a function of liquid Reynolds number and aerodynamic Weber number. Each jet is classified according to its photographic appearance. For $Re_\ell = 10^3$, as We_a is progressively increased, it can be seen that up to $We_a = 8$ disintegration is of the axisymmetric Rayleigh type. At $We_a = 17$, the disintegration is of the non-axisymmetric Rayleigh type. By $We_a = 33$ the membrane type region is reached and by $We_a = 130$ fiber type disintegration is found. The particular type of disintegration can be found easily from Fig. 11 with knowledge of Re_ℓ and We_a.

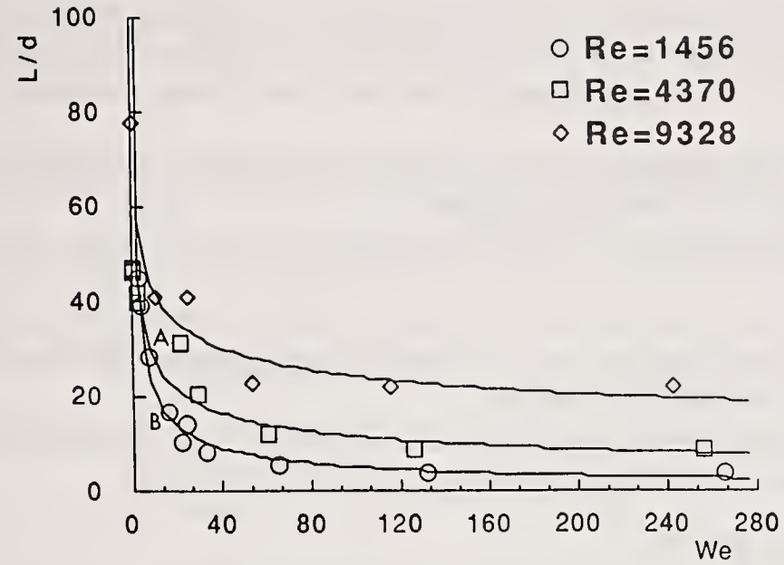

Fig. 10 Average jet liquid intact length in coaxial gas flow (Re = 1456, 4370, 9328)

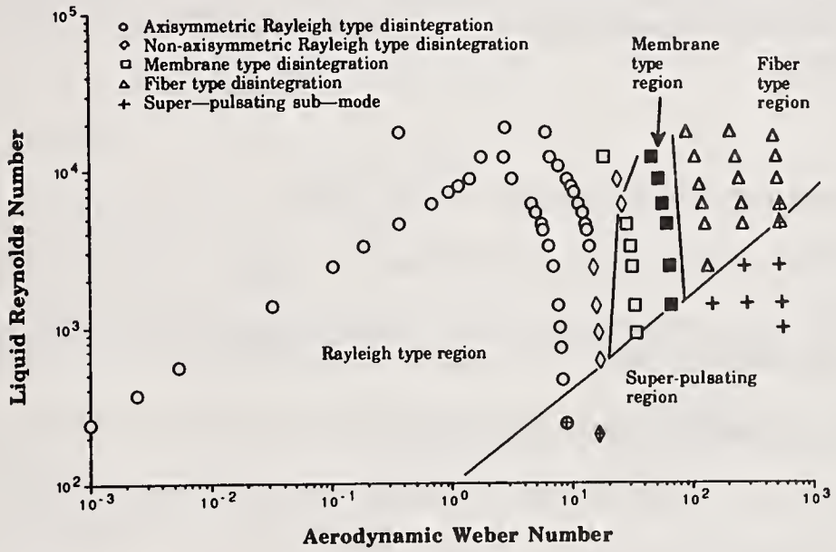

Fig. 11 General classification of liquid jet breakup in coaxial air streams

New information on frequency, wave length and wave amplitude measured along the lingth of liquid jets and sheets for a wide range of liquid and gas velocities is reported by Eroglu and Chigier, 1991.

CONCLUSIONS

- Close similarities are found between the breakup of 1) liquid sheets 2) round jets and 3) large droplets under the influence of air streams.
- Cylindrical jets and flat sheets curl up to form "ladle" shapes.
- Ordered cell structures form in liquid sheets with thin membranes stretched between thick rims.
- Large drops measured in the spray are formed from thick rims while small drops are formed from thin membranes in the sheet.

- Disturbances generated within the nozzle grow in amplitude along the liquid surface.
- Airflow causes small disturbances to grow into major disturbances that lead to disruption.
- When the thickness of the liquid sheet falls below a critical value, perforations start to appear in the sheet.
- Disintegration of the liquid sheet occurs when the amplitude of waves exceeds a critical value and half waves are torn off the disturbed sheet.
- Increasing the liquid flow rate causes decreases in the spray angle while the air flow is maintained constant.
- Increasing the air velocity causes the spray angle to increase for a fixed liquid flow rate.
- The initial mean velocity distribution in the liquid jet determines the character of the surface wave formation at the liquid/air interface.
- A new equation is derived for intact length as a function of Reynolds and Weber numbers.
- A new classification of modes of disintegration has been presented.

ACKNOWLEDGEMENTS

The principal ideas contained in this paper have evolved over a number of years of intensive research at Carnegie Mellon University. I wish to particularly thank Hasan Eroglu, Zoltan Farago, Adel Mansour and all other members of my research team who have made important contributions. I wish to acknowledge the financial support of NASA Marshall Space Flight Center and Parker Hannifin Corporation.

REFERENCES

Bergwerk, W., Proc. Inst. Mech. Engrs., 173, 655, 1959.

Buschulte, W., ISABE, 9th Int. Symp. of Air Breathing Engines, Athens, 1989.

Cheremisinoff, N.P. (Ed.), "Gas Liquid Flows", Encyclopedia of Fluid Mechanics, Vol. 3, Gulf Publ. Co., Houston, TX, 1986.

Chigier, N., Energy, Combustion and Environment, McGraw Hill, 1981.

Chuech, S., Przekwas, A., Yang, H., and Gross, K., AIAA, 90-2060, 1990.

De Juhasz, K.J., ASME Trans., Vol. 53, OGP-53-5, 1931.

Dombrowski, N. and Fraser, R.P., Philos. Trans. R. Soc. London Ser. A., Math. Phys. Sci., Vol. 247, No. 924, pp. 101-130, 1954.

Dombrowski, N., Hasson, D. and Ward, D. E., Chem. Eng. Sci., Vol. 12, pp. 35, 1960.

Eroglu, H. and Chigier, N., ASME Journal of Fluids Engineering, 1991.

Eroglu, H. and Chigier, N., Atomization and Sprays, 1991.

Eroglu. H. and Chigier, N., "Liquid Sheet Instability in a Coflowing Air Stream", Proceedings of ICLASS 91, NIST, Gaithersburg, MD, July 1991.

Eroglu, H. and Chigier, N., "Wave Characteristics of Liquid Sheets in Cocurrent Air Flow", Atomization and Sprays, Vol. 2, 1992.

Eroglu, H., Chigier, N. and Farago, Z., Physics of Fluids A , Vol. 3, No. 2, pp. 303-308, 1991.

Farago, Z. and Chigier, N., ASME Paper No. 90-GT-81, 1990.

Farago, Z. and Chigier, N., ILASS-Americas 4th Annual Conference, pp. 122-126, Hartford, CT, May 1990; ILASS-Europe 6th Annual Conference, Pisa, Italy, July 1990.

Giffen, E. Muraszew, A., The Atomization of Liquid Fuels, John Wiley & Sons, New York, 1953.

Hagerty, W. and Shea, J. F., J. Appl. Mech., Vol. 22, No. 4, pp. 509-514, 1955.

Kennedy, J.B., Roberts, J., ILASS-Americas, 4th Annual Conference, Hartford, CT, May 1990.

Krulle, G., Mayer, W., and Schley, C.A., AIAA 90-1959, 1990.

Lin, S.P. and Woods, D.R., "Induced Atomization", ICLASS-91.

Mansour, A. and Chigier, N., Physics of Fluids A, 1991.

Mansour, A. and Chigier, N., Physics of Fluids A, Vol. 2, No. 5, pp. 706-719, 1990.

Miesse, C.C., Ind. Eng. Chem., Vol. 49, No. 9, 1955.

Ohnesorge, W.V., A.V.D.I., Vol. 81, No. 16, 1937.

Ranz, W.E., Can. J. Chem. Eng., 36, 175 1958.

Rayleigh, Lord, Proc. Roy. Soc., 1878.

Reitz, R.D. and Bracco, F.V., Phys. Fluids, Vol. 25, No. 2, pp. 1730-1741, 1982.

Reitz, R.D., "Atomization and Other Breakup Regimes of a Liquid Jet", Ph.D. Thesis, Princeton University, 1978.

Rupe, T.H., JPL Tech Report n. 32, 207, 1962.

Sattelmayer, T. and Wittig, S., ASME 86-GT-150, 1986.

Scheubel, F.N., NACA Tech. Memo No. 644, 1931.

Schweitzer, P.H., J. Appl. Physics, Vol. 8, 1937.

Squire, H.B., Brit. J. Appl. Phys., pp. 167-169, 1953.

Weber, C., AZMIM, Vol. 11, 1931.

Keynote Lecture

EXPERIMENTAL AND THEORETICAL STUDIES ON THE STRUCTURE OF FUEL SPRAYS IN DIESEL ENGINES

H. Hiroyasu

Department of Mechanical Engineering
University of Hiroshima
Hiroshima, Japan

ABSTRACT

The combustion process in a diesel engine is very complex, and its detailed mechanisms are not well understood. The study of diesel engine emissions and fuel economy requires a basic understanding of the processes of mixture formation, because the diesel combustion is strongly controlled by a fuel spray injected into the combustion chamber.

This paper reviews the experimental results and the spray formation modeling of the diesel fuel sprays. The experimental results for break-up length, spray angle, spray tip penetration and drop size distribution of the diesel sprays are introduced to discuss the internal structure of the spray. A review is also made of the potentials of specific models for atomization of the spray-jet.

INTRODUCTION

The high thermal efficiency on the diesel engine, especially the direct injection diesel engine, is mainly caused by the relatively high compression ratio, the lower pumping loss as a result of the absence of the throttle valve and overall lean mixture required to achieve an efficient heterogeneous combustion process. However, diesel combustion processes are very complex and their detailed mechanisms are not well understood.

The primary factor which controls the diesel combustion is the mixture formation as shown in Fig. 1. The mixture formation is controlled by the characteristics of the injection system, the nature of air swirl and turbulence in the cylinder, and spray characterization.

Combustion in a direct injection diesel engine is closely related to the transient injection of a fuel spray into air at high pressure and temperature. The air-fuel mixing processes, including atomization and vaporization, at the edges of the spray are followed by the ignition of these regions and progressive diffusive burning of the remainder of the spray. Therefore, accurate descriptions of the behavior of atomizing and vaporizing fuel in the spray are important for any kind of models to comprehend and describe the processes of air-fuel mixing and subsequent combustion.

The fuel injected from the nozzle into the combustion chamber of the diesel engine disintegrates into numerous drops of different sizes and concentrations in the spray. Figure 2 shows the main parameters the express the aspect of a diesel spray. The motion of the spray tip and break-up length give clues as to the understanding of the disintegrating process of a fuel jet. Spray angle and drop sizes distribution are the results of this disintegrating process. These four paramcters of the spray are related to each other in the disintegrating process and affect the mixture formation through acrodynamic and thermodynamic processes in the combustion chamber of the diesel engine.

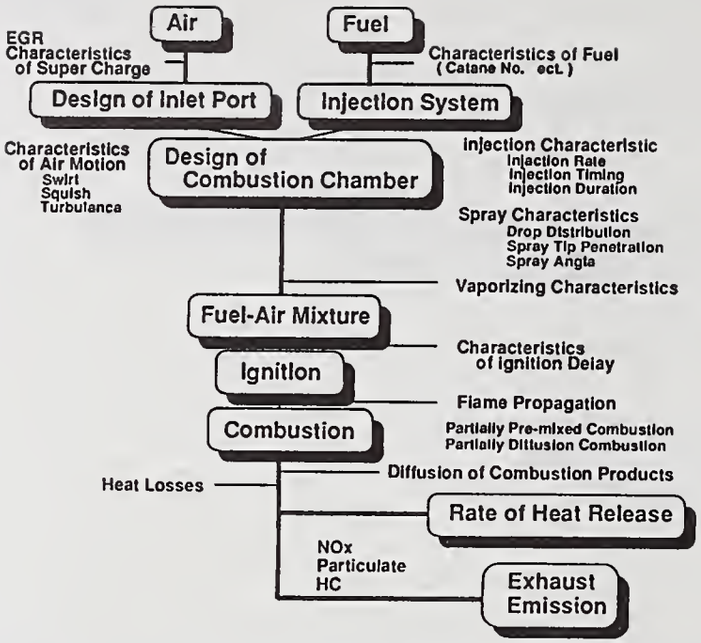

Fig. 1 Block diagram of diesel combustion

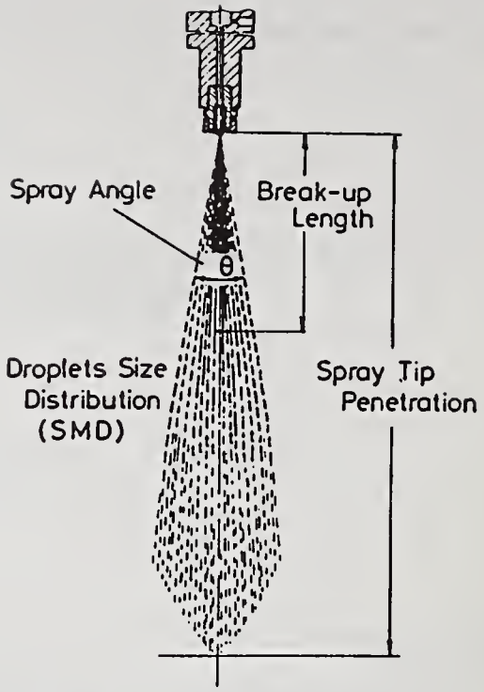

Fig. 2 Parameters of a spray

EXPERIMENTAL STUDIES

Break-up Length

The injected liquid does not break-up instantly after injection. There is some unbroken portion which is referred to as the liquid break-up length. Break-up lengths average between 10 to 30 mm and appear to be present for injection velocities above 200 m/s.

In a high speed small direct injection diesel engine of a light duty vehicle, break-up length of the fuel spray and the distance from the nozzle to the combustion chamber wall are almost the same. Thus, the break-up length may have a great effect on the spatial distribution of the liquid fuel and the formation of the fuel-air mixture in that small engine.

Extensive experimental studies on the break-up phenomena of low velocity jets have been carried out [1-3]. Figure 3 shows break-up length which describes the continuous portion of the liquid column or unbroken length as a function of the jet velocity. In this paper, the main interest is in the spray region. Break-up length of the spray region was measured by electric resistance between the nozzle and a fine wire net detector located in a spray jet [4-6].

Figure 4 shows the effect of injection velocity on break-up length at various ambient pressures. Increasing ambient pressure from 0.1 MPa to 3.0 MPa, the break-up length decreases. From 20 to 60 m/s of injection velocity, the injection liquid column is disintegrated by the micro-turbulence of the liquid surface and is called wavy flow [7]. In this region, break-up length increases with an increase in injection velocity. When injection velocity is further increased, the wavy flow is not observed and break-up length decreases. This region is called a spray. Further increasing injection velocity, the break-up length reaches an almost constant value.

There is an apparent difference between the spray of which break-up length has decreasing tendency with an increase of the injection velocity and one of which break-up length is hardly changed by the further increase of the velocity. Categorizing sprays by their break-up length and related atomization, they are divided into two regions; incomplete and complete sprays[8]. In the incomplete spray region, the liquid jet was ejected from the nozzle to form a spray through a relatively slow disintegrating process. In other words, the process of transformation from liquid column to drops had to be developed along the liquid jet and fine drops were only made at a distance far from the nozzle exit. As injection velocity increased further, the disintegrating process from a

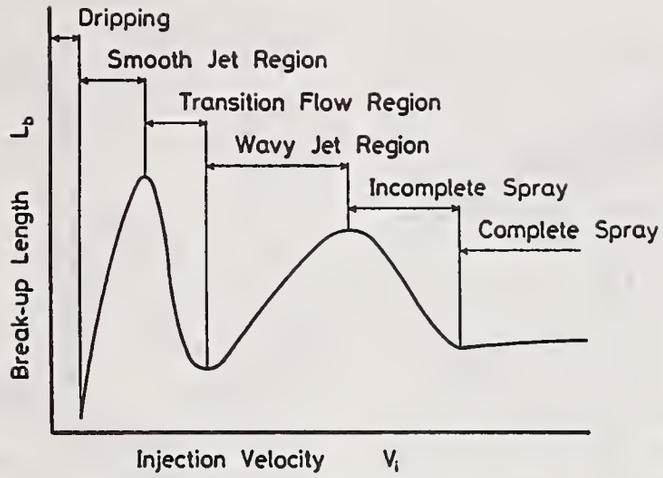

Fig. 3 Break-up behavior of a liquid jet

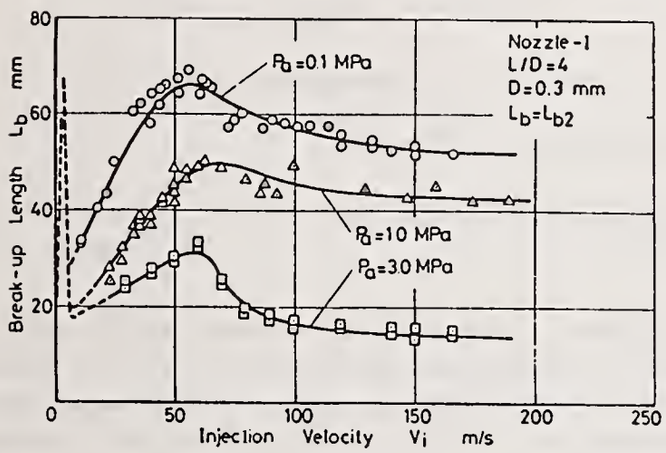

Fig. 4 Break-up length vs. injection velocity

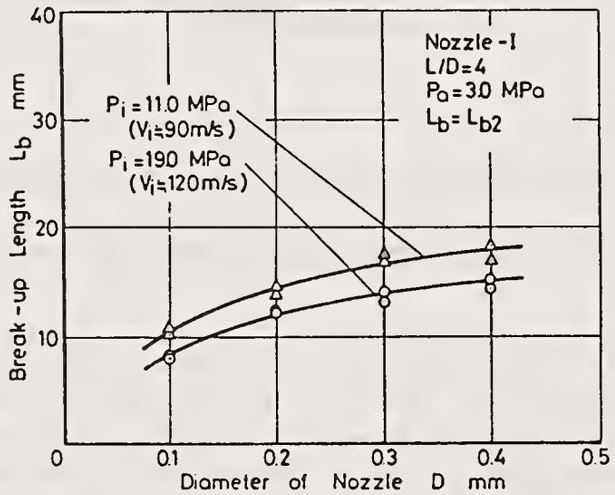

Fig. 5 The effect of nozzle diameter on break-up length

liquid column to a fine spray appeared as soon as the liquid was injected. This region is called the complete spray that is corresponded to a diesel spray. Spray as the general meaning, covers both the region mentioned above.

The effect of nozzle diameter on break-up length in a complete spray region is shown in Fig.5. Break-up length in this region increases with an increase in the diameter of the nozzle. Break-up length is also affected by the dimensionless length of a nozzle, that is, the ratio of the length L to the diameter D of the nozzle hole, L/D. The following expression was derived for break-up length from experimental data which covered a wide range of conditions.

$$L_b = 7.0\ D\ \left(1 + 0.4\ \frac{r}{D}\right)\left(\frac{P_a}{\rho_l V_i^2}\right)^{0.05}\left(\frac{L}{D}\right)^{0.13}\left(\frac{\rho_l}{\rho_a}\right)^{0.5} \qquad (1)$$

This expression is valid for any complete spray region.

Spray Angle

Many photographs of spray were taken to measure the spray angle. Figure 6 shows the effect of injection pressure on the spray angle. The spray angle increases with an increase in injection velocity, takes the maximum value and reaches an almost constant value in a complete spray region. The experical equation for the

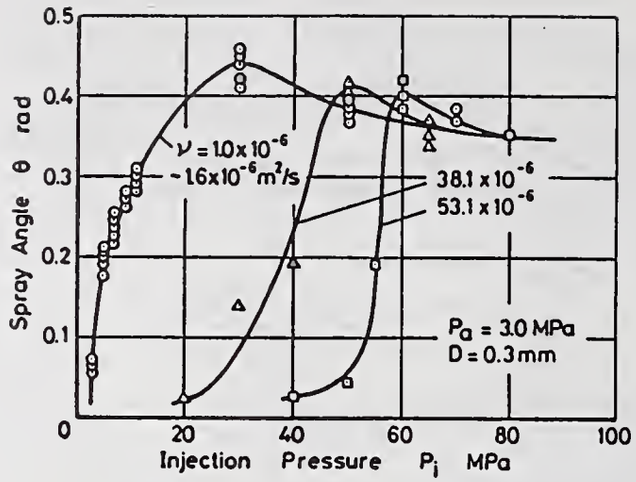

Fig. 6 The effect of injection pressure on the spray angle

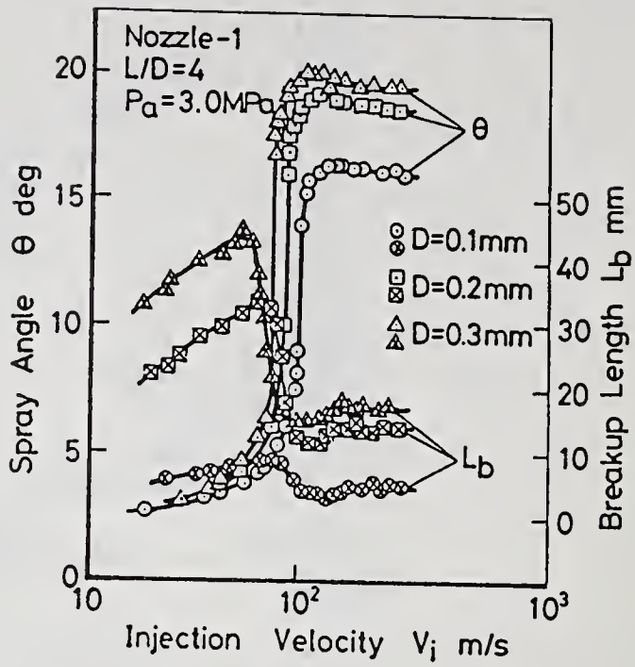

Fig. 7 The spray angle and break-up length

spray angle when this angle reaches the constant value is expressed by the following:

$$\theta = 83.5 \left(\frac{L}{D} \right)^{-0.22} \left(\frac{D}{D_0} \right)^{0.15} \left(\frac{\rho_a}{\rho_l} \right)^{0.26} \quad (2)$$

Figure 7 shows spray angle and the break-up length versus injection velocity for several different nozzle hole diameters. This figure is very important to discuss the internal structure of the spray. When the liquid was injected with the speed less than 70 m/s, the break-up length was not shortened and only a narrow spray angle appeared even if the ambient pressure was elevated up to 3 MPa. However, the liquid injected with the speed of over 100 m/s, was disintegrated quickly to form a complete spray. As the result of it, the break-up length was shortened and the wide spray angle was achieved.

The region where the injection velocity ranged from 70 to 100 m/s, corresponded to an incomplete spray. The maximum spray angle appeared at the injection velocity where the feature of a spray shifted from an incomplete spray type to a complete one. In Figure 6, the injection pressure where the maximum spray angle occurs increases with an increase in the liquid kinematic viscosity; this indicates that the transition velocity also increases with the viscosity. However, Figure 7 suggests that the transition velocity is almost independent of the nozzle hole diameter.

Spray Tip Penetration

The speed and extent to which the fuel spray penetrates in the combustion chamber has an important influence on air utilization and fuel-air mixing rate. So, spray tip penetration of the intermittent diesel spray was measured with the aid of photographic techniques at various ambient temperature, ambient pressures, injection pressures and injection durations.

Figure 8 shows the effect of injection pressure on spray tip penetration under constant ambient pressure and injection duration[9]. The logarithmic penetration on the ordinate is correlated with the logarithmic time from the injection start on the abscissa. This figure shows the linear relationship with two different slopes between logarithmic expressions of penetration and time. At the early stage of the spray, the slope is 1, but after a short period, the slope changes to 0.5. This result shows that the spray velocity at the initiation of the injection is constant and then the spray develops into a steady jet. The spray tip penetration decreases with an increase in ambient gas pressure. The time at the intersection of the two lines decreases with an increase in injection pressure.

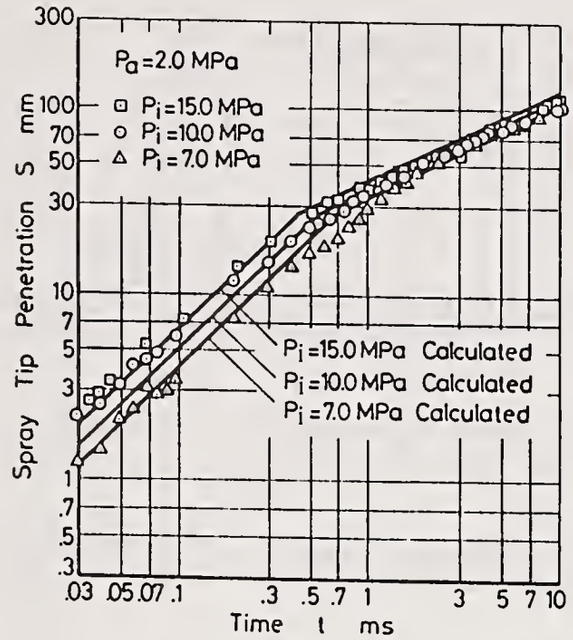

Fig. 8 Spray tip penetration at various injection pressures

The following expressions for the spray tip penetration are derived from the data obtained during our investigation[10].

$0 < t < t_b$

$$S = 0.39 \left(\frac{2\Delta P}{\rho_l} \right)^{0.5} t \qquad (3)$$

$t > t_b$

$$S = 2.95 \left(\frac{\Delta P}{\rho_a} \right)^{0.25} (D \cdot t)^{0.5} \qquad (4)$$

$$t_b = 28.65 \frac{\rho_l \cdot D}{(\rho_a \Delta P)^{0.5}} \qquad (5)$$

Results calculated from these equations are also expressed by the solid lines in Figs. 8.

Drop Size Distribution

The various methods employed in drop size measurement may be grouped conveniently into two broad categories; mechanical and optical. The second category includes optical systems that have been developed in recent years and are finding an increasing range of applications. In mechanical method, there are liquid immersion sampling technique[11], molten-wax method[12] and frozen-drop technique[13]. In optical method, there are several techniques that have been applied to drop sizing in diesel fuel sprays; photography and holography imaging technique[14], line-of-sight extinction technique[15], Fraunhofer diffraction technique[16, 17], and the phase Doppler technique[18]. The effects of ambient pressure and injection pressure were measured using a diesel nozzle with a diameter of 0.3 mm, as shown in Fig. 9 by using Fraunhofer diffraction method.

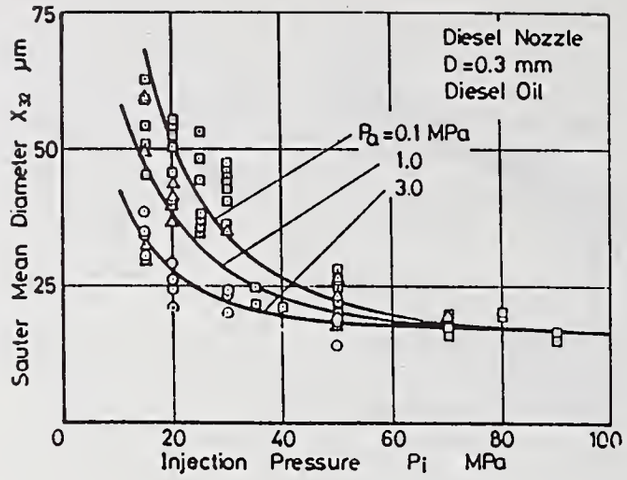

Fig. 9 The effect of ambient pressure and injection pressure on the Sauter mean diameter

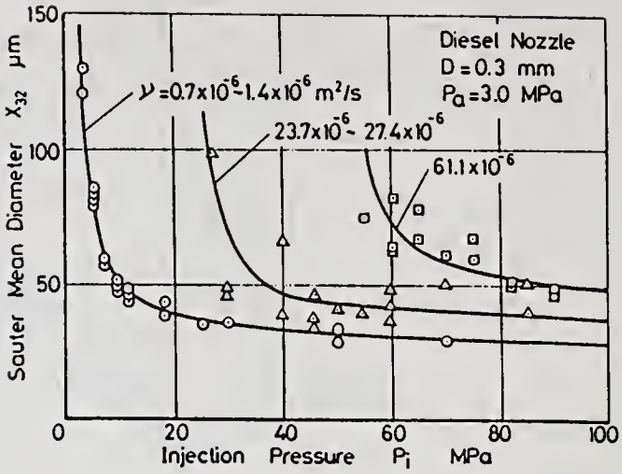

Fig. 10 The effect of viscosity and injection pressure on the Sauter mean diameter

The effect of liquid viscosity on the Sauter mean diameter was measured using glycerin-water solutions of various kinematic viscosity. Figure 10 shows the measured results of the relationships between the solution's viscosity and the Sauter mean diameter [17]. Increasing injection pressure, the Sauter mean diameter decreases, but there is still some difference in the Sauter mean diameter according to the viscosity of the fuel. When the viscosity of the fuel is over a certain value, the Sauter mean diameter increases rapidly.

Dimensionless analysis was conducted based on the above measurement results, leading to the following experimental equations for the Sauter mean diameter[19].

$$\overline{X_{32}} = \mathrm{MAX}\left[\frac{\overline{X_{32}}^{LS}}{D}, \frac{\overline{X_{32}}^{HS}}{D}\right] \tag{6}$$

$$\frac{\overline{X_{32}}^{LS}}{D} = 4.12\,\mathrm{Re}^{0.12}\cdot\mathrm{We}^{-0.75}\cdot\left(\frac{\mu_l}{\mu_a}\right)^{0.54}\cdot\left(\frac{\rho_l}{\rho_a}\right)^{0.18} \tag{6-a}$$

$$\frac{\overline{X_{32}}^{HS}}{D} = 0.38\,\mathrm{Re}^{0.25}\cdot\mathrm{We}^{-0.32}\cdot\left(\frac{\mu_l}{\mu_a}\right)^{0.37}\cdot\left(\frac{\rho_l}{\rho_a}\right)^{-0.47} \tag{6-b}$$

where MAX [ ] denote the lager value of the two.

Equation (6-a) is the Sauter mean diameter for an incomplete spray with low injection velocity, and Eq. (6-b) for a complete spray.

Incomplete and Complete Sprays

Overall feature of the break-up length, spray angle and mean diameter are summarized into Fig. 11. The break-up mechanism of a complete spray is different from that of an incomplete spray. Then, the empirical equation of the Sauter mean diameter for a complete spray is expressed by the different form from that for an incomplete spray as mentioned before. The maximum spray angle was obtained at the transition velocity from incomplete spray to complete one.

Further observation of the internal flow in the nozzle shows the cavitation area expanded to the exit of the nozzle when the liquid jet was injected at the transition velocity. The highly turbulent internal flow due to the cavitation caused the wide spray angle and sometimes forced to shorten the break-up length as shown in Fig. 7.

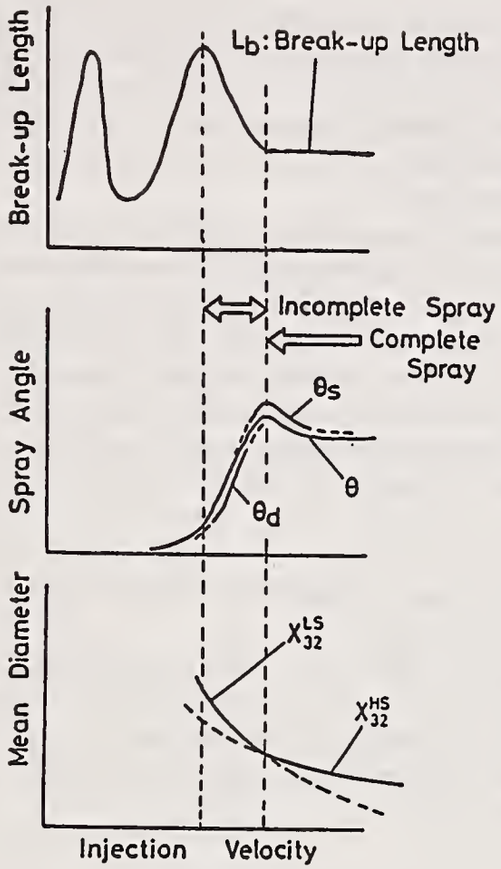

Fig. 11 Behavior of diesel spray

NUMERICAL MODELS

Multidimensional models of diesel engine combustion account for the temporal and spatial variations of the flow field, temperature, composition, pressure, and turbulence within the combustion chamber. Most of the multidimensional models that have appeared in the literature are based on the following spray equation [20], which depend on time and on the radius, velocity, and temperature of the drops and may account for thick spray effects [drop collisions, coalescence, and volumetric displacement of the gas phase] and for drop breakup. A statistical description of the spray may be given by the distribution function [or density function]

$$f_j (r, x, v, t) \, dr \, dx \, dv \tag{7}$$

which is the probable number of particles of chemical composition j in the radius range dr about r located in the spatial range dx about x with velocities in the range dv about v at time t. The spray equation can be written as

$$\frac{\partial f_j}{\partial t} = -\frac{\partial}{\partial t} (R_j \cdot f_j) - \nabla_x \cdot (V \cdot f_j) - \nabla_v (F_j \cdot f_j) + Q_j + \Gamma_j \tag{8}$$

where v, F, R, and T denote the velocity, force, rate of change of the radius, and temperature of the drops, respectively. Q represents the rate of increase of f due to nucleation or liquid breakup, and Γ will represent the rate of change of f caused by collisions and coalescence.

Main approach which has been used to analyze the flow field in diesel engines is Lagrangian-Eulerian formulations, where Lagrangian equations are employed for groups of drops and Eulerian equations are employed for the gas phase. Lagrangian-Eulerian formulations can also account for thick spray effects such as drop collision, coalescence, and breakup.

The conservation laws for the gas, mass, momentum, internal energy and the scalar variables that characterize turbulence (k and ε) are expressed in the form of time-dependent, partial differential equations. These equations were solved subjected to appropriate initial and boundary conditions using an explicit numerical method. For computational efficiency, stochastic parcel injection was used for the spray drops. In this technique each computational parcel represents a group of drops with similar physical attributes and the attributes are assigned using a Monte Carlo sampling method.

The spray equation is coupled with statistically averaged gas phase equations of mass, momentum, and energy. However, there are many difficulties in treatments of the spray initial and boundary conditions.

One of the main difficulties in spray modeling has been the specification of drop size at the nozzle, since the atomization process is not resolved in the computations and it is not understood. Experiments are difficult since the spray near the nozzle is optically dense and drop size cannot be measured, except near the spray edge. For this reason, most measurements have been confined to locations far downstream of the nozzle.

Some model may account for thick spray effect, that is, drop collisions, coalescence and volumetric displacement of the gas phase and far drop breakup, but some model did not account for thick spray effects.

Thin spray Models

In thin or dilute spray models volumetric displacement effects can be neglected and the interactions between individual drops can be disregarded or highly simplified.

Nguyen et al. [21] used a thin spray approximation, that is, volumetric displacement effects on the gas phase equation were neglected, and also drop collisions and coalescence were neglected. The numerical calculations were compared with the experimental data of Hiroyasu and Kadota [22], and good agreement was obtained. Figure 12 shows a comparison between the predicted and measured penetration of sprays injected into stagnant combustion chambers at different pressures.

Thick Spray Models

Thick or dense spray models that account for volumetric displacement effects seem to have originated with Dukowicz's work [23], where a Lagrangian-Eulerian formulation was used to compute the behavior of atomized, non-evaporating liquid sprays injected into a gaseous environment. He accounted for volumetric displacement effects but did not consider drop collisions, coalescence and breakup, and obtained good agreement with the experimental date of Hiroyasu and Kadota [22] for a variety of ambient conditions. This agreement seems to have been obtained by employing small drops at the nozzle exit.

Cloutman et al.[24] and Butler et al.[25] used the stochastic model proposed by Dukowicz [23], law of the wall to account for the turbulent boundary layers and heat transfer to walls, and a mean-reaction-rate model in DI diesel engines. The calculation were performed with the CONCHAS-SPRAY code[26].

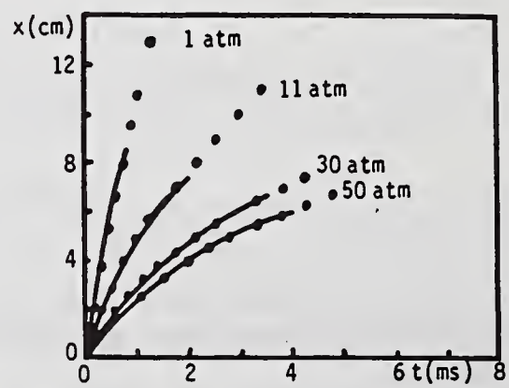

Fig. 12 Comparison between predicted (solid line) and measurement (symbols) spray tip penetration at several chamber pressure[21]

Amsden et al.[27] developed the KIVA code to analyze two- and three dimensional flows in DI engines. The KIVA code uses an ALE (an arbitrary Lagrangian-Eulerian) formulation, a subgrid- scale model and a mean-reaction-rate model.

O'Rourke and Amsden[28] analyzed the spray penetration, vaporization, mixing and combustion in the UPS-292 stratified charge engine with the KIVA code and showed that combustion occurs in the wake of the spark plug.

Takenaka et al.[29] performed three-dimensional calculation in a DI diesel engine with modified KIVA code. They calculated the gas flow, spray pattern, air-fuel mixing process for the heavy duty DI diesel engine. The results of computation were compared with the experimental data of pressure, flame temperature and mass change of chemical species in cylinder [30] and good agreement was obtained.

In 1987, KIVA-II computer program was reported by Amsden et al.[31]. KIVA-II code improves the earlier version in the accuracy and efficiency of the computational procedure, the accuracy of the physics submodels, and in versatility and ease of use. This model also includes a two-equation (k- ε) model of turbulence, a stochastic spray model, an implicit-continuous Eulerian (ICE) method with conjugate residual iteration, a quasi-second-order-accurate convection scheme, and several other improvements over the original KIVA code.

Figure 13 shows a comparison between the predicted and measured pressure diagram in the UPS-292 stratified charge engine and indicate that the KIVA-II code accurately predicts the cylinder pressure if the correct compression ratio is used in the calculation.

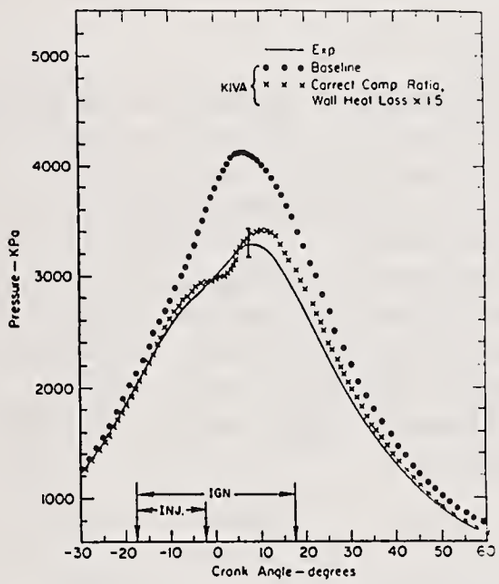

Fig. 13 Measured and predicted pressure diagrams in stratified charge engine[31]

Small Drop Models

Bracco's group of Princeton University were used very small drops in initial drop distribution near the nozzle exit. Kuo and Bracco[32] and O'Rourke and Bracco[33] used the thick spray model to calculate transient axisymmetric non-evaporating spray, asses the importance of drop collisions and coalescence, and compute the spray tip penetration and drop size distribution in spray injected into high pressure chambers. O'Rourke and Bracco [33] used the correlations proposed by Reitz and Bracco[34] for the spray cone angle and initial mean drop size, that is, initial drop size is average radius is about 3 μm. Figure 14 shows the computed and experimentally measured drop volume distributions. The computed penetration versus time curves are plotted in Fig. 15, along with the experimentally measured curve. These curves show the expected trend that as the drop size is increased, spray tip penetration is enhanced because the larger drops exchange their momentum with the gas more slowly. The penetration is somewhat insensitive to change in the initial drop size, however, and only the case with initial Sauter mean drops of 21 μm diverges markedly from the experimental curve.

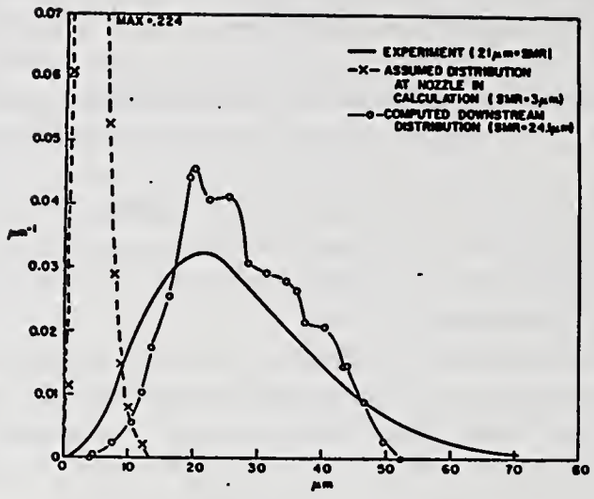

Fig. 14 Measured and predicted drop volume distributions[33]

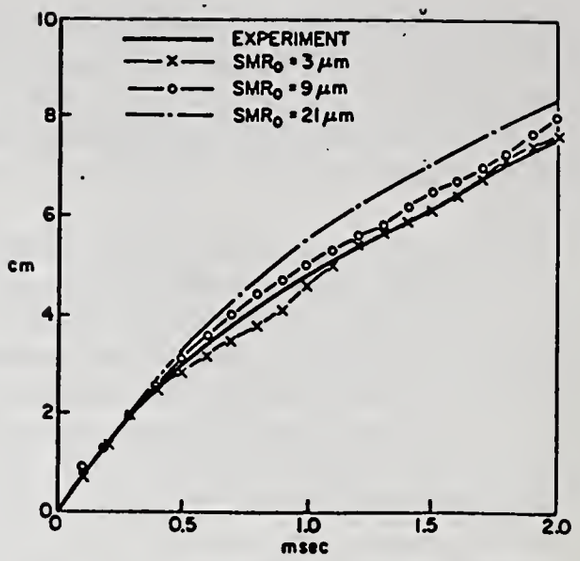

Fig. 15 Effect of varying injected drop size on computed tip penetration[33]

Blobs Models

The assumption of very small size in initial drop condition near the nozzle exit is unrealistic. Reitz and Diwakar[35, 36] injected drops having a diameter equal the nozzle exit diameter, and they assumed that the dynamics and breakup of these large drops are similar to those of a liquid jet as illustrated conceptually in Fig. 16[37]. Several kinds of blobs models are proposed. Breakup of the blobs is modeled using different stability analysis by different researchers. Reiz and Diwakar[35] incorporated into KIVA a model for both bag and boundary layer stripping breakup. In their model, bag breakup occurs if the drop Weber number, We, was greater than a critical value of 6. An unstable lifetime, t_1 is expressed following equation. Boundary layer stripping (BLS) is due to flow over the drop inducing a thin laminar boundary on the drop surface. The boundary layer is assumed to be stripped from the periphery of the drop as shown in Fig. 17. Boundary layer stripping is proposed to occur when the Weber to jet Reynolds number ratio $We / \sqrt{Re}$ is grater than 0.5. For stripping, an unstable lifetime t_2 is expressed by equation (12).

For Bag Breakup

$$We > 6.0 \tag{9}$$

$$t_1 = C_1 \left[\frac{\rho_l r^3}{2\sigma} \right]^{\frac{1}{2}} \tag{10}$$

For Boundary Layer Stripping

$$We / \sqrt{Re} > 0.5 \tag{11}$$

$$t_2 = C_2 \frac{r}{W} \left(\frac{\rho_l}{\rho_a} \right)^{\frac{1}{2}} \tag{12}$$

These large ' blobs ' fragment dynamically according to the rate equation

$$\frac{dr}{dt} = -\left(\frac{r - r_{stable}}{\tau} \right) \tag{13}$$

The term ' r_{stable} ' is found by equating the applicable drop stability criteria to the Weber number, We, for bag breakup or $We / \sqrt{Re}$ for stripping. The characteristic time, τ, is also found t_1 (eqn. 4) or t_2 (eqn. 5) depending on the appropriate breakup mechanism. Figure 18 shows the variation of drop size with axial distance from the injector for the solid-cone spray.

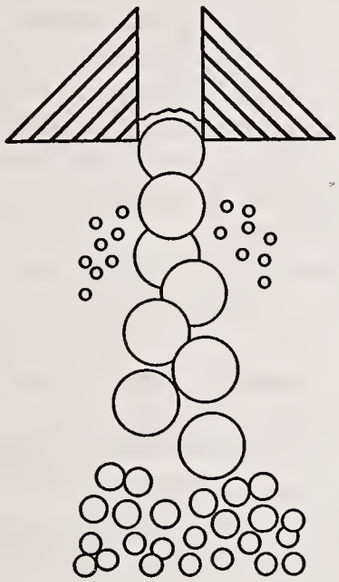

Fig. 16 Conceptual picture of the spray jet atomization

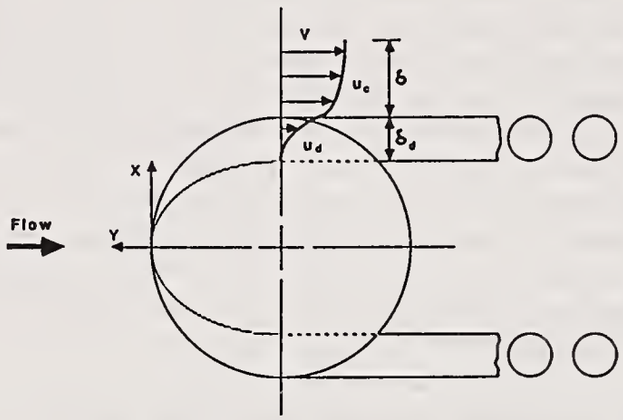

Fig. 17 Velocity profile created by shear forces during boundary layer stripping

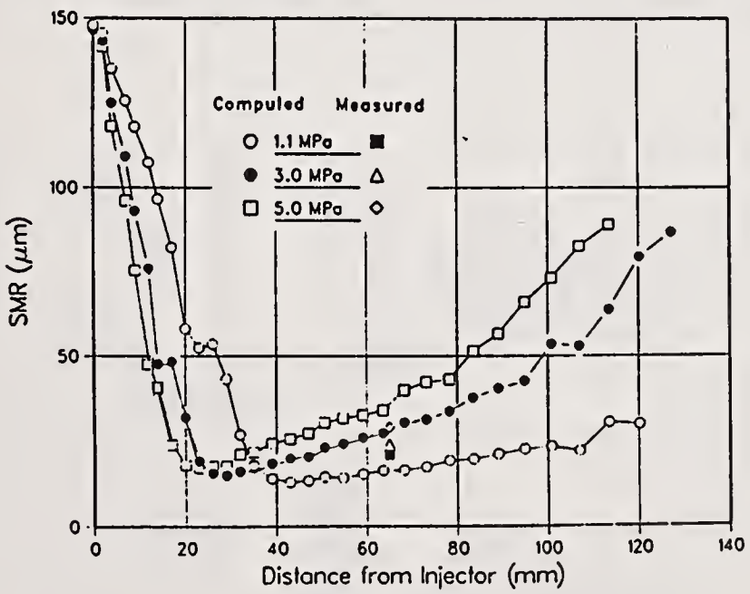

Fig. 18 Computed far-field solid-cone spray drop Sauter mean radius variation with distance from the nozzle. Three data points at 65mm measured by Hiroyasu and Kadota[22]

Recently, Reitz [38] has taken a different approach to jet breakup by considering Kelvin-Helmholtz instability growth on the jet surface and using the fastest growing wavelength as the length scale for drop formation of the parcel "blob". Thus, the jet "blobs" can breakup immediately upon exit from the nozzle by shedding small drops of diameter. The parcel "blobs" decrease linearly in size from their initial size at the nozzle diameter by this mass loss due to drop stripping relation.

O'Rourke and Amsden's model [39] is based on an analogy suggested by Taylor[40], between an oscillating and distorting drop and a spring-mass system. The restoring force of the spring is analogous to the surface tension force. The external force on the mass is analogous to the gas aerodynamic force. They also consider the damping forces due to liquid viscosity. They called this model the TAB (Taylor Analogy Breakup) model.

To predict the drop sizes after breakup, they used an equation motivated by an analysis based on energy conservation. In this analysis, they equated the energy of the parent drop before breakup to the combined energies of the product drops after breakup. Before breakup, the energy of the parent drop in its own frame of reference is the sum of its minimum surface energy and the energy in oscillation and distortion.

University of Wisconsin group [37] developed a theoretical model on the basis of applying the unstable wave penetration mechanism for a Rayleigh-Taylor instability as shown in Fig. 19 and boundary layer stripping (BLS) to a wide range of Weber number.

In this model, only the large drop breakup mechanism is considered initially. Drop mass loss due to Kelvin-Helmholz instability and the boundary layer stripping mechanisms have been neglected initially. This model is used to predict the transient drop breakup phases and obtain a correlation of the fragment size with time.

Typical results for single drop breakup are shown in Fig. 20 for a range of drop Weber numbers. The slight decrease in diameter with time is due to the boundary layer stripping mechanism mass loss and the catastrophic breakup at a given time is due to the Rayleigh-Taylor instability.

Spray Impingement on the Wall

Fuel spray may impinge on the piston bowl in DI diesel engines and may have a great influence on the mixture formation and combustion processes. Naber and Reitz [41] showed that their wall-jet model yields better agreement with experimental data of Kuniyoshi et al.[42]. Their results indicate that the width and high of the wall jet decrease as the gas density and the wall inclination angle are increased.

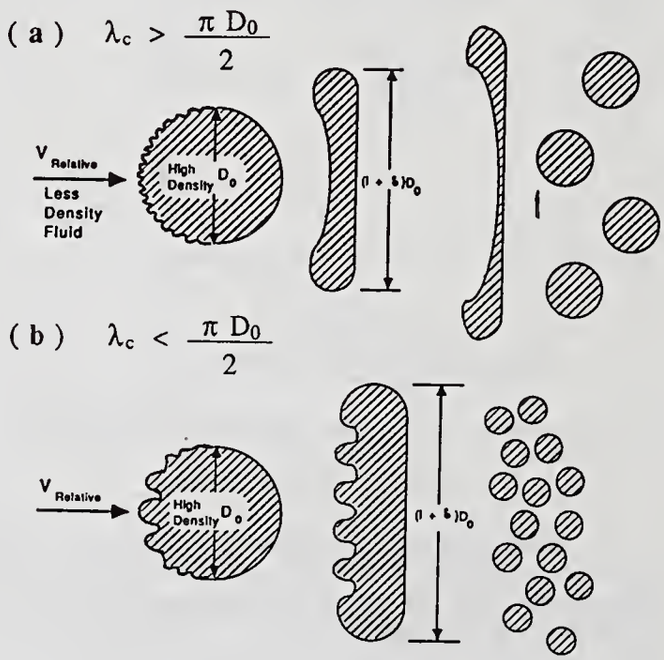

Fig. 19 Rayleigh-Taylor instability droplet breakup conceptual model

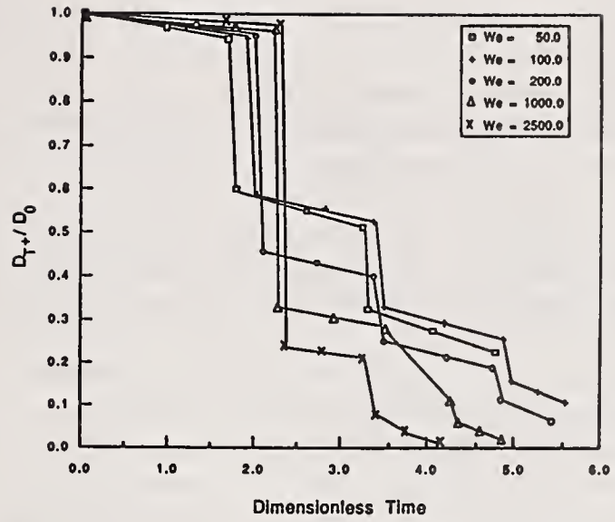

Fig. 20 Liquid droplet transient fragment size

CONCLUSIONS

The combustion process in a diesel engine is very complex, and its detailed mechanisms are not well understood. The study of diesel engine emissions and fuel economy requires a basic understanding of the processes of mixture formation, because the diesel combustion is strongly controlled by a fuel spray injected into the combustion chamber. More experimental data are required to validate the predictions of multidimensional models. Especially needed is a better understanding of spray breakup, include drop size distributions and drop velocities in engines, and they can be used to determine the effects of turbulence and drop collisions, coalescence, and breakup on the engine flow field and combustion.

NOMENCLATURE

$C_{1,2}$	constants
D	nozzle diameter (m)
D_0	sac chamber diameter of nozzle (m)
F	force (N)
L	nozzle length (m)
L_b	break-up length (m)
P_a	ambient pressure (MPa)
ΔP	difference between injection pressure and ambient pressure (Pa)
Q	rate of increase of distribution function
R	rate of change of radius
r	round radius of nozzle (m) , drop radius (m)
Re	Reynolds number
S	Spray Tip Penetration (m)
T	temperature (℃)
t	time (s)
t_1	unstable lifetime for BLS
t_2	unstable lifetime for stripping
t_b	break-up time (s)
v	drop velocity (m/s)
v_i	initial spray velocity (m/s)
W	relative velocity (m/s)
We	Weber number (m/s)
x	position
x_{32}	Sauter mean diameter (m)
x_{32}^{LS}	Sauter mean diameter at incomplete spray (m)
x_{32}^{HS}	Sauter mean diameter at complete spray (m)
μ_a	viscosity of air (pa · s)
μ_l	viscosity of fuel (pa · s)
ρ_a	density of air (kg/m^3)
ρ_l	density of fuel (kg/m^3)
θ	spray angle (degree)
σ	surface tension (N/m)
Γ	rate of change of distribution function
τ	liquid breakup time (s)

REFERENCES

1. DeJuhasz, K. J., "Dispersion of Sprays in solid Injection Oil Engines", Trans. of ASME, 53, p.65, 1931.
2. Castleman, R. A., "Mechanism of Atomization Accompanying Solid Injection", NACA Rept., No.40, 1932.
3. Tanasawa, Y. and Toyoda, S., "A Study on the Atomization of High Speed Liquid Jets", Bull. of JSME 20-92,1954.
4. Hiroyasu, H., Shimizu, M. and Arai, M., "The Break-up of High Speed Jet in a High Pressure Gaseous Atmosphere", 2nd Int. Conf. on Liquid Atomization and Spray Systems, ICLASS-82, p.69, 1982.
5. Shimizu, M., Arai, M. and Hiroyasu, H., "The measurements of Break-up Length in High Speed Jet", Trans. of JSME 49-446,1983.
6. Arai, M., Tabata, M., Hiroyasu, H. and Shimizu, M., " Disintegrating Process and Spray Characterization of Fuel Jet Injected by a Diesel Nozzle", SAE Paper No.840275, 1984.
7. Tanasawa, Y., "High Speed Diesel Engines I, Fuel Spray Systems and Spray Combustion, Sankaido, p.87, 1956.
8. Hiroyasu, H. and Arai, M., "Structures of Fuel Sprays in Diesel Engines", SAE Paper, No.900475, 1990.
9. Hiroyasu, H., Kadota, T. and Tasaka, S., "Penetration of Diesel Sprays", Trans. of JSME, 44-385, p.3208, 1978.
10. Hiroyasu, H. and Arai, M., "Fuel Spray Penetration and Spray Angle on Diesel Engines", Trans. of JSAE, 21, p.5, 1980.
11. Hiroyasu, H., Kadota, T., "Fuel Droplet Size Distribution in Diesel Combustion Chamber", Bulletin of JSME, 19-135, p.1064, 1976.
12. Tanasawa, Y. and Hiroyasu, H., "Measurement of Size Distribution of Sprayed Drops by Means of Molten Wax", Trans. of JSME, 26-162, pp.224-232, 1960.
13. Karasawa, T., Kurabayashi, T. and Kaeriyama, H., "Freezing Method by Liquid Nitrogen for Measuring Spray Droplet Sizes", Journal of Fuel Society of Japan, 62-679, pp.90-912, 1983.
14. Nishida, K., Murakami, N. and Hiroyuki, H., "A Pulsed Laser Holography Study of the Evaporating Diesel Spray in a High Pressure Bomb", Trans. of JSME, 52-478, p.2457, 1986.
15. Kamimoto, T., Yokota, H. and Kobayashi, H., "A New Technique for the Measurement of Sauter Mean Diameter of Droplets in Unsteady Dense Sprays", SAE Paper, No.890316, 1989.
16. Arai, M., Hiroyasu, H. and Kishi, T., "Measurement of Drop Size Distribution of the Spray by Using a Laser Diffraction Method", Trans. of JSME, 29-252, p.1795, 1986.
17. Tabata, M., Arai, M., Hiroyasu, H., "Atomization of High Viscosity Liquid by a Diesel Nozzle", Bull. of JSME, 29-252, p.1795, 1986.
18. Bhatia, J. C. and Durst, F., "A Comparative Study of Some Probability Distributions Applied to Liquid Sprays", Proc. Int. Conf. Mech. of Two-Phase Flows, Taiwan, pp.279-284, 1989.
19. Hiroyasu, H. and Arai, M. and Tabata, M., "Empirical Equations for the Sauter Mean Diameter of a Diesel Spray", SAE Paper, No.890464, p.97, 1989.
20. Williams, F. A., "Process in Spray-Combustion Analysis", Eighth Int. Symp. on Comb., Williams & Wilkins Co., Baltimore, 50-69, 1962.
21. Nguyen, H. L., Schock, H. J., Carpenter, M. H., Ramos, J. I. and Stegeman, J. D., "Numerical Simulation of the Flow Field and Fuel Sprays in an IC Engine", SAE Paper No.870599, 1987.
22. Hiroyasu, H., Kadota, T., "Fuel Droplet Size Distribution in Diesel Combustion Chamber", SAE Paper No.740715, 1974.
23. Dukowicz, J. K., "A Particle-Fluid Numerical Model for Liquid Sprays", Journal of Computation Physics, Vol.35, pp.229-253, 1980.
24. Cloutman, L. D., Dukowicz, J. K. and Ramshaw, J. D., "Numerical Simulation of Reactive Flow in Internal Combustion Engines", Lecture Notes in Physics, Vol. 141, pp.119-124, 1981.
25. Butler, T. D., Cloutman, L. D., Dukowicz, J. K. and Ramshaw, J. D., "Multidimensional Numerical Simulation of Reactive Flow in Internal Combustion Engine", Progress in Energy and Combustion Science, Vol. 7, pp.293-315, 1981.

26. Cloutman, L. D., Dukowicz, J. K. and Ramshaw, J. D. and Amsden, A. A., "CONCHAS-SPRAY : A Computer Code for Reactive Flows with Fuel Sprays", Report No. LA-9294-MS, Los Alamos National Laboratory, 1982.
27. Amsden, A. A., Butler, T. D., O'Rouke, P. J. and Ramshaw, J. D., "KIVA-Comprehensive Model for 2-D and 3-D Engine Simulations", SAE Paper No.850554, 1985.
28. O'Rouke, P. J., Amsden, A. A., "Three Dimensional Numerical Simulations of the UPS-292 Stratified Charged Engine", SAE Paper No.870597, 1985.
29. Takenaka, Y., Aoyagi, Y., Tsuji, Y. and Joko, I., "3D Numerical Simulation of Fuel Injection and and Combustion Phenomena in DI Diesel Engines, SAE Paper No.890668, 1989.
30. Aoyagi, Y., Kamimoto, T., Matsui, Y. and Matsuoka, S., "A Gas Sampling Study on the Formation Process of Soot and NO in a DI Diesel Engine", SAE Paper No.800254, 1980.
31. Amsden, A. A., Butler, T. D. and O'Rouke, P. J., "The KIVA-Computer Program for Transient Multidimensional Chemically Reactive Flows with Sprays", SAE Paper No.872072,1987.
32. Kuo, T. W. and Bracco, F. V., "Computation of Drop Sizes in Pulsating Sprays and of Liquid-Cone Length in Vaporizing Sprays", SAE Paper No.820133, 1982.
33. O'Rouke, P. J. and Bracco, F. V., "Modeling of Drop Interactions in Thick Sprays and a Comparison with Experiments, Stratified Charge Automotive Engines", pp.1054-1064, 1979.
34. Reitz, R. D. and Bracco, F. V., "Mechanism of Atomization of a Liquid Jet", Physic of Fluids, Vol.22, No.6, pp.1054-1064, 1979.
35. Reitz, R. D. and Diwakar, R., "Effect of Drop Breakup on Fuel Sprays", SAE Paper No.860469, 1986.
36. Reitz, R. D. and Diwakar, R., "Structure of High-Pressure Fuel Sprays", SAE Paper No.870598, 1987.
37. Bower, G., Chang, S. K., Corradini, M. L., EI-Beshbeeshy, M., Martin, J. K. and Krueger, J., "Physical Mechanisms for Atomization of a Jet Spray : A Comparison of Models and Experiments:, SAE Paper No.872089, 1987.
38. Reitz, R. D, "Modeling Atomization Process in High-Pressure Vaporizing Sprays", Atomization and Spray Technology 3, pp.309-337, 1987.
39. O'Rouke, P. J. and Amsden, A. A., "The TBA Method for Numerical Calculation of Spray Droplet Breakup", SAE Paper No.831318, 1983.
40. Taylor, G. I., " The Shape and Acceleration of a Drop in a High Speed Air Stream", The Scientific Papers of G. I. Taylor, ed. G. K. Batchelor, Vol.II, Uviv. Press, Cambridge, 1963.
41. Naber, J. D. and Reitz, R. D, "Modeling Engine Spray / Wall Impingement", SAE Paper No.880107, 1988.
42. Kuniyoshi, H., Yamamoto, H., Fujimoto, H. and Sato, G. T., "Investigation of the Characteristics of Diesel Spray (Third Paper : Impinging upon a Flat Plate)", Journal of JSME, Vol.15, pp.57-64, 1980.

Keynote Lecture

ATOMISATION OF LIQUID METALS FOR THE MANUFACTURE OF METAL POWDER AND FOR SPRAY FORMING

K. Bauckhage

University of Bremen, Verfahrenstechnik
Bremen, Germany

ABSTRACT

Among the numerous atomization techniques for melt spraying the most important ones will be described and discussed in regard to their design criteria and operating conditions. They can be classified according to the forces acting on the melt stream via the high energy fluid streams (gas or water jets), by ultrasound activated vibrations, by impact or by rotating elements.

The equations for overall drop size distributions will be discussed. While this information is important for an optimized production of powders, there is a strong demand for a more differentiated description of local drop size and drop velocity distributions which can be used for the balances of mass, momentum, and energy during spray forming or metal spray coating. Using the measurements of local velocity and size distributions of the melt droplets in correspondence with the differential equations of the a.m. balances gives a basis for a numerical simulation of the gas atomized spray forming, the results of which are in good agreement with the experimental findings.

INTRODUCTION

Atomization is a process in which a liquid stream is disintegrated into a large number of droplets of various sizes. Because all solid state materials like minerals, ceramics, glass and of course metals can be converted into the liquid state (it is only a question of heat and temperature) there have been developed numerous atomization techniques for molten materials which differ greatly in the modes in which energy is supplied to the disintegration process and which after comminuting the melt streams alter widely in the tasks and hence in the process lines of accompanied unit operations. In many cases where melting is a necessary operation in the line to generate for instance metals of high purity, the atomization process in comparison with for instance milling represents the most economic way to produce particulate materials, i.e. metal powders.

Atomization techniques for powder production and also for melt spraying have been reviewed several times in the last decade, [1] to [3]. This has mainly been done from the standpoint of metallurgical engineers, because of the economic and technical importance of metal powder production. But this is not the only field of interest for melt spraying techniques which are used mainly to produce the majority of available metal powders with a special metallurgical, crystalline or mechanical behaviour and with properties controlled by the individual conditions of consolidation, rapid quenching, segregation or crystallization processes of the par-

ticulates and specified by their overall size distribution, the mean particle diameter, the particle shape and the capacity to spill.

It is also the field of interest of mechanical, chemical and process engineers

- to produce metallic layers with specific mechanical characteristics on tools or machine elements, with electrical or optical characteristics in combination with surfaces of special substrate materials;
- to manufacture spray deposited preforms of near-net shape as a single operation in a new and very successful process line which combines the creation of spray and the consolidation of particulate materials, thus contributing to micro-structural refinement in the billets, sheets or tube preforms.

These techniques are not restricted to molten metals. Ceramic and glass powders also are produced by melt atomization, mostly with spherical shapes. Atomization is not necessarily limited to the production of droplets or powders. The high viscosity of molten minerals, glasses or ceramics for instance allows the generation of ultrafine fibres (rock wools and high temperature resistant fibrous refractory). And spray deposit preforms already include ceramic-fiber reinforced metal-matrix composites.

MAIN CRITERIA OF MELT ATOMIZATION

The main difference between melt atomization and conventional atomization (of aqueous and organic liquids) consists in the preceding energy transport for heating and melting the material as well as in the subsequent release of this energy in order to consolidate the dispersed droplets (and to convert them into powder particles) and to cool the particles after impact (and coalescence) on the substrate or on the preform layer.

In most of the existing experimental rigs or production plants the main unit operations - melting, atomization, cooling and consolidation - are arranged below each other or integrated into one common vessel following the same sequence. (Taken all together these unit operations define the so called process of "pulverization".) Following gravitational forces the melt leaves the induction heater and poures from the crucible/tundish to the disintegration zone of the atomizer. Very often the basic operations have to be performed under an inert gas atmosphere (such as nitrogen or argon) in order to prevent chemical reactions of the metal melt with for example oxygen. It should be noted that increasing safety hazards go hand in hand with the production of finer powders of for instance aluminum and magnesium. Here one needs closed plants including sieving and bottling, all together operating under inert gas.

Because of great differences in the thermal expansion of the various materials of the crucible/tundish and the atomizer elements (ring nozzles, gas tubes, etc.) and considering the enormous temperature differences due to standstill and stationary operating, this gives reason to keep the melting design separated from the atomizer design. Typical pressure atomizers (plain orifices, simplex nozzles, etc.) or internal mixing atomizers, well known from conventional atomization, cannot be used.

Conventional atomization is characterized by the liquid state of the aqueous or organic fluids after atomization and therefrom by the tendency of the liquid droplets to coalesce or to evaporate thus causing the loss of the initial drop shape and size (as a consequence of impact, deformation or heat transfer). In comparison to this the melt atomization in general provides for its own analytical instrument, i.e. the powder product, which is extremely helpful for analysis of the disintegration process. This "by-product" can be obtained as a representative powder sample directly from the powder production process during atomization, or can be taken as momentary powder samples from the succeeding manufacturing processes if for instance the tasks of generating metallic layers or spray deposited preforms have to be slightly manipulated. After this powder "by-product" has been screened it functions as a prerequisite for an assessment of the disintegration process and of product quality. These powder samples supply a basis for documentation not only of atomization efficiency but also for the quality of the total spraying system (including cooling and consolidation). Such an "alibi" cannot be obtained from conventional atomization.

Last but not least, an important difference of melt atomization in comparison with conventional atomization results from the material properties of the melts of metal, ceramic and glass, i.e., surface tension, density and dynamic or kinematic viscosity, which are given in Table 1 for some representative materials. Compared with water, the values of surface tension rise to a 20-fold level, those of density to an 11-fold one and those of dynamic viscosity to a 4-fold level; but the values of kinematic viscosity go down to a factor of 0.2. The ranges of these properties differ greatly from those of aqueous or organic fluids, which show for the surface tension for instance a range of only 10 to 74 dyn/cm.

Table 1 Materials properties with T = temperature; σ = surfache tensions; η_L = dynamic viscosity; ρ_L = density; ν_L = kinematic viscosity

Melt	T [°K]	$\sigma 10^{-3}$ [N/m]	$\eta_L 10^{-2}$ [P]	$\rho_L 10^{-3}$ [kg/m^3]	$\nu_L 10^{2}$ [m^2/s]
Aluminum	930	570 (865	2 (3)	2.25	1 (1.3)
Cupper	1,360	1,150 (1,300)	4.2 (3.4)	8.3 (7.8)	0.5
Iron	1,870	1,200 (1,820)	4.3 (6.0)	7.2 (6.9)	0.6 (0.87)
Lead	600	400	2	10.7	0.2
Magnesium	923	570	1.2	1.54	0.8
Pb-Bi-Sn-Eutectic	348	450	1.5	9.4	0.16
Steel	1,730	1,500	5	7.5	0.66
Tin	500	560	1.6	6.6	0.24
Zinc	690	785	2 (3.6)	7.1 (6.5)	0.28 (0.55)
Water	293	74	1	1	1
Glas	900	160	100	6.27	159

With regard to the task of this contribution one has to confine to the most common atomizer types and to limit the selection of interesting atomizers. Such a limited selection is given in Fig. 1, which illustrates various principles of atomization of molten metals and melt spraying. This overview can give only a faint impression of this wide field and of different technical solutions, in which mainly two types have reached a wide spread industrial standard of economic application, i.e., the gas or water atomization and the centrifugal atomization.

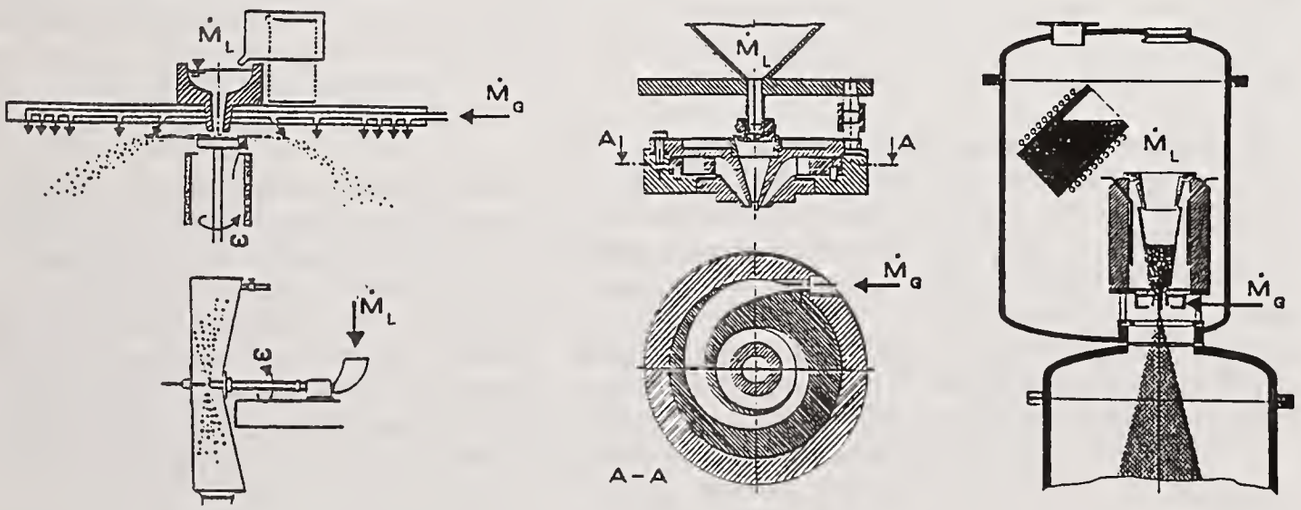

Fig. 1 Rotating and gas atomizers

DESCRIPTION OF THE MOST COMMON ATOMIZERS

A presentation and a systematic description of common atomizers for melt spraying seems best to start with a classification of governing disintegration forces in regard to the transport of momentum, i.e.

a) the momentum transport by pressure gas or liquid streams
b) the introduction of centrifugal forces using rotating elements or via angular momentum of the gas stream
c) the use of vibrating forces
d) momentum induced by the melt droplets themselves via impact.

It can also be useful to take advantage of combinations of these alternatives, i.e. a) and c) or b) and d).

As has been described elsewhere in detail, [4] and [5], liquid atomization in general is characterized by typical formations of thin jets and sheets of liquid, which are disrupted into ligaments and droplets by rapidly growing disturbances in or on the surface of these liquid fragments. Primary jets and sheets as well as ligaments and fragments are caused by internal forces of the liquid itself and by external ones due to tangential and normal forces of atomizing gas jets (or vibrating gas columns) or due to centrifugal forces induced by rotating elements. All the various types of internal and external forces have to overcome the consolidating influences of surface tension, which is permanently contracting the different fragments to spherical shapes, thus minimizing the surface energy. Conversely the liquid viscosity tends to stabilize the momentary shape of liquid fragments (thus being the main cause for fiberformation during the solidification process of the melt jets and ligaments). This means that liquid viscosity is opposing the disruption process but on the other hand - exerted by gas jets - gas viscosity may support the disruption. Inertial forces due to liquid or gas density promote the disruption process.

"Breakup occurs, when the magnitude of the disruption forces" commonly "just exceeds the consolidating force of surface tension. Most of the larger drops produced in the initial disintegration process are unstable and undergo further disruption into smaller drops. Thus the final range of drop sizes produced in a spray depends not only on the drop sizes produced in primary atomization but also on the extent to which these drops are further disintegrated during secondary atomization." Reducing the different phenomena and also the very complicated and complex details of disintegration in this quotation in a pregnant manner to the main object, Lefebvre [4] focused his description onto the conventional atomization of aqueous and organic liquids. Nevertheless his description also holds for liquid melts and thus for melt atomization. But though we principally may expect the same laws describing the disintegration processes of melts as of aqueous or organic liquids, we may not assume the dimensionless correlations leading to the same constants without having proved this. Relating to the wide variety of materials properties (ρ_L, σ, η_L) of molten metals some of the extreme large values give raise to prove the range of validity of earlier relevant literature.

Gas- or Liquid-Atomization

Gas- or liquid-atomization techniques cover the main field in the manufacture of metallic particulate and spray deposited preforms. In recent years increasing numbers of reports describe these atomization and melt-spraying techniques, see for instance [6] to [8] (also for ceramics and glasses). When the atomization plants and their typical process design are considered, it can be said, that in most cases melting and atomization are integrated into the same system, that both processes take place under the same pressure (i.e. $\Delta p = 0$); the latter mainly because of the insufficient strength of the refractory material of the heated crucible/tundish or because of sealing problems. This causes an effluent velocity of the melt stream leaving the bottom exit of the tundish governed only by the level h of the liquid (melt) above the exit:

$$\overline{v_o} = \beta\sqrt{2gh + \Delta p/\rho} \qquad (1)$$

where h very often varies with time: h = h(t), thus making necessary a manipulation of the factor β (by means of for instance a plugging device) in order to compensate the influence of h(t) in the mass flow rate

$$\dot{M}_L = \overline{v_o} \left(\frac{\pi D_o^2}{4} \right) \rho_L = \dot{M}_L (\beta, h) \qquad (2)$$

As the materials properties show strong temperature dependencies, these properties - depending on the task of atomization and of the cooling process - have to be fixed as constants near the melting temperature T_L, often necessarily taking into account a small temperature difference ΔT depending on a process immanent undercooling or overheating.

In order to prevent the tundish exit or the atomizer from "freezing in" by a solidifying melt stream or by impacting and also solidifying melt droplets one has primarily to avoid extreme low mass flow rates with insufficient heat transfer or on the other hand streaming conditions of the effluent melt jet that belong to zones of spontaneous disruption of free jets.

The main task is to bring the continuous melt stream into the disintegration zone where the momentum of pressure gas or water jets (i.e. their amount and their direction) prevents backsplashing of melt droplets.

There exist several solutions to this problem - one answer consists of the following design principles for atomizers:

- making use of the gravitational force for the effluent of the melt out of the crucible/tundish,
- leading the melt flow as a continuous central stream downwards into the atomization zone,
- surrounding it with concentric orifices for the atomization pressure gas or liquid,
- using co-current flows of melt and gas (downwards) but inclining the gas jets under small angles in order to rise tangential and normal forces.

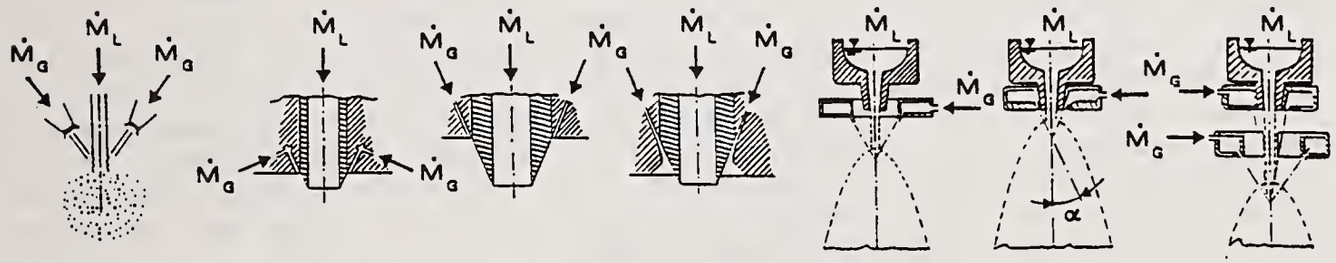

Fig. 2 Various types of gas atomizers

It is of prime importance to manage the flow conditions of the melt stream and of the essential energy supply within the melt stream itself (by convection and conduction) as well as through its conducting tundish walls in order to keep the melt liquid at the exit of the tundish as well as down to the atomization zone. On the other hand one has to provide for the necessary insulation against the cooling effect of the gas tubes in the vicinity of the exit and against the expanding and therefrom cooling gas streams near the melt stream in the atomizer zone.

Another design element to solve the problem is to limit the liquid level h of the melt above the bottom exit of the crucible/tundish by means of an overflow. This prevents the melt jet from breaking up spontaneously or from generating single drops (caused by interaction with the surrounding gas) before it has reached the disintegration zone. Keeping the liquid level constant or the velocity $\overline{v_o}$ provides a constant mass flow rate $\dot{M}_L$ and hence a stationary melt flow and an unchanged turbulent situation of the melt jet in the atomization zone.

A third method is, not to allow the melt stream to accelerate under free fall conditions and to prevent it from generating drops by using a short tube, which leads from the tundish exit to the atomization zone. (This is the so called closed coupled atomizer.) Using such a short

tube means that additional drag deminishes the melt velocity $\bar{v}_o$ in the disintegration zone, but on the other side to allow higher mass flow rates.

Further effective design principles to avoid "freezing in" result in leading the gas stream into a spiral form onto the melt, thus forcing the atomized droplets immediately to twist away from the atomizer, as already shown in Fig. 1 after [8]. Or they find their expression in a two-stage atomization, in which the upper (first) gas stream only takes over the task of minimizing the relative velocity of melt and gas, of raising the drag forces of eventually back-splashing droplets and of transporting them downstream into the spray cone. Whereas here the upper gas stream does not serve at all to disintegrate the melt stream, the upper water-stream in a combined two-stage water- and gas-atomizer mainly has only this function. After primary atomization has been executed in this zone the water stream also carries away the particles.

Within the atomization zone the pressure-gas streams (the liquefied-gas streams or the water jets) bounce against the continuous melt stream accelerate it downwards and disintegrate it into droplets by tangential and normal forces. (In the above mentioned case of spiral gas supply, parts of the tangential forces are centrifugal ones.) The gas jets (or liquefied gas or water jets) originate from an arrangement of identical orifices or from a slit nozzle arranged concentrically to the central melt stream. Concerning the direction of the melt stream one can recognize gas jets with moderate inclinations, see Fig. 2, nearly parallel ones, but also some with angles α of about 45°.

In order to provide sufficiently high momentum forces for a satisfactory disintegration very high gas velocities and gas mass flow rates are employed. While the velocity of the melt stream in the atomization zone rarely exceeds values of about 20 m/sec, the gas jets reach velocities of more than the 10-fold value, limited only by the sound velocity.

Atomization by Means of Rotating Elements

The application of centrifugal forces to the disintegration process is mainly done in accordance with the same scheme the melt poures under free fall conditions from the crucible/tundish with a constant velocity. It enters the rotary atomizer of diameter D_2 which rotates at a constant speed ω. Here the melt wets the rotating surface which has the form of a flat disc, a drum or a cup shape, see Fig. 3. Because of the adhesion of the wetting melt layer and its viscosity the melt is accelerated by the rotating surface from which it is spread out at least fairly uniformly, depending on the flow rate. (As there exists a pronounced region of filament formation this type of atomization is also used for fiber production of melts with high viscosities near the solidification temperature.) To prevent the melt from creeping over the rim of the rotary atomizer, auxiliary secondary gas streams blow from below and carry the droplets slightly upwards in the radial and tangential direction.

The generation of droplets by means of rotating elements can be classified into three main groups governed by the rotational speed ω as well as by the flow rate of the melt V and corresponding to the main phenomena observed during the variation of these parameters, (see Fig. 3) i.e.,

- centrifuging off droplets directly from the rim .. (a),
- drops emerging from previously formed ligaments .. (b),
- drops forming from breaking liquid sheets (films). .. (c).

Generally expressed: for a given melt (constant temperature and fixed material properties) the regularity of the powders (i.e. the narrow size distribution of the powder particles) will improve if the rotational speed of the elements is raised or the melt stream is diminished.

Looking at Table 2 a considerable number of equations are seen describing the borders of the above mentioned fields of droplet generation with some serious contradictions. The equations have been derived for conventional atomization of aqueous or organic liquids, where the material properties cover a far smaller range than they do for molten metals, ceramic or glass melts. In Fig. 3, after [9], there can be seen differing results for the conventional atomization (i.e. for the border between (a), (b) and (c).

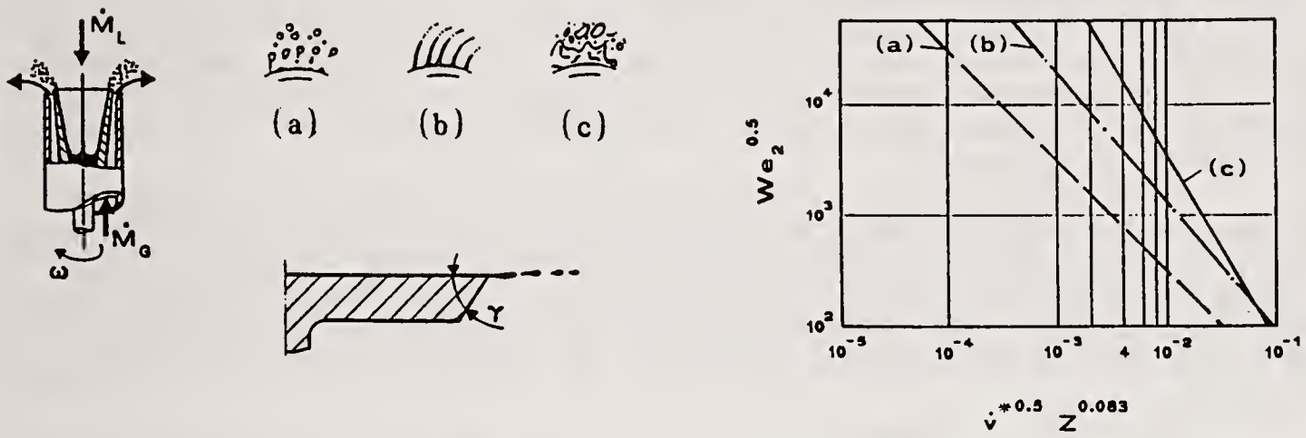

Fig. 3 Liquid atomization by rotating elements

Table 2 Equations describing the borders between droplets centrifuged off directly (a), drops emerged from filaments (b) and drops created by breaking liquid sheets (films), i.e. (c)

ZONE	Equations	Lit. cit. No.
a/b: drops - drops from ligaments	$\dot{v}^* We_2^{0.25} Z^{0.167} = 2.08\ 10^{-5}$	[10]
	$\dot{v}^* We_2^{0.75} Z^{0.180} = 3.068$	[11]
	$\dot{v}^* We_2^{0.85} Z^{0.45} = 0.113 \div 0.195$	[12]
	$\dot{v}^* = 13.40 \left\{ \frac{D_2}{\omega} \right\}^{0.667} \frac{\sigma}{\rho_L (1 + 10\, Z^{0.167})}$	[13]
	$\dot{v}$ [m^3/s]; D [m]; ω [rad/s]; σ [N/m]; ρ_L [kg/m^3]	
b/c: ligaments - film	$\dot{v}^* We_2^{0.6} \cdot Z^{0.167} = 1.77$	[14]
	$\dot{v}^* We_2^{0.583} Z^{0.166} = 1.45$	[10]
	$\dot{v}^* = 4.443\ 10^{-2} \cdot D_2^{-0.5}\, \omega^{-0.667} (\sigma/\rho)^{0.833}$	[13]
	$\dot{V}$ [m^3/s] and other terms as given above	
	with $\dot{v}^* = \frac{\dot{v}^2 \rho_L}{\sigma D_2^3}$; $We_2 = \frac{\rho_L \omega^2 D_2^3}{\sigma}$; $Z = \frac{\eta \dot{V}}{\rho_L \sigma D_2}$	

The atomization of metal melts takes place in the region left from the border (a), after [9]. This is why in the following only drop size equations will be discussed, which have their origin in this parameter combination.

Utilizing Forces Induced by Ultrasonic Vibrations

Also in the area of melt atomization by utilizing ultrasonic forces the above described free fall of the melt stream from the crucible/tundish to the vibrator zone is used as sketched in Fig. 4 after [15]. The melt wets the surface of the conical ultrasound vibrator before being disintegrated into very small droplets under the influence of capillary forces. The droplets are sprayed off in all directions.

The free falling melt jet is applied for leading the melt stream into the central one of several pressure nodes of a horizontal standing ultrasonic wave generated by two sonotrodes after [16], as sketched in Fig. 4b. This arrangement prevents wetting of the two vibrating surfaces of the sonotrodes by the melt and helps for instance to keep the molten metals extremely pure. The efficiency of this disintegration process can be increased by raising the pressure of the gas atmosphere in the atomization chamber, i.e. the density of the vibrating gas column between the sonotrodes.

Another type of ultrasonic atomizer uses vibration of (20 to 100) kHz of the gas jets impinging onto the melt. The so called USGA-nozzles surrounding the melt stream each incorporate a Hartmann shockwave tube in order to generate pulsed high velocity gas jets, Fig. 4c. To change the flow characteristics one needs different atomizer design (altering inclination angle, number of gas nozzles and insert length), because of the restriction in the mass flow ratio, i.e. keeping constant the ultrasound parameters. The vibrating gas jets assist the production of fine dispersed powders.

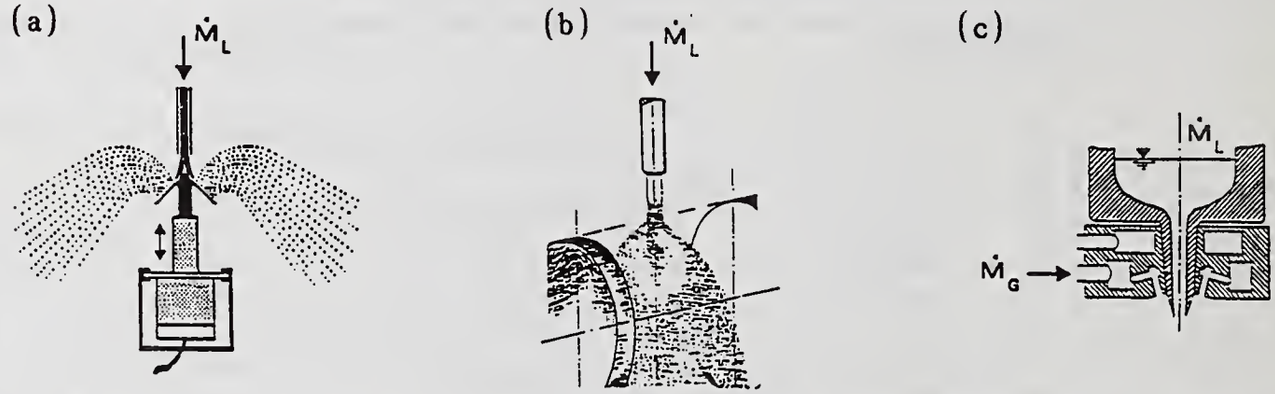

Fig. 4 Atomizers using ultrasonic vibrations: (a) a vibrating conical surface, (b) an ultrasound standing wave, (c) USGA nozzles

Utilizing Drop Impaction for Further Disintegration

Utilizing controlled drop impaction for further disintegration of larger[1] drops into significantly smaller ones can only be an additional process step after primary atomization. Assuming that the drops leave the primary atomization with high velocities, this together with the high density of several metals can be used for subsequent impact disintegration, because of the remainder high momentum of the particles.

If for instance rotary atomizers are used for the primary disintegration this first step together with the impact disintegration can be handled under vacuum conditions, which may be important with respect to a postulated extreme purity of the materials. Using vacuum means also that the drag resistance of the particles can be diminished significantly thus raising the impact velocity necessary for further disintegration.

The limiting condition for impact disintegration is given by the declining line in the diagram after Fig. 5, where the vertical and the horizontal axes are given by the number A and the Weber-number We_3 after [17]:

1. The adjectives larger and smaller have to be understood in this context only as a relative characterization, there are no quantifying equations available!

$$A = \frac{d\,\sigma\,\rho_L}{\eta_L^2} \tag{3}$$

$$We_3 = \frac{v_3^2(d)\,d\,\rho_L}{\sigma} \tag{4}$$

If a drop of diameter d impinges perpendicularly on the flat (not wetted) surface of the disintegration element with the impact velocity $v_3(d)$ further disintegration in several significantly smaller drops will appear only when the couple of A and We_3 mark a point to the right of the declining line. The diagram has been established for aqueous liquids and for mercury. There exists no equation that describes the diameters of the secondary significantly smaller droplets.

Other Principles of Atomization

Leading the melt flow as a continuous central stream into the atomization zone, and surrounding it with a concentric gas stream has been explained as a typical design principle of gas atomization. Utilizing this principle in a radical manner in order

- to bring the ambient gas stream into a close contract with the metal stream
- to intensify the heat transfer between both phases
- to introduce shear forces from the gas stream to the melt stream and
- to avoid backsplashing of droplets

leads to solutions sketched in Figrs. 6a and b. Using Laval principle (injection principle) for the surrounding gas stream, thinning the walls between the melt and the gas phase (with completion already in or above the acceleration zone of the gas stream) and raising the gas temperature above or up to the melting temperature opens the possibility to accelerate both phases and therewith to augment their inertial forces as well as to lift the viscous forces of the gas stream due to higher temperatures. There have also been successful attempts to verify laminar boundary layers because of the high gas viscosity and to produce extremely small droplets. Accelerating of the melt jet means diminishing its diameter and creating an excellent basis for break-up of an extremely thinned melt jet just below the smallest nozzle cross section. It has been reported that this method allows a powder production of ultrafine particles, [18].

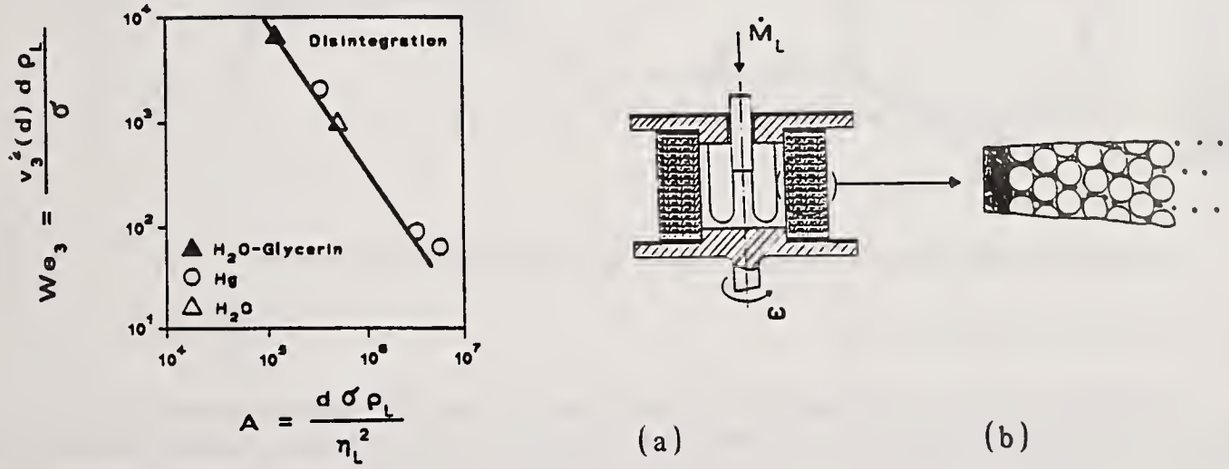

Figrs. 5 (left): Diagram for further drop integration after impact on a plane (not wetted) surface and 7 (right): Atomization by means of a rotating porous cylinder

A similar way of atomizing the melt received from the melting zones of a wire is shown in Fig. 6b after [19] and [20] for a flame spray gun. The wire (identical with the central melt stream) is supplied continuously from behind (left) into the melting zone of the burning gases. Starting from the surface the material of the wire is molten and thrown away by the gas stream

onto the surface of the substrate. The melt droplets are kept liquid until reaching the impact zone by radiation, conduction and convection within the gas flame of the gun thus forming a spray cone of only 10 to 30 cm in length.

The flame spray is used to generate special metallic or ceramic coatings on surfaces (improving the resistance to wear, heat or corrosion). The droplet impact and the complete spray deposition process is similar to that described below as the Osprey spray compaction process. In this context there has to be mentioned the plasma spraying as an alternative spray deposition process (widening the application of materials and properties of coatings by raising the plasma gas temperatures up to some 10^3 Kelvin. While the two phase flow in the spray and the deposition process are once again similar to the above mentioned process and to that of Osprey, the melting process differs greatly by using powder particles which are molten within a very short distance because of the extreme high temperatures in the plasma flame. The assumption is that the droplet diameters are prescribed by the sizes of the powder particles, whether the droplets underlay further disintegrations cannot be answered till now.

A combination of the principles of rotating and impacting has been verified by [21] using a hollow cylinder of porous material of sintered monodispersed spheres of ceramics or metals. This sintered material should not be wetted by the melt, thus allowing only very dedicated combinations of metal/metal or metal/ceramics. The principle is illustrated in Fig. 7a: the melt is fed from above and centrifuged through the pores. Fig. 7b shows how the melt is pressed through the upper pores and disrupted into larger and smaller droplets (generating also secondary smaller droplets by impact). The pores are forcing the smaller drops to coalesce before leaving the last (outer) zone of the pores thus giving cause for a very narrow size distribution.

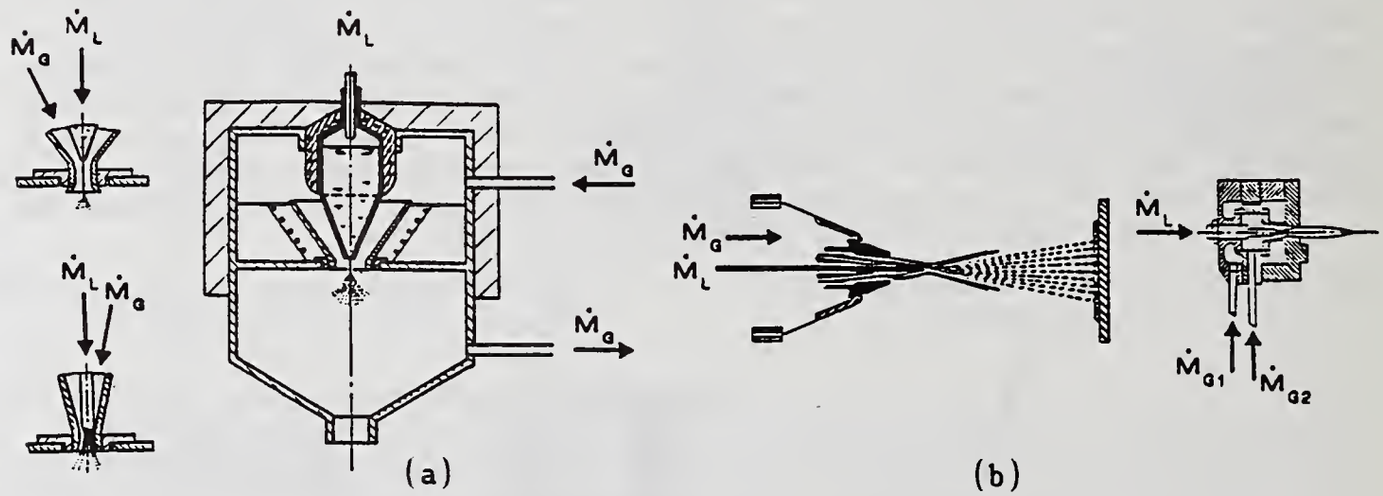

Fig. 6 a) Laval principle after [18] and b) flame spray gun after [19] and [20]

OVERALL SIZE DISTRIBUTION

The most important prerequisite for atomizer design, for process layout, process optimization, and process control as well as for the product quality is knowledge of the droplet diameters. This holds not only for the conventional atomization of aqueous or organic fluids but also for melt atomization, where for instance the size distribution of the pulverized metal directly influences its acceptance and its price. The dependencies on the conditions of unit operations integrated in the same process play an important role. And last but not least problems arise from environmental and safety conditions especially for the treatment of fine and ultrafine powder particles.

Great efforts have been made to describe the size distributions of droplets obtained by atomization in different atomizer types depending on atomizer design and geometry and also on

the material properties of the process media. Some attempts have been successful. Especially for conventional atomization, there have been derived numerous dropsize equations for the very different types of atomizers and operating conditions. A very helpful and worth reading survey of such equations is given in [4] including also results of his own research. Other equations also valid for aqueous or organic liquids are mainly derived from ratios of similitude and lead to dimensionless correlations. Some attempts failed completely in transforming them from conventional to melt atomization because of the not allowed extrapolation of parameters and because up till now no theoretical description of the disintegration process in general is available. Especially with respect to melt atomization this may also depend on the deficits in awareness of the necessary material properties of melts with regard to the great variety of alloys and composites.

As long as it is satisfactory for a well operating atomization process to keep constant the overall-size distribution with respect to the total mass flow of the powder production, it may be sufficient to take periodical samples of the powder and to screen these samples or to measure the size distribution by means of (for instance) a diffraction instrument and to describe or to control the size distribution by the results of these measurements.

In order to describe the overall size distributions of melt droplets generated by gas- or liquid atomization one can recognize especially one equation (after Lubanska [22]) on which the experimental reports are focused chiefly and which has been used successfully in a great number of experiments:

$$d_{50,3} = B \left\{ \left(1 + \frac{\dot{M}_L}{\dot{M}_G} \right) \frac{\nu_L}{\nu_G} \right\}^{\frac{1}{2}} We_1^{-\frac{1}{2}} D_1 \qquad (5)$$

with

$$We_1 = \frac{u^2 D_1 \rho_L}{\sigma} \qquad (6)$$

and

$$B = 50 \qquad (7)$$

Lubanska observed size distribution closely following a log-normal pattern

$$q_3(d) = - \frac{dR}{dd} = \frac{100}{s \sqrt{2\pi}} e^{-\left\{ \frac{(\log d - \log d_{50})^2}{2 s^2} \right\}} \qquad (8)$$

with dR being the cumulative weight oversize percentage per screen after sieving and $d_{50} = d_{50,3}$ as given by equation (5). He gave the standard deviations as depending on $d_{50,3}$:

$$d_{50,3} = 13 \, [\, \mu m \,] \bullet s^2 \qquad (9)$$

where s is given as

$$s = \log \frac{d_{84,3}}{d_{50,3}} \qquad (10)$$

In this equation D_1 is the diameter of the continuous melt jet before reaching the gas jets (i.e. the zone of disintegration) and u is the velocity difference between both types of jets at this zone. Because it is difficult to measure these terms one may use D_o instead of D_1, i.e. the diameter of the exit of the crucible/tundish, and one has to make assessments for the velocity difference.

As mentioned above the melt jet rarely exceeds velocities at the disintegration zone of more than 20 m/sec, whereas the gas streams may reach more than the 10-fold value, because the gas jets normally are operated at velocities somewhat below the sound velocity. It's now depending on the distance between the disintegration zone and the gas nozzle exits, Δz, as well

as on the characteristics of gas-velocity governed by the nozzle cross sections and the gas pressure prior to the nozzle exits of how strong the decline of the gas velocity will be along the distance z, see for instance paper [23] of these proceedings.

For the utilization of rotating elements for melt atomization one has a quite simple overall drop size equation:

$$d_{50,3} = C\ We_2^{-\frac{1}{2}}\ D_2 \tag{11}$$

with

$$We_2 = \frac{\rho_L\ w^2}{\sigma}\ \left(\frac{D_2}{2}\right)^3 \tag{12}$$

As can be seen from [9] there are - derived from experiments and from reports in the literature - factors C of 2.67 up to 6.55, the latter also given for molten metal, but aware of material constants. Often no information can be found whether the melt mass flow rate had been changed or not. (The angle j of the edge of the rotating plate - as can be seen from Fig. 3 - may influence the factor C.) As mentioned earlier, for melt atomization there will be of importance only the drop formation region directly from the edge of the rotating plate. This is why here are given only equations for this region.

Because of the similarity of the rotating elements compared with the rotary atomizers for conventional atomization and because of the same forces governing the disintegration processes it should at least in this context be allowed to cite one of the various equations which have been derived for aqueous or organic liquids, for instance those which have been discussed by [9]. One should expect that the deviations between metal melt atomization and conventional atomization could be explained by the material properties.

As also derived by [9] the size distributions mainly can be described by the log-normal type. While there is no information about the standard deviation, the $d_{50,3}$ diameter, which principally contains the described influences in the right manner, has been given as

$$d_{50,3} = 0.376\left(\frac{\eta_L}{\rho_L\ w}\right)^{\frac{1}{2}} We_2^{-\frac{1}{4}} \cdot \dot{V}^{*\,-0.07} \cdot Z^{-0.33}\ , \tag{13}$$

with $\dot{V}^*$ and Z given already in Table 2.

LOCAL DROP SIZE DISTRIBUTIONS AND VELOCITIY DISTRIBUTIONS IN METAL SPRAYS

The principles of rapid quenching or of spray - or of plasma - deposition make it necessary to posses of detailed knowledge of the multi-phase-flow situation in the spray cone (of gas, plasma, melt droplets, solidified particles) in order to describe and control the flow field generated by the atomizer. Research programmes are concerned with the laws which govern the particle transport onto a shaped collector (mold, substrate or preform), and with the phenomena together with the mechanical processes of particle impact, particle flattening and welding together, and last but not least with the overall heat transfer and solidification process of the droplets.

For a stationary spray casting process (as sketched in Fig. 8) there are mainly six independent process parameters which govern the spray process and which must be optimized and controlled: The melt temperature, its effluent velocity and its mass flow rate describe the material delivery and its flow situation before comminution. The gas mass flow rate and its pressure govern the gas jets which leave the ring nozzle and bounce against the melt stream. These parameters guide the disintegration process, which results in an overall droplet size distribution. This is given by eqs. (5), (8) and (9), if the relative velocity difference between the melt stream and the gas jets at the disintegration zone and the material properties of gas and

melt are known. Now the droplets are accelerated by the carrier gas towards the substrate. Here they impinge and consolidate completely to form a bulk-net or near-net shape. The stand-off distance between the atomization point and the substrate is important for the flow situation of the multi-phase flow in the spray and the heat transfer efficiency between the particles and the carrier gas up till the moment of impact. This distance therefore governs the temperature and the status (liquid or solidified) of the particles directly before impact.

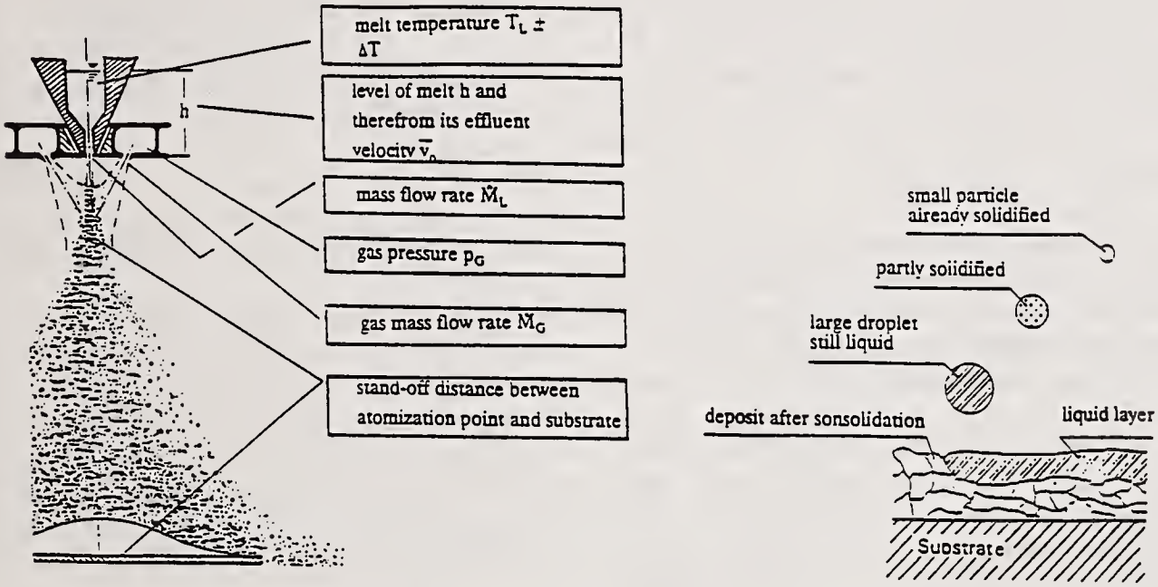

Fig. 8 Stationary spray casting process with six independent parameters; impact situation on the right

In order to guarantee successful operation an uniform distribution of the fractions of still liquid droplets and already solidified ones on the substrate should be attaint. This has to be observed by the on-line measurements of velocity- and size distributions of droplets in the spray as a part of a process model of the atomization and the multiphase flow situation (i.e. the mass- and momentum-balances) which also give the basis for the corresponding heat balance. In [24] have already been described the principles of a numerical simulation model especially for the Osprey process including the model for the heat transfer in the spray and the different solidification processes of larger and smaller droplets during their flight downwards. This simulation model has been adapted to the results of temperature and phase-Doppler (PDA)-measurements. The local velocity vectors of gas or droplets in the spray chamber can be seen from Fig. 5, the gas- and droplet velocities versus flight distance from Fig. 6 of paper [23] of these proceedings, the local mass fluxes of droplets, measured and calculated can be seen from Figures 4 to 6 of paper [25], also in these proceedings.

CONCLUSIONS

Having focused the discussion first onto the gas atomization it can in general be said that the necessity to introduce sufficiently high momentum forces in order to guarantee a satisfactory fine pulverization by means of the gas streams requires high mass flow rates and high velocities of the gases and hence high Reynold-numbers, i.e. immense turbulence ratios. (This turbulent disintegration process cannot yet be described theoretically nor can the equations be deduced which describe the drop sizes or size distributions generated by these turbulence forces.) After joining, the gas streams form a common jet stream and create a flow field that is

similar to those which are well known from free jets [25], loaded in our case with the dispersed melt phase, mostly accompanied by high densities.

In comparison with the conventional atomization the problems of melt conduction seem to simplify the situation by reducing the types of applicable atomizers. This also holds for attributing the complicated two phase flows to the free jet stream and in addition for having only one important drop size correlation (eq. (5) to (10) of Lubanska [22]) till now which fairly governs the gas atomization scenario and most metal powder size distributions.

On the other hand it has to be remembered that in general there exists no information about the difference velocity between the gas jets and the melt jet near the disintegration zone (needed in eq. (6)). Further the exact material properties (i.e. the density, the kinematic viscosity and mainly the surface tension) are very often unknown. If we rush to a conclusion this would make it trivial to use the formula for the overall particle size. But keeping in mind the extremely helpful special feature of melt atomization (which by its product generates an alibi for an assessment of the process, i.e. the powder metal which can be taken as local or overall samples, which can be screened and which provides the necessary size distribution) there is support for changing the operating conditions for a given atomizer in a very successful manner and nevertheless to utilize therefore the equations (5) to (10)!

Now considering the rotary atomizers and their very similar design compared with the conventional atomizers, one should be allowed to speak of similar or identical equations that describe the drop generation phenomena as well as the overall drop size. But the attempts to describe melt atomization by the equations derived for the conventional atomization seem to be successful only for the region of drop formation directly from the edge of the rotating plate. An explanation can be found in what has been said in regard to the deficit knowledge about the material properties. This is the cause why also in the case of rotary atomization (for a given design) the equations can be successfully used only for relative alterations of the operating conditions after having fixed the type of melt stream.

These results can be generalized also for the ultrasonic atomizers and for the secondary atomization of impacting drops. Only under very special preconditions, for instance where pure or well known metal melts or glass melts have to be atomized, the material properties are well established or given in tables versus melt temperature. (These are opportunities to check the above mentioned equations for their validity.)

With regard to the more common case where the material properties have to be extrapolated or interpolated or where have to be made assumptions there can be received important results from model experiments (from model melts and for fixed atomizer types and geometries). In this case it would be very helpful, if results of model experiments with for instance water (and air) were available. But here the problem arises that water droplets coalesce and tend to evaporate after atomization (i.e. losing their alibi); which in the past made it nearly impossible to compare results from the same atomizer obtained from extremely different liquids.

Here the development of new instruments, for example of the PDA and of very short lightning imagination techniques open an interesting field of future research work. The PDA especially seems to be able to provide quasi on-line results from metal melt atomization as well as from water atomization thus permitting the crossing of the bridge from conventional atomization to metal melt atomization and melt spraying and to answer the questions for a generalized theory for all types of liquids under the task of atomization.

List of Symbols

A	Constant factor in eq. (3)	v_G	Gas velocity
B	Constant factor in eq. (5) and (7)	v_d	Particle velocity
C	Constant factor in eq. (12)	$\overline{v_o}$	Melt velocity in eq. (1)
d	Drop diameter	v_3	Impact velocity in eq. (4)
$d_{50,3}$	Drop diameter (50 %) of volume-dist.	$\dot{V}$	Volume flow rate of melt after Table 2
D_o	Diameter of bottom exit in tundish	$\dot{V}^*$	Dimensionless volume flow rate of melt
D_2	Diameter of rotary atomizer	Z	Dimensionless factor after Table 2

g	Acceleration due to earth	α	Angle of inclination of gas jets versus melt
h	Level of melt above exit of tundish	β	Effluent factor in eq. (1)
$\dot{M}_G$	Gas mass flow rate	η_L	Dynamic viscosity of melt
$\dot{M}_L$	Melt mass flow rate	ν_L	Kinematic viscosity of melt
Δp	Pressure difference	ν_G	Kinematic viscosity of gas
q	Size distribution, vol.fraction in eq.(8)	σ	Surface tension of melt/gas
R	Cummulative weight oversize in eq. (8)	ρ_L	Density of melt
T	Temperature of melt	ω	rotational speed of atomizer
T_L	Melting temperature	We_1	Weber-number in eq. (5) and (6)
ΔT	temperature difference	We_2	Weber-number after Table 2 and eq. (11)
u	Velocity difference in eq. (6)	We_3	Weber-number in eq. (4)

References

1. Lawley A., Doherty R.D., "Atomization Models and Mechanisms in Advanced High-Temperature Alloys" in N. Grant Symp. 1985 Mass. Am. Soc. for Metals
2. Mehrotra P.S., "Mathematical Modelling of Gas Atomization Process for Metal Powder Production", Part 1, Powd. Met. Int. Vol 13 No 2 (1981) 80-84, Part 2 ibidum, 3, 132-135
3. Savage S.J., Froes F.M., "Production of Rapidly Solidified Metals and Alloys" J. of. Metals April (1984) 20-33
4. Lefebvre A.H., "Properties of Sprays" Particle & Part. Syst. Charact. 4 (1989) 176 - 186
5. Grassmann P., "Physikalische Grundlagen der Verfahrenstechnik" Salle & Sauerlander Frankfurt/Main (1983)
6. Ruthardt R., "Basic Characteristics of LAB-Scale Argon Atomization Units"; Mod. Developm. in Powder Metall. Vol. 15-17 (1985) 67-72
7. Lewis R.E., Fitzpatrick J.M., Crooks D.D., Singer A.R.E., Jenkins W.N., "A Novel Approach for Rapid Solidification Processing of High Strength PM Aluminum Alloys", SAE Technical Paper Series 841514, Aerospace Congress & Exposition, L.B. Cal. Oct. 15-18 (1984) 27-33
8. Schellenberg R., "Zerstäubung von Metallen, insbesondere von Zink", Diss. T.H. Stuttgart (1964)
9. Mehrhardt E., "Zerstäubung von Flüssigkeiten mit rotierenden Scheiben", Diss. TU Berlin 1978
10. Dombrowski N., Lloyd T.L., "Atomization of liquids by spinning cups", Chem. Engng. J. 8 (1974) 1, 63-81
11. Dunskii V.F., Nikitin N.V., "Monodisperse atomization of a liquid by a rotating disc", JH. Engng. Phys. 23 (1972) 5, 1474-1475
12. Matsumoto S., Saito K., Takashima Y., "Phenomena Transition of Liquid Atomization from Disk", J. Chem. Engng. Japan 7 (1974) 1, 13-19
13. Tanasawa Y., Miyasaka Y., Umehara M., "On the filamentation of liquid by means of rotating discs", Trans. Soc. Mech. Eng. Japan 25 (1959) 879-905
14. Hinze J.O., Milborn H., "Atomization of liquids by means of a rotating cup", J. Appl. Mech. 17 (1950) 145-153
15. Bendig L., "New Developments of Ultrasonic Atomizers", Proc. of the 4th Int. Conf. on Liquid Atomization and Spray Systems, August 22-24, 1988, Sendai, Japan
16. Bauckhage K., Schreckenberg P., "Control of Powder-Metal Production; A New Application of Phase-Doppler-Anemometry"; Intern. Conf. on Mechanics of Two-Phase-Flows, 12.-15.6.1989, Taipei/Taiwan, ROC, Proc.
17. Walzel P., "Zerteilgrenze beim Tropfenprall", Chem.-Ing.-Tech. 52 (1980) 4, 338-339
18. Geropp D., "Die Berechnung reibungsbehafteter Strömungen in Lavaldüsen mit Anwendungen" Manuskript eines Kolloq.-Vortrages am ..... 1990 in Bremen sowie
Walz A., "Entwicklung eines Verfahrens zur Herstellung keramischer Fasern", BMFT-Bericht NT 321 Juli 1974

19. Meringolo V., "Stop Tube Corrosion and Wear in Coal-fired Power Boilers", Power-magazine, May 1981, Mc Graw-Hill, Inc.
20. Anonymus, "Advanced Plasma Gun", bulletin No. 283 of Metco, Percin Elmer Westbury, Long Island N.Y.
21. Schmidt P., "Zerteilen von Flüssigkeiten in gleich große Tropfen"; Chem.-Ing.-Tech. 39 (1967) 5/7, 375-379
22. Lubanska H., "Correlation of Spray Ring Data for Gas Atomization of Liquid Metals", J. of Metals (1970) 45-49
23. Fritsching U., Liu H.-M., Bauckhage K., "Numerical Modelling in the Metal Spray Compaction Process"; paper presented on ICLASS '91, included in these proceedings
24. H. Liu: "Berechnungsmodelle für die Geschwindigkeiten und die Abkühlung von Tropfen im Sprühkegel einer Stahlzerstäubungsanlage"; Diss. Universität Bremen, Febr. (1990)
25. Uhlenwinkel V., Fritsching U., Bauckhage K., "The Influence of Spray Parameters on Local Mass Fluxes and Deposit Growth Rates During Spray Compaction Process", paper presented on ICLASS '91, included in these proceedings

Keynote Lecture

TWIN-FLUID ATOMIZATION: FACTORS INFLUENCING MEAN DROP SIZE

A.H. Lefebvre

School of Mechanical Engineering, Purdue University
West Lafayette, IN, U.S.A.

ABSTRACT

The principal factors governing the mean drop sizes produced by twin-fluid atomizers are examined. It is shown that atomization may occur by one of two different mechanisms. For both "classical" and "prompt" modes of atomization, the principal factors governing the fineness of atomization are air velocity, air/liquid ratio, and surface tension. For the classical mechanism of breakup, involving flow instabilities and wave formation, atomization occurs slowly and is strongly influenced by variations in liquid viscosity, air density, and the initial diameter (or thickness) of the liquid jet (or sheet). If atomization occurs very rapidly, these parameters have little effect on mean drop size.

INTRODUCTION

The description "twin fluid atomizer" can be applied to any device in which the driving force for liquid breakup is either air, gas, vapor, or even another liquid. The following discussion will be confined to the atomization of liquids by gases which, for convenience, will be referred to henceforth as air. Most twin-fluid atomizers fall into the categories of "air-assist" or "airblast," the main difference between them being that the former use relatively small quantities of air or steam flowing at very high velocities (usually sonic), whereas the latter employ large amounts of air flowing at much lower velocities of around 100 m/s. Airblast nozzles are thus ideally suited for atomizing liquid fuels in continuous-flow combustion systems, such as gas turbines, where air velocities of this magnitude are usually readily available. The most common form of airblast atomizer is one in which the liquid is first spread into a thin conical sheet and then exposed to high-velocity airstreams on both sides of the sheet. The atomization performance of this *prefilming* type of airblast nozzle is superior to that of the alternative *plain-jet* airblast nozzle, in which the liquid is injected into the airstream in the form of one or more discrete jets [1].

In recent years, considerable interest has been aroused in an alternative method of twin-fluid atomization in which a gas (usually air) is injected into the bulk liquid at some point upstream of the nozzle discharge orifice. The injected gas forms bubbles which produce a two-phase flow at the injector orifice. The liquid flowing through the injection orifice is "squeezed" by the gas bubbles into thin shreds and ligaments. When the bubbles emerge from the nozzle they "explode", thereby shattering the surrounding liquid into small drops.

This paper examines the factors governing the mean drop sizes produced by twin-fluid atomizers. Attention is focused primarily on the effects of air and liquid properties on mean drop size. It is shown that at least two different mechanisms may be involved in airblast atomization. Recognition of these different mechanisms helps to explain some of the apparent anomalies that exist in the atomization literature. It will be shown that the effects of certain air and liquid properties on mean drop size may be large or insignificant depending on the mode of atomization. These considerations open up the possibility of designing airblast atomizers specifically to employ either one or the other of these two different modes of atomization, depending on which is best suited for any given application.

CONVENTIONAL TWIN-FLUID ATOMIZATION

During the past 25 years airblast and air-assist atomizers have been subjected to considerable experimental study. An early investigation on prefilming airblast atomization by Rizkalla and Lefebvre [2] led to the following dimensionally-correct equation for the Sauter mean diameter (SMD).

$$SMD = 3.33 \times 10^{-3} \frac{(\sigma \rho_L t)^{0.5}}{\mu_A U_A}(1 + 1/ALR) + 13.0 \times 10^{-3}\left(\frac{\mu_L^2}{\sigma \rho_L}\right)^{0.425} t^{0.575}(1 + 1/ALR)^2 \quad (1)$$

An interesting feature of this equation is that the SMD is directly related to the initial thickness of the liquid sheet, t. For liquids of low viscosity, SMD α $t^{0.5}$. For liquids of high viscosity, the dependence of mean drop size on t is slightly higher.

A drawback to Eq. (1) is that t is usually unknown and difficult to estimate. This problem is avoided in the following "basic" equation for the mean drop sizes produced by prefilming airblast atomizers [1]

$$\frac{SMD}{L_c} = \left[A\left(\frac{\sigma}{\rho_A U_A^2 D_p}\right)^{0.5} + B\left(\frac{\mu_L^2}{\sigma \rho_L D_p}\right)^{0.5} \right] [1 + 1/ALR] \qquad (2)$$

where A and B are constants whose values depend on the atomizer design and must be determined experimentally.

Equation (2) shows that the SMD is proportional to a characteristic dimension L_C, which represents the linear scale of the atomizer. It also shows that mean drop size is inversely proportional to the square root of the prefilmer diameter D_p. This is consistent with Eq. (1) because, if other parameters are kept constant, an increase in D_p will reduce the liquid sheet thickness t, and hence the SMD. It will merely be mentioned here, and discussed more fully later, that the strong dependence of SMD on t, as expressed explicitly in Eq. (1) and embodied in Eq. (2), is not always observed in practice. For some atomizers, it is found that the influence of initial sheet thickness on SMD is small, which tends to suggest that the mechanism whereby a liquid sheet is converted into drops may differ from one atomizer design to another.

Influence of Air Properties

Perhaps the least controversial aspect of airblast atomization is the role played by atomizing air velocity. A unanimous conclusion from all experimental studies on airblast atomization is that air velocity has an important and sometimes overiding effect on the drop size distributions in the spray. Generally, it is found that mean drop size is roughly inversely proportional to atomizing air velocity, i.e. SMD α U^{-1}, although the literature contains values of velocity exponents varying from -0.75 to -1.33. It is important to bear in mind that the velocity of most relevance to airblast atomization is not the absolute velocity of the atomizing air but rather the relative velocity between the atomizing air and the liquid jet or sheet. This point is well brought out in the results obtained by Suyari and Lefebvre {3} who used an external-mixing, air-assist nozzle of the type shown in Fig. 1, which comprises a simplex, pressure-swirl nozzle surrounded by a co-flowing stream of swirling air.

Fig. 2 exhibits some interesting features which appear to be characteristic of this type of atomizer. First, it shows that an increase in ΔP_A, which corresponds to an increase in atomizing air velocity, has a beneficial effect on atomization quality, especially at low liquid flow rates. Of more interest, however, is the observation that, for all values of ΔP_A, SMD increases with increase in liquid flow rate until a maximum value is reached, beyond which any further increase in $\dot{m}_L$ causes SMD to decline. The unusual shape of this curve can be explained in terms of the relative velocity between the conical sheet of liquid produced by the simplex atomizer and the surrounding coflowing air. At low liquid flow rates, the device operates primarily as an airblast atomizer, and any increase in liquid flow rate impairs atomization quality, despite the increase in liquid injection pressure, by reducing both the air/liquid ratio and the relative velocity between the air and the liquid. At the peak of the curve, where the mean drop size attains its maximum value, the relative velocity and hence the interaction between the liquid sheet and the surrounding air is minimal. Beyond this point the device functions mainly as a pressure atomizer, and any increase in liquid flow rate serves to improve atomization by increasing the liquid injection pressure and hence the relative velocity between the liquid and the air.

In most practical forms of air-assist atomizer, the air and the liquid issuing from the nozzle have both radial and tangential as well as axial components of velocity. In this complex two-phase flow field the term "relative velocity" is difficult to define. Nevertheless, for any given air velocity there will always be one particular value of liquid velocity at which the level of interaction between the liquid and the air is a minimum. An increase in atomizing air velocity will cause the condition of minimum relative velocity to occur at a higher level of liquid velocity. Thus one would expect the value of $\dot{m}_L$ at which the SMD attains its maximum value to increase with increase in $\Delta P_A/P_A$, and this is indicated by the dashed line drawn in Fig. 2. These results underline the importance of relative velocity in the airblast atomization process.

Another important factor influencing atomizer performance is the air/liquid mass ratio. With conventional airblast atomizers, atomization performance starts to decline when the ALR (air/liquid ratio) drops below around 3, and deteriorates quite rapidly at ALR's below about 1.5. At ALR's higher than about 5, only marginal reductions in SMD are gained by the utilization of more air in atomization. This is because air which is physically far removed from the liquid cannot play an effective role in the atomization process. For this reason, it is customary in equations for mean drop size to express the dependence on air/liquid ratio as SMD α $[1 + 1/ALR]^n$, where n has values

ranging from 0.4 to 1.0. This expression allows the influence of ALR on mean drop size to diminish with increase in ALR, in accordance with experimental observations.

Influence of Initial Sheet Thickness

In their early studies on prefilming airblast atomization, Lefebvre and Miller [4] stressed the importance of spreading the liquid into the thinnest possible sheet before exposing it to the atomizing air, arguing that "any increase in the thickness of the liquid sheet flowing over the prefilmer lip will tend to increase the thickness of the ligaments which, upon disintegration, will then yield drops of a larger size."

Subsequently, Rizk and Lefebvre [5] conducted tests to examine the effect of initial liquid sheet thickness on the drop sizes produced by prefilming airblast atomizers. They employed a specially-designed airblast atomizer in which a flat liquid sheet was produced across the centerline of a two-dimensional air duct, with the liquid sheet exposed on both sides to high velocity air (see Fig. 3a). This atomizer was designed with the capability of varying the initial liquid sheet thickness in order to examine its influence on atomization quality. The results obtained showed that thicker liquid sheets resulted in coarser sprays. Measurements of mean drop size carried out over wide ranges of air velocity, air/liquid ratio, and initial sheet thickness, indicated that the effect of sheet thickness on mean drop size could be expressed as $SMD \propto t^x$, where x has a mean value of 0.38. This result was considered to be consistent with Eqs. (1) and (2) and generally supportive of the classical wavy-sheet mechanism for liquid sheet disintegration, as postulated theoretically by Squire [6] and Fraser et.al. [7], which leads to the relationship $SMD \propto t^{0.5}$. Some of the results obtained by Rizk and Lefebvre [5] on the influence of t on SMD are shown in Fig. 4.

Other workers have also observed an appreciable effect of initial liquid sheet thickness on mean drop size. For example, Inamura and Nagai [8] in their performance comparison of various types of airblast atomizers noted that "SMD is nearly proportional to the film thickness at the point of impingement of the liquid film and the air stream." Zhao and Gan [9] examined the influence of initial sheet thickness on the mean drop sizes produced by a prefilming airblast atomizer. Their results for kerosine are shown in Fig. 5. According to Zhao and Gan, these data indicate that $SMD \propto t^{0.39}$, which is remarkably close to the findings of Rizk and Lefebvre, as noted above. However, close inspection of the experimental data in Figs. 4 and 5 reveals that the dependence of mean drop size on initial sheet thickness diminishes with increase in atomizing air velocity. This trend was also observed by Beck et.al [10,11] who employed a two-dimensional flat-sheet atomizer, shown schematically in Fig. 3b, to study the influence of sheet thickness on mean drop size. They also found that the effect of t on SMD diminishes with increase in atomizing air velocity, as illustrated in Fig. 6.

In all these studies, the initial liquid sheet thickness was found to influence the mean drop size in the spray. The magnitude of this influence varied appreciably with atomizing air velocity, but in all cases an increase in sheet thickness was accompanied by an increase in mean drop size. Contrasting results were obtained by Wittig and his co-workers [12,13] who found no effect of sheet thickness on mean drop size. They attributed this result to the fact that in their atomizer the liquid does not flow continuously over the atomizing edge but is stored in the wake of the edge in the form of a bulge. This bulge increases in thickness until the aerodynamic forces exceed the surface forces, at which point the bulge disintegrates into ligaments and then drops.

Consideration of these and other apparent anomalies in the atomization literature suggest that the disintegration of the liquid sheet into drops may not always occur via the classical wavy-sheet mechanism. According to this mechanism, waves are formed which protrude into the coflowing air stream. The most rapidly growing wave becomes detached from the leading edge of the sheet to form a ligament which subsequently breaks down into drops. The size of these drops is directly related to the diameters of the ligaments from which they are formed. These ligament diameters, in turn, are dependent on sheet thickness, so there is a very direct relationship between the mean drop size of the spray and the initial sheet thickness, as postulated theoretically by Dombrowski et al. [7,14] and demonstrated experimentally by Rizk and Lefebvre [5] and Zhao and Gan [9]. An essential prerequisite for wavy-sheet formation is sufficient time for the waves to develop. In many cases ample time is available, because the air and liquid are coflowing (see Fig. 3a, for example) and there is no significant component of air velocity in a direction which could promote rapid disintegration of the liquid sheet. If, however, the atomizing air is arranged to impinge on the liquid sheet at an appreciable angle, as illustrated in Fig. 3b, it now has a sizeable transverse component of velocity. In consequence, the liquid sheet emerging from the nozzle has no time to develop a wavy structure but is instead rapidly torn into small fragments by the vigorous interaction created between the liquid and the impinging air jets. The maximum critical size of the liquid fragments produced in this *prompt* atomization process is governed primarily by the magnitude of the air velocity component normal to the liquid sheet, the air/liquid mass flow ratio, and the surface tension. An essential feature of this mode of atomization is that the rapid and violent disruption of the liquid sheet into drops ensures that the ensuing drop sizes are much less dependent on the initial sheet thickness. This could serve to explain the different results obtained by different workers on the effect of initial liquid sheet thickness on mean drop size.

Analysis

If atomization occurs very rapidly just downstream of the atomizing edge, the flow instabilities which normally precede wave formation have no time to develop. Sheet breakup occurs so rapidly that the mean drop sizes produced in atomization are governed solely by the ratio of the kinetic energy of the atomizing air to the energy required to overcome the consolidating surface tension forces. This hypothesis leads to the following expression for mean drop size [15]

$$SMD = \frac{3}{\left[\frac{1}{t} + \frac{C\,\rho_L U_A^2}{4\sigma(1 + 1/ALR)}\right]} \qquad (3)$$

in which the constant C represents the ratio of the energy required for atomization to the kinetic energy of the atomizing air. For a flat-sheet airblast atomizer, the data of Beck et.al. [10,11] indicate a value for C of 0.0070. Thus Eq. (3) may be rewritten as

$$SMD = \frac{3}{\left[\frac{1}{t} + \frac{0.00175\ \rho_L U_A^2}{\sigma(1 + 1/ALR)}\right]} \qquad (4)$$

or, more basically, as

$$\frac{SMD}{t} = \frac{3}{\left[1 + \frac{0.00175\ We}{(1 + 1/ALR)}\right]} \qquad (5)$$

Where $We = \rho_L U_A^2\, t/\sigma$

Equation (4) has some interesting features. For example, at the normal operating conditions of most practical airblast atomizers, the second term in the denominator is always appreciably higher than the first. This explains why in Beck et. als'. [10] experiments the SMD was found to be fairly insensitive to variations in liquid sheet thickness. Equation (4) also predicts that the dependence of SMD on t should diminish with increase in U_A, as observed experimentally by Zhao and Gan [9] and Beck et. al [10] .

Another interesting feature of Eq. (4) is the absence of any term to represent liquid viscosity. Normally, with coflowing airblast atomizers, an increase in liquid viscosity has two adverse effects on atomization quality. First, it tends to increase the thickness of the liquid sheet formed at the atomizing edge which, for this type of atomizer, produces an increase in mean drop size. Second, an increase in viscosity hinders the development of any natural instabilities in the liquid sheet. This delays the disintegration process so that when breakup finally occurs it does so under conditions that are less conducive to atomization. In extreme cases, the breakup time may be extended so much that little or no breakup occurs, even though the initial aerodynamic force was large enough to produce breakup.

Measurements carried out by different workers using various types of coflowing airblast atomizers almost invariably show a significant effect of liquid viscosity on mean drop size. The results of these investigations have been summarized elsewhere [16]. However, in other types of atomizers in which the air and liquid are not coflowing, but instead the impact of the atomizing air on the liquid is such as to promote prompt atomization, it is found that mean drop size is much less dependent on viscosity. For example, Fig. 7 shows results obtained by Beck et. al. on the influence of viscosity on mean drop size. They show that increasing the liquid viscosity by a factor of more than thirteen produced only a 16 percent increase in SMD, i.e. $SMD \propto \mu_L^{0.06}$. A similar result was obtained by Sattelmeyer and Wittig [12]. These workers studied prefilming airblast atomization under conditions where "the disintegration of the liquid film always takes place close to the atomizing edge, regardless of the liquid's properties," i.e. under conditions which might reasonably be described as "prompt." They found that liquid viscosity had no effect on SMD, which agrees both with the findings of Beck et.al. [10] and with predictions based on Eq. (4). Another example of the insensitivity of mean drop size to variations in liquid viscosity is provided in the results obtained by Kennedy [17] who carried out a comprehensive series of tests on twenty-five different hydrocarbon fuels, using six different pressure-swirl nozzles of large flow number. In contrast to all previous work on pressure-swirl nozzles, Kennedy found no effect of viscosity on mean drop size. The only essential difference between Kennedy's investigation and those of previous workers is that his measurements of SMD were carried out on nozzles operating at exceptionally high Weber numbers (>10) i.e. under conditions of very rapid sheet breakup. These results are fully

consistent with Eq. (5) which predicts that when the Weber number is high the mean drop size is independent of liquid viscosity.

Another interesting feature of Eq. (5) is that for very high Weber numbers the mean drop size should be directly proportional to surface tension. This is exactly the result obtained by Kennedy. Sattelmeyer and Wittig also observed a pronounced effect of surface tension on SMD. They reported that atomization characteristics were "drastically improved" by an almost three-fold reduction in surface tension, Beck et.al. also noted a strong effect of surface tension on mean drop size, as illustrated in Fig. 8. Thus, ample results are available to support the validity of Eqs. (4) and (5) for conditions of prompt atomization.

According to Eq. (4) air density has no influence on mean drop size. Most previous work on prefilming airblast atomizers has shown a density dependence which is usually expressed as SMD α ρ_A^z with values of z ranging from 0.5 to 0.7. However, over a range of air densities from 1.2 to 6.0 kg/m^3, Beck et.al. [11] found no effect of SMD on ρ_A, which confirms that when the airblast atomization process occurs very rapidly, air density has little or no effect on mean drop size.

The results of the various studies outlined above show that when sheet breakup occurs too rapidly to permit the development of waves and other flow instabilities that normally precede atomization, the mean drop size in the spray is strongly dependent on surface tension, largely independent of liquid viscosity and ambient air density, and only slightly dependent on the initial sheet thickness. These experimental observations are in complete agreement with the predictions of Eq. (4) which was derived on the assumption that the liquid issuing from the atomizer is converted into droplets without the help or intervention of flow instabilities and wave formation.

Plain-Jet Airblast Atomization

In many practical airblast atomizers the liquid is injected into the high-velocity air stream in the form of one or more discrete jets. Similar arguments to those employed above for flat-sheet atomizers yield the following equation for the mean drop sizes produced under conditions of "prompt" atomization.

$$\frac{SMD}{d_0} = \frac{1.5}{\left[1 + \frac{C'We}{(1 + 1/ALR)}\right]} \qquad (6)$$

where $We = \rho_L U_A^2 d_0/\sigma$ and C' is a constant which includes a term to represent the energy efficiency of the atomization process and must be determined experimentally.

Equation (6) again illustrates that under conditions of high Weber number the mean drop size becomes independent of air density and initial liquid jet diameter. It also serves to explain some of the anomalies that exist in the literature on plain-jet airblast atomization. For example, Nukiyama and Tanasawn [18], using an atomizer in which the atomizing air impacted the liquid jet at an angle of almost 90°, thereby causing rapid jet breakup, found no effect of ρ_A and d_0 on SMD, in accordance with Eq. (6), whereas Rizk and Lefebvre's [5] results for a coflowing air stream exhibited a strong influence on mean drop size of both ρ_A and d_0, ($SMD \alpha d_0^{0.6}/\rho_A^{0.4}$).

The conclusion to be drawn from these various studies on both plain-jet and prefilming airblast atomizers is that for both types the dependence of mean drop size on initial jet diameter (or sheet thickness) and ambient air density is governed by the rapidity of the atomization process. If the atomizing air impacts the liquid at an appreciable angle, of if coflowing atomizing air encounters the liquid at high velocity, breakup occurs very rapidly and the ensuing atomization process is characterized by a lack of sensitivity of mean drop size to the initial diameter (or thickness) of the liquid stream and to air density. If, however, the atomizing air is flowing at a relatively low velocity and in generally the same direction as the liquid, the atomization process occurs more slowly, via a different mechanism, with the result that drop sizes become much more dependent on the physical dimensions of the liquid stream and the ambient air density.

MECHANISMS OF AIRBLAST ATOMIZATION

The experimental evidence cited above suggests that airblast atomization occurs by one of two different mechanisms, depending on the time available. If ample time is available, the breakup process follows the classical mechanism whereby instabilities are created within or on the surface of the liquid jet or sheet which promote the formation of waves that subsequently break down into ligaments and then drops. Liquid viscosity delays the onset of wave formation and opposes ligament breakup. Thus an increase in viscosity is always accompanied by an

increase in mean drop size. If, however, the bulk liquid is shattered almost instantaneously into droplets as soon as it leaves the nozzle and becomes exposed to the atomizing air, then waves and ligaments have no time to form and the delaying action normally exerted by viscosity has no opportunity to manifest itself. Under these conditions of "prompt" atomization, viscosity and initial sheet thickness have little effect on mean drop size.

For both mechanisms, the mean drop size depends on atomizing air velocity, air/liquid ratio, and surface tension. For the wavy-sheet mechanism, the mean drop size is also strongly dependent on the initial liquid dimensions (jet diameter or sheet thickness), liquid viscosity, and air density. For the prompt mechanism, the mean drop size is much less dependent on the liquid jet diameter or sheet thickness, and completely independent of liquid viscosity and air density.

For any given atomizer, the dominant mode of atomization will be governed largely by its design features and operating conditions. As discussed above, if the atomizing air and liquid are coflowing, then, unless the atomizing air velocity is exceptionally high, the wavy-sheet mechanism will dictate the atomization process. On the other hand, if the atomizing air impacts the liquid jet or sheet at an appreciable angle, or at a velocity which precludes wave formation, then the prompt mode of atomization will dominate.

Under certain operating conditions it is possible that both mechanisms may play a role in the overall atomization process. For example, atomizers which are normally characterized by the "prompt" mode of atomization will switch to the "classical" mode of atomization if either the atomizing air velocity or the air/liquid ratio are reduced so far below their normal operating values that sufficient time is available for wave formation to occur. At this point the mean drop size will start to become dependent on initial jet diameter or sheet thickness, liquid viscosity, and air density.

EFFERVESCENT ATOMIZATION

The atomizers discussed above have one important feature in common, namely, the bulk liquid to be atomized is first transformed into a jet or sheet before being exposed to the atomizing air. In effervescent atomization, the atomizing air is introduced directly into the bulk liquid at some point upstream of the nozzle discharge orifice. As this air is not intended to impart kinetic energy to the liquid stream, it is injected at low velocity, so that the pressure differential between the air and the liquid is very small, and only what is needed to persuade the air to enter the flowing liquid. The injected air forms bubbles which are conveyed by the liquid stream to the injection orifice, downstream of which the bubbles 'explode' thereby shattering the surrounding liquid into small drops.

For this type of atomization, it is reasonable to assume that the mean drop sizes produced should be related to the average distance between the bubbles in the plane of discharge from the injector orifice. If the average liquid thickness between adjacent gas bubbles is denoted as t_B, then, from simple geometric considerations, it can be shown that

$$t_B = d_A \left\{ \left[\frac{\pi}{6} \left(1 + \frac{C^* \rho_A}{\rho_L \, ALR} \right) \right]^{1/3} - 1 \right\} \qquad (7)$$

where d_A is the average diameter of the air bubbles, ALR is the air/liquid ratio by mass, and ρ_A and ρ_L are the air and liquid densities, respectively.

The value of C* in Eq. (7) depends on the manner in which the gas bubbles are distributed throughout the two-phase medium. If the bubbles are spherical in shape, all the same size, and aligned in rows, the value of C* is unity. If the spherical bubbles are all the same size and so closely packed that the volume of liquid in the intervening spaces is the minimum geometrically possible, then the value of C^* in Eq. (7) becomes 2.6. For this bubble packing geometry, the maximum air/liquid ratio for operation in the bubbly flow regime is given by

$$ALR_{max} = 2.85 \; (\rho_A / \rho_L) \qquad (8)$$

In practice, a wide range of bubble sizes may be generated so that small bubbles occupy the spaces between larger bubbles. Analysis of Whitlow's [19] data for an effervescent atomizer operating over a range of pressures from 0.27 to 0.69 MPA yields a value for C* in Eq. (7) of 4.4. For this flow structure, the maximum air/liquid ratio for operation in the bubbly flow regime is obtained as

$$ALR_{max} = 4.80 \; (\rho_A / \rho_L) \qquad (9)$$

this relationship is illustrated in Fig. 9 for air bubbles in water at a temperature of 288K. This figure shows that, when operating at low injection pressures, i.e. low gas densities, the bubbly flow regime is confined to relatively low air/liquid mass ratios. Equation (9) indicates that replacing air with a gas of higher density would extend the bubbly flow regime to a higher gas/liquid ratio, and thereby improve atomization quality.

It is of interest to note in Eq. (7) that the average thickness of liquid between adjacent gas bubbles is independent of the injector orifice diameter, which suggests that the mean drop size in the spray should also be independent of the discharge orifice diameter. This is confirmed in the results obtained by Lefebvre, Wang, and Martin [20] and Roesler [21]. Roesler's results for water at pressure levels of 0.069, 0.137, 0.275, and 0.551 MPA are shown in Fig. 10. They clearly demonstrate that mean drop size is fairly insensitive to changes in discharge orifice diameter.

Roesler also studied the effect of air injector geometry on mean drop size, using a series of porous tubes of different porosity to inject atomizing air into flowing water. His results for aerator tubes having porosities of 20, 70, and 120 μm are shown in Fig 11. They illustrate that mean drop sizes are mainly dependent on operating pressure and air/liquid ratio and are largely unaffected by the manner in which the atomizing air is introduced into the flowing liquid stream

The fact that the atomizing performance of effervescent nozzles is largely independent of injector geometry is a most useful asset from a practical viewpoint. As discussed above, the discharge orifice diameter has little effect on mean drop size, an increase in orifice diameter serving merely to increase the flow capacity of the nozzle for any given operating pressure. Another important practical advantage of effervescent atomizers is their low discharge coefficient. If the air and liquid flow through the discharge orifice at the same velocity, the discharge coefficient of this orifice is given by

$$C_D = [1 + ALR\ (\rho_L / \rho_A)]^{-1} \qquad (10)$$

The variation of discharge coefficient with air/liquid ratio and operating pressure is illustrated in Fig. 12 for air-water mixtures. Typical values of discharge coefficient for conventional plain-orifice atomizers are between 0.62 and 0.8, depending on the length/diameter ratio of the discharge orifice. The values of discharge coefficient shown in Fig. 12 are clearly much lower, especially for high air/liquid ratios, where C_D values fall to around 0.1.

Energy Considerations

The nature of the effervescent atomization process suggests that the fineness of atomization should be related to bubble energy. For a stream of air bubbles to convert a jet or sheet of liquid into a fine spray they must possess enough energy to overcome the surface tension forces that hold the liquid together. Figure 13 shows SMD data obtained by Roesler [21] over wide ranges of operating pressure and air/liquid ratio as a function of bubble energy which is defined as

$$E = RT\ (\dot{m}_A / \dot{m}_L)\ \ln\ (P_A / P_L) \qquad (11)$$

At the high air/liquid ratios and high pressures corresponding to the right side of Fig. 13, the bubbles have sufficient energy to break the liquid into small droplets through bubble explosions. However, at low pressures and/or low air/liquid ratios, the effects of bubble expansion are greatly diminished. Under these conditions, the manner in which the bubbles enhance atomization is mainly by squeezing the liquid into thinner shreds and ligaments as it leaves the atomizer.

For effervescent atomizers operating at high pressures and/or high air/liquid ratios, the high bubble energy is manifested as a multiplicity of violent bubble explosions which rapidly disintegrate the liquid into a fine spray. For these conditions of prompt atomization, Eq. (4), can be rewritten as

$$\frac{SMD}{d_o} = \frac{1.5}{\left[1 + \dfrac{C\,\rho_L\,T_A\,(\Delta P_A/P_A)}{\sigma\,(1 + 1/ALR)}\right]} \qquad (12)$$

A significant feature of this equation is that mean drop size is shown to be independent of liquid viscosity. In this context it is of interest to note that Buckner et al. [22], who employed an aerated-liquid atomizer to examine the effects of variations in liquid properties on mean drop size, found virtually no effect of viscosity on SMD for liquids ranging in viscosity from 0.384 to 0.968 Ns/m. These results, shown in Fig. 14, provide further confirmation of the fact that when atomization takes place very rapidly the effect of liquid viscosity on SMD is small.

CONCLUSIONS

1. All the experimental evidence obtained on many different types of atomizers in which air is used as the principal driving force for atomization points to air velocity as the principal factor governing mean drop size. For low-viscosity liquids, the SMD is roughly inversely proportional to the atomizing air velocity. Unless the liquid injection velocity is negligibly small in comparison with the atomizing air velocity, it is the relative velocity between the two streams that governs the mean drop size.

2. The other major factor governing the fineness of atomization is air/liquid ratio. Most correlations for mean drop size embody the term [1 + 1/ALR]. This form of dependence on air/liquid ratio is consistent with experimental observations in showing that the effect of ALR on SMD is large for small values of ALR and diminishes with increasing ALR.

3. The influence of liquid jet diameter or sheet thickness on mean drop size depends on the mode of atomization. For relatively slow mechanisms of atomization, involving flow instabilities and wave formation, mean drop sizes are roughly proportional to the square root of the initial liquid dimension. If atomization occurs very rapidly, the mean drop size is much less dependent on jet diameter or sheet thickness.

4. If atomization proceeds fairly slowly, the effect of air density can be expressed as SMD α ρ_A^{-n}, with reported values of n varying between 0.3 and 0.6. For prompt atomization, Eqs. (4) and (5) predict no effect of ρ_A on SMD.

5. Mean drop sizes increase with increasing surface tension, regardless of the mode of atomization. For the classical mechanism of jet or sheet breakup, SMD α σ^x, where x usually lies between 0.25 and 0.5. For prompt atomization, the dependence of mean drop size on surface tension is much stronger, especially at high values of Weber number where the mean drop size becomes directly proportional to the surface tension.

6. The well-known adverse effect of an increase in liquid viscosity on atomization quality applies only to the classical mechanisms of jet and sheet breakup. For prompt atomization, the mean drop size is largely independent of viscosity.

REFERENCES

1. A.H. Lefebvre, Airblast Atomization, Prog. Energy. Combust. Sci. vol. 6, pp. 233-261, (1980).

2. A.A. Rizkalla and A.H. Lefebvre, The Influence of Air and Liquid Properties on Airblast Atomization, ASME J.Fluids Eng., vol. 97, no. 3, pp. 316 - 320, (1975).

3. M. Surayi and A.H. Lefebvre, Drop-Size Measurements in Air-Assist Swirl Atomizer Sprays, Paper CSS/CI 86-5D1, Spring Technical Meeting, Central States Section/ The Combustion Institute, Cleveland, Ohio (May 1986).

4. A.H. Lefebvre and D. Miller, The Development of an Airblast Atomizer for Gas Turbine Application, College of Aeronautics Report, Aero no. 193, Cranfield, England, (1966).

5. N.K. Rizk and A.H. Lefebvre, The Influence of Liquid Film Thickness on Airblast Atomization, ASME J. Eng. Power , vol. 102, pp. 706 -710, (1980).

6. H.B. Squire, Investigation of the Instability of a Moving Liquid Film, Br. J. Appl. Phys., vol. 4, pp. 167 -169, (1953).

7. R.P. Fraser, P. Eisenklam, N. Dombrowski, and D. Hasson, Drop Formation from Rapidly Moving Sheets, J.AIChE. vol. 8, pp. 672-680, (1962).

8. T. Inamura and N. Nagai, The Relative Performance of Externally and Internally-Mixed Twin-Fluid Atomizers, Proc. 3rd International Conference on Liquid Atomization and Sprays, pp. II C/2/1-11, London (1985).

9. Q.S. Zhao and X.H. Gan, Effects of Geometrical Size and Configuration of Airblast Atomizers on Atomizing Performance, ASME Paper 85-IGT-138, (1985).

10. J.E. Beck, A.H. Lefebvre, and T.R. Koblish, Airblast Atomization at Conditions of Low Air Velocity, AIAA J. Propul. Power, in press.

11. J.E. Beck, A.H. Lefebvre, and T.R. Koblish, Liquid Sheet Disintegration in a Coflowing Air Stream, Atomization and Sprays, vol. 1, no. 2, pp. 155-170, (1991).

12. T. Sattelmayer and S. Wittig, Internal Flow Effects in Prefilming Airblast Atomizers: Mechanisms of Atomization and Droplet Spectra, ASME J. Eng. Gas Turbines and Power, vol. 108, pp. 465-472, (1986).

13. M. Aigner and S. Wittig, Swirl and Counterswirl Effects in Prefilming Airblast Atomizers, ASME Paper 87-GT-204, (1987).

14. N. Dombrowski and W.R. Johns, The Aerodynamic Instability and Disintegration of Viscous Liquid Sheets, Chem. Eng. Sci., vol. 18, pp. 203-214, (1963).

15. A.H. Lefebvre, Energy Considerations in Twin-Fluid Atomization, ASME J. Eng. Gas Turbines and Power, in press.

16. A.H. Lefebvre, Atomization and Sprays, Hemisphere, Washington D.C., (1989).

17. J.B. Kennedy, High Weber Number SMD Correlations for Pressure Atomizers, ASME Paper 85- GT-37, (1985).

18. S. Nukiyamo and Y. Tanasawa, Experiments on Atomization of Liquids in an Airstream, Trans. Soc.Mech. Eng. Jpn., vol. 5, pp.68-75, (1939).

19. J.D. Whitlow, An Experimental Investigation of Internal-Mixing, Twin-Fluid Atomization, M.S.M.E. thesis, Purdue University, W.Lafayette, Indiana, (1990).

20. A.H. Lefebvre, X.F. Wang and C.A. Martin, Spray Characteristics of Aerated- Liquid Pressure Atomizers, AIAA J. Propul. Power, vol. 4, 293-298, (1988).

21. T.C. Roesler, An Experimental Study of Aerated-Liquid Atomization, Ph.D. thesis, Purdue University, W. Lafayette, Indiana, (1988).

22. H.N. Buckner, P.E. Sojka, and A.H. Lefebvre, Aerated Atomization of High Viscosity Newtonian Liquids, Proc. 3rd Annual Conference on Liquid Atomization and Spray Systems, Irvine, California, pp.56-61, (May 1989).

NOMENCLATURE

ALR	air/liquid mass ratio
C_D	discharge coefficient
D_p	prefilmer diameter, m
d_o	initial jet diameter, m
d_A	air bubble diameter, m
E	bubble energy, J/kg
L_C	characteristic dimension of atomizer, m
$\dot{m}$	mass flow rate, kg/s
P	pressure, Pa
P_B	bubble pressure upstream of discharge orifice, Pa
ΔP	pressure differential, Pa
R	gas constant, J/kgK
SMD	Sauter mean diameter, ,
T	temperature, K

t	initial sheet thickness, m
t_B	average distance between bubbles
U	velocity, m/s
We	Weber number
μ	absolute viscosity, kg/ms
ρ	density, kg/m^3
σ	surface tension, kg/s^2
Subscripts	
A	air
L	liquid

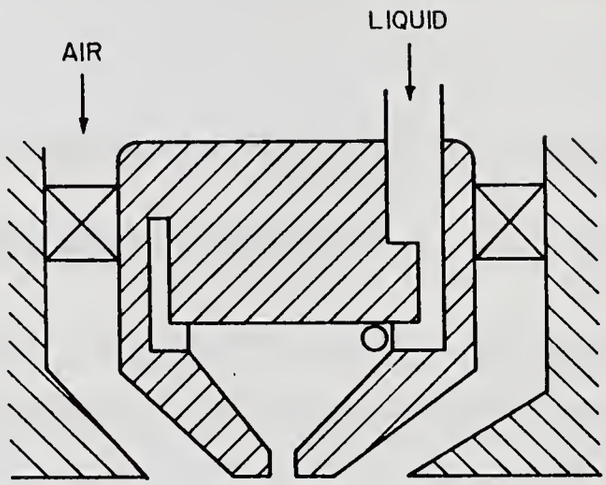

Fig. 1 Schematic diagram of external-mixing, air-assist atomizer

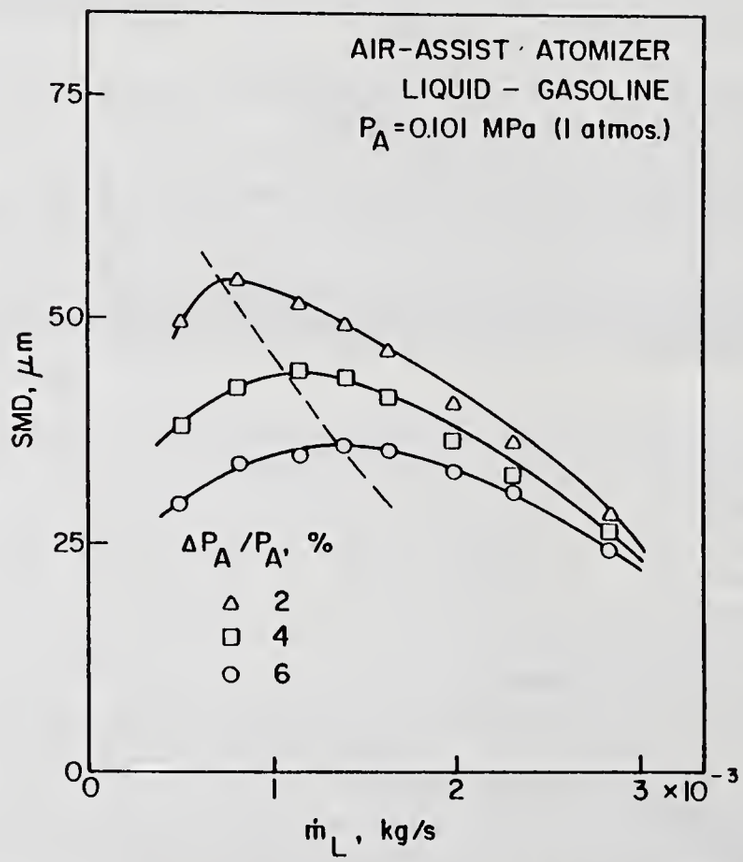

Fig. 2 Influence of liquid flow rate and air velocity on mean drop size

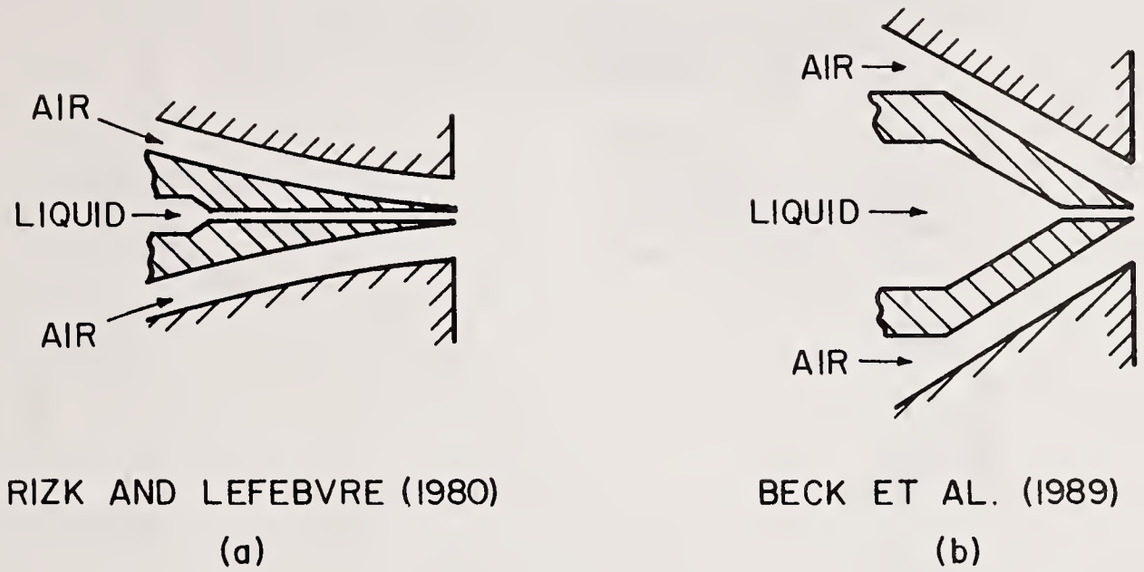

Fig. 3 Two different types of flat-sheet airblast atomizers

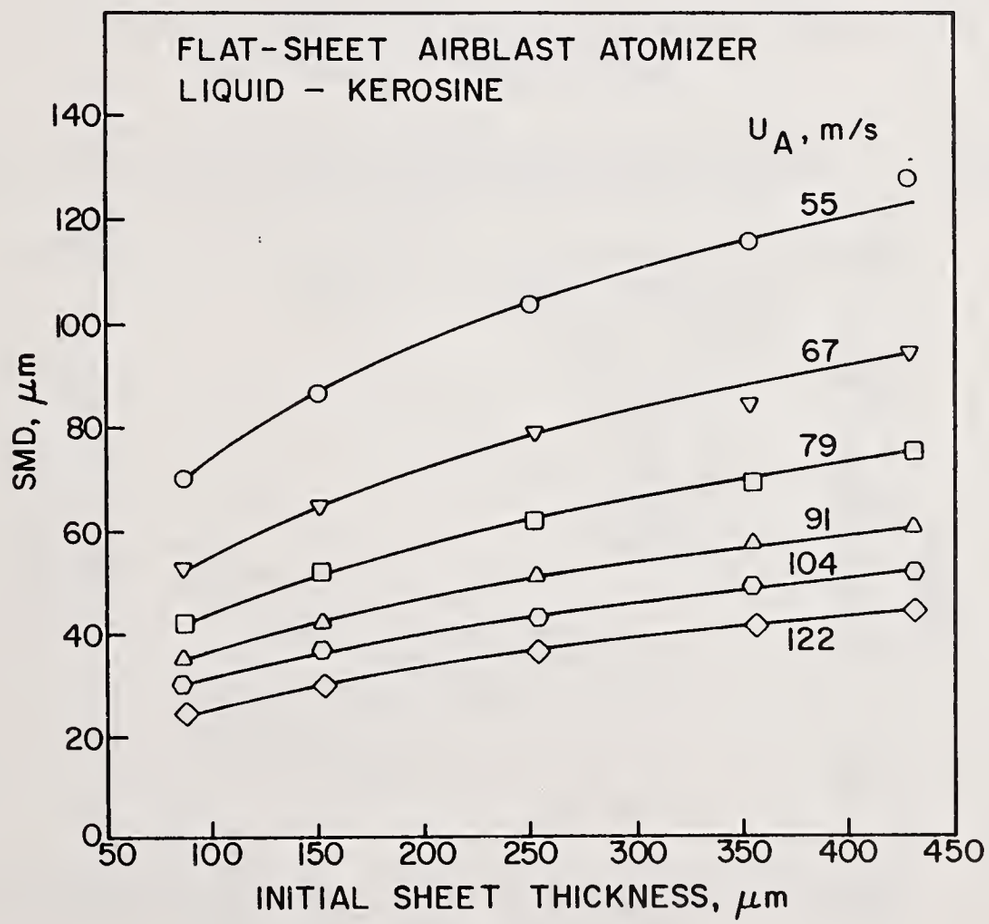

Fig. 4 Influence of initial sheet thickness on mean drop size. Data from Ref. 5

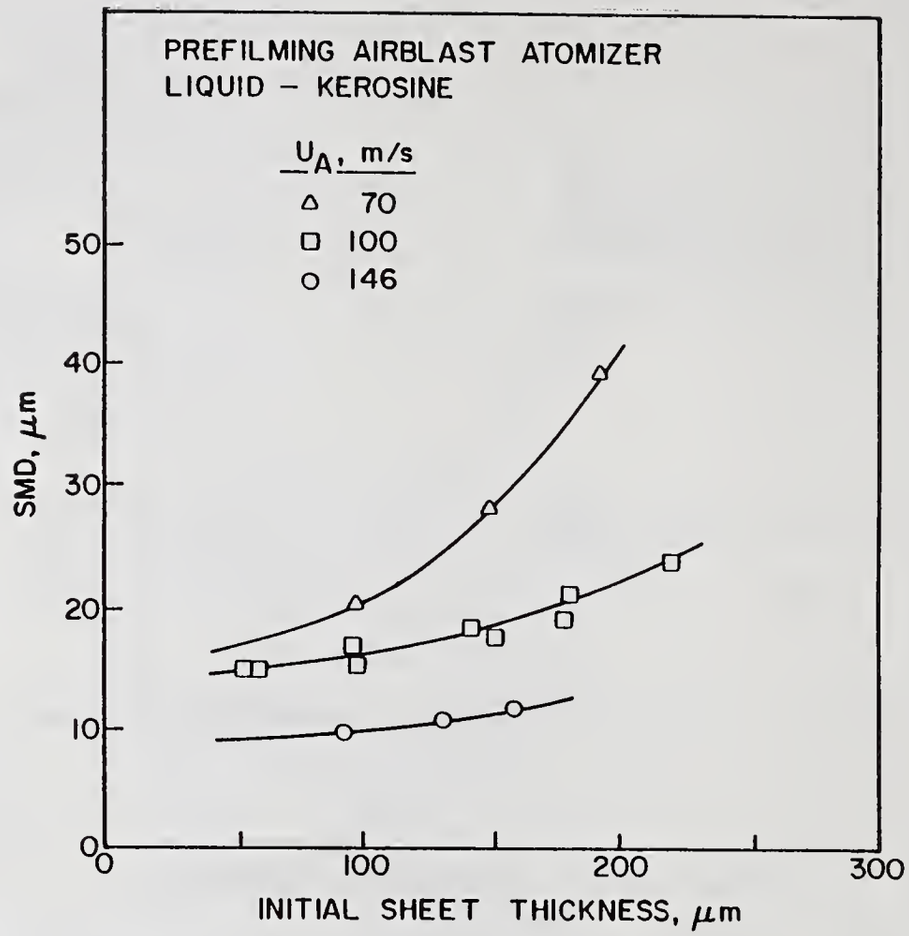

Fig. 5 Influence of initial sheet thickness on mean drop size. Data from Ref. 9

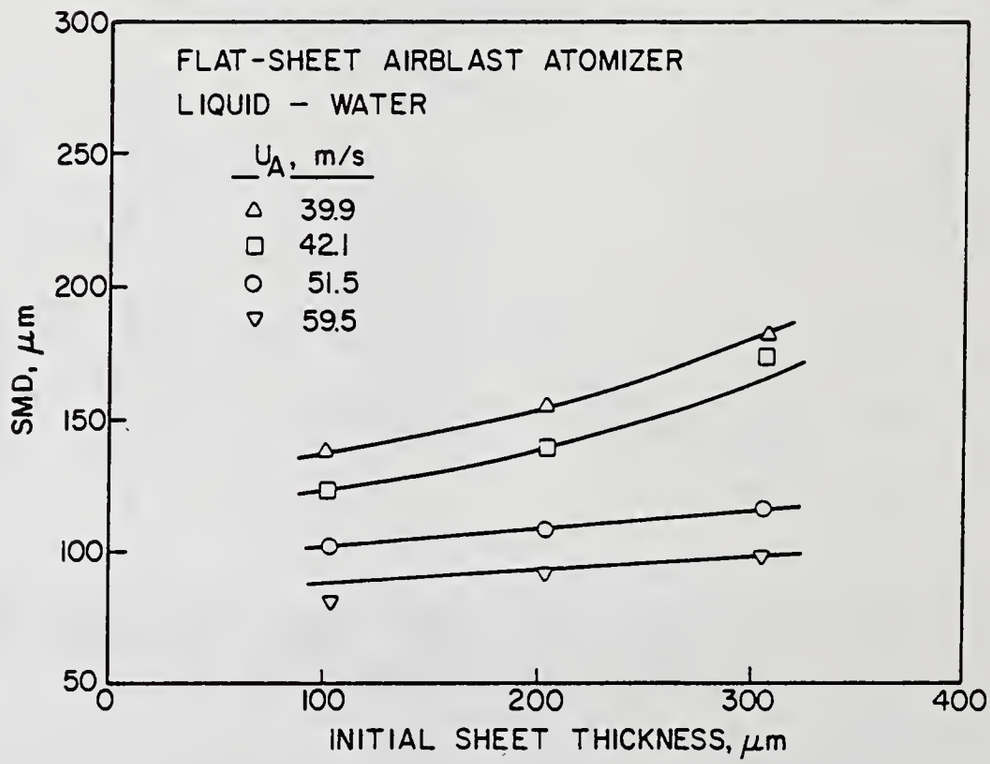

Fig. 6 Influence of initial sheet thickness on mean drop size. Data from Ref. 10

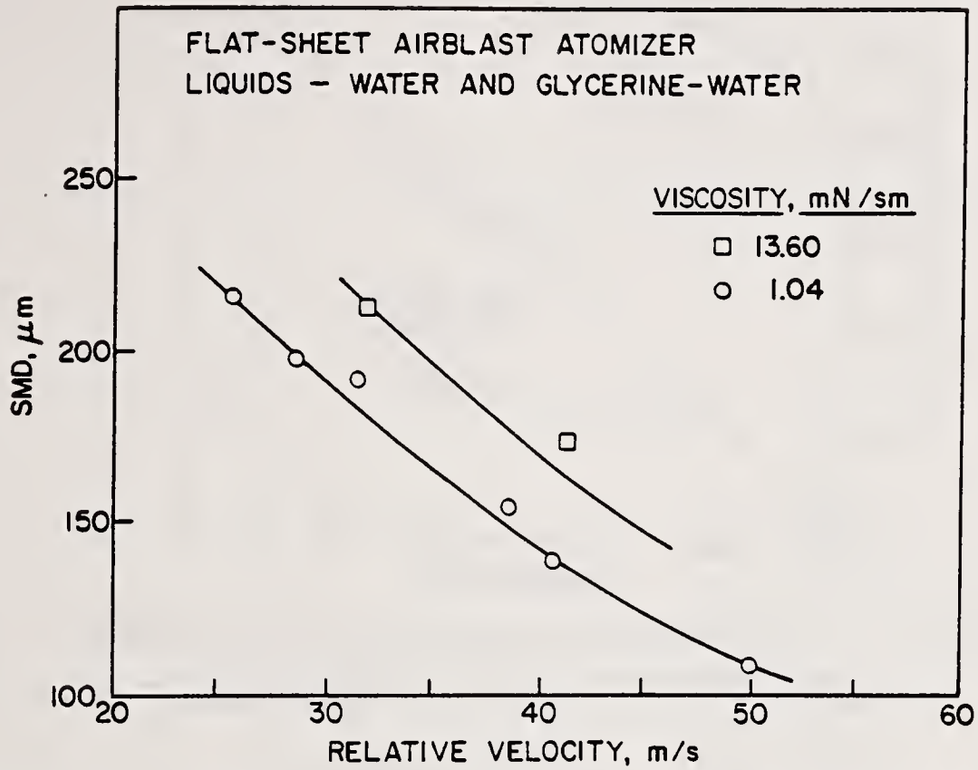

Fig. 7 Influence of liquid viscosity on mean drop size. Data from Ref. 10

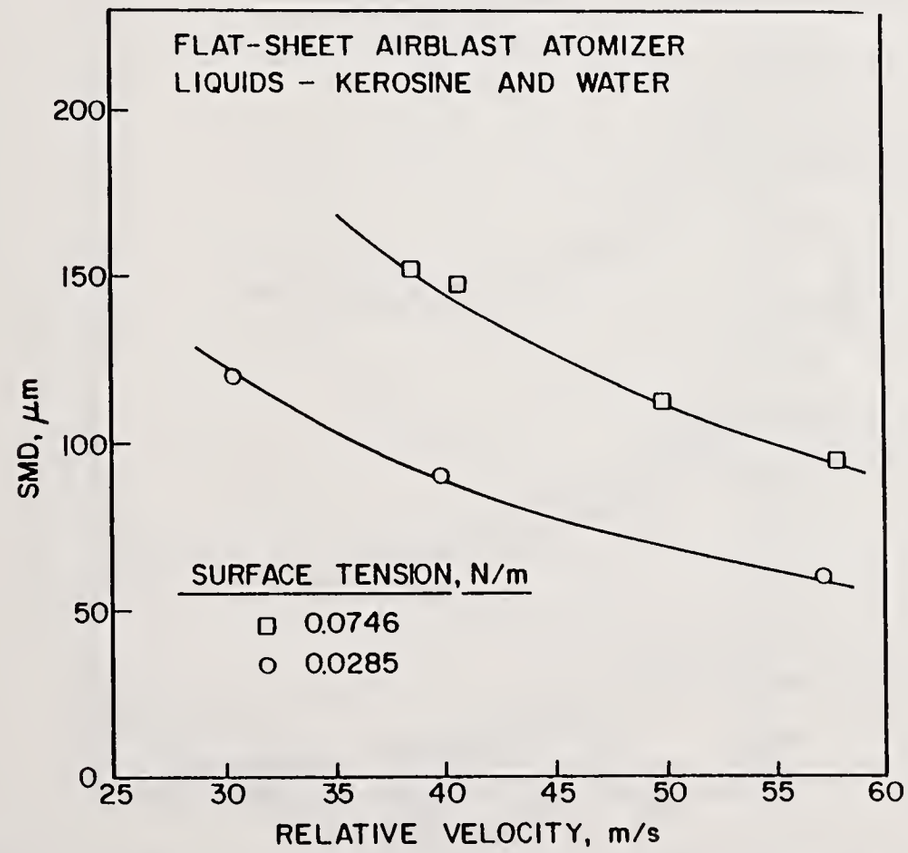

Fig. 8 Influence of surface tension on mean drop size. Data from Ref. 10

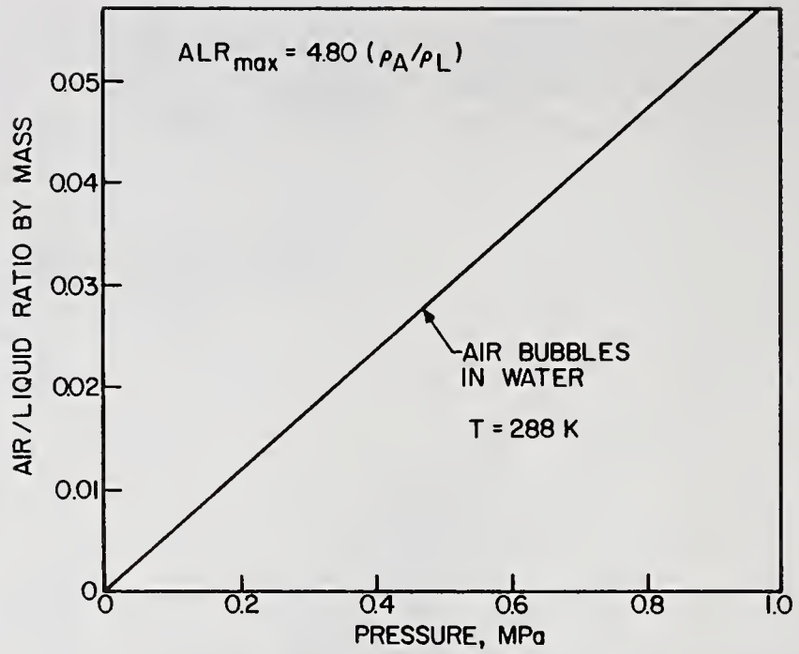

Fig. 9 Maximum air/water ratio for effervescent atomization

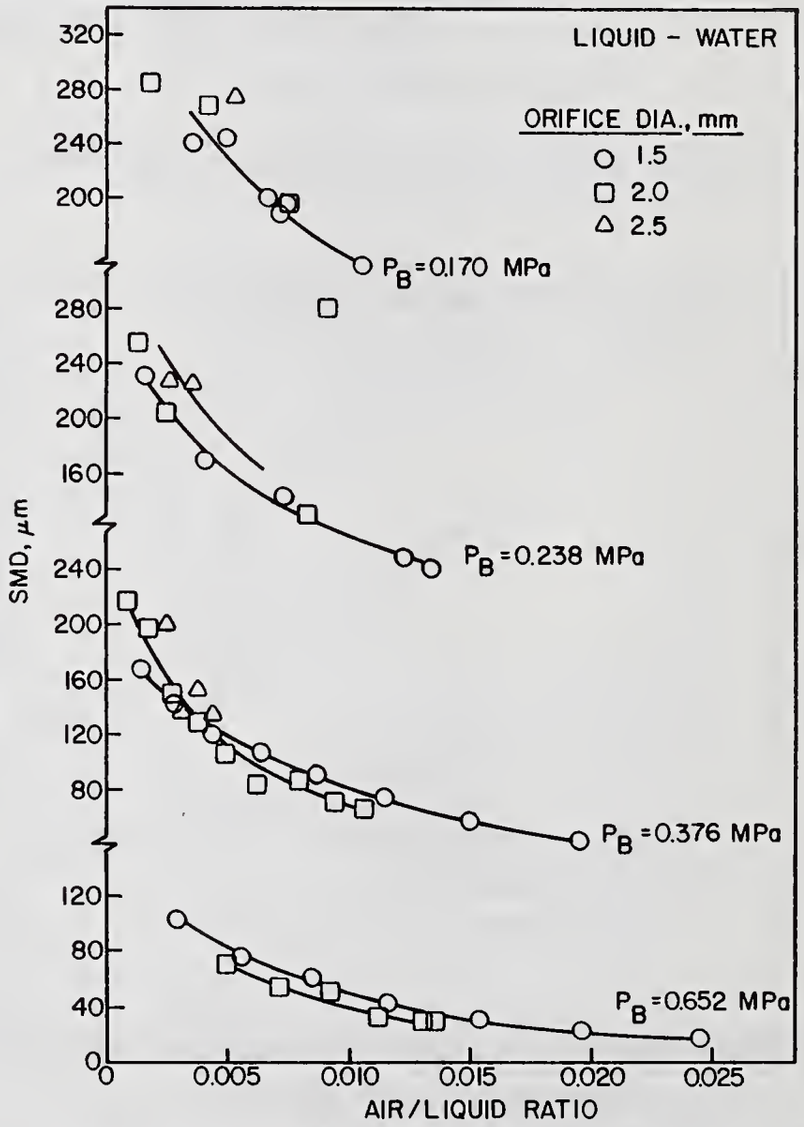

Fig. 10 Influence of final discharge orifice diameter on mean drop size. Data from Ref. 21

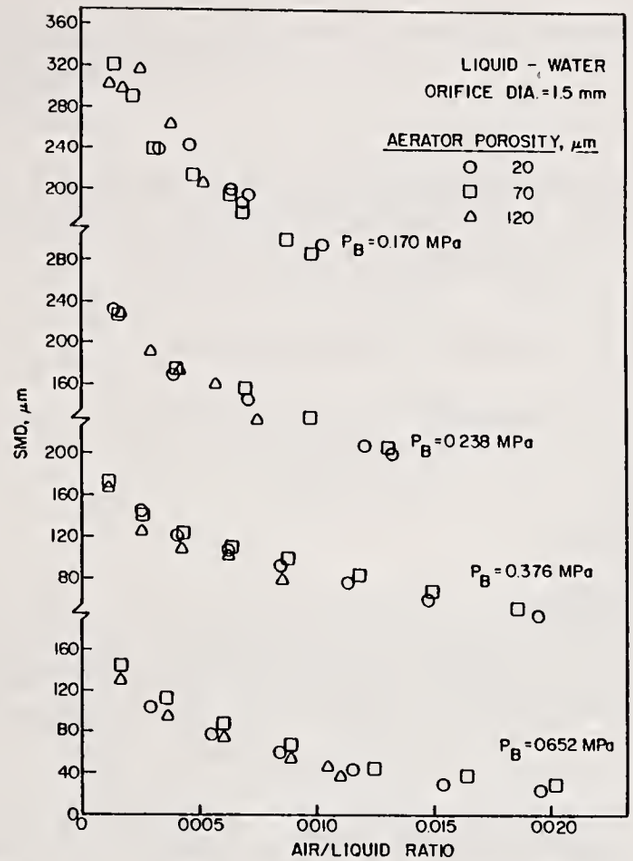

Fig. 11 Influence of aerator tube porosity on mean drop size. Data from Ref. 21

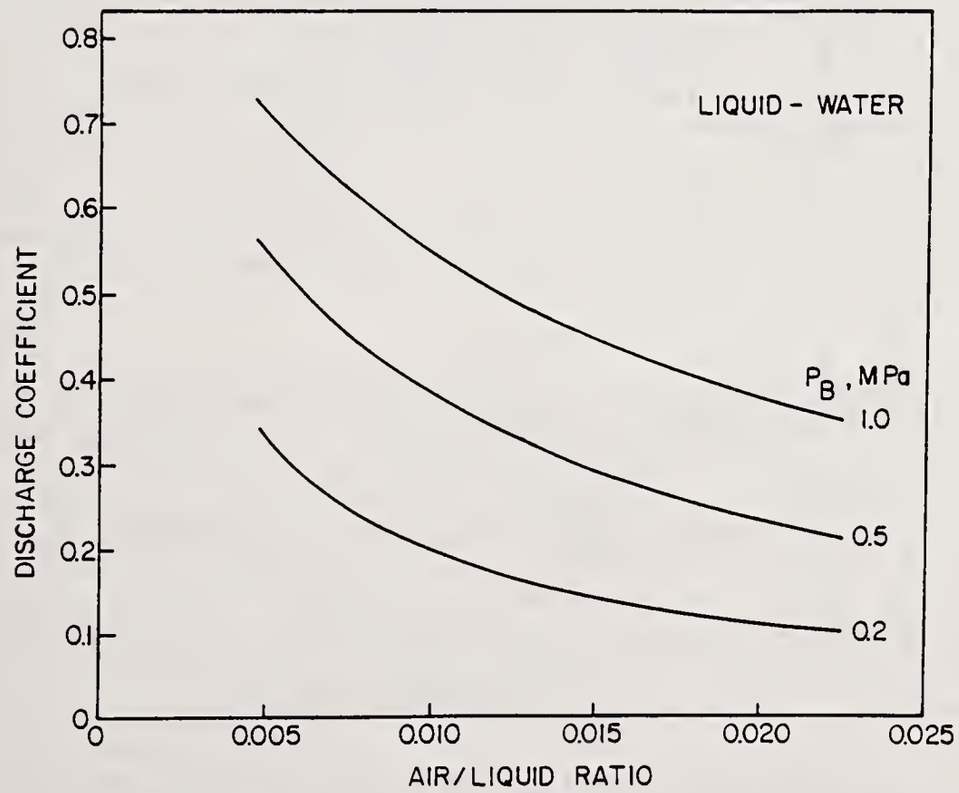

Fig. 12 Influence of bubble pressure and air/liquid ratio on discharge coefficient

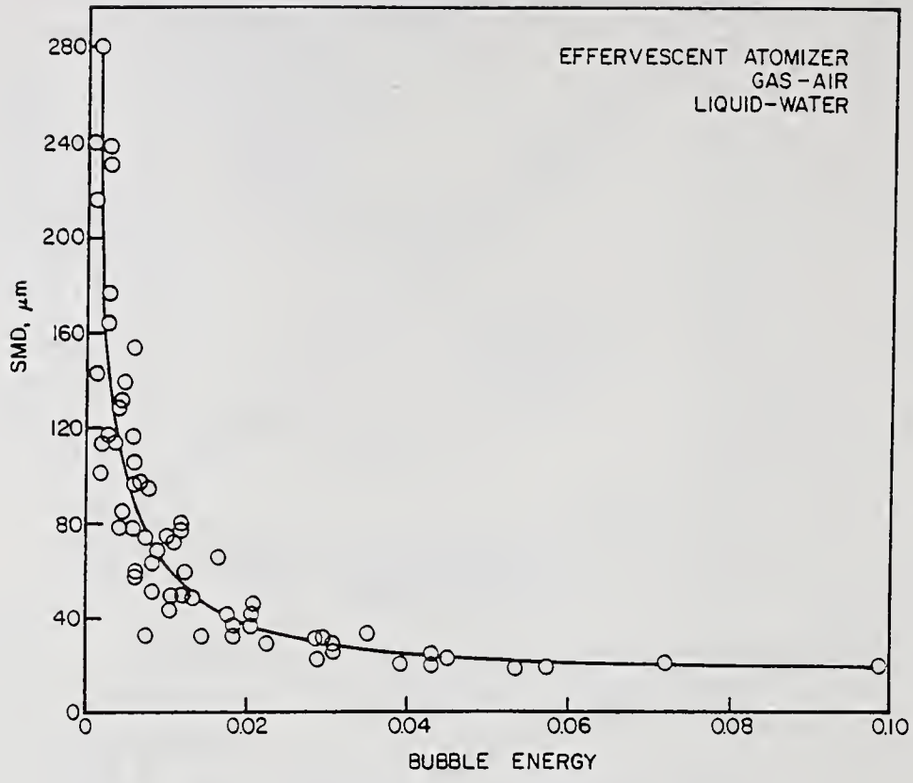

Fig. 13 Relationship between bubble energy and mean drop size

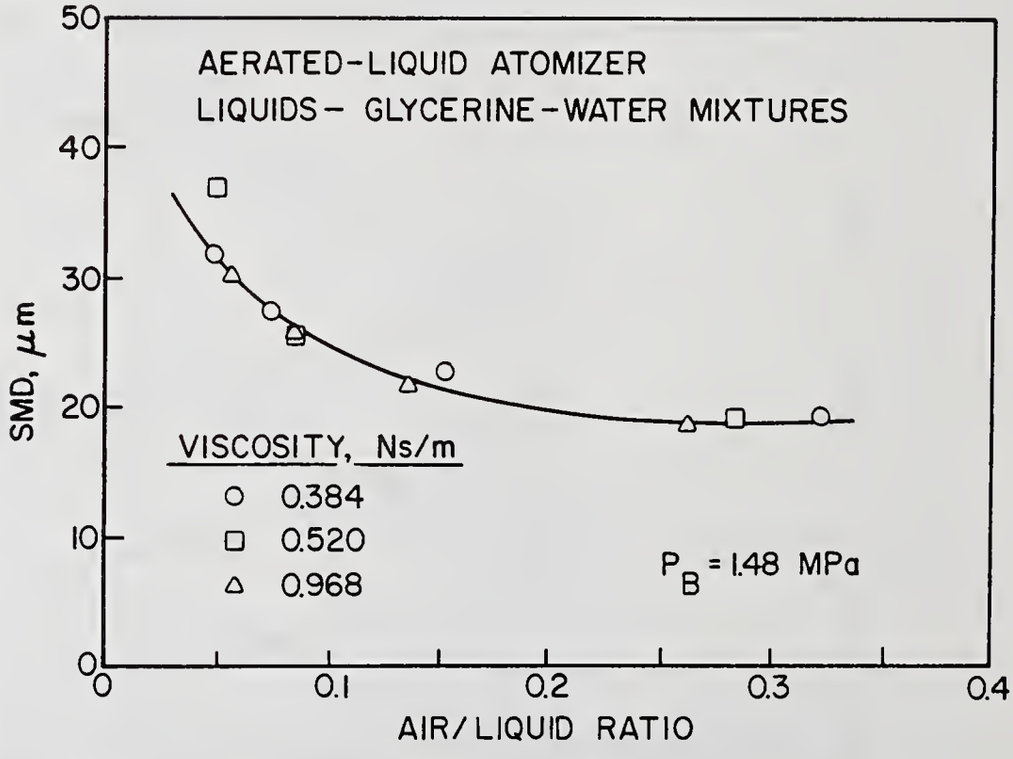

Fig. 14 Influence of air/liquid ratio on mean drop size for liquids of high viscosity. Data from Ref. 22

RELAXATION OF A POLYDISPERSE SPRAY UNDERGOING VAPORIZATION AND COALESCENCE IN A FLOW FIELD BEHIND A NORMAL SHOCK WAVE: A SECTIONAL APPROACH

S. Zahavi and Y. Tambour

Faculty of Aerospace Engineering
Technion - Israel Institute of Technology
Haifa, Israel

ABSTRACT

A gas flow field behind a normal shock wave inflicts a step function in velocity, temperature and pressure upon a polydisperse spray suspended in the flow. As a result, there are large differences in velocity and temperature between the carrying gas and the droplets of the spray immediately after the shock. These differences gradually decrease in a relaxation zone which ends at a distance, where the so called "far-field" begins, at which the droplets eventually travel at a velocity which is close to the host fluid velocity. Thus, the investigation of the relaxation zone may be regarded as the analysis of a "near-field" problem in contradistinction to "far-field" problems which have been analyzed by Greenberg, Tambour and their coworkers employing a sectional approach. Treatment of a "near-field" problem via a sectional approach requires derivation of new generalized sectional-equations which extend the previous sectional-equations which were derived by Tambour for "far-field" problems. Such new generalized sectional-equations are derived in the present paper. They rigorously account for the heritage of momentum and enthalpy that droplets carry with them as they "move" from one size section to another due to evaporation and coalescence processes, e.g. a large droplet formed by coalescence (of two small droplets) will differ from the originally large droplets since the properties of the newly formed droplet depend on the properties of the small droplets which participate in the coalescence process, and generally in the "near-field", small droplets differ in velocity and enthalpy from large ones. These effects, as well as the influence of the velocity lag between droplets and the host fluid, between droplets of various sizes, and between droplets of the same size on the evolution in pointwise droplet size distributions along the axial direction are presented here. The computed results also include changes of velocities and temperatures of each droplet size-section in the relaxation zone.

INTRODUCTION

The flow of a polydisperse liquid spray suspended in a gas is of importance to a wide range of technologies in the chemical industry, in jet engine main combustion chamber and afterburner design, and in liquid fuel rocket propulsion. In general, when the spray is injected, the two phases (the liquid spray and the host gas) are not initially in equilibrium. There are differences in velocity and temperature, not only between the two phases, but also between droplets of various sizes. Equilibrium tends to be achieved by relatively slow processes of drag, heat and mass transfer as the flow proceeds through a relaxation zone or a "near-field" zone. Since there are velocity differences between droplets, coalescence resulting from collisions between droplets, may occur. In the light of the above, our specific interest in the present paper is the analysis of the relaxation of a polydisperse spray undergoing simultaneous vaporization and coalescence in a flow field in which the nonequilibrium state is brought about by a normal shock wave.

Early work which dealt with the relaxation of solid particles in a gas flow behind a shock wave was presented in the late fifties by Hoenig [1] and by Carrier [2]. Hoenig [1] discussed the variation

of the velocity of a single solid particle behind a shock wave. Carrier [2] formulated the general problem for solid particles that are numerous enough to affect the gas flow behind the shock wave. The case of solid particles was also studied in the sixties by Kriebel [3] who analyzed three particle sizes, and by Rudinger [4,5] who analyzed various shock strengths, drag laws and specific heats. Rudinger pointed out that the velocities and temperatures do not always change monotonically towards their equilibrium values.

Mass transfer between the two phases was considered by Lu and Chiu [6] for the case of water droplets in air. Panton & Oppenheim [7] considered the case of two droplet size groups and demonstrated the interesting possibility of a situation where some of the droplets diminish by vaporization while others grow by condensation. Nayfeh [8] studied a gas containing ablating particles and Evans and Mackie [9] modified his calculations by allowing downstream variation of particle temperatures and by the use of a diffusive evaporation rate. Later, in 1975, Narkis and Gal-Or [10] pointed out that for a given Mach number there is a certain particle flow rate for which a minimum equilibrium velocity is achieved.

More recently, Ben-Dor and Igra [11,12], analyzed the relaxation zone behind normal shock waves in a dusty reacting gas. An analysis of normal shock waves in a carbon particle-laden oxygen gas was presented by Alperin, Igra and Ben-Dor [13]. Although not dealing with a flow behind a shock wave, a pioneering theoretical study of what can be regarded as a "near-field" problem, was recently presented by Bellan and Harstad [39]. They analyzed dense and dilute clusters of drops evaporating in large, coherent vortices.

Detailed formulations of the governing equations for the two phases can be found in the literature, e.g. see Carrier [2], Soo [14,15], Kliegel [16,17], Marble [18-19] and Pai [20]. However, since our objective here is to analyze a **polydisperse** spray undergoing **simultaneous evaporation and coalescence** processes, we find a "sectional" approach [21-33] to be useful for handling this problem. In the sectional approach, the spray is divided into size groups (size-sections), where for each size group a sectional mass balance (and in the present study also a momentum and energy) equation is derived. This enables one to deal with a fairly small number of conservation equations for the analysis of a **polydisperse** spray of a **wide range** of sizes. Another advantage of the sectional approach lies in the ability to rigorously account for intra- and inter-sectional mass (and in the present study also momentum and energy) transfer for **simultaneous** evaporation and coalescence processes.

Thus far, the sectional approach has been used [21-25,27-33] for the analysis of "far-field" zones, where essentially most of the droplets travel at a velocity close to the host fluid velocity field. Theoretical simulations have been carried out for (i) "far-field" downstream changes in integral droplet size distributions of evaporating sprays in "cold" and "heated" environments [23] and for (ii) "far-field" downstream evolution in pointwise droplet size distributions of polydisperse sprays undergoing simultaneous evaporation and coalescence processes [24]. The good agreement that has been observed comparing these theoretical simulations [23,24] with independently reported experimental data [34,35] has demonstrated the simplicity and reliability of the sectional approach.

As to "near-field" problems, rapid developments in measurement techniques supply plenty of experimental data on pointwise and integral droplet size distributions of polydisperse sprays in the "near-field" [36-38]. Such data can serve as initial conditions for simulations and also for verifying theoretical predictions.

In light of the above, the purpose of the present study is to extend the mass balance sectional-equations which were previously derived for the analysis of "far-field" problems [21-24] and present **new generalized sectional equations** which account for the intra- and inter-sectional transfer of momentum, kinetic-energy and enthalpy. The derivation of these equations has been presented elsewhere [40]. These generalized equations will be employed here in order to analyze a "near-field"

problem, that is, the relaxation zone of a polydisperse spray undergoing evaporation and coalescence processes behind a normal shock wave.

RESULTS AND DISCUSSION

Computations were carried out for a polydisperse spray suspended homogeneously in a one-dimensional gas flow at a Mach number of M=1.5, and under conditions of equilibrium of velocity and temperature, between the two phases (the liquid spray and the host fluid). Due to a normal shock wave at x=0, the host fluid undergoes a step change in velocity, temperature and pressure. We assume that immediately after the shock wave, at $x=0^+$, the volume concentration of the spray z_o, and the size distribution of the spray, and the mass fraction of vapors χ_o, are given. Based on these initial conditions, we analyze the evolution in spray size distribution and the variation of velocity and temperature of each size group (section) of the spray along the axial direction in the relaxation zone. These changes are not only coupled to the variation of velocity and temperature of the host fluid in the relaxation zone due to the interaction between the two phases, but also intercoupled due to mass, momentum and energy transfer between droplets of various sections.

The spray size distribution is divided into 10 sections (size groups). The smallest section is 0-8 monomers and the limits of the largest section are 5832-8000 monomers. If one denotes the diameter of a single monomer by d_o, then, section No. 1 includes droplets of a diameter up to $2d_o$. The "width" of all other sections is also $2d_o$ (in terms of droplet diameters), so that droplets of a diameter which lies within the range of $18d_o$ to $20d_o$, are in section No. 10. Hence, the ratio of the largest droplet in section 10 to the largest droplet in section 1 is 10:1 in diameters and 1000:1 in volume (or mass).

We begin with the analysis of a trivial case in which there is neither coalescence nor evaporation. The computed results of this case are shown in Figs. 1 and 2, and will serve as a comparison for more complex cases. The variation of velocity in the relaxation zone is shown in Fig. 1. The gas loses almost half of its original velocity as it passes through the shock. Then, its velocity continues to decrease in the relaxation zone due to dissipation of kinetic-energy which results in an increase of the internal energy of the gas, as indicated by the increase in gas temperature in the first part of the relaxation zone (see Fig. 2). (Afterwards, the gas temperature decreases as the gas heats the droplets.) As to the variation of the velocity of each size section of the spray, as expected, the small droplets (e.g. section No. 1) adjust to the gas velocity within a shorter distance than the large droplets.

We now return to analyze the results presented in Fig. 2. Since immediately after the shock the gas is hotter than the droplets, the droplets are heated along the axial direction till thermal equilibrium is gained. The thermal relaxation zone is wider than the momentum relaxation zone (compare Figs. 1 and 2) due to the difference in characteristic time scales between heat transfer and momentum transfer. It is also interesting to note that large droplets (e.g. sections 2 to 10) increase their temperature gradually, while the small droplets (sections 1 and 2) exhibit a temperature overshoot. This behavior is due to the fact that small droplets are heated faster than large ones, so when the gas is "hot", they reach high temperatures and then, the gas cools down at a faster rate. There is an interesting region in which the temperature of these small droplets is locally higher than that of the surrounding gas. However, in this region, the slope of temperature variation always points downwards.

Next, coalescence effects are analyzed and compared with the previously described case in which neither coalescence nor evaporation were assumed. In a polydisperse spray such as considered here, collisions between droplets are expected due to the velocity differences between droplets of various sizes. Collision rates depend on the characteristic distance between droplets (which is a function of

number concentration of droplets per unit volume, or the volume concentration of the spray, z), the relative velocities between droplets, the collision cross section, and the characteristic time of droplets in the relaxation zone. We assume here that all collisions result in coalescence.

We focus here on three coalescence rates: (i) "Low", C_{FC}=0.0002, (ii) "Medium", C_{FC}=0.005, and (iii) "High", C_{FC}=0.02. The variation of velocity of each size-section of the spray and the velocity of the host fluid, in the relaxation zone, are shown in Figs. 3a(i, ii and iii) for the above three coalescence rates. Comparison of Fig. 1 (No coalescence) with Fig. 3a-i (Low coalescence) indicates that the effects of "Low" coalescence rate, on the velocity profiles are hardly noticeable. However, at higher coalescence rates (see Figs. 3a-ii and 3a-iii), the velocity profiles of the various spray sections become more crowded and the relaxation zone becomes shorter. This behavior is due to the fact that coalescence serves as a "mixing" process for the momentum of droplets, in which the velocity of each newly formed droplet is constructed on the basis of the momentums of the original droplets that participate in the coalescence process.

The same arguments hold for explaining the results that show the effects of coalescence on the temperature profiles of the various spray-sections. Coalescence also serves as a mixing process for thermal energy and thus shortens the relaxation zone [compare Figs. 4 (i,ii,iii) with Fig. 2].

The results described above are based on solutions of the "near-field" equations that have been derived in the present paper. These equations rigorously account for the heritage of momentum and enthalpy that droplets carry with them as they "move" from one size-section to another due to coalescence (and evaporation). To demonstrate the importance of this rigorous treatment, for comparison we present in Figs. 3b (i, ii, iii) and 4b (i, ii, iii), velocity and temperature profiles obtained by solving a set of more simplified sectional-equations in which intra- and intersectional mass transfer due to coalescence is accounted for, but bound to the simplifying assumption that inter-sectional momentum and energy transfer are negligible (as in the "far-field" equations). Thus, newly formed droplets adopt the momentum and energy of the new section which they join without altering its average momentum and energy.

One can clearly see that the rigorous derivation of the "near-field" sectional-equations is necessary since otherwise solutions may show erroneous results such as presented in Figs. 3b and 4b. For example, the second peak in temperature (see Figs. 4b, i and ii) is erroneous. It is explained as follows. Small droplets have a higher temperature than large ones, so when they coalesce the newly formed large droplets have a higher temperature than the originally large droplets. Failing to consider this effect by assuming that the newly formed large droplets immediately adopt the energy state of the originally large droplets results in an energy difference which, due to energy conservation in the system as a whole, is added erroneously to the host gas.

The variations of the liquid-phase mass flow rate along the axial direction are shown in Fig. 5 for each of the spray size-sections. Variations of the spray volume fractions are presented in Fig. 6. Both figures are for the "medium" coalescence rate (C_{FC}=0.005) and both show the increase in mass flow rate and in volume concentration of droplets in the upper sections due to the creation of new droplets by the coalescence process. It should be emphasized that due to the overall mass conservation, section No. 10 actually also includes all droplets larger in size than the upper limit of section No. 10.

The integral volume fraction of the liquid phase, z, is shown in Fig. 7 for various coalescence rates. All profiles asymptotically approach the same value, and the increase in spray concentration, as one marches downstream, is due to the decrease in droplet velocities see Figs. 3a.

The effects of heat transfer on the variation of temperature in the relaxation zone are shown in

Fig. 8. These results indicate that a shorter relaxation distance is obtained for droplets of a high initial temperature, which is closer to their boiling point temperature (compare Fig. 8-i with Fig. 8-ii). If a more accurate heat-transfer model is used, e.g. with Ranz-Marshall convective correlation (see Fig. 8-a), temperature profiles of the various spray sections become more crowded due to the higher convective heat transfer rate.

The latter results are for an evaporating spray without coalescence. When simultaneous evaporation and coalescence occur, the general behavior remains the same (see Fig. 9) since on the one hand coalescence hinders vaporization (due to the decrease in the surface area of the droplets), but on the other hand, coalescence serves as a "mixing" process and causes the profiles of the various spray sections to become more crowded.

CONCLUSIONS

To summarize, new generalized "near-field" spray section-equations have been derived in which intra- and inter-sectional transfer of mass, linear-momentum, kinetic-energy and enthalpy has been rigorously accounted for. These equations have been employed here to analyze the behavior of a **polydisperse** spray undergoing **evaporation** and **coalescence** processes in a relaxation zone behind a normal shock wave.

REFERENCES

1. Hoenig, S.A. (1957), "Acceleration of Dust Particles by Shock Waves", *J. of Applied Physics*, Vol. 28, No. 10, pp. 1218-1219.
2. Carrier, G.F. (1959), "Shock Waves in a Dusty Gas", *J. of Fluid Mechanics*, Vol. 4, No. 4, pp. 376-382.
3. Kriebel, A.R. (1964), "Analysis of Normal Shock Waves in Particle Laden Gas", *J. of Basic Eng.*, Vol. 86, No. 4, pp. 655-665.
4. Rudinger, G. (1964), "Some Properties of Shock Relaxation in Gas Flows Carrying Small Particles", *Physics of Fluids*, Vol. 7, No. 4, pp. 658-663.
5. Rudinger, G. (1965), "Some Effects of Finite Particle Volume on the Dynamics of Gas-Particle Mixtures", *AIAA J.*, Vol. 3, No. 7, pp. 1217-1222.
6. Lu, H.Y. and Chiu, H.H. (1966), "Dynamics of Gases Containing Evaporable Liquids under a Normal Shock", *AIAA J.*, Vol. 4, No. 6, pp. 1008-1011.
7. Panton, R. and Oppenheim, A.K. (1968), "Shock Relaxation in a Particle-Gas Mixture with Mass Transfer Between Phases", *AIAA J.*, Vol. 6, No. 11, pp. 2071-2077.
8. Nayfeh, A.H. (1966), "Shock Wave Structure in a Gas Containing Ablating Particles", *Physics of Fluids*, Vol. 9, No. 12, pp. 2351-2356.
9. Evans, P.J. and Mackie, J.K. (1971), "Shock Waves Interaction with an Evaporating Aerosol", *Physics of Fluids*, Vol. 14, No. 3, pp. 539-541.
10. Narkis, Y. and Gal-Or, B. (1975), "Two - Phase Flow Through Normal Shock Waves", J. of Fluid Engineering (ASME), Vol. 97, pp. 361-365.
11. Ben-Dor, G. and Igra, O. (1982), "The Relaxation Zone Behind Normal Shock Waves in Reacting Dusty Gas. Part 1. Monatomic Gases", *J. Plasma Phys.*, Vol. 27, pp. 377-395.
12. Igra, O. and Ben-Dor, G. (1984), "The Relaxation Zone Behind Normal Shock Waves in a Dusty Reacting Gas. Part 2. Diatomic Gas", *J. Plasma Phys.*, Vol. 31, pp. 115-140.
13. Elperin, I., Igra, O. and Ben-Dor, G. (1986), "Analysis of Normal Shock Waves in a Carbon Particle-Laden Oxygen Gas", *J. of Fluids Eng., Trans. ASME*, Ser. D, 86, pp. 655-663.
14. Soo, S.L. (1961), "Gas Dynamics Processes Involving Suspended Solids", *AIChE J.*, Vol. 7, No. 3, pp. 384.
15. Soo, S.L. (1967), *Fluid Dynamics of Multiphase Systems.* Blaisdell Publishing Co., Waltham.
16. Kliegel, J.R. and Nickerson, G.R. (1962), "Flow of Gas-Particles Mixtures in Axially Symmetric Nozzles", *In Progress in Astronautics and Rocketry*, Vol. 6, Academic Press, New York, pp. 173-194.

17. Kliegel, J.R. (1963), "Gas Particle Nozzle Flow", Ninth Symposium (International) on Combustion, Academic Press, New York, pp. 811-826.
18. Marble, F.E. (1963), "Dynamics of a Gas Containing Small Solid Particles", Fifth AGARD Combustion and Propulsion Colloquium, Pergamon Press, London, pp. 175-215.
19. Marble, F.E. (1964), "Mechanism of Particles Collision in the One-Dimensional Dynamics of Gas-Particle Mixtures", *Physics of Fluids*, Vol. 7, No. 8, pp. 1270-1282.
20. Pai, S.I. (1977), Two-Phase Flows, Oswatitisch.
21. Tambour, Y. (1980), "A Sectional Model for Evaporation and Combustion of Sprays of Liquid Fuels", *Israel J. Tech.*, Vol. 18, pp. 47-56.
22. Tambour, Y. (1984), "Vaporization of Polydisperse Fuel Sprays in a Laminar Boundary Layer", *Comb. Flame*, Vol. 58, pp. 103-114.
23. Tambour, Y. (1985), "A Lagrangian Sectional Approach for Simulating Droplet Size Distribution of Vaporizing Fuel Sprays in a Turbulent Jet", *Comb. Flame*, Vol. 60, pp. 15-28.
24. Tambour, Y. (1985), "Coalescence of Vaporizing Kerosene Fuel Sprays in a Turbulent Jet", *Atomization and Spray Technology*, Vol. 1, pp. 125-146. See also: "Simulation of Coalescence and Vaporization of Kerosene Fuel Sprays in Turbulence Jet: A Sectional Approach", AIAA/ASME/ASEE 21st Joint Propulsion Conference, Monterey, 1985. AIAA Paper No. 85-1315.
25. Tambour, Y., Greenberg, J.b. and Albagli, D. (1985), "Vaporisation and Coalescence of Sprays in 3-D Axisymmetric Stagnation Flow", ICLASS-85, 3rd International Conference on Liquid Atomisation and Spray Systems, England, 1985.
26. Avital, G., Greenberg, J.B., Tambour, Y. and Timnat, Y.M. (1989), "Spray Dynamics and Fuel Vapor Distributions in a Spinning Spherical Combustion Chamber", 12th International Colloquium on Dynamics of Explosions and Reactive Systems, Ann Arbor, Michigan.
27. Greenberg, J.B. and Tambour, Y. (1986), "Far Field Coalescence Effects in Polydisperse Spray Jet Diffusion Flames", Twenty First Symposium (International) on Combustion, The Combustion Institute, Philadelphia, pp. 655-663.
28. Greenberg, J.B., Albagli, D. and Tambour, Y. (1986), "An Opposed-Jet Quasi- Monodisperse Spray Diffusion Flame", *Comb. Sci. Tech.*, Vol. 50, Nos. 4-6, pp. 255-270.
29. Tambour, Y. and Greenberg, J.B. (1988), "Fuel-Injector Far Field Temperature Distributions Resulting from Coalescence, Vaporization and Combustion of a Polydisperse Spray", ICLASS-88, 4th International Conference on Liquid Atomisation and Spray Systems, Japan.
30. Greenberg, J.B. (1989), "The Burke-Schumann Diffusion Flame Revisited-With Fuel Spray Injection", *Comb. Flame*, Vol. 77, pp. 229-240.
31. Silverman, I., Greenberg, J.B. and Tambour, Y. (1990), "Asymptotic Analysis of a Premixed Polydisperse Spray Flame", *SIAM J. on Appl. Mathematics*, in press.
32. Silverman, I., Greenberg, J.B. and Tambour, Y. (1991), "Solutions of Polydisperse Spray Sectional-Equations via a Multiple-Scale Approach: An Analysis of a Premixed Polydisperse Spray Flame", submitted to ICLASS-91.
33. Tambour, Y., Silverman, I. and Greenberg, J.B. (1991), "Effects of Initial Droplet Size Distribution on Polydisperse Jet Far-Field Diffusion Flames", submitted to ICLASS-91.
34. Yule, A.J., Seng, C.Ah., Felton, P.G., Ungut, A. and Chigier, N.A. (1982), "A Study of Vaporizing Fuel Sprays by Laser Techniques", *Combustion & Flame*, Vol. 44, pp. 71-84.
35. Yule, A.J., Ereat, P.R. and Ungut, A. (1983), "Droplet Sizes and Velocities in Vaporizing Sprays", *Comb. Flame*, Vol. 54, pp. 15-22.
36. Bachalo, W.D., Brena de la Rosa, A. and Rudoff, R.C. (1988), "Advances in Diagnostics for Complete Spray Characterization", ICLASS-88, pp. 287-295.
37. Edwards, C.F. and Rudoff, R.C. (1990), "Structure of a Swirl-Stabilized Spray Flame by Imaging, Laser Doppler Velocimetry and Phase Doppler Anemometry", 23rd Symp. Combust., Orleans, France.
38. Presser, C., Gupta, A.K., Avedisian, C.T. and Semerjian, H.G. (1990), "Fuel Property Effects on the Structure of Spray Flames", 23rd Symp. on Combustion, Orleans, France.
39. Bellan, J. and Harstad, K. (1990), "The Dynamics of Dense and Dilute Clusters of Drops Evaporating in Large, Coherent Vortices", 23rd Symp. on Combustion, Orleans, France.
40. Zahavi, S. and Tambour, Y., "Relaxation of a Polydisperse Spray Behind a Normal Shock Wave: A Sectional Approach", to be submitted to Atomization and Sprays.

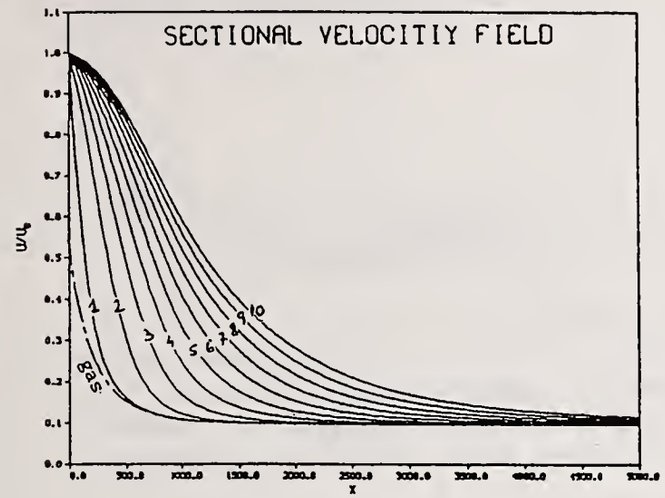

Fig. 1: Variation of gas-phase velocity, and velocity of each size-section of the spray in the relaxation zone. **No evaporation, No coalescence.**

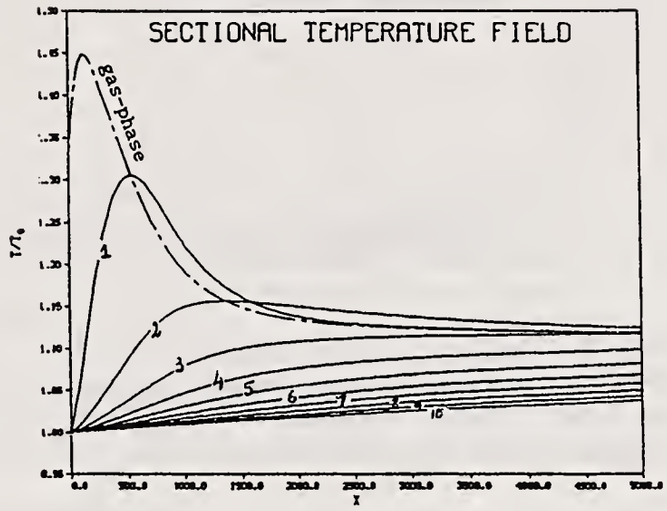

Fig. 2: Variation of gas-phase temperature, and temperature of each size-section of the spray in the relaxation zone. **No evaporation, No coalescence.**

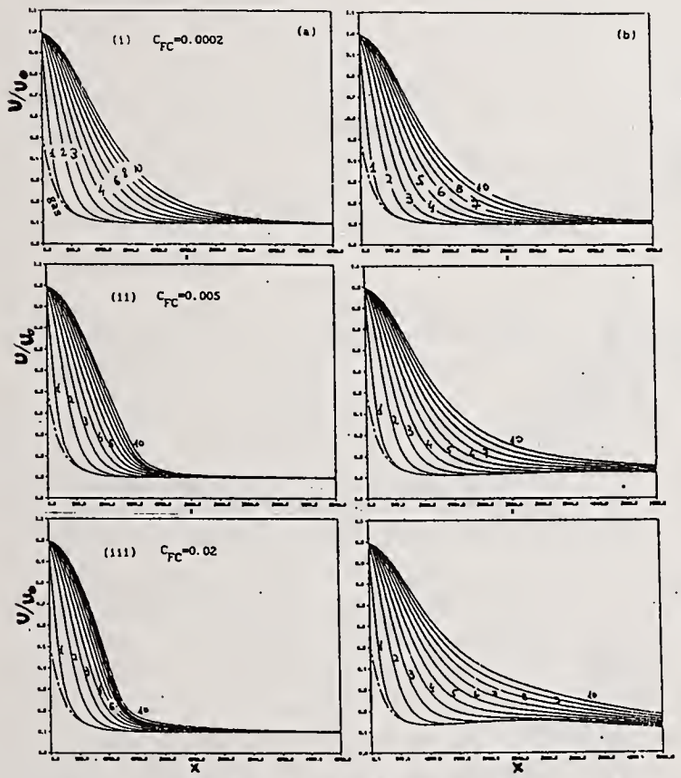

Fig. 3: Variation of gas-phase velocity, and velocity of each size-section of the spray in the relaxation zone, for three coalescence rates: (i) "Low", C_{FC}=0.0002, (ii) "Medium", C_{FC}=0.005, and (iii) "High", C_{FC}=0.02.

(a) Solutions of rigorous "near-field" sectional-equations.

(b) Neglecting inter-sectional momentum and energy transfer.

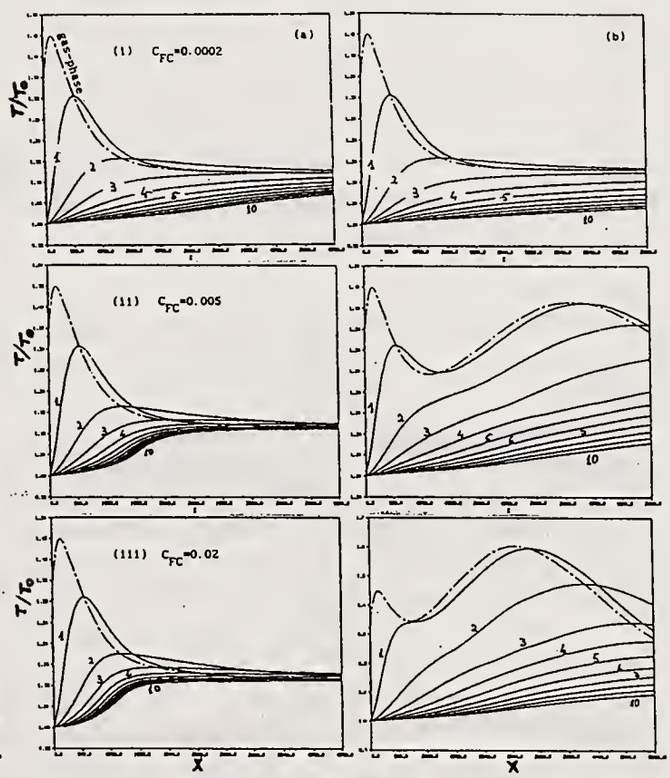

Fig. 4: Variation of gas-phase temperature, and temperature of each size-section of the spray in the relaxation zone, for three coalescence rates: (i) "Low", C_{FC}=0.0002, (ii) "Medium" C_{FC}=0.005, and (iii) "High", C_{FC}=0.02.

(a) Solutions of rigorous "near-field" sectional equations.

(b) Neglecting inter-sectional momentum and energy transfer.

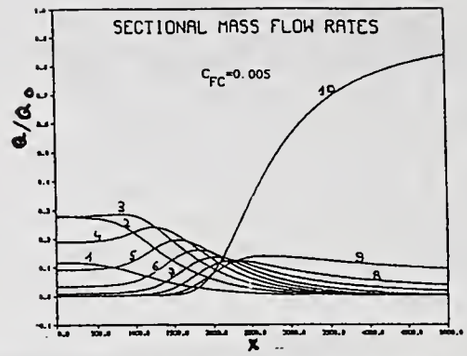

Fig. 5: Variations of the liquid-phase mass flow rate along the axial direction for each of the spray size-sections. "Medium" coalescence rate C_{FC}=0.005 (No evaporation).

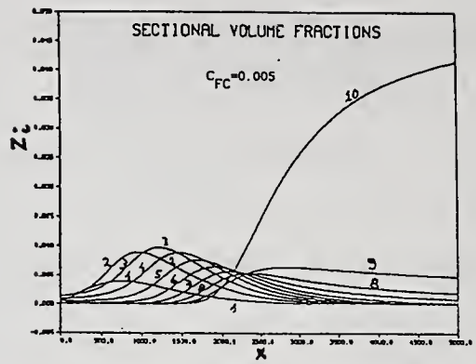

Fig. 6: Variations of the liquid-phase volume fractions along the axial direction for each of the spray size-sections. "Medium" coalescence rate C_{FC}=0.005 (No evaporation).

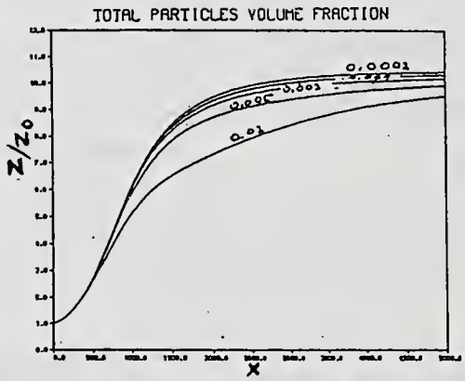

Fig. 7: Profiles of the integral volume fraction of the liquid phase (z) in the relaxation zone for various coalescence rates.

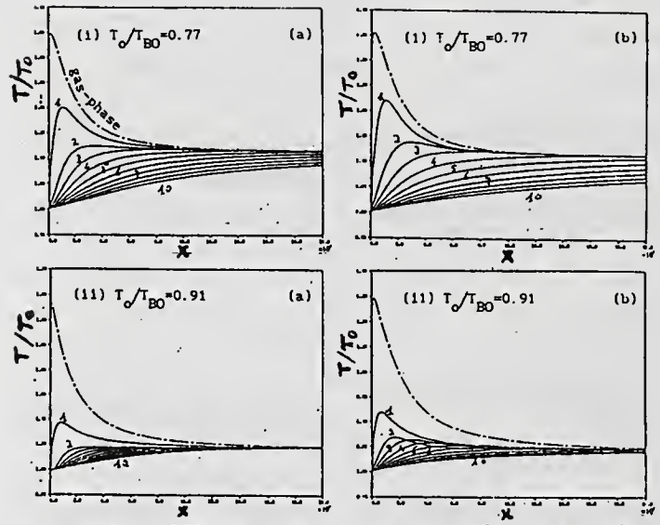

Fig. 8: Effects of heat transfer on the variation of gas-phase temperature, and temperature of each size-section of the spray along the axial direction (evaporation without coalescence). Initial droplets temperature is: (i) 0.77 of their boiling point temperature. (ii) 0.91 of their boiling point temperature.
(a) with Ranz-Marshall convective correlation.
(b) without Ranz-Marshall convective correlation.

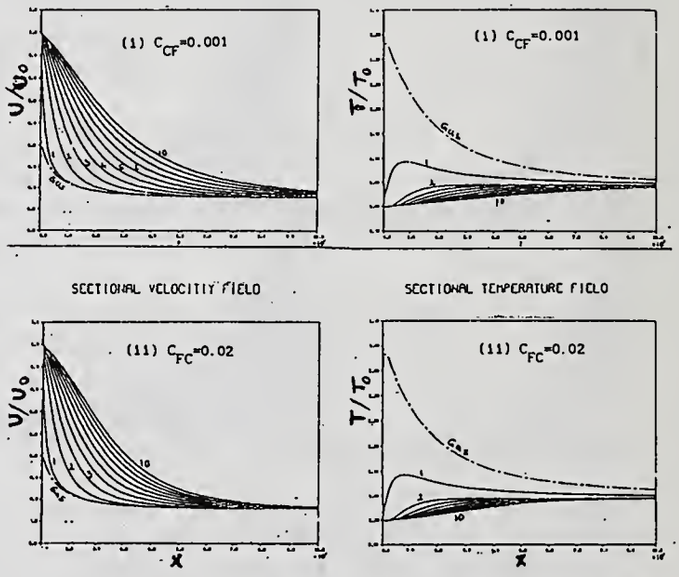

Fig. 9. Effects of simultaneous evaporation and coalescence rates on variation of (a) velocities and (b) temperatures in the relaxation zone, for two coalescence rates (i) C_{CF}=0.001 and (ii) C_{FC}=0.02.

EFFECT OF INTERACTION ON THE RATES OF EVAPORATION OF A GROUP OF DROPS AND PREDICTION OF VOID FRACTION

I. Taniguchi and K. Asano

Department of Chemical Engineering
Tokyo Institute of Technology
Tokyo, Japan

ABSTRACT

Measurements were made for the effect of adjacent solid spheres with arbitrary arrangement on the rates of evaporation of a water and an octane drop for Re_{PA}=72-234,Sc=0.59-1.61, diameter ratios D_P/D_A=0.57-0.89 and dimensionless distance L/D_A=1.12-9.44 ,W/D_A=0-1.02. New correlations for the effect of solid spheres on the rates of evaporation were proposed. By use of the correlations, prediction of void function was made and compared with the experimental data for gas-solid fluidized bed.

INTRODUCTION

Prediction of void function, which relates heat and mass transfer rates of a group of drops or of particles with that for a single drop or particle, is important for design of spray columns or fluidized bed- or fixed-bed reactors. Although in the past decades many theoretical or experimental approaches (2),(5),(6),(9),(10) to motion ,heat and mass transfer of a group of drops or particles have been made , few approach has ever been made to the prediction of void function. In our previous papers, some experimental (1),(13) and theoretical (11), (12) approaches to the effect of interaction on the drag coefficients and diffusion fluxes of two coaxially arranged drops were made under low- to high mass flux conditions and for intermediate Reynolds number ranges. The purpose of the present work is to make an experimental approach to the effect of a group of solid spheres on the rates of evaporation of a drop and to develop a new method for prediction of void function for low to intermediate Reynolds number ranges.

EXPERIMENTAL APPARATUS AND PROCEDURES

Experimental Apparatus

Figure 1 shows a schematic diagram of an experimental apparatus. The test section was a brass-made rectangular duct of 70x70mm in cross section and 166mm in length with two large side view windows. In the middle of the test section, a 0.5mm-outer diameter stainless steel tubes for liquid supply was mounted by a three-dimensional fine adjustment traversing mechanism,through which liquid to an evaporating pendant drop was supplied by a microfeeder-

operated hypodermic syringe. A 0.05mm-outer diameter Chromel-Alumel thermocouple was mounted by a two-dimensional fine adjustment traversing mechanism for measurements of drop temperature.

Measurement

Rates of evaporation of a pendant drop were taken equal to equilibrium liquid flow rates supplied by a microfeeder, of which flow rates were so adjusted that the diameter of the drop did not change appreciably for a given time interval.

Distance between the center of a drop and a solid sphere or distance between solid spheres were measured by a cathetometer with an accuracy of 1/100mm. Diameters of a pendant drop were also measured by the same cathetometer, from which surface area of the drops were calculated by assuming that the shape of the drop was symmetrical with respect to vertical axis(3).

The drop temperatures were measured by a 0.05mm-outer diameter Chromel-Alumel thermocouple mounted on a two-dimensional fine adjustment traversing mechanism, from which the surface temperatures of the evaporating drop were estimated by assuming that the temperature distribution inside the drop is uniform (3). Surface concentrations of the vapor of an evaporating drop were estimated from saturated vapor pressures of the pure liquid at the surface temperatures.

Ranges of variables were shown in Table 1.

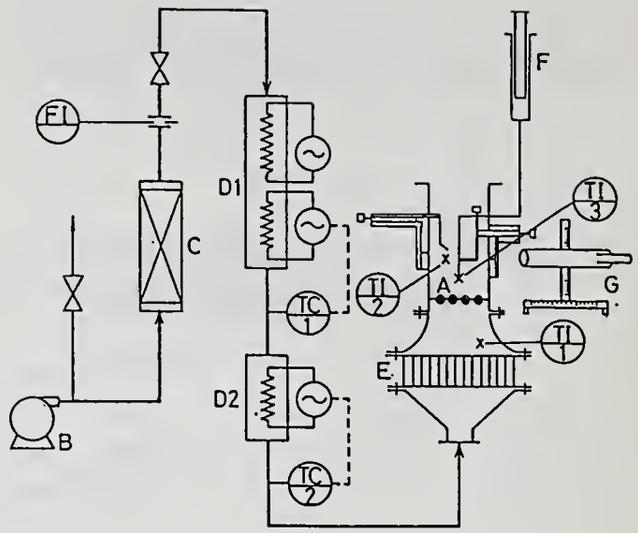

A : Test section
B : Blower
C : Silica gel dehumidifier
D1,2:Heater
E : Divergent-convergent nozzle with calming grid
F : Microfeeder
FI : Orifice flow meter
G : Cathetometer
TC1, 2:Temperature controller
TI : Thermocouple for
1:bulk flow
2:temperature profile
3:liquid drop

Fig. 1 Schematic diagram of an experimental apparatus.

Table 1 Ranges of experimental variables

System		Water-Air	Octane-Air
D_P	[mm]	1.92-2.66	1.72-2.28
D_A	[mm]	3.0	3.0
L	[mm]	0.80-28.32	4.95-24.21
W	[mm]	0-4.11	0-1.80
T_∞	[K]	343-371	335-337
U_∞	[m/s]	0.31-1.40	0.80-1.17
Re_{PA}	[-]	73-234	138-232
Sc	[-]	0.59	1.61
L/D_A	[-]	1.12-9.44	1.65-8.07
D_P/D_A	[-]	0.64-0.89	0.57-0.76
W/D_A	[-]	0-1.02	0-0.60

EXPERIMENTAL RESULTS

Effect of Two and Four Upstream Spheres

Figure 2 shows the effect of two solid spheres of equal diameters arranged symmetrically around center axis of the drop on the diffusion fluxes of a water drop. The ordinate is the diffusion fluxes normalized by the ones for a single drop (8) and the abscissa is the dimensionless distance L/D_A. The parameter, W/D_A, is the dimensionless distance between the center axis and the solid sphere. The effect of L/D_A on the diffusion fluxes becomes considerable as W/D_A decrease. By considering our previous numerical

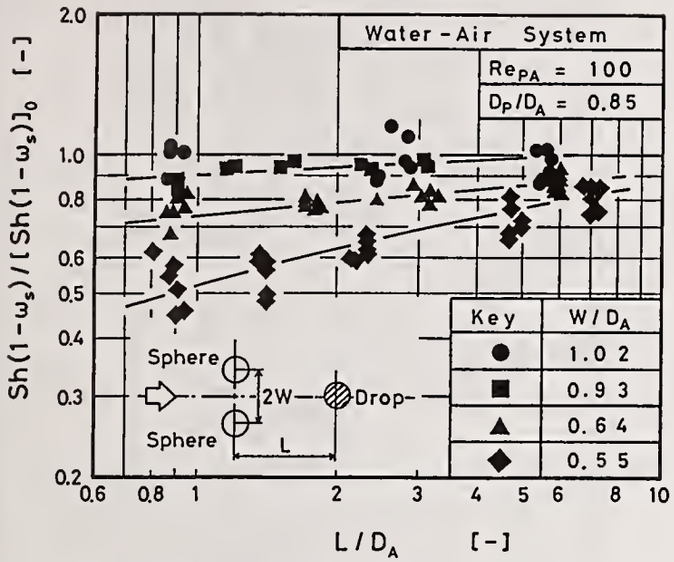

Fig. 2 Effect of two solid spheres arranged symmetrically around center axis of a drop.

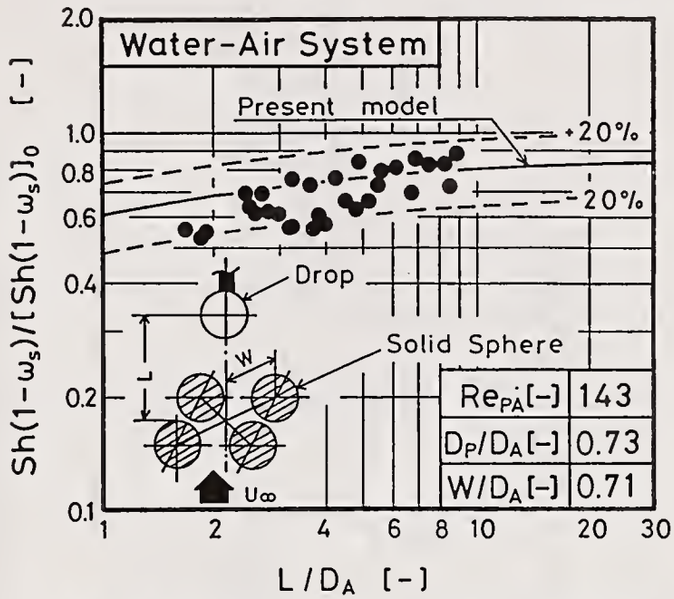

Fig. 3 Effect of four solid spheres arranged symmetrically around center axis of a drop.

correlation for the effect of interaction on the rates of mass transfer of two coaxially arranged solid spheres (11),(12);

$$f = 1/\{\ 1+0.77(D_P/D_A)^{-0.21}(L/D_A)^{-1.38\cdot Re_{PA}^{-0.26}}\ \} \tag{1}$$

the present data were well correlated by the following equation:

$$Sh(1-\omega_s)/[Sh(1-\omega_s)]_0 = f_1^2 \tag{2}$$

$$f_1 = 1/\{1+0.77(D_P/D_A)^{-0.21}(L/D_A)^{-1.38\cdot Re_{PA}^{-0.26}}(1-W/D_A)^{1.5}\} \tag{3}$$

where $(1-W/D_A)^{1.5}$ represents the effect of eccentric arrangement of solid spheres.

Figure 3 shows the effect of four solid spheres of equal diameters arranged symmetrically around the center axis of the drop on the diffusion fluxes of a water drop. The solid line in the figure represents the diffusion fluxes estimated by the following equation:

$$Sh(1-\omega_s)/[Sh(1-\omega_s)]_0 = f_1^4 \tag{4}$$

where f_1 is estimated by use of Eq.(3). Good agreement is observed between the data and the theory.

Figure 4 shows the effect of two solid spheres of arbitrary arrangement on the rates of evaporation of a water drop, where the first solid sphere(the one near to the drop) is arranged eccentrically to the center axis and the second one is arranged coaxially with the drop. The dot-dash line in the figure represents the effect of the first solid sphere calculated by Eq.(3). Deviation from the dot-dash line may indicate the effect of the interaction due to the presence of the second sphere. If we assume that the effect of interaction with two solid spheres of

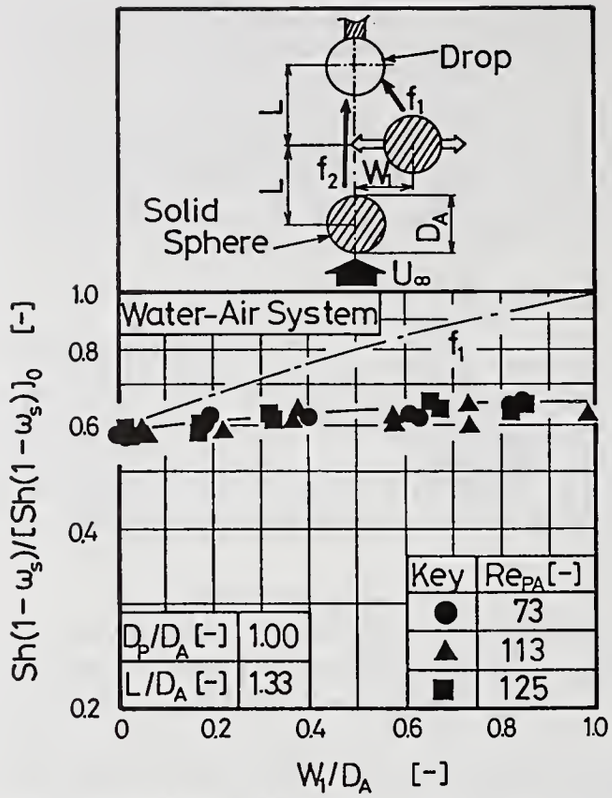

Fig. 4 Effect of two solid spheres with arbitrary arrangement.

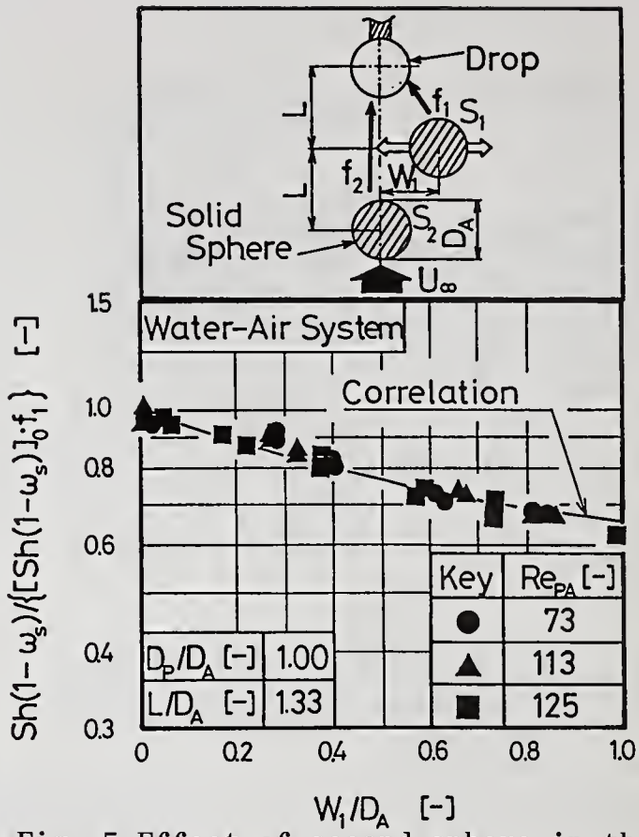

Fig. 5 Effect of second sphere in the presence of the first solid sphere.

arbitrary arrangement is represented by the following equation as was the case with two- and four-symmetrically arranged solid spheres:

$$Sh(1 - \omega_s)/[Sh(1 - \omega_s)]_0 = f_1 \cdot f_2 \tag{5}$$

the effect of the second solid sphere may be obtained by use of Eq.(3) for f_1.

Figure 5 shows the results. The effect of the second sphere is well correlated by the following equation:

$$f_2 = \frac{1}{1+0.77\cdot(D_P/D_A)^{-0.21}\cdot(L/D_A)^{-1.38\cdot Re_{PA}^{-0.26}}\cdot(1-W_2/D_A)^{1.5}\cdot(W_1/D_A)^{(1-W_1/D_A)^{0.43}}} \tag{6}$$

where a parameter $(W_1/D_A)^{(1-W_1/D_A)^{0.43}}$ in the denominator represents the effect of the first sphere on the interaction function f_2 for the case of arbitrary arrangement of two solid sphere.

Effect of Solid Sphere Layers

Figure 6 shows the effect of upstream solid sphere layers of equal diameters in rectangular arrangement, where the drop is arranged on the perpendicular bisector of the line connecting the centers of two spheres. The solid lines in the figure represent the effect of number of solid sphere layers on the rates of evaporation of a drop estimated by the following equations:

n=1: $$Sh(1 - \omega_s)/[Sh(1 - \omega_s)]_0 = f_1^2 \tag{2}$$

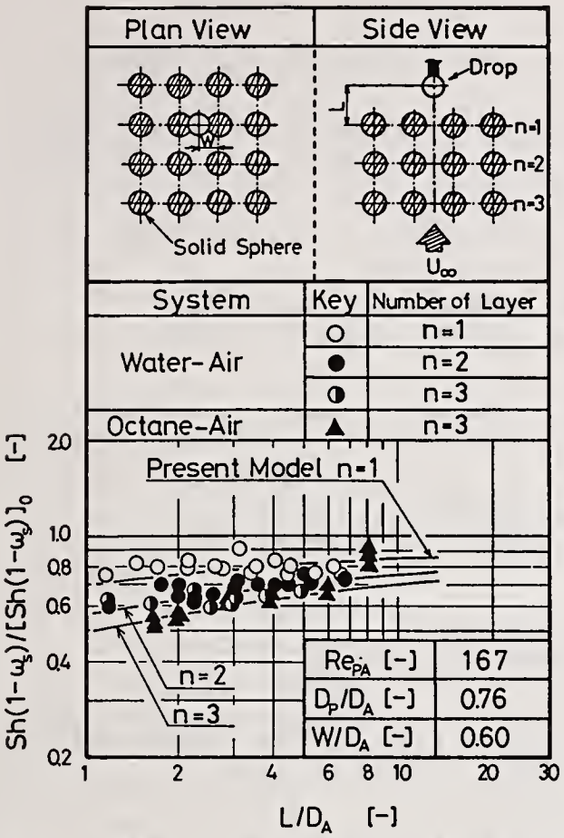

Fig. 6 Effect of number of layers; a drop is arranged on the perpendicular bisector of the line connecting the centers of two spheres.

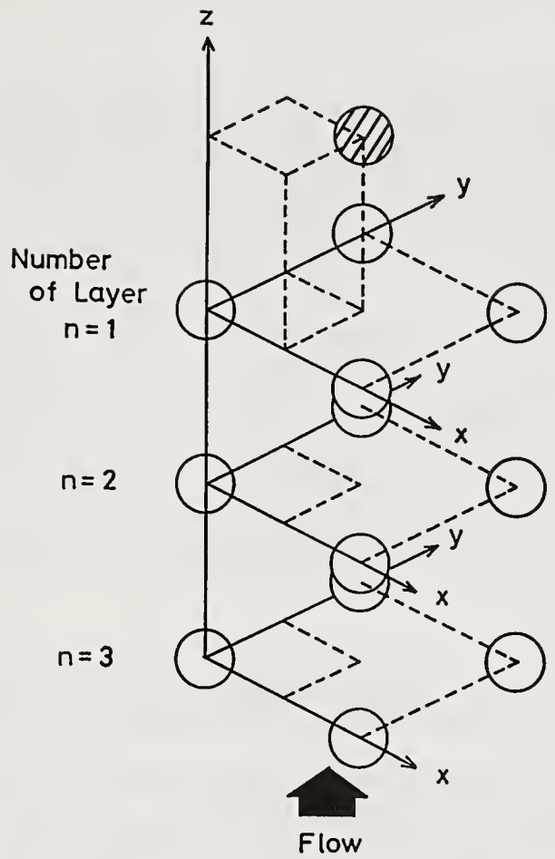

Fig. 7 Physical picture of the model for calculation of void function.

n=2:

$$Sh(1 - \omega_s)/[Sh(1 - \omega_s)]_0 = f_1^2 \cdot f_2^2 \tag{7}$$

n=3:

$$Sh(1 - \omega_s)/[Sh(1 - \omega_s)]_0 = f_1^2 \cdot f_2^2 \cdot f_3^2 \tag{8}$$

$$f_3 = 1/\{1+0.77(D_P/D_A)^{-0.21}(L/D_A)^{-1.38}\cdot Re_{PA}^{-0.26}(1-W_3/D_A)^{1.5}\cdot f_{n,k}\} \tag{9}$$

where $f_{n,k}$ represents the effect of k-th layers on interaction function of n-th layer by:

$$f_{n,k} = 1/[\prod_{k=1}^{n-1}\{(W_k/D_A)^{(1-W_k/D_A)^{0.43}}\}] \tag{10}$$

Good agreement is observed between the data and the theory.

PREDICTION OF VOID FUNCTION

Method of Calculation

Discussions in the previous sections may lead to estimation of void function for heat and mass transfer of a group of drops or of particles. The

following simplifying assumptions were made for the present calculation.

1) Particle or drop size is uniform.
2) Particles or drops are arranged in rectangular arrangement on each layer and the distance between each layer is equal to the distance between particles or drops on the layer.
3) Relative position of an arbitrary particle or drop on each layer with respect to the one on the other layers is independent.
4) Effect of downstream layers is negligibly small.
5) Effect of interaction of n-th upstream layers on mass transfer can be estimated by the following equations:

$$Sh(1-\omega_s)/[Sh(1-\omega_s)]_0 = f_1^4 \cdot f_2^4 \cdot f_3^4 \cdots\cdots f_n^4 \tag{11}$$

n=1:

$$f_1 = 1/\{1+0.77(D_P/D_A)^{-0.21}(L/D_A)^{-1.38}\cdot Re_{PA}^{-0.26}(1-W_1/D_A)^{1.5}\} \tag{3}$$

n>1:

$$f_n = 1/\{1+0.77(D_P/D_A)^{-0.21}(L/D_A)^{-1.38}\cdot Re_{PA}^{-0.26}(1-W_n/D_A)^{1.5}\cdot f_{n,k}\} \tag{12}$$

Figure 7 shows physical picture of the model. Calculations were made by dividing one-quarter of a layer-element into 10x10 grid mesh. Void function is calculated by the following equation.

$$F(\varepsilon) = \frac{\int_0^{L/2}\cdots\cdots\int_0^{L/2} f_1^4 \cdot f_2^4 \cdots\cdots f_n^4 dXdY\cdots dXdY}{(L/4)^n} \tag{13}$$

Void Function

Figure 8 shows results of the calculation. The ordinate is the void

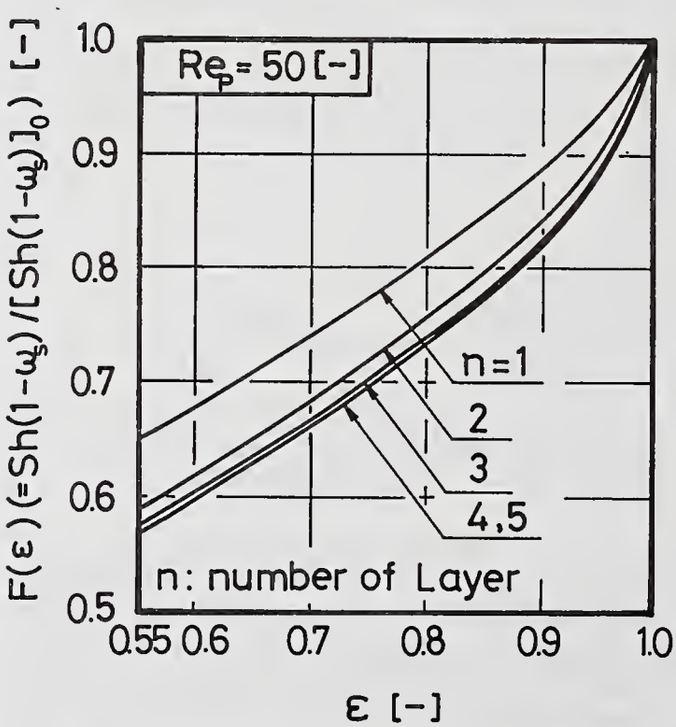

Fig. 8 Prediction of void function.

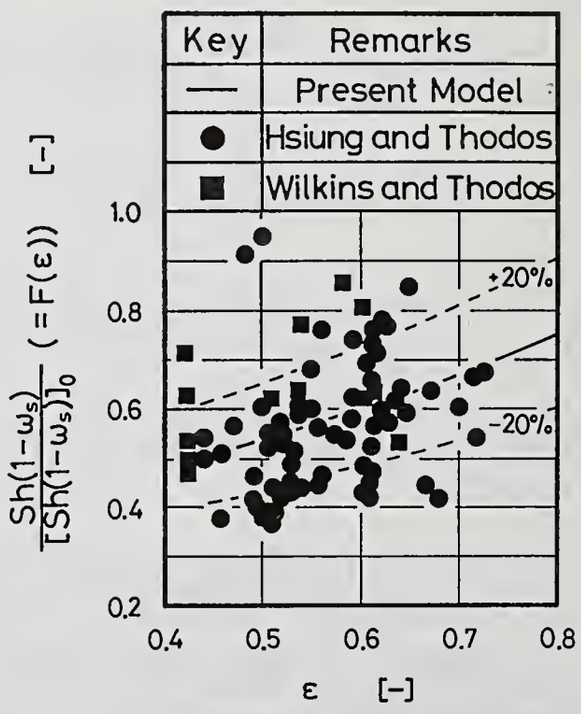

Fig. 9 A comparison between experimental data and proposed correlation.

function calculated by the present model and the abscissa is void fraction of particle layers, where n is number of upstream layers of rectangular arrangement. The figure clearly indicates that the void function approaches to an asymptotic value as the number of layers increase. The calculated void functions for n>5 are well correlated by the following equations:

$$F(\varepsilon) = 1/\{ 1 + 1.29\cdot(1 - \varepsilon)^{0.75}\} \qquad (14)$$

Fig. 9 shows a comparison of the observed void function which were obtained for mass transfer in gas-solid fluidized bed (4),(14) with the prediction by the proposed correlation, where solid line in the figure represents the correlation(Eq.(14)). Although some scattering of the data is observed, fairly good agreement between the data and the theory is observed.

CONCLUSIONS

Measurements for the effect of adjacent solid spheres on the rates of evaporation of a water- and an octane drop into dry air were made to show the following conclusions.

1) The effect of adjacent solid spheres on the rates of mass transfer is well predicted by Eqs. (3) and (12).
2) A new method for prediction of void function is proposed to show good agreement with observed data.

ACKNOWLEDGMENTS

The authors are grateful to Mr. J. Narita of Tokyo Institute of Technology for his assistance in measurements.

NOMENCLATURE

$\mathscr{D}$ = binary diffusion coefficient,m^2/s
D_A = diameter of front sphere,m
D_P = diameter of liquid drop,m
$F(\varepsilon)$ = void function defined by Eq.(13)
f_1, f_2, f_3 = interaction function defined by Eqs.(3),(6),(9)
$f_{n,k}$ = interaction function defined by Eq.(10)
L = distance between center of two spheres,m
N_A = mass flux of component A,$kg/(m^2\cdot s)$
n = number of layer
Re_{PA} = Reynolds number based on front sphere or drop($D_A U_\infty/\nu$)
Sc = Schmidt number($=\nu/\mathscr{D}$)
Sh = Sherwood number($=N_A\cdot D_P/\mathscr{D}_s\cdot\rho_s(\omega_s - \omega_\infty)$)
T = temperature,K
U = velocity,m/s
W, W_1, W_2 = distance between center axis and center of solid sphere,m

ε = void fraction
ν = kinematic viscosity of gas,m^2/s
ρ = density,kg/m^3
ω = mass fraction

Subscripts

A = front sphere or drop
B = rear sphere or drop
G = gas phase
s = surface of drop
0 = a single sphere without mass injection
∞ = free stream

REFERENCE

1. Asano, K., Taniguchi, I. and Kawahara, T., " Numerical and Experimental Approaches to Simultaneous Evaporation of Two Adjacent Volatile Drops", Proceedings of the 4th International Conference on Liquid Atomization and Spray Systems, pp. 411-418, 1988.
2. Chen, S. J. and Tong, A. Y., " Numerical Study on Hydrodynamics and Heat Transfer of Droplet Arrays Using Grid Generation", AIChE Symposium, Series No. 257, Vol. 83, pp. 230-236,1987.
3. Chuchottaworn, P., Fujinami, A. and Asano, K.," Experimental Study of Evaporation of A Volatile Pendant Drop Under High Mass Flux Conditions", J. Chem. Eng. Japan, Vol. 17, pp. 7-13, 1984.
4. Hsiung, T. H. and Thodos, G.," Mass Transfer in Gas-Fluidized Beds: Measurement of Actual Driving Forces", Chem. Eng. Sci., Vol. 32, pp.581-592, 1977.
5. Labowsky, M., " The Effect of Nearest Neighbor Interactions on the Evaporation Rate of Cloud Particles ", Chem. Eng. Sci., Vol. 31, pp. 803-813, 1976.
6. Marberry, M., Ray, A. K. and Leung, K.," Effect of Multiple Particle Interactions on Burning Droplets", Combust. and Flame, Vol. 57, pp. 237-245, 1984.
7. Miura, K., Miura, T. and Ohtani, S.," Effect of Surrounding Glass Beads on Heat and Mass Transfer from A Water Droplet", Kagaku Kogaku Ronbunshu, Vol. 1, pp. 241-246, 1975.
8. Ranz, W. E. and Marshall, W. R.," Evaporation from Drops; Part 1 and Part 2", Chem. Eng. Progr., Vol. 48, pp. 141-146, 173-180, 1952.
9. Ray, A. K. and Davis, E. J.," Heat and Mass Transfer with Multiple Particle Interactions Part I. Droplet Evaporation" ,Chem. Eng. Commun., Vol. 6, pp. 61-79, 1980.
10. Shuen, J. S., " Effects of Droplet Interactions on Droplet Transport at Intermediate Reynolds Numbers", AIAA 25th Aerospace Sciences Meeting , AIAA-87-0137, 1987.
11. Taniguchi, I. and Asano, K.," Numerical Analysis of Drag Coefficients and Mass Transfer of Two Adjacent Spheres", J. Chem. Eng. Japan, Vol. 20, pp. 287-294, 1987.
12. Taniguchi, I. and Asano, K., " Calculation of Drag Coefficients and Mass Transfer of Two Adjacent Spheres of Various Diameter Ratios," J. Chem. Eng. Japan, Vol. 22, pp. 701-703, 1989.
13. Taniguchi, I., Kawahara, T. and Asano, K.," Simultaneous Evaporation of Two Adjacent Volatile Drops", J. Chem. Eng. Japan, Vol. 23, pp. 315-319, 1990.
14. Wilkins, G. S. and Thodos, G.," Mass Transfer Driving Forces in Packed and Fluidized Beds", AIChE. J. Vol. 15, PP. 47-50, 1969.

INFLUENCE OF TURBULENCE ON THE MASS TRANSFER FROM LIQUID FUEL DROPLETS

I. Gökalp, C. Chauveau, O. Simon and X. Chesneau

Centre National de la Recherche Scientifique
Laboratoire de Combustion et Systèmes Réactifs
Orléans, France

ABSTRACT

An experimental set-up and an experimental strategy have been developed to investigate the influence of turbulence on the global mass transfer rates from fuel droplets. Heptane and decane droplets of 1.5 mm initial diameter suspended in grid induced turbulent flows have been investigated in the regime where the integral length scales of turbulence are, on average, 5 times larger than the initial droplet diameter. The turbulence intensity has been increased up to 44%. A new mass transfer parameter which distinguishes between the influences of the mean relative velocity and that of turbulence structure has been introduced. Mass transfer from heptane droplets has been found insensitive to turbulence. On the contrary, the same turbulence conditions exert a significant influence on the mass transfer from decane droplets. It has been shown that the influence of turbulence energy on the mass transport from decane droplets can be represented by a turbulence Reynolds number. The Frössling coefficient has been found to increase with the turbulence intensity. The differences in the sensitivity of heptane and decane droplets against the turbulence influence on mass transfer are tentatively explained by introducing a "vaporization Damköhler number". The present experimental results suggest that turbulence enhances the mass transport from liquid droplets only for low values of this number.

INTRODUCTION

Spray combustion occurs in most cases in a turbulent medium. This enhances the challenging nature of multiphase reacting flows, but also increases their complexity [1]. The studies of the influence of a turbulent convective flow on the pure vaporization rates of single droplets are relevant for spray combustion, for one of the possible scenarios of the single droplet behaviour is their total vaporization before reaching the flame zone. Furthermore, pure droplet vaporization is also of interest for other applications such as spray drying or spray cooling [2].

One way to tackle the problem of the influence of turbulence on interphase transport phenomena is to simplify it by investigating the interactions between a given turbulence structure and a single vaporizing or burning droplet. This strategy could be justified if one is interested in dilute dispersed flows, reacting or non reacting. But, even for a single droplet, current numerical calculations try to avoid the problem of turbulence by assuming that a locally laminar region exists

near the droplet surface due to the much smaller size of the droplets compared to the typical large eddy sizes [3].

In order to contribute to this area, we have initiated the investigation of the influence of turbulent flows on the vaporization and burning characteristics of single fuel droplets [4, 5]. The issues we are addressing are the modification of the heat and mass transfer characteristics of pure and bicomponent fuel droplets and of the transition criteria between the envelope and wake flame regimes, by varying the turbulence structure in terms of its intensity and length and time scales. In the work described below, some preliminary results on the mass transfer (low temperature vaporization) from n-heptane and n-decane droplets suspended in a grid induced turbulent flow are reported.

The experimental set-up, the diagnostics used and the characteristics of the grid-generated turbulence are briefly presented in section 2. Section 3 presents the experimental results on the influence of turbulence on the global mass transfer parameters from suspended heptane and decane droplets and proposes an interpretative framework for the observed results.

EXPERIMENTAL SET-UP AND FLOW CONDITIONS.

The experiments are performed in a facility specially designed for this purpose: The Forced Flow Droplet Burning Facility (FF-DBF) which is fully described in Gökalp et al. [4, 5] and Chauveau [6]. It is briefly presented here for completeness. The FF-DBF allows the investigation of single and interacting droplet vaporization and/or burning in stagnant, laminar and turbulent conditions. It consists of a closed loop flow channel in stainless steel (length: 3.20 m; height: 0.85 m) which is fixed on a supporting structure. The flow channel is composed of an electrical axial fan, an electrical heater, a set of laminarization ducts. The channel is connected to a stainless steel test section of square cross section (side: 0.15 m; length: 0.50 m). A by-pass channel and a return channel of circular cross-section (diameter: 20 cm) closed the loop to the electrical fan. Turbulence grids can be positioned at the inlet of the test section. Two circular glass windows are mounted vis a vis on the parallel sides of the test section to allow optical access. The test section also supports the injection and the ignition systems.

Droplets of approximately 1 mm to 1.5 mm initial diameter can be formed by using a syringe located at the top of the test section. A quartz fibre (diameter 0.2 mm) is tilted to the syringe extremity allowing the transfer of the droplet to the fibre. The lower extremity of the fibre has an enlarged diameter of 0.5 mm. The fibre is then tilted back and positioned in front of the test section windows. The sequence of operations is performed automatically by using step-motors controlled by a micro-computer.

The air flow can be generated by the axial fan up to a maximum velocity of approximately 5 m/s in the test section. The characteristics of the turbulent flows are measured with laser Doppler anemometry, and the flow monitoring system is calibrated against the mean longitudinal velocity at the location of the droplet.

The principle diagnostic system used to investigate the droplet vaporization phenomena is based on the visualization of the droplet. The imaging system is a high speed video camera, Kodak Ektapro 1000, which can record up to 1000 full frames per second allows the detailed analysis of the time variation of droplet dimensions. The Ektapro 1000 Motion Analyser's live, real time viewing makes it possible to follow the investigated phenomena frame by frame. The digitized images from the Ektapro system are transferred to a micro-computer where the image analyses are performed. More details on the image analysis technique can be found in Chauveau [6].

In the calculation of the droplet surface regression rates, (or the global vaporization rate), we evaluated a characteristic dimension for the droplet in terms of the diameter of a sphere of equivalent projected surface area. The projected droplet surface area is determined by image

analysis. The droplet equivalent projected diameter is calculated as the diameter of a circle having the same area as its projected image.

To investigate the mass transfer characteristics of fuel droplets in a turbulent medium, turbulence parameters, such as the turbulence intensity and the length and time scales, have been controlled by using square mesh grids. These parameters have been varied independently by varying the mesh size, the mean flow velocity and the distance between the grid and the droplet. The mesh sizes we used are, in mm, M = 1.4; 2.9; 5; 10 and 37. The grids with M = 37 mm and 1.4 mm or 5 mm have also been used in combination. In the combined grid mode, another parameter we varied is the distance between the two grids. For mean flow velocities equal to or higher than 1 m/s, the turbulence structure in all cases is very close to that of isotropic turbulence [4, 6]. The relevant turbulent length and time scales have been determined from spectral analysis of instantaneous velocity signals and by using the theoretical relations for isotropic turbulence. The following flow and turbulence characteristics correspond to those determined at the position of the droplet in the test section.

The mean velocity has been varied from 1 m/s to 4.5 m/s with a step of 0.5 m/s. This means that the Reynolds number based on the mesh size has been varied from 90 to approximately 6000. In terms of the droplet Reynolds number, the variation is approximately between 100 and 450. The turbulence intensity, defined as the ratio between the longitudinal r.m.s. velocity fluctuation and the mean axial velocity, has been varied from Tu = 1.5% to 44%. The lowest turbulence intensity corresponds to our quasi-laminar conditions as it was impossible to obtain a pure laminar flow in the test section. The longitudinal integral length scale varies from 1 mm to 19.5 mm. This means that the ratio between the initial droplet diameter and the integral length scale varies between 1.5 and 0.08. The maximum value obtained for the turbulence Reynolds number based on the integral length scale is 350. For each mean velocity, 3 to 9 different turbulence conditions are obtained. In total, 42 different flow conditions have been explored for the vaporization of heptane droplets; for decane, this number is 17.

However, it is important to mention that only 3 of these 59 experimental conditions correspond to cases where the initial droplet diameter is lower than the integral length scale of the turbulence. This means that in most of the cases, the vaporizing droplet interacts with small scale and less energetic eddies.

RESULTS ON MASS TRANSFER RATES

The main objective of this study is to investigate the influence of a turbulent flow on the global vaporization rates of suspended fuel droplets. More specifically, it is desirable to separate the respective influences of the mean velocity from that of the turbulence. This is because in real spray situations, small droplets may easily be transported "in the mean" by the carrier phase, thus with a zero mean relative velocity. However, they may be subjected to the instantaneous fluctuations of the flow field.

In this section, experimental results on the global vaporization rates of heptane and decane droplets in grid induced turbulent flows are presented. The values of the vaporization rates that are presented below are the average values of 3 to 5 runs under the same flow conditions and for initial droplet diameters equal approximately to 1.5 mm.

Vaporization constants in laminar and turbulent flows.

Fig. 1 presents the time variation of the droplet diameter for heptane droplets under quasi-laminar conditions. The stagnant and two forced convective runs are shown. For these last cases, the droplet Reynolds numbers are approximately 100 and 425. The droplet diameter is normalized by its initial value; the time axis is normalized by the total vaporization time of the stagnant case.

From the time variation of the instantaneous droplet diameter ds, we have determined the variation of the instantaneous vaporization mass flux. The results corresponding to the previous

cases are presented on Fig. 2. The curves are normalized by the initial droplet mass and the total vaporization time of the stagnant case. Except the initial transient phase, which is too short to be observed in these low temperature vaporization experiments, these curves are very close to those predicted by [7]. Similar results have also been obtained for the other mean convective velocities and for decane droplets.

The experiments with heptane droplets have shown no influence of turbulence on the vaporisation rate determined from the d^2-law as $K = - d(ds^2)dt$ [5]. The same conclusion can also be drawn for the influence of the droplet Reynolds number for increasing turbulence intensity. The Frössling coefficients [8, 9] have been found slightly scattered around the value of 0.19. It is noteworthy that the Frössling coefficient determined in this study is significantly lower than the value of 0.276 obtained by Frössling himself and widely accepted today.

As shown on Figs. 3, 4 and 5, the results for decane droplets vaporizing under the same conditions are significantly different. Indeed, for the same turbulence structures as for the heptane case and for three values of the mean convective velocity (1, 2 and 3 m/s), an important increase of K/Ko with the turbulence intensity is observed (Fig. 3). On Fig. 4, the influence of the turbulence intensity on the time variation of the droplet diameter is shown for U = 2 m/s. On the other hand, as shown on Fig. 5, the Frössling coefficient for decane, which is equal to 0.19 for the quasi-laminar case, increases gradually with turbulence intensity, and reaches the value of 0.274 for Tu = 20%.

The curves of Fig. 3 can be represented by the following linear relationship:

$$(K/Ko)_T = C1(u/U) + (K/Ko)_L \qquad (1)$$

where subscripts T and L refer respectively to turbulent and laminar cases. In other words, $(K/Ko)_L$ represents the increase of the mass transfer constant due only to laminar forced convection. Eq. 1 can be written also as

$$Go = (K_T - K_L)/Ko = C1(u/U) \qquad (2)$$

It is proposed here to consider the left hand side of this equation as representing the influence of turbulence alone on the mass transfer rate, with respect to its stagnant case value. This parameter is introduced in order to separate the effects of mean convective velocity from that of the turbulence. In the following, we shall use this parameter in the discussion of the turbulence effect on the global vaporization rates of droplets.

Influence of the turbulence Reynolds number

Fig. 6 shows the variation of Go with the turbulence intensity for three mean velocities. It is clear that the influence of turbulence is enhanced with increasing mean velocity. The coefficient C1 passes from 0.0053 for U = 1 m/s to 0.018 for U = 3 m/s.

Previous studies have shown that the transfer rates from particles or drops increase with increasing turbulence intensity. They also show that this increase is stronger when the droplet Reynolds number is high. This effect has been generally correlated with the parameter Re(u'/U).

If the Reynolds number is taken to be the one based on the droplet diameter, this parameter can be written as (u/U)(Ud/ν) or ud/ν, which is a turbulent Reynolds number based on a turbulence length scale equal to the droplet diameter, where ν is the kinematic viscosity of the free stream. Fig. 7 shows the following correlation for three mean convective velocities:

$$Go = (K_T - K_L)/Ko = C2(ud/\nu) = C2Re_{Td} \qquad (3)$$

The values for C2 are 0.0052, 0.0056 and 0.0060 for respectively U = 1, 2 and 3 m/s. Even if a slight dependence against the mean velocity is still observed, this last correlation is significantly improved compared to that given by Eq. 2. As the parameter Go represents only the influence of turbulence on

the mass transfer rate, the improvement of the correlation when the turbulence parameters are introduced instead of the mean velocity, seems encouraging.

Influence of the turbulence length scale

Past experimental work on heat and mass transfer from spherical particles or drops, have shown some influence of the ratio between the turbulence length scales and the particle diameter [10, 11, 12]. A detailed inspection of our experimental results shows also some length scale influence on the mass transfer from decane droplets.

For example, for U = 1 m/s, the parameter Go = $(K_T - K_L)/Ko$ is larger for u/U = 8% and Le/do = 2.7 than for u/U = 10% and Le/do = 9. Similarly, for U = 3 m/s, this parameter is larger for u/U = 11% and Le/do 4.7 than for u/U = 11.5% and Le/do = 11.8. These comparisons seem to indicate that, for a given turbulence intensity, smaller scale turbulence structures are more efficient to increase the mass transfer rates. It should however be noted that this length scale influence does not explain the differences that we observed between the sensitivities of mass transfer rates from heptane and decane droplets against turbulence, as the Le/do ratios for both fuels are the same.

Influence of time scales and discussion

The main result of this investigation is indeed the differential sensitivities of heptane and decane droplets for the same turbulence structure. We have just pointed out that this difference is observed in spite of the similar turbulence length scale to droplet diameter ratios. In this part, we shall propose a tentative explanation in terms of the time scale ratios of the phenomena involved.

Fig. 9 shows for decane droplets the variation of the parameter Go with the integral time scale t_{ed} of velocity fluctuations. This time scale corresponds to turbulent eddies having integral length scales equal or smaller than the instantaneous droplet diameter. This figure shows that, for a fuel droplet of given initial diameter, the efficiency of turbulence to increase the mass transfer rates decreases as the time scale of the eddies effectively interacting with the droplet increases.

In order to compare the heptane and decane cases on a time scale basis, we attempted to define a time scale ratio based on t_{ed} and on a time scale characterizing the thermodynamics of vaporization, t_v. This ratio could be considered as the equivalent of a "vaporization Damköhler number", Da_v. As t_v is constant for a given fuel, the variation of Fig. 9 can also be interpreted as the effect of Da_v. This variation indicates that the effect of turbulence on mass transfer from droplets is more efficient for low values of Da_v. For the comparison of the heptane and decane time scale ratios, we use a baseline case corresponding to the same turbulence structure for both fuels having an initial droplet diameter of 0.15 cm. To estimate the time scale characterizing the thermodynamics of vaporization, we propose to define it, as a first approximation, as the ratio between the film thickness and the radial blowing velocity (or the Stefan velocity) V_r. The radial velocity is calculated by equating the expression of the instantaneous mass transfer rate as $m = 4\pi r^2 \rho_g V_r$ to its expression from the quasi-stationary theory and by assuming the Lewis number equal to unity. In the estimation of the film thickness we used the calculation procedure recommended by Abramzon and Sirignano [7]. The results of these calculations are summarized on the following table .

		C7H16	C10H22
V_r	(cm/s)	0.1	0.004
$(\delta)_M$	(microns)	266	191
t_v	(ms)	266	4775
Da_v		0.03	0.0016

As expected, the radial velocity for heptane is much higher than that of decane. At the present stage of this investigation, it is speculative to attribute any intrinsic significance to the

precise values of the vaporization Damköhler numbers. However, what is certainly significant is the ratio between Da_v(C7H16) and Da_v(C10H22) and which is equal to 18.8. This ratio is in fact very close to that between the respective mass transfer numbers B_M or the vaporization constants under stagnant conditions Ko of the two fuels.

If a reference value of 1 ms is attributed to the time scale characterizing the thermodynamics of vaporization for decane, Fig. 9 shows that for a vaporization Damköhler number higher than 15, the turbulence effect on the mass transfer is negligible. As the characteristic vaporization time for heptane is approximately 20 times shorter than that of decane, for the same turbulence conditions as on Fig. 9, the data point corresponding to heptane will be located at the high vaporization Damköhler number end of the curve, where no turbulence effect on the mass transfer is expected. This reasoning based on the comparisons of the characteristic times of turbulence and of vaporization thermodynamics may then explain the sensitivity differences of heptane and decane droplets against the same turbulence structure.

CONCLUSIONS

It has been shown above that the influence of turbulence on the mass transport from decane droplets can be represented by the turbulence Reynolds number. The Frössling coefficient which correlates the effect of mean relative velocity (or of the droplet Reynolds number) on the mass transfer has been found to increase with the turbulence intensity.

The differences in the sensitivity of heptane and decane droplets against the turbulence influence on mass transfer rates are tentatively explained by introducing a "vaporization Damköhler number". The present experimental results suggest that turbulence enhances the mass transport from liquid droplets only for low values of this number.

REFERENCES

1. Faeth G.M. (1989) in **Turbulent Reacting Flows** (Ed. R. Borghi and S.N.B. Murthy) New York: Springer Verlag, pp. 764-814.
2. Lefebvre A.H. (1989) **Atomization and sprays**, New York: Hemisphere Publishing Corporation
3. Megaridis C.M. and Sirignano W.A.(1990) **Paper presented at the ASME Winter Annual Meeting**, Dallas, Texas
4. Gökalp I, Chauveau C., Richard J.R., Kramer M. and Leuckel W. (1988) **Twenty-second Symposium (International) on Combustion**, The Combustion Institute, pp. 2027-2035.
5. Gökalp I., Chauveau C. and Monsallier G. (1989) in **Drops and Bubbles. Third International Colloquium on Drops and Bubbles**, (Ed. T.G. Wang), AIP Conferenc Proceedings 197; pp. 362-372.
6. Chauveau C. (1990) **PhD Thesis**, University of Orléans.
7. Abramzon B. and Sirignano W.A. (1988) **AIAA Paper 88-0636**. 14p.
8. Frössling N. (1938) **Gerlands Beitr. Geophys.**, 52:170.
9. Ranz W.E. and Marshall W.R. Jr. (1952) **Chemical Engineering Progress**, 48:141 et 48:173.
10. Van Der Hegge Zijnen B.C. (1958) **Appl. Scient.Res.**, 7A:205.
11. Raithby G.D. and Eckert E.R.G. (1968) **Int. J. Heat Mass Transfer**, 11:1213.
12. Sandoval-Robles J.G., Delmas H. and Couderc J.P. (1981) **AIChE Journal**, 27:819-823.

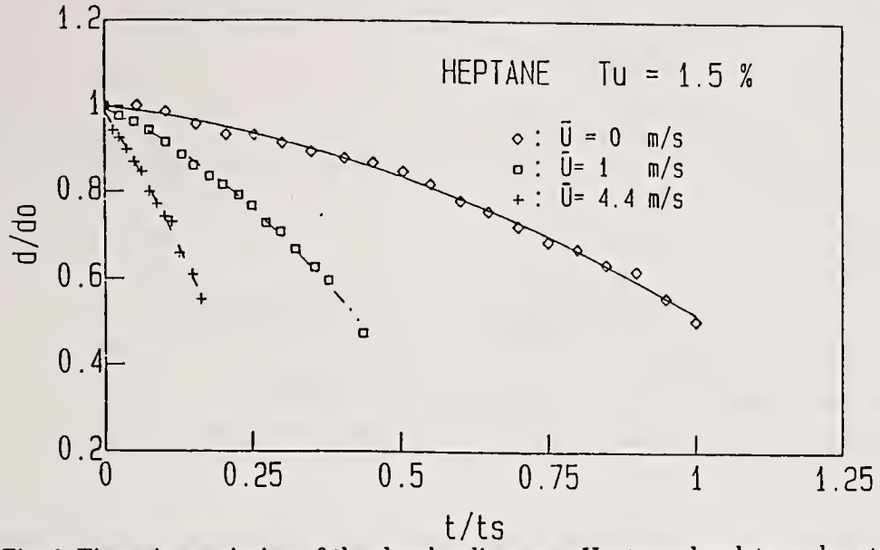

Fig. 1. Timewise variation of the droplet diameter. Heptane droplets under stagnant and two laminar convectives cases.

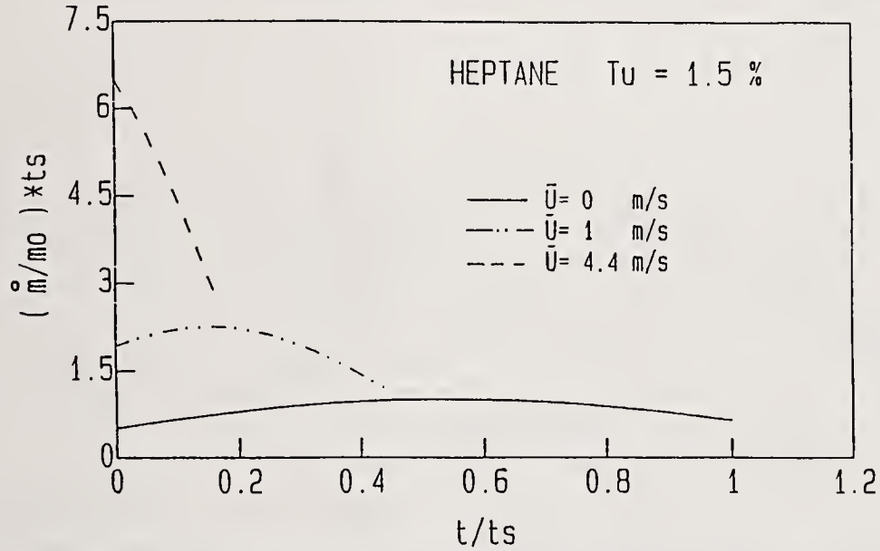

Fig. 2. Timewise variation of the instantaneous vaporization rate. Same conditions as on Fig. 1.

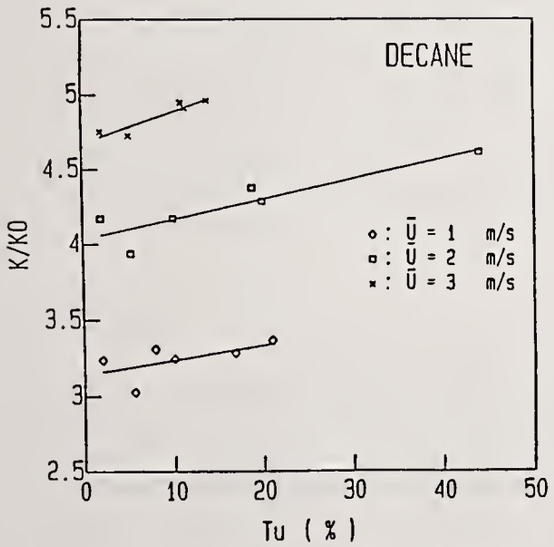

Fig. 3. Variation of the vaporization rate with turbulence intensity. The case of decane.

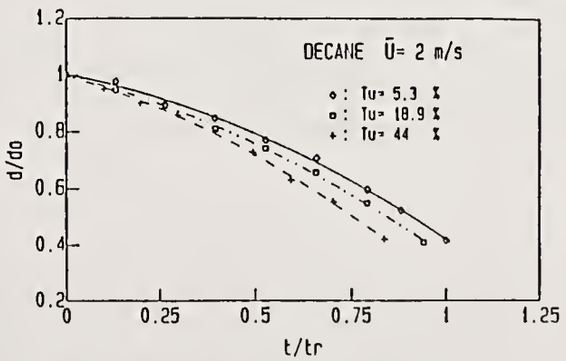

Fig. 4. Influence of turbulence intensity on the timewise variation of the droplet diameter. The case of decane.

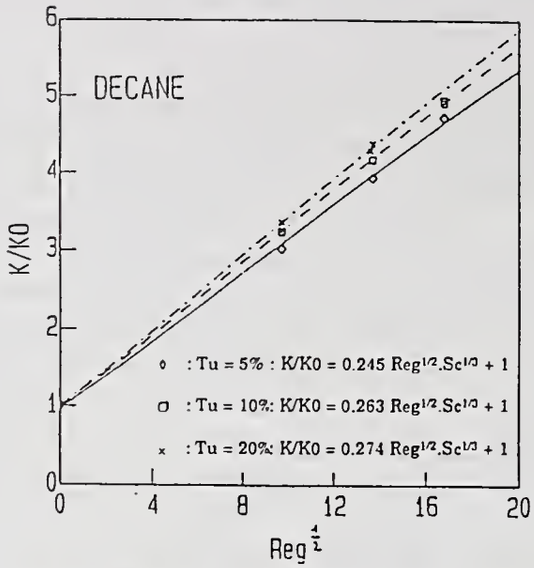

Fig. 5. Frössling correlation for different turbulence intensities. The case of decane.

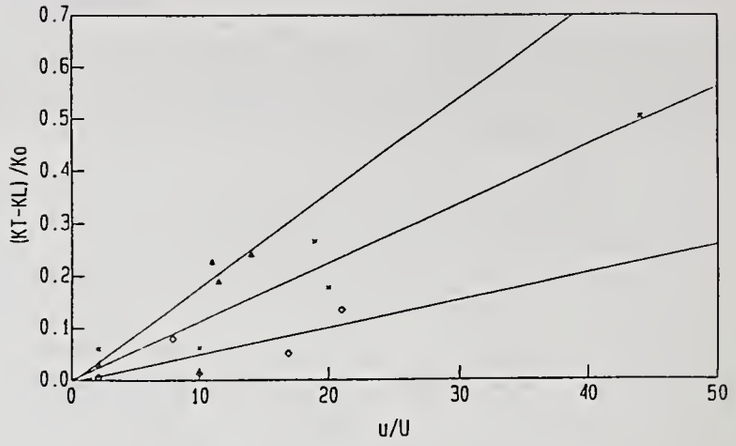

Fig. 6. Influence of the turbulence intensity on the mass transfer rate. The case of decane. ◇ 1 m/s, × 2 m/s, △ 3 m/s

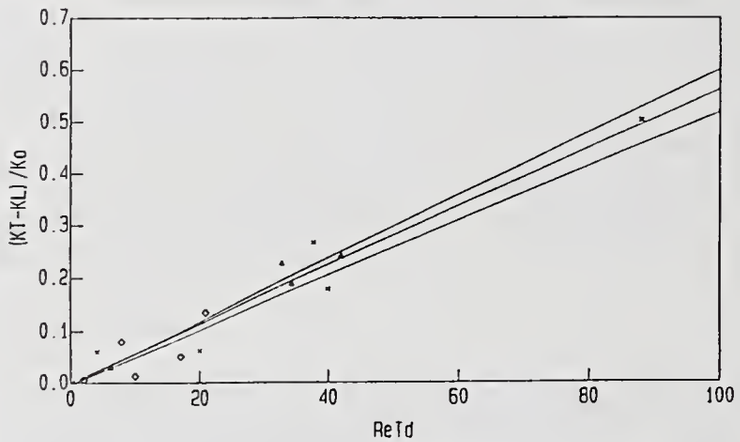

Fig. 7. Influence of the turbulence Reynolds number on the mass transfer rate. The case of decane. Same symbols as Fig. 6.

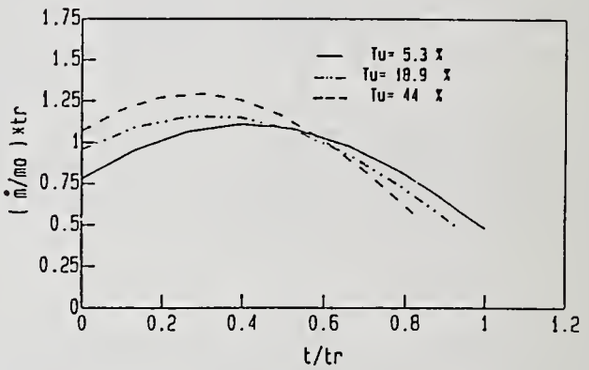

Fig. 8. Influence of the turbulence intensity on the instantaneous vaporization rate. The case of decane. U = 2 m/s

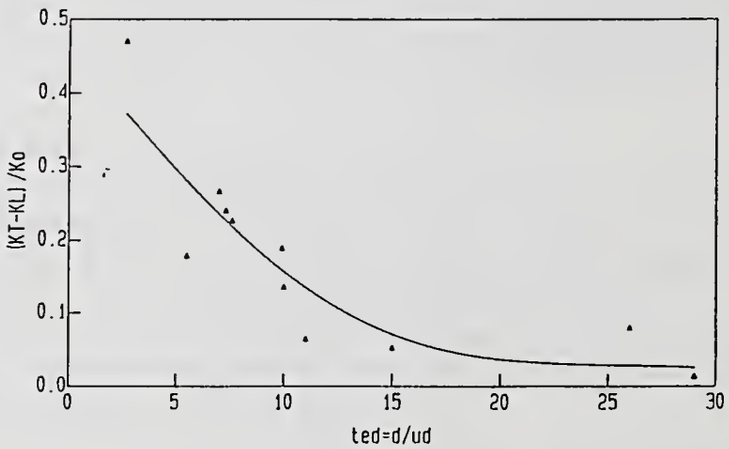

Fig. 9. Influence of the turbulence time scale on the mass transfer rate. The case of decane.

SUPERCRITICAL DROPLET EVAPORATION

A. Umemura, X.-Y. Chang and T. Fujiwara

Faculty of Engineering
Yamagata University
Yonezawa, Japan

ABSTRACT

Numerical calculation is performed to examine the evaporation process of a liquid fuel droplet which is immersed in an otherwise quiescent, inert gas at a various state beyond the critical point of the fuel. Either is realized at any instant, of (i) the subcritical evaporation regime in which phase change takes place discontinuously at the droplet surface or (ii) the supercritical evaporation regime in which phase change occurs spatially continuously. Satisfactorily to simulate the transition from (i) to (ii), it is essentially important to take into account the fact that the coefficient of diffusion between the fuel and the inert gas should vanish at the droplet surface when the thermodynamic state of the droplet surface attains to the critical point of the mixture system.

Conditions under which the droplet experiences the transition are identified in terms of the initial system parameters. Consistent with past expemental results no singular behavior is observed in the droplet temperature change at the instant of transition. The core characterized by high fuel concentration behaves like a liquid droplet even after the transition, and can be distinguished from the other part by a sharp but continuous change at its boundary. Once the core is about to disappear, the concentration as well as the temperature changes abruptly to assume the gaseous state. The concept of "vapor puff" which has been frequently used to model a supercritically evaporating droplet seems only valid to describe the state after disappearance of the liquid core.

INTRODUCTION

As well known a pure liquid under its supercritical pressure may undergo a spatially continuous phase change from a liquid to gaseous state. A similar situation is expected for a hydrocarbon droplet evaporating in an air whose temperature and pressure exceed the critical point of the fuel, as encountered in Diesel engines and the like. The phenomenon is, however, not so simple because the occurrence of the transition from subcritical evaporation regime, in which phase change takes place discontinuously at the droplet surface, to supercritical evaporation regime, in which phase changes in a spatially continuous way, depends not only the system pressure but also on the ambient gas

temperature and is closely related with the droplet heat-up process itself.

A numerous attempt has been made to reveal the underlying physics of supercritical droplet evaporation while there still remain ambiguities about the transition feature[1-10]. Among them the following are important to note. (1) In most of the previous investigations the occurrence of the transition is judged by whether the droplet surface temperature reaches the fuel critical temperature or not. However, for a mixture system in which the initial droplet and ambient gas comprise different chemical species, the mixture critical point system should be considered instead of the fuel critical point. For a hydrocarbon/nitrogen system of interest the mixture critical temperature is usually lower than the fuel critical temperature and the mixture critical pressure exceeds the fuel critical pressure. This raises a question upon the conventional criterion. (2) There seems to be anticipation of singular behaviors by association of the critical behaviors of specific heat and thermal conductivity observable for a pure substance. This is not the case for a mixture system because of different criticalities of he components. One of the authors demonstrated in an asymptotic analysis[13] that, when the droplet experiences the transition at a finite radius, the surface temperature continues to increase regularly with a gap to the droplet center temperature until it reaches the mixture critical temperature. An abrupt change in the droplet center temperature, which is detected experimentally, may occur only when the droplets gasifies completely. Considering a not large difference between the fuel and mixture critical temperatures, there is a possibility that this behavior is mistakenly identified as a singular behavior at the transition. (3) Without the knowledge of critical material properties it is impossible to simulate the transition satisfactorily. It was also shown [11-14] that vanishing of the relevant binary diffusion coefficient at the critical droplet surface is essential to realize the unsteady transition in the realm of the current continuum theory which is based on the local equilibrium hypothesis and the linear phenomenological relationships. Failures in past numerical calculations are due to lack of this basic consideration.

In consideration of the above-mentioned status we perform numerical calculation to reveal the characteristic feature of droplet evaporation at elevated pressures. At the stage when knowledge about material properties for mixtures is not complete it is, however, difficult to do in a quantitatively satisfactorily way. Therefore, the calculation is based on an appropriate, simplified physical model which allows for minimum items necessary to simulate the phenomenon satisfactorily, and aims at a rather qualitative nature of the problem. Nevertheless, the results will be found to be in good agreement with the existing experimental data.

FORMULATION

Consider the spherically symmetric evaporation process of a liquid fuel droplet which is immersed in an otherwise quiescent, inert gas at high pressures above the fuel critical pressure. At initial time, $t = 0$, the droplet of radius, a_0, has a uniform temperature, T_d, while the ambient gas, T_∞. The droplet gasifies to produce the Stefan flow velocity, u, whose magnitude is so small that the pressure, p, can be regarded as constant everywhere. The phenomenon is thus governed by the following heat and mass transport equations.

Overall mass:

$$\frac{\partial \rho}{\partial t} + \frac{1}{r^2}\frac{\partial}{\partial r} r^2 \rho u = 0 \qquad (1)$$

Energy:
$$\rho\left[\frac{\partial h}{\partial t} + u\frac{\partial h}{\partial r}\right] = \frac{1}{r^2}\frac{\partial}{\partial r} r^2 \lambda \frac{\partial T}{\partial r} \tag{2}$$

Fuel:
$$\rho\left[\frac{\partial Y}{\partial t} + u\frac{\partial Y}{\partial r}\right] = \frac{1}{r^2}\frac{\partial}{\partial r} r^2 \rho D \frac{\partial Y}{\partial r} \tag{3}$$

To close the equation system we need an equation of state, $\rho = \rho(T,Y;P)$, and a caloric equation, $h = h(T,Y;P)$, together with appropriate expressions for the mixture thermal conductivity, λ, and binary diffusion coefficient, D, as functions of temperature, T, fuel mass fraction, Y, and pressure, P. All these equations hold irrespective of liquid or gas phase. We shall use the subscript * to distinguish liquid properties.

The initial and boundary conditions to be satisfied are

Initial:
$$T = T_g, \quad Y = 0 \quad \text{for} \quad r > a_0$$
$$T_* = T_d, \quad Y_* = 1 \quad \text{for} \quad 0 < r < a_0 \tag{4}$$

Boundary:
$$T \to T_g, \quad Y \to 0 \quad \text{as} \quad r \to \infty$$
$$\frac{\partial T_*}{\partial r} = \frac{\partial Y_*}{\partial r} = u_* = 0 \quad \text{at} \quad r = 0 \tag{5}$$

Besides, in the subcritical evaporation regime the following conservation equations, (7)-(9), must be satisfied at the droplet surface, $r = a(t)$. Since we assume the hold of phase equilibrium at the droplet surface, the interfacial fuel concentrations, Y_{*s} and Y_s, are determined from Eq.(6) as functions of droplet surface temperature, T_s, for a given system pressure, P.

$$\mu_F(T_s,Y_s;P) = \mu_{*F}(T_s,Y_{*s};P)$$
$$\mu_I(T_s,Y_s;P) = \mu_{*I}(T_s,Y_{*s};P) \tag{6}$$

$$\rho_*\left(u_* - \frac{da}{dt}\right) = \rho\left(u - \frac{da}{dt}\right) \equiv m \tag{7}$$

$$\lambda\frac{\partial T}{\partial r} - \lambda_*\frac{\partial T_*}{\partial r} = mL \qquad \text{with} \quad L = h - h_* \tag{8}$$

$$\rho D\frac{\partial Y}{\partial r} - \rho_* D_*\frac{\partial Y_*}{\partial r} = -m\Delta \qquad \text{with} \quad \Delta = Y_* - Y \tag{9}$$

All quantities appearing in the above equations are made dimensionless as described below, so that the equations preserve the original forms with the same symbols employed to denote the corresponding dimensionless quantities. The temperature, T, and pressure, P, are reduced by the fuel critical temperature, T_{Fc}, and pressure, P_{Fc}. The radial coordinate, r, and instantaneous droplet radius, a, are divided by the initial droplet radius, a_0 (thereby $a_0 = 1$ in the nondimensional form of the equations). The material properties, ρ, D, h_T, and λ, are made dimensionls so that a Lewis number constructed from nondimensionalizing reference quantities becomes unit. That is, we make dimensionless the mixture density, ρ, by the fuel critical density, ρ_{Fc}, the specific heat at constant pressure, h_T, by the universal gas constant, R, and

the mixture thermal conductivity, λ, by an appropriate reference value, λ_r. Then, the diffusion coefficient, D, is nondimensionalized by the quqntity, $\rho_{Fc}R/\lambda_r$. Correspondingly, the time, t, is made dimensionless by $a_0^2 \rho_{Fc}R/\lambda_r$. Note that we do not assume unit Lewis number for the trasport field; the local Lewis number changes significantly from point to point at any instant. From the invariance of the governing equation form it follows immediately that the d^2-law holds between the initial droplet diameter and the evaporation time for the case of subcritical evaporation regime dominating throughout the droplet lifetime.

The material properties are estimated as follows. The Redlich-Kwong equation of state with adequate mixing rules for binary mixtures[15] is adopted to describe the local-equilibrium state of the fuel/air binary mixture. The required thermodynamic variables are all derived as functions of pressure, temperature and composition through the well-known procedures in thermodynamics. Normal butane and nitrogen are chosen as the fuel and inert gas , respectively, since the recommended values of the parameters appearing in the mixing rules are readily available for this binary system. The mixture thermal conductivity is estimated by applying the corresponding states principle to an empirical relation for pure substance[16]. The binary diffusion coefficient is calculated according to the proposed expression in Ref.[12] which satisfies the vanishing condition at the mixture critical point. Identifying with the self-diffusion coefficient of a hypothetical pure substance, the factor, D_0, is estimated by applying the corresponding states principle to self-diffusion coefficient for pure substance[17]. In the present calcualtion the mixing heat, H_Y , is assume zero for simplicity.

RESULTS AND DISCUSSION

Numerical calculation was performed for a particular value of initial droplet temperature, $T_d = 0.5$, to examine the variations of characteristic quantities with ambient gas conditions, T_∞ and P.

We start with the case, $P < 1$. In this case the droplet has a liquid-gas interface throughout its lifetime. This can be seen from Fig. 1 which shows the saturation curves calculated from Eq.(6). Characteristic for $P < 1$ is that a pair of saturated-liquid branch (solid line) and saturated-vapor branch (dotted line) merge at a point on the $Y = 1$ line, i.e., the boiling point at the pressure under consideration. Therefore, if we plot, on the same figure, a curve Y(t,T) which is obtained by eliminating r from the instantaneous temperature and concentration profiles, T(t,r) and Y(t,r), the curve connecting the two states, (T_0,Y_0) at the droplet center and $(T_\infty,0)$ at infinity, must intersect the two branches, indicating the existence of a liquid-gas interface. Since the latent heat of vaporization, L, takes a non-zero

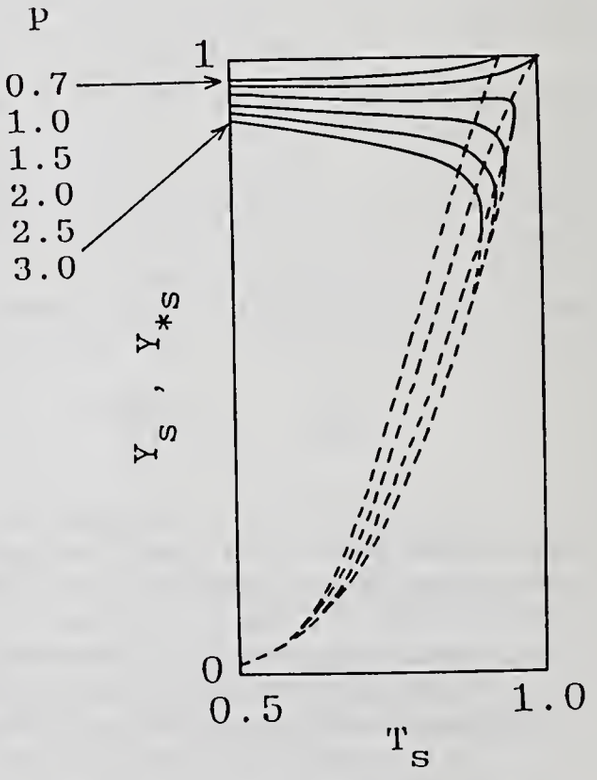

Figure 1 Saturation curves

value, the state within the droplet becomes uniform as time proceeds and eventually settles down at the wet-bulb condition that all heat transferred from the gas phase is consumed for vaporization at the droplet surface. Correspondingly the instantaneous evaporation constant, K, also becomes constant and the d^2-law holds exactly at any instant. The temporal changes in the characteristic quantities in this subcritical pressure case are shown in Fig. 2.

For the supercritical pressure case, P > 1, there is a critical point in Fig. 1 where the latent heat of vaporization vanishes. One can consider two possibilities. (i) The curve, Y(t,T), intersects the saturation curve. In this case the droplet has its surface and requires a non-zero heat for vaporization similarly to the subcritical pressure case. (ii) The curve, Y(t,T), has no intersection with the saturation curve. In this case, liquid phase changes to gas phase spatially continuously so that there is no distinguishable liquid-gas

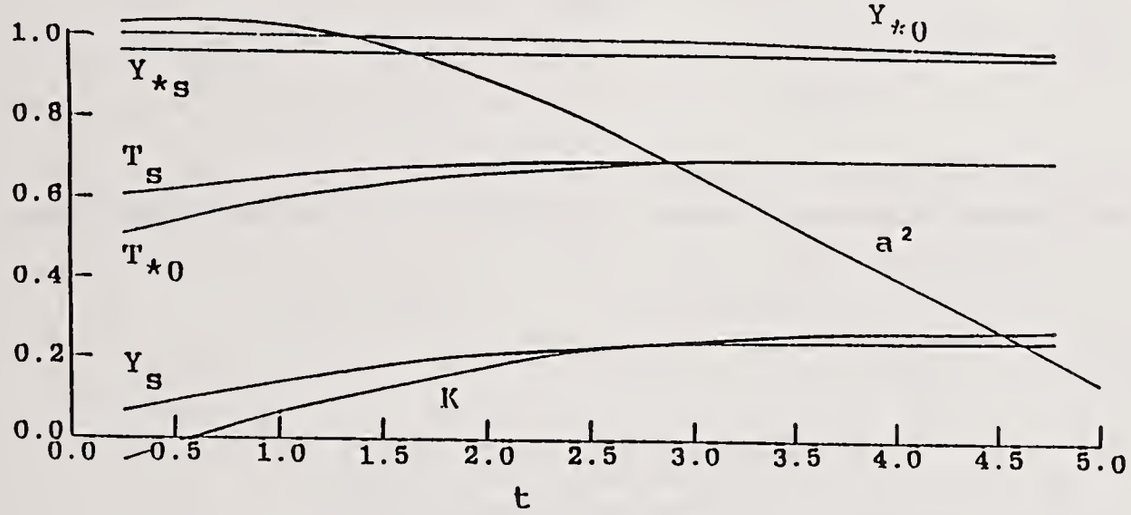

Figure 2 Temporal changes in characteristic quantities
(P = 0.9, T_z = 1.2)
see nomenclature footnoted below Fig. 4

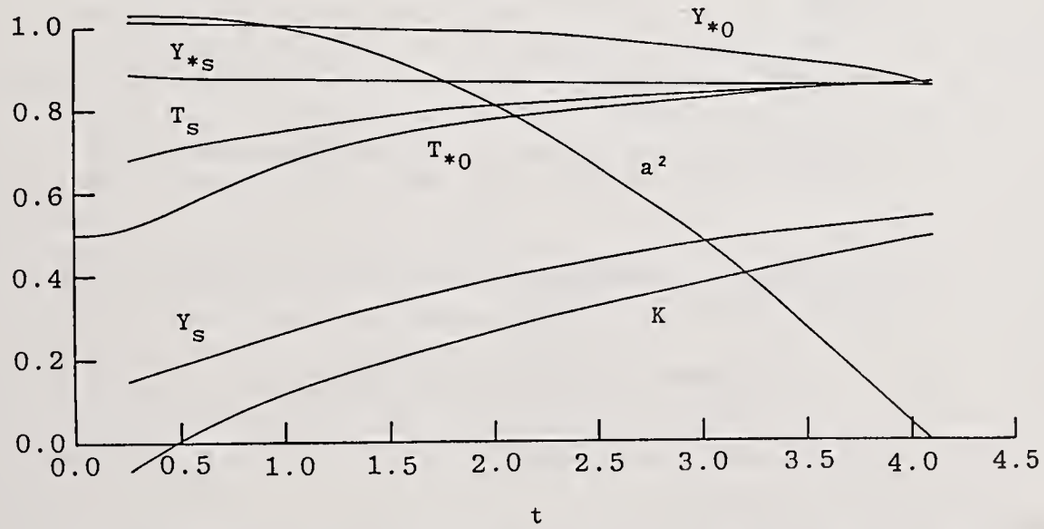

Figure 3 Temporal changes in characteristic quantities
(P = 2.5, T_z = 1.1)
see nomemclature footnoted below Fig. 4

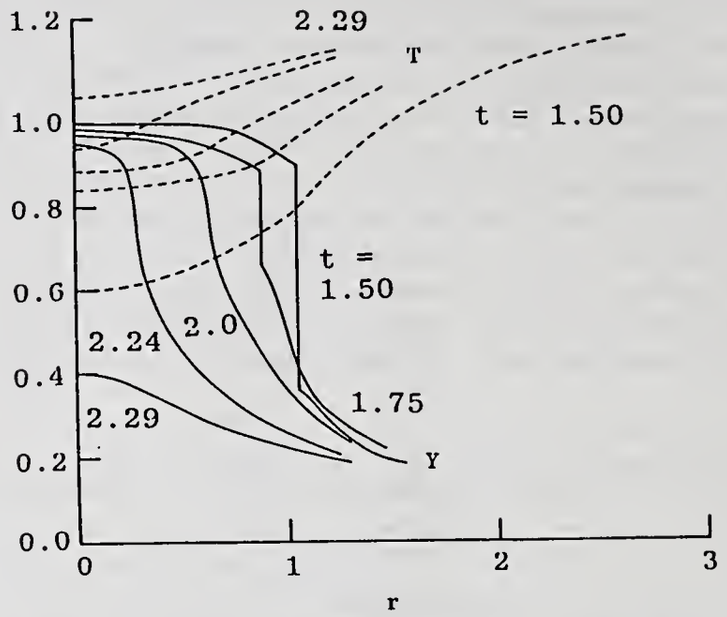

(a) Temporal changes in temperature and fuel concentration profiles
(P = 2, T_s = 1.25)

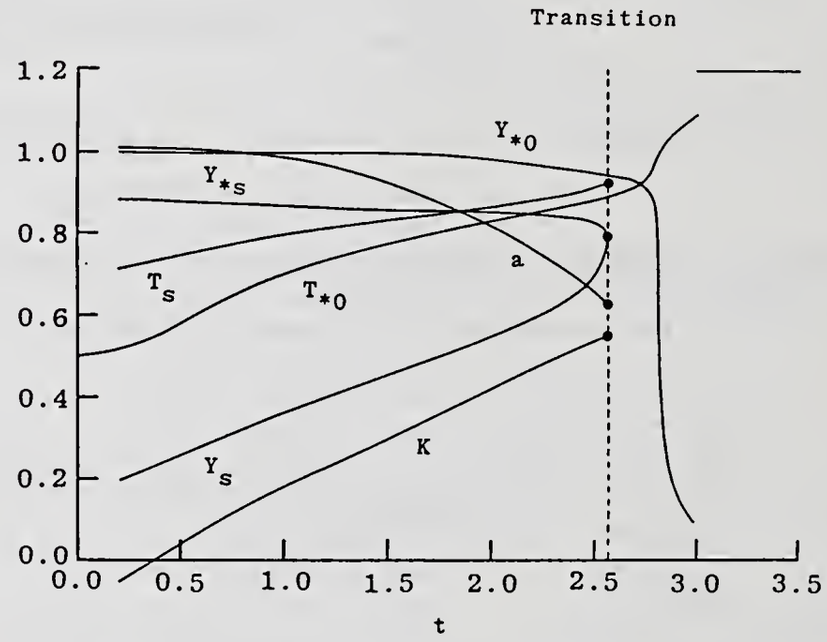

(b) Temporal changes in characteristic quantities
(P = 2.5, T_s = 1.2)

Figure 4 Transition feature

Characteristic quantities:
Droplet center temperature, T_{*0}, and fuel mass fraction, Y_{*0}
Droplet surface temperature, T_s , and fuel mass fractions, Y_{*s} and Y_s
Instantaneous evaporation constant, K = - a(da/dt)

interface. If the system pressure is not high enough, the subcritical evaporation regime (i) dominates until the droplet gasfies completely. Figure 3 shows the variations of the characteristic quantities in such a case. The behaviors are similar to those in Fig. 2. In particular it should be noted that the wet-bulb state is established toward the end of the droplet lifetime. This is because the relaxation time of the transport phenomenon within the droplet diminishes in proportion to the vanishing size of the droplet.

As the pressure is increased for the fixed ambient gas temperature, the wet-bulb state shifts to the mixture critical point and the droplet comes to reach the critical state at the instant of complete gasification of the droplet. Beyond this critical value of pressure the transition from sub-to-supercritical evaporation regime occurs at a finite radius of the droplet. Results for this case are shown in Fig. 4. Figure 4(a) shows the temperature (solid line) and concentration (dotted line) profiles at the time written alongside the curves for the case of P = 2 and T_g = 1.25. The value of r at which the concentration profile is discontinuous gives the instantaneous droplet radius. In the figure the state of the droplet surface attains to the mixture critical point just before t = 1.8 when the droplet radius reduces to three quarters the initial one. Correspondingly the discontinuities in the concentration and in the temperature gradient at the droplet surface disappear and degenerate into inflection points of the profiles. The subsequent change in the concentration profile indicates that a portion of high fuel concentration, nearly Y = 1, still remains qround the droplet center. This portion will be called "liquid core" because it has a similar property to the liquid fuel which the droplet has before the transition. The core radius, which may be defined by the radial distance to the inflection point of the concentration profile, decreases faster than the degression speed of the droplet surface. Once the core radius is about to vanish, the fuel concentration at the origin rapidly decreases to zero indicating total gasfication. At the same time the temperature at the origin increases abruptly toward the asymptotic value of the ambient gas temperature. These behaviors can be more clearly seen in Fig 4(b) in which the variation of the characteristic quantities with time is plotted for a different ambient gas condition. It is confirmed from this figure that there appears no singular behavior in the droplet surface temperature toward the transition instant. The droplet surface temperature continue to increase regularly with a finite gap to the droplet center temperature. In particular the droplet center temperature increases monotonically and shows no singular behavior at the transition instant, consistent with the past experimental result. The rapid increase in the temperature, T_0, about t = 2.3 is due to the vanishing of the liquid core at that time.

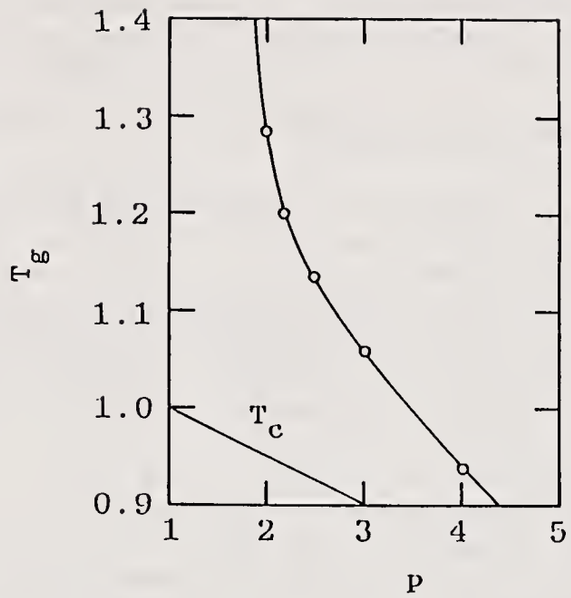

Figure 5 Ambient gas condition for transition to occur

In Fig. 5 the range of initial gas temperature is shown against pressure, for which the droplet experiences the transition during its lifetime. Above the solid curve the transition occurs. In the figure the variation of the mixture

critical temperature with pressure is also plotted by the dotted line for reference. For P $\sim$ 1 the ambient gas temperature must be very high to cause the transition while the required ambient gas temperature decreases to the mixture critical temperature asymptotically at high pressures.

CONCLUDING REMARKS

Satisfactorily to describe the transition from sub-to-supercritical evaporation regime it is essentially important to take into account the fact that the binary diffusion coefficient should vanish at the liquid-gas interface in a mixture critical state. In the present study, adopting a model diffusion coefficient which satisfies such property we have succeeded in revealing the characteristic feature of droplet evaporation at elevated pressures and in predicting the ambient condition under which the droplet experiences the transition within its lifetime. As anticipated, the "droplet" preserves the liquid-like property even after it lost the liquid-gas interface. Since continuous phase change occurs in a thin layer, rough optical observations will gives images as if ther still exists the droplet with surface. The concept of vapor puff which has been frequently used to model the supercritical evaporation regime is only valid for the state which follows the vanishing of the liquid core. Since both temperature and concentration profiles have inflection points at the boundary of the liquid core, it would be possible to define apparent quantities pertaining the liquid-gas interface such as latent heat of vaporization and concentration jump etc. even in the supercritical evaporation regime so far as there exists the liquid core.

REFERENCES

1. Spalding,D.B., ARS J., 29, 825 (1959)
2. Brzustowski,T.A., Can. J. Chem. Eng., 43, 30 (1965)
3. Wieber,P.R., AIAA J., 1, 2764 (1963)
4. Rosner,D.E., AIAA J., 5, 163 (1967)
5. Manrique,J.A. and Borman,G.L., Int. J. Heat and Mass Transf., 12, 1081 (1969)
6. Faeth,G.M. et al., Twelfth Symp. (Int'l) on Combustion, p.9 , The Combustion Institute, Pittsburgh, PA (1969)
7. Matlosz,R.L. et al., Int. J. Heat and Mass Transf.,15, 831 (1972)
8. Hiroyasu,H. et al., Trans. Japan Soc. Mech. Engrs., 44, 3885 (1978)
9. Kadota,T. and Hiroyasu,H., Trans. Japan Soc. Mech. Engrs., 44, 3885 (1978)
10. Kadota,T. and Hiroyasu,H., Trans. Japan Soc. Mech. Engrs., 46, 1591 (1980)
11. Umemura,A., Trans. Japan Soc. Mech. Engrs., 478, 82-94 (1986); also Heat Transfer Jap. Re., 17 , 82 (1988)
12. Umemura,A., Twenty-first Symp. (Int'l) on Combustion, p.463, The Combustion Institute, Pittsburgh, PA (1986)
13. Umemura,A.,Lecture Notes in Physics 299: Mathematical Modeling in Combustion Science (J.D. Buckmaster and T. Takeno, Eds.), p.52, Springer-Verlag, Heidelberg, Germany (1988)
14. Chang,X. et al., Progress in Astronautics and Aeronautics Vol. 113, p.168, AIAA, Washington, DC (1988)
15. Chueh,P.L. and Prausnits,J.M., I&EC Fund., 6, 492 (1967)
16. Stiel,L.E. and Thodos,G., A.I.Ch.E. Jl, 10, 26 (1964)
17. Lee,H.L. and Thodos,G., Ind. Eng. Chem. Fund., 22, 17 (1983)

WATER DROPLET EVAPORATION IN FIRE PLUMES

G. Krishan*, R.P. Gakkhar† and S. Prakash†

*Fire Research Division, Central Building Research Institute, Roorkee, India
†Dept. of Mechanical Engineering, University of Roorkee, Roorkee, India

ABSTRACT

In the present paper, the vaporization of water droplet in a sprinkler system encountering the ambient conditions which exist along the centreline of a fire plume, has been studied. The authors had developed an unsteady droplet vaporization model for constant ambient conditions. In the present work the unsteady droplet vaporization model has been modified to accommodate the conditions of varying ambient temperature and the free stream velocity, for a water droplet passing through a fire plume. The evaporation of various sizes of water droplets ranging from 1 mm to 4 mm diameter falling through the different intensities of fire plumes has been studied, and the optimum size of water droplets which should come out of the water sprinkler heads has been proposed.

INTRODUCTION

Although the automatic sprinkler systems have been using water as the suppressant for many decades, the exact mechanism of direct extinction by water as it is delivered from an automatic sprinkler system is not fully understood [1]. The water in the form of spray comes out from sprinkler heads. The water droplets of varying sizes during their fall, encounter conditions of varying ambient temperature and composition, and get heated up. These droplets keep on vaporizing as they pass through the hot convective environment, before falling on the burning materials. The droplets coming from sprinkler heads should be of a size, such that, even after vaporization in a hot environment, they retain optimum size before falling on the seat of fire, to quench it and also to avoid water damage.

As a water droplet enters a fire plume and continues to fall, it heats up and vaporize. Moreover, it encounters a hot convective flow field with increasing ambient temperature and plume velocity. The relative velocity between the droplet and the hot ambient gases decreases due to drag. These varying ambient conditions along with the unsteady heating and shrinking of the droplet make the problem of droplet vaporization in fire plume essentially unsteady.

There have been several studies [1] on vaporization of water droplets in steady state and with constant ambient conditions and therefore, they do not adequately represent the droplet vaporization problem under conditions relevant to the actual fires. Therefore, it becomes important to study the vaporization rate of water droplets vaporizing in a hot convective environment with varying ambient conditions relevant to actual fires.

MODEL USED

The present study makes use of a model developed by Prakash and Krishan [2]. This model has been coupled with the model of Gakkhar and Prakash [3], to accommodate the varying ambient conditions encountered by the water droplets as it falls through the plume. The plume is assumed to be steady. However, the gas-phase flow conditions in the vicinity of the falling droplet are assumed to be quasi-steady. The droplet is assumed to be falling in the environment of the plume and the interaction between the neighbouring droplets has been ignored. Thus, the model considers an isolated droplet vaporizing in a convective flow field which falls vertically downwards along the centreline of fire plume. As the droplet enters a hot convective flow field, a gas-phase viscous boundary layer develops around the droplet. Energy is transferred from the ambience to the droplet, a part of which goes into heating up the droplet while the remaining part is utilized in vaporizing the droplet. The heating up of the droplet is essentially unsteady. This model was modified to accommodate the varying ambient conditions of temperature and the free stream velocity for a water droplet passing through a fire plume. The quasi-steady, gas-phase momentum, energy and species boundary layer equations were solved by an integral approach developed by Prakash and Sirignano [4], while the one-dimensional unsteady heat diffusion equation was solved for the liquid-phase heating. Coupling at the gas-liquid interface is in the form of conservation of heat flux and the water vapour mass flux at the droplet interface. The coupled problem was solved for three plumes of different intensities, namely, weak, medium and strong plumes [5], for droplet diameters ranging from 1 to 4 mm. The height of sprinkler from the fire source is taken as 4.57 m.

Various correlations giving the temperature and velocity along the centreline of plumes were taken from reference [6]. The water droplet penetration into the plume was computed by using the momentum balance in the vertically downward direction,

$$m\frac{dU}{dt} = mg - C_D \rho_g \frac{(U+V_m)^2}{2} S, \qquad \ldots(1)$$

assuming the initial droplet velocity coming out of the sprinkler to be zero.

The drag coefficient, C_D, variation with Reynolds number for vaporizing droplet was computed, as suggested by Yuen and Chen [7], using the standard drag curve and modifying the Reynolds number. For calculating the Reynolds number, the free stream density was used while the dynamic viscosity, μ, was evaluated at the reference temperature T_r, and the reference ambient composition $Y_{w,r}$ given below:

$$T_r = T_s + (T_\infty - T_s)/3 \qquad \ldots(2)$$

$$Y_{w,r} = 2/3\ Y_{w,s} \qquad \ldots(3)$$

The mixture viscosity was then calculated from the values of viscosity for air and the water vapours at the reference temperature [8]. The C_D vs Reynolds number correlations for solid sphere was taken from reference [9].

PLUME CORRELATIONS USED

The experimental data of three plumes [5], covering a wide range of plume intensities (named, weak, medium and strong plumes for convenience), were used for the present study of water droplet vaporization in fire-plumes. The relevant data is given in Table 1.

Table 1

Fuel	Pool diameter D(m)	Convective heat flux Q_c(kW)	Flame Height Z_f(m)
Methanol	1.737	796	1.7
Hydrocarbon Transformer Fluid	1.737	1546	3.7
Heptane	1.737	4367	5.5

The various correlations for the variation of centreline temperature and plume velocity were used following the recommendations of Beyler [6]. Accordingly, the correlations for the centreline temperaure and the velocity for the three regions viz. plumes above flame, intermittent and continuous flame are described below:

Correlations for Plumes Above Flame

The centreline temperaure and the velocity above the flame in a fire plume is given as follows:

$$\Delta T_m = 22.0\ Q_c^{2/3}\ z^{-5/3} \qquad \ldots(4)$$

$$V_m = 1.14\ Q_c^{1/3}\ z^{-1/3} \qquad \ldots(5)$$

where T_m is the centreline temperature rise (°C) above the ambient temperature and V_m is the centreline velocity (m/s), and z is measured above the virtual source (m) and not the height above the actual fuel source. However, the virtual source location was estimated using the following relationship [6].

$$\frac{(Z_f - Z_o)}{Q_c^{2/5}} = 0.12 \qquad \text{for } Z_f/D < 1 \qquad \ldots(6)$$

$$\frac{(Z_f - Z_o)}{Q_c^{2/5}} = 0.15 \qquad \text{for } Z_f/D > 1 \qquad \ldots(7)$$

where Z_f(m) is the flame height, and Z_o(m) the location of virtual source.

Correlations for Velocity and Temperature in Flame

The flame above a burning object can be divided into two regions for the purpose of correlating centreline velocities and temperatures, the continuously flaming region and the intermittent region. Within the continuously flaming region the centreline temperture is approximately constant and velocity rises as the square root of height. The correlations for continuously flaming region as proposed by Beyler [6] were used and are given below in a tabular form:

Table 2

Region	T_m	$V_m/Z^{1/2}$
$Q^{2/5}/D > 10.2$ and $0.03 < Z/Q^{2/5} < 0.08$	980	6.83
$Q^{2/5}/D < 10.2$ and $0.02 < Z/Q^{2/5} < 0.06$	960	6.83

where Q is total heat release rate (kW).

Correlations for the intermittent region as proposed by Beyler [6] are as follows:

For the region $Q^{2/5}/D > 10.2$ and $0.08 < Z/Q^{2/5} < 0.2$

$$\Delta T_m = 78.0\ Q^{2/5}\ Z^{-1} \qquad \ldots(8)$$

$$V_m = 1.85\ Q^{1/5} \qquad \ldots(9)$$

For the region $Q^{2/5}/D < 10.2$ and $0.06 < Z/Q^{2/5} < 0.12$, the centreline temperatures are calculated from the correlations for plume above the flame, while the centreline velocity is calculated as given below:

$$V_m = 1.65\ Q^{1/5} \qquad \ldots(10)$$

The variation of the ambient temperature and the plume velocity with height, which are the input parameters for the water droplet vaporization, are shown in Figs. 1 and 2. These curves have been made smoother in the matching regions of the various plume zones by adjusting the various correlation coefficients.

RESULTS AND DISCUSSION

In the present study, the time was non-dimensionalized with the characteristic thermal diffusion time (in water) for a 2 mm water droplet (for all the droplets), so that the non-dimensional time is directly proportional to the real time and the evaporation rates of various size droplets can be compared.

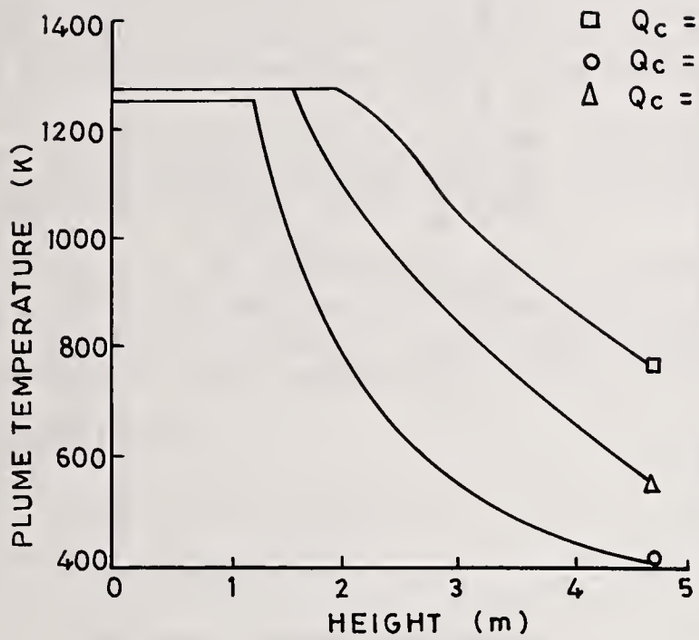

FIG.1. PLUME TEMPERATURE VS HEIGHT

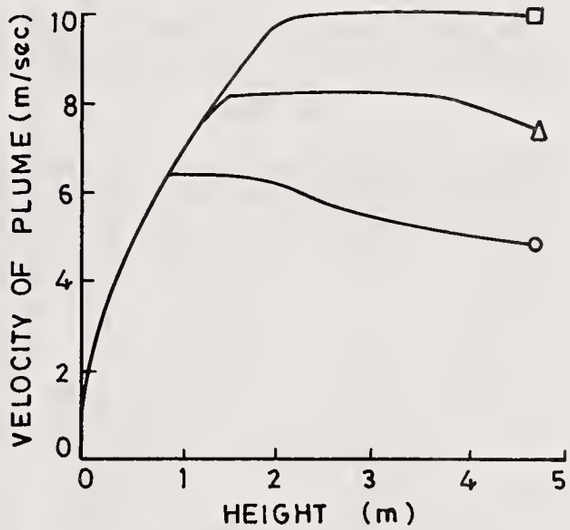

FIG.2. VELOCITY OF PLUME VS HEIGHT

Figures 3 to 5 show the temporal variations of the falling water droplet velocity with respect to ambient gas for weak, medium and strong plumes. Initially the droplet starts falling from zero velocity in a region where plume velocity is also small but in the opposite direction. As the droplet continues to fall, its falling velocity and also the plume velocity increase. Consequently the relative gas droplet velocity increases. This trend continues upto the start of continuous flaming region. As the droplet enters the continuous flaming region, the plume velocity decreases which results in a lower gas-droplet velocity. In the region between the continuous flaming region and the ground, the relative gas-droplet velocity goes on decreasing. Thus the portion of the relative velocity curves after the maxima represents the travel of droplets in a continuous flaming region of plumes. It may be noticed from the figures that 2 mm drop can penetrate only weak plume. In the case of medium plume after falling for some time, it is carried away by the rising plume. In strong plumes it is not able to enter at all. However, larger size drops are able to penetrate all the three plumes and reach the seat of fire.

Figure 6 shows the total mass vaporized for various drops when they fall in various plumes from a height of 4.57 m. The 2 mm diameter drop is able to enter only the week plume and vaporizes upto 33% in the weak plume. The 3 mm drop is able to enter all the three types of plumes and vaporises upto 10, 15 and 35% in the weak, medium and strong plumes respectively.

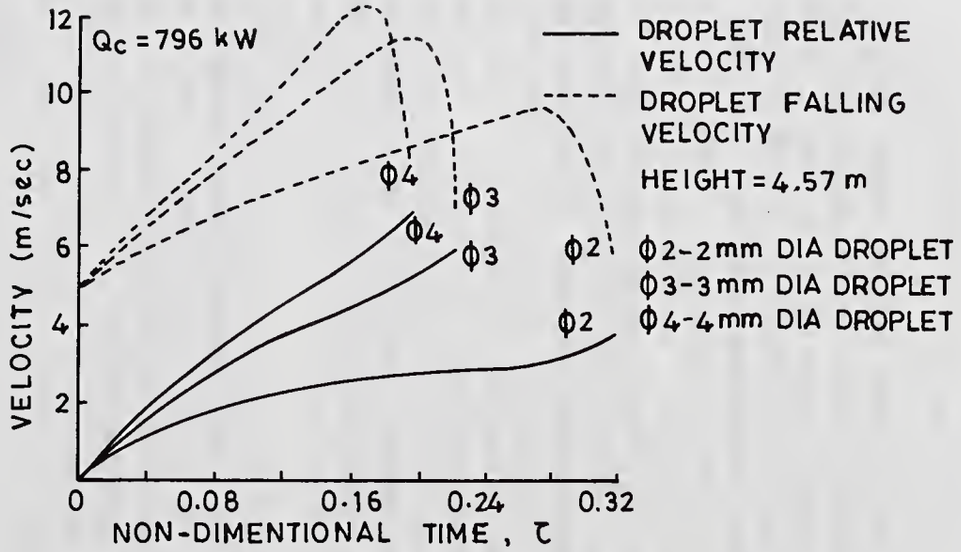

FIG.3. DROPLET RELATIVE AND FAILING VELOCITY VS TIME FOR WEAK PLUME

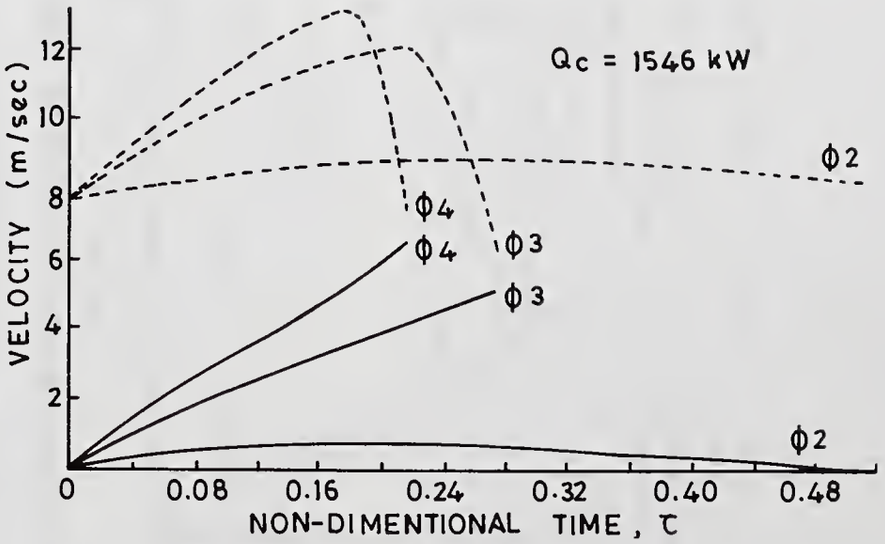

FIG.4. DROPLET RELATIVE AND FAILING VELOCITY VS TIME FOR MEDIUM PLUME

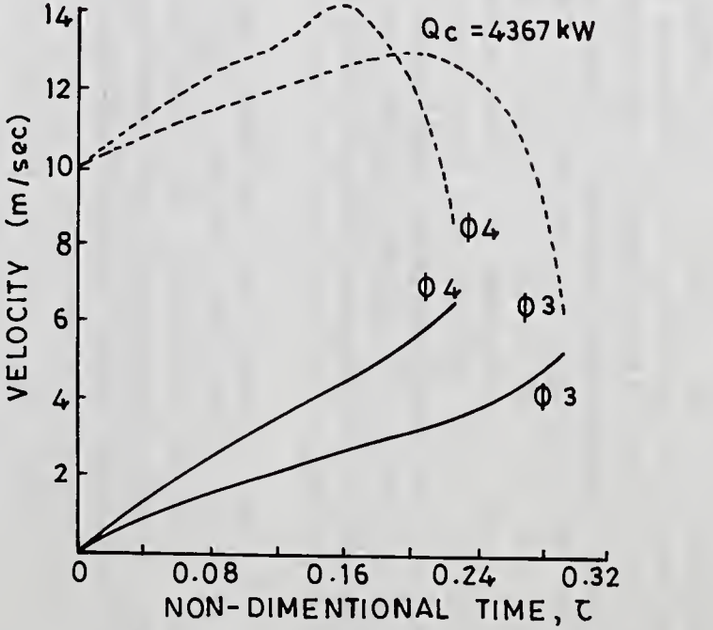

FIG.5. DROPLET RELATIVE AND FAILING VELOCITY VS TIME FOR STRONG PLUME

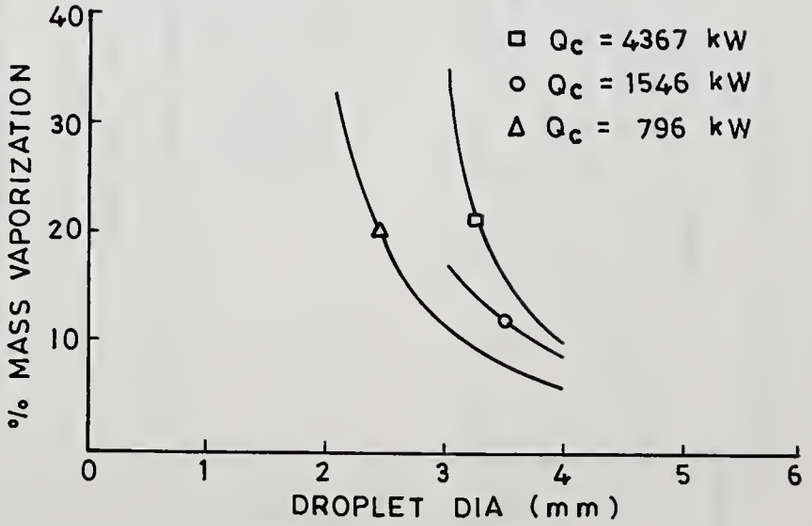

FIG. 6. TOTAL MASS VAPORIZATION OF DROPLETS IN VARIOUS PLUMES

CONCLUSIONS

From the above study it seems that the 2 mm droplet may not be the optimum size droplet. This is so because a 2 mm droplet can penetrate only the weak plume while in other plumes, it will be carried away by the hot gases. Moreover, it evaporates upto 33% even in the weak plume, thereby the net mass of water falling on the seat of fire is reduced considerably.

It is found that the droplets larger than 2 mm diameter can penetrate all the three types of plumes. For a 3 mm droplet the reduction in mass is of the order of 35% in the strong plumes.

In the present study the spray effects and the interaction between the droplets have not been considered. In a spray, the vaporization of droplets is modified because of lower temperatures in sprays and also because of the presence of water vapors in the ambient environment.

NOMENCLATURE

C_D coefficient of drag

D pool diameter (m)

g acceleration due to gravity

m mass of the falling water droplet

Q total heat release rate (kW)

Q_c convective heat flux release rate (kW)

R_0 initial droplet radius

S frontal surface area of drop

t time

ΔT_∞ centreline temperature rise above ambient (°C)

U velocity of the falling water droplet

V_m centreline mean upward velocity of the fire plume (m/sec)

Z height, measured above virtual source (m)

Z_o location of virtual source (m)

Z_f flame height (m)

Greek Symbol

α_l thermal diffusivity of the liquid (water)

τ $t\ \alpha_l/R_0^2$, dimensionless time

ρ density

μ dynamic viscosity of free stream

Subscript

g gas phase

l liquid phase

0 initial value

∞ ambient

REFERENCES

1. Harpole, G.M., "Droplet Evaporation in High Temperature Environment", Jour. of Heat Transfer, Transaction of the ASME, Vol.103, p.86-91 (1981).

2. Prakash, S. and Krishan, G., "Convective Droplet Vaporization with Transient Non-convective Liquid-Phase Heating", Twentieth International Symposium on Combustion, The Combustion Institute, Pittsburgh, PA, p.1735-1742 (1984).

3. Gakkhar, R.P. and Prakash, S., "Unsteady Vaporization of Fuel Droplet in a Convective Environment with Varying Ambient Conditions", Int. Jour. of Heat and Mass Transfer, Vol. 33, p. 1003-1012 (1990).

4. Prakash, S. and Sirignano, W.A., "Theory of Convective Droplet Vaporization with Unsteady Heat Transfer in the Circulating Liquid-Phase", Int. Jour. of Heat and Mass Transfer, Vol.23, p.253-268 (1980).

5. Kung, H. and Stavrianidis, P., "Buoyant Plumes of Large Scale Pool Fires", Nineteenth International Symposium on Combustion, The Combustion Institute, Pittsburgh, PA., p.905-912 (1982).

6. Beyler, C.L., "Fire Plumes and Ceiling Jets", Fire Safety Journal, Vol.11, p.53-75 (1986).

7. Yuen, M.C. and Chen, L.W., "On Drag of Evaporating Liquid Droplets", Combustion Science & Technology, Vol.14, p.147-154 (1976).

8. Reid, R.C., Prausnitz, J.M. and Sherwood, T.K., The Properties of Gases and Liquids, McGraw Hill (1977).

9. Morsi, S.A. and Alexander, A.J., "An Investigation of Particle Trajectories in Two-Phase Flow System", Jour. of Fluid Mech., Vol.55, p.193-208 (1972).

NEW RESEARCH APPROACH TO AIR SPRAY PAINTING

K.-C. Kwok[*] and B.Y.H. Liu[†]

[*]Graco, Inc., Minneapolis, MN, U.S.A.
[†]Particle Technology Laboratory, University of Minnesota, Minneapolis, MN, U.S.A.

ABSTRACT

Although spray painting is a widely used technique to apply decorative or protective coatings on a substrate, very little scientific researches have been done to enhance the understanding of its deposition mechanism. This paper first describes some parameters which are essential in controlling transfer efficiency (or deposition) and finish quality. Then, the approach to study the particle size distribution and the deposition mechanism of air spray painting is given. To illustrate the study approach, some experimental and theoretical results are also presented.

INTRODUCTION

Spray painting is an effective method for applying coatings on surfaces. In the past, the finish quality of a paint job was the primary concern. In recent years, environmental regulation has made it necessary to reduce solid waste and volatile organic compounds (VOCs) emissions. This has led to the development of high-solids and waterborne paints. The high cost of the new paints and the environmental issues have made it imperative to have high transfer efficiencies in painting operation. In southern California, for instance, no spray painting equipment is allowed to be used if its transfer efficiency is less than 65%.

Throughout the spray painting industry, a great deal of practical experience has been accumulated over many years, but very little systematic research has been done to understand the atomization process, and the transport and deposition mechanisms of spray painting. Only when these process and mechanisms are fully understood there is the hope of making significant improvement in the transfer efficiency and finish quality.

IMPORTANT PARAMETERS

Through experience, it is known that particle size distribution (PSD) is closely related to finish quality and transfer efficiency. Researchers in other fields also know that the PSD of airborne particles affects the deposition of particles on surfaces, as for example, the deposition of inhaled particles in the human lung [1].

During spray painting, paint particles are driven towards the target and impact on it. For those particles that fail to impact on the target, they become airborne. These are known as the overspray. The airborne particles will eventually be deposited on the booth walls or be collected by the air filter in the exhaust. While the transfer efficiency is routinely measured to gauge the performance of spray painting equipment, the amount of paint deposited on the booth walls and collected by the exhaust are not measured. The last two pieces of information will help determine the frequency of cleaning and filter change the spray booth may need.

For measuring the particle sizes of a spray, the conventional method is to collect samples on a microscopic slide (or a substrate). Then the spot sizes of the paint particles are measured under a microscope. Unfortunately, this sampling method only collects those particles that can impact on the slide, and the measured size distribution represents only a part of the total PSD of the spray. If this result is used, erroneous conclusions can be reached.

Even though the total PSD can be estimated using instruments like the Malvern particle sizer, there is no information on what kind of particles will and can deposit on the target, the booth walls, or be collected by the exhaust. The PSDs of these three particle fractions are important for understanding the aerodynamic motion of particles in the spray booth. In addition, if the PSD in each of the three fractions is known, the total (or true) PSD

of the spray can be obtained by combining the three PSDs. With this information, it may be possible to find ways to improve the transfer efficiency, reduce the paint deposit on the booth walls, improve the filtering efficiency of the exhaust system, and eliminate the harmful respirable particles.

AIR SPRAY PAINTING

Among all existing spray painting methods, air spray painting is the most widely used and versatile. The advantage of air spray is its ability to change the degree of atomization without changing the paint flow rate, thus allowing the operator to control both the finish quality and the coating speed. Another advantage of the air spray is that it can spray metallic paints with uniform and desirable shades of color. Hence, in view of the benefits listed above, air spray is potentially the method to produce high finish quality and transfer efficiency. This is the motivation for conducting a fundamental research on air spray painting [2].

The air flow field formed by the air cap of a spray gun is the main source of energy to drive the paint particles forward and deposit them on the target. It is important to know the mean velocity structure of the air flow field. For convenience, we shall refer to this air flow field as the "air-cap jet". Figure 1 illustrates the impingement of an air-cap jet onto a target. The mean velocity profiles shown represent approximately the true profiles of the air-cap jet. At a short distance from the air cap, the jet expands rapidly in the X-Z plane. The cross-section of the jet is approximately in the form of an ellipse. As the jet travels forward, the ellipse is further elongated.

The velocity profiles in the plane of the minor-axis resemble the shape of a bell. The peaks occur at the centerline of the jet. However, the peak decreases and the profile spreads out and becomes wider as the jet travels downstream. In the major-axis plane, the velocity profiles look like the cross-section of a saddle-back. The peak velocities of each profile are not at the centerline but near the two edges of the profile. As the jet travels farther downstream, the length of the profile increases. Also, the difference between the peak and the centerline velocities decreases. After impinging on the target, as shown in Figures 1(a) and (b), two walls jet are produced. The wall jet produced from the ends of the jet is called the radial wall jet while that produced from the long side of the ellipse is called the plane wall jet.

NEW EXPERIMENTAL APPROACH

To measure the important parameters affecting spray painting, a new experimental approach has been developed [2]. The main idea is to construct a miniature spray booth which is designed to measure simultaneously the paint deposit on the target, on the walls, and in the exhaust. Furthermore, the measurement of the PSDs on the booth walls and in the exhaust can be done in the same experiment.

Figure 2 shows the basic construction of the miniature spray painting booth[1]. The booth was designed to be a rectangular box with 0.61 m x 0.91 m (24" x 36") floor, and an interior height of 0.61 m (24"). For the sake of clarity, the vertical walls are not shown. Two large panel filters were put on the top of the booth to filter the incoming air. In the middle of the booth, a target panel was hung. The gun-to-target distance could be adjusted. On the floor, an 0.203 m x 0.086 m (8" x 3.375") rectangular hole was cut, which was the exhaust outlet of the booth. Connected to the exhaust outlet was a 5-stage Hi-Flow Cascade Impactor (HFCI) which draws 0.0188 m^3/s (40 cfm) of air. Cascade impactor is a device designed to classify airborne particles according to their aerodynamic particle size. The HFCI was designed to classify particles with diameter below 20 μm. The 5 stages have stage cut-points of 16.30, 9.87, 5.58, 3.10, and 1.62 μm. A filter was used to collect particles less than 1.62 μm.

To start an experiment using the miniature spray booth, the spray gun was mounted on a stand in front of the booth. Only the front end of the gun was allowed to stick into the booth. Before an experiment, the target panel was weighed and the HFCI was prepared. Then, the blower for the HFCI was turned on and the spray gun was triggered for about two seconds. After the gun stopped spraying, the blower was allowed to run for about 1.5 minutes. This ensured all airborne particles were evacuated. To calculate the transfer efficiency, the net weight of paint on the target, the percentage of paint solid, and the total paint output from the gun were recorded. The transfer efficiency is calculated by dividing the net dry paint on the target by the total dry paint output from the gun. The net weight gain by each stage of the HFCI was used to construct the mass distribution of the airborne paint particles. The summation of the weights of all stages plus the filter gives the total weight exhausted by the booth. The amount of deposit on the booth walls can be calculated by subtracting the sum of the weights of the target and the exhaust from the total weight output from the gun.

---

[1] The miniature spray booth is covered by an University of Minnesota patent (pending) licensed to the MSP Corporation. The equipment is available commercially (MSP Corporation, 1313 Fifth Street S. E., Minneapolis, MN 55414).

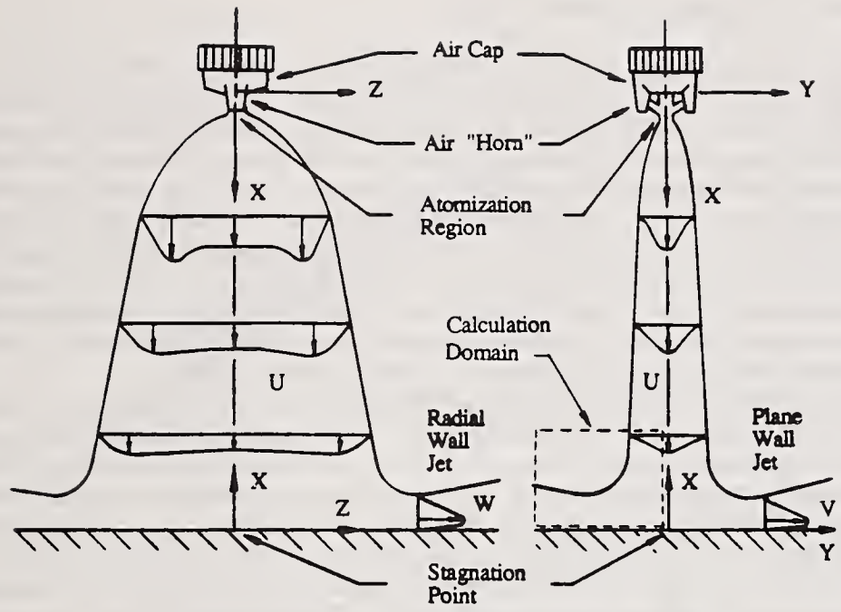

Figure 1. Schematic Diagram of Impinging Air-Cap Jet

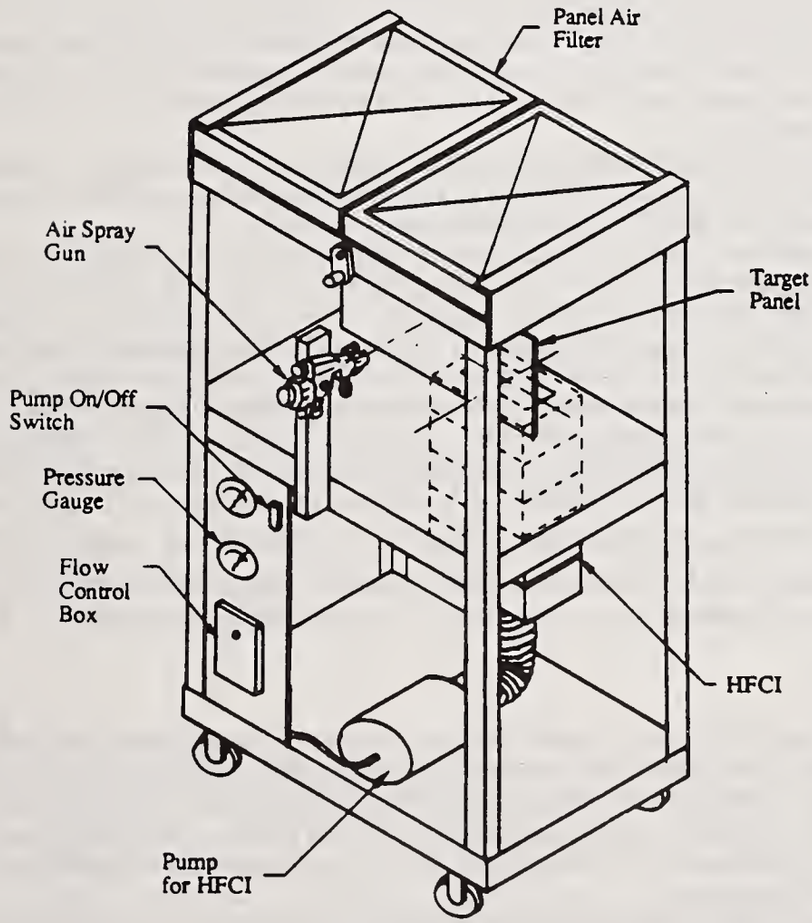

Figure 2. Miniature Booth for Spray Painting Tests

PARTICLE SIZE DISTRIBUTIONS (PSDs)

As explained in the last section, the mass distribution of the airborne particles was measured by the HFCI. To measure the PSD on the booth walls, microscopic slides were placed on the walls to collect paint particles for future analysis. To measure the PSD on the target, the particle sampling shutter was used to collect particle samples. The detailed construction and operational principle of the shutter has been given by Kwok [2].

To facilitate the measurement of the sizes of particles collected on the slides, an automatic image analyzer was used. This analyzer consisted of a microscope fitted with a motorized table. The slide was mounted on the table and the particle images were viewed by a video camera. With the images displayed on a video monitor, the analyzer could measure 500 images per second. This fast rate of image measurement allowed a large number of particles to be analyzed in a reasonable length of time. This improved the accuracy of the statistical analysis of the particles. Furthermore, the motorized table and a computer program allowed many measurements to be done automatically. The measured information was stored on a diskette for future statistical analysis.

The paint particles collected on the slides were flattened due to inertial impact. Although the diameter of the flattened particles is believed to be better related to the finish quality, for analysis of the aerodynamic particle motion, the spherical diameter is needed. A new method has been developed to correlate the flattened diameter and the spherical diameter of the paint particles [2]. The main idea of the method is to collect flattened particles on the edges of the microscopic slide. The side profiles of the particles collected in this manner can be analyzed using the automatic image analyzer. If the height and the flattened diameter of a particle are known, the volume of the flattened particle can be calculated. Then the spherical diameter can be calculated by equating the volume of the flattened particle to the same volume of a spherical particle. The correlation of the flattened diameter (d_f) and the spherical diameter (d_p) is shown in Figure 3.

MATHEMATICAL MODEL

The air-cap jet is an elongated ellipse which is a three-dimensional jet. To calculate the three-dimension flow field, even using a supercomputer, the computational effort and the data storage requirements are quite substantial. Since the ratio of the major-axis length to the minor-axis width was about 8, the air-cap jet was modeled as a two-dimensional plane jet. The velocity profiles in the minor-axis plane (see Figure 1(b)) were assumed for the entire jet. Furthermore, only the region near the wall is critical for particle impaction so the calculation domain was selected as shown in Figure 1(b).

The air-cap jet is quite turbulent and many turbulence models have been proposed to calculate turbulent flow fields [3, 4]. Among these models, the k-ε turbulence model is the most popular and extensively tested. Therefore, it was selected for calculating the air flow field of the impinging air-cap jet.

Once the air flow field was known, the trajectories of a range of particle sizes could be calculated [5, 6]. The calculation procedure was quite simple. First, a particle of known size was placed at an arbitrary position along the starting line of the flow field and the trajectory was calculated. If the particle impacted on the target, it was moved to a position farther away from the centerline for the next calculation. If the particle did not impact on the target, the particle position was moved closer to the centerline. This process was repeated until a position, called the critical position, was found such that the particle just impacted on the edge of the target. The percentage of flow rate at that critical position was the collection efficiency for that particle size. After the collection efficiencies for a range of sizes were obtained, a curve of collection efficiency versus particle diameter was constructed. It should be pointed out that the aerodynamic motion of a particle is better represented by the aerodynamic diameter rather than the geometrical particle diameter. The relationship between the two diameters is $d_a = \sqrt{\rho_p} d_p$ where d_a = aerodynamic diameter, ρ_p = particle density, and d_p = geometrical particle diameter. Using the information of the measured total PSD of the spray and the collection efficiency curve, the PSD on the target was calculated.

SAMPLE RESULTS

Figure 4 shows a plot of the paint deposit versus target distance for the target, the walls, and the exhaust. As shown, the percentage of paint deposit on the target (i.e. transfer efficiency) decreased linearly with increasing target distance. The slope of the line is -1.35% per cm (-3.44% per inch). This means that the transfer efficiency decreased 1.35% for every centimeter the gun was moved away from the target. In normal spray painting, the gun-to-target distance can vary between 20.3 cm to 30.48 cm (8" to 12"). As a result, the transfer efficiency can vary by as much as ± 7% by this factor alone.

The particles collected in the exhaust can be considered as airborne and an undesirable air pollutant, if emitted to the ambient atmosphere. They arise because they cannot impact on the target or settle on the walls. The bottom line in Figure 4 shows only slight increment in weight with a large increase in target distance. This means

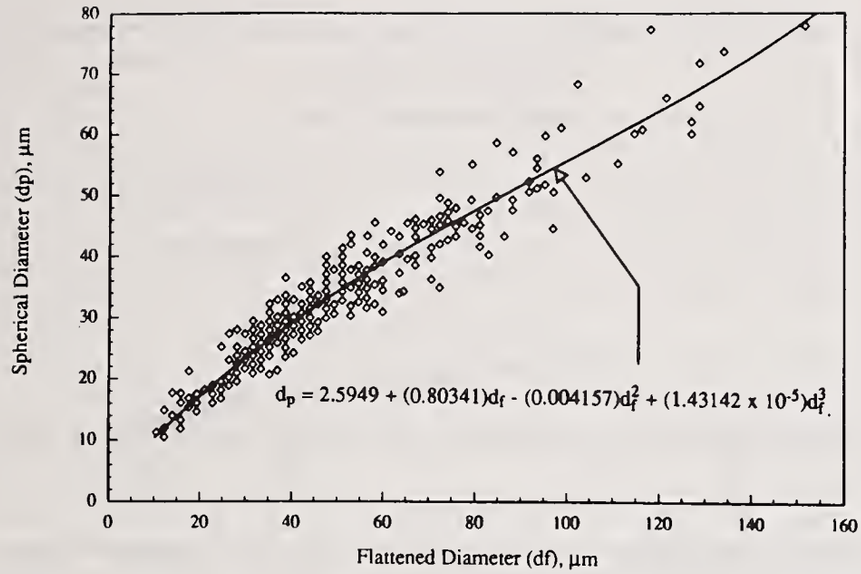

Figure 3. Correction between Spherical and Flattened Particle Diameter

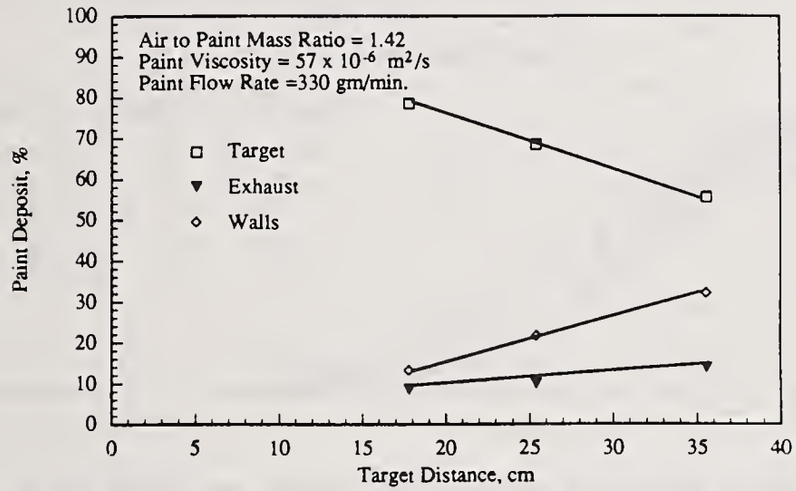

Figure 4. Effect of Target Distance on Paint Distribution on Target, Walls, and Exhaust

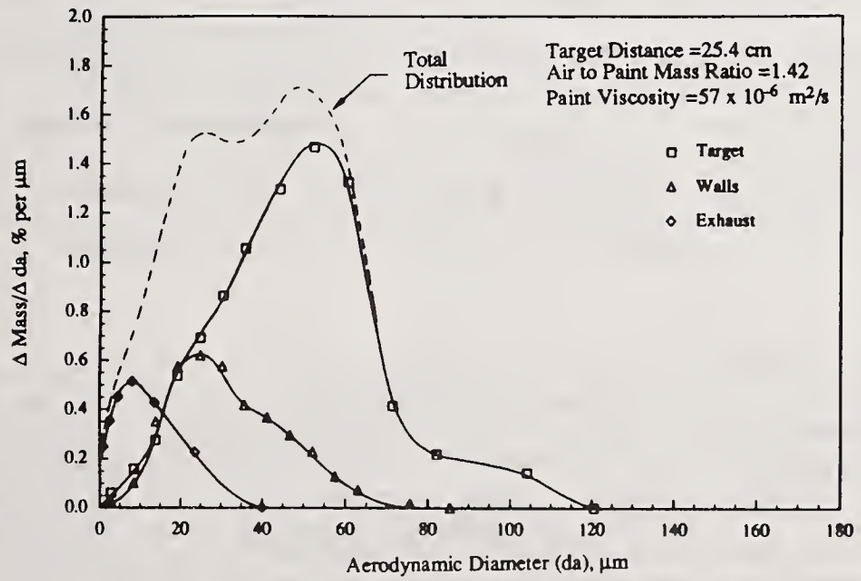

Figure 5. Mass Size Distributions on Target, Walls, and Exhaust

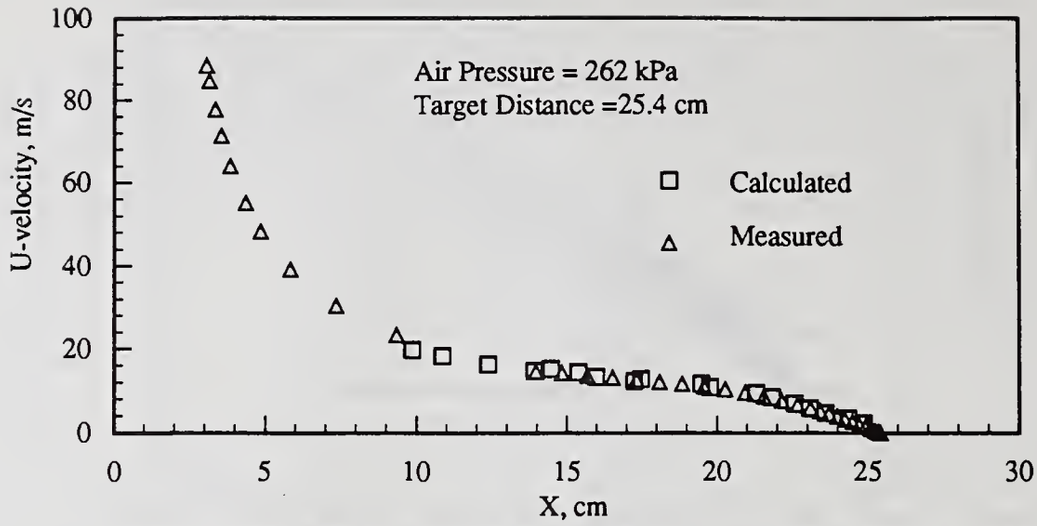

Figure 6. Comparison between Calculated and Measured Centerline Velocities

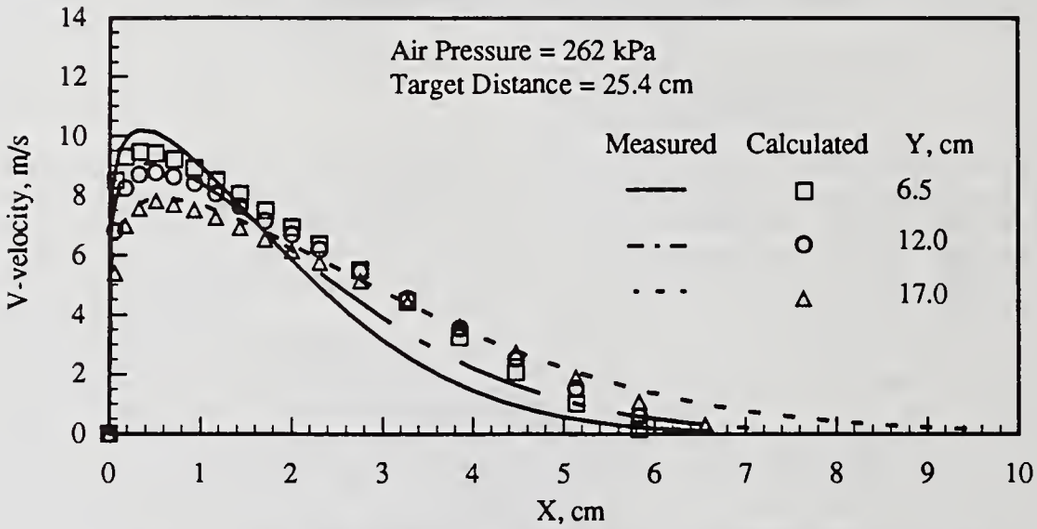

Figure 7. Comparison between Measured and Calculated V-velocity Profiles

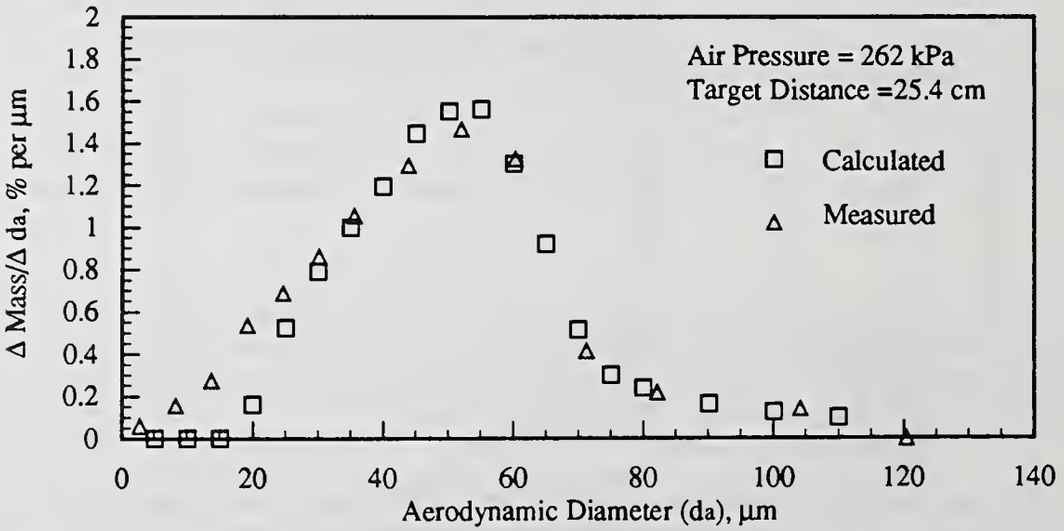

Figure 8. Comparison of Measured and Calculated MSD on Target

that increasing target distance did not cause a substantial increase in airborne particles produced. Instead, most of the particles that could not impact on the target end up on the walls. This is evident from the steeper positive slope of the middle line in Figure 4.

Figure 5 shows the mass size distributions of a spray at 25.4 cm target distance. The dotted line is the total distribution which was constructed by summing all the other distributions. Also, it should be pointed out that the area under each curve represents the total mass for that curve. As can be seen, the particles deposited on the target had sizes ranging from a few micron to about 120 μm. For all practical purpose, the significant particle sizes are between 15 to 80 μm, and they are the most important particles affecting the finish quality of a coating. The peak of the curve is located at an aerodynamic diameter of approximately 50 μm. Coincidentally, the mass median aerodynamic diameter (MMAD) was also found to be 50 μm. The MMAD is defined as the aerodynamic diameter for which 50% of the mass is less than the stated aerodynamic diameter.

From the mass distribution curve for the walls, it can be seen that the largest particle size was about 70 μm. This means that any particles bigger than 70 μm were all collected by the target. The peak of the mass distribution curve was about 25 μm and the MMAD was about 30 μm. According to the settling velocity calculation, a 30 μm particle will settle (due to gravitational force) at 2.72 cm/s. This is quite a fast settling rate, indicating that most particles on the floor was probably deposited by settling. However, the smallest particle found on the microscopic slides was about 2.5 μm. The settling velocity for this size is quite small, only 0.021 cm/s. It is unlikely that the 2.5 μm particles collected were due to settling. One possible deposition mechanism is turbulent deposition.

The mass distribution curve for the exhaust shows that the majority of the airborne particles was about 8 μm and the MMAD was about 12 μm. Further, the curve also shows that particles above 35 μm could not remain airborne. For a 12 μm particle, the settling velocity is 0.49 cm/s.

The total distribution curve shows that the mass distribution is bimodal. One peak is located at an aerodynamic diameter of 25 μm and the other peak at an aerodynamic diameter of about 50 μm. The comparison between the total mass distribution and the mass distribution on the target immediately tells about the sizes and the amount of particles that cannot impact on the target. This information can be used to guide equipment design and improvement. For example, if the of an equipment is so designed that the inertial energy of those particles between 10 and 60 μm are increased, the transfer efficiency will be improved substantially.

To show the validity of the mathematical model described earlier, some of the measured and the calculated results are compared. The measurement method and data for the mean air velocities have been given in Kwok's thesis [2]. Figure 6 compares the measured and calculated centerline velocities as a function of axial distance for the 262 kPa air pressure. It can be seen that the agreement between the measured and the calculated data points is excellent. Also, the air-cap jet showed rapid decay of centerline velocity in the first 10 cm from the air cap. Then the decay rate is reduced. At about 5 cm from the target (X=25.4 cm is the target location), the centerline velocity decelerated quickly to zero.

The mean velocity profiles in the major-axis and the minor-axis planes have been shown and explained in Figure 1. So, they will not be repeated here.

Figure 7 shows three calculated and measured velocity profiles of the plane wall jet for three Y distances. The two results show fair agreement. In fact, for Y=17 cm, the calculated velocity profile fit is in excellent agreement with the measured velocity profile. However, for the other two Y distances, the "widths" of the calculated profiles are slightly larger than the measured ones.

The calculated and measured mass distributions on the target for the 262 kPa air pressure and 25.4 cm (10") target distance are shown in Figure 8. In general, the agreement between the calculated and the measured values is excellent for aerodynamic diameters larger than approximately 30 μm. Below 30 μm, the calculated value is always less than the measured value. The smaller the aerodynamic diameter, the bigger is the deviation in $\Delta mass/\Delta da$. The explanation for the deviation is that the particle number concentration was very high for particles with aerodynamic diameter less than 30 μm. In fact, these particles constituted 98% of all particles by number. So, the flow situation was probably a dense two-phase flow which was not included in the mathematical model.

CONCLUSIONS

Air spray painting, though an old painting method, can be improved to give high transfer efficiency and good finish quality through fundamental understanding of the atomization, transport and deposition process. The independent control of the air flow and pressure makes air spray the preferred and versatile atomization method for obtaining fine finish coatings.

New research approach has been suggested and explained. This approach allows the measurement of paint deposition on the target, the walls, and the exhaust. Furthermore, the PSD in each of these three places can be measured and the total PSD constructed. This information is necessary in order to better understand the aerodynamic motion and the deposition mechanism of the paint particles. Even though the aerodynamic motion of the particles

is difficult to study experimentally, their behavior can be studied using modern mathematical and computational tools.

REFERENCES

1. Bürkholz, A., Widder, J., Müller, W. and Dislich, M., "Particle Size Distribution of Overspray Generated During Spray Painting", Polymers, Paint and Colour Journal, Vol 167, pp.285-290 (1977).

2. Kwok, K. C., "A Fundamental Study of Air Spray Painting", Ph. D. thesis, Particle Technology Laboratory, University of Minnesota, Minneapolis, MN (1991).

3. Rodi, W., Turbulence Models and Their Application in Hydraulics, International Association for Hydraulic Research (IAHR), Delft, The Netherlands(1980).

4. Launder, B. E. and Spalding, D. B., Mathematical Models of Turbulence, Academic Press, London (1972).

5. Marple, V. A., "A Fundamental Study of Inertial Impactors", Ph.D. thesis, University of Minnesota, Minneapolis, MN, Particle Technology Laboratory Publ. 144 (1970).

6. Rader, D. J. and Marple, V. A., "Effect of Ultra-Stokesian Drag and Particle Interception on Impaction Characteristics", Aerosol Science and Technology, Vol 4, pp.141-156 (1985).

COATINGS APPLIED WITH THE PLASMA-SPRAY PROCESS USING NICKEL-ALUMINUM POWDERS

D.J. Varacalle, Jr.[*], J.R. Knibloe[*], V.L. Smith-Wackerle[*], J.A. Walter[†] and G. Irons[‡]

[*]Idaho National Engineering Laboratory, EG&G Idaho, Inc., Idaho Falls, ID, U.S.A.
[†]Miller Thermal Inc., Appleton, WI, U.S.A.
[‡]TAFA, Inc., Concord, NH, U.S.A.

ABSTRACT

As part of an investigation of the dynamics that occur in the plasma-spray process, an experimental study of the plasma spraying of nickel-aluminum powder was conducted. The coating experiments used typical process parameters that were varied in a Taguchi fractional factorial design parametric study. Operating parameters were varied around the typical spray parameters in a systematic design of experiments to display the range of plasma-processing conditions and their effect on the resultant coating. Parameters varied include the working gas mixture, power, powder injection location, spray distance, traverse rate, and powder feed rate. The coatings were characterized by hardness tests, optical metallography, and x-ray diffraction. Coating qualities are discussed with respect to thickness, hardness, porosity, and phase content.

INTRODUCTION

The plasma-spray process is one of the most versatile and rapid methods of applying coatings, and its applications continue to increase [1]. The plasma-spray guns typically use a nontransferred dc plasma torch configuration with powers up to 100 kW. The basic design of the plasma gun consists of a cone-shaped cathode inside a cylindrical anode nozzle. An inert gas (usually argon, argon/hydrogen, or argon/helium) flows through the space between the electrodes where it is ionized to form a plasma. Powders injected into the plasma are then accelerated and melted by its high temperature. The molten droplets (i.e., splats) are propelled onto the substrate where they solidify and accumulate to form a thick, well-bonded coating. For quality coatings, the particles must absorb enough heat from the flame to melt thoroughly, but not so much that they overheat, oxidize, and/or vaporize. At the same time, the particles must travel fast enough to have good particle adherence once they strike the substrate.

Plasma-sprayed coatings are used for wear resistance, heat and oxidation resistance, corrosion resistance, electrical or thermal conductivity or resistivity, restoration of dimension, and clearance control. Many operational parameters control the quality of the coating, making it difficult to find the optimum processing conditions for any specific application [2,3].

As coatings become more sophisticated, a better knowledge of the underlying principles is necessary to improve process control and coating quality. Plasma spraying was developed to a large extent by empirical means, while the scientific research lagged behind. This work attempts to further

the scientific understanding of the physical mechanisms involved in nickel-aluminum coating formation by determining which process parameters affect the structure and properties of the coatings.

Plasma-sprayed nickel-aluminum coatings are widely used in the automotive, transportation, aerospace, and aircraft industries. The nickel-aluminum powder system is used for restoration of dimension, wear, and oxidation and as bond coats for thermal-sprayed ceramic coatings to enhance the adhesion strength of the coating to the substrate.

EXPERIMENTAL PROCEDURE

A Taguchi [4] statistical-style fractional-factorial design experiment was employed to evaluate the effect of seven plasma-processing variables on three quantitatively measured responses. The parameters varied were amperage, primary gas flow, secondary gas flow, powder feedrate, spray distance, gun traverse rate, and powder injection angle. The resulting responses evaluated were thickness and porosity with optical microscopy and hardness with a Rockwell 15T test. Phase content was determined with x-ray diffraction (XRD).

Experiments NA15 through NA22 in Table 1 represent the eight runs evaluated with the Taguchi approach. Two levels of each variable were selected to band around the nominal settings (i.e., experiment NA01). The quantitative Taguchi evaluation of the plasma-spray process is ideal because it displays the range of measured coating characteristics attainable, and it statistically delineates the impact of each factor on the measured coating characteristics across all combinations of other factors. The Taguchi analysis used PC-based software [5] on the measured responses.

A Miller Thermal Plasmadyne SG-100 plasma-spray system was used the experiments in Table 1. The primary gas was argon and the secondary gas was helium. A four hole gas ring induced vortex flow. The powder carrier gas was argon at 0.000102 m^3/s (13 scfh) for all experiments. The powder injection was internal to the torch and was directed either perpendicular to the flow or at a 20-degree angle forward into the flow. An x-y manipulator ensured the spray distance and repeatability in the experiments. Traverse rates varied from 43.2 to 54.8 cm (17 to 23 in.)/s with a y-step of 0.3175 cm (0.125 in.) /step. Ten passes were used to fabricate each of the coatings.

Table 1 Nickel-Aluminum Thermal Spray Experiments

Experiment Number	Current (amps)	Power (kW)	Gas Flow Primary (m^3/s) (scfh)	Gas Flow Secondary (m^3/s) (scfh)	Powder Feed (m^3/s-lb/h)	Spray Distance (cm/in.)	Gun Traverse (cm/s-in/s)	Inject (p or f)[a]
NA01	800	30.9	0.000787 100	0.000370 47	0.00088 7	7.62 3.0	50.8 20	f
NA15	700	23.8	0.000590 75	0.000236 30	0.00063 5	6.35 2.5	43.2 17	p
NA16	900	39.2	0.000983 125	0.000472 60	0.00114 9	6.35 2.5	43.2 17	p
NA17	700	27.4	0.000590 75	0.000472 60	0.00114 9	8.89 3.5	58.4 23	p
NA18	900	35.5	0.000983 125	0.000236 30	0.00063 5	8.89 3.5	58.4 23	p
NA19	700	27.7	0.000983 125	0.000236 30	0.00114 9	6.35 2.5	58.4 23	f
NA20	900	33.0	0.000590 75	0.000720 60	0.00063 5	6.35 2.5	58.4 23	f
NA21	700	30.5	0.000983 125	0.000720 60	0.00063 5	8.89 3.5	43.2 17	f
NA22	900	29.3	0.000590 75	0.000236 30	0.00114 9	8.89 3.5	43.2 17	f

a. p = perpendicular to flow, f = 20 degrees forward into flow.

The study used a commercially available powder (Alloys International AI-1037), consisting of a nickel core with an aluminum skin. The powder chemistry and sieve analysis, as supplied by the powder manufacturer, are shown in Table 2. The powder was plasma-sprayed onto 304 stainless steel plates (51 x 63 x 3 mm) cooled by air jets on the back side. One side of each steel coupon was grit-blasted with #30 alumina grit before spraying.

Table 2 Nickel-Aluminum Powder Chemistry and Sieve Analysis

Chemistry	%	Sieve (μm)	%
Ni	95.13	>106	0.1
Al	4.87	> 90	1.3
	> 45	99.8	

MATERIALS CHARACTERIZATION RESULTS

Conventional air plasma spraying (APS) yields rapid solidification and is considered a continuous, metastable materials forming technique. However, APS is known to produce rapidly solidified structures that show defects, such as unmelted particles, porosity, and oxide inclusions, which modify the coating thermophysical properties and affect bond strength and toughness. The microstructure of plasma-sprayed deposits is based on the rapid solidification of individual splats. The splat morphology depends on the processing parameters that dictate the particle velocity, temperature, and size at the standoff distance.

Average coating thicknesses for each experiment, taken from 12 measurements using optical metallography, are listed in Table 3. The deposits ranged from 187 to 603 μm for an average of 19 to 60 μm per pass, reflecting influences of spraying parameters. Controlled deposition is important to the substrate heat input that influences the residual stress buildup within the coating. Also, deposition considerations substantially impact the economics of the plasma-spray process.

Table 3 Coating Characterization Results

Experiment Number	Ni-Al thickness (μm)	Hardness[b]	Porosity (%)
NA01	421	15T76.5	2.6
NA15	309	15T80.0	5.9
NA16	601	15T83.6	1.8
NA17	435	15T80.4	4.1
NA18	187	15T80.9	3.5
NA19	476	15T75.6	1.1
NA20	280	15T84.0	4.2
NA21	310	15T81.1	3.8
NA22	603	15T78.0	3.0

a. Rockwell 15T hardness

Variances in porosity were evident by optical microscopy. Average porosities from four measurements per coating for each experiment are listed in Table 3. The average porosity of the nickel-aluminum coatings ranged from 1.1 to 5.9%. Figs. 1 and 2 illustrate the microstructure of nickel-aluminum coatings from experiment NA15 (highest porosity coating) and experiment NA19 (lowest porosity coating). The NA15 coating shows a significant amount of oxide stringers and a somewhat higher NiO content (measured by XRD) than the NA19 coating. Unmelted particles are more evident in the NA19 coating. Typically, low porosity is desirable in nickel-aluminum coatings.

Hardness measurements were taken on the coatings normal to the deposit using the superficial Rockwell 15T method. Twelve measurements were taken and averaged. The hardness of the coatings varied from 75.6 to 84.0, as listed in Table 3. Higher superficial hardness of a coating may be an advantage for wear applications, but is not necessary when used as a bond coat.

X-ray diffraction measurements were taken to qualitatively assess the phases in the coatings from the nine plasma-spray experiments. The feedstock powder and all as-sprayed coatings exhibited XRD spectra indicating that the samples primarily contained elemental Ni. This is not surprising since the source powder had less than 5% Al. Results from the XRD studies are presented in Table 4. The coatings contained minor amounts of various nickel-aluminides (Ni_3Al, Al_3Ni_2, NiAl) and dispersed Al_2O_3 and NiO. A previous study [6] also reported primarily nickel coatings with some oxides for a similar source powder, but no aluminides were detected.

Fig. 1 Microstructure (400X) for coating NA15

DISCUSSION OF TAGUCHI FRACTIONAL FACTORIAL EXPERIMENT DESIGN

Taguchi-type fractional-factorial testing is an efficient means of determining broad-based factor effects on measured attributes. This methodology statistically delineates the impact of each variable on the measured coating characteristics across all combinations of other factors. It does not consider second or third order interactions, but it does determine which factors have the most influence on the measured attributes. The factor significance lies only between the levels of test parameters selected and used. Also, the test methods used to evaluate the attributes must be consistent and accurate.

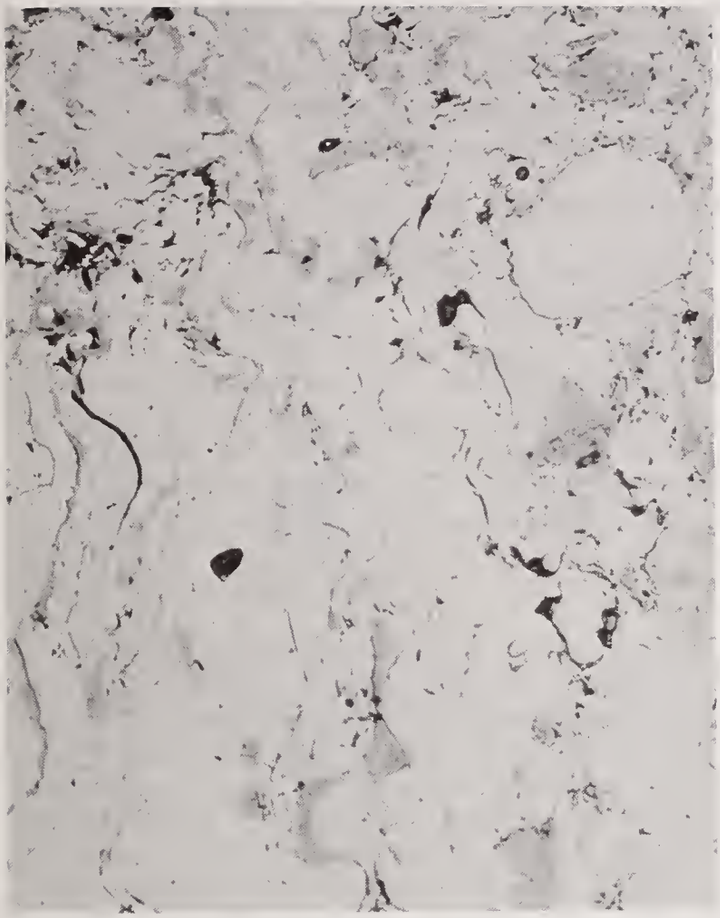

Fig. 2 Microstructure (400X) for coating NA19

The spray tests were conducted and evaluated once, and all data points were considered in the analysis of variance (ANOVA) calculations. The rho percent calculation indicates the influence of a factor or parameter on the measured response, with a larger number indicating more influence. The error calculation is the percentage of the variation observed in the test due to the data scatter. The confidence interval is determined by comparing the rho percent with the error percentage of the response test. Thus, a parameter with a low rho percent that is significant at a 95% confidence level indicates that the effect is probably real, but relatively insignificant when compared to other parameters. The ANOVA calculations guide further experimentation by indicating which parameters are the most influential on coating attributes. This information is extremely useful in developing new coating specifications and spray equipment.

Table 4 Coating X-Ray Diffraction Results

Experiment Number	Ni	Ni3Al	Ni2Al3	NiAl	NiO	Al2O3
Powder	p[a]	s[b]	s	s	t[c]	
NA01	p	t	s	t	t	
NA15	p	t	t	t	t	t
NA16	p		t	t	s	t
NA17	p			t	s	t
NA18	p		t	t	s	t
NA19	p		t	s	t	
NA20	p		t	t	t	t
NA21	p	t	s	t	t	
NA22	p	t	t	t	t	t

a. p = predominant phase
b. s = secondary phase
c. t = possible trace of phase

The analysis evaluated the effect of seven plasma-processing variables on three quantitatively measured responses. The variation in the coating characteristics displayed in the experiments indicates that minor variations in plasma-processing conditions can affect coating properties. Table 5 illustrates the results of the Taguchi analysis.

Table 5 Results of the Taguchi Analysis

Factor	Rho Percent	Confidence Level (%)	Level High	Average Low
Superficial Hardness (Rockwell 15T) (12 Data Points)				
Helium Flow	37.2	99	82.3	78.6
Amperes	15.0	99	81.6	79.2
Feedrate	11.6	99	79.4	81.5
Injection Angle	5.8	95	79.7	81.2
Error	29.4			
Porosity (%) (4 Data Points)				
Feedrate	32.1	99	2.6	4.3
Argon Flow	26.2	99	2.5	4.4
Injection Angle	5.1	95	3.0	3.9
Error	35.5			
Thickness (μm) (12 Data Points)				
Feedrate	75.1	99	528	272
Gun Traverse Rate	13.9	99	345	455
Amperage	1.4	95	419	384
Injection Angle	1.3	95	417	384
Spray Distance	1.1	95	384	417
Error	7.0			

The Taguchi evaluation indicated that secondary helium flow was the most significant contributor to hardness at a 37.2 rho percent with higher helium flow resulting in greater hardness. Other contributors at the 99% confidence level were amperage at a 15.0 rho percent with higher amperage resulting in higher hardness values, and powder feedrate at 16.7 rho percent with lower feed rates resulting in higher hardness values. At the 95% confidence level, the injection angle had a small, yet probably real, contribution of 6 rho percent with rearward injection leading to greater hardness. The error within the test accounted for 29.4% of the variation observed in the test.

At the 99% confidence level, the most significant contributors to porosity were powder feedrate and primary flow with rho percentages of 29 and 24%, respectively. Higher powder feedrate and higher argon flow contributed to lower porosity. A small but real contribution to porosity was made by an injection angle with a rho percent of 5.1% at a 95% confidence level. The error in this response test accounted for 35.5% of the variation observed in the porosity data.

The Taguchi analysis of this study indicated that the key to maximizing the economics of the coating deposition was controlling powder feedrate and gun traverse rate. Their contribution to the total variation in thickness observed (i.e., rho percent) was 75.1 and 13.9%, respectively, at a 99% confidence level. Increasing the powder feedrate increased the deposition thickness, as would be expected. Lower gun traverse rates lead to increased deposition thickness. The error percentage for the thickness response test was low at 7%, which made the small contributions of amperage, injection angle, and spray distance significant at a 95% confidence level.

This Taguchi evaluation is significant because it directs further experimentation on the most important process or coating attributes and the process parameters that affect these attributes. The most important attributes may differ for the same material in different applications, and the baseline data generated in this study can be used to develop specific confirmation runs that approach the desired application attributes.

SUMMARY AND CONCLUSIONS

This paper presents an experimental study of the plasma-spraying of nickel-aluminum powder coatings. Experiments were accomplished using a Taguchi fractional-factorial approach varying typical process parameters. The coatings were then characterized for thickness, porosity, hardness, and phase structures using optical microscopy and x-ray diffraction. The coating thicknesses, reflecting influences of spraying parameters, ranged from 187 to 603 μm. Porosity of the coatings ranged from 1.1 to 5.9%. Hardness measurements varied from 75.6 to 84.0 on the Rockwell 15T scale. Results from the XRD coating studies indicated a predominantly nickel matrix with various nickel-aluminides (Ni3Al, Al3Ni2, NiAl) and dispersed oxides (Al2O3 and NiO).

The Taguchi analysis indicated that powder feedrate and traverse rate were the significant factors affecting the deposition thickness. The significant factors for hardness were secondary flow and amperage. Powder feedrate and primary flow significantly affected porosity.

The objective of this and future work is to optimize the quality of plasma-sprayed coatings. By generating baseline data on factors that influence coating characteristics, operational parameters can be selected and optimized for future nickel-aluminum plasma-spray processing experiments and applications. Future work is needed to determine the effect of powder fabrication methods on the coating morphology.

ACKNOWLEDGEMENTS

The technical input of G. C. Wilson and A. W. Erickson is gratefully acknowledged. The work described in this paper was supported by the U.S. Department of Energy under DOE Contract No. DE-AC07-76ID01570.

REFERENCES

1. Kubel, E. D., Advanced Materials and Processes, (132), 6, 69-80, (1987).

2. Pfender, E., "Fundamental Studies Associated with the Plasma Spray Process," Proceedings of the National Thermal Spray Conference, September 14-17, 1987, Orlando, Florida.

3. Fauchais, P., "State of the Art for the Understanding of the Physical Phenomena Involved in Plasma Spraying at Atmospheric Pressure," Proceedings of the National Thermal Spray Conference, September 14-17, 1987, Orlando, Florida.

4. Taguchi, G., and Konishi, S., Taguchi Methods: Orthogonal Arrays and Linear Graphs, ASI Press, (1987).

5. Culp, R. F., Sadie, Speedy Analysis and Design of Industrial Experiments, Copyright 1990, R. F. Culp.

6. Sampath, S., Herman, H., and Rangaswamy, S., "Ni-Al Re-evaluated," Proceedings of the National Thermal Spray Conference, September 14-17, 1987, Orlando, Florida.

ATOMIZATION CHARACTERISTICS OF A HIGH-SPEED ROTARY-BELL PAINT APPLICATOR

P.L. Corbeels, D.W. Senser and A.H. Lefebvre

School of Mechanical Engineering, Purdue University
West Lafayette, IN, U.S.A.

ABSTRACT

An experimental study was conducted on the influence of fluid properties and operational parameters on the atomization characteristics of a high-speed rotary-bell paint applicator. Drop size measurements near the bell edge were complimented with high speed photography to investigate the filming characteristics, atomization modes, and ligament disintegration mechanisms of this type of applicator. Surface tension was varied by a factor of 2.5 and viscosity by a factor of 100. Rotational speeds ranged from 4,000 rpm to 40,000 rpm, while the liquid mass flow rate was varied from 0.67 to 6.67 g/s. It was found that high viscosity fluids film the bell very evenly and produce long regular ligaments, whereas low viscosity fluids film incompletely and produce very irregular ligaments that disintegrate near the bell edge. Mean drop size was found to be fairly insensitive to large changes in flow rate and viscosity at bell speeds higher than 20,000 rpm.

INTRODUCTION

Rotary-bell atomizers are widely used in spray coating systems and generally provide excellent finishes and high transfer efficiencies. Bells are generally preferred to cups because they provide a larger fluid filming area for a given diameter. Consequently, a smaller diameter bell can be used without loss of atomization quality, resulting in a smaller spray pattern that is more easily controlled. A typical rotary-bell atomizer is shown in Figure 1. The coating material is delivered to the inside surface of the rotating bell by an array of fluid feed ports. Under the influence of centrifugal and Coriolis forces the fluid films toward the bell edge, generally decreasing in thickness as it move radially outward. Near the bell edge, radial serrations promote the formation of discrete ligaments which subsequently disintegrate into droplets. An axial flow of shaping air from a ring of small orifices positioned behind the bell imparts axial momentum to the droplets, directing them towards the workpiece. In addition, a high voltage is applied to the bell directly, or to a series of electrodes in the vicinity of the bell, to impart an electric charge to the liquid. The resulting charged droplets are attracted to the grounded workpiece, thereby increasing transfer efficiency. For paint spray applications, rotational speeds in excess of 20,000 rpm, and small bell diameters of less than 10 cm, are typically used. This combination of high rotational speed and small bell diameter provides good atomization and a compact spray pattern.

While rotary atomization in general has been the subject of considerable research, as evidenced in the reviews by Matsumoto et al. [1], Masters [2], Dombrowski and Munday [3], and Marshall [4], few studies have addressed high-speed, rotary-bell paint applicators (HSRBPAs). Hinze and Milborn [5] established that rotary atomizers produce drops by one of three principal mechanisms; atomization by direct drop formation, by ligament formation, and by sheet formation. Small serrations near the bell edge allow HSRBPAs to operate almost exclusively in the ligament formation mode. Under most conditions the number of ligaments is constant and equal to the number of serrations on the bell edge. The Sauter mean diameters (SMDs) produced by these applicators range from 15 to 50 μm under typical operating conditions. These values are quite small in comparison with those obtained by Dombrowski and Lloyd [6] who performed an experimental study on the factors that control the spray characteristics of spinning cup atomizers, ranging in diameter from 50 to 150 mm. Most of their work dealt with atomization by film formation but a limited number of measurements were made in the ligament mode. Within this mode, the measured SMDs ranged from approximately 30 to 300 μm. However, the maximum rotational speed of 10,200 rpm is slow in comparison to typical operating conditions for HSRBPAs. Contrary to general experience, they observed a decrease in drop size as the liquid viscosity was increased from 7.3 to 101 mNs/m^2. They attributed this

anomaly to more viscous ligaments stretching farther and becoming smaller in diameter before finally breaking up into droplets.

Kayano and Kamiya [7] developed an analytical expression for the mean size of drops produced by a rotating disk when operating in the ligament mode. Their calculations were based on a analysis which predicted the number of ligaments produced at the disk edge and on the drop sizes produced by the disintegration of these ligaments into drops. They assumed the ligament diameter to remain constant with distance from the bell edge. Their model predicted drop size to increase with increasing surface tension and with increasing viscosity. Comparisons of predicted and measured drop sizes in the range from 100 to 300 μm showed good agreement at all test conditions for disks of 3 to 7 cm in diameter and rotational speeds from 2,500 to 6,000 rpm.

Frost [8] defined conditions for the occurrence of drop formation by ligament formation and derived an expression for the prediction of mean drop size in the ligament mode. Comparison with measured values of mean drop size for disks of 40, 60, 80, 100 and 120 mm in diameter showed good agreement over the range of drop sizes investigated (circa 70 to 300 μm). Again, the maximum rotational speed of 9,500 rpm is low in comparison to typical HSRBPA conditions.

In summary, few previous studies have addressed high-speed rotary-bell atomization. The authors are unaware of any published reports on drop size measurements for commercial HSRBPAs, despite their widespread use. While some studies have dealt with rotary atomization in the ligament mode, the rotational speeds employed were typically much less than 20,000 rpm. Consequently, the observed drop sizes were large and the magnitudes of the centrifugal and Coriolis forces much smaller than in HSRBPA systems. Finally, the drop-sizing techniques used in previous studies are less accurate than the laser-based diffraction technique (Malvern particle sizer) used in this study.

The goal of the present research is to quantify the influence of the operational parameters (rotational speed and liquid mass flow rate) and the key liquid properties (surface tension and viscosity) on the drop-size distributions produced by a commercial HSRBPA. In order to isolate the hydrodynamic effects and develop a baseline from which to assess their influence, neither shaping air nor applied voltage are used.

EXPERIMENTAL

The Turbobell III rotary paint applicator manufactured by Ransburg-Gema is depicted in Fig. 1. It uses an air turbine to spin a 70 mm diameter bell at speeds of up to 40,00 rpm. A digital controller is used to maintain any given preset bell speed. Fluid is delivered to the bell through a number of discrete circular feed ports by a positive displacement pump. Once it emerges onto the the bell surface the fluid encounters a series of bell steps which allow it to build up before flowing radially outwards across the smooth bell surface. Along the edge of the bell are small triangular wedges called serrations. These serrations, spaced approximately 0.3 mm apart, tend to force the fluid into discrete ligaments and extend the range over which the atomizer can operate in the ligament mode.

This study combines qualitative visualization techniques with quantitative drop size measurements. A 0.5 μs flash is used to "freeze" the motion of the bell. Both front and back-lit photographs are taken to visualize the flow on the bell surface as well as the ligament disintegration.

A Malvern 2600 particle sizer (MPS) with a 300 mm lens is used for quantitative measurements of drop size distributions. The principles of operation and limitations of the MPS are well established; see for example, Swithenbank et al. [9], and Dodge and Cerwin [10]. The drop size distributions are characterized by the Sauter mean diameter (SMD) using the two parameter Rosin-Rammler [11] model. The Rosin-Rammler model is defined as

$$Q = 1 - \exp\left[-\left(\frac{D}{X}\right)^{q}\right] \qquad (1)$$

where Q is the fraction of the total volume contained in drops of diameter less than D, and X and q are constants for a given drop size distribution. The exponent q in Eq. (1) provides a measure of the spread in the drop sizes. The higher the value of q the narrower the size distribution.

As shown in Fig. 2, the axis of the atomizer lies in the horizontal plane. The 9 mm diameter laser beam of the MPS passes through the spray at an angle of 30 degrees. This is done to obtain measurements near the bell edge while providing sufficient space for the receiving optics. A light tube is used to prevent laser light scattering from any other region except near the bell edge. The SMD was determined to be invariant within plus or minus 10 mm about this 35 mm location. Also, at a distance of 35 mm the time of droplet flight is so short that evaporation effects are negligibly small. For these reasons, all drop size measurements are made 35 mm radially from the bell edge. Two thousand measurements of drop size

distributions are made at each test condition. As obscuration values are always less than 30% no corrections for multiple scattering are required. The Rosin-Rammler [11] reduction procedure indicates log differences between 3.0 and 4.5 which lies well below the stipulated maximum value of 5.0 for a good data fit.

RESULTS

The effects of operational parameters and liquid properties were investigated over wide ranges, as shown in Table 1. The bell speed and liquid mass flow rate (referred to henceforth as flow rate) were varied within the allowable limits of the current installation. Surface tension and viscosity, the liquid properties having the greatest influence on drop size, were varied by formulating mixtures of corn syrup and water as well as mixtures of hydrocarbon oils. The resulting fluids represent a two order of magnitude change in viscosity and a 250 percent change in surface tension. All liquids exhibited Newtonian behavior.

Order of magnitude changes in bell speed and flow rate produced all of the atomization modes identified by Hinze and Milborn [5]. However, atomization by direct drop and sheet formation produced large drops that are unsuitable for painting purposes. Hence, all the drop size measurements were made with the atomizer operating in the ligament mode of droplet formation.

The effects of bell speed and liquid flow rate on Sauter mean diameter are illustrated in Fig. 3 for four of the fluids listed in Table 1. The results show that, regardless of liquid properties, an increase in bell speed at a given flow rate always tends to decrease the SMD towards a limiting size of between 15 and 20 um. At low bell speeds, the expected result of higher flow rates producing larger drop sizes is observed, but at higher bell speeds the SMD becomes much less dependent on flow rate.

The drop size data corresponding to a liquid flow rate of 3.3 g/s have been replotted in Figs. 4 and 5 to illustrate the main effects of liquid properties on SMD. Qualitatively similar results were obtained at the other flow rates examined. The influences of bell speed and surface tension on SMD for low-viscosity liquids (circa 1 mNs/m^2) are presented in Fig. 4. This figure shows that the higher surface tension fluid produces larger drops over the entire range of bell speeds. The effects of viscosity on mean drop size for fluids of low surface tension (circa 30 mN/m) are shown in Fig. 5. At low bell speeds, the expected result of an increase in viscosity producing larger drops is obtained. Of special interest however, is that the influence of viscosity on SMD diminishes with increase in bell speed and becomes negligibly small at the highest bells speeds for which SMD data were taken.

The effects of bell speed and flow rate on the Rosin-Rammler distribution parameter, q, are shown in Fig. 6. For water, the effect of increasing bell speed at constant flow rate produces no significant change in q. For other liquids, having either significantly higher viscosity or much lower surface tension than water, it is observed that increasing the bell speed diminishes q, thus indicating a broader range of drop sizes in the spray. For all four liquids, Fig. 6 shows that a reduction in flow rate produces a higher value of q, i.e. a more narrow drop size distribution.

It is often claimed that the sprays generated by rotary bell atomizers are characterized by an exceptionally narrow drop size distribution. In this context it is of interest to note in Fig. 6 that when the bell atomizer is operating at conditions of most practical interest [bell speeds of 19,000 rpm and higher], the drop size distributions are just as broad as those produced by air or airless paint applicators [12,13].

DISCUSSION

Rotary-bell atomization in the ligament mode consists of four sequential processes: (1) filming on the bell surface, (2) ligament formation at the bell edge, (3) attenuation of stable ligaments, and (4) ligament disintegration into drops. Filming on the bell surface is strongly influenced by liquid properties and bell speed. Water flowing at around 7 g/s films the bell as a complete wavy film at all bell speeds. At lower flow rates, and all bell speeds, water flows over the bell surface in discrete wavy streams. An example of these discrete streams is shown in Fig. 7a. The width of these streams is unaffected by changes in flow rate between 1.17 and 3.3 g/s and bell speeds between 8,000 and 16,000 rpm. However, at bell speeds of 24,000 rpm and higher, stream widening is observed over a range of flow rates from 1.17 to 3.3 g/s. Stream widening occurs because water, having low viscosity, is unable to resist the Coriolis force. The other low viscosity fluid, fluid IV, exhibits slightly different filming characteristics. For bell speeds less than 8,000 rpm this fluid traverses the bell as a complete wavy film. As the bell speed is increased from 8,000 to 40,000 rpm, the increased centrifugal force causes the fluid film to divide into discrete wavy streams at all flow rates below about 7 g/s. At high rotational speeds, an increase in flow rate causes the

discrete streams to widen until, at flow rates higher than 7 g/s, the fluid flows over the bell in the form of a complete wavy film.

Separate streams are also observed near the fluid feed ports for high viscosity fluids. Figure 7b shows how these streams merge into a smooth, uniform film shortly after flowing over the bell steps.

As a result of these filming characteristics, different types of ligament formation can occur, depending on the fluid viscosity. Low viscosity fluids reach the bell edge in the form of discrete streams, each of which is converted into a cluster of ligaments. Fluids of low surface tension tend to produce wider streams which result in a larger number of ligaments in each cluster. One such cluster for water is shown in Fig. 8a. The spacing of the ligaments in this high magnification photograph is approximately 0.3 mm. Water forms very short, irregular ligaments that disintegrate into drops close to the bell edge. The ligaments produced by fluid IV, which has a lower surface tension than water, tend to be similar in structure to those of water except that the ligaments are generally longer. Figure 8a shows that the breakup mechanism for these ligaments is either Rayleigh or first wind-induced [14], since the resulting drops are either equal or larger in diameter to the ligaments from which they are formed.

High viscosity fluids film the bell completely. Two types of ligament formation are observed, depending on the operational parameters. At bell speeds lower than 8,000 rpm, the fluid film is so thick at the bell edge that the serrations are incapable of dividing the film into one ligament per serration. Instead, a liquid torus forms on the bell edge which eventually becomes unstable and produces ligaments which are spaced at an integral number of serrations. At bell speeds above 16,000 rpm, the fluid at the bell edge is thin enough to divide itself into a single ligament per serration. These ligaments are illustrated in Fig. 8b where the spacing between adjacent ligaments is again about 0.3 mm. These viscous ligaments tend to be evenly spaced and regular in shape. They also remain attached to the rotating bell for about four times the distance of their low viscosity counterparts. This results in a considerable reduction in ligament diameter along the streamwise direction due to the effect of centrifugal force in increasing the streamwise velocity. The relative velocity between the ligaments and the surrounding air increases with increasing bell speed. This causes the ligaments to become wavy and follow a sinusoidal trajectory as they move further away from the bell edge.

The preceding discussion of bell filming and ligament formation helps to explain the dependence of SMD on flow rate exhibited in Fig. 3. For example, in Fig. 3a the change in dependence of SMD on flow rate at bell speeds above and below 10,000 rpm can be explained by differences in the filming characteristics. Below 10,000 rpm, fluid IV films the bell completely, so the effect of increasing the flow rate is to increase the film thickness at the bell edge and hence the initial ligament diameter. Since these ligaments are fairly short, and have no chance to attenuate, this increase in initial ligament diameter will cause an increase in drop size. Above 10,000 rpm, high centrifugal forces cause stream widening to occur as the flow rate is increased. This widening of the stream tends to offset the effect of the increase in flow rate, so the film thickness at the bell edge remains about the same regardless of flow rate. This behavior explains the insensitivity of mean drop size to variations in flow rate at bell speeds above 10,000 rpm.

Figure 3b illustrates the effect of bell speed and flow rate on SMD for water. It shows trends similar to those in Fig. 3a, except that the bell speed at which the mean drop size becomes insensitive to flow rate is around 20,000 rpm. This critical bell speed marks a change in the effect of flow rate on stream widening. At bell speeds below the critical value, the stream widths remain unaffected by changes in flow rate, but at higher bell speeds an increase in flow rate causes the streams to widen. Since the ligaments for water are even shorter than those of fluid IV, due to its higher surface tension, it is to be expected that increases in flow rate below 19,000 rpm should increase drop sizes, while increases in flow rate above 19,000 rpm should have little effect on drop size. These expectations are confirmed in Fig. 3b.

Figures 3c and 3d show that the high viscosity fluids have two regions of dependency of flow rate on SMD. Below 29,000 rpm the SMD is very dependent on flow rate, while at higher bell speeds there is little effect of flow rate on SMD. Both liquids totally film the bell surface, so an increase in flow rate always produces a thicker film at the bell edge and hence a larger initial ligament diameter. Thus, the only way the SMD can be insensitive to flow rate above 29,000 rpm is if the final breakup diameter of the ligaments is independent of its initial value at the bell edge. This does occur with viscous ligaments because they are stable and can extend radially outward to a distance which is several times greater than for low viscosity liquids. Hence, at high bell speeds where centrifugal forces are large, a viscous ligament can thin out to a diameter which is largely independent of its initial diameter. This attenuation mechanism appears to be present at bell speeds higher than 29,000 rpm, and is mainly responsible for the independence of SMD on flow rate. Below 29,000 rpm, ligament attenuation is much less pronounced and an increase in flow rate raises the SMD.

The fluid property effects examined in this work are those of surface tension and viscosity. As shown in Fig. 4, an increase in surface tension tends to produce larger mean drops sizes for liquids of low viscosity. This is attributed to the effect of surface tension on stream width. An increase in surface tension reduces the spreading capability of individual streams. This results in thicker streams that produce larger initial ligament diameters and ultimately larger drops. Figure 5 shows the effect of viscosity at low surface tension. Below 20,000 rpm, the expected result of a higher viscosity fluid producing larger drops is observed. Above 20,000 rpm, the mean drop size remains essentially the same for a two order of magnitude increase in viscosity. For this to occur there must be a competing mechanism at high bell speeds to offset the well-known effects of viscosity on ligament disintegration. The photographic evidence suggests that the competing mechanism is the attenuation of a viscous ligament under the action of high centrifugal forces. Thus although viscosity has its normal adverse effect of increasing the optimum wavelength for ligament breakup, this effect is largely offset by the fact that when breakup finally occurs it does so at a smaller ligament diameter.

The other important spray characteristic along with SMD is the drop size distribution. Figure 6 shows how the Rosin-Rammler distribution parameter q varies with flow rate and bell speed. A general trend exhibited by all four fluids in Fig. 6 is that as the flow rate is increased the drop size distribution widens (i.e. q decreases), regardless of the bell speed. At high bell speeds, where SMD remains constant, the fact that q decreases with increasing mass flow rate should be interpreted as an indication that more fine droplets are being produced. Another general trend exhibited by all the fluids except water is that an increase in bell speed causes the drop size distribution to broaden. This can be accounted for by considering the effects of aerodynamic forces on the ligaments. Increasing aerodynamic forces cause the ligaments to wave sinusoidally and interact with each another. This tends to make the atomization process more random and thereby lower q. Photographs indicate that this ligament interaction is most pronounced at high bell speeds because the ligaments are located in close proximity at the serration spacing of 0.3 mm and the amplitude of their wave behavior is larger at higher bell speeds. At lower bell speeds, the ligaments are spaced further apart which lowers the chances of ligament interactions and the amplitude of displacement is smaller. The only fluid in Fig. 6 that shows a slightly different trend from the other fluids is water. For water, q changes only slightly as the bell speed is varied at a constant flow rate. High speed photographs show that water produces very short ligaments which do not extend far from the bell edge and thus are less susceptible to the aerodynamic forces that change appreciably with bell speed. Consequently, ligament interaction is much less pronounced, so that q remains fairly constant as the bell speed increases.

SUMMARY AND CONCLUSIONS

In interpreting the effects of operational parameters and liquid properties on the drop sizes produced by rotary bell applicators operating in the ligament mode of atomization, four separate processes must be considered: (1) filming on the bell surface, (2) ligament formation at the bell edge, (3) attenuation of stable ligaments, and (4) ligament disintegration into drops. An increase in rotational speed always produces a decrease in mean drop size by increasing the centrifugal and Coriolis forces. These forces promote increased thinning of the liquid film on the bell surface, with the result that the ligaments formed at the edge of the bell are smaller in diameter.

An increase in liquid flow rate generally increases the mean drop size at the lower bell speeds. At higher bell speeds, increasing the flow rate has little effect. This insensitivity to flow rate of low viscosity fluids is attributed to stream-widening, while for high viscosity fluids it is attributed to ligament attenuation.

Increasing the flow rate at a given bell speed always leads to a broader distribution of drop sizes in the spray. Increasing the bell speed at constant flow rate generally widens the drop size distribution due to the effects of aerodynamic forces on ligament trajectories.

In flow situations where the bell surface is incompletely filmed, which is generally the case for low viscosity fluids, an increase in surface tension raises the mean drop size by narrowing the discrete fluid streams flowing over the bell surface, thereby increasing their thickness. Viscosity has an adverse effect on mean drop size for low surface tension fluids at low bell speeds, but has little effect at the higher speeds. This is attributed to the thinning mechanisms that operate at high bell speeds.

REFERENCES

1. S. Matsumoto, D.W. Belcher, and E.J. Crosby, Rotary Atomizers: Performance Understanding and Prediction, Proceedings of ICLASS-85, Madison, WI, pp. 1A/1/1-21, (1985).

2. K. Masters, Spray Drying, John Wiley & Sons, New York, NY, (1979).
3. N. Dombrowski, and G. Munday, Spray Drying. In Biochemical and Biological Engineering Science (N. Blakebrough, ed.). Academic Press, New York, NY, vol. 2, pp. 209-320, (1968).
4. W.R. Marshal, Atomization a Spray Drying, Chem. Eng. Monograph Series no. 2, vol. 50, A.I.Ch.E., (1954).
5. J.O. Hinze, and H. Milborn, Atomization of Liquids by Means of a Rotating Cup, J. Appl. Mech., vol. 17, pp. 145-153, (1950).
6. N. Dombrowski, and T.L. Lloyd, Atomization of Liquids by Spinning Cups, Chemical Engineering Journal, vol. 8, pp. 63-81, (1974).
7. A. Kayano, and T. Kamiya, Calculation of the Mean Size of the Droplets Purged from the Rotating Disk, Proceedings of the First International Conference on Liquid Atomization and Spray Systems, Tokyo, pp. 133-137, (1978).
8. Frost, A.R., Rotary Atomization in the Ligament Formation Mode, Journal of Agricultural Engineering Research, vol. 26, pp. 63-78, (1981).
9. J. Swithenbank, J.M. Beer, D. Abbot,. and G.C. McCreath, A Laser Diagnostic Technique for the Measurement of Droplet and Particle Size Distribution, Paper 76-69 presented at the AIAA 14th Aerospace Sciences Meeting, Washington D.C., January 26-28, (1976).
10. L.G. Dodge, and S.A. Cerwin, Extending the Applicability of Diffraction-Based Drop Sizing Instruments. In Liquid Particle Size Measurement Techniques, ASTM STP 848 (J.M. Tishkoff, R.D. Ingebo and J.B. Kenndey, eds.), American Society of Testing and Materials, pp. 72-81, (1984).
11. P.Rosin and E. Rammler, The Laws Governing the Fineness of Powdered Coal, J. Inst. Fuel, vol. 7, no. 31, pp. 29-36, (1933).
12. H.E. Snyder, Drop Size Investigation of an Electrostatically-Assisted Fan-Spray Atomizer. M.S.M.E. thesis, School of Mechanical Engineering, Purdue University, (May 1988).
13. N.H. Goris, Operational Characteristics and Energy Considerations of Pneumatic Atomizers. M.S.M.E. thesis, School of Mechanical Engineering, Purdue University, (May 1990).
14. R.D. Reitz, Atomization and Other Breakup Regimes of a Liquid Jet, Ph.D. thesis, Princeton University, (1978).
15. C. Weber, Disintegration of Liquid Jets, Z. Angew. Math. Mech., vol. 11, no. 2, pp. 136-159, (1931).

TABLE 1 Operational Parameters and Liquid Properties

Operational Parameters:

Rotational speed, rpm	2,000 - 40,000
Mass flow rate, g/s	0.67 -6.7

Liquid properties (295 K):

Fluid	Surface Tension (mN/m)	Viscosity (mNs/m^2)
I. water	76	1.0
II. glycerin/water	65	100
III. corn syrup/water	80	100
IV. hydrocarbon oil	32	3.0
V. hydrocarbon oil	30	100

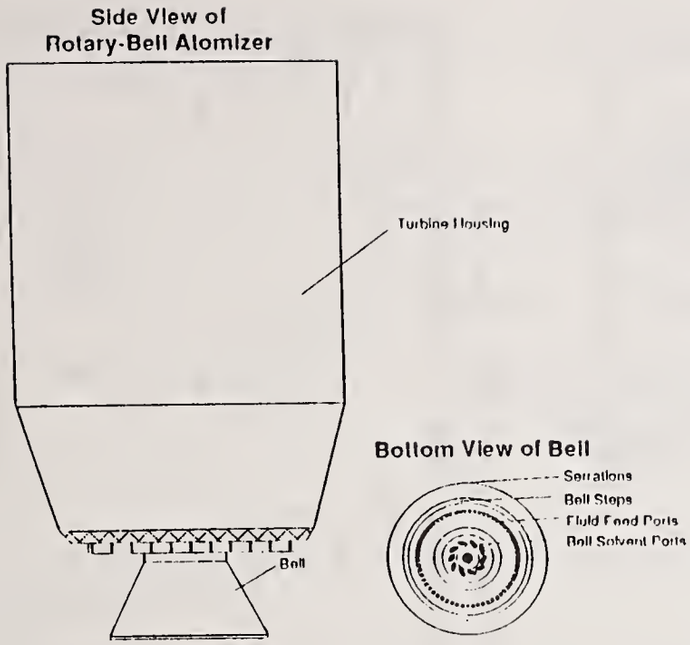

Fig. 1 Ransburg - Gema Turbobell III rotary-bell paint applicator.

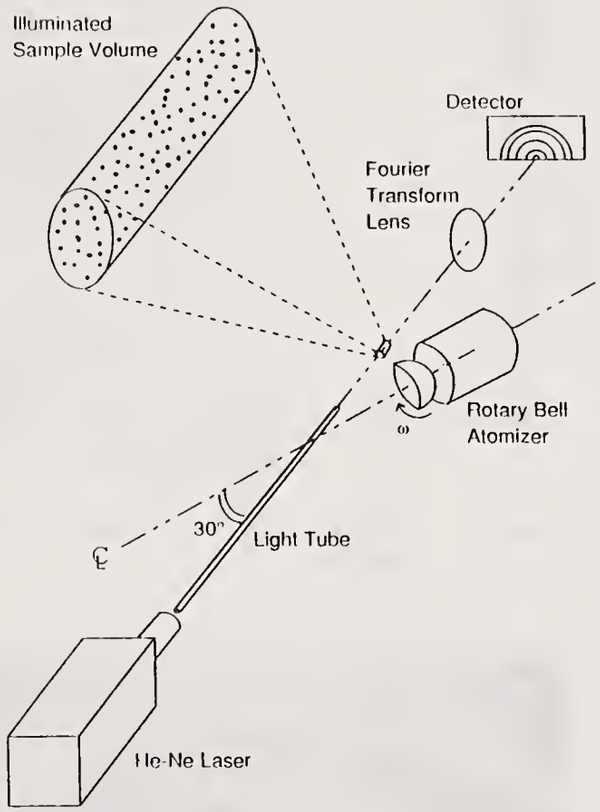

Fig. 2 Optical configuration for drop size measurements.

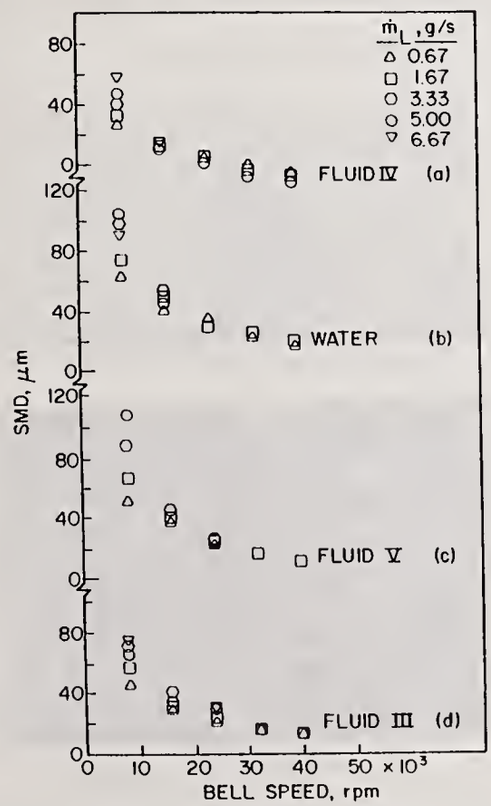

Fig. 3 Influence of liquid flow rate on mean drop size.

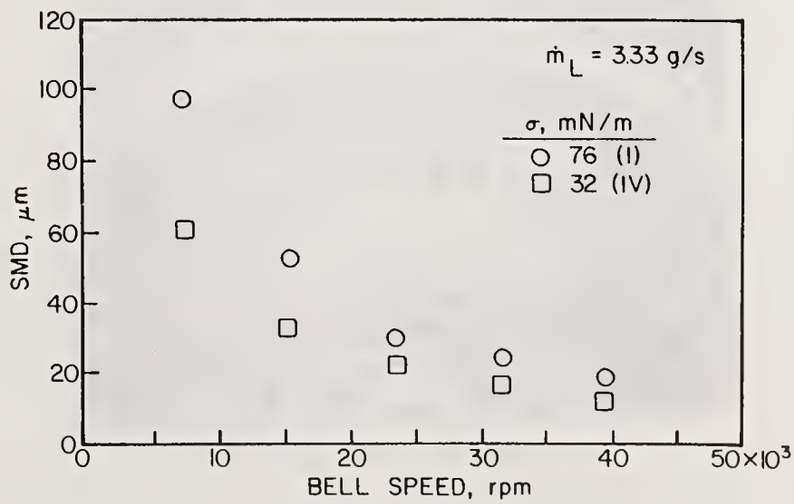

Fig. 4 Influence of surface tension on SMD for liquids of low viscosity.

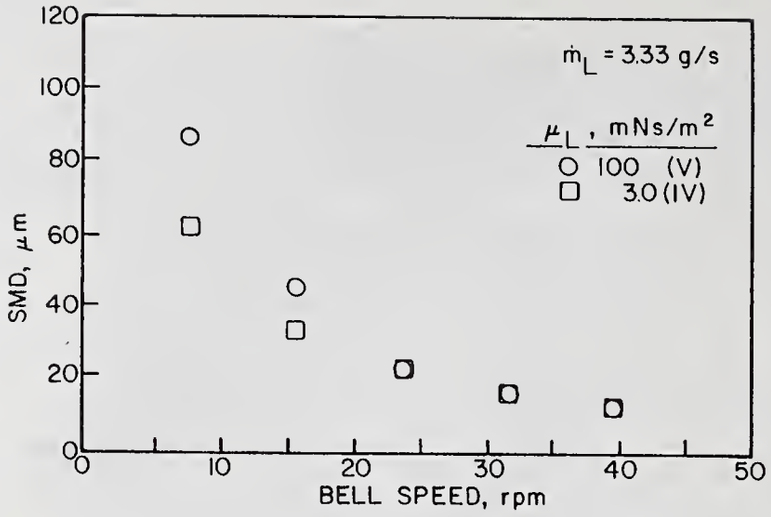

Fig. 5 Influence of viscosity on SMD for liquids of low surface tension.

μ_L = 1.0 mNs/m², σ = 76 mN/m [Water]
(a)

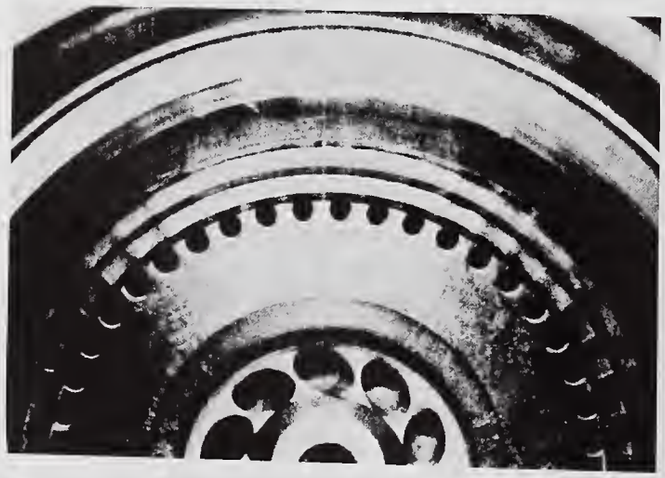

μ_L = 100 mNs/m², σ = 65 mN/m [Fluid II]
(b)

Fig. 7 Effect of viscosity on bell filming characteristics at a bell speed of 24,000 rpm. $\dot{m}_L$ = 3.3 g/s.

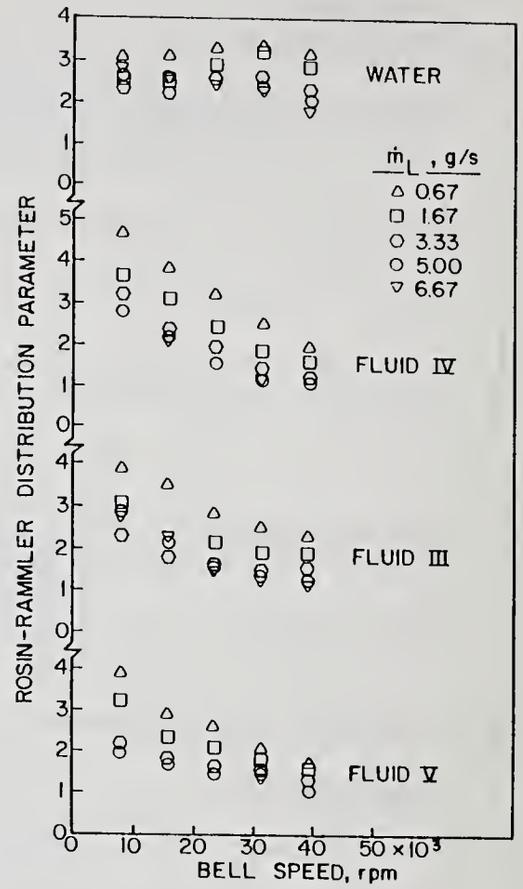

Fig. 6 Influence of bell speed and flow rate on drop-size distribution.

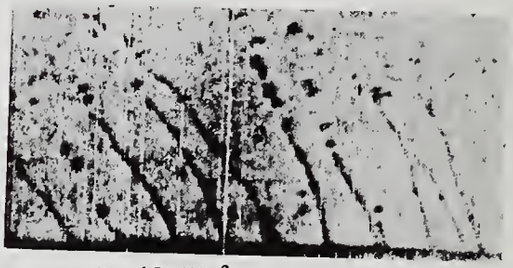

μ_L = 1.0 mNs/m², σ = 76 mN/m [Water]
(a)

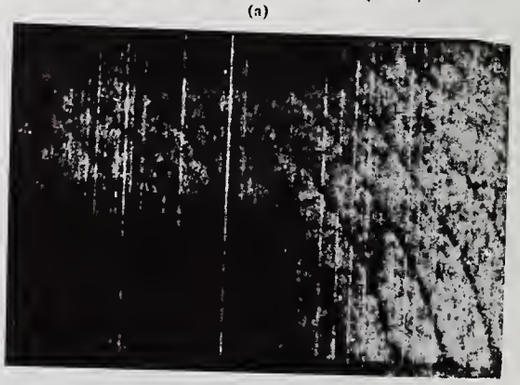

μ_L = 100 mNs/m², σ = 80 mN/m [Fluid III]
(b)

Fig. 8 Effect of viscosity on ligament structure and breakup at bell speed of 16,000 rpm.

MEASUREMENTS IN PAINT SPRAYS USING A PHASE-DOPPLER ANEMOMETER

J. Domnick, C. Tropea and T.-H. Xu

Lehrstuhl für Strömungsmechanik
Universität Erlangen - Nürnberg
Erlangen, Germany

ABSTRACT

Simultaneous measurements of droplet size and velocity in paint sprays using a phase-Doppler anemometer are presented. Mie calculations of the scattered light field, based on measured refractive indices and absorption coefficients of 2 different paints, have shown the possibility of obtaining good results with 1st order refracted light. Furthermore, verification experiments with a monodispersed droplet generator and a small hand-held spray gun were in good agreement with the calculated transfer function of the phase-Doppler system. Extended measurements in a spray cabin were performed, changing a variety of parameters like gun type, air cap and paint and air flow rates. Profiles of velocity and size were taken at 3 different distances, 5, 15 and 30 cm downstream from the nozzle. The results have shown some of the expected dependencies of the local velocity and droplet distributions on global parameters, e.g. an increase of the mean sizes with decreasing air flow. The measured size distributions were fitted to a modified log-hyperbolic function, thereby enabling the entire size distribution to be represented in terms of three parameters. The variations in these parameters with changing paint flow rate are documented and are shown to adequately represent the physical background of the phenomena under consideration.

1 INTRODUCTION

In industrial painting in Europe pneumatic spraying systems of the air-assist type with external mixing cover most of the applications, including robot driven systems in the car manufacturing. A standard spray gun, shown schematically in fig 1 has several holes arranged radially around the paint stream in the center, providing high air velocity for the atomization.

The air velocity is usually close or equal to the velocity of sound at the outlet. This high air flow leads on the one hand to a good atomization and to size distributions necessary for a good quality of the paint film on the object and on the other hand it results in a loss of paint due to droplets following the air flow parallel to the object's surface. This is the so-called overspray. For reasons of pollution control and reduction of secondary costs for disposal of overspray strong efforts are undertaken to reduce the amount of overspray.

Apart from new developments in painting like ultrasonic or rotary atomizers with or without electrostatic charge it is also necessary to improve the behavour and the efficiency of the usual pneumatic atomizer, e.g to spray water-based paint. Here, a close look to the local size distributions and the velocity field between the spray gun and the surface to be painted is a keypoint for a better understanding of the reasons for overspray production.

Until now, only few measurements in paints sprays have been published. Some measurements of the velocity field have been made using Pitot-tubes [1] or Laser-Doppler anemometer [2]. Most of the droplet size measurements reported were using Fraunhofer-Diffration, e.g. [3], or sampling techniques [4],[5]. None of these papers deals with simultaneous measurements of drop size and velocity.

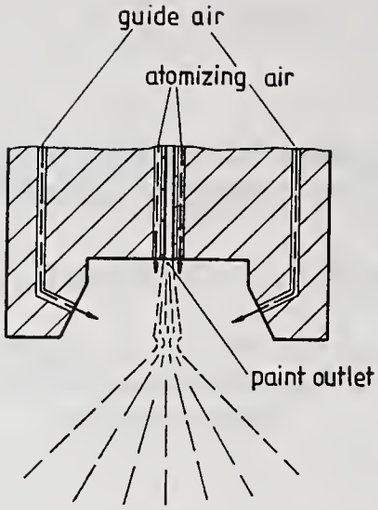

Figure 1: Pneumatic paint atomizer

This paper presents recent results of phase-Doppler measurements in paint sprays. In principle, this technique has been proved to give very good and reliable results in any kind of spray flows, e.g. [6], [7], [8]. In the derivation of the principle of the phase-Doppler technique, it is assumed that the dispersed phase is a simple fluid with very well known optical properties like refractive index and absorption coefficient. Paint, however, is a mixture of liquid and solid with a rather complex nature, so some basic experiments have to be made to check the accuracy of the phase-Doppler technique applied to paint drops, including calculations of the scattered light field by means of a Mie-program.

2 OPTICAL CONSIDERATIONS

The phase-Doppler technique is suitable for any kind of spherical particles, including droplets in gas or bubbles in liquid. Depending on the relative refractive index between dispersed and continuous phase, measurements are possible if one of the scattering mechanisms reflection, 1st or 2nd order refraction is dominant. For this purpose programs based on Mie scattering theory [9] or geometrical optics have been developed to enable the PDA user to adapt his system to the flow situation.

All of these programs deal only with homogeneous fluids, which have constant refractive index and absorption inside the droplet. The application to paint, which is a mixture of solid and liquid parts, including pigments, metallic powder, solvents and water, is therefore limited. Nevertheless it should be possible to get some first ideas about the scattered light field out of these programs. The following table shows the measured optical properties of the examined paints; water-based silver metallic and a lacquer.

	refractive index	absorption coeff.
lacquer	1.42	$8.63 \cdot 10^{-8}$
silver metallic	1.36	$5.98 \cdot 10^{-4}$

In order to be able to perform Mie calculations it is also necessary to define the optical arrangement of the complete PDA-system. A one-component HeNe system with rotating grating and 500 mm lenses on both the sending and the receiving side was used. A 3x beam expansion was used to achieve a high intensity in the probe volume. The specifications were as follows

probe volume diameter (μm):	134
fringe number (-):	6
fringe spacing (μm):	21.07

In the case of silver metallic droplets the maximum measurable size, using a standard two-detector receiving optics, was 360 μm at 30° scattering angle.

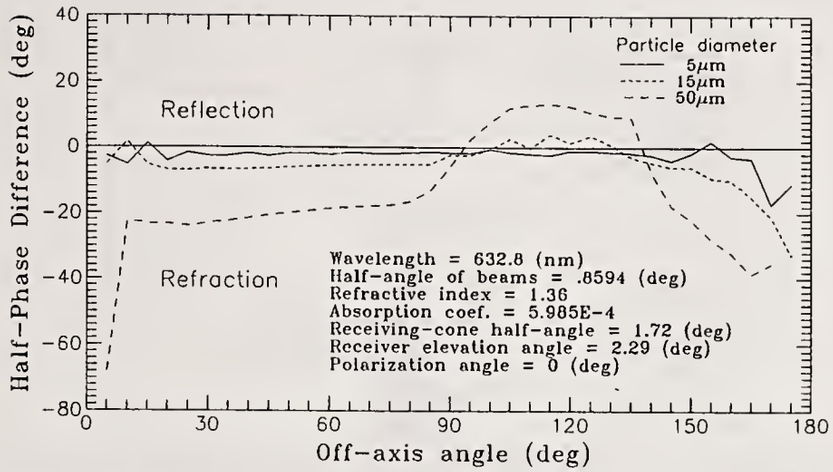

Figure 2: Phase as a function of scattering angle (silver metallic)

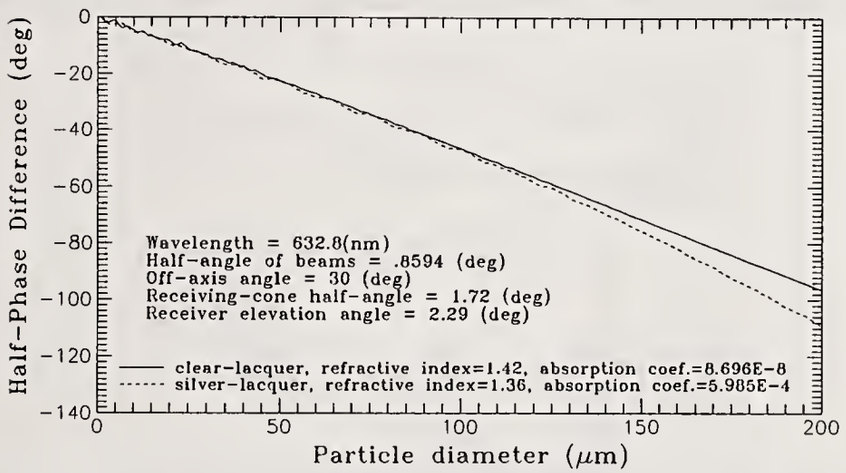

Figure 3: Phase as a function of droplet size (silver metallic and lacquer)

Figure 2 indicates the phase as a function of the scattering angle for three different droplet sizes, 5, 15 and 50 μm. For clarity only the result for the silver metallic is shown in this figure. This figure also indicates a wide range between 25 and 80° scattering angle where 1st order refraction is dominant, characterized by an increase of the phase in the negative direction. This result is not surprising, since the absorption coefficient lies in the range of $6 \cdot 10^{-4}$, leading to only 5 % absorption of the refracted light in a 50 μm particle. But one has to keep in mind, that the effect of the absorption will increase at larger droplets. This is also visible in Figure 3, showing the response curve of the phase-Doppler system at a scattering angle of 30°. From 100 μm onwards, the curve for the silver metallic starts to deviate from a straight line, which is the result of the beginning influence of scattered light from reflection.

From these curves one can expect a very linear relation between droplet size and phase for both silver metallic and lacquer. As will be shown later most of the droplets can be obtained in the range under 60 μm, so the influence of reflection can be neglected. These results are valid only for homogeneous fluids. The effect of the inhomogeneities inside the droplets is still to be investigated.

3 PRELIMINARY TESTS

Preliminary tests were performed to check the accuracy of the phase-Doppler technique applied to paint sprays. A vibrating orifice monodispersed droplet generator was used to produce a stream of paint droplets of known size. Fig. 4 shows PDA-measurements of 125 μm lacquer droplets.

Apart from the error in mean size, which is only 2.5 %, there is a small broadening of the size distribution of about $\pm 15 \mu m$. It is possible that this was due to the droplet generator performance since it is not designed

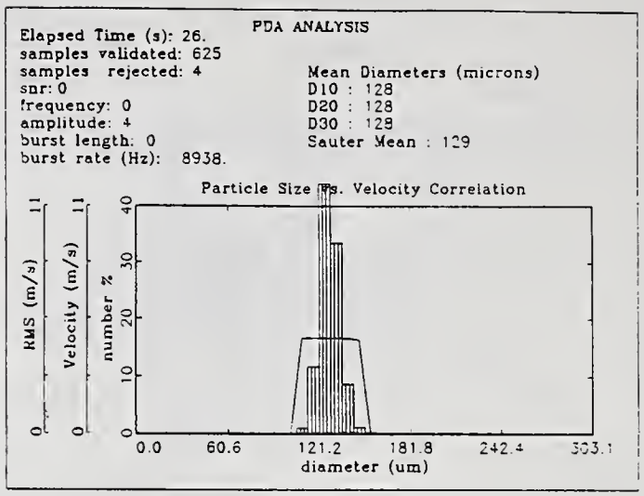

Figure 4: Measured size distribution of a monodispersed droplet generator (lacquer)

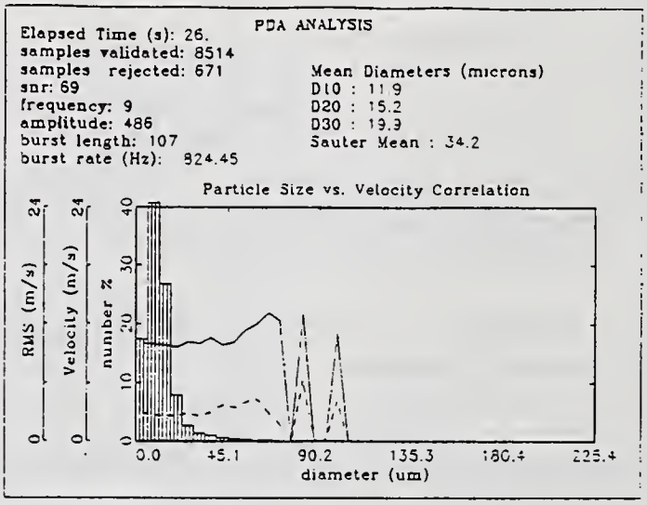

Figure 5: Local size distribution at z = 25 mm (lacquer, low flowrate)

to produce droplets of a high viscous and nonhomogeneous fluid. In addition, Doppler amplitude variations visible on the screen of a digital oscilloscope indicated also size variations inside the droplet stream.

Another method to clarify the response of the phase-Doppler in paint sprays is the controlled variation of one dominant operating parameter of a spray gun for which the influence on mean size and velocity is known. The phase-Doppler technique should be able to demonstrate the corresponding change in the droplet size distribution and the mean values. For instance Figures 5 and 6 show the influence of a change in paint flow rate on the local size distribution at 25 mm distance from the nozzle. The measurements were made with a simple hand-held spray gun.

There is a significant increase in the mean droplet sizes with increasing paint flow rate; the arithmetic mean D_{10} is more than doubled. The mean velocity has decreased as can be explained by the higher momentum exchange from the fast air flow to the paint stream. In both cases there exists a correlation between the droplet size and the mean velocity.

Both experiments have been performed with a 30° off-axis arrangement of the PDA-receiving optics, using the normal phase factor based on geometrical optics calculations for refraction, as indicated in the previous section. Signal processing was done with a transient recorder system using the cross-spectral density function [10] for frequency and phase estimation. A probe volume correction was made to account for the Gaussian intensity profile in the probe volume [11].

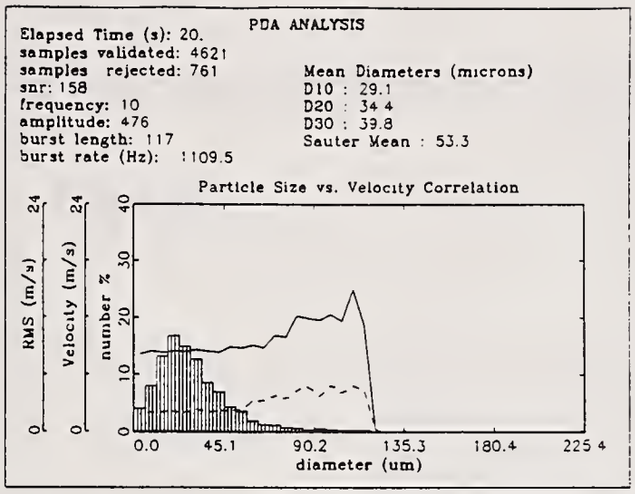

Figure 6: Local size distribution at z = 25 mm (lacquer, high flowrate)

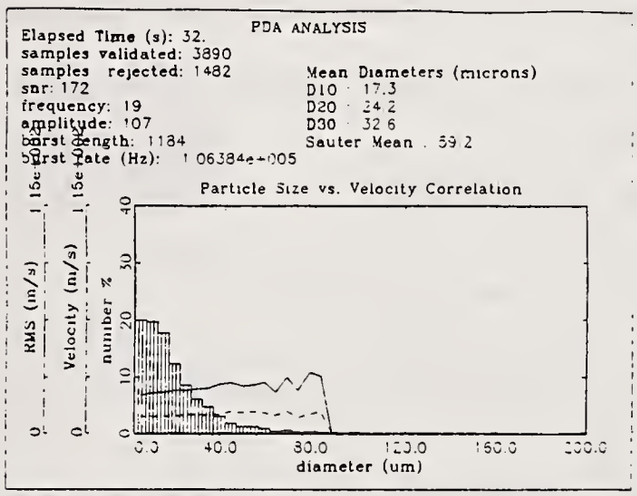

Figure 7: Typical size and velocity distribution

4 MEASUREMENTS IN A SPRAY CABIN

After the very encouraging results of the preliminary test measurements further experiments were made in a more practical situation inside a spray cabin, using two different spray guns designed for robot systems. The purpose of the study was to verify existing differences between different spray guns and air caps and to demonstrate the influence of the major operating parameters, e.g. liquid and air flow rates. Profiles of local size and velocity distributions were taken at 5, 15 and 30 cm distances from the nozzle, using silver metallic paint throughout the experiments. Care was taken to keep all the parameters in their normal operating range. The paint flow rate was adjusted by a speed controlled gear pump, the atomizing and guide air flow rates were measured using an instrument based on two temperature compensated hot film anemometers. The spray gun was mounted on a x-z traversing system, allowing vertical and horizontal movements relative to the fixed table of the PDA-system. The flow direction was vertical downwards.

In the beginning, all spray guns were tested with water as an atomized fluid, yielding a very narrow spray cone with small and fast droplets. The measured arithmetic mean diameters with water were in the range of 7.0 - 10.0 μm, the corresponding velocities up to 80 m/s at a distance of 5 cm from the nozzle. In contrast, spraying paint led to a wider spray cone with reduced velocities. Fig. 7 shows a typical plot of the size and velocity distribution from 3000 samples at one single point, indicating a D_{10} of 17.3 μm, D_{30} of 32.6 μm. The velocity is around 25 m/s.

It was a common feature of the measured size distributions that they display a peak in the first size

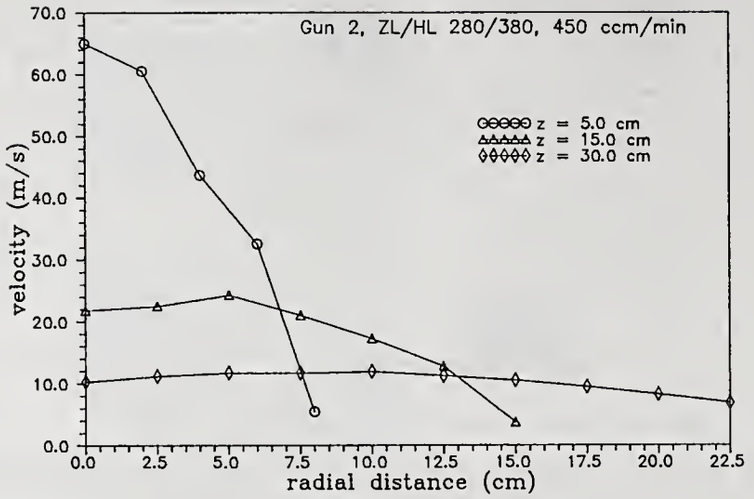

Figure 8: Axial development of the velocity (spray gun 2)

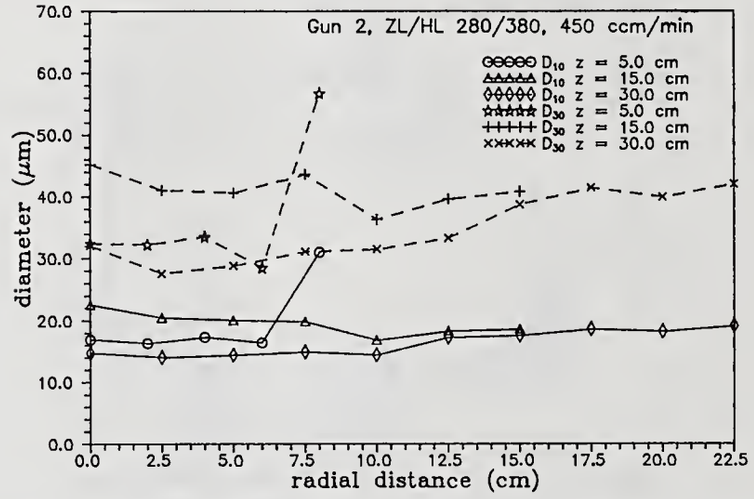

Figure 9: Axial development of mean diameters (spray gun 2)

class, which extends up to 5 μm. On the other hand, big droplets could be obtained up to 150 μm and higher, resulting in strongly skewed distributions. Since the higher moments like D_{30} or the Sauter diameter are strongly influenced by the few very big droplets, 3000 samples was found to be a good compromise between stable mean diameters and a limited measuring time.

In Figs. 8 and 9, the axial development of size and velocity of spray gun 2 is shown. The mean velocity profile indicates a steep gradient at z = 5.0 cm, from 60 m/s in the core to 6 m/s at the edge of the spray cone, flattening out to a nearly constant velocity of 10 m/s at z = 30.0 cm. The diameter profiles D_{10} and D_{30} which are shown are very homogeneous except for the very edge of the spray cone where a sharp increase of the mean diameters can be noticed. This is common for all three spray guns examined.

This result can be explained by the presence of a shield of big droplets surrounding the spray cone. The cone edge itself was defined using the arrival rate of droplets in the probe volume.

The measurements of spray gun 2 are also taken to explain the influence of a change in paint flow on the size distribution in the spray cone. Two flow rates, 250 ccm/min and 450 ccm/min, were examined. The result for a distance z = 30 cm is shown in Fig. 10. It is very interesting to note that the additional amount of paint is concentrated in larger droplets in the outer region of the spray cone, expressed in an increase of the volume mean diameter in the region $x \geq 5.0$ cm, whereas D_{10} is changing only slightly. In general, higher paint flow rates lead to a more inhomogeneous distribution of the mean sizes of the spray. From this point of view it would be preferable to operate the spray guns at a low paint flow rate, though this would

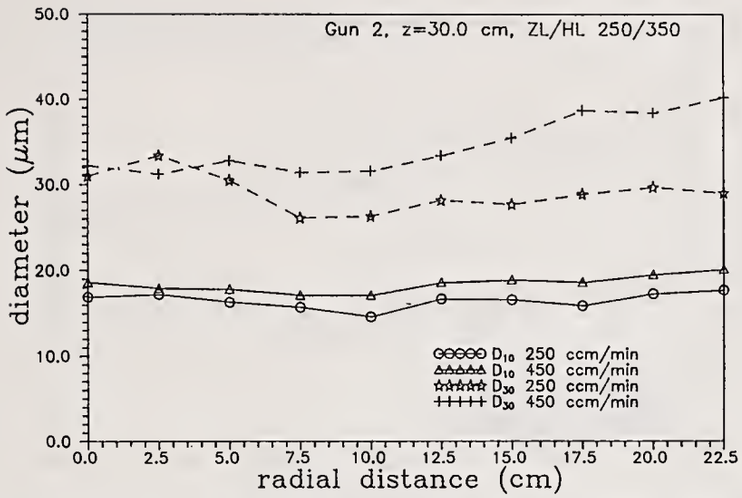

Figure 10: Influence of paint flow rate on mean diameters (spray gun 2)

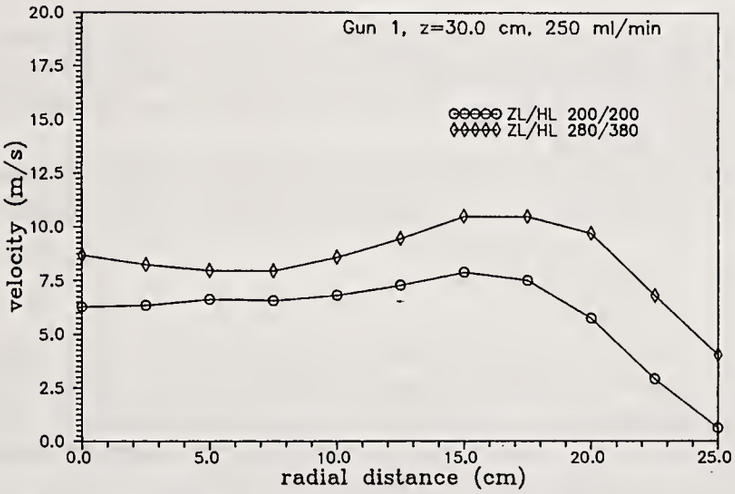

Figure 11: Influence of air flow rate on velocity (spray gun 1)

imply a lower travelling speed during painting.

Finally, the influence of the air flow rates on size and velocity should be discussed here. As indicated already in Fig. 1, there are 2 independent air supplies, the atomizing air flowing through 4 or 6 nozzles very close to the paint outlet and the guide air, flowing from 2 sides through radially arranged nozzles, thus leading to a elliptically shaped spray cone. The appropriate choice of the air flow rates is essential for the painting process since both the atomization of the paint stream and the air flow field in the vicinity of the surface is strongly influenced. Higher air flow will lead to better atomization resulting in smaller mean droplet diameters but also to higher air velocities parallel to the surface and therefore to more overspray caused by small droplets following the air flow field.

Figs. 11 and 12 indicate the results obtained for 2 different air flow rates of spray gun 1 at 30 cm distance from the nozzle. From Fig. 11 it can be seen that the velocity profile remains unchanged but on a lower level. It is also clear, that the cone angle, expressed in terms of the mean velocity, has decreased, since at a location x = 25.0 cm the velocity is nearly zero. This can be explained by the smaller guide air flow rate.

The interpretation of the behavour of the mean diameters becomes more complicated. Fig. 12 indicates, as expected, higher D_{30}-values for the low-flow case in the range between 0 and 10 cm radial distance, but also higher D_{10}-values for the high-flow case between 12.5 and 25.0 cm. The development of D_{30} in the outer region is, however, nonuniform. One possible explanation could be the combination of the creation

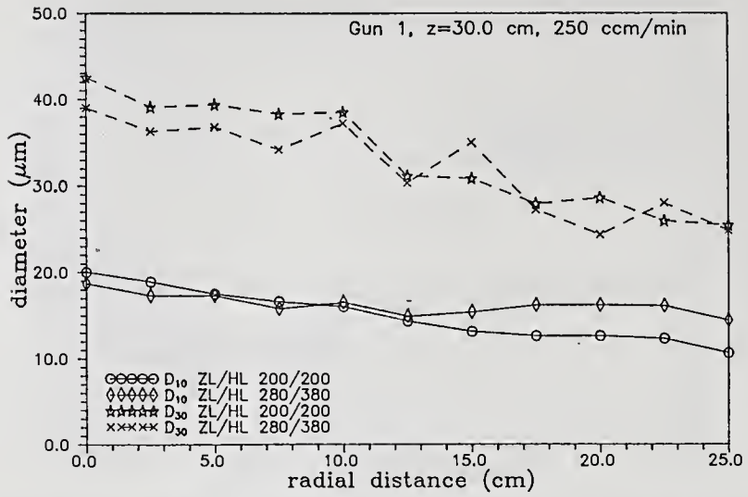

Figure 12: Influence of air flow rate on mean diameters (spray gun 1)

of smaller droplets in the high-flow case due to the higher air flow with the tendency of bigger droplets to concentrate more in the outer region of the spray cone with increased air flow rate, thus covering the effect of better atomization. It should be emphasized that the increase of the atomizing air flow is only 40 %, whereas the guide air is nearly doubled.

This is one of the points where more detailed measurements, e.g. with a two-component PDA-system, are necessary to clarify the correlations between different parameters in more detail.

5 DATA REDUCTION

Up to here, all effects have been discussed in terms of the mean values of velocity and size. Two different mean diameters, D_{10} and D_{30}, have been used to show changes in the shape of the size distribution. However, if one is interested in any other moment, e.g. Sauter mean diameter, it is necessary to store and replay or even regroup the entire droplet size distribution. Thus, it would be convenient to define a analytical function representing the measured size distribution very accurately without any loss of information. From this function it is possible to calculate any desired number necessary for further applications of the measurements, i.e. calculation of mass transfer.

The function proposed here is the so called three-parameter log-hyperbolic distribution, a modification of the usual four-parameter log-hyperbolic function. As shown in [12], this distribution gives very good results in many different kinds of size distribution, including this paint measurements. As illustrated in Fig. 13, the three parameters a, θ and μ have geometrical meanings, θ being the angle of the hyperbola axis relative to the coordinate system, μ the location parameter defining the peak of the distribution, and a defining the slope of the asymptotes or the opening of the hyperbola.

From the values of these three parameters the original size distribution can be reconstructed, which is not possible from the mean diameters. For example, different shapes of distributions can give identical D_{10} and D_{30} values. In addition, it is possible to deduce changes in the shape of the distribution from changes in the parameters, making physical processes clearer.

This function was applied to the measured size distributions in the case of paint flow rate changes (spray gun 2), which was already discussed in section 4. Figs. 14 and 15 show the corresponding change of the three parameters of the log-hyperbolic distribution. Parameter a, characterizing the opening of the hyperbola, is constant, whereas a slight increase of parameter μ, characterizing the location of the mode point, corresponds to the increased arithmetic mean diameter. Most of the effect of the flow rate change seems to come up in changes of θ.

Therefore it can be concluded, that the additional amount of paint could mainly be found in big droplets, concentrated in the outer region of the spray cone. This is expressed by the decrease of θ, denoting a longer right-hand side tail and a higher skewness to the left. Furthermore, higher θ-values near the center

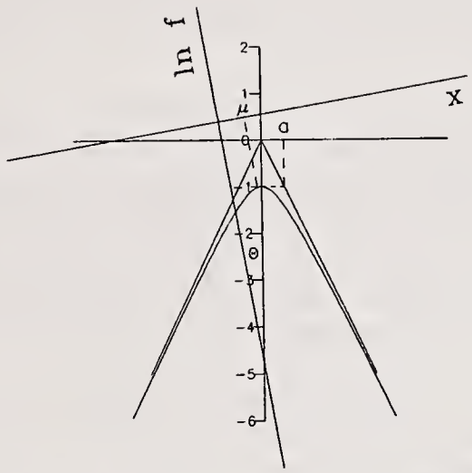

Figure 13: The three parameter log-hyperbolic distribution

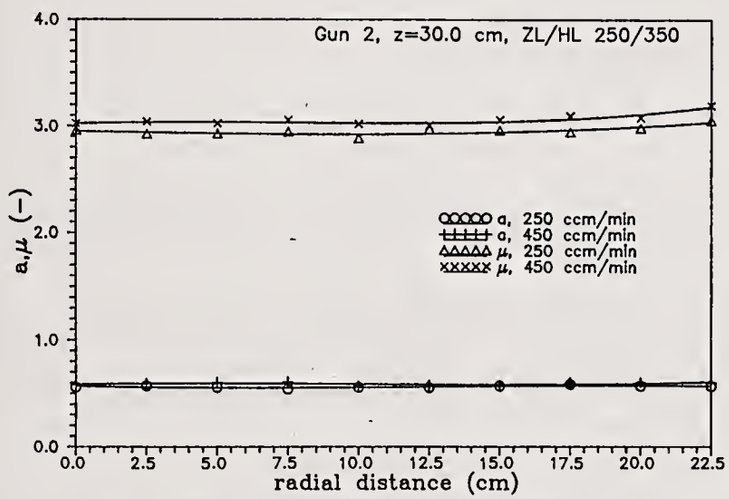

Figure 14: Variation of the parameters a and μ

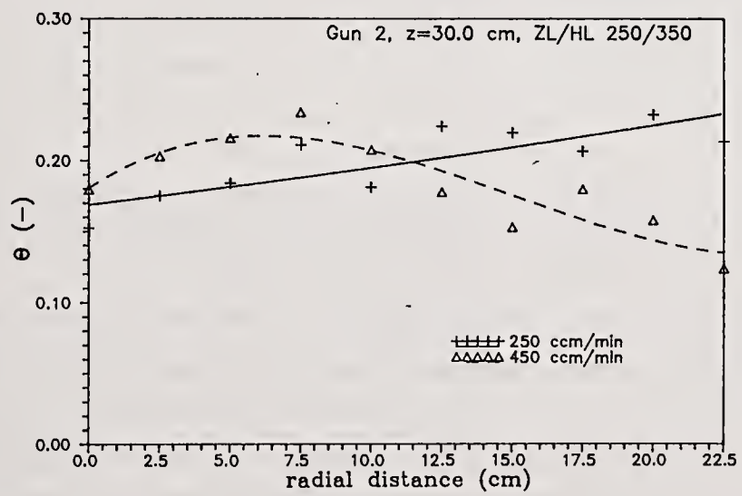

Figure 15: Variation of the parameter θ

of the spray for the high flow case indicate also a lack of big droplets in that region, resulting in a very inhomogeneous development of the mean sizes from the center to the edge of the spray cone. Based on this result, neglecting other operation boundary conditions, it is not recommendable to use the investigated spray guns at higher paint flow rates.

6 CONCLUSIONS

Although the data base of the presented PDA-measurements in paint is still limited, the obtained results indicate the possibility to use the phase-Doppler technique in paint sprays. This could be shown with preliminary tests, including measurements in a monodispersed droplet generator, as well as with measurements in a very realistic spray inside a cabin. Using a silver metallic paint, some basic correlations between the operating parameters, e.g. paint and air flow rate, and the local size and velocity distributions were demonstrated.

The obtained size distribution could be fitted by the so-called three-parameter log-hyperbolic distribution resulting in a storage of the local information in 3 parameters. From the changes in the parameter values changes of the spray flow could be made much clearer.

The final aim of the presented investigations is to improve the knowledge of the flow from pneumatic paint atomizers in order to be able to reduce the amount of paint overspray and energy consumption without deteriorating the quality of the paint film. Therefore further detailed measurements in paint sprays will be made, including also the flow field in the vicinity of a surface. It is also planned to enlarge the number of verified paints suitable for PDA-measurements.

References

[1] K. W. Warnecke Air velocity measurements at the jet of a paint spray gun, *Industrie-Anzeiger*, 100(7), 1978

[2] D. Müller *"Untersuchung des Zerstäubungsvorganges bei der pneumatischen Lackapplikation"* Diplomarbeit, Lehrstuhl für Strömungsmechanik, Universität Erlangen-Nürnberg, 1990

[3] H.E. Snyder; D.W. Senser; A.H. Lefebvre; R.S. Coutinho "Drop size measurements in electrostatic paint sprays", *IEEE Trans. Ind. Appl.*, 24(4), 1989

[4] W.S. Janna; J.E.A. John "Drop-size distributions of Newtonian and Bingham liquid sprays produced by fan-jet pressure nozzles with and without preorifice", *Trans. ASME, J. Engng. Ind.*, 103(40), 1981

[5] A. Bürkholz; J. Widder; W. Müller "Primäre Tropfengrößenverteilung und atembarer Feinanteil beim Lackspritzen durch Druckluftzerstäubung", *Farben und Lacke*, 82(8), 1976

[6] K. Bauckhage, H.-H. Flögel "Simultaneous Measurement of Droplet Size and Velocity in Spray Nozzles" *Proc. of the 2nd Int. Symposium on Appl. of LDA to Fluid-Mechanics*, Lisbon 1984

[7] W.D. Bachalo; M.J. Houser "Phase/Doppler spray analyzer for simultaneous measurements of drop size and velocity distributions", *Optical Engineering*, 23(5), 1984

[8] W.D. Bachalo; M.J. Houser "Spray drop size and velocity measurements using the phase/Doppler particle analyzer" *Int Conference on Liquid Atomization and Spray Systems ICLASS 85*, 1985

[9] A. Naqwi; F. Durst *"Computation of light scattering from a dual-beam system"*, Internal report LSTM/259/T/89, Lehrstuhl für Strömungsmechanik, Universität Erlangen-Nürnberg, 1989

[10] J. Domnick; H. Ertel; C. Tropea "Processing Phase/Doppler Signals Using the Cross-Spectral Density Function" *Proc. of the 4th Int. Symposium on Appl. of LDA to Fluid-Mechanics*, Lisbon 1988

[11] M. Saffman "Automatic calibration of LDA measurement volume size", *Applied Optics*, 26(13), 1988

[12] T.H. Xu; C. Tropea; F. Durst "The three-parameter log-hyperbolic distribution and its application to liquid sprays", submitted to *Int Conference on Liquid Atomization and Spray Systems ICLASS 91*, 1991

ATOMIZATION, CHARGE AND DEPOSITION CHARACTERISTICS OF DUAL POLARITY ELECTROSTATICALLY CHARGED AIRCRAFT SPRAYS OF SERRATED SPINNER CUP ATOMIZERS

K.D. Kihm, B.H. Kim and A.R. McFarland

Department of Mechanical Engineering
Texas A&M University
College Station, TX, U.S.A.

ABSTRACT

Atomization, charge and deposition characteristics of an electrostatic aircraft spray system were studied. The system used serrated spinner cup atomizers with tap water as atomized fluid. Despite the well-known advantages of electrostatic sprays, electrical discharge from excessive build-up of residual charge on the aircraft skin has been a major problem in utilizing electrostatic systems for aircraft spraying. An idea of bipolar electrostatic charging has been employed which shows that the bipolar charging could effectively abate the residual charge build-up. In addition, the deposition efficiency of aircraft sprays could be significantly enhanced. Atomization and charging behaviors of the atomizer were studied under a laboratory simulation using a Malvern diffraction technique and a Farady cage collector, respectively. The deposition characteristics were investigated by carrying out a field experiment with an aircraft spray system and a water-sensitive dye paper sampling technique. Sampled dye papers were digitized and processed to obtain the aerosol diameters and other statical data. The bipolar spray configuration was able to effectively eliminate the electric discharge of the residual charge on the aircraft skin. Compared with a corresponding neutral spray, for bipolar charging the overall *SMD* was increased by over 10 % showing significant decrease in the number of small droplets and increase in large drops. This effect would reduce the drift problem of aircraft sprays. The total deposition mass was also increased by more than 25 % when the spray was charged by dual polarities.

INTRODUCTION

Aircraft spray systems are extensively utilized for applying pesticides to vast agricultural fields and hard-to-reach terrain like mountain areas. It is well known that electrostatically charged sprays enhance the deposition efficiency of droplets on targets because of the Coulomb attractive force between the charge on the atomized aerosol and its image in the collector [1]. Carlton and Bouse [2] demonstrated experimentally with a ground-based electrostatic spray system that the deposition efficiency can exceed that of its uncharged counterpart by as much as 800 percent.

For the case of aircraft application of the electrostatic sprays, where the aircraft releases unipolar-charged aerosols, a surface charge of the opposite polarity develops on the aircraft skin. Excessive build-up of the residual charge creates an electric field high enough to generate localized electric discharges (Fig. 1-A). Since the electric discharge results in undesirable fluctuations in both charge distribution and electric field around the aircraft, a build-up of aircraft surface charge may degrade the deposition efficiency of charged aerosols [3].

An innovative idea which uses alternatively charged nozzles on an aircraft spray boom (Fig. 1-B) has been proposed and investigated as a way to minimize or eliminate the build-up of aircraft surface charge so that electrostatic aircraft sprays can ensure an improved deposition efficiency. In addition, this approach offers a possibility of reducing spray drift since oppositely charged aerosols will coalesce together, and smaller aerosols will coalesce far more quickly compared larger ones because of their higher electric mobility [4].

The present work consists of two primary parts: (1) a laboratory study of atomization and charge characteristics of spray aerosols from a serrated spinning cup atomizer, and (2) a field study of aerosol deposition and coalescence characteristics of bipolar charge aircraft spray system. Both studies used tap water as the atomization fluid. A spinning cup atomizer was employed as this type of system is simple, lighte and provides aerosol diameters

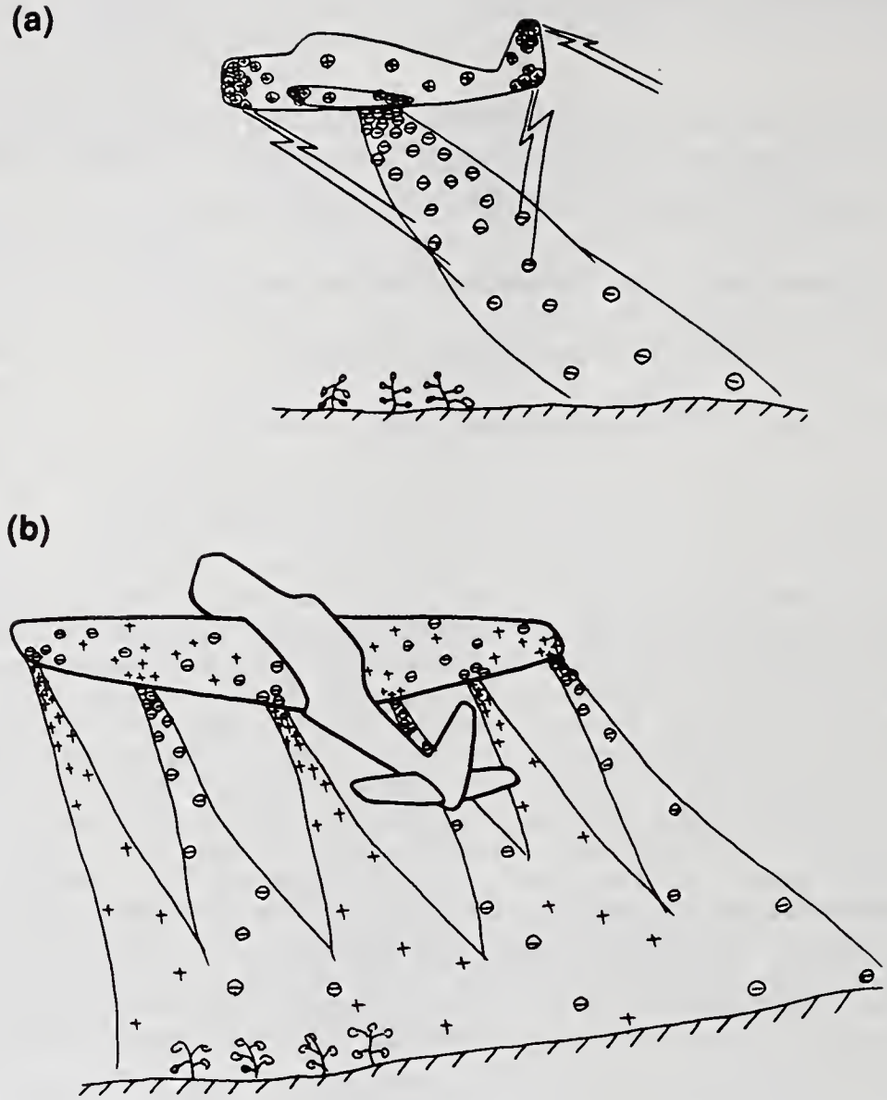

Fig. 1 Comparison of electrostatic aircraft sprays: (A) a single-polarity charged spray system, (B) a double-polarity charged spray system.

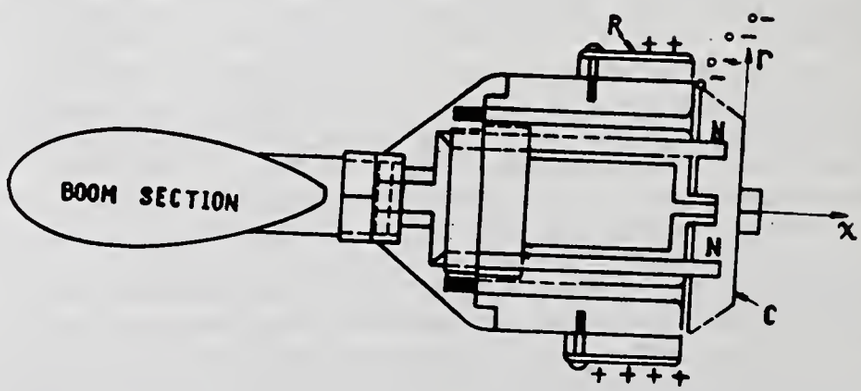

Fig. 2 A configuration of a *DC* motor-driven spinning cup atomizer with serrated teeth.

of a fairly uniform distribution with a reliably small standard deviation [5]. Spray charging was attained with an induction charging ring installed near the periphery of the spinning cup. A He-Ne laser Fraunhofer diffraction particle sizer (Malvern 2600 D system) was used to measure the aerosol size for the laboratory study. The amount of spray charge was measured by collecting charged aerosols with a Farady cage. For the aircraft spray field study, aerosols were sampled with water-sensitive dye papers, and then the marked papers were digitized and processed for statistical data.

EXPERIMENTAL SETUP

Serrated Spinning Cup Atomizer

The general configuration of a *DC* motor-driven spinning cup atomizer can be seen from the cross-sectional view in Fig. 2. The design of the atomizer was based on the work of Bals [6], and a laboratory type atomizer, which had been constructed by Carlton and Bouse [2] was employed for the present study. The cup has a dimension of 55 mm in diameter with 360 uniformly shaped triangular teeth with a serration pitch of 480 micrometers. The spinning cup, C, rotates and receives water from the two liquid supply needles, N. Atomizer parts were made of nonconducting materials whenever possible to achieve high-voltage insulation and to minimize the electric field distortions and/or the electric discharge. When a positive potential is placed on the cylindrical ring, R, with the negative terminal from the power supply connected to the needles, droplets near the serrated periphery are negatively charged because of the electron induction mechanism and, vice versa for a negative potential.

Laboratory Setup

Figure 3 presents a schematic diagram of the experimental configuration. The spinning cup atomizer was affixed to a spray boom section, which was located downstream of the air blower outlet. Tap water was fed through the boom. The blower outlet section had dimensions of 154 mm in diameter and 0.6 m in length, and contained a honeycomb-type flow straightener. Air was blown into the outlet through the reservoir with a 40 horse-power electric motor-driven squirrel-cage type blower. The maximum air speed at the outlet was 175 km/hr, which was approximately equal to the typical cruising speed of an agricultural spray aircraft [7].

The atomizer was installed 15 cm downstream of the blower outlet and both the atomizer and the outlet were vertically adjustable. The Malvern system was mounted on a horizontal two-dimensional positioning system. Thus, the whole system was capable of precise three dimensional positioning of the atomizer. The Farady cage unit consisted of three collectors to maximize the collection efficiency: a needle collector, a plane-mesh collector, and a concave-mesh collector. The meshes were 0.3 mm diameter aluminum wires with a mesh size of 1.5 mm x 1.5 mm. All three meshes were connected to a microamperemeter to measure the spray current.

Field Setup

Figure 4 shows a schematic representation of the field setup for a ground-level sampling of droplets from aircraft sprays. A movable sampling stand, 60 meters in length, was setup on a landing strip perpendicular to the aircraft cruising direction. The spray aircraft was flown in the upwind direction in an attempt to maximize the sampling efficiency with longer airborne period of aerosols. Forty water-sensitive dye papers (25 mm x 75 mm each) were placed vertically at 0.5 m above the ground and at 0.6 m intervals along the stand. Ten atomizers were installed along a boom section attached behind the trailing edge of the right hand wing of a Cessna Model P-206B aircraft. Wind speed and other atmospheric conditions, such as humidity and temperature, were measured and recorded with a portable weather station. The aircraft cruising altitude and speed during spraying were maintained at 3 meters and 175 km/hr, respectively.

RESULTS AND DISCUSSION

The results are presented for three different aspects of the study: (a) laboratory measurements of aerosol mean diameters for various atomizer operating conditions (e.g., spinner rpm, liquid flow rate, air velocity and charging), (b) laboratory measurements of the amount of spray charge for different charging voltages, and (c) field measurements of aerosol deposition and size spectra.

Aerosol mean diameters

Figure 5 shows different disintegration mechanisms of a spinner atomizer as functions of spinner rpm and water feed rate. For a given spinner revolution rate, when the feed rate is small, the liquid can not cover the entire surface of the spinner. The liquid leaves the edge of the spinner as a form of dripping drops (drop formation atomization). Like usual dripping of liquid, a significant number of secondary drops are formed. As the feed rate increases, a thin liquid sheet covers the entire spinner surface and ligaments are formed at the spinner periphery which

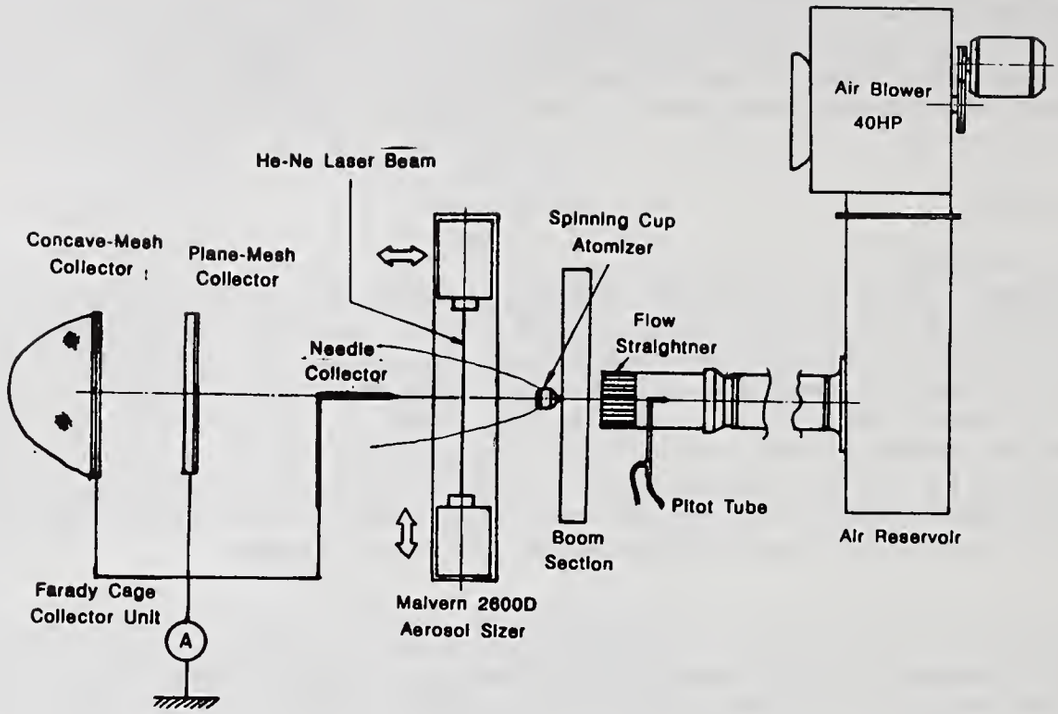

Fig. 3 Schematic diagram of experimental configuration for measurements of spray size and charge.

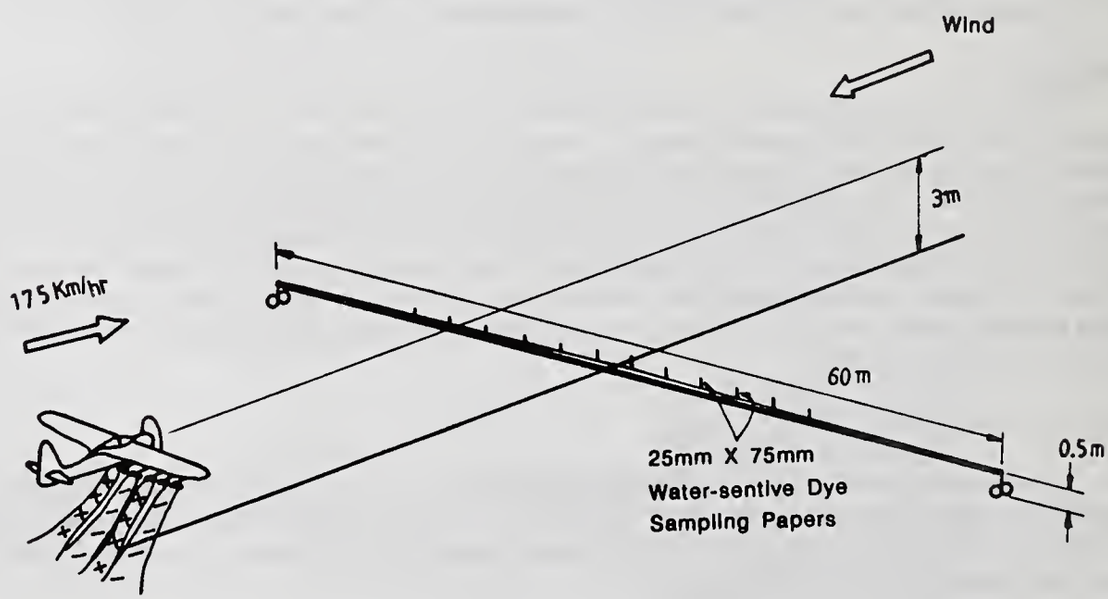

Fig. 4 Schematic representation of the field setup of a ground sampling system for electrostatic aircraft spray.

disintegrate into numerous drops (ligament disintegration atomization). The distribution of drop diameters becomes fairly uniform with a minimal standard deviation. When the feed rate exceeds a critical value, the spinner surface is flooded and the liquid sheet extends outside the periphery. The extended sheet disintegrates into drops irregularly (sheet disintegration atomization). The drop diameters become highly polydispersed. Using a direct visualization technique, Tanasawa et al. [8] observed that minimal drop diameters were obtained in the ligament disintegration condition. For the present study, all measurements were carried out within the ligament disintegration region.

As schematically illustrated in Fig. 6, radially spiral spray is developed in the absence of air stream while an axially cylindrical spray is formed under the action of convective air stream. To account for such dramatically different spray developments, two different sampling locations were considered for the measurement of mean diameters: point A was used when there was no superimposed air stream. This is located 150 mm in the radial direction from the spinner axis. Point B, located on the spray axis 122 mm downstream from the spinner edge, was used when there was a superimposed air stream. At both locations, stable and highly repeatable values of Sauter Mean Diameter (*SMD*) were measured. It must be noted that inconsistent *SMD* values could be measured if the sampling location is not properly selected, especially for sprays with a superimposed air stream, .

Measured data of *SMD* both with and without the air flow are presented in Fig. 7 as functions of liquid feed rate for four different spinner revolution rates. The symbols with dashed lines represent *SMD* measured with a convective air stream of 175 km/hr (or equivalently 49 m/s), and the symbols with solid curves represent data taken with no air flow. As the spinner revolution rate increases while the liquid feed rate remains unchanged (within the ligament breakup condition), the cross sectional area of ligaments formed at the tips of serrated teeth of the spinner must be decreased because of mass continuity considerations. In primary atomization, ligament usually disintegrates into drops with sizes comparable to its own diameter. Therefore, reduced cross sectional area of ligaments can explain the reduction in *SMD* when the spinner rotation is increased. The reverse may be true for the case where the liquid feed rate is increased for a fixed spinner revolution. For the case of no air flow, the increase of *SMD* with the increase of liquid feed rate can be attributed mainly to the enlargement of ligaments.

When cross-sectionally enlarged ligaments are exposed to a high velocity air stream, viscous pulling action of the air may elongate the ligaments longitudinally, which could produce longer ligaments of nearly unchanged or even slightly reduced cross sectional area. The nearly constant or slightly decreasing *SMD* in the presence of the convective air flow could be explained by this. Evaporation from the liquid surface by a high speed air stream may also contribute to a further reduction in *SMD*. The ranges of the aerosol diameters were found to be smaller than the critical diameters [9,10, 11], at which aerosols break up due to the inertial force of the air stream overcomming the surface tension force. The probability of this secondary atomization will be very low for the conditions investigated.

Spray charge

Amounts of spray current (*C/s*) were measured with the Farady cage collector and results are presented in terms of charge to mass ratio *Q/M* (*C/kg*) in Fig. 8. The charging voltage was allowed to vary while the spinner rotational rate was held at 9000 rpm for three different liquid feed rates (0.75 *ml/s*, 1.0 *ml/s* and 1.5 *ml/s*) and for an air speed of 175 *km/hr*. No significant difference was observed for different polarity of charging voltage. The charge to mass ratio increased with the charging voltage and showed maximum values at approximately 7 kV. The charge to mass ratio sharply decreased thereafter due to the electrical break down as a result of the excessive electric field between the induction charging ring and ground (the liquid in this case). As the liquid flow rate was increased, a higher amount of total spray charge was measured. The charge to mass ratio, which would be a more accurate measure of aerosol charging, showed a decrease with an increase in liquid flow rate. Since the aerosol *SMD* remained nearly unchanged as the liquid flow rate was varied under a constant spinner revolution rate (Fig. 7), the amount of surface charge of individual droplets will be directly proportional to the charge to mass ratio. Although not presented, the charge to mass ratio demonstrated a slightly increasing function of spinner revolution rate for a given liquid flow rate. Since the induction charging increases with the surface area of aerosols, the increase of the charge to mass ratio is attributed to reduced *SMD* with increased spinner rpm and increased total surface area of aerosols for the same liquid flow rate.

An excessively charged liquid drop can disintegrate into smaller droplets when the Coulomb repulsive force (the outward pressure) produced by the surface charge equals or exceeds the holding force (the inward pressure) produced by the surface tension. This condition is called the Rayleigh limit [1], and is defined as a limiting charge at or above which aerosols will disintegrate by the electric repulsion. When this occurs, the mean drop diameter will be significantly reduced [12]. Drop diameters of charged sprays were measured while the air speed and the feed rate remained unchanged. Results, including the uncharged counterparts, are presented for two different spinner revolution rates and for three different liquid feed rates in Fig. 9. Up to the peak charging voltages corresponding to the maximum charge to mass ratio, the aerosol *SMD*s remained nearly unchanged for both spinner revolution rates. The maximum value of the charge to mass ratio was measured to be on the order of 10^{-2} *C/kg* whereas the Rayleigh limit is a charge to mass ratio of about 0.1 *C/kg* for the same mean diameter. The amount of aerosol charge with

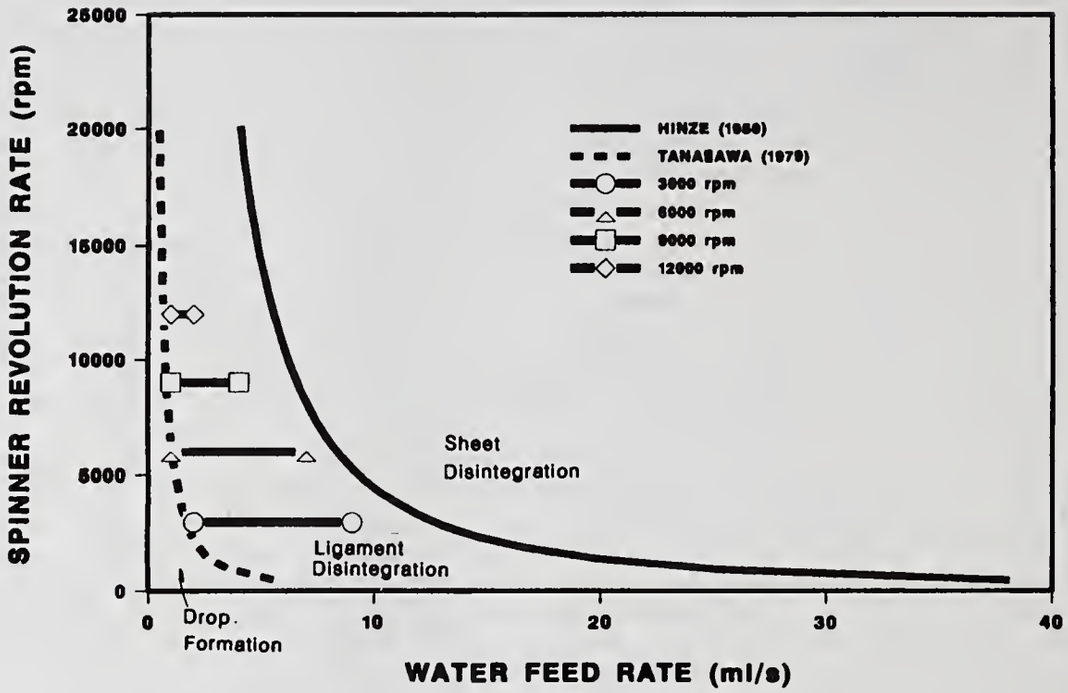

Fig. 5 Different atomization mechanisms of spinner atomizer functions of the spinner revolution rate and the liquid feed rate.

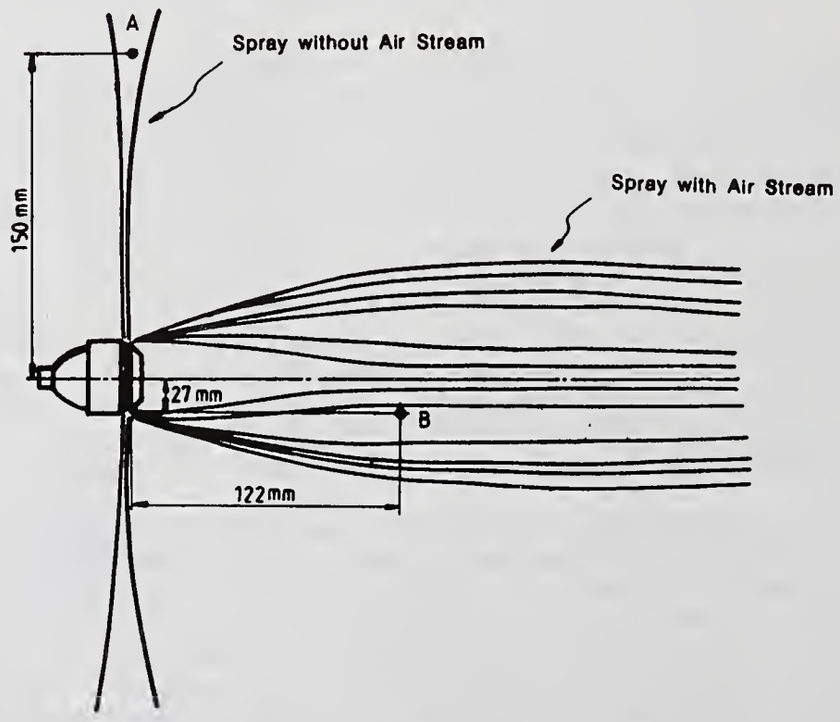

Fig. 6 Spray configurations and sampling locations for the spray under convective air stream (A) and for the spray without air flow (B).

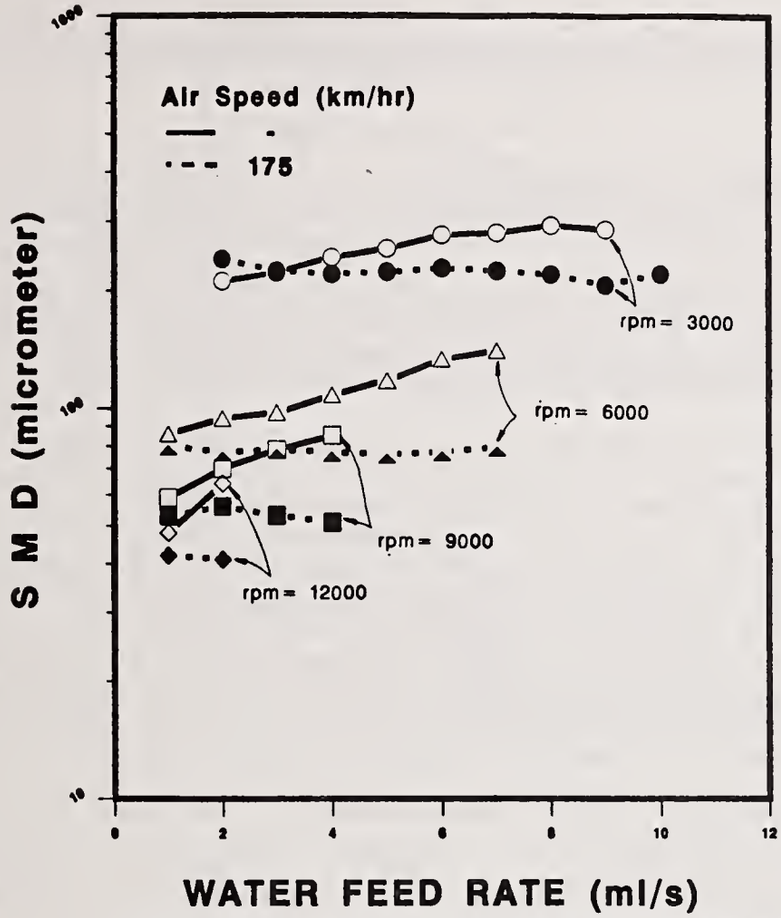

Fig. 7 Spray *SMD* both with and without the air flow as a function of water feed rate for four different spinner revolution rates.

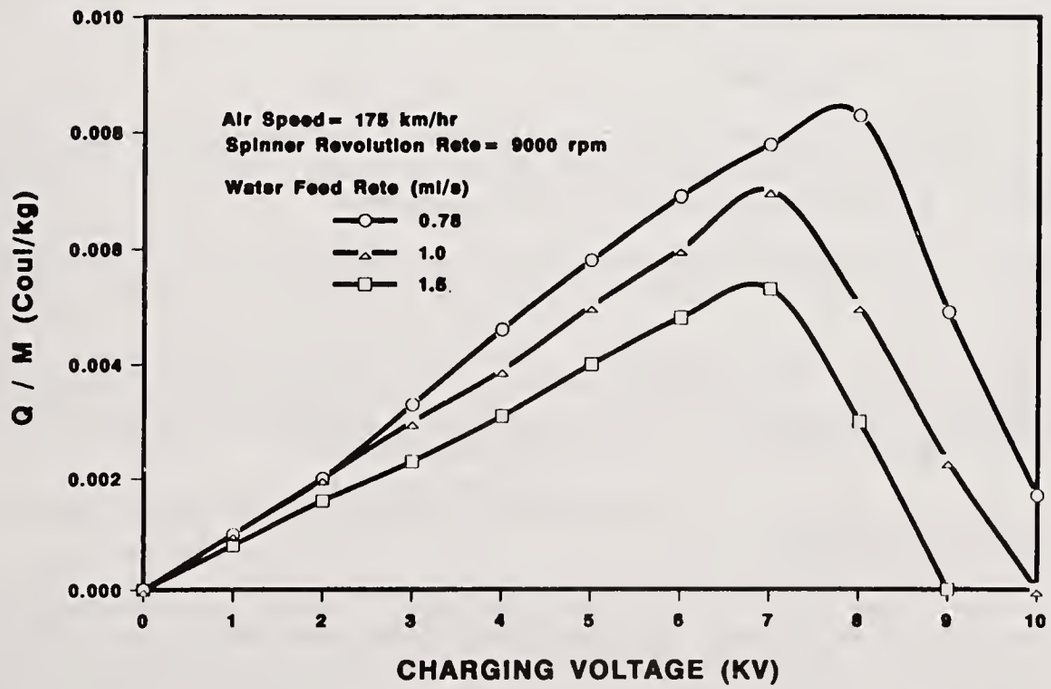

Fig. 8 Spray charge to mass ratio versus induction charging voltage for three different water feed rates.

the present configuration was not sufficient to disintegrate the drops further by overcoming the surface tension holding force.

Aerosol deposition

For the field experiment, the liquid feed rate was maintained at 1 *ml/s* per atomizer, the rotational rates were set at 9000 rpm and a charging voltage of 7 *kV* was used to provide a maximum value of the charge to mass ratio. An electric discharge pole was installed at each wing tip to monitor the electric current discharged to the environment. A reading of 25 μA was recorded when five sprays were positively charged with a negative polarity. As soon as the ten alternatively-charged sprays were activated with nearly equal values of positive and negative charging voltages, the reading was gradually decreased and a zero reading was attained within a second. This proved that the bipolar electrostatic charged spray system elliminates any noticeable build-up of residual charge on the aircraft.

Figure 10 presents lateral distributions of *SMD* and the number of deposited drops for both charged and uncharged cases. For each test, aircraft spraying was repeated three times over the same path to average meteorological differences. The average wind speed was 13 *km/hr* and the relative humidity was 45 %. The zero lateral location was set at the center of the aircraft. Since aerosols will spread and leave larger marks when they are collected by the water-sensitive dye paper, a spread factor must be considered in order to determine the true aerosol diameters. The spread factor is defined as the ratio of the marked diameter to the true aerosol diameter. For the conditions of our experiment, a spread factor of two was used as suggested by the manufacturer. The reduction in numbers of deposited drops from the case of uncharged spray to the case of charged spray may result from the coalescence of bipolar charged aerosols in the aerosol state. Also, the bipolar coalescence causes the mean diameter to increase. The charged spray was more uniformly dispersed showing less dependence of *SMD* and number count upon the lateral location. It is believed that this is because electrostatic coagulation preferentially occurs between the largest and smallest sizes.

The size spectra of all the deposited aerosols are presented for both cases in Fig. 11. The values of *SMD* of all the collected drops were 92.2 μm for the neutral spray and 103.3 μm for the charged spray. It is apparent that for the case of charged spray the size spectrum was shifted toward a larger mean value with a significant reduction in small drops less than 50 μm in diameter and a noticeable increase in large drops of 120 μm or more in size. Volume mean diameters (*VMDs*) were calculated to be 99.7 μm and 110.7 μm for uncharged and charged sprays, respectively. By multiplying the *VMD* by the total particle count for each case, the ratio of deposited mass with charging to that without charging was determined to be 1.27. Thus, the deposited mass was increased by over 25 % when charged sprays were used.

SUMMARY AND CONCLUSION

Characteristics of atomization, charging and deposition were investigated for a bipolar electrostatic aircraft spray system. The system utilizes a serrated spinning cup atomizer. Both laboratory measurement and field experiment were carried out and major conclusions of the study are:

(1) The Sauter mean diameter of atomized aerosols remained nearly unchanged for varying liquid feed rates under a convective air stream of 175 *km/hr*, which is a typical crusing speed of an agricultural spray aircraft.

(2) The maximum value of the charge to mass ratio was measured to be on the order of 0.01 *C/kg* with a charging voltage of about 7 *kV*. The charge to mass ratio decreases with an increase of the liquid flow rate. The maximum charge to mass ratio was found to be below the Rayleigh limit by an order of magnitude and aerosol *SMD* remained unchanged with an increase of the charging voltage.

(3) A successful elimination of the build-up of residual charge on the aircraft skin was achieved with bipolar-charging aircraft sprays.

(4) Field studies showed the *SMD*s of deposited aerosols were 10 % larger for aerosols of bipolar charged sprays as compared with neutral sprays. A reduction in the number of small droplets and an increase in the number of large droplets were noted when bipolar charging was used. This can be attributed to the coalescence of bipolarly charged aerosols. The total amount of deposited mass was also increased by over 25 % when the aircraft spray was bipolarly charged.

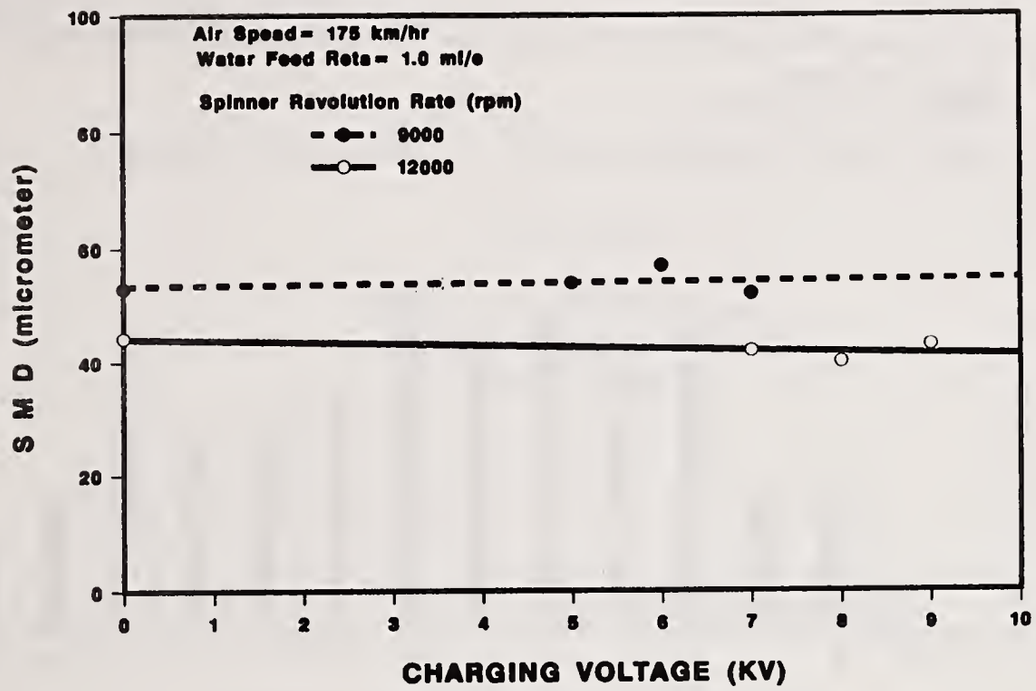

Fig. 9 Independence of spray *SMD* with regard to charging voltage.

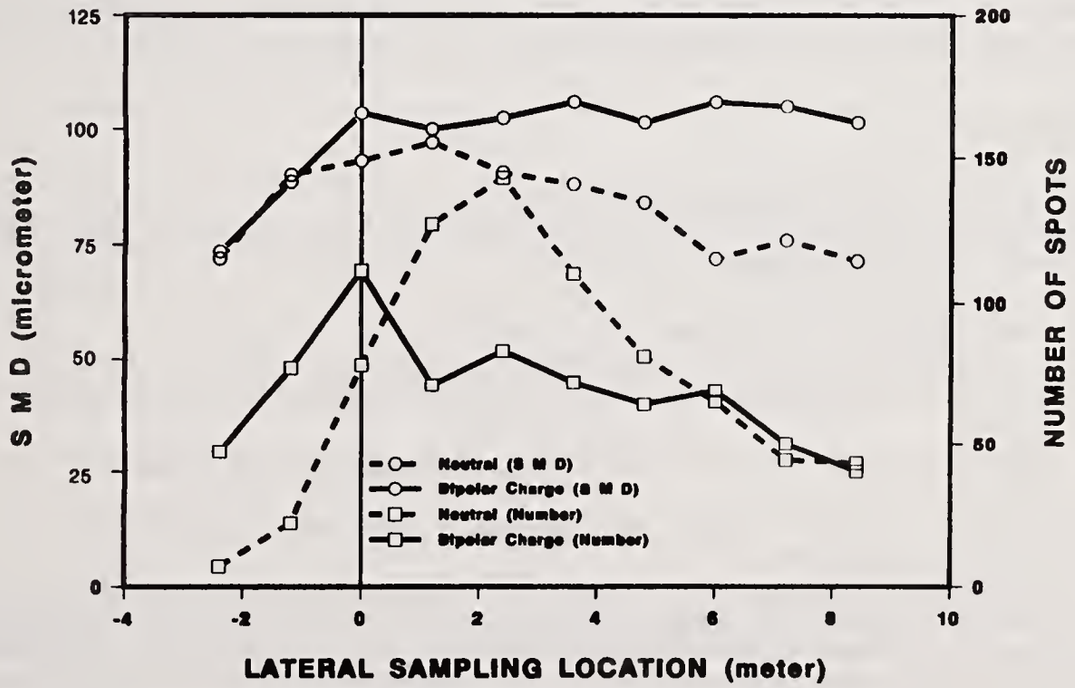

Fig. 10 Lateral distributions of *SMD* and the number of sampled drops for both dual-polarity charged and uncharged aircraft sprays.

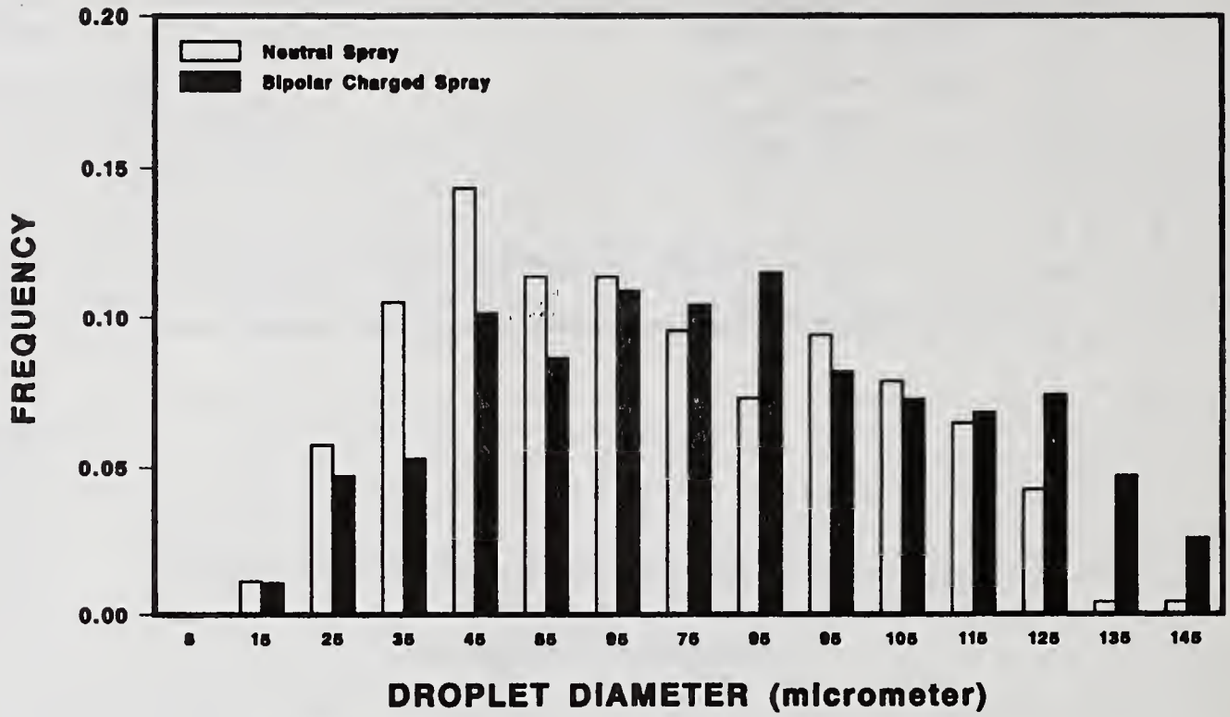

Fig. 11 Comparison of size distributions between neutral and dual-polarity charged spray.

ACKNOWLEDGEMENTS

The financial support for the present work was provided by the United States Department of Agriculture through the Agricultural Research Service. Authors wish to thank Dr. L.F. Bouse and Dr. J. Carlton of the USDA Agricultural Research Service for their many valuable suggestions and help throughout the work.

REFERENCES

1. Davies, C.N., Aerosol Science, Academic Press, Ch. 3 (1966).
2. Carlton, J.B., and Bouse, L.F., "Electrostatic spinner-nozzle for charging aerial sprays," Trans. ASAE, Vol. 23, No. 6, pp. 1369-1378 (1980).
3. Carlton, J.B., and Bouse, L.F., "Distribution of the electric field for an electrostatic spray charging aircraft," Trans. ASME, Vol. 20, No. 2, pp. 248-357, (1977).
4. Oglesby, S., and Nichols, G.B., Electrostatic Precipitation, Marcel Dekker Inc., Ch. 2 (1978).
5. Lefebvre, A.H., Atomization and Sprays, Hemisphere Publishing Co., pp. 127-134, pp. 189-193, 222-228, (1989).
6. Bals, E.J., "Design of rotary atomizers," Proc. 4th Int. Agric. Aviat. Congr., Kingston, UK., pp. 156-165 (1969).
7. O'Neal, H., and Brazelton, R.W., "Aerial Application of Pesticides," Report No. ADP 84-016, Shell Chemical Company, p. 22, (1984).
8. Tanasawa, Y., Miyasaka, Y., and Umehara, M., "Effect of shape of rotating disks and cups on liquid atomization," Proc. 1st Int. Conf. Liquid Atomization and Spray Systems, Tokyo, Japan, pp. 165-172 (1978).
9. Lane, W.R., "Shatter of drops in the stream of air," Ind. Eng. Chem., Vol. 43, No. 6, pp. 1312-1317, (1951).
10. Hinze, J.O., "Fundamentals of the Hydrodynamic Mechanism of splitting in dispersion processes," AICHE J., Vol. 1, No. 3, pp. 289-295, (1955).
11. Richardson, S.M., Fluid Mechanics, Hemisphere Pub. Corp., pp. 260-264, (1989).
12. Cross, J.A., Electrostatics, Adam Hilger, pp. 198-218 (1987).

A NUMERICAL MODEL OF THE CAPILLARY INSTABILITY

R.W. Sellens

Department of Mechanical Engineering
Queen's University at Kingston
Ontario, Canada

ABSTRACT

The momentum and continuity equations are reduced to a one dimensional form for the case of a finite axi-symmetric disturbance on a liquid ligament, retaining both viscous and inertial terms. Numerical solution of these equations yield results that are in good agreement with experimental data and the exact solutions of Rayleigh and Weber for infinitesimal disturbances. The model carries through to the point of breakup and predicts the formation of satellite drops between the main drops of the stream.

INTRODUCTION

The capillary instability of cylindrical ligaments of liquid is of fundamental importance in the atomization of liquids. This mechanism is key in both practical atomizers and a variety of special purpose devices such as monosize drop generators and ink jet printers.

A cylindrical element of liquid in a quiescent environment is inherently unstable, so that small disturbances will grow larger. The first quantitative solution to this problem was presented by Rayleigh [1], who linearized the system by neglecting viscous forces and restricted his analysis to sinusoidal disturbances of small amplitude. Weber [2], considered a viscous system, but neglected the inertial effects, again for small disturbances. Both Rayleigh and Weber found that disturbances at unstable wavelengths would grow exponentially so that

$$\xi = \xi_0 e^{\alpha t} \qquad \text{where} \qquad \xi = (R_{max} - R_{min})/2 \tag{1}$$

with the growth rate α dependent on the geometry of the system and the fluid properties.

$$\text{Rayleigh} \quad \alpha^2 = \frac{\sigma}{\rho a^3} \frac{(1 - k^2a^2)ka\, I_1(ka)}{I_0(ka)} \tag{2}$$

$$\text{Weber} \quad \alpha^2 + \alpha \frac{3\mu}{\rho a^2} k^2a^2 = \frac{\sigma}{2\rho a^3}(1 - k^2a^2)k^2a^2 \tag{3}$$

R is the local ligament radius, a is the undisturbed ligament radius and k is the disturbance wave number, $2\pi/\lambda$. By examination of equation 3 it is clear that the importance of viscosity increases with decreasing initial ligament radius. The scale and fluid properties in most atomization flows require that the effects of viscosity be considered.

Subsequent analytical solutions (c.f. Sterling and Sleicher[3]) have generally been restricted by one or more assumptions; inviscid flow, negligible inertia, or small disturbance amplitude. The assumption of small

disturbance amplitude prevents the application of these models to the later stages of the breakup process where the ligament is pinching off to form separate drops, generally leaving a "satellite" drop in the pinched off region.

The instability is driven by the surface tension force, which produces pressure variations dependent on the local curvature of the liquid surface. Thus, as surface geometry is of first order importance, the modelling of the moving interface is critical to success. Numerical methods developed for fluid systems with fixed boundaries, or with boundaries where surface tension may be neglected are ill suited to the solution of this problem.

Mansour and Lundgren [4] have presented a solution method for the growth of finite amplitude, spatially periodic, axisymmetric waves on an inviscid cylindrical ligament using a boundary integral technique to solve the potential flow equations. The solution can follow the ligament growth to breakup and predict the formation of satellite drops. Growth rates are in good agreement with the classic result of Rayleigh. However, this approach holds only for inviscid flow, and it fails where small size or high viscosity violate this condition.

Shkoohi and Elrod [5,6] have solved the complete Navier-Stokes equations for both Lagrangian and Eulerian coordinates. However, the computational requirements of this approach have limited their studies.

The present approach considers a simplification of the equation system in hopes that the essential character of the solution may be preserved, while dramatically reducing computation time. This will permit an assessment of the effects of a wide variety of different disturbance functions on the ligament breakup, particularly on the sizes of drops produced. If this system is considered statistically, it may shed some light on the processes limiting the formation of small drops in low speed atomization flows. In previous work by the author [7,8] a physical constraint limiting the formation of small drops was found necessary in the statistical prediction of drop size and velocity distributions.

EQUATIONS OF MOTION

The surface of an axisymmetric ligament may be characterized by its radius as a function of axial position. If the radial velocity is neglected and the axial velocity within the ligament is assumed to be radially uniform, it may also be characterized as a function of axial position, thus reducing the problem to a transient, one dimensional problem.

Continuity for an incompressible, disk shaped element requires that the radius, R, increase to accommodate the net mass flux into the element so that

$$\frac{\partial R^2}{\partial t} = -\frac{\partial R^2 w}{\partial z} \tag{4}$$

or rearranging explicitly for the temporal change in R

$$\frac{\partial R}{\partial t} = -w\frac{\partial R}{\partial z} - \frac{R}{2}\frac{\partial w}{\partial z}. \tag{5}$$

A balance of axial momentum on an element of fluid yields

$$\frac{\partial w}{\partial t} + w\frac{\partial w}{\partial z} = -\frac{1}{\rho}\frac{\partial P}{\partial z} + 2\nu\frac{\partial^2 w}{\partial z^2} + \frac{4\nu}{R}\frac{\partial R}{\partial z}\frac{\partial w}{\partial z} \tag{6}$$

where the second viscous term accounts for the variation of the radius. The pressure immediately beneath the surface may be calculated by considering the forces on an element of surface curved in both directions.

$$P = P_0 + \frac{\sigma}{R}\left(1 - \left(\frac{\partial R}{\partial z}\right)^2 - R\frac{\partial^2 R}{\partial z^2}\right) \tag{7}$$

In keeping with the one dimensional velocity approximation, the pressure may be approximated as radially uniform. Thus, differentiating equation 7 and substituting into equation 6 yields an explicit expression for

the temporal change in velocity.

$$\frac{\partial w}{\partial t} = -w\frac{\partial w}{\partial z} + \frac{\sigma}{\rho R^2}\frac{\partial R}{\partial z} - \frac{\sigma}{\rho R^2}\left(\frac{\partial R}{\partial z}\right)^3 + \frac{2\sigma}{\rho R}\frac{\partial R}{\partial z}\frac{\partial^2 R}{\partial z^2}$$

$$+ \frac{\sigma}{\rho}\frac{\partial^3 R}{\partial z^3} + 2\nu\frac{\partial^2 w}{\partial z^2} + \frac{4\nu}{R}\frac{\partial R}{\partial z}\frac{\partial w}{\partial z} \qquad (8)$$

Equations 5 and 8 then provide a coupled system of nonlinear equations describing the development of the two variables, R and w. An appropriately chosen numerical solution technique may then be used to follow this development under varying initial conditions.

DISCRETIZATION AND SOLUTION OF EQUATIONS

The ligament is discretized into a number of elements, each characterized by values of R and w at the centre of the element. Equations 5 and 8 may then be approximated about each element by evaluating first order central differences for each of the derivative terms. (Although various differencing schemes were tried, no improvement on the initial scheme was found.) This approach provides estimates of the temporal derivatives based on the current values of R and w.

The problem is then solved by a semi-implicit time marching scheme. For each time step, the following process is employed.

1. Approximate the sets of new values w_1 and R_1 to be equal to the sets of current values w_0 and R_0.
2. Evaluate $(\frac{\partial w}{\partial t})_0$ and $(\frac{\partial R}{\partial t})_0$ based on w_0 and R_0.
3. Evaluate $(\frac{\partial w}{\partial t})_1$ and $(\frac{\partial R}{\partial t})_1$ based on w_1 and R_1.
4. Calculate $w_1 = w_0 + 0.5\left((\frac{\partial w}{\partial t})_0 + (\frac{\partial w}{\partial t})_1\right)\Delta t$ and $R_1 = R_0 + 0.5\left((\frac{\partial R}{\partial t})_0 + (\frac{\partial R}{\partial t})_1\right)\Delta t$
5. Repeat from step two until the values of w_1 and R_1 converge.

By repeating this entire process the solution may be marched forward, Δt at a time. At present, periodic boundary conditions are applied, so that the difference approximations are wrapped around to the opposite ends of the solution domain.

Initial conditions on the ligament may be set to a sinusoidal variation in the radius along the ligament, a sinusoidal variation in velocity, or a combination of the two.

Instabilities occasionally develop in the solution, particularly for cases where the viscous forces are small. These instabilities are on the scale of the discretization and are first evident in the time derivative of the velocity. Reducing the time step will eliminate or delay the onset of these instabilities, however it has been found more effective to apply a 3 or 5 point moving average on the derivative field to suppress this instability.

RESULTS AND DISCUSSION

For comparison with the classic results and experimental data, the overall progress of the solution may be characterized by the exponential growth rate α, as defined in equation 1. Although a constant for the classical solutions, the growth rate is found to vary with solution progress. Figure 1 shows the results obtained for α when the solution parameters are varied. As can be seen by comparison with denser grids, the 60 point discretization yields good results, provided that no averaging is used to stabilize the solution. All results presented in this paper are for a 60 point discretization with no averaging, except where noted otherwise.

The 90 and 120 point solutions are very close to the 60 point results, but averaging and/or time step reduction were necessary to stabilize the solutions. The equations were solved on a 20 MHz, 80386 based personal computer with numeric coprocessor. Overall solution times to carry a ligament through to the

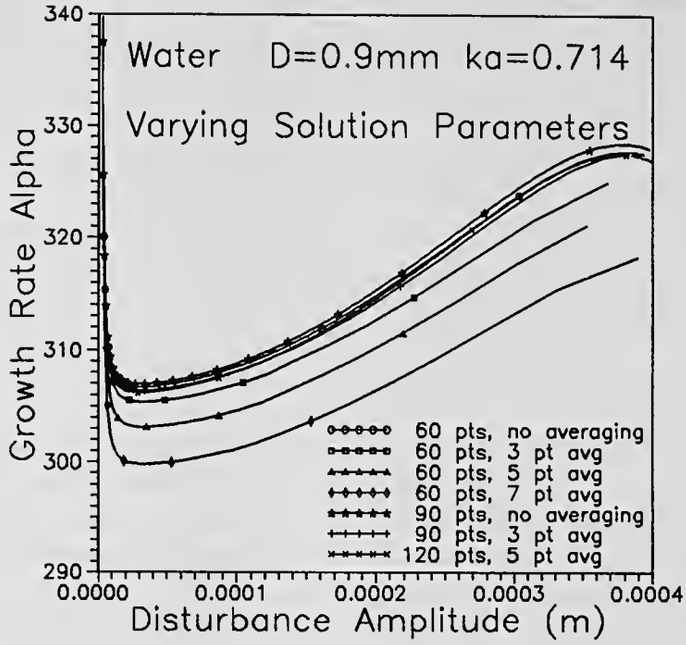

Figure 1: Varying the solution parameters has little effect on the solution behaviour, as shown by the growth rate α, except when the domain of the moving average represents a significant portion of the solution domain.

point of breakup were typically around 20 minutes, 3 hours and 60 hours for 60, 90 and 120 point solutions respectively. Naturally, these times varied substantially with differences in initial conditions, being longer for smaller initial disturbances.

The code presently allows sinusoidal variations in amplitude and/or velocity to be applied to the ligament. Figure 2 shows that the solutions tend toward a common result, independent of the characteristics of the initial disturbance. Only the wavelength of the disturbance is significant. Thus, an infinitesimal disturbance may be simulated by any combination of amplitude and velocity, provided it is small.

A characteristic growth rate has been arbitrarily defined as the value of α when the disturbance amplitude, peak to trough, has reached 1/4 of the undisturbed ligament radius. As can be seen from the figures, this provides a result that characterizes the early part of the growth for a specific wave number, but is insensitive to the other characteristics of the initial disturbance.

Figure 3 shows comparisons with the experimental data of Sakai et al [9] for glycerine/water solutions. A vibrating orifice generator was used to produce a ligament with imposed disturbances of known wavelength and growth rates calculated from photographic measurements.

The results agree quite well for the lower viscosity case of 65% glycerine, but the present approach over-predicts the growth rates for the higher viscosity case. For pure water, the present model predicts growth rates approximately 3% higher than Rayleigh's solution. Otherwise, the model shows the same characteristics as the classical results, yielding a maximum growth rate around $ka = 0.69$ for low viscosity cases and moving towards $ka = 0.5$ as viscosity increases.

This deviation from the classical results appears to be due to the one dimensional approximation, which eliminates the effects of the radial velocity and its variation. From the qualitative agreement it is clear that this is a secondary effect. It may be possible to model the radial resistance to growth in terms of the current solution variables R and w to produce a quasi-two-dimensional model that retains the simplicity and computational efficiency of the 1D model while producing more accurate results.

The variation of α with solution progress is shown in figures 4 and 5 for water and 65% and 90% glycerine/water solutions respectively. The growth rate remains more nearly constant for the more viscous flows.

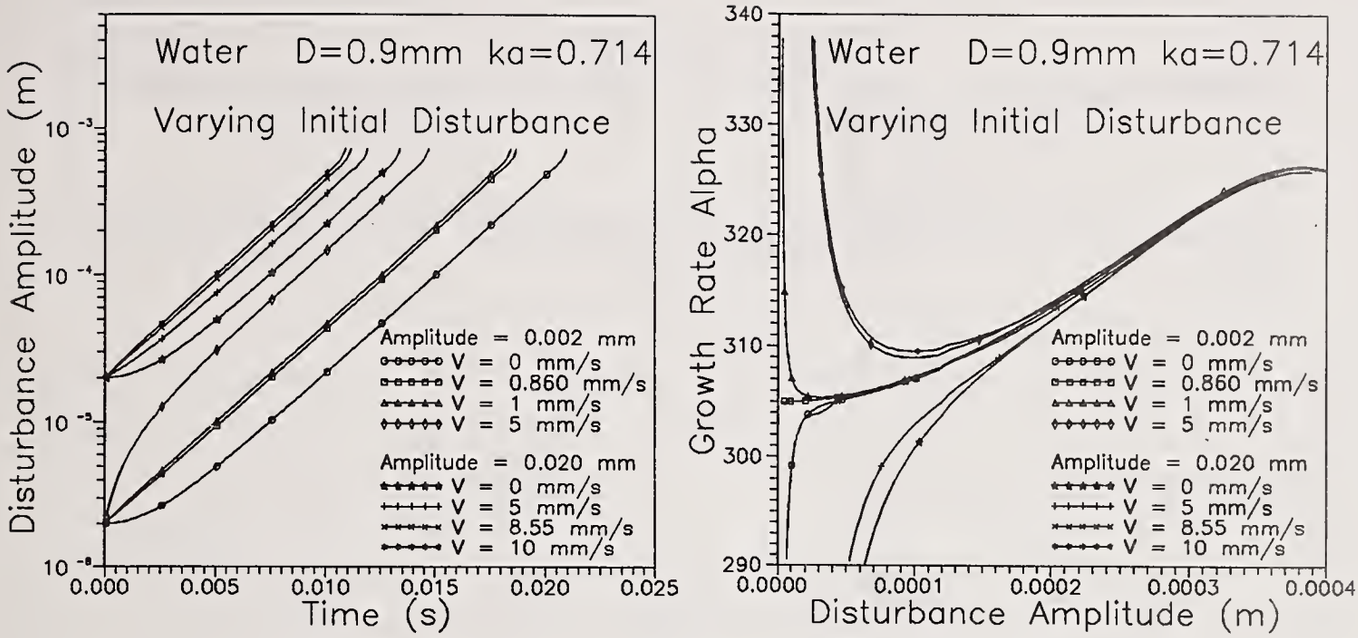

Figure 2: Variations in the initial disturbance characteristics affect only the early part of the solution. The disturbance wavelength defines a solution that different types of disturbance move towards. The left hand plot shows that disturbance amplitude grows exponentially with time, while the right hand plot shows the variation of that growth rate with disturbance amplitude.

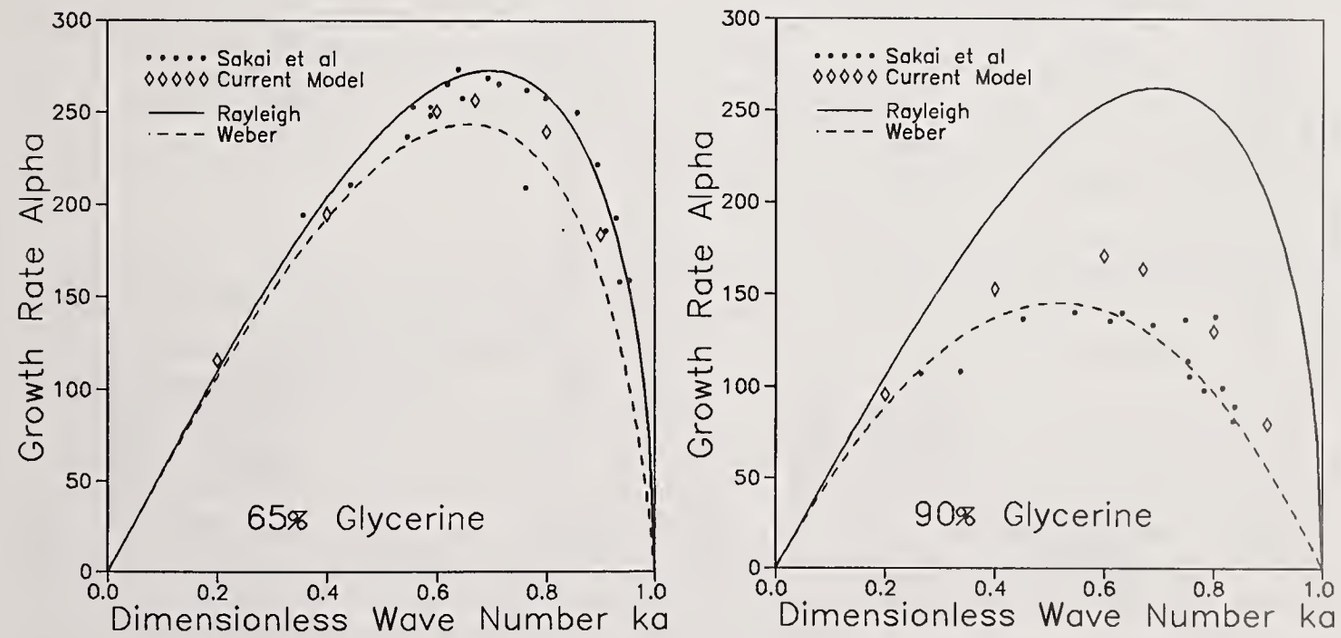

Figure 3: This figure compares the growth rates found for different wave numbers on 0.9 mm diameter ligaments of 65% and 90% glycerine/water solutions.

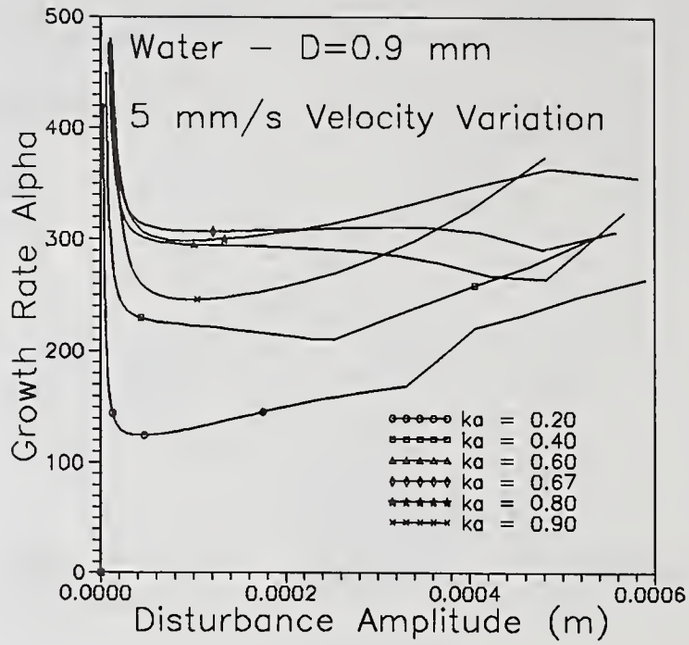

Figure 4: Growth rate behaviour in water at various dimensionless wave numbers.

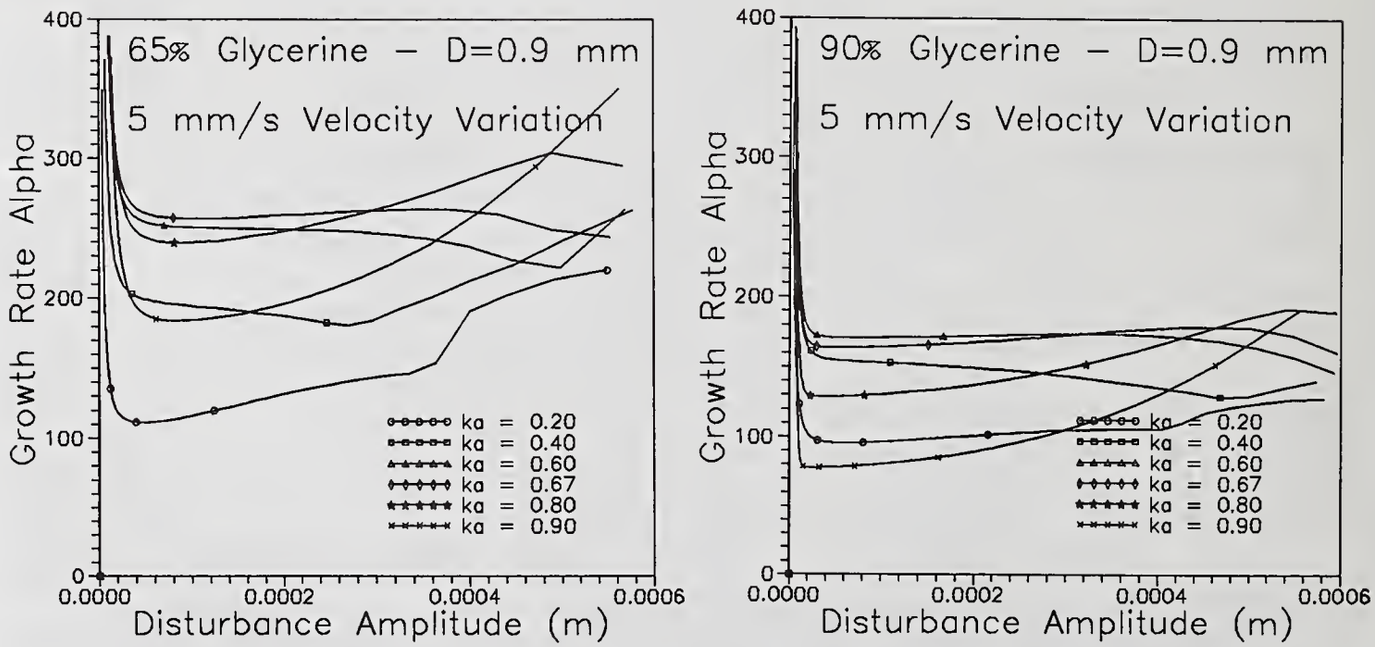

Figure 5: Growth rate behaviour in 65% and 90% glycerine/water solutions at various dimensionless wave numbers.

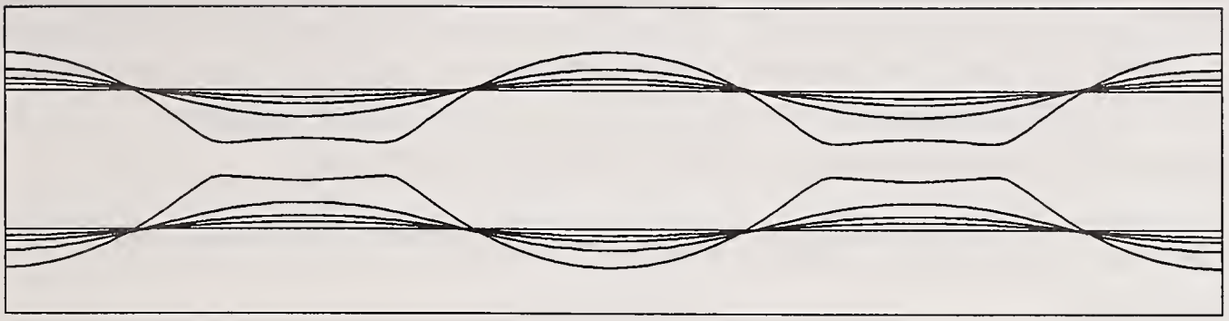

Figure 6: Surface profiles for a 0.9 mm ligament of water at different times. $ka = 0.7$; lines are 2 ms apart.

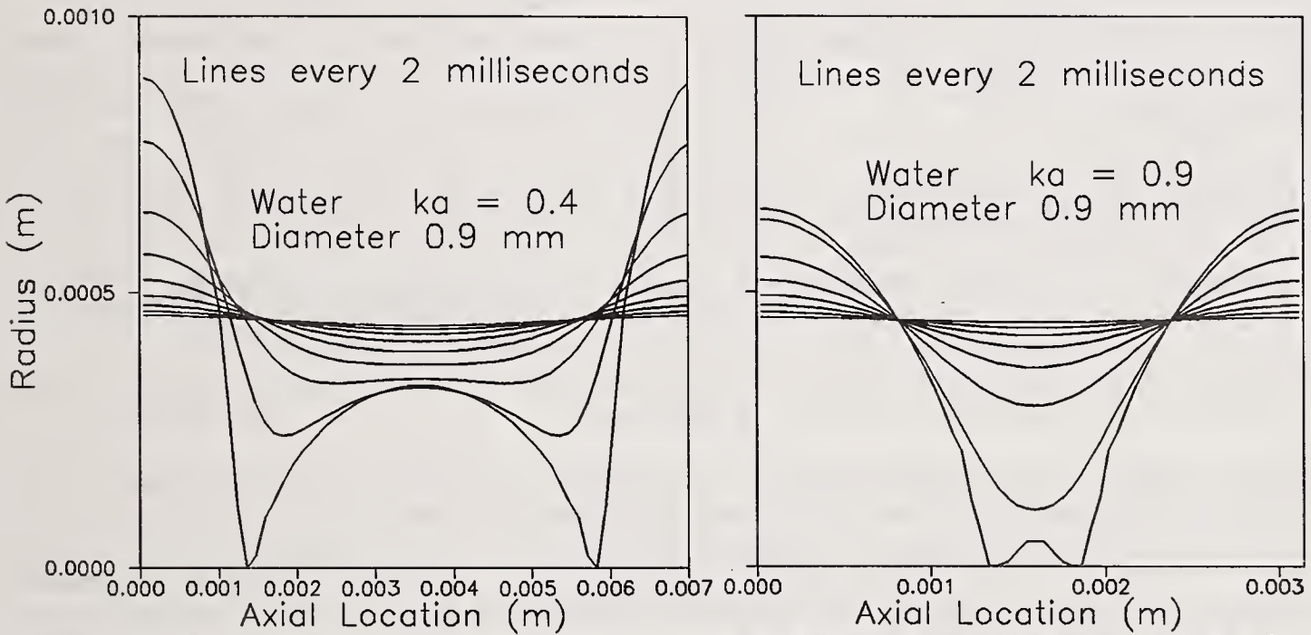

Figure 7: Surface profiles for a 0.9 mm ligament of water at different times. The aspect ratio has been exaggerated to provide more detail. On the left the dimensionless wave number is $ka = 0.4$, while on the right $ka = 0.9$.

Figures 6 and 7 show the development of the surface profiles for ligaments of water, subject to disturbances of different wave number. Figure 6 is plotted in the correct aspect ratio, showing the ligament for two wavelengths and provides a clear picture of the flow. The plots in Figure 7 are exaggerated in the radial direction to show more detail.

It was observed that all instances yield satellite drops, but that these drops become much smaller at higher wave numbers. This is consistent with the two dimensional inviscid results of Mansour and Lundgren [4]. The breakup process could not be followed past the point of pinching off due to current limitations in the code. Inclusion of a boundary condition for a pinched off end is planned to permit following of the secondary breakup of the satellite ligaments produced at low dimensionless wave numbers. However, this extension is not important for the higher wave number cases where both main and satellite drops are well formed as drops by the time the ligament pinches off.

CONCLUSION

A model has been developed which incorporates both the inertial and viscous forces in the capillary instability. Comparisons indicate a tendency to over-prediction of disturbance growth rate, particularly in highly viscous cases, due to the approximations in the one dimensional formulation.

However, qualitative agreement is very good and a refinement of the model to incorporate inertial and viscous effects of motion in the radial direction is expected to yield quantitatively accurate results.

The computational requirements of this model are much smaller than fully two dimensional solutions, while providing useful results.

ACKNOWLEDGEMENT

The author is grateful for the support of Queen's University for this work, through both Research Initiation and Advisory Research Committee Grants.

REFERENCES

[1] Rayleigh, Lord, "On the Instability of Jets," Proc. London Math. Soc., Vol. 10, pp. 4-13, (1878).

[2] Weber, C., "Zum Zerfall Eines Flüssigkeitsstrahles," Z. Angew. Math. Mech., Vol. 11, pp. 138-145, (1931).

[3] Sterling, A.M. and Sleicher, C.A., "The instability of capillary jets," J. Fluid Mech., Vol. 68, pp. 477-495, (1975).

[4] Mansour, N.N. and Lundgren, T.S., "Satellite Formation in Capillary Jet Breakup," Phys. Fluids A, Vol. 2, No. 7, pp. 141-1144, (1990).

[5] Shkoohi, F. and Elrod, H.G., "Numerical Investigation of the Disintegration of Liquid Jets," J. Comput. Phys., Vol. 71, pp. 324-342, (1987).

[6] Shkoohi, F. and Elrod, H.G., "Algorithms for Eulerian Treatment of Jet Breakup Induced by Surface Tension," J. Comput. Phys., Vol. 89, pp. 483-487, (1990).

[7] Sellens, R.W., "Prediction of the Drop Size and Velocity Distribution in a Spray, Based on the Maximum Entropy Formalism," Part. Part. Sys. Charact., Vol. 6, pp. 17-27, (1989).

[8] Sellens, R.W., "Drop Size and Velocity Distributions in Sprays, A New Approach Based on the Maximum Entropy Formalism," Ph.D. Thesis, Department of Mechanical Engineering, University of Waterloo, Waterloo, Ontario, Canada, (1987).

[9] Sakai, T., Sadakata, M., Saito, M. and Matsushita, K., "Studies of Disintegration of Liquid Column Between Production of Uniform Drops by Vibration Method," International Conference on Liquid Atomisation and Spray Systems (ICLASS-85), paper VIIB(b)/2, The Institute of Energy, London, England, 1985.

ICLASS-91 *Gaithersburg, MD, U.S.A. July 1991* *Paper 12*

ATOMISATION OF FLAT AND ANNULAR LIQUID SHEETS PRACTICAL USE OF LINEAR THEORIES

C. Dumouchel and M. Ledoux

URA CNRS 230/CORIA - University of Rouen
Mont Saint Aignan, France

In this paper atomisation of flat and cylindrical liquid systems have been investigated through linear theories. After an examination of the parameters involved in the problem it is found that the behaviour of flat systems is totaly known by the determination of a set of non dimensionalized numbers and that cylindrical systems behaves as flat ones in many cases.

Associated to a disintegration process that allows to calculate one drop diameter, applications of these mathematical models on practical situations are described. Some experimental observations concerning the influence of the external pressure are found again and an interesting agreement between a set of calculated and measured drop diameters is obtained.

1 INTRODUCTION

Atomisation is based on interfacial instabilities of liquid systems either in calm atmospheres or induced by air streams. This physical process is not perfectly known and its complexity makes theoretical investigations tricky to set up.

Even though it can be critized the linear theory based on the development of a dominant wave length allows a quick approach to the problem and supports comparisons with experimental data.

Examples of linear theories are presented here for flat and cylindrical liquid systems. It is attempted to allow the exploitation of such theoretical models by designers through a synthetic presentation of the results of computations and to show the possibilities as well as the limits of such theories.

2 INSTABILITY OF A FLAT LIQUID SHEET

2.1 Analysis

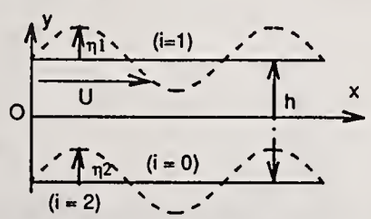

Fig. 1. Flat liquid sheet in air at rest (—— undisturbed flow) (--- perturbed flow)

The disintegration of an inviscid flat sheet of liquid is studied through the set up of a linear theory. This approach assumes that a superposition of sinusoidal perturbations takes place on the interfaces of the liquid system (see fig. 1). Some of these perturbations will grow sufficiently to lead to the break down of the sheet. However, among them, one will have a growth rate that is larger than the others and the

disintegration of the system will be dominated by the growth of this particular perturbation.

The mathematics involved here are similar to those used by Crapper et al [1] and Dumouchel et al [2] for the case of a cylindrical liquid sheet and they are not reported in detail here.

The initial flow is steady but any perturbation induces a non-steady flow assumed irrotational and thus associated to a perturbation potential ϕ. In each phase the continuity equation allows the functions ϕ_i to be written as :

$$\phi_i = \epsilon \, (A_i e^{ky} + B_i e^{-ky}) \, \exp\left[i(kx - \omega t)\right] \qquad (1)$$

where i refers to the regions indicated on fig. 1. The displacement of the upper and lower surfaces shown in fig. 1 are taken under a similar form :

$$\eta_i = \epsilon \, \alpha_i \, \exp\left[i(kx - \omega t)\right] \qquad (2)$$

The pulsation ω may be complex and its imaginary part ω_i is the temporal growth rate corresponding to the imposed perturbation defined by a wave number k. The fluid particles that compose the interfaces are supposed to be the same all over the time and this is expressed through four kinematic conditions. They allow the determination of the coefficients A_i and B_i. Two dynamic conditions expressing the balance between the pressure and the surface tension forces are written on each interface and the resulting system of equations conducts to the dispersion equation that has the form :

$$C_4\omega^4 + C_3\omega^3 + C_2\omega^2 + C_1\omega + C_0 = 0 \qquad (3)$$

(the coefficients C_i may be obtained from the authors). For a given liquid system, equation (3) is solved to find the value of ω of the imposed perturbation which will grow if the solution found is complex. According to Hagerty and Shea [3] and Dombrowski and Hooper [4] remarks, one has only to consider the antisymmetric mode of perturbation which is predominating for small gas densities ($\rho_G << \rho_L$).

2.2 Results

Figure 2 shows dispersion diagrams ie ω_i versus k, over a range of velocity U for a sheet of water. In each case it is seen that the characteristics of the dominant wave ie k_{amax} and ω_{iamax} both increase with the velocity U. For the same cases fig. 3 shows the propagation velocities Cel of the growing perturbations versus the wave numbers k.

The growth rate of the perturbation is only controled here by the aerodynamical and surface tension forces. On fig. 2 and 3 we can see that aerodynamical forces are destabilizing

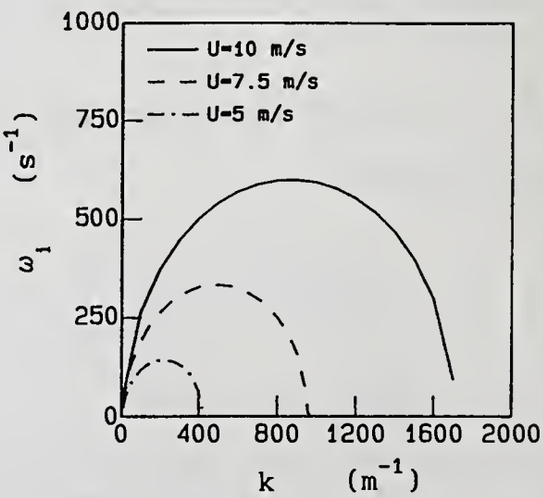

Fig. 2. Dispersion diagram. h=300μm (water/air)

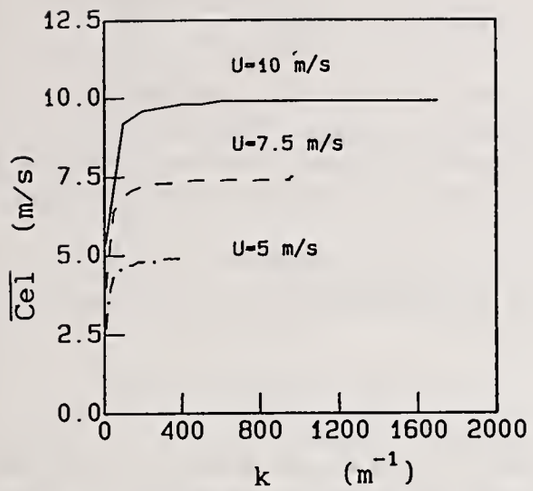

Fig. 3. Propagation wave velocity. h=300μm (water/air)

and proportional to the difference of velocity between the external medium and the perturbation propagation speed (for small wave numbers ω_{iamax} and Cel both increase with k).

The surface tension forces are indirectly proportional to the curvature radius of the interfaces and therefore more effective for high wave numbers. For these values of k the growth rate decreases as k increases showing the stabilizing effect of the surface tension forces that increases with k. This effect becomes more and more effective in a domain where the aerodynamical forces are maximum (Cel=U) but constant and that is why ω_{iamax} decreases until it becomes zero.

The dominant wave results from the best compromise between the aerodynamical and surface tension effects.

We studied the influence of each parameter involved in the problem on the characteristics of the dominant perturbation ie k_{amax}, ω_{iamax} and Cel. Using a set of non dimensionnal parameters the different results showed only one behaviour presented on fig. 4 where :

$$\left.\begin{aligned} We &= \frac{2\sigma}{\rho_L U^2 h} \qquad & We\omega &= \frac{\omega_{iamax}\sigma}{\rho_G U^3} \\ Wek &= \frac{k_{amax}\sigma}{\rho_G U^2} \qquad & \overline{Cel} &= \frac{Cel}{U} \end{aligned}\right\} \quad (4)$$

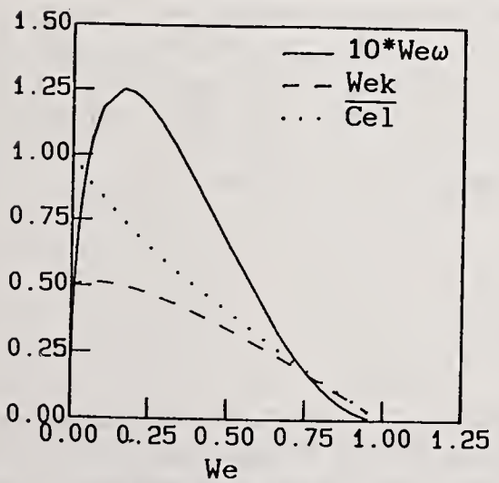

Fig. 4. Characteristics of the dominant wave for flat liquid sheets.

Figure 4 is relevant for any kind of flat sheet evolving through any kind of gaseous medium as long as the assumption $\rho_G << \rho_L$ is kept. It is seen that if We>1 the corresponding liquid system is stable for any perturbation. We find here again the stability criterion found by Squire [5]. We see as well that ω_{iamax} reaches a maximum corresponding to :

$$\begin{aligned} We &= 0.17 \quad & We\omega &= 0.125 \\ Wek &= 0.50 \quad & \overline{Cel} &= 0.75 \end{aligned} \quad (5)$$

The presence of this maximum may be explained as previously for the maxima shown on fig. 2.

3 INSTABILITY OF A CYLINDRICAL LIQUID SHEET

3.1 Introduction

Encountered in amny practical situations, the disintegration of cylindrical liquid sheets has been the subject of many theoretical and experimental investigations [1], [5], [6]. Furthermore such studies provide a first approximation of the complex problem posed by the conical liquid systems as proposed by Dumouchel et al. [2].

Here their analysis is summarized and results are presented and compared with those of flat systems to allow a better understanding of the process described by linear theories in such cases.

3.2 Analysis

The cylinder of liquid is defined by a thickness h, an internal radius a and two velocity components, U along the axis of symmetry and V along the azimuth (as for a conical sheet). We make the assuumption that the liquid velocity is sufficiently high and the liquid sheet thin enough so that the sheet breakdown occurs before the tendency of the cylinder to collapse under surface tension forces takes place. The analysis, not reported in detail here, is conducted using cylindrical coordinates. The velocity V allows a perturbation to take place along the azimuth and this is introduced in the propagating terms of the functions ϕ_i and η_i that become :

$$\phi_i = \epsilon \left(A_i I_n(kr) + B_i K_n(kr)\right) \exp\left[i(kx + n\theta - \omega t)\right] \tag{6}$$

$$\eta_i = \epsilon \alpha_i \exp\left[i(kx + n\theta - \omega t)\right] \tag{7}$$

The internal radius and the possible azimuthal perturbation introduce new curvature radii that modify the surface tension terms in the dynamic conditions (for more details see reference [2]).

As for the flat sheet the dispersion equation obtained for ω is of the fourth order. Here again we only deal with the solutions corresponding to the antisymmetric mode of perturbation.

3.3 Results

3.3.1 Without azimuthal component of velocity

As for a flat liquid sheet, the dispersion diagram for a cylindrical liquid sheet shows a maximum corresponding to a perturbation that growths quicker than the others. We are only interested by this particular perturbation characterised by the numbers Weω, Wek and $\overline{\text{Cel}}$ defined by equations (4).

A new parameter Wea is introduced to take into account the internal radius a.

$$\text{Wea} = \frac{\sigma}{\rho_G U^2 a} \tag{8}$$

Fig.5 shows the relation between Weω and We for different values of Wea. When Wea=0.048 we can see that the curve obtained is not very different from fig.4. Further calculations actually showed that a liquid cylinder having a parameter Wea less than 0.1 behaved like a flat system. This means that when Wea<0.1 the surface tension effects added by the curvature radius a are very

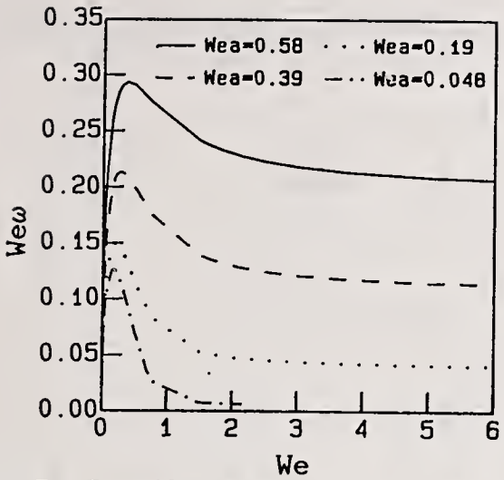

Fig.5. Growth rate of the dominant wave for cylindrical liquid sheets. Weω=f(We)

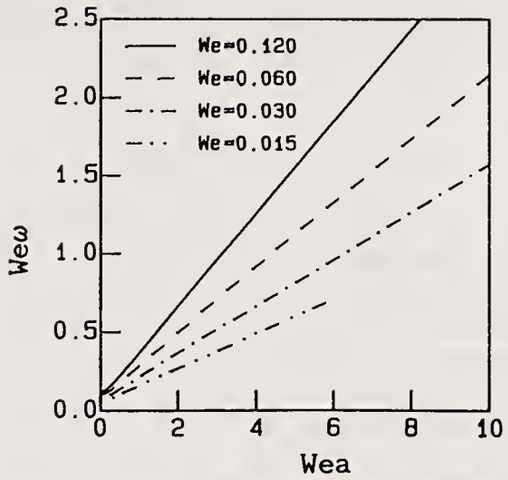

Fig.6. Growth rate of the dominant wave for cylindrical liquid sheets Weω=f(Wea)

small compared to the aerodynamical effects or the surface tension effects due to the perturbation and therefore they may be ignored. This criterion agrees with the one found by Guilié in a similar study [6].

When Wea increases, we see on fig.5 that Weω increases for any given We. This shows that the surface tension forces introduced by the radius a are destabilizing. We note as well that when We increases Weω reaches a limit different from zero as for a flat system and that increases as Wea increases. In this domain the disintegration is especially controlled by the surface tension forces introduced by the radius a and it corresponds to the domain of very thin systems as those studied by Martinon [7].

Fig.6 shows that the relation between Weω and Wea is linear, the expression of which, for We<0.6, was found to be :

$$We\omega = 0.8\sqrt{We}\ Wea - 1.1\ We^2 + 0.11\ We + 0.07 \qquad (9)$$

As for a flat sheet it can be seen from fig.5 and equation (9) that the maximum growth rate of a cylindrical system reaches a maximum for given We and Wea.

Fig.7 shows the values of Wek and $\overline{Cel}$ for Wea=0.58 and it is seen that both of them reach a limit for high We. However we can see that the limit of $\overline{Cel}$ is very near zero that confirms that in this domain the disintegration is controled by the presence of the internal radius a.

From these different results we can also draw the double effect of the surface tension on the dispersion diagram. When the surface tension increases the growth rates increase (see fig.5 and 6) but the range of wave numbers of the growing perturbations decreases due to the more effective surface tension forces.

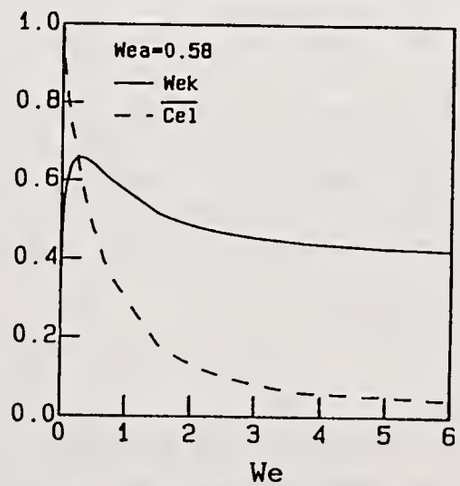

Fig.7. Wek and $\overline{Cel}$ for cylindrical liquid sheets with Wea=0.58

3.3.2 With an azimuthal component of velocity

Now the velocity U introduced in each non-dimensionalized Weber numbers (equations (4) and (8)) is replaced by the total velocity U_T defined by :

$$U_T = \sqrt{U^2 + V^2} \qquad (11)$$

As found by Dumouchel et al. [2] the dominant perturbation may be characterised by two orthogonal wave lengths associated to two wave numbers; k along the axis and n/a along the azimuth. Then, the direction of propagation of the perturbations makes an angle β_P with the axis of symmetry. Over a range of Wea $tg(\beta_P)$ is compared in fig.8 to $tg(\beta_V)= V/U$. For Wea>1 the dominant wave is longitudinal ($\beta_P=0$) and its characteristics are exactly the same as those of the same liquid cylinder with the axial velocity component U only. For these cases an azimuthal component of velocity has no influence at all. This comes from the fact that an azimuthal component of velocity tends to reduce the surface tension forces due to the radius a. For Wea>1 the disintegration is mainly controled by the surface tension forces induced by the radius a, therefore the dominant wave will stay longitudinal as an azimuthal perturbation introduced by V would reduce the growth rate. However for small Wea, the system tends to adopt the behaviour of a flat system and therefore the presence of V will be regarded as an increase of the destabilizing aerodynamical effects. The dominant wave is no longer longitudinal (β_P is different from zero) and when Wea tends toward zero β_P tends toward β_V : the system behaves like the flat sheet with the velocity component U_T.

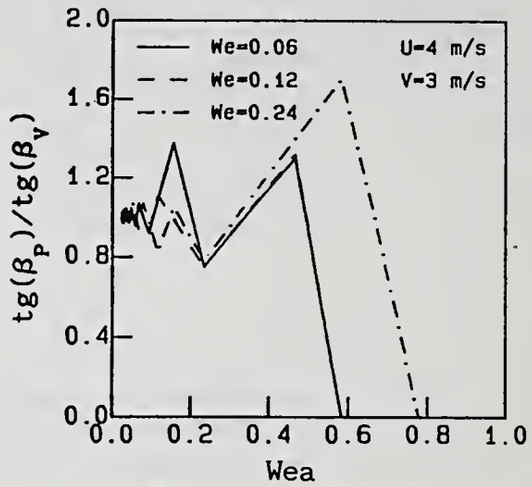

Fig.8. Direction of propagation of the dominant wave for cylindrical liquid sheets with two components of velocity.

3.3.3 Discussion - Application

In practical situations two effects of the azimuthal component of velocity can be therefore dissociated : first, a spin velocity modifies the liquid geometry giving birth to a thinning conical system (as for a swirl atomizer for instance) and secondly, when the internal radius has become large enough, the spin becomes an effective component of velocity for the disintegration increasing the wave number of the dominant wave. Dumouchel et al [2] showed that a drop diameter d_G could be calculated from this investigation :

$$d_G = 3.78 \sqrt{\frac{h}{K_T}} \qquad (12)$$

Although it is generally not straight-forward such investigations may be used as predictive tools. For instance, Dumouchel et al [2] adapted this approach to the case of swirl atomizers that deal with conical liquid sheets

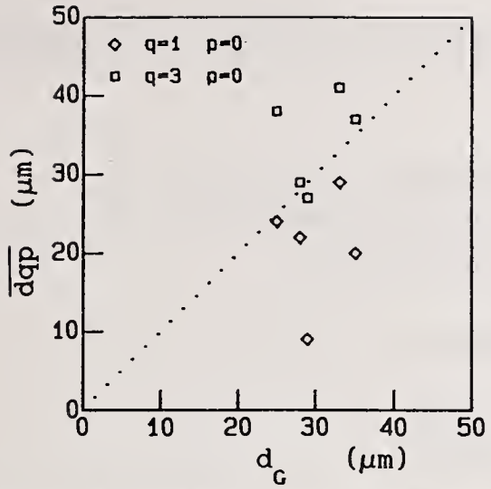

Fig.9. Calculated drop diameters d_G versus measured diameters $\overline{dqp}$ for a set of swirl atomizers (from ref.[2]).

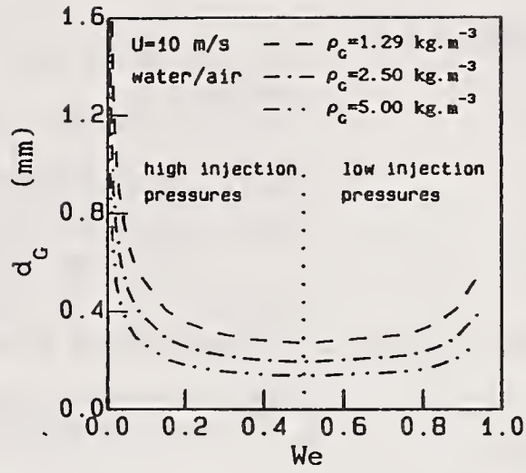

Fig.10. Influence of ρ_G on the drop diameter for a flat system.

and an interesting agreement was found between measured and calculated drop diameters (see fig.9).

It is possible as well to bring out the influence of parameters involved in the process of drop formation as for instance the influence of the external pressure P_{amb} on the drop diameter for a thinnig flat liquid sheet. Figure 10 shows d_G odtained from equation (12) as a function of We for three values of ρ_G. Let's call Wer the value of We at the break-up. When P_{amb} increases, ρ_G increases and fig.4 shows that ω_{iamax} increases : then Wer decreases. Fig.10 shows that an augmentation of P_{amb} will make the drop diameter decrease if Wer is high (corresponding to low injection pressures) and will increase d_G if Wer is low (corresponding to high injection pressures).

A similar behaviour has been experimentaly found by Tabata et al. [7] in a slightly different case. It appears here that the explaination of the opposite influence of the external pressure according to the injection pressure may be linked to the fact that the liquid system is thinning.

4 CONCLUSION

In this paper the instabilities of liquid systems (flat and cylindrical) in an atmosphere at rest have been investigated by the use of linear theories.

The behaviour of flat systems was found to be totaly determined by a set of non dimensionalized numbers and cylindrical systems were found to be affected by the destabilising effects introduced by the internal radius. However cylindrical systems behave as flat ones in many cases.

It is point out here that these approaches may be easily adapted to different situations and used as predictive tools. For instance, calculated mean drop diameters are presented for a set of swirl atomizers. A second application shows the influence of the external pressure on the drops formed by a thinning liquid sheet.

Most of the time, the results obtained are not accurate but the tendances they bring out are of practical interest and may be used with confidence.

NOMENCLATURE

a	internal radius of the cylindrical lquid system
A, B	constants
Cel	propagation wave speed = ω_r/k
C_i	coefficients of the dispersion equation
d_G	calculated drop diameters
$\overline{dqp}$	measured mean drop diameters
h	thickness of the liquid systems
$I_n(kr)$, $K_n(kr)$	modified Bessel functions of order n
k	longitudinal wave number
k_{amax}	k for the dominant wave
K_T	total wave number $=\sqrt{k^2+(n/a)^2}$
n	azimuthal number of perturbation
(r , θ , x)	cylindrical coordinates system
t	time
U	component of velocity along the axis Ox
V	azimuthal component of velocity
(x , y)	cartesian coordinates system
α	amplitude of the functions η
β_P	angle between the axis of symmetry and the direction on propagation of the perturbation
β_V	angle between U_T and the axis of symmetry
ϕ	perturbation potential functions
η	displacement of the interfaces
ρ_G, ρ_L	gas and liquid densities respectively
σ	surface tension
ω	pulsation
ω_i	growth rate of the perturbation (imaginary part of ω)
ω_{iamax}	maximum growth rate

REFERENCES

[1] G.D. Crapper, N. Dombrowski and G.D. Pyott, "Kelvin-Helmholtz wave growth on cylindrical sheets", J.F.M. vol.68, p.497-502 (1975)

[2] C. Dumouchel, M. Ledoux, M.I.G. Bloor, N. Dommbrowski and D.B. Ingham, "The design of pressure swirl atomizers", 23rd Symposium on combustion Orleans July 1990

[3] W.W. Hagerty and J.F. Shea, "A study of the stability of the plane fluid sheets", Journ. Appl. Mech. p 509-514 (Dec 1955)

[4] N. Dombrowski and P.C. Hooper "The effect of ambient density on drop formation in sprays." Chem. Eng. Sci., vol.17, p 291-305 (1962)

[5] H.B. Squire, "Investigation of the instability of a moving liquid film." Brit. Jour. of Appl. Phys., vol.4, p.167-169 (1953)

[6] C. Guilié, "Etude expérimentale et théorique de l'injection aérodynamique.", Thesis ENS Mines de Paris Jan.1987

[7] J. Martinon, "Instabilités d'une nappe liquide cylindrique en présence de deux écoulements gazeux." Int. report ENSM Paris (1982)

[8] M. Tabata, M. Arai and H. Hiroyasu, "Effect of fuel viscosity and surface tension on diesel spray drops." ICLASS 85 paper II/B/1

FLOW CHARACTERISTICS OF ATOMIZING LIQUID JET BY SUPERSONIC FLOW AND RELATED SHOCK WAVE/ BOUNDARY LAYER INTERACTION

T. Arai, H. Sugiyama, N. Uno and T. Takahashi

Muroran Institute of Technology
Muroran, Hokkaido, Japan

ABSTRACT

Flow characteristics of atomizing liquid jet by supersonic flow and related shock wave/boundary layer interaction were observed by flow visualization technique of schlieren method with spark flash. Two types of liquid injector were used : a flat plate injector and a backward step injector. The liquid was injected vertically into supersonic flow of Mach number 2 from one orifice of 1 mm diameter at the flat plate or at just behind backward step. In the case of a flat plate injector, the liquid was atomized by boundary layer flow, and the liquid injection produced the bow shock wave or pseudo-shock wave (multiple normal shock train). In the case of a backward step injector, the liquid was not only atomized by boundary layer flow but also supersonic main flow, since the low pressure part was formed outside the boundary layer due to the existence of the expansion fan at the backward step. Therefore, more fine particles will be produced by a backward step injector than a flat plate injector. Interaction between the shock wave and the boundary layer leads to flow separation and this might promote to mix of the fine liquid particles into the main flow.

INTRODUCTION

There are a number of practical applications of transverse injection of a liquid jet into a high-speed gas stream. Among a large variety of applications, fuel injection for scramjets, ramjets, and afterburners, thrust vector control in rockets, cooling sprays in turbines, and localized cooling on re-entry bodies exemplify this important field of study. In all of these applications, cross-stream penetration and the droplet size resulting from the break up of the liquid jet was items of primary engineering interest. These general problems are still very important and were investigated by many researchers[1-7]. The flowfield in the inlet/combustor isolator section of scramjet engine is more complex due to the liquid injection/supersonic flow interaction. The performance of the scramjet and ramjet engines strongly depends on the flow characteristics. However, detailed information concerning with the change of the flowfield due to the liquid injection into supersonic flow is not available yet. Furthermore, the atomization mechanism of liquid fuel and the following process of gas-liquid fuel mixing in supersonic flow is very important for developing the scramjet engines.

The purpose of this paper is to clarify the liquid atomization process with

following gas-liquid mixing process in supersonic flow and shock wave/boundary layer interaction due to the liquid injection.

EXPERIMENTAL APPARATUS AND PROCEDURE

The tests were performed in a 50×50 mm supersonic suction type wind tunnel at Muroran Institute of Technology. Figure 1 shows the schematic diagram of the experimental apparatus and measuring system. The supersonic flow trials were at atmospheric ambient stagnation pressure and temperature. The symmetric Laval nozzle is used so that the upper and lower wall boundary layers entering the test section have identical properties. The side wall of the test section is provided with an optical glass to measure the flow characteristics optically. Two symmetric Laval nozzles were provided to obtain the nozzle exit Mach numbers of 1.8 and 2.0. In the present study, two types of liquid injector were used as shown in Fig.2. One was a flat plate injector, and the other a backward step injector. Water and ethanol were used as the injectant. The liquid was injected vertically into supersonic flow from an orifice of 1 mm diameter. The driving force for the liquid injection was the pressure difference between ambient pressure and local pressure at exit of the orifice in the wind tunnel. The velocity of the liquid injecting was about 6～8 m/s. The flow characteristics were investigated by using the flow visualizations technique of schlieren and shadowgraph method with 0.8 μs flash light. The wall static pressure distributions were measured at upper wall of the square duct using mercury manometers. The velocity profiles, in the case of no liquid injection, were measured using a fiber optic dual-beam Laser Doppler Velocimeter (LDV) (TSI). The TSI six jet atomizer using water was used to generate seed particles with a polydispersed size distribution with mean diameter of about 2 μm. It was confirmed by the preliminary experiments that the incoming supersonic flow showed a high degree of two-dimensionality. All measurements were made on the midplane of the wind tunnel except for a limited series of spanwise traverses made to check the degree of two-dimensionality of the flow.

RESULTS AND DISCUSSIONS

Velocity distribution of main supersonic flow

Figure 3 shows the velocity distributions of the main supersonic flow. The top view is the case of flat plate injector type and bottom view the case of the backward step injector type. The thickness of the boundary layer just ahead of the injector for the flat plate type was about 5 mm and the boundary layer thickness just ahead of the step was also about 5 mm. It was confirmed by the measurements of the velocity distribution in the boundary layer that it was turbulent.

Flow visualization of atomizing liquid and flow pattern

Flat plate injector. Figure 4 shows the liquid injected vertically into supersonic flow of Mach number 2.0 with following mixing process and related flow pattern. The top and bottom views show the water and ethanol injection, respectively. The vertical line in the photos indicates the marker of the injecting location. It is seen from the top view of Fig.3 that the thickness of the fully developed turbulent boundary layer was about 5 mm. The top and bottom photos of Fig.4 show the bow shock produced by the liquid injection. The bow shock reflects at the upper and lower walls and propagates downstream. It is seen from the top and bottom views that the liquid was atomized by the boundary layer flow so that the liquid particles scarcely diffused into the main supersonic flow.

Figure 5 shows the flow patterns of Mach number 1.8. The top view of water injection case shows that the pseudo-shock wave[8] (multiple shock train[9]) was

formed by the liquid injection/shock wave/boundary layer interaction. In the case of ethanol injection, the pseudo-shock wave was formed far downstream, which was found by the wall static distribution. The pseudo-shock wave causes the loss of pressure and oscillation phenomena of main flow so that the generation of the pseudo-shock wave might have bad influence on the supersonic mixing and supersonic combustion mode. However, as seen from the top view of Fig.5, the separation region under the first shock wave of the pseudo-shock wave contributes to the diffusion of the liquid particles.

Backward step injector. Figure 6 shows the schematic view of the flow field of the main flow Mach number M=2.0. The orifice was located 5.4 mm from the backward step. Figure 7 shows the schlieren photographs of air flow patterns and liquid injected by backward step injector. The left and the right side photos are taken, respectively, with a horizontal knife edge and a vertical one. From the top view of the left side, it is seen that the turbulent boundary layer was separated at a backward step and formed a free shear layer, which went through a reattachment process. The average reattachment line is located approximately 2～2.5 step heights from the step. The expansion fan at the backward step and reattachment shock wave are also observed. The middle and bottom photos show the flowfield in the cases of water injection and ethanol injection, respectively. The weak bow shock wave produced by the liquid injection can be seen in the expansion fan. The strength of the reattachment shock wave with liquid injection grew weaker than the case of no liquid injection. Figure 8 shows the behavior of the liquid atomization by backward step injector, which was taken by backlight photograph method. As compared between the spatial position of the atomizing liquid in Fig.8, the boundary layer thickness and station of the bow shock wave in top view of Fig.7, it seems that the liquid was not only atomized by boundary layer flow but also the supersonic mainflow. Therefore, liquid particles produced by a backward step injector may be more fine than that of a flat plate injector because the liquid is atomized by higher velocity gas flow.

Wall static pressure distributions

Figure 9 shows the time mean wall static pressure distributions on the upper wall along the duct for the case of the flat plate injector. The symbols □, ○ and △ indicate the conditions of no liquid injection, water injection and ethanol injection, respectively, and Pa is the atmospheric pressure. The abscissa x means the downstream distance from the injection hole. The time mean wall static pressure increased abruptly from x=350 mm for all three cases. This indicates generation of pseudo-shock waves (shock train). Figure 10 shows the time mean wall static pressure distributions at the upper wall along the duct for the case of the backward step injector. The symbols in Fig.10 have the same meaning as before. The high pressure region are not observed in all cases in Fig.10 and the pseudo-shock wave was not generated. The liquid injection has little influence on the time mean wall static pressure distribution for the two types of injector, in the present experiments using the mercury manometers system.

Effect of pre-injection on liquid particles mixing into main flow

Figure 11 shows the schlieren photograph of the liquid (water) atomization from the flat plate injector with two holes located 15 mm apart. The liquid injected from the second hole has a higher penetration height than that from the first injection one (pre-injection). From the above experimental result, it may be said that the injection of liquid just upstream to the main injection controls the turbulent boundary layer and promotes the mixing between the main flow and the liquid particles.

Penetration height of liquid jet for the case of flat plate type injector

The penetration height was determined by the observation of the amount of light that scattered when a beam of light passes through a suspension of droplets. Figure 12 shows the variations of the penetration height for the case of water injection and ethanol injection. It is considered that the penetration height corresponds to the mixing layer thickness. The symbols ● and ▲ mean the water and ethanol injection for the case of Md=2.0 (Md : design Mach number of the Laval nozzle, free stream Mach number M=1.8), respectively. Also, the symbols ○ and △ mean the water and ethanol injection for the case of Md=2.2 (free stream Mach number M=2.0), respectively. The mixing layer for the case of Md=2.0 was thicker than that of Md=2.2. In the case of the water injection for Md=2.0, the supersonic mixing was not happened by the generation of the pseudo shock wave in the duct (as it was seen in Fig.5). It can be seen that the mixing layer thickness by ethanol injection was larger than by water injection case. The reason for this result has not been clarified.

CONCLUSIONS

The liquid atomization process with following gas-liquid mixing process in supersonic flow and shock wave/boundary layer interaction by the liquid injection were investigated by the schlieren photograph and shadowgraph method. It was cleared that the liquid injection in supersonic flow produces the bow shock wave and/or pseudo-shock wave (multiple shock train), resulting supersonic flows more complicated. The behavior of the liquid atomization process and mixing process are strongly influenced by the shock wave/boundary interaction. It is shown that the production of more fine liquid particles and the promotion of the gas liquid mixing can be expected if the reflection of the shock wave and the expansion fan at the backward step would be effectively used. Therefore, the change of flow pattern, which includes the generation of the shock wave, the development of the boundary layer and the separation of the boundary layer, should be used effectively for the liquid atomization technique by the supersonic flow.

REFERENCES

1. Schetz, J., Kush, E. and Joshi, P., Wave Phenomena in Liquid Jet Breakup in a Supersonic Crossflow, AIAA Journal, Vol.18, No.7, pp.774-778 (1980).
2. Reichenbach, R. and Horn, K., Investigation of Injectant Properties on Jet Penetration in a Supersonic Stream, AIAA Journal, Vol.9, No.3, pp.469-472 (1971).
3. Schetz, J. and Padhye, A., Penetration and Breakup of Liquids in Supersonic Airstreams, AIAA Journal, Vol.15, No.10, pp.1385-1390 (1977).
4. Less, D. and Schetz, J., Transient Behavior of Liquid Jets Injected Normal to a High-Velocity Gas Stream, AIAA Journal, Vol.24, No.12, pp.1976-1986 (1986).
5. Nejad, A. and Schetz, J., Effects of Properties and Location in the Plume on Droplet Diameter for Injection in a Supersonic Stream, AIAA Journal, Vol.21, No.7, pp.956-961 (1983).
6. Heister, S., Nguyen, T. and Karagozian, A., Modeling of Liquid Jets Injected Transversely into a Supersonic Crossflow, AIAA Journal, Vol.27, No.12, pp.1727-1734 (1989).
7. Thomas, R. and Schetz, J., Distributions Across the Plume of Transverse Liquid and Slurry Jets in Supersonic Airflow, AIAA Journal, Vol.23, No.12, pp.1892-1901 (1985).
8. Arai, T., Sugiyama, H., Abe, H., Takahashi, T. and Onodera, O., Internal Structure of Pseudo-Shock Waves in a Square Duct, AIP CONFERENCE

PROCEEDINGS 208 (Current topics in shock waves, 17th International Symposium on Shock Waves and Shock Tubes, Bethlehem, U.S.A., 1989), pp.850-855 (1989).
9. Carroll, B. and Dutton, J., Turbulence Phenomena in a Multiple Normal Shock Wave/Turbulent Boundary Layer Interaction, AIAA Paper No.90-1455 (1990).

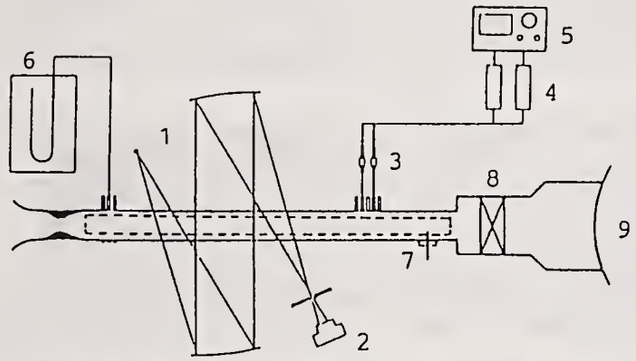

1:Schlieren System
2:Camera
3:Pressure Transducer
4:D.C.Amplifier
5:Synchroscope
6:Mercury Manometer
7:Shock Location Controller
8:Valve
9:Vacuum Tank

Fig.1 Schematic diagram of experimental apparatus

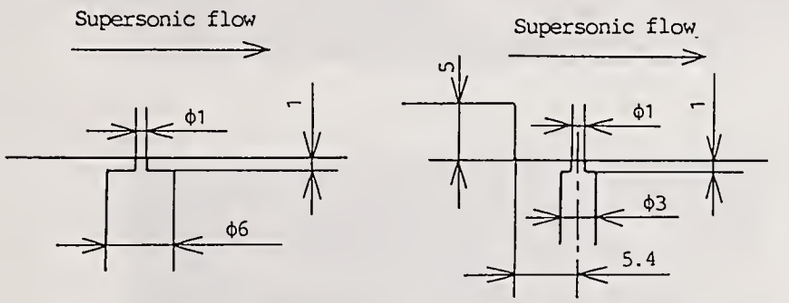

(a) flat plate injector (b) backward step injecter

Fig.2 Schematic view of injectors

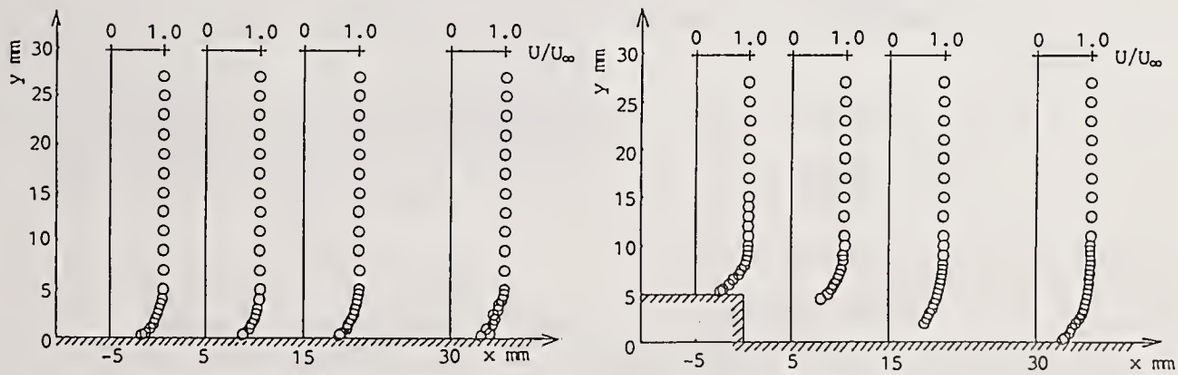

(a) flat plate injector (b) backward step injector

Fig.3 Velocity distributions of main supersonic flows, U_∞ means the velocity of free stream flow outside boundary layer and corresponds Mach number M=2.0.

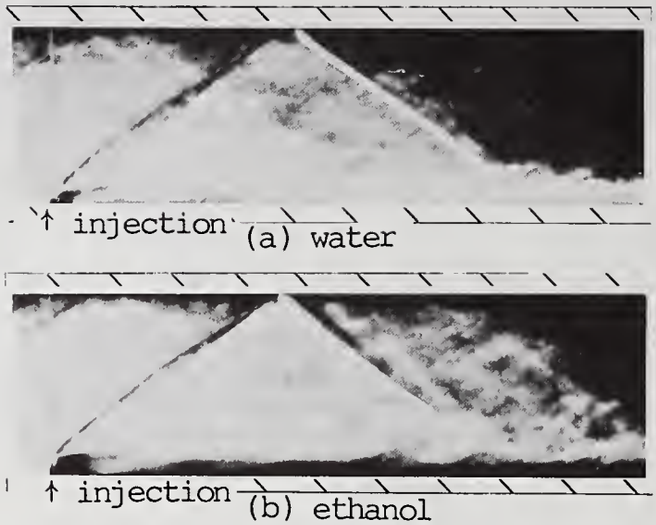

Fig.4 Schlieren photographs of liquid injected vertically into supersonic flow of M=2.0

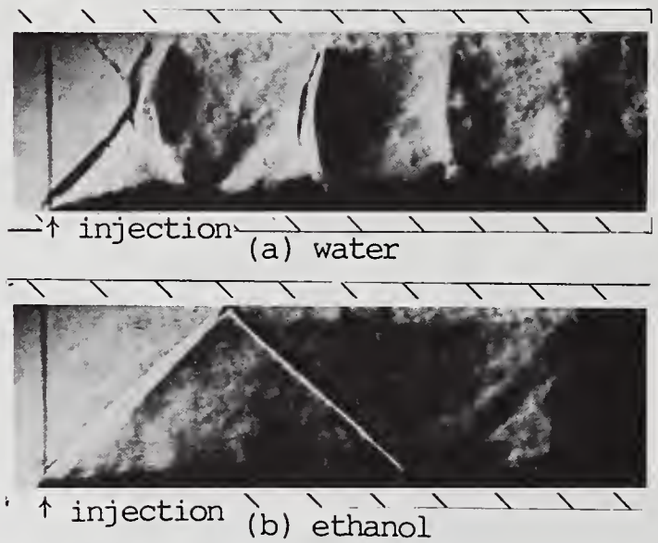

Fig.5 Schlieren photographs of liquid injected vertically into supersonic flow of M=1.8

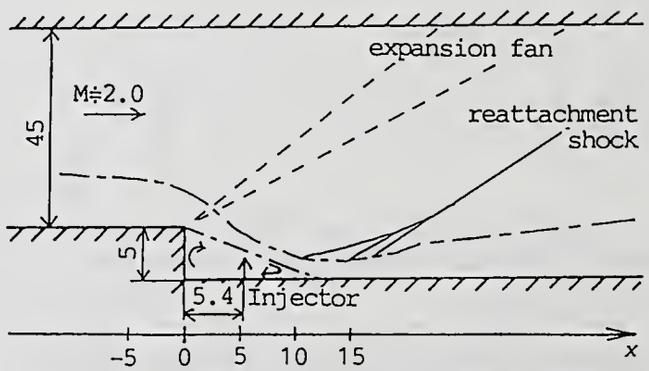

Fig.6 Schematic view of flow field at backward step injector

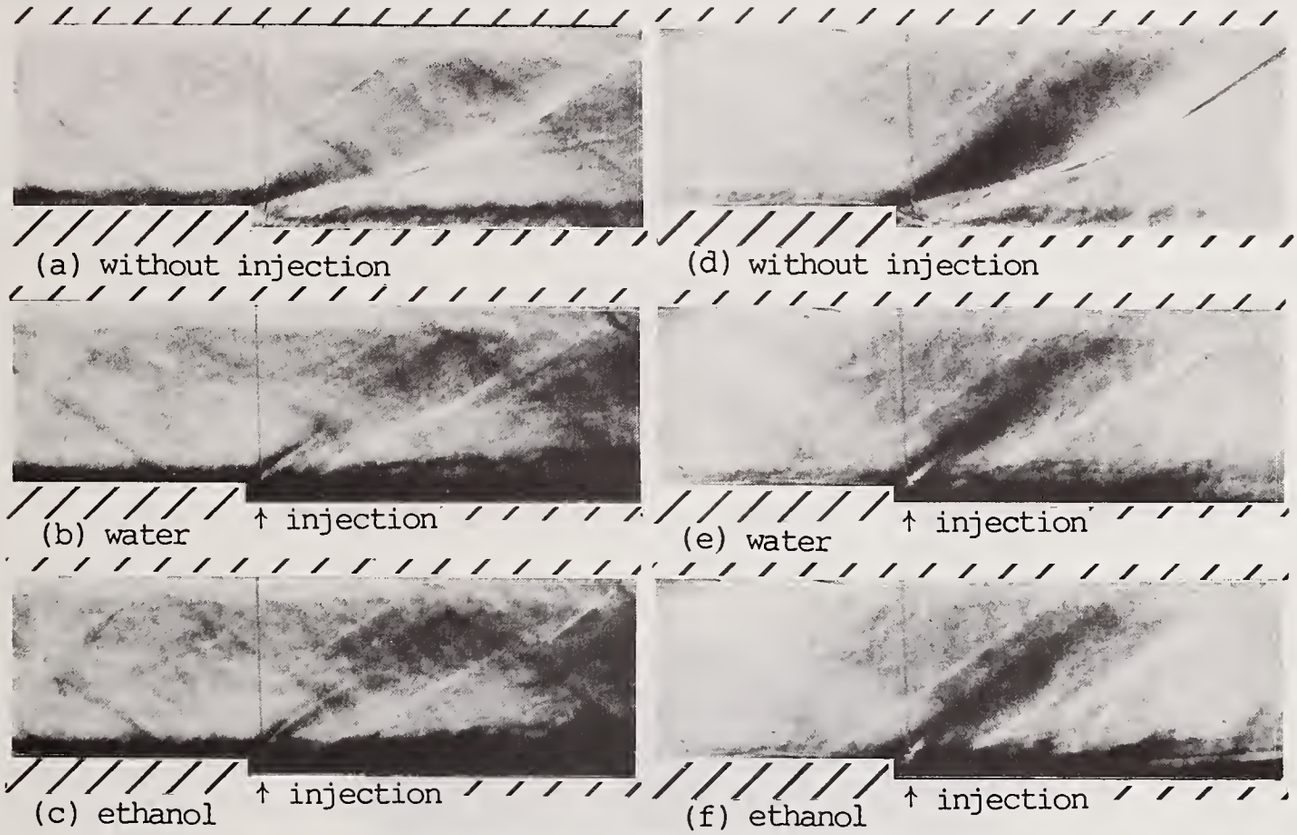

Fig.7 Schlieren photographs of air flow pattern and liquid injected by backward step injector at M=2.0 ; left side photos are taken with a horizontal knife edge and right side photos with vertical one.

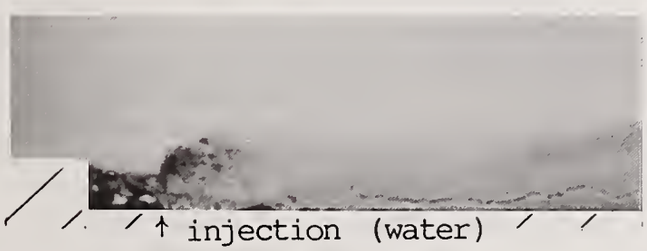

Fig.8 Liquid atomization by backward step injector taken by backlight method at M=2.0

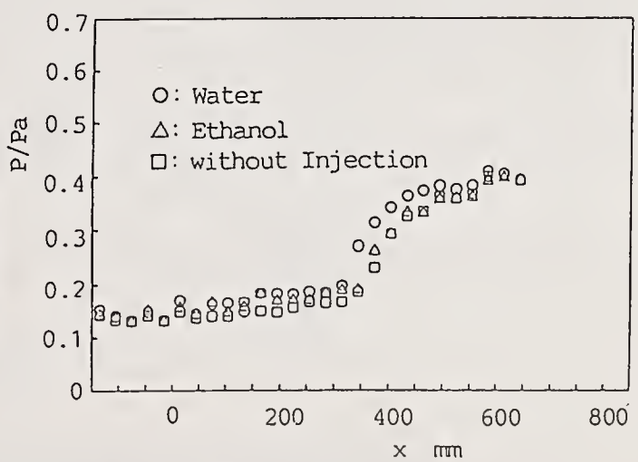

Fig.9 Wall static pressure distributions for flat plate injector at M=2.0

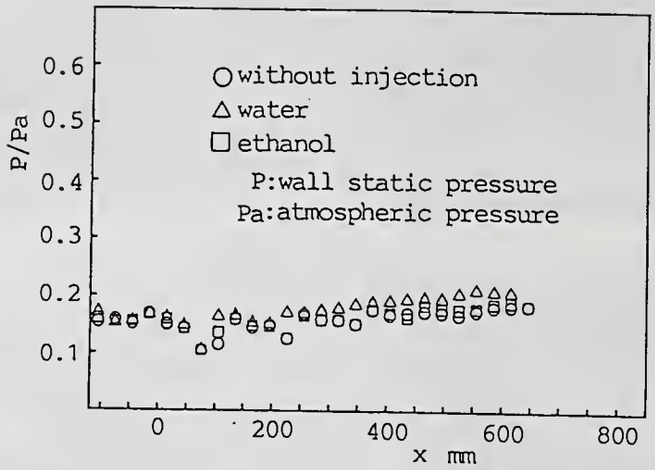

Fig.10 Wall static pressure distributions for backward step injector at M=2.0

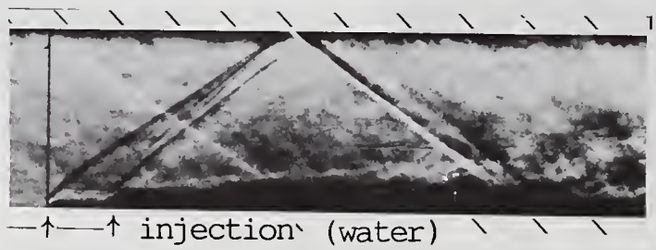

Fig.11 Schlieren photograph of double injections into supersonic flow for flat plate injector at M=2.0

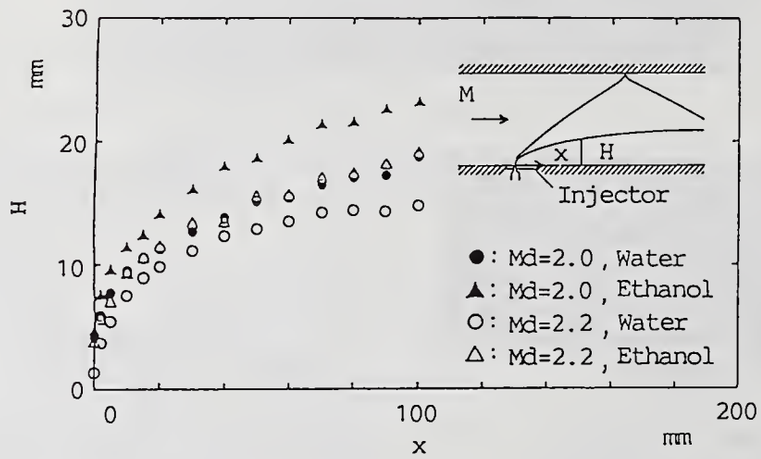

Fig.12 Penetration heights of liquid jet for flat plate injector

SHOCK WAVE INTERACTION WITH LIQUID LIQUID ATOMIZATION AND ANALYSIS SCHLIEREN, LIGHT SHEET AND HOLOGRAPHIC RECORDS

N.M. Fargère

Centre d'Etudes du Bouchet
Vert-Le-Petit, France

ABSTRACT

Though subaquatic explosions have been the subject of many studies, the interaction of the subaquatic shock wave with the liquid air interface is not well known, particularly in its earliest effects. In particulary, microscopic and precocious events occur during the acceleration of the free surface of the liquid.

We used several techniques (fast camera, image convector, schlieren and ombroscopie records...) to record the water surface motion and the main phenomena above it. For the description of the first phenomena, holographic techniques appeared very instable, and we observed the free surface movements using light sheet for the latter events, like plume.

GENERAL DESCRIPTION

The experimental set up is a test tank (1 x 1 x 0,5 m3 P.M.M.A. of optical quality) filled tap water [1].

A 215 mg PETN detonator is ignited at several immersion dephts, basically 0,25 m, the depth for which all the main characteristics of the problem have been studied. This in order to study the influence of the shock intensity on the surface effects. The detonator is a very simple way to generate a spherical shock wave far enough from the detonation point the profile of which is checked by pressure transducers and compared with the theorical calculations [2]. The correlation obtained allows us to calculate the rough parameters of similitude in Cook formula .

A typical case of the shock front properties impacting against the water-air interface is a peak pressure lower than 100 bars, usually 50 bars, a shock velocity in water : 1500 m/s, a maximum free surface velocity : 7 m/s.

Several optical methods are used :

1) Direct camera records.
2) Schlieren and ombroscopic cinematography using an argon laser modulated light (10 µs duration, 900-1000 Hz frequency) and a drum camera.
3) Holographic technique using a pulsed laser.
4) Light sheet laser techniques.

THE OBSERVED MACROSCOPIC PHENOMENA

The observed effects at the water surface are classified in two main categories : macroscopic and microscopic.

During its detonation in a liquid medium, the solid explosive is rapidly transformed into gaseous products at high temperature and pressure. The so created bubble expands rapidly and its inner pressure decreases down to a pressure slightly lower than the hydrostatic equilibrium corresponding pressure. The bubble then shrinks until the limit of gas compressibility is reached, the movement inverto and a secondary shock wave is generated.

This phenomenon occurs after the second shock and so on. Just after detonation, the first shock wave separates from the bubble and spreads out in surrounding water at a velocity which falls rapidly to a slightly supersonic one. Its peak pressure decreases rapidly, a great part of the shock energy being dissipated during the propagation in

water. Coming up at the surface, it transmits a wave in the air and a rarefaction wave goes back towards the detonation source. The above parameters highly depend on the depth and on the charge weight. It is known that for small charges, at relatively important depth (Ro/do <<1, Ro radius of charge, do depth), the reflection can be considered as total and the shock transmitted into the air is weak [(3), (4), (5)].

In the case we are interested in (Ro/do << 1), the first macroscopic effect is bound to the arrival of the shock wave itself. It is the shock black ring which spreads on the water surface. Then we observe the dome, mass of water accelerated by initial shock and sub surface movements. Its initial speed is very close to the speed of matter bound to the shock. The maximum heigth of the water above the surface is reached when the forces of air friction and gravity balance those of upward motion. In our case, the secondary dome, bound to the going up of secondary shock wave and to the bubble second expansion, adds to the principal dome when it's going down. There is then a break and the beginning of the water plume. It is noted that the coming out of the column (plume) is closely linked to the depth of the detonation and to the used explosives characteristics (mass...). In a general way the column is the result of either breaking of dome or coming up in the air of detonation products when these are still energetic (first period (s) of pulsation interacting with the surface) [(6), (7), (8)]. These phenomena have been observed by ombroscopy and schlieren techniques on high speed camera. The microscopic effects show the coming up at the surface of small jets (which have been observed by means of an image convector tube) and a suspension of mistlike droplets. A first approach of jets formation mechanism has been made thanks to a rapid camera and ombroscopy records.

The description of the microscopic effects and their origins is the aim of this paper. The results described are the one obtained with the laser means of recording. Lasers are used as energy sources (light sources) as well as specific precision means. They offer several technical advantages : three dimensional image (holography), high energy (light sheet), great precision of synchronisation and a short exposure time. We must underline the great possibilities in magnification and the excellent definition.

CAVITATION

Liquids can more or less withstand tensions. Untreated, their continuity happens to be broken up by formation of cavities. This cavitation tendency is especially increased by presence of impurities. In the case of sea water or industrial water, the ambient pressure under which the cavitation increases indefinitely is very close to saturated vapor pressure. This approximation does not take into account the size of impurities seeding. We admit that if the pressure nearby a bubble exceeds saturated vapor tension, the cavity disappears. There is an implosion with creation of a jet characterized by a high speed and the emission of a compression wave [(9), (10), (11)].

The formation of bubbles, their gradual growth are also influenced by water physico-chemical properties (inclusions, surface tensions, specific viscosity....). The modeling of the phenomenon is not easy, especially in presence of a free surface.

After their formation, the bubbles of an initial diameter of some micrometers can be submitted to pulsation, according to the flow where they happen to be [12]. This pulsed movement is characteritic and can lead to maximal diameters of several tenth millimeters associated to a life time from some hundred of nanosecondes to several milliseconds, limited by a relatively violent implosion [13].

Assuming that the cavitating pressure is saturated vapor pressure we decided to apply first the Cole formulations [14]. The experimental cavitation zone was not compliant with the one we numerically found. We did not take into account the bubble erosive action on the expansion front. Using Dubesset et Lavergne [15] method and a trick in mathematics we found to introduce time, we obtained the specific shape of the cavitation zone at different instants and depths. An analysis of the numerical results (minimum and maximum depth) shows a relative agreement with the experimental results, although by excess, they are very closed to Kedrinskii's [16]. The experimental cavitation zone has been deduced from under water surface holographic records.(Fig.1)

INSTABILITIES AND BREAK UP OF LAMINAR JETS

Basically, Plateau [17] attributed the main mechanism to the interfacial tension. He showed that if there is an axisymetric disturbance in the jet, it reduces the free energy of the jet if its wave length is greater than the original undisturbed jet circonference. The system attempts to minimize the free surface energy, aiming at a minimum surface area per volume unit, reaching then the break up in spherical drops. Rayleigh [18] gave the equations and correlated the amplitude growth rate with the perturbation wave length. He found that if all axisymetric disturbances - which are characterized by a wave length greater than the circumference of the undisturbed jet - are unstable, only one has got an amplitude growing faster than the others, dominating the break up and fixing the jet's length and drop's size.

The first studies are based on the assumption that there is a pressure initiated perturbation originated at the jet's surface which equation should be :

$$\delta=\bar{\delta}_0 \exp(qt+ikz) \quad (1)$$

Weber [19] also solved the Navier-Stokes equation for a liquid jet. He showed that the perturbation characterized by the wave number k* rises rapidly and makes the jet break up into drops. Tomotika [20] solved the equation in his study of jets in 1966. The dimensionless growth rate and the wave number of the disturbances that grows most rapidly are given by, respectively [21].

$$Q^* = q^* \sqrt{2\rho \frac{a^3}{\sigma}} \quad (2) \quad \text{and} \quad x^* = a\,k^* \quad (3)$$

Assuming that break up occurs when the disturbance grows up to be comparable with the jet radius, break up time T is given by.

$$T = \frac{\mathrm{Ln}\left(a/\bar{\delta}_0\right)}{q^*} \quad (4)$$

Assuming that jet's radius and velocity are quasi constant we can say that break up length is given by T x u.

$$L = \mathrm{Ln}\left(\frac{a}{\bar{\delta}_0}\right) \cdot \frac{u}{q^*} \quad (5)$$

The liquid in a column of one special wave length turns into one drop of corresponding volume, the diameter of drops formed from jets of those type is :

$$d = \left(\frac{1{,}5.\pi.D^3}{x^*}\right)^{1/3} \quad (6)$$

HOLOGRAPHY

General Principle

General Principle of classical photography is based on the record of light, intensity and wave length. Moreover holography calls for light phase, which allows to integrate for recording, the relative position of different parts of the object. The light diffused by the objects is recorded on a very high resolution power plate on which is superposed a reference wave. The complex diffraction so formed net diffracts light when placed in reference wave, then restoring a real image and a virtual one of the object.

Microholography

Because of the phenomenon low rate of darkening (< 10%) we used GABOR mounting. The separate reference assembling regains an interest for recording the phenomenon after 2500 µs. We then got rid of field observations (astigmatism, coma...) but not of the spherical one [22].

Restitution is obtained by the analysis of the real image recovered on a TV set. Reconstruction is made semi-automatically by means of an image analyser [(23), (24)].

A synchro-optic cell is adjusted to obtain a double exposition, allowing to record of the object in two consecutive positions, and to calculate the speed calculation.

We used a ruby oscillator laser (50 mJ, 15 ns) for recording with an optic system [Div. Doublet (20, 30 mm), Conv. lens (800 mm)]. For reconstruction we used an unfocal system (65 mm) and an objective. Taking into account the errors in the different positionnings of detonator and hologram (recording and reconstruction) the relative error is never more than 10 % in depth, and 5% in the observing plane.

Hologram assessment and results for jets

General remarks. It is difficult to assert the occurence of such and such mechanism. We will see that the observations allow the appraisal of :

1) the periodic instabilities along the jet,
2) the forces of tension which depend upon the velocity gradient in the jet.

These two mechanisms take place separately, the instabilities being able to grow and to set only if the whole jet exists. However, the conjugate mechanisms are sometimes simultaneously observed. The velocity gradient works in terms of stretching and shearing, the break up is then irregular.

Regular drops generated by jets are mostly relevant to Rayleigh's instabilities.

Specific results assessments and exploitation gave us the following set of average results, where d and T are measured and calculated directly, d' an T' are deduced from calculations.

n	1	2	3	4	5	6	7
d (µm)	194	279	320	410	450	200	260
d' (µm)	198	250	240	310	310	140	270
%	2	11	28	27	36	33	4
T (µs)	190	790	528	434	368	475	2570
T' (µs)	405	353	670	360	460	439	2500
Δ (%)	66	72	25	15	24	8	3

The variation of relative difference between calculated and measured diameters is in the range of 2 to 36 %.

If we exclude two results (n = 1,2) that we assume to correspond to a different break up mechanism (striction), the times T and T' are in agreement in the range of 3 to 25%.

Error can be imputed to the specific experimental measurement error (about 8%) and to the fact that Tomotika theory is relevant to very constant laminar jets (created in reproductible conditions) characterized by constant speed. If the following set shows that we realize one condition (one jet drops production) speed is not totally constant and we know its importance in the rupture time calculation.

n	1	2	3	4	5	6	7	8	9	10	11	12	13
d(µm)	89	74	89	81	71	77	89	77	71	71	89	74	75

LIGHT SHEET EXPERIMENTS

Light sheet laser assembling - Dispersion laws

The light sheet laser mounting is very closed to the microholography one. The main difference is due to the specific optics used. We calculated the numerous parameters aiming at a maximum energy in the conic sheet created by the quartz bar (the Neodym laser used was characterized by 1,15 J (1050 nm) and 250 mJ (532 nm) for a 25 µs duration. The beam diameter is 7 mm).

Exploitation was built over the use of an image analyser. For several depths and times we analysed the photos. We were then able to appraise MMD (Mass Median Diameter) and NMD (numerical Median Diameter) for each trial.

The theorical laws are :

Drop's volume $$\therefore V = \frac{4}{3}\pi R^3 = \frac{1}{6}\pi \phi^3 \qquad (7)$$

Drop's mass $$: M = Vd \qquad (8)$$

Mass variation $$: \frac{dM}{d\phi} = \frac{MT}{(\ln \sigma)^2 . \sqrt{2\pi} . \phi} . \exp\left(-\frac{\ln \phi - \ln MMD}{\sqrt{2} . \ln \sigma}\right)^2 \qquad (9)$$

$$(\ln \sigma)^2 = \frac{\sum_i (\ln \phi - \ln MMD)^2 . M_i}{\sum_i M_i} \qquad (10)$$

Numerical variation : $\frac{dN}{d\phi} = \frac{NT}{(\ln \sigma)^2 . \sqrt{2\,\Pi} . \phi} \exp - \left[\frac{\ln \phi - \ln NMD}{\sqrt{2}\ln \sigma}\right]^2$ (11)

$$(\ln \sigma)^2 = \frac{\sum_i (\ln \phi - \ln NMD)^2 . N_i}{\sum_i N_i} \quad (12)$$

MMD and NMD relation : $\text{Ln MMD} = \text{Ln NMD} + 3 (\ln \sigma)^2$ (13)

Results

Comparing curves of theorical dispersion and the experimental one we found that if we are very closed as far as we compared NMD's results, we weren't not so acute in MMD. Knowing that the NMD's laws are the more followed, we used it with the aim of comparing the theoric MMD and the experimental one (Fig.2, Fig.3).

Depth mm	Time ms	MMD measured mm	NMD measured mm	Ln σMMD	Ln σ NMD	MMD calculated mm	(1)
250	26	1.6	0.7	0.4982	0.5239	1.59	0.33
250	24	1.5	0.5	0.5448	0.5338	1.17	22
250	18	1.2	0.6	0.5055	0.4929	1.24	3.6
250	9	1.6	0.6	0.5030	0.5298	1.39	12.9
225	4.837	1.5	0.5	0.5245	0.5248	1.14	24
175	4.837	1.5	0.6	0.5014	0.5698	1.59	5.9
160	4.837	1.5	0.6	0.4614	0.5363	1.42	5.2

(1) Δ MMD/MMD measured %.

We can notice that the accurracy is somewhat variable, but generally closed to 10 % and less.
We encountered some difficulties with the beam's width and its influence on the light transmission.

SCHLIEREN AND OMBROSCOPY

We used an Argon laser, an acousto-optic modulator and a Gallus, drum camera to realize the first schlieren views (interframe time 1,1 ms, impulse time 10 µs, rotating frequency 396 Hz). They enabled us to identify with certainty the jets we already saw with the image tube convector. But we had some difficulties with a too weak light intensity so we decided to use
ombroscopy with a very close setting. We realized different trials and we were able to quantify the peales and dome behavior (position and velocity). We identified the jets instabilities but the accuracy was not so good, but the instabilities under the surface were identified too .

CONCLUSIONS

The free surface motion of water-air interface accelerated by the impact of a shock impulse generated by an explosive has been observed by means of holographic technique.

The results of the holograms analysis allowed us to confirm and to clarify the role of cavitation phenomena which :

- is identified as soon as the reflection of the shock wave takes place at the interface,
- creates micro jets in the air, the distribution of which is correlated with the propagation of the cavitation phenomenon,
- is in relatively good agreement with a numerical model taking into account the erosion of he expansion front.

Holography appears to be a very suitable technique to prove the microjets existence and to visualize the jets instabilities.

The microjets deformation and rupture seem to be consequence of:

- periodic instabilities along the jet,
- forces of tension which depends upon the velocity gradient in the jet.

Dispersion laws are followed somewhat accurately. The light sheet results are very interesting.

Shlieren and ombroscopic records enabled us to characterize the phenomena occuring at the surface between the very early instants (bubbling and peacks birth) and the whole effects (plume).

Shock wave interacting with a liquid air interface is able to generate cavitation and small bubbles, the implosion of which is responsible of microjets and small droplets production in air. New studies of the implosion of the bubbles are needed to contribute to the behavior of cavitated liquid supporting chemical reactions [25].

NOMENCLATURE

a = radius of jet (m),
d = diameter of drop (m),
x = dimensionless wave number.
k = wave number (m^{-1}),
L = break up length of jet (m),
M = drop Mass
MT = Total measured drop's mass
N = Drop Number
NT = Total measured drop's number
Q = dimensionless growth rate,
q = growth rate of disturbance (s^{-1})
R = Drop radius
T = break up time (s),
t = time (s),
z = axial coordinate (m),
V : Drop Volume
δ = disturbance on jet (m),
ϕ =Drop diameter
ρ = density of liquid (kg/m3),
σ = interfacial tension (N/m),

BIBLIOGRAPHY

1- Jonhson J.N.: Calculated shock pressures in the aquarium test - Los Alamos National Laboratory NM 87 545. 1982 (US Dpt. Of Energy).

2- Cook M.A, Keyes T.T, Ursenbach W.O.: "Measurements of Detonation Shock and impact pressures" University of Utah - Salt Lake City.

3- Mader C.L."Compressible Numerical Calculations of Underwater explosion". Los Alamos Scientific Laboratory University of California (1971).

4- Snay H.G.and Rosenbaum S.H.: "Shock wave parameters in Fresh Water for pressures up to 95 kbars" Naval report 2383 US Naval Ordnance Laboratory - White Oak, Maryland (1952).

5- Wang Xu, De Yang Yu, Yun-Xiang Xu, Xiuny-Fei Zeng : "Effects of charge diameter on detonation, Pressure Measured by aquarium technique". Lanzhou Modern Chemistry Research Institute. Chine.

6- Sakurai A and Pinkson J.M, US Army Engineering :"Water ways Experiments Station" Technical Report n° 1-771 (1967).

7- Zaslavskii BT : ZH Prick Mekls - Telek - Fig 4.50 (1963).

8- Holt M."Underwater explosions" - Ann Rev. Fluid - Mech § 187-214 (1977).

9- Flynn H.G.: "Physics of Acoustic Cavitation in Liquids". Physical Acoustics. Col. Warnen, P. Manon, Vol 1B (1964).

10- Weston D.E : "Underwater Explosions as Acoustic Sources" A.R.L. Teddington, Middlesex U.K.

11- Wentzell R.A : "Cavitation phenomena due to Shock Pulses Reflected from the Sea Surface". University J. Waterloo, Ontario, Canada.

12- Bangah et Sarh : "Cavitation induite par une onde de détente dans un fluide au repos". Rapport intermédiaire. Contrat DRET 81-500. (1981).

13- Giovanneschi P.: "Contribution à l'étude de la cavitation à bulles isolées, initiées par un rayonnement laser de grande intensité". Université d'Aix-Marseille II. UM CNRS n° 34 - Thèse (1987).

14- Cole R.H."Underwater Explosions" 1949.

15- Dubesset et Lavergne "Calcul de cavitation due aux explosions sous-marines à faible profondeur". Acustica Vol. 20 (1968).

16- Kedrinskii V.K.: "Surface Effects from an Underxater Explosion". Zhurnal Prikladnoi Mekkaniki i Tecknicheskoi Fiziki n° 4 pp.67-87 (1978).

17- Plateau M.T.- Phil Mag. 12 P. 286 (1856).

18- Raileigh J.W., Strutt, Baron - Proc. London Math. Soc. 10, p.4 (1878).

19- Weber C.- Zeit. Angew Math. Mech : "Disintegration of liquid jet" Math Mech - 11/136-54 (1931).

20- Tomotika S."The Instability of Cylindrical Column of a perfect liquid surrounded by another perfect fluid" Proc. Physico Math Soc. Japon 18.550.62 (1936).

21- Abott W. - "Analysis of the Instability of laminar, Newtonien liquid Jets in Air" - The Louisiana State Agricultural and Mechanical Col. PHD New Orleans (Louisiane) (1982).

22- Royer H.: "La microholographie et ses applications" Institut Franco-Allemand de Recherche de Saint-Louis - France. Rapport interne.

23- Fargère N : "Contribution à l'automatisation du développement d'hologrammes de GABOR". GAMS COFERA, "Journées d'étude sur les Aérosols" (12/87).

24- Fargère N : "Dépouillement semi-automatique d'hologrammes de GABOR et programme dégradé". Data processing on Interpretation in Holography 2 nd Franco-German Congress on Applications of Holography- Saint-Louis - France (1988).

25- Suslick K. "Les effets chimiques des ultrasons" - Pour la science n° 138, p. 89 à 94 (1989).

Fig.1 Experimental and Theorical Cavitation Zone

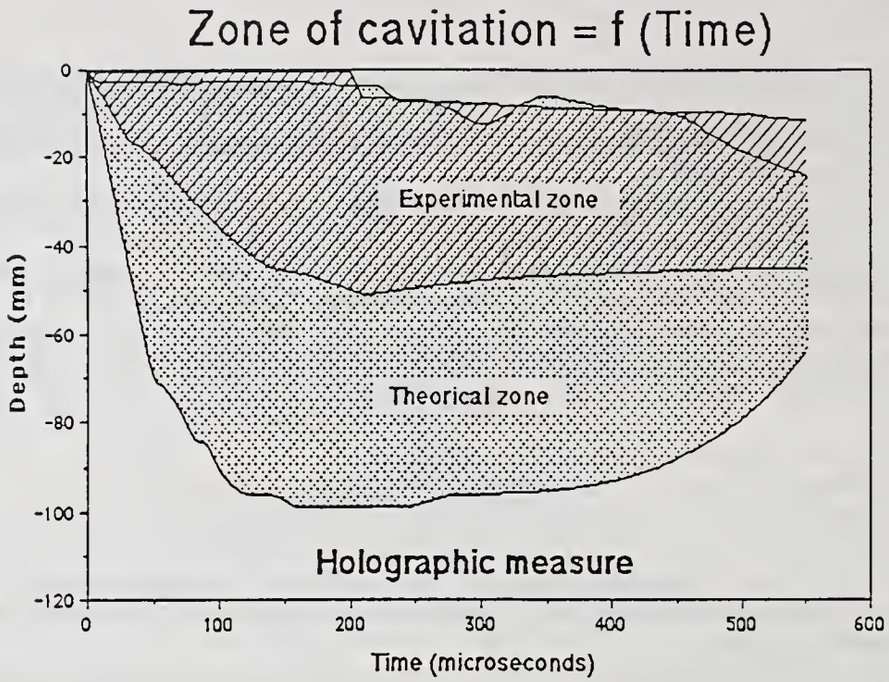

Fig.2 Drop's number versus Diameter (250 mm)

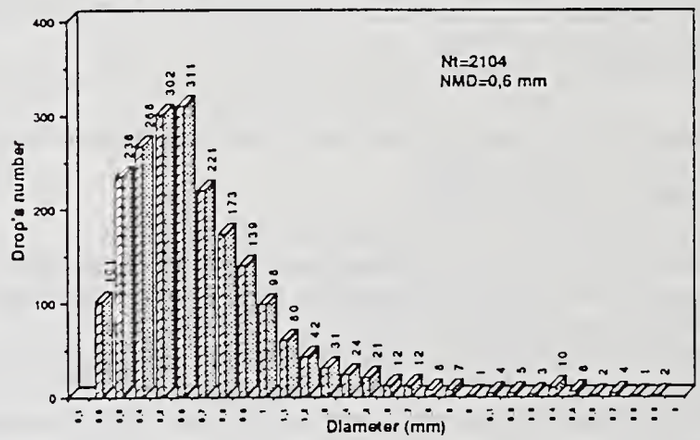

Fig.3 Drop's mass versus Diameter (250mm)

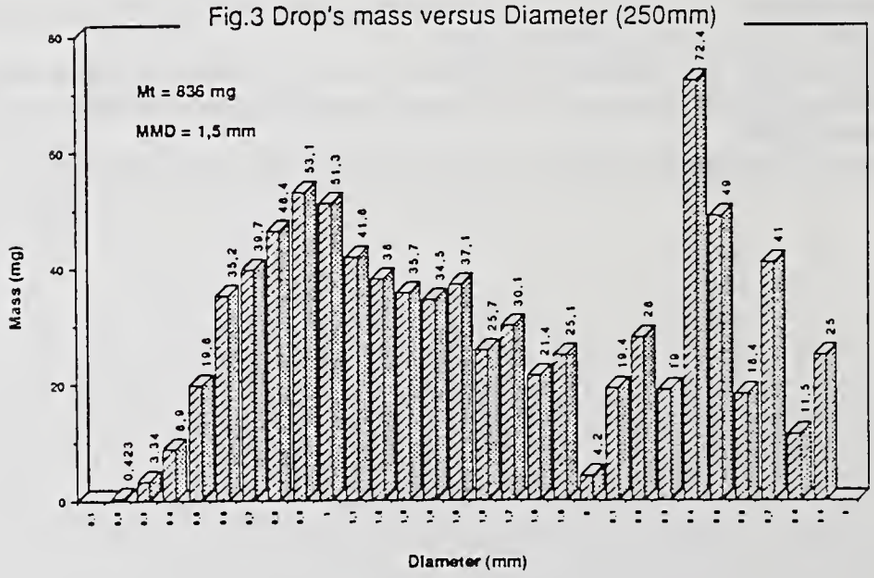

DYNAMIC SIMILARITY BETWEEN LIQUID SHEETS AND HARD SPRING SYSTEMS

A. Mansour and N. Chigier

Department of Mechanical Engineering
Carnegie Mellon University
Pittsburgh, PA, U.S.A.

ABSTRACT

Detailed measurements of the frequency of oscillation of a liquid sheet issuing from a 2D air assisted nozzle have been made. The measured vibrational frequencies were then correlated with the resulting spray angle. It was shown that the liquid sheet oscillations are dynamically similar to that of hard spring systems. The effect of introducing air in the nozzle simulates the effect of forced vibrations on the nozzle jaws. Thus, for each air flow rate, there is a specific vibration frequency for the nozzle. The frequency of these vibrations is proportional to the air velocity. As the liquid sheet natural frequency approaches that of the nozzle, resonance is established. At resonance, the maximum spray angle is achieved.

INTRODUCTION

An experimental study is being conducted on a 2D twin fluid atomizer, similar to that of Reference 1. A liquid sheet emerges from a central slit with a high aspect ratio. High velocity air impinges on both sides of the liquid sheet at the nozzle exit. Microphotography was used to determine the global structure of the sprays, and a light attentuation technique was employed to measure the frequencies of oscillations.

FREQUENCY MEASUREMENT TECHNIQUE

The experimental technique utilizes the attentuation of a collimated laser beam passing through the liquid sheet in the transverse direction (i.e., parallel to the nozzle slit). The optical system is shown in Fig. 1. The beam was positioned 2 mm upstream of the breakup region. This method ensures the sampling of the most dominant frequency, that which causes the breakup of the liquid sheet. Figure 2 shows the mean breakup length (i.e., the distance from the nozzle exit to the disintegration point) of the liquid sheet, as determined from many photographs. Numerous tests were performed by translation of the laser beam along the intact length. The bandwidth of oscillation frequencies was reduced as the laser beam was translated in the downstream direction along the intact length. Spurious modes of oscillation disappear as a dominant frequency emerges which is sustained by the liquid sheet. Even if the breakup length recedes to the nozzle exit, this method still proves to be reliable.

Two types of waveform are possible depending on the location of the laser beam with respect to the Z coordinate. Figure 3 shows photographs of the waveform taken from the oscilloscope

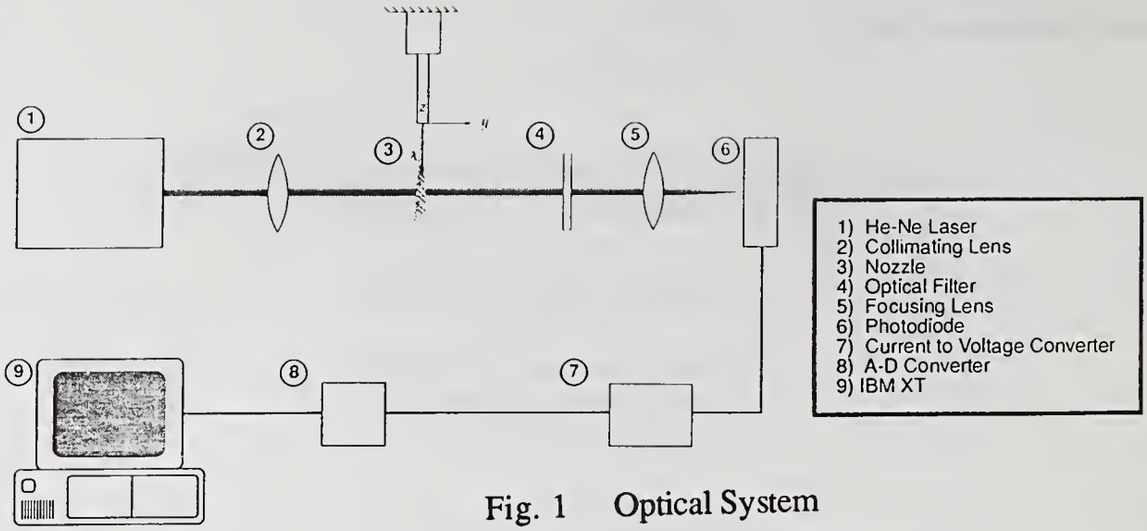

Fig. 1 Optical System

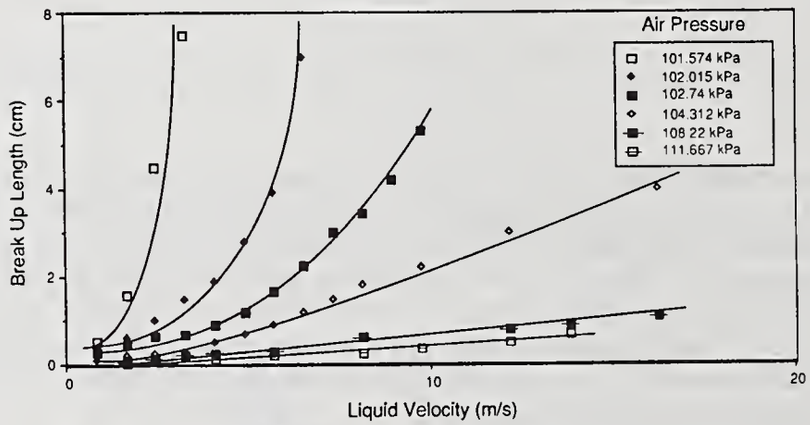

Fig. 2 Mean Breakup Length as a function of Liquid Velocity and Air Supply Pressure to Atomizer

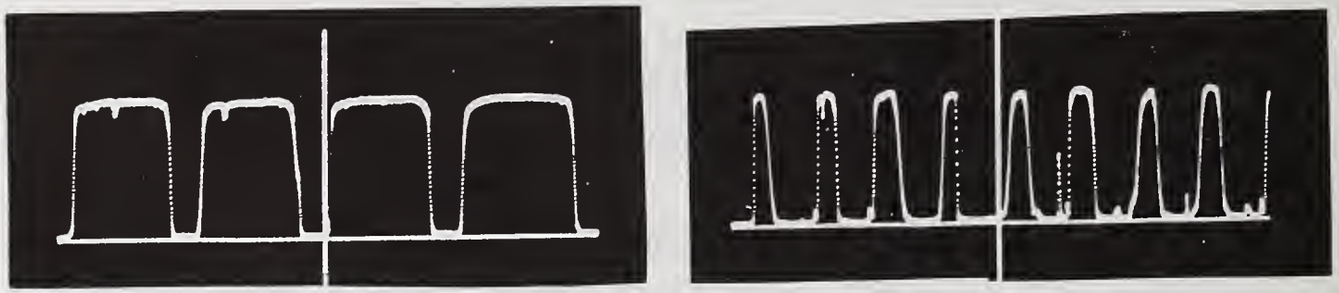

a) Z_{laser} = A (amplitude of oscillation) b) Z_{laser} = 0

Fig. 3 Typical Wave Forms (P_0 = 101.823 kPa, m_{liquid} = 15.77 g/s)

screen. When Z_{laser} = A (A being the amplitude of oscillation at the measuring location) the waveform is shown in Fig. 3a. Figure 3b shows the waveform when Z_{laser} = 0. Particular attention has been paid to the Z location of the laser beam because, as shown in Fig. 3, sampling at Z=0 would lead to a vibrational frequency that is double the actual frequency of the liquid sheet.

Figure 4 shows the actual waveform sampled when the breakup length recedes to the nozzle exit. In this case the signal is produced by ligament shedding. Figure 5 shows the power spectral densities of the liquid sheet vibration. Figures 5a through 5c correspond to Figs. 3a, 3b and 4, respectively.

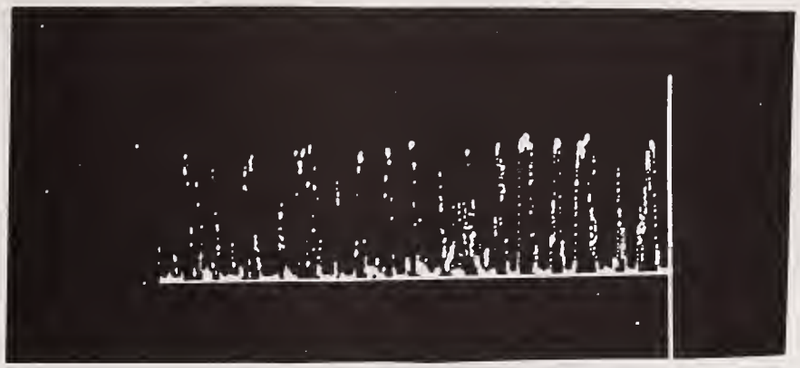

Fig. 4 Typical Wave Form when Breakup Length Recedes to the Nozzle Exit
Z_{laser} = A; P_0 = 104.312 kPa; m_{liquid} = 15.77 g/s

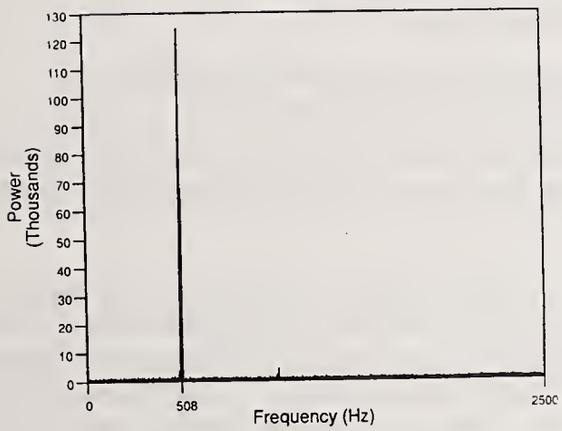

a) Z_{laser} = A; P_0 = 101.823 kPa;
m_{liquid} = 15.77 g/s $\Rightarrow$ f = 508 Hz

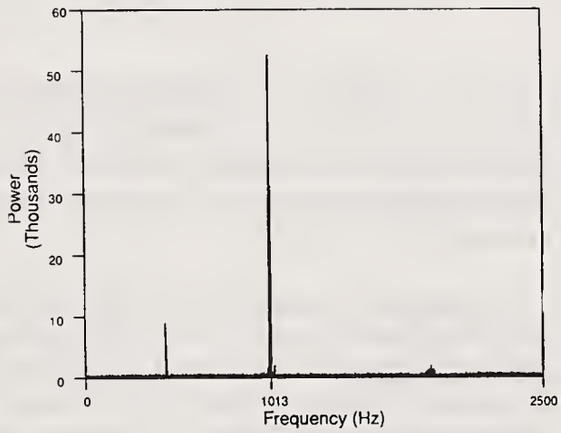

b) Z_{laser} = 0; P_0 = 101.823 kPa;
m_{liquid} = 15.77 g/s $\Rightarrow$ f = 1013 Hz

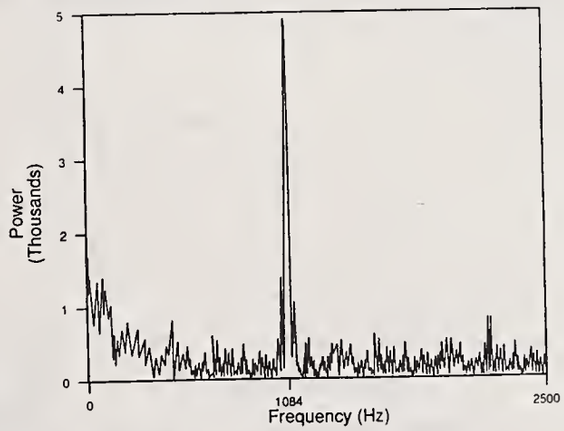

c) Z_{laser} = 0; P_0 = 101.823 kPa;
m_{liquid} = 15.77 g/s $\Rightarrow$ f = 1084 Hz

Fig. 5 Power Spectral Density

RESULTS AND DISCUSSION

Figure 6 shows the vibration frequency of the liquid sheet as a function of liquid exit velocity for different air supply pressures to the atomizer. Figure 6 is divided into three distinct subregions. In regions A and B the frequency of the liquid sheet is highly stable. A sampling rate of 20000 Hz with a time duration of 0.1 sec was sufficient to insure perfect repeatability. In these two regions the bandwidth of oscillation frequencies is very narrow and a perfect spike similar to

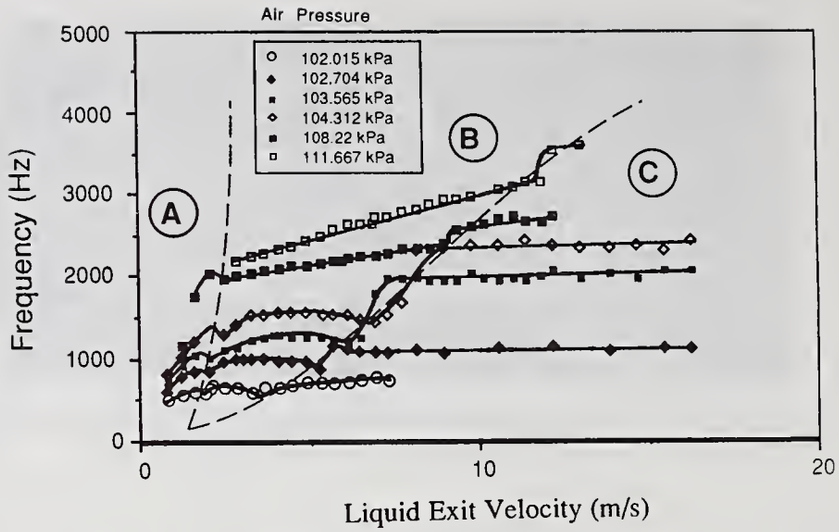

Fig. 6 Vibration Frequency of Liquid Sheet as a Function of Liquid Exit Velocity for 6 Different Air Supply Pressures to Atomizer

that of Fig. 5 is recorded. The clarity of the signal displayed in these regions is due to the fact that the instrument is very sensitive to wave amplitudes: the greater the wave amplitude, the better the signal.

In region C, secondary modes of oscillation appear. The transition from region B to region C is accompanied by a widening of the bandwidth of oscillations and a considerable increase in the measured frequencies. The repeatability in region C of Fig. 6 is poor and a maximum discrepancy of about 15% between each run was recorded. The data points of region C correspond to the arithmetic mean of five different runs, all of which have a sampling rate of 20000 Hz and a time duration of 0.1 sec. Region C is characterized by small wave growth and thus small wave amplitude at the measuring location. The signal in this region deteriorates considerably since, at the measuring location, the wave amplitude is of the same order of magnitude as the laser beam diameter.

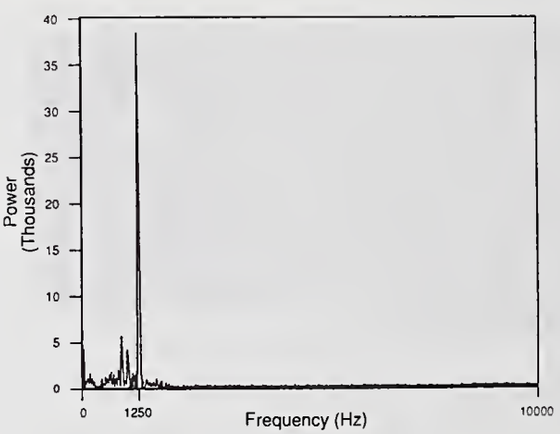

a) in region B of Figure 6:
Z_{laser} = A; P_0 = 103.565 kPa;
m_w = 44.16 g/s $\Rightarrow$ f = 1250 Hz

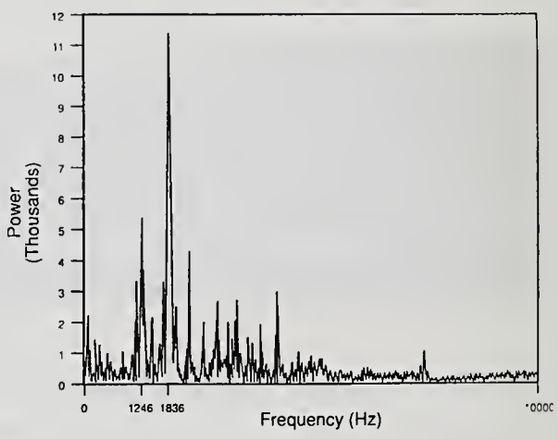

b) in region C of Figure 6:
Z_{laser} = A; P_0 = 103.565 kPa;
m_w = 56.78 g/s $\Rightarrow$ f = 1836 Hz

Fig. 7 Power Spectral Density

Figure 7 shows the power spectral densities of the liquid sheet vibrations for an air supply pressure of 103.565 kPa and for two different liquid flow rates. Figures 7a and 7b correspond to data points sampled in regions B and C of Fig. 6, respectively. Figure 7b shows that while the primary mode which corresponds to region B (see Fig. 7a for detail) still exists, a secondary, more

powerful mode with a higher frequency is displayed. Photographic visualization of the liquid sheet shows that in regions A and B, the sinusoidal mode of oscillation dominates the liquid sheet vibrations. In the transition between regions B and C, both sinusoidal and dilational waves exist. In region C, the liquid sheet oscillations are predominantly of the dilational type.

Figure 6 shows that for each air supply pressure, the frequency of oscillations of the liquid sheet undergoes sudden but continuous jumps as the liquid flow rate is increased. It is also shown that these jump points are displaced to the right as the air pressure or the air velocity is increased.

In order to understand the jump phenomenon that were recorded, a separate test was conducted to measure the spray angle. The criterion for measurement of the spray angle was to follow the crests of the major disturbances. The surrounding droplet mists were not generally considered. It should be mentioned, however, that when the breakup length recedes to the nozzle exit, the droplet cloud was globally considered for spray angle measurement.

Figure 8 shows spray angle measurements as a function of liquid velocity for three different air supply pressures. It is shown that for each air supply pressure the spray angle undergoes an increase followed by a decrease as the liquid flow rate or the liquid velocity is increased. It is also shown that the spray angle curves and the curves' maxima are displaced to the right as the air supply pressure is increased. These maxima diminish with an increase in air supply pressure.

Careful examination of Figs. 6 and 8 shows that for low air supply pressure, namely P_{air} = 102.704 kPa and 103.565 kPa, the local maxima of the frequency curves in region B of Fig. 6, closely correspond to the maxima of the spray angle curve. The reason for this correspondence will be explained in subsequent paragraphs. There may be a mechanical element in the system which has a resonant frequency near the maximum frequency displayed in this region. Near resonance, the spray angle reaches its absolute maximum and the frequency of the liquid sheet reaches a local maximum.

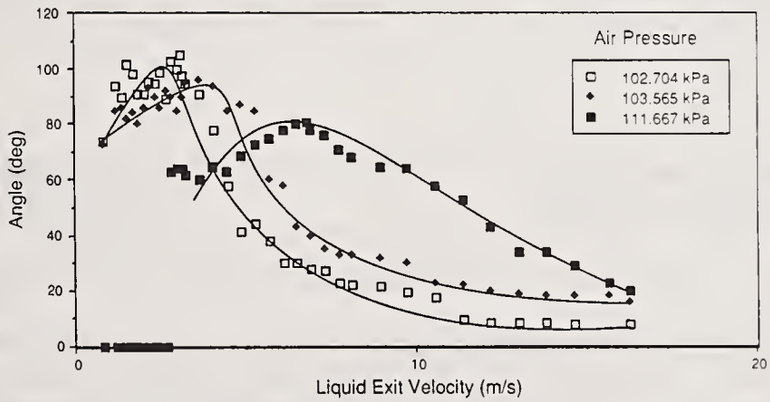

Fig. 8 Spray Angle vs. Liquid Velocity for Three Different Air Supply Pressures

In order to demonstrate the phenomenon of resonant frequency and its influence on maximizing the wave amplitude, the spray angle was plotted as a function of the vibrational frequency of the liquid sheet. The results are presented in Fig. 9. It is shown in this figure that for low air pressures, the liquid sheet oscillation is similar to that of a non-linear, damped, hard spring system.

In non-linear, non-damped, hard spring systems, it is found that the amplitude A undergoes a sudden discontinuous jump near resonance. The jump phenomenon can be described as follows. For the hardening spring system with increasing frequency of excitation, the amplitude gradually increases until a point "a" in Fig. 10a is reached. It then jumps to a smaller value, indicated by

point "b", and diminishes along the curve to its right. In decreasing the frequency from point c, the amplitude continues to increase beyond point b to point d and suddenly jumps to a higher value at point e. The shaded area in the amplitude frequency plot is unstable. The extent of instability depends on a number of factors such as the amount of damping present and the rate of change of the exciting frequency [2].

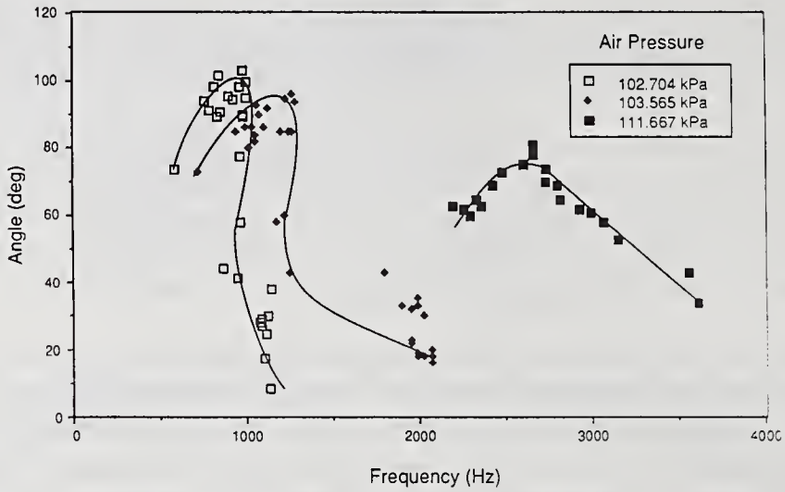

Fig. 9 Spray Angle vs. Vibrational Frequency of the Liquid Sheet for Three Different Air Supply Pressures

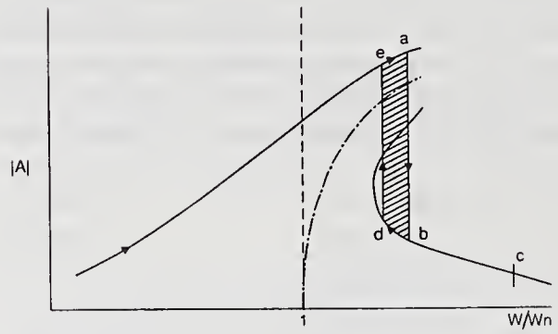

a) The jump phenomenon for the hardening spring (no damping)

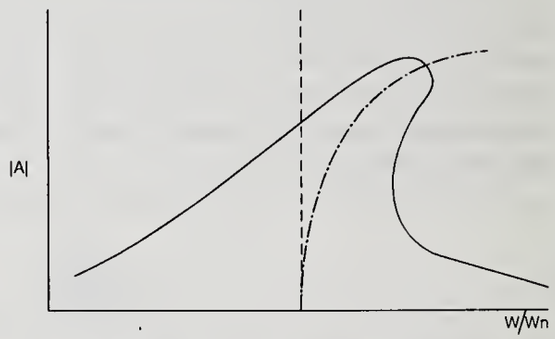

b) The jump phenomenon for the hardening spring (with damping)

Fig. 10 Amplitude vs. Frequency for a Hardening Spring System

In the undamped case, the amplitude frequency curves approach the backbone curve (shown dotted) asymptotically. This is also the case for the linear system where the backbone curve is the vertical line at $w/w_n = 1$. With a small amount of damping, the behavior of the system cannot differ appreciably from that of the undamped system. The upper curve, instead of approaching the backbone curve asymptotically, will cross over in a continuous curve as shown in Fig. 10b. The jump phenomenon is also present, but damping generally tends to reduce the size of the unstable region [2]. To summarize, it is seen that for low air pressures, the liquid sheet oscillation is similar to that of a damped, non-linear hard spring system.

As the air supply pressure is increased, P_{air} = 111.667 kPa, Fig. 9 shows that the jump phenomenon is no longer present and the angle vs. frequency curve approaches that of a linear, damped spring system. This change in character is due to the fact that at high air flow rates, the oscillation frequencies of the liquid sheet show a monotonous increase with increase in liquid flow rate. The cyclic increases and decreases, characteristic of low liquid flow rates, are no longer present.

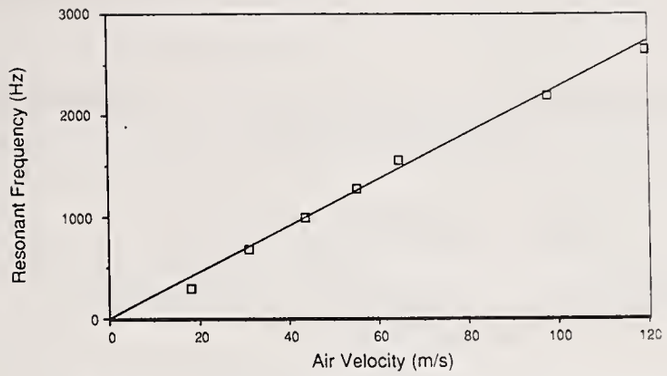

Fig. 11 Resonant Frequency vs. Air Velocity

Thus, it can be seen in Figs. 6, 8 and 9 that the spray angle reaches a maximum near the resonant frequency. For low air supply pressures, the local frequency maxima of region B in Fig. 6 correspond to the resonant frequency. For high air supply pressures, the resonant frequency can be inferred from Fig. 8. It is interesting to note that the resonant frequency increases with air supply pressure or air velocity.

Figure 11 shows the influence of the air velocity on the resonant frequency. It is seen that the resonant frequency increases linearly with air velocity. For each air flow there is a specific vibrational frequency for the nozzle. The frequency of these vibrations is proportional to the air velocity. The effect of introducing air in the nozzle simulates the effect of forced vibrations on the nozzle jaws.

ACKNOWLEDGEMENTS

The authors gratefully acknowledge financial support from NASA Marshall Space Center, grant number NAG 8-126, and Parker Hannifin corporation for providing the atomizer.

REFERENCES

1. Mansour, A. and Chigier, N., "Physics of Fluids A," Vol. 2, No. 5, pp. 706-719, 1990.

2. Thomson, T.W., "Theory of Vibration," Prentice-Hall, pp. 392-397, 1979.

AN EXPERIMENTAL STUDY OF AIR ENTRAINMENT BY MULTIPLE SPRAY NOZZLES

N. Dombrowski and J. Singh

Department of Chemical Engineering, Leeds University
Leeds, United Kingdom

ABSTRACT

Gaseous entrainment by banks of multiple fan sprays is investigated. The results show that an effectively isolated single fan spray has a higher entrainment efficiency then within an assemblage. A hypothesis is presented that the reduction in efficiency is caused by gas flow mutually decreasing the relative gas-drop velocity of its neighbours and hence the drag force. Spray nozzle configurations have been devised for maximising the relative velocity and hence entrainment. It is found that, although entrainment is affected by nozzle size, it is primarily controlled by liquid loading.

INTRODUCTION

The process of heat and mass transfer between a continuous and dispersed phase is involved in a wide variety of processes such as spray drying, extraction, combustion, absorption, humidification and cooling. Sprays have particular advantages over other methods of contacting liquids and gases. They are characterised by a large specific surface within a relative small volume without having the pressure drop associated with other types of contacting equipment. They also have the ability to entrain gas. These features are examined in this work in relation to a novel forced-draft water cooling tower, to be described later, where the entrainment property of a bank of sprays is made use of in place of the conventional fan. This work examines gas entrainment relative to the water flowrate per unit cross-sectional area.

REVIEW OF PAST WORK

The aerodynamic behaviour of sprays is complex, and, in general, researchers have investigated the entrainment characterists of sprays for a specific systems using single atomisers, [1-7]. Generalised experimental or theoretical analysis is complex and its universal application has yet to be fully demonstrated.

EXPERIMENTAL

Nozzle Selection

Benatt and Eisenklam [3] have reviewed gaseous entrainment rates for various types of liquid sprays. Their studies showed that hollow cone swirl spray atomisers entrain more air per momentum supplied in the liquid than from equivalent fan or solid cone nozzles for the same length of spray. However, their study made no allowance for the water loading for each spray type, which cooling tower manufacturers seek to maximise to obtain a compact unit. In order to obtain a higher water loadings then those possible with hollow cone sprays, whilst maintaining a fine spray, fan spray nozzles, produced from single-orifice pressure nozzles, were selected for this work.

Bray nozzles* 000, 2, 7 and 10 corresponding to flow numbers of 0.38, 1.69, 3.40 and 4.24 mls^{-1}/(kN/m^2)$^{1/2}$ were selected.

Figure 1 demonstrates the process of drop formation from fan spray nozzles. The liquid emerges as a thin attenuating sheet. Waves which are initiated by disturbances on the sheet are rapidly amplified by aerodynamic action. When the waves reach a critical amplitude they break down into drops via the formation of threads. [8] The lateral dispersion indicated in figure 1 is caused by a normal, or perpendicular, velocity component derived from the waves.

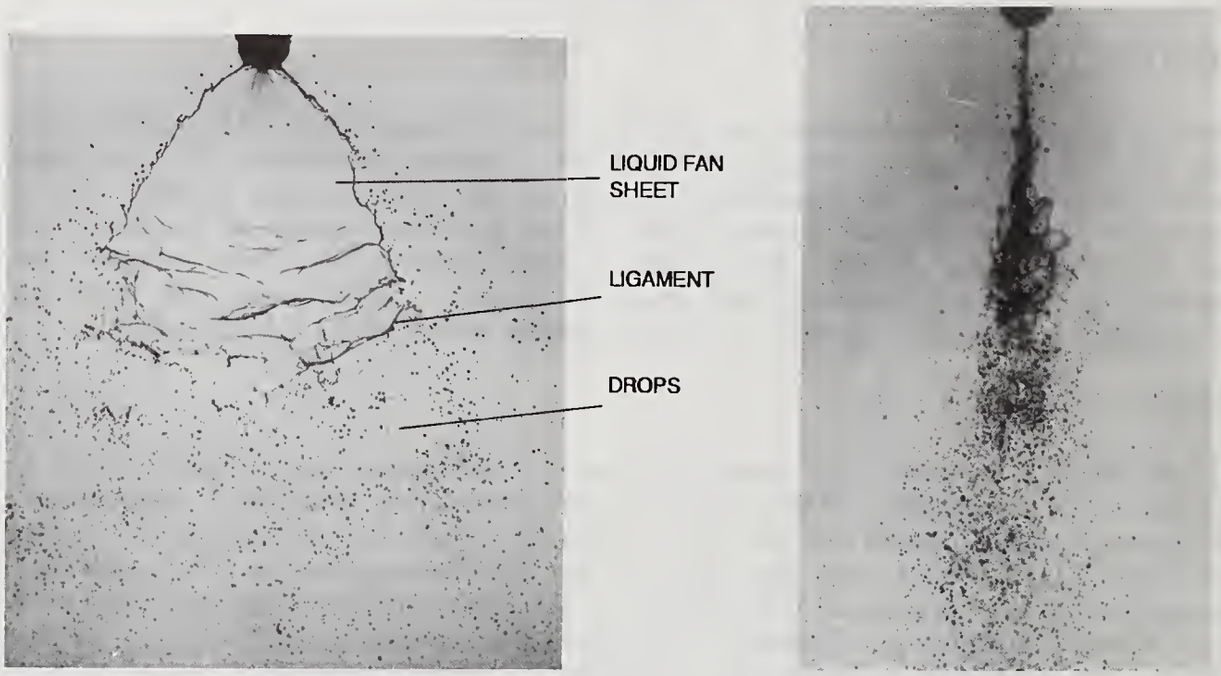

Front View Edge View

Fig 1. Drop formation from a fan spray nozzle
(No. 2 nozzle, 103 kN/m2)

Apparatus

Figure 2 illustrates the apparatus used to study air entrainment. Water is pumped from a re-circulating tank through control valves to a nozzle manifold under test. The supply pressure was taken from a tapping located just upstream of the manifold, whilst the water flowrate was determined by means of a rotameter placed in the delivery line. The manifold was housed in a rectangular test section with an adjustable width and/or length of spray penetration. The nozzles were arranged on a common manifold aligned to spray vertically downwards with the plane of the sheets lying parallel to each other. The spray bank was arranged so that nozzle separation was accommodated by varying the duct width; the duct breadth was maintained constant.

Geo. Bray & Co. Ltd, Leeds, U.K.

The superficial duct air velocity upstream of the nozzle assembly was measured by a hot wire anemometer close to the duct inlet. The air profile across the duct at this location was found to be sensibly uniform over the full range of air flows encountered.

A range of nozzle supply pressures up to 240 kN/m ^{2} was employed which gave superficial air velocities of up to 5 m/s in the duct.

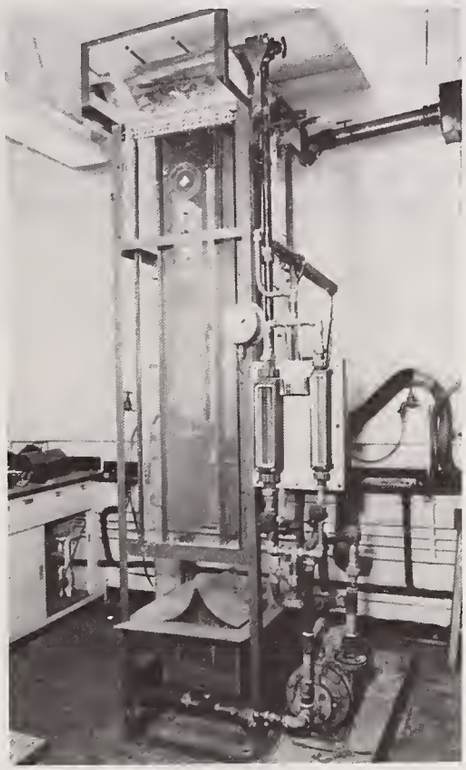

Fig 2. Test rig

RESULTS

Nozzle Size and Spacing

Figure 3 shows the variation of entrainment efficiency, expressed as the gas/liquid (G/L) mass ratio, with water supply pressure for different nozzle spacings. The test was carried out with No. 2 nozzles arranged along a spray bar (referred to as the row configuration) with a spray length of 900 mm. The figure shows that the mass ratio increases significantly with reduction of nozzle spacing and it may therefore be inferred that a single isolated (or unbounded) nozzle is more efficient in entraining gas than a nozzle assemblage. Air flow measurements for a single nozzle could not be undertaken with the present rig because the relatively low flows could not be measured with sufficient accuracy. The figure also demonstrates that; apart from a significant reduction at low pressures, entrainment is effectively independent of pressure.

The effect of nozzle size on entrainment was studied with four sets of nozzles at three water loadings, selected to demonstrate the effect of various loadings. The results are plotted on figure 4 to show the variation of mass ratio with nozzle size for water loadings of 0.63, 1.3 and 2.6 l/s.m^2 at a pressure of 138 kN/m^2. The figure shows that the entrainment increases significantly as a result of increased distance between nozzles of the same size (points B, C and D for No. 2 and points E and F for No. 7).

It also shows that at high water loadings (circa 2.6 l/s.m^2) an increase in nozzle size from No. 2 to 7 causes a slight increase in entrainment which falls sharply with a further increase in size to No. 10 nozzles (points D, F and G). It may be inferred that any advantage gained from increased spacing with the larger nozzles is offset by loss in momentum transfer, due to the relatively coarse drops produced by No. 10 nozzles. (D_{32} mean drop sizes are 265, 405 and 456μm for No. 2, 7 and 10 nozzles respectively). At low water loadings (0.6 l/s.m^2) No. 2 nozzles with a mean drop size of 265μm entrain more gas than the smaller 130μm drops of the 000 nozzle, because the advantageous effect of increased spacing offsets any momentum transfer loss due to the larger drop size (points A and B). A balance is reached between nozzle spacing and drop size at a water loading of 1.3 l/s.m^2 where it is seen that increase in nozzle size from No. 2 to 7 has little effect on entrainment. It may be concluded that while air entrainment is affected by nozzle size it is primarily controlled by water loading irrespective of liquid pressure.

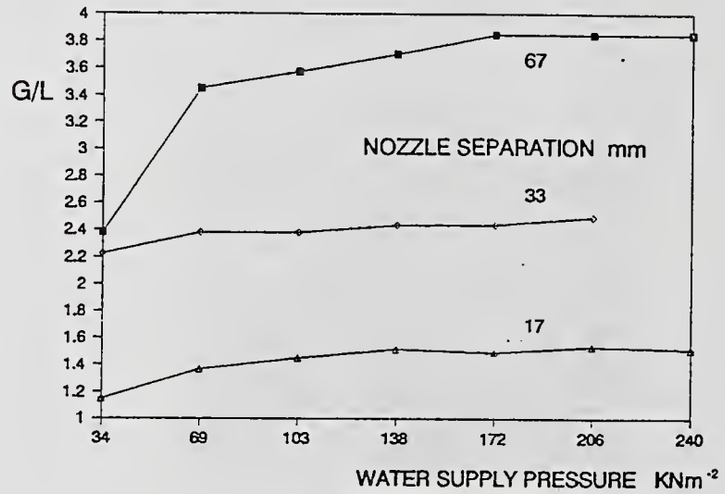

Fig 3. Variation of G/L with pressure and Nozzle separation (aspect ratio = 4.5)

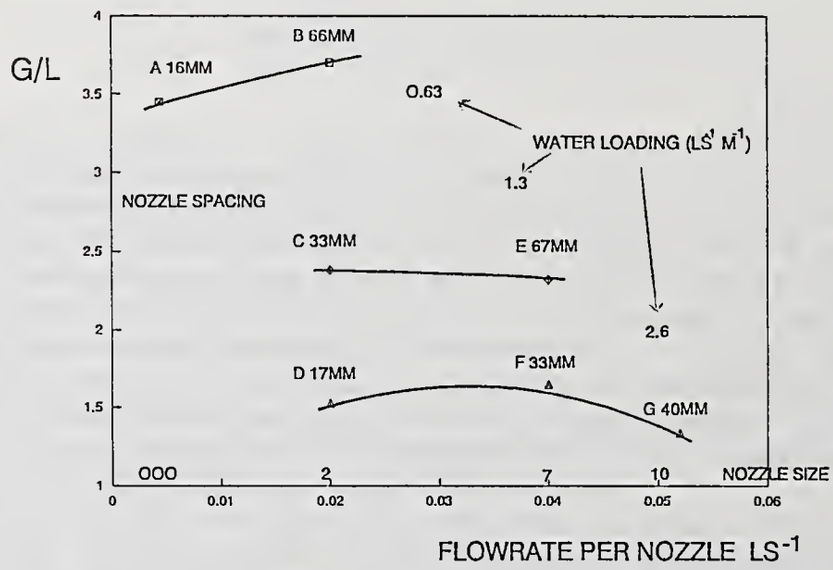

Fig 4. Variation of L/G with nozzle size and spacing For row configuration

Spray Length

The effect of spray length on entrainment was evaluated at a water loading of 1.3 l/s.m^2 with number 2 nozzles spaced 33 mm apart. Two spray lengths, 450 and 900 mm were examined. The spray length was varied by spraying at different heights above the duct discharge. The results are shown in figure 5 as a plot of the G/L ratio against nozzle supply pressure. The figure shows that the variation of spray length in a duct has a small effect only on entrainment, a 100% increase length resulting in an increase in entrainment of 14%.

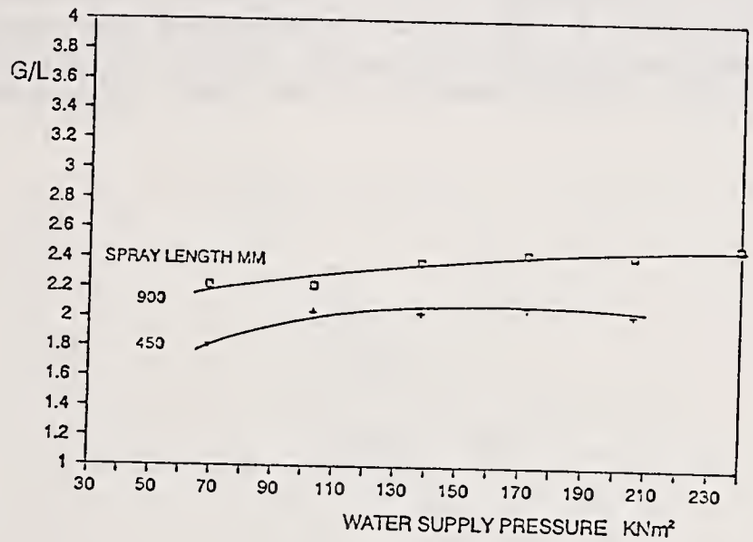

Fig 5. Variation of G/L with pressure and spray length

MECHANISM OF GAS ENTRAINMENT BY MULTIPLE SPRAYS

Development of Hypothesis

The above tests show that, generally, momentum transfer between air and spray droplets can be enhanced by increasing the distance between adjacent nozzles. The effect can be explained in terms of the likely mechanism that takes place. The momentum transfer between the drops of a spray and the air is dependent on the relative drop-air velocity. For single unbounded sprays, entrainment occurs throughout the spray length from the surrounding quiescent environment. However, for single or multiple sprays located in duct, the entrained air flows co-currently through the duct causing a reduction of the relative drop-air velocity within the spray and hence a reduction in entrainment. The larger the distance between adjacent sprays the lower is the average gas velocity through the duct and hence the higher entrainment efficiency.

The following trials were carried out to test the hypothesis.

Two-tier Spray Arrangement

It has been demonstrated that entrainment efficiency can be improved with increased nozzle spacing. A possible alternative method of increasing the spacing, whilst maintaining compactness, is to employ a two-tier deck of sprays. A schematic diagram of the arrangement is given in figure 6. Initial trials with banks of number two nozzles in a row proved to be inconclusive as the sheet break-up at the lower tier was found to be affected by drops from the upper tier. An alternative nozzle assembly was employed using impinging jet nozzles (see below) where the sheets appeared to be unaffected by the falling drops. The results, shown in figure 7, indicate that the large improvement that might have been expected by doubling the distance between the adjacent nozzles was not obtained. These tests confirm that although entrainment by a bank of sprays in a duct is a function of the actual physical spray separation, it is also a function of the local relative drop-air velocity. The air velocity induced by each tier reduces the relative air-drop velocity of the other, thus reducing the overall entrainment.

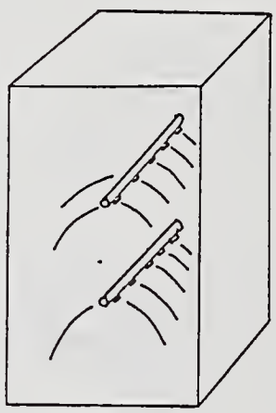

Fig 6. Two-tier spray arrangement

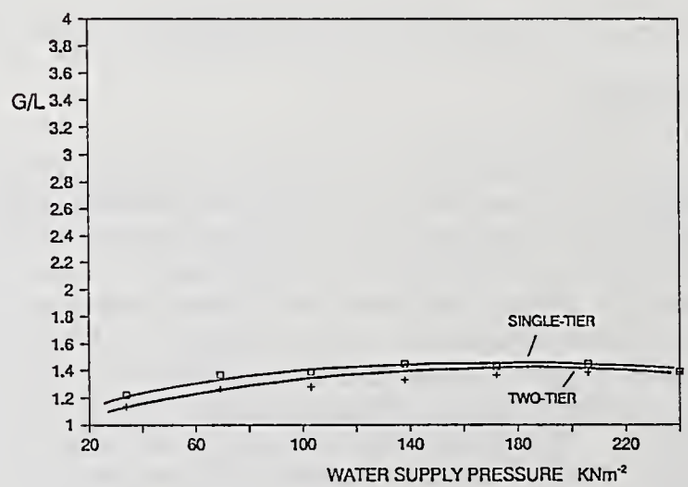

Fig 7. Entrainment by single and two-tier systems

Effect of Upstream Duct Aspect Ratio

To ensure adequate flow straightening, and hence, a uniform air flow pattern upstream of the spray manifold, the experiments described above were performed in a duct of relatively high aspect ratio (ratio of duct height upstream of manifold to duct width). Thus, by virtue of its forward momentum, the air was constrained to flow co-currently over the spray sheets.

It was postulated that, under these conditions, the air flow would flatten the spray profile i.e. the spray width normal to the plane of the sheet, and hence increase the inter-boundary spacing above that based on 'unbounded' measurements. At low aspect ratios the flow pattern is less constrained to flow co-currently, and, the spray boundary would be less affected with a consequent reduction in entrainment efficiency. This reasoning is confirmed in Fig 8 which shows that a reduction in the aspect ratio from 6.8 to 1.5 causes entrainment to fall by up to 30% and in Figure 9 which shows a comparison of the spray profiles of unbounded and bounded sprays.

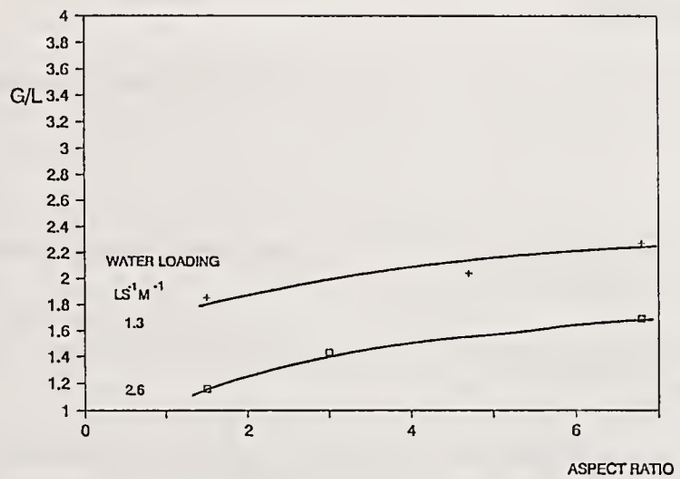

Fig 8. Variation of L/E with aspect ratio

Fig 9. Comparison of edge profiles, LHS, single nozzle; RHS row configuration (6.8 aspect ratio)

CONCLUSIONS

It has been found that the entrainment potential of a bank of sprays is reduced as the nozzles are brought close together. The spray from a single nozzle in a free environment entrains air along its full length normal to its axis, the air being taken from its locality. However, for a bank of sprays in a duct, the air is forced to flow parallel to the spray outside the drop envelope and as a result the relative drop-air velocity within each spray envelope decreases. These air profiles reduce the drag between the air and the spray droplets and result in lower momentum transfer and hence lower entrainment at any given spray length.

The relative influence of a spray on its neighbours can be reduced by greater physical separation of adjacent nozzles, although this leads to lower water loadings.

In general air entrainment is controlled primarily by water loading, nozzle size having a less significant effect.

ACKNOWLEDGEMENTS

The provision of a research grant from Hall-Thermotank Limited is gratefully acknowledged.

REFERENCES

(1) Rasbash D. J. and Stark G. W. V. Some aerodynamic properties of sprays. The Chemical Engineer. (1962)

(2) Briffa F. E. J. and Dombrowski N. Entrainment of air into a liquid spray. A. I. Ch. E. Journal 1966 12, 708.

(3) Benatt F. G. S. and Eisenklam P. Gaseous entrainment into axisymmetric liquid sprays. Journal of the Institute of Fuel 1966 309.

(4) McQuaid J. Air entrainment into axisymmetric sprays. Proceedings of the Institution of Mechanical Engineers 1975, 189 28.

(5) Heskested G., Kung M. C. and Todtenkopf N. F. Air entrainment into water sprays and spray curtains. The American Socety of Mechanical Engineers, 76-WA/FE 40.

(6) Arrowsmith A. and Foster P. J. The motion of a stream of monosized liquid drops in air. The Chemical Engineering Journal 1973 5. 243-250.

(7) Hedley A. B, Arrowsmith A. and Foster P. J. Entrainment and evaporation in single streams of monosized drops. Chemeca 1970.

BEHAVIOR OF SURFACE WAVES ON THE BREAKUP MECHANISM OF A LIQUID COLUMN

D.-J. Kim[*] and C.-W. Lee[†]

[*]Dept. Mechanical Design Engineering, Pusan National University, Pusan, Korea
[†]Dept. Mechanical Engineering, Kyungpook National University, Taegu, Korea

ABSTRACT

In twin-fluid atomizers it is difficult to analyze the behavior of liquid column since it is affected complicatedly by many factors. The simplest shape of liquid. which is injected through these atomizers is a solid jet before it encounters with the gas stream. The liquid jet is deformed at first, and then disintegrates into drops. The objective of this study is to investigate experimentally the basic disintegration mechanism of the liquid column in co-axial air flow. The behavior of the liquid jet ejected from the circular capillary tubing into co-axial air flow was observed by the high-speed camera. Breakup patterns, surface wave length, amplitude, and growth rate of the disturbance were measured to explain the behavior of the jet. The wave length of the disturbance formed on the liquid surface becomes shorter at the downstream and the trend of change of amplitude as time passes deviates from the linearity. The growth rate of the disturbance is not much influenced by the liquid flow rate. And an empirical equation of the breakup length is obtained as a function of air Reynolds number, liquid Weber number, and initial breakup length.

INTRODUCTION

Lately, the twin-fluid nozzle, in which combustion air is used to atomize liquid jet, has been used in the combustor of jet engines, because of the characteristics of fine atomization optimized distribution, and strong mixing of air and fuel. But the limit ranges of ignition and flame hold in the combustor with this nozzle become narrower than those with pressure nozzle. Owing to these facts the characteristics of atomization, fuel dispersion, and fuel distribution become worse at low speed operation conditions.

In order to eliminate the defects it is necessary to study the effect of air flow on the basic breakup mechanism of liquid jet, the evaporation process of droplets, and the mixing process of droplets and air. For the first time, Rayleigh [1] developed a theory about the breakup mechanism of liquid jets. Casleman [2] reported that the breakup of liquid resulted from the growth of unstable waves formed on the liquid jet surface by the aerodynamic interaction at the liquid-air interface. Sato [3-5] suggested that the breakup of smooth liquid jets came from the dispersion of propagation of nonlinear waves. Situ [6]

pointed out that growth rate of swell and neck formed on the liquid jet surface was changed with the characteristics of nonlinear effects. He also investigated theoretically the effect of heat and mass transfer on the instability of liquid jets. These studies were performed on the breakup mechanism of the liquid jet itself at different experimental conditions. A systematic view between these studies has not been developed yet. Most studies inclined to qualitative analysis. Especially,the effect of the disturbance behavior on the breakup of liquid jets has not been made clear. So, experimental equation proposed for breakup length was applied to limited nozzle only.

The purpose of this study is to investigate the disintegration mechanism of liquid jets, with change in surface wave length, amplitude, growth rate of disturbance, and maximum growth rate to dimensionless wave number, which were examined by using a high speed camera. The empirical equation of breakup length as a function of air Reynolds number, liquid Weber number, and initial breakup length is obtained.

EXPERIMENTAL APPARATUS AND PROCEDURE

An apparatus was newly designed in order to study the disintegration mechanism over wide ranges of operating conditions. The experimental apparatus consists of the air and liquid supply system, injection system, and high speed photographing equipment.

When liquid, compressed by a compressor, is injected vertically through an injection nozzle into the stagnation air or the co-axial air flow, the liquid flow rate is controlled by the injection valve. Air used to atomize the liquid is pressurized by a compressor and then flows vertically in co-axial liquid flow.

The diameter of the liquid nozzle, used in this study, is 0.7mm. Diameters of the air orifice are 4mm, 6mm, and 8mm. Liquid flow rates are 0.69 g/s, 0.89 g/s. and 1.14 g/s. When the air flow was increased gradually for each different liquid flow rate, wave length, amplitude, and growth rate of disturbance were measured with photographs by the high speed camera.

RESULTS AND DISCUSSION

Breakup Patterns

Figure 1 shows photographs by using the high speed camera in order to compare the formation process of the liquid droplet in stagnation air with that in co-axial air flow. Figure 1(a) shows the photographs of a liquid jet in the absence of air flow. This also shows the surface wave formed on the liquid column symmetrically. The length of the ligament between swell and neck is slightly longer before producing droplets. The ligament is disintegrated into small satellite droplets at the downstream. Figure 1(b) shows the photographs of liquid jet in co-axial air flow. The amplitude of surface waves becomes shorter than that of Fig. 1(a). The reason of the generation of satellite droplets from the ligament is considered as follows. Before the longer ligament was formed, the shorter ligament was broken up, and then absorbed into the main droplet due to surface tension at the downstream. In the case of Fig. 1(a), the preliminary droplets were observed before the droplet generation. This droplet was a result of the balance of gravity and surface tension. But, in the case of Fig. 1(b), the preliminary droplets were not observed and were formed at the tip of the smooth jet just before the preliminary droplet formation. The effect of air flow

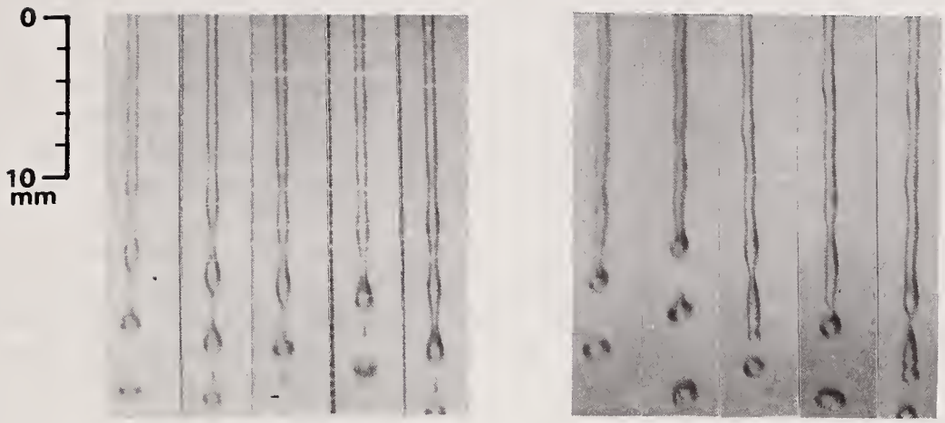

(a) Ua = 0 m/s (b) Ua = 10 m/s

Fig.1 High speed photographs of liquid jet
(dl=0.7mm, Ml=0.89g/s, Δt=0.67ms)

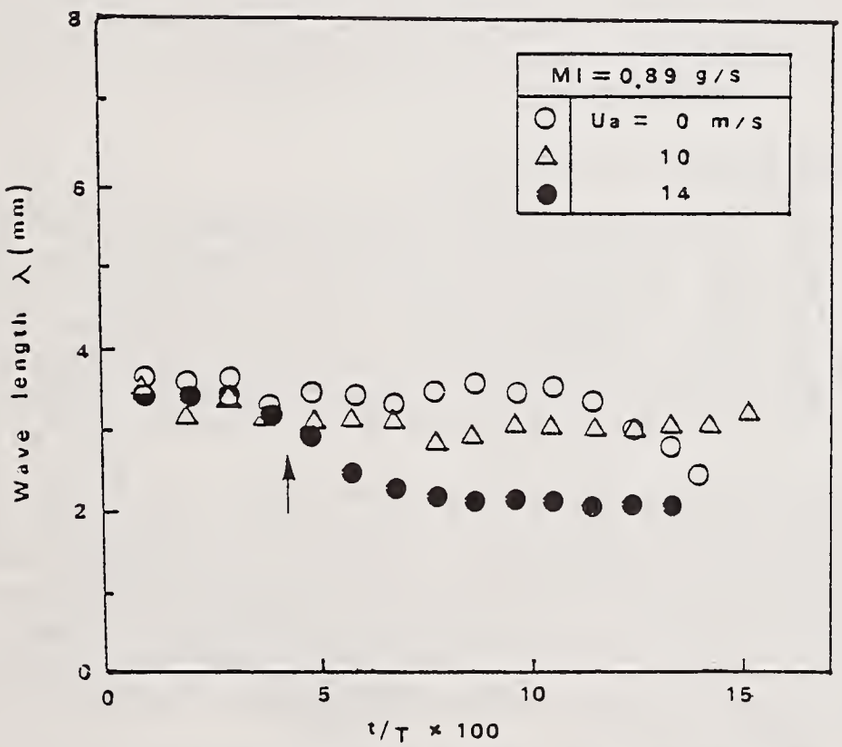

Fig.2 Variation of the wave length with elapsed time
for different air velocity (Ml = 0.89 g/s)

on the liquid breakup is stronger than many other parameters. Both cases show that the amplitude of surface waves increases at the downstream. The reason is that the first formed surface waves were pushed by following surface waves, and that the gravity and the surface tension act on the liquid jet. Thus, the effect of co-axial air flow on disintegration of the liquid jet, as expressed in Weber's equation, results in changes of relative velocity of the liquid and air. initial amplitude of the disturbance, and growth rate of the disturbance.

When the liquid is injected into stagnation air, droplets are slowly generated because of the action of surface tension and gravity, even though the initial disturbance is small. But the liquid jet in co-axial air flow is more largely subject to the effect of an increase in growth rate of the initial disturbance due to aerodynamic interaction than the effect of surface tension.

Surface Wave Length

Figure 2 shows that the wave length on a liquid jet through a nozzle is changed with time at the liquid flow rate of 0.89g/s. Time, T, represents the value that breakup length is divided by liquid velocity. t is time that is passed. When the liquid jet was in co-axial air flow, the surface wave length of disturbance decreases with time, and the reduction rate of it increases as air velocity increases. The reason is that the aerodynamic force acting on it becomes stronger than surface tension by the balance of forces acting on the disturbance. And the instantaneous time that the surface wave length decreases rapidly, as indicated by the arrow in Fig. 2, makes earlier with increasing air velocity. This instant is nearly equal to the time that the velocity of the first formed surface wave and the following surface wave is inverted.

Growth Rate and Amplitude of Surface Wave

Figure 3 shows that the amplitude of the disturbance on a liquid jet is changed with the ratio of the time to the production period of droplets at Ua=0 m/s. The slope represents the growth rate of the disturbance. The amplitude increases linearly for all liquid flow rates. The flow condition of liquid flow rate of 0.69 g/s and 0.89 g/s corresponds to the applicable region of Rayleigh's theory (so called smooth region). The disintegration of the liquid jet results from the growth of axial symmetry caused by surface tension and gravity.

Figure 4 shows the amplitude of the surface wave for the liquid flow rate of 0.89 g/s. The shape of the curves at Ua>0 m/s deviates from the linearity as compared with Ua=0 m/s. The absolute values of amplitude were slightly increased. The slopes of the curves showed the similarity to each other until the first formation of droplets, but change irregularly with time. The reason is that the frequency in generation of a droplet changes with the increase of the air velocity. The change in slope corresponds to the time that the velocity of the surface wave changes rapidly.

The maximum growth rate occurs at the dimensionless wave number of 0.697 in the case of Rayleigh's linear theory [7], less than 0.697 of Wang's analysis [8], the lower wave number of Yuen [9]. Finally the nonlinear effect at above dimensionless wave number used in the instability theory dominates the disintegration processes. But the maximum growth rate occurred at near 0.7 as shown Fig. 5. This means that Rayleigh's linear theory has the limit of application for liquid jets in co-axial air flow.

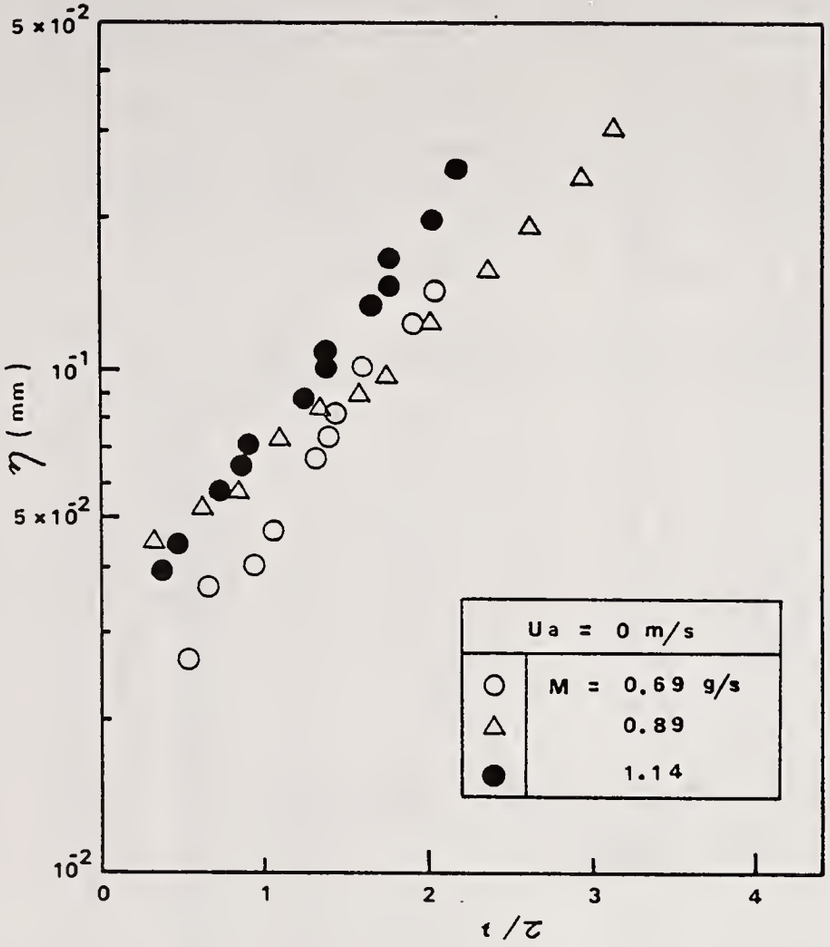

Fig.3 Variation of the surface wave displacement with elapsed time for different liquid flow rate (Ua=0m/s)

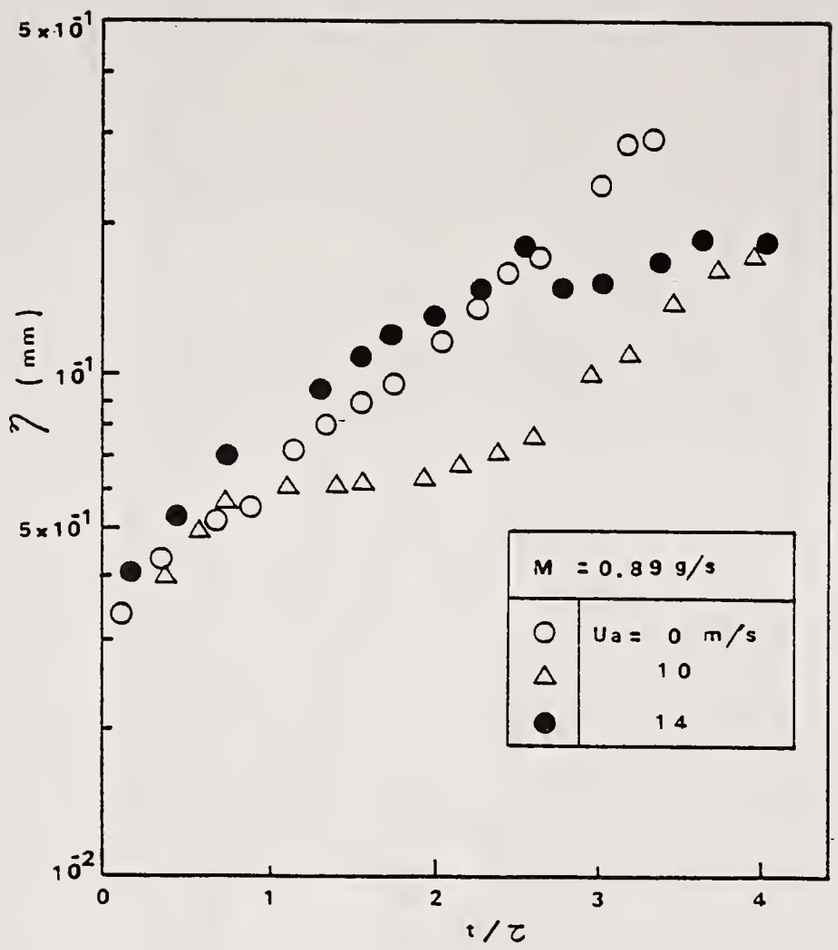

Fig.4 Variation of the surface wave displacement with elapsed time for different air velocity (Ml=0.89g/s)

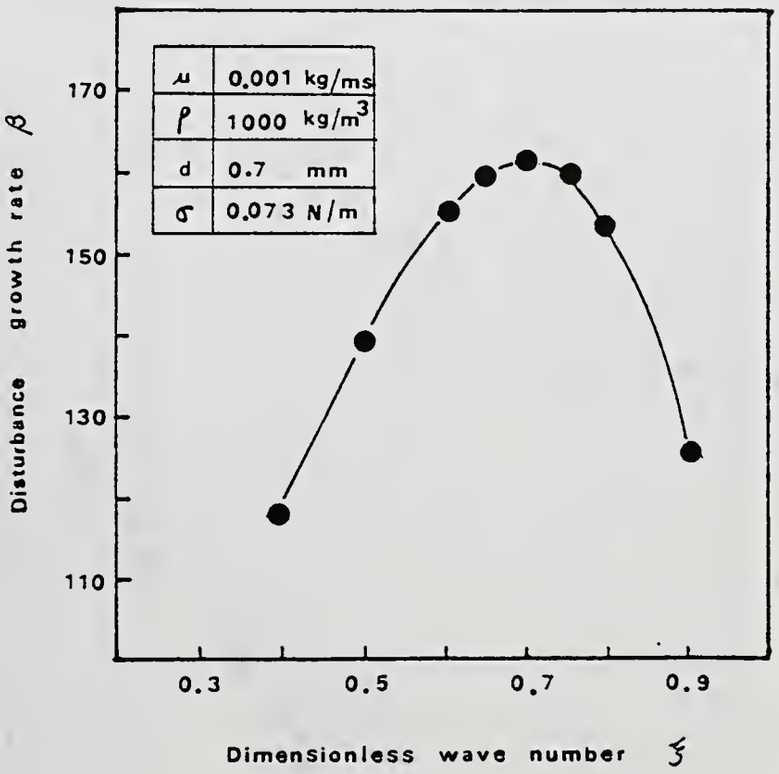

Fig.5 Relation between distrubance growth rate and dimensionless wave number.

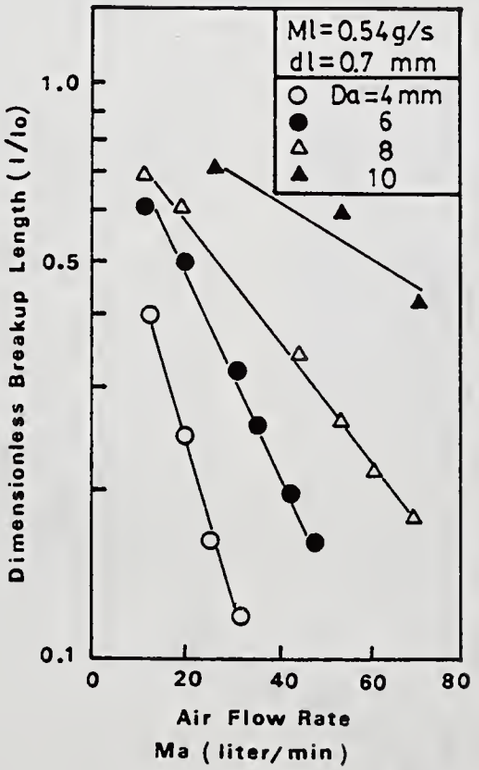

Fig.6 Effect of breakup length ratio on the air flow rate.

Empirical Equation of Breakup Length

Grant and Middleman [10], Sato [11], etc., proposed the empirical equation of the breakup length of a liquid jet in stagnation air. Especially, Sato had developed the equation in terms of Weber number and air velocity for a nozzle diameter of 2.09 mm in co-axial air flow. Figure 6 shows the change of breakup length for various diameters of the air orifice. When the equation of the breakup length is formulated, the effect of air flow rate with the change of air orifice diameter must be included. The empirical equation for breakup length includes parameters such as the initial breakup length, liquid Weber number, and air Reynolds number including air velocity and air orifice diameter as shown in Fig. 7.

The equation is set up as follows.

$$\frac{l}{l_0} = (We)^{0.0075}\sqrt{Re}\exp(-0.0143\sqrt{Re}) \tag{1}$$

This equation means that the breakup length of liquid column changes complicatedly under the influence of parameters such as the aerodynamic interaction, the geometrical shape of air orifice, and of liquid column.

CONCLUSIONS

To investigate the disintegration mechanism of a liquid jet in co-axial air flow, breakup patterns, surface wave length, amplitude, and growth rate of disturbance were measured with photographs by a high speed camera.

(1) The wave length of the disturbance formed on the liquid surface becomes shorter at the downstream and the trend of change of amplitude as time passes the disturbance deviates from the linearity.
(2) The growth rate of the disturbance is not influenced much by the liquid flow rate.
(3) An empirical equation of the breakup length is obtained as a function of air Reynolds number, liquid Weber number. and initial breakup length.

REFERENCES

1. Rayleigh, Lord., "On the Instability of Jets", Proc. Lond. Math. Soc., Vol. 10. pp. 4-13 (1878).
2. Casleman, R.A., "The Mechanism of Atomization Accompanying Solid Injection", Report National Advisory Committee for Aeronautics, No. 440, pp. 735-746 (1932).
3. Sato, H., Makai, T. and Saito, M., "Non-linear Waves on Smooth Jet of Liquid Column", 8th Japan Conference on Liquid Atomization and Spray Systems, pp. 7-12. (1980).
4. Sato, H. and Saito, M., "Non-linear Wave Propagation and Disintegration of a Circular Liquid Jet", International Conference on Liquid Atomization and Spray Systems. 1-3. pp. 19-27 (1982).
5. Sato, H., Sakai, T. and Saito, M., "Nonlinear Waves on Smooth Jet of Liquid Column II", The 10th Conference on Liquid Atomization and Spray System in Japan, pp. 19-24, (1982).

6. Situ, M. and Schetz, J.A., "Computational and Experimental Study of the Effect of Mass Transfer on Liquid-Jet Breakup", AIAA Journal, Vol. 23, No. 2, pp. 254 -261, (1985).
7. Rayleigh, Lord, "Theory of Sound", Macmillan, London, Vol. 2, pp. 43-375, (1926).
8. Wang, D.P., "Finite Amplitude Effect on the Stability of a Jet of Circular Cross-Section", J. Fluid Mech., Vol. 34, pp. 299-313 (1968).
9. Yuen, M.C., "Non-linear Capillary Instability of a Liquid Jet", J. Fluid Mech., Vol. 33, Part 1, pp. 151-163, (1968).
10. Grant, R.P. and Middleman, S., "Newtonian Jet Stability", AIChE Journal, Vol. 12, No. 4, pp. 669-678, (1966).
11. Nagaosa, S., Matsui, H., Tokuoka, N. and Sato, G.T., "A Study of the Disintegration of a Liquid Jet in an Air Flow", International Conference on Liquid Atomization and Spray Systems, 2-1, pp. 29-36. (1978).

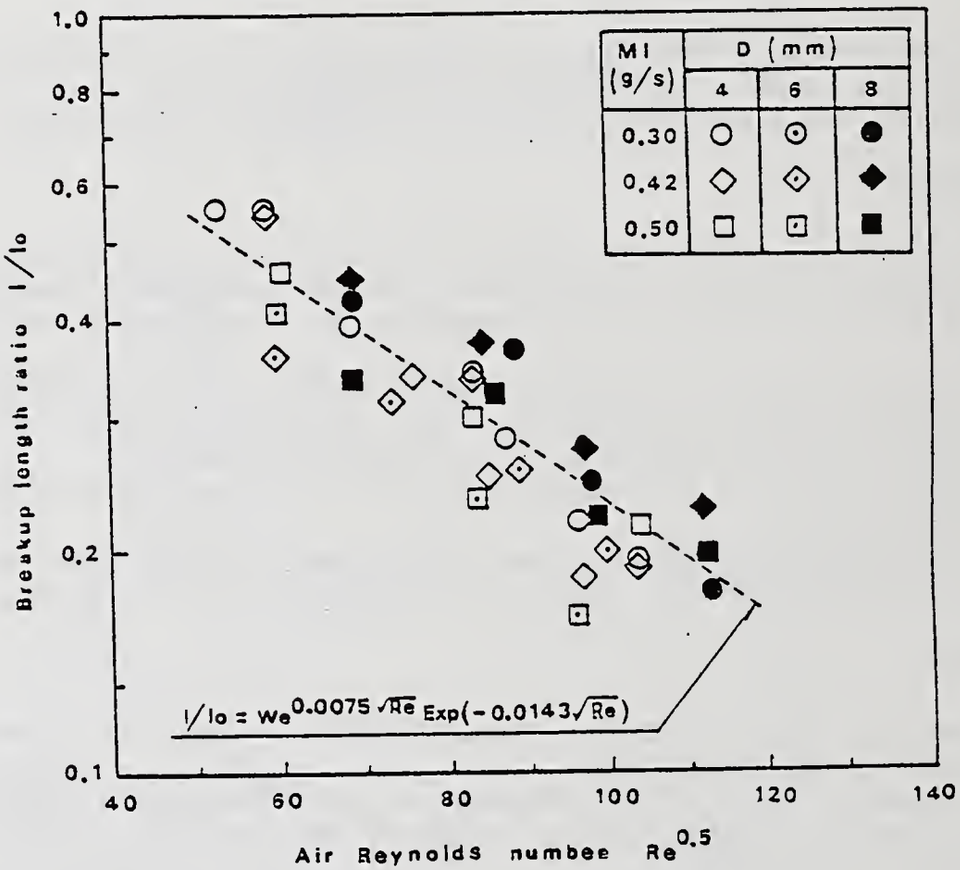

Fig. 7 Breakup length ratio of smooth jet as function of Reynolds number, air orfice diameter and liquid flow rate

LIQUID ATOMIZATION WITH HOLLOW CONE NOZZLES

H.D. Dahl and E. Muschelknautz

Lehrstuhl und Institut für Mechanische Verfahrenstechnik
Universitat Stuttgart
Stuttgart, Germany

1. ABSTRACT

Hollow cone nozzles consist of a spin chamber with an excentrical or axial inlet generating rotational flow. Because of the great centrifugal forces a thin liquid film is formed in the outlet.

For the calculation of the flow in the nozzle cyclone theory is used. Cyclone theory consists of simple, physically founded equations for outlet velocities and pressure loss, which are taking into account the influence of wall friction.

We found, that the mechanism of disintegration of the liquid film depends on the outlet velocity of the nozzle. For lower velocities the breakup of the film takes place under the influence of aerdoynamic forces forming sinuous waves according to the model of Dombrowski and Johns /1/. If the outlet velocity surmounts a certain value the disintegration is due to turbulent liquid forces, i.e. the film is atomized. The maximum drop size is then a function of the Weber and Ohnesorge numbers.

All calculation methods are based either on physical balances or on a complete set of similarity numbers. They have been verified by a systematical variation of nozzle geometry and of liquid and gas properties. Therefore they can be applied for nozzle design and scale-up.

2. FLOW IN THE NOZZLE

2.1 Theory

Cyclone theory /2/ takes into account the influence of the wall friction of rotational flow. Figure 1 shows a hollow cone nozzle with axial inlet.

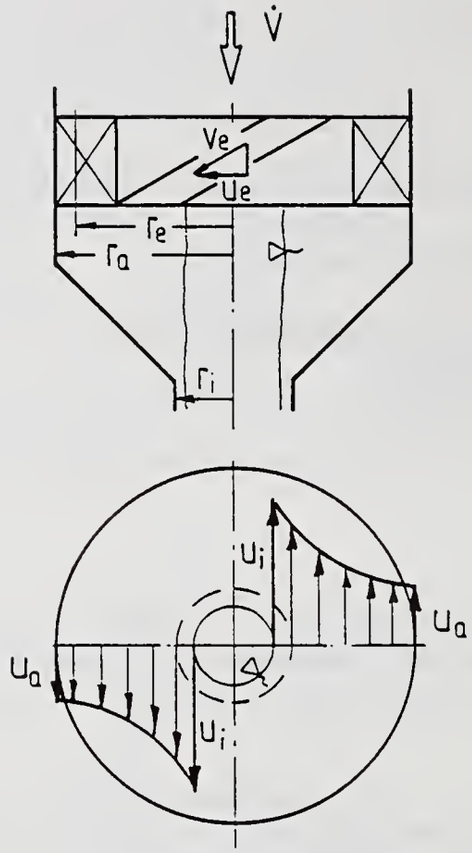

Figure 1: Angular velocity in a hollow cone nozzle

After having entered the spin chamber through the grooved core the pressure gradient of the rotational flow is impressed on the liquid. Due to this the flow contracts and accelerates to the outer angular velocity ua. The contraction coefficient α is defined as the angular momentum's ratio before and after the contraction of flow:

$$\alpha = \frac{\dot{M}\, u_e\, r_e}{\dot{M}\, u_a\, r_a} = \frac{u_e\, r_e}{u_a\, r_a} \qquad (1)$$

The tangential stress due to wall friction is

$$\tau = - \lambda \frac{\rho_L}{2} u^2 \qquad (2)$$

With geometric mean values for tangential velocity and radius the loss of angular momentum results as

$$M_R = \int \tau \, dA_R \, r = \lambda \, A_R \, \frac{\rho_L}{2} \, u_m^2 \, r_m \qquad (3)$$

The balance of momentum equation (4), leads to the equation for the angular velocity in the outlet of the nozzle:

$$\dot{M} \, u_a \, r_a = \dot{M} \, u_i \, r_i + M_R \qquad (4)$$

$$u_i = \frac{u_a \, r_a / r_i}{1 + \frac{\lambda}{2} \, \frac{A_R \, u_a}{\dot{V}} \, \sqrt{r_a / r_i}} \qquad (5)$$

The pressure loss of the nozzle consists of a part caused by the acceleration of the liquid and of a part caused by wall friction.
The wall friction pressure loss results from a balance of energy:

$$\Delta p_e = \lambda \, \frac{A_R}{\dot{V}} \, \frac{\rho_L}{2} \, (u_a \, u_i)^{3/2} \qquad (6).$$

The acceleration pressure drop is calculated by the Bernoulli equation:

$$\Delta p_i = \frac{\rho_L}{2} \, w^2 = \frac{\rho_L}{2} \, (u_i^2 + v_{ax}^2) \qquad (7).$$

By means of experiments this pressure drop can be as well expressed as a function of the angular velocity in the outlet:

$$\Delta p_i = \zeta_i \, \frac{\rho_L}{2} \, v_i^2 \qquad (8)$$

with

$$\zeta_i = \left(1 + 2 \, \frac{u_i}{v_i} + \frac{u_i^2}{v_i^2}\right) \qquad (9)$$

and

$$v_i = \frac{\dot{V}}{\pi r_i^2} \qquad (10).$$

In comparison to hollow cone nozzles the pressure loss coefficient in cyclones is higher, because the swirl flow in the cyclone is reversed.
With equations (7), (8) and (9) the axial velocity is

$$v_{ax} = v_i^2 + 2 u_i v_i \qquad (11).$$

The film thickness in the outlet is given by continuity equation as

$$\delta = r_i - \sqrt{r_i^2 - \frac{\dot{V}}{\pi v_{ax}}} \qquad (12).$$

2.2 Experimental Results

The examined nozzles had ratios of spin chamber radius to outlet radius from 2 to 5. The spin chamber radius varied from 6 to 12 mm.The physical properties of the liquids which were used for experiments are displayed in Table 1.

	ρ_L [kg/m^3]	η_L [10^{-3}Pa s]	σ [10^{-3}Nm]
Water	1000	1	72
Glycerin/Water	1215	75	65
Ethanol/Water	972	1.9	42
Suspension of lime 35%	1280	2.2	49

Table 1: Liquid properties

With an experimentally determined contraction coefficient α the wall friction coefficient λ could be calculated out of the experimental data by means of equation (5). λ decreases for laminar flow with increasing Re-number until a constant value for great Re-numbers (turbulent flow) is attained (Figure 2).

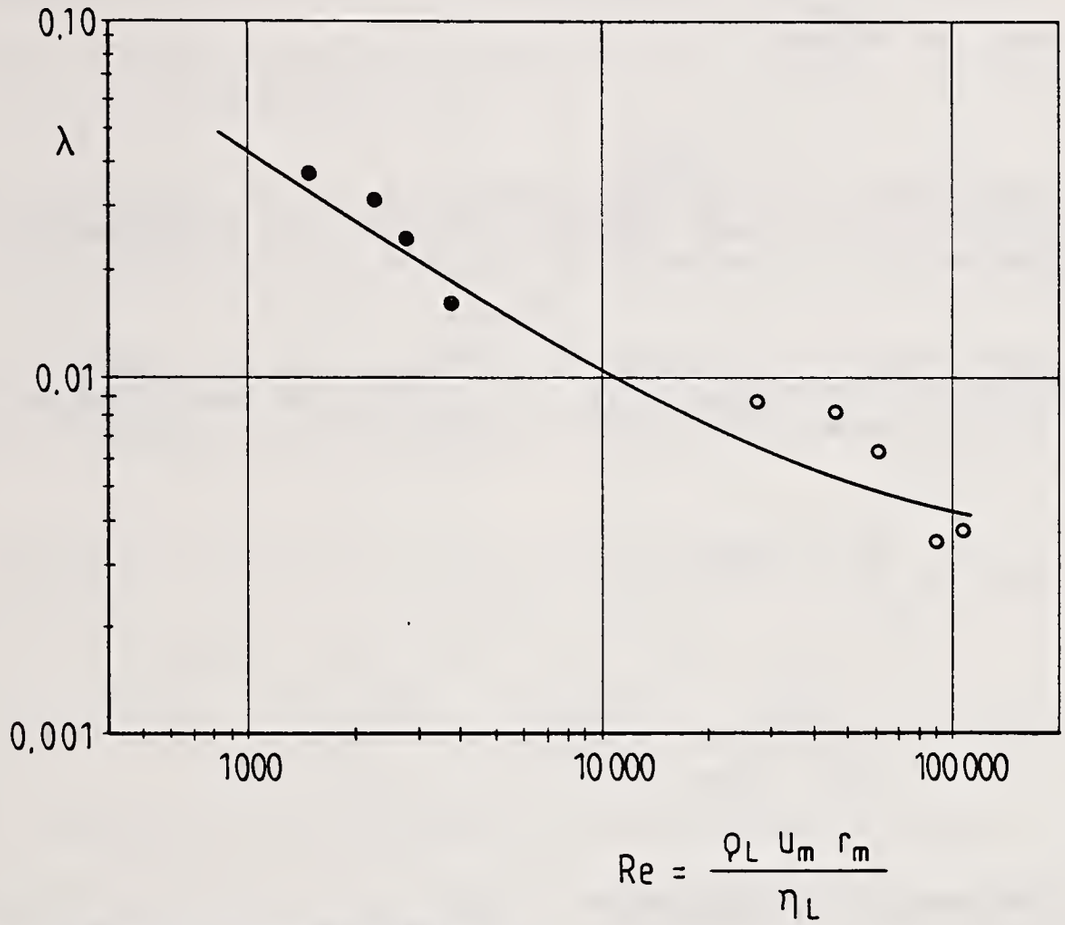

Figure 2: Friction coefficient λ

3. FORMATION OF DROPS

3.1 Theory

Sinuous wave breakup, which is due to aerodynamic forces, has been closely examined by Dombrowski and Johns /1/. From their model, equation (13) for a nonviscous, conical sheet was derived.

$$d \sim \delta \left(\frac{\rho_L}{\rho_G}\right)^{1/6} \left(\frac{\sigma}{\rho_L w^2 \delta}\right)^{1/3} \left(\frac{r_i}{\delta \tan\gamma}\right)^{1/3} \qquad (13)$$

As this model does not take into account viscous forces of the gas, we found, that it had to be supplemented by a Reynolds number for the gas flow in contact with the liquid film :

$$Re_\delta = \frac{\rho_G \, w \, \delta}{\eta_G} \qquad (14)$$

With equation (13) and (14) a complete set of similarity numbers according to similitude theory is given. Our experimental resultsjustify the omission of the liquid viscosity in this context.

At higher outlet velocities the liquid film is atomized by turbulent liquid forces (/3/, /4/). This is described by two similarity numbers, the Weber number and the Ohnesorge number:

$$We = \frac{\rho_L \, w^2 \, d_{max}}{\sigma} \qquad (15)$$

$$Oh = \frac{\eta_L}{\sqrt{\rho_L \, \sigma \, d_{max}}} \qquad (16)$$

3.2 Measurement Techniques

The maximum drop size was measured by sampling the largest drops in oil. A Malvern particle Sizer was used for the determination of the drop size distribution.

3.3 Results

The application of equation (13) on experimental data leads to Figure 7. Hence the maximum drop size for wave breakup is calculated by equation (17):

$$d_{max} = 1{,}13 \; \delta \left(\frac{\rho_L}{\rho_G}\right)^{1/6} \left(\frac{\sigma}{\rho_L \, w^2 \, \delta}\right)^{1/3} \left(\frac{r_i}{\delta \, \tan\gamma}\right)^{1/3} \left(\frac{\rho_G \, w \, \delta}{\eta_G}\right)^{1/5}$$

The exponent of the Reynolds number was found out by means of correlation of experimental results.

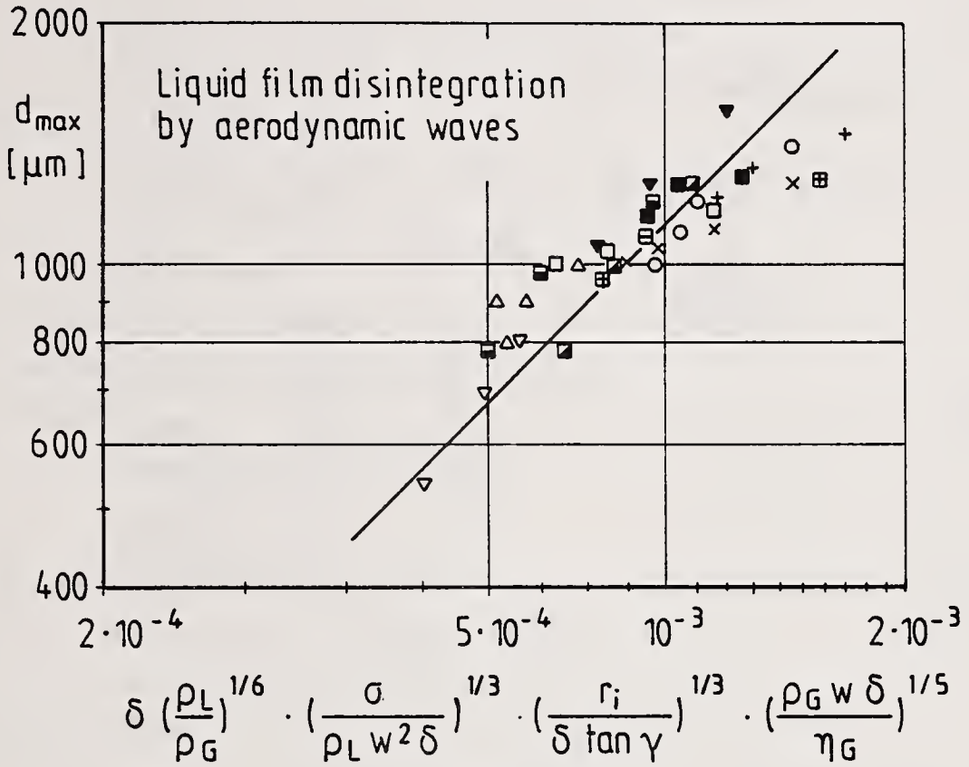

Figure 3: Maximum drop diameter for sinuous wave breakup

Equation (17) is valid for sinuous wave breakup. If the velocity of the liquid film is raised up to a certain point the turbulent forces in the liquid film will surmount the aerodynamic forces, which cause sinuous wave breakup. The drop size is then smaller compared to calculation with equation (17). The stability criterion for maximum drop size is given by Figure 4:

$$We = 4{,}1 \; 10^4 \; Oh^{1/6} \qquad (18)$$

for $0{,}003 < Oh < 0{,}03$. The experiments showed, that gas density and liquid film thickness have if any only small influence. Table 2 gives characteristic parameters of the measured drop size distributions:

	wave breakup	atomization
d_{32}/d_{max}	0.35	0.31
d_{50}/d_{max}	0.48	0.42

Table 2: Characteristic drop diameters

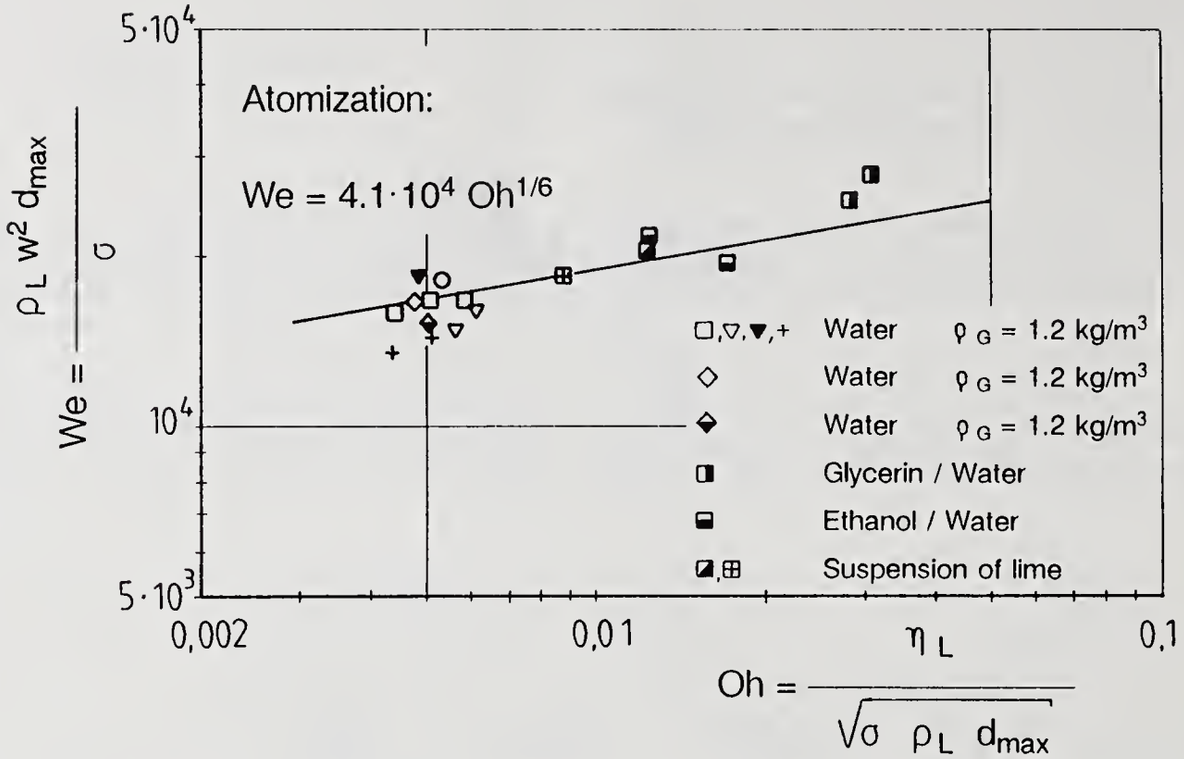

Figure 4: Atomization of the liquid film

4. NOTATION

A	:	area	m^2
d	:	drop diameter	m
d_{32}	:	Sauter diameter	m
d_{50}	:	mass medium drop diameter	m
d_{max}	:	maximum drop diameter	m
M	:	angular momentum	Nm
$\dot{M}$	:	mass flow	kg/s
Oh	:	Ohnesorge number	
Δp_i	:	acceleration pressure loss	N/m^2
Δp_e	:	friction pressure loss	N/m^2
r	:	radius	m
r_m	=	$\sqrt{r_a\ r_i}$: mean radius	m
u	:	angular velocity	m/s
u_m	=	$\sqrt{u_a\ u_i}$: mean angular velocity	m/s

v_i	:	mean velocity in the outlet	m/s
v_{ax}	:	axial velocity of the liquid film	m/s
$\dot{V}$	:	volume flow	m^3/s
w	:	velocity in the outlet	m/s
We	:	Weber number	
γ	:	spray angle	o
δ	:	film thickness	m
ζ_i	:	pressure loss coefficient	
η	:	dynamic viscosity	Pa·s
λ	:	friction coefficient	
ρ	:	density	kg/m^3
σ	:	surface tension	N/m
τ	:	tangential stress	N/m^2

Subscripts:

a	:	on spin chamber radius
e	:	inlet
G	:	gas
i	:	on outlet radius
L	:	liquid
R	:	friction

5. REFERENCES

/1/ Dombrowski,N., Johns, W.R.:;
Chem.Eng.Sci. 1963, Vol. 18, S. 203 - 214

/2/ Muschelknautz, E., Krambrock, W.:
Chem.-Ing.-Techn. 42 (1970) 5, S. 247 - 255

/3/ Troesch, H.A.:
Chem.-Ing.-Techn. 26 (1954) 6, S. 311 - 320

/4/ Grassmann, P.:
Physikalische Grundlagen der Vefahrenstechnik
Salle u. Sauerländer, 3. Aufl. 1983

DROP SIZE-VELOCITY CORRELATION AND DROP FLUX IN THE SPRAY CONE OF A FAN SPRAY ATOMISER

G. Schulte and I. Özdemir

University of Bremen, Verfahrenstechnik
Bremen, Germany

ABSTRACT

Sprays of liquids are of high importance in many technical processes. Therefore the measurement of drop size and velocity have always been of interest to research work [1-5]. In such work laser measurement instruments give the advantage of non-invasive access to the wanted location in spray cones [6-9]. However, although a lot of work is done in this field there still seems to be sometimes unclearness in respect to interpretation of measurement results in terms of the parameters of the dispersed flow. The work here reports on an investigation of a spray by means of the phase Doppler anemometer (PDA) intrinsically giving the flow parameter "particle flux" and additionally by means of diffraction size meter (DSM) intrinsically giving the flow parameter "particle concentration". The relationship between these flow parameters is given by the drop size-velocity correlation at the respective location in a spray. This correlation and the development of the flow parameters mentioned above will be discussed in the following paper.

GENERAL REMARKS

In investigation of drop flows i.e. sprays are two points of main interest. On one hand the description of the dispersed flow situation on the other knowledge of the individual elements, the drops. If we look at sprays, by the view of particle measurement technology [10], we look for a physical property that characterizes the particles - mostly the "size" given as an equivalent drop diameter - and we look for the particle velocity as a second item which characterizes the particle motion and causes their location to depend on time. So we not only look at particles in terms of their physical properties but also in terms of flow parameters. A common parameter related to space is the "particle number flow concentration" c_o. Another parameter related to time is the "particle number flow". The particle flow often will additionally be related to a flow cross-sectional area so the resulting parameter is the "particle number flux" f_o. Basically in a steady spray these parameters can be defined for each location in the spray cone and at a point in time ($(f_o=f_o\ (x,y,z,t)$; $c_o=c_o(x,y,z,t)$). These flow parameters normally vary with the different spray locations because of the spreading character of a spray and ac- or deceleration of the drops. Particle measurement methods give distributions of the measurement

quantity according to size (and velocity) and intrinsically measure a flow parameter either drop "flux" or drop "concentration". Normalized distributions from spray measurements and mean diameters derived from therefore always should be marked as either flux (index "f") or concentration (index "c") related. If correlated values of size and velocity are known these results are convertible [9]. It depends on the field of application whether one is more interested in the drop "flux", i.e. in spray-coating or in the drop "concentration", i.e. in burning sprays of fuel.

The following report on the experimental analysis of a spray of water is organized as follows: First a description of the experimental rig and the measurement locations. It will be followed by the presentation of profiles of medians of drop size from PDA and DSM measurements. Thereafter 2-dimensional number distributions are analyzed with respect to the drop size-velocity correlation. And at last we will look at drop number and drop volume flux through the spray planes under observation.

EXPERIMENTAL PROGRAM

Water was sprayed in a vertical arranged flow channel of 1000 mm length having a cross section 900 mm to 750 mm (Fig. 1). Grids at top and bottom of the chamber provided a block profile of the superimposed air flow of v = 0,2 m/sec. The spray investigated was a flat full cone spray generated by a fan spray atomiser. The nominal operating pressures in our experiments were 2 bar, 3 bar and 4 bar. This corresponds to theoretical spray angles of 51°, 65° and 69°. Figure 2 shows the shape of the spray. Drawn are three horizontal planes E2 at z=20 cm, E3 at z=30 cm and E4 at z=40 cm. The experimental program reported here covered phase Doppler (PDA) measurements at 350 locations (65 in E2; 125 in E3 and 160 in E4) and diffraction measurements (DSM-"line of sight") at 120 locations 30 in E2; 40 in E3; 50 in E4).
The phase-Doppler-instrument was built by components from Dantec and a self-made processor:

He-Ne laser; 25 mW	wave length: 632,8 mm
intersecting angle: 2,5°	elevator angle: 5,8°
off-axis angle: 60°	

A measurement location for PDA in a spray plane z is defined by PDA (x,y).
The diffraction size meter (DSM) was a Helos 12 LA:

He-Ne laser: 5 mW	diameter of laserbeam: 13,28 mm
size range: 7,9-1750 mm	focus length of receiver: 1000 mm

In a given spray plane z the DSM-measurement location is given by the "line of sight" parallel to the y direction defined by DSM (x).

DISCUSSION OF RESULTS

Figure 3 shows the profiles of the volume medians $d_{50,3f}$ obtained by the PDA. The number of counts included in the evaluation was 4000, however, we found that even a number of 2000 counts leads to a sufficient accuracy if we look at the marginal number distributions because some larger drops have here no significant influence. Working out volume distributions causes that the number of large drops will become a most important influence. On the other hand, a counting method like PDA may become a time consuming method depending on the drop flux at the respective measurement locations. So in our case, the measurement-time for 4000 drops reached from 50 sec in the centre on the spray axis up to 500 sec at the spray boundary with corresponding acceptance rates of

0,5 up to 0,9. For balance calculations the results were extrapolated assuming the distributions of drops not included in the evaluation are the same as from those included. So the number of 4000 counts seems to be a reasonable compromise. This the more as we have a large number of measurement locations so that significant deviations from the general trend are easier recognizable as unsteadiness in the profiles of the parameters of interest. The top of the profiles look very smooth and show that in the core of the spray the medians are lowest as expected. The shapes of the profiles are very similar. The step in the $d_{50,3f}$ profile of spray plane E4 was caused by an adjusting error which affected all the measurements at locations x=-1 up to x=-12 cm spray plane z=40 cm. The profile of $d_{50,3f}$ along x-axis (run a in Fig. 4a) show more clear the effect of the adjustment error. To find out whether this unsteadiness was due to an asymmetry of the spray pattern or due to a supposed adjustment error we ran an additional series of measurements by PDA (run b in Fig. 4a) and as reference by DSM (Fig. 4b). We found that the PDA results fit very well with those obtained in the first series except these values which we assume to be due to an adjustment error. So the conclusion: before believing in absolute values of point measured results it is recommended to look at the results from locations in the vicinity to find out whether the results fit with the general trend of the parameter in question. Figure 4b gives the volume median diameter $d_{50,3c}$ obtained from DSM "line of sight" measurements at different x-locations. The "line of sight" represents the axis of the intersecting volume between the laser beam and spray, and was parallel to the y-axis. The DSM-result gives an average of all drops in the intersecting volume. A transformation of these integral data into point data is possible by a Fourier transform method [11]. However because of the shape of the spray and the alignment of the "line of sight" overall and point data show the same behavior [6] and therefore for the aim of this work the overall "line of sight" data are sufficient. The curves of $d_{50,3c}$ show for the PDA results a clear symmetry with respect to the spray axis represented by the ordinate x=0.

Figure 5 shows the 2-dimensional number distribution of size and velocity $h_{of}(d,v)$ on the spray axis and at the boundary of the spray cone in 3 spray planes in question. From these again we recognize the drops on the spray axis are smaller. The difference between velocity of small and large drops will become smaller with increasing distance from nozzle tip and from spray axis or in other words more general: the correlation of size and velocity of the drops as we see is dependent on the location in the spray. As 2-dimensional distributions contain a large amount of information it is difficult to get clearness in looking at a number of them at the same time. So it is usual to restrict oneself to looking at the key parameters of interest. The drop size-velocity correlation seems to be a parameter worth looking at respectively to be meaningful to describe the spray cone in terms of it. Looking at the so called empirical regression curve $v_i = v\ (d_i)$ which is often given as standard software of PDA-instruments we mostly realize unsteadinesses at the tails where the distribution counts lower numbers of drops in its bins. $v(d_i)$ in Fig. 6 shows a typical shape of such curves. Computing the linear regression curve $v_{o,o}$ of the $v(d_i)$-values this gives only a poor fitting although there seems to be a linear correlation for the main bulk of drops. The result will become much better if we include only this main bulk of drops into the calculation of the linear regression. The resulting straight line $v_{0,2}$ now fits very well with the empirical regression curve besides at its ends. Included in the calculation are here only these size bins of the boundary distribution $h_{of}(d_i)$ in which there were counted numbers of more than $0,2*h_{ofmax}$ drops meaning high enough by view of

statistics. This procedure of data preparing results in a linear correlation coefficient of $r_{0,2}$=0,994 which points out a really good fitting whereas only about 7% of all drops are excluded from the calculation. If the bulk contains more than 90% of the drops this can be seen as representative for the size-velocity correlation, so we looked for the linear regression in this way for all measurement locations and we found fairly good results for the $r_{0,2}$-values all over the spray, seen in Fig. 7a, which means the correlation of the main field of drops is given fairly good by a linear regression. No significant differences are seen which depend on the measurement location. For comparison in Fig. 7b are given the $r_{o,o}$-values in spray plane E2 which confirm the result of Fig. 6: the correlation coefficient of all drop size bins are included is mostly less than 0,8 saying that not linear correlation is given if the tailvalues are included. Figure 8 gives the linear regression coefficient $b_{vd0,2}$ - the measure of ascent of the regression line-for the x-axis location corresponding to the $r_{0,2}$-values of Fig. 7a. The basic information is that there is a clear dependency on the measurement position recognizable. As expected in general at downstream positions $b_{vd0,2}$ is smaller: the angle of ascent of the regression line becomes smaller. The situation on the spray axis is different dependent on atomiser distance. So the air entrainment seems to cause an equalizing effect on the drop velocities which is seen at the boundary of the spray cone and on the spray axis here more evident at downstream positions where the $b_{vd0,2}$ are lower on the spray axis. The development of the linear regression coefficient $b_{vd0,2}$ and of the respective coefficient of correlation $r_{0,2}$ along the spray axis is seen in Fig. 9a. We recognize increasing of $b_{vd0,2}$ and after getting the highest value at z=15 cm going down to $b_{vd0,2}$=0,01 at z=50 cm. Again the correlation coefficient $r_{0,2}$ points out the good quality of the linear regression for all locations. The $b_{vd0,2}$ curve shows - if extrapolated to a starting point - that first all drops seem to have the same starting velocity and that very soon because of deceleration of the small drops we have a significant increase of $b_{vd0,2}$. The development of the arithmetic means $d_{1,0f}$ (Fig. 9b) is affected by the air entrainment effect and has its lowest value at z=22,5 cm. At the same time the velocity means $v_{1,0f}$ are represented by a steady line lastly reaching the velocity of the air stream.

We will now leave the distribution parameters and look at results computed from the distribution as spray parameters (Fig. 10). First the drop number flux f_o as profiles in the observed spray planes. We see a very clear characteristic spray pattern of the atomisers and the development of the spray with growing distance. In the core of the two phase flow of the spray there are by far higher values of drop <u>number</u> flux f_o caused by the entrainment effect mentioned before, which shifts the smaller drops to the centre of the spray. Again the symmetry of the spray pattern in the x and y directions as well (the view shown here is only +y). This is confirmed and the spray situation will become clearer from Fig. 11 where the drop <u>volume</u> flux f_3 is seen. The peaks especially in E2 and E3 are caused by the weighing effect in volume distributions: the comparatively low number of larger drops at the spray boundary have a larger contribution to the volume flux than the high number of small drops at the spray centre. Working out the drop volume flux balance is a principle possibility given by the PDA results. So in Fig. 11 the drop volume flow through spray planes is given as well. But one should not forget that although PDA gives the results as absolute values these results are affected by a number of error sources reaching from the optical characteristics of the process fluid and bias effects caused by size and/or velocity up to the signal processing which can cause a "complex" influence on the results. So at least PDA results give values of important parameters in

sprays at different operating parameters for different locations as information relative to each other so compensating potential bias influences. The balance here is worked out based on a large number of measurement locations and on results which are confirmed by a reference method (DSM). This allows a more extensive data preparation than without additional information. The high knowledge of the process in question last but not least leads to the good fitting of the balance calculation results presented here.

SUMMARY

PDA and DSM were used for a descriptive analysis of a spray of water. PDA and DSM deliver intrinsically flux related or concentration related results which are in principle convertible by using the drops velocity, however here measured only by PDA. The spatial averaging effect of DSM is possibly not wanted. In this case, the procedure of getting "point" results from different measurements is necessary but also time consuming. If as in our case, the geometry of the spray allows to have similar DSM-measurement volumes for different locations also the DSM deliver a detailed analysis of the spray in terms of drop distributions according size in a less time consuming procedure in comparison to PDA. The PDA however allows a far more differentiated analysis of sprays in measuring also drop velocities and because of its high spatial resolution. From this arises the possibility of working out the drop size-velocity correlation as a quite meaningful spray parameter and derived quantity like the drop volume flow.

REFERENCES

1. Bachalo, W.D., Houser, M.J., Smith, J.N., Atomisation and Spray Technology, Vol. 3, pp. 53 (1987).
2. Bauckhage, J., Dannehl, M., Fritsching, U., Schöne, F., Schulte, G., 2nd Intern. Cong. on Laser Anemometry - Adv. and Appl., Strathclyde/UK (1987).
3. Dannehl, M., Schöne, F., Schulte, G., Liquid Particle Size Measurement Techniques: 2nd Volume, ASTM STP 1083, Hirlemann/Bachalo/Felton, Eds. American Society for Testing and Materials, Philadelphia, pp. 246-256 (1990).
4. Dodge, L.G., Rhodes, J., Reitz, R.D., Applied Optics, Vol. 26, No. 11, pp. 2144 (1987).
5. Leschonski, K., Part. Charact., Vol. 1, pp. 89 (1984).
6. Meyer, P., Chigier, N., Atomisation and Spray Technology, Vol. 2, pp. 261 (1986).
7. Raasch, J., Umhauer, H., Chemie Ingenieur Tecknik, Vol 49, No. 12, pp. 931 (1977).
8. Schulte, G., ICLASS 85, London/UK, Proceedings (1985).
9. Schulte, G., Bachkhage, K., Flögel, H.-H., Fritsching, U., 3rd Intern. Symp. of Appl. of Laser Anemometry to Fluid Mechanics, Lisbon/Portugal (1986).
10. Young, B.W., Bachalo, W.D., in The direct comparison of three 'in-flight' droplet sizing techniques for pesticide spray research, in Sym. Optical Particle Sizing-87, pp. 42-1 - 42-15, Rouen, France (1987).
11. Zhu, H.M., Sun, T.Y., Chigier, N., Atomisation and Spray Technology, Vol. 3, pp. 89 (1987).

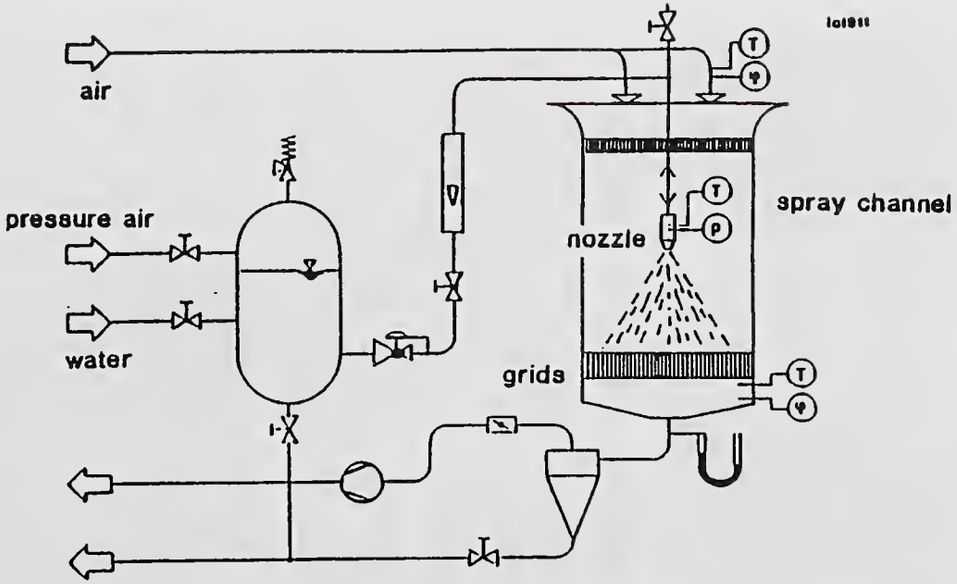

Fig.1: Experimental rig for spray investigations

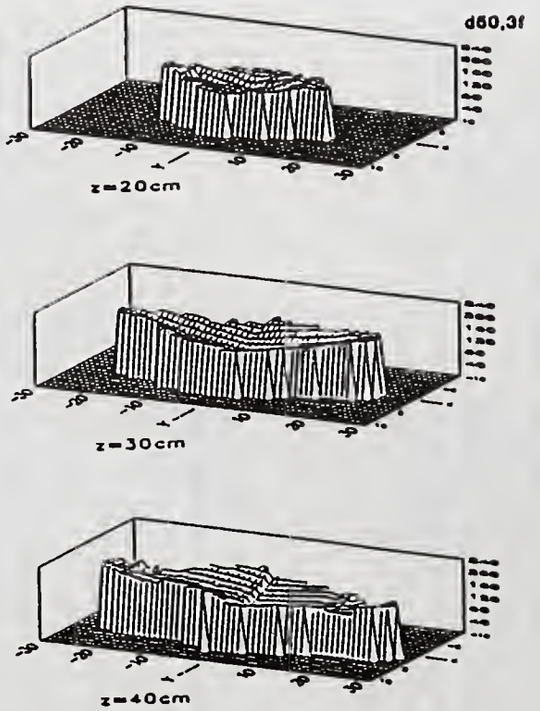

Fig.3: Profiles of volume medians d50,3f from PDA-measurements

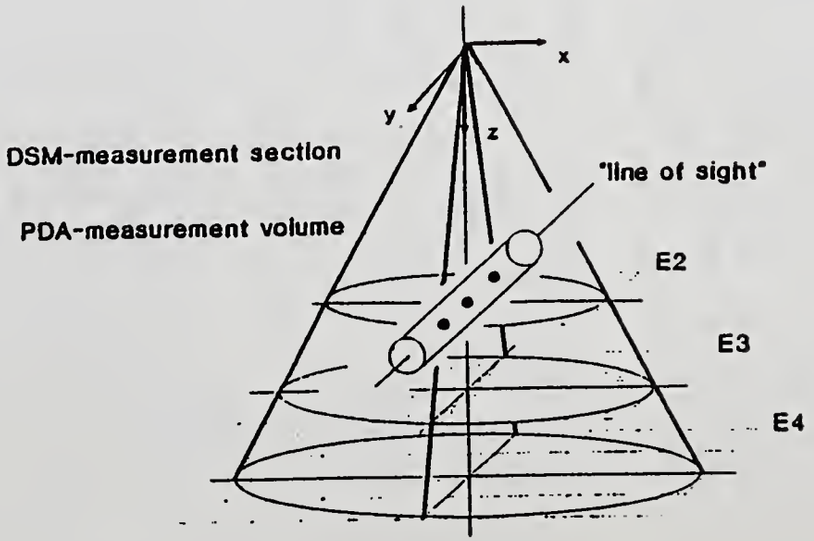

Fig.2: Spray cone
Location of measurements

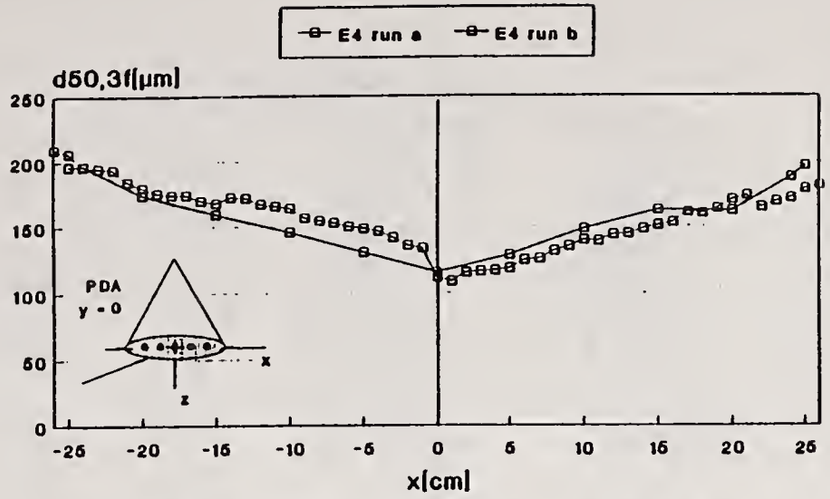

Fig.4a : d50,3f profile on x-axis in E4

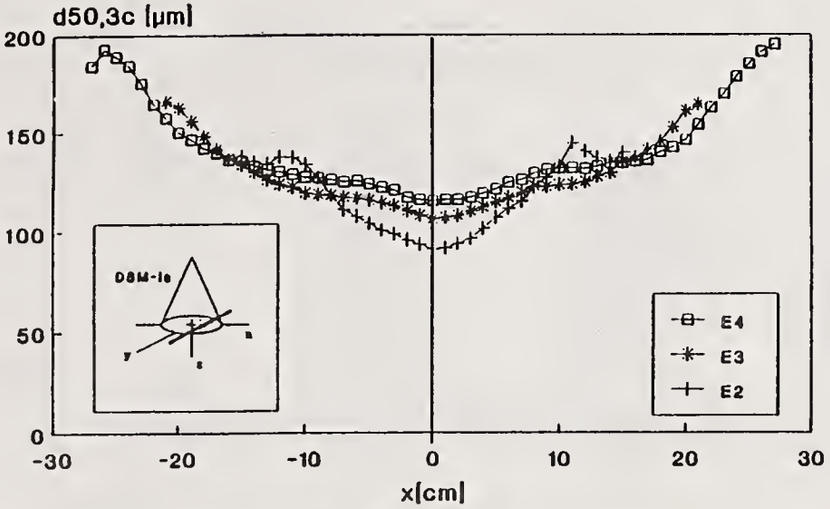

Fig.4b: volume medians d50,3c from DSM "line of sight"- measurements

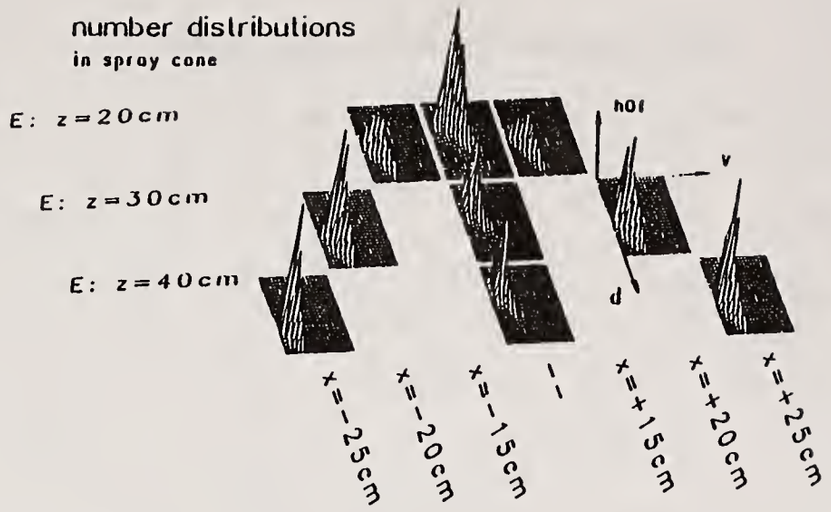

Fig. 5: Number distributions h0f drop flux at different locations

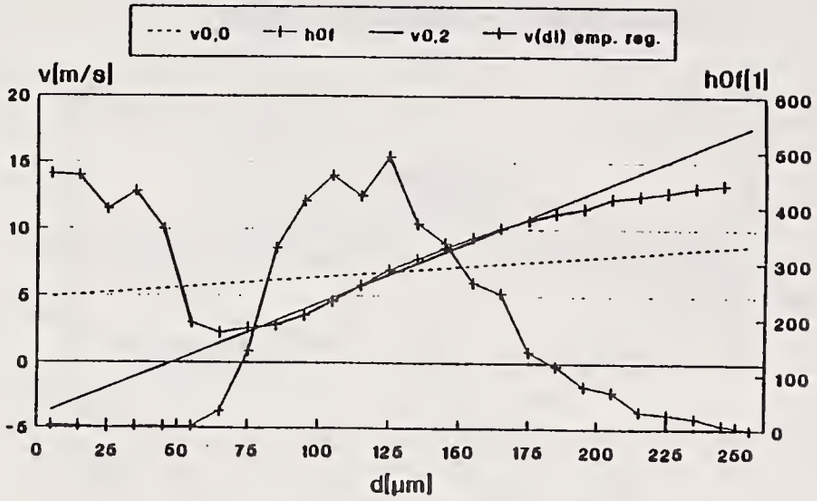

Fig.6: Linear regression of the v(di)-values of d-v distributions

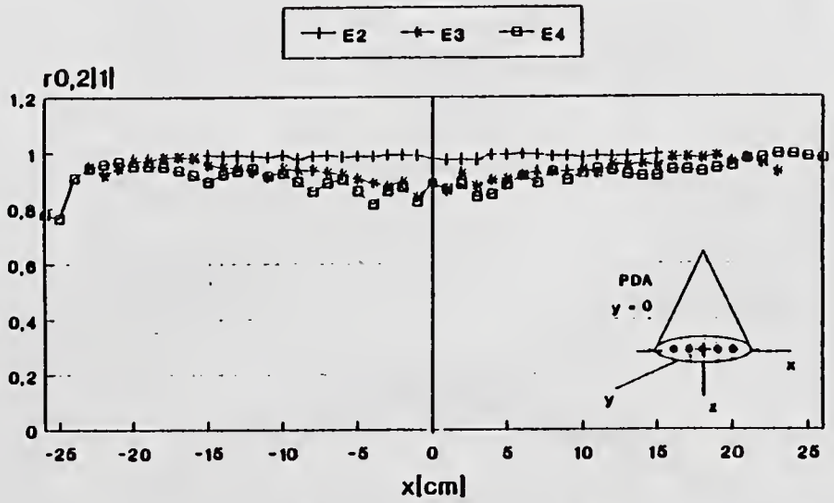

Fig.7a: Coefficient of linear correlation r0,2 on x-axes

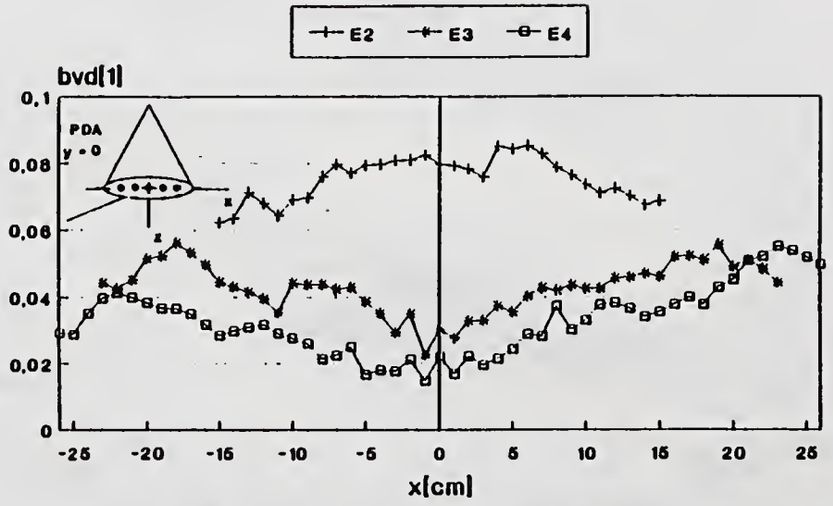

Fig.8: Coefficient of regression bvd0,2 on x-axes

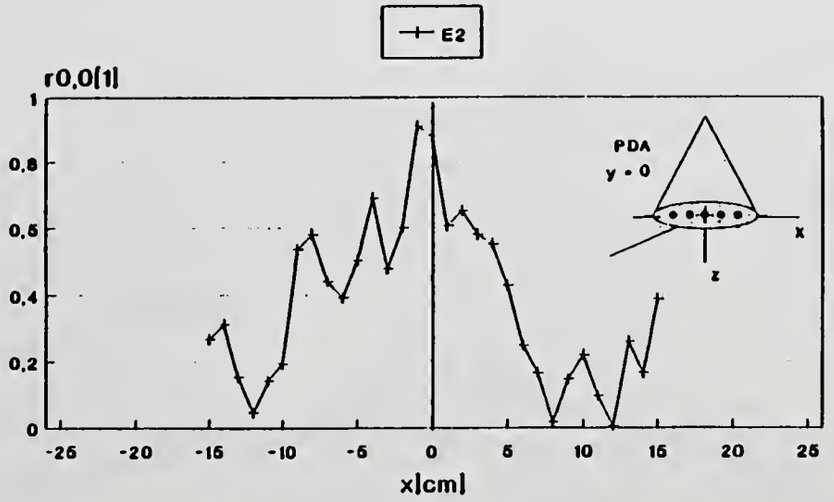

Fig.7b: Coefficient of linear correlation r0,0 on x-axis

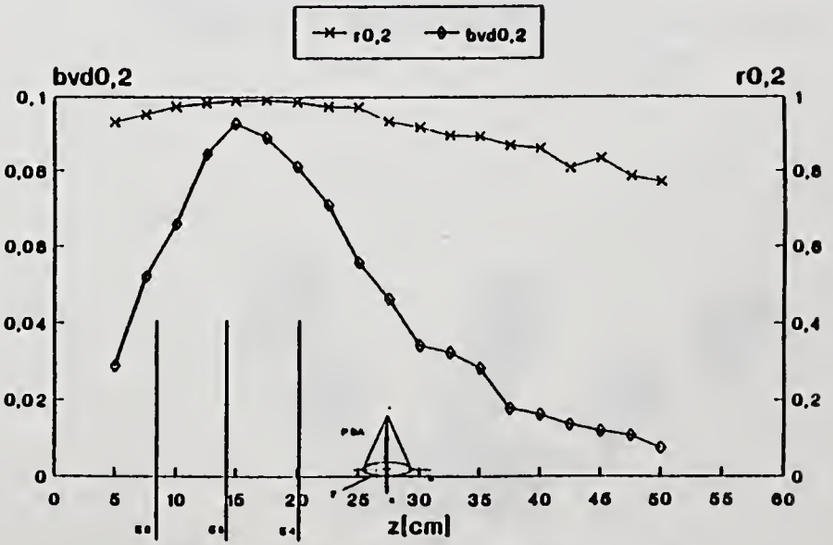

Flg.9a: bvd0,2 and r0,2 along z-axis

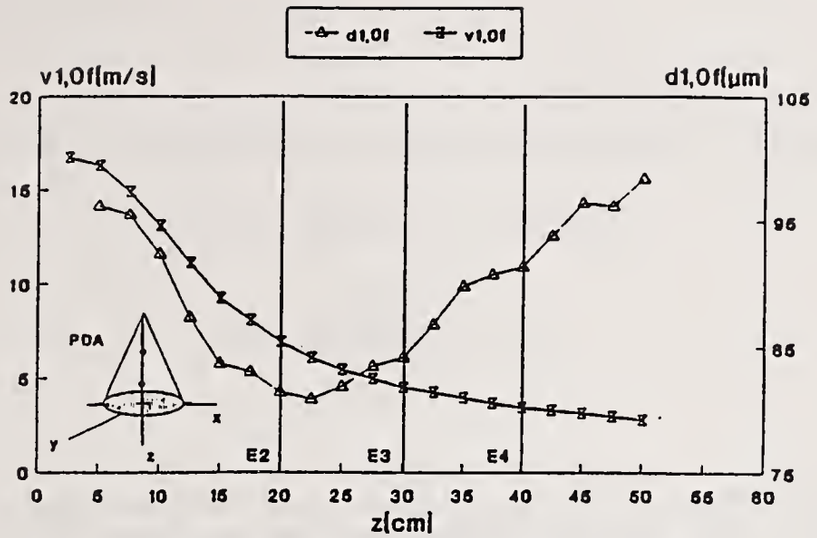

Fig.9b: d1,0f and v1,0f along z-axis

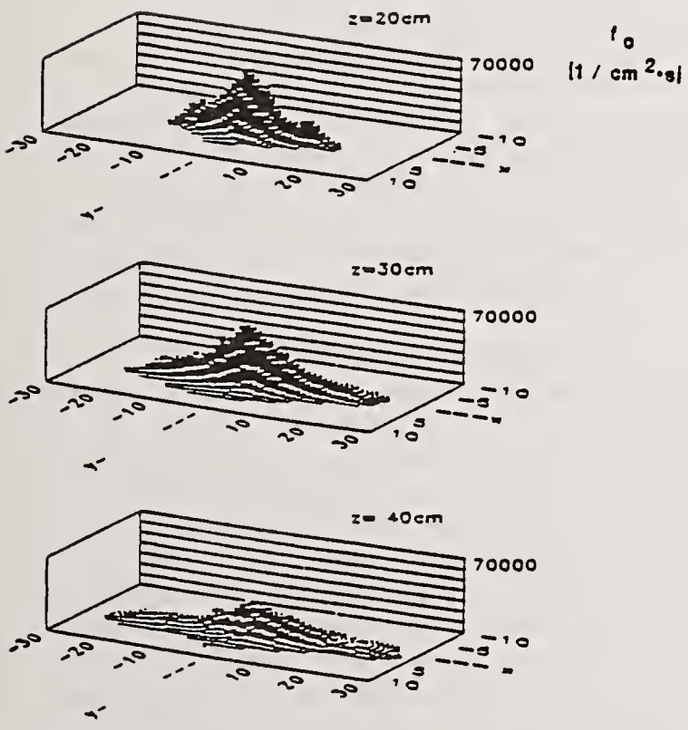

Fig.10: Drop number flux f_0
Profiles from PDA-measurements

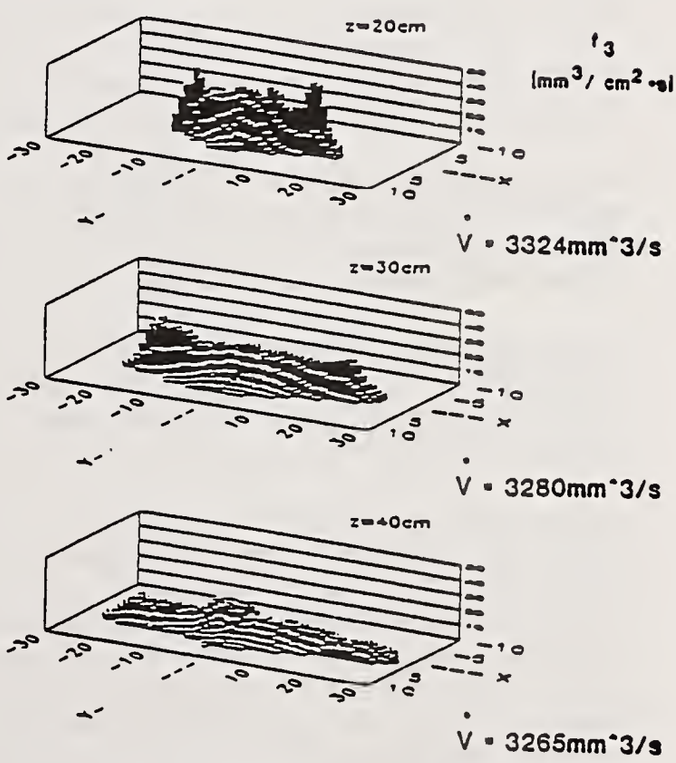

Fig. 11: Drop volume flux f_3
Profiles from PDA-measurements

NUMERICAL ANALYSIS OF PRESSURE SWIRL ATOMIZERS

C.-P. Mao and S.G. Chuech

Delavan Inc.
West Des Moines, IA, U.S.A.

ABSTRACT

This study investigated the liquid breakup process in pressure swirl (simplex) atomizers. A "FILM" code which combined a film dynamics model with wave instability theory was developed to describe the flow characteristics and primary breakup process. This analysis led to the prediction of film trajectory, angle, breakup length, thickness, velocity and drop size as a function of flow conditions, fluid properties and nozzle geometry. Experimental data obtained with a high-magnification 4x5 camera, a Phase/Doppler Particle Analyzer, and a PMS imaging probe were used for model verification. The predicted Sauter mean diameters showed good agreement with the PMS data.

INTRODUCTION

Pressure swirl atomizers are widely used in industrial, agricultural and propulsion applications. These atomizers are very popular because of their simple design, low cost and effective atomization.

In most pressure swirl atomizers, the liquid is injected under high pressure through tangential slots or passages into a small swirl chamber. Prior to discharge through a circular orifice, the liquid forms a hollow film as a result of the vortex and air core developed within the swirl chamber.

As this film emerges from the exit orifice, wave instability immediately occurs, leading to the disintegration of the liquid sheet into ligaments and droplets. Following initial breakup, the ligaments and large drops undergo a secondary breakup process. During this stage, many drops collide and coalesce. The atomization process is finally completed further downstream in the dispersed two-phase regime where spherical drops exist.

The characteristics of the liquid film are considered to be extremely important in determining spray quality. A considerable number of studies have been conducted on the formation of liquid film and variations in film thickness and velocity as a function of nozzle design dimensions and fluid properties. It is well known that the initial axial and tangential velocities at the exit orifice determine the shape and angle of the spray and that the initial film thickness is related to drop size.

Despite some minor differences among previous theories [1-7], the investigator made important contributions to the understanding of the flow phenomena in pressure atomizers. These theories permit the prediction and correlation of initial film properties as a function of physical dimensions of the nozzles, fluid properties and flow conditions. However, there is a common deficiency in most existing theories; namely, the lack of information concerning the process of film breakup outside the nozzle. It is essential to determine the film properties at the nozzle exit, but it is equally important to understand the breakup process. Spray characteristics such as symmetry, uniformity, pattern, drop size distribution, velocity, and volume flux are closely related to the film trajectory, breakup length, and film thickness outside the nozzle. Also, the interaction between the liquid film and ambient air can be extremely critical in determining the downstream spray characteristics.

In the present study, a simple film dynamic model which, with wave instability theory, was developed to describe the film characteristics outside pressure swirl atomizers. This analysis led to the prediction of film trajectory, breakup length and initial drop size distribution. Experimental data obtained with a Phase/Doppler Particle Analyzer, PMS imaging probe, and a high-magnification camera were used to verify the model predictions.

EXPERIMENTAL APPARATUS

Three pressure swirl atomizers were selected for the study. These nozzles have similar designs, but slightly different dimensions in the fuel distributor and exit orifice. Nozzle flowrates were measured on a calibrated test stand equipped with turbine flow meters. All tests were conducted using MIL-C-7024 Type II calibration fluid having the following physical properties: density = 0.769 g/cc; kinematic viscosity = 1.15 centistoke; and surface tension = 28.2 dynes/cm. Each nozzle was tested within a 20 to 1380 kPa pressure range.

A high-magnification 4x5 format camera was used to determine the spray angle, film trajectory and breakup length. The camera was equipped with a variable-length bellows extension to permit close-up views near the breakup zone. All photos were taken with a back-lighting technique. Spray motion was frozen by means of a high-intensity, short-pulse (0.5 μsec) flash unit manufactured by EG&G (Model 549). Kodak T-Max 400 film was selected for this study.

An Aerometrics Phase/Doppler Particle Analyzer (PDPA) was used to measure the drop size distributions and mean diameters. A thorough calibration study using a single- drop generator and a rotating disc was conducted to determine the accuracy and limitations of the instrument. For calibration, a piezoelectric generator was used to produce uniform size drops ranging from 150 to 1000 microns.

During data acquisition, the PDPA instrument was used to obtain both local and global drop size information. The atomizers were mounted on an automated traversing mechanism to allow movement at fixed increments for the purpose of obtaining local point data. In addition, the traverse device could also sweep continuously across the probe area from one side of the spray boundary to the other. Using this continuous traversing method, it was possible to obtain a global mean drop size which closely represents the entire cross-sectional area. All drop size measurements were made 10 cm downstream from the nozzle face.

A Particle Measuring Systems (PMS) optical array spectrometer probe (OAP-260X) was utilized for direct measurement of global mean diameters. The probe covers a range of 21 to 1875 microns in 62 channels, with approximately 30 microns per channel. A collimated laser beam exiting from a 2 mW He-Ne laser unit is directed perpendicularly across the main flight direction of the droplets. Droplets are sized using a linear device with masked diode elements to sense the shadows projected on the diode elements by the moving droplets.

FILM DYNAMICS AND WAVE INSTABILITY THEORY

In the analysis of the primary breakup process, two basic models are required to describe the physical phenomena. First, a film dynamics model is needed to simulate the motion of the liquid film as it emerges from the orifice. Second, instability theory is required to describe the growth and propagation of waves on the film surface.

The present study is concerned only with primary breakup and the mean diameters that represent the entire spray. Other physical sub-models, such as secondary breakup, evaporation and drop history, were not considered. The theoretical analysis focused only on the breakup regime.

Film Dynamics Model

In the present analysis, the hollow film formed outside the nozzle was assumed to be a steady-state structure with no pressure gradient in the circumferential direction. Viscous forces within the thin liquid film were neglected. However, viscous friction at the interface was taken into account.

The governing equations for the hollow film were derived in a curvilinear coordinate system conforming to the curvature of the liquid sheet. An integral method was used to establish the mass and momentum equations. Primary forces acting upon the control volume included: convection, centrifugal motion, interface friction, gravity, pressure gradients and Coriolis forces. The governing equations for the swirling film are described in detail in reference [8].

In the present model, the pressure differences between the inner and outer film surface were represented by the capillary force (i.e., surface tension). The interaction between the liquid film and surrounding air was calculated from the interface friction on both sides of the film surface. The friction coefficients are non-linear functions of the Reynolds number based on the local film velocity and thickness. The three momentum equations were solved simultaneously to yield information on the film velocity and trajectory (film shape and angle). The variation of film thickness along the sheet surface was then determined from the mass continuity equation.

Wave Instability Theory

Instability theory has been successfully employed to describe the breakup process in flow systems such as liquid jets and fan sprays. From photographic studies, the theory of wave instability also seems to be suitable for describing the behavior of a hollow film. The amplitude of the waves gradually increases as they progress toward downstream along the film surface. Breakup occurs at a point where the wave amplitude exceeds a certain critical value.

Based upon Meyer and Weihs [9], a characteristic equation for hollow films can be derived from the temporal growth rate of the unstable waves, according to the following equations:

$$G_1\alpha^2+G_2\alpha = G_3$$

$$\text{where } G_1 = \rho_l h+(\rho_g/k)$$

$$G_2 = -2[\mu_l/r-U_r\rho_g i]$$

$$G_3 = \rho_g k U_r^2-\sigma_l k^2 \qquad (1)$$

Equation (1) relates the growth rate to the local film properties and the surrounding air flow conditions. It can be solved numerically to find all potentially unstable waves which, in turn, determine the breakup length and drop size distribution.

In determining the breakup length, it is crucial to find the proper criteria for disintegration of a swirling film. A spin frequency defined by the tangential velocity at the nozzle exit was found to be directly related to the breakup process. Two characteristic parameters for determining breakup length are defined as follows to determine breakup length:

$$f_c = w_2/D_2 \qquad (2)$$

$$\lambda_c = u_2/f_c \qquad (3)$$

It was assumed that liquid disintegration occurs when the wave amplitude exceeds one-half of the characteristic wave length or one-half of the local film thickness.

When the fastest growing wave propagating in the streamwise direction meets the breakup criteria, a circular ribbon of liquid detaches from the leading edge of the surface. Meanwhile, unstable waves keep growing in the circumferential direction of the circular ribbon. Further breakdown occurs in the tangential direction as a result of flow instability and stretching.

One important assumption was made here for the prediction of mean drop size and distribution. It was assumed that, after breakup, the drop size distribution would follow the same distribution function as that determined by the unstable (positive) growth rates. A probability density function (PDF) can be constructed from the solutions of Equation (1). This PDF was then used to calculate the drop size distribution and Sauter mean diameter.

Methods of Estimating Initial Film Properties

Previous studies [10-11] indicated that the initial film properties are extremely critical in determining the downstream spray characteristics. Hence, it is necessary to make an accurate estimate of the initial film characteristics to ensure a valid prediction of the spray breakup process.

In the present study, two methods were used to estimate these initial parameters. (A) Giffen and Muraszew's approach and (B) Lefebvre's correlation [12]. These two methods provided slightly different initial film properties.

Method (A) is based upon the concept that, anywhere inside the nozzle, the fluid mass, angular momentum and total momentum are conserved. In the analysis by Giffen and Muraszew, the following equation for the nozzle discharge coefficient was derived by assuming maximum flow through the exit orifice:

$$C_d = 1.17\left[\frac{(1-X)^3}{1+X}\right]^{0.5} \qquad (4)$$

Because C_d can be determined from flowrate measurements, Equation (4) may be solved for the value of X (area ratio of air core and exit orifice). The film thickness can then be calculated from the following equation:

$$X = (D_2 - 2t)^2 / D_2^2 \tag{5}$$

After obtaining the initial film thickness t, the axial and tangential velocities are determined from angular and total momentum balance.

The detailed description of method (B) for estimating the initial film thickness was presented in reference [12]. Unlike other investigators, Lefebvre indicated that the initial film thickness does not remain constant for a given nozzle, but depends on the operating pressure and fluid properties. He derived the following equation for predicting the film thickness in simplex nozzles:

$$t = 2.7\left[\frac{D_2 M \mu_l}{\Delta P \rho_l}\right]^{0.25} \tag{6}$$

In method (B), Equation (6) was used to calculate the film thickness at the nozzle exit. The axial and tangential velocities were then determined the same way as method (A).

Although the initial film thickness calculated by the two methods was slightly different, the results seem to be in the same order of magnitude, and follow the same qualitative trends. It was observed that the initial film thickness gradually decreased with an increase of the liquid pressure. As the pressure increased, however, the air core began to develop and gradually increased in diameter. At a certain high pressure, the diameter approached a constant value and the film thickness therefore also remained constant. As the pressure approached 1380 kPa, there was better agreement between the two methods.

RESULTS AND DISCUSSION

Comparison of Initial Film Angle and Film Trajectory

By using 4x5 high-magnification photography, it was possible to observe the detailed variations in film trajectory. A series of pictures taken at different liquid pressures was compared with the model predictions.

Present results indicated that the initial film properties estimated by method (A) agreed quite well with the experimental data. The predicted trajectory gradually became wider and more conical as the liquid pressure increased.

Although the FILM code prediction agreed reasonably well with the actual film shape, the code cannot predict liquid breakup at extremely low pressures. It predicted multiple "onions" that could not break up if the Weber number is less than 4.0×10^3. For lower Weber numbers, there is probably a different breakup mechanism which the present model does not take into account.

The most encouraging feature of the FILM code is its ability to predict the transition from an onion shape to a fully developed conical film as the flowrate gradually increases. Hence, this computer model is sufficient to describe the primary mechanisms at normal operating conditions.

Comparison of Breakup Length

Figure 1 compares the breakup length for predicted and measured values for the 2 and 10 GPH nozzles at several liquid pressures. Breakup length was defined as the film length along the nozzle axis, not the film surface. The values from method (A) agreed better with the experimental data. Within the pressure range under study, it was found that the breakup length generally decreased with an increase in liquid pressure. Both the experimental and predicted results approached asymptotic values. Thus, the breakup length will eventually remain constant after a certain high pressure is reached. For the 10 GPH nozzle, the discrepancy between the predicted breakup length from methods (A) and (B) diminished at liquid pressures above 1380 kPa.

The variation of breakup length appears to be closely related to the initial film thickness and angle. For a given flowrate, short breakup lengths are associated with thin films. Wide film angles also result in a shorter breakup lengths. The breakup length approaches a constant value at high pressures because of the constant film thickness and velocity at the exit orifice.

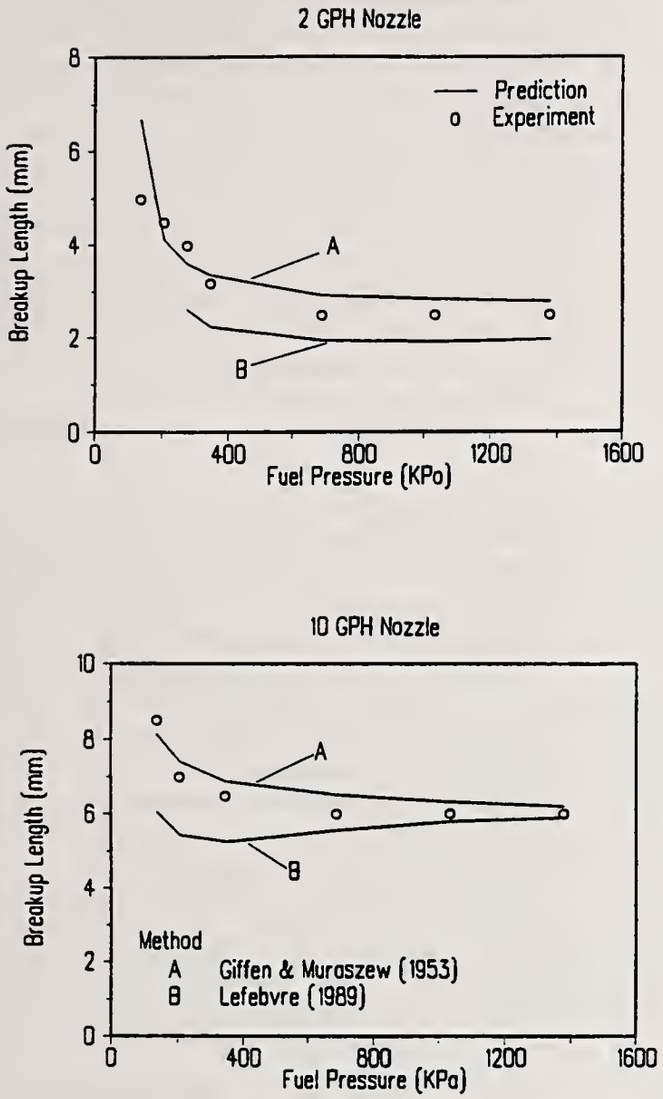

Fig. 1 Comparison of breakup length between predictions and measurements for 2 and 10 GPH nozzles at several fuel pressures.

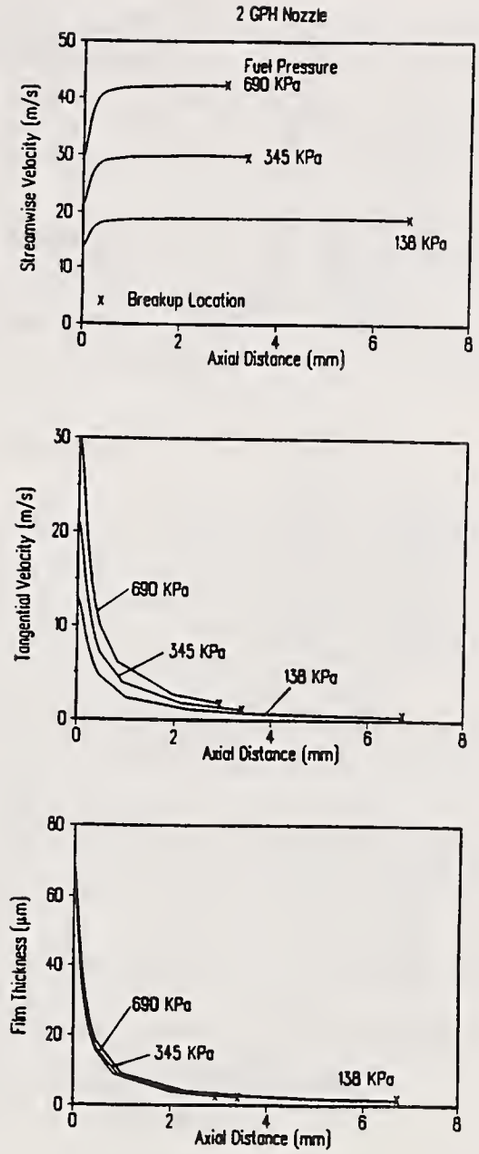

Fig. 2 Variation of film thickness, streamwise and tangential velocities with axial distance for 2 GPH nozzle at several fuel pressures.

Variation of Film Thickness and Velocity

To date, experimental and analytical techniques can only provide information beyond the locations where film breakup occurs. The accuracy of existing computer models depends on the upstream initial conditions measured by the drop sampling instruments which normally have probe volumes located far away from the breakup region.

The present FILM code analyzes the variation of film thickness, angle, and velocity in the film breakup zone. This information is extremely useful because it permits more accurate prediction of drop behavior in the dispersed two-phase regime.

Figure 2 shows the variation of film thickness, axial and tangential velocities for downstream locations at several flowrate conditions. The film thickness generally decreased with an increase in downstream distance. The streamwise velocity accelerated with an increase in axial distance. However, the tangential (swirling) velocity decreased. A common feature was observed in the variations of all three parameters. That is, these parameters all tended to approach constant values prior to film breakup. It was also observed that, at higher pressures, the film thickness and velocities changed at a faster rate as the downstream distance increased.

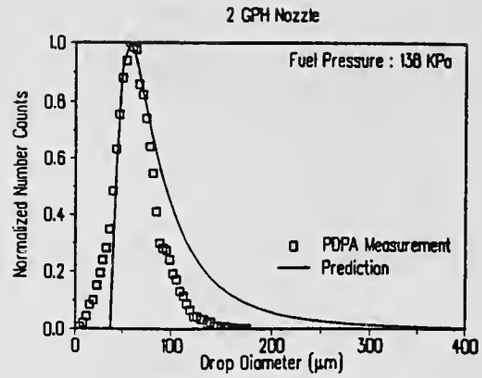

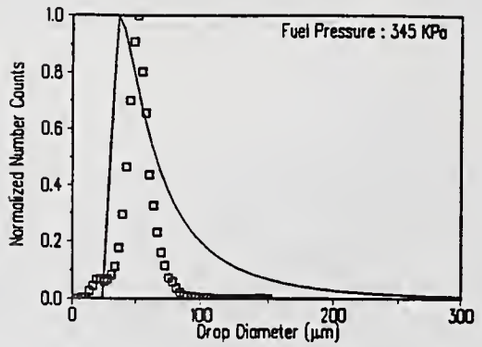

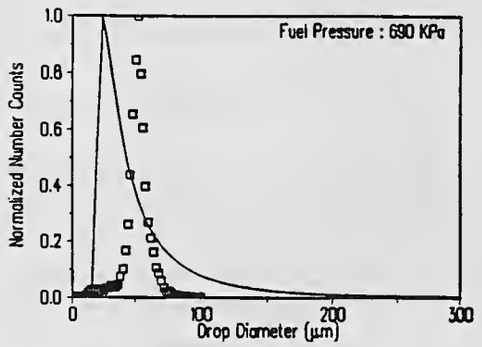

Fig. 3 Comparison of predicted and measured drop size distributions for 2 GPH nozzle at several fuel pressures.

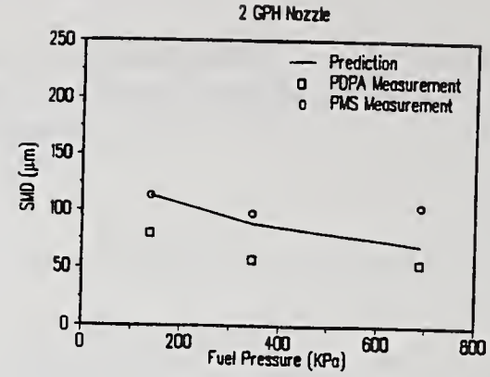

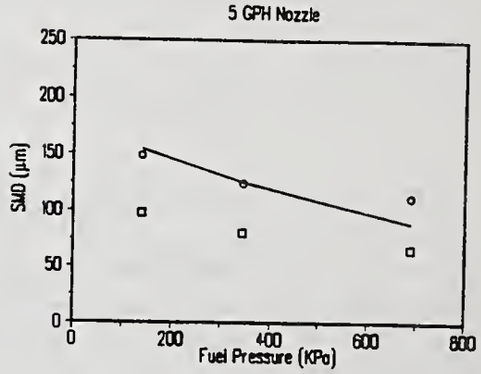

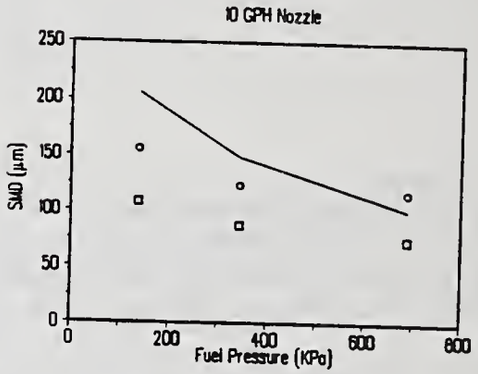

Fig. 4 Comparison of predicted and measured Sauter mean diameters for 2, 5 and 10 GPH nozzles at several fuel pressure conditions.

Comparison of Drop Size Distributions and Mean Diameters

Although methods (A) and (B) gave slightly different values of film trajectory, angle, and breakup length, they provided similar drop size distributions and mean diameters. In the following discussion, however, the predicted drop size values will be presented only for method (A).

Drop size distributions were calculated from a PDF constructed from solutions of the characteristic equation. The PDF obtained at each flow condition was compared with the drop size distributions measured by the Aerometrics Phase/Doppler Particle Analyzer (PDPA) and the PMS imaging spectrometer.

Because the drop size distribution predicted by the FILM code represents the particle spectrum for the entire spray, the local mean diameters measured by the PDPA can not be directly used for comparison.

A continuous traverse method was used to measure the Sauter mean diameter along the center line where the local point samples were taken. The intersection point between the radial SMD distribution and the SMD measured by the continuous traverse will be determined as the location where the drop spectrum matches that of the entire spray. Figure 3 shows a comparison of predicted and measured drop size distribution at several flowrate conditions for the 2 GPH nozzle. The predicted shape of the distribution function agreed quite well with the PDPA measurements. Notice that the agreement appears to be much better at 138 kPa condition where the peak point is fairly close.

Generally, the present model overestimated the percentage distribution of the large drops. In the prediction, the size class of the peak point for the distribution function significantly dropped as the liquid pressure increased. However, the peak point of the measurements did not drop significantly.

The predicted drop size distribution function was later used to calculate the SMD values for the comparison of mean drop sizes. Figure 4 shows the comparison of SMD between predictions and measurements at several liquid pressures for 2, 5, and 10 GPH nozzles.

Shown in Figure 4, good agreement was observed between PMS data and model predictions at liquid pressures of 138 and 345 kPa conditions for 2 and 5 GPH nozzles. It appears that the agreement is better at lower pressure conditions for a low capacity nozzle. However, for a higher flow capacity nozzle, the agreement is better at the high pressure conditions. This seems to indicate that the present model cannot predict well when the initial film thickness is too thick or too thin. It could also be caused by the improper estimation of initial film properties at those conditions used in method (A).

SUMMARY

The present study has demonstrated a realistic approach for analyzing the liquid breakup process and flow characteristics in pressure swirl atomizers. Reasonably good agreement was observed between the model predictions and experiments. The following major conclusions can be drawn from the present study:

(1) The initial film properties are extremely important in determining the spray characteristics. FILM code predictions using the initial film properties estimated by method (A) showed better agreement with the experiments.

(2) Prior to breakup, film properties such as thickness, axial and tangential velocities tend to approach to constant values. For a given nozzle, the gradient of film property variation as a function of downstream distance increased with an increase in liquid pressure.

(3) In pressure swirl atomizers, the variation of breakup length is closely related to the initial film thickness and angle. For a given flowrate, a thinner film thickness and wider film angle resulted in a shorter breakup length. Similar to initial film thickness, breakup length tends to approach a constant value after a certain high pressure is reached.

(4) The present model prediction agreed better with the PMS data. The SMDs measured by the PDPA were consistently lower than those of the model predictions and PMS data.

(5) The present analysis successfully predicted the primary breakup process in the pressure swirl atomizers. Reasonably good agreement was obtained for the predictions of drop size distribution function.

NOMENCLATURE

C_d discharge coefficient
D_2 orifice diameter
f_c critical spin frequency for breakup
h half of film thickness at downstream locations
k wave number
M mass flowrate
ΔP liquid pressure drop
r radial distance in y direction
t film thickness at nozzle exit
U streamwise velocity in the ξ direction
u_2 axial velocity at nozzle exit
W_e Weber number, $(\rho_l u_2^2 D_2/\sigma)$
w_2 tangential velocity at nozzle exit
X area ratio of air core and exit orifice
μ liquid dynamic viscosity
α temporal growth rate
ρ liquid density
σ liquid surface tension
λ_c critical wavelength

SUBSCRIPTS

g	gas phase
l	liquid phase
r	relative value between gas and liquid
2	location at the nozzle exit orifice

REFERENCES

1. Voros, I., Royal Hungarian University of Engineering, Ph.D. Thesis, Budapest, 1935.
2. Novikov, I. I., Journal of Technical Physics (Russian), XVIII, No. 3, 1948.
3. Doumas, M. and Laster, R., "Liquid-Film Properties for Centrifugal Spray Nozzles," Chemical Engineering Progress, October 1953.
4. Giffen, E. and Muraszew, A., The Atomization of Liquid Fuels, Chapman & Hall Ltd., London, 1953.
5. Dombrowski, N. and Hasson, D., "The Flow Characteristics of Swirl Spray Pressure Nozzles with Low Viscosity Liquids," AIChE Journal, Vol. 15, No. 4, July 1969.
6. Fenger, N. P., "Dimensional Analysis of Swirl Atomizers," Journal of Engineering, Vol. 216, pp. 896-899, 1976.
7. Rizk, N. K. and Lefebvre, A. H., "Internal Flow Characteristics of Simplex Swirl Atomizers," AIAA 22nd Aerospace Science Meeting, Paper No. AIAA-84-0124, Reno, Nevada, 1984.
8. Chuech, S.G., and C.-P. Mao, "Numerical Analysis of Pressure Swirl Atomizers," Delavan Technical Report No. 565, 1990.
9. Meyer, J. and Weihs, D., "Capillary Instability of an Annular Liquid Jet," Journal of Fluid Mechanics, Vol. 179, pp. 531, 1987.
10. Mao, C.-P., Chuech, S.G., and Przekwas, A.J., "An Analysis of Pressure Swirl and Pure Airblast Atomization," To be published in Journal of Atomization and Sprays, 1991.
11. Mao, C.-P., "An Analysis of Film Thickness Inside Airblast Atomizers," ILASS-Americas, 4th Annual Conference, Hartford, Connecticut, 1990.
12. Lefebvre, A. H., Atomization and Sprays, Hemisphere Publishing Corporation, 1989.

THE SPRAY STRUCTURE FROM SWIRL ATOMIZERS (Part 1: General Structure of the Spray)

N. Tokuoka, Y. Yamaguchi*, M. Takada and F. Zhang

Dept. Mechanical Engineering, Keio University, Yokohama, Japan
*Tonen Corporation, Tokyo, Japan

ABSTRACT

Spray structure is one of the major factors to control the combustion and its simulation. Several papers have been reported in this field. But those only engaged in the macro viewpoint because of the limit of measuring devices. In this paper, micro behavior of drops such as the radial distributions of the dropsize, velocity and volume flux etc. were measured by Phase Doppler Particle Analyzer (PDPA) and the entrained air also measured to clarify the general structure of spray from the swirl atomizer. The spray consists of larger drops in the sheath, which have larger momentum and entrained ambient air into spray, and smaller drops in the central part which are induced by air flow. Therefore, mean drop velocity in the sheath decreases remarkably but one in the center decays scarcely toward downstream. The volume rate of entrained air is in proportion to axial distance Z and the spray momentum over a cross section decreases with Z. The trajectory angle of drops is affected by its size.

INTRODUCTION

The spray characteristics are of similar importance not only in evaporation processes, combustions and chemical and food engineering etc. but also on their simulation studies.

The relation between the atomizer and the spray characteristics have been a fruitful subject for study. But in most researches on this subject, the spray characteristics were clarified using a special atomizer.

The researches that disclosed the relations between the spray characteristics and the geometrical shape of the atomizer were done by Tanasawa(1), Kobayasi(2)(3)(4),ect.

Tanasawa analyzed theoretically the stream in the swirl chamber as potential flow and showed the relation between the geometrical size, the discharge coefficient, and the spray cone angle. On the basis of Tanasawa's theory, Kobayasi designed and produced several atomizers for his systematic experiments. The result of which was the establishment of the empirical formula about the spray cone angle and the Sauter mean diameter (SMD). Further, its accuracy was improved by examining surface tension and viscosity. Nevertheless all of those studies were done in the macro viewpoint.

Recently, it becomes very important to know the structure of spray and reciprocal actions between drops and air on the study of spray to establish the requirement for energy saving and environment preserve.

The purposes of this research is to generalize the structure and characteristics of spray from pressure atomizers and deliver the effective data for the design of atomizers serving its purpose. At moment, swirl atomizers are used. Centrifugal and single hole atomizers will be also examined.

From this point of view, the spray structure and relations between the dimensions of atomizer, operating conditions etc., macro- and micro-scopic characteristics such as spray angles, dropsize and drop velocity distributions, trajectory, behavior of entrained air etc. will be made clear.

This paper (Part1) makes clear the general characteristics of spray from a swirl atomizer using only the typical atomizer under constant operating conditions.

APPARATUS AND EXPERIMENTAL METHODS

Tested Atomizer

In this paper, the swirl atomizer is used because it is used the most widely in the continuous combustion. It is well known that properties of atomizer are affected by its dimensions such as diameter of inlet holes into swirl chamber, orifice diameter, diameter of swirl chamber and its shape.

The atomizer used in this research is shown in Fig.1. It is designed for changing the dimensions of each parts systematically. The dimensions used in Part1 are listed in Table1.

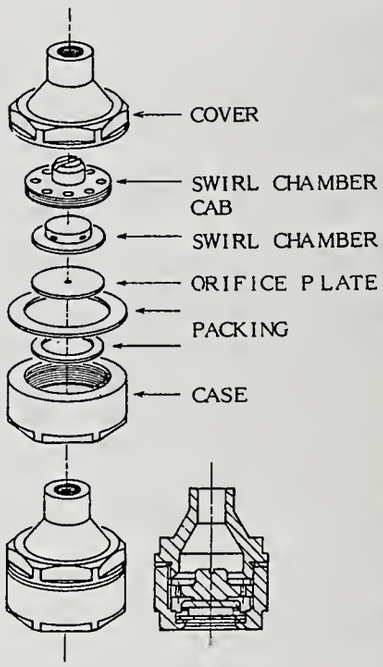

Fig.1 The Structure of the Tested Swirl Atomizer

Table 1 Dimensions and Flow Rate of Atomizer

Inlet holes	Diameter	0.0011 m
	Number	4
Swirl chamber	Diameter	0.0104 m
	Height	0.0030 m
Orifice	Diameter	0.0007 m
	Thickness	0.0010 m
Flow Rate	6.9cc/s at P=1.0 MPa	

Experimental Apparatus and Measuring Methods

The schematic diagram of apparatus to produce a spray and to measure the dropsize and its velocity is shown in Fig.2. The sample liquid, stored in an accumulator, is compressed by pressurized nitrogen gas and injected into a still air through the tested atomizer. The liquid and nitrogen gas in an accumulator are separated by a rubber balloon to prevent gas from dissolving into liquid. The atomizer is set on a positioning device in an injection room which has 1.200m width, 1.200m depth and 1.000m height. The top and bottom walls of the room are constructed by honeycomb board and the room is slightly blown out by a blower to prevent ambient air from circulating. So that the

spray is not affected by ambient air. It is possible to move the atomizer in the axial direction and radial direction.

The dropsize and velocity are measured simultaneously by Phase Doppler Particle Analyzer made by Aerometrics Inc..

The flow rate of entrained air is measured by the 'porous vessel' method which is similar method by Ricou et al (5), as shown in Fig.3. (a) shows a schematic diagram of apparatus and (b) shows the details of the porous vessel.

When a spray is injected into the atmosphere, the ambient air is entrained into it. This is due to the pressure difference between the inside of a spray and a surrounding atmosphere.

If the pressure at points beyond spray is kept atmospheric, the spray characteristics are similar to unbounded spray, although it is formed in a closed space. Base on this preceding principle, a spray is formed in a closed vessel which is sufficiently larger than the reduced pressure field and has a permeable inner wall with a circular hole exit at the front wall of diameter such that the spray just touched the perimeter of the hole. All walls are porous except those at the downstream end where the aperture is adjustable so that entrainment is prevented and air is supplied only from the sides and upstream. The front wall was made of transparent plastic, so that the spray and its impact with the perimeter of the hole could be observed.

The static pressure was measured at the point just inside the permeable wall and outside of the reduced pressure field by a Betz type micro-manometer with a sensitivity of 0.49 Pa. During operation of the spray, quantity

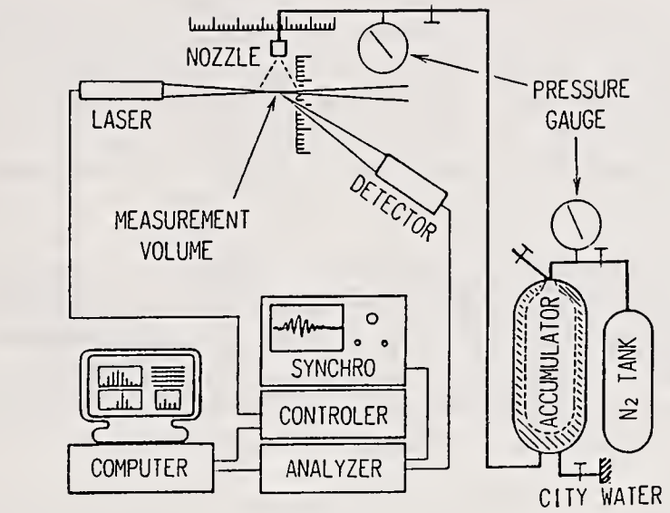

Fig.2 Schematic Diagram of Experimental Apparatus to Measure the Dropsize and its velocity

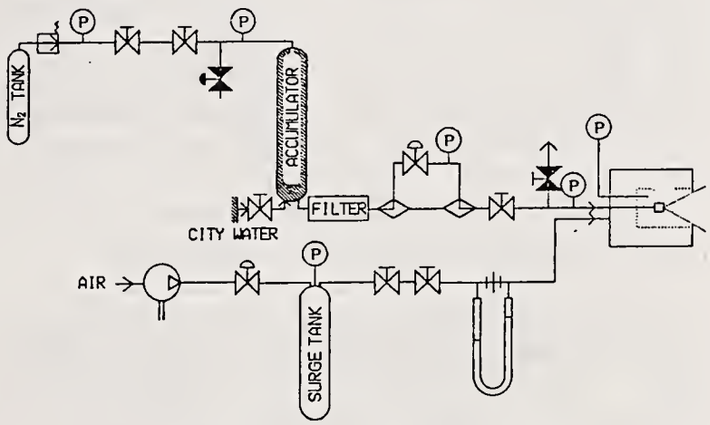

(a) Measurement of Entrainment

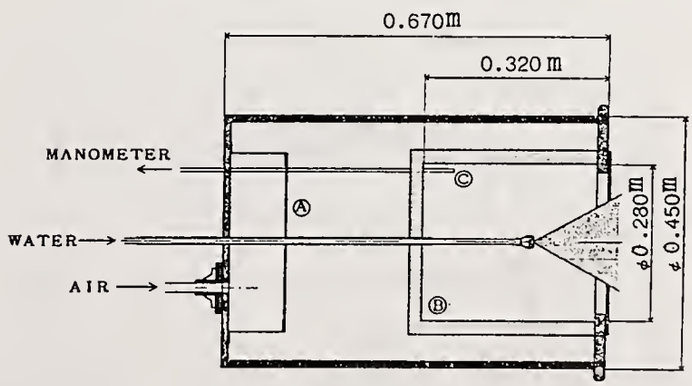

(b) Details of Prorous Vessel

Fig.3 Schematic diagram of Experimental Apparatus to Measure the Rate of Entrainment air

of air was supplied to the chamber through the permeable wall until the static pressure inside the wall reached atmospheric. This amount of air supplied is equal to the amount of air entrained through the spray surface between the tip of the atomizer and the front wall. The total amount of entrained air is measured at Z = 0.020-0.200m. The amount of air entrained through a spray surface between any two sections can be obtained as the difference of the total amount of air between those two sections.

Experimental Conditions, Measured Items and Analysis Method

Experimental conditions and measured points are shown in Table 2. Dropsizes and their velocities are measured at each point. The distribution of mean dropsize, velocity, volume flux, momentum etc. in a space and at any cross sections of spray are calculated from them. Trajectory angle and velocity are obtained by measuring the radial and axial velocity separately.

Table 2 Experimental Conditions

Tested Atomizer	Swirl Atomizer (see Table 1 and Fig.1)
Sample Liquid	City Water
Pressure	P = 1.0 MPa
Measuring Device	PDPA for Dropsize and its Velocity Porous Vessel Method for Entrained Air
Measured Items	Dropsize , Drop Velocity and Flow Rate of Entrained Air
Measured points	Axial Distance Z=20,40,60,80,100 ($\times 10^{-3}$m) Radial Distance R=0-0.100(m) 1-5($\times 10^{-3}$m)pitch

EXPERIMENTAL RESULTS AND DISCUSSION

Volume Flux Distribution and Spray Angle

Volume flux distribution in the radial direction at any axial distance Z are shown in Fig.4. The volume flux in the central part of spray becomes lower at any Z, increases towards the boundary surface and decreases again

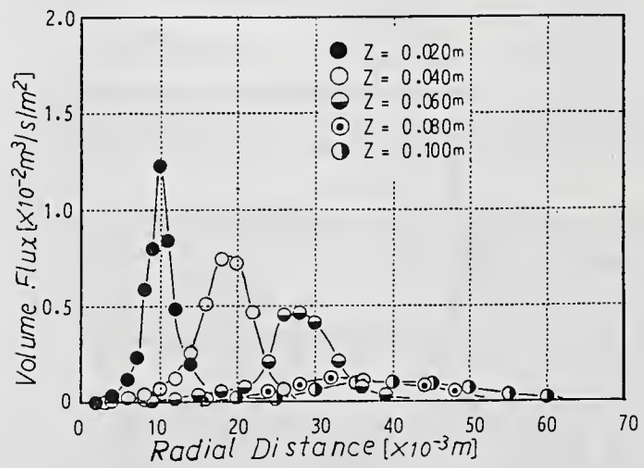

Fig.4 Volume Flux Distribution

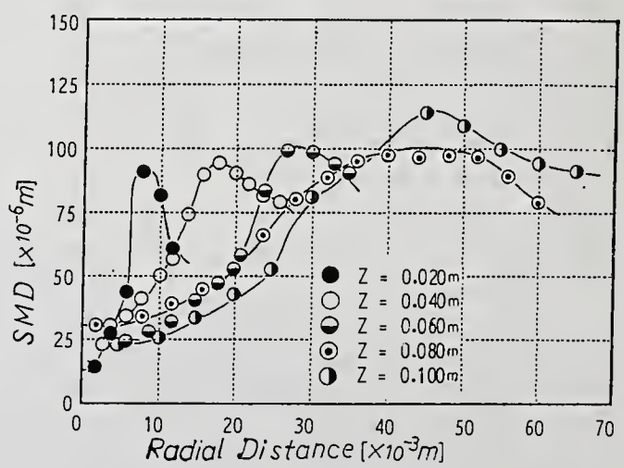

Fig.5 SMD Distribution

after reaching the maximum value. The radial point showing the maximum volume flux is defined as the spray sheath, and the radial distance as the sheath radius of spray, Rsheath. The spray angle is defined by the outline of spray from photograph in general. However, it is difficult to decide the outline exactly. The half spray angle, a'/2, in this research is defined as the angle constructed by Z axis and the line connected the orifice and spray sheath, viz a'=2*arctan(Rsheath/Z).

The spray angle a' defined in this research shows 48 degree between Z=0.040m and 0.100m (see Fig.8). The volume flux at Z less than 0.040m can not be measured by PDPA because drops in this region are not spherical. According to the observation by photographs, disintegration completes around at Z=0.020m and deformation of drops follows it up to Z=0.030m. The spray cone angle (angle of liquid sheet) shows several degrees larger than the spray angle.

SMD and Mean Velocity Distribution

Figure 5 shows the distribution of Sauter Mean Diameter(SMD) in the radial direction at any Z. SMD increases towards the sheath at any section and reaches maximum in the sheath. It is also known that SMD in the sheath increases with Z. This is due to the small drops being induced by entrained flow, leaving the larger drops which have larger momentum moving linearly along the sheath.

The mean velocity shows maximum near the sheath and it decays with increasing Z as shown in Fig.6. The mean velocity here is calculated arithmetically. This tendency is similar to the SMD distribution, On the other hand, the decay of the velocity in the center of the spray is smaller than one near the sheath. It is considered that ambient air is accelerated by the drops near the sheath. Smaller drops flow with the entrained air and concentrated in the center of the spray. The decay of small drops in the center of spray becomes less as they are accelerated by entrained air.

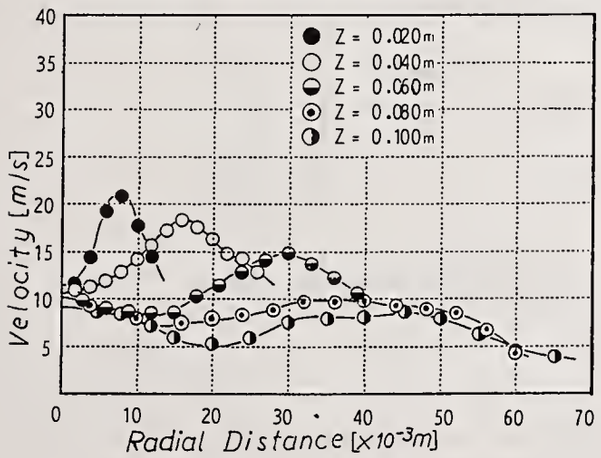

Fig.6 Mean Velocity Distribution

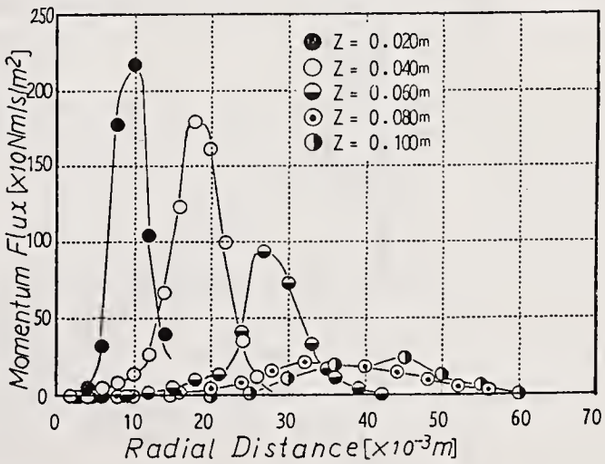

Fig.7 Momentum Flux Distribution

Momentum Flux Distribution

The momentum flux distribution of drops is shown in Fig.7. The momentum flux is calculated by the mass and velocity of independent drop. This tendency shows more similar to one of the volume flux than to one of the mean velocity because the momentum is largely influenced by the larger drops with larger mass and the mean velocity is calculated arithmetically.

Axial Distributions

The SMD and the momentum over each cross section are calculated by assuming that the spray from a swirl atomizer is Z axial symmetry. The axial distribution of SMD, momentum and flow rate of entrained air are shown in Fig.8.

The theoretical SMD is calculated by means of the empirical formula (3) and the theoretical momentum is obtained from the axial velocity by Tanasawa(1) multiplied by the flow rate at the orifice. SMD at each cross section except Z=0.020m becomes constant and coincides well with the empirical formula by Kobayasi(3). SMD at Z=0.020m is smaller than others. In this region, disintegration has not completed yet and the value is calculated by only spherical particles at the point.

The total amount of entrained air in volume increases proportional to the axial distance Z , but the total momentum of drops in cross section, Ml, is inversely. The induced air velocity just before entering the sheath Vin is in inverse proportion to Z because the volume fraction dQa entrained from dZ, dQa/dZ, is constant and surface area at dZ is proportional to Z.

This figure shows that the spray angle at Z=0.020m is larger than one for Z>0.02mm and it becomes constant at Z>0.040m. This fact also suggests that disintegration has not completed yet at Z=0.020m.

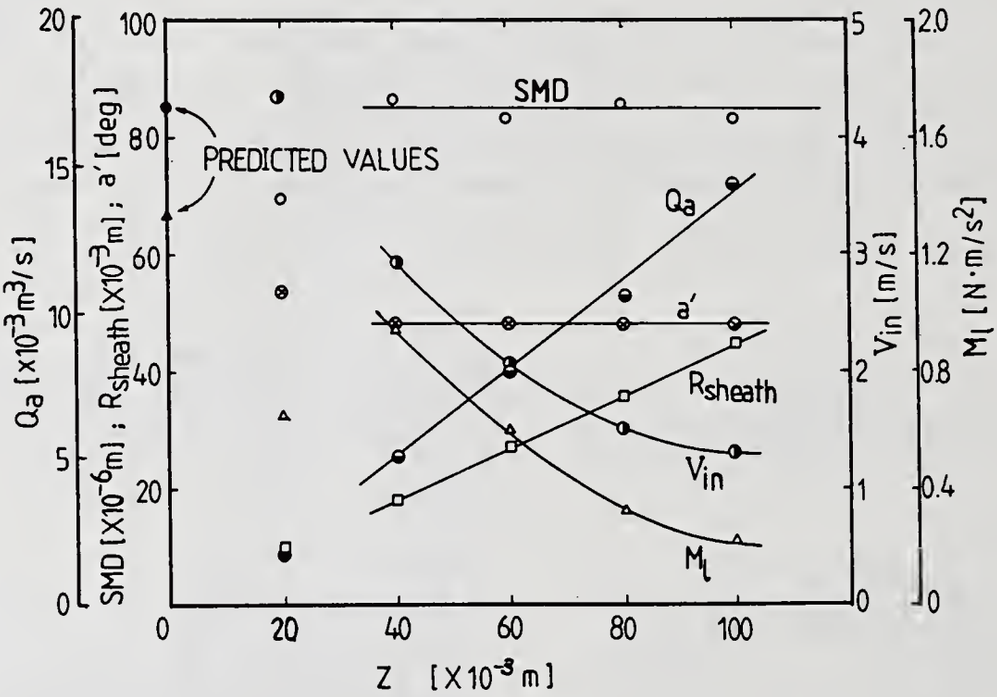

Fig.8 Axial Distribution of SMD, Ml, a' and Qa in section

Drop Velocity and Trajectory Angle

Figure 9 shows the drop mean velocity and the trajectory angle of each dropsize range at local points. The trajectory angle is calculated by using the mean velocity of each dropsize in radial direction and one in Z axial direction. It is considered that small drops flow with entrained air so the velocity of entrained air can be known roughly from the velocity of small drops. From the figure for the dropsize range of 0-10 $x10^{-6}$m, the air flows faster at the central part than at the outer part. It is observed that the

decrease of drop velocity near the spray axis is smaller than that at the sheath. And an ambient air seems to be entrained at Z=0.040-0.060 m vigorously. Further, the velocity of large drops is faster at the outer part and slower at the center than one of small drops. In the sheath, the number of small drops having low velocity decrease and the number of larger drops having high velocity increase with Z, because of the total amount of entrainment increase with Z as shown in Fig.8.

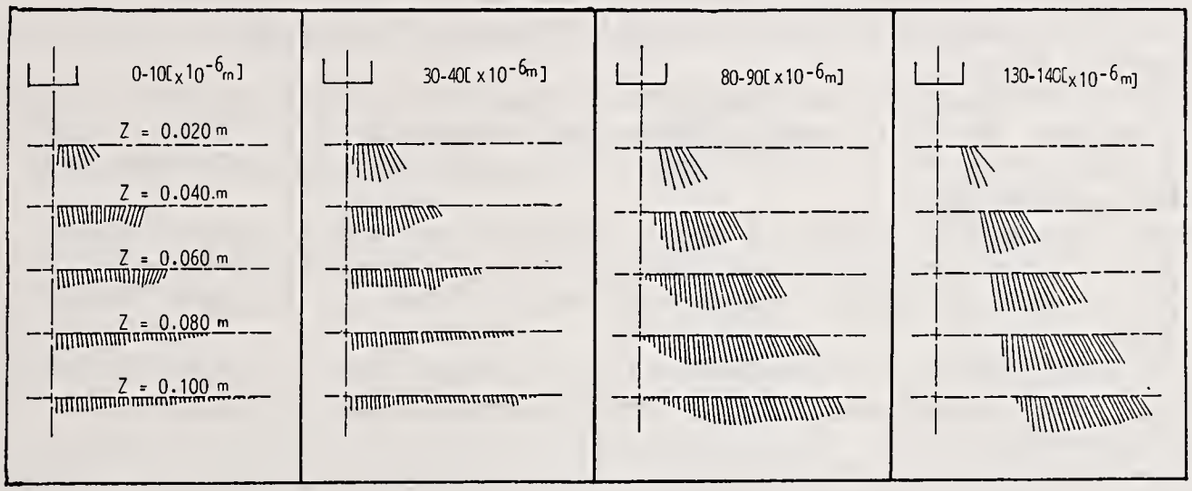

Fig.9 Number Mean Velocity and Trajectory Angle

Figure 10 shows the trajectory angle distribution of drops at Z=0.060m referring to the size ranges. Though all drops flow parallel to the spray axis in the region of less than R=0.010m but at the outer part the trajectory angle of small drops of less than 40×10^{-6} m becomes smaller than the spray angle. Large drops flow along the sheath, that is the half spray angle.

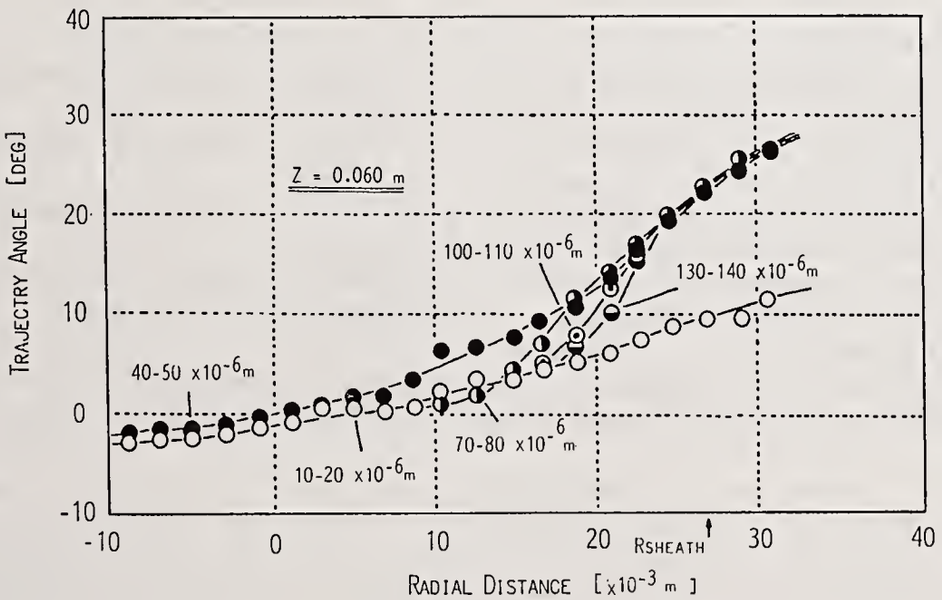

Fig.10 Trajectory Angle Distribution of Each Dropsize

CONCLUSIONS

In this paper, distributions of mean dropsize, velocity, volume flux, flow rate of entrained air, trajectory angle etc. were measured by using the typical atomizer under constant operating conditions to make clear the general characteristics of spray from the swirl atomizer and to generalize the structure. The results are summarized as follows;

(1) The spray consist of large drops with large momentum in the sheath and small drops induced by an entrained air in the central part.
(2) The mean drop velocity at the sheath is larger than one in the central part of spray.
(3) The decrease of the mean velocity in the central part is smaller compared with one in the sheath. This fact suggests that drops accelerate entrained air at the outer part of spray and entrained air does drops at the central part.
(4) The trajectory angle of drops depends upon the dropsize. Though all drops flow parallel to the spray axis in the central part, at the outer part, the trajectory angle of small drops is smaller than large drops.
(5) The total amount of entrained air is in proportion to axial distance Z and the induced air velocity before entering the sheath is inversely proportional to Z.
(6) The total momentum of drops over a cross section is inversely proportional to axial distance Z.

ACKNOWLEDGMENT

The authors would like to express their deep gratitude to Mr. T.Hyodo, Mr. K.Fukuzato from Seika Sangyo Co.Ltd. and staffs of Aerometrics Inc. who offered valuable advises for this study.

REFERENCES

(1)Tanasawa Y. et al., "Design Method For Swirl Injection Nozzle Using Potential Flow Theory", JSME, Vol 17, No.58, pp.107-111 (1951).
(2)Kobayasi K., "Atomizing Characteristics of Swirl Injection Nozzle (1st Report)", JSME, Vol 17, No.58, pp.112-114 (1951).
(3)Kobayasi K., "Atomizing Characteristics of swirl Injection Nozzle (2nd Report)", JSME, Vol 17, No.58, pp.114-118 (1951).
(4)Kobayasi K., "Atomizing Characteristics of Swirl Injection Nozzle (3rd Report)", JSME, Vol 19, No.80, pp.60-64 (1953).
(5)Ricou, F.P. and Spalding, D.B., "Measurements of entrainment by axisymmetrical turbulent jets", J. Fluid Mech., Vol 11, No.1, pp.21-32 (1961).
(6)Benatt, F.G.S. and Eisenklam, P., "Gaseous entrainment into axisymmetric liquid spray", J. Inst. Fuel, Vol 42, No.8, pp.309-315 (1969).

THE SPRAY STRUCTURE FROM SWIRL ATOMIZERS (Part 2: Effect of Injection Pressure and Atomizer Characteristics on the Spray Structure)

F. Zhang, Y. Yamaguchi*, M. Takada and N. Tokuoka

Dept. Mechanical Engineering, Keio University, Yokohama, Japan
*Tonen Corporation, Tokyo, Japan

ABSTRACT

It is known that the spray characteristics change according to the structure of atomizer and operating conditions. The swirl atomizers whose dimensions of each parts can be changed systematically are designed and the relations among atomizer's characteristics, operating conditions and spray structure are made clear experimentally.

The boundary of the sheath region and central part of spray becomes clearer and the thickness of sheath region decreases with an injection pressure. The flow factor B and the characteristic factor K affect on a spray angle. A spray angle increases with the increase of B and with the decrease of K. Empirical formula for spray angle a' is presented as a function of Re. The flow rate of entrained air is also affected by B, K and injection pressure.

INTRODUCTION

Spray characteristics are changed by the structure of atomizer, its dimensions, operating conditions, liquid properties, ambient air conditions etc.. It is known that the characteristics of swirl atomizer are affected by its dimensions such as an area of inlet hole into a swirl chamber, a diameter and a height of swirl chamber, orifice diameter and its length etc..

Many studies(1)-(3) have been reported about the relations between the structure of atomizer and characteristics of spray. However, those made clear only macro characteristics of spray such as spray cone angle, Sauter mean diameter, discharge coefficient, etc. because of the lack of measuring technique. Fortunately, a phase doppler system is development and it becomes possible to measure the velocity and size of each drop simultaneously. This study aims to generalize the structure of spray from the microscopic point of view.

The swirl atomizers of which dimensions of each parts can be changed systematically are designed. The general structure of spray from a swirl atomizer was made clear in Part1(4). In this paper, the relations among the characteristics of atomizer, an injection pressure and spray characteristics such as spray angle, spatial distributions of mean dropsize, velocity, momentum and volume flux, trajectory angle of drops, flow rate of entrained air etc. are examined to generalize the characteristics of spray.

EXPERIMENTAL METHODS AND APPARATUS

The details of experimental apparatus, measuring item etc. are shown in Part1(4). The velocity and diameter of drops, volume flux are measured by Phase Doppler Particle Analyzer (PDPA) from Aerometrics Inc. and the flow rate of entrained air by the "porous vessel" method(5).

The dimensions of each parts of tested atomizers(4) are shown in Table 1. Those are designed to be able to examine spray characteristics under the constant characteristic factor K, the flow factor B, etc. by selecting some of atomizers. The city water is sprayed into a still air under an injection pressure of 0.7, 1.0 and 1.5 MPa.

Table 1 Dimensions and Properties of Atomizers

Atomizer Number	Measured Values			Theoretical Values by (1)				
	do	di	de	K	ao	k	dc	B
	[x10^{-3}m]			[-]	[deg]	[-]	[10^{-3}m]	[-]
S-01	1.28	10.4	0.96	0.66	74.5	0.61	0.58	0.49
S-02	1.28	10.4	0.70	0.90	65.3	0.54	0.38	0.49
S-03	1.28	10.4	0.51	1.24	55.9	0.47	0.24	0.49
S-04	1.10	10.4	0.96	0.48	83.2	0.67	0.64	0.42
S-05	1.10	10.4	0.70	0.66	74.1	0.61	0.42	0.42
S-06	0.93	10.4	0.96	0.35	92.2	0.72	0.69	0.36
S-07	0.93	10.4	0.70	0.48	83.7	0.67	0.47	0.36
S-08	0.93	10.4	0.51	0.65	74.7	0.61	0.31	0.36

ao:Theoretical spray cone angle (=2*arctan(k/(1-k**2)**0.5)); B:Flow factor (=2*m**(1/2)*d0/di)); dc:Air core diameter at the orifice; de:Orifice diameter di: Diameter of swirl chamber; do: Inlet hole diameter to swirl chamber; k: Cavity factor (=dc/de); K:Characteristic factor (=m*do**2/(de*di))

RESULTS AND DISCUSSION

Effect of Injection Pressure

Distribution of SMD and Mean Drop Velocity. The difference of SMD distributions under various injection pressure Pi is shown in Fig.1(a) and of number mean velocity in Fig.1(b). Both are at an axial distance Z=0.060m and an atomizer is S-05.

SMD decreases with Pi at each radial point and the radial distance where SMD shows the maximum increases with Pi.

The mean velocity decreases with radial distance R and increases towards the sheath after showing minimum. Those tendencies do not affected by Pi but the velocity difference of drops along R becomes more distinct with Pi being higher. It is considered that the increase of drop velocity near the sheath is due to the increase of initial injection velocity under higher Pi but one in the central part is due to higher entrained air velocity caused by the decrease of pressure within a spray led by larger momentum of drops at sheath.

Distributions of Volume Flux and Momentum Flux of drops. Fig.1(c) and (d) shows the distributions of volume flux and momentum flux of drops at Z=0.060m respectively. Those indicate that the maximum values and radial distances showing maximum increase with the injection pressure Pi. The fact means that the spray angle increases with Pi. The distributions near the sheath becomes more peaky and the thickness of sheath region reduces with increasing Pi.

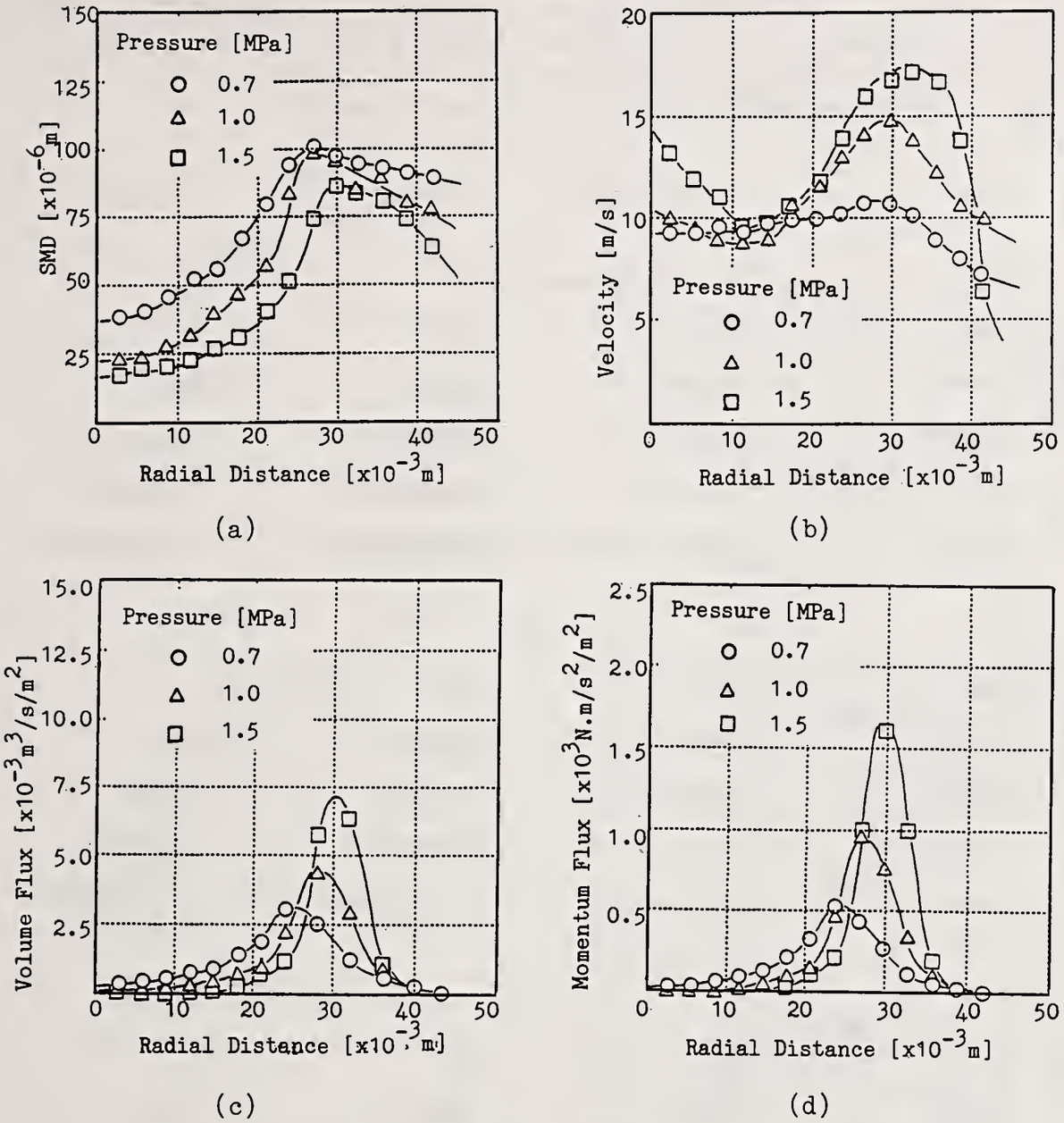

Fig.1 Effect of Injection Pressure on Distribution

The total momentum of drops and the flow rate of entrained air are shown in Fig.2. The latter means the total volume of air entrained through spray surface between Z=0m and Z=0.060m. The flow rate of entrained air is roughly proportional to the total momentum Ml when an injection pressure increases.

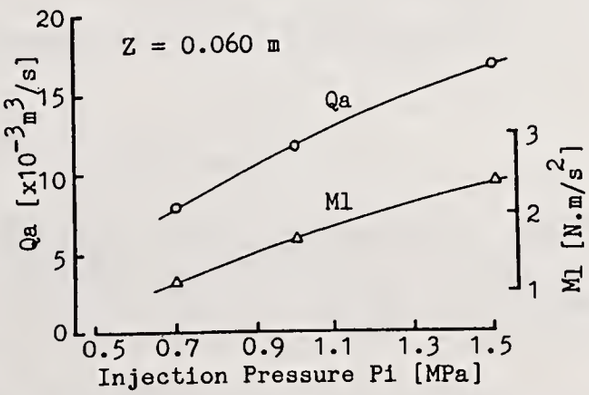

Fig.2 Effect of Pi on Qa and Ml

Effect of Dropsize on Velocity Distribution. The mean velocity and trajectory angle of each dropsize are shown in Fig.3. The line length in Fig.4 shows the mean velocity and the

direction a trajectory angle. When the injection pressure increases, the velocity also increases. The area where drops of more than $80X10^{-6}$m decreases with Pi though one for drops less than $40X10^{-6}$m does not change and a path width passing through large drops becomes narrow. This fact also indicates that the thickness of sheath region reduces with increasing Pi.

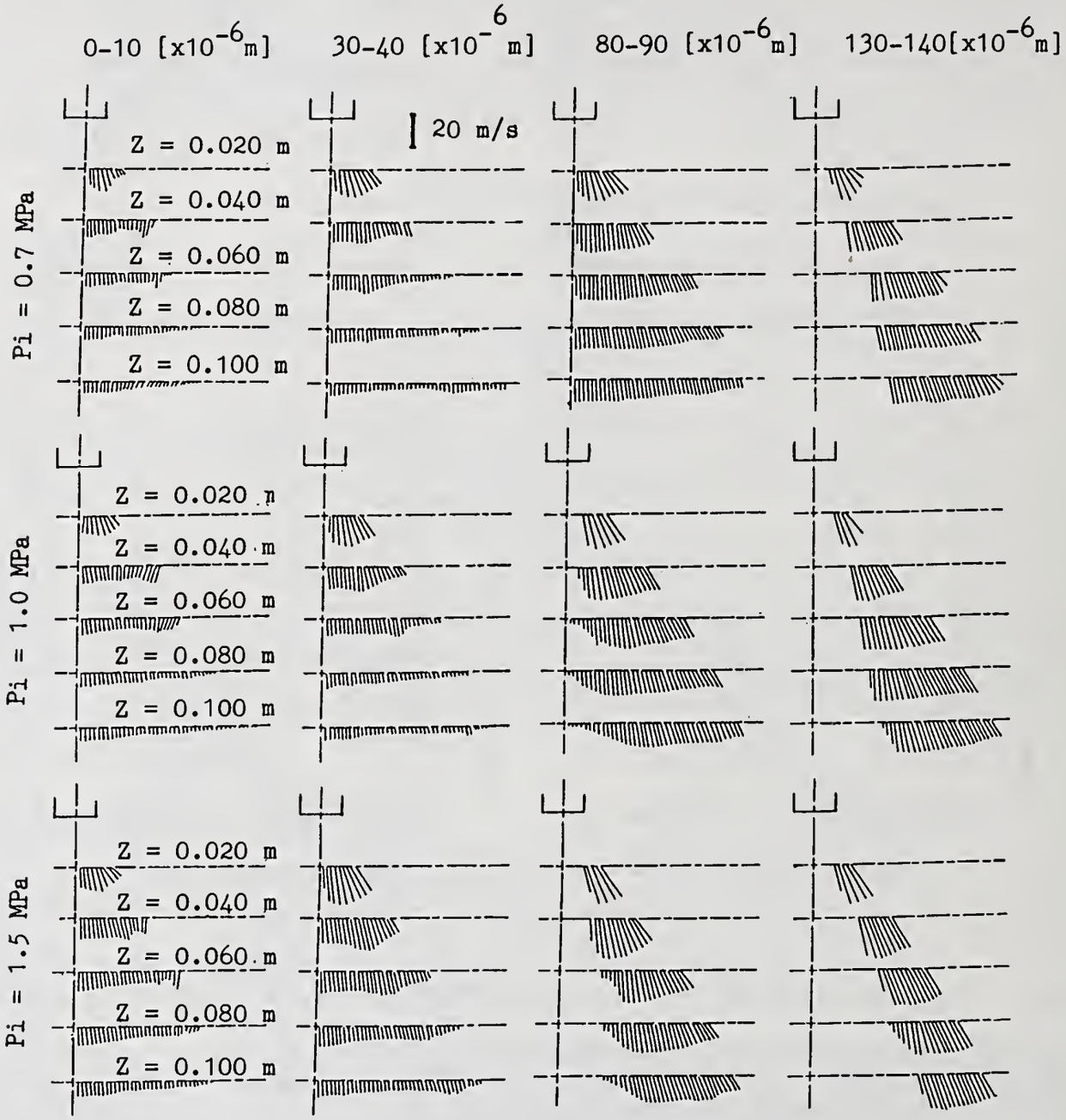

Fig.3 Number Mean Velocity and Trajectory Angle

Effect of Atomizer's Characteristics

The spray produced by different atomizers with various dimensions of each parts are examined under the constant injection pressure of Pi=1.0MPa to clarify the effect of atomizer's characteristics on spray.

Effect of Orifice Diameter de. To make clear the effect of an orifice diameter on spray characteristics, the sprays from atomizers with various

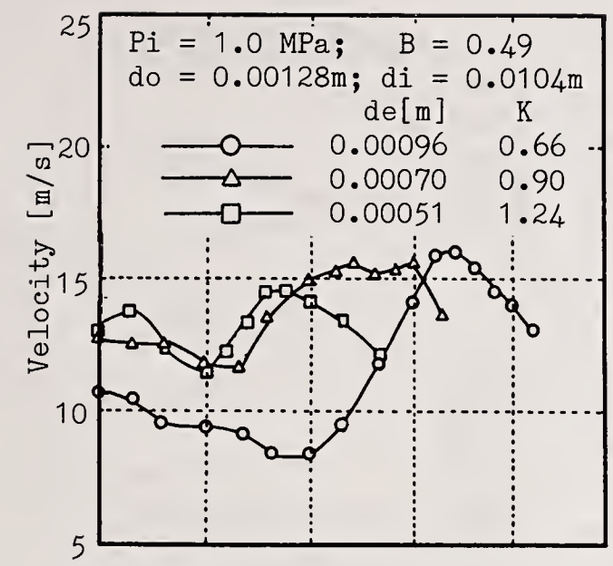

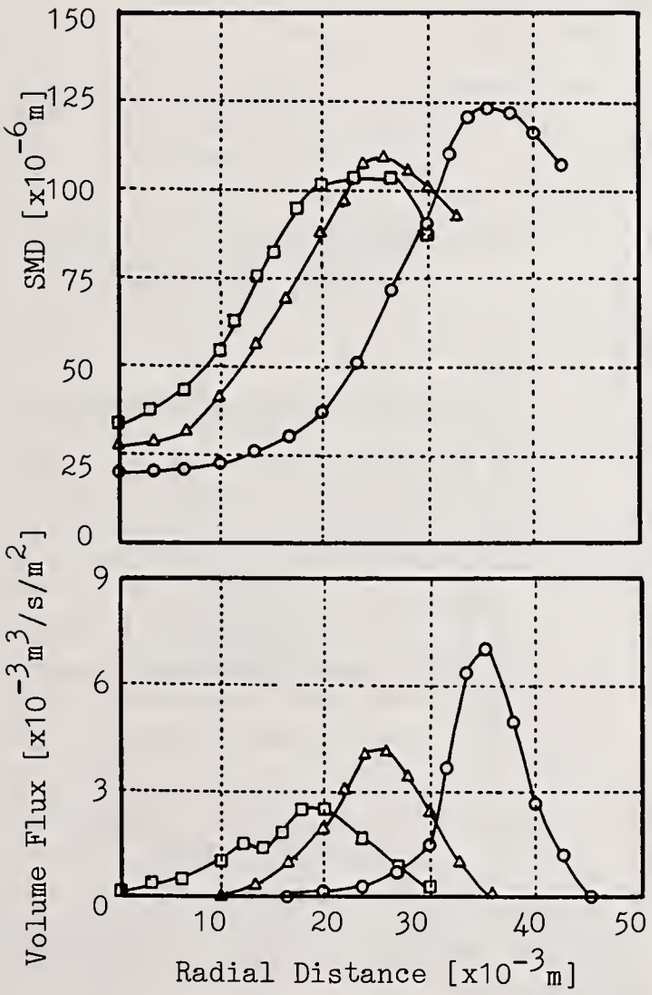

Fig.4 Effect of Orifice Diameter on Radial Distribution

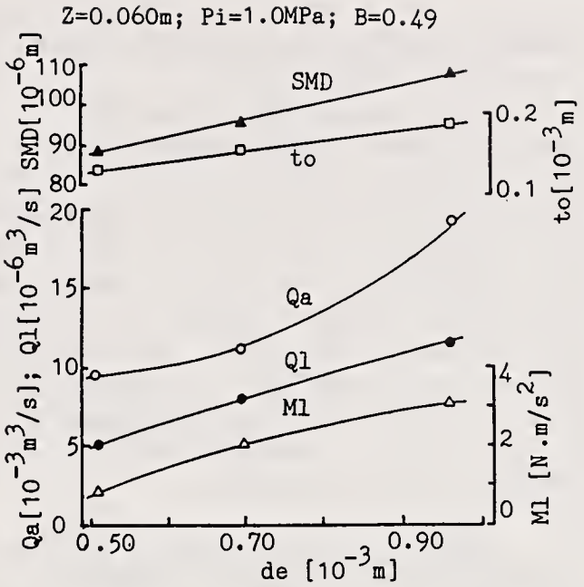

Fig.5 Effect of Orifice Diameter de on SMD, Qa, Ql, Ml, to

orifice diameter de but constant inlet hole diameter do and diameter of swirl chamber di are examined. In the case that do and di are constant and de changes, the characteristic factor of atomizer K is in inverse proportion to de and the flow factor B is constant.

Figure 4 shows the distributions of mean velocity, SMD and volume flux at the axial distance of Z=0.060m. The flow factor B is 0.49 and K changes between 1.24 and 0.66. Those figures suggest that the maximum values of mean velocity, SMD, volume flux, spray radius, and spray angle a' increases with the increase of orifice diameter de, that is with the decrease of K. This is because the radial velocity component at the orifice increases relatively compared with the axial velocity component when de is larger, viz K is smaller.

SMD(D32) over a cross section increases with the increase of the orifice diameter. It is also predicted by a theoretical work(1). According to it, the thickness of liquid film at an orifice, to, increases with K and shown in Fig.5 with SMD.

The ambient air is entrained by the momentum of drops flowing in the sheath region and. Therefore, the flow rate of entrained air increases with de

because the momentum of drops Ml in the sheath region is larger when de is larger as shown in Fig.5.

The number mean velocity in the sheath of all atomizers are almost same at Z=0.060m. This is because that the reduction rate of velocity is smaller in the sheath region because the size of drops there are relatively large. On the other hand, drop velocity in the central part of spray becomes smaller with de. It is considered that the mean velocity of air within a spray decreases with de, as the spray radius becomes larger though the Qa increases.

Effect of Flow Factor B. The flow factor is affected by diameter of an inlet hole and of swirl chamber. To make clear the effect of B, atomizers with a constant characteristic factor K and a different flow factor B are required. Atomizers with suitable sets of do and di are selected from Table 1 and those are S-01,-05,-08.

The flow rate of liquid Ql, the flow rate of entrained air Qa, SMD etc. are shown in Fig.6. All of them increase with the increase of flow factor B. The spray angle a' also increases with B because the radial distance indicating the maximum of volume flux increases with B as shown Fig.7.

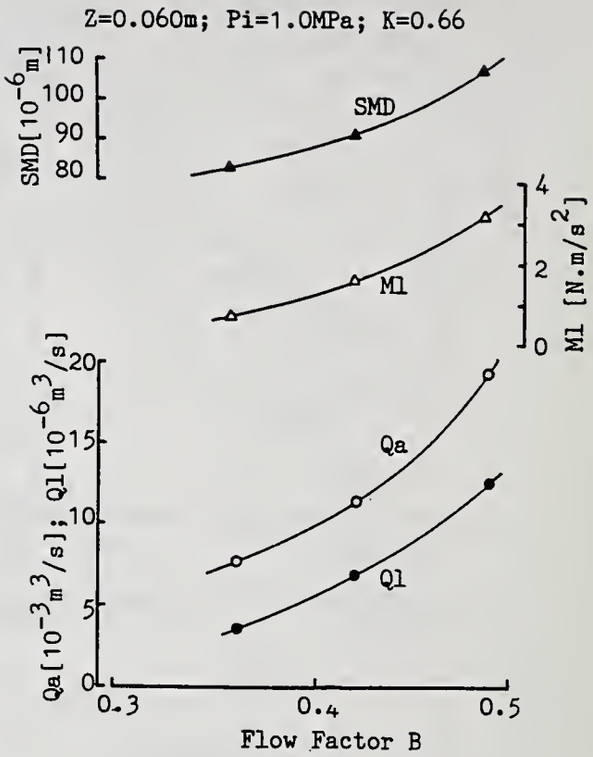

Fig.6 Effect of Flow Factor B on SMD, Qa, Ql, Ml

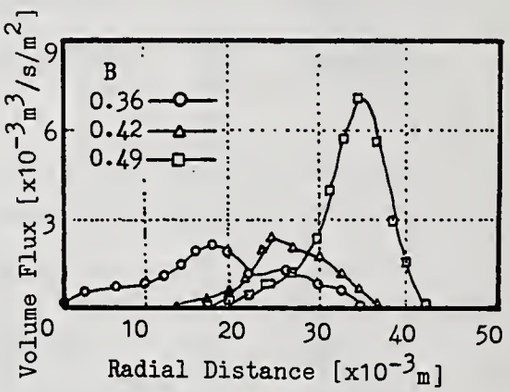

Fig.7 Effect of Flow Factor B on Volume Flux

According to the potential theory, the characteristics of spray depend upon K but the viscosity affects on the flow in a swirl chamber when real liquid is injected. Tanasawa(1) also suggested that the flow in a swirl chamber approximates the potential flow most at B=0.5. When B is less than 0.5, a friction due to the viscosity near the wall increases and the swirl velocity decreases. This fact leads a spray angle decreases and a discharge coefficient increases. On the other hand, when B is greater than 0.5, the radial and axial velocities are affected a little by friction and the discharge coefficient became smaller while the spray angle became larger.

In case of S-01,-05,-08, though the theoretical cone angles calculated by the potential theory are all 75 deg. but spray angles measured from Fig.7 become 60, 50 and 32 deg. respectively. This result indicates that the spray angle decreases with the decrease of B.

Effect of Inlet Port Diameter do. The sprays from atomizers, of which an inlet hole diameter do varies and diameter of an orifice de and of a swirl

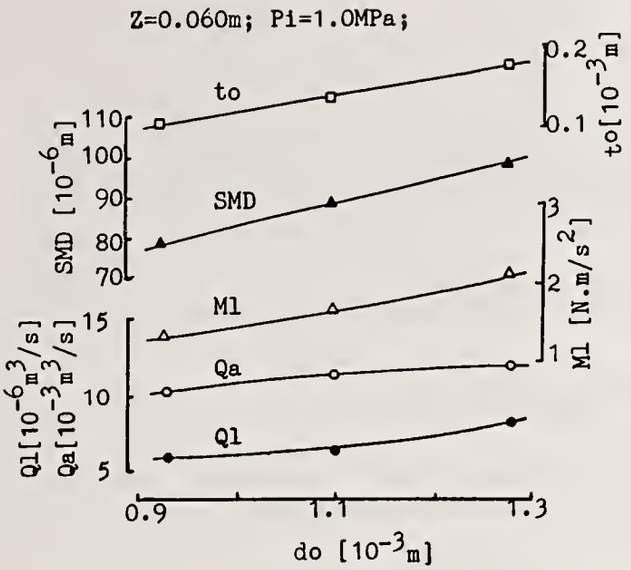

Fig.8 Effect of do On SMD,Qa,Ql,Ml,to

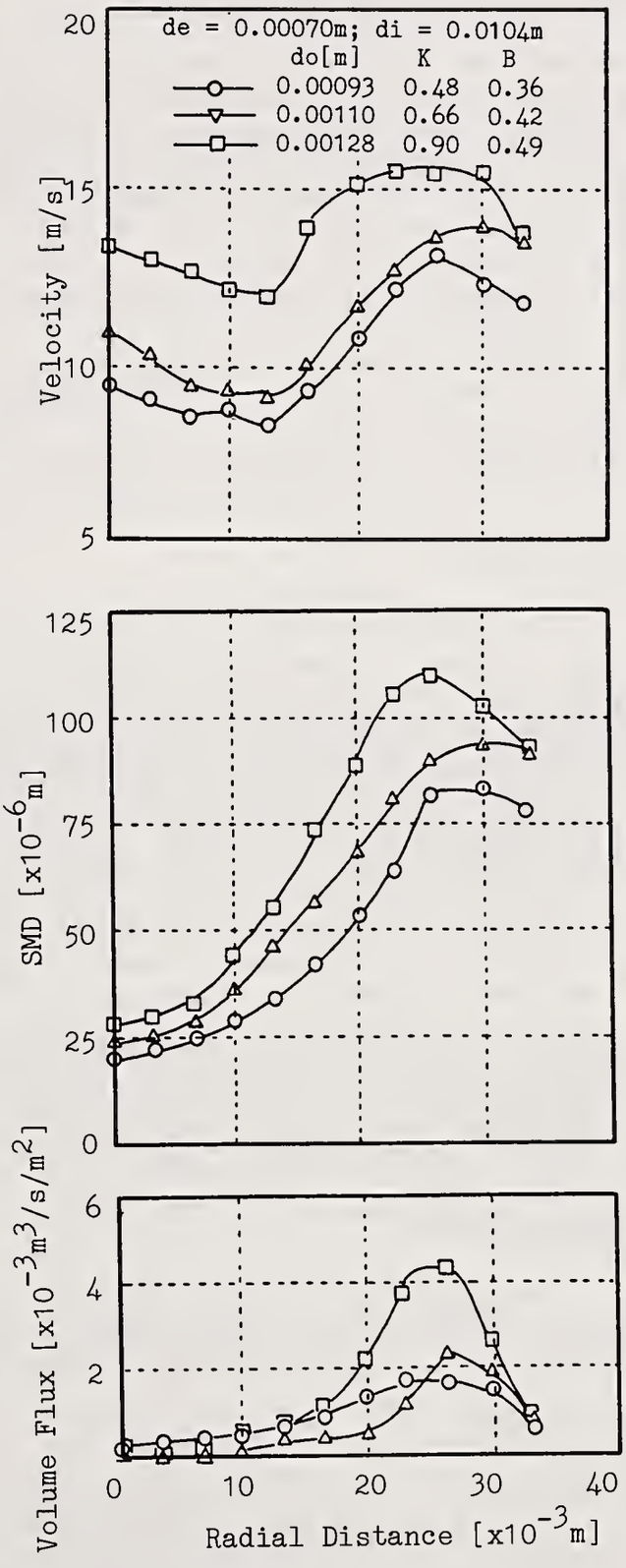

Fig.9 Effect of Inlet Port Diameter do on Radial Distribution

chamber di are kept constant, are examined. In this case, both the flow factor B and the characteristic factor of atomizer K change. K is in proportion to the square of do and B to do.

SMD(D32), total momentum of drops and flow rate of entrained air Qa over a cross section increase with an inlet diameter do as shown in Fig.8. This figure indicates the tendency for K shows opposite compared with Fig.5. It is considered that an orifice diameter de does not give any effects on B but an inlet hole diameter do affect on not only K but also B. When do becomes smaller as in this case, K increases and B decreases. The decrease of K causes the increase of the ratio of the radial velocity component to the axial one and makes a thickness of liquid film thicker but the decrease of B acts on them conversely. Consequently, the relations in Fig.8 are obtained.

Figure 9 shows the distributions of mean velocity, SMD and volume flux of drops in radial direction. It is evidence from Fig.9 that the mean velocity and SMD increases with do and that the spray radius is not influenced by do. Therefore, the spray angle vary scarcely with do.

Empirical Formula for Spray Angle a'

Figure 10 shows the relation between the ratio of a spray angle a' to a theoretical spray cone angle ao and Re number in the swirl chamber. Reynolds number is given by using an inlet velocity into swirl chamber, ui, calculated from the potential theory as the representative velocity, a radius of swirl chamber, and viscosity of liquid. It may not suitable in this stage for experimental results to indicate by Re number because all data are obtained from sprays of city water and viscosity,v, is constant. However, Fig.13 gives the following empirical formula by means of the least square method. a'=ao*e**(-3900/Re);Re=ui*di/2/v.

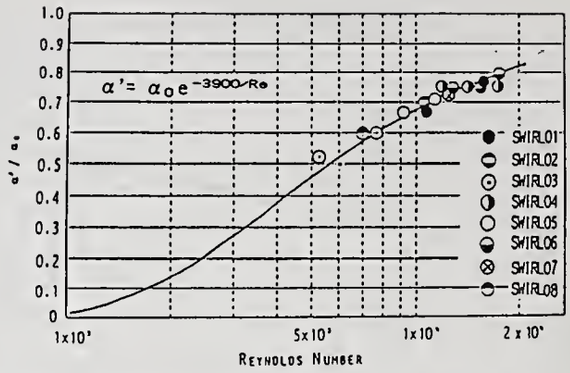

Fig.10 Relation Between Re and a'/a

CONCLUSIONS

The effect of injection pressure and dimensions of parts constructing a swirl atomizer on the spray characteristics are examined. Size and velocity of each drop are measured by PDPA and the entrained air into spray is also measured using the 'porous vessel' method. These results summarized as follows

(1)The volume flux and momentum flux are concentrated near the sheath and this tendency becomes more remarkable and a thickness of sheath region decreases with an injection pressure.

(2)The flow factor B and the characteristic factor K affect on a spray angle. A spray angle increases with the increase of B and with the decrease of K.

(3)The increase of orifice diameter leads the increase of spray angle and the decrease of thickness of sheath region. However, the inlet hole diameter effects scarcely on them. This is because the former affect only on a characteristic factor K but the latter on K and a flow factor B.

(4)The increase of B and/or the decrease of K and/or the increase of injection pressure cause the increase of flow rate of entrained air.

(5)Empirical formula for spray angle a' in the researched range is led as a' = ao*e**(-3900/Re); Re = ui*di/2/v

ACKNOWLEDGMENT

The authors would like to express their deep gratitude to Mr.T. Hyodo, Mr.K. Fukuzato from Seika Sangyo Co.Ltd and staffs of Aerometrics Inc. who offered valuable advice for this study.

REFERENCES

(1)Tanasawa Y., et.al.;"Design Method For Swirl Injection Nozzle Using Potential Flow Theory", JSME, Vol 17, No.58, pp.107-111 (1951).

(2)Kobayasi K.;"Atomizing Characteristics of Swirl Injection Nozzle (1st Report)", JSME, Vol 17, No.58, pp.112-114 (1951).

(3)Kobayasi K.;"Atomizing Characteristics of swirl Injection Nozzle (2nd Report)", JSME, Vol 17, No.58, pp.114-118 (1951).

(4)Tokuoka N. et.al.;"The Spray Structure from Swirl Atomizer (Part 1)", submitting to 5th ICLASS (1991).

(5)Ricou F.P., Spalding D.B.; "Measurements of entrainment by axisymmertrical turbulent jets", J.Fluid Mech., Vol 11, No.1, pp.21-32 (1961).

ICLASS-91 *Gaithersburg, MD, U.S.A. July 1991* *Paper 23*

TWO-COMPONENT PHASE-DOPPLER MEASUREMENTS FROM THE SPRAY OF A SWIRL-PRESSURE BURNER-NOZZLE IN THE VICINITY OF THE NOZZLE

K. Lampe, K. Bauckhage and B. Haase

University of Bremen, Verfahrenstechnik
Bremen, Germany

ABSTRACT

A two-component phase-Doppler measuring system (PDM) has been used to measure simultaneously drop sizes and velocities at a vertically mounted swirl-pressure burner-nozzle under various atomizing conditions. The measurements from different radial positions in two horizontal planes, 10 mm and 20 mm below the nozzle, result in a linear dependency of the main horizontal velocity components on radial distances r. With a second one-component PDM variations of Sauter-mean-diameter (SMD) were examined in order to describe the dependency of SMD on the fuel oil viscosity.

INTRODUCTION

Short comings of energy resources and higher requirements for minimizing air-pollutant emissions call for further optimization of the atomization process in fuel oil burners. Simplex swirl pressure nozzles producing hollow or solid spray cones are used for instance in house-heating systems. Only with the exact knowledge of the spray parameters a further optimization of the already well doing atomizing process of these burner nozzles is possible. Using the phase-Doppler technique as described by [1] to [4] sizes and two velocity components of droplets can be measured simultaneously thus answering questions for local distributions and evolutions of sprays.

Simplex nozzles of fuel oil burners generate diffusion flames, in which beside the drop size distribution the fuel oil air mixing ratio plays an important part. Thus operating conditions as the pressure and the temperature of the preheated fuel oil get influence on the atomization process and on the properties of the sprays of this type of swirl-pressure burner nozzles.

Therefore our point of interest was to find out the dependency of the local spray cone parameters, especially of the Sauter-mean-diameter on the oil pressure,the temperature and on the temperature-dependent physical fuel oil properties (viscosity, density, surface tension) respectively. All investigations have been done under temperature controlled conditions using only one type of hollow-cone-nozzle, i. e. Danfoss, type: 60° H, 1,6 kg/h. Another question was the dependency of the horizontal (radial and swirl) velocity components of drops on radial distance r from the centreline of the spray cone and on the axial distance z from the nozzle. Thus this dependency had also to be analysed in relation of the temperature dependent properties of fuel oil to the spray cone parameters. At least one object of our investigations was, to point out a relationship between radial and swirl velocity components and the radial distance r at different horizontal planes.

Experimental Set-up

The experimental apparatus consists of the nozzle mounted centrally in a cylindrical chamber. The chamber is movable in two directions (x- and y-direction), the nozzle position can be changed in z-direction (Fig. 1). Without moving the optics of the measuring system thus each point of spray cone can be reached for measurements without changing the operating conditions of the stationary atomization process. The oil pressure, p_l, and its temperature, T_l, can be varied and controlled in a range of 5 to 20 bars and from 20 to 90 °C. The circulated and rectified gasstream (N_2, u ≈ 0,2 m/s) is temperature controlled. It is prevented from supplying the measuring volume with recirculating fuel oil mist by filters. In order to avoid explosion N_2 was used instead of air.

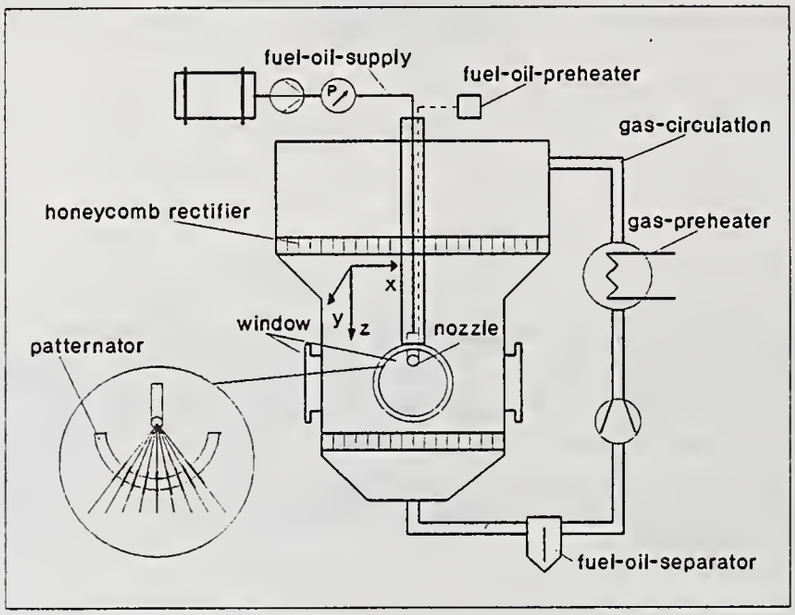

Fig. 1 Experimental set-up

Before entering the nozzle the fuel oil temperature and pressure are measured by thermocouples and pressure sensor respectively. A patternator can be installed below the nozzle, measuring the dependency of mass flow density on radial distance, r, axial distance, z, and on operating conditions as oil pressure, p_l, and its temperature T_l.

Measurement Procedures

The temperature-dependency of the local drop size distributions and the local distributions of the vertical component, v_z, of droplet velocities has been measured separately for various locations in the spray cone by means of an one-component PDM (Aerometrics). The main interest was focused on the changes of SMD by varying the temperature dependent physical properties of the fuel oil (and additional of the gas stream).

All two velocity component measurements together with the correlated diameter observations have been done by a four-beam two-colour configuration [5] of a fibre-optic-PDM (Dantec). For both measuring systems (Aerometrics and Dantec) an argon-ion-laser was used as light source; photomultipliers, installed under 30° off-axis-angles were used as receivers.

The measuring system of the two-component-PDM is shown in Fig. 2. After passing a set of optical filters the light is divided into two beams with different wavelengths (blue: 488 nm, green: 514,5 nm) and after that by beam-splitter prisms into the well known dual beam systems. In order to distinguish between the altering directions of the horizontal velocities of very low values a frequency shift was necessary, realized in the path of the blue light using a bragg-cell.

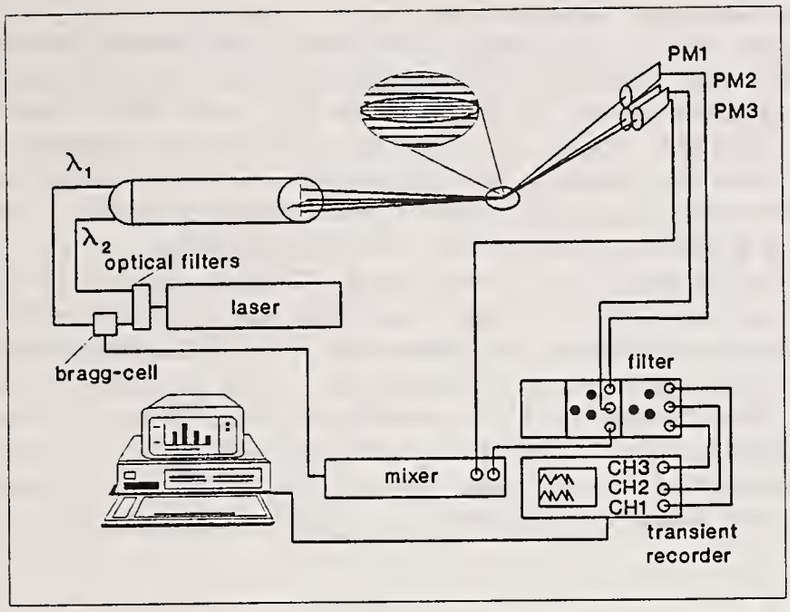

Fig. 2 Fiber optic phase-Doppler-measuring-system

Signal detections and data acquisition of the two-component PDM were done by a transient-recorder and a PC-diagnostic-system. The advantage of this system is based on the ability of logging a whole signal run, which is laid down in a data file. After a great number (of more than 2000) signal runs has been stored to the buffer of the computer, the quality of the signals is tested by varying the fault criteria [6]. Test measurements with a small rotating glas-ball resulted in good accordance with the given values of the rotating speed of the drive motor and with the particle size given by microphotos. Instead of the transient recorder also a FFT-processor, described by [7], has been used for detecting and analyzing the signals. The comparison of these acquiring methods resulted also in good accordance.

Discussion of the experimental results

An optical configuration for laser light sheet photography had been used to get first informations about the shape and the extension of the spray cone. Fig. 3 shows a photograph of the spray cone in the vicinity of the nozzle, received for the same fuel oil and gas temperature of 30 °C and a fuel oil pressure of 8 bar.

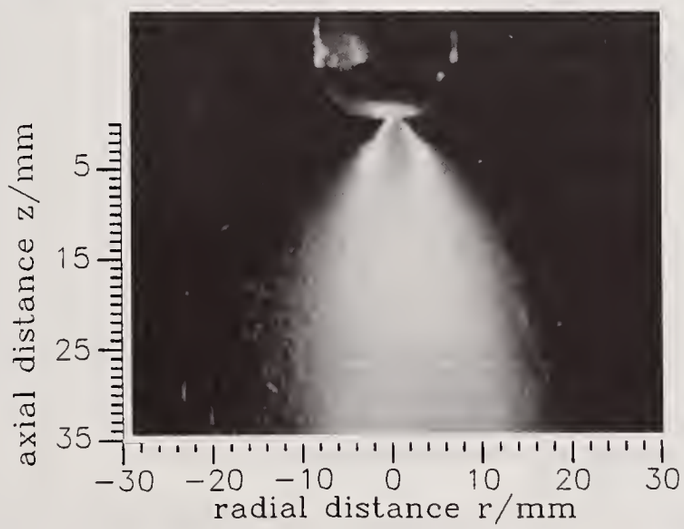

Fig. 3 Laser-light-sheet photograph

It has to be noticed that the extension of the liquid film and of the hollow cone in the centre of the spray cone is very small. Within less than 5 mm below the nozzle the liquid film becomes unstable and disintegrates into ligaments and droplets. 10 mm below the nozzle orifice the hollow cone has disappeared and the shape of the spray cone looks like a solid cone. This is illustrating that the interesting region for drop-size and velocity measurements should be executed not far away from the nozzle orifice. It has also to be noticed that changes of the spray parameters which influence the burning process (with regard to the very short flame) are expected to take place in a distance range of only a few millimeters.

In two horizontal planes, at z = 10 mm and z = 20 mm, and for differing radial positions r measurements of drop-sizes and of 2-component drop-velocities have been carried out under constant gas and fuel oil temperature conditions and for an atomizing pressure of 8 bars. The vertical velocity component (z-direction) is given by v_z, the resultant horizontal drop-velocity by v_h (Fig. 4 and 5). The resultant horizontal velocity v_h is given by the vector addition of the radial and the swirl velocity components (v_r, v_φ). For the assumption of a symmetric spray cone and of a linear dependency of v_r and v_φ on r (which is a weak one), v_h can been calculated at least from the measured velocity component v_m, which is perpendicular to the interference fringe pattern.

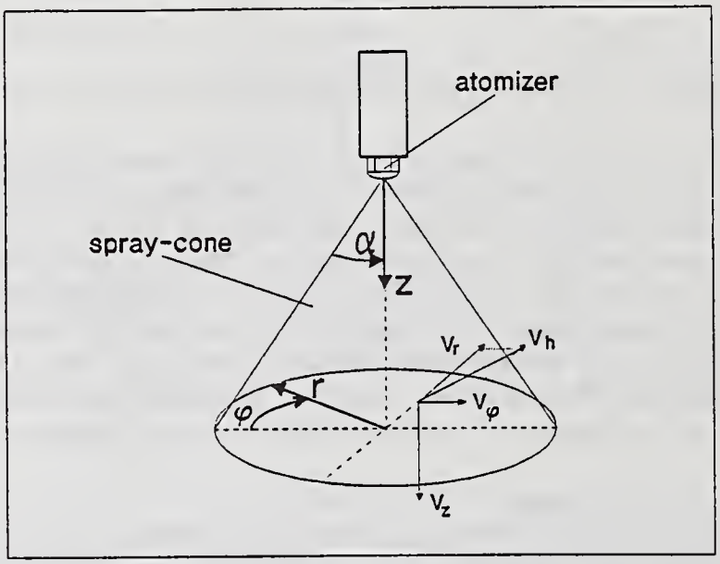

Fig. 4 Spray-cone parameters

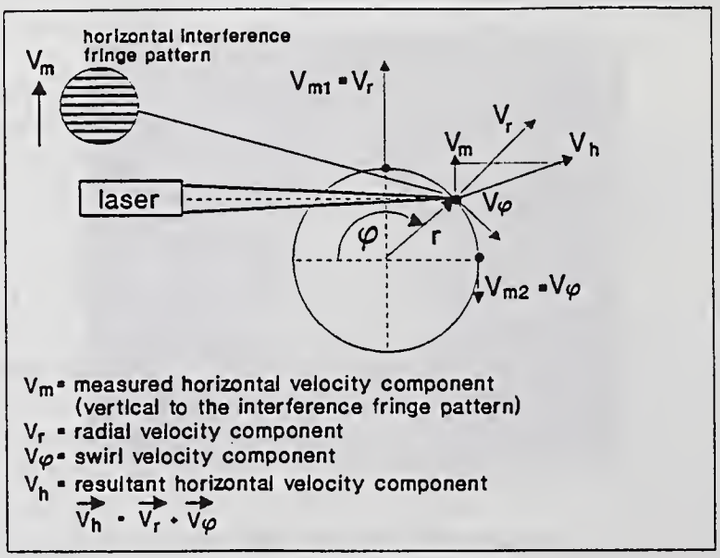

Fig. 5 Horizontal velocity components

Fig. 6 shows mean values of the horizontal velocities v_h versus the radial distance r for z = 10 mm and z = 20 mm. The best fit of all mean values results in the regression lines. That means we receive a linear dependency of horizontal mean velocity, v_h, on radial distance r.

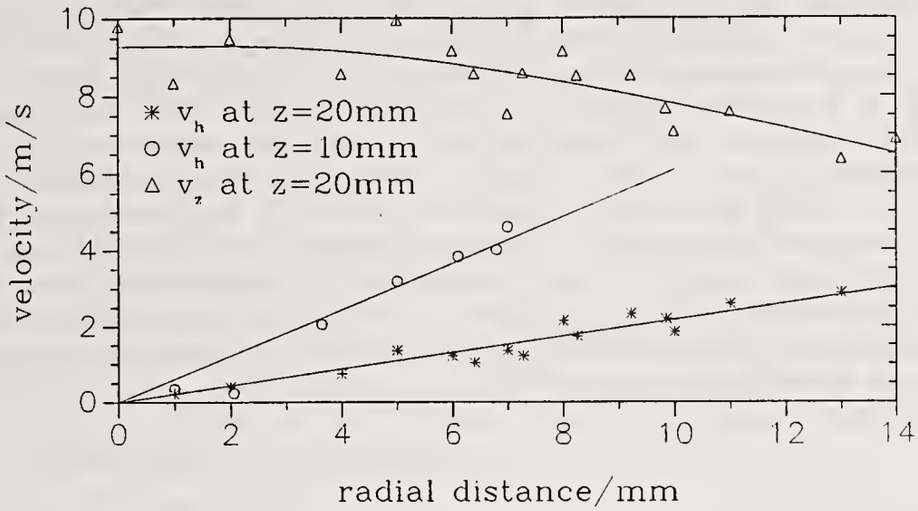

Fig. 6 Axial and horizontal velocity mean values at z = 10 mm and z = 20 mm

For larger radial distances from the centre line the radial droplet-velocity increases strongly for growing drop-sizes and is directed outwards of the spray cone. For small radial distances a narrow velocity distribution is resulting for the whole range of drop-size distribution without a correlation between drop-size and -velocity (Fig. 7b). Fig. 7 shows a comparison of the cross-correlation of the horizontal velocities and the diameters at a) r = 13 mm and b) r = 4 mm in the horizontal plane, z = 20 mm. It is astonishing to get nearly the same diameter distributions at both positions, because we expected smaller droplets in the centre and larger droplets at the periphery of the spray cone. This fact again demonstrates that the interesting changes of the spray cone parameters take place near the nozzle orifice. This means that the influences of the quality of atomization on combustion have their domain already a few millimeters below the nozzle.

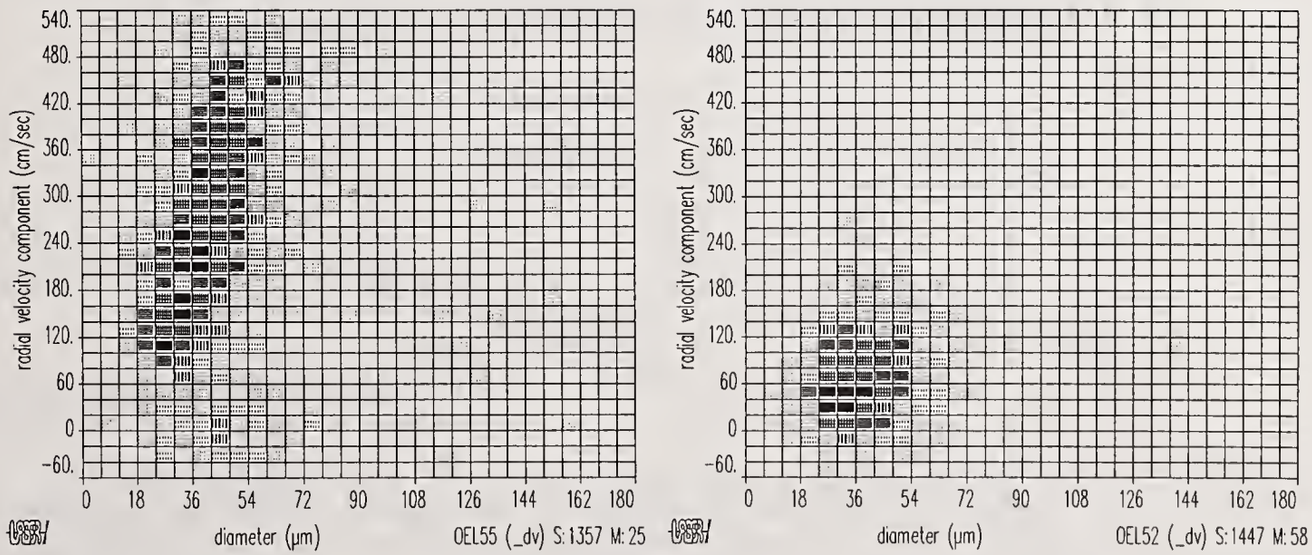

a) φ = 90°, r = 13 mm, z = 20 mm b) φ = 90°, r = 4 mm, z = 20 mm

Fig. 7a,b Diameter-velocity correlation

A comparison of the results of droplet velocities shows a strong decrease with growing z-values, caused by drag of the droplets executed by the entrainment of the gas into the spray cone. This can be seen for example from Fig. 6 for the mean horizontal velocities for the two distances z = 10 and 20 mm. The axial mean velocity, v_z, decreases with growing radial distances and fluctuates around a regression curve of nearly constant value for small distances, r.

A significant sensitivity of the dropsize-distribution for temperature influences (mainly via viscosity) can be demonstrated by the SMD of local distributions versus oil temperature as given in Fig. 8. It has been measured by the one-component PDM-configuration. In Figrs. 8 and 9 the SMD is plotted versus temperature and viscosity respectively for three positions at different horizontal planes, i. e. z = 20mm; 35 and 50 mm. The temperature influence via density and surface tension on the drop-size distribution could not be analysed explicitly, because of the small changes of these physical properties within the temperature ranges varied (Table 1). It had also been tested whether the gas temperature affected the spray parameters; but within the range of variation the effects could be neglected compared with those resulting from the fuel oil temperature, because of the small distances of possible heat transfer processes in the disintegration zone before ligament disruption.

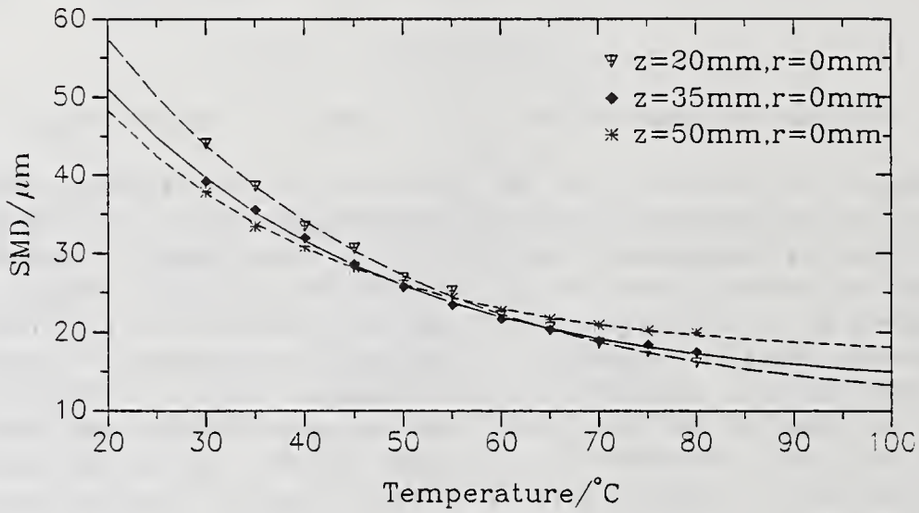

Fig. 8 Dependency of the Sauter-mean-diameter on temperature (T_{gas} = 30 °C)

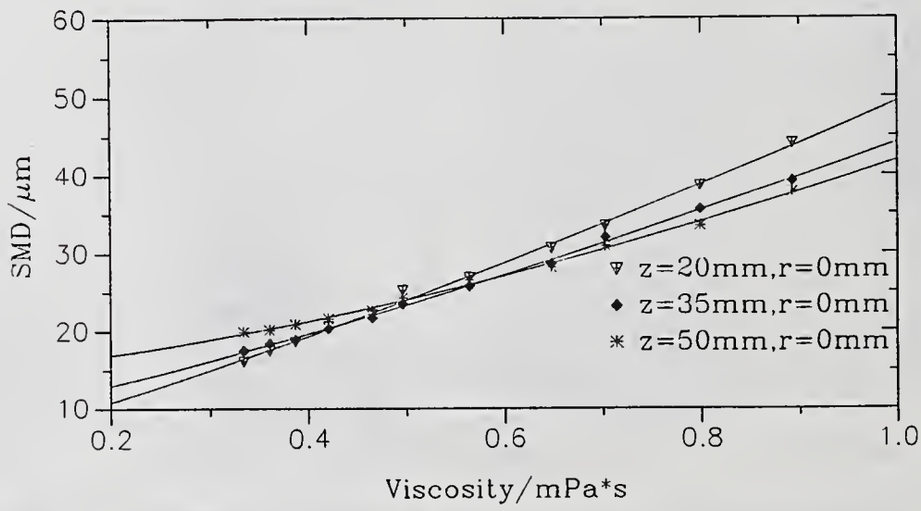

Fig. 9 Dependency of the Sauter-mean-diameter on viscosity (T_{gas} = 30 °C)

Table 1 Properties of fuel oil

temperature	density	viscosity	surface tension
°C	g/cm^3	mPa*s	dyn/cm
30	0.822	3.42	26.15
40	0.813	2.69	25.35
50	0.804	2.16	24.60
60	0.795	1.78	23.90
70	0.786	1.48	23.15
80	0.776	1.28	22.40

Table 1 also shows a strong decrease of the viscosity, μ, of the fuel oil for growing temperatures. Therefore the decrease of viscosity has been postulated to be mainly responsible for SMD changes for growing temperature. In this context it should be mentioned that one receives an exponential dependency of SMD on the viscosity. Similar correlations have been found by Jasuja [10], Jones [11] and Knight [12] in the form

$$SMD \sim \mu^B \quad ,$$

but the resulting coefficients for B in our investigations are different from those in the literature. Wang and Lefebvre [8],[9] did similar investigations using blended diesel oil with polybutene. They also found an exponential dependency of SMD on the liquid viscosity. A better fit for the regression line is given by

$$SMD = B(1) \cdot (\mu/\mu_0)^{B(2)} + B(3), \quad \mu_0 = 3.83 \text{ mPa} * \text{s}$$

μ_0 is the viscosity of standard state at a pressure of 1 atm and a temperature of 25 °C. The values of the coefficients B(1), B(2) and B(3) for different spray positions can be taken from Table 2. Fig. 10 shows, that the SMD depends on viscosity as well as on location in the spray cone. The local dependency can be interpreted by the different trajectories of drops of varying sizes and by the changes of drop path's for increasing temperatures of the fuel oil.

Table 2 Coefficients of dependency of SMD on viscosity

axial distance z	spray cone angle	B(1)	B(2)	B(3)
mm	degree	μm	---	μm
20	0	9.19	1.19	4.12
35	0	6.80	1.24	8.10
50	0	3.52	1.53	14.55

CONCLUSIONS

A new two-component PDM with direct storing of signals and succeeding analysis has successfully been tested. Measurements of particle size and velocity distributions in the vicinity of the nozzle with hollow cone spray demonstrate a linear dependency of the horizontal resultant velocity component on the radial distance r. This linear dependency with different gradients has been found in two horizontal planes. Because of the entrainment of the surrounding gas and the drag of droplets the horizontal resultant velocity decreases for increasing axial

distance z. According to this fact the curvature of the particle trajectories vary with increasing distances z tending more and more to the vertical direction.

Temperature dependencies of the spray-cone parameters have been investigated in three horizontal planes at different radial distances. The point of interest was the correlation between SMD and the physical properties of the fuel-oil. Because it has been found, that within the range of temperature variation there have been only small changes of the surface tension and the density, these properties have been neglected. Thus only the growing viscosities due to decreasing temperatures are responsible for SMD-augmentation. The results of these temperature investigations demonstrate an exponential increase of SMD for higher values of viscosity. Additionally a dependency of the local value of SMD on its position in the spray cone has been found. Patternator investigations show, that this local dependency may be reduced to the temperature dependency of the curved droplet trajectories. The phenomena of changes of drop path curvature for higher temperatures has to be investigated in future.

REFERENCES

1. Durst, F. and Zare, M., "Laser Doppler Measurements in Two- Phase Flows", Proc. LDA-Symp., Copenhagen, pp. 403-429 (1975)

2. Bachalo, W. D. and Houser, M. J., "Development of the Phase/Doppler Spray Analyzer for Liquid Drop Size and Velocity Characterizations", Proc. AIAA/SAE/ASME 20th Joint Propulsion Conf. Cincinnati, June 1984

3. Bauckhage, K.and Flögel, H.-H., "Simultaneous Measurement of Droplet Size and Velocity in Nozzle Sprays", Proc. of the 2nd Int. Symp. on Appl. of Laser Anemometry to Fluid Mechanics, 2.-4.7.1984, Lisbon

4. Buchhave, P., Saffman, M. and Tanger, H., "Simultaneous Measurement of Size, Concentration and Velocity of Spherical Particles by Laser Doppler Method", Proc. of the 2nd Int. Symp. on Laser Anemometry to Fluids Mechanics, 2.-4.7.1984, Lisbon

5. Bauckhage, K. and Schulte, G., "Lasermethoden in der Strömungsmeßtechnik", Editor B.Ruck, Chap. 7: 'Phasen-Doppler-Anemometrie', AT-Fachverlag Stuttgart (1990)

6. Ruck, B., "Laser-Doppler-Anemometrie", AT-Fachverlag, Stuttgart (1987)

7. Bauckhage, K., Schöne, H. and Wriedt, Th., "Using Fast-Fourier-Transform (FFT) for the Phase-Doppler-Difference Analysis of powder and metal sprays", Proc. of the Int. Conf. on Laser Technologies in Industry, June 1988, Porto

8. Lefebvre, A.H., "Atomization And Sprays", Hemisphere Publ. Corp., New York (1989)

9. Wang, X.F. and Lefebvre A.H., "Mean Drop Sizes from Pressure-Swirl Nozzles", AIAA J. Propul. Power Vol. 3, No. 1, pp 11-18 (1987)

10. Jasuja, A.K., "Atomization of Cruede and Resichnal Fuel Oils", ASME J. Eng. Power, Vol. 101, No.2, pp 250-258 (1979)

11. Jones, A.R., "Design Optimization of a Large Pressure Jet Atomizer for Power Plant", 2nd ICLASS, Madison, Wis., pp 181-185, proc. (1982)

12. Knight, B.E., "Communication on the Performance of a Type of Swirl Atomizer", by A.Radcliffe, Proc. Inst. Mech. Eng., Vol. 169, pp 104 (1955)

CHARACTERIZATION OF INDUSTRIAL AIR ATOMIZED LIQUID SPRAYS FOR FLUIDIZED BED GRANULATORS

T. Isenschmid

Institute for Process and Cryogenic Engineering
Swiss Federal Institute of Technology
ETH Zürich Zentrum, Zürich, Switzerland

ABSTRACT

Atomization is a key unit process for the design of spray dryers - in our study a continuous fluidized bed granulator. A test rig for industrial scale nozzles has been installed to characterize two-fluid atomizers for various spray operating conditions. Distributions of drop size, drop velocity and mass flow in different locations of the spray cone were measured with a Phase-Doppler-Particle-Analyzer. The nozzles tested up to now are of two-fluid type with independent control of air and liquid flow. The atomization of the liquid jet is performed by compressed air. Air pressures varied from 2 to 7 bar, the liquid flow in a range of 115 to 800 l/h. Water, water based solutions, water based suspensions or a mixture of all of these have been used. The different water based liquids were especially prepared to vary systematically the main parameters influencing atomization. Feed-suspensions with a very narrow particle size distribution of the suspended solids were produced by hydrocyclone classification. The viscosity has been increased by adding polyglycol. Thus viscosities from 1 to 150 mPa·s and suspensions with a solids concentration as high as 30 % could be tested. This allowed to compare a water spray pattern to a spray pattern produced by liquids with suspended particles and/or with higher viscosity liquids. Monitoring of the viscosity by a newly developed orifice simply measuring a pressure difference allowed an easy on-line control of viscosity respective viscosity changes during spray operations.

Keywords
Spray characterization, two-fluid nozzles, fluidized bed granulators, pneumatic nozzles for suspensions, spray dryer conditioned products.

1. INTRODUCTION

Disintegrating a liquid jet by various means into single drops is an increasingly and often used technology in todays industry. In many operations the atomization process plays a significant role [1]. The generation of a well defined spray has to be considered as a "key unit operation" especially in following areas:

- atomization of fuels
- production of powders and granules
- heat and mass transfer operations
- application of thin layers to a surface.

Requirements concerning drop size, drop velocity and mass flow distribution in the spray are determined by process conditions and requirements of products. For continuous production of powders and granules spray dryers have long been standard in process industry [2]. However, recent developments for dryers have led to different design solutions [3] adapted to more sophisticated requirements.

1.1 Industrial application: Fluidized Bed Granulator

The Fluidized Bed Granulator (FBG), as shown in Figure 1, is a new drying system [4] for the production and conditioning of dyes and agricultural products in chemical process industry. The advantages of this technology are:

- *product quality requirements*: Conditioned products which are dust free, free flowing and which show fast redispersion and uniform appearance can be achieved
- *safety/hygiene*: Hazardous products are easier to handle since the fines are recycled within the apparatus and a coarse product reduces risk of dust explosion
- *building space requirements*: The height of FBG installations can be reduced considerably due to reduced specific drying volumes.

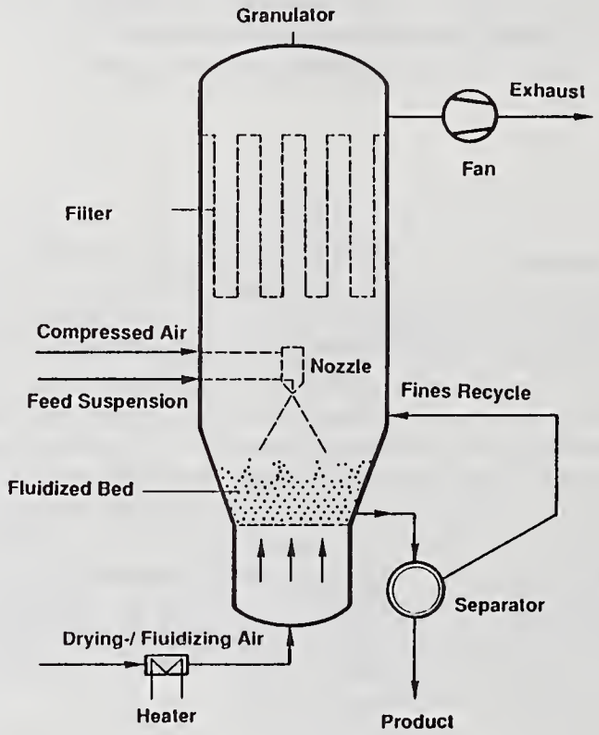

Figure 1:
Simplified flow scheme of a fluidized bed granulator

Such a drying installation can be regarded in macro- and microscale. The behaviour of the macrosystem - which is considered to be the FBG with its in- and outgoing mass flows - is governed by the corresponding mass and energy balances. Interaction of the nozzle spray cone with the fluidized bed - one calls it the microsystem - is however a critical item of such a dryer. For example, for scale-up purposes, for changes of feed suspensions or for required product qualities, one needs to know the distributions of drop size, drop velocity and mass flow for the actual spray cone at different levels. Those define number and distance of nozzles above the fluidized bed, the drying behaviour of the droplets in the freeboard and the specific liquid load per unit area of fluidized bed surface.

2. NOZZLE TEST RIG

To investigate spray patterns of nozzles with liquid flow rates up to 1000 l/h, a nozzle test rig of industrial size has been designed and built (Figure 2). The spray chamber is built from plexiglass in order to have visual control of the spray patterns as well as to avoid any unwanted outside disturbancies of preset spray and flow conditions. The cross section of the spray chamber is 1.4 m square. It has been decided to perform the spray pattern measurements in a constant co-current laminar downstream air flow, despite the gas flow situation in the FBG is opposite. Theoretical considerations about the spray cone behaviour under the before mentioned differing conditions showed that at least in the distances to be investigated no significant influence has to be expected.

The liquid to be tested is kept in a closed cycle. A frequency controlled screw pump conveys the liquids from the stirred liquid tank to the pneumatic nozzle with air supply from a pressurized air tank.

The spray produced by the two-fluid nozzles, after having passed the measurement level, is sucked to a vane blade droplet separator at the bottom of the test rig and is separated from the gas stream.

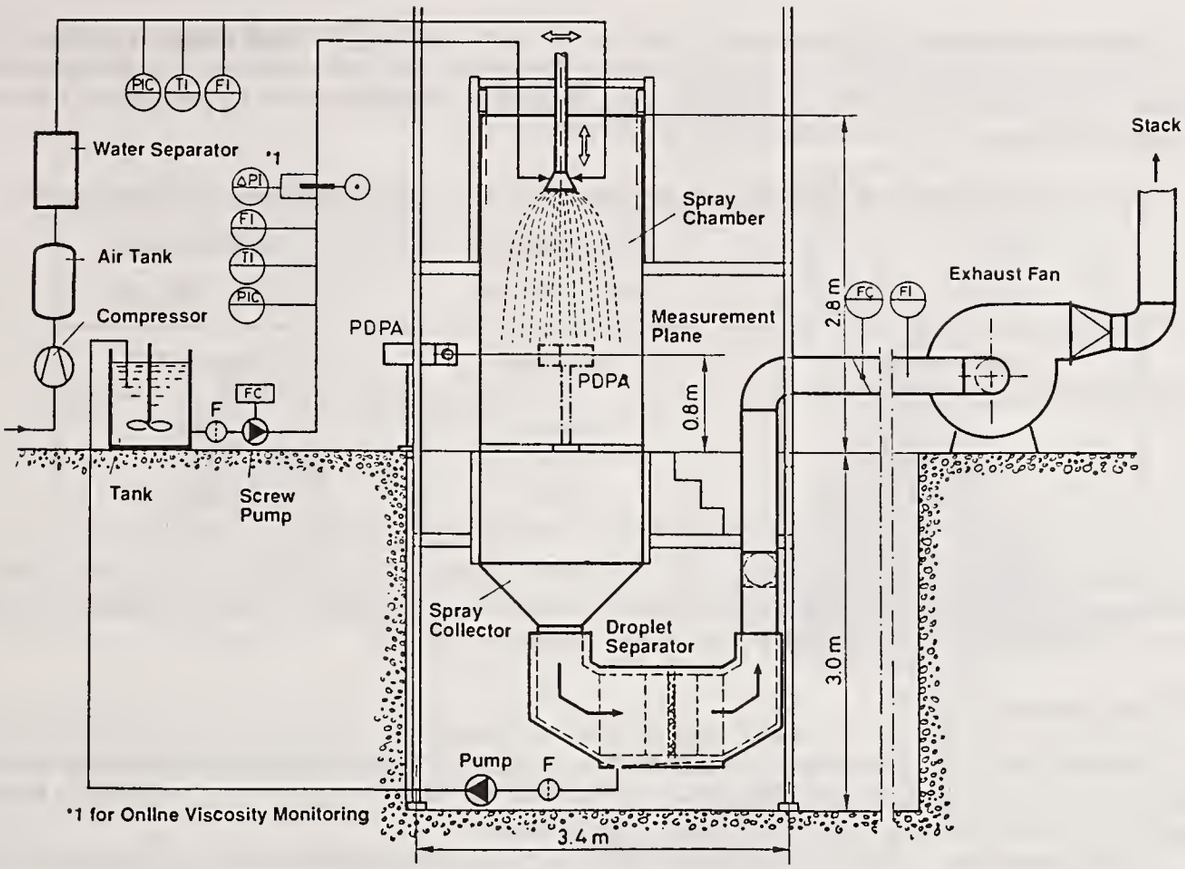

Figure 2: Scheme of industrial size nozzle test rig

The collected liquid is recycled to the storage tank. All flow rates are indicated and controlled. They can be varied following the demands for measuring the industrial relevant parameters. After careful evaluation of existing particle sizing measurement systems an Aerometrics Phase-Doppler-Particle-Analyzer (PDPA) has been applied. The optical system has been strictly separated from the test rig and mounted on separate stands. In order to measure spray characteristics at all locations in the spray cone the nozzle is attached to a three dimensional traverse system. This allows to move the nozzle outlet to nearly any point of the spray chamber and to control its exact position.

3. MEASUREMENT SYSTEMS

3.1 Spray pattern measurements

The PDPA from Aerometrics was used as a non-intrusive and simultaneous measurement technique to obtain size, velocity and concentration of the dispersed drops in the spray as further described in [5, 6]. Since the measured droplets were transparent and their refractive index close to that of water, the receiver has been positioned at an off-axis angle of 30 degrees. At this angle the refracted light dominates the reflected light component. The index of refraction was determined with an "ABBE-refractometer".

To calibrate the PDPA a commercial generator of monodispersed drops as further described in [7, 8] was used. This method has been established as a primary standard for instrument calibration. The liquids tested to produce these droplets of uniform size were identical to the process liquids described in chapter 5 - except no solids could be added due to clogging of the small orifices. The measured drop diameter d_{30} by the PDPA compared to the calculated drop size

$$d = \left[\frac{6}{\pi} \frac{\dot{V}}{f} \right]^{1/3} \qquad (3.1)$$

where $\dot{V}$ was measured by a scale and f controlled with an oscilloscope (LeCroy 9600). A mean deviation of 2 % resulted for the PDPA.

A comparative study was performed by means of a Zeiss IBAS 2000 image analyzing system (IBAS) and a Helos-Sympatec laser diffraction meter (Helos). Therefore, two sieve fractions of glass beads were measured by three different sizing systems.The results of these measurements by comparing the volume mean diameters d_{30} of the spatial distribution are as follows:

Table 3.1: Comparison of particle diameters by different sizing techniques using glass beads

	Sieve fraction I 160 - 224 µm	Sieve fraction II 355 - 560 µm
Sizing technique	d_{30} [µm]	d_{30} [µm]
IBAS HELOS PDPA	192 198 208	518 497 599

The rather large diameter measured with the PDPA for the II sieve fraction is believed to be due to asphericity and deviations from the correct index of refraction of the glass beads. Additional information concerning such sizing technique comparisons can be found in [9, 10].

3.2 On-line viscosity control

The viscosity of the atomized fluid has a decisive influence on the spray characteristics. For that reason it is very important to measure and monitor the viscosity of the liquid on-line immediately before it is sprayed as realized in the test rig. Another question is how to measure a correct viscosity for a liquid with suspended particles due to a certain non-newtonian behaviour.

Careful evaluation of different possible measurement principles lead to the decision to install a custom manufactured orifice in the liquid pipe leading to the nozzle (Figure 2). From the pressure difference measured across the orifice an on-line viscosity can be derived. Liquids with a known viscosity are initially used to calibrate the orifice. The opening of the orifice has been chosen of the same size as the liquid nozzle opening. Therefore, similar shear stresses occur at the location of the viscosity measurement and at the nozzle. On-line viscosities with our new method are compared with a conventional viscosimeter (Contraves Rheomat 115):

Table 3.2: Viscosities of polyglycol water mixtures measured by the two different methods

	Viscosity [Pa·s] · 10^{-3}					
Rheomat	23,2	29,3	39,7	48,8	87,0	121,7
Orifice on-line	19,2	32,6	36,9	51,1	86,6	107,1

4. NOZZLES TESTED

The nozzles tested are of two-fluid type with external mixture of the fluids (Figure 3). Such nozzles are currently applied sucessfully in FBG operation following the arrangement in Figure 1.

Air and liquid flow of the nozzle can be varied independently to adjust the spray cone conditions to the liquid distribution required for granulation. Compared to pressure nozzles the liquid exit opening is large - therefore clogging can be avoided even if the liquid contains suspended particles.

A swirl body in the nozzle's liquid path produces a liquid cone shaped lamella outside the nozzle. This technique - sometimes called pre-atomization - forces the compressed air to impinge on the liquid lamella in a close to rectangular way to guarantee optimal atomization. The air pressure has to be kept above the critical pressure ratio. Therefore, the atomizing air reaches velocity of sound in the narrowest cross section and expands vigorously immediately outside the nozzle. Typical air pressures vary from 3 to 6 bar. The liquid pressure determined by the requested flow rate can be kept generally very low (≤ 0,5 bar).

To evaluate the measurement data of the symmetric spray cone a coordinate system following Figure 4 for positioning the PDPA probe volume is used.

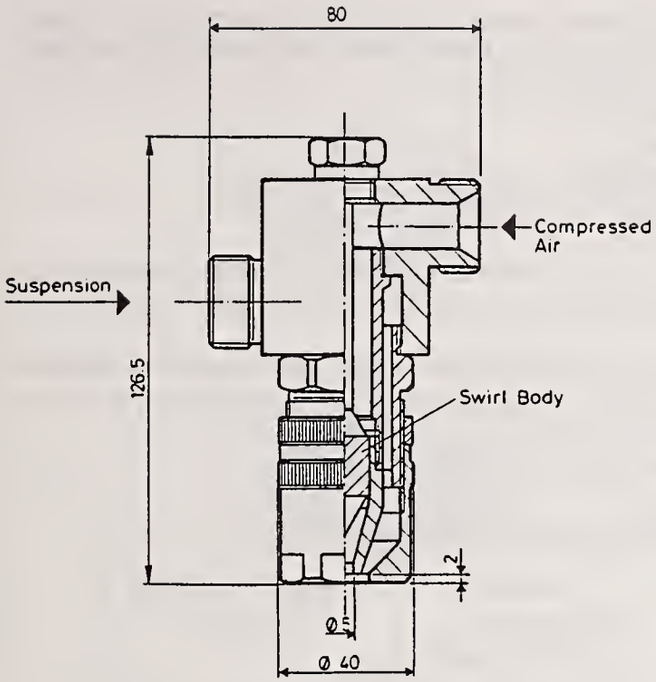

Figure 3: Two-fluid nozzle as used in tests (Schlick 0/5)

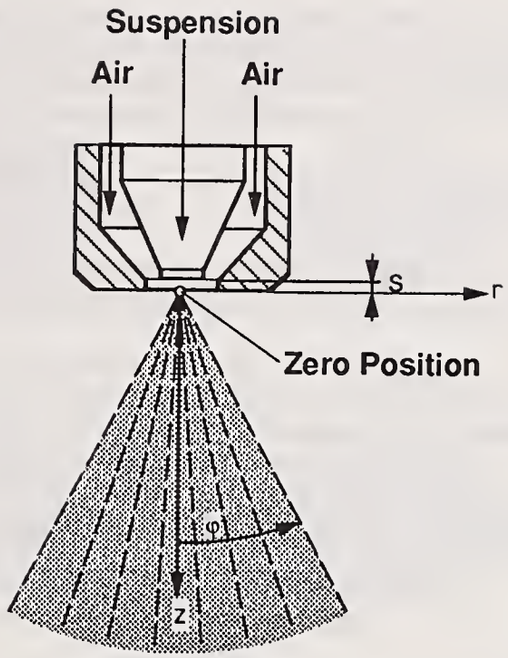

Figure 4: Coordinate system for position of probe volume in spray cone

5. COMPOSITION AND SIMULATION OF TEST LIQUIDS

In a chemical production process the final step is often the separation of the product from a suspension, the so called formulation. To transfer the solids content of such a formulation into a product, drying in fluidized bed granulators is more and more preferred.

To characterize a formulation however, one has to analyze first the composition of suspension and to divide it into fractions of pure liquid, disolved and solid phase (Figure 5).

For the atomization process of a formulation it is important to know the influence of its viscosity, of its surface tension, % solids concentration, the solid particulate size in the suspension and the particulate size of its solids.

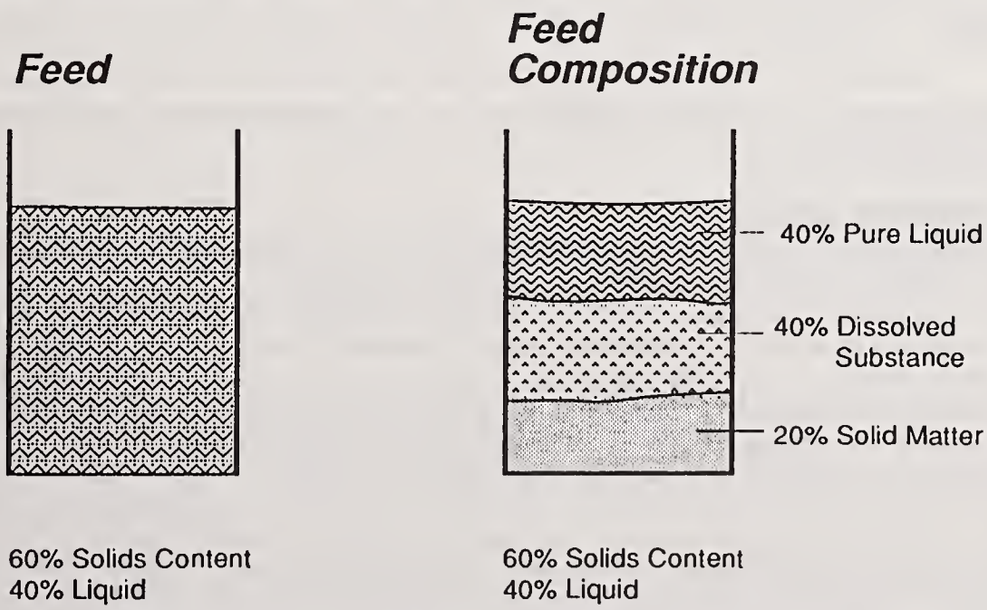

Figure 5: Typical Composition of an industrial formulation

Since real formulations cannot be used in tests for many reasons (price, safety, handling, ...) these features had to be simulated. Therefore new components had to be found to synthesize suspensions meeting the specifications determined by the industrial process as well as by the measurement technique. For the tests reported here we replaced the real components as follows:

liquid	⇒	water
solvent	⇒	polyglycol
solids	⇒	china clay or filter cel (FC).

Viscosity. To vary the viscosity polyglycol has been dissolved in water in changing quantities. For example, adding 20 % polyglycol by weight increased the viscosity to 150 mPa·s (water: η = 1 m Pa·s).

Solids. China clay and filter cel (FC), used as filter aid in filtration processes, were applied as solids in different concentrations. In a hydrocyclone classifying pilot unit suspensions with different size fractions have been produced to investigate the influence of different particulate size of solids as well.

The model suspensions being sprayed are characterized in the following table:

Table 5.1: Characteristics of the model suspensions being tested

Suspension type	Solids material	solids concentration [% by weight]	d_{50} [µm]	d_{84}-d_{16} [µm]
B	china clay	5	4	7
D	filter cel	8	13	29
E	filter cel	6	8	14
-	filter cel	various	16	33

Surface Tension. The surface tension (σ) of water was measured as 0,072 N/m. Mixtures of polyglycol and water showed a decrease of surface tension which was independent of the amount of polyglycol added. The average surface tension for all water polyglycol mixtures was found to be 0,058 N/m.

Index of Refraction. The index of refraction had to be measured for each tested liquid. A classical "Abbe-refractometer" was used.

6. MEASUREMENT RESULTS

A water spray with the same operating parameters of the nozzle served as a comparison to each of the other tests conducted with the formulations mentioned in chapter 5.

Figure 6.1 shows a typical size, mass and velocity distribution for a water spray at three different distances z from the nozzle. As a representative mean diameter of the droplets the sauter mean diameter (d_{32}) has been chosen since it represents an optimal average value for heat and mass transfer calculations. One can see, that with increasing distance from the nozzle the larger droplets travel to the edge of the spray. At the same time velocity and mass distribution become more even.

It is interesting to know how the sauter mean diameter of spray changes if only one of the critical parameters is varied. A higher liquid flow rate causes larger droplets and a narrower spray cone (Figure 6.2). Liquids with viscosities of 49.6 and 82.4 mPa·s are compared to water in Figure 6.3. In accordance to existing experience a higher viscosity corresponds to a distinct increase of droplet size. Simultaneously however, the maximum drop diameter measured is significantly larger than that of a water spray.

Increasing solids concentration has a similar effect (Figure 6.4). With a slightly increased amount of solids the sauter mean diameter becomes obviously larger, but doesn't increase as much as expected when the solids concentration is further raised. A variation of the suspensions with similar solids concen-

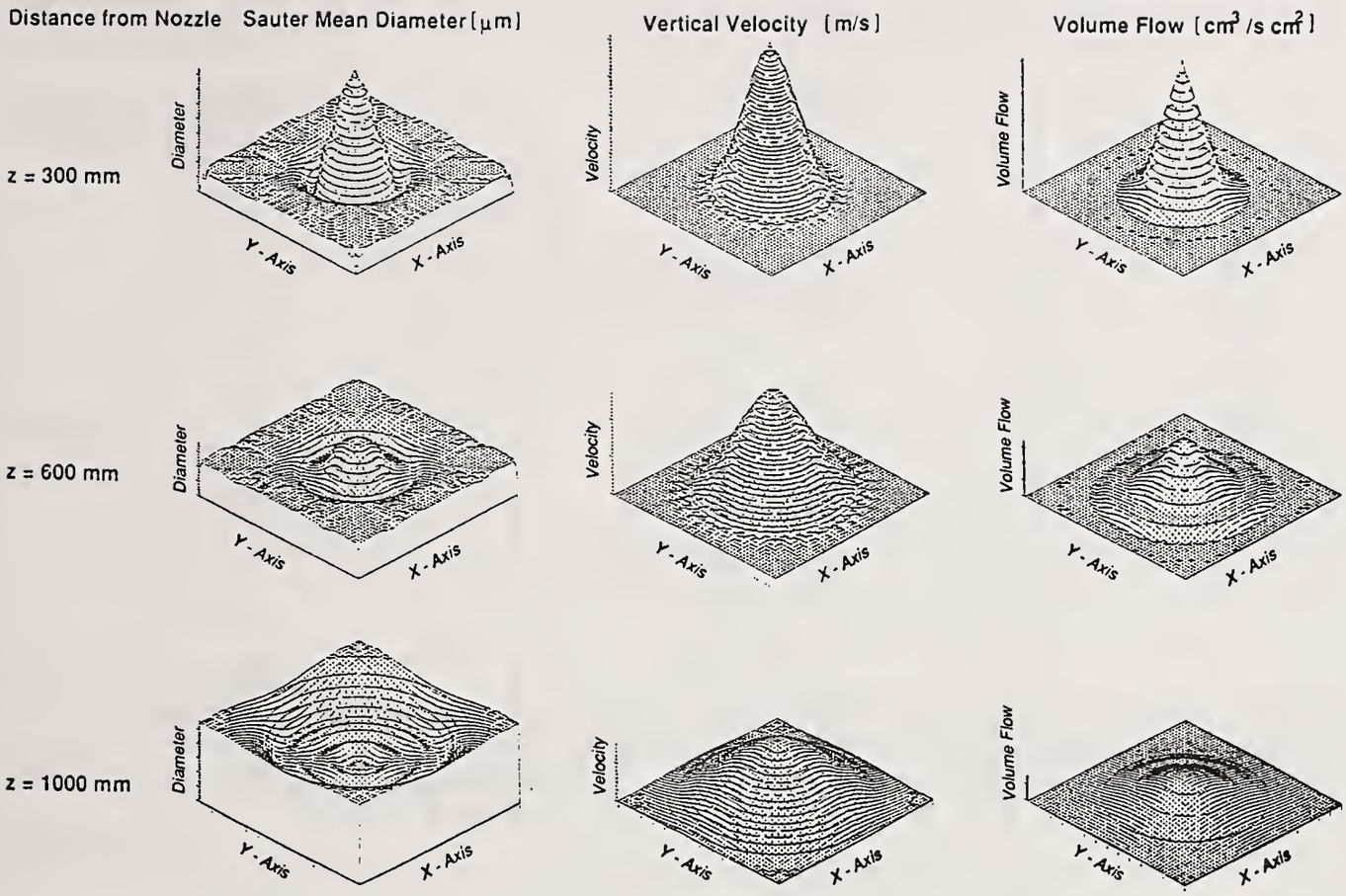

Figure 6.1: Local size, velocity and mass distribution for a water spray at three different distances from nozzle z = 0,3/0,6/1,0 m
(Schlick 854/0, s = - 4mm, $\dot{V}_l$ = 326 l/h, p_A = 3,2 bar)

tration (Figure 6.5) results in increased drop size of the suspensions compared to water. An obvious influence of suspended solid particulate size distribution could not be found, however.

Scattered refractive light signals from drops containing higher solid concentrations show a low signal-to-noise ratio due to multiple scattering by solid particles within the drops. At the same time, higher light absorption by these particles reduce also the strength of the refractive light component in relation to the reflective one [11]. Therefore, further research in optical spray measurements should be directed to liquids that favour reflection in order to reduce signal rejection and to become independent of droplet content when measuring with the PDPA. A possibility to improve spray characterization could be the development of appropiate model suspensions that meet optical as well as process requirements.

7. CONCLUSIONS

The presented industrial-scale nozzle test rig with PDPA measuring technique has given valuable insights into characterization of sprays from two-fluid nozzles. The main results is that by PDPA measurements it is possible to characterize the generated spray by distributions of droplet size, velocity and mass flow rate as function of the distance from nozzle, which allow adaption of spray behaviour to different process requirements.

The spray characteristics for two-fluid nozzles as function of on-line controlled viscosity changes (1...100 mPa·s), of varying solid concentrations (0...0,3 kg/l) in sprayed suspensions and of varying solid particulate size (d_{50}:4...16µm) in the suspensions could be verified experimentally.

Despite the automation technique used, the time consumption for performing such measurements is still extremely high due to calibration, adjustment and handling procedures that cannot be automated

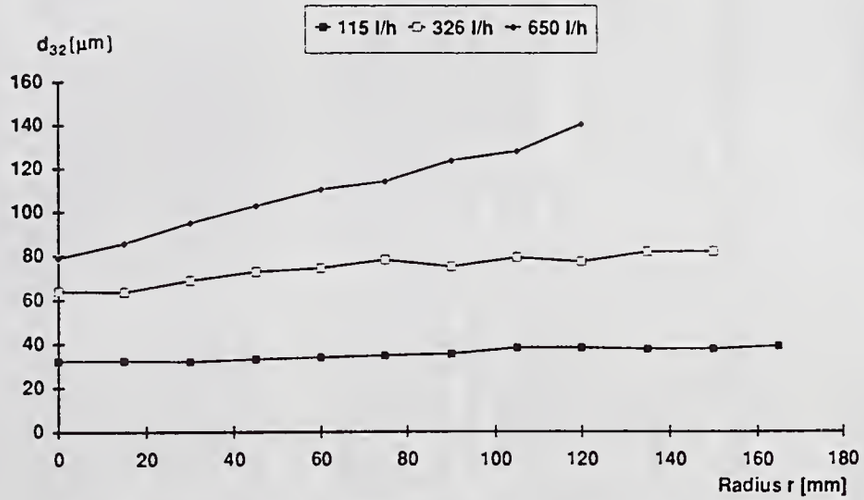

Figure 6.2: Local sauter mean diameter over spray cone radius for variation of water flow rate at distance from nozzle z = 0,6 m (Schlick 0/5, s = -2 mm, p_A = 3,5 bar)

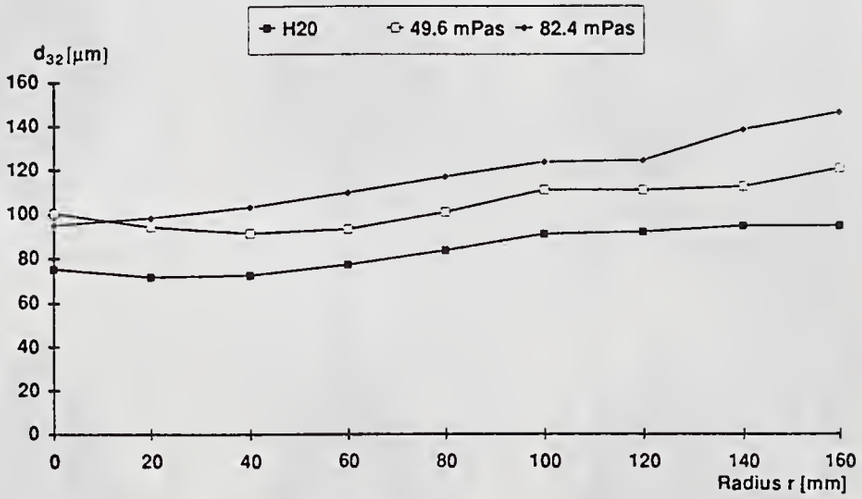

Figure 6.3: Local sauter mean diameter over spray cone radius for variation of viscosity at distance from nozzle z = 0,6 m (Schlick 0/5, s = -2 mm, $\dot{V}_l$ = 326 l/h, p_A = 3,5 bar)

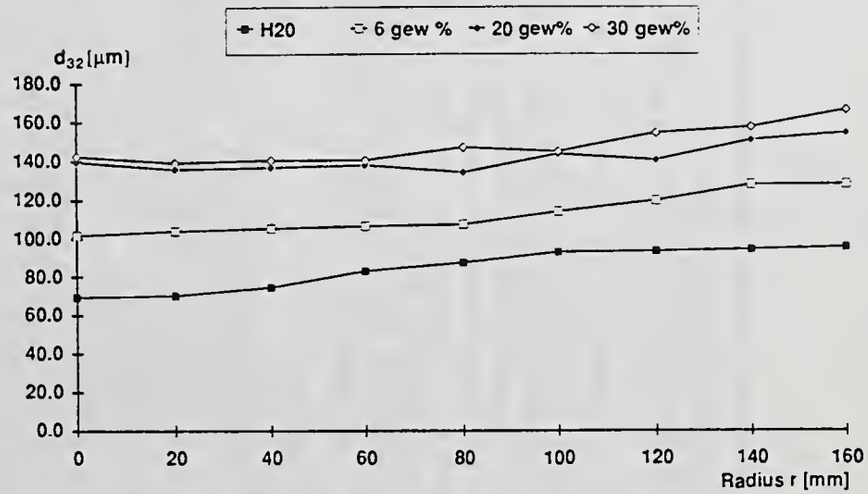

Figure 6.4: Local sauter mean diameter over spray cone radius for variation of solids concentration at distance from nozzle z = 0,6 m (Schlick 0/5, s = -2 mm, $\dot{V}_l$ = 326 l/h, p_A = 3,5 bar)

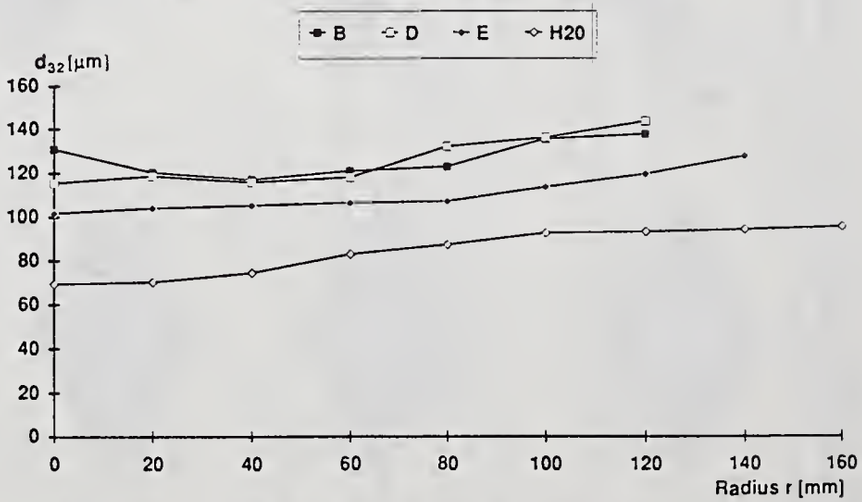

Figure 6.5: Local sauter mean diameter over spray cone radius for varying types of suspension at distance from nozzle z = 0,6 m (Schlick 0/5, s = -2 mm, $\dot{V}_l$ = 326 l/h, p_A = 3,5 bar)

yet. Therefore, further research efforts should especially take into consideration optical sizing, process and time requirements.

NOMENCLATURE

SYMBOLS AND ABBREVIATIONS

d	[m]	drop diameter
f	[s^{-1}]	frequency
p	[bar]	pressure
r	[m]	radius
s	[m]	gap between liquid tip and nozzle exit
$\dot{V}$	[m^3/h]	volume flow
x,y,z	[m]	coordinate system

INDICES

32	sauter mean
30	volume mean
50	volume median
84,16	points on the cummulative volume distribution curve
A	air
l	liquid

ACKNOWLEDGEMENTS

The author is glad to acknowledge the financial support provided by *SANDOZ AG, BASEL*, and the *Kommission zur Förderung der wissenschaftlichen Forschung (KWF)* , project number 1613. Prof. L. Reh's valuable advice is gratefully appreciated.

REFERENCES

[1] Walzel, P.: "Zerstäuben von Flüssigkeiten", CIT 62 (1990) Nr. 12, S. 983-994.

[2] Masters, K.: Spray drying handbook, 4th ed., George Godwin London (1985).

[3] Gehrmann, D.: "Entwicklungstendenzen der Trocknungstechnik in der chemischen Industrie", CIT 62 (1990) Nr. 10, S. A512-A520.

[4] Uhlemann, H.: "Kontinuierliche Wirbelschicht-Sprühgranulation", CIT 62 (1990) Nr. 10, S. 822-834.

[5] Bachalo, W.D.: "Method for measuring the size and velocity of spheres by dual-beam light-scatter interferometry", Applied Optics, Vol 19, No. 3, pp. 363 (1980).

[6] Bachalo, W.D. and Houser, M.J.: "Phase/Doppler spray analyzer for simultaneous measurements of drop size and velocity distributions", Optical Engineering, Vol 23, No. 5, pp. 583-590 (1984).

[7] Berglund, R.N. and Liu, B.Y.H.: Environmental Science and Technology, Vol. 7, (1973).

[8] MDG-Manual, Aerometrics Inc., 550 Del. Rey Av., Sunnyvale, CA. 94086.

[9] Dodge, L.G. and Hirlemann, E.D.: "Performance Comparison of Malvern Instruments Laser Diffraction Drop Size Analyzers", ICLASS, London, England, (1985).

[10] Young, B. W., Bachalo, W.D.: "The direct Comparison of three "In-Flight" droplet sizing techniques for pesticide spray research"

[11] Bauckhage, K., Floegel, H., Fritsching,U., Hiller, R.: "The Phase-Doppler-Difference-Method", Part. Part. Syst. Charact., 5, pp. 66-71 (1988).

CORRELATIONS FOR DIESEL SPRAY PENETRATION INCLUDING THE EFFECTS OF THE BREAK-UP ZONE

A.J. Yule, M.R. Mirza and I. Filipovic*

Dept. of Mechanical Engineering, UMIST, Manchester, United Kingdom
*Faculty of Mechanical Engineering, University of Sarajevo, Sarajevo, Yugoslavia

ABSTRACT

The semi-empirical penetration rate equation, often used to match the fully atomized downstream spray, has been modified to include the effects of the break-up zone near the injector nozzle. A single equation is developed, which accurately covers the whole spray flow field, rather than the two equation, two-zone approach used in previous work. The equation is compared with data derived using three nozzles, with variation in gas density and cross-flow velocity. The break-up time is an adjustable constant in the new penetration equation which is proportional to the time at which the spray penetration distance is the same as the break-up length. Matching the equation with the measurements provides useful data on how the break-up time, and thus break-up length, varies.

INTRODUCTION

The Equivalent Gas Jet Assumption and Spray Penetration

The 'equivalent gas jet' concept correlates experimental data on the penetration rates of the downstream "well atomized" zones of sprays from single hole diesel injector nozzles. Figure 1 shows the notation for the spray. This gives $U_p \propto x_p^{-1}$ and, integration leads to the dimensionally correct equation:

$$x_p = C_1 \left(\frac{\Delta P}{\rho_g}\right)^{0.25} D_N^{0.5}\, t^{0.5} \tag{1}$$

and U_{inj} is related to ΔP by the nozzle discharge coefficient C_D

$$U_{inj} = C_D(2\Delta P/\rho_L)^{0.5} \quad \text{and} \quad \dot{M}_J = \pi C_D^2 D_N^2 \Delta P/2 \tag{2}$$

Assuming a self-preserving velocity profile:

$$\dot{M}_J = 2\pi\rho_S \int_0^b U^2 r\, dr = 2\pi\rho_S b^2 U^2_{max} \int_0^1 f^2 \eta d\eta = 2\pi\rho_S b^2 U^2_{max}\, \varphi_2 \tag{3}$$

The density ρ_S is the "average" local density of the spray and, if, one ignores vaporization,

$$\rho_S = (\dot{m}_L + \rho_g(2\pi b^2 U_{max}\varphi_1 - \dot{m}_L \rho_L^{-1}))/(2\pi b^2 U_{max}\varphi_1) \tag{4}$$

Far downstream the spray should spread at a rate equal to that of a turbulent gas jet, $b=C_2X$, and C_2 should be a "universal" constant. Equation (3) gives:

$$U_{max} = \left[\frac{\dot{M}_L}{2\pi\varphi_2\rho_S}\right]^{0.5} C_2^{-1}\, x^{-1} \tag{5}$$

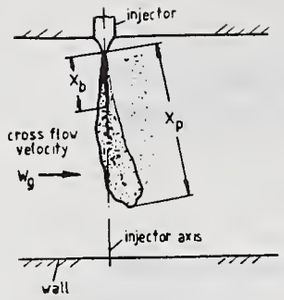

Fig. 1 Definition of spray characteristics

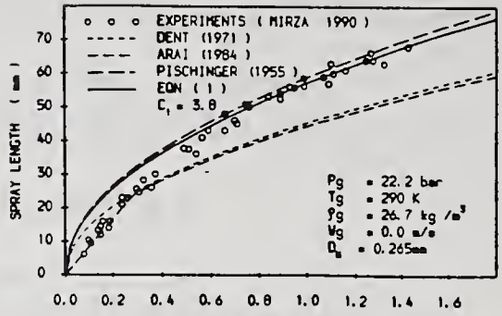

Fig. 2 Comparison between different correlations

and for large x eq (4) reduces to $\rho_s \simeq \rho_g$ and, using eq (2),

$$U_{max} = C_2^{-1} C_D \varphi_2^{-0.5} (\triangle P/\rho_g)^{0.5} D_N^{-1} x/2 \tag{6}$$

The (rather sweeping) assumption that the penetration velocity of the front edge of the spray is the same as the peak velocity of a steady spray at the same position $x=x_p$ gives $U_{max}=U_p=dx_p/dt$ and integration of (6) yields eq (1) with

$$C_1=(C_2^{-1} \; C_D \varphi_2^{-0.5})^{0.5} \tag{7}$$

Values for C_1 given by different authors vary considerably. Reasons were given in (1) which recommended an average value $C_1 = 3.0$. For a steady, incompressible gas jet one may assume $\triangle P=\frac{1}{2}\rho_g U^2_{inj}/C_D^2$ and eq (6) is $U_{max}/U_{inj}=C_3(x/D_N)^{-1}$ where

$$C_3 = (2C_2^2\varphi_2)/2^{-0.5} \quad \text{and} \quad C_1 = 2(2^{-0.5} \; C_3 C_D)^{0.5}. \tag{8}$$

Measurements in an air jet (2) gave $C_3 = 5.17$, with a virtual origin at $x=7D_N$. A typical value $C_D = 0.65$, for a diesel injector gives, $C_1 = 3.08$, when using eq (8) with $C_3 = 5.17$.

Sources of Variation in C_1

Break-Up Process. Equation (1) is not applicable near the orifice, where the predicted penetration rate is too high. For a zone of incomplete atomization near the nozzle, up to $x = x_B$, one expects a penetration velocity similar to the nozzle exit velocity and (3) assumed, for $x_p < x_B$,

$$x_p = 0.39 \; (2\triangle P/\rho_L)^{0.5} t \tag{9}$$

A typical value of C_D is 0.65, rather than 0.39 so that $U_B < U_{inj}$ and (4) explains and confirms this observation. (3) proposed a two-equation correlation and $x_p = x_B$ occurs where eq (9) intersects eq (1), with $C_1 = 2.95$. This gives:

$$t_B = 28.65\rho_L \; D_N/(\rho_g \triangle P)^{0.5} \tag{10}$$

Figure 2 compares this approach to one of the authors' experiments. Eq (9) gives reasonable fit to the initial penetration but a sharp break-point is not clear in the measurements. Fig 2 shows the curves of (5) and (6) which use $C_1 = 3.01$ and $C_1 = 3.91$ respectively.

Virtual Origin of Spray Steady gas jets have a virtual origin, at $x = x_o$, so that the spreading of the jet is represented by $b = c_2(x - x_o)$. Modification of penetration equations

to model this should be considered and (7) shows that a virtual origin gives an apparent change in the value of C_1.

Pressure Differential $\triangle P$ (3) used a rig which maintained $\triangle P$ constant after the needle valve opened. In general $\triangle P$ varies during a "real" injection and definitions for $\triangle P$ include $\triangle P_o$, based on the needle opening pressure, and $\overline{\triangle P}$, averaged during the injection period: The most physically realistic definition for $\triangle P$ should be used.

Measurement Technique/Accuracy The method of measurement of x_p is a source of differences between C_1 values. Penetration distances, measured along the nozzle centre-line (by using a shadowgraph method with a photodiode) were 10% less (8) than values measured using photographs and the "largest radial distance from nozzle orifice" definition used here. The front edge of a spray pulse is usually irregular and not always sharp. One must define the "edge" of the spray: Here the furthest visible extent of either liquid phase or gaseous phase (vaporized) fuel is defined as the spray edge.

Spray Angle For all sprays $\rho_s \rightarrow \rho_g$ as $x \rightarrow \infty$ and eq (1) assumes a universal, downstream spray angle, $\tan^{-1}C_2$. However authors have, paradoxically, provided data on spray angle as a function of ρ_g and other parameters. As shown by (8), for example, the downstream spray angle is $18^\circ - 20^\circ$, which agrees with that expected for a turbulent gas jet. The lower spray angles reported nearer to the nozzle or at low gas pressures represent a transient stage of the spray due to (a) break up, (b) a region where $\rho_s > \rho_g$ or (c) very large droplets (particularly when ρ_g is small). A varying spray angle should also give variation of C_1 from the ideal 'gas jet' value.

EXPERIMENTS

Experiments at UMIST used three single hole diesel injectors operated with commercial pumps and Table 1 summarises the operating conditions. Penetration measurements were made in pressurised gas chambers with, for D_N = 0.265mm, a variable cross-flow velocity W_g. All measurements were made at a gas temperature 290K ± 5K. Penetration rate measurements were made by high speed movie photography and spark photography. The "zero time", for all penetration measurements, is defined as the time at which liquid commences to emerge from the nozzle. It is necessary to ensemble average penetration measurements, for a number of pulses, and a minimum of 10 spray pulses were used. This scatter is due to cyclic variations, (9).

D_N (mm)	L/D_N	Opening Pressure (bar)*	$\overline{\triangle P}$ (bar)*	$\overline{\triangle P}_{0.5}$ (bar)*	P_g (bar)+	ρ_g (kg/m³)	W_g (m/s)	Vol. per Pulse (mm³)	Injection Duration (ms)
0.265	2	160	210	215	11.8 22.2 22.2 22.2 32.5	14.2 26.7 26.7 26.7 39	13.5 0 8.8 13.5 13.5	11.4	1.36
0.213	3.6	220	312	300	5 25 45	6 30 54	0 0 0	10.1	1.5
0.46	1.65	120	254	245	5 25 50	6 30 60	0 0 0	53.7	1.9

Table 1. Summary of Test Conditions

*Gauge Pressures +Absolute Pressure

A MODIFIED PENETRATION EQUATION

Pressure Differential and Basic Constant C_1

The penetration data, in Fig 2, are typical in showing that far downstream the correlations of (5) and (3) underpredict the penetration, whilst (6) gives a small overprediction. The correlations are evaluated assuming eq (1) with $\Delta P = \overline{\Delta P}$. The pressure in the middle and later parts of the injection period cannot influence the penetration rate during the first 0.5msec. There is a rapid increase in injection pressure, with a peak pressure occurring between 0.5 and 1.0msec after needle opening time. An increasing P_{inj}, with time, should principally affect the shape of the penetration curve during the break-up process, with less effect further downstream and (4) gives a detailed consideration of this. Table 1 includes values of the mean injection pressure and the injection pressure averaged during the first 0.5msec of injection and values of these quantities agree to within 4%. The mean pressure differential, $\overline{\Delta P}_{0.5}$, should be more representative of the initial spray conditions during penetration. This agreement between averages during the initial period and during the whole period occurs for similar injector - pump combinations and thus $\overline{\Delta P}$ (averaged over the full injection period) may generally be used in eq (1). The value $C_1 = 3.8$, gives best agreement for $t > 0.5$msec. The three injectors used here have a similar value, $C_D = 0.67 \pm 0.03$, and using eq (8), $C_1 = 4.71\ C_D^{0.5}$. Two methods of modifying eq (1) to include a time-dependent parameter are discussed below.

Time-Varying Power Modification

Assuming a time-dependent power $t^{F(t)}$, so that eq (1) becomes:

$$x_p = 3.8\ (\Delta P/\rho_g)^{0.25}\ D_N^{0.5}\ t^{F(t)} \qquad (11)$$

then F should reduce to the value 0.5 as t increases. This modification occurs for a time t_B. The following empirical form for F was found:

$$F = 0.5 + (0.032/(\frac{t}{t_B} + 0.19)) \qquad (12)$$

Figure 3 shows the data of Fig. 2 fitted by eq (11). A value $t_B = 0.25$msec gives best fit and this procedure provides characteristic break-up times from penetration curves. The penetration curves obtained for all of the operating conditions in Table 1 gave $0.21\text{msec} \leq t_B \leq 0.27\text{msec}$. An investigation (4), which includes comparisons with break-up times derived by other techniques, led to the following general expressions:

$$U_B/U_{inj} = Re_B^{0.3}/31.7 \text{ and } x_B = 2.8 \times 10^4 We^{-0.46} D_N \qquad (13)$$

The approximation $U_B \approx x_B/t_B$, provides an expression for t_B. Using σ_L=0.03N/m, ρ_L=861kg/m^3 and ν_L=10^{-5}m^{2}s^{-1} gives (SI units):

$$t_B = (3.75 \times 10^5) D_N^{-0.28}\ \rho_g^{-0.05}\ \Delta P^{-1.37} \qquad (14)$$

Unlike eq (10), t_B has a very weak dependency on gas density. The effects, on t_B or x_B, of the internal nozzle geometry and turbulence level are secondary, as suggested by conductivity probe measurements (3).

Hyperbolic Modification of Penetration Equation

Break-up is a gradual, chaotic process so that exponential expressions, may be used. For example:

$$x_p = 3.8(\triangle P/\rho_g)^{0.25} D_N^{0.5} t^{0.5} \tanh[(t/t_B)^{0.6}] \quad (15)$$

where t_B is found to have the same values as those used in eq (11) (i.e. $t_B \simeq 0.25$msec) and can be described approximately by eq (14). Figure 3 includes eq (15) and its more rapid tendency to reach the "classical" form of eq (1), is more realistic so that eq (15) maybe preferred to eq (11). Figures 4 and 5 show penetration data (8) for 0.213mm and 0.46mm diameter nozzles compared with equation (15) and the agreement is excellent.

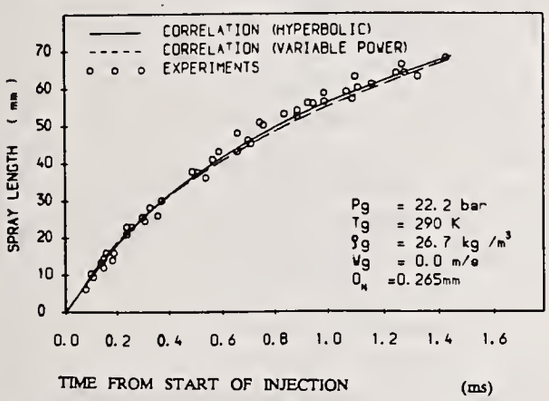

Fig. 3 Comparison between penetration rate and two forms of Correlation: Equation (11) and (12)

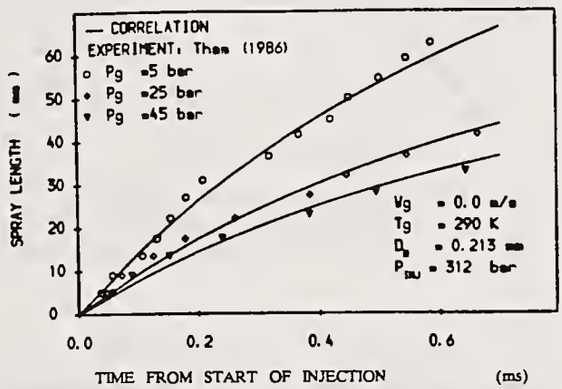

Fig. 4 Comparison between measured penetration rate, for injection into ambient gas and new correlation; diameter 0.213mm

Penetration Rate with a Cross-Flow of Gas

An empirical correction to the penetration correlation has been proposed (3) for injection into a swirling cross-flow, with the cross flow at right angles to the injector axis:

$$x_p = C_4\, x_{po} \text{ and } C_4 = (1 + (W_g/U_{inj}))^{-1} \quad (16)$$

where x_{po} is the penetration without cross-flow, given by eq (15). (3) proposed that U_p should be used in eq (16), rather than U_{inj} which was used for convenience. The use of U_{inj}, in eq (16), was unsatisfactory and the following definition of C_4 gave good agreement with the present experiments:

$$C_4 = (1 + (W_g/\bar{U}_p))^{-1} \quad (17)$$

Where $\bar{U}_p$ is the average penetration velocity up to the time t.

$$\bar{U}_p = \frac{1}{t}\int_0^t U_p\, dt = \frac{1}{t}\int_0^t \frac{dx_p}{dt}\, dt = \frac{x_p}{t} \quad (18)$$

Correlation of cross-flow effects by the ratio of the cross-flow velocity and the average penetration velocity appears physically reasonable. Equation (17) and (18) give:

$$x_p = x_{po} - W_g t \qquad (19)$$

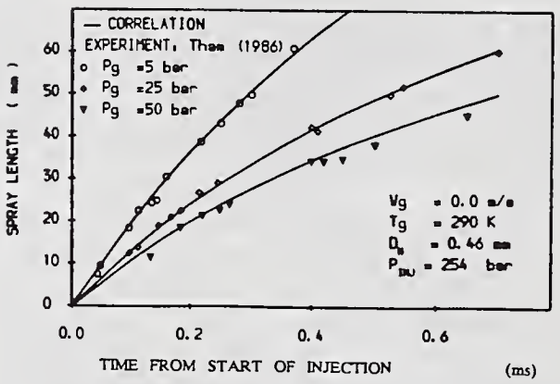

Fig. 5 Comparison between measured penetration rate and new correlation; nozzle diameter 0.46mm

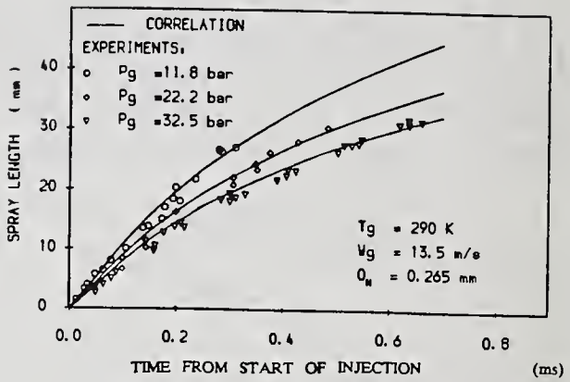

Fig. 6 Measured penetration rate in cross-flow and new correlation; nozzle diameter 0.265mm

This modification for the "compression" effect of the cross-flow should be assumed valid only for the range of cross-flow velocities and penetration distances which have been investigated. Figure 6 shows measurements of spray penetration for W_g = 13.5m/s with variation of gas pressure and Fig. 7 shows measurements, for variation of the cross-flow at one pressure. There is excellent agreement with eq (19). When the spray is not injected normally to the cross-flow, or when the spray has deviated significantly a component of cross-flow velocity in the same direction as the direction of penetration becomes important. This produces a "stretching" effect which opposes the compression effect of the orthogonal flow. Experiments (10) with angled injection into a cross-flow show that further modification of the penetration correlation is required under these conditions. It has been found that these correlations are in good agreement with CFD predictions of the flows (7) when a submodel of the break-up process is included.

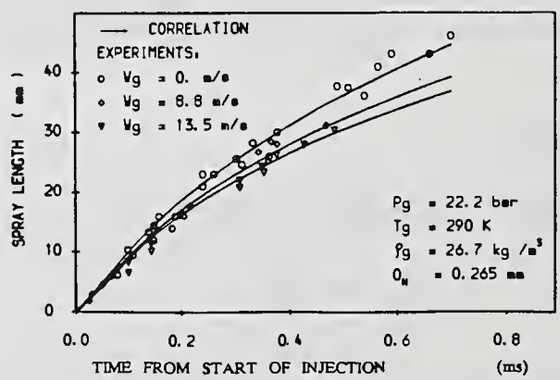

Fig. 7 Measured penetration rate at constant gas pressure, with variation of cross-flow velocity, compared with new correlation; nozzle diameter 0.265mm

CONCLUSIONS

A modified form of the penetration rate equation, for sprays produced by simple orifice diesel injectors, has been derived by considering the effects of the break-up zone near the nozzle. The equation gives excellent agreement with data for three nozzles, with variation in gas density and cross-flow velocity. Use of the correlation provides information on break-up time, which shows little variation for the range of conditions which have been examined, and break-up length, which has a much stronger dependency on both gas density and nozzle diameter.

NOMENCLATURE

b	half-width of spray or jet
C_1, C_2, C_3	empirical constants
C_4	cross-flow parameter, eq 17
C_D	nozzle discharge coefficient ($C_D = U_{inj}(2\triangle P/\rho_L)^{-0.5}$)
D_E	equivalent nozzle diameter, $D_E = D_N(\rho_L/\rho_g)^{0.5}$
D_N	nozzle orifice diameter
$F(t)$	variable power in modified penetration equation (11)
$\dot{m}_g$ and $\dot{m}_L$	gas and liquid phase mass flow rates through spray cross-section
$\dot{M}_J$	momentum flow rate through nozzle orifice (instantaneous)
P_g	gas pressure (absolute)
P_{inj}	injection pressure
$\triangle P$	pressure difference between nozzle inlet and outlet ($\triangle P = P_{inj} - P_g$)
$\underline{\triangle P_o}$	value at needle valve opening time
$\overline{\triangle P}$ and $\overline{\triangle P}_{0.5}$	average values for whole injection period and first 0.5msec
$\dot{Q}_g$, $\dot{Q}_L$	gas and liquid phase volume flow rates at spray cross-section
r	radial distance from centre-line
Re_B	Reynolds number, $Re_B = \rho_L U_B D_E/\mu_L$
t, t_B	time after commencement of injection and break-up time
U_{inj}	velocity in nozzle orifice
U_B	penetration velocity in break-up zone ($\approx x_B/t_B$)
U_{max}	centre-line velocity
$\underline{U}_p$	penetration velocity = dx_p/dt
$\overline{U}_p$	average penetration velocity at time t, = (x_p/t)
We	Weber number, $We = \rho_g U_B{}^2 D_N/\sigma_L$
Wg	gas cross-flow velocity
x	distance along axis of nozzle
x_p	maximum penetration distance, measured radially from nozzle orifice
ρ_g, ρ_L, ρ_s	densities of gas, liquid fuel and spray
η	dimensionless radial coordinate r/b
σ_L	surface tension of liquid
μ_L	viscosity of liquid

REFERENCES

1. Williams, T.J., "Parameters for correlation of penetration results for diesel fuel sprays", Proc. Inst. Mech. Engineers, Vol. 187 69.73, pp771-774, London (1973).

2. Wygnanski, I. and Fiedler, H., "Some measurements in the self-preserving jet", J. Fluid Mech., 38, 3, pp557-612 (1969).

3. Arai, M., Tabata, M., Hiroyasu, H. and Shimizu, M., "Disintegrating process and spray characterization of fuel jet injected by a diesel nozzle", SAE Technical Paper 840275 (1984).

4. Yule, A.J., Mirza, M.R. and Filipovic, I., "On the break-up times and lengths of diesel sprays", Submitted to Sprays and Aerosols' 91, University of Surrey, Sept. (1991).

5. Dent, J.C., "A basis for the comparison of various experimental methods for studying penetration", SAE Trans., Vol. 80, Paper No. 710571 (1971).

6. Pischinger, F., "Verfahren zur untersuchung von diesel-einspritzstrahlen", MaschBau Warmew, 10 (1955).

7. Yule, A.J., Mirza, M.R. and Filipovic, I., "Measurements and correlations of diesel sprays", submitted to Atomization and Sprays, Jan. (1991).

8. Tham, S.Y., "The study of diesel spray structure and penetration in high pressure and temperature quiescent gas", PhD Thesis, University of Manchester (UMIST) (1986).

9. Aval, S.M., "A study of pulsed sprays in a high pressure and temperature gas cross-flow", PhD Thesis, University of Manchester (UMIST) (1990).

10. Mirza, M.R., "Study of diesel sprays interacting with cross-flows and solid boundaries", PhD Thesis, Submitted to University of Manchester (UMIST) (1991).

BREAK-UP LENGTH OF A LIQUID JET AND INTERNAL FLOW IN A NOZZLE

H. Hiroyasu*, M. Arai† and M. Shimizu‡

* Dept. of Mechanical Engineering, University of Hiroshima, Hiroshima, Japan
† Dept. of Mechanical Systems Engineering, Gunma University, Kiryu, Gunma, Japan
‡ Dept. of Mechanical Engineering, Kinki University, Osaka, Japan

ABSTRACT

A new break-up phenomenon in a liquid jet, in which was friction inside the nozzle hardly contributed to the formation of the surface disturbance of the issuing jet, was discovered in a jet of a higher speed than a spray jet. Owing to lower turbulence, the break-up length was very long and the disintegration of the jet was driven only by an interfacial force between the jet and surroundings. A cavitation fixed at an entrance of the nozzle, generated strong internal turbulence, and the surface disturbance of the jet was a result of this. However, if the cavitation was too strong to prevent disruption of the cavity, a constricted jet, that was separated from the wall, issued from the nozzle, similar to super-cavitation flow around a wing. The break-up lengths were shortened by the cavitation but elongated by the separated flow. They are discussed using photographs of internal flows in a transparent nozzle.

INTRODUCTION

It has been known recently that the break-up phenomena of liquid jets are controlled by both internal turbulence in a nozzle and interfacial force between the jet and surroundings. The main cause of disintegration from a smooth jet to a droplet state is thought to be the surface instability expressed by the Rayleigh's theory [1]. In a wavy flow region, the instability of the jet increases with the turbulence in it. If the velocity of the jet further increases, interfacial forces, such as shear forces and pressure perturbations around the jet, become more important factors in the turbulence motion of the surface. Also the turbulence in the internal flow increases with an increase in the velocity. Increased velocity will finally result in a cavitation fixed at the entrance of the nozzle. This generates strong turbulence in the internal flow of the jet. This strong turbulence is amplified by the interfacial forces mentioned above and the jet disintegrates quickly as in the spray region [2,3].

In the spray flow region, since the intensity of the cavitation is strongly dependent on the nozzle structure, the break-up length shows different behaviors with different nozzle geometries. This link has already been suggested in previous researches [4-10]. However there has been little attention paid to the internal flow behavior after cavitation. Strong cavitation that stretched from the entrance to the exit of the nozzle could exist in a set condition. The constricted jet, which started from the entrance and continued to the exit, could sometimes be observed with a further increase of the velocity [11]. In such a condition, no strong turbulence was generated and a high speed smooth jet was obtained. In spite of the strong interfacial force caused by the high speed jet, the break-up length was elongated, since there was no surface disturbance that could be amplified. In this paper, the main concentration of the study was on the phenomenological analysis of the break-up mechanism of this smooth jet.

BREAK-UP LENGTH OF A LIQUID JET

Constricted and Non-constricted Jets

The velocity of a jet from the nozzle is usually lower than the theoretical velocity derived by the Bernoulli's equation. This is due to pressure drops caused by the wall friction, and by the turbulent wake or cavitation at the entrance, which are not negligible. The turbulence caused by these pressure drops results in the surface disturbance and this leads to the disintegration of the jet. The length-to-diameter L/D ratio of the nozzle and the Reynolds number Re of the flow, control the intensity of the wall friction. The wake and cavitation are affected by the geometry of the nozzle entrance.

Based on this consideration, two kinds of injection nozzles, shown in Fig. 1, were selected to study the general forms of the break-up length. Water was continuously injected through these nozzles. The injection velocity of the jet was calculated as the sectional average velocity in the nozzle. The Reynolds number Re of the jet was calculated with kinematic viscosity of water, nozzle diameter and the above velocity. An electrical circuit was used to determine the break-up length [8].

The break-up lengths of the jets injected through the nozzles-A and -B are shown in Fig. 2 as functions of the injection velocity. With the nozzle-A, the spray jet was observed in the higher velocity region than 10 m/s, and the break-up length decreased with an increase of the velocity from this value. However at a certain value of this velocity, the break-up length discontinuously elongated and a smooth jet was observed. There was no spray jet formed after this transition. When the injection velocity was reduced after the transition, the break-up length decreased but was still longer than the break-up length existing before the transition. The break-up length had the hysteresis in both the wavy and spray regions.

The break-up length of the jet produced by nozzle-B changed smoothly with an increase in the velocity. The length was shorter than that produced by nozzle-A after the transition, in spite of the jet still resembling the pre-transition form. However it was much longer than the jet before the transition.

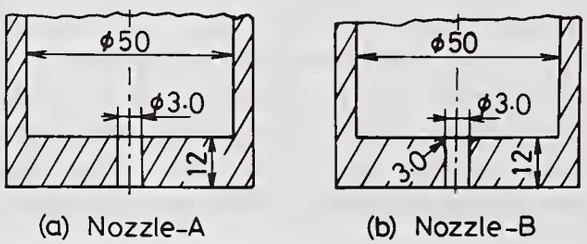

Fig. 1 Nozzle specifications

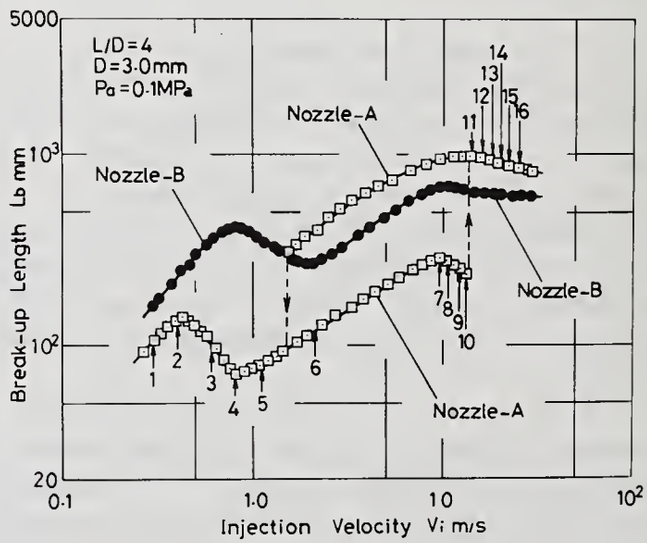

Fig. 2 Break-up lengths of constrict and non-constricted jets

The photographs of the jets formed by nozzle-A are displayed in Fig. 3. The numbers that indicate the jets correspond to the numbers in Fig. 2, numbers 9 and 10 being the spray jets. The photograph indicated by 11 was taken just after the completion of transition. The surface of the jet was very smooth and initiation of surface disturbance, that can be seen in the photograph, was related to downstream region of the jet. The break-up mechanism that was observed in the downstream regions of the jets, indicated by the numbers 11 to 16, was almost same as the mechanism observed in the jets 7 to 9. It is concluded that there was no surface disturbance that could be amplified by the interfacial force produced around the high speed jet. The break-up length after transition was elongated by the related development of the surface disturbance.

The internal flow in nozzle-A observed by the transparent nozzle is displayed in Fig. 4. When the velocity increased from 10 m/s, a fixed cavitation appeared at the entrance of the nozzle. The turbulence caused by the destruction of the cavity produced the surface disturbance of the jet in co-operation with the wall friction in the nozzle. This disturbance was amplified by the interfacial force and resulted in the short break-up length of the jet. The cavity was stretched to the exit with an increase of the velocity in the spray jet region. However, when the velocity reached the transition value, the reattachment point of the separated flow caused by the cavitation moved away from the exit. The flow that was separated from the wall was generated at the entrance. After this transition, no wall friction affected the flow and a very smooth jet appeared as mentioned before.

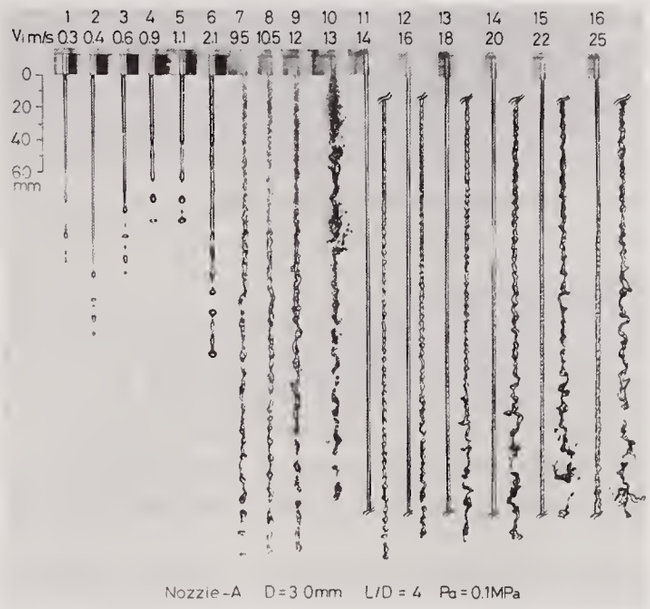

Fig. 3 Photographs of the jets injected through the nozzle-A

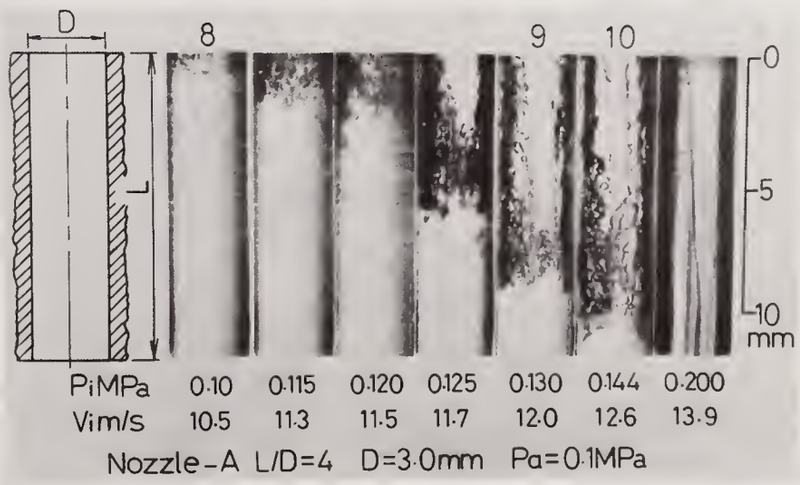

Fig. 4 Internal flows in the nozzle-A

The photographs displayed in Fig. 5 are the jets injected by the nozzle-B. It had a quadrant shape at its entrance. No cavitation and no constricted flow were produced but the wall friction was always acting on the jet. As a result, the surface of the jet, close to the exit, had slight disturbance that could be amplified by the interfacial force and it caused a longer break-up length than the constricted jet injected by the nozzle-A.

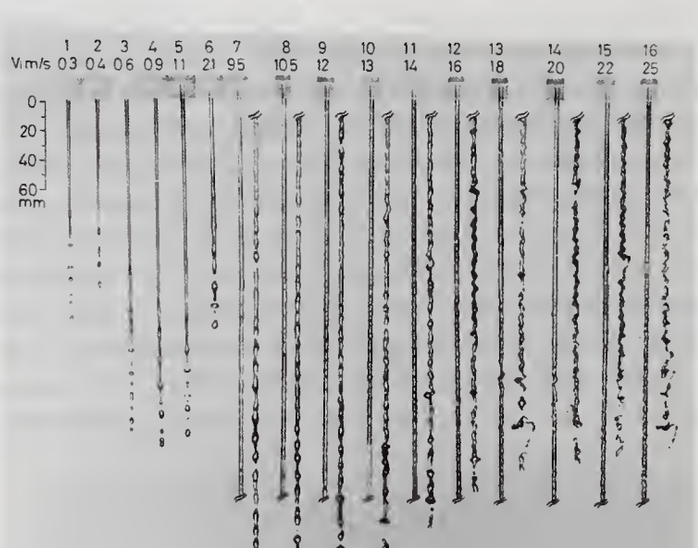

Fig. 5 Photographs of the jets injected through the nozzle-B

General Forms of the Break-up Length

General forms of the break-up length are schematically shown in Fig. 6 as a function of the injection velocity. By applying Tanasawa's classification [3] of the disintegrating states for a jet, the dripping region was determined and is indicated by symbol A, the smooth jet B, the transition jet C, the wavy jet D and spray jets which are shown by E, G and F. The numbers 1 and 2 are the points where the break-up length elongated discontinuously as the injection velocity increased. However 3 and 4 are the points where the break-up length discontinuously shortened with a velocity decrease. The hysteresis of the break-up length is shown by the broken lines.

When the surrounding pressure or density was too low to generate the possible interfacial force around the jet, no spray jet was formed and break-up length increased with the velocity as shown by symbols SH and H. When the pressure was not below this limiting value, the break-up process, indicated by SF, appeared on the constricted smooth jet with high velocity.

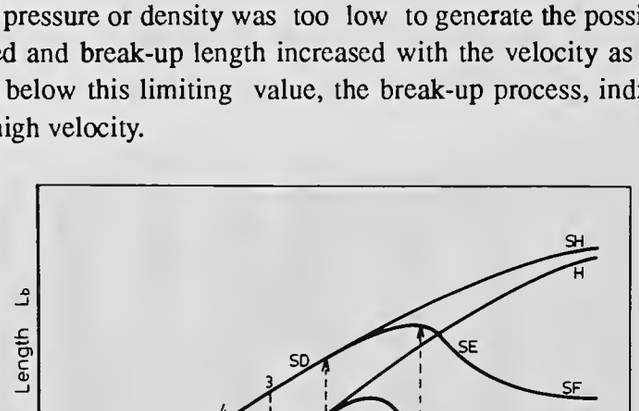

Fig. 6 General behavior of the break-up length

The photographs of the high speed jet indicated by SH, H, SF and F are shown in Fig. 7. The jet shown by SH exited from the nozzle as constricted flow and no disturbance was imparted to the jet. However, the jet shown by H was non-constricted flow and had turbulence as a result of the wall friction. The difference in surface perturbation between SH and H was caused by turbulence, due to the geometrical disparity of the nozzles. When the ambient pressure was so high that the interfacial force between the jet and surroundings had sufficient intensity to modify the break-up phenomena, the break-up behavior of SH and H changed to SF and F, respectively. The spray jet indicated by F was usually observed to resemble a diesel spray injected into pressurized surroundings.

INTERNAL FLOW AND CAVITATION

Super-cavitation

The schematic appearance of the jets are illustrated in Fig. 8. The jet indicated by (a) exits from an orifice and has a very smooth surface, since no wall friction is acting on it. The jet (b) is produced by a nozzle that has a smooth entrance, or is long enough to damp out turbulence generated at the entrance. The surface of the issuing jet has a slight disturbance that is generated by the wall friction. The jets indicated by (c), (d) and (e) are formed by the same nozzle but different injection velocities. The jet (c) is observed to be in a relatively low velocity condition. The entrance of sharp edge type forms a wake in the internal flow of the nozzle. It generates the flow pattern that results in a turbulent jet, when acting in co-operation with the wall friction. When the velocity increases beyond a certain value, a cavity fixed at the entrance appears as shown in (d). A disruption of the cavity generates the intense turbulence which can perturb the jet surface close to the exit. This situation is usually observed in a spray jet and it is the reason why the break-up length of the spray jet decreases with an increase of the velocity. However if the cavitation is too strong to prevent a separated flow expanding and reattaching to the wall, a constricted jet, that is separated from the wall, issues from the nozzle. This is similar to super-cavitation flow around a wing [12] or in a long orifice [13]. The terminology of this situation, super-cavitation inside a nozzle, is proposed in this paper. Wall friction and turbulence generated by cavitation can not work on the constricted jet. The break-up length in this situation is elongated since there is no surface disturbance that can be amplified by the strong interfacial force around the high speed jet.

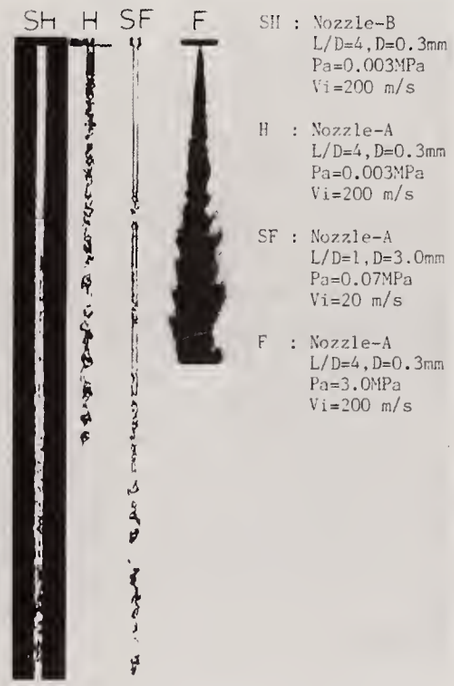

Fig. 7 Effects of surrounding pressure on the disintegration of high speed jet

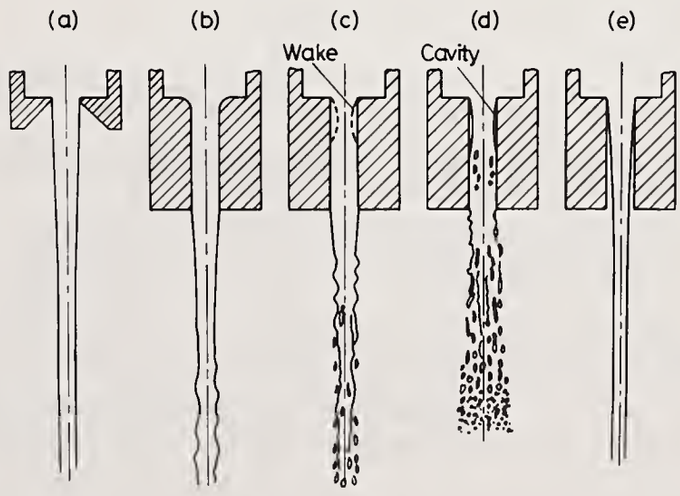

Fig. 8 Schematic appearances of the jets

Cavitation Number

A cavitation number is usually used as a criterion of an onset of a cavitation [14]. Figure 9 shows the schematics of the flow and the pressure distribution in the nozzle.

The static pressure P_2 is defined using the Blasius's equation of the wall friction as

$$P_2 = P_a + \frac{1}{2} f \frac{(L - Lc)}{D} V_i^2 \tag{1}$$

$$f = \frac{0.316}{Re^{0.25}} \quad \text{(Blasius's equation)} \tag{2}$$

The velocity V_1 is derived by

$$V_1 = \left(\frac{D}{D_c}\right)^2 V_i \tag{3}$$

and the static pressure P_1 is expressed by

$$P_1 = P_2 + \frac{1}{2} \rho V_i^2 \left\{ 1 - \left(\frac{D}{D_c}\right)^4 \right\} \tag{4}$$

Then, the cavitation number k_c is defined as

$$K_c = \frac{P_1 - P_V}{\frac{1}{2} \rho v_i^2} = \left(\frac{D_c}{D}\right)^4 \left\{ \frac{P_a - P_v}{\frac{1}{2} \rho V_i^2} + \frac{f(L - L_c)}{D} + 1 \right\} - 1 \tag{5}$$

where, P_v is the vapor pressure of the liquid.

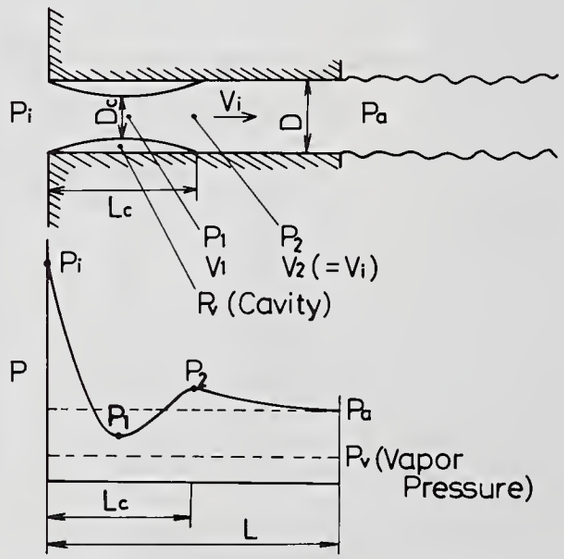

Fig. 9 Internal flow and pressure distribution in the nozzle

Table 1 is a list of the calculated cavitation numbers using the equation (5) and reasonable assumptions for D_c/D, L_c and P_v. The intensity of the cavitation increases with a decrease in the cavitation number. The value smaller than 1.0 usually indicates the existence of the fixed cavitation. The negative value means too strong cavitation exists. The appearance of the jet could be explained as follows. The cavitation number in the flow with no wake had a relatively large value. The transition from cavitation to super-cavitation was indicated by a medium value of the cavitation number. The negative values except Fig. 7-F correspond to the super-cavitation situations. The spray jet indicated by Fig. 7-F also had a low enough cavitation number to form a constricted jet. However, it was a special situation where the interfacial force caused by surroundings of high density was strong enough to dominate over the disintegration process of the jet. Even if the constricted flow started at the entrance of the nozzle, the surface disturbance developed before it reached the exit of the nozzle and a turbulent jet resulted. Further study on the cavitation number calculated by correct values of D_c/D and other variables is needed to explain the transition from cavitation to super-cavitation.

Table 1 Cavitation numbers calculated by the equation (5)

Nozzle	D (mm)	Pa (MPa)	Condition	Kc*	Comments
A	3.0	0.1	Fig.5-No.10	0.632	Transition from cavitation to super-cavitation
B	3.0	0.1	Fig.7-No.10	11.6	No wake
B	0.3	0.003	Fig.3-SH	3.28×10^{-5}	No wake
A	0.3	0.003	Fig.3-H	-0.870	Super-cavitation with turbulence
A	3.0	0.07	Fig.3-SF	-0.826	Super-cavitatation
A	0.3	3.0	Fig.3-F	-0.851	Spray jet, High turbulence

* $\frac{D_c}{D}=0.6$, $f\frac{L-L_c}{D}=0$ and $P_v=2.35$ KPa were assumed

CONCLUSIONS

From the phenomenological analysis of the liquid jets, the relationship between the break-up length and the internal flow in the nozzle was explained as follows.

(1) The jet coinciding with the fixed cavitation at the entrance of the nozzle appeared as a spray jet. The break-up length in this situation decreased with an increase in the velocity since turbulence generated by the cavity increased with the velocity increase.

(2) However, if the cavitation was too strong to be disrupted in the nozzle, a constricted jet issued from the nozzle. The appearance of this flow field was similar to the super-cavitation around a wing. The break-up length was elongated since there was no surface disturbance that could be developed.

(3) The cavitation number in the internal flow of the nozzle was introduced to explain the intensity of the cavitation.

REFERENCES

1) Rayleigh, Theory of Sound, 2nd edn., Dover reprint, New York, (1945).
2) Levich, V. G., Phyicochemical Hydrodynamics, Prenetics-Hall, Inc., Englewood Cliffs, N. J. (1962).
3) Tanasawa, Y., High speed diesel engines I, "Fuel systems and spray combustion", Sankaido (in Japanese), (1956), 87.
4) Rupe, S. H., "On the dynamic characteristics of fuel liquid jet and a partial correlation with orifice geometry", JPL Tech. Rept., 32 (1962), 207.
5) Lee, D. W., " The effect of nozzle design and operating conditions on the atomization and distribution of fuel sprays", NACA Tech. Rept., No.425 (1932), 565.
6) Ruiz, F. and Chigier, N. " Mechanism of high speed atomization", Proc. 3rd ICLASS, Vol. 1 (1985), VIB/3/1.
7) Reitz, R. D. and Bracco, F. V. "Mechanism of atomization of a liquid jet", Phys Fluids Vol.25 No.10 (1980), 1730.
8) Hiroyasu, H., Shimizu, M. and Arai, M.," The break-up of high speed jet in a high pressure gaseous atmosphere" Proc. 2nd ICLASS (1982), 69.
9) Arai, M., Tabata, M.,Hiroyasu, H. and Shimizu, M., " Disintegrating process and spray characterization of fuel jet injected by a diesel nozzle", SAE Paper No. 840275 (1984).
10) Arai, M. Shimizu, M. and Hiroyasu, H. " Break-up length and spray angle of a high speed jet" Proc. 3rd ICLASS, Vol.1 (1985), IB/4/1.
11) Arai, M., Shimizu, M. and Hiroyasu, H. "Break-up length and spray formation mechanisms of a high speed liquid jet", Proc. 4th ICLASS, (1988), 177.
12) Yamazaki, T., "Cavitation Engineering", Nikkan-Kogyo Press. (1978).
13) Yokota, M., Ito, Y. and Shinohe, T., "High Speed Photographic Observations of Cavitation Arising in The High-Speed Oil-Flow Through a Very Small Long Orifice", 9th Int. Symp. on Jet Cutting Tech., Sendai Japan (1988), 13.
14) Daugherty, R. L. and Franzini, J. B., "Fluid Mechanics", McGraw-Hill,Inc., New York, (1965).

AN EXPERIMENTAL STUDY ON INITIAL BEHAVIOR OF DIESEL FUEL SPRAY CHARACTERISTICS

J.-C. Huh*, G.-Y. Lee† and O.-Y. Yang‡

*Dept. of Marine Engineering, Cheju National University, Cheju, Korea
†Dept. of Mechanical Engineering, Inha Technical Junior College, Inchon, Korea
‡Dept. of Mechanical Engineering, Inha University, Inchon, Korea

ABSTRACT

An experimental study has been conducted to investigate the characteristics of diesel fuel spray injected from a single hole nozzle into a cylindrical steel chamber with transparent windows. With modified fuel injection system, the spray tip penetration, the spray angle and the initial behaviour of diesel fuel spray have been observed by shadowgraph. The effects of preheated fuel at temperatures of room temperature ~ 150 ℃ and ambient gas pressures of 0.1, 1.5 and 3 MPa on the characteristics of diesel fuel spray were also investigated.

The spray angles in the case of preheated fuel supply were larger than those of non-preheated fuel conditions. Particularly, spray angle in the initial stage of fuel injection was sharply increased due to the result of change of fuel properties, but the spray tip penetration was decreased.

With the increase of ambient gas pressure, the spray tip penetration was decreased and the spray angle was increased. The transition point in the spray tip penetration was observed at the higher ambient gas pressures considered and it strongly depends upon the fuel temperature.

The initial stage of injection of diesel fuel spray showed the form of non-disintegrated intact core, but the formation of ligament increasingly was developed with the increase of injection time.

INTRODUCTION

Combustion of liquid fuels in diesel engines is highly dependent on effective atomization to increase the specific surface area of the fuel and thereby achieve high rates of mixing and evaporating. It is commonly known that the disintegrating process of fuel spray mainly depends on the properties of injected oil, fuel temperature, injection pressure, ambient gas pressure and injection nozzle geometry(1-4). The combustion process is inherently affected by the spatial and temporal distributions of atomized liquid fuel and/or atomized fuel within the combustion chamber,which, in turn, are strongly dependent on the details of the initial atomization process itself.

Reitz (5) reported that the jet appears initially to emerge shaped like a blunt cylindrical rod, with an exit diameter approximately equal to the nozzle exit hole diameter. Newman, et al.(6,7) showed the existence of a continuous portion of liquid in the vicinity of the nozzle in a high speed jet. In addition, Pai and Nijaguna(8) supported the evidence that the liquid, initially, just after leaving the nozzle is in

the form of a continuous body. However, initial behaviour of fuel spray at a location just behind the nozzle exit has not been well understood.

The purpose of this experimental work is to obtain the experimental data on the spray tip penetration and spray angle of the diesel fuel spray. The influence of preheated fuel and ambient gas pressure on the behaviour of diesel spray is studied. Time - variation process of diesel fuel spray within the injection time of 1 msec from the nozzle exit has been principally investigated by the shadowgraph by means of a incident light.

EXPERIMENTAL APPARATUS AND PROCEDURE.

The experimental apparatus consists of a fuel injection system, electric heaters, an electronic cntrol unit, a pressure chamber, a light source and a camera as shown in Fig.1. One of car plunger pumps mounted on the injection pump test device was used as a pressurizer. The diesel fuel from the plunger (4) flows into an accumulator (6) which is the inside volume of 5.1 liter and is then pressurized to the required high pressure. The pressurized fuel is heated up by the first electric heater (7) supplied to a supplementary accumulator (26). The second heater inserted in the supplementary accumulator heats up the preheated fuel again and the accumulator reduces the pressure pulsations during the whole injection period. The nozzle is controlled by electronic control unit (19,20). The fuel injection is synchronized with the input signal in the solenoid. The setting time can be varied from 1μsec to 1sec.

Experiments were made for injecting a single charge of diesel fuel into the chamber through a nozzle, and for photographing the developing spray by the stroboscope or nanolite through windows in the cylindrical chamber wall. The pressure chamber was designed for gas pressure up to 5MPa and the highly pressurized N_2 gas was supplied to the chamber. The inner diameter and the length of chamber were 196mm and 500mm respectively. The chamber was made of steel with transparent rectangular windows of 230 x 130 mm on to opposite faces.

The shadowgraphic method was introduced in this work. Photo-interrupter (11) was installed at the tip of the spindle connected to the needle. The spindle interrupts the inspection light beam of the photo-interrupter. At the moment of operating solenoid, the injection start signal from photo-interrupter trigers the digitalized regarding circuit (21) during the desired time from 1 μsec to 10 msec. A stroboscope or a nanolite (22) is, then, activated by an output of the retarder and emits the flash. The flash duration of the stroboscope and the nanolite is about 3 μsec and 17 nsec, respectively. The camera was at the state of B-shutter and photographed the spray at the lightening moment.

The experimetal conditions are shown in Table 1.

Table 1. Experimental conditions

Titles	Descriptions
Injection Pressure (MPa)	7, 14, 21
Ambient gas pressure (MPa)	0.1 1.5 3.0 (N_2 gas)
Ambient gas temperature	Room temperature
Preheated fuel temp. (∘C)	Room temp., 50,100,150
Liquid	Diesel fuel (specific weight: 0.84)
Injection Nozzle	Aspect ratio(L/D):2 D=0.65mm,Single hole
Lenses	105mm microlens (f=4) Tele-micro lens(magnifying ratio:4.5)
Film	KODAK TRI- X (ASA - 400)

RESULTS AND CONSIDERATION

Spray tip penetration and spray angle

Many photographs of sprays by shadowgraph are taken to measure the spray tip penetrations and spray angles. Photo.1 shows representative photographs of the developing process of spray for the preheated fuel.The spray tip penetration and the spray angle were measured on the basis of those figures.

Fig.2 shows the variation of spray tip penetration and spray angle for various fuel temperatures and ambient pressures at the injection pressure of 7 MPa as a function of time.

It can be seen from Fig.2(a) that the logarithmic spray tip penetration for all four fuel temperatures linearly increases up to before transition time with the slope of 1 and then increases with that of 0.4-0.6. It is considered that the liquid column is disintegrated before the transition point and the spray is then fully developed after it. The lower ambient pressure and the higher fuel temperature allow the shorter length and the more delayed occurrence of transition point for spray tip penetration with respect to time. This reveals that the fuel temperature is one of the important parameters governing the disintegrating process of spray.

From Fig.2(b), the effect of preheated fuel on the spray angle is clearly found at the initial period of injection with Pa =0.1 and 3 MPa respectively. From 1.5 and 2.0 msec after injection repectively for those ambient pressures, the nearly constant spray angle with the variation of fuel temperature can be found. On the other hand, the spray angle is increased with the increase of fuel temperature through the whole duration in the case of ambient temperature of 1.5 MPa. It is particularly noticed that the spray angle after transition point at 1.5 MPa is coincident with that at 3 MPa for the preheated temperature of 150 ℃. This effect is attributed to the variation of surface tension and viscosity of fuel as the fuel temperature increases.

The effect of ambient pressure and fuel temperature on the spray tip penetration and spray angle at the injection pressure of 14 MPa is shown in Fig. 3.

It is found from Fig.3(a) that for all three ambient pressures the logarithmic expression of spray tip penetration and time shows the linear relationship with two distinct slopes. This result shows good agreement with that of Arai,et al.(9). For the given conditions of fuel temperature the variation of spray tip penetration shows a similar trend to that obtained for the various ambient pressures. The spray tip penetration decreases with the increase of fuel temperature at Pa = 0.1 and 1.5 MPa respectively. It is evident from the figure that the fuel temperature of 150℃ remarkably reduces the spray tip penetration for the ambient pressures considered, while the other fuel temperatures at the given ambient pressures has no effect on the spray tip penetration. As same as the observations from Fig.2, the higher fuel temperature and the lower ambient pressure show the delayed transition.

The influence of fuel temperature on the spray angle at the ambiemt pressure of 0.1 MPa is not significant. The spray angle with fuel temperature of 150℃ at Pa= 1.5 MPa is considerably increased comparing with the other fuel temperature considered. The spray angle in this case is higher than that obtained at Pa= 3 Mpa. The effect of fuel temperature on the spray angle is clearly found at preheated temperature of 100 and 150 ℃ repectively from the Fig.2(b).

The effect of the fuel temperature and the ambient pressure on the spray tip penetration and spray angle at Pi = 21 MPa with respect to time is shown in Fig.4. The spray tip penetration and the spray angle at the ambient pressure of 0.1MPa is constant for all preheated temperature of fuel considered. The transition point for fuel temperature at the ambient pressure of 3 MPa can be found at 1.2 msec for room temperature, at 1.8 msec for 50℃, and at 2.5 msec for 100℃ and 150℃ respectively. This appears to be due to the ratardation of transition time by the higher fuel temperature, leading to the increase of penetration.

The spray angle in this ambient pressure is, however, nearly constant regardless of

preheated temperature of fuel. It is evident from Fig.4(b) that the spray angle is increased with increasing the ambient pressure.

Initial behaviour of spray

Photo.2 shows the enlarged photographs of spray at two different injection pressures. In the case of injection pressure of 7 MPa shown in Photo.2(a), a continuous sinusoidal wave is formed on the surface of the liquid column at injection time of 0.05 msec. After the injection time elapsed over 0.15 msec, the unstable growth of suface waves with short wavelength on the liquid column which is caused by the relative motion of the jet and the ambient air grows larger,and this leads to the formation of ligaments. With the continuous interaction with the ambient air, the ligaments yield droplets at the injection time of 0.3 msec. The process of fully developing spray is clear from the photographs of injection time of 1.0 and 2.0 msec respectively.

In the case of injection pressure of 21 MPa shown in Photo. 2(b), liquid column of 1 mm can be observed at a location just behind the nozzle exit at the injection time of 0.01 msec and the tip of the liquid column has the shape of rivet, which is considered to be caused by the interaction between the surface tension of diesel fuel and the aerodynamic resistence of ambient air. At injection time of 0.05 msec, the formation of ligament reveals in the circumferential surface of the unbroken portion. As injection time increases to 0.15 msec, the surface of the unbroken portion has been largely deformed and the vigorous formation of ligament is evidently detected. At injection time of 0.4 msec, ligaments are observed to coexist with many droplets disintegrated from the ligaments. Fully developed spray is shown after injection time of 1 msec and the liquid column is observed as the form of cone.

The enlarged photographs of spray at two different fuel temperatures are shown in Photo.3. Comparing with the effect of fuel temperature on the spray characteristics, it is found that the spray is considerably expanded in the case of fuel temperature of 150 ℃. This appears to be due to the decrease of surface tension and viscosity of fuel resulting from the increase of fuel temperature.

CONCLUSIONS

Important conclusions to emerge from this experimental study on the initial behaviour of diesel fuel spray characteristics are:

1. The spray angles in the case of preheated fuel supply within given conditions were larger than those of non-preheated conditions. In addition, the spray angle in the initial period of fuel injection was rapidly increased owing to the result of variation of fuel properties, but the spray tip penetration was decreased.With the higher ambient gas pressure,the transition point in the spray tip penetration strongly depends on the preheated fuel temperature.

2. The spray penetration was decreased and the spray angle was increased with incresing the ambient gas pressure considered.The transition point in the spray tip penetration was not found at the ambient pressure of 0.1 MPa regardless of fuel temperature.

3. The initial period of injection of diesel fuel spray reveals the shape of non-disintegrated intact core. However, the formation of ligament was increasingly developed with respect to injection time.

REFERENCES

1. Schmeitzer , P.H., " Mechanism of Disintegration of Liquid Jets", Journal of Appplied Physics, Vol.8, pp. 513-521 (1937)
2. Walsh,G.J.and Cheng,W.K.,"Effects of Highly-heated Fuel on Diesel Combustion ". SAE Paper , No. 850088,(1985)
3. Dent , J.C., " A Basis for the Comparison of Various Experimental Methods of Studying Spray Penetration.", SAE Paper No. 710571 (1970)

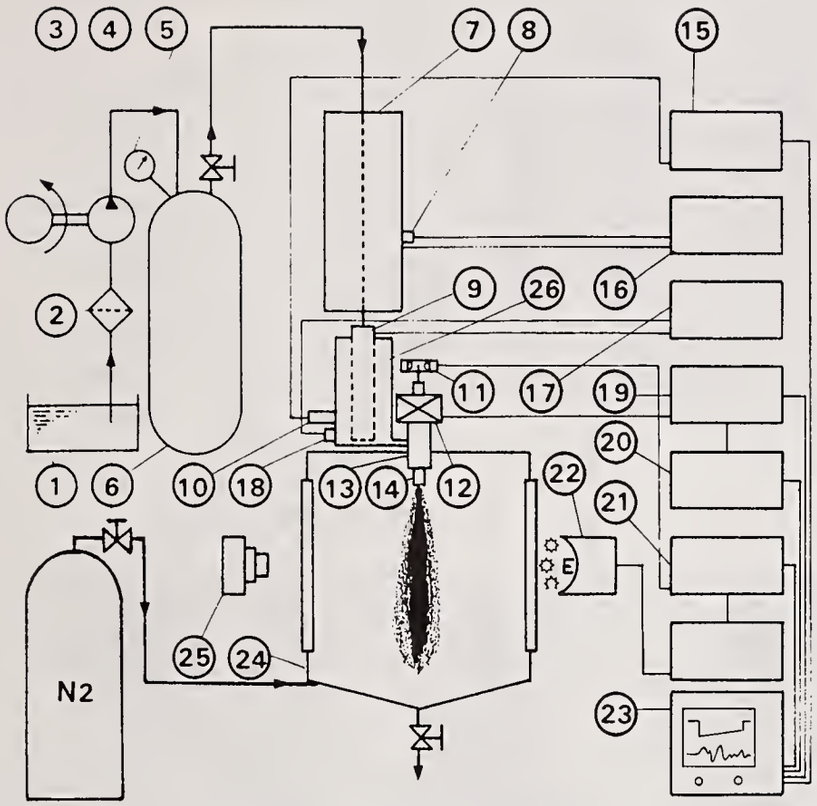

1. Fuel Tank
2. Fuel Filter
3. Motor
4. Fuel Injection Pump
5. Pressure Gauge
6. Accumulator
7,9. Electric Heater
8,18. Thermo-couple
10,15. Pressure Transducer
11. Photo-interrupter
12. Solenoid
13. Nozzle Holder
14. Nozzle
16,17. Temp.Controller
19,20. Nozzle Driving & Controller
21. Retarder
22. Stroboscope & Nanolite
23. Oscilloscope
24. Pressure Chamber
25. Camera
26. Supplementary Accumulator

Fig.1 Schematic diagram of experimental apparatus

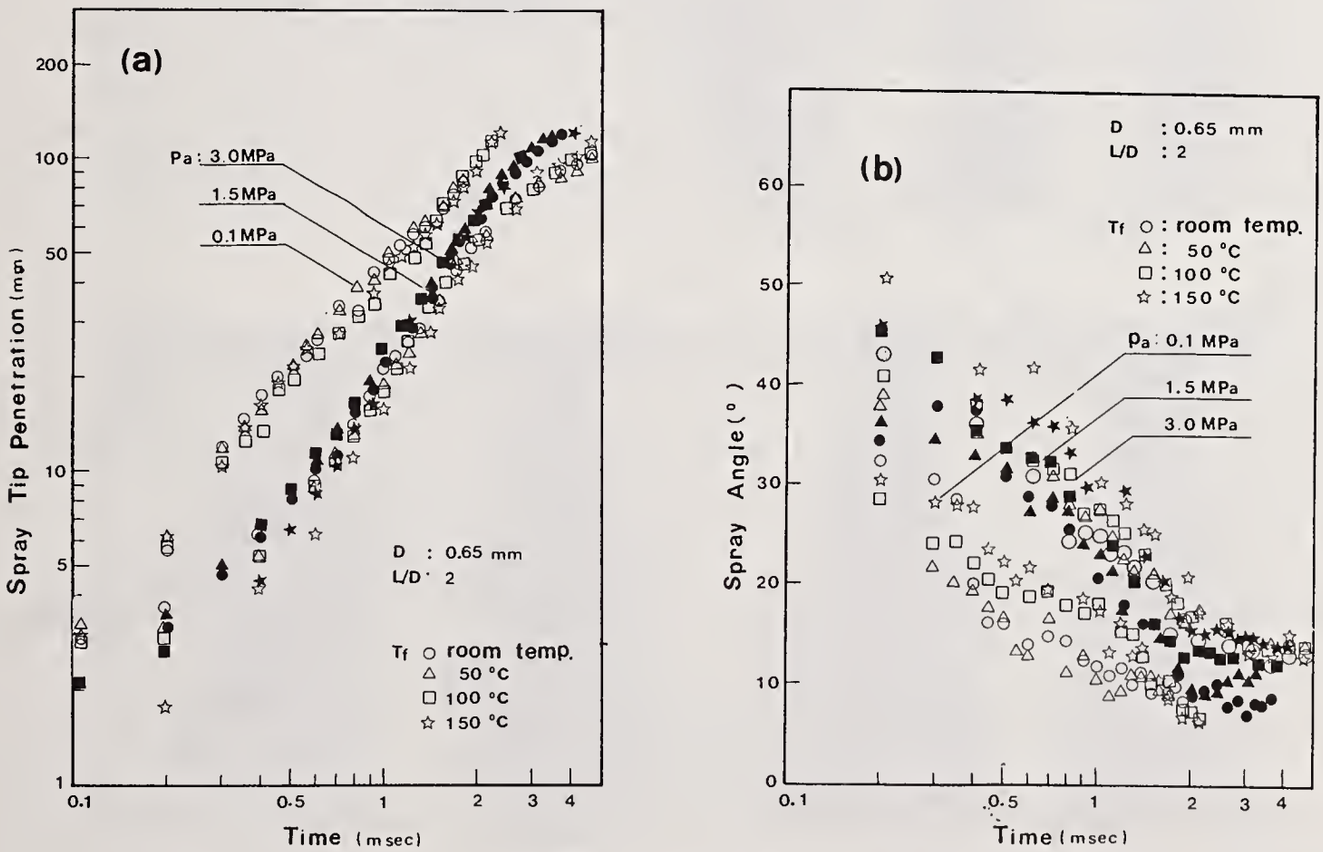

Fig.2 Influence of ambient pressure and fuel temperature on spray tip penetration(a) and spray angle(b) (Pi = 7 MPa)

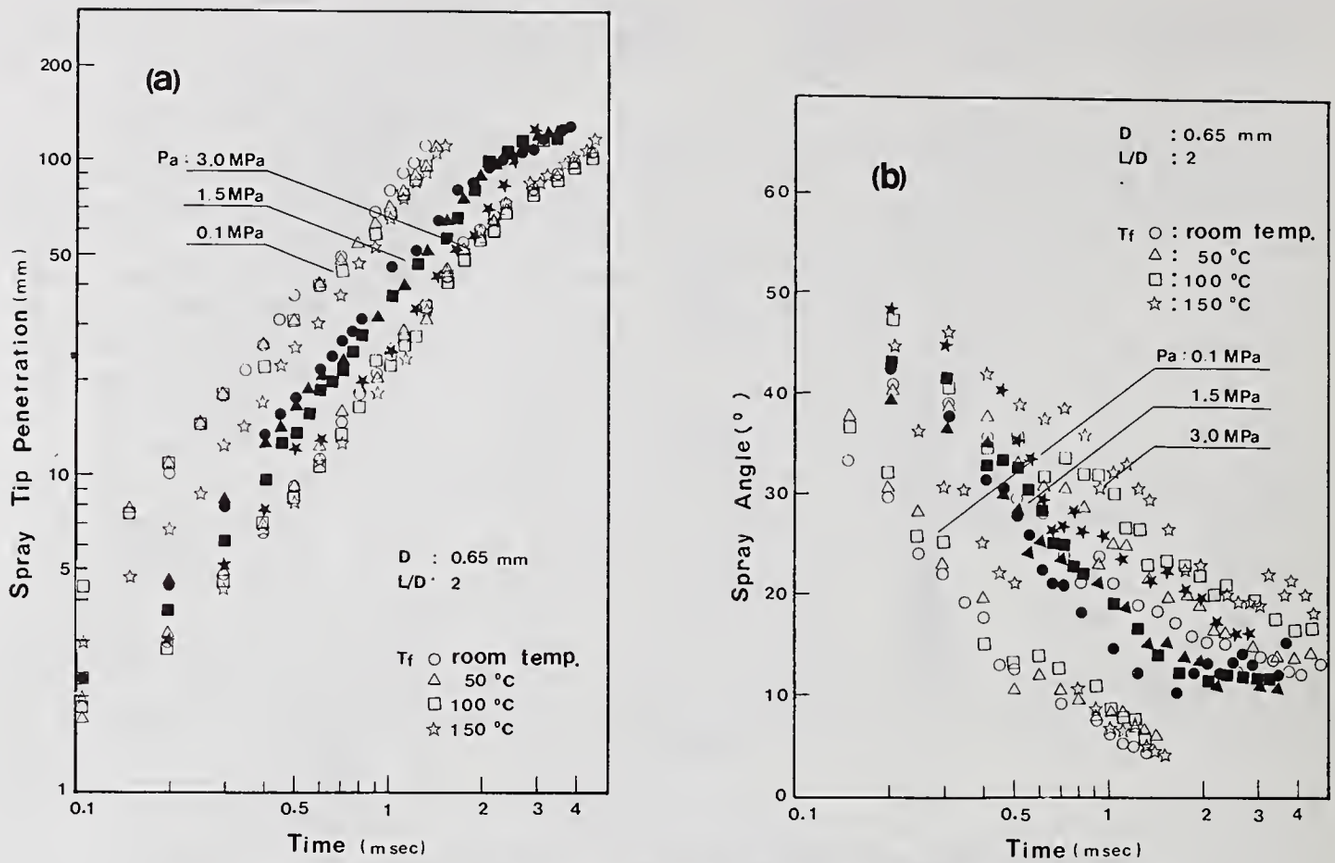

Fig.3 Influence of ambient pressure and fuel temperature on spray tip penetration(a) and spray angle(b) (Pi = 14 MPa)

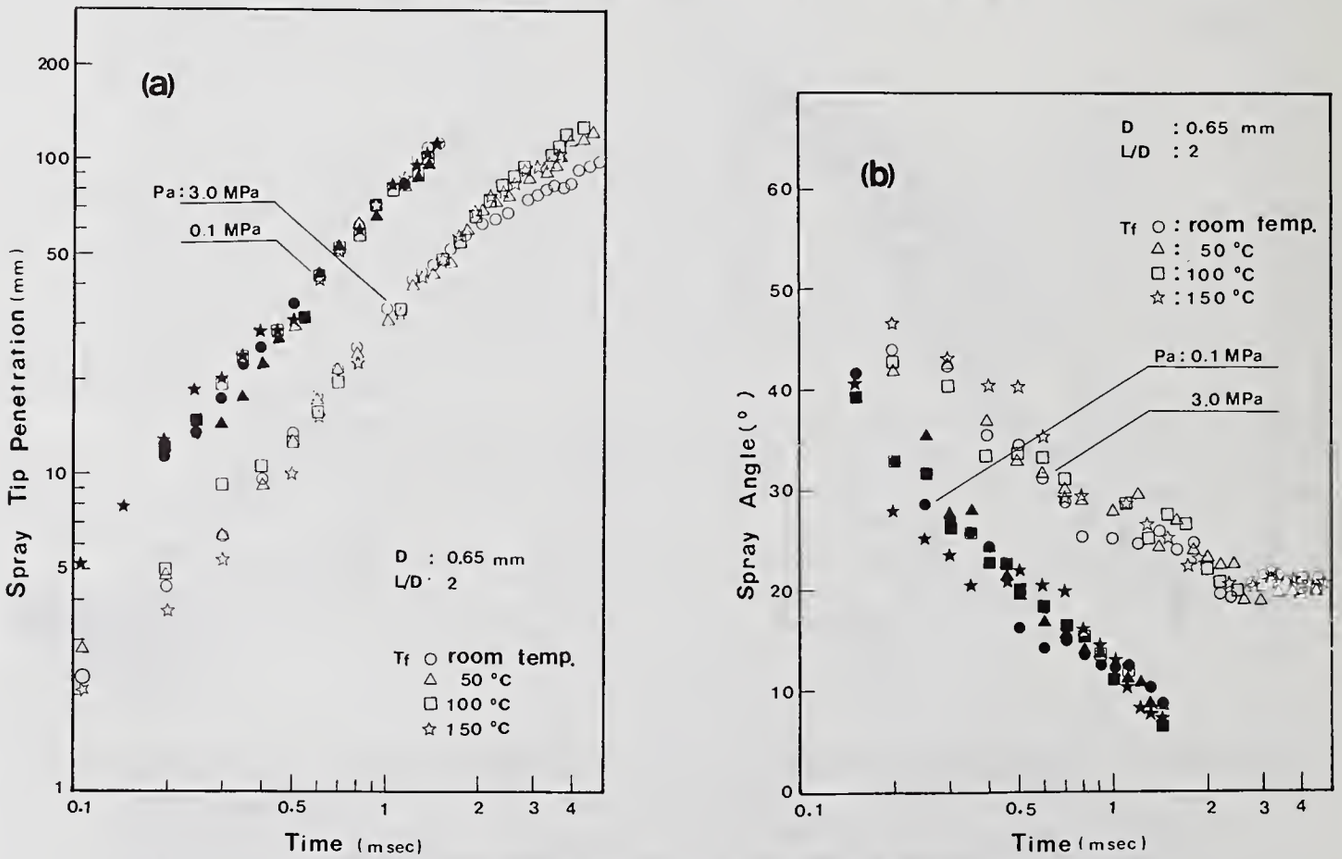

Fig.4 Influence of ambient pressure and fuel temperature on spray tip penetration(a) and spray angle(b) (Pi = 21 MPa)

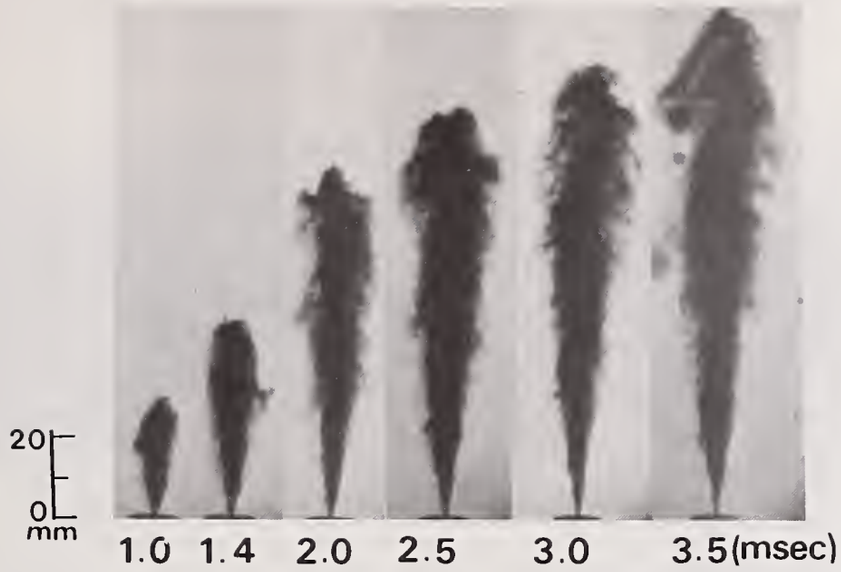

Photo.1 Photographs of spray (Pi = 21 MPa,Pa = 3 MPa,T_f = 150℃)

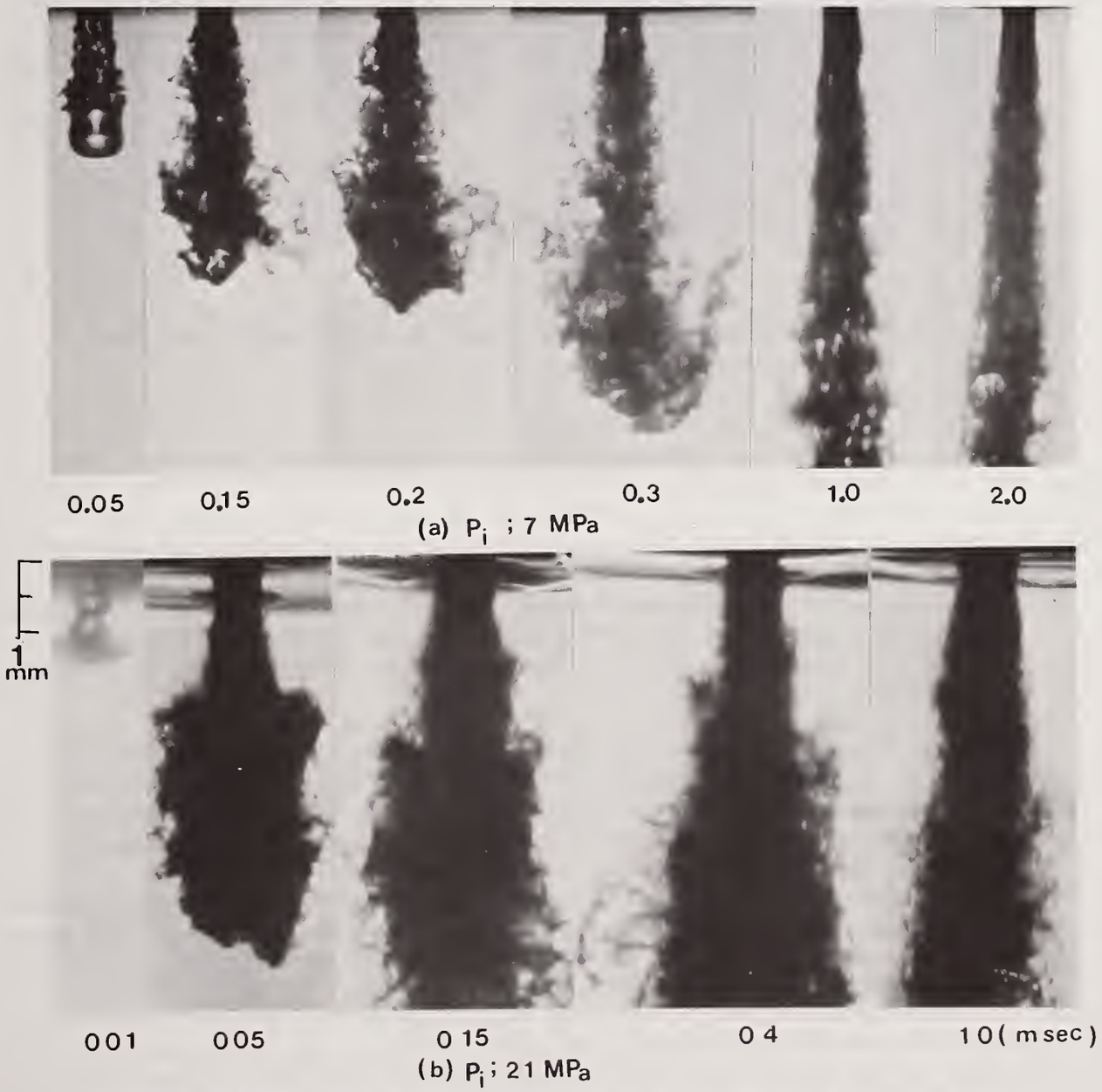

Photo.2 Enlarged photographs of spray (Pa = 0.1 MPa,T_f = room temp.)

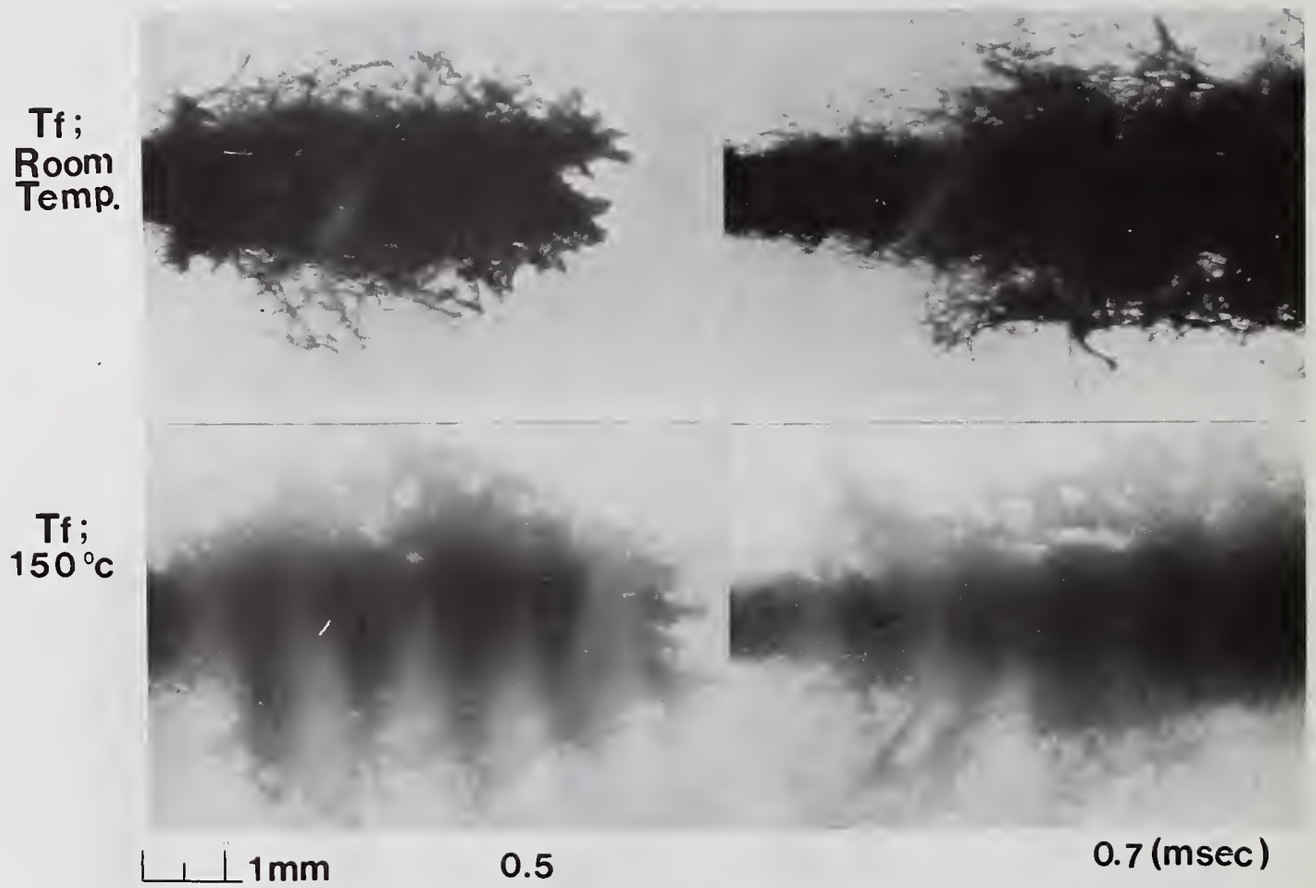

Photo.3 Enlarged photographs of spray (Pi = 14 MPa,Pa = 0.1 MPa)

4. Nagai,N. Sato,K. and Lee,Ch.W., " Atomization Characteristics of Superheated Liquid Jets", ICLASS - 85,pp. VB/3/1-VB/3/11 (1985)
5. Reitz, R.D., "Atomization and Other Breakup Regimes a Liquid Jet", Ph.D.Thesis, Princeton University, (1978)
6. Newman, J.A. and Brazustowski,T.A., " Behavior of Liquid Spray at High Pressures.", AIAA Journal Vol.8, No.1, pp. 164-165 (1970)
7. MacCarthy, M.J. and Molly, N.A., " Review of Stability of Liquid Jets and the Influence of Nozzle Design.", Chem. Eng. J. Vol. 7, pp. 1-20 (1974)
8. Pai, B.U. and Nijaguna, B.T., " The Characterization of Spray" Proc. 2nd ICLASS pp. 29-35 (1982)
9. Arai, M., Tabata, M., Hiroyasu, H. and Shimizu, M., " Disintegrating Process and Spray Characterization of Fuel Jet Injected by a Diesel Nozzle", SAE Paper No.840275 (1984)

MODELING DIESEL ENGINE SPRAY VAPORIZATION AND COMBUSTION

M.A. Gonzalez[*] and R.D. Reitz[†]

[*]Intevep S.A., Venezuela
[†]Engine Research Center, University of Wisconsin, Madison, WI, U.S.A.

ABSTRACT

Diesel engine in-cylinder processes have been studied using computational models with particular attention to spray development, vaporization, fuel/air mixture formation and combustion in conditions of high temperature and high pressure. A thermodynamic zero-dimensional cycle analysis program was used to determine initial conditions for multidimensional calculations. A modified version of the time-dependent, three-dimensional computational fluid dynamics code KIVA-II, with a detailed treatment for the spray calculations and a simplified model for ignition, was used to determine details of the closed cycle events. These calculations were used to obtain an understanding of the potential predictive capabilities of the models. It was found that there is a strong sensitivity of the spray calculations to numerical grid resolution. However, if proper grid resolution is used, the spray calculations were found to reproduce experimental data adequately for non-vaporizing sprays. However, for vaporizing sprays in high temperature engine environments the computations underpredicted measured gas phase (vapor) penetration results substantially. This underprediction of spray penetration reduces the accuracy of combustion predictions greatly. The atomization drop size was found to be a key parameter influencing spray penetration predictions and this indicates that improved atomization models are needed for engine conditions.

INTRODUCTION

Detailed models of engine combustion are of interest because they give insight about the combustion process. This information is helpful to aid engine development efforts. However, due to the complexity of the controlling phenomena, models are still being formulated and they require detailed validations before they can be used for performance predictions. This study describes initial attempts to assess the capabilities of current spray and combustion models for diesel engine combustion.

The computations were performed using a modified version of the KIVA-II computer code [1]. In the spray atomization submodel, drop parcels were injected with sizes equal to the nozzle exit diameter following Reitz [2] and the subsequent breakup of the parcels and the resulting drops is computed using a stability analysis for liquid jets. This model was chosen over earlier models because, in principle, it removes the need to specify an assumed initial dropsize distribution at the nozzle. The kinetics chemistry submodel used for combustion considers a single step Arrhenius mechanism for the stoichiometric reaction of the fuel. The pre-exponential factor, activation energy and component rate constants are those given by Bergeron and Hallett [3].

The engine computations were made for a Cummins NH engine for which extensive experimental data are available with measurements of injection characteristics, cylinder pressure, and flame temperatures (Yan and Borman [4]). Results using a cycle analysis simulation program are available for the same engine [5]. Data calculated using the steady state mode were used as input for the initial conditions in the multidimensional calculations as shown in Table 1. The injection velocity data was determined based on the injector link load vs. crank angle data assuming a constant nozzle hole discharge coefficient equal to 0.7. The turbulent kinetic energy was initialized at intake valve closing, using the equations of Grasso et al. [6].

Table 1 Engine Conditions

Cylinder Bore	139.7 mm	Fuel flow rate	0.144 g/cycle
Stroke	152.4 mm	Engine temperatures:	
Compression ratio	13.23	Cylinder wall	405 K
Displacement	2.33 liters	Cylinder head	486 K
Fuel unit injector		Piston surface	578 K
Number of spray nozzle orifices	8	Mass average gas temperature at IVC	359 K
Nozzle hole diameter	0.2 mm	Cylinder pressure at IVC	157.9 kPa
Spray axis, angle from head	18 degrees	Swirl number	1.0
Combustion chamber	Quiescent	Fuel	Tetradecane
Piston crown	Mexican hat	Injection starts (BTDC)	18 deg
Engine speed	1500 rev/m	Injection ends (ATDC)	11 deg
Overall equivalence ratio	0.6	Number of parcels injected	500
Air flow rate	3.53 g/cycle		

For the engine computations the 3-D computational mesh had 15 x 4 x 18 grid cells (in the radial, azimuthal and axial directions, respectively) at TDC. The radial spacing was 5 mm with 3 cells in the squish region and the geometry was based on direct measurements of the piston profile. Other computations were also made with a finer 31x8x15 grid to test the influence of grid spacing. The calculations were started at inlet valve closing (150 deg BTDC) and considered a 45 degree sector of the engine that included one of the eight spray plumes.

RESULTS

Engine Computations

Temperature contours and droplet locations (circles) projected in the plane containing the axis of the spray at TDC are shown superimposed in Fig. 1. Three main regions can be identified: the first, located closest to the nozzle, has the lowest temperature because it is where the spray vaporization occurs; the second is the combustion region with the highest temperatures in the domain (also located close to the injection nozzle) and; the third is the undisturbed gas phase region. Most of the injected drops reach the critical temperature of 695 K for the tetradecane fuel soon after leaving the nozzle and then disappear. Between 9 deg BTDC and TDC, the liquid penetration length remains approximately constant, and the liquid phase is confined to the region close to the nozzle due to the fast vaporization of the drops in the spray.

Two major problems are in evidence in these calculations. First, the flame location does not agree with the experimental results of Yan and Borman [4]. Using a radiation probe mounted in the cylinder head, they found that the flame reaches the piston bowl outer surface between 6 deg BTDC and 1 deg ATDC. However, the calculated flame never reaches the field of view of this probe. Second, as shown in Fig. 2, the calculated cylinder pressure (chain-dashed line) is substantially lower than the measured cylinder pressure (solid line). The amount of fuel burned in the combustion chamber was too low, and this explains the small energy release and subsequent small pressure rise. The amount of fuel evaporated was close to the amount of fuel injected, indicating a fast vaporization of the fuel once it was injected in the combustion chamber. The vaporized fuel creates a rich region near the nozzle which reaches the rich flammability limits. At first, combustion depletes the oxygen in this region. Thereafter, the combustion is controlled by turbulent diffusion of oxygen into the flame zone. The

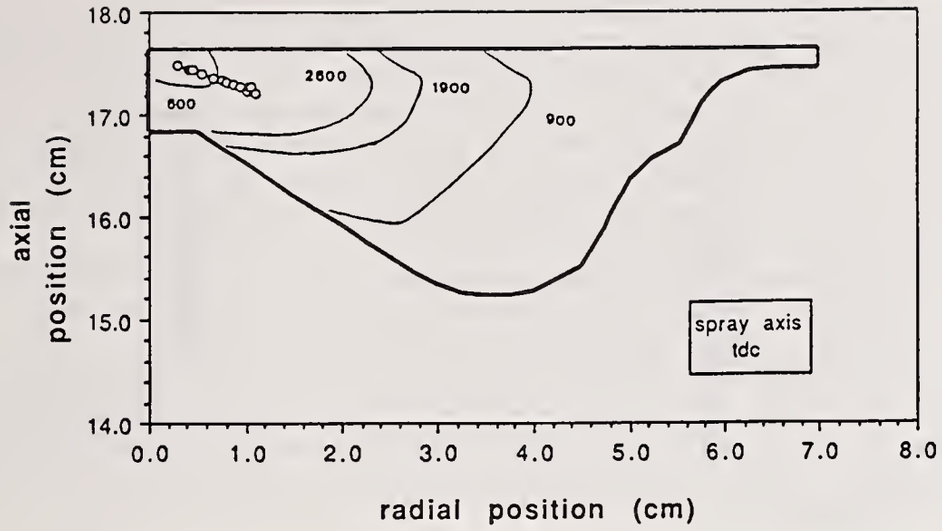

Figure 1. Cylinder gas temperature contours and drop locations (solid circles) in the plane mid-axis of the spray at TDC.

diffusion process is comparatively slow and there are regions close to the nozzle where the oxygen concentration is zero.

Similar computations that show incomplete or slow rates of combustion have been presented by Takenaka et al. [7] and McKinley and Primus [8]. These workers speculated that the problem was related to errors in the drop drag coefficient or to inadequate numerical resolution. However, the precise reasons for the shortcoming were not established definitively in those studies. Takenaka et al. artificially reduced the drop drag coefficient by a factor of five in their computations in order to increase the spray penetration sufficiently to match experiments. McKinley and Primus introduced an ad hoc correction to the drop-gas coupling terms in the conservation equations to include an effect of numerical grid size.

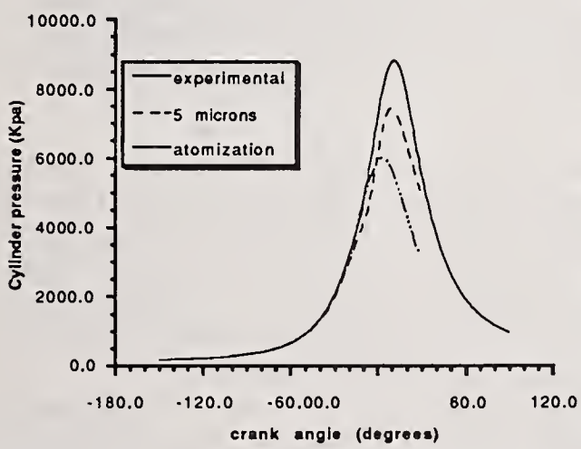

Figure 2. Calculated and experimental cylinder pressures using the atomization model [2] and using instead an initial drop radius of 5 mm (without drop breakup or coalescence)

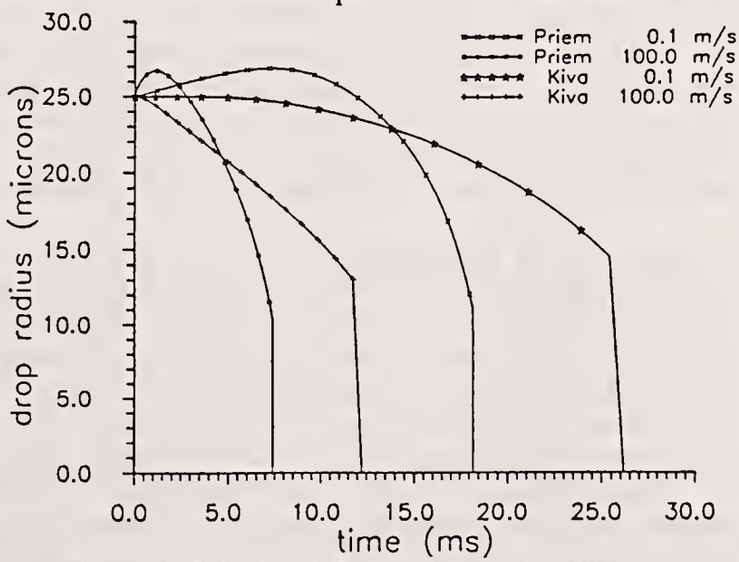

Figure 3. Calculated drop radius using KIVA and Priem vaporization models with and without convective effects. Hexadecane fuel. Initial diameter=50 μm, Pressure=4.0 MPa, Gas temperature=800 K.

Several numerical experiments were conducted in the present study to try to identify factors which might increase the spray penetration and improve the fuel distribution. Higher initial turbulent kinetic energy, higher swirl ratio, reduced aerodynamic droplet drag due to the influence of vaporization, reduced fuel vapor diffusivity, reduced fuel vapor pressure and higher enthalpy of vaporization, did not show sufficiently large effects to be able to explain the discrepancies. The influence of the chemistry model was also studied by introducing an artificial ignition delay, by varying the kinetic constants, by changing the temperature dependency on the reaction rates and by introducing the diffusion burning combustion model of Magnussen [9].

Although each of these modifications did influence the predicted rates of pressure rise and the peak cylinder pressures, they did not consistently change the combustion chamber pressure, which was still underpredicted, or the spray penetration, which still remained low.

Based on these tests it was concluded that three areas needed further study: first, to determine if drop vaporization rates predicted in KIVA were consistent with those from other more comprehensive models; second, to examine the influence of numerical error on the results and; third, to explore the influence of the drop breakup process and, in particular, the dropsize predicted from the atomization model. These aspects are discussed next.

Effect of Vaporization Model. A numerical experiment was conducted in which a single drop was injected into a high temperature and high pressure environment. A cylindrical computational domain of 4 cm diameter and 12 cm length was discretized using a grid of 20x1x60 cells with 1 mm radial x 2mm axial spacing near the nozzle. The diesel engine environment at the time of injection was simulated using air at 800 K and constant pressure of 4.0 MPa. The initial condition was selected to be quiescent to remove any uncertainties associated with fluid motions. The 50 mm diameter hexadecane drop initially was at 298 K and two cases were considered: 1) injection velocity of 0.1 m/s (for practical purposes zero velocity) and 2) injection at 100 m/s.

The evaporation routine in KIVA uses the Ranz-Marshall correlation [1], with a correction for convective effects. Computations with this model were compared with results obtained using the model of Priem et al. [10] which includes a variable density term (which is important during the heat-up period of the drop) and a correction to account for superheating of the diffusing vapor around the drop. The Priem model was also modified to include the effect of convection. Several combinations of dropsizes, injection velocities, gas temperatures and pressures were compared in the study and each case reached the same qualitative conclusions as those that are given in Fig. 3.

As can be seen in Fig. 3, although the evaporation routine in KIVA does not include the mentioned corrections, it predicts lower vaporization rates than the more comprehensive Priem model. Thus, one can conclude that the observed low spray penetration predictions in the engine computations cannot be explained by any obvious shortcoming of KIVA's vaporization model, since the more comprehensive model gives even faster vaporization under all conditions.

Effect of Grid Resolution. To assess the effect of numerical error, non-vaporizing sprays were also studied to remove the coupling between drop breakup and vaporization. The experiments of Hiroyasu and Kadota [11], with measurements of spray tip penetration using diesel fuel injected in nitrogen gas at 300 K and 3.0 MPa, was used for comparison. A computational domain of 4 cm diameter and 12 cm length was discretized using a grid of 40x8x24 (0.5 mm radial x 5 mm axial). Diesel fuel was simulated using tetradecane and the environment gas flow was quiescent. The initial injected drop radius was 150 mm (equal to the nozzle hole radius) and the injection velocity was held constant at 90.3 m/s.

The results shown in Fig. 4 correspond to 4 ms after the beginning of injection. At this time the experimental spray tip penetration was 7.5 cm and the spray angle was 13 degrees. As seen in the left-hand-side of Fig. 4, the computations gave a low spray tip penetration (about 6.4 cm) and significant radial dispersion of the drops with about 40% of the injected mass outside of the measured spray angle. The dispersion of the drops near the nozzle reflects errors in the calculation of the gas velocity in the region of large velocity gradients near the nozzle exit.

Further calculations demonstrated that the grid spacing of 5 mm in the axial direction was too large. Results obtained by increasing the grid resolution in the axial direction by using a grid of 0.5 mm radial x 2 mm axial resolution are shown in the right-hand-side of Fig. 4. Now the spray penetration is

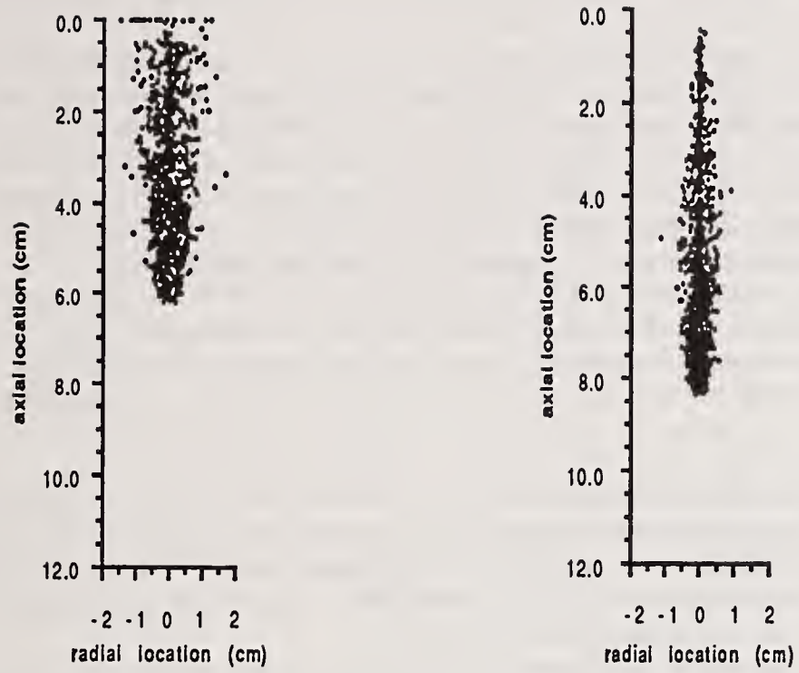

Figure 4. Influence of mesh refinement on spray penetration. Sprays shown at 4 ms after injection. Left: 0.5 mm radial by 5 mm axial resolution. Right: 0.5 mm radial by 2mm axial resolution.

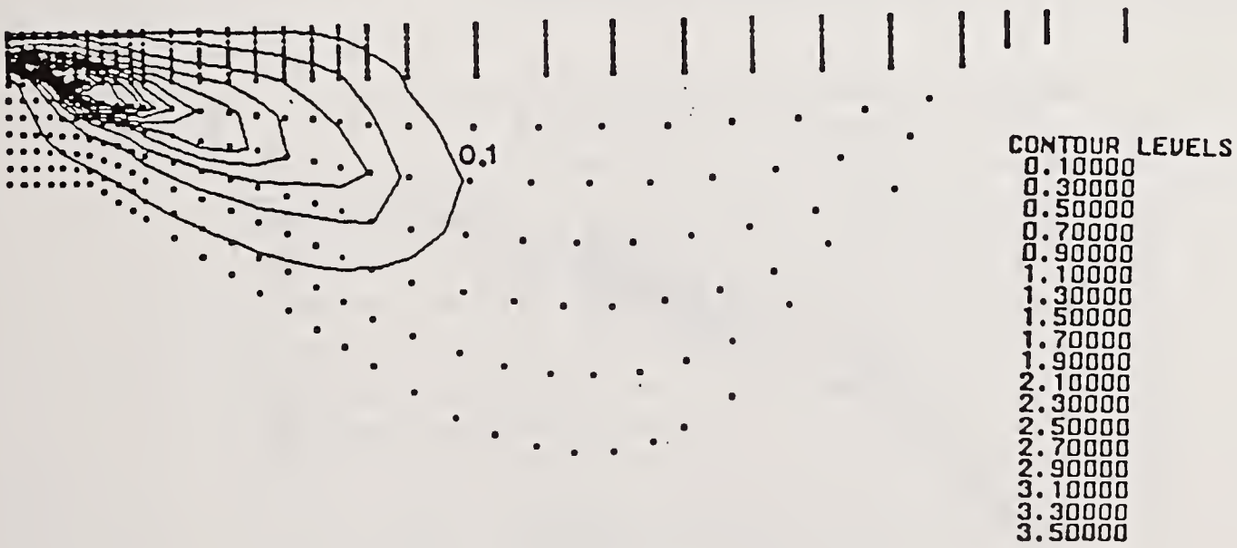

Figure 5. Predicted equivalence ratio contour on the plane mid-axis of the spray at TDC without considering combustion.

increased to 8.5 cm and the percentage of mass outside of the spray angle is only 4.6%. The calculation overpredicts the measured spray tip penetration somewhat, but dramatically improves the predicted dispersion of the drops.

These results demonstrate a strong sensitivity of spray calculations to numerical grid resolution and suggest the need for grid sensitivity analyses of engine calculations. Accordingly, the engine computations were repeated using a fine grid with 31x8x15 cells and 8 planes in the squish region at TDC (a radial mesh spacing of 0.78 mm was used in the vicinity of the nozzle). It should be noted that the use of such a fine grid is prohibitive for routine calculations due to the long computational times. The complete run took 4.0 hr of cpu time on a Cray Y-MP computer compared to 0.9 hr for the 15x4x18 grid. In order to decouple the contributions, these computations not consider combustion.

Figure 5 shows the equivalence ratio contours in the mid-axis plane at TDC. The fuel vapor tip (e.g., equivalence ratio of 0.1 contour) is located about halfway between the nozzle and the piston bowl. These results again show low fuel vapor penetration, even in the absence of combustion. This indicates that grid resolution effects cannot explain the observed low penetration in the engine's highly vaporizing environment.

Effect of Initial Dropsize. The formation of small drops with their high vaporization rates and high deceleration due to their strong interaction with the gas could be responsible for reduced spray penetration. To explore this possibility, the experiments of Kamimoto et al. [12] were used. These consist of n-tridecane injections into nitrogen gas at 875 K and 3.0 MPa. In the experiments gas and liquid phase penetrations were determined from Schlieren photographs.

A cylindrical computational domain of 4 cm diameter and 12 cm length was discretized using a grid of 20x8x30 cells (0.5 mm radial and 2 mm axial spacing near the nozzle). The environment was quiescent and the initial injected drop radius was 80 mm (equal to the nozzle hole radius). Three different experimental conditions were studied with injection pressures of 26, 50 and 80 MPa.

The calculated gas phase penetration seen in Fig. 6 (arbitrarily represented using that axial location where the fuel vapor contour reached 0.002 kg/m^3) shows a lower gas penetration than the experiment; and the difference between them increases with increasing injection pressure and consequently higher injection velocities. These high temperature and high pressure results confirm the low spray penetration predictions found in the engine computations and suggest the need for a revision of the spray calculation in order to identify the source of the discrepancy.

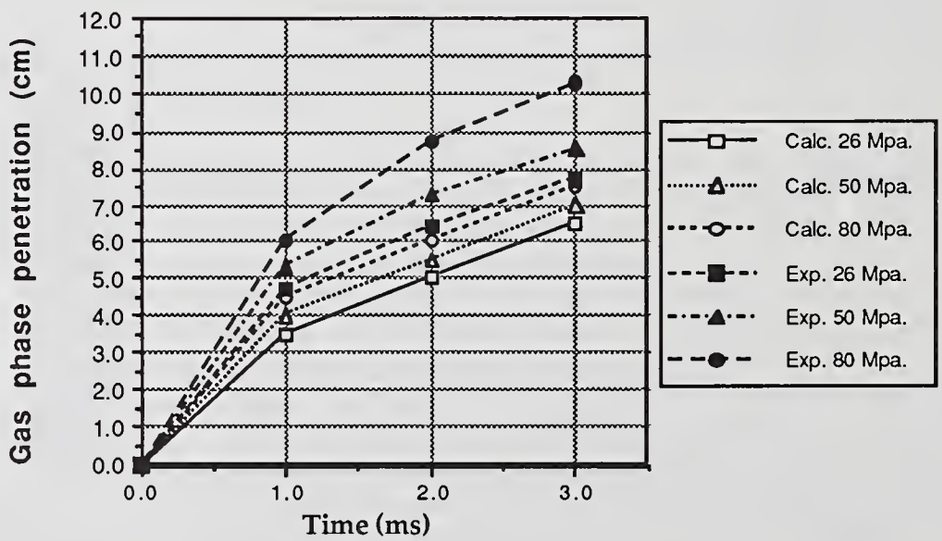

Figure 6. Calculated and experimental gas (vapor) penetration for different injection pressures. Experimental data from Kamimoto et al. [12].

The spray atomization model predicts the formation of very small drops at the high injection velocities of interest in engines. For example, for the case with injection pressure of 50 MPa in Fig. 6, the radius of the injected drops was 80 μm and the calculated wavelength of the fastest growing surface waves was between 0.45 and 0.80 μm. This results in the formation of a spray of drops with sub-micron sizes since the initial drop size is assumed to be of the order of the unstable wavelength in the atomization model [2]. Similar small spray drop sizes are predicted using other atomization models such as the Taylor Analogy Breakup (TAB) model of O'Rourke and Amsden [13]. These small drop sizes lead to very fast vaporization rates with corresponding low penetrations.

The marked influence of atomization drop size on penetration was demonstrated by injecting drop parcels with a fixed initial drop radius of 5 μm and by also suppressing drop breakup, collisions and coalescences in the calculation. The results given in Fig. 7 compare the predicted spray penetrations in two engine computations made using the atomization model for the initial drop size (top) and the 5 μm initial drop size case (bottom). As can be seen, greater spray penetration is achieved with the the use of the larger initial drop size.

The improved penetration also has a beneficial effect on combustion predictions. This can be seen in the cylinder pressure comparison shown in Fig. 2 for the case of 5 μm radius injected drops (dashed-line). There is an increase in the calculated peak pressures and a different rate of pressure rise. The improvement results from an improved fuel vapor distribution and consequent higher energy release. From Fig. 2 it can be inferred that a bigger initial dropsize would be able reproduce the experiment even better. These results indicate the need to improve the prediction of dropsizes from atomization models.

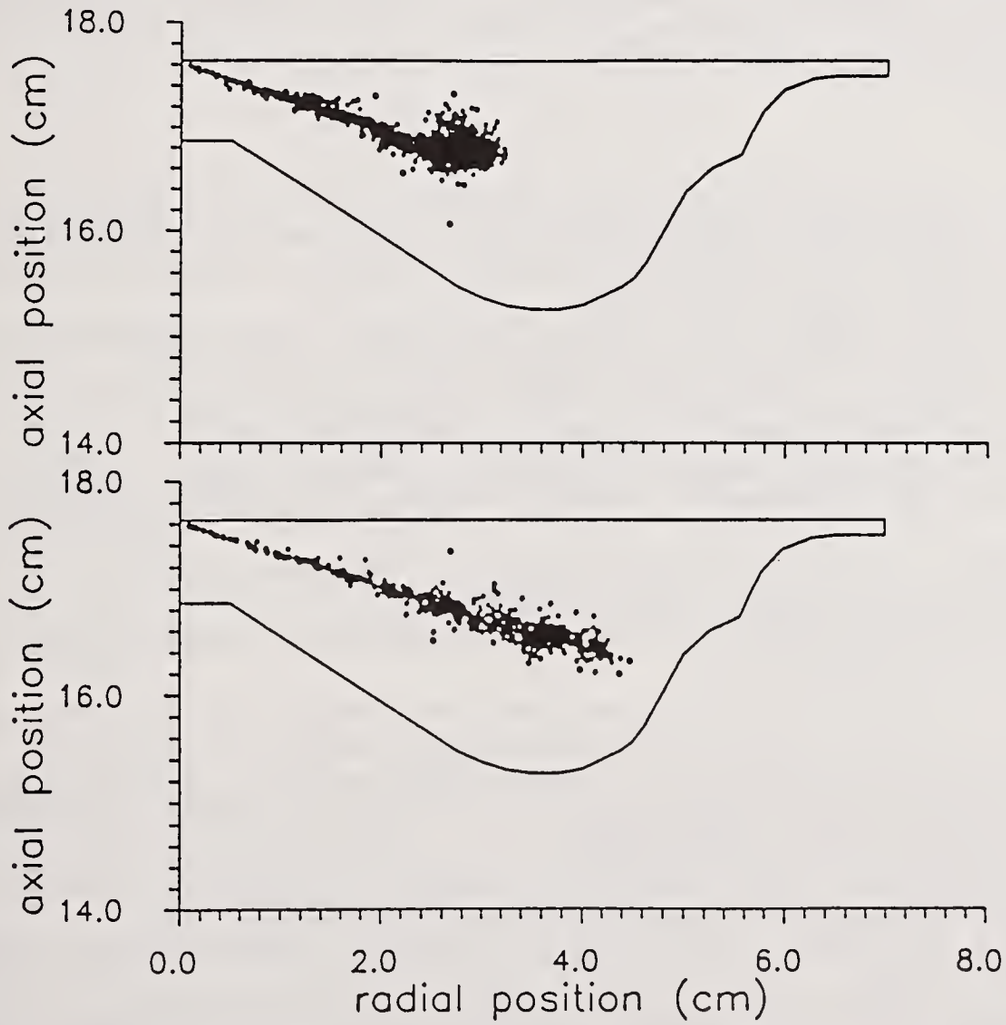

Figure 7. Drop locations in the plane mid-axis of the spray using the atomization model [2] (top) and, instead, an initial drop radius of 5 μm (without breakup or coalescence in the computation - bottom).

CONCLUSIONS

The study found difficulty in reproducing measured diesel combustion trends. Various possible causes were examined and the importance of the atomization model was pinpointed. The results showed:
1) The spray calculations were sensitive to numerical grid resolution. However, if proper grid resolution was used, the calculations reproduced experimental data adequately for low injection pressures and non-vaporizing sprays.
2) Spray calculations in high temperature environments were found to underpredicted measured gas phase penetration. This trend was found in both constant volume bomb and engine computations.
3) The underprediction of spray penetration was found to reduce the accuracy of engine combustion predictions considerably.
4) The details of the spray vaporization model were unable to explain the low spray penetrations.
5) The sensitivity of the results to the size of the injected drops suggests that improved atomization models are needed for engine conditions. Experimental data is needed under highly vaporizing conditions to validate new models (pressure 3.0-5.0 MPa, temperature >700 K, injection velocities (100-300 m/s), including measurements of fuel vapor concentration, dropsizes and liquid core penetration.

ACKNOWLEDGMENTS

The authors thank Gary Borman for helpful comments. Support for this work was provided by Intevep S.A. Venezuela, by Army Research Office contract DAAL03-86-K-0174 and by NASA-Lewis grant NAG 3-1087. Funding for the computations was provided by Cray Research, Inc. and the San Diego Supercomputer Center.

REFERENCES

1. Amsden, A.A., O'Rourke, P.J., and Butler, T.D. "KIVA-II: A computer program for chemically reactive flows with sprays," Los Alamos National Laboratory Report LA-11560-MS (1989).
2. Reitz, R.D. "Modeling atomization processes in high-pressure vaporizing sprays". Atomisation and Spray Technology, Vol 3, pp. 309-337 (1987).
3. Bergeron, C.A. and Hallett, W.L.H. "Ignition characteristics of liquid hydrocarbon fuels as single droplets," The Canadian Journal of Chemical Engineering, Vol 67 (1989).
4. Yan, J. and Borman, G.L. "Analysis and in-cylinder measurement of particulate radiant emissions and temperature in a direct injection diesel engine," SAE Paper 881315 (1988).
5. Lei, N. "A cycle simulation program for the dynamic operation of a single cylinder direct injection diesel," MS Thesis, Department of Mechanical Engineering, University of Wisconsin-Madison (1988).
6. Grasso, F., Wey, M.-J., Bracco, F. V., and Abraham, J. "Three-dimensional computations of flows in a stratified-charge rotary engine," SAE Paper 870409 (1987).
7. Takenaka, Y., Shiozaki, and Joko, I. "Numerical Analysis of the Fuel Spray Formation in DI Diesel Engine," SAE Paper 902078 (1990).
8. McKinley, T.L. and Primus, R.J. "Three-Dimensional Calculations of Air Motion, Sprays, and Combustion in a Quiescent Direct-Injection Diesel Engine," ASME Paper 90-ICE-2 (1990).
9. Magnussen, B.F., and Hjertager, B.H. "On mathematical modeling of turbulent combustion with special emphasis on soot formation and combustion," 16th Symposium on Combustion, The Combustion Institute, Pittsburgh, PA (1976).
10. Priem, R.J., Borman, G. L., El Wakil, M.M.O., Uyehara, A. and Myers, P.S. "Experimental and calculated histories of vaporizing fuel drops," NACA TN 3988 (1957).
11. Hiroyasu, H., and Kadota, T. "Fuel droplet size distribution in diesel combustion chamber," SAE Paper 740715 (1974).
12. Kamimoto, T., Yokota, H., and Kobayashi, H. "Effect of high pressure injection on soot formation processes in a rapid compression machine to simulate diesel flames," SAE Paper 871610 (1987).
13. O'Rourke, P.J. and Amsden, A.A. "The TAB Method for Numerical Calculation of Spray Droplet Breakup," SAE Paper 872089 (1987).

MATCHING OF ENGINE CHAMBER AND FUEL SUPPLY SYSTEM VIA KIVA-II MODELING

K.C. Tsao, Y. Dong and Y. Xu

Dept. of Mechanical Engineering
University of Wisconsin-Milwaukee
Milwaukee, WI, U.S.A.

ABSTRACT

A comprehensive model--KIVA-II--code based on the numerical calculation of transient, two- and three-dimensional, chemically reactive fluid flow with sprays was used to study the spray penetration in three classic types of combustion chambers of direct injection diesel engine. The effects of changes in several operating parameters such as the speed of the engine, the fuel mass per cycle and the initial swirl ratio were accounted for, as were the effects of changes in the clearance and the geometry of the piston bowl. In addition, the effects of different injection parameters viz. initial injection velocity at the nozzle, injection rates, nozzle diameters and Sauter mean radius of the droplets were investigated in relation to spray penetration and spread and the relationship between the spray and the shape of the chambers. The initial injection velocity, the Sauter radius and the rate of injected fuel per cycle all play a significant role in spray penetration and air fuel mixing. Moreover, the nozzle orifice diameters and duration of injection do affect the spray penetration, spread and air fuel mixing though they are governed predominantly by the other parameters such as injection pressure, mass injection rate, etc. The velocity and distribution of gas motion described by the initial swirl ratio and clearance height of the piston also affect the spray characteristics, especially in the outer peripheral region of the spray cone.

INTRODUCTION

Matching of injection characteristics, air motion and combustion chamber geometry are of prime importance in the development of more efficient and cleaner emission direct injection diesel engines. Direct injection diesel engines offer great promise in terms of both efficiency improvement and pollution control. The important factors which influence the open-chamber engine performance are the fuel penetration, vaporization and mixing. This means that the rate and completeness of combustion are controlled by the way the fuel vapor gains access to the available air, which is in turn determined by such factors as the trajectory of the sprays, the droplet velocity and the size distributions, and the nature of the prevailing gas flow field. The

spray trajectory is strongly influenced by the gas flow, especially after injection is terminated.

Injection rate is an important parameter as it has a strong influence on the rate of pressure rise after ignition. Injection duration is another, particularly at full load, since it influences engine performance, the fuel economy and the density of smoke directly. Fine atomization of fuel is not sufficient in achieving an efficient combustion unless proper propagation of sprays in the engine combustion chamber is attained. So, both the atomization and penetration of sprays play a key role to reach a desired pattern of distribution and a shorter delay of the injected fuel. In addition, the penetration of finely atomized fuel is required to match that of air motion and combustion chamber shape under varying fuel injection characteristics.

Recognition of these problems has prompted the application of multidimensional modeling techniques to the in-cylinder processes in D.I. engines. The results presented in this paper were obtained using KIVA-II computer code of Los Alamos National Lab. [1]. The work reported here attempts to introduce some cohesion into the studies of sprays in engine chambers by carrying out a limited variation of engine parameters. Three different shapes of omega chambers, prevailing in modern high speed D.I. diesel design, are used as typical configurations. The effect of engine speeds, initial swirl ratio, and clearances in the normal range of an operating engine is assessed for a bowl shape. Other fuel-supply parameters such as the size of injector nozzle, the duration of injection, the velocity at the injector hole exit and the spray mass per cycle are assessed for a bowl shape. The detailed parameters incorporated for discussion here are shown in Table 1.

TABLE 1. Parameter Variations

Variations	Levels
Engine speed (r.p.m.)	1500 2000 2500* 3000 3500 4000
Clearance (cm)	0.12 0.23* 0.38
Geometries of bowl	#1* #2 #3
Diameter of injector nozzle (cm)	0.018 0.021 0.024* 0.027 0.031
Velocity at injector hole (cm/s)	4000 16000* 28000 40000
Spray mass (g/cyc.)	0.0116 0.0232* 0.0348 0.0464
Initial swirl ratio	0.0* 1.5 2.0 2.5 3.0
Sauter mean radius (cm)	1.5×10^{-4} 5.0×10^{-4}* 1.0×10^{-3}
Duration of injection (CA°)	10 15* 20 24

METHOD OF CALCULATION AND CASES CONSIDERED

In the swept and clearance volumes, the grids expand and contract with the piston motions. And the number of the axial meshs decreases correspondingly as the piston moves toward TDC. The process of contracting and expanding is calculated from 90° BTDC to 60° ATDC. All operations of the KIVA-II program (including compiling, running and data processing) are carried out on a Cray Y-MP supercomputer.

Simulations of the in-cylinder flow were carried out on various combinations of parameters shown in Table 1. The variations with * mean that they are a baseline case in calculation. The main structure parameters and operat-

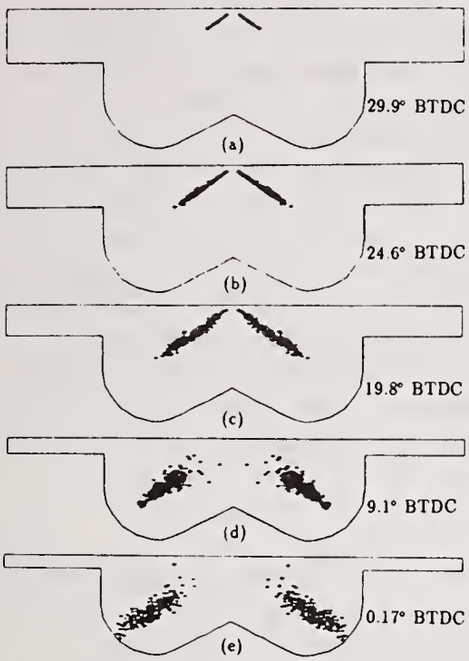

Fig. 1. Spray in bowl #1.

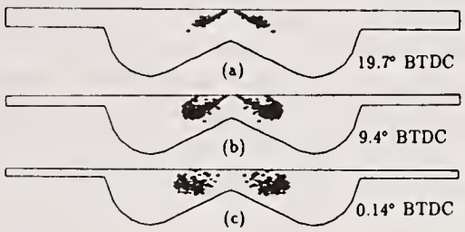

Fig. 2. Spray in bowl #2.

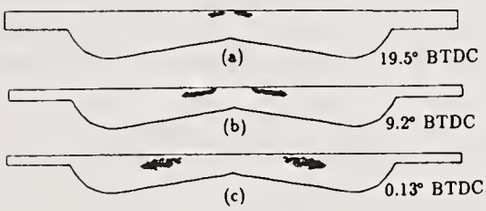

Fig. 3. Spray in bowl #3.

ing conditions of the engine used were given in reference 5. The engine is typical of a modern high speed diesel engine for off-road applications. In all cases, the calculations are commenced at the inlet valve closure, at which stage the air is assumed to have zero radial component and the axial component is assumed to vary linearly between the cylinder head and the piston crown. All wall temperatures, including the cylinder wall, cylinder head, piston face, valves and other exposed surfaces, are taken as 400 K.

RESULTS

The evolution of the spray fields will now be presented in the form of plots at selected crank angles spanning a period between 40° BTDC and 20° ATDC. The spray will be shown as viewed from the side through the full depth of field.

Baseline Results

The calculated spray obtained using bowl #1 are depicted in Fig. 1. The spray field in Fig. 1 shows that during the injection period, spray is developing as the crank angle increases and there is a "solid core" in the spray which is seldom influenced by the gas flow. However, as soon as the injection ends (Fig. 1(d)), the velocity of the spray decreases greatly. Afterward, the spray is influenced by the gas flow, which includes the entrainment and dispersion of the gas and the spray. Here the fuel spray, under the influences of squish flow and the presence of a curved bowl surface, is deflected downward into the piston bowl. At the same time the entrainment of gas causes the fuel liquid to be drawn up from the bowl near the center line. Only very early in the injection period does the bulk of the spray move in the injection direction. Beyond 15°, BTDC the spray is pushed downward by the stronger squish motion, so that the spray tends to spread out across the piston bowl volume. It could be presumed that for a bowl with a smaller squish volume the fuel liquid would tend to spray up to the top of bowl.

The Geometry of Chambers viz. Spray

The matching of the injection spray and the geometry of chambers is of prime importance. Under the conditions that all fuel parameters, gas flow and operating parameters are kept constant, only the angle of direction of spray is adjusted, the spray in two different geometric chambers #2 and #3 is illustrated in Fig. 2 and Fig. 3. For chamber #2, comparing with chamber #1 (see Fig. 1), the d/D keeps constant; however, H/D decreases about 55%. Because the fuel is injected into a narrow space between the cylinder head and the bottom of the bowl, the entrainment of gas is not sufficiently strong in the direction of the core of spray. It is evident that the spray penetration in chamber #2 is less than that in chamber #1 at the same crank angle. The situation is more evident in chamber #1. So, some measures should be taken if a shallow ω chamber is preferred. The measure includes increasing the initial momentum of spray, or adjusting the angle of spray so that the mixing and atomization of spray can be performed well.

Effect of Initial Swirl Ratio

The effects of the different swirl levels on the droplet trajectories and locations are shown in Figs. 4 and 5. The amount of initial swirl level would affect the gas velocity profiles and the turbulence levels in the bowl. It is noted that the interaction of the swirl and the squish has a significant effect on the axial and radial flow patterns and results in a system of two counter-rotating toroidal vortices in contrast to the no swirl case [5]. The direction of velocity in the region between the vortices is upward towards the cylinder head in the case of stronger initial swirl. In contrast, it is downward towards the bottom of the bowl in the case of no initial swirl. So, from Fig. 5 it is seen that the location of droplets is on the top of bowl if there is swirl. On the other hand, the existence of initial swirl would accelerate the dispersion of spray well, which is favorable to mixing and vaporization of fuel spray with air in the chamber.

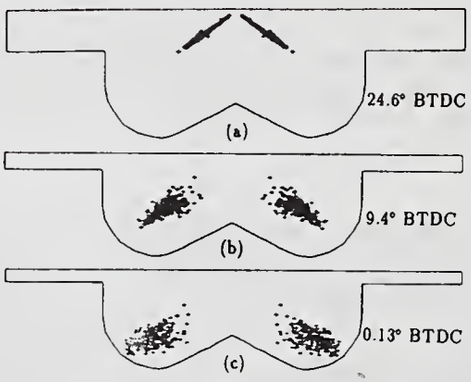

Fig. 4. Influence of initial swirl ratio on spray SR=0.0.

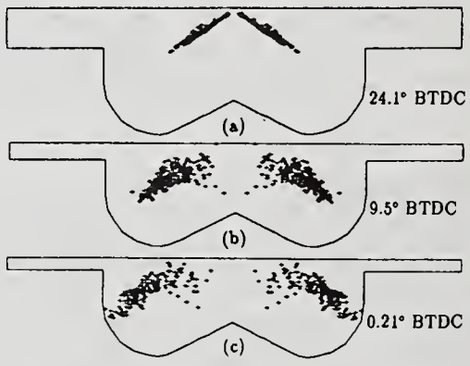

Fig. 5. Influence of initial swirl ratio on spray SR=2.5.

Effect of Clearance on Spray

The difference of clearance height means the change of the compression ratio. The range of the clearance height is from 0.12 cm to 0.38 cm. In fact, the compression ratio is altered from 19.1 to 14.0 respectively. On the other hand, the change of the clearance height also results in the difference of squish volume from 0.272 cm^3 to 0.862 cm^3.

A larger clearance means a lower compression ratio, which results in a lower pressure and temperature at late duration of the compression stroke. This case is out of favor from the point of view of the evaporation and atomization of spray. By comparing Figs. 6 and 7, this case is shown obviously. In addition, large a clearance also decreases the squish intensity, which would have an unfavorable influence on the distribution of spray in the bowl after injection ends.

Engine Speed Effect

The engine speed range was chosen to cover from 1500 to 4000 r.p.m. which is the normal operating speed of open chamber diesels. The engine speeds have a significant effect on the fuel-supplied system such as fuel mass per cycle, injection duration, etc. Comparison of Fig. 8 and Fig. 9 indicates that an increase of engine speeds lowers the penetration distance which appears to be not in favor of engine designer. The results hint that when a high speed engine is designed, corresponding measures, such as increasing injection pressure, selecting a suitable diameter of injector nozzle and so on, should be redesigned.

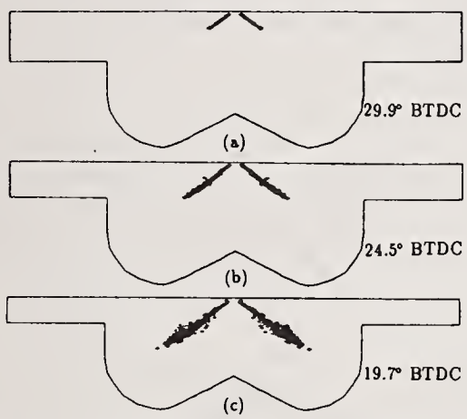

Fig. 6. Influence of clearance height on spray at CH=0.12 cm.

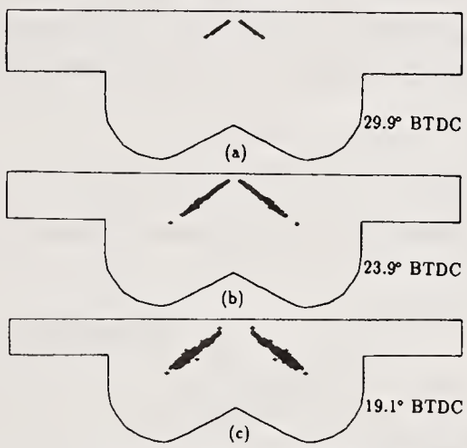

Fig. 7. Influence of clearance height on spray at CH=0.38 cm.

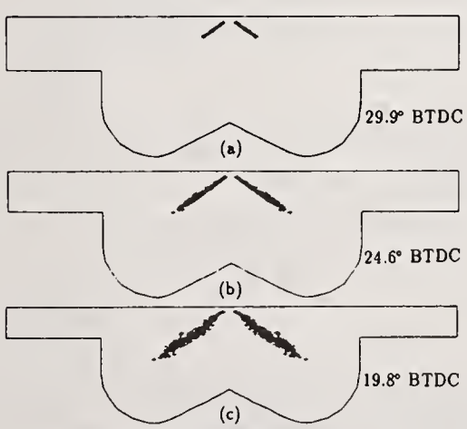

Fig. 8. Fuel penetration at n=1500 rpm.

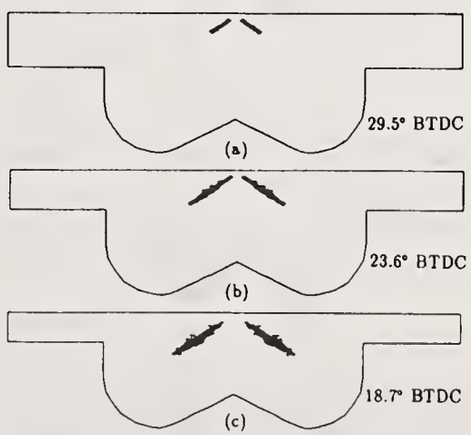

Fig. 9. Fuel penetration at n=3000 rpm.

Effect of Fuel System Parameters

The penetration and atomization of spray are influenced by many fuel system parameters such as injection pressure, diameter of pump shaft, structure

and size of injector, etc. Here, the effect of several essential parameters, the diameter of injector hole d_n, the injection velocity v_i, the fuel mass per cycle, the Sauter mean radius and the injection rate will be discussed. For baseline condition and at crank angles of 29.7°, 24.6° and 21.2° BTDC the penetration of fuel spray column is shown in Fig. 10 versus the diameters of injector hole. Figure 10 indicates that during injection, both the larger and smaller diameters of nozzle would decrease the penetration of spray, when all other conditions are unchanged. This is because smaller nozzle diameters would have the spray more atomized, and hence shorter penetration.

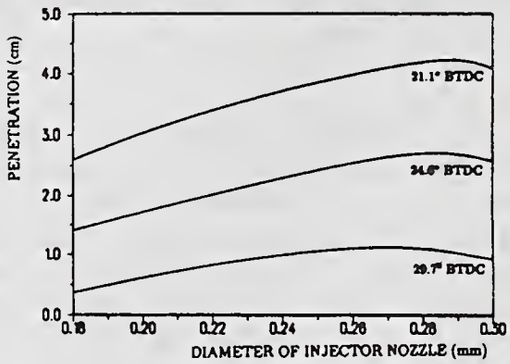

Fig. 10. Influence of nozzle dia. on penetration of spray.

The injection velocity at the nozzle has a significant influence on penetration and atomization of the spray. An increase of injection velocity from 40 m/s, Fig. 11(I), to 80 m/s, Fig. 11(II), shortens the injection duration, increases penetration and offers greater dispersion and hence better overall performance.

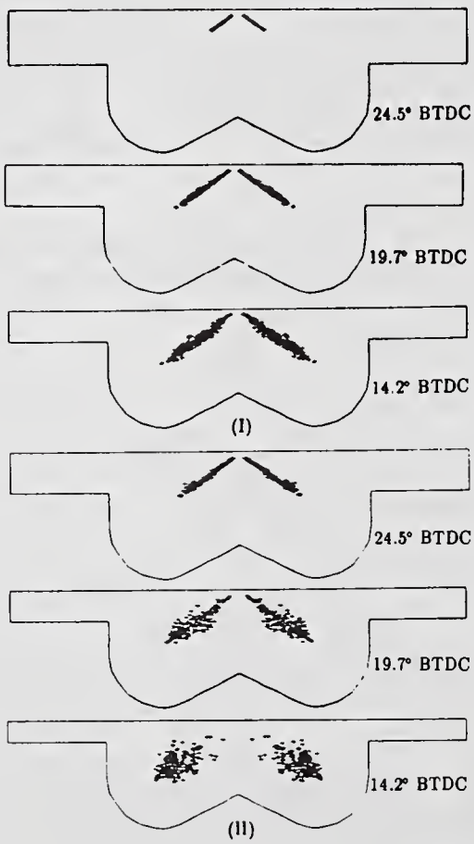

Fig 11. Injection velocity at nozzle.

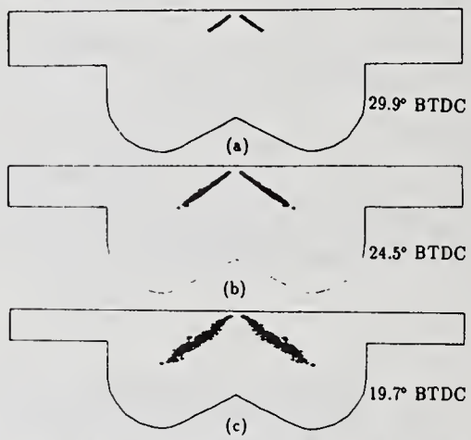

Fig. 12. Spray field at Ms = 0.0116 g/cyc.

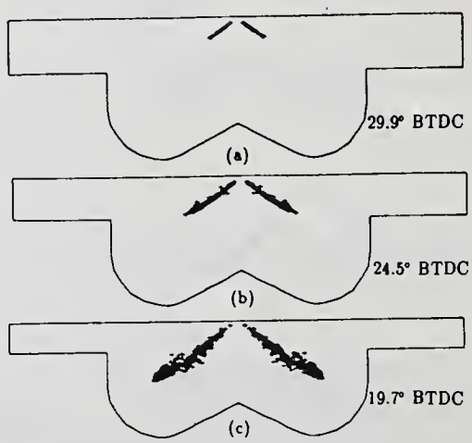

Fig. 13. Spray field at Ms = 0.0452 g/cyc.

The spray mass per cycle, which symbolizes the engine load, is an important operating parameter. Two classical instances of spray mass are shown in Figs. 12 and 13 for 0.0116 and 0.0452 g/cycle respectively. It is seen, obviously, that an increase of spray mass per cycle would result in greater penetration and density of the spray. The larger droplets penetrate farther than the smaller droplets and hence the leading region of a spray plume is enriched with large droplets. The tip droplets, i.e. those with the farthest axial penetration, are always moving and following the movement of gas vortex vector in the bowl.

The initial Sauter mean radius was estimated according to the theory developed by Taylor [6] who studied the rate of growth of the perturbations of planar liquid surfaces induced by co-flowing gas. The theory states that the initial droplet radius is directly proportional to the liquid surface tension and wavelength of the fastest growing surface wave, and inversely proportional to the gas density and the square of the relative velocity between the gas and the liquid. The investigation by Bracco [4] showed that stable droplets are of the order of 5 to 10 μm depending on the relative velocity between the gas and the liquid phases. For injection velocities larger than 100 m/s, droplets larger than 10 μm in radius will breakup into smaller droplets. The spray penetration viz. the initial Sauter mean radius is shown in Fig. 14. As expected, the penetration increases as the initial Sauter mean radius increases.

The injection rate is a function of the total injected mass and the duration of injection. For a fixed amount of fuel injected, the penetration of spray versus the duration of injection was indicated in Fig. 15. It is evident that an increase in injection rate would result in an increase in penetration and vice versa.

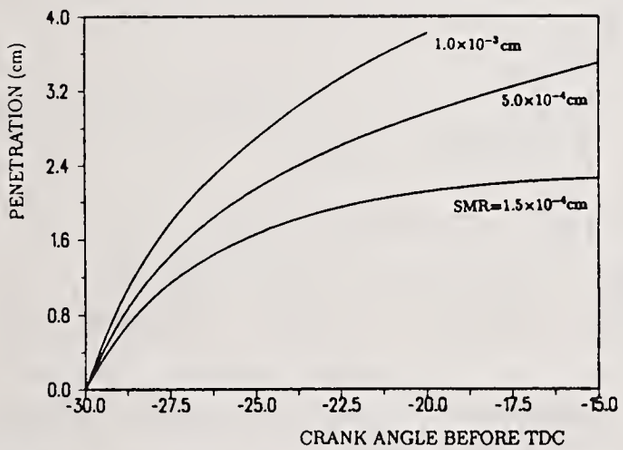

Fig. 14. Effect of Sauter mean radius.

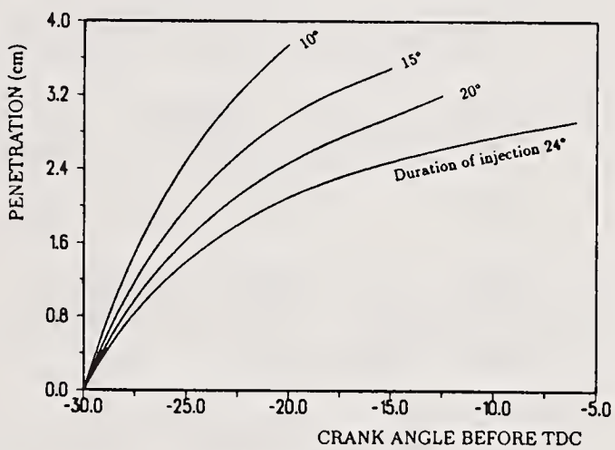

Fig. 15. Influence of injection duration.

CONCLUSIONS

The engine designer is confronted with a formidable task to reconcile and optimize a set of engine parameters relating to engine performance and exhaust emission. These include, insofar as gas motion is considered, the induction and combustion chamber configuration which characterize the in-cylinder gas motion to facilitate air fuel mixing. On the fuel system, the main consideration is the performance of an injector which would supply a fuel spray of adequate penetration and dispersion to match that of the in-cylinder gas behavior, and vice versa. This paper has demonstrated the following observations.

1. The solid core of a fuel spray plume is seldom influenced by the in-cylinder gas motion during the injection period. However, after injection terminates, the spray profile is significantly affected by the gas flow, especially the engine squish velocity.

2. A shallow chamber has a minimal effect on spray penetration. Additional measures must be incorporated in the design for proper mixing and dispersion between fuel and air.

3. As anticipated, engine initial swirl and squish velocity would alter the direction of sprays and subsequent improvement of fuel air mixing.

4. An increase of engine speed reduces the fuel penetration distance.

5. Fuel injection parameters, such as injection pressure and duration, exert a greater influence on the spray pattern than the in-cylinder gas motion.

ACKNOWLEDGEMENT

The authors wish to thank the National Center for Supercomputing Applications, Champaign, Illinois, for a grant on KIVA-II applications.

REFERENCES

1. Amsden, A. A., O'Rourke, P. J., and Butler, T. D., "KIVA-II: A Computer Program for Chemically Reactive Flows with Sprays," Report LA-11560-MS, Los Alamos National Laboratory (May 1989).

2. Gosman, A. D., "Multidimensional Modeling of Cold Flows and Turbulence in Reciprocating Engines," SAE 850344 (1985).

3. Watkins, A. P., Gosman, A. D. and Tabrizi, B. S., "Calculation of Three Dimensional Spray Motion in Engines," SAE 860468 (1986).

4. Bracco, F. V., "Modeling of Engine Sprays," SAE 850394 (1985).

5. Tsao, Keh C., Dong, Yu and Xu, Yong, "Investigation of Flow Field and Fuel Spray in a Direct-Injection Diesel Engine via KIVA-II Program," SAE 901616 (1990).

6. Reitz, R. D. and Bracco, F. V., "Mechanism of Atomization of a Liquid Jet," Physics of Fluids, Vol. 25, pp. 1730-1742 (1982).

EXPERIMENTAL INVESTIGATION ON MICRO-EXPLOSION OF EMULSIFIED DIESEL OIL BY HOLOGRAPHY

X. Hang, S. Yunbiao, Z. Chongji and M. Yuanji

I.C. Engine Research Institute
Dept. of Energy Engineering
Zhejiang University
Hangzhou, P.R. China

ABSTRACT

In this study, appreciating the single-pulsed in-line Fraunhofer holographic system and the high speed schlieren photographic technique , we have studied the atomizing and evaporizing characteristics of emusified diesel spray in a high temperature combustion bomb.

During the research, we have obtained both the micrographes of oil droplets in the spray field and the macrographes of the spray development process. While comparing the pure and water emulsified diesel oil, we found the emusified oil had better atomizing characteristics than the neat oil. "Fragmentation" atomizing phenomenon has been discovered in emulsified spray. The authors propose, according to these features, the water-oil uncontinuing internal phase boundary decays the uniform of liquid. We think the diverging and disturbing ability of the superheated water addition in the emulsified oil contributes to the improvement of spray atomization.

In addition, we also found a distinctive spray distribution of a pintle diesel nozzle. That is at the outer region of the spray the droplets have larger size than those in the inner region. This tendency is more stronger in low environmental temperature than in high one.

INTRODUCTION

Diesel oil emulsified with water has been widely studied as an effective method to reduce both the fuel consumption and exhaust emissions of the engine. According to the feature that the combustible air-fuel mixture of diesel engine is formed in the combustion chamber, spray atomizing characteristics become very important to diesel engine performance. So it is necessary to have a further investigation on the spray atomization of emulsified oil.

Formerly, Ivanov(1) found the "micro-explosion" phenomenon of suspended fuel emulsion droplet by high speed motion photography. Gallahalli(2) studies the flame structure of

unsupported single drop for both neat and emulsified oil. Lasherac(3) has also observed the micro-explosion of emulsified free droplet. Although there have been a number of studies on the isolated emulsified droplet,as mentioned above, that is not enough to guide the application of water emulsified oil in diesel engines. We say this because the condition of single free droplet is quite different from that of particles in diesel spray, no matter in particle size, density or in droplet life time. On account of this, we have paid more attention to the spray particle field of emulsified oil in diesel engine.

In our study, the high speed schlieren photography and in-line Fraunhofor holography have been adopted to observe the spray development process macrocopically and the particles in spray field microscopically. We found that emulsified oil had some different features of spray atomization from the neat oil.

EXPERIMENTAL APPARATUS

High Temperature Combustion Bomb

Figure 1 shows a scheme of the high temperature combustion bomb used in this study. Two quartz windows are installed in both sides of bomb for optical access.

Nitrogen was used as the surrounding gas. This made it possible to observe the atomizing and vaporizing process in detail. Fuel was injected by a standard diesel injector with pintle diesel nozzle(hole diametre 1.5mm, spray angle 15deg, openning pressure 20.0Mpa). The neat fuel used was No.0 diesel oil with a density of 0.819g/cm3 and cetane number of 55.

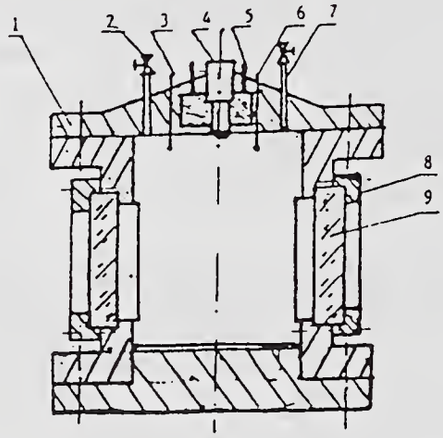

Fig.1 High Temperature Bomb
1. Pressure Vessal 2. Intake Valve
3. Thermalcouple 4. Fuel Injector
5. Cool Water Jacket 6. Presure Transducer
7. Emission Valve
8. Glass Holder 9. Quarze Window

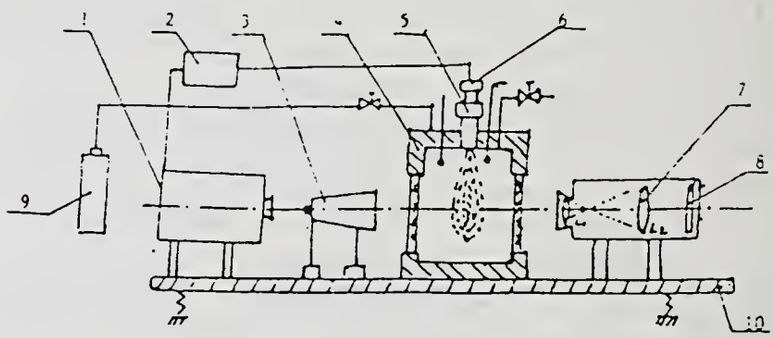

Fig.2 Layout of In-Line Fraunhofer Holographic Recording System
1. Pulsed Laser 2. Synchronism Delaying System
3. The Exoander
4. Combustion Bomb 5. Fuel Injector
6. Neddle Lift Transducer 7. Image Lens
8. Holographic Plate
9. N2 bottle 10. Working Plat

Optical Arrangement of Recording System

The layout of the holographic system and the high temperature combustion bomb is shown in Figure 2. An in-line holographic arrangement using a single-pulsed ruby laser was employed. The laser with a wavelength of 694.3nm, an output of 100mj and a pulsed width less than 50ns.

A set of image lens[7] is placed just before the plate not only to premagnify the conjugate image of the particles recorded in the plate, but also to eliminate the aberrations which will distort the image greatly in micro-photography.So in our system, the resolving power is high enough to record a 3um particle.

Holographic Reconstruction and computer processing system

Fig. 3 shows the devices used in holographic reconstruction. As mentioned in the Figure, a He-Ne laser beam is used as reconstruction light. Spray field hologram which has been put on the three-dimension displacement is reconstructed by the optical system. A vedio camera catches the holographic image. A computer imaging system is used to process and count the size and distribution of droplets in spray field. The processing of droplets is based on the theory of grayscale mathematical method(4).

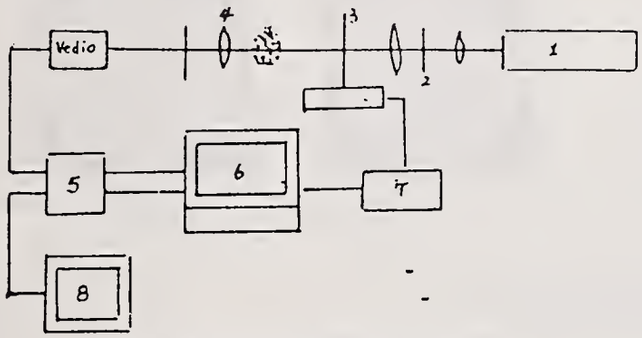

Fig.3 Holographic Reconstruction & Processing system
1. He-Ne Laser 2. Spacial Filter
3. Hologram Plate 4. Image Lens
5. PC Vision 6. Computer
7. Three Dimension Displacement 8. Monitor

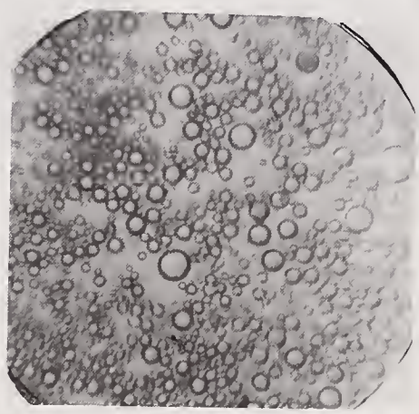

Fig.4 Micrograph of Internal Phase of Emulsion

EXPERIMENTAL RESULTS AND ANALYSIS

We have adopted No.0 diesel oil. Water/oil emulsion with 15 percent of water content by volume which was provided by adding surfactants of SPAN 0.1% and MAPE 0.2%(volume fraction). A 400X enlargement microscopic photograph showed a fine and stable dispersion of water addition. The particles of internal phase are as small as 2-7um(see Fig. 4). Both the dillution and electric resistance tests manifested the emulsion were water-in-oil structure.

Experiment Results in Ambient Condition

In ambient condition, we studid the spray atomizing feature of both the neat and emulsified oil. High speed schlieren photographes showed the emulsified spray had a smaller spray angle than that of the neat oil, which were shown in Fig. 5.

While under the same condition, holographes manifested the and a smaller S. M. D.(Sauter Mean Diameter) of droplet size than the pure diesel oil. Table 1 showed the S.M.D. results counted statistically by computer.

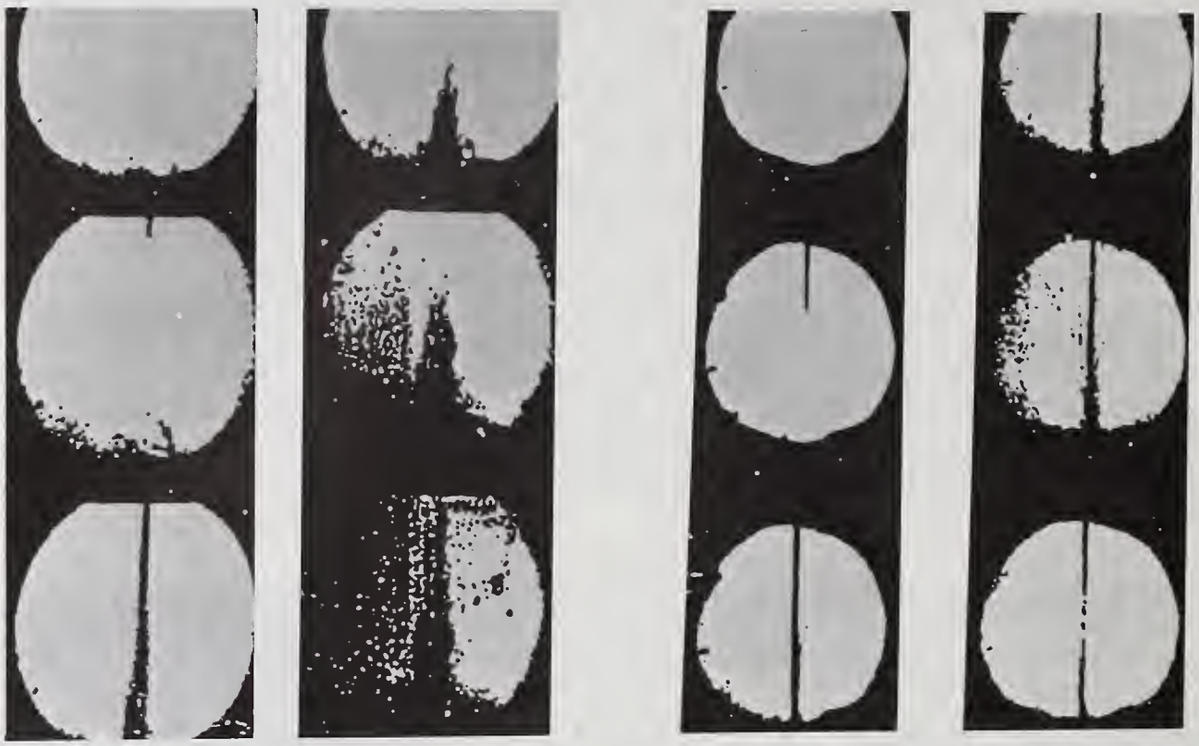

(a) Pure Oil Spray (b) Emulsified Oil Spray

Fig.5 High Speed Schlieren Cinematography
Sequences of Spay Development
(Ambient Condition,2000f/s)

Time Delay From Injection	0.7ms	0.9ms
Emulsion (S.M.D.)um	18.78	24,12
Pure Oil (S.M.D.)um	25.27	30.12

Table 1 Results of S.M.D.

The atomizing features of the emulsion, in author's opinion, are closely related to its internal phase structure and physical properties. In ambient condition, the emulsion is more viscous than the pure oil, and this causes the emulsion has a more narrow spray angle. But, on the other hand, the water-oil uncontinued phase boundaries bring the more uniform and smaller emulsified spray distribution. We can find the uncontinuing property of internal phase of emulsion from the micro-photograph.(Fig.4).It is obvious that the sheer stress between these water-oil uncontinuing surface must be weaker than those of the continuing phase in pure oil. So fragmentation of droplets occured more frequently at these micro-regions.

Therefore, when the emulsified spray moves in the air with high speed, the spray will be disturbed and become instability. We assume that the boundaries of uncontinued water-oil surfaces at those internal phase are easier to be broken and cause further fragmentations of particles and a fine atomization.

Atomization and Vaporization of Emulsion in High Temperature Environment

High speed schlieren photographes in 573K and 0.9Mpa environment of pure and emulsified oils showed a very interesting experimental phenomenon. At the beginning of injection, the emulsified spray angle was smaller than the pure one, but after a certain period as shown in Fig. 6, the emulsified spray expanded disruptively and developed to a larger spray angle than the pure oil(Frame No.4, 5, 6).

In high temperature, holography showed microscopically the emulsified particles had two distinctive features.

One was the fragmentations of some of large droplets in the surrounding parts of spray. The other was the existance of many small particles in outer region of spray, where used to be dominated by larger size droplets. Fig. 7 is the pictures of emulsified droplets taken in different high temperature environments.

We haven't found the same phenomenons mentioned above in pure oil spray.

In high temperature, the appearance of a lot of small particles in the emulsified spray has improved the atomizing quality. The water addition in spray is in overheated state after having been injected into the high temperature bomb. The puffing of vaporized water might be strong enough to cause fragmentations of large particles directly as "micro-explosion", or if not as strong as "micro-explosion", might intense the internal disturbance of droplets which are in high speed. In the mean time, the micro-structure of uncontinued internal phase between water addition and oil might also optimize the spray atomization.

Spray	Emulsion	Neat Oil
Middle S.M.D.(um)	11.4	19.1
Surrounding S.M.D.(um)	11,5	24.3
Front Edge S.M.D.(um)	17.9	29.3

Table 2 Results of S.M.D.
(T=723K P=0.1Mpa, t=0.4ms)

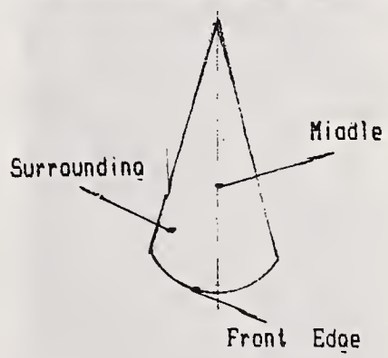

Table 2 shows the results of S.M.D. of particles in different regions of a developing spray. According to the results, we concluded that even in high temperature the droplet size distribution of emulsified fuel is more uniform and smaller than that of pure diesel oil. Statistic results of Fig. 7 manifest that in the middle and surrounding regions of emulsified oil, 65% of total counted droplets are among 3-10um, only small quantity of big droplets have diametres of 40-50um, while in the same condition for pure oil. only 26% of total droplets have 3-10um diametres, most of the particles in that region own diametres of 10-40um. At the front edge, 80% of droplets occupied the diametres of 3-25um in the emulsion, while in diesel oil, the same amount droplets occupied the diametres of 15-65um.

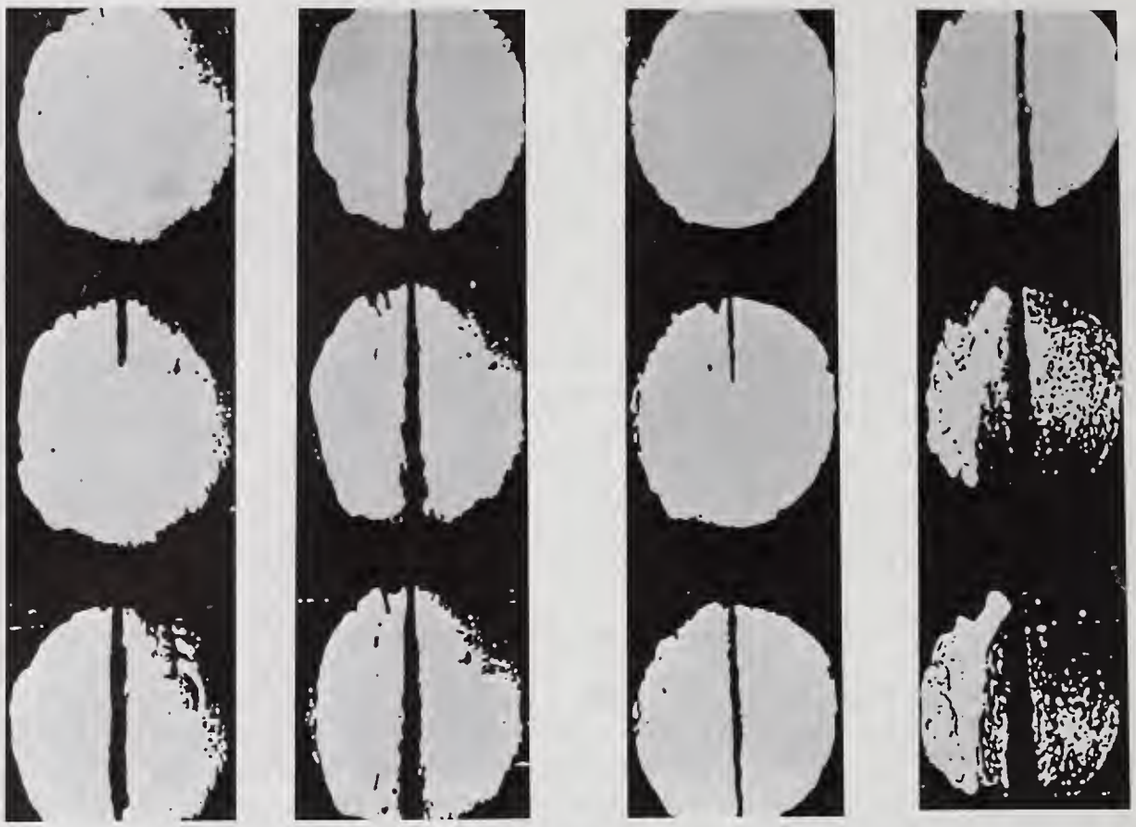

(a) Pure Oil Spray (b) Emulsified Oil Spray

Fig.6 High Speed Schlieren Cinematography
Sequences of spray Development
(573k.0.9Mpa;2000f/s)

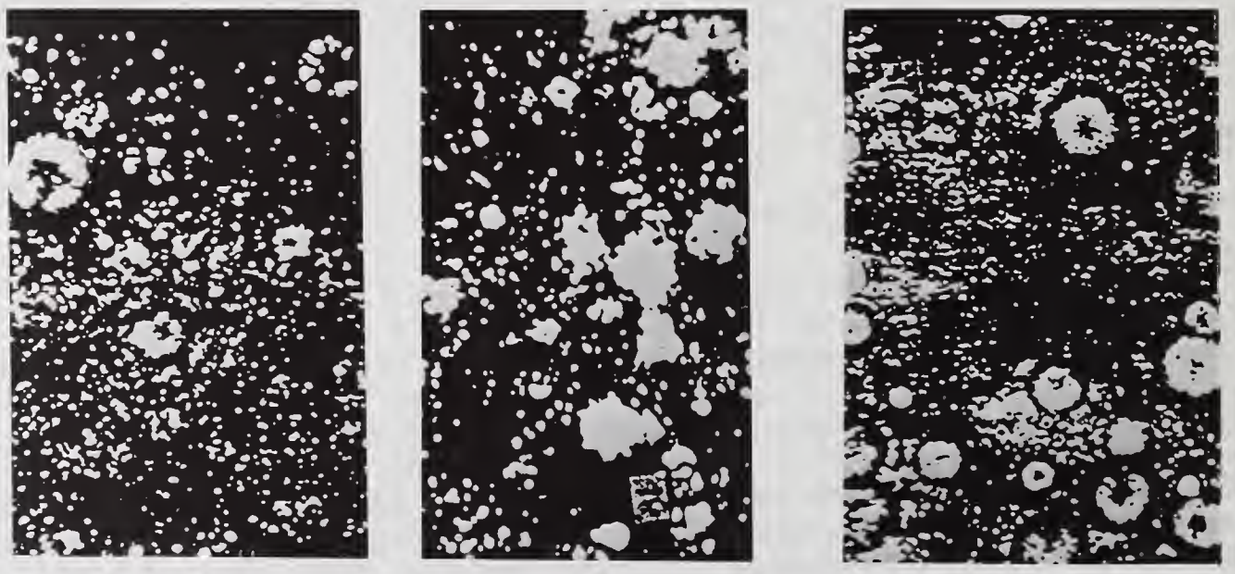

(a) T=623K t=0.4ms (b)T=723K t=0.4ms (c) T=723K t=0.2ms

Fragmentations of Emulsified Particles Pure Diesel Oil Partcles

Fig.7 Holographic Microgrophes of Spray Particles
of Both Emulsified and Pure Oil
in High Temperature

Conclusively, in the analysis of emulsion vaporizing characteristics, we find the strength of micro-explosion of emulsified spray is not as effective as it is in the single droplet test. It also implies that the vaporizing water addition causes disturbance inside oil droplets. It's the internal disturbance of the large size and high velocity droplets that brings out a fine atomizing quality in high temperature.

Droplet Size Distribution of Pintle Diesel Nozzle

Having tested both the pure and emulsified oil, we found the pintle diesel nozzle always formed a distinctive spray distribution. Table 2 and Fig. 8 show this trend. At the outer region of the spray, the droplets have bigger sizes than those in inner region. This trend is stronger in low environment temperature than in the high one. That is because the high temperature cause a faster vaporization.

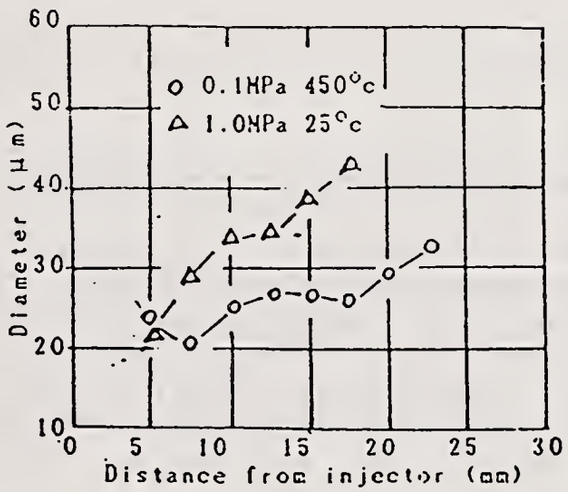

Fig.8 Sprav Droplets Variations With Distance from Nozzle

According to Rayleigh's atomization theory(6,7), when the oil jets out of the nozzle, small disturbance will appear on the surface of the jet. Filaments of oil that splash out of the spray surface will reduce its speed rapidly. These Filaments are difficult to break again in low speed and gradually become the large circle particles by the force of surface tension.

CONCLUSIONS

By the methods of high speed schlieren photographic and in-line Fraunhofor holographic techniques, we studied the atomizing characteristics of emulsified spray in a high temperature combustion bomb and obtained the conclusions as follows:

1) With some necessary technical measures, it is possible to record the diesel spray fields clearly in high temperature environment by in-line holography.

2) Studies manifest the emusified diesel spray has a more uniform size distribution and a samller S.M.D. particle size than

the pure diesel oil. Especially in a high temperature condition, the spray angle expands disruptively and fragmentations take place in some of big emulsified droplets.

3) The author assume that the better atomizing performance of emulsion is mainly caused by the following two reasons.

The uncontinuing water-oil internal phase boundary is a micro-structure easier for droplet disperse.

In high temperature, puffing of the vaporizing water addition brings internal disturbance to big droplets and make them easier to disrupt during the high speed atomizing process.

4) The particle size distribution of spray of pintle diesel nozzle is featured by a tendency. The tendency is that the deoplets in outer edge has bigger S.M.D. than those in inner region of the spray.

REFERENCES

1. DRYER F.L. "Water Adition to Practical Combustion Systems--Concepts and Applications" 16th Symp. on Combustion.

2. GALLAHALLI S.R. "Combustion of Drops and Sprays of No.2 Diesel Oil and Its Emulsions with Water" 18th. Symp. on Combustion.

3. LASHERAS, C.K.LAW. "Combustion Characteristics of Water-in-Oil Emulsion Droplets " Combustion and Flame. VOL. 37(1980).

4. Kenneth Sloan "Measureing photoreceptor Mosaic:An Application of Adaptive Gray Scale Morphology" SPIE Vol.937 Applications of Artificial Intelligence,1988.

5. NISHIDA "Holographic Measurement of Evaporating Diesel Sprays at High Pressure and Temperature" JSME Vol.30. No. 259 (1987).

6. REITZ R.D."Atomization of a Liquid Jet" Phys. Fluid 30(7) July, 1987.

7. REITZ R.D. "Effect of Drop Break Up on Fuel Spray" SAE 860469.

8. TSAO.K.C. "Puffing and Micro-Explosion Phenomenon of Water Emulsion Fuels" SAE 860304.

THE THREE-PARAMETER LOG-HYPERBOLIC DISTRIBUTION AND ITS APPLICATION TO PARTICLE SIZING

T.-H. Xu, F. Durst and C. Tropea

Lehrstuhl für Strömungsmechanik
Universität Erlangen
Nürnberg, Germany

ABSTRACT

This paper investigates the possibilities of representing measured size distributions in the form of a three-parameter log-hyperbolic (3P-LH) distribution. This distribution is shown to be a special case of the more general four-parameter log-hyperbolic (4P-LH) distribution but which exhibits a more stable behavior in the fitting of its parameters to empirical data. The problem of parameter estimation stability using the 4P-LH distribution has been identified and explanations are given for its causes. The 3P-LH distribution circumvents these problems while yielding an equally good representation of the data for a large variety of applications. The 3P-LH distribution is therefore concluded to be a valuable means of presenting large amounts of size distribution data in a more comprehensible manner.

1. INTRODUCTION

Many industrial processes deal with particles in which either the speed of reaction or the quality of the product depend strongly on the particle size distribution. Spray painting, spray drying, oil combustion and numerous other unit operations concerned with heat and mass transfer from dispersed phases are well-known examples. For the purpose of the optimization of these processes, a mathematical description of size distributions is needed. In the field of spray research especially, such a quantitative description is required for extracting information from the large amount of measured data in order to study the spatial variation or to compare different nozzles. A further necessity lies in the research aim of predicting spray properties and their dependence on nozzle configuration, physical properties of the liquid, supply pressure, etc.

Although the mean diameters D_{10}, D_{20}, D_{30} and D_{32} are widely used to characterize the essential features of the distributions, they are not a sufficient mathematical description because different distributions may have the same values of mean diameters while exhibiting significant differences in the distribution shape. To predict the average velocity and heat/mass transfer rates of a particle system, the use of the equations for a single particle with simple replacement of the particle diameter by a mean diameter for describing a particle ensemble may cause considerable error. Furthermore, even if particle dependent transfer phenomena can be correlated with a certain mean diameter, this correlation may not be valid for other applications. For this purpose and for a better understanding and modeling of the process concerned with particles, a probability density function (PDF) must be used.

In recent years, attempts have been made to find a suitable PDF for particle systems. Among the various forms of distributions, the log-hyperbolic distribution, which was proposed by Barndorff-Nielsen [1] in 1977, has been shown by Durst and Macagno [2] to be suitable for many fields of particle physics. Bhatia and Durst [3] summarized the application of different distributions to sprays and carried out a comparative study of four distributions, Rosin-Rammler, log-normal, a distribution proposed by Li and Tankin[4] and the

log-hyperbolic distribution. They have demonstrated clearly that the log-hyperbolic distribution provides a more appropriate description of the measurement results for eight sets of data from three different sources.

The main difference among the possible analytic descriptions of the measured distribution lies in the "tails" of the distribution. As is seen clearly by the data presented in references [1,2,3], the tails of the measured distribution can be approximated well by straight lines when the logarithm of PDF is plotted against the particle size or the logarithm of particle size. This is exactly the description afforded by the hyperbolic/log-hyperbolic distribution. The present authors have examined a number of PDA-measured droplet size distributions and found that this behavior held not only for water sprays, but also for paint sprays[5] and coffee sprays[6].

The purpose in approximating a measured size distribution with an analytic function is to characterize a large amount of information, the empirical distribution, with a small number of parameters. Changes in the distribution should therefore be reflected in changes of the fitted parameters, preferably also with immediate physical interpretations of the changes. Hence small variations in the observed distribution should correspond to small variations of the fitted parameters and there should not exist two or more sets of parameter estimates that yield equally good fittings. Unfortunately, this stability problem does exist for the four parameter log-hyperbolic distribution. In the next section, this is demonstrated by a few examples and the cause is analyzed. To solve the problem, a new probability density function is proposed, which can be considered a special case of the log-hyperbolic distribution but which only has three parameters. Hence, it is called "the three-parameter log-hyperbolic (3P-LH) distribution". This distribution, some of its characteristics, the method to estimate the parameters, and its relation to the usual four parameter log-hyperbolic distribution are introduced in section 3. Some applications and comparisons with the usual log-hyperbolic distribution as well as an example of using this distribution to analyze a spray are provided in section 4.

2. THE LOG-HYPERBOLIC DISTRIBUTION AND THE STABILITY PROBLEM IN PARAMETER ESTIMATION

The probability density function of hyperbolic distribution proposed by Barndoff-Nielsen [1] may be written in the form

$$f(x;\alpha,\beta,\delta,\mu) = A(\alpha,\beta,\delta)\exp\{-\alpha\sqrt{\delta^2+(x-\mu)^2}+\beta(x-\mu)\}\ , \qquad -\infty < x < \infty\ . \tag{1}$$

where $\alpha > 0, |\beta| < \alpha, \delta > 0$ and $\mu \in (-\infty,\infty)$ represent the four parameters to be fitted. A is the normalization constant introduced to insure that

$$\int_{-\infty}^{+\infty} f(x)dx = 1 \tag{2}$$

and is given by

$$A = \frac{\sqrt{\alpha^2-\beta^2}}{2\alpha\delta K_1(\delta\sqrt{\alpha^2-\beta^2})}\ . \tag{3}$$

The slope of the left asymptote is given by $\alpha+\beta$, that of the right by $-(\alpha-\beta)$ and μ gives the abscissa of the asymptotes intersection.

According to Barndoff-Nielsen [1], when x follows Eq.(1) the distribution of $s = \exp(x)$ is the log-hyperbolic distribution.

In applying the 4P-H distribution to approximate the measured droplet distributions in sprays, several undesirable characteristics of the parameter estimation have been observed. In some cases the variations of the fitted parameters for distributions measured in close proximity to one another were very irregular. Significant variations were even registered for repeat measurements at the same location in the spray. In some extreme cases, for example in paint sprays, the estimated parameters depended strongly on the initial values used in the maximizing procedure and on the number of grouping classes. Despite these instabilities in the parameter estimation, the fitted curves were largely coincident. The exact nature of these instabilities were therefore studied in more detail using a computer simulation.

A computer simulation has the deciding advantage over experiments that the true distribution is always known. In the present case a random number generator was used to produce 20,000 samples that were log-

hyperbolic distributed in the range -100 to 200 and with the known distribution parameters as were estimated in the example 2 of [7]. Applying existing fitting procedures to the simulated data resulted in parameter estimates which were rather stable and accurate. A further simulation introduced random fluctuations in the sample elements, corresponding to a measurement error in an experiment, which was normally distributed and with a standard deviation of 5%. Parameters were again estimated from the resulting sample. Although the parameter variation rose slightly among different simulations, the estimates remained excellent.

A third simulation was performed using the same known parameters but truncating the left side of the generated data to yield a distribution as illustrated in Fig. 1. As seen from the five sets of parameter estimates corresponding to five parallel runs, the variation of the parameters is high, although the fitted curves lie close to one another. This is typical of the behavior found in spray experiments. From these simulations it is concluded that the tail portion of the distribution is essential to a stable estimation of the four parameters.

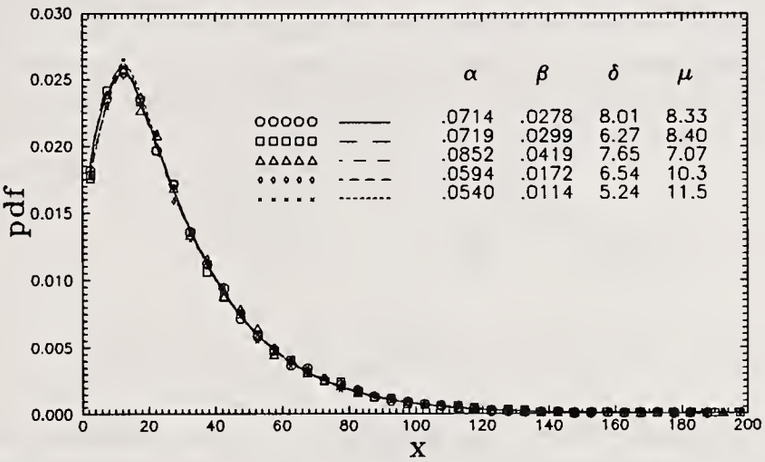

Figure 1: 4P-H fittings for simulated distributions

Initially, an improvement of the estimation stability was attempted by first taking the logarithm of x prior to grouping and fitting the distribution. This has the effect of elongating the left side tail of the distribution. This approach was also studied by simulation and Fig.2 illustrates several simulations using actual parameter values found empirically in a paint spray. In fact, using the logarithm of x tends to shorten the right side tail of the distribution and the table included in Fig.2 indicates that to some extent the stability problem still exists.

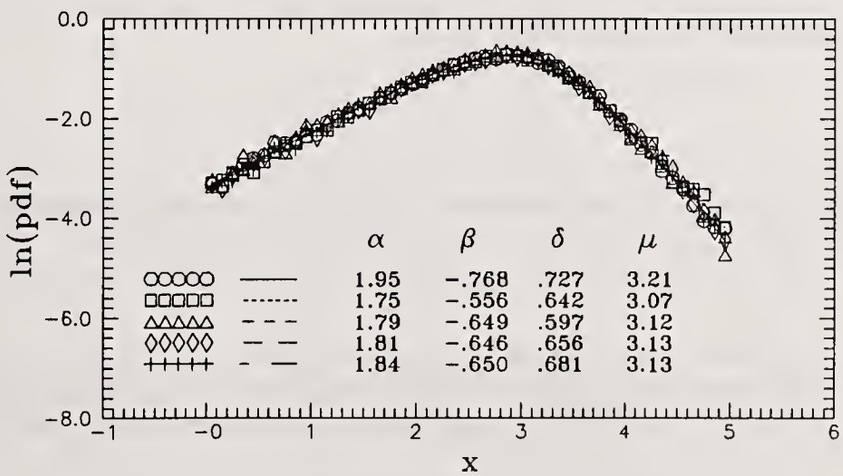

Figure 2: 4P-H fittings for simulated distributions

Thus the length of the available "tails" in the distribution is a deciding parameter in determining the applicability of the 4P-LH distribution. To investigate the influence of the tail portion in more detail Eq.(1) can be written as

$$\ln f = \ln A + (-\alpha\sqrt{\delta^2 + (x-\mu)^2}) + \beta(x-\mu) \ . \tag{4}$$

From this equation it is seen that $\ln f$ comprises three terms, $\ln A$, a standard hyperbola and a straight line, the slope of which is given by β. To investigate the stability problem the symmetrical case of the distribution can be considered, i.e. $\beta = 0$, allowing Eq.(4) to be written as

$$\ln f = \ln A + (-\alpha\sqrt{\delta^2 + (x-\mu)^2}) \ , \tag{5}$$

indicating that the slopes of the asymptotes are given by $\pm\alpha$ while the peak value of $\ln f$ depends on $\ln A$ and $\alpha\delta$.

If the measured distribution has long tails then the square root factor is dominated by $(x-\mu)^2$ rather than δ^2 in tail regions. A possible measure of this effect is the extreme values of $(x-\mu)^2/\delta^2$, shown in Table 1 for two of the simulation cases. Case A represents the non-truncated case mentioned above which yielded stable parameter estimates and case B is the distribution shown in Fig.2. The poorer estimates (Case B) were associated with extreme values of $(x-\mu)^2/\delta^2$ being less than about 20.

	left side $(x_{min}-\mu)^2/\delta^2$	right side $(x_{max}-\mu)^2/\delta^2$
Case A	283	853
Case B	22	7.64

Table 1: Comparison of tail effects of two simulation cases

If $(x-\mu)^2/\delta^2$ takes large extreme values, thus dominating the square root factor, the parameter α can be uniquely determined by the asymptote slopes. If on the other hand the parameter δ remains considerably influential as in Case B, then the distribution can be fitted with arbitrary combinations of α and δ, which results in a less stable parameter estimation. Note that the freedom in choosing α and δ combinations is only possible because the norming quantity $\ln A$ will automatically shift the fitted distribution to a correct vertical position, fulfilling Eq.(2).

3. THE THREE-PARAMETER LOG-HYPERBOLIC (3P-LH) DISTRIBUTION

In an effort to avoid the estimation stability problem of the 4P-LH distribution outlined above, the 3P-LH distribution is introduced. This is introduced on the assumption that the particle distribution, especially in sprays, is described by a hyperbola when plotted in logarithmic coordinates. The derived distribution will then be related to the more well known 4P-LH distribution.

A hyperbola is given in its general form as

$$\frac{Y^2}{b^2} - \frac{X^2}{a^2} = 1 \ . \tag{6}$$

Since a normalization constant will be introduced later which automatically shifts the distribution to the correct position in the y direction, the constant b could be arbitrarily set to 1, yielding

$$Y = -\sqrt{1 + X^2/a^2} \ . \tag{7}$$

An asymmetry must be introduced to correspond to experimental observation, however the addition of a linear term, as in the 4P-LH distribution is undesirable as the geometric meaning of the parameters becomes unclear. In the present case a rotation of the coordinates by an amount given by the angle θ is introduced instead:

$$X = x\cos\theta - y\sin\theta \tag{8a}$$

$$Y = x\sin\theta + y\cos\theta \ . \tag{8b}$$

Combining equations (7) and (8) results in

$$y = -\frac{a}{a^2\cos^2\theta - \sin^2\theta}\sqrt{(a^2\cos^2\theta - \sin^2\theta) + x^2} - \frac{(a^2+1)\sin\theta\cos\theta}{a^2\cos^2\theta - \sin^2\theta}x \quad . \tag{9}$$

The abscissa of the vertex of Eq. (9) is given by

$$\mu_0 = -\frac{(a^2+1)\sin\theta\cos\theta}{\sqrt{\frac{a^2 - (a^2+1)^2\sin^2\theta\cos^2\theta}{a^2\cos^2\theta - \sin^2\theta}}} \quad . \tag{10}$$

Introducing a location parameter μ, which shifts the curve horizontally, the final probability density function takes the form of

$$f(x) = A\exp\{-\frac{a}{a^2\cos^2\theta - \sin^2\theta}\sqrt{(a^2\cos^2\theta - \sin^2\theta) + (x+\mu_0-\mu)^2} - \frac{(a^2+1)\sin\theta\cos\theta}{a^2\cos^2\theta - \sin^2\theta}(x+\mu_0-\mu)\} \; . \tag{11}$$

This distribution is pictured in Fig.3 in which the physical meaning of the 3 parameters is apparent. The parameter $a > 0$ determines the slope of the asymptotes in the unrotated coordinate system. The parameter $|\theta| < min\{\tan^{-1} a, (\sin^{-1} 2a/(a^2+1))/2\}$ is the rotation angle. The parameter μ is the position of the vertex (mode). A is a normalization constant, as given before by Eq.(2).

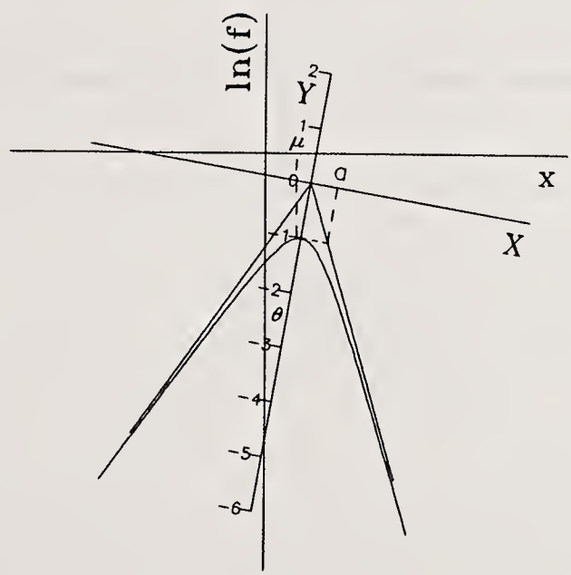

Figure 3: The three-parameter hyperbolic distribution

The distribution $f(x)$ given by Eq.(11) is termed "the three-parameter hyperbolic (3P-H) distribution". When x follows this distribution, the distribution of $s = \exp(x)$ is "the three-parameter log-hyperbolic (3P-LH) distribution".

This distribution can be related to the four parameter distribution using the following relations:

$$\alpha = \frac{a}{a^2\cos^2\theta - \sin^2\theta} \tag{12a}$$

$$\beta = -\frac{(a^2+1)\sin\theta\cos\theta}{a^2\cos^2\theta - \sin^2\theta} \tag{12b}$$

$$\delta = (a^2\cos^2\theta - \sin^2\theta)^{1/2} \tag{12c}$$

$$\mu_{(4p)} = \mu_{(3p)} - \mu_0 \quad . \tag{12d}$$

The norming constant A of the three-parameter hyperbolic distribution can also be found by combining Eqs.(12) and (3):

$$A = \frac{\sqrt{a^2 - (a^2+1)^2 \sin^2\theta \cos^2\theta}}{2a\sqrt{a^2\cos^2\theta - \sin^2\theta}\, K_1(\sqrt{\frac{a^2 - (a^2+1)^2 \sin^2\theta\cos^2\theta}{a^2\cos^2\theta - \sin^2\theta}})} \quad . \tag{13}$$

In addition, all the statistical quantities such as moments and mean diameters can be obtained immediately by using Eqs.(12) and the available formulas for the hyperbolic distribution in [8].

Several methods of parameter estimation for the 3P-LH distribution have been investigated. The maximum likeness estimation, as proposed in [1], has been found to be superior to the maximum likelihood approach and to the method of least squares. This conclusion is based on comparisons of the computed mean diameters and moments and held also for the agreement of the estimated parameters with the true values in fitting the simulated data, especially in the cases in which the tails of the measured distribution are incomplete.

Since the three parameters are related simply to the shape of the distribution, they can be roughly estimated directly by referring to Fig.4 and using the relations

$$a = \tan\left(\frac{1}{2}\tan^{-1}\frac{x_m - x_1}{1 + y_m - y_1} + \frac{1}{2}\tan^{-1}\frac{x_2 - x_m}{1 + y_m - y_2}\right) \tag{14a}$$

$$\theta = \frac{1}{2}\left(\tan^{-1}\frac{x_m - x_1}{1 + y_m - y_1} - \tan^{-1}\frac{x_2 - x_m}{1 + y_m - y_2}\right) \tag{14b}$$

$$\mu = x_m \quad . \tag{14c}$$

These relations are useful for obtaining initial values for the minimizing procedure in the maximum likeness estimation.

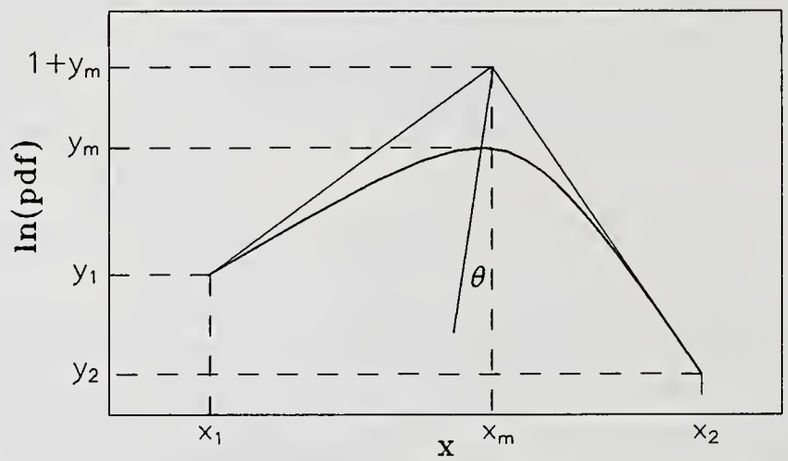

Figure 4: Rough estimation of the parameters

The parameter estimation of the 3P-LH distribution is found to be well behaved and stable, even for samples with very short distribution tails. This is illustrated in more detail in the following section.

4. APPLICATIONS AND EVALUATION

The stability of the parameter estimation for the 3P-LH distribution is evaluated by repeating the simulation presented in Fig.1, using a truncated input sample. Fig.5 illustrates that the three estimated parameters, expressed in this figure as the conventional four parameters according to Eqs.(12), vary little for different simulations, reflecting the similarity of the different fitted curves. The improvement over the 4P-H distribution is clearly evident.

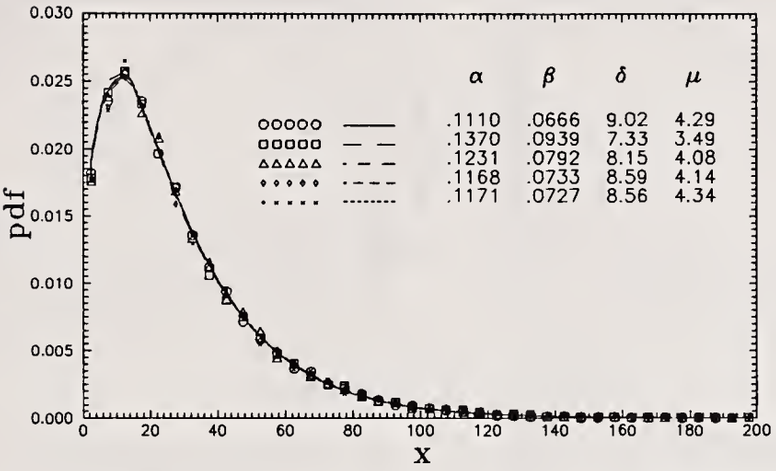

Figure 5: 3P-H fittings for simulated distributions

Durst and Macagno[2] have applied the log-hyperbolic distribution to seven different cases of particle distributions, namely the mass-size distribution of a sand sample, the size distribution of diamonds, the size distribution of river bed sediments, the size distribution of glacio-fluvial sediments, the measurement of aerosol distributions, the particle size distribution in a spray and a molecular weight distribution. The results show that the log-hyperbolic distribution successfully represents the particle size distributions of all of these particle systems. In the present study, the three-parameter log-hyperbolic distribution was also applied to these seven cases using the same input data.

Fig.6 illustrates a direct comparison between the 3P-LH and 4P-LH fitted distributions and indicates that the former provides an equally good representation in all cases except perhaps for the two sediment examples.

Further examples of the application of the 3P-LH distribution are presented using spray data. These data are taken from a low pressure water spray, having also been analyzed by Bhatia and Durst and corresponding to Example 2 in [7] and data sets 4,5 and 6 in [3] respectively. The results of the fitting are illustrated in Fig.7. From Fig.7 it is seen that, for the most parts, the three-parameter curve is almost indistinguishable from the four-parameter curve.

A more detailed comparison is possible by examining the computed mean diameters and the moments presented in Table 2. Both fitted curves result in almost equally excellent estimates of the mean diameters and moments, therefore the 3P-H distribution can be considered equivalent to the 4P-H for these applications. Despite these similarities, it is interesting to note from Table 3 that the close agreement between the two fitted curves is achieved with significantly different parameter values. In Table 3 Eqs.(12) has been used to compute the four parameters corresponding to the three parameter fit. Accordingly, the fit results in a different set of hyperbolic shape triangle parameter χ and ξ (see Ref.[8]).

A final application example illustrates how the spatial variation of the three estimated parameters in a spray can be used to interpret the physical changes in the size distribution. Fig.8 shows the variations of the three parameters and the mean diameters along the axis of a water spray, the data having been collected using a phase Doppler anemometer.

In the region $z = 8mm$ to $14mm$ parameter a increases slightly, parameter θ decreases and μ remains constant. The rotation indicates a broader distribution especially towards larger droplets, although there is no shift in the mode (vertex). In the region $z = 14mm$ to $16mm$ there is a steep descent in θ and μ, while a decreases only very slowly. This indicates a sudden increase in the percentage of small droplets and a rapid decrease of large droplets, indicating that a violent break-up takes place in this region. Beyond $z = 26mm$, θ and μ begin to increase while a continues to decrease slowly. Here the percentage of smaller droplets is decreasing and the distributions are becoming narrower. The interpretation given above can be verified by examining the behavior of the various mean diameters along the spray center line, also given in Fig.8.

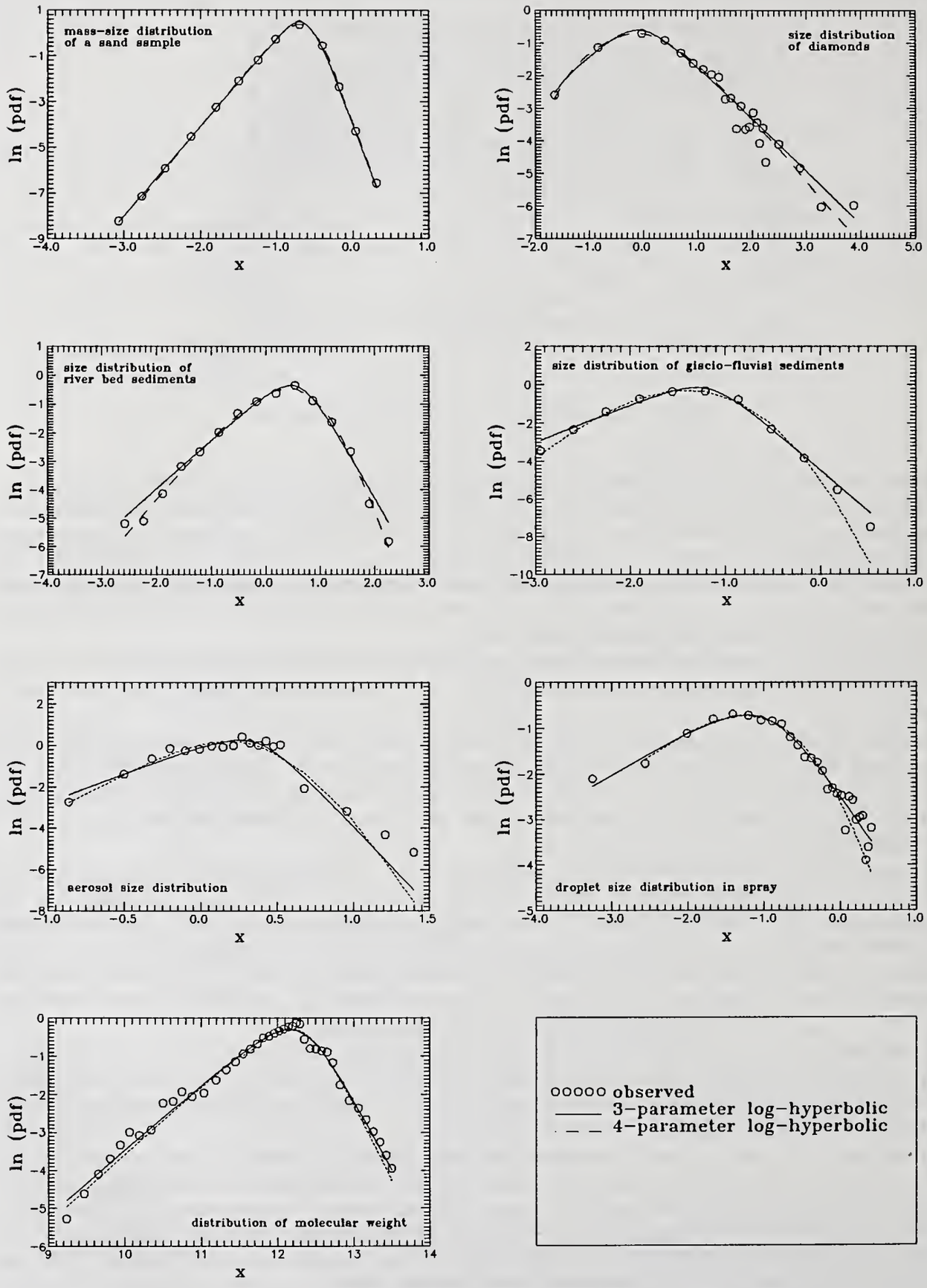

Figure 6: Comparison of 3P-LH distribution with 4P-LH distribution in seven applications

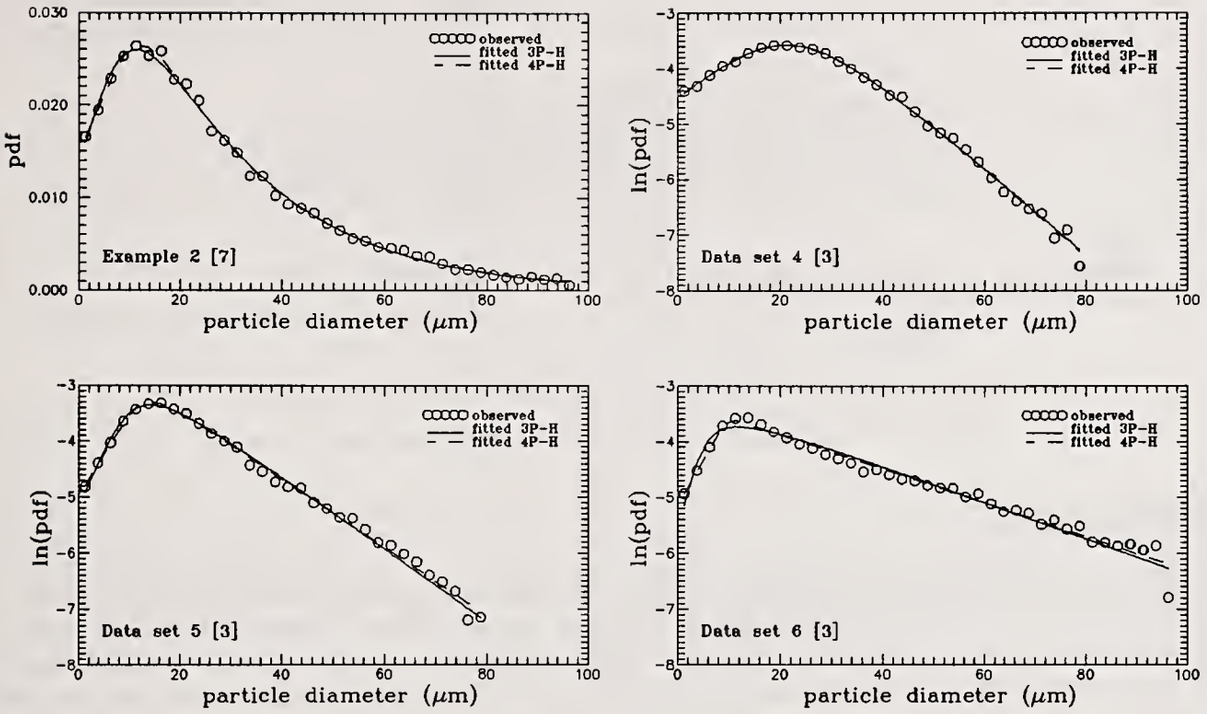

Figure 7: Application of the three-parameter hyperbolic distribution to spray

		D_{10}	D_{20}	D_{30}	D_{32}	m_2	m_3	m_4	m_5	m_6
Ex. 2	Summ.	26.93	33.70	39.50	54.25	411.1	8904	621562	2.62E7	1.69E9
of [7]	3P-H	26.92	33.67	39.45	54.17	409.0	8870	624360	2.90E7	1.73E9
	4P-H	26.92	33.72	39.56	54.46	412.6	9105	639223	2.99E7	1.78E9
Data	Summ.	25.61	29.79	33.36	41.83	231.8	2535	1.78E5	5.03E6	2.50E8
No. 4	3P-H	25.60	29.79	33.39	41.94	232.5	2603	1.83E5	5.25E6	2.61E8
of [3]	4P-H	25.60	29.79	33.37	41.87	231.9	2568	1.81E5	5.15E6	2.56E8
Data	Summ.	23.51	27.96	32.09	42.28	229.4	3895	2.13E5	7.67E6	3.58E8
No. 5	3P-H	23.50	27.83	31.82	41.60	222.1	3577	1.99E5	7.12E6	3.36E8
of [3]	4P-H	23.50	27.91	31.99	42.03	226.6	3785	2.10E5	7.62E6	3.61E8
Data	Summ.	31.90	39.27	45.36	60.52	524.5	1.07E4	8.03E5	3.39E7	1.99E9
No. 6	3P-H	31.90	38.93	44.80	59.33	497.8	9.81E3	7.53E5	3.16E7	1.88E9
of [3]	4P-H	32.22	39.57	45.72	61.06	509.2	1.03E4	7.84E5	3.34E8	1.98E9

(Summ. represents summation over grouped data)

Table 2: Comparison of the mean diameters and the moments

	fitted with 4P-H	corresponding to 3P-H
α	.06454	0.1119
β	.02184	0.0672
δ	6.5187	8.9568
μ	9.6533	4.5379
χ	.286338	0.4472
ξ	.846385	0.7450

Table 3: Comparison of the parameters for Example 2 from [7]

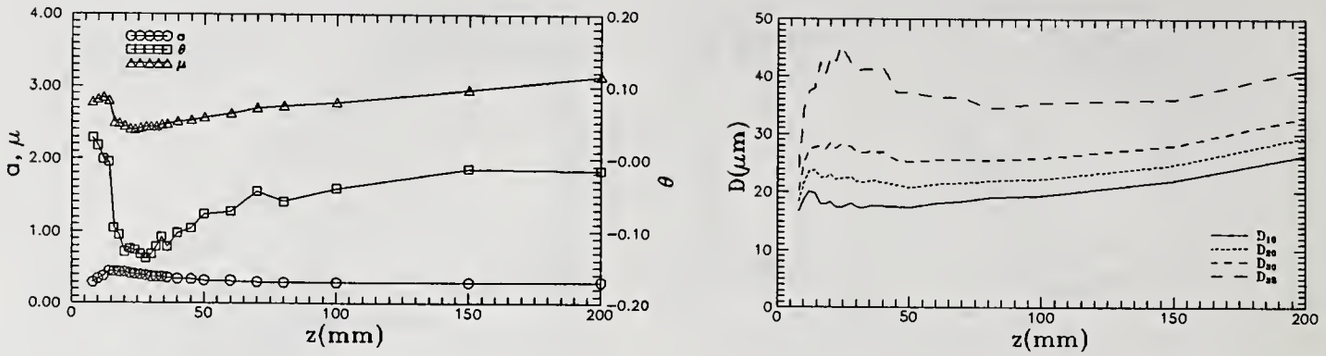

Figure 8: Variation of size distribution along the axis of a spray

5. CONCLUSIONS

In this paper the stability problem in estimating parameters of the four-parameter log-hyperbolic distribution was examined by computer simulation and the importance of the sufficiently long tails was identified. The three-parameter log-hyperbolic distribution was then introduced and shown to be a special case of the 4P-LH distribution. Further simulations indicated that this new distribution did not suffer from the estimation stability problem and gave an equally good representation of measured data for a wide variety of size distribution applications. Detailed examples were given for spray data and for this application the three parameter log-hyperbolic distribution can be recommended for future use.

The financial support of the Deutsche Forschungsgesellschaft through grant Du. 101/14 is gratefully acknowledged, as is a study scholarship from PR China for the first author.

References

[1] Barndorff-Nielsen,O., "Exponentially Decreasing Distributions for the Logarithm of Particle Size", Proc. R. Soc. Lond. A.353, pp. 401-419 (1977).

[2] Durst,F. and Macagno,M., "Experimental Particle Size Distributions and Their Representation by Log-Hyperbolic Functions", Power Tech., 45, pp. 223-244 (1986).

[3] Bhatia,J.C. and Durst,F., "Comparative Study of Some Probability Distribution Applied to Liquid Sprays", Part. Part Syst. Charact., 6, pp. 151-162 (1989).

[4] Li,X. and Tankin,R.S., "Droplet Size Distribution: A Derivation of a Nukiyama- Tanasawa Type Distribution Function", Combust. Sci. Technol., 56, pp. 65-76 (1987).

[5] Domnick,J, Dorfner,V, Durst,F, Tropea,C. and Xu,T.-H., "Bestimmung der Zerstäubungseigenschaften von Lacken: Voruntersuchung", Report No. LSTM 282/I/90, Univ. Erlangen-Nürnberg (1990).

[6] Domnick,J, Dorfner,V, Tropea,C. and Xu,T.-H., "Phasen-Doppler-Messungen an einem Sprühtrockner der Firma LINOR", Report No. LSTM 278/I/90, Univ. Erlangen-Nürnberg (1990).

[7] Bhatia,J.C. and Durst,F., "LHPDF - A PC Package for Estimating Parameters of the Log-Hyperbolic Distribution, Moments and Mean Diameters", Report No. LSTM 230/T/88, Univ. Erlangen-Nürnberg (1988).

[8] Bhatia,J.C., Domnick,J, Durst,F. and Tropea,C., "Phase-Doppler-Anemometry and the Log-Hyperbolic Distribution Applied to Liquid Sprays", Part. Part Syst. Charact. 5, pp. 153-164 (1988).

A DROP SIZE DISTRIBUTION DATA BASE FOR FOREST AND AGRICULTURAL SPRAYING: POTENTIAL FOR EXTENDED APPLICATION

M.E. Teske*, P.J. Skyler† and J.W. Barry†

*Continuum Dynamics, Inc., Princeton, NJ, U.S.A.
†USDA Forest Service, Forest Pest Management, Davis, CA, U.S.A.

ABSTRACT

Over the last several years the USDA Forest Service, and other agencies and companies, have contracted for wind tunnel tests to determine drop size distributions of pesticides and simulant spray material atomized by nozzles. These test results have been assembled into a data base presently containing 224 atomization entries. Nearly all spray materials and nozzle types used by the Forest Service are represented. Access to the data base is through an interface program DROPSIZE, developed specifically for the data base and freely available from the Forest Service. Preliminary examination of some of the data indicates that spray drop size distributions may be correlated based upon physical properties, but that unique details in the distributions dictate the continued use of wind tunnel tests.

INTRODUCTION

The drop size distribution of spray material atomized by nozzles influences the magnitude of evaporation, spray deposition and drift. Several factors affecting the atomization process and the resulting spray distribution include nozzle type, hydraulic line pressure, flow rate, shear across the nozzle orifice and specific properties of the formulation. The details of the resulting distribution are critical, especially to forest and agricultural applications, where specific levels of spray material must be deposited to achieve success and avoid environmental insult. Concerns over aerial spraying have escalated in the past several years, as has the cost of pesticides. It is becoming increasingly clear that the physical processes generating the spray distribution must be better understood. Risk of potential damage from driftable material is becoming too high.

Under the direction of the USDA Forest Service, wind tunnel tests of pesticides and simulant tank mixes have been conducted to:

1. Determine the atomization of tank mixes as influenced by hydraulic line pressure, flow rate, air velocity and shear across the atomizer, components including adjuvants (chemical, physical and biological) in the tank mix, viscosity, specific gravity, surface tension and other atmospheric conditions.
2. Evaluate the mixing and handling of the tank mix.
3. Develop recommendations for field use of the tank mix.

Atomization results from these tests are then used in selecting the optimum combination of factors that have a high probability of meeting field project objectives. Wind tunnel facilities for testing pesticide sprays have been established and are maintained at University of California, Davis, California (the pioneering work of Wes Yates and Norm Akesson); Cranfield

Institute of Technology, England; University of New Brunswick, Canada; USDA Agricultural Research Service, College Station, Texas; and New Mexico State University, Las Cruces, New Mexico.

Recently, the entire complement of spray distributions generated for the Forest Service (224 entries) has been compiled [1] and assembled into an interactive data base [2]. This paper summarizes the contents of this data base, reviews the historical approaches suggested for collapsing spray distribution data, and implements three such approaches as examples of the usefulness of the data base.

DATA COLLECTION

Numerous researchers have investigated spray distributions that are essentially water-based [3,4], oil-based [5] and generated from standard tank mixes [6]. Many other studies have been conducted, but these results are unpublished or held company proprietary. Generic results from these wind tunnel tests indicate the following:

1. Shear across hydraulic nozzles caused by nozzle orientation, and shear across the rotating basket cages of rotary nozzles caused by rotation, are major factors in break up that produce small drops.
2. Increase in surface tension increases drop size.
3. Viscosity is a minor influence on atomization.
4. Rotary atomizers can become overloaded, resulting in larger drop size atomization even when the rotation rate is held constant.
5. Most nozzles produce a large number of small drops (less than 56 micrometers in diameter); however, these drop sizes generally represent less than one percent of the total volume in the spray.
6. Slight changes in some chemical, physical and biological properties of a tank mix can significantly alter the atomization.

It is this last observation that guarantees the continued use of wind tunnel tests. Although the development of atomization models (invoking similarity or dimensional analysis) is currently underway, these models are envisioned to enhance rather than replace the need to characterize tank mixes and spray systems. An examination of spray distributions in the above references indicates a strong dependence upon variables that may not be easily quantified.

Spray drop size distributions are typically developed by using laser probes to scan the spray downstream of the nozzle. A flow-through wind tunnel provides an ambient air stream at the anticipated flight speed of the aircraft. The typical output from a single nozzle study at a single air stream speed, and at other specified conditions depending on the nozzle type, is shown in Figure 1. Here the volume fraction is shown, although the same experiment will recover the number density as well. The typical gross features of interest are:

1. $D_{0.1}$: The diameter below which 10 percent of the spray material is found.
2. Sauter Mean Diameter SMD: the diameter whose ratio of volume to surface area is the same as that of the entire spray.
3. Volume Median Diameter VMD: the diameter below which 50 percent of the spray material is found.
4. $D_{0.9}$: The diameter below which 90 percent of the spray material is found.

The cumulative volume fraction CVF is generally shown, since it tends to smooth the distribution, de-emphasize details of the peak, and offers a result that goes between a value of zero and unity. Further operations on CVF offer the prospects of representing its behavior mathematically. To this point previous researchers have dealt with limited data. Here, the extensive data base generated for the Forest Service offers a new look at some old suggestions for collapsing data.

DATA BASE CONTENTS

Collected from published and unpublished reports, a spray drop size distribution data base has been compiled [1]. This data base covers 40 spray materials and 27 nozzle types in 224 unique distributions. Most applications for these distributions include a variation in air stream speed, angle of the nozzle to the air stream (where applicable) or hydraulic line pressure or atomizer rotation rate. The data base is accessed with an interactive program (called DROPSIZE) that enables the user to extend the data base under linear interpolation (and extrapolation) between known results for flow rate, air stream speed, atomizer rotation rate and nozzle exit angle, where applicable [2]. The code and data base are free from the Forest Service. Table 1 summarizes the spray materials, while Table 2 summarizes the nozzle types available in the data base.

DATA CORRELATION

Trying to find a way to correlate spray drop size distributions, where numerous variables can influence the results, has attracted attention to areas beyond aerial spraying, and has generated numerous insights into the problem. Goering and Smith [7] summarize the various techniques that have been attempted to essentially curve fit CVF. They ended up suggesting a three-parameter technique (upper limit logarithmic normal [8]) that extends the standard logarithmic normal approach [9]. The most redeeming feature of the logarithmic normal representation is the expectation of a straight-line fit through the data plotted on these particular axes.

Lefebvre [10] offers reasons for finding a suitable mathematical representation for the CVF distribution:

1. Provide a satisfactory fit to the drop size data.
2. Allow extrapolation outside the range of measured values.
3. Permit easy calculation of mean and representative drop diameters and other parameters of interest.
4. Provide a means of consolidating large amounts of data.
5. Furnish insight into the basic mechanisms involved in atomization.

The existence of the present data base should continue a process that began over 55 years ago. What is driving the problem now is the requirement by the U. S. Environmental Protection Agency for drift data to support registration and reregistration of certain pesticides. To provide drift data the driftable part of the atomization must be known; however, wind tunnel tests are costly. Therefore, it becomes prudent to seek approaches that might reduce the need for extensive wind tunnel testing.

DATA BASE EXAMINATION

Preliminary correlation of the data in the data base includes three examples. These examples correlate the data following the techniques

suggested previously, and demonstrate how to extend the data base to conditions not contained in the data base.

1. STRAIGHTFORWARD INTERPRETATION OF LOGARITHMIC NORMAL DISTRIBUTIONS

An examination was made for water released from flat fan nozzles at 90 degrees (normal) to a 100 mph air stream. Four flat fan nozzles (8001, 8004, 8010 and 8020) are contained in the data base with these characteristics. Their logarithmic normal distributions are shown in Figure 2.

The data is correlated by straight lines on these axes, assuming:

$$y = a + b\,x \qquad (1)$$

where $x = \log (D)$; $y = \log (- \log (1 - CVF))$ and D = drop diameter (in micrometers). A least squares fit for all four spray distributions gives:

$$a = -14.164$$
$$b = 2.293\ FR^{-0.0363}$$

where FR is the flow rate through the nozzle (for the 8001 nozzle the flow rate is 0.01 gal/min). This correlation collapses the four spray distributions, and, when compared with the original data, shows a standard deviation in volume fraction of 0.024.

2. ROSIN-RAMMLER LOGARITHMIC NORMAL DISTRIBUTIONS

An examination was made for water released from a Micronair AU5000. Seven distributions are contained in the data base: 3750 and 4100 RPMs at 50 mph air stream; 4200, 8000 and 9100 RPMs at 100 mph; and 10850 and 11700 RPMs at 130 mph. The technique in Example 1 collapsed the data by correlating the slope of all of the logarithmic normal curves; here, the drop diameters are first divided by their respective diameters $D_{0.632}$, the diameter below which 63.2 percent of the spray material is found, (as suggested in [10]) before transformation. The result is shown in Figure 3.

The data is seen to nearly collapse to a straight line, discounting the leveling off at larger drop diameters. This line may be determined by Equation 1 where now $x = \log (D / D632)$ and $y = \log (- \log (1 - CVF))$. The least squares fit for all seven spray distributions gives:

$$a = 0.211$$
$$b = 2.206$$

With this normalization, however, the sensitivity of the correlation is moved to the normalizing diameter $D_{0.632}$. Comparison with the original volume fraction data for all seven spray distributions yields a standard deviation of 0.090, a significant variation, due principally to the curve fit in $D_{0.632}$ (which has a standard deviation of 33.9 micrometers). With these simple fits, significant errors can result in spray drop size distribution, as noted in [6] for VMD correlations.

3. MUGELE-EVANS ERROR FUNCTION NORMAL DISTRIBUTIONS

An examination was made for the biological pesticide Foray 48B (*Bacillus thuringiensis*) combined with water in several dilutions, for an 8004 flat fan nozzle at 90 degrees (normal) to a 100 mph air stream. Foray 48B is contained

in the data base in five dilution factors (0 percent, or undiluted; 5, 10, 25 and 50 percent water added by volume). In this example, the error function technique [8], strongly endorsed by [7], is used to correlate the spray distributions.

Goering and Smith [7] give approximate formulae for generating the three parameters needed to represent each spray distribution:

$$D_m = \frac{VMD\ (\ D_{0.1} + D_{0.9}\ ) - 2\ D_{0.1}\ D_{0.9}}{VMD - D_{0.1}\ D_{0.9} / VMD}$$

$$A = \frac{D_m - VMD}{VMD}$$

$$\delta = \frac{0.394}{\log_{10}\ (\ \frac{A\ D_{0.9}}{D_m - D_{0.9}}\ )} \qquad (2)$$

to give

$$CVF = 0.5\ (\ 1 + erf\ (\ \delta z\ )\ )$$

$$z = \log\ (\ \frac{A\ D}{D_m - D}\ ) \qquad (3)$$

and erf is the commonly defined error function. Thus, this approach involves a best fit to an error function for each spray distribution. For this example the data was fit with a single curve using the average values for these three parameters, not including the 50 percent data. The transformed distributions are shown in Figure 4. It may be seen that the error function fit is quite good at the lower drop diameters, and becomes progressively worse for larger drop diameters.

Considerably more work with the data base is needed before deciding on a recommended curve fit technique. The three examples, given above, suggest that some data collapse is possible. Sufficient wind tunnel tests will still be required to define spray distribution limits.

CONCLUSIONS

A preliminary examination of an extended USDA Forest Service spray drop size distribution data base indicates that data correlation and collapse is possible. The sensitivity of the curve fits to slight changes in the volume fraction determines the accuracy of the substituted expressions. Compression of the spray distribution data may result in some inaccuracies; thus, wind tunnel tests will continue to be important. Correlation techniques should however be able to reduce the number of wind tunnel tests required.

REFERENCES

1. Skyler, P. J. and Barry, J. W., "Compendium of Drop Size Spectra Compiled from Wind Tunnel Tests," USDA Forest Service Forest Pest Management Report No. FPM-90-9 (1990).

2. Teske, M. E., "DROPSIZE User Manual," Continuum Dynamics, Inc. Technical Note No. 90-10 (1990).

3. Yates, W. E., Akesson, N. B. and Cowden, R. E., "Measurement of Drop Size Frequency from Nozzles Used for Aerial Applications of Pesticides in Forests," USDA Forest Service Equipment Development Center Report No. 8434-2803 (1984).

4. Bouse, L. F., Carlton, J. B. and Jank, P. C., "Effect of Water Soluble Polymers on Spray Droplet Size," Transactions of the ASAE, Vol. 31, No. 6, pp. 1633-1641, 1648 (1988).

5. Bouse, L. F. and Carlton, J. B., "Factors Affecting Size Distribution of Vegetable Oil Spray Droplets," Transactions of the ASAE, Vol. 28, No. 4, pp. 1068-1073 (1985).

6. Picot, J. J. C., van Vliet, M. W. and Payne, N. J., "Droplet Size Characteristics for Insecticide and Herbicide Spray Atomizers," Canadian Journal of Chemical Engineering, Vol. 67, pp. 752-761 (1989).

7. Goering, C. E. and Smith, D. B., "Equations for Droplet Size Distributions in Sprays," Transactions of the ASAE, Vol. 21, No. 2, pp. 209-216 (1978).

8. Mugele, R. and Evans, H. D., "Droplet Size Distributions in Sprays," Industrial and Engineering Chemistry, Vol. 43, No. 6, pp. 1317-1324 (1951).

9. Rosin, P. and Rammler, E., "The Laws Governing the Fineness of Powdered Coal," Journal of the Institute of Fuel, Vol. 7, No. 31, pp. 29-36 (1933).

10. Lefebvre, A. H., Atomization and Sprays, Hemisphere, New York. pp. 421. See pgs. 79-103 (1989).

Table 1 Spray materials in the USDA Forest Service data base.

Dipel 6L	Thuricide 32LV, 48LV, 64LV
Dipel 6L with Triton	Water
Dipel 8L	Water with Aatrex
Esteron	Water with Esteron
Foray 48B	Water with Manganese Sulfate
Garlon	Water with Manganese Sulfate and Nalco Trol
Glycerine	Water with Nalco Trol
Roundup	Water with Velpar
San 415 SC 32LV	

Table 2 Nozzle types in the USDA Forest Service data base.

Flat fan:	8001, 8002, 8003, 8004, 8006, 8010, 8020
Hollow cone:	D2-23, D2-25, D2-45, D3-45, D4-45, D4-46, D8-45, D8-46, D10-45
Jet:	D8, D10
Raindrop:	RD-7, RD-10
Rotary:	Airbi, Beecomist, Micronair AU5000, Micronair AU7000, Spinner, Unimizer

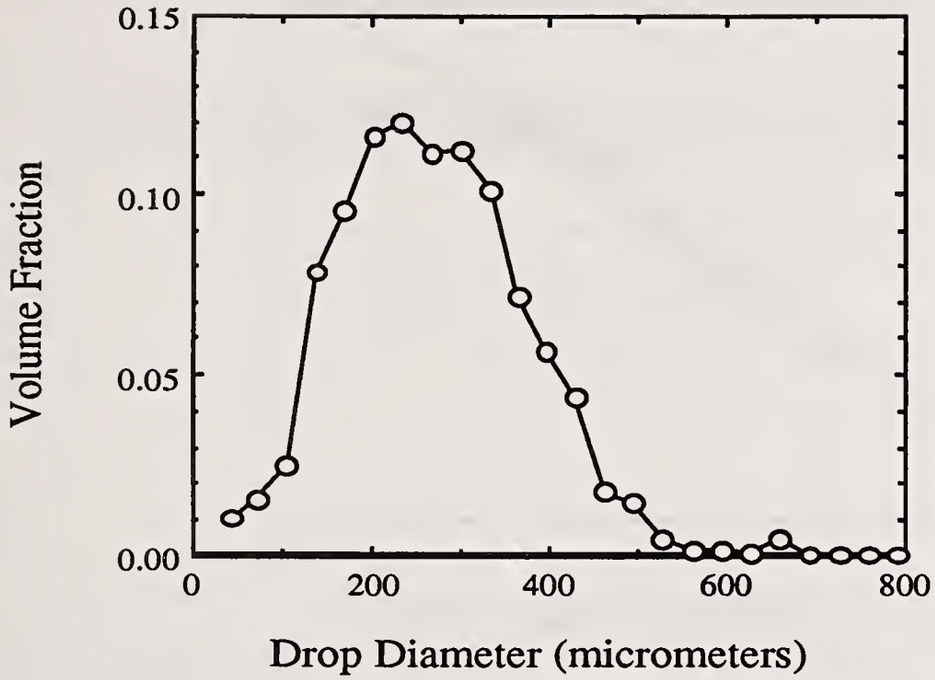

Figure 1 Spray drop size distribution volume fraction for a D4-45 hollow cone nozzle, spraying water, oriented 90 degrees (normal) to a 50 mph air stream. Pertinent drop diameters: $D_{0.1}$ = 131 micrometers; SMD = 223 micrometers; VMD = 263 micrometers; $D_{0.9}$ = 398 micrometers.

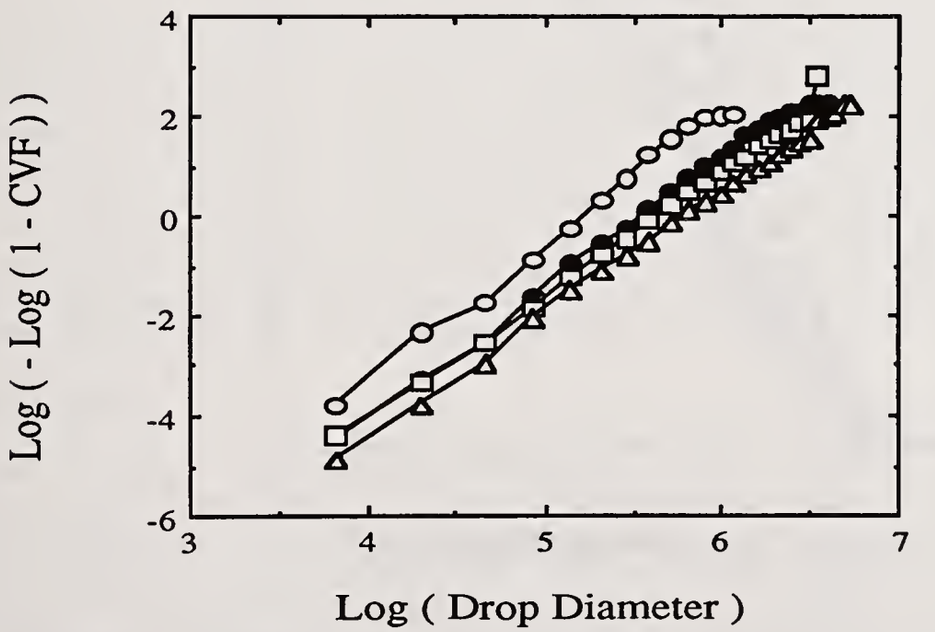

Figure 2 Logarithmic normal distributions for water released from flat fan nozzles at 90 degrees (normal) to a 100 mph air stream. 8001: open circles; 8004: closed circles; 8010: open rectangles; 8020: open triangles.

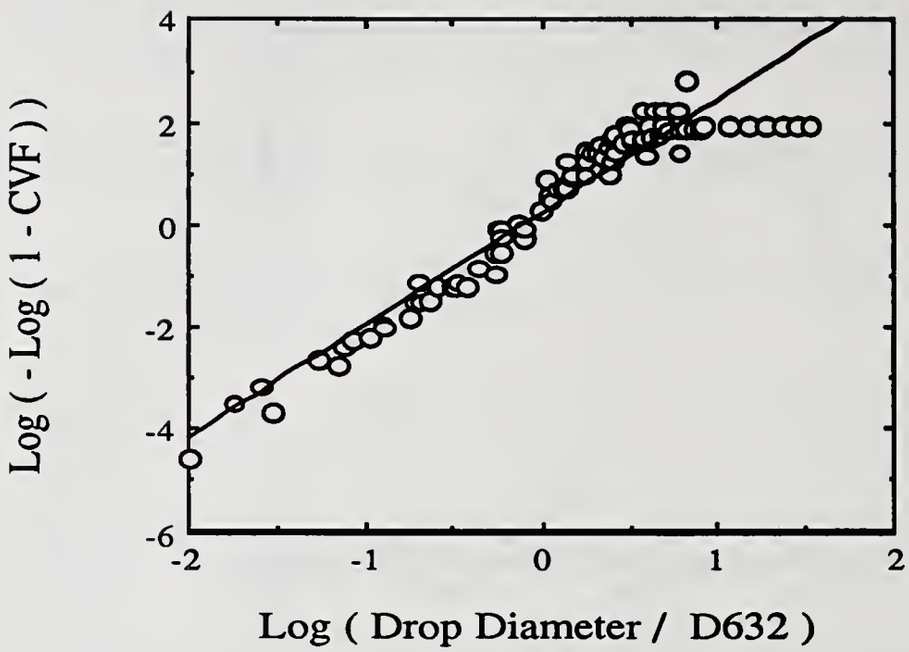

Figure 3 Rosin-Rammler logarithmic normal distributions for water released from seven Micronairs rotating at different RPMs. Data are open circles. Line is least squares fit to all of the data.

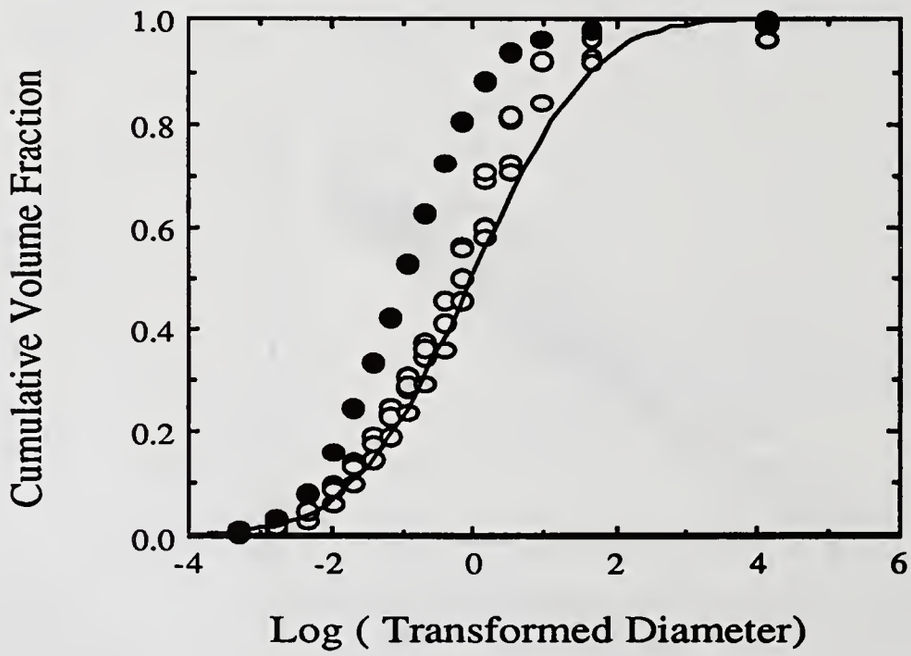

Figure 4 Mugele-Evans transformed distributions for Foray 48B combined with water in five dilutions, and released from an 8004 flat fan nozzle at 90 degrees (normal) to a 100 mph air stream. Open circles are 0, 5, 10 and 25 percent dilution data; closed circles are 50 percent dilution data. Error function curve fit to open circle data is line.

EFFECTS OF INITIAL DROPLET SIZE DISTRIBUTIONS ON POLYDISPERSE SPRAY JET FAR-FIELD DIFFUSION FLAMES

Y. Tambour, I. Silverman and J.B. Greenberg

Faculty of Aerospace Engineering
Technion - Israel Institute of Technology
Haifa, Israel

ABSTRACT

A theoretical study of polydisperse spray jet far-field diffusion flames is presented. In order to analyze the influence of initial droplet size distribution on the flame, a comparison of four kinds of initial droplet size distributions is carried out. These are: (A) a spray of **"small"** droplets of diameters initially within the range of 20-25.2 μm; (B) a **"bimodal"** size distribution with spray droplets initially in two size groups: "small" 20-25.2 μm, and "large" 80-100.8 μm; (C) all droplets of the spray are initially of an **"average"** size of 40-50.4 μm; (D) all droplets are initially **"large"** and are within the limits of the size group of 80-100.8 μm. All other parameters such as: the flow field, the total amount of injected fuel, the evaporation model and the chemical reaction model are kept the same for each of the four cases. The theoretical analysis includes solutions for the spatial evolution in local droplet size distributions which determine the amounts of fuel vapors which are locally released via the evaporation process. Thus, solutions of the present study encompass the mutual relations between local droplet size distributions, local fuel vapor concentrations, and the spatial temperature-field distribution resulting from the combustion process. The spatial variations of these physical properties are explained in the paper, emphasizing the differences between the four kinds of initial droplet size distributions. Significant differences are found in the concentration of droplets and fuel vapors in the far-field and in relatively cold areas in the jet's outer envelope. These differences strongly depend on the initial size distribution and may also be important in future studies of emission of pollutants. Two other important conclusions of the present study are: first, that a spray of an initial **"bimodal"** size distribution cannot be replaced by and initial **"average"** size distribution, and second, that the presence of **"small"** droplets in the initial size distribution significantly affects the behavior of the **"large"** droplets in the spray flame.

INTRODUCTION

There is a series of questions that spray flame researchers often raise. For instance, can a **polydisperse** spray be represented by a group of droplets of an **"average"** size in the theoretical analysis of spray flames? How does a spray flame resulting from a **"bimodal"** initial size distribution of droplets initially in two size groups: "small" and "large" (and nothing in between) differ from a spray flame of droplets of only an **"average"** size? What are the changes that can be expected in a flame resulting form a spray of only **"large"** droplets, if **"small"** droplets are added to the initial size distribution? In the light of the latter question, what should be the accuracy required by modellers in measurements at upstream stations (which may serve as initial conditions for computations) in terms of the **boundaries** of the spectrum of droplet sizes in pointwise spray histograms?

These are a few of the important questions that spray flame modelers face nowadays, especially in

light of the rapid development in measurement techniques [1-12] which supply plenty of experimental data on pointwise droplet size distributions of polydisperse sprays in combusting systems [13,14].

In recent years, comprehensive experimental data on downstream changes in spray characteristics of fuel droplets produced by a twin-fluid (air-kerosene) jet atomizer have been reported by a group of researchers: Yule, Ah Seng, Ereaut, Felton, Ungut and Chigier [3,15-19]. These experimental data indicate the existence of 3 zones in the twin fluid atomizer flow field:

(i) The "atomization zone", (up to some 50 nozzle diameters downstream [19]). Within this zone the break up of the liquid fuel jet into droplets occurs.

(ii) The "near-field" is defined here as the zone that starts immediately after full atomization has been accomplished. The "near-field" is characterized by large differences in momentum between the two phases (the droplets and the surrounding atomizing air).

(iii) The "far-field" is defined here as the downstream zone that follows the "near-field" where experimental data essentially show that most of the droplets travel at a velocity which is close to the host fluid velocity field.

On the basis of these experimental data, theoretical simulations of the **far-field** downstream changes in the integral droplet size distributions and in pointwise spray histograms, have been presented [20, 21], for "cold" and "heated" sprays (i.e. sprays that are introduced to a preheated environment so that vaporization rates are increased, but with combustion occurring).

As to combusting spray jets, effects of far-field coalescence effects on flame height, on maximum flame temperatures, and on the flux percentage of droplets which may "survive" the flame were analyzed by Greenberg and Tambour [22]. They also analyzed [23] the effects of total fuel mass fractions on flame behavior by comparing various flames of the same initial polydisperse size distribution, but of different fuel consumptions.

These two studies serve as a basis for the present study regarding the solution procedure for the flow field equations and the spray model (although coalescence of droplets will not be considered here). Since the purpose of the present study is to shed light on the issues raised in the beginning of the introduction, we focus here on the comparison between four initial droplet size distributions. These are: (A) **"small"** droplets (20-25.2 μm); (B) **"bimodal"** distributions: "small" and "large" (20-25.2 μm and 80-100.8 μm); (C) **"average"** (40-50.4 μm) and (D) **"large"** (80-100.8 μm).

The evaporation model and the chemical reaction model are kept the same for each of the four cases. Also kept the same are the flow field parameters and the total amounts of injected fuel (a mass fraction of 20%).

As previously indicated, the present study is limited to the far-field flow. A more advanced model for jet spray flames which includes the near-field is present being developed by the authors and will be reported.

To analyze the effects of initial droplet size distributions on spray jet diffusion flames, one has to rely on pointwise polydisperse spray histograms at a given up-stream station, which serve as initial conditions for the computations. Thanks to advanced measurement techniques, such pointwise spray histograms have been reported by experimentalists [12-14]. They are usually of a "bar-graph" shape, where each "bar" corresponds to the concentration of droplets within a defined range of droplet diameters, i.e. each "bar" corresponds to **a size group** of droplets, or **a size section.**

Thus, in a similar way, in the present study the local pointwise, polydisperse size distributions are divided into ten size-groups (sections) according to the following droplet diameters: 0-20; 20-25.2; 25.2-31.8; 31.8-40; 40-50.4; 50.4-63.5; 63.5-80; 80-100.8; 100.8-127; 127-160 μm. Conservation equations for each section are used to represent the spray. Derivation of these equations has been described in detail in previous publications [20-26]. Relevant data is also given in Ref. [23].

RESULTS AND DISCUSSION

In order to analyze the influence of initial droplet size distribution on the flame, a comparison between four kinds of **initial** droplet size distributions is carried out. These are: **(A)** a spray of **"small"** droplets of diameters initially within the range of 20-25.2 μm. **(B)** a **"bimodal"** size distribution with spray droplets initially in two size groups: **"small"** 20-25.2 μm, and **"large"** 80-100.8 μm. (C) all droplets of the spray are initially of an **"average"** size of 40-50.4 μm. **(D)** all droplets are initially **"large"** and are within the limits of the size group of 80-100.8 μm. For each of the above cases, the initial mass fraction of the spray is 15%, whereas in the **"bimodal"** distribution, these 15% are equally divided between the small droplets and the large ones.

In Figs. 1a,b, variation of integral fluxes of the liquid phase (i.e. droplets) and the corresponding fluxes of fuel vapors along the axial direction is shown. The integral values at each downstream axial station were obtained by integration of the relevant fluxes over all radial distances. The spatial contours of spray mass fractions and spray pointwise histograms are presented in Figs. 2,a,b,c,d, whereas the corresponding contours of the fuel vapors are shown in Fig. 3.

At the initial upstream station, where the spray is introduced, we assume that the flow already contains a certain amount of fuel vapors (5% for all cases **"A"** to **"D"**). Thus, the fuel vapor fluxes in Fig. 1a all start from the same value. For all cases the initial fuel vapor flux decreases as vapors are consumed by the flame. However, immediately afterwards a significant increase in fuel vapor flux is noticed in case **"A"** (when only small droplets are present) due to the rapid evaporation of small droplets. This is consistent with the corresponding sharp decrease of the liquid fuel flux for this case in Fig. 1b. Eventually, all fuel vapors are consumed by the flame further downstream.

The **"average"** size spray, case "C", exhibits a similar pattern, although the evaporation rate is smaller. In case **"D"**, of only **"large"** droplets, the evaporation rate is even smaller, so that vapors are consumed by the flame before having a chance to build up a high local concentration.

It is interesting to compare the behavior of the **"bimodal"** size distribution, case **"B"**, with all other cases. First, there is a build up of fuel vapors due to the evaporation of the small droplets, (similar to what happens in case **"A"**), and then, the large droplets manage to survive deeper into the flame and are noticeable further downstream (see Fig. 1b).

The influence of **"large"** droplets (80-100.8 μm) on the flame in case **"B"** is different from that of case **"D"**. When **all** the injected droplets are **"large"**, case **"D"**, droplets and fuel vapors are found further downstream and at larger radial distances at the edges of the jet (see Figs. 1, 2d and 3d) and in relatively **"cold"** areas (see Fig. 4). In case **"B"**, **"small"** droplets (20-25.2 μm) are present in the initial size distribution beside the **"large"** ones and significantly affect the behavior of their **"large"** neighbors. The small droplets evaporate faster and their fuel vapors feed the flame. As a result, high temperatures develop at shorter downstream distances (compare cases **"B"** and **"D"** in Fig. 4, note that the **"D"** flame does not reach the temperature of 2100 K) and thus enhance the evaporation of the **"large"** droplets. These effects are most pronounced at downstream stations x=0.1 m and x=0.2 m, as can be seen in Figs. 2b and 2d by comparing the corresponding spray pointwise histograms of case **"B"**

with those of case "D". (Note that the change in scales as one marches downstream. As the spray evaporates, scales change from 10^{-1} (or 10^{-2}) to 10^{-2} and further downstream to 10^{-3}, (or 10^{-4})).

Another interesting observation regarding the downstream pointwise histograms is their staircase-shape, ending in a precipice. Such a shape is visible not only for a "single-bar" initial size distribution (cases "C" and "D"), but also for the initially **"bimodal"** size distribution (case "B").

CONCLUSIONS

To summarize, the influence of initial droplet size distributions on polydisperse spray jet far-field diffusion flames has been analyzed. A comparison of four different kinds of initial droplet size distributions has demonstrated the direct link between these initial conditions and the spatial spreading of the fuel droplets and vapors in the jet's far-field, emphasizing the importance of the small droplets when they are present in the initial size distribution beside the large ones. Finally, a **"bimodal"** size spray and an **"average"** size spray have been compared showing the differences in fuel vapor distributions and in other flame features.

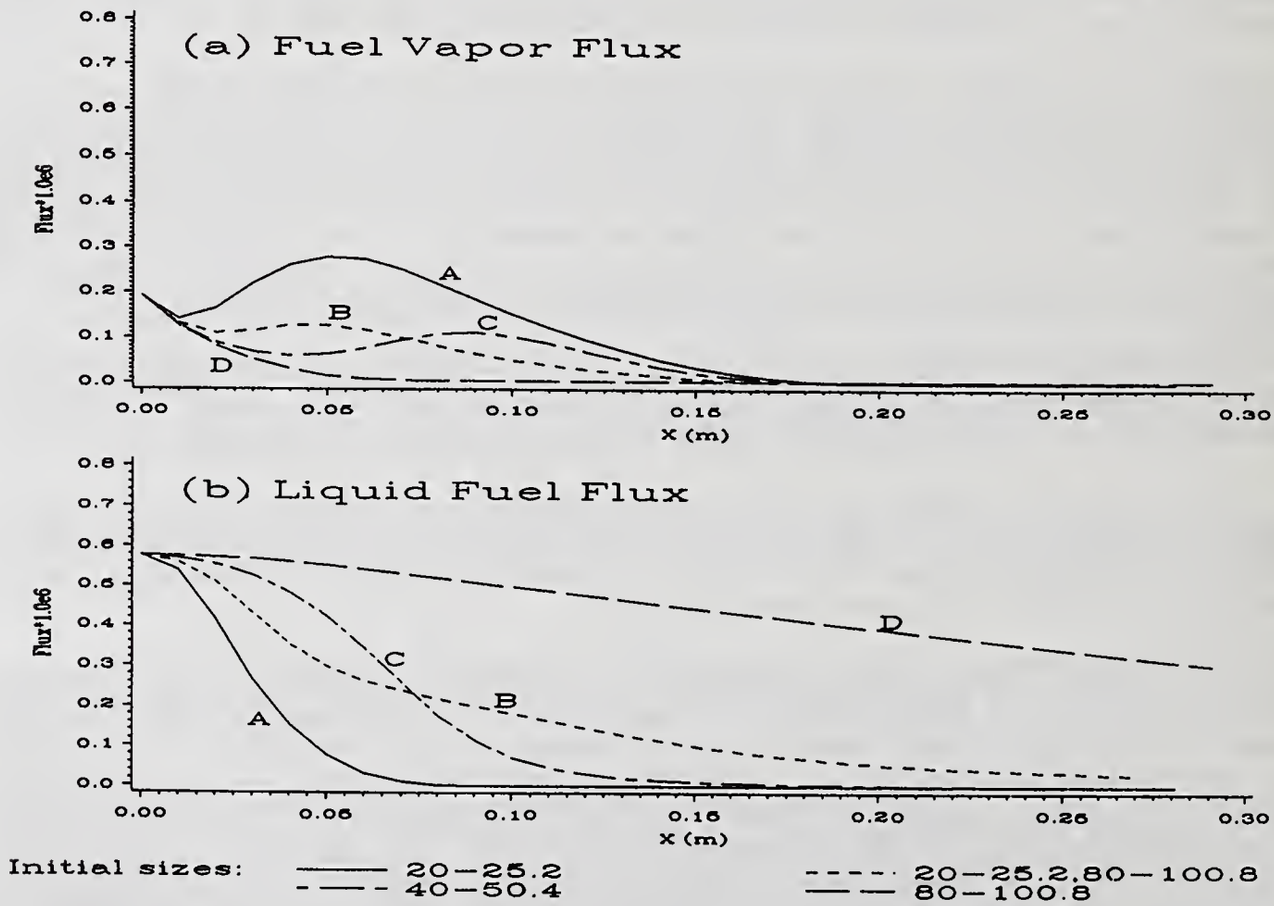

Fig. 1: Variation of fuel-vapor flux and liquid-fuel flux along the axial direction, (each point on the graph represents integral values of the fluxes over all radial distances of the jet).

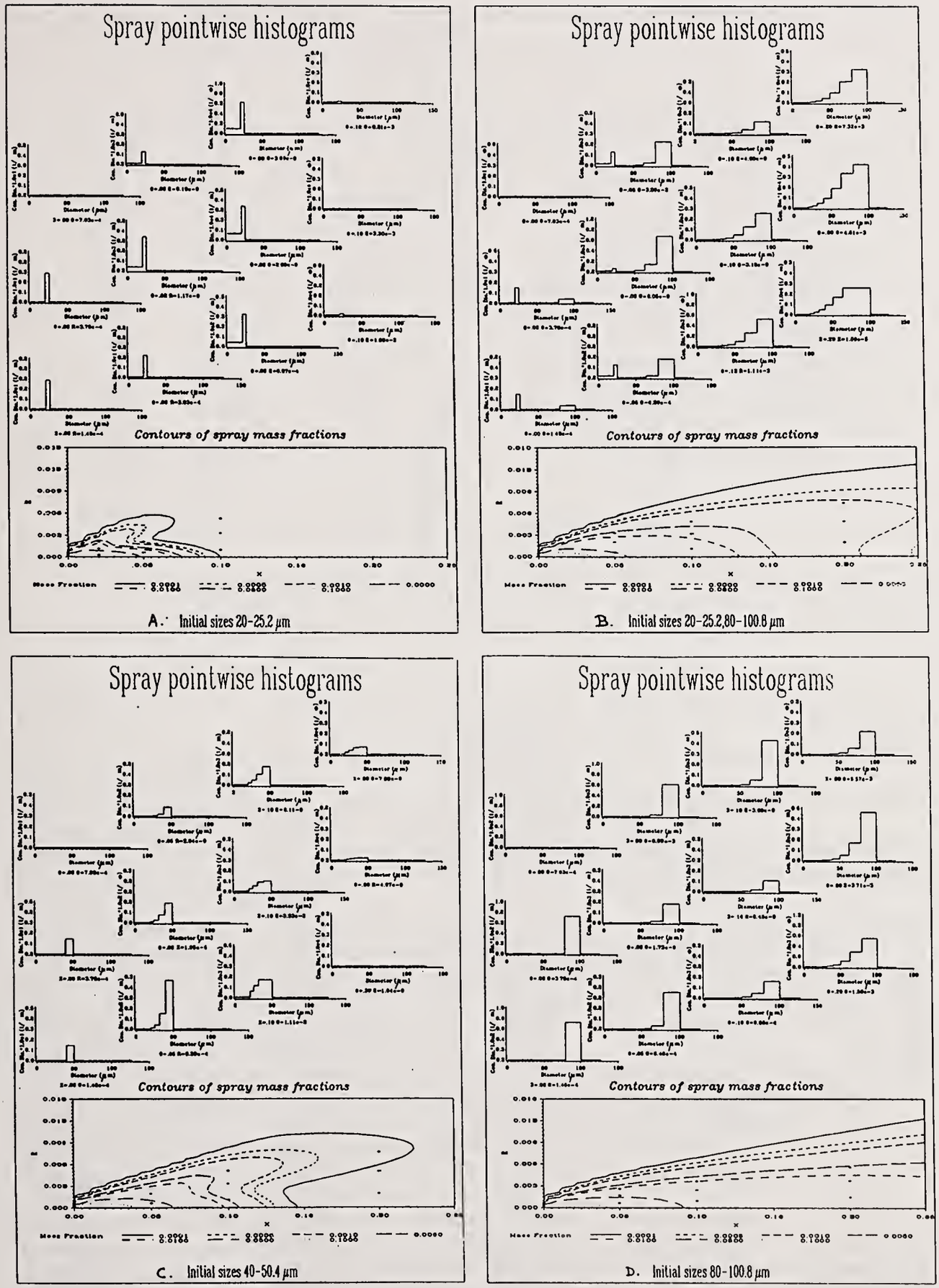

Fig. 2: Spatial distribution of spray mass-fractions and spray pointwise histograms.

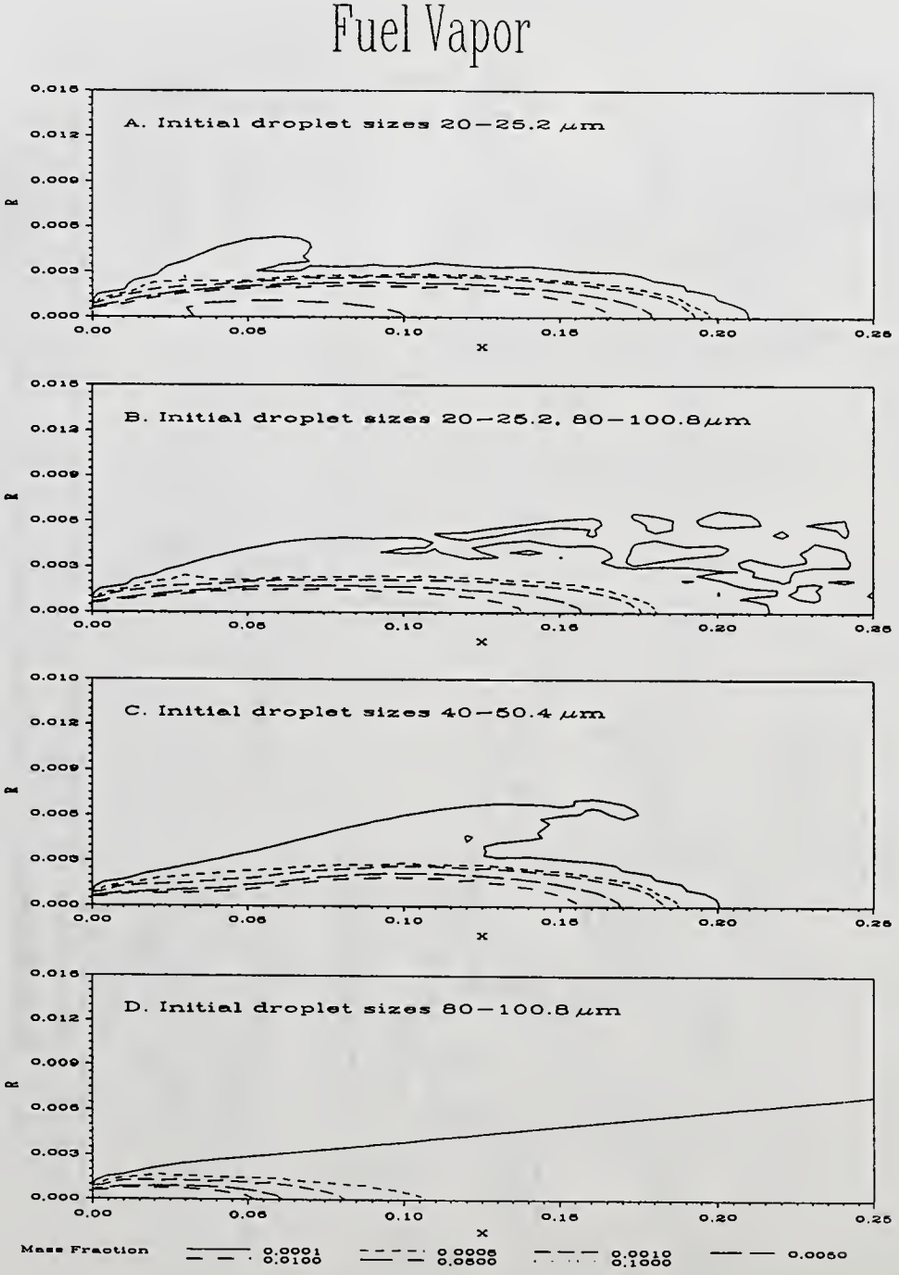

Fig. 3: Spatial distribution of fuel vapors.

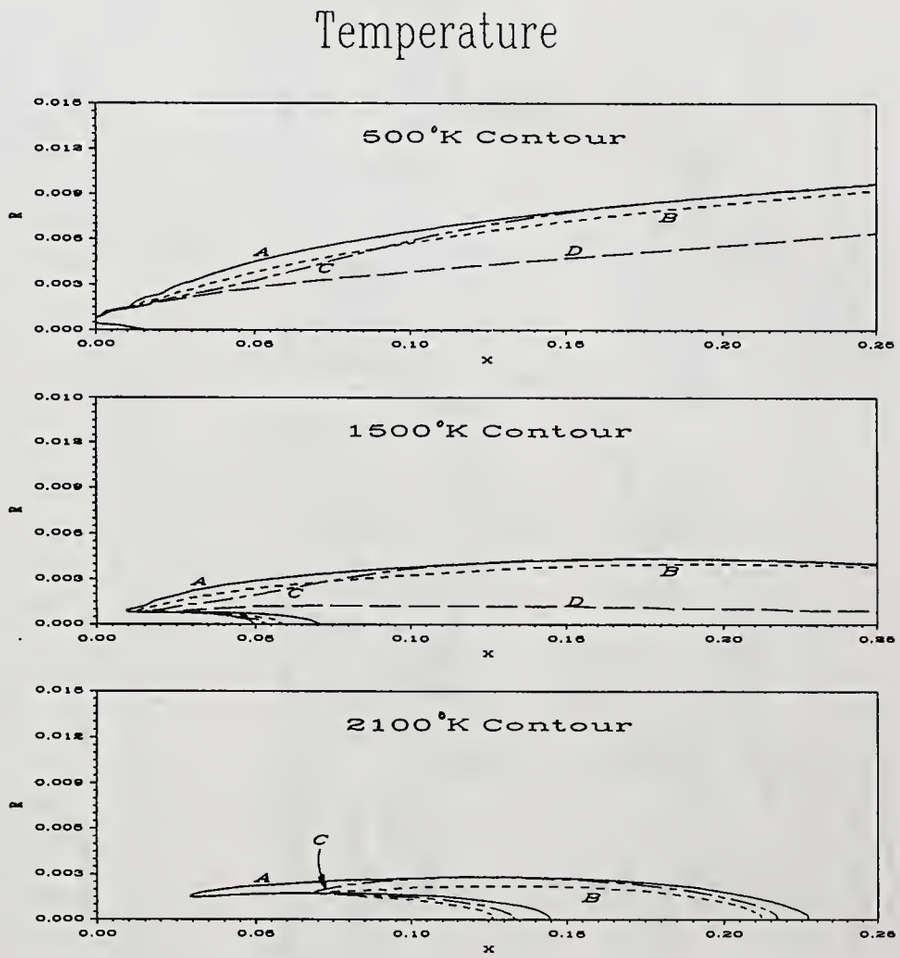

Fig. 4: Flame temperature contours.

TABLE 1
Sectional Vaporization Coefficients

Section no.	Droplet Diameter (μm)	Number of Monomers	$C_j/E(T)$ (μm^{-2})	$B_j/E(T)$ (μm^{-2})
1	0.0 - 20.0	1	0.011250	0.003749
2	20.0 - 25.2	2	0.006672	0.002340
3	25.2 - 31.8	3 - 4	0.004178	0.001498
4	31.8 - 40.0	5 - 8	0.002657	0.000937
5	40.0 - 50.4	9 - 16	0.001668	0.000591
6	50.4 - 63.5	17 - 32	0.001051	0.000372
7	63.5 - 80.0	33 - 64	0.000662	0.000234
8	80.0 - 100.8	65 - 128	0.000417	0.000148
9	100.8 - 127.0	129 - 256	0.000263	0.000093
10	127.0 - 160.0	257 - 512	0.000166	-

Monomer Diameter: 20.0(μm)
E(T) = 980.0(1.0+7.423E-7(T-300.0)**2.7548) ($\mu m^2/s$)

REFERENCES

1. Chigier, N.A., "Drop Size and Velocity Instrumentation", Progress in Energy and Combustion Science, **9**, (1983), pp. 155-177.
2. Chigier, N.A., "Group Combustion Models and Laser Diagnostic Methods in Sprays (A Review)", Combustion and Flame, **51**, (1983), pp. 127-139.
3. Chigier, N.A., Ungut, A. and Yule, A.J., "Particle Size and Velocity Measurements in Flames by Laser Anemometer", Seventeenth Symposium (International) on Combustion, The Combustion Institute, Pittsburgh, (1979), pp. 315-324.
4. Beretta, F., Covaliere, A. and D'Alessio, A., "Drop Size and Concentration in a Spray by Sideward Laser Light Scattering Measurements", Combustion Science and Technology, **36**, (1984), pp. 19-37.
5. Levy, Y. and Timnat, Y.M., "Two Phase Flow Measurements Using a Modified Laser Doppler Anemometry System", *Single and Multiphase Flows in Electromagnetic Fields: Energy, Metallurgical and Solar Applications*, (H. Branover, M. Monds and P. Lykudis, eds.), Progress in Astronautics and Aeronautics Series, AIAA, New York, 1985.
6. Stevenson, W.H., "Spray and Particulate Diagnostics in Combustion Systems. A Review of Optical Methods", Central States Section Meeting of the Combustion Institute, West Lafayette, 1978.
7. Jones, A.R., "A Review of Drop Size Measurements - The Application of Techniques to Dense Fuel Sprays", Progress in Energy and Combustion Science, **3**, (1977), pp. 225-234.
8. Trolinger, J.D., "Laser Diagnostic Methods - A Summary", AIAA 16th Fluid and Plasma Dynamics Conference, AIAA Paper No. 83-1683, 1983.
9. Holve, D.J., "*In situ* Optical Particle Sizing Technique", J. Energy, **4**, (1980), p. 176.
10. Swithenbank, J., Beér, J.M., Taylor, D.S., Abbot, D. and McCreath, G.C., "A Laser Diagnostic Technique for the Measurement of Droplet and particulate Size Distribution", in *Experimental Diagnostics in Gas Phase Combustion Systems, Prog. in Astronautics and Aeronautics*, **53**, (1977), p. 421.

11. Presser, C., Gupta, A.K., Santoro, R.J. and Semerjian, H.G., "Droplet Size Measurements in a Swirling Kerosene Spray Flame by Laser Light Scattering", ICLASS-85 Meeting, **2**, (1985).
12. Bachalo, W.D., Brena de la Rosa, A. and Rudoff, R.C., "Advances in Diagnostics for Complete Spray Characterization", ICLASS-88, (1988), pp. 287-295.
13. Edwards, C.F. and Rudoff, R.C., "Structure of a Swirl-Stabilized Spray Flame by Imaging, Laser Doppler Velocimetry, and phase Doppler Anemometry", Paper presented at the Twenty-Third Symposium (International) on Combustion, Orléans, France, (1990).
14. Presser, C., Gupta, A.K., Avedisian, C.T. and Semerjian, H.G., "Fuel Property Effects on the Structure of Spray Flames", Paper presented at the Twenty-Third Symposium (International) on Combustion, Orléans, France, (1990).
15. Chigier, N.A., Ungut, A. and Yule, A.J., "Particle size and Velocity Measurement in Flames by Laser Anemometer", Seventeenth Symposium (International) on Combustion, The Combustion Institute, Pittsburgh, (1979), pp. 315-324.
16. Yule, A.J., Ah Seng, C., Felton, P.G., Ungut, A. and Chigier, N.A., "Laser Tomographic Investigation of Liquid Fuel Sprays", Eighteenth Symposium (International) on Combustion, The Combustion Institute, (1981), pp. 1501-1510.
17. Yule, A.J., Ah Seng, C., Felton, P.G., Ungut, A., and Chigier, N.A., "Sprays, Drops, Dusts, Particles: A Study of Vaporizing Fuel Sprays by Laser Techniques", Combustion and Flame, **44**, (1982), pp. 71-84.
18. Yule, A.J., Ereaut, P.R. and Ungut, A., "Droplet Sizes and Velocities in Vaporizing Sprays", Combustion and Flame, **54**, (1983), pp. 15-22.
19. Chigier, N.A., *Energy Combustion and Environment*, McGraw-Hill, 1981.
20. Tambour, Y., "A Lagrangian Sectional Approach for Simulating Droplet Size Distribution of Vaporizing Fuel Sprays in a Turbulent Jet", Combustion and Flame, **60**, (1985), pp. 15-28.
21. Tambour, Y., "Coalescence of Vaporizing Kerosene Fuel Sprays in a Turbulent Jet", Atomisation and Spray Technology, **1**, (1985), pp. 125-146. See also: "Simulation of Coalescence and Vaporization of Kerosene Fuel Sprays in a Turbulent Jet: A Sectional Approach", AIAA/ASME/ASEE 21st Joint Propulsion Conference, Monterey, 1985, AIAA Paper No. 85-1315.
22. Greenberg, J.B. and Tambour, Y., "Far-Field Coalescence Effects in Polydisperse Spray Jet Diffusion Flames", Twenty-First Symposium (International) on Combustion, The Combustion Institute, (1986), pp. 655-663.
23. Tambour, Y. and Greenberg, J.B., "Fuel-Injector Far-Field Temperature Distributions Resulting From Coalescence, Vaporization and Combustion of a Polydisperse Spray", ICLASS-88, (1988), pp. 431-438.
24. Tambour, Y., "A Sectional Model for Evaporation and Combustion of Sprays of Liquid Fuels", Israel Journal of Technology, **18**, (1980), pp. 47-56.
25. Tambour, Y., "Transient Mass and Heat Transfer From a Cloud of Vaporizing Droplets of Various Size Distributions: A Sectional Approach", Chem. Eng. Commun. **44**, (1986), pp. 183-196.
26. Tambour, Y., "Vaporization of Polydisperse Fuel Sprays in a Laminar Boundary Layer: A Sectional Approach", Combustion and Flame, **58**, (1984), pp. 103-114.
27. Spalding, D.B., *GENMIX: A General Computer Program for Two Dimensional Parabolic Phenomena*, Pergamon Press, 1977.

APPLICATION OF THE SINGULAR VALUE DECOMPOSITION TO THE INVERSE FRAUNHOFER DIFFRACTION PROBLEM

S. Huzarewicz, G.W. Stewart* and C. Presser

Chem. Sci. and Tech. Lab, National Institute of Standards and Technology, Gaithersburg, MD, U.S.A.
*Department of Computer Science, University of Maryland, College Park, MD, U.S.A.

ABSTRACT

A method for solving the inverse Fraunhofer diffraction problem is presented. The singular value decomposition is used to obtain a solution for the linear system of equations relating an unknown size distribution to a measured diffraction pattern. By using only the larger singular values, an approximate solution is calculated which solves the problem to within the accuracy warranted by uncertainties in the data. The method is stable in the presence of noise, and it is capable of resolving multimodal distributions. Results for both numerical simulations and experimental data are presented.

INTRODUCTION

The size distribution of an ensemble of particles can, in principle, be determined from light scattering measurements. When the particles are larger than a few microns, the angular distribution of scattered light is readily calculated from Fraunhofer diffraction theory. The inverse problem, which is the determination of the size distribution from the diffraction pattern, is more difficult. With varying degrees of success, an iterative method [1], integral transforms [2], and a regularization method [3] have all been used to solve the problem. In this paper a quick, easy-to-use procedure, which relies on the singular value decomposition, is discussed.

Swithenbank *et al.* [4] describe an apparatus, represented schematically in Fig. 1, which measures the angular distribution of scattered light in the near-forward direction (the diffraction pattern). The first lens to the right of the spatial filter collimates the expanded incident beam. The detector, which is a two-dimensional array of concentric, semi-circular photodiodes, is one focal length from the transform lens, so it is effectively an infinite distance from the particle cloud. The two lenses provide adequate, but not the only, conditions for Fraunhofer diffraction; they ensure that the incident light and the diffracted light are parallel. Additionally, the particles must be larger than the wavelength of the light. For the sake of simplicity, the particles are assumed to be opaque spheres in the formulation of the scattering problem.

THEORETICAL BACKGROUND

Highlighting the mathematical development of Swithenbank *et al.*[4], the intensity of light diffracted by a sphere of radius a is:

$$I = I_0 \left[\frac{2J_1(ka\omega)}{ka\omega} \right]^2 , \tag{1}$$

where $k = 2\pi/\lambda$ is the wavenumber, λ is the wavelength of the light source, $\omega \approx r/f$ is the scattering angle, r is the radial distance at the plane of detection, f is the focal length of the transform lens, I_0 is the intensity at the center of the pattern, and J_1 is a Bessel function of the first kind of order one. This function is shown

in Fig. 2. The fraction of the total incident energy, $L(\omega_0)$, contained within a circle of radius ω_0 in the image plane, centered on the geometrical image, is obtained by integrating the right hand side of Eq. (1) over the enclosed area to give

$$L(\omega_0) = 1 - J_0^2(ka\omega_0) - J_1^2(ka\omega_0) \,, \tag{2}$$

where J_0 is a Bessel function of the first kind of order zero. The energy, $E(\omega_1, \omega_2)$, contained within concentric circles of radius ω_1 and ω_2 is

$$E(\omega_1, \omega_2) = C\pi a^2 \left[\left(J_0^2(ka\omega_1) + J_1^2(ka\omega_1) \right) - \left(J_0^2(ka\omega_2) + J_1^2(ka\omega_2) \right) \right] \,, \tag{3}$$

where $\omega_2 > \omega_1$ and C is a constant that depends on the laser power.

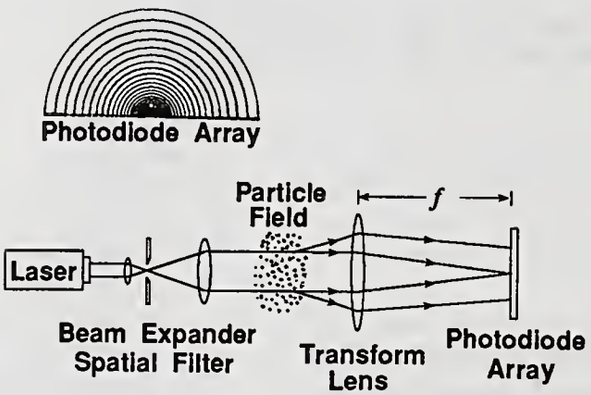

Figure 1: Schematic of the Fraunhofer diffraction apparatus.

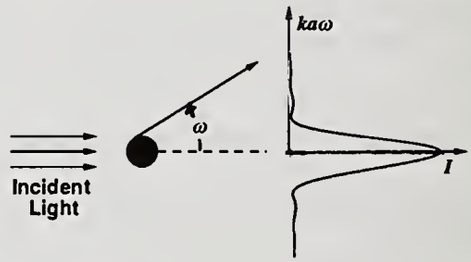

Figure 2: Fraunhofer diffraction for a sphere. The function $I = I_0 \left[\frac{2J_1(ka\omega)}{ka\omega} \right]^2$.

In the absence of multiple scattering, Eq. (3) can be written for a polydispersion as

$$E(\omega_1, \omega_2) = C\pi \sum_{i=1}^{m} N_i a_i^2 \left[\left(J_0^2(ka_i\omega_1) + J_1^2(ka_i\omega_1) \right) - \left(J_0^2(ka_i\omega_2) + J_1^2(ka_i\omega_2) \right) \right] \,, \tag{4}$$

where the sum is over m sizes and N_i is the number of spheres of radius a_i. Equation (4) may be easily recast in a form relating the energy to the weight rather than to the number of particles since $N_i = 3W_i/4\pi a_i^3 \rho$, where W_i is the total weight of particles of radius a_i and ρ is the density of the particles, which is assumed to be size independent. Upon substitution, the result is

$$E(\omega_1, \omega_2) = C' \sum_{i=1}^{m} \frac{W_i}{a_i} \left[\left(J_0^2(ka_i\omega_1) + J_1^2(ka_i\omega_1) \right) - \left(J_0^2(ka_i\omega_2) + J_1^2(ka_i\omega_2) \right) \right] \,, \tag{5}$$

where $C' = 3C/4\rho$. Since the incident beam is not of uniform intensity, it is necessary to assume that the particles are moving through the beam without a correlation between size and velocity and that the measurement time is sufficiently long so that a representative portion of the sample passes through the beam.

If there are n photodiodes, one can write n linear equations in the form of Eq. (5)

$$\boldsymbol{T}\boldsymbol{w} = \boldsymbol{e} \,, \tag{6}$$

where $\boldsymbol{e}$ is a vector with n components e_i, which is the light energy falling on diode i in the detector array, $\boldsymbol{T}$ is an $n \times n$ matrix with components t_{ij}, which is proportional to the light which has been diffracted by a particle of diameter d_j falling on the i^{th} diode, and $\boldsymbol{w}$ is a vector with n components w_j, which is the weight fraction of particles of size d_j. The expression for t_{ij} is

$$t_{ij} = \frac{1}{d_j} \left[\left(J_0^2 \left(\frac{\pi d_j r_{2i-1}}{\lambda f} \right) + J_1^2 \left(\frac{\pi d_j r_{2i-1}}{\lambda f} \right) \right) - \left(J_0^2 \left(\frac{\pi d_j r_{2i}}{\lambda f} \right) + J_1^2 \left(\frac{\pi d_j r_{2i}}{\lambda f} \right) \right) \right] \,, \tag{7}$$

where r_{2i-1} and r_{2i} are the inner and outer radii of the i^{th} diode. The constant C' need not be included since the results are to be normalized, that is, $w_i = W_i / \sum_{i=1}^{n} W_i$.

Physically, Eq. (6) means that any diode receives scattered light from the entire range of particle sizes. However, the maximum energy diffracted by a sphere of diameter d_j falls on the perimeter of a circle (at the detector) with radius r, which is determined from the solution of

$$3J_2\left(\frac{\pi d_j r}{\lambda f}\right) - J_0\left(\frac{\pi d_j r}{\lambda f}\right) = 0 ,$$

(which is the derivative of Eq. (2)) where J_2 is the Bessel function of order two. The solution, calculated numerically with Newton's method, is $\pi d_j r / \lambda f = 1.356602$, or

$$d_j = 1.356602 \frac{\lambda f}{\pi r} . \tag{8}$$

Using this result, a mean particle diameter can be associated with each diode. Likewise, the lower and upper limits of each size class are determined from the outer and the inner radii of the diode, respectively. Any size classes may be chosen as long as the minimum and maximum particle diameters present in the sample are encompassed and the smallest size is larger than the wavelength.

This work was motivated by the need to rapidly obtain a size distribution from the measured diffraction pattern for the purpose of process control. Using the singular value decomposition, the size distribution can be determined directly, without the need to invoke an iterative procedure.

THE SINGULAR VALUE DECOMPOSITION

The singular value decomposition of a matrix $\boldsymbol{T}$ is a factorization

$$\boldsymbol{T} = \boldsymbol{U}\boldsymbol{\Sigma}\boldsymbol{V}^{\mathsf{T}}$$

of $\boldsymbol{T}$ into the product of orthogonal matrices $\boldsymbol{U}$ and $\boldsymbol{V}$ and a diagonal matrix $\boldsymbol{\Sigma} = \mathrm{diag}(\sigma_1, \sigma_2, \ldots, \sigma_n)$, where T indicates the transpose. The numbers σ_i, which are called the singular values of $\boldsymbol{T}$, are nonnegative and are traditionally ordered so that $\sigma_1 \geq \sigma_2 \geq \cdots \geq \sigma_n$. There are efficient, stable algorithms for computing the singular value decomposition [5, 6].

The solution of the system $\boldsymbol{T}\boldsymbol{w} = \boldsymbol{e}$, may be expressed in terms of the singular value decomposition as follows. Let $\boldsymbol{U}$ and $\boldsymbol{V}$ be partitioned by columns in the form

$$\boldsymbol{U} = (\boldsymbol{u}_1\ \boldsymbol{u}_2\ \ldots\ \boldsymbol{u}_n) \qquad \boldsymbol{V} = (\boldsymbol{v}_1\ \boldsymbol{v}_2\ \ldots\ \boldsymbol{v}_n).$$

If $\boldsymbol{T}$ is nonsingular, its singular values are all nonzero, and by the orthogonality of $\boldsymbol{U}$ and $\boldsymbol{V}$ we have

$$\boldsymbol{w} = \boldsymbol{T}^{-1}\boldsymbol{e} = \boldsymbol{V}\boldsymbol{\Sigma}^{-1}\boldsymbol{U}^{\mathsf{T}}\boldsymbol{e} = \sum_{j=1}^{n} \frac{\boldsymbol{u}_j^{\mathsf{T}}\boldsymbol{e}}{\sigma_j}\boldsymbol{v}_j . \tag{9}$$

When some of the singular values are small compared to σ_1, the solution is ill-conditioned; that is, it is very sensitive to perturbations in $\boldsymbol{e}$ and $\boldsymbol{T}$. Stable approximate solutions may sometimes be obtained by truncating the sum, Eq. (9):

$$\boldsymbol{w}^{(k)} = \sum_{j=1}^{k} \frac{\boldsymbol{u}_j^{\mathsf{T}}\boldsymbol{e}}{\sigma_j}\boldsymbol{v}_j . \tag{10}$$

In ill-posed problems, such as the one under consideration here, the truncated solutions behave in the following manner. As k increases, the accuracy of $\boldsymbol{w}^{(k)}$ increases up to a point, after which the solutions become increasingly inaccurate. To see why this happens, note that from Eq. (9)

$$\|\boldsymbol{w}\|^2 = \sum_{j=1}^{k} \frac{|\boldsymbol{u}_j^{\mathsf{T}}\boldsymbol{e}|^2}{\sigma_j^2} .$$

Solutions obtained by application of Eq. (10) to the scattering signature calculated from Eq. (11) with superimposed noise for a log-normal distribution with $\sigma_g = 0.5$ and $D_g = 45\ \mu m$ are presented in Fig. 3. The limits of integration were $d_{min} = 6\ \mu m$ to $d_{max} = 500\ \mu m$. The input distribution was obtained through quadrature of the probability density function over size classes corresponding to those of the diffraction instrument. In the absence of noise, the reconstructed distribution was indistinguishable from the input distribution.

The Sauter mean diameter, $\overline{D}_{32}$, is

$$\overline{D}_{32} = \frac{\int_0^\infty P(D)dD}{\int_0^\infty P(D)D^{-1}dD} \approx \left(\Sigma_{i=1}^n w_i d_i^{-1}\right)^{-1} ,$$

where $P(D)$ is on a weight basis. For the original distribution, $\overline{D}_{32} = 39.7\ \mu m$ while for the distributions determined from the noisy data $\overline{D}_{32} = 39.6\ \mu m$ (0.3% noise) and $\overline{D}_{32} = 39.4\ \mu m$ (2% noise).

The solutions for a Rosin-Rammler distribution with $\alpha = 50\ \mu m$ and $\beta = 3.3$, are shown in Fig. 4. For the original distribution, $\overline{D}_{32} = 38.6\ \mu m$ while for the distributions determined from the noisy data $\overline{D}_{32} = 38.7\ \mu m$ (0.3% noise) and $\overline{D}_{32} = 38.6\ \mu m$ (2% noise).

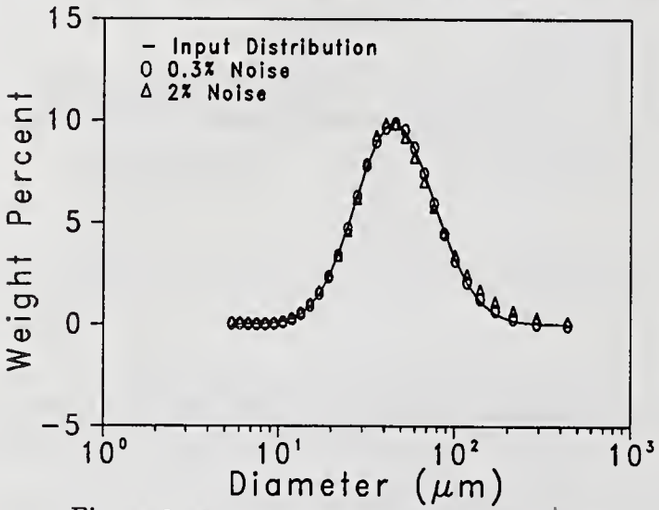

Figure 3: Reconstructed log-normal distribution ($\sigma_g = 0.5, D_g = 45\ \mu m$).

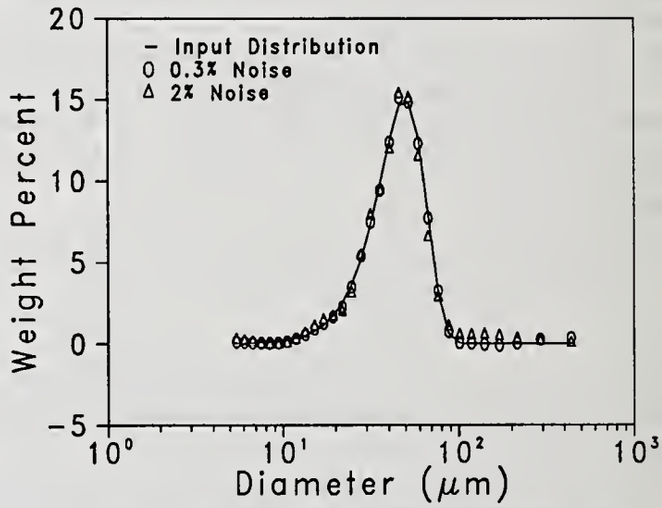

Figure 4: Reconstructed Rosin-Rammler distribution ($\alpha = 50, \beta = 3.3$).

For both cases, in the presence of 0.3% noise, the first twelve singular values ($k = 12$) were used, while for 2% noise only the first nine singular values ($k = 9$) could be used. This suggests that the solution can be determined directly, without the need to calculate the residual at each step in building the solution, once the magnitude of the noise has been determined.

The solutions for the 50 μm monodispersion shown in Fig. 5 are less satisfactory. Although the principal mode is located correctly, several small, fictitious modes appear. Even the solution corresponding to the noiseless data indicates this. Part of the problem lies in the derivation of $\boldsymbol{T}$. None of the d_j from Eqn. (8) is 50 μm, so a meaningful, exact solution of $\boldsymbol{Tw} = \boldsymbol{e}$ does not exist. This suggests that a choice of size bands other than those dictated by Eq. (8) may improve the results.

The solutions for the polydispersion made up of the sum of three log-normal distributions are shown in Fig. 6. The probability density function is simply $P(D) = P_1(D) + P_2(D) + P_3(D)$ where the parameters associated with the subscripts 1, 2, and 3 are $(\sigma_{g1}, D_{g1}) = (0.3, 25\ \mu m)$, $(\sigma_{g2}, D_{g2}) = (0.15, 63\ \mu m)$, and $(\sigma_{g3}, D_{g3}) = (0.2, 125\ \mu m)$. For noiseless data, the original distribution was recovered exactly. With added noise, the modes are correctly resolved although some of the weight fractions are off the mark.

In all of these simulations, the noise added to a particular e_i was in many cases on the order of 20 – 30% of that e_i which is unrealistically large. In order to get a better estimate of the noise, some experimental data were gathered.

From physical considerations we know that $\boldsymbol{w}$ is bounded. Consequently, the inner products $\boldsymbol{u}_j^\top \boldsymbol{e}$ must decrease at least as fast as the σ_j. (Actually, since the small singular values correspond to high frequency components in the solution, the inner products tend to decrease more swiftly than the singular values.)

Now this decrease in the inner products would cause no harm if we could calculate them accurately. However, because $\boldsymbol{e}$ is inevitably contaminated with error, small inner products cannot be computed accurately. To see this, let us assume that what we actually measure is the vector $\boldsymbol{e} + \boldsymbol{g}$, where the components of $\boldsymbol{g}$ are uncorrelated, with mean zero and standard deviation s. Then the inner products we calculate are $\boldsymbol{v}_j^\top \boldsymbol{e} + \boldsymbol{v}_j^\top \boldsymbol{g}$. Since $\|\boldsymbol{v}_j\| = 1$, the standard deviation of $\boldsymbol{v}_j^\top \boldsymbol{g}$ is s, which is independent of j. For small values of j, the inner products are generally quite large and are computed accurately. But as their value decreases toward s, they become increasingly inaccurate, until finally they are overwhelmed by the error term $\boldsymbol{v}_j^\top \boldsymbol{g}$. This error appears in the solution as the vector

$$\frac{\boldsymbol{u}_j^\top \boldsymbol{g}}{\sigma_j} \boldsymbol{v}_j ,$$

whose size is approximately s/σ_j. Since the σ_j are decreasing, the error in the solution grows.

This informal analysis suggests a heuristic for bounding k. Estimate the errors in $\boldsymbol{e}$ and scale the rows of the equation $\boldsymbol{T}\boldsymbol{w} = \boldsymbol{e}$ so that all the errors are roughly equal to a single value, say s (n.b., the scaling must be done before the singular value decomposition is computed). Then k should be chosen so that the inner products $\boldsymbol{u}_j^\top \boldsymbol{e}$ remain larger than s.

Note that our heuristic does not give a predetermined value of k—just an upper bound. A more delicate analysis would take into account the size of the error compared to the size of the solution and the errors introduced in the derivation of $\boldsymbol{T}$. However, formulas based on such analyses are very sensitive to the underlying assumptions, and it is better to base the choice of k on simulations and experiments with real data, to which we now turn.

RESULTS AND DISCUSSION

Simulations

To gain a sense of the accuracy of solutions found through the singular value decomposition, numerical experiments were carried out. Light energy distributions were determined from the log-normal and Rosin-Rammler (or Weibull) distribution functions. The log-normal probability density function by weight is

$$P(D) = \frac{1}{\sqrt{2\pi} D \sigma_g} \exp\left[-(\ln D - \ln D_g)^2 / 2\sigma_g^2\right] ,$$

where D is a random variable representing the diameter, $D_g > 0$ is a scale parameter equal to the geometric mean diameter, and $\sigma_g > 0$ is a shape parameter equal to the geometric standard deviation. For the Rosin-Rammler distribution, the probability density function by weight is

$$P(D) = \frac{\beta}{\alpha^\beta} D^{\beta-1} \exp[-(D/\alpha)^\beta] ,$$

where $\alpha > 0$ is a scale parameter, and $\beta > 0$ is a shape parameter. The mode of this distribution is $\alpha(1 - 1/\beta)^{1/\beta}$ if $\beta \geq 1$. The constant β is a measure of the width of the distribution and α essentially determines the mode. The theoretical light energy distribution was calculated by numerically integrating the product of the density distribution function and Eq. (7) over the range of sizes in the sample

$$e_i = \int_{d_{min}}^{d_{max}} \frac{P(D)}{D} \left[J_0^2\left(\frac{\pi D r_{2i-1}}{\lambda f}\right) + J_1^2\left(\frac{\pi D r_{2i-1}}{\lambda f}\right) - J_0^2\left(\frac{\pi D r_{2i}}{\lambda f}\right) - J_1^2\left(\frac{\pi D r_{2i}}{\lambda f}\right) \right] dD , \qquad (11)$$

where d_{min} and d_{max} are the diameters of the smallest and largest size particles present. To determine the resolution capability of the method, the theoretical scattering signature for a monodispersion of spheres with diameter d_j was obtained from Eq. (7). The same procedure was carried out for a polydispersion composed of the sum of three log-normal distributions. Uniform noise levels on the order of 0.3% and 2% of the maximum diode value were superimposed onto the theoretical scattering signatures and the size distributions were recalculated.

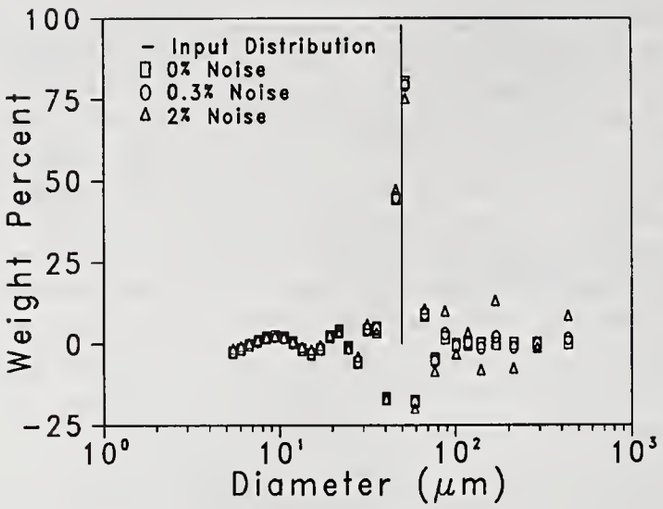

Figure 5: Reconstructed monodispersion of 50 μm spheres.

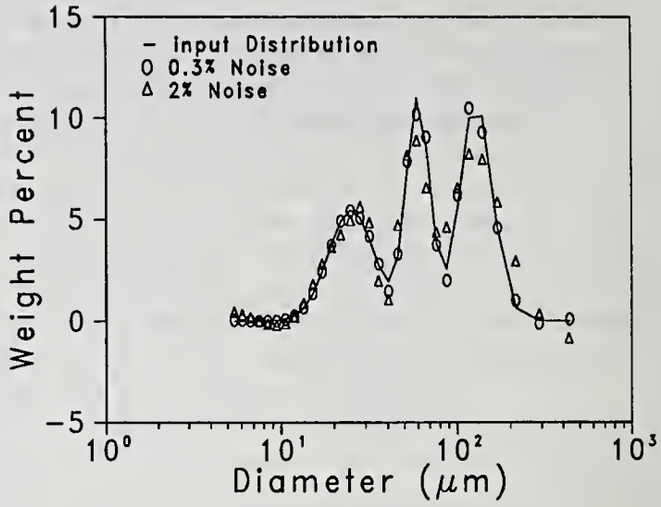

Figure 6: Reconstructed polydispersion of the sum of three log-normal distributions $(\sigma_{g1}, D_{g1}) = (0.3, 25\ \mu m)$, $(\sigma_{g2}, D_{g2}) = (0.15, 63\ \mu m)$, and $(\sigma_{g3}, D_{g3}) = (0.2, 125\ \mu m)$.

Experimental data

In the derivation of $\boldsymbol{T}$ it was assumed that the particles were opaque spheres. The derivation is also valid for circular apertures or opaque discs. A calibration reticle [7], consisting of a random two-dimensional array of chromium discs on a quartz substrate, was used to obtain experimental scattering data from an instrument like the one described by Swithenbank *et al.* [4]. The size distribution of the discs is approximately Rosin-Rammler with $\alpha = 53\ \mu m$ and $\beta = 3.2$. The average deviations of the signals from the diodes were experimentally found to be less than 0.3% of the maximum diode signal. The distributions of the signals were not Gaussian due to fluctuations in the intensity of the light.

Results for the reticle are shown in Fig. 7. The circles correspond to the weight fractions of the discs on the substrate, to which a correction has been applied to account for the Gaussian intensity profile of the incident beam [7]. Calculated from the known distribution, $\overline{D}_{32} = 40.3\ \mu m$ [7]; calculated from the inverted data, $\overline{D}_{32} = 40.2; \mu m$. Despite the good agreement, the residual was somewhat larger than those for the simulated two-parameter distributions. This is because about 10% of the discs overlap — the diffraction model does not account for overlap, just how these should be counted is uncertain.

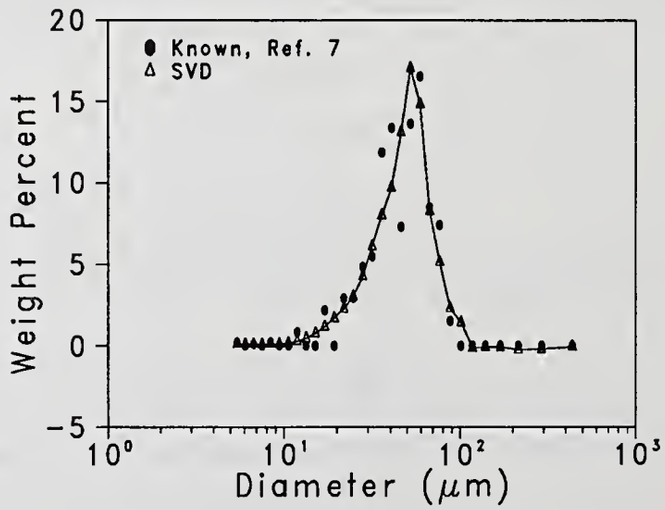

Figure 7: Reconstructed size distribution for the calibration reticle.

CONCLUSIONS

An easy-to-use method of directly solving the inverse Fraunhofer diffraction problem has been demonstrated. This method works well for polydispersions even in the presence of noise. When applied to monodispersions or multimodal distributions, it accurately determines the modes although it tends to spread them out over more than one size class. No technique exists which does not suffer from this deficiency. Because the method is direct, it requires less computational time than iterative procedures, making the use of diffraction-based particle sizing instruments for process control feasible. A singular value analysis is often useful when dealing with ill-posed problems. Its application to the system of equations produced by quadrature of Fredholm integral equations of the first kind, which arises from an alternative formulation of the inverse diffraction problem, will be the subject of a future publication.

ACKNOWLEDGEMENTS

We acknowledge the partial support of the Office of Nondestructive Evaluation, Materials Science and Engineering Laboratory, N.I.S.T.

NOMENCLATURE

a, a_i	radius of sphere
c	ratio of consecutive mean diode radii
C, C'	constants dependent on the laser power
D_g	geometric mean diameter, parameter of log-normal distribution
$\overline{D}_{32}$	Sauter mean diameter
d_j	diameter of sphere
d_{max}, d_{min}	maximum and minimum sphere diameters
E	energy falling on the image or detection plane
e_i	energy falling on i^{th} photodiode
f	focal length of transform lens
$\boldsymbol{g}$	noise vector
I	intensity of diffracted light in the image plane
I_0	intensity at the center of the diffraction pattern
J_ν	Bessel function of the first kind of order ν
k	wavenumber
L	fraction of diffracted energy
N_i	number of particles
n	number of terms in summations, matrix dimension
$P(D)$	probabilty density function in the random variable D, representing particle diameter in this application
r, r_i	radial coordinate in the plane of detection or diode radius
$\boldsymbol{T}, t_{ij}$	scattering matrix of which t_{ij} is an element
T	transpose operation
s	standard deviation of the noise
$\boldsymbol{U}, u_{ij}$	orthogonal matrix of the singular value analysis, u_{ij} is an element of $\boldsymbol{U}$
$\boldsymbol{V}, v_{ij}$	orthogonal matrix of the singular value analysis, v_{ij} is an element of $\boldsymbol{V}$
W_i, w_i	total weight of spheres, w_i is the cooresponding weight fraction
α	scale parameter of Rosin-Rammler distribution function
β	shape parameter of Rosin-Rammler distribution function
λ	wavelength
ρ	density of a particle

$\boldsymbol{\Sigma}, \sigma_i$	diagonal matrix of the singular values, σ_i, of $\boldsymbol{T}$
σ_g	geometric standard deviation, parameter of the log-normal distribution function
ω	dimensionless radial distance in the image plane

REFERENCES

[1] Sangeorzan, B.P., Uyehara, O.A. and Myers, P.S., "Time-Resolved Drop Size Measurements in an Intermittent High-Pressure Fuel Spray," SAE Paper No. 841361, Warrendale, PA (1985).

[2] Koo, J.H. and Hirleman, E.D., "A Synthesis of Integral Transform Methods for Reconstruction of Particle Size Distributions from Forward-Scattered Light," Second Int'l Congress on Optical Particle Sizing, pp. 189-198, Arizona State University, Tempe, AZ (1990).

[3] Hirleman, E.D., "Optimal Scaling of the Inverse Fraunhofer Diffraction Particle Sizing Problem: The Linear System Produced by Quadrature" in Optical Particle Sizing: Theory and Practice (G. Gousebet and G. Gréhan, Eds.), pp. 135-146, Plenum Press, New York, NY (1988).

[4] Swithenbank, J., Beér, J.M., Taylor, D.S., Abbot, D. and McCreath, G.C., "A Laser Diagnostic Technique for the Measurement of Droplet and Particle Size Distribution," Experimental Diagnostics in Gas Phase Combustion Systems (B.T. Zinn, Ed.), Progress in Astronautics and Aeronautics, Vol. 53, pp. 421-447, AIAA, New York, NY (1977).

[5] Golub, G. H. and Van Loan, C., Matrix Computations, Johns Hopkins, Baltimore, MD (1989).

[6] Dongarra, J.J., Moler, C.B., Bunch, J.R. and Stewart, G.W., LINPACK Users' Guide, S.I.A.M., Philadelphia, PA (1980).

[7] Hirleman, E.D. and Dodge, L.G., "Performance Comparison of Malvern Instruments Laser Diffraction Drop Size Analyzers," Third Int'l Conf. on Liquid Atomization and Sprays, pp. 8564/1-8564/14, The Institute of Energy, London, England (1985).

THE ANGULAR PATTERN OF THE SCATTERED LIGHT AND THE LORENZ-MIE THEORY FOR THE STUDY OF OIL SPRAYS

F. Ossler*, F. Beretta†, A. D'Alessio* and A. Tregrossi†

*Dipartimento di Ingegneria Chimica, Università "Federico II", Napoli, Italy
†Istituto di Richerche sulla Combustione, CNR, Napoli, Italy

Abstract

The angular pattern of the polarization ratio $\gamma(\theta)=C_{HH}(\theta)/C_{VV}(\theta)$ of the light scattered by droplets has been computed according to the Lorenz-Mie theory in the size range from 0.02÷50μm. It was found that the scattering due to the smaller droplets with typical size around 1μm is dominated by surface waves effects and the angular pattern presents relevant polarization peak in the backscattering region.This scattering feature has been successfully applied to the characterization of aerosols of light and heavy oils with a Junge size distribution function. The angular pattern of light scattered by sprays of heavy oil atomized by air assisted nozzle presents a similar maximum of the polarization ratio in the backscattering region, thus showing that a large concentration of micron-sized droplets are present also in this condition. A quantitative comparison of the data with the Lorenz-Mie Theory indicates that the overall size distribution of the sprays is bimodal and that the atomization efficiency has large influence on the ratio of the number concentration between the smaller particles and those larger than 20μm.

Introduction

The determination of the size distribution of the droplets is certainly one of the most important problem for studying atomization and spray evolution. The greatest part of the equations proposed in the current literature derives directly or indirectly from measurements method based on visualization of the droplets (1). Now in practice it is almost impossible to visualize a droplet smaller than 3-4μm employing radiation in the visible range, according to the Rayleigh criterium (2); by consequence the lower part of the size distribution is neglected or improperly taken into account.

Light scattering does not suffer this limitation and allows, in line of principle, to determine the size and the optical properties of droplets of any size. In fact when the droplets can be considered as spherical objects the Lorenz-Mie theory provides an exact framework for the interpretation of their experimental angular distribution of the scattered light and their extinction coefficient. The systematic measurements of the angular pattern of the polarized components of the scattered light and their comparison with the theory have been carried out by our group in the last years in single droplets furnaces, sprays and flames (3-6). It was found that the polarization ratio $\gamma(\theta)$ between the horizontally polarized scattered light and the vertically polarized one is a quite sensitive function of the size and optical properties of the

scatterers. More particularly, the polarization ratio in the side scattering region around θ=90° allowed to estimate the presence in the spray of droplets much smaller than those normally reported in the literature. However these studies were based on the hypothesis that the size distribution function was monomodal; an attempt to obtain the droplets size distribution of a light oil spray from the inversion of the scattering spectrum in the u.v., across the threshold of the absorption band, did not give conclusive results for the numerical instability of the inversion method (7).

This paper has the purpose of measuring and interpreting not only the side scattering region, but the whole polarization pattern, with particular emphasis to the backscattering regions, in order to asses the presence and role of droplets smaller than 3-4μm. A preliminary theoretical section contains some numerical results of the Lorenz-Mie theory and summarizes the different regimes of scattering from the limit of very small particles where they behave as Rayleigh dipoles to the limit of very large spheres where the scattering is described by ray optics. The experimental section discusses firstly the results obtained on aerosols produced from both light and heavy oils in comparison with the prediction of the theory. The same type of analysis is then extended to sprays of heavy oils, produced by a home designed internal air assisted nozzle.

The final part of the communication discusses potentialities and limits of the scattering diagnostics and point out the relevances of the results on the size distribution of the smaller droplets for a more deep insight on the processes of atomization and spray evolution.

The angular patterns of the polarization ratio computed by the Lorenz-Mie theory

The Lorenz-Mie theory provides expressions for the angular scattering cross sections in terms of infinite series (2,8):

$$C_{VV}(\theta) = \left(\frac{\lambda}{2\pi}\right)^2 \left| \sum_1^{\infty} \frac{2n+1}{n(n+1)} \left\{ a_n \pi_n(\cos\theta) + b_n \tau_n(\cos\theta) \right\} \right|^2 \qquad (1)$$

$$C_{HH}(\theta) = \left(\frac{\lambda}{2\pi}\right)^2 \left| \sum_1^{\infty} \frac{2n+1}{n(n+1)} \left\{ b_n \pi_n(\cos\theta) + a_n \tau_n(\cos\theta) \right\} \right|^2 \qquad (2)$$

where $C_{VV}(\theta)$ and $C_{HH}(\theta)$ are the vertically and horizontally polarized scattering cross sections respectively and θ is the scattering angle. The dependence of the scattering on the size parameter $\alpha=\pi D/\lambda$ and on the complex refractive index m=n-ik is contained in the functions a_n and b_n, wich represent the strength of the electric and magnetic multipoles of the scattered field, while its angular distribution is determined exclusively by the functions $\pi_n(\cos\theta)=P_n^{(1)}(\cos\theta)/\sin\theta$ and $\tau_n(\cos\theta)=d[P_n^{(1)}(\cos\theta)]/d\theta$, where $P_n^{(1)}$ are associated Legendre functions of the first kind and order n. A discussion of the properties of the Lorenz-Mie series can be carried out only numerically and fig.1 illustrates how the ratio $\gamma(\theta)=C_{HH}(\theta)/C_{VV}(\theta)$, defined as the polarization ratio, varies with the sizes of the droplets in the range 0.02÷50μm at the reference wavelength of 500nm, for two kinds of hydrocarbon mixtures. The right side of fig.1 contains the results computed for a typical light oil mixture transparent in the visible and the left side refers to a heavy oil mixture partially absorbing at λ=500nm. When the size of the droplets is very small respect to the incident light wavelength, only the electric dipole term of the series of eq. 1-2 contributes to the cross sections and the sphere scatters according to the Rayleigh law with $\gamma(\theta)=\cos^2\theta$. If the size is slightly increased the magnetic dipole term and electric quadrupole terms are relevant and the

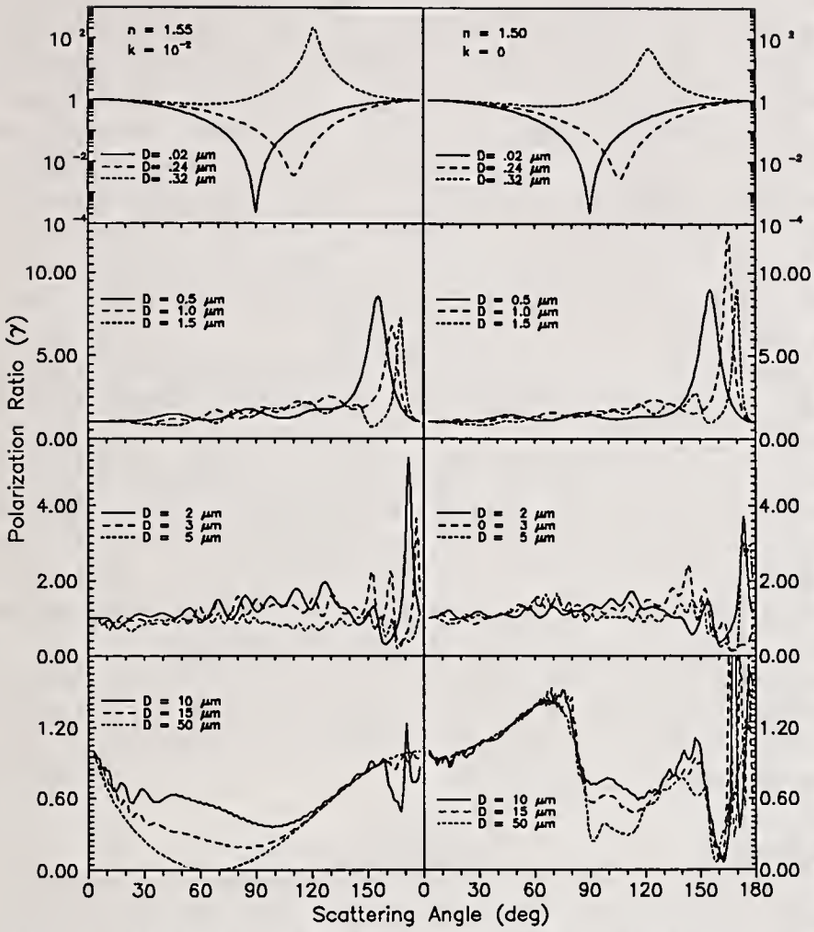

Fig. 1 Angular patterns of the polarization ratio computed by the Lorenz-Mie theory for heavy oil (left) and light oil (right).

minimum of the polarization becomes shallower and shifts in the backward direction, as it appears for the first curves of the upper part of fig.1. As the diameter of the droplets increases, more a_n and b_n functions contribute appreciably to the series. It can be shown that the infinite series can be truncated approximately after n^* terms with $n^* \simeq \alpha+(\alpha)^{1/3}$ and the terms included in the interval $\alpha-(\alpha)^{1/3}$ and $\alpha+(\alpha)^{1/3}$ defines the "edge domain" (9). The a_n and b_n functions in this range present strong resonances with the size reaching values much higher than the other non resonant terms of the series (10). A physical interpretation of this behaviour is that when the sphere is rather small the incident radiation interacts more strongly with a limited region above and below the surface of the particle than with its internal part. Thus the scattered light has mainly the character of a series of surface waves travelling near the boundary of the sphere (11). Furthermore the cross sections in this size range shows also strong variations with the scattering angle due to the oscillatory behaviour of the first associated Legendre functions which define their angular distribution. The angular pattern of polarization becomes a very sensitive function of the size of the scatterers but many of its details are confusing and not relevant when an ensemble polydispersed spheres is considered. Therefore the computations for the size range from D=0.5μm to D=5μm presented in the central part of fig.1 are obtained by averaging the monodisperse case over a ΔD interval of $\pm$0.254μm and a $\Delta\theta$ interval of $\pm$1.6°. It appears that the resonances peaks are smeared out in the greatest part of the angular pattern, where the polarization ratio is close to one, with the evident exception of a relevant peak of positive polarization in the backward region. The angular position and the values of the polarization ratio at the peak changes noticeably with the size and the real part of the refractive index while the absorption index has a lesser influence, as is expected for particles with very large surface to volume ratio. Physically the constructive interference of surface waves in the backscattering is related to complex, and still not understood, mechanisms which are responsible of the glory for larger spheres (9). For droplets larger than 5μm the number of a_n and b_n functions which contribute significantly to the series becomes larger and consequently the non resonant terms outside the edge domain are progressively more relevant. Following the van de Hulst (12) correspondence principle these terms are associated to rays with different impact parameters and are diffracted, refracted or

reflected, according to the laws of ray optics.

The difference between transparent and absorbing droplets becomes quite important in this scattering regime, as it is illustrated by the lower part of fig.1 where the angular pattern of polarization ratio are reported for transparent and absorbing droplets ranging from 10μm to 50 μm. For the transparent case, shown in the right side of the figure, the γ-ratio in the forward follow quite closely that predicted by the geometrical optics considering the contribution of refraction and external reflection. The minimum of the polarization ratio in the backward around θ=160° is instead due to the developing of a strong rainbow which is preferentially polarized in the vertical plane. Scattering effects due to surface waves are still recognizable in the side scattering region where the polarization ratio is higher than that predicted by external reflection, and in the backward, beyond the rainbow, where strong oscillations due to glory effects are present.

The angular patterns of the polarization ratio for partially absorbing droplets show quite different trends, as it appears from the lower left side of fig.1. There is no maximum of the polarization ratio in the forward because the refracted rays are more and more absorbed inside the droplets as its size increases. For the same reason the minimum of polarization at the rainbow angle barely is present for 10μm droplets and disappears for larger spheres.

Also surface waves are heavily damped by absorption and no glory characteristics develop in the backward. Therefore 50μm droplets have an angular polarization pattern identical to that of a purely reflecting sphere with a deep polarization minimum at the Brewster angle.

Experimental Apparatus and Procedures

Experiments were carried out on clouds of droplets of commercial oils: a light oil with $m=1.48-i\cdot1.38\cdot10^{-5}$ and a heavy oil with $m=1.55-i\cdot1.00\cdot10^{-2}$ at λ=488 nm. The complex refractive indexes of the fuels were determined in the following ways: the real parts were determined measuring the Brewster angle while the imaginary parts were determined using a spectrophotometer.

The clouds were generated by two methods: the finer distribution were obtained employing a commercial pneumatic aerosol generator (the heavy oil was diluted with 90% dichloromethane in order to reduce its viscosity); the sprays were produced using an internal mixing air assisted nozzle, whose scheme is reported in the left side of fig.2. The fuel passes through the central duct and interacts with the swirled atomization air, that passes trough four tangential small ducts, in a small chamber located at the top of the nozzle. The spray then comes out from an cylindrical orifice of 0.9 mm ID.

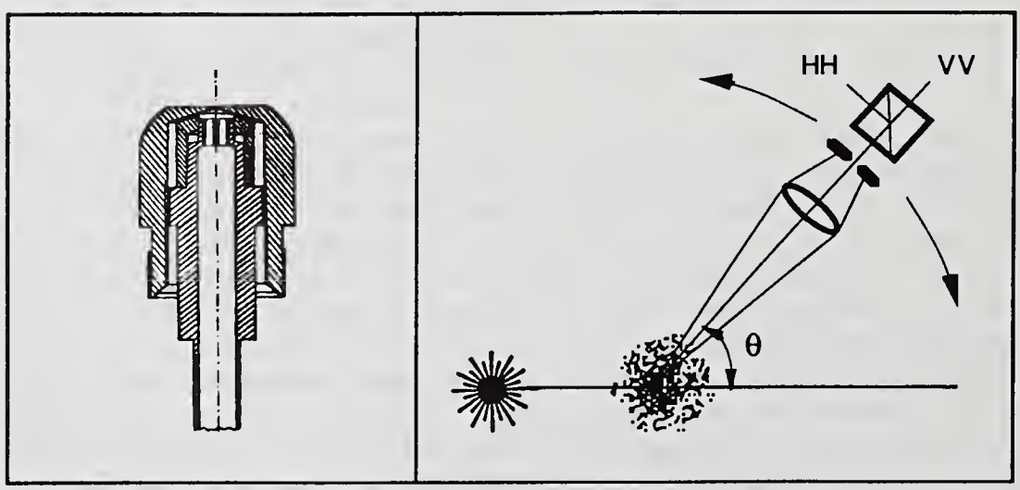

Fig. 2 Air assisted nozzle (left) and optical setup (right).

A sketch of the optical setup used for the scattering measurements is

reported in the right side of the fig.2. The light source used was the blue line of an Ar-ion laser (λ=488 nm) plane polarized at 45° in order to obtain two polarized components, vertical and horizontal, with same intensity in the scattering volume. The collecting optics can rotate around the scattering volume in order to continuously measure the angular profiles of the scattered light. A polarizing cube, inside this optic, discriminates the two polarized components that are simultaneously measured by two lock-in amplifiers and sent to a micro computer. A check of the experimental setup was performed verifying the agreement between the polarization ratio angular pattern of a stream of monodisperse droplets and the corresponding calculated one.

Experimental Results

Typical angular distributions of the polarization ratio of the light scattered by aerosols of light and heavy oils are illustrated in fig.3. The polarization is almost uniform in the forward and side scattering regions with γ close to one while a marked peak of horizontal polarization is found in the backward region near θ=155° for the heavy oil aerosol. A qualitative comparison of the experimental results with the theoretical predictions of fig.1 evidences that the scattering is mainly determined by surface waves effects, typical of droplets with diameter between 0.3μm and 5μm.

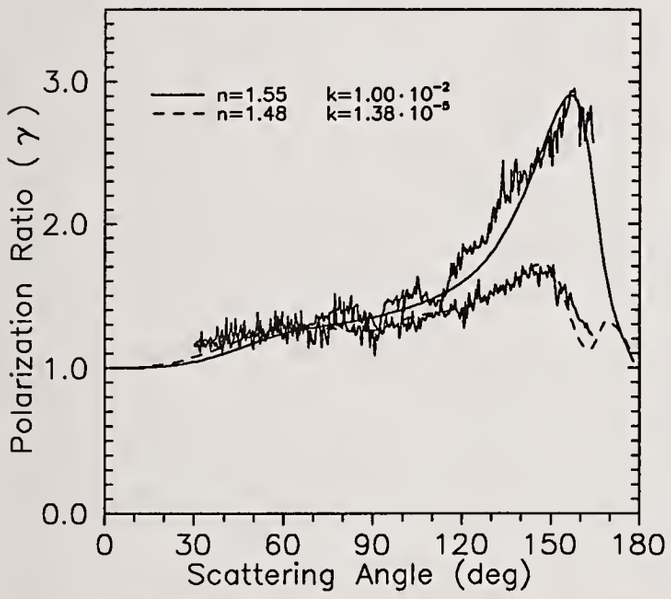

Fig. 3 Measured (noisy curves) and computed angular patterns of the polarization ratio for aerosols of heavy and light oils.

For a quantitative comparison, the polydispersion of the droplets should be taken into account because the measured polarization ratio is given by the expression:

$$\gamma(\theta) = \frac{\int F(D)\ C_{HH}(D,\theta)\ dD}{\int F(D)\ C_{VV}(D,\theta)\ dD} \qquad (3)$$

where F(D) is the number size distribution function of the droplets.

Junge has proposed for size distribution of aerosols an inverse power law $F(D) \propto D^{-P}$ and found p=3 for atmosphere aerosols. In the present case the Junge distribution was modified by neglecting the contribution of droplets larger than 10μm and by considering constant the number concentration of the droplets smaller than a cut-off diameter D_o:

$$\begin{aligned} F(D) &= c && .02\ \mu m \le D \le D_o \\ F(D) &= c\ (D_o/D)^P && D_o \le D \le 10\ \mu m \\ F(D) &= 0 && D > 10\ \mu m \end{aligned} \qquad (4)$$

The integrals of eq.3 were computed with integration steps of ΔD=0.02 μm and $\Delta\theta$=0.2° (angular interval of ±1.6°) and the parameters D_o and p were obtained by the best fitting with the experimental angular patterns. It was found that both the heavy and light oils aerosols patterns were described by the same size distribution with $p \simeq 3.0$ and $D_o \simeq 0.5\mu m$. The same value of the exponent p was obtained from the fitting, when the lower part of the size distribution was modelled assuming a decrease of the number concentration for

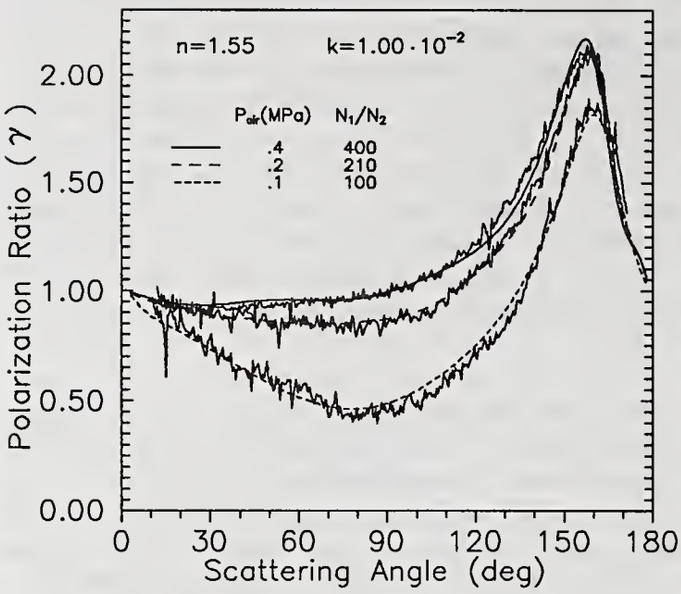

Fig. 4 Measured (noisy curves) and computed angular patterns of the polarization ratio for heavy oil sprays at different pressure of atomization air.

sizes smaller than D_0, thus showing that droplets smaller than 0.2μm do not contribute to the integrals. Having demonstrated the sensitivity of the polarization pattern for the characterization of aerosols, other experiments were devoted to the characterization of sprays of heavy oil produced through atomization. Typical angular patterns of the polarization ratio of the light scattered by sprays atomized at different pressure of the atomization air are reported in fig.4. The patterns are qualitatively similar to those exhibited by the heavy oil aerosol with a relevant peak of polarization in the backward scattering region. However differences are evident in the side scattering region where the γ-ratio is lower than in the previous case and depends on the quality of atomization. In fact a minimum with γ=0.5 is found around θ=80° in the case of the worst atomization with P_{air}=0.1MPa, thus showing that also larger droplets contribute to the polarization pattern, as it is expected.

However, any attempt to fit theoretically the experimental patterns with a single distribution function did not give satisfactory results. In fact Junge distributions with different *p* exponents were able to model the polarization peaks in the backward but gave too high γ-values in the side scattering. Viceversa Γ-functions with a modal value of the size around 5-10μm were able to model the side region but gave values of γ too low in the backscattering for reproducing the maximum observed experimentally.

Therefore it was concluded that the size distribution function of droplets produced by atomization is bimodal and for its modelling it was assumed that the lower tail of the distribution is described by a Junge function $F_1(D)$, similar to that employed in the aerosol case, and the upper tail of the larger droplets was approximated by a monodispersion with a typical size D_2. So that:

$$F(D) = N_1 F_1(D)^{aerosol} + N_2\ \delta(D-D_2)$$

Then the comparison between the experimental angular patterns and the theoretical ones was carried out in dependence of the size of the larger droplets D_2 and of the concentration ratio between the number concentration of the small droplets and the larger ones N_1/N_2.

A preliminary series of numerical integrations of eq.3 showed that it was not possible to reproduce the experimental γ-ratio in the side scattering region with D_2 smaller than 20μm while it was always possible to find a couple of D_2 and N_1/N_2 which fits the experimental curves for $D_2 \geq 20\mu$m.

This result means that the larger droplets of the spray scatter the light according the geometrical optics limit, where the C_{VV} and C_{HH} cross sections are both proportional to their surface area and thus their polarization ratio γ is constant. Therefore it is not possible to obtain more information on their size from polarization measurements but only their surface area per unit volume $N_2\pi D_2^2/4$ can be obtained from these experiments.

Figure 4 illustrates the comparison between the experimental data and the

theoretical bimodal model when D_2=20μm: the number concentration ratio N_1/N_2 between the very small droplets and the large ones is around 400 where the atomization is carried out very efficiently (P_{air}=0.4MPa) and drops to 100 for the worst atomization condition (P_{air}=0.1MPa).

Discussion

The measurement of the complete angular patterns of the polarized components of the scattered light together with the systematic comparison with the Lorenz-Mie theory allows to conclude that a very large number of droplets with diameter smaller than one micrometer are produced during atomization of heavy oil. In fact the analysis shows that the patterns are dominated by non geometrical optics contribution when both light oils and hevy oils are dispersed as aerosols and that the same is true for the light scattered in the backward direction, in the case of heavy oil sprays produced by air assisted atomization. This lower part of the size distribution function is not detected when optical sizing methods based on geometrical optics or, in equivalent ways, when visualization techniques are employed. On the contrary the angular pattern of the polarized components of the scattered light does not offer a great sensibility to the characterization of the lower tail of the size distribution, composed by droplets larger than 10 μm, whose scattering properties are mainly determined by geometrical optics.

Scattering due to surface waves has been employed before by the same group in the diagnostics of sprays by measuring the polarization ratio at θ= 90° employing a monomodal size distribution function. The measurement of the complete pattern of polarization shows that a bimodal size distribution, including both very small and large droplets, is the only choice to interpret theoretically the scattering both in the backward and in the side scattering region.

The presence of a bimodal size distribution contributes to a better understanding of the physics of the atomization and of the convection and the vaporization processes in sprays. The production of a great number of droplets smaller than 1μm is not satisfactory taken into accountct by the current models of atomization, mainly based on linear instability analysis (1). The great number of very small droplets suggests that the local efficiency of the momentum transfer between the gase phase and the liquid phase is high, otherwise it should be impossible to justify the large value of the energy necessary to overcome the surface tension effects. With regard to spray dynamics it is worthwhile to remark that in the spray atomized in the best condition of our experiments (see fig.4) the ratio of the total perimeter per unit areas between the small and large droplets is in the order of 10 and the ratios of the total surface area and of the total volume are in the order of 1 and 0.1 respectively. For the worst atomization case the ratios are 2, 0.1 and 0.01 respectively. By consequence in the first case 10% of the fuel is in the form of droplets so small that they are directly convected by the air and have a vaporization lifetime orders of magnitude lower than the larger droplets. This part of the fuel is readily available for oxidation and pyrolysis reactions in the gas phase and they play an important role for the ignition and stabilization of flames. On the contrary for the worst atomized spray there is practically no fuel available for this purpose.

From an optical point of view it is worthwhile to remark that the fact that heavy oil is partially absorbing in the visible allowed to find the non geometrical optics nature of the polarization in the backward scattering region, and consequently the high concentration of the very small droplets. This surface wave effect is not so evident in the angular polarization pattern of transparent sprays because peaks of preferentially vertically polarized

light due to rainbow tend to reduce the overall polarization ratio. In fact fig.4 shows that transparent aerosols have a less prominent polarization peaks in the backward than absorbing aerosols with the same size distribution. The difference between the transparent and absorbing cases becomes clearer for sprays where the much larger droplets, produced by atomization, damp almost completely the refracted rays.

Final Comments

In summary this communication gives a contribution on the following points:

i) Analysis of the Lorenz-Mie solution for particles around 1μm shows that light scattering is dominated by surface wave effects; the polarization peak in the backscattering is an useful tool to identify the size of spherical objects in this diameter range.

ii) This method has been applied to aerosols formed by light and heavy oil droplets with good agreement with the predictions of the aerosol literature.

iii) The same method applied to a sprays of heavy oil droplets allowed to detect the lower part of the size distribution function which is not detectable with other optical techniques. Furthermore the bimodal characteristics of sprays produced by air assisted atomization has been proved.

References

1. Lefevbre, A.H., Atomization and Sprays, Hemisphere, New York, NY (1989).
2. Born,M. and Wolf, E., Principles of Optics, Pergamon, Oxford, UK (1970).
3. Massoli, P., Beretta, F. and D'Alessio, A., "Single Droplet Size, Velocity and Optical Characteristics by the Polarization Properties of Scattered Light", Appl. Opt., Vol 28, p. 1200 (1989).
4. Massoli, P., Beretta, F. and D'Alessio, A., "Pyrolysis in the Liquid Phase Inside Single Droplets of Light Oil Studied with Laser Light Scattering Methods", Comb. Sci. Tech., Vol 72, p. 271 (1990).
5. Beretta, F., Cavaliere, A. and D'Alessio, A. "Ensemble Laser Light Scattering Diagnostics for the Study of Fuel Sprays in Isothermal and Burning Conditions" Twentieth Symp. (Int'l) on Combustion p.1249, The Combustion Institute, Pittsburgh,PA (1984).
6. Beretta, F., D'Alessio, A. and C. Noviello, "Spray Vaporization and Soot Formation in Flames Generated by Light Oil with Different Chemical Composition", Twenty-first Symp. (Int'l) on Combustion p.1133, The Combustion Institute, Pittsburgh, PA (1986).
7. Beretta, F., Cavaliere, A., D'Alessio, A., Massoli, P. and Ragucci, R., "A Spectral Scattering Method for Determining Size Distribution Functions and Optical Characteristics of Droplets Ensembles in Fuel Sprays", Twenty-first Symp. (Int'l) on Combustion p.675, The Combustion Institute, 1986.
8. Kerker, M., The Scattering of Light, Academic Press, New York, NY (1969).
9. Nussenwveig,H.M., "Complex angular momentum theory of the rainbow and the glory", J. Opt. Soc. Am. Vol.69, p.1068 (1979).
10. Pluchino, A.B., "Surface wave and the radiative properties of micron-sized particles", Appl. Opt. Vol.20, p.2986 (1981).
11. Ashkin A. and Dziedzic, M., "Observation of Optical Resonances of Dielectric Spheres by Light Scattering", Appl.Opt. Vol.20, p.1803 (1981).
12. van de Hulst, H.C., Light Scattering by Small Particles, Dover, New York, NY (1981).

EXPERIMENTAL AND NUMERICAL STUDIES ON DROPLET DISTRIBUTION IN DIESEL OIL SPRAYS

K.-J. Choi, J. Xin and Y.B. Shen*

Department of Mechanical Engineering, University of Illinois at Chicago, Chicago, IL, U.S.A.
*Department of Energy Engineering, Zhejiang University, Hangzhou, P.R. China

ABSTRACT

In this paper, the spray atomization processes of pure diesel oil through a pintle diesel injector were investigated both experimentally and theoretically. The experiments were conducted in a combustion chamber applying an in–line holographic measurement system. An axisymmetric turbulent model for theoretical study was introduced by assuming the spray atomization as the pre–mixing injection of vapor and droplets; the eddy viscosity was simulated with a sub–grid scale method. The experimental results indicated that clear holographic images can be obtained by means of an in–line holographic system. It was observed that droplet size in the core region is smaller than that in the outer region. The numerical results of the droplet distributions and the droplet trajectories were in good agreement with the experimental observation. From this, it was indicated that the atomization processes in a diesel engine can be simulated to a certain degree using the present numerical model.

NOMENCLATURE

C_D	drag coefficient
D_k	resistant coefficient defined in equation (7)
g	acceleration of gravity
m	particle mass, $= \frac{4}{3} \pi r_k^3 \rho_p$
$\vec{M}$	momentum exchange term between gas and droplets
P	pressure
Q	mass flux of spray
r	radial coordinate or radius of droplet
Re_d	droplet Reynolds number
t	time
Δt	time interval between each group of injected droplets
t_{tot}	total time of spray injection
$\vec{U}$	instantaneous velocity, $= \vec{u} + \vec{u}'$
$\vec{u}$	time mean velocity
$\vec{u}'$	fluctation velocity

U,u,u′	velocity component in radial direction
V,v,v′	velocity component in axial direction
U_m	modulus of relative velocity, $= \lvert\vec{U}_g - \vec{U}_{pk}\rvert$
$\vec{x}$	spatial vector
$\vec{x}_{pk}$	particle location vector
z	axial coordinate
θ	gaseous volume fraction
ρ	density
μ	dynamic viscosity
ν	kinematic viscosity
ν_e	effective viscosity, $= \nu + \nu_t$
ν_t	eddy viscosity defined in Equation (3)
τ	dimensionless time, $= t/t_{tot}$
g	gas phase
p	particle
k	kth computational group of drops
i,j,k	coordinate directions

1. INTRODUCTION

Atomization and spray processes in combustion chambers are of considerable importance to the design of diesel engines. The basic process involved is the disintegration of the liquid fuel to produce millions of small droplets to increase the total surface area. To a certain extent, the performance of diesel engines depends on the quality of spray atomization. Up to now, many fundamental studies have been done in this area. In the past, much focus was placed on single droplets or macroscopic characteristics of sprays, such as spray penetration and spray angle [1–3]. With the development of new measuring techniques and instruments, it has become possible to study droplet size distribution, droplet evaporation and combustion within sprays in high temperature and pressure environments [4–6].

The diesel spray atomization is a transient, unsteady, phase–changing process accompanied with disintegration, collision and coalescence of liquid droplets. This complex process is influenced by many parameters, such as the properties of liquid, the nozzle specifications, and environmental conditions. Due to the complexity and random nature of spray atomization, it is time–consuming, expensive, and sometimes almost impossible to study the spray characteristics and effects of various parameters on the atomization processes by means of experiments only. Rather, comprehensive understanding of microscopic mechanisms of spray formation and development can be obtained by means of combination of experiments and numerical simulations.

In this paper, the authors intended to develop an experimental method measuring droplet size distribution in a diesel oil spray by using a single pulse Fraunhofer in–line holographic system. Then, a computational model for the droplet distribution and drop trajectory was developed.

2. EXPERIMENTAL APPARATUS AND PROCEDURE

An experimental system similar to the one used in our previous study [7] was applied. A constant volume combustion chamber was filled with nitrogen to avoid burning of fuel so that the atomization and evaporation processes without chemical reaction could be observed. A pintle diesel injector in a cooling water jacket for insulation was installed

inside the combustion chamber. The geometric angle of the pintle nozzle was 15°. The combustion chamber was 100 mm in diameter and 140 mm in height. The size of the two parallel quartz viewing windows was 50 mm in width and 100 mm in height. The windows' surfaces were normal to the laser beam.

An in–line holographic system was chosen to study the atomization mechanisms due to its simpler optical arrangement and less requirement for the resolution of holograms. Concerning the atomization features of diesel sprays, a very high resolving power of measurement was required. In order to solve this problem, a pre–magnifying system was adopted to a conventional in–line holographic system. The present system consisted of 8 lenses making the magnification of the objects constant regardless of the distance between recorded objects and the holographic plate. A single pulse of 100 Mj at 50 ns pulse width was generated with a ruby laser. The light rays were expanded and collimated to 90 mm in diameter. A He–Ne laser was employed for reconstruction of the holograms. The optical systems for recording and reconstruction are shown in Fig. 1. The recording region is shown in Fig. 2.

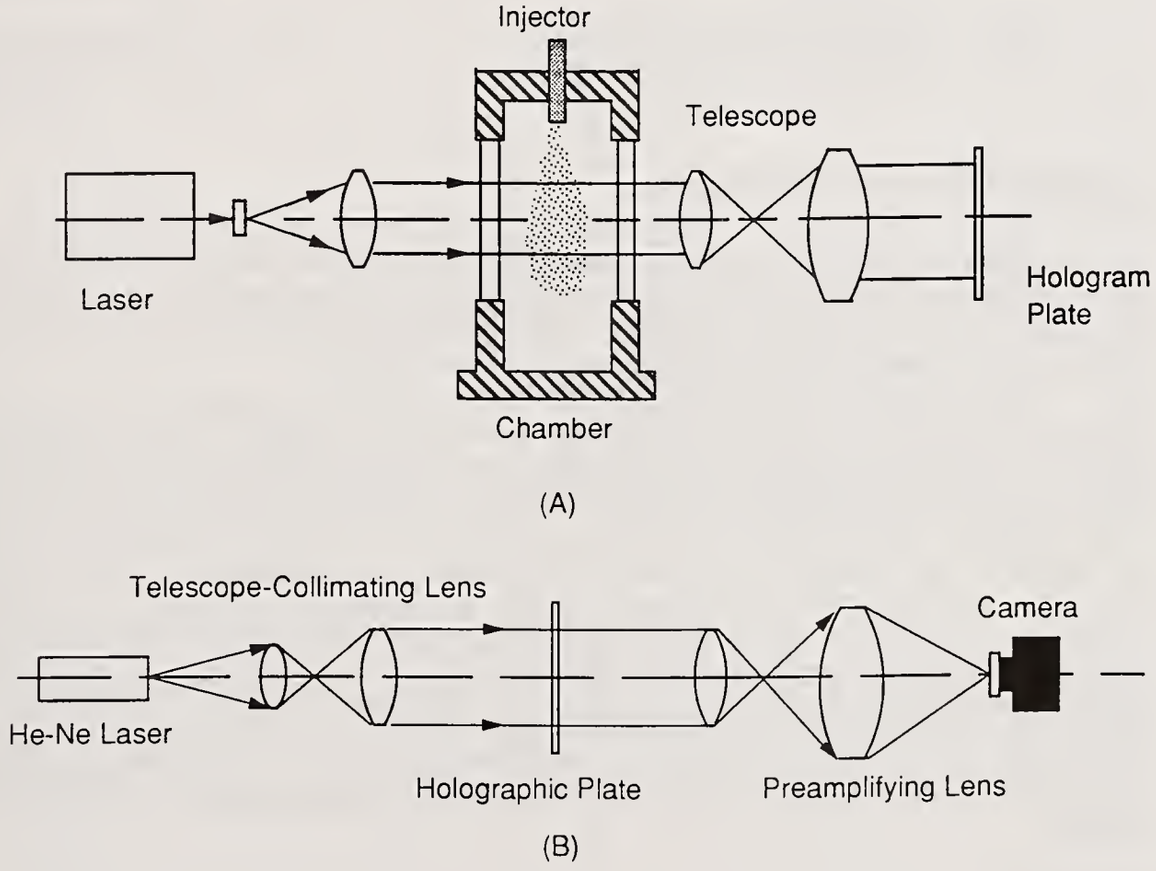

Fig 1. In-line holograph arrangement: (A) for recording, (B) for reconstructing

At ambient temperature, diesel spray was so dense that most laser beams cannot pass through. Therefore, a slit made from two knives was installed right beneath the injector to block a portion of the spray. At a high temperature in the measuring field, however, sprays have become dilute because of the evaporation of droplets. It was not necessary to block any portion of the sprays at media temperatures above 573 K.

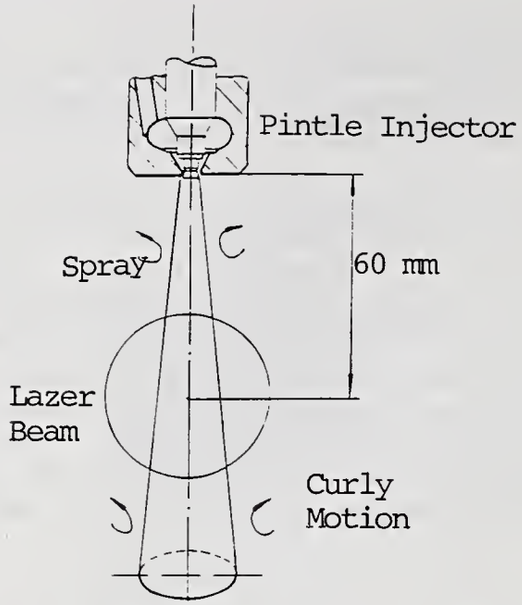

Fig 2. Schematic diagram of an oil spray near the pintle injector

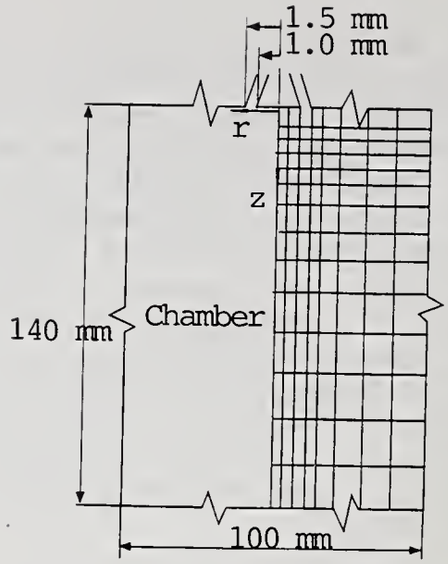

Fig 3. Coordinates and schematic of computed sub-grids in a chamber

3. THEORETICAL MODELING

There are few models which can simulate the main steps of the atomization process, such as breakup, collision, coalescence of droplets and interaction between liquid droplets and the surrounding gaseous medium. Previous research was mainly emphasized on spatial fuel vapor concentration using a gaseous jet model [8,9].

When liquid fuel is injected into the combustion chamber under a high pressure difference, there are many tiny droplets in the initial stage of spray atomization. In this study, however, it was assumed that tiny drops vaporize instantly right after injection, and otherwise no vaporization occurs in the spray. Therefore, the spray atomization process was simplified by considering the spray as a mixture of liquid fuel droplets and fuel vapor. In addition, no breakup or collision of droplets was assumed. The droplet phase was treated in the Lagrangian approach, and the gas phase in the Eulerian approach. In order to simulate an actual spray which has broad ranges of droplet size, velocity, and droplet numbers, a certain number of groups of droplets was selected. Each group of droplets injected at different time has N_{pk} droplets of the same diameter and velocity. Coordinates and schematic diagram of the system are shown in Fig. 3. For unsteady and axisymmetric two–phase flow, the fundamental equations were written in cylindrical coordinates as the follows.

Gas Phase

Continuity equation:

$$\frac{\partial \theta}{\partial t} + \frac{1}{r} \nabla \cdot (r \theta \vec{u}_g) = 0 \tag{1}$$

Momentum equation:

$$\frac{\partial \theta \vec{u}_g}{\partial t} + (\vec{u}_g \cdot \nabla) \theta \vec{u}_g = \theta \vec{g} - \frac{\theta}{\rho_g} \nabla P + \nabla \cdot (\theta \nu_e \nabla \vec{u}_g) + \frac{\vec{M}}{\rho_g} \tag{2}$$

A sub–grid scale turbulence model [10] was used to evaluate the eddy viscosity ν_t given as

$$\nu_t = (C_s \Delta_a)^2 [2 \bar{S}_{ij} \bar{S}_{ij}]^{1/2} \tag{3}$$

where

$$\bar{S}_{ij} = \frac{1}{2}\left[\frac{\partial u_i}{\partial x_j} + \frac{\partial u_j}{\partial x_i}\right] \tag{4}$$

C_s is a constant and Δ_a a local grid length.

Droplet Phase

The velocity and acceleration of a droplet belonging to the kth group of droplets are expressed by the following

$$\frac{d\vec{x}_{pk}}{dt} = \vec{u}_{pk} \tag{5}$$

$$\frac{d\vec{u}_{pk}}{dt} = \vec{g} + \frac{D_k}{m_k}(\vec{U}_g - \vec{u}_{pk}) \tag{6}$$

The resistant drag coefficient, D_k, for the specific droplet is given as

$$D_k = 6\pi\mu_g r_k + \frac{1}{2}\pi r_k^2 \rho_g C_D u_m \tag{7}$$

The first term in the right hand side of Eq. (7) is Stokes drag coefficient for $Re_d < 1$, and the second term is for large Re_d.

Numerical Methods and Initial Conditions

The above differential equations are discretized into finite difference equations using a variable spacing grid system based on a time step. The detailed numerical procedure can be referred in literature [11].
The gaseous volume fraction in a grid is presented as

$$\theta = 1 - \sum_{k=1}^{m}\left[\frac{4}{3}\pi r_k^3 N_{pk}\delta(\vec{x} - \vec{x}_{pk})\right]/\Delta V \tag{8}$$

where, ΔV is the volume of a grid, $\delta(x)$ Dirac delta function, m the group number of liquid drops in the grid (0–2500), and N_{pk} the number of drops represented by the kth group. Assuming that each group of droplets enters the chamber at a different time, N_{pk} can be determined by the following equations:

$$N_{pk}\frac{4}{3}\pi r_k^3 \rho_p = Q\Delta t \tag{9}$$

The time interval between groups of injected droplets, Δt, was 6×10^{-6} seconds and the total injection time was 1.5×10^{-2} seconds. Therefore, the maximum number of groups used in this study was 2500. Momentum exchange between gas and droplets is calculated as

$$\vec{M} = -\sum_{k}^{m} [D_k(\vec{U}_g - \vec{u}_{pk})\delta(\vec{x} - \vec{x}_{pk})]/\Delta V \qquad (10)$$

Prior to injection of the mixture of fuel drops and fuel vapor, the environmental gas medium is assumed to be quiescent. The gas temperature and pressure are 450 K, 0.9 MPa, respectively. According to the results of our previous experiments [12], the initial velocity of spray was selected as 170 m/s. The drop diameters were taken at random within a range between 6 μm and 60 μm, and the initial location of droplets at the exit are determined randomly between 1 mm and 1.5 mm in the radial direction from the centerline of the chamber. The liquid flow rate used in this calculation was 13.3 mℓ/sec.

4. RESULTS AND DISCUSSION

Experimental Results of Drop Distribution

Fig. 4 shows the droplet size distribution of diesel oil spray in the core and the outer layer of the spray under ambient conditions. By intuition, it is assumed that the droplet SMD in the inner space of the spray is much larger than that in the outer region, because the shear force between the liquid drop and gas medium was small. To the contrary, however, the experimental results indicate that the droplets in the outer layer are larger than those in the inner as shown in Fig. 4. It can be found that there are dense droplets near the core and sparse droplets near the outer layers of the sprays. At ambient temperature, the size range near the core is about 3 to 30 μm, elsewhere diameters are up to 60 μm in the outer region.

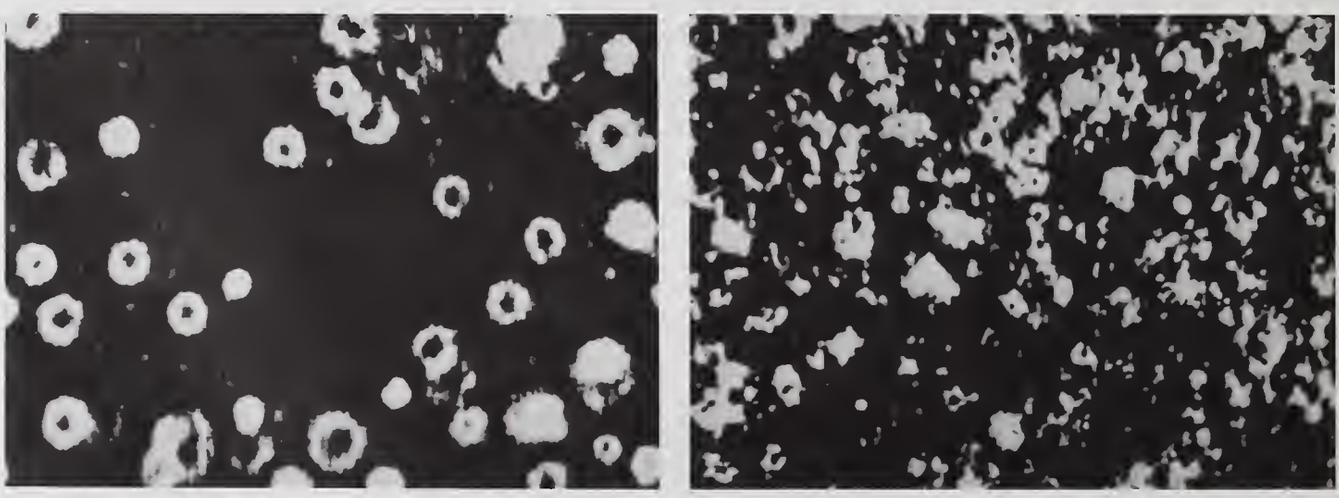

(A) outer region (B) Core region

Fig 4. Droplet distributions in a diesel oil spray, P_g = 1,2, MP_a, T_g = 300 K, and t = 0.9 ms

When gas in the chamber is heated to 450 K, 540 K, 650 K and 750 K respectively, the same phenomena are observed, i.e., large drops are distributed in the outer layer of the spray. However, due to the strong heat and mass transfer processes between droplets and gas in the outer layers, droplets in the outer region vaporize faster than those near the core. Consequently, the spatial droplet size distribution in the outer region tends to be more uniform than that in the core region with increasing temperature, as shown in Fig. 5.

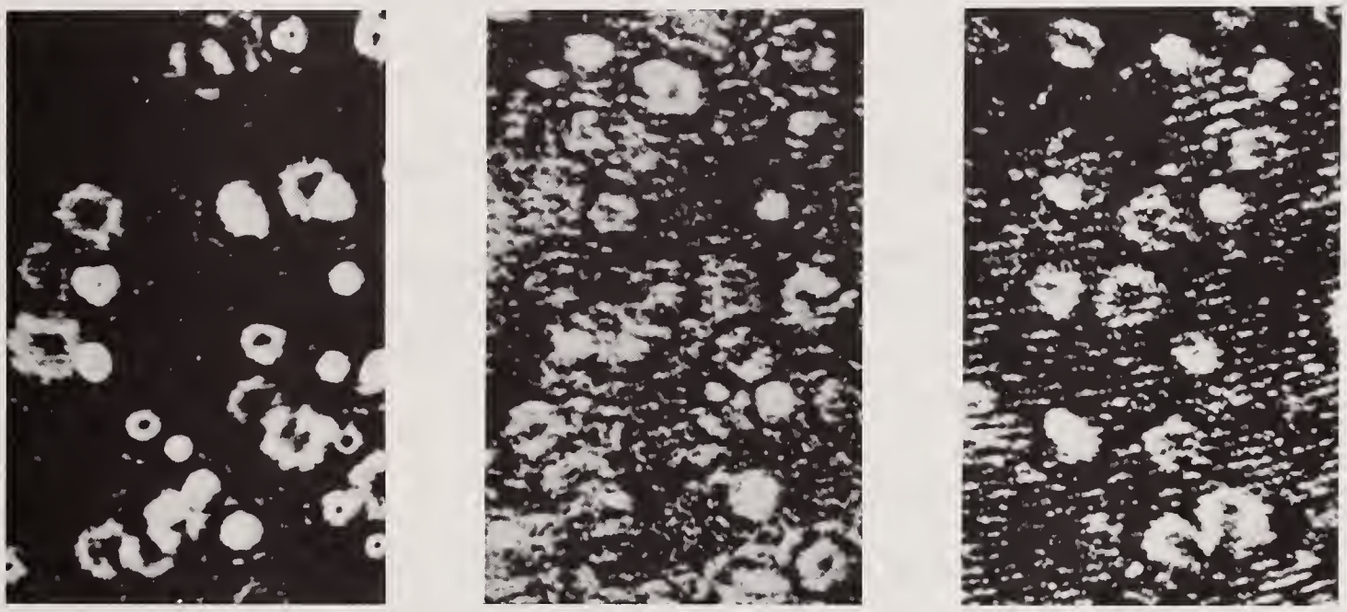

(A) T_g = 280 K (B) T_g = 520 K (C) T_g = 740 K

Fig 5. Droplet distributions in an outer region of a diesel oil spray at different gas temperatures, p = 0.5 MP_a and t = 0.4 ms

It was also observed that large droplets existing in outer layers form an umbrella shape spray. It is because when liquid fuel is injected, the perturbation motion is vigorous in the interface between the unbroken hollow cone and gas medium. As a result, the edges of the spray is torn first, and then the whole spray. Droplets torn out at the edge are smaller than those in the cone surface of umbrella spray. On the other hand, because of the effect of strong curly motion, small droplets in the periphery are drawn into the core of the spray while the trajectory of large droplets changes slowly due to their greater inertia.

Numerical Studies on Droplet Distribution and Spray Development

Fig. 6 and 7 show the trajectories of two different groups of droplets injected at different stage of spray development. The parameters of typical groups of droplets are summarized in Table 1. Dimensionless time τ was used to describe the stages of spray development, which was defined as the ratio of spray developing time to the total period of injection. Since the atomization process is unsteady, the flow field of gas varies with time. The numerical results indicate that small droplets are influenced greatly by turbulence. For small droplets, velocities decelerate quite rapidly, resulting in conformity to the gas velocity in a short time. Since the gas medium was quiescent before injection, later gas motion was developed along with the droplet motion and spray development. When fuel is injected into the chamber, the gas medium is entrained into the spray as shown in Fig. 2. The small droplets diverge their initial direction quickly, and are blown into the inner region of spray due to the curly motion near the spray. The computational results agree well with experimental results.

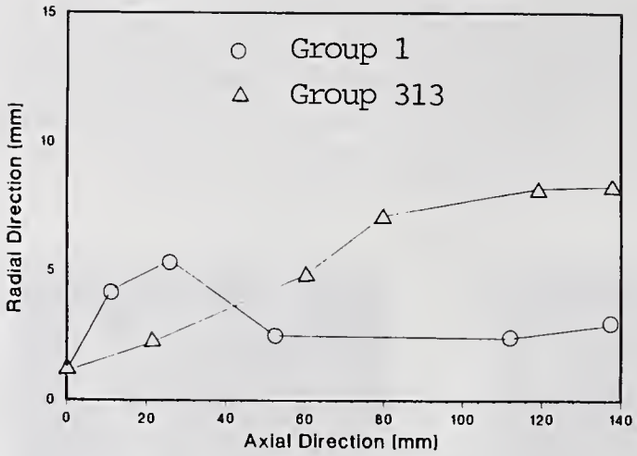

Fig 6. Droplet trajectories of two different groups injected at the early stage (τ = 0 ~ 0.12)

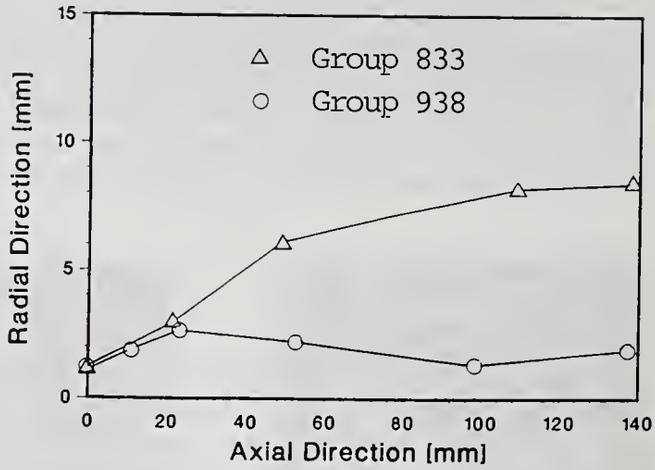

Fig 7. Droplet trajectories of two different groups injected at the middle stage (τ = 0.3 ~ 0.4)

Table 1.Parameters of each group of droplets injected at different time

Group No. of Droplets	Dimensionless Time	Injection Location of Droplets		Dia. (μm)	N_{pk}
		r (mm)	z (mm)		
1	0	1.21	0.0	8.9	150,285
2	4×10^{-4}	1.23	0.0	7.0	313,562
313	0.1248	1.08	0.0	51.4	786
833	0.3328	1.15	0.0	59.2	515
938	0.3748	1.10	0.0	7.3	272,344

Furthermore, the computational results account for the interaction of droplets through their momentum exchange with the gaseous medium. Table 2 shows the spatial location of two groups of droplets with time, which have the similar parameters. Droplets groups 1 and 2 are injected consecutively, with $\Delta t = 6 \times 10^{-6}$. The droplets in group 1 were injected prior to the droplets in group 2. The latter moves faster than the former, because the droplets of group 2 move in the wake of the droplets of group 1, therefore reducing the drag force. The droplets in group 2, therefore, maintain a higher velocity, and surpass the droplet 1.

Fig. 9 is the droplet distribution at τ = 0.24. As a spray develops, large droplets are mainly distributed in the front and outer region of the spray due to their larger inertia. It is observed that the results are in good agreement with experimental results.

Table 2.Spatial locations of two groups of droplets

Dimensionless Time (τ)	Group 1		Group 2	
	r (mm)	z (mm)	r (mm)	z (mm)
0.0	1.21	0.0	1.23	0.0
0.075	4.18	11.57	7.1	24.0
0.25	5.06	19.53	4.12	48.3
0.333	3.1	47.7	3.74	84.31
0.41	2.2	116.1	3.54	136.5

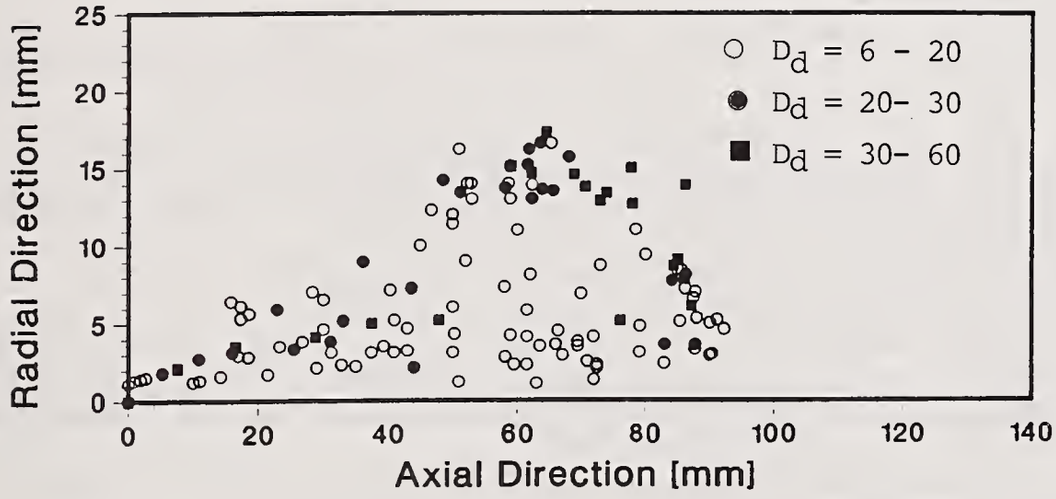

Fig 8. Predicted droplet distributions at τ = 0.24

5. CONCLUSIONS

Atomization features of pure diesel oil sprays have been studied. The following conclusions were obtained:

1. For the pintle diesel injector, most of the small droplets are in the inner core of the spray and droplet sizes are proportionally larger with an increasing radial distance from the spray axis in the tested temperature range.
2. With increasing temperature, droplets in the outer layers will vaporize and their size decreases because of stronger heat and mass transfer processes in the outer layers, and in turn, the droplet size difference between in the boundary region and in the core region becomes smaller.
3. The numerical results indicate that small droplets tend to follow the gas flow in a short period after injection, and the distribution of small droplets depends upon the gas velocity field.
4. The computational results agree well with the experimental results, i.e., the droplet size increases with the radial distance from the spray axis. In the spray, the large droplets distribute in the front and outer region of sprays.

REFERENCES

1. William, A., "Combustion of Droplets of Liquid Fuels: A Review," Combustion & Flame, Vol 21, pp. 1–31, (1973).
2. Varde, K.S., Popa, D.M. and Varde, L.K., "Spray Angle and Atomization in Diesel Spray," SAE 841055, (1984).
3. Hikaru, K. Hideaki, T., Takeshi, S. and Fujimoto, H., "Investigation on the Characteristics of Diesel Fuel Sprays," SAE 800968, (1980).
4. McDonell, V.G. and Samuelsen, G.S., "Application of Two–Component Phase Doppler Interferometry to the Measurement of Particle Size, Mass Flux, and Velocities in Two–Phase Flows," Twenty–Second Symposium (International) on Combustion, pp. 1961–1971, (1988).
5. Keiya, N. Naoki, M. and Hiroyuki, H., "Holographic Measurement of Evaporating Diesel Sprays under High Pressure and Temperature, Nippon Kikai Gakkai Ronbunshu B Hen Vol. 52, No. 478, 2457–2463 (1986).
6. Wu, K.J., Coghe, A., Santavicca, D.A. and Bracco, F.V., "LDV Measurements of Drop Velocity in Diesel–Type Sprays," AIAA Journal, Vol. 22, No. 9, pp. 1263–1270 (1984).
7. Ma, Y., Xin, J. and Choi, K.J., "Experimental Studies of Diesel Oil Spray and Microexplosion of Water–in–Oil Emulsions by Using Optical Imaging Techniques," ILASS–AMERICAS, 4th Annual Conference, Hartford, CT (1990).
8. Arcoumanis, C., Whitelaw, J.H., and Wong, K.Y., Gaseous Simulation of Diesel–Type Sprays in a Motored Engine, SAE 890793, 1989.
9. McMillian, O.J. and Ferziger, J.H., "Direct Testing of Subgrid Scale Models," AIAA Journal, Vol. 17, No. 12, pp. 1340–1346 (1979).
10. Travis, J.R., Harlow, F.H. and Amsden, A.A., Numerical Calculation of Two–Phase Flows, Nucl. Sci. Engineering, Vol. 64, pp. 1–10 (1976).
11. Fan, Z.–Q., Zhang, B.–Z. and Ding, J.–M., "Prediction of Gas–Particle Two–Phase Flows in Combustion," Vol. 3, Proceedings of International Symposium Workshop on Particulate and Multiphase Processes and the 16th Annual Meeting of the Fine Particle Society, Florida, (1985).
12. Xin, J., "Studies on Atomization and Combustion of Diesel Oil and Emulsion Sprays," Master Thesis, Zhejiang University, China (1987).

A NEW ATOMIZATION MECHANISM FOR AIRLESS SPRAYING: THE SUPERCRITICAL FLUID SPRAY PROCESS

K.A. Nielsen, C.W. Glancy, K.L. Hoy and K.M. Perry

Union Carbide Chemicals and Plastics Company, Inc.
South Charleston, WV, U.S.A.

ABSTRACT

The supercritical fluid spray process uses supercritical fluids such as carbon dioxide and nitrous oxide to replace the volatile organic solvent content in coating formulations. This not only reduces solvent emissions to the atmosphere by 50 to 80 percent, while continuing to use existing coating systems, it can also greatly improve airless spray technology by producing a new atomization mechanism. Besides being an effective viscosity reducer, the dissolved supercritical fluid creates an expansive force that overcomes liquid cohesion and surface tension forces that oppose atomization. This produces vigorous atomization that remedies the deficiencies of the airless spray process so that high quality coatings can be applied. It produces a fine droplet size and a "feathered" spray that resembles an air spray system, but without having the high volume of compressed air that deposits coating inefficiently. The coarse droplet size and "fishtail" spray pattern characteristic of airless sprays are eliminated. The feathered spray fan can be produced in any width from narrow sprays to sprays that are much wider than current spray tip technology can produce. This new technology can be applied to most coating systems and can be retrofitted into existing spray operations. It is expected to be widely used industrially.

INTRODUCTION

Each year, American industry sprays 400 million gallons of coatings such as paints, varnishes, lacquers, and enamels. They are applied by spray techniques such as air spray, airless spray, air-assisted airless spray, and rotary atomizers, each of which has advantages and disadvantages in how they apply energy to atomize the coating. Air spray uses a large volume of compressed air, which gives the fine droplet size and uniform spray needed for high-quality coatings but deposits coating inefficiently, so much coating is wasted. Conventional airless spray uses high fluid pressure, but produces coarse droplets and a non-uniform spray, which has limited it to applying low-quality coatings even though it is much more efficient than air spray. Air-assisted airless spray is a combination of both, but uses less air volume and lower pressure, so it has intermediate performance. Rotary atomizers can produce a fine droplet size and deposit coating efficiently, but the spray is unfocused and the apparatus is expensive.

These spray techniques share the fundamental problem that coating formulations must have a very low viscosity to produce the fine droplet size needed for high-quality coatings. This requires a large amount of organic solvent, which is a major source of air pollution. Therefore, the government has mandated that solvent emissions be reduced to low levels. Coating formulators have responded by developing water-borne coatings and high-solids coatings, but these have created new problems for applicators and have had limited success. Water-borne coatings must contain enough organic coupling solvent to be compatible with water, so they often do not meet regulatory limits. Quality has suffered from problems in evaporating the high water content. Electrostatic spraying is difficult because water is highly conductive. High-solids coatings retain many advantages of solvent-borne coatings, but they use reactive polymers with low molecular weight, so they suffer from new problems such as running and sagging, cratering, poor pot life, and curing that is slow or requires high temperatures.

The requirement of very low spray viscosity means that most of the solvent in coating formulations is used just for viscosity reduction. Film formation actually requires a high coating viscosity to prevent running and sagging on the substrate. Therefore, the solvents used for viscosity reduction are fast-evaporating solvents that evaporate in the spray so that the viscosity of the deposited coating is much higher. The coating requires a much smaller proportion of slow-evaporating solvents to obtain proper film coalescence, leveling, and reflow to form a smooth coating after application and during curing. This large viscosity increase that must occur during spraying has so far been a spray technology barrier to reducing solvent usage while retaining good coating performance. The previous methods of using less solvent to obtain low spray viscosity have invariably reduced coating performance on the substrate as well.

We have developed new spray technology that solves this dilemma by using environmentally compatible supercritical fluids such as carbon dioxide and nitrous oxide to replace the volatile organic solvents used to obtain low atomization viscosity. Only the much smaller amount of slow-evaporating solvent needed for film coalescence and leveling is used. This reduces solvent emissions by up to 80 percent while using conventional polymers with high molecular weights that give superior coating performance (1-2). Furthermore, we have discovered that supercritical fluids not only reduce viscosity, they also produce vigorous atomization by a new mechanism that remedies the defects of conventional airless spraying. Therefore, the supercritical fluid spray resembles an air spray but without the high air volume, so high quality coatings can be deposited efficiently.

CONVENTIONAL AIRLESS SPRAY MECHANISM

Airless spray uses a high pressure drop across the spray orifice to propel the coating formulation through the orifice at high velocity. The conventional atomization mechanism is well known (3). The coating exits the orifice as a liquid film that becomes unstable from shear induced by its high velocity relative to the surrounding air. Waves grow in the liquid film, become unstable, and break up into liquid filaments that likewise become unstable and break up into droplets. Atomization occurs because cohesion and surface tension forces, which hold the liquid together, are overcome by shear and fluid inertia forces, which break it apart. However, the cohesion and surface tension forces are not entirely overcome and they profoundly affect the spray, particularly for viscous coating formulations.

Conventional airless spray techniques are known to produce coarse droplets and defective spray fans that limit their usefulness to applying low-quality coating films. Higher viscosity increases viscous losses within the spray orifice, which lessens the energy available for atomization, and it decreases shear intensity, which hinders the development of natural instabilities in the expanding liquid film. This delays atomization so that large droplets are formed (4).

Fig. 1 Conventional airless "fishtail" spray

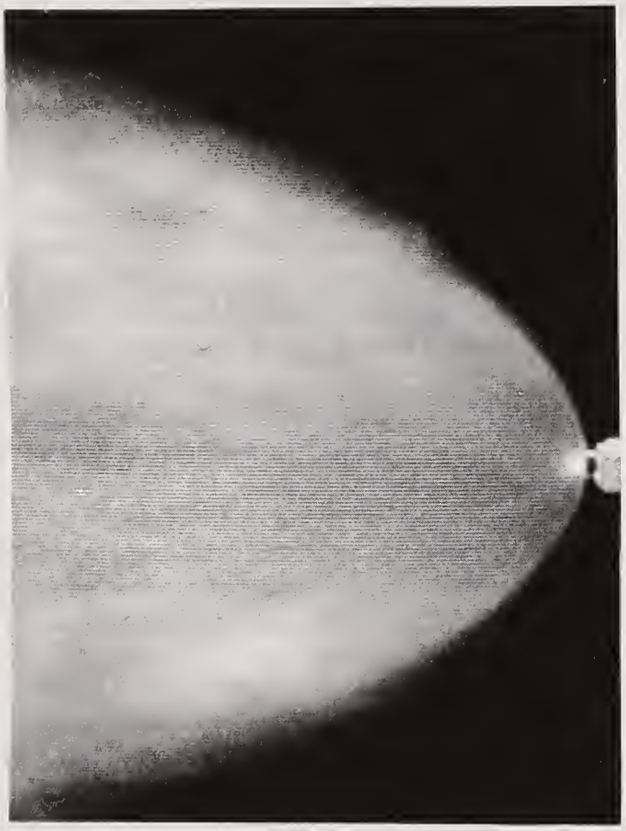

Fig. 3 "Feathered" spray with carbon dioxide

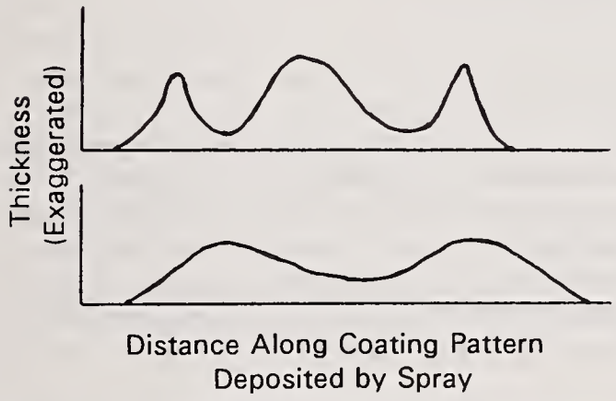

Fig. 2 Two measured "fishtail" spray deposition patterns

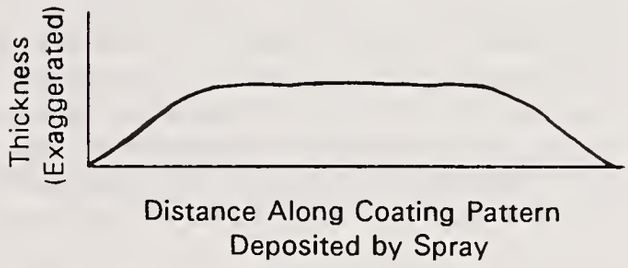

Fig. 4 Measured "feathered" spray deposition pattern with carbon dioxide

The spray characteristically forms a "tailing" or "fishtail" spray pattern. An example is shown in the photograph in Figure 1. More liquid gathers at the edges of the fan than in the center, which produces coarsely atomized jets of coating. Sometimes the jets separate from the spray and deposit separate bands of coating. At other times they thicken the edges so that more coating is deposited at the top and bottom than in the center of the spray. Examples of measured spray depositions of coating are illustrated in Figure 2. These deficiencies make it difficult to apply a uniform coating.

SUPERCRITICAL FLUID SPRAY PROCESS

The supercritical fluid spray process uses gaseous fluids such as carbon dioxide and nitrous oxide in their supercritical state to dilute coating formulations to spray viscosity instead of using volatile organic solvents. Byproduct carbon dioxide from natural gas wells, fermentation plants, and ammonia plants is preferred due to low cost and wide availability, but nitrous oxide might be more environmentally acceptable, because it dissociates to nitrogen and oxygen, so that in effect air is used as a solvent. Carbon dioxide becomes supercritical at temperatures and pressures above its critical point, where liquid and gas properties become identical. The critical temperature, 31 C (88 F), is just above room temperature and the critical pressure, 72 bars (1070 psi), is well within the operating range of airless spray equipment.

For a wide variety of coating systems, we have demonstrated that 50 to 80 percent of the organic solvent can be removed from coating formulations with equal or better coating performance, because little or no change is made to the polymers and pigments. Only the solvent blend is changed, eliminating the volatile solvents and retaining just enough slow-evaporating solvent to obtain proper film coalescence and leveling (1). The solvent content of conventional high-solids coatings can also be further reduced and their performance can be improved because higher molecular weight polymers can be used (2).

By using the supercritical fluid spray process, conventional low-solids and high-solids coatings can be reformulated at very high solids levels. These reformulated coatings are called coating concentrates. They typically have viscosities from 800 to 3000 centipoise, although viscosities up to 12,000 centipoise have been sprayed. These concentrate viscosities are much higher than conventional formulations. Even conventional high-solids coatings have a low application viscosity: 80 centipoise for clear coats and 35 centipoise for base coats. In general, air spray and air-assisted airless spray require a low viscosity below about 100 centipoise and even rotary atomizers have an upper viscosity limit below 500 centipoise.

Spray Conditions

The supercritical fluid is mixed with the coating concentrate at the time of spraying. The spray solution usually contains 10 to 50 weight percent of dissolved carbon dioxide. The proper concentration for a given coating application depends upon the solubility, viscosity reduction, solids level, pigment content, and the spray temperature and pressure. The spray solution is heated above the critical temperature to offset cooling that occurs as the carbon dioxide is released as a free gas from the spray. The spray temperature is usually 40 to 70 C (100 to 160 F). The spray solution is pressurized above the critical pressure to increase the carbon dioxide solubility. The spray pressure is usually 80 to 110 bars (1200 to 1600 psi). Airless spray guns and nozzles are used that have been modified for the special properties of the spray solution.

Generally carbon dioxide solubility is not a limiting factor for spray application. Solubilities usually range from 25 to 50 percent. Spraying is usually done below the solubility limit at the spray conditions, so that the carbon dioxide is entirely dissolved. Excess carbon dioxide forms a second fluid phase, but usually no harm results if a small excess is present. A large excess can be detrimental because solvent is extracted from the polymer solution into the excess carbon dioxide phase. This can increase the viscosity and reduce the amount of solvent available for film coalescence and leveling.

The large concentration of dissolved supercritical carbon dioxide produces a liquid spray solution with markedly different properties. Conventionally sprayed coating solutions are incompressible liquids, but the supercritical fluid spray solution is highly compressible, that is, the density changes markedly with changes in pressure. Furthermore, temperature and pressure changes about the solubility limit can cause phase changes. Usually more carbon dioxide is present than organic solvent, so polymer solvation can be different than in normal solutions. Because

carbon dioxide is a small molecule, it has much higher diffusivity and can penetrate polymer configurations better than normal solvents. Supercritical carbon dioxide is an insulating solvent that can give the spray solution the proper electrical resistivity for good electrostatic deposition.

Viscosity Reduction

An important function of the supercritical carbon dioxide is to reduce the viscosity of the coating concentrate to a sprayable level. The spray viscosity is usually less than 50 centipoise, often as low as one centipoise. It is a function of the polymer system, concentrate viscosity, carbon dioxide concentration, and temperature. The viscosity is insensitive to spray pressure provided the carbon dioxide remains dissolved. In most systems, less carbon dioxide than an equal weight replacement of the replaced volatile solvent is needed to obtain the proper spray viscosity.

The viscosity reduction can be illustrated by using a medium molecular weight acrylic polymer system. A concentrate with 65 percent polymer has a viscosity of 1000 centipoise at room temperature. Heating it to a spray temperature of 50 C reduces the viscosity to 300 centipoise. Adding carbon dioxide to 28 percent concentration gives a spray viscosity below 30 centipoise. A concentrate with 75 percent polymer is very viscous at room temperature and the viscosity is still 2000 centipoise at the spray temperature, but adding carbon dioxide gives a spray viscosity below 40 centipoise.

SUPERCRITICAL FLUID SPRAY CHARACTERISTICS

Supercritical carbon dioxide not only functions as a good viscosity reducer, more importantly, it can produce a vigorous new atomization mechanism that can remedy the deficiencies of conventional airless spraying so that high quality coatings can be applied. The supercritical fluid spray has the good characteristics of an air spray but eliminates the detrimental large air volume produced by the compressed air. The vigorous decompressive atomization can produce the fine droplet size needed for high quality coatings and a "feathered" spray that gives uniform coating thickness. The coarse droplet size and "fishtail" spray of conventional airless sprays are eliminated. The carbon dioxide escapes from the spray droplets as free gas, but the volume is relatively small.

New Airless Atomization Mechanism

The vigorous decompressive atomization is believed to be produced by the dissolved supercritical carbon dioxide suddenly becoming exceedingly super-saturated as the spray solution leaves the nozzle and experiences a sudden and large drop in pressure. This creates a very large driving force for gasification of the carbon dioxide, which overwhelms the cohesion, surface tension, and viscous forces that oppose atomization and normally bind the fluid flow together into a fishtail type of spray.

A different atomization mechanism is evident because atomization occurs right at the spray orifice instead of away from it. Atomization is no longer due to break-up of a liquid film from shear with the surrounding air. Instead it is due to the expansive forces of the compressible spray solution created by the large concentration of dissolved supercritical fluid. Therefore, no liquid film is visible coming out of the nozzle. Furthermore, because the spray is no longer bound by cohesion and surface tension forces, it leaves the nozzle at a much wider angle than normal airless sprays and produces a feathered spray with tapered edges like an air spray. This produces a rounded parabolic-shaped spray fan instead of the sharp angular fans typical of conventional airless sprays. An example of the feathered spray is shown in the photograph in Figure 3.

The spray pattern deposits coating uniformly in a wide central portion and deposits progressively less coating at the tapered edges, as illustrated in the measured deposition profile in Figure 4. This feathering is particularly desirable for overlapping adjacent layers of sprayed coating to produce a coating film of uniform thickness. This is one of the principle reasons why air sprays

are used instead of airless sprays to apply high-quality coatings.

The feathered spray pattern is characteristically obtained when the supercritical carbon dioxide concentration in the spray solution exceeds a transition-point concentration for the given spray conditions. With no carbon dioxide, the binding forces of cohesion, surface tension, and viscosity in the incompressible spray solution produce a typical fishtail spray pattern with very poor atomization. At carbon dioxide concentrations below the transition-point, the binding force exceeds the expansive force of the carbon dioxide, so a fishtail spray pattern persists, but it becomes more uniform, the spray fan becomes wider, the visible liquid film recedes towards the orifice, and the spray solution becomes compressible as the concentration increases from zero. At the transition-point concentration, the expansive force equals the binding force, so neither controls the spray pattern. The visible liquid film has disappeared and atomization is occurring at the spray orifice. Surprisingly, as the concentration increases through the transition point, the angular flat fishtail spray fan first contracts into a narrow transitional oval or flared non-planar spray and then greatly expands into a much wider parabolic flat feathered spray fan. The transition can be seen not only in the shape of the spray but also in the greatly improved atomization and deposition of the coating. The droplet size becomes much smaller, which shows that the binding force is completely overcome by the expansive force of the carbon dioxide, and coating quality is greatly improved. At carbon dioxide concentrations above the transition point, the spray fan is fully feathered, much wider and thicker, and exits the spray orifice at a much greater angle. Higher concentration further decreases the particle size, increases the fan width, and makes the spray solution more highly compressible, which affects the spray rate.

Laser light scattering measurements and comparative spray tests show that the vigorous atomization can produce fine droplets that are in the same size range as air spray systems (20 to 50 microns) instead of the coarse droplets produced by normal airless sprays (70 to 150 microns). For a properly formulated coating, the droplet size range and distribution are ideal for minimizing orange peel and other surface defects commonly associated with spray application.

This fine particle size provides ample surface area for the dissolved carbon dioxide to very rapidly diffuse from the droplets within a short distance from the spray nozzle. Therefore, the coating is essentially free of carbon dioxide before it is deposited onto the substrate. Ideally, coatings sprayed conventionally and with supercritical carbon dioxide have the same composition when they are deposited so that coating performance is the same but much less solvent is emitted to the atmosphere.

The released carbon dioxide gas forms a shroud that tends to displace air, moisture, and dust from the spray. The lower oxygen level and absence of volatile solvents significantly lowers spray flammability. The displacement of moisture lowers the local dew point so that moisture absorption is less likely in humid environments. The drier spray also helps droplets retain their electric charge during electrostatic spraying.

Spray Temperature Profile

The rapid release of carbon dioxide from solution is evident in the very rapid cooling of the heated spray that occurs within a very short distance from the spray nozzle. Figure 5 compares temperature profiles for conventional heated airless sprays and a supercritical fluid spray that is heated to a temperature that compensates for expansive cooling. The conventional spray cools to ambient temperature within 15 centimeters from the nozzle because the solvent evaporates and ambient air is entrained into the spray. Therefore the coating is deposited at ambient temperature. The supercritical fluid spray typically cools to ambient temperature within about two centimeters of the nozzle. In some cases the spray might briefly subcool, but the entrainment of ambient air ensures that the coating is also deposited at ambient temperature. The amount of cooling depends upon the carbon dioxide concentration and the spray temperature.

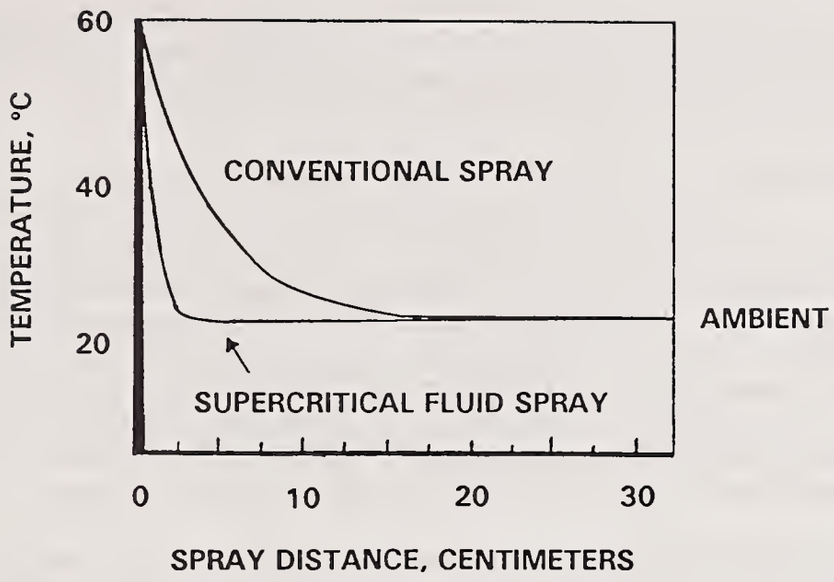

Fig. 5 Temperature profile of spray

The rapid cooling is beneficial because it reduces solvent evaporation in the spray, so little solvent is lost from a properly formulated coating. Therefore solvent is used efficiently and worker exposure to solvent vapors in the spray booth is reduced to a low level. Measurements for one coating system showed that the solids content of the deposited coating was only about two percent higher than the solids content of the coating concentrate. Therefore, the viscosities of the coating concentrate and the deposited coating should be similar.

Spray Fan Width

One manifestation of the expansive force of the supercritical carbon dioxide is that the feathered spray has a much greater fan width than normal airless sprays. The fan width is typically 50 to 150 percent greater, and in some cases can be 300 percent greater, than the fan width rating of the airless spray tip, depending upon the nozzle type, carbon dioxide concentration, coating formulation, and spray conditions. In particular, much larger fan widths can now be produced for small orifice sizes than conventional spray tip technology can produce. Generally the fan width can be altered by varying the carbon dioxide concentration.

Although the spray leaves the nozzle at a much wider angle and the fan width is much wider than normal airless sprays, the fan width can be indexed to give any fan width from narrow to very wide by changing the fan width rating of the airless spray tip, as is normally done. Examples of fan widths measured with and without carbon dioxide are illustrated below for two coatings, using dome-style spray tips with a 0.23-mm (9-mil) orifice size and measuring the fan width 30 centimeters (12 inches) from the spray tip.

Fan Width Rating of Spray Tip	Measured Widths Without Carbon Dioxide	Measured Widths With Carbon Dioxide	
		Coating 1	Coating 2
5 cm	5 cm	10 cm	20 cm
10 cm	10 cm	18 cm	28 cm
15 cm	15 cm	28 cm	36 cm
20 cm	20 cm	33 cm	41 cm

In general, with the supercritical fluid spray process, cross-cut type airless spray tips produce larger fan widths than dome-style spray tips with the same fan width rating. For example, a cross-cut type spray tip with a 0.23-mm (9-mil) orifice size and a fan width rating of 15 centimeters (6 inches) can produce a fan width of 61 centimeters (24 inches).

CONCLUSIONS

In addition to eliminating up to 80 percent of the organic solvent used to apply coatings, the supercritical fluid spray process greatly improves airless spray technology by producing a new atomization mechanism that gives the fine droplet size and feathered spray fan required to produce high quality coatings. Therefore, we believe the process will be used to reduce solvent emissions not only in current airless spray applications but also where air spray, air-assisted airless spray, and rotary atomizers are currently used. Some of the anticipated end uses are automotive topcoats and component finishing, automotive refinish, wood and metal furniture, appliances, pails and drums, aerospace, machinery and equipment, trucks and buses, and structural steel.

With continued development of new coatings we expect solvent usage to decrease to very low levels. Ultimately the supercritical fluid spray process will be able to apply coatings that are the liquid analog of powder coatings, but it will do so with easier implementation, greater versatility, and better coating performance.

REFERENCES

1. Nielsen, K. A., Busby, D. C., Glancy, C. W., Hoy, K. L., Kuo, A. C., and Lee, C., "Supercritical Fluid Spray Application Technology: A Pollution Prevention Technology for the Future" in Proceedings of the Seventeenth Water-Borne and Higher-Solids Coatings Symposium (R. F. Storey and S. F. Thames, Eds.), pp. 218-239, New Orleans, LA (1990).

2. Nielsen, K. A., Busby, D. C., Glancy, C. W., Hoy, K. L., Kuo, A. C., and Lee, C., "Application of High Solids Coatings Using Supercritical Fluids", Proceedings Division of Polymeric Materials: Science and Engineering, Vol. 63, pp. 996-999, American Chemical Society, Washington D.C. (1990).

3. Dombroski, N. and Johns, W. R., "The Aerodynamic Instability and Disintegration of Viscous Liquid Sheets", Chemical Engineering Science, Vol. 18, pp. 203-214 (1963).

4. Lefebvre, A. H. and Senser, D. W., "Research Unravels Spray Mysteries", Industrial Finishing, Vol. 66, No. 6, pp. 16-20 (1990).

DROPLET DIAMETER, FLUX AND TOTAL CURRENT MEASUREMENTS IN AN ELECTROHYDRODYNAMIC SPRAY

P.F. Dunn and S.R. Snarski

Particle Dynamics Laboratory
Department of Aerospace and Mechanical Engineering
University of Notre Dame
Notre Dame, IN, U.S.A.

ABSTRACT

The measured diameter and flux distributions and total current of ethanol droplets generated electrohydrodynamically from a single hypodermic needle at two different spray charge densities are presented and discussed. At the lower spray charge density, the droplet diameter distribution having the smallest mode diameter occurs at the spray centerline, with a diminishing number of droplets and an increasing modal diameter occurring in the lateral direction toward the periphery of the spray. At the higher charge density, these droplet diameter distributions become more narrow and approach lognormal distributions. The droplet fluxes are maximum at the spray centerline and decrease appreciably toward its periphery. The droplet flux distributions are used to construct droplet charge flux distributions by assuming various models of the droplet charging process. The resultant charge fluxes are logarithmically related to lateral position, irregardless of the droplet charging model assumed. The integrals of the various charge flux profiles are compared to the measured total current. This approach reveals the best agreement between measured and predicted total droplet currents when an equilibrium end-state process for droplet charging is assumed.

INTRODUCTION

With the recent development of advanced *in situ* laser diagnostic systems, it is now possible to obtain non-intrusive measurements of the velocity and/or diameter of droplets within electrohydrodynamic (EHD) sprays to a level of detail that was not possible in earlier studies. This paper presents the results of such laser diagnostic measurements of droplet diameter and flux within a single EHD spray. The present work further examines the process of droplet charging by using the various models that relate droplet diameter and charge to predict the total droplet current, which also is measured. As a consequence, the model that best describes the charging process for these experiments can be identified. The major findings from this study, when considered in conjunction with those reported recently by Dunn and Snarski [1] conducted under similar conditions using two parallel needles, support that droplet sprays of ethanol obtained at the subject levels of spray charge density closely approach or already have reached their equilibrium end-state, as described by Kelly [2].

EXPERIMENTS

In the present experiments, a fine spray of droplets in the approximate diameter range of 1 - 50 μm were generated electrohydrodynamically by supplying ethanol at a fixed mass flow rate (4.5 mg/s) from a syringe pump and applying a high positive voltage to a stainless steel hypodermic needle (216 μm I.D., 406 μm O.D., 1.905 cm length) located 38 cm above an electrically grounded droplet-collection funnel (see Figure 1). Droplet diameter and flux distributions were obtained using a Phase Doppler Particle Analyzer (PDPA) (see Bachalo and Houser [3]) at two axial (z) positions below the needle's tip (15 and 30 mm), at approximately twenty lateral (x) positions for each axial position and at four applied voltages (15, 20, 25 and 30 kV). Total droplet currents were measured as the collected droplet current to ground through an electrometer. The resultant spray charge densities for these conditions were 12, 42, 106 and 210 C/m^3, respectively. A description of the experiment's main components and operating procedure is presented in further detail elsewhere [1].

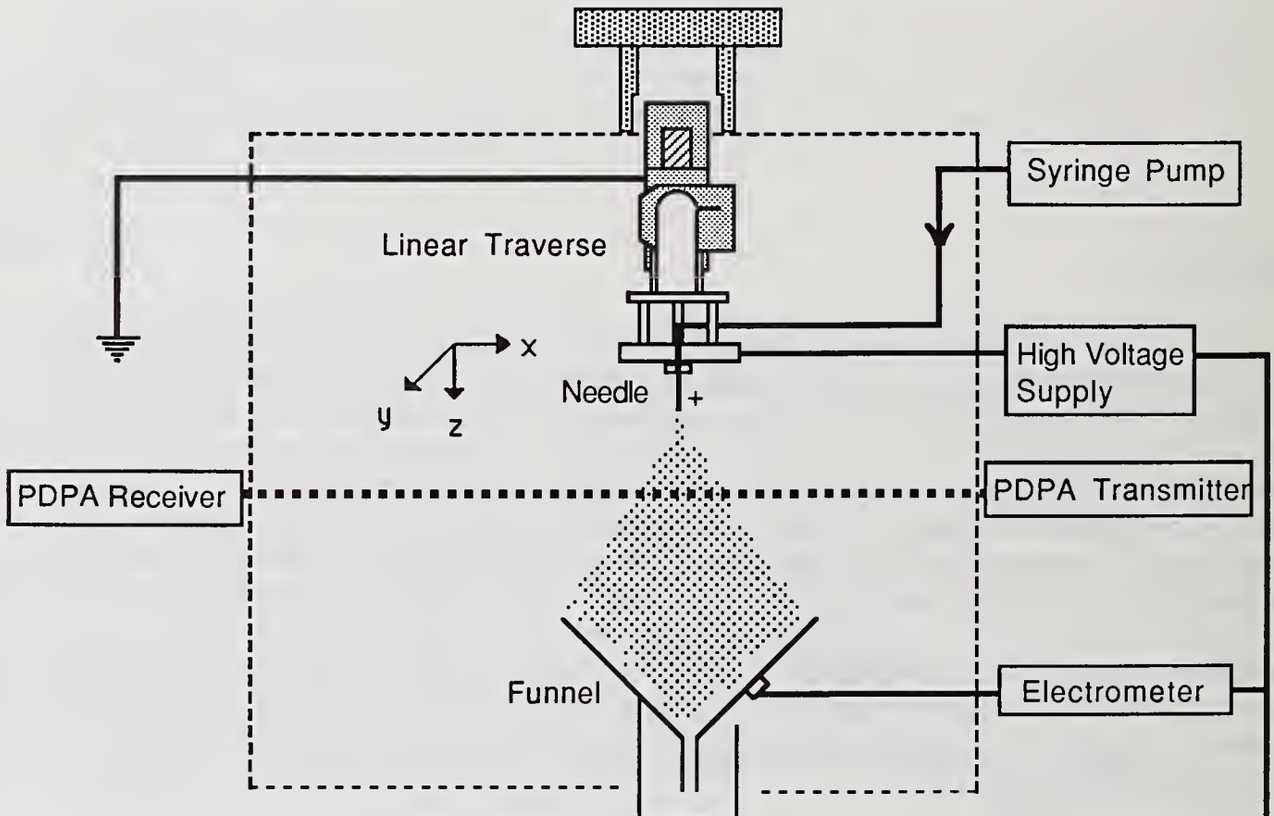

Figure 1. Schematic of the experiment.

Only the measurements acquired at the two highest spray charge densities and first axial position are presented and discussed herein. These essentially constitute those measurements in the Fine Spray Mode (see Snarski [4] for a discussion of the various EHD regimes encountered in such experiments) in which micrometer-size droplets are produced from short, brush-like filaments emanating directly from the tip of the needle. This situation is achieved at relatively high spray charge densities (in the range of ~100-200 C/m^3), at which the electric field strength at the tip of the needle is ~10^6 V/m.

Estimated uncertainties in the measured quantities were 10% for the volumetric flow rate and less than 1% for the measured voltage. The uncertainty for the probe volume location also was less than 1%,

while the typical uncertainty in the measured diameter was 4%, as estimated by Bachalo and Houser [3]. The overall range of uncertainty in the measured diameter for those measured in the present experiments was from 2 to 16%, based upon the PDPA droplet sizing calibration studies of O'Hern *et al.* [5]. The uncertainty in the current measurements was from 1% at the lowest voltage, where all the spray was collected by the funnel, to approximately 30% at the highest voltage, where the spray width exceeded that of the funnel. To compensate for the large uncertainties in current measurement at the higher voltages, the values of the currents reported herein were obtained by extrapolation of those measured at the lower voltages and at the higher voltages but at different needle-to-funnel distances.

RESULTS AND DISCUSSION

The droplet diameter distributions measured at the 15 mm axial position for the spray charge densities of 106 and 210 C/m^3 are shown in Figure 2 for three lateral positions. These lateral positions, representing typical axial centerline (x=0 mm), near-centerline (x=8 mm) and peripheral (x= 32 or 36 mm) distributions, adequately display the evolution of distributions that occurred across the span of the axially symmetric spray. At the lower charge density, the distributions at the centerline and peripheral locations are reasonably similar, but both are somewhat different than that at the near-centerline location. The mode of the distribution (the diameter of maximum count) is smallest at the centerline. At the higher charge density, the distributions become comparatively more disparate and evolve toward a lognormal distribution at the centerline. A comparison of the distributions between the two spray charge densities reveals a progressive increase with increasing spray charge density in the number of smaller droplets occurring at the centerline and at the periphery. This is especially evident at the axial centerline. This trend is like that obtained previously by Snarski [4] in similar experiments using two needles.

Individual droplet size distributions can be modelled by various empirical fits (see Lefebvre [6]). For the present study, the Rosin-Rammler distribution provided excellent agreement with the measurements. In particular, the measured and predicted volume mean diameters agreed to within approximately 5% for all cases and to within approximately 2% when averaged over the lateral span of the spray. A comparison between measured and predicted % droplet volume and count distributions is given in Figure 3. The resultant values for the two Rosin-Rammler fit parameters (the size dispersion coefficient, q, and the diameter of 63.2% cumulative liquid volume, X) at a fixed spray charge density were minimum at the centerline and increased by approximately 10 to 20% across the lateral span of the spray. When averaged across the spray, these values ± their standard deviations were $q_{avg} = 3.65 \pm 0.27$ and $X_{avg} = 26.6 \pm 1.80$ μm for 106 C/m^3 and $q_{avg} = 3.52 \pm 0.18$ and $X_{avg} = 22.5 \pm 1.90$ μm for 210 C/m^3. These resultant values are within the bounds of those obtained for most sprays [6] and are like those found in Snarski's experiments [4]. Also, the parameters q and X were minimum at the spray centerline at each charge density, implying a diameter distribution of smaller droplets with slightly more dispersion than at other locations. This occurred even more so at the higher spray charge density.

At the higher charge density, however, a progressively larger number of smaller diameter droplets comprised a majority of the droplet population. For this situation, the Rosin-Rammler empirical fit inherently did not predict well the lower diameter end of the distribution. Here, the measured diameter distribution was better described in this region by a lognormal fit, as evidenced by the precision of the lognormal fit of the count distribution shown in Figure 3. Based upon this trend, it is plausible to expect that at even higher charge densities a normal distribution will provide the best fit, as predicted by Kelly [2], if the droplets reach an equilibrium end-state. Such an evolution to a normal distribution would signify a reduction in the complexity of or number of parameters affecting the droplet population [7].

Further insight into the dynamics of the droplets within the spray can be gained by examining the measured droplet flux distributions. These are presented in Figure 4 for the same conditions as those in Figure 2. At a fixed spray charge density, the greatest droplet flux occurred at the centerline where the droplet population was comprised of a majority of small droplets. In the lateral direction toward the periphery of the spray, the droplet flux decreased appreciably, eventually by 2 to 3 orders of magnitude

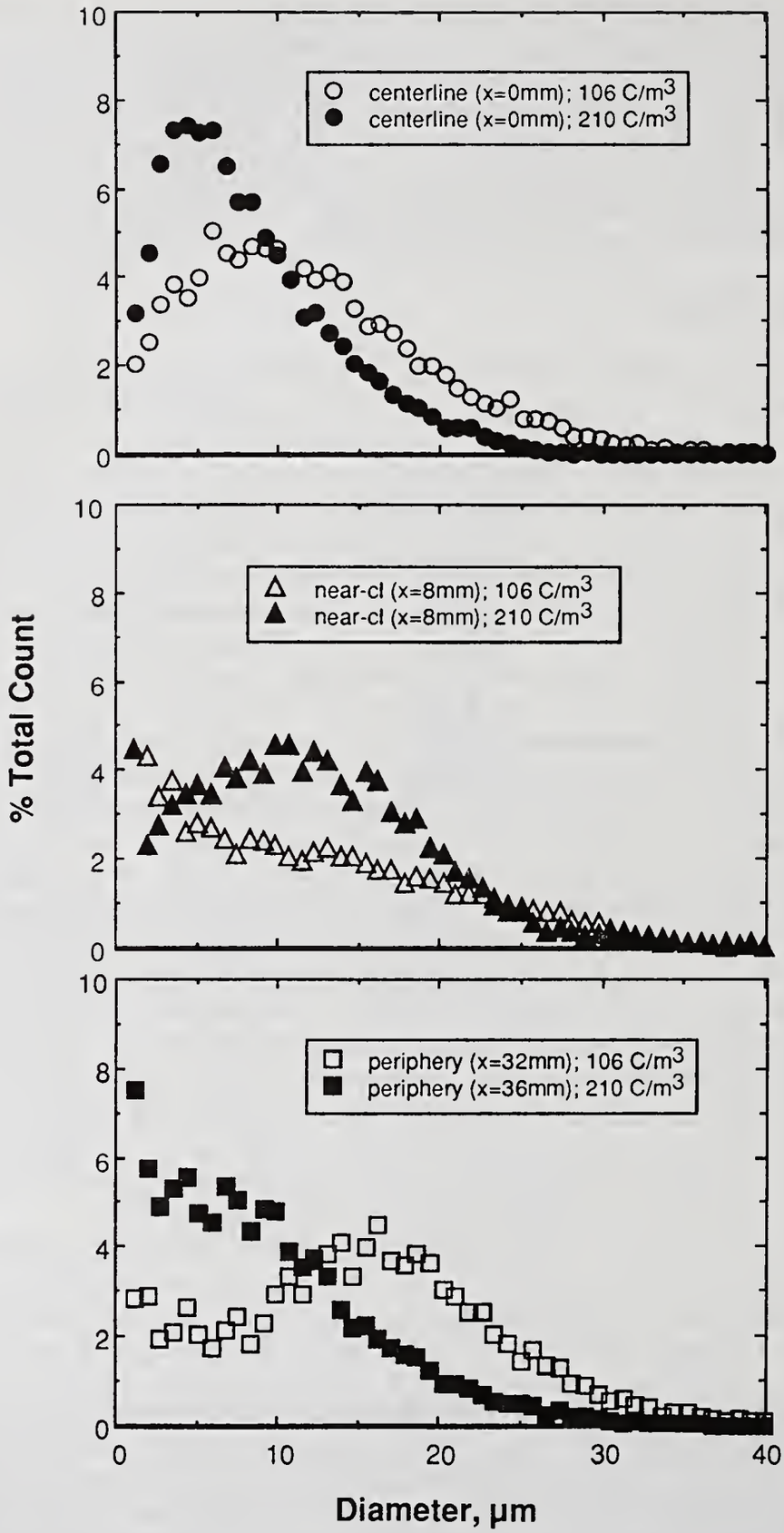

Figure 2. Droplet diameter distributions at the 15 mm axial location and spray charge densities of 106 and 210 C/m^3.

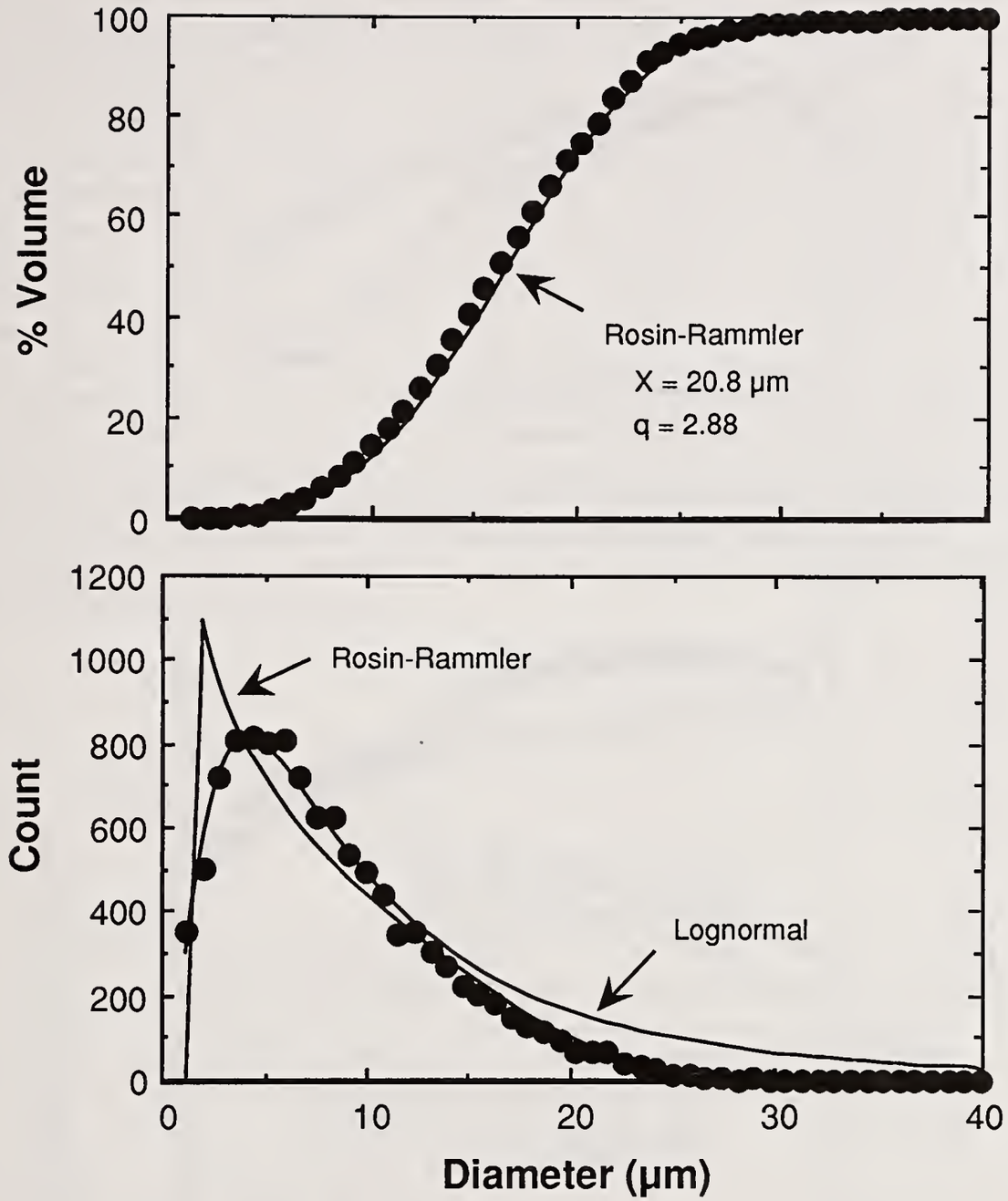

Figure 3. Rosin-Rammler and lognormal fit comparison at the spray centerline, 15 mm axial location and spray charge density of 210 C/m^3.

at the periphery. At the higher charge density, for all lateral positions, the maximum value of the droplet flux occurred at smaller diameters. This is consistent with the photographic observations reported by Snarski [4], in which the length and diameter of the brush-like filaments extending from the tip of the needle decrease with increasing charge density and produce a larger number of smaller droplets.

The measured droplet flux distributions also can be used in conjunction with various models that relate droplet charge to diameter to construct charge flux distributions. This is accomplished by incorporating the appropriate droplet charge-to-diameter relation into the droplet flux distribution, directly yielding the charge flux distribution. In the present study, two models were examined. In one, droplets were assumed to be charged to their maximum (Rayleigh) limit where charge ~ diameter$^{3/2}$, and in the

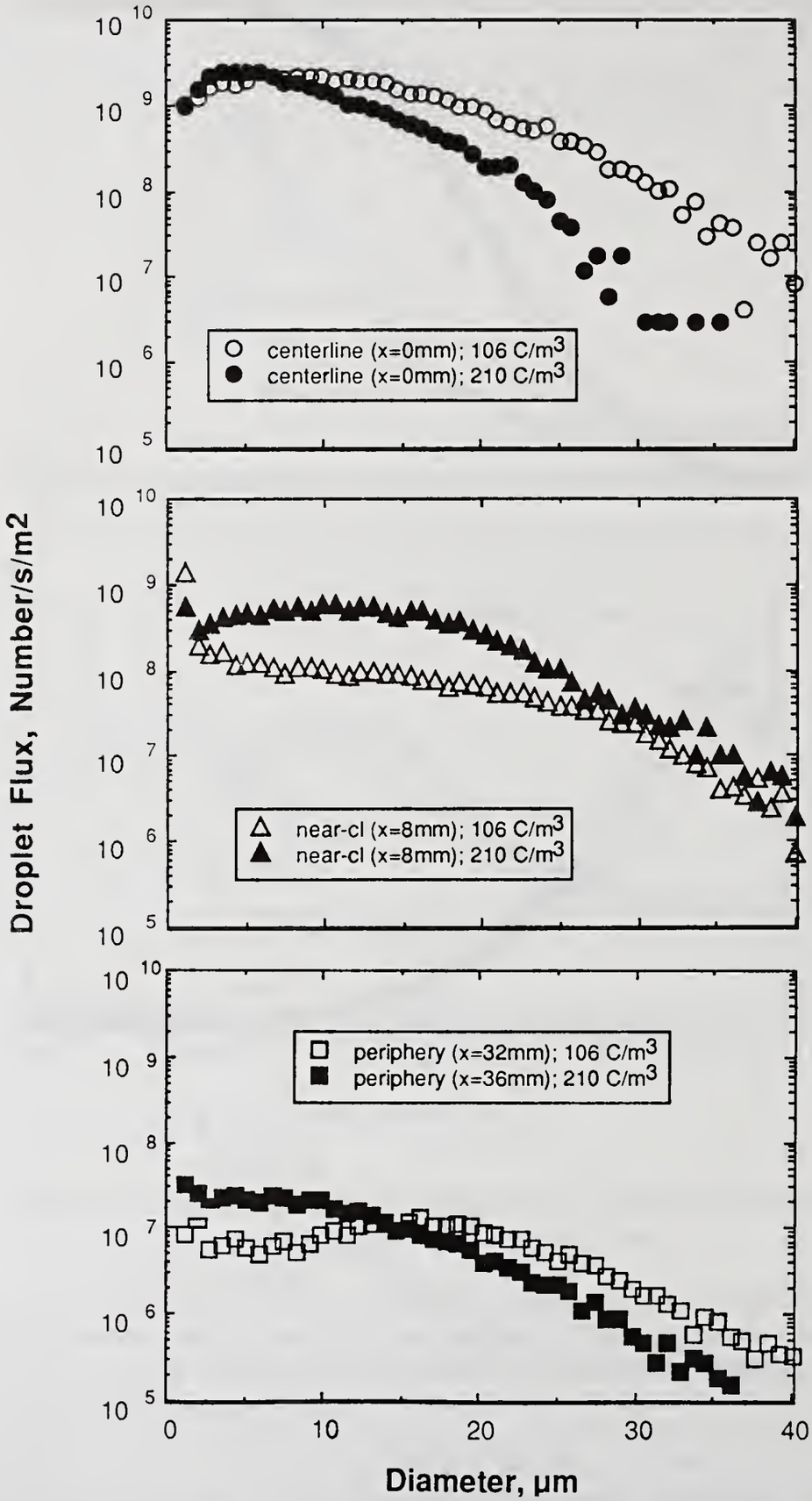

Figure 4. Droplet flux distributions at the 15 mm axial location and spray charge densities of 106 and 210 C/m^3.

other, to an equilibrium end-state where charge ~ diameter [2]. Other droplet charging models, such as those yielding minimum energy and most probable distributions, were not considered. This was because the Rayleigh model describes an upper limit and Kelly's model recently has been shown in two independent experiments [2,7] of EHD sprays to best describe the measured velocity-diameter correlations.

The resultant droplet charge flux profiles at both charge densities are displayed in Figure 5 for each of the two models. Implicit in determining these profiles is the choice of a diameter that is representative of the diameter distribution at each lateral position. Here, for the Rayleigh model, the PDPA measured diameters were used directly and, for Kelly's model, several representative diameters were examined (d_{mode}, d_{10}, d_{20}, d_{30} and d_{32} - see Lefebvre [6]). The linear average diameter, d_{10}, gave the best agreement between experiment and theory in terms of total current measurement. At both spray charge densities, each model predicted that the maximum charge flux was at the centerline. The Rayleigh model, as anticipated, predicted the highest charge flux. Comparison between the two charge density cases further showed that the droplet charge flux distribution with increasing spray charge density became logarithmically related to lateral position. The least-squares fits of the data yielded high correlation coefficient values of 0.98 and 0.99 at the higher charge density and 0.94 and 0.94 at the lower charge density for the Rayleigh and Kelly models, respectively. All of these values corresponded to confidence levels greater than 99.9% when considering the number of lateral positions examined. These findings imply, irregardless of the droplet charging model assumed, that the droplet charge flux distribution is logarithmically related to lateral position.

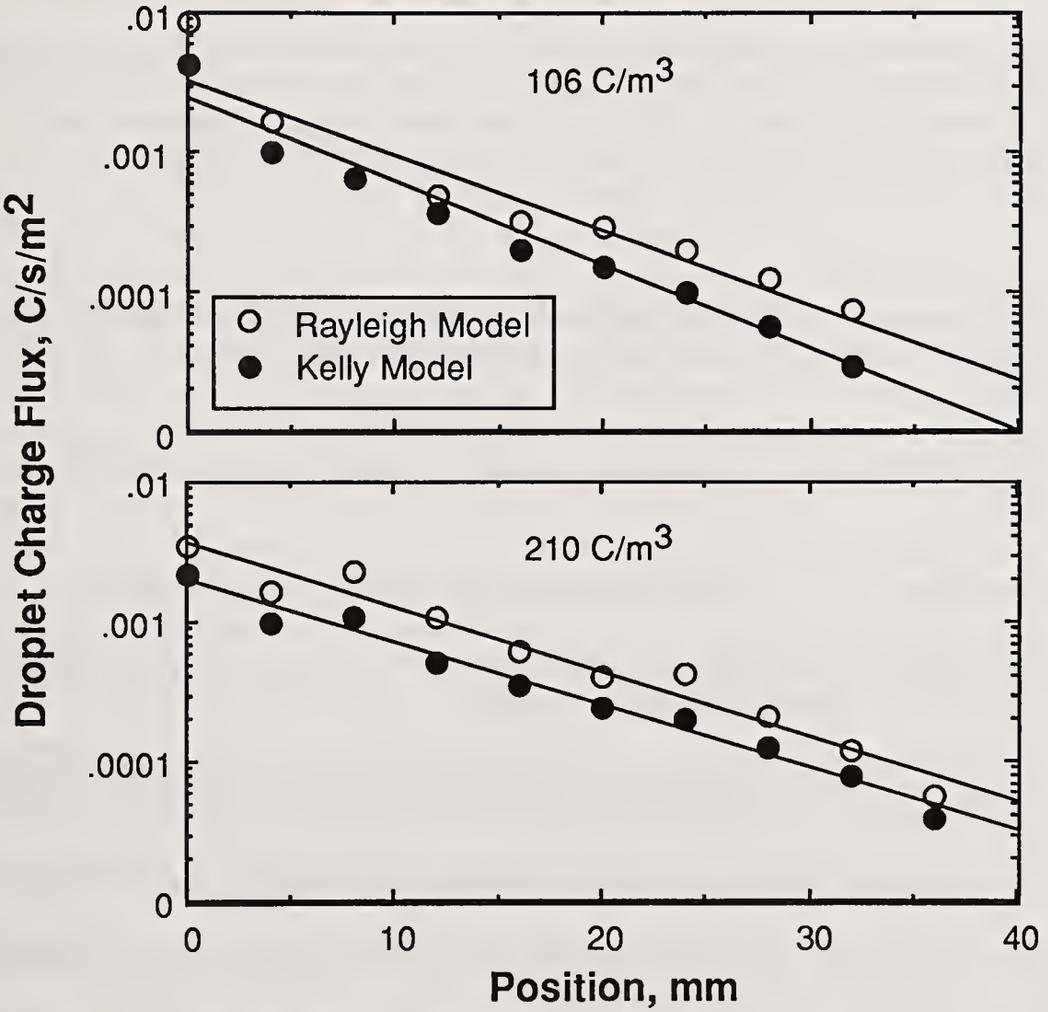

Figure 5. Droplet charge flux profiles for Rayleigh's and Kelly's models at the 15 mm axial location and spray charge densities of 106 and 210 C/m^3.

The model most descriptive of the present experiments can be identified by numerically integrating these profiles across the lateral span of the spray to yield values that can be compared to the measured total droplet current. This comparison revealed very good agreement (within the experimental uncertainty) with Kelly's theory (to within approximately 5% for the lower charge density [0.63 μa predicted versus 0.60 μa measured] and to within approximately 20% for the higher charge density [0.94 μa predicted versus 1.20 μa measured]). The total droplet currents predicted from Rayleigh's model were approximately twice the magnitude of the measured values (1.27 μa and 2.08 μa for the lower and higher charge densities, respectively). These results further support that Kelly's theory best describes the present experimental results.

CONCLUSIONS

The measurements presented herein support that droplet sprays of ethanol obtained at the subject levels of spray charge density closely approach or may have already reached their equilibrium end-state. This conclusion was drawn from the observed evolution of the droplet diameter and flux distributions with increasing spray charge density. Further evidence was acquired by determining that the best agreement between measured and predicted total droplet currents was achieved by assuming an equilibrium end-state process for droplet charging.

ACKNOWLEDGEMENTS

We gratefully acknowledge the technical advice of Drs. V.J. Novick and E.D. Doss within the Engineering Physics Division of Argonne National Laboratory. This work was performed under MIPR No. FY76168800343 between the University of Chicago and the Department of Defense and under Contract No. 62622401 between Argonne National Laboratory and the University of Notre Dame.

REFERENCES

1. Dunn, P.F. and Snarski, S.R., "Velocity Component and Diameter Distribution Characteristics of Droplets Within Two Interacting Electrohydrodynamic Sprays," Physics of Fluids A, Vol. 3, No.3, pp. 492-494, 1991.

2. Kelly, A.J., "Electrostatic Metallic Spray Theory," Journal of Applied Physics, Vol. 47, No. 12, pp. 5264-5271, 1976.

3. Bachalo, W.D. and Houser, M.J., Optical Engineering, Vol. 23, No. 5, pp.583-590, 1984.

4. Snarski, S.R., "The Interaction of Electrohydrodynamically Generated Liquid Droplets," Masters Thesis, University of Notre Dame, Notre Dame, IN, 1988.

5. O'Hern, T.J., Rader, D. J., and Ceman, D.L., "Droplet Sizing Calibration of the Phase Doppler Particle Analyzer," Annual Meeting of the American Association for Aerosol Research, Reno, NV, 1989.

6. Lefebvre, A.H., *Atomization and Sprays*, Hemisphere Publishing Corporation, New York, 1989.

7. West, B.J. and Shlesinger, M., "The Noise in Natural Phenomena," American Scientist, Vol. 78, pp. 40-45, 1990.

8. Gomez, A. and Tang, K., "Characterization of Liquid Fuel Electrostatic Sprays," Fall 1990 Meeting of the Western States Section of the Combustion Institute.

INDUCED ATOMIZATION

S.P. Lin and D.R. Woods

Mechanical and Aeronautical Engineering Department
Clarkson University
Potsdam, NY, U.S.A.

ABSTRACT

An intact liquid jet emanating from a nozzle is subjected to a periodic external forcing in the axial direction. It is discovered that the jet may be induced to atomize and produce droplets of diameters much smaller than the jet diameter. The induced atomization occurs only in widely separated discrete frequency bands. The diameter of the droplets produced in these bands decrease with increasing frequency. The locations of the discrete bands for the induced atomization depends on the relevant flow parameters.

INTRODUCTION

It is well known since the time of Rayleigh (1) and Plateau (2) that a liquid jet emanated from a nozzle may break up into droplets of diameter comparable to the diameter of the liquid jet. The mechanism of the breakup is due to the capillary pinching (3). Taylor (4) demonstrated that at a relatively high jet velocity there is another mode of breakup which results in a formation of a spray of fine droplets of diameters much smaller than the jet diameter. Lin & Kang (5), and Lin & Lian (6) showed that formation of droplets of this scale by spontaneous atomization of a liquid jet without external excitation can be achieved only in the parameter range $Q >> We$, where $Q = \rho_2/\rho_1$ is the ratio of the density of the ambient gas to that of the liquid, We is the Weber number $We = S/\rho_1 U^2 a$, S being the surface tension, U the jet speed and a is the nozzle inner radius. By use of the energy equation and neglecting the gas viscosity Lin and Creighton (7) showed that while the mechanism of the jet breakup by the Rayleigh mode is capillary pinching, the mechanism of atomization is the high frequency pressure fluctuation at the liquid-gas interface. Taking into account the effect of gas viscosity, Lin & Ibrahim (8) showed that the interfacial shear stress fluctuation may be of the same order of magnitude as the pressure fluctuation in some parameter range. A similar energy analysis for a coaxial core annular flow was reported by Chen, Bai & Joseph (9). These results suggest that atomization may be induced even in the range $We \sim Q$ by a high frequency oscillation of the nozzle tip in the axial direction. This is found to be the case in the present experiments. However, unexpectedly we discover that the atomization can be induced only in widely separated narrow bands of frequency.

EXPERIMENT

Figure 1 displays the general layout of the experimental equipment. A flask filled with a test liquid is connected from it upper neck to a flexible tubing. The tubing is connected through a pressure gauge and a valve to a compressed air line. A nozzle is connected to the flask

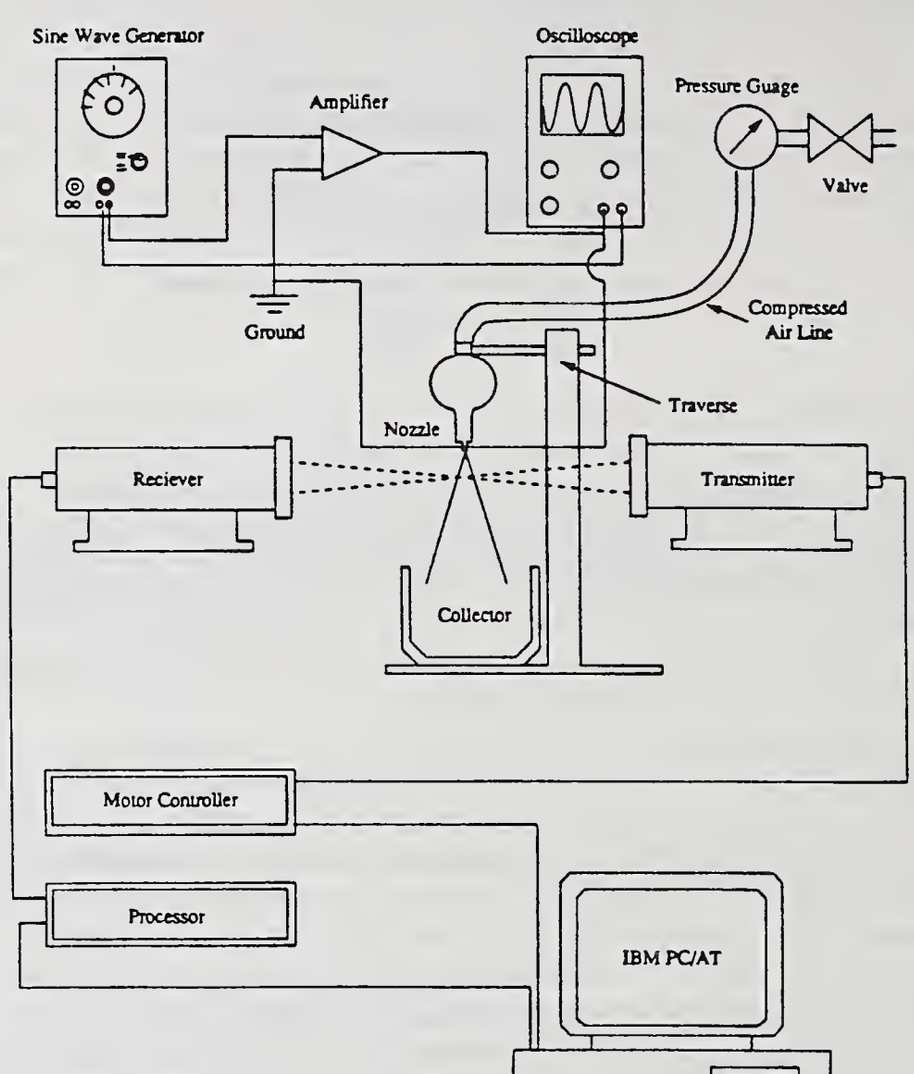

Fig. 1 Experimental Layout

through its lower open protrusion. The liquid discharge rate through the nozzle is regulated by use of the pressure gauge which controls the pressure exerted at the air-liquid interface in the flask. The flask is mounted on a frame which can be traversed vertically as well as horizontally. The liquid discharged through the nozzle is collected in a beaker under the nozzle. The cylindrical nozzle tip is made of Vernitron piezoelectric ceramic. Its inner diameter and length are respectively 0.05 cm and 1.905 cm. The cylindrical wall thickness is 0.05 cm. The axis of the nozzle tip is aligned in a vertical direction. The electrodes at the upper end of the piezoelectric cylinder are connected to a function generator, through an oscilloscope and a amplifier (Burr-Brown 3854 JM). The amplifier is required to raise the voltage to approximately 100 Volts which is necessary to vibrate the 1.905 cm long piezoelectric piece by as small an amplitude as 1 μm in the axial direction. The function generator supplies sinusoidal voltages on the order of 10 Volts peak to peak at frequencies between 1 Hz and 100 KHz. The signal supplied to the nozzle is monitored on the oscilloscope. The size and the axial velocity

distributions of the atomized droplets at a given spatial position are measured non-intrusively by use of a Phase Doppler Particle Analyzer (PDPA, Aerometrics). The PDPA system consists of the laser beam transmitter (XMT-1100), a signal receiver (RCV-2100), a motor controller (MCB-700-1) Phase/Doppler processor and a data processor. Two transmitted laser beams of equal intensity intersect at a specified spatial position where the measurement is to be taken. A droplet passing through this position scatters the transmitted light and produces an interference fringe pattern. The fringe spacing is related to the drop size by the Mie equation (10). The image of the fringe pattern appears to move past the receiver at the Doppler difference frequency. Each of the three detectors in the receiver sees a similar but out of phase Doppler burst. The phase shift is related to the drop size and the Doppler shift is related to the droplet velocity. The conversion of the phase and frequency shifts to the particle size and velocity is achieved by the Phase/Doppler processor (PDP-3100). The statistics of the size and velocity distributions at the spatial position over a sufficiently long period of time is then obtained by use of an IBM PC/AT. The detail of the principle of a PDPA system can be found int he paper by Bachalo and Houser (10). Pure alcohol and 70% -30% by volume of alcohol-water mixture were used as the test liquids.

The experimental procedure is relatively straightforward. First the receiver is aligned to receive the forward scattering light making a fixed angle of 30° with the transmitted laser beam. The flask is traversed to a desired position. The valve of the compressed air line is then opened and the pressure gauge is set to a preassigned pressure depending on the discharge rate desired. The function generator is then turned on, and the frequency is gradually raised until atomization takes place. The size and the velocity distributions at the intersection of the transmitted beams are measured with the Aerometric PDPA system.

RESULTS

The results will be presented in terms of the following relevant dimensionaless groups:

Weber number, $We = S/\rho_1 U^2 a$,

Reynolds number, $Re = U a/\nu_1$,

Froude number, $Fr = U^2/ga$,

Strouhal number, $St = U/\omega a$,

amplitude ratio, $A = \delta/a$,

density ratio, $Q = \rho_2/\rho_1$,

viscosity ratio, $M = \nu_2/\nu_1$,

where the subscript 1 and 2 stand for the liquid and gaseous phases respectively, ν is the kinematic viscosity, g is the gravitational acceleration, and δ and ω are respectively the amplitude and the frequency of the nozzle oscillation. The amplitude δ is related to the applied voltage V

and the piezoelectric constant d_{31} (-274 x 10^{-2} m/Volt) by

$$\delta = V \cdot L \cdot d_{31}/t \ ,$$

where L and t are respectively the length and thickness of the piezoelectric cylinder. The amplitude δ in the present experiment is approximately 1 μm according to the above equation. Hence the parameter δ/a is fixed to be 4 x 10^{-3}. The values of Q and M for the test fluids are given in Table 1.

Table 1 - Physical Properties of Fluids

Fluid	Viscosity	Surface tension	Density	10^3Q	M
(% Alcohol - % H_2O)	($10^{-6}m^2/s$)	(10^{-2} N/m)	(Kg/m^3)		
100 - 0	1.45	2.30	789.0	1.53	10.42
70 - 30	2.72	2.71	851.7	1.42	5.52

When the frequency of the function generator is increased gradually from zero, the jet remains intact until the first critical frequency is reached. When the first critical frequency is exceeded, the jet suddenly atomizes to form the fine spray. As the frequency is raised further, the jet continues to atomize in a narrow frequency band. When this band is exceeded, the jet returns to its intact configuration. Before the maximum function generator frequency of 100 KHz is reached, three such narrow bands of atomization are encountered. The location of the frequency bands depend on the relevant flow parameters. The results obtained with pure ethyl alcohol are presented in Figure 2. Measurements were taken at a point 3.0 mm radially and 5.0 mm axially from the nozzle exit. In each figure the values of A, Q, and M are fixed. The measured dimensionaless average droplet diameter D = d/(2*a*), d being the average diameter, are plotted against St in the figure for the set of We, Re, Fr specified in the figure.

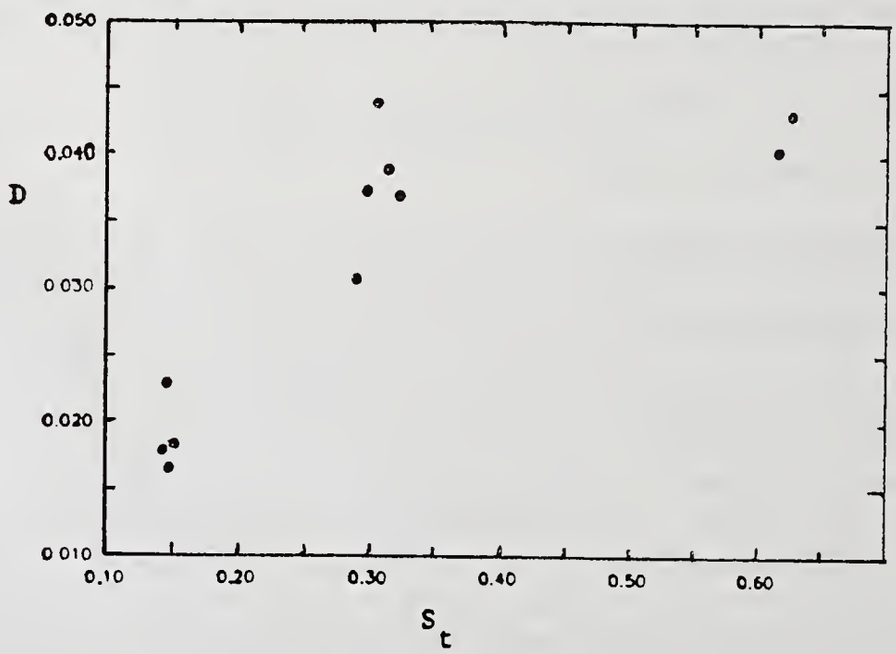

Fig. 2 Selective Atomization

Re = 500, We = 0.01383, Fr = 3433, Q = 0.001525, M = 10.42, A = 0.004

ACKNOWLEDGEMENT

This work was supported in part by grant no. DAAL03-89-K-0179 of ARO, grant no. MSM-8817372 of NSF and a New York State Science Foundation Grant. The computation was carried out with the computer facility at Clarkson University and with the Cornell National Computer facility, which is funded by the NSF, the State of New York, and IBM Corporation.

REFERENCES

1. Rayleigh, Lord, "On the Instability of Jets", London Math Soc., **10**, pp. 361-371 (1879).

2. Plateau, J., Statique Experimentale Et Theorique Des Liquids Soumix Aus Seules Forces Moleicularies, Canthier Vallaris (1873).

3. Chandrasekhar, S., Hydrodynamic and Hydromagnetic Stability, Oxford U. Press, Oxford (1961).

4. Taylor, G.I., The Scientific Papers of G.I. Taylor, Cambridge U. Press, London, Vol. 3 (1963).

5. Lin, S.P. and Kang, D.J., "Atomization of a Liquid Jet", Phys. Fluids, **30**, pp. 2000-2006 (1987).

6. Lin, S.P. and Lian, Z.W., "Mechanism of Atomization", AIAA, **28**, pp. 120-126 (1990).

7. Lin, S.P. and Creighton, B., "Energy Budget in Atomization", Aerosol Science and Tech., **12**, pp. 630-636 (1990).

8. Lin S.P. and Ibrahim, E.A., "Instability of a Viscous Jet Surrounded by a Viscous Gas", J. Fluid Mech., **218**, pp. 641-658 (1990).

9. Chen, K., Bai, R, and Joseph, D.D., "Lubricated Pipelining III", J. Fluid Mech., **214**, pp. 251-266 (1990).

10. Bachalo, W.D. and Houser, M.J., "Phase/Doppler spray Analyzer for Simultaneous Measurements of Drop Size and Velocity Distributions", Optical Eng., **23**, pp. 583-590 (1990).

PRODUCTION OF UNIFORMLY-SIZED DUAL CONCENTRIC DROPLETS FROM COAXIAL SMOOTH JET UNDER APPLIED AC ELECTRIC FIELD

T. Sakai, M. Sadakata, M. Sato, K. Kimura and M. Saito

Department of Biological and Chemical Engineering
Gunma University
Kiryu, Gunma, Japan

ABSTRACT

The production of uniformly-sized droplets by means of a mechanical vibration method and an electrical method has been studied. The relationship between these two methods at the limits of the uniform region are aimed to establish. The upper and the lower limits of the frequency of a uniform droplet region (synchronous region) for the mechanical vibration method and the AC electric field method were the same. From the analogy of the surface wave propagation caused by mechanical and electrical vibrations, it is considered that the AC electric field may cause an initial disturbance or displacement on the electrically conductive liquid surface. Thus the surface wave growth along the liquid column surface will result in synchronous disintegration of the smooth liquid jet.

The generation of concentric dual droplets by the AC electric field method and surface wave propagation rates on co-axial dual liquid columns are discussed. It is proposed that the present method may provide a new technique for the production of fine uniform droplets or particles, even for non electrically conductive liquids.

INTRODUCTION

Research papers on the production of uniform droplets have essentially describe two methods. One is the vibration method which includes acoustic, mechanical and liquid pressure vibration and the other method is the application of electrostatic field. Reports on these methods have been published [1 - 14], however, the relationship between the vibration method and the electrostatic method has not clarified.

In this paper, at first, the disintegration mechanisms during uniform droplet production of both methods are compared and analyzed. The results are then applied to produce uniform sized droplets by application of high AC voltages. The second purpose of this work is to produce smaller uniform droplets of non or poorly electrically conductive liquids using electrostatic method, by applying AC voltages on a smooth dual coaxial liquid column covered with conductive liquid. This method would provide more convenient process to produce finer uniformly-sized droplets with lower injection pressure particularly for high viscous non conductive liquids when dual convergent nozzle are adopted.

The vibration method used on dual or multiple coaxial liquid columns to manufacture uniform droplets is popular [15] such that artificial salmon roe is well known. Though the technique is known, fundamentals of this

method have not been discussed.

This work is concentrated in two areas. The first is to clarify the relationship between the upper and lower limits of vibration frequency of the uniform droplet region, and upper and lower limits of applied AC frequency. The second purpose is to clarify the fundamentals of generating conditions for dual uniform sized droplets by means of the electrostatic method from dual or multiple coaxial smooth jets which are surrounded by electrically conductive liquid, where inner liquids are not conductive.

EXPERIMENTAL APPARATUS AND METHOD

Experiments were conducted using the apparatus shown in Fig. 1. As shown in the figure, inner and outer liquids are supplied from the storage vessels (5) using static air pressure to prevent liquid flow disturbance. Flow rates of each liquid are controlled with regulating the air pressure supplied from the air compressor (7) through the reducing valve (6) and measured using flowmeters (4). The inner and outer liquids are forced into the dual capillary nozzle (1) and discharged into ambient air. The discharged liquids are consisted of a co-axial dual liquid jet column. The dual capillary nozzle (1) and the circular plate electrode (3) are connected to a high voltage AC power source (2). The disintegration patterns of the liquid column are recorded by means of shadow and scattered light photographs using a stroboscope (10) as a lighting source by a still camera (8) or a video camera (9).

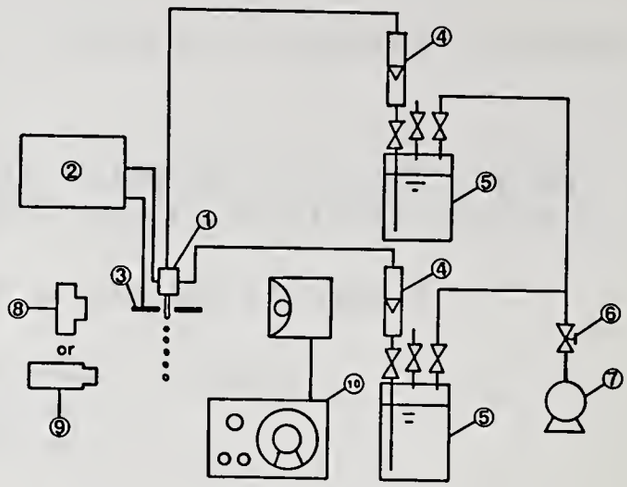

Fig.1 Schematic diagram of experimental apparatus.

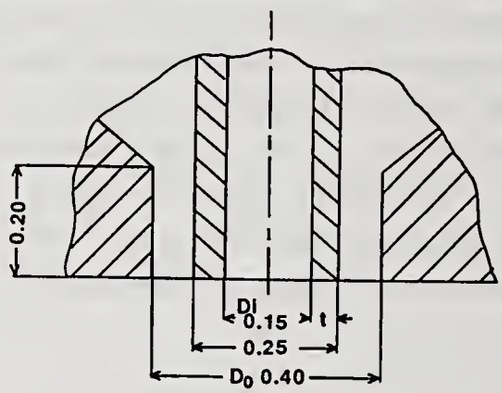

Fig.2 Geometry of dual capillary nozzle.

The detailed geometry of the dual capillary nozzle is shown in Fig. 2. In this case, kerosene is discharged from the inner nozzle as an example of non or poor electrically conductive liquids and from the outer nozzle distilled water is discharged as the conductive liquid.

RESULTS AND DISCUSSIONS

Observations of the disintegration patterns

In Fig. 3, disintegration patterns of the coaxial dual liquid columns of mean velocity of 300 cm/s, when 2 kV AC potential with frequency of 1.0 - 3.0 kHz is applied, are compared with pattern when no AC potential is applied. The liquid velocity at the exit port of the inner and outer nozzle were both kept at 300 cm/s. As seen in the Fig. 3, spontaneous irregular disintegration of smooth jet column was observed when no AC potential is

applied.

When the applied AC frequency was changed in steps of 0.5 kHz interval, as seen in the Fig. 3(b) - (f), the patterns of (b) and (c) show irregular disintegration at 1.0 and 1.5 kHz. However, at the frequencies of 2.0 and 2.5 kHz one can observe that the disintegrated droplets were generated at nearly equal interval synchronizing with the applied AC frequency (Fig. 3(d), (e)). Furthermore, when the applied AC frequency was increased up to 3.0 kHz, the disintegration interval and droplet size became irregular. Thus, it was found that there was a synchronizing region in which coaxial dual liquid column disintegrated with a uniform interval distance and droplet size, when the applied AC potential was kept constant.

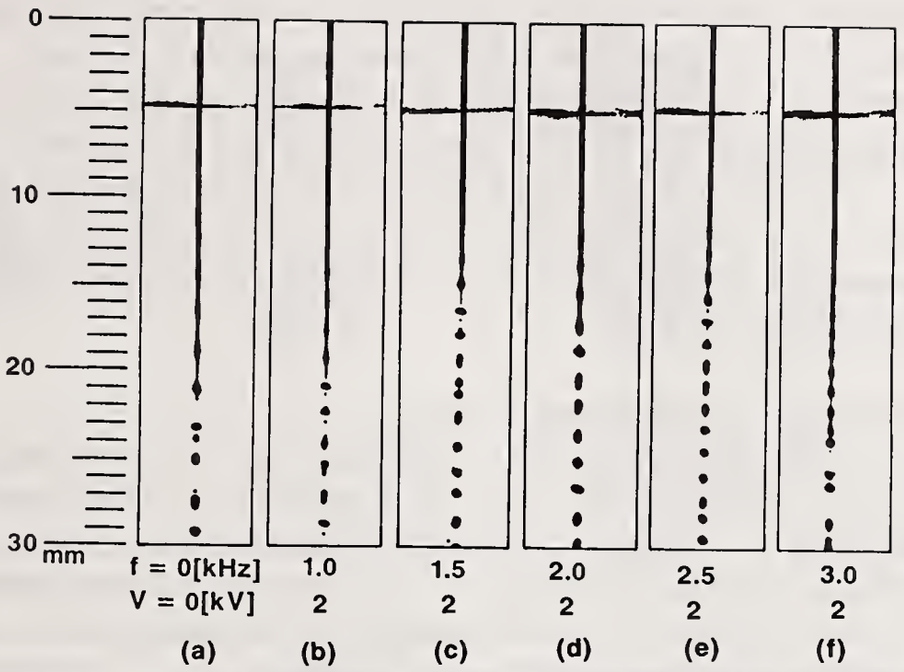

Fig.3 Disintegration patterns of the dual liquid jet column with and without AC potential.

Upper and lower limits of synchronizing frequency

In the Fig. 3, it is shown that there are upper and lower limits of frequency in which synchronized disintegration occurs changing applied AC frequency with the voltage maintained constant. This region of the frequency in which synchronized disintegration of smooth jet column occurs is referred to the "uniform (synchronous) region". The effects of the liquid mean velocity on the synchronizing upper and lower limits of the frequency of the uniform region was investigated, when outer and inner liquid velocity are kept the same.

The upper and lower limits of the frequency of the uniform region was shifted to a larger frequency range when the liquid velocity was increased. Furthermore, it was observed that there is a minimum potential over which uniform droplets can be produced. It is also shown that inspite of changing AC voltage

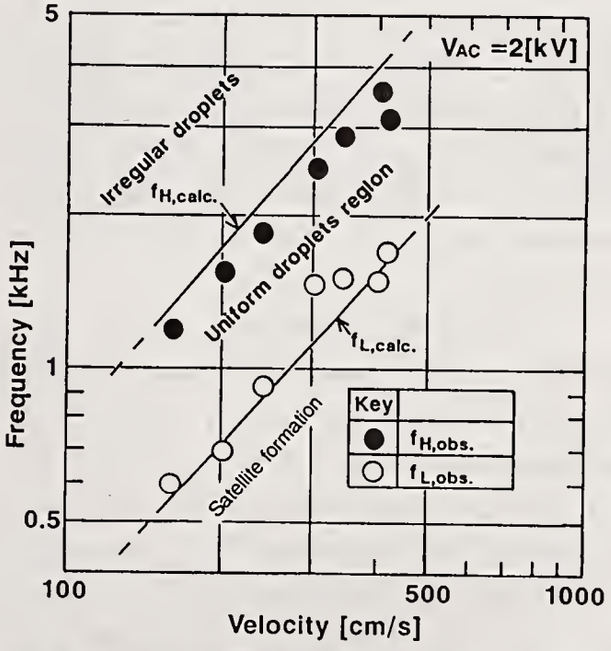

Fig.4 Upper and lower limits of AC frequency of the uniform droplets region and comparisons with calculated values by empirical equations of mechanical vibration method.

the upper and lower limits of AC frequency were kept constant for each liquid velocity. Those phenomena agree with previous reports on uniform droplets generated by mechanical vibration [1 - 5, 8]. The authors showed a parallelogram in which uniform droplets were generated. The existence of the minimum applied potential would suggest the essential minimum initial displacement or disturbance on a jet surface by an electrostatic force.

In Fig. 4, an example of upper and lower limits of frequency of uniform region is shown. The upper and lower limits of frequency line are parallel as in the case of mechanical vibration. Furthermore, the straight lines calculated by the empirical formulae from the mechanical vibration method [4, 5] agree with the experimental AC potential method, as expected.

Size distribution of uniformly-sized dual droplets

Uniformly-sized dual droplets were generated within a region of upper and lower limits of applied AC frequency. The size distributions of droplets with and without AC potential for the 300 cm/s liquid column are shown in Fig. 5. The upper figure (a) shows size distribution of falling spontaneous non synchronized disintegrated drops when AC potential was not applied. As seen in the figure, the size spread is within a wide rage of 400 - 850 μm. On the contrary, as is evident in the lower figure (b), the droplet size showed a narrower rage of 500 - 600 μm and a sharp peak when an adequate AC potential was applied.

From the experimental results, it was found that uniform droplets were generated when adequate AC potential was applied on a smooth jet of coaxial dual liquid column, the same as for the mono liquid column of electrically conductive liquid.

Observation of free falling dual droplets

Instantaneous shadow photographs of the free falling droplets were taken by means of a telescopic microscope cameras as shown in Fig. 6. The outer and inner liquid velocities were 200 cm/s, respectively. The photograph on the left shows a droplet produced by spontaneous disintegration of a smooth jet when AC potential was not applied. As seen in the Fig. 3, at the frequency of 0 and 1.0 kHz, the sizes were unequal, though each drop consists of both droplets as shown in the Fig. 6 left.

The middle photograph of Fig. 6 shows synchronized uniform droplets as an example when the AC frequency reaches 1.5 and 2.5 kHz within the established uniform region at the same AC potential of 2 kV and the liquid velocity of 300 cm/s. The spontaneously and synchronously disintegrated droplets showed double sphere drops involving one kerosene drop within each water sphere, though double spheres could not be detected in Fig. 3, which were taken by means of a usual camera.

However, in the photograph on the right side,

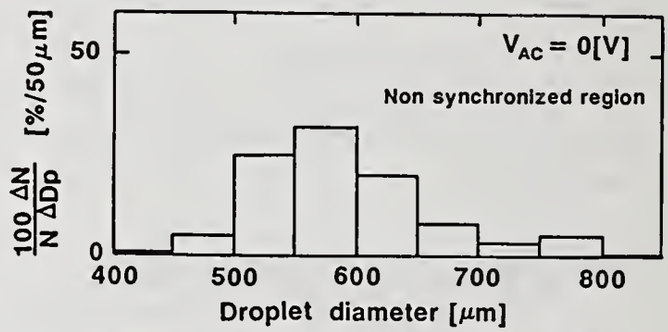

a) Non synchronized spontaneous disintegration

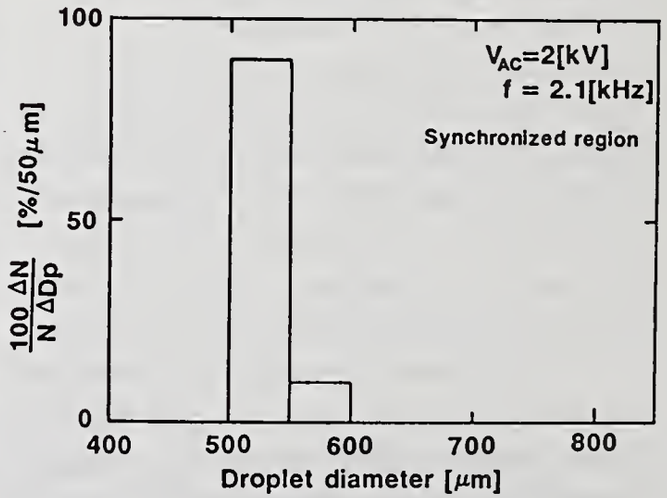

b) Synchronized disintegration

Fig.5 Size distribution of droplets between free falling.

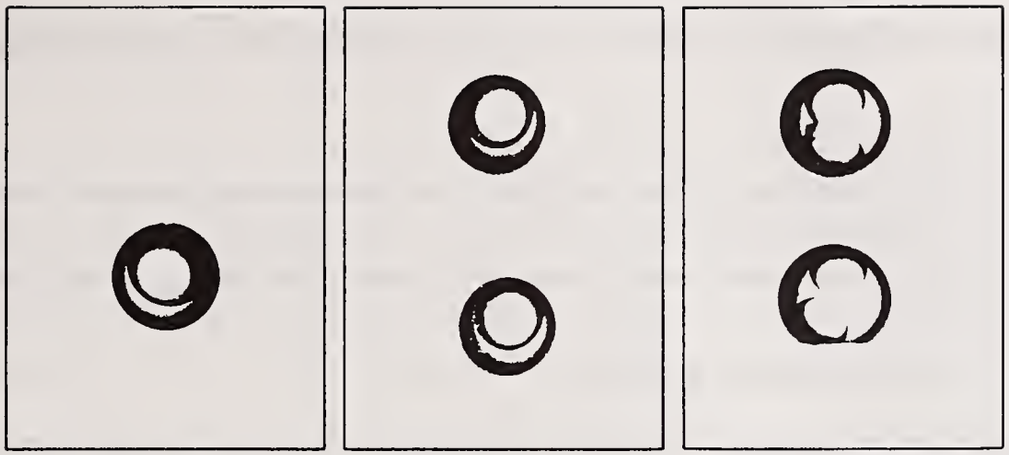

Fig.6 Instantaneous shadow photographs of droplets between free falling discharged from a dual coaxial nozzle.

the droplets were generated over the upper limit of the frequency of uniform region, the outer drop size became irregular and the number of inner drops were varied. In this case, two, three or more drops were involved, though the outer size of each droplet seemed nearly equal in size from this photograph. It is considered that in this region of disintegration, satellites were produced and sometimes they were absorbed into the main droplets therefore the drop sizes were not uniform and the satellite formation could be one of the reasons which determine the number of inner particles. However, further investigation is needed to clarify the reason why the inner particle number is varied.

Sizes of inner droplets

The sizes of the inner droplets were determined by calculation since to measure directly from the photograph was difficult because of the strong lens effect by the outer droplets. When the outer and the inner liquid mean velocities are kept uniform, the interface of both liquid should be formed between the thickness of inner tube wall. Then outer and the inner flow rate ratio $Fo/Fi=\gamma$ will be expressed using the modified nozzle diameter ratio δ, when t is the wall thickness of inner tube, Do and Di are defined in Fig. 2.

$$\delta = Do/(Di+t) \quad (1)$$

$$\gamma = \delta^2-1 \quad (2)$$

Then, the outer and the inner drop size ratio β should be

$$\beta = (1+\gamma)^{1/3} \quad (3)$$

From equations (2) and (3)

$$\beta = \delta^{2/3} \quad (4)$$

In this experiment, the center photograph of Fig. 6 is δ = 2.0, $\beta = 2.0^{2/3} = 1.59$. Therefore, the outer droplet diameter do determined from the photograph is do = 525 μm, and inner diameter is di = do/β = 331 μm.

Surface wave growth rate and effect of applied AC field

Growth rate α and uniform region. The authors investigated theoretically and experimentally on the relation between surface wave growth rate and mechanical vibration in order to generate uniform droplets [8], using

instability theory of Rayleigh [16] and Weber [17]. Rayleigh had indicated that the surface wave displacement along a smooth jet is

$$\xi = \xi_0 \exp(\alpha t + ikz) \qquad (5)$$

Here, ξ is surface displacement, α is growth rate of surface displacement in mm/s, t is time, k is wave number, z is distance in axial direction from nozzle port and i is imaginary. He neglected the viscosity term of Navier-Stoke's equation and reduced an equation of maximum surface wave growth rate as equation (6), hereafter referred as growth rate α.

$$\alpha^2 = (\sigma/\rho\, a^3)(1-k^2a^2)k\,a\, I_1(k\,a)/I_0(k\,a) \qquad (6)$$

Here, I_0 and I_1 are Modified Bessel Functions of the first kind, λ is wave length, σ is surface tension, ρ is density and a is radius of jet at any distance, $k = 2\pi/\lambda$, and ka is referred as dimensionless wave number.

On the other hand, Weber neglected the inertia term of Navier-Stoke's equation and obtained an equation regarding growth rate.

$$\alpha^2 + \alpha(3\mu/\rho\, a^2)k^2a^2 = (\sigma/2\rho\, a^3)(1-k^2a^2)k^2a^2 \qquad (7)$$

Here, μ is viscosity of liquid. The surface wave displacement ξ measured by means of the serial instantaneous shadow photographs [4, 5], should give a straight line from the equation (5) when log ξ vs. time t is plotted. The gradient gives growth rate α. The intercept on the vertical axis is corresponded to initial displacement ξ_0. The actual smooth jet radius a can not be read from the photographs directly because of the existence of surface waves at any distance z from the nozzle. The radius a at distance z is calculated by [17]

$$a = a_0 u_0^{1/2}(1+2gz/u_0^2) \qquad (8)$$

Here, g is the gravity acceleration and u_0 is the initial mean velocity of liquid jet. Conversions from measured z to t are calculated considering gravity acceleration and neglecting air friction.

The critical viscosity for using either Rayleigh or Weber's equation for the calculation of surface wave growth rate is 50 c.p. as pointed out previously [8]. As seen in Fig. 4, the experimental frequency limits of f_H and f_L by the AC method agreed with the calculated lines of f_H and f_L by the empirical equation of the mechanical vibration method for low viscosity liquids under 50 c.p. [4, 5].

Growth rate α along dual jet surface. As described in the former section, growth rate α is strongly related to the upper and lower limits of vibration frequency regarding to the uniform droplet region, while Weber [17] had proposed that the breakup length L of smooth jet column should be expressed as

$$L = (u/\alpha)\ln(a/\xi_0) \qquad (9)$$

The value $\ln(a/\xi_0)$ is known as a function of Ohnezorge number. He pointed out that when initial displacement ξ_0 grows up to ξ, as expressed in equation (5) equal to jet radius a, disintegration of liquid column occurs following equation (9). However, the jets discussed in many former investigations were merely on mono phase and single smooth jets.

The growth rate α of the spontaneous wave along coaxial dual smooth jets were measured without applying mechanical vibration or AC field by plotting log ξ vs. t, when the outer and inner liquid velocity were 200 cm/s. The measured points were lined up straightly and both of the gradients of two groups, i.e., water in water jet and oil in water jet, agreed with the theoretical gradient α which was calculated by the Rayleigh's equation for water

when the non dimensional wave number $ka = \pi d/\lambda_{obs} = 0.776$. The average ξ_0 of oil in water jet was about 0.1 μm, on the other hand the average ξ_0 of water in water jet was about 0.01 μm.

From this evidence the effect of inner nozzle geometry and physical property of liquid on the variation of scattering and initial disturbances may suggest the importance of the geometry of inner nozzle port and sharp knife edge is desirable.

From the experiments it was found that the growth rate α of co-axial dual jet surface wave is ruled merely with physical property of outer liquid when the viscosity of inner liquid is in a same order with outer liquid. Moreover, the growth rate α agreed to the Rayleigh's equation in spite of the coexistence of inner liquid.

Effect of applied AC field. Fig. 7 shows an example of growth rate α along the surface of the coaxial dual jet column when AC potential applied within a uniform region is compared with a spontaneous natural jet. The gradient of fitted straight line of AC applied jet was calculated from Rayleigh's equation using physical properties of the outer liquid but the fitted line of the spontaneous jet was drawn without using regression analysis. When 3 kV and 1.3 kHz AC was applied to the jet the uniform droplets were generated synchronously with the applied AC frequency, i.e. one droplet per each cycle, and the jet without the AC generated irregular sized droplets with spontaneous natural disintegration. The cross point with a_0 line corresponds to the breakup length of the jet and that of the AC applied jet is shorter than the non applied jet, although the gradients of the two lines were nearly equal. The breakup length of the spontaneous jet was L = 25 mm, t = 12 ms and when 3 kV, 1.3 kHz AC is applied it became L = 20 mm and t = 9.5 ms.

The intercept of vertical ξ axis increased as AC potential was applied. Thus this experimental results may be summarized that as the AC potential is applied to the conductive liquid column the initial displacement ξ_0 on the jet surface increases, however, surface wave growth rate was not changed visibly. Furthermore, it was clarified that theoretical growth rate α along coaxial dual jet surface followed to the Rayleigh's equation despite that AC potential was applied considering only its outer liquid physical properties.

According to the electromagnetic dynamics the electric field should reduce the surface tension and resulted surface wave growth rate due to Rayleigh's equation, but the experimental results did not show this. It is considered that the effect of the high potential on the surface tension reduction should be less or negligible, and the electro-attractive or repulsive forces caused by the high potential on the liquid column should have the affect of increasing the initial displacement on its surface similarly as the mechanical vibration, though further physical considerations still remaining.

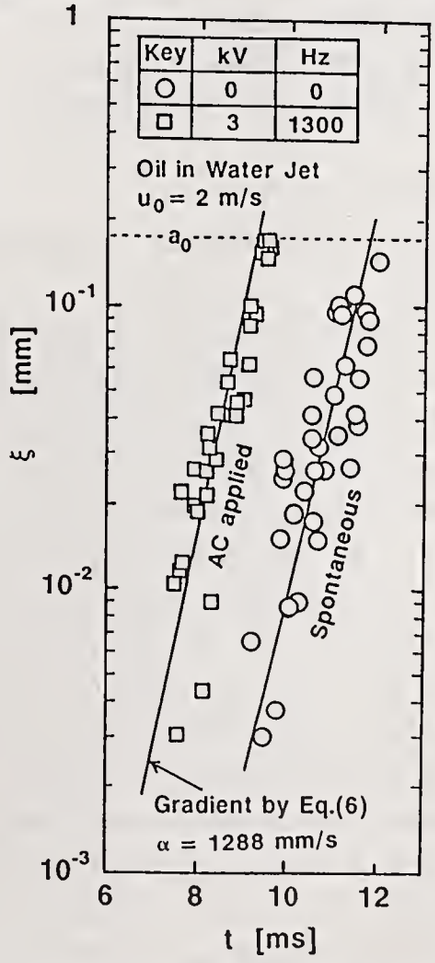

Fig.7 Comparison of surface wave growth along coaxial dual jet by spontaneous disintegration and AC applied disintegration within uniform region.

CONCLUSION

The following conclusions were obtained.

1) Uniform droplets were generated when adequate AC potential is applied on a coaxial dual smooth jet. A minimum voltage existed for generating uniform droplets. Also, within the upper and lower limits of AC frequency uniform droplets were generated and the frequency of both limits were agreed with those of the mechanical vibration, relating with jet velocity. The uniform dual droplets were generated synchronously with AC frequency, i.e. one droplet per each cycle. Each droplet contained one same sized inner droplet.

2) The surface wave growth rate along coaxial dual smooth jet follows the theoretical growth rate calculated by Rayleigh's equation using physical property of outer liquid when the viscosity of both liquid is almost the same.

3) Surface wave growth rate along coaxial dual jet when AC potential is applied agreed with that of calculated by Rayleigh's equation using induced wave number and physical property of outer liquid only. The minimum AC potential to produce uniform droplets is considered corresponding to the essential initial displacement of mechanical vibration method to generate uniform droplets to overcome the back ground noise.

4) The AC potential may cause initial displacement which will propagate along the surface of coaxial dual smooth jet most quickly than spontaneous disturbances and causes disintegration regularly following applied AC frequency and at the end of the jet the displacement grows up to jet radius.

ACKNOWLEDGEMENT

The authors wish to express their appreciate to Kanegafuchi Chemical Co. Ltd. A part of this experimental work is assisted by their financial support.

LITERATURE CITED

1) Sakai, T. and N. Hoshino: The 7th JCLASS (Japan Conference on Liquid Atomization and Spray Systems), pp. 105 (1979).
2) Sakai, T. and S. Senuma: The 9th JCLASS, pp. 11 (1981).
3) Sakai, T. and N. Hoshino: J. Chem. Eng. Japan, 13(4), 263 (1980).
4) Sakai, T., M. Sadakata, M. Saito, N. Hoshino and S. Senuma: ICLASS '82 (Wisconsin), pp. 37 (1982)
5) Matsushita, K., M. Sadakata and T. Sakai: ICLASS '88 (Sendai), A2 (1988).
6) Sakai, T., M. Sadakata and K. Matsushita: The 11th JCLASS, pp. 37 (1983).
7) Sakai, T., M. Sadakata, M. Saito and K. Matsushita: The 12th JCLASS, pp. 11 (1984).
8) Sakai, T., M. Sadakata, M. Saito and K. Matsushita: ICLASS '85 (London), VIIB(b)/2/1 (1985).
9) Sato, M. and T. Sakai: The 4th JCLASS, pp. 49 (1975).
10) Sato, M., M. Kito and T. Sakai: The 6th JCLASS, pp. 9 (1977)
11) Sato, M., H. Negishi, M. Sadakata and T. Sakai: The 15th JCLASS, pp. 73 (1987).
12) Sato, M.: J. Electrostatics, 15, 237 (1984).
13) Sato, M.: IEEE/IAS Annu. Meet. (Atlanta), pp. 1406 (1987).
14) Sato, M., H. Miyazaki, M. Sadakata and T. Sakai: ICLASS '88 (Sendai), B3-1 (1988).
15) Fullwiller, M. J. and C. W. Hatcher: Japan Patent, 52-129686 (1977).
16) Rayleigh, L: Phyl. Mag., 177 (1892).
17) Weber, C.: Z.A.M.M., 11, 136 (1931).
18) Sato, H. and M. Saito: ICLASS '82 (Wisconsin), pp. 19 (1982).

ATOMIZATION OF LIQUID CYLINDERS, CONES, AND SHEETS BY ACOUSTICALLY-DRIVEN, AMPLITUDE-DEPENDENT INSTABILITIES

J.L. Dressler

Fluid Jet Associates
Spring Valley, OH, U.S.A.

ABSTRACT

The atomization of several liquid jet configurations by an acoustic disturbance is studied. The atomizer forms a cylindrical, conical, or flat(a sheet) liquid jet by means of an electroformed nozzle. A piezoelectric driver, which has been constructed to efficiently couple energy to the liquid, modulates the fluid velocity. Operating the piezoelectric drivers at high power levels produces perturbations with sufficient energy to break the liquid jets into drops, with a net increase in surface energy. The resulting drop sizes are influenced by the frequency and amplitude of the driving signal, as well as the nozzle size. The spatial distribution of the spray is controlled by the spacing and geometry of the holes in the nozzle plate, the amplitude of the acoustic signal, and the swirl in the fluid manifold. This device is more robust than the typical acoustic drop generator because small drops can be made from large holes, reducing the plugging problem. No air flow is used.

INTRODUCTION

The atomization of a jet or sheet of liquid is a process that in most cases requires the addition of energy to the fluid. The energy input is required because the surface area of the atomized fluid is larger than the original fluid surface area. The energy stored in the increased surface must be supplied from a decrease in the kinetic energy of the fluid or from an external source.

Most fuel injectors for oil burners or gas turbines use an air blast to atomize the liquid jet or sheet. A fast moving air stream impinges on the slower moving fuel. The kinetic energy of the air tears the liquid into filaments and then into drops.[1,2]

Another technique that has been used for specialized applications is the acoustic excitation of a liquid cylinder at an unstable wavelength. This technique does not add energy to the liquid because the fluid surface area is lower after the disintegration has occurred. Rayleigh[3] derived the dispersion equation for infinitesimal disturbances on a liquid cylinder. His theory correctly shows that the cylinder is stable for all but one of the modes of perturbation. The jet is unstable only for azimuthally symmetrical perturbations (the sausage mode) whose axial wavelength is longer than the jet's circumference. For this one mode, small perturbations will grow and the surface area of the fluid decreases as the jet disintegrates into a stream of drops. The use of small amplitude acoustic perturbations to produce a stream of monodisperse drops from a circular liquid jet has been studied extensively.[4,5,6] The drawback of this technique for atomizing fuel is that the size range of drops for a given liquid jet diameter is restricted. The resulting drops have a diameter approximately twice the diameter of the original jet. This restriction means

that small nozzles must be employed to obtain small drops and there is a great chance of nozzle plugging due to particles in the fuel.

Dressler[7] has derived a dispersion equation for small perturbations on the surface of a sheet of liquid. This analysis is similar to Rayleigh's analysis of a circular jet. Dressler found that for perturbations driven solely by capillary forces, the sheet of fluid is stable for all perturbations. Thus, the technique of inducing atomization with a small acoustic signal works only for circular jets; it does not work for sheets.

In addition to the air blast techniques, other methods have been devised to overcome the capillary force and drive a fluid jet or sheet unstable. Melcher[8,9,10], Crowley[11], Ketterer[12], Dressler[13], and Centani[14] studied driving and stabilizing instabilities on fluid jets and sheets with electrical forces. These previous electrohydrodynamic studies were concerned with systems that were unstable; an infinitesimal perturbation of the liquid surface would grow without bound.

Our atomizer described here builds on our previous work[15,16] to disintegrate the fluid and obtain a spray with a higher surface area than the initial fluid. We use high amplitude acoustic energy to provide the energy needed to increase the surface energy of the fluid. This process produces sprays with the shapes of fans, cones, cylinders, and sheets. The process does not use an air blast. By setting the frequency and amplitude of the acoustic signal, we achieve some control of the drop size in the resulting atomized fluid independently of any air flow.

ATOMIZER DESCRIPTION

Figure 1 shows a photograph of the injector. A piezoelectric driver is placed in the circular fluid manifold. A nozzle plate, fabricated by a photofabrication process, is placed across the end of the manifold. With this design, the acoustic energy produced by the piezoelectric transducer is efficiently coupled into the fluid, creating additional surface area on the atomized fluid.

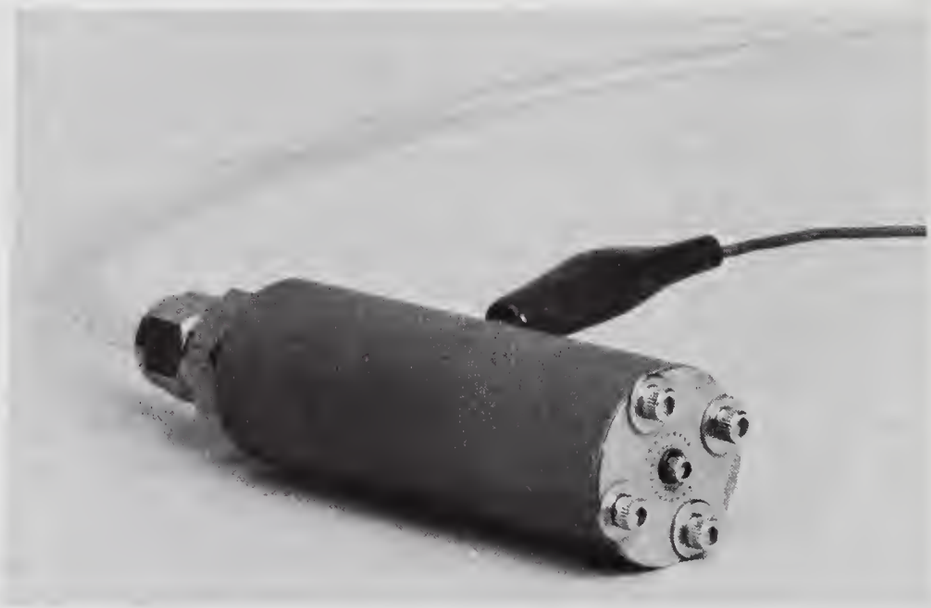

FIGURE 1.
High Amplitude Ultrasonic Atomizer

Several photographs of nozzle plates are shown in Figure 2. Figure 2a is a rectangular slot, Figure 2b is a rectangular slot with width perturbations, and Figure 2c shows a common round nozzle.

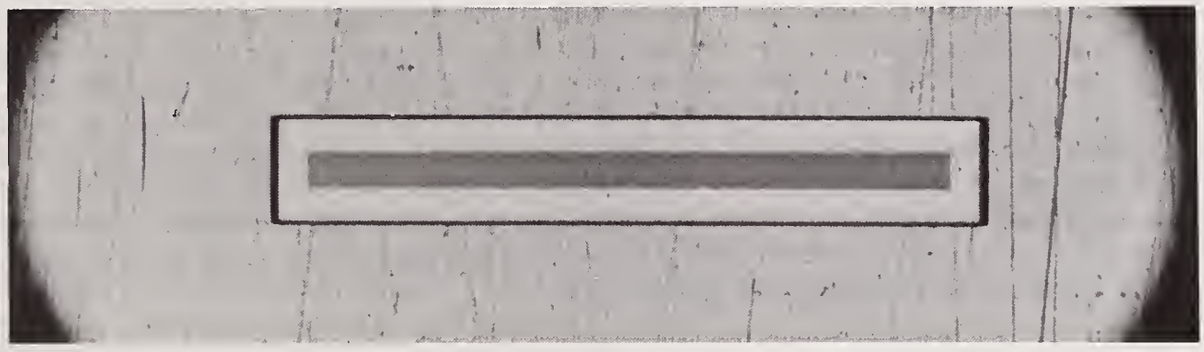

FIGURE 2a.
Rectangular Slot. 500 x 50 Microns

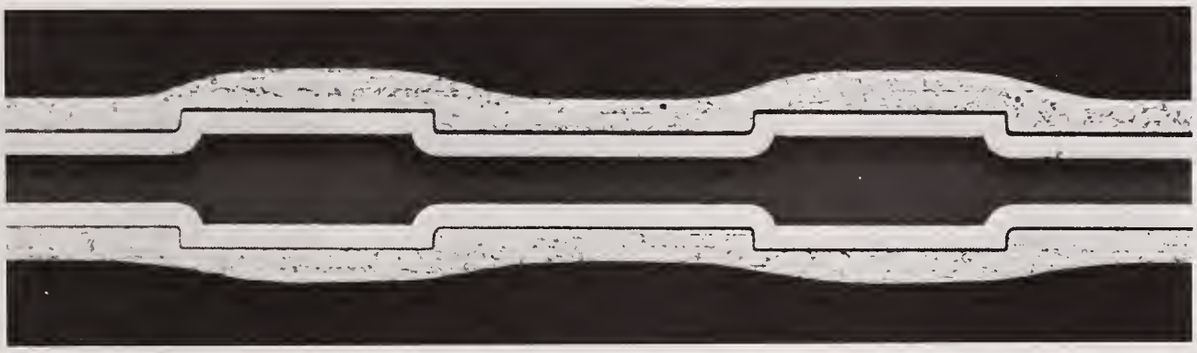

FIGURE 2b.
Rectangular Slot with Perturbations.

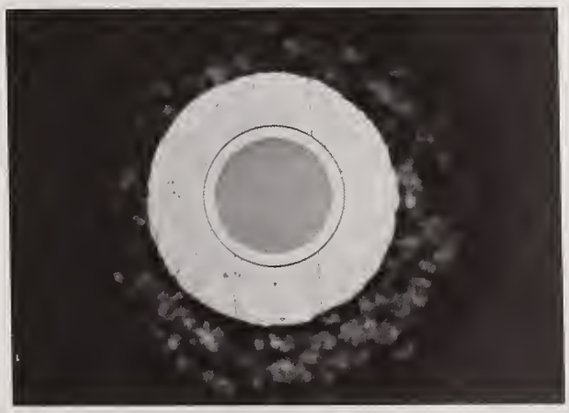

FIGURE 2c.
Common Round Nozzle. 50 Microns.

EXPERIMENTS ON CIRCULAR JETS:

Zero Order Azimuthally Symmetrical Mode (Sausage or Varicose)

Dressler and Jackson have previously shown that azimuthally symmetrical disturbances, which are predicted to be stable by Rayleigh's criteria for small perturbations, can be made unstable by the application of a large perturbation in the jet's velocity. The energy in the perturbation, if large enough, can cause the jet to break into a stream of drops. Because the breakup is dependent on the acoustic amplitude, it is called an amplitude dependent instability.

Figure 3 shows a jet that is unstable for the applied perturbation. The varicose disturbances grow in amplitude as the jet moves from the top to bottom of the photograph. This process for jet disintegration is commonly called Rayleigh breakup.

Figure 4 shows a jet that is stable for the applied perturbation. The wavelength of the perturbation is smaller than the jet's circumference and the perturbation decays as the jet moves from top to bottom of the photograph.

Figure 5 shows the jet of Figure 4 driven with a larger amplitude signal. With the higher acoustic signal, the jet is unstable and breaks into a stream of drops at the driving frequency. For this jet, the Rayleigh wavelength is 314 microns. The wavelength of this disturbance is about 280 microns. The drops in Figure 5 have a volume that is 10% less than the smallest drop predicted by Raleigh's theory for small perturbations.

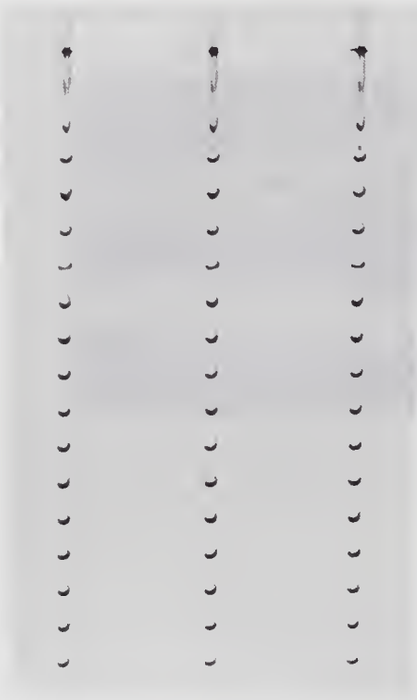

FIGURE 3.
Circular Jets Exhibiting Raleigh Break-Up

FIGURE 4.
Circular Jet Exhibiting Decaying Perturbations.

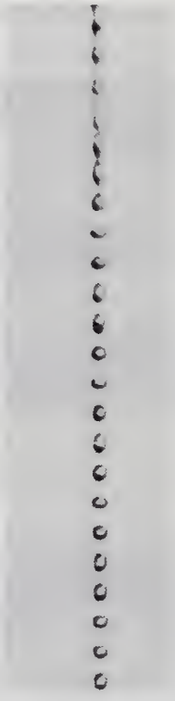

FIGURE 5.
Circular Jet Exhibiting Amplitude Dependent Instability.

Higher Order Modes

Rayleigh's Theory predicts that all of the higher order modes of a liquid cylinder are stable for small perturbations. One method of countering the stabilizing effect of surface tension is to apply an electric field to the liquid surface. This technique has been shown to be useful for producing very reproducible instabilities of the first mode.[10]

We have succeeded in driving a jet of liquid unstable in the higher modes by the application of a high amplitude acoustic drive. Again, this instability is dependent on the amplitude of the excitation. Figure 6 shows a liquid jet with radial perturbations that are caused by our acoustic excitation. These perturbations do not exceed the stability threshold and they decay as the jet

moves. Figure 7 shows a jet with a larger perturbation. These perturbations exceed the threshold and the jet is unstable. The instability causes drops to be ejected in the radial direction. There are 14 to 16 drops ejected from each perturbation on the jet and therefore we must be driving the m=14 or 16 azimuthal mode.

LIQUID CONE INSTABILITY

The photographs of the atomized jet show that there is a region of large drops in the center of the spray pattern. To modify the spatial distribution of the spray, we added swirl to the injector manifold. With this added swirl, a hollow cone of liquid is produced from the circular nozzle.

Figure 8 shows the cone after an acoustic drive was applied. The excitation forces the cone to break into rings of liquid which then disintegrate into drops. The spray pattern formed is thus hollow.

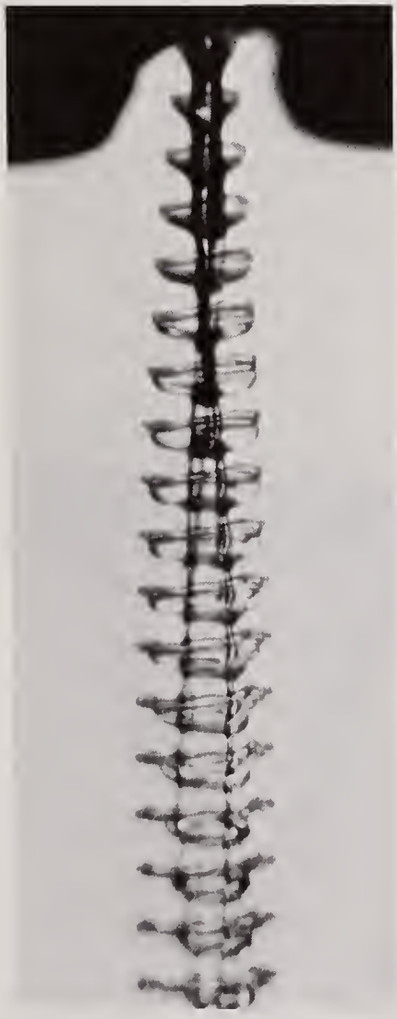

FIGURE 6.
Stable Perturbations on a 750 Micron Circular Jet.

FIGURE 7.
Unstable High-Order Perturbations on a 750 Micron Circular Jet.

FIGURE 8.
A Cone Shaped Jet Breaking into Rings Due to an Acoustic Drive.

SHEET INSTABILITY

Dressler[7] developed a dispersion equation for small disturbances on a thin sheet of liquid. The derivation was made into a homework problem[9] and in the final publication, the capillary force was changed to a magnetic force. Since it is not available elsewhere, the original equation is given here without derivation. This equation predicts that the sheet is stable for all small disturbances.

$$\left(\rho\frac{\omega^2}{\kappa}\right)^2 - \left(\rho\frac{\omega^2}{\kappa}\right)\coth 2\kappa d(2\kappa^2 T) + (\kappa^2 T)^2 = 0 \qquad (1)$$

where κ is radians/length, ω is radians/second, ρ is the fluid density T is the surface tension, and d is the half-width of the fluid layer.

The dispersion equation can then be further factored into two equations. The first represents disturbances where the sheet of liquid has a thickness perturbation and the deflections of the sides of the sheet move in opposite directions. The second equation is for kinking perturbations where both sides of the sheet move in the same direction. These two dispersion equations are then simplified with the long wavelength assumption that κ is small. Because they are not readily available elsewhere, the dispersion equations for the thickness mode and the kink mode, for a liquid sheet driven only by capillary forces are presented here.

$$\rho\omega^2 = \kappa^4 T d \qquad (2)$$

$$\rho\omega^2 = \kappa^2\frac{T}{d} \qquad (3)$$

The kink mode, (3), of the sheet has a typical wave type of dispersion equation while the thickness mode equation, (2), is more interesting. For the thickness mode of the fluid sheet and the sausage or azimuthally symmetrical mode on the circular jet, the dispersion equation is fourth-order in space and second-order in time. Thus two of the characteristics are horizontal, representing infinite velocity of propagation. This strange behavior results from the incompressibility assumption, which gives more spatial derivatives than time derivatives to the dynamic equations for both the circular jet and flat sheet. If one has an interest in studying flat or circular jet deformations, he should be aware that this infinite propagation velocity means that the initial conditions at the nozzle exit are not sufficient to determine the liquid behavior. One downstream boundary condition must be considered.

Figure 9 is a photograph of a liquid sheet originating from a slot nozzle. Small perturbations are applied to the nozzle by acoustically perturbing the fluid velocity and

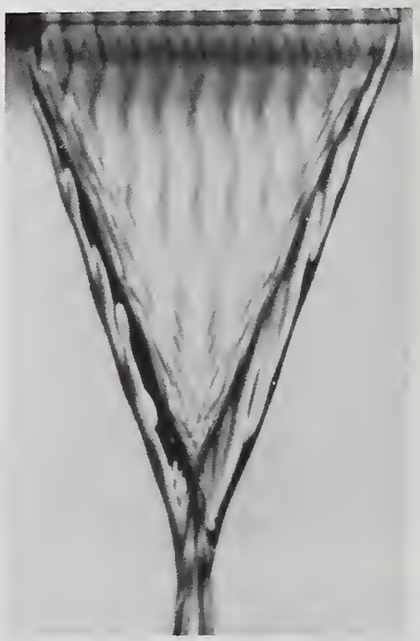

FIGURE 9.
Sheet of Fluid Exhibiting Stable Perturbations

spatial perturbations are applied to the sheet thickness by putting perturbations in the nozzle width as shown in Figure 2b. Figure 9 shows the sheet is stable for these perturbations. The sheet was also stable for all other small perturbations.

Figure 10 shows the sheet after it was made unstable in the thickness mode. Here a large acoustic signal is applied to the sheet and it breaks into tubes as a result of this large signal. Since a large excitation is required to produce this sheet breakup, this instability is called amplitude dependent. The nozzle plate used for Figure 10 contains thickness perturbations and they cause the tubes formed from the sheet breakup to break into drops.

The higher order azimuthal modes on the circular jet were shown to have an amplitude dependent instability. For this instability, drops were ejected radially from the jet. Similarly, the second order or kink modes of the sheet can be forced to become unstable if driven with a large enough amplitude. Photograph 11 shows fingers of liquid extending from the sides of a sheet due to the application of a moderate driving force. These perturbations are not large enough to be unstable and Figure 11 shows them collapse back into the sheet. When a larger perturbation is applied to the sheet, the perturbations become unstable and drops are ejected from the edge of the sheet. This is shown in Figure 12.

FIGURE 10.
Sheet of Fluid Unstable in the Thickness Mode. Tubes Break into Drops.

FIGURE 11.
Stable, High-Order Kink Mode on a Fluid Sheet. Side View.

FIGURE 12.
Unstable, High-Order Kink Modes on a Fluid Sheet. Amplitude Dependent Instability. Side View.

SUMMARY

The effect of high amplitude acoustic signal to the stability of fluid sheets and cylinders has been examined. Without the large acoustic signal, a fluid cylinder is unstable only for sausage mode disturbances with wavelengths longer than the circumference of the cylinder. The sheet is stable for all small disturbances. When a large acoustic signal is applied to a cylinder, it becomes unstable in the sausage mode with wavelengths shorter than the jet's circumference. For cylinders with large diameters, we found that we could drive the surface unstable for higher order azimuthal modes. The instability caused drops to be ejected radially from the cylinder.

Swirl was added to our atomizer and this changed the circular jet into a cone. A high amplitude acoustic signal forced the cone to break into a series of expanding rings which then broke into drops.

Amplitude dependent instabilities were exhibited on a fluid sheet. The thickness mode was driven and this stimulated the sheet to break into ligaments which then broke into drops. The kink mode of the sheet was driven and small drops were ejected from the sides of the sheet.

The acoustically driven atomizer can provide a reasonable flow rate with no air mass. The device will be useful in situations where it is desired to control the atomization without depending on the air mass flow. The drop size and mass flow can be controlled by the acoustic amplitude and frequency and the fluid supply pressure. One potential use for the acoustic atomizer is as a fuel injector for reciprocating engines that operate at low speeds. By speeding the vaporization of the fuel, it may be possible to have a fuel/air mixture which can be ignited by a spark plug and which is not as rich in liquid fuel droplets as present mixtures.

ACKNOWLEDGEMENT

This work was supported by contract F33615-89-C-2973 from the Air Force Wright Laboratory(WL-POSF). The photographs were made by Marcia Dressler. The author also wishes to acknowledge the assistance of Dr. Tom Jackson, Cindy Obringer, Gary Switzer, and Lt. Robert Hancock.

REFERENCES

1. LeFebvre, A.H., "Airblast Atomization", Progress in Energy and Combustion Science, Vol 6, pp. 233-261 (1980).
2. Mansour, A. and Chigier, N., "Disintegration of Liquid Sheets", Phys.Fluids, A2(5) (May 1990).
3. Rayleigh, J.W.S., "On the Stability of Jets", Proceedings of the London Mathematical Society, Vol 10, p 4 (1878). Available in U.S. in Chandrasekhar, S., Hydrodynamic and Hydromagnetic Stability, Chapter 12, Oxford University Press, London (1961).
4. Pierce, J.R., "An Interesting Wave Amplifier", IRE Trans. Elec.Dev., pp 73-74 (April 1960).
5. Mason,B.J. and Brownscombe J.L., "Production of Uniform Size Drops at a Controllable Frequency and Spacing from a Vibrating Capillary", Journal of Scientific Instruments, Vol 41 (1964).
6. Dressler, J.L., and Kraemer, G.O., "A Multiple Drop-Size Drop Generator for Calibration of a Phase-Doppler Particle Analyzer", in Liquid Particle Size Measurement Techniques (Hirleman, Bachelo, and Felton, Eds.), ASTM,Philadelphia PA, STP 1083 (1990).

7. Dressler, J.L., "Active Electromechanical Control of Fourth-Order Continua", Master of Science Thesis, MIT, Cambridge, MA (May 1966).
8. Melcher, J.R., Field-Coupled Surface Waves, Chapter 6, MIT Press, Cambridge, MA (1963).
9. Melcher, J.R., Continuum Electromechanics, Prob. 8.12.1, MIT Press, Cambridge, MA (1981).
10. Melcher, J.R., "Complex Waves", IEEE Spectrum, pp 86-101 (Oct. 1968).
11. Crowley, J.M., "Growth and Excitation of Electrohydrodynamic Surface Waves", Phys. Fluids, Vol 8, No. 9, pp 1668-1676 (Sept. 1965).
12. Ketterer, F.D. and Melcher, J.R., "Electromechanical Costreaming and Counter Streaming Instabilities", Physics of Fluids, Vol 11, No. 10, pp 2179-2191 (Oct. 1968).
13. Dressler,J.L.,"Videotype Sampling in the Feedback Stabilization of Electromechanical Equilibria", in Feedback and Dynamic Control of Plasmas, (T.K. Chu and H.W. Hendel, Eds.), American Institute of Physics, NY (1970).
14. Centani, F.A., "The Dynamics of an Electrified Sheet of Fluid", B.S. Thesis, MIT Dept of EE, Cambridge, MA (1966).
15. Dressler, J.L., "Shock Model of Liquid Jet Breakup", Lawrence Livermore National Laboratory, UCRL-78480, Rev. 1 (Oct 20,1976).
16. Dressler, J.L. and Jackson, T.A., "Acoustically Driven Liquid Sheet Breakup", ILASS-Americas 4th Annual Conference, Hartford CT (May 1990).

ATOMISATION AND COMBUSTION PERFORMANCE OF A STEM-JET TYPE TWIN-FLUID ACOUSTIC ATOMISER

N.R. Ramesh* and R. Natarajan†

*Propulsion Division, National Aeronautical Laboratory, Bangalore, India
†Department of Mechanical Engineering, Indian Institute of Technology, Madras, India

ABSTRACT

A modified version of the Hartmann-type stem and cavity air jet acoustic generator coupled with a twin-fluid air-assist atomiser has been used to form a unique practical device for atomisation, emulsification and combustion applications. The effects of acoustic and fluid dynamic fields on the atomisation parameters have been investigated theoretically. These results have been employed to evolve a step-by-step procedure for designing the important parameters of the twin-fluid acoustic device. Detailed experimental work has been performed to study the effect of various flow and fluid properties on the mean drop size of the spray. The results have been correlated to arrive at a semi-empirical equation for estimating the SMD of sprays from the acoustic device, applicable in the range of fluid properties and test conditions employed. Incorporation of the acoustic device in a practical combustion chamber has proved to be successful.

1. INTRODUCTION

It has been postulated and observed that the acoustic field in the spray zone enhances liquid sheet disintegration into ligaments and drops resulting in better atomisation and efficient combustion [1]. The Hartmann whistle and its modified form, namely, the stem jet generator [2] which generates acoustic field by directing moderately high pressure air through the centre of the device into a suspended resonant cavity has been found to be best suited for atomisation applications. The present work deals with a detailed investigation of the design aspects of the acoustic device and its performance evaluation by experiments.

2. DESIGN CONSIDERATIONS

The design of the acoustic device using air is generally based on the empirical relations developed by Hartmann himself, and with a few modifications as suggested by the later investigators [2,4]. However, for the purpose of its application to atomisation, emulsification and combustion, with the addition

of a liquid it is essential to consider some of the two-phase flow parameters.

2.1 Equivalent Diameter Concept

The empirical equations of Hartmann [2] for designing the acoustic generator have been suitably modified to account for the presence of the stem rod by using an equivalent diameter concept by replacing D_n by D_{ne} and D_r by D_{re}.

2.2 Acoustic Frequency

Acoustic frequency is calculated by considering the resonant cavity as a quarter wave tube with one end closed, for which the natural frequency of operation at the fundamental mode is given by

$$f_n = \frac{C_a \ (2n - 1)}{4 \ (h + \delta)} \qquad \ldots\ldots \quad (1)$$

In practice it has been observed that for the given cavity dimensions, f_n varies with the pressure of the driving fluid, and the sonic velocity of the air-liquid mixture. Hence it is required to calculate the actual f_n corresponding to the operating conditions.

2.3 Velocity of Sound in Air-liquid Mixture

In an air-liquid mixture the resultant sound velocity is a function of the void fraction (α) and the individual sonic velocities which can be estimated using the equation based on mean density and bulk modulus of the mixture [4] and can be used for calculating the actual operating frequency

$$C_m^2 = 1/\rho_m \left[(\alpha/\rho_a C_a^2) + (1 - \alpha)/\rho_1 C_1^2 \right] \qquad \ldots\ldots \quad (2)$$

2.4 Relation Between Drop Size and Frequency

A liquid drop, suspended in a gaseous medium subjected to an acoustic field, undergoes periodic compression and rarefaction. By considering the equation of motion and neglecting the gravity effects it has been shown [3] that

$$\lambda^3 = 2 \pi \sigma / \rho F^2 \qquad \ldots\ldots \quad (3)$$

Using the general relation between driving frequency f and the wave frequency F, as suggested by Lang, $F = f/2$, and the equation for can be written as:

$$\lambda = (8 \pi \sigma / \rho f^2)^{1/3} \qquad \ldots\ldots \quad (4)$$

It is also well known that the median diameter of the liquid droplet is proportional to λ , and hence we can write:

$$d = K\lambda, \text{ so that } d = K\,(8\pi\sigma/\rho_l f^2)^{1/3} \quad \ldots\ldots \quad (5)$$

where K is a constant to be determined experimentally.

2.5 Design Procedure

Based on the foregoing discussion, guidelines for a step-by-step procedure for the design of the twin-fluid acoustic atomiser is suggested.

3. EXPERIMENTAL PROGRAMME

3.1 Configuration of the Acoustic Device

The sectional view of the acoustic device chosen for the present work is shown in Fig.1.

Using the design procedure, a nozzle diameter of 6 mm was selected, and the other dimensions were derived. Atomising air was injected into the main body through a 10 mm dia tube. The test liquids, and water (when used for emulsification), fed through 6 mm dia tubes, filled the annular groove in the convergent-divergent nozzle and entered the main air stream tangentially through three orifices of 0.8 mm diameter.

3.2 Test Facility and Instrumentation

The overall layout of the facility is shown schematically in fig.2. In all the atomisation experiments an optical bench incorporating the forward diffractive light reattering technique, built indigenously, was used for the measurement of spray drop size.

3.3 Experimental Work

Extensive tests were conducted to determine the parametric effects on the atomisation performance of the acoustic atomiser.

As a practical application, the acoustic device was then incorporated into a gas turbine combustion chamber, and lean stability limits, were determined. The results were compared with those obtained by repeating the same experiments using a conventional pressure jet atomiser.

4. RESULTS AND DISCUSSION

4.1 Results of Atomisation Studies

The influence of flow and fluid properties on the Sauter mean diameter is shown plotted in figures 3,4,5. The increase in liquid flow rate increases the drop size almost linearly, whereas increase in atomising air flow rate and in turn the air velocity decreases the drop size. The behaviour is similar for all the four liquids. The optimum air liquid ratio lies between 4 and 8

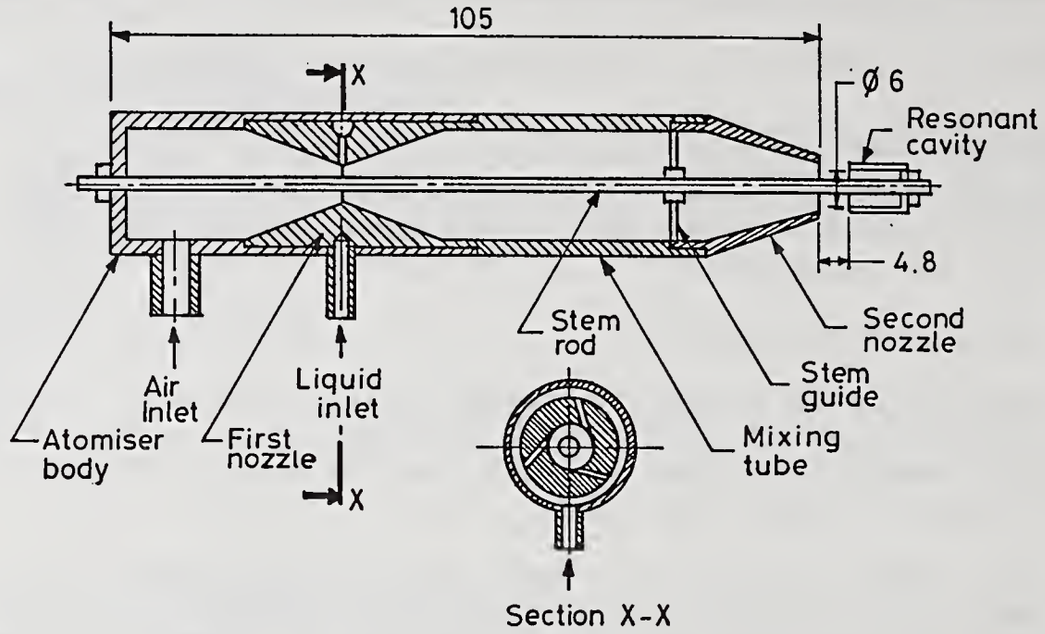

FIG.1 SECTIONAL VIEW OF THE ATOMIZER

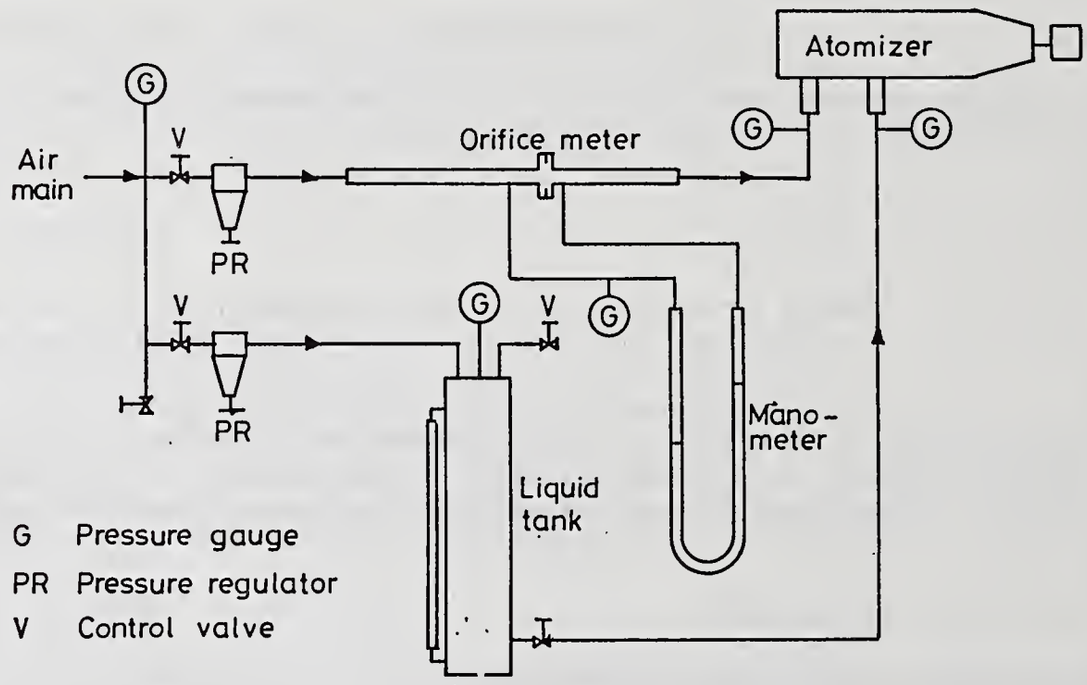

FIG.2 SCHEMATIC OF THE EXPERIMENTAL SET UP

for low viscous liquids, and is around 10 for furnace oil. Generally the SMD of furnace oil is 4 to 5 times the SMD of low viscous liquids.

Results of the present work have been compared with those obtained by Nagai et al [8] (Fig.6). It can be seen that there is good agreement between the two. Similarly the results of SMD obtained for furnace oil have been compared with those calculated from Jasuja's equation.

4.2 Drop Size Correlation

In the present investigation, the large amount of experimental data obtained during atomisation studies have been used to arrive at a semi-empirical equation for the prediction of SMD, taking into account as many parameters as possible :

$$SMD = 0.0189\left(\frac{8\pi\sigma}{\rho_l f^2}\right)^{1/3}\left(\frac{\mu_l}{\mu_a}\right)^{1/4}\left(\frac{2P_a g}{\rho_a V_a^2}\right)^{1/2}\left(1+\frac{M_l}{M_a}\right)^{5/4} \quad \ldots\ldots \quad (6)$$

4.3 Results of Combustion Studies

The results of combustion studies have been analysed in terms of the lean stability limits. Stable combustion was possible at low fuel to atomising air ratios below a fuel rate of about 7 g/s. At higher fuel flow rates, combustion was stable for fuel/air ratios above 0.4. Visual and photographic observations indicated that the flame cone angle was as high as 180°, and tended to spread backwards if the gap setting was reduced. As the fuel flow rate was increased, the flame became more luminous, with an increase in length and diameter.

The changes in the shape of the flame, viz., length and diameter, and cone angle were observed as the fuel flow rate was increased. It was seen that for kerossene and diesel fuels a stable blue flame could be obtained with flow rates upto 5 g/s. The flame was short and broad, and had a wide angle of coverage with symmetric distribution.

Sound level and frequency were strong functions of the nozzle diamter and other geometrical and flow parameters. In the present case, the predominant sound frequency for the atomizer was around 10 kHz. The sound level was 130 dB, which decreased by 15 dB with liquid injection, and a further decrease of 10 dB was observed during combustion. Using the measured acoustic power output, the acoustic generator efficiency was calculated to be around 4%.

While burning kerosene with water addition, an almost transparent flame was observed. The reasons presumably are: (i) homogeneous dispersion of water in kerosene spray (ii) the isolated liquid droplets being re-atomised by the boiling of water, thus achieving better mixing and in turn high intensity combustion, (iii) reduction in soot formation by the lower combustion temeperature with water. Flame length considerably decreased during emulsion burning compared to neat fuel burning.

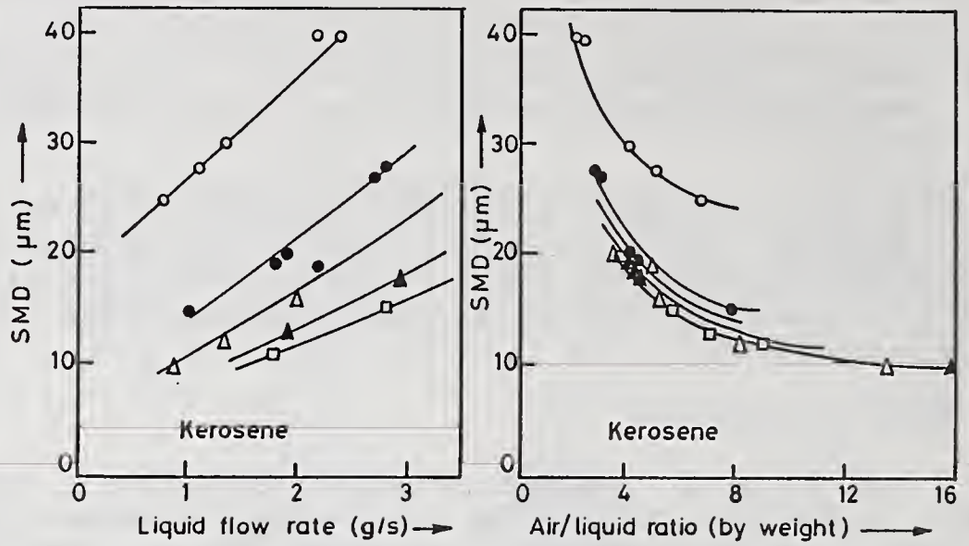

Symbol	o	●	Δ	▲	□
Atomizing air pressure kPa	160	239	298	367	436
(psig)	10	20	30	40	50
Atomizing air flow rate g/s	5.4	8.0	10.7	13.3	16.0

FIG. 3 EFFECT OF FLOW RATE ON SMD

FIG 4 EFFECT OF AIR/ LIQUID RATIO ON SMD

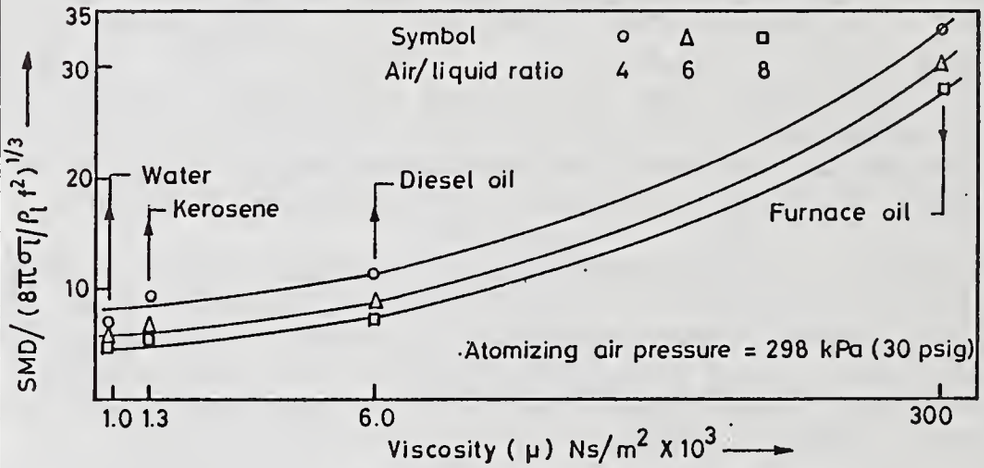

FIG.5 EFFECT OF LIQUID VISCOSITY ON SMD

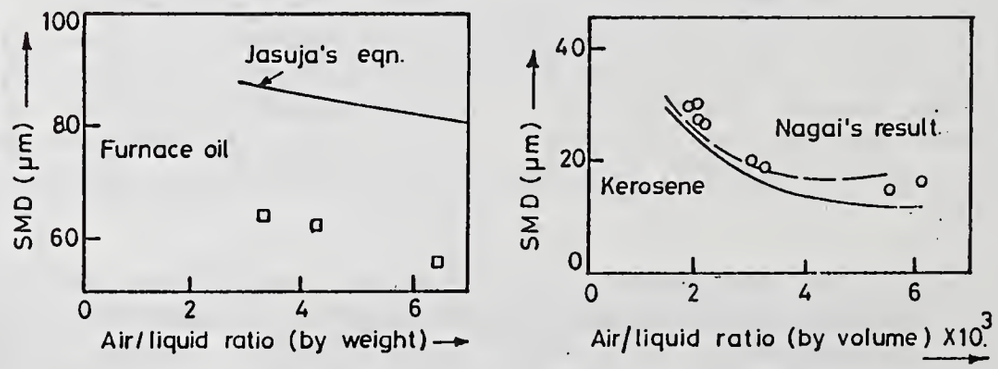

FIG. 6 COMPARISON WITH AIR BLAST ATOMIZER

The effects of water addition on lean stability limits are shown in Fig.8. It is seen that water addition in general has a deteriorating effect on the lean stability of the acoustic atomiser.

4.4 Results of Combustion Chamber Tests

Stability limits were obtained by carrying out a series of extinction tests at constant, pre-determined levels of air temperature and pressure. With the fuel flowing and the mixture ignited, the fuel flow was gradually reduced until flame extinction occurred. This process was repeated at increasing levels of air mass flow rate until the complete stability loop was drawn. Figure 9 illustrates the main features of the stability loop obtained by this technique.

NOMENCLATURE

C	Velocity of sound
D	Diameter
f	Frequency
h	Depth of resonating cavity
l	Gap between the nozzle and the resonating cavity
m	Mass flow rate
P	Pressure
Q	Volume flow rate
SMD	Sauter mean diameter
V	Velocity
W	Power
α	Void fraction
η	Efficiency
μ	Absolute viscosity
ρ	Density
σ	Surface tension

REFERENCES

1. Ramesh, N.R., Sridhara, K., and Natarajan, R., Fuel (London), Vol.2 pp.1677-1680 (1985).

2. Borisov, Yu.Ya in "Source of High Intensity Ultrasound" Vol.1 (Part 1), Ed., Rozenburg, Plenum Press, New York, (1969).

3. Lang,R.J., J. Ac. Soc. Am., Vol.34, No.1, pp 6-8 (1962).

4. Ramesh, N.R., Rao, K.V.L., and Natarajan, R., Proceedings of the 10th National Conference in I.C. Engines and Combustion, Rajkot, India, (1987).

5. Nagai, I.N. , Kumazawa, T., Hayakawa, Y., and Okazaki, H., Proc.I ICLASS, Tokyo, Japan,pp.209-219 (1978)

6. Jasuja, A.K., ASME Paper, 78/GT/83.

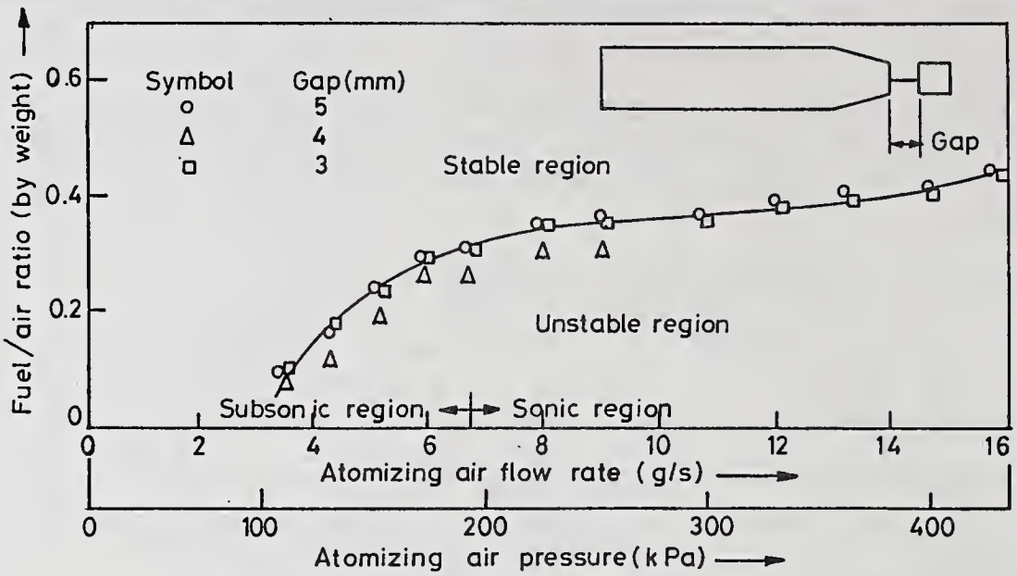

FIG. 7. LEAN BLOW OFF LIMITS FOR KEROSENE

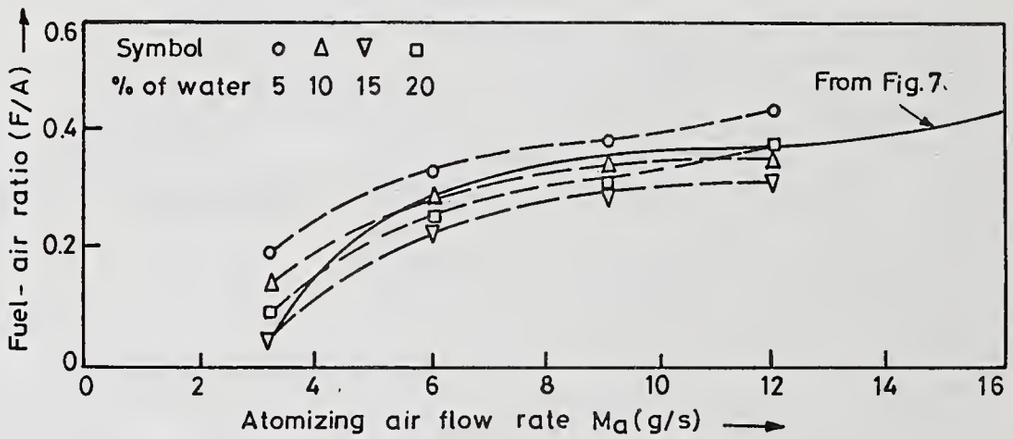

FIG. 8 EFFECT OF EMULSIFICATION ON STABILITY LIMIT

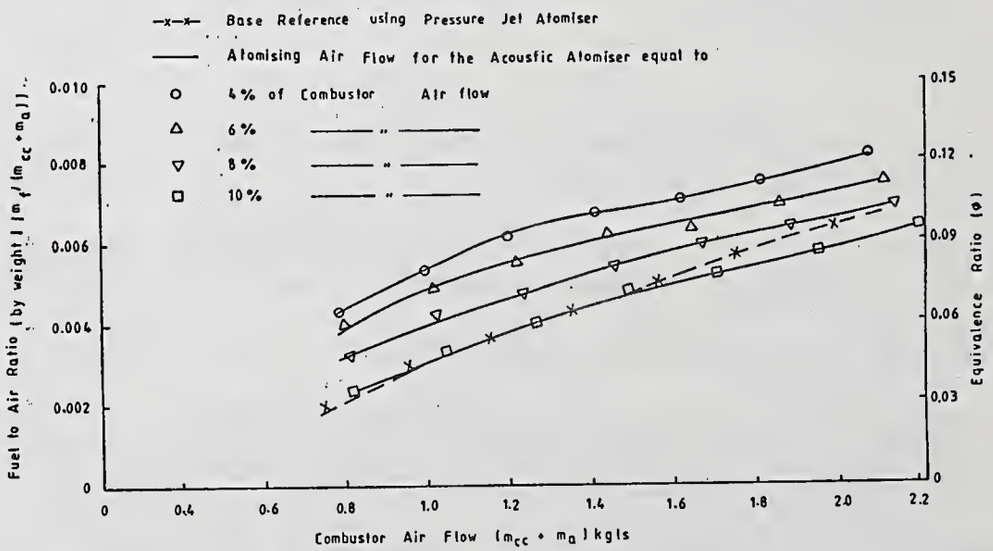

FIG. 9 LEAN STABILITY LIMITS FOR ACOUSTICALLY ATOMISED KEROSENE

CALIBRATION FACTORS FOR LASER DIFFRACTION RING DETECTORS: THEORETICAL MODELING

S.B. Kenney and E.D. Hirleman

Mechanical and Aerospace Engineering Department
Arizona State University
Tempe, AZ, U.S.A.

ABSTRACT

Photodiode arrays used in laser diffraction particle sizing instruments must be calibrated to account for detector-to-detector variations in sensitivity. We have calibrated an Insitec EPCS-P detector by scanning a small laser beam across the detector surface. A deconvolution of the known intensity distribution of the laser beam from the measured signal resulted in detector response as a function of position. Detector response was approximately constant over the region of the ideal active detector and it decreased exponentially in the region beyond the ideal detector boundary. A diffusion length constant of 50μm gave the best fit to the measured data. Theoretical predictions of calibration factors based on measured detector response agreed reasonably well with Malvern and Insitec calibration factors obtained from the traditional uniform light illumination method. This indicates that edge effects in ring detectors made by different sources are similar.

INTRODUCTION

Particle sizing instruments based on near forward scattering signatures are commonly used to measure droplet size distributions in sprays [1]. Scattering signatures are collected by the instrument and are processed by a mathematical inversion scheme to determine the size distribution. The equation which models the scattering signature is a classical Fredholm integral equation. This integral equation is often approximated by a linear system of discretized equations and the calculated size distribution is only an approximation of the actual distribution. The corresponding coefficient matrix resulting from discretization contains elements that must be estimated. Two of these components are the distribution of particle size within each size class and detector response characteristics. The ultimate accuracy of the calculated size distribution is limited by the accuracy to which these components are properly estimated.

Since it is the particle size distribution that is sought, it is doubtful that any information on within class size distributions would be known *a priori*. However, it is possible to experimentally probe the detector response. Literature references [2-4] discuss calculation of the scattering matrix assuming an ideal step response at the boundary of detector elements. Any deviation in the actual detector edge response characteristics from this assumed ideal behavior would result in a bias error in the matrix, and hence, also in the calculated size distributions. Further, all scattering matrix calculations reported to date have assumed no detector-to-detector variation in responsivity, the ideal situation. However, since interlaboratory studies [5] highlighted the significant effect of between-detector responsivity variations on the overall accuracy of laser diffraction instruments, calibration factors have been introduced to correct for these between-detector effects. The process of calibrating a photodetector array using uniform illumination [6] can experimentally correct for two effects, 1) spatial variations in the local responsivity (amps/watts) either within or between detectors, and 2) edge effects. Clearly, details of these local effects are masked by the averaging effect of uniform flood illumination. In this paper we are concerned with the details of detector array characteristics on a spatial scale much smaller than the detector dimensions. In particular, we report

experimental measurements of local responsivity both within and at the boundaries of the detector elements. We have used the results to develop a theoretical model for the edge effects and we therefore are able to theoretically predict calibration factors.

MATHEMATICAL FORMULATION

Scattering measurements in laser diffraction instruments are typically made with annular ring shaped detectors which cover a finite range of scattering angles as determined by the detector apertures. It is convenient to assign a particular scattering angle θ_i to represent the range of scattering angles in the ith detector aperture. The detection process can be represented as:

$$I_w(\theta_i) = \int_0^\infty w_\theta(\theta,\theta_i)\, i(\theta)\, d\theta \tag{1}$$

where the weighting function $w_\theta(\theta,\theta_i)$ describes the relative responsivity variations across the detector and $I_w(\theta_i)$ is representative of the signal obtained from the ith discrete detector (the subscript w indicates a dependence on the weighting function). The azimuthal, or φ dependence on the responsivity variations are significantly less important than the θ effects, and have been neglected. $i(\theta)$ is the intensity (W/sr) diffracted at near-forward scattering angles θ. The weighting function w_θ is what is to be determined experimentally. It is also noted that the particle distribution should also be discretized in a manner similar to that used for the scattering intensity [7]. In that case we obtain a system of m_θ equations in m_α (α is the size parameter) unknowns where m_θ is the number of discrete detectors and m_α is the number of discrete size classes. The linear system is written as:

$$\mathbf{I} = \mathbf{K} \cdot \mathbf{N} \tag{2}$$

In Eq. (2) the m_θ elements of the vector **I** are $I_w(\theta_i)$ as given by Eq. (1); the m_α elements of **N** contain the bth partial moments of the number of particles in the size class; and **K** is the instrument or system matrix whereby element $\mathbf{K}_{ij}$ represents the diffraction contribution of a unit measure of particles in the jth size class onto the ith detector. The elements of **K** are given by:

$$K_{ij} = \int_0^\infty \int_0^\infty k_b(\alpha,\theta_i)\, w_\alpha(\alpha,\alpha_j)\, w_\theta(\theta,\theta_i)\, d\alpha\, d\theta \tag{3}$$

where $w_\alpha(\alpha,\alpha_j)$ is a weighting function for the jth size class and $k_b(\alpha,\theta_i)$ is a general scattering function which gives the scattering contribution of a unit quantity of particles of size α into angle θ. The solution or measured particle size distribution indicated by **N** in Eq. (2) can in theory be obtained by inverting the matrix **K**.

EXPERIMENTAL PROCEDURE

Fig. 1 shows a schematic for a laser diffraction particle sizing instrument. A laser beam is spatially filtered, expanded and collimated to a few millimeter $1/e^2$ diameter. Particles within the collimated beam scatter light which is collected by a receiving lens and refracted onto the detector plane. A commercially available Insitec particle sizing detector head and electronics were used for the experiment . The layout of the Insitec detector is well-suited for examining detector response, given its odd numbered rings on one half of the detector and even numbered rings on the other. This design has large non-responsive sections between adjacent rings, which provides good isolation between adjacent detectors.

The Insitec detector was mounted in a cantilevered position on a programmable x-y translation stage which moved in a plane normal to the beam axis. A HeNe laser beam was focussed to a $1/e^2$ spot 25μm in diameter and the spot was positioned in the small hole in the center of the detector. (The hole allows the strong unscattered light at the center of the detector to pass through, thereby reducing stray reflections and inner ring cross-talk). Coarse centering was performed by moving the detector until the light reflecting off the region surrounding the hole disappeared (indicating the light was passing through the hole). The beam power was adjusted so that when the laser was positioned in the middle of an active detector the resultant signal was just below the saturation level.

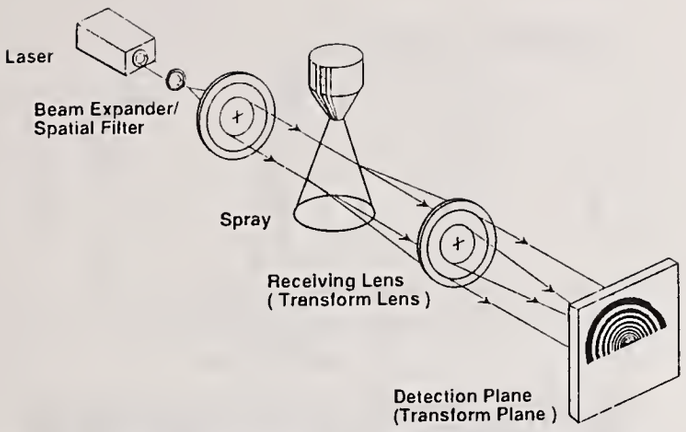

Fig. 1. Schematic of conventional laser diffraction particle sizing system.

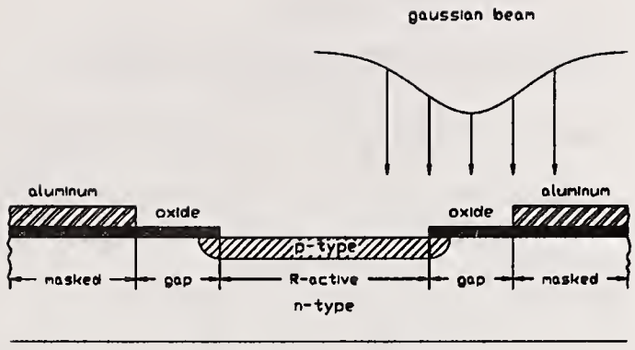

Fig. 2. Cross section of an Insitec photodiode detector showing the ideal responsive region (R-active), the transition region (gap), and the non-active region (masked).

Several runs were made by scanning across the entire detector on a line passing through the center in one direction and then rotating the detector 90 degrees and repeating the scan in the other direction. Signals were recorded at 1μm increments and the entire experimental apparatus was shielded from stray room light.

Before scanning the detector, the rings were examined under a microscope. Three distinct regions were noticed which are shown in Fig. 2 and are labeled as follows: the ideal responsive or active region (R_{active}), the transition region (gap), and the non-active region (masked). Bounding each detector is a thin aluminum film, which has been deposited to cover most of the area between detectors. It is assumed that the metal helps block radiation so that masked regions are not responsive. Though Fig. 2 shows just one detector, all detectors were examined and found to be similar.

To measure the gap width, the detector was placed on a two-axis translation stage that was coupled to LED displays showing relative stage position. The resolution of the display was 1μm. A camera connected to a 19-inch TV screen was mounted on the microscope which allowed for easy visual inspection of the object. A small piece of tape was placed on the screen to mark the starting and ending points for various features. An inner gap edge was visually lined up with an imaginary tangent line on the edge that would be parallel to the tape. The stages were moved until the outer gap edge was reached and the difference between stage positions was recorded. In this manner the width of each gap (both inner and outer per detector), was determined.

RESULTS AND DISCUSSION

The average gap width was approximately 8μm (results from all detector rings can be found in Table 1). The largest measured gap width was 10mm while the smallest gap width was 6mm, though most widths were 8mm. The table begins with detector 5 because the first four inner rings were damaged when a hole was laser drilled through the detector center. Also included in Table 1 is the visual measured width of the Insitec detectors (from microscope).

Fig. 3 displays the individual ring signal vs. radial distance for the first five inner odd-numbered rings. The rectangular boxes represent the specified width of the detectors and therefore the ideal top hat response distribution, while the curves represent the measured signal. The measured signal is a convolution of the detector spatial response and the Gaussian intensity profile of the laser beam. Since the measured curves are centered around the specified points, it was concluded that the laser beam was approximately centered about the detector. The maximum signal is close to 8 volts, however this value is not quite reached on rings 4 and 5 because the width of the rings is less than twice the beam width, (where twice the beam width represents more than 99% of the total beam energy). Also, overlap between rings occurs because of the beam width and edge effects resulting from electron hole pair and photon diffusion. Note how overlap decreases with increasing ring size, which is due to the larger regions of non-responsive area between rings. The curves appear smooth except for the saturation region where small deviations in signal are noticed. It should be mentioned that 1000 signals are averaged at each position.

In order to be able to calculate w_θ for use in Eq. (1) it is necessary to model the gap response. This response can be estimated by deconvolving the measured signal from the known Gaussian intensity profile of the laser beam. After several runs were taken of the inner odd rings (results of rings 11,13,15) an average response in the gap region

Table I

Insitec ideal detector width and gap width. Visual dimensions were acquired by viewing the detector under a microscope.

Detector	Visual detector width (μm)	Visual gap width inner (μm)	outer (μm)
1			
2			
3			
4			
5	27	7	7
6	29	8	8
7	38	7	8
8	47	7	6
9	55	8	8
10	65	7	8
11	77	7	8
12	92	8	8
13	108	7	7
14	127	7	7
15	149	8	9
16	177	8	9
17	209	8	6
18	244	7	7
19	285	7	8
20	333	10	6
21	392	7	8
22	455	9	10
23	532	8	10
24	625	8	8
25	730	7	8
26	855	8	7
27	997	8	9
28	1165	8	7
29	1361	10	8
30	1586	7	9
31	1855	7	8
average		8	8

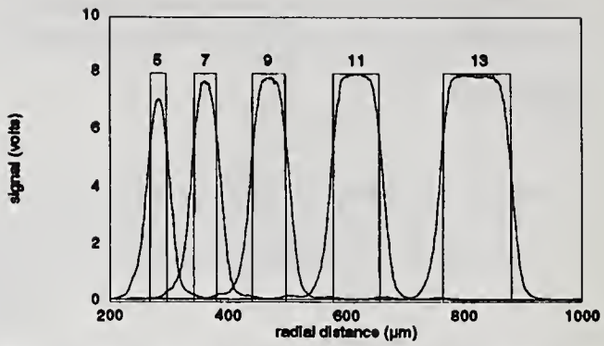

Fig. 3. Plot of detector signal vs. radial distance for five inner odd rings. The rectangles represent the specified detector dimensions. The curves are the signals resulting from a $1/e^2$ 25μm diameter laser beam of wavelength 0.6328μm. Measurements were made at 1μm increments.

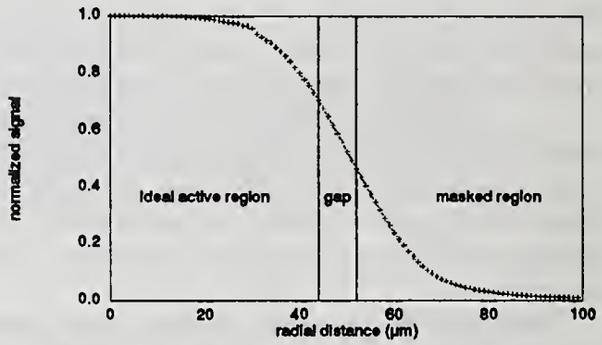

Fig. 4. Plot of the average edge signal of rings 11, 13, and 15 vs. relative distance. The signals of the three rings are superimposed to form one curve.

was calculated by determining the average signal for each ring at each 1μm position (over a 100μm distance) and then superimposing the data to calculate an overall average. This average gap response curve is shown in Fig. 4.

Initial insight into a possible model for the gap response is found by looking for symmetry within Fig. 4. The symmetry present in the curve points to a potential model based on a simple function, most likely exponential. A logical model to predict the gap response based on physical conditions would include uniform response over the idealized detector region, decaying exponential response over the 8μm gap width and no response in the masked or non-responsive region.

Photons incident on the gap region are absorbed by the silicon where they create electron-hole pairs. The electron-hole pairs begin diffusing through the material until they either reach the p-n junction where there is a possibility that they will contribute to the overall current, or they lose their energy through collisions and recombine. For an overview of the physics of photodiode operation see Sze [8]. As far as a model is concerned only one parameter will need to be determined; the "diffusion length constant" governing the decaying exponential.

However, it should be mentioned that when convolving the Gaussian beam with the gap response function the value of the diffusion length constant has only a slight impact on the slope of the curve, thereby making it difficult to estimate the proper value of the constant to match the measured data. Fig. 5 confirms this observation, where three curves representing the same beam diameter, but different diffusion length constants are displayed. As can be imagined the gap response resulting from different diffusion constants is highly variable, yet because the beam width is much greater than the gap width the slopes of the curves are nearly equal. If the beam width was less than the gap width then the slopes of the three curves would be much different. Furthermore, if the beam was reduced to a point source then the response would simply be the exponential itself. However, even with large beam widths a

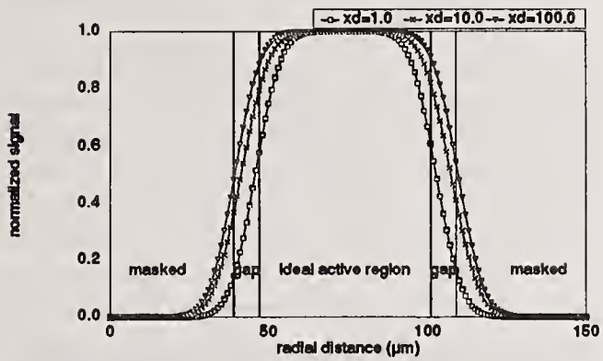

Fig. 5. Plot of theoretical signal curves calculated by convolving a 25μm beam diameter with the theoretical detector response. The specified detector width is 55μm which corresponds to ring 9 of the Insitec detector. Calculations are made with different diffusion length constants as indicated. The ideal active, gap, and masked regions are also indicated on the figure.

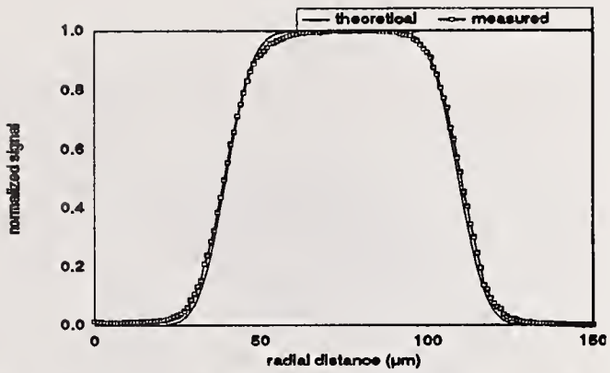

Fig. 6. Comparison of theoretical and measured signal vs. relative distance for ring 9. The theoretical signal was calculated based on a 25μm beam diameter, 8μm edge width, 50μm diffusion length, and 55μm detector width.

difference exists between the curves. The results are sensitive to diffusion length in that the curves expand with increasing diffusion length constant.

Since the specified width of each detector is known, a theoretical calculation could use diffusion constants as a means to expand or contract the curve to match the measured data. First, the total laser power in the Gaussian beam is normalized to one and the beam is moved in one micron increments over the idealized, gap, and masked regions. At each position the expected signal is calculated by convolving the response function (assuming a diffusion length) with the Gaussian beam intensity. (As can be seen from Fig. 2 there are instances when the width of the beam covers all three regions of the detector.) These values are then compared to the measured data to find the diffusion length constant that provides the best fit.

Experimental data from ring 9 were compared to theoretical data calculated based on different diffusion length constants. Assumed values in the theoretical calculations include a 25μm $1/e^2$ Gaussian intensity profile diameter laser beam, gap width of 8μm, and total detector width obtained from visual inspection. Results showed that a diffusion length constant of 50μm±10μm (which falls within observed measurements [8]) gave the best fit between experimental and theoretical values. A plot of ring 9 normalized signal vs. distance is found in Fig. 6, and as can be seen from the graph the fit is quite good. As a test for the model, comparisons were made between experimental and measured results for many of the other rings and similar results were noted. Thus, it was concluded that a simple exponential function appears to adequately predict the gap response of the Insitec ring detector. The weighting function over the gap width can be written as:

$$w_{\theta edge} = \rho/\rho = e^{-x/xd} \qquad (4)$$

where $\rho(\theta)$ is the local responsivity, ρ is the maximum responsivity in the ideal active region of the detector, xd is the diffusion length constant, and x is the position measured from the ideal edge into the gap.

Now that the weighting function w_θ has been determined a new instrument matrix K can be calculated by substituting the measured gap weighting function of Eq. (4) into Eq. (3) in place of the usually assumed step function. To quantify the effect of the detector weighting function on the instrument matrix, two matrices were calculated; one assuming a step detector response, the other the actual measured gap response (and weighting values of 0 and 1 in the masked and idealized regions, respectively). A plot of the difference matrix (element by element) between the two matrices is presented in Fig. 7. The matrices were calculated on an area basis with rectangular weighting functions, uniform by volume within-class distributions, and a Fraunhofer diffraction approximation. The surface plot shows almost no change on the outer rings, while the difference increases as ring geometry decreases. This is expected, as the ratio of gap area to visual detector area is much greater for smaller rings than larger ones.

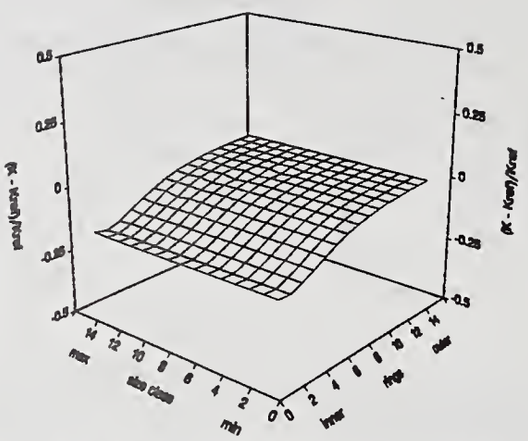

Fig. 7. Plot of the difference matrix between K based on a step response detector weighting function and K obtained with theoretical detector response weighting function (which accounts for detector response in the gap region between the mask and idealized detector boundary).

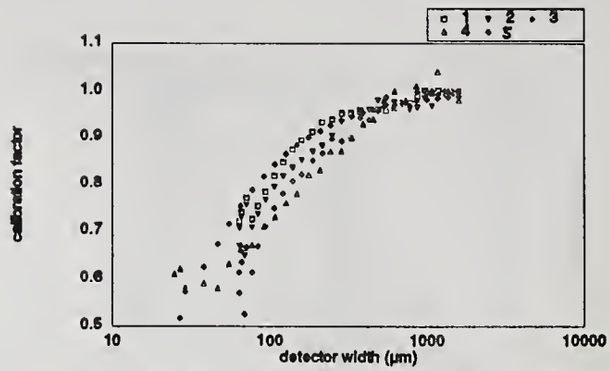

Fig. 8. Plot of calibration factors vs. detector width for various instruments and calibration techniques. The numbers in the legend correspond to the following: 1) Malvern 2600, instrument #1, uniform incoherent illumination [6,11]. 2) Malvern 2600, instrument #2, factory supplied calibration factors [9]. 3) Malvern 2600, instrument #3, uniform incoherent illumination [10]. 4) Insitec, uniform incoherent illumination. 5) Insitec, theoretical predictions based on gap response method.

It has already been mentioned that it is possible to predict calibration factors based on gap or transition region response as opposed to systematic between-detector variations in the responsivity. The accuracy of the "gap" calculated factors is based on the premise that the major contribution to calibration factors is from gap response. A predicted calibration factor is defined here as the ratio of the ideal detector output to the actual detector output when illuminated with light of uniform intensity. The ideal detector output is calculated by integrating the incident light intensity over the ideal, visual detector area while assuming that the weighting function w_θ is constant and equal to one. The actual detector output is found in the same manner except the area over which the integration is performed includes the gap region and the associated weighting function $w_{\theta edge}$. In equation form we have:

$$C_{pred} = \frac{\int I \, dA}{\int w_\theta \, I \, dA} = \frac{\int dA_{(ideal)}}{\int w_{\theta edge} \, dA_{(gap)} + \int dA_{(ideal)}} \qquad (5)$$

where C_{pred} is the predicted calibration factor and I is the intensity (W/m^2).

Traditionally, calibration factors have been determined based on illuminating the detectors with uniform light intensity. We determined two sets of calibration factors for the Insitec detector. One set of factors was calculated using Eq. (5), while the other set was determined using the uniform light method. Results of the two methods are displayed in Fig. 10 along with calibration factors from 3 different [9-11] Malvern 2600 instruments determined empirically with the uniform light method. Since the Insitec detector geometry differs slightly from the Malvern detector geometry, the calibration factors are plotted vs. detector width. As is seen from the plot the curves are in reasonable agreement. Noticed trends are that all factors decrease in value as detector area decreases. Consequently, the inner detectors over-respond relative to the outer detectors. Calibration factors determined from Eq. (5) are limited by the fact that experimental data were collected along two lines running through the center of the detector instead of scanning the entire detector surface. Additionally, in Eq. (5) it was assumed that the weighting function equals a constant over the ideal detector region, however, Fig. 4 shows slight variation in this region. One other area of uncertainty which we did not investigate is the ends of each detector. Though we accounted for the end region in the calculations the region is different from the rest of the perimeter regions in that a masked area is not found 8μm from the ideal detector boundary. A drawback to the uniform light method is that linear detector response is assumed with no cross-talk. If either of the above assumptions is not correct then errors in calibration factors will propagate through the remaining factors that need to be determined. This results from the requirement that values acquired from different light levels must be spliced together [3]. Overall, it appears that calibration factors calculated using Eq. (5) compare reasonably well with factors determined with the uniform light method, especially considering the fact that factors are for different detectors from different laboratories.

CONCLUSIONS

In conclusion, the transition region response has been measured and modeled for an Insitec detector. A simple exponential with a diffusion length constant of 50μm accurately predicted the experimental data. The detector weighting function has been calculated and incorporated into the instrument matrix K. Calibration factors for the Insitec detector have been predicted based on edge effects and were compared with calibration factors derived from the uniform light source technique. Both methods indicated that the inner rings over-respond relative to the outer, larger rings. It is difficult to conclude which method produces the more accurate results. The uniform light method has the disadvantage that detector signals resulting from several light levels must be measured and the calibration curves spliced together. The gap response model has the disadvantage that it is based on 2-dimensional results and it must be assumed that gap response is axisymmetric. Another independent technique for calculating calibration factors could help verify whether the gap or uniform light source is more accurate. The effect of using the theoretical calibration factors instead of the uniform light source factors would, in general, translate into slightly larger particle sizes because of the higher signals on the inner rings.

ACKNOWLEDGMENTS

This research was supported by the Air Force Office of Science Research, Air Force Systems Command, USAF, under grant AFOSR-90-0358, Dr. Julian Tishkoff, program manager. The U.S. government is authorized to reproduce and distribute reprints for governmental purposes notwithstanding any copyright notation thereon.

REFERENCES

1. E. D. Hirleman, "Particle Sizing by Optical, Nonimaging Techniques," in *Liquid Particle Size Measurement Techniques*, STP 848, J. M. Tishkoff, R. D. Ingebo, and J. B. Kennedy, Eds. (American Society of Testing Materials, Philadelphia, 1984), pp. 35-60.

2. J. Swithenbank, J. Beer, D. S. Taylor, D. Abbot, and C. G. McCreath, in *Experimental Diagnostics in Gas-Phase Combustion Systems*: AIAA Progress in Astronautics and Aeronautics, B. T. Zinn, ed., AIAA V. 23, pp. 421-447. (1977).

3. E. D. Hirleman, V. Oechsle, and N. A. Chigier, "Response Characteristics of Laser Diffraction Particle Size Analyzers: Optical Sample Volume Extent and Lens Effects," *Optical Engineering*, V. 23, No. 5, pp. 610-619 (1984).

4. M. Heuer, K. Leschonski, "Results Obtained with a New Instrument for the Measurement of Particle Size Distributions from Diffraction Patterns," Particle Characterization, V. 2 pp. 7-13 (1985).

5. E. D. Hirleman and L. G. Dodge, "Performance Comparison of Malvern Instruments Laser Diffraction Drop Size Analyzers," ICLASS Conference Proceedings, The Institute of Energy, London, V. 2, pp. IVA.3.1-IVA.3.6 (1985).

6. L. G. Dodge, "Calibration of the Malvern Particle Sizer," *Applied Optics*, V. 23, pp. 2415-2419 (1984).

7. E. D. Hirleman, "Uncertainties in Matrix Formulations of the Fraunhofer Diffraction Particle Size Problem," Proceedings of ILASS America Conference, Institute of Liquid Atomization and Spray Systems, pp. 1-5 (1989), Irvine, CA.

8. S. M. Sze, *Physics of Semiconductor Devices*, John Wiley and Sons, New York (1981).

9. G. S. Samuelsen, University of California, Irvine, CA (private communication).

10. E. A. Hovenac, NASA Lewis Research Center, Cleveland, Ohio (private communication).

11. L. G. Dodge, Southwest Research Institute, San Antonio, Texas (private communication).

PARTICLE DIAGNOSTICS AND TURBULENCE MEASUREMENTS IN AN ISOTHERMAL SPRAY UNDER THE INFLUENCE OF STABILIZING BODIES

A. Breña de la Rosa and W.D. Bachalo

Aerometrics, Inc.
Sunnyvale, CA, U.S.A.

Abstract

The present work reports a study of the effect of three stabilizing bodies on the turbulence properties and on the dynamics of an isothermal spray. A vane type swirler having a high swirl number $S = 1.23$, a bluff body, and a bluff body with orifices were used to create a turbulence field with recirculation. A pressure swirl nozzle was used to atomize water downstream of the stabilizing bodies and produce a spray to study its turbulence properties and the interaction with the surrounding air. Properties of the spray such as particle size distributions, particle velocity distributions, and particle number density were also obtained for the sprays in the flow fields of these recirculating flows. The results of the paper show that the recirculation regions produced by the three stabilizers are very different with very high turbulence intensities generated by the bluff body with orifices. Spatial distribution of the particle size is also very different, most notably the liquid drops in the swirling field seem to follow well ordered trajectories which reflect the effect of the circumferential velocity imparted to the drops. In contrast, the drops in the wake of the bluff bodies exhibit trajectories which differ greatly for the various particle size classes.

Introduction

The importance of stabilizing bodies such as disks, cylinders, V-gutters, and swirlers in reacting and non-reacting flows has been recognized for some time, Beer and Chigier (1983). Combustion in the wake of stabilisers causes changes in the shape and strength of the recirculation zones. In addition, reaction in the recirculation region results in an increase in temperature and thus in volumetric flow rate. Moreover, the rate of fuel evaporation, mixing and the rate of formation of chemical species are greatly influenced by the structure of this recirculation region in the flow. Measurements in the reactive case for gaseous fuels have been made by Winterfeld (1965) and Bespalov (1967) in the wake of a V-shaped flame holder. In combustion systems swirl generation is, by far, the most extensively used mechanism for stabilizing the flame and for controlling the efficiency and generation of pollutants, Gupta et al. (1984). While swirl burners have been used widely in combustion, a major effort has been put recently to elucidate the basic mechanisms that govern swirl flows, Sislian and Cusworth (1986) - Cameron et al. (1988). In the application of swirl combustion devices to utility and industrial gas turbine systems, special emphasis has been placed

in understanding the mechanism of formation and emission of pollutants such as CO, unburnt hydrocarbons (UHC), NO_x, and soot; especially when it is recognized that measures customarily taken to reduce, for example, CO, UHC, and soot tended to increase the emission of NO_x.

An important aspect in the design of combustion systems is the ability to predict and control their performance and efficiency. One of the routes to achieving this is through numerical modelling of the flow under study. However, this task is usually very complex if the combustion designer does not possess some basic knowledge of the flow, which in turn must be obtained only from experimental evidence. The purpose of this paper is, therefore, to provide some insight of the effect of three different stabilizing bodies on the structure of the liquid spray.

Experimental Setup

The tests were carried out in a 46×46 cm^2 wind tunnel with a free stream velocity of $V_{fs} = 20$ m/s for all the experiments reported here. Each of the stabilizing devices was placed on the liquid supply tube of a pressure swirl atomizer and the assembly surrounded by an acrylic chamber 300 mm ID which had a screen fitted in the upstream end to dampen turbulence fluctuations of the air flow. This whole assembly was placed, in turn, inside the wind tunnel test section, see Figure 1.

The swirler was manufactured of stainless steel and consisted of a hub 19 mm ID and eight straight vanes welded equidistantly to it and forming an angle of 60° with the longitudinal axis of the swirler. The design of the swirler followed the general guidelines depicted by Beer and Chigier (1983). A more detailed description of the swirler configuration is given by Breña de la Rosa et al. (1990). The 60° vane swirler chosen for this study provided a strong recirculation region and gave a nominal swirl number of $S = 1.23$, Beer and Chigier (1983).

The solid disk and the disk with orifices were 76 mm in diameter and 3.18 mm thick. Two sets of eight symmetrically located orifices were drilled in one of the disks. One set of holes was located at 32 mm from the center of the disk and its orifices were 6.35 mm in diameter, the other set was located at 21 mm from the center of the disk and the orifices were 4.76 mm in diameter, see Figure 1. The location and the size of these holes was arbitrary.

The measurements were obtained with an Aerometrics two-component Phase Doppler Particle Analyzer (PDPA) whose principle of operation is given by Bachalo and Houser (1984). The system consists of a 3 Watt Argon-ion laser, however, the power used in the present experiments was 100 milliwatts measured at the probe volume. The PDPA was configured in the 30 degree off-axis forward scatter, where the scattering of light by refraction is the dominant mode and yields a linear relationship of particle size versus phase between the photodectors over the detectable size range of the instrument. Particle sizing was done with the 0.5145 μm green beams which also gave the first component of velocity, while the 0.488 μm blue beams provided the second orthogonal component of velocity. Frequency shifting was provided by a rotating grating. The optical components selected to obtain the turbulence data were an $f = 300\,mm$ collimating lens and an $f = 200\,mm$ transmitter lens which gave an effective particle detection range of 0.5 to 40 μm in diameter. For the spray data an $f = 160\,mm$ collimating lens and an $f = 500\,mm$ transmitter lens yielded a particle detection range of 4.0 to 300 μm in diameter.

Two sets of experiments were carried out for the three stabilizing bodies. Firstly, the flow was seeded with steam particles having a mean diameter $D_{10} = 1.8\,\mu m$ and a Sauter mean diameter $D_{32} = 3.9\,\mu m$ to obtain the turbulence properties of the flow in the absence of the spray. Secondly, a pressure swirl atomizer operating at $P = 415$ kPa with a nominal flow rate of 3 gph, 45° solid cone, was used to atomize water downstream of the stabilizing bodies. For each of these experiments the axial, radial, and tangential velocity components of the flow were evaluated. The experiments consisted of radial scans of the flow field which were obtained at five different axial locations,

namely, $X = 10$, 20, 50, 100, and 150 mm downstream from the face of the atomizer to evaluate the velocity and turbulence fields. At these same positions (except at $X = 10$ mm where only velocity information was taken), measurements of drop size, drop velocity, and particle number density were obtained from the water spray in the recirculating field. At each axial position the radial measurements were taken at 3-5 mm intervals from the centerline of the nozzle to the periphery of the flow field.

Results

Figure 2 shows the radial distribution of the mean axial velocity of the air $\overline{U}$ obtained at 10 mm from the face of the atomizer for the three stabilizing bodies. Several interesting features can be observed in this plot. Most notably is the difference in the velocity gradients observed amongst the three bodies. In the case of the bluff body, the gradients of mean axial velocity are lowest, in fact, the velocity distribution changes between $\overline{U} = -2.5$ m/s to about $\overline{U} = -7.5$ m/s over most of the flow field at this location. The vane swirler $S = 1.23$ yields an almost constant axial mean velocity from $R = -25$ mm to $R = 25$ mm and subsequently increases to the edge of the swirling field. The bluff body with orifices yields the sharpest changes in mean axial velocity with two peaks in the radial distribution. The first occurs at $R = 20$ mm just before the place where the row of small holes is located. The trough observed at $R = 30$ mm in the radial distribution of $\overline{U}$ is located where the large holes are placed. From this point the velocity gradients are steepest and the velocity increases towards the edge of the solid disk and eventually decreases towards the boundary of the acrylic chamber.

Although not shown, the radial distribution of the radial and tangential velocities of the air were obtained. As expected, the bluff body and the bluff body with orifices provide essentially no rotational velocity to the flow. The air field produced by the swirler showed a steep gradient in azimuthal velocity at the edge of the swirler close to the nozzle.

Figure 3 (left) gives a plot of the turbulence Reynolds shear stresses $\overline{u'v'}$ for the three stabilizing bodies at three axial locations $X = 10$ mm, $X = 20$ mm, and $X = 50$ mm from the atomizer. The interesting features about this figure are that the bluff body shows regions of relatively high shear at $R = 20$ mm and $R = -20$ mm probably caused at the boundaries of the recirculation eddy. The vane swirler produces a practically uniform region of shear except at the boundaries with the external air flow field. The bluff body with orifices exhibits a radial distribution of shear stress $\overline{u'v'}$ whose peaks are consistent with the locations where the gradients of the mean velocity field $\overline{U}$ are found, i.e., at $R = \pm 20$ mm and $R = \pm 32$ mm, see top of Figure 3. The third peak is result of the flow being sheared by the external air flow field. At $X = 20$ mm the bluff body depicts fluctuations of the shear stress profile throughout the flow field. The bluff body with orifice shows peaks in the shear stress profile caused by the jets issuing from the holes. The swirling field does not show regions of high shear except at the boundaries with the external air flow. At $X = 50$ mm the shear stress profiles do not exhibit regions of high shear except at the boundaries of the flow. Notice that for the swirler, half-radial profiles of the shear stress at $X = 20$ mm and $X = 50$ mm were only available.

Also shown on Figure 3 (right) is a comparison of the mean axial velocity of discrete drop sizes having 10 μm, 20 μm, 30 μm, 40 μm, and 50 μm in diameter with the mean velocity of the air. At $X = 20$ mm, in the case of the bluff body and the bluff body with orifices, some of the particle sizes reflect sharp changes in the mean velocity as a result of the vigorous mixing and of the jets issuing from the orifices. In the case of the swirler at $X = 20$ mm, the mean axial velocity profiles of the drops are similar to each other and the particles are decelerated up to the boundaries of the recirculation region, i.e., $R = 26$ mm. Outside of the recirculation region the external air flow field

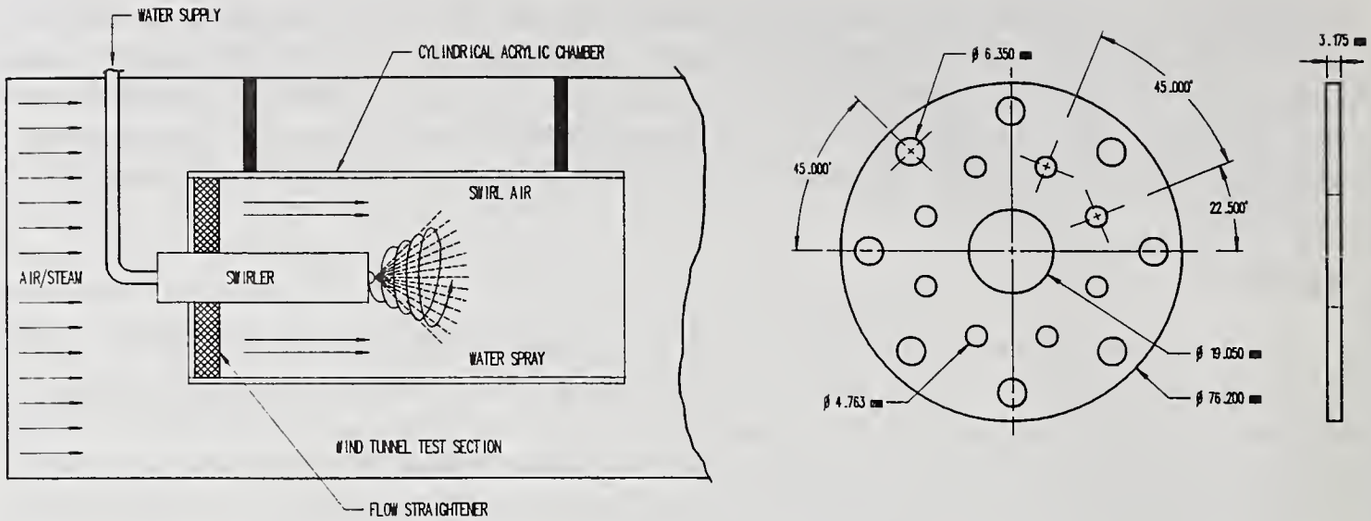

Figure 1: Schematic of the swirl vane assembly fitted to the liquid supply tube of the atomizer inside the wind tunnel test section. The same overall configuration was used (with the swirler removed) for the bluff body and the bluff/orifice stabilizers. Right: Schematic of the bluff body with orifices.

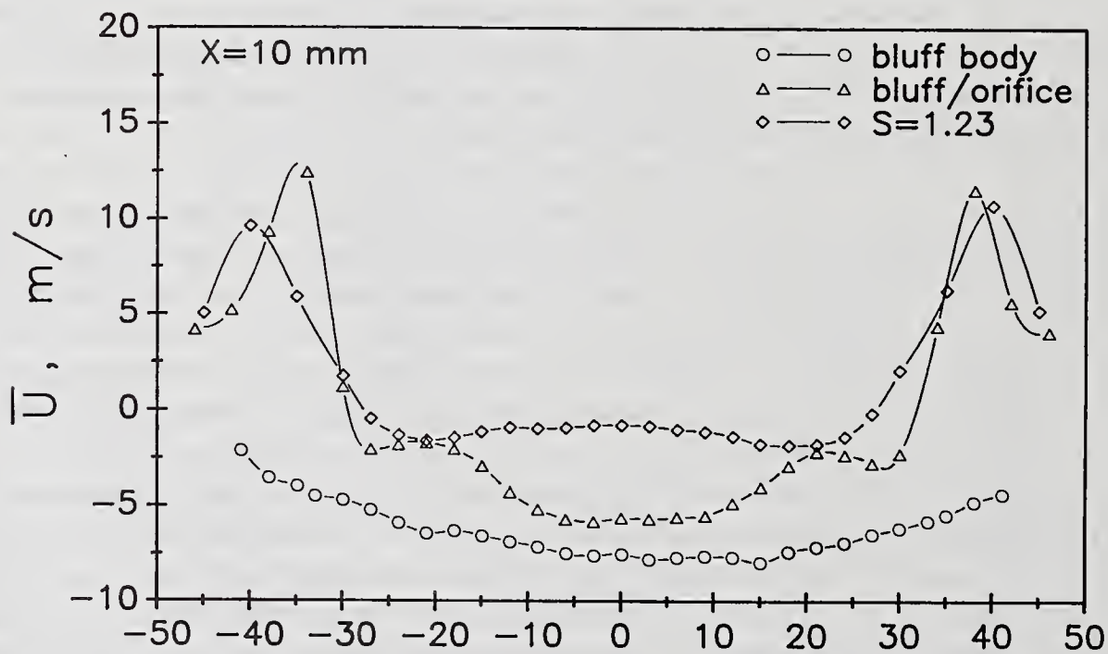

Figure 2: Radial distribution of the mean axial velocity of the air at $X = 10$ mm from the atomizer for the three stabilizing bodies.

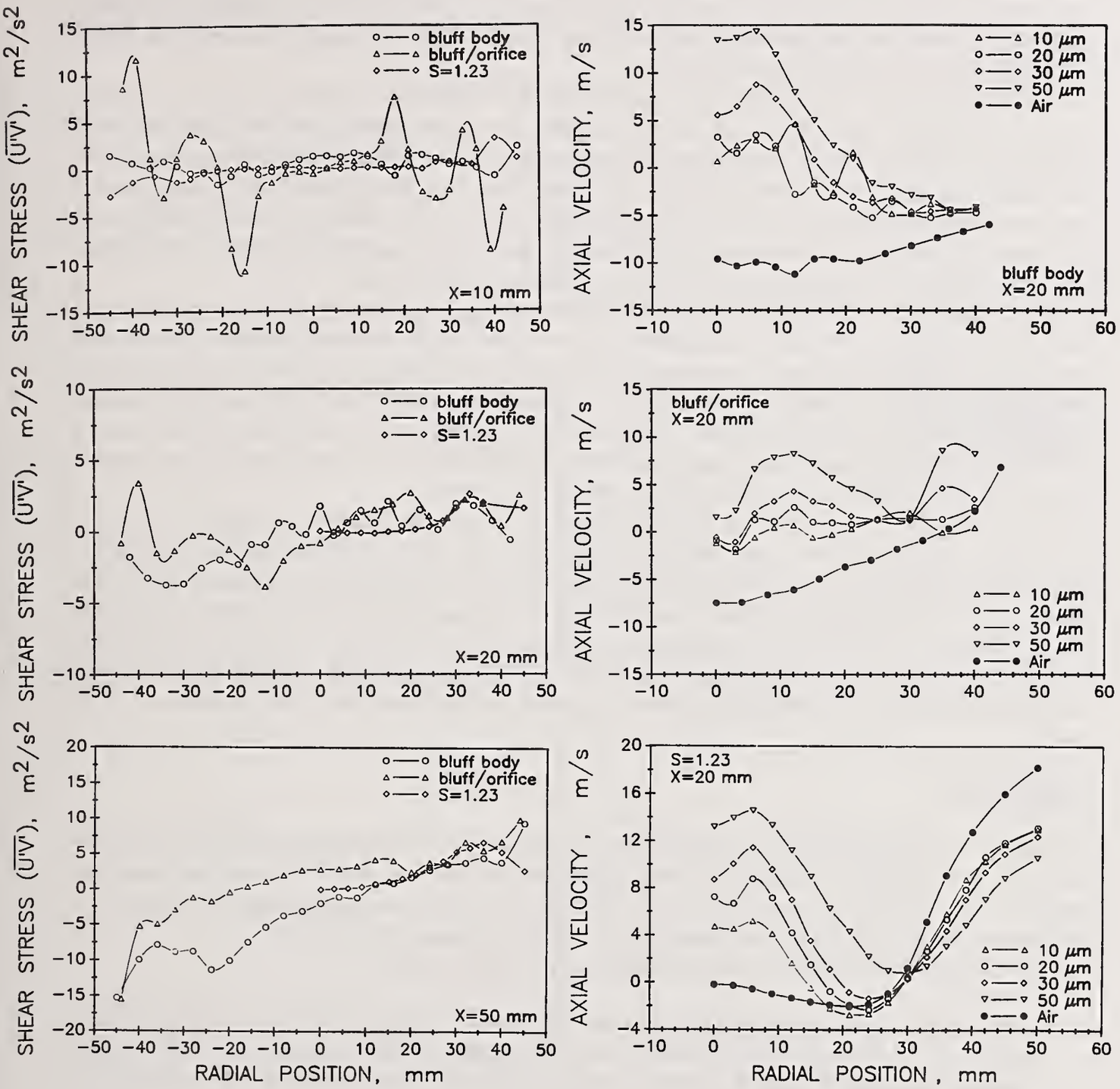

Figure 3: Radial profiles of the turbulence Reynolds shear stresses $\overline{u'v'}$ (left) and comparison of the mean axial air velocity $\overline{U}$ with the mean axial velocity of discrete drop diameters for the three stabilizing bodies.

is dominant and the drops exhibit large gradients of mean axial velocity, with the highest velocities associated with the smallest drop sizes. Notice that negative mean velocities of the air are present for the bluff body and the bluff body with orifices for most of the flow field at this location, which is an evidence of the strong recirculation flow.

For reasons of space limitations, the profiles of the turbulence intensity and of the kinetic energy of turbulence, E_t, are not presented. Turbulence intensity shows a fast decay for the three stabilizers and only the bluff body with orifices shows a region of turbulence at the shear layer with the external air flow field. In the case of E_t, the results show that the regions of high energy content are located where the flow is sheared by opposing high velocity air streams, i.e., at the boundaries of the recirculation region in the core and at the boundaries with the external air stream. In addition, the bluff body with orifices produces the highest E_t close to the nozzle.

Figure 4 depicts the radial distribution of the Sauter mean diameter D_{32} for the three stabilizing bodies at three axial locations. Larger particles were measured in the spray produced by the bluff body at all axial positions when compared to the other two stabilizing bodies. It is evident that the smaller particles are found in the core of the recirculation region for all the stabilizing bodies. The radial distributions of D_{32} for the bluff body and the bluff body with orifices do not follow a particular trend but rather reflect the intense mixing of the spray and the effect of the jets issuing from the orifices, see for example, the D_{32} profile at $X = 20$ mm.

Also shown on Figure 4 are the radial distributions of particle number density N_d (number of particles per cubic centimeter), for the flows produced by the three stabilizing bodies. Peak values of N_d for the bluff body with orifices and for the swirler are about four times greater than those produced by the bluff body. For the latter, this may be the result of the strong recirculation region which prevents a relatively large concentration of drops at that location, (see N_d for the bluff body at $X = 20$ mm, Figure 4). In general, the radial distributions of N_d are strongly affected by the dynamics imposed by the different stabilizers, especially at locations close to the atomizer, $X < 50$ mm.

Conclusions

Measurements of the turbulence properties and of the particle dynamics of an isothermal spray in the wake produced by a bluff body, a bluff body with orifices, and a 60° vane swirler have been made. Due to space limitations, only some of the results have been presented here, however, a complete discussion of the present investigation will be published in a journal.

The following conclusions can be drawn from the present work:

- The air flow fields produced by the three stabilizing bodies tested here produced drastic differences in both the turbulence field and the dynamics of the liquid particles. Flow reversal was observed for the three flow fields, with the bluff body yielding the highest negative axial mean velocities at all axial locations, see Figure 4.

- Regions of highly sheared flow are present in the field produced by the bluff body with orifices which persist to about $X/D = 0.66$ ($X = 50$ mm, where $D = 76$ mm) from the nozzle.

- The turbulence properties of the flows show that the bluff body with orifices yields the highest kinetic energy of turbulence and turbulence intensity, caused by the strong jets issuing from the holes.

- The trajectories of discrete liquid particles are also very different for the three flow fields, the largest differences amongst them observed close to the nozzle. In the case of the vane swirler,

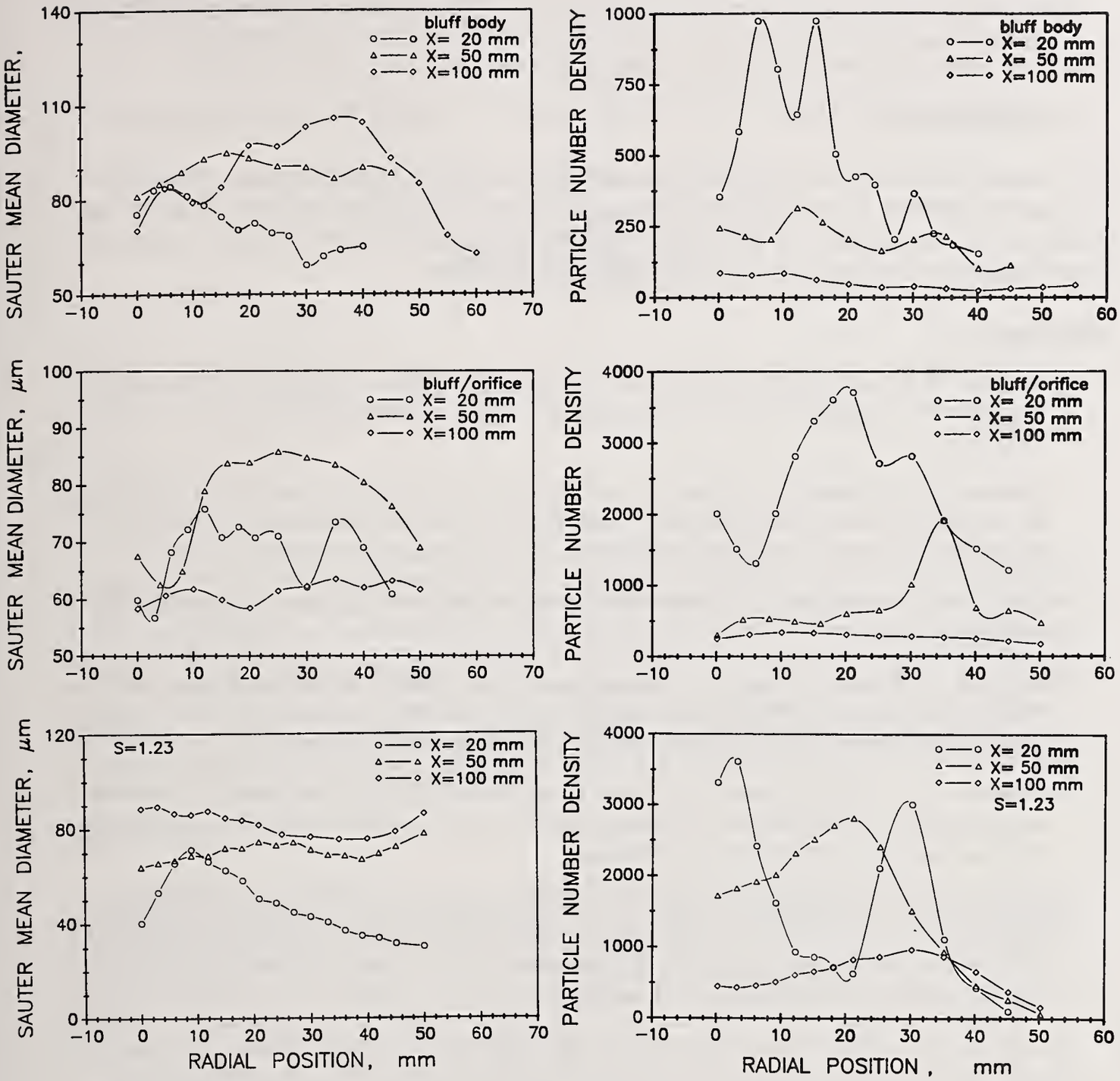

Figure 4: Radial distribution of the Sauter mean diameter D_{32} (left) and of the particle number density N_d (right) for the three stabilizing bodies at three axial locations.

a clear evidence of the effect of the recirculation region (in the core) and of the external air flow field on the droplet trajectories was present in all the results, see for example Figure 3. Particle number densities resulted in peak values which are about four times greater for the bluff body with orifices and for the swirler than those produced by the bluff body.

Acknowledgements

The authors gratefully acknowledge the support of this work by the National Science Foundation, Contract ISI-8860783 and by NASA Lewis Research Center, Contract NAS3-25204. The authors would also like to express their gratitude to Mr. Mark Yoneyama and Mr. Robert Kennedy for their contributions during the experimental stage of the program.

References

- Bachalo, W.D., and Houser, M.J., 1984, "Phase/Doppler Spray Analyzer for Simultaneous Measurements of Drop Size and Velocity Distributions", Optical Engineering, Vol. 23, No. 5, p. 583.
- Bachalo, W. D., Breña de la Rosa, A., and Rudoff, R. C., 1988, "Advances in Diagnostics for Complete Spray Characterization", Proceedings of the 4th International Conference on Liquid Atomization and Spray Systems, Sendai, Japan, August 22-24.
- Beer, J. M., and Chigier, N. A., 1983, *Combustion Aerodynamics*, Robert E. Krieger Publishing Company, p. 111.
- Breña de la Rosa, A., Wang, G., and Bachalo, W. D., 1990, "The Effect of Swirl on the Velocity and Turbulence Fields of a Liquid Spray", Presented at the 35th ASME Gas Turbine and Aeroengine Congress and Exposition, Brussels, Belgium, June 11-14.
- Bespalov, I. V., 1967, "Physical Principles of the Working Process in Combustion Chambers of Jet Engines", Translated from Russian, Clearinghouse for Federal Scientific and Technical Information, USA, AD 658 372, p. 366, May.
- Cameron, C. D., Brouwer, J., Wood, C. P., and Samuelsen, G. S., 1988, "A Detailed Characterization of the Velocity and Thermal Fields in a Model Can Combustor with Wall Jet Injection", ASME Paper No. 88-GT-26, Presented at the Gas Turbine Congress and Exposition, Amsterdam, The Netherlands, June 5-9.
- Gupta, A. K., Lilley, D. G., and Syred, N., 1984, *Swirl Flows*, Abacus Press.
- Lilley, D. G., 1988, "Lateral Jet Injection into Swirling Combustor Flowfields", AIAA Paper No. AIAA-88-3183, AIAA/ASME/SAE/ASEE 24th Joint Propulsion Conference, Boston, July 11-13.
- Sislian, J. P., and R. A., Cusworth, February 1986, "Measurements of Mean Velocity and Turbulence Intensities in a Free Isothermal Swirling Jet", AIAA Journal, Vol. 24, No. 2, pp. 303-309.
- Winterfeld, G., 1965, "On Processes of Turbulent Exchange Behind Flameholders", Tenth Symposium International on Combustion, The Combustion Institute, pp. 1265-1275.

ATOMIZATION WITH SPILL-CONTROLLED SWIRL PRESSURE-JET NOZZLES

M. Löffler-Mang and W. Leuckel

University of Karlsruhe, Engler-Bunte-Institute
Combustion Technology Section
Karlsruhe, Germany

ABSTRACT

The entire atomization process using spill-controlled swirl pressure-jet nozzles was investigated. Part I deals with the flow fields inside scaled-up plexiglass nozzles. Tangential and axial mean velocities and velocity fluctuations were measured within the nozzle chamber by using Laser-Doppler-Velocimetry (LDV). Outlet conditions were evaluated from the measurements and, in addition, photographs of the flow patterns were taken. Part II deals with the drop behaviour in the spray cone of real nozzles. Axial and radial drop velocities (mean values and RMS-values) and, simultaneously, drop sizes were measured at various nozzle distances with a Phase-Doppler Particle Analyser (PDPA). Finally, some comparative considerations of angular exit momenta (perspex models) and drop sizes (real nozzles) were drawn from the results, exhibiting agreement between the two parts of the investigation. Also an energy balance for the nozzle as a whole was formulated and evaluated.

INTRODUCTION

Atomization with pressure-jet nozzles is widely used in mechanical engineering, e.g., for paint and laquer spray nozzles, within spray towers, in humidifiers, but also in combustion engineering for liquid fuel nozzles (domestic heating burners, industrial furnaces, gas turbine combustors). The great advantage of spill-controlled nozzles compared to those without spill return is their much wider control range and the relative constancy of spray quality over a wide throughput range. Their main drawback is the lack of equations for predicting drop sizes, velocities, etc. They still have to be developed, designed and dimensioned empirically.

The swirl pressure-jet atomization process can be characterized as follows. The fluid enters the swirl chamber of the pressure-jet nozzle through tangential channels. The energy necessary to create a free film surface is taken from the pressure-induced kinetic energy of the fluid to be atomized. As a result of the radial pressure gradient caused by the swirling motion (centrifugal forces) within the nozzle, an air-filled hollow core forms about the nozzle chamber axis. Hence, the liquid issues from the nozzle exit as a concentric film which forms an expanding hollow cone, which finally disintegrates into an atomized spray as a result of inertia and viscous forces acting upon the film.

Obviously, the generation of the final drops is strongly influenced by the outlet conditions and the liquid film properties at the orifice. Those in return depend on the flow fields inside the nozzle chamber. Keeping those dependencies in mind, the motivation for stepwise investigations is evident. The first step (PART I) consisted of flow field measurements inside the nozzle chambers of enlarged perspex models (scale 20 : 1). In the second step (PART II), investigations in the spray cone of real nozzles were carried out. In order to characterize the flow within the nozzle, and to compare the results obtained inside and

outside the nozzle, three dimensionless numbers were used:

$$\textit{Reynolds number} \qquad Re = \frac{\overline{w_0} d_0}{\nu}$$

$$\textit{swirl number} \qquad S_0 = \frac{\pi r_{exz} r_a}{A_E}$$

$$\textit{spill:feed ratio} \qquad RV = \frac{\dot{V}_R}{\dot{V}_V}$$

PART I : FLOW-FIELD INSIDE NOZZLE CHAMBER

Experimental Set-Up

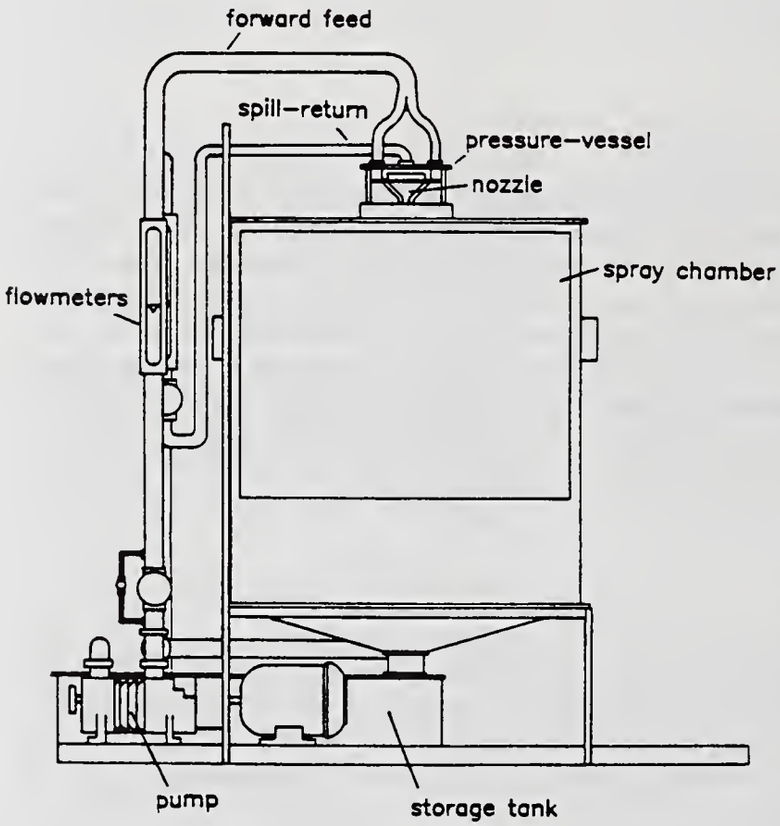

Fig. 1: Experimental set-up I

For the experimental investigation of the flow-field inside the nozzle chamber scaled-up perspex nozzles were mounted into a pressure vessel, which was placed above a large spray chamber as can be seen in Fig. 1. Vessel and spray chamber had two windows each, so that on the one hand velocity measurements inside the nozzle using Laser-Doppler Velocimetry could be conducted, and on the other hand photographs of the spray cone could be taken.

A ternary test liquid was fed into the nozzle chamber by a pump. One part of the liquid stream left the nozzle through the orifice, the other part escaped through the central spill-bore in the rear wall of the nozzle, flowing directly back to the storage tank. The part of the liquid being atomized was collected at the bottom of the spray chamber from where it also passed into the tank. The volume flow rates of the feed and the spill were measured and controlled by flowmeters. Typical feed volume flow rates were in the range between 10 and 90 l/min.

Air bubbles in the liquid stream served as tracer particles for the LDV-measurements. The bubbles were fed into the test fluid by means of a valve at the low-pressure side of the circuit.

Results

Fig. 2 exemplifies flow fields for different spill:feed ratios (RV) at a constant feed rate of 35 l/min. In the lower left corner of each diagramm the values of the spill:feed ratio (RV), the swirl number (S_0) and the Reynolds-number (Re) are indicated. On the left hand side of each diagramm, the contour of the air-filled hollow core has been included, the corresponding dimensions being extracted from photographs of the flow. The behavior of the core under the influence of various spill:feed ratios is obvious : at a ratio RV = 0.0 the core diameter increases progressively towards the nozzle outlet, whilst for RV = 0.86 the core assumes an almost cylindrical shape of very large diameter. On the right hand side of each diagramm tangential and

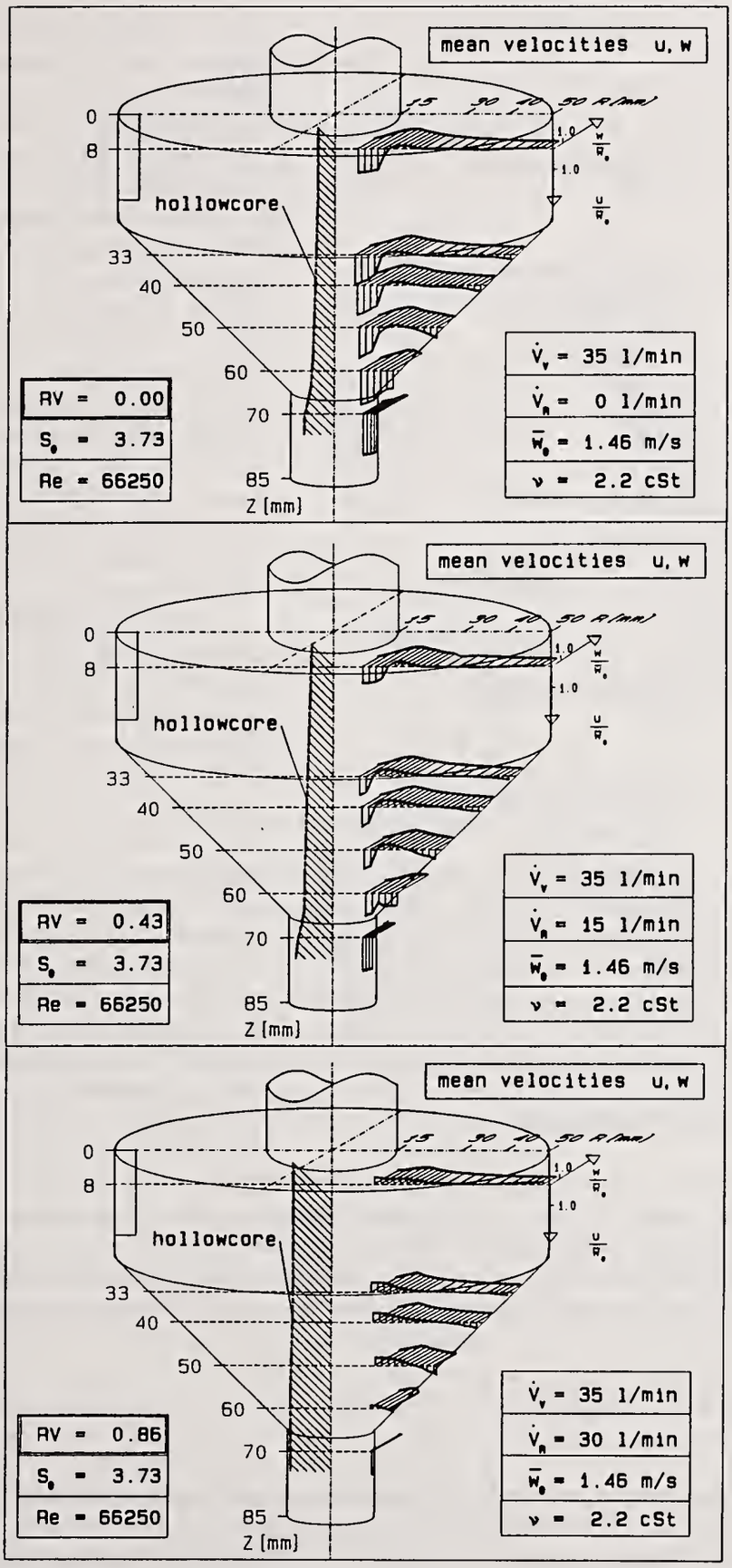

Fig. 2: Mean velocity profiles u,w; variation of spill:feed ratio

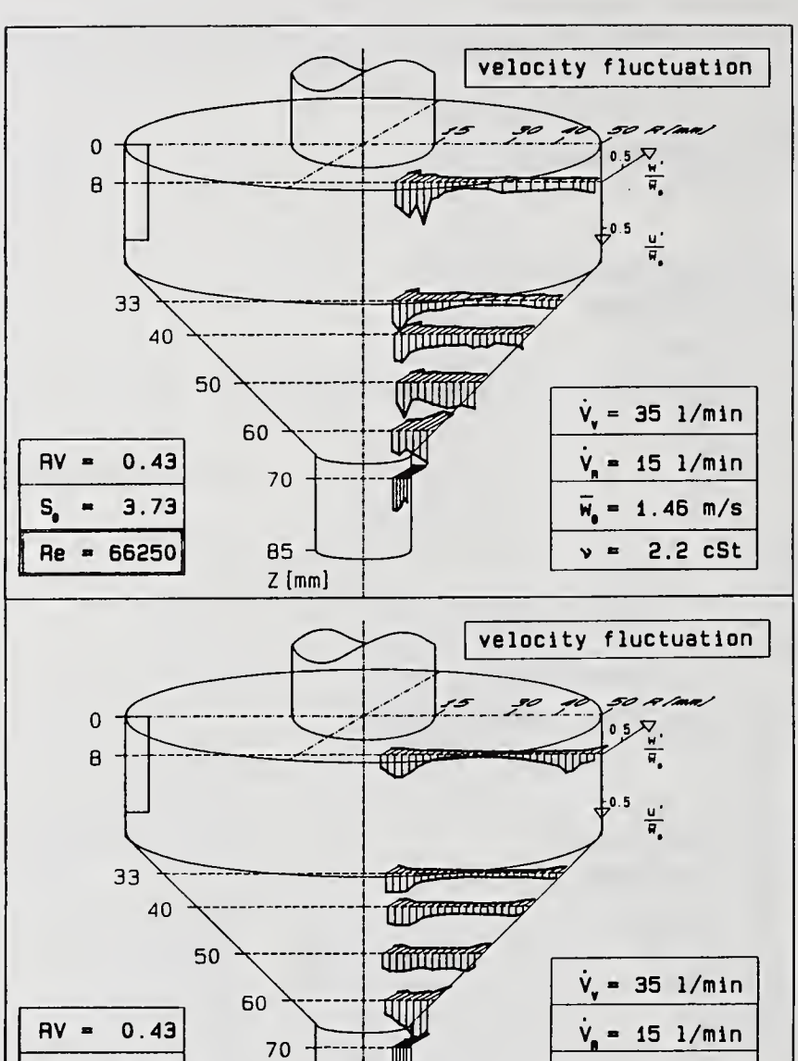

Fig. 3: Velocity fluctuations u',w'

axial velocity profiles are illustrated. The velocity components were measured at 6 different nozzle cross-sections each. The plots represent the velocities as ratios of the mean tangential inlet velocity through the tangential ports. The axial components are drawn in the downward direction, the tangential components to the rear of the drawing plane.

In all cases, the tangential velocity profile resembles a Rankine vortex, with a solid body vortex characteristic in the vicinity of the nozzle axis, and tangential velocity decrease towards the chamber periphery. The tangential velocity profile varies only slightly in the downstream axial direction, the peripheral zone being simply cut-off due to the convergent nozzle geometry.

From the axial component profiles a clear influence of the spill-return may be observed. Whilst at low spill:feed ratios two forward flow zones appear (one at the nozzle periphery, the other in the vicinity of the hollow core), which merge with each other in the region of the orifice, at high values of RV (RV > 0.75) a clear backflow along the hollow core is apparent for nearly the whole nozzle chamber length. Near to the nozzle outlet the values of tangential and axial velocity components are rather similar.

In addition to the mean values of the velocity components also the fluctuations of the tangential and axial components were measured. Again the spill:feed ratio showed the strongest influence on the profiles, as to be expected from the observations of the mean velocities. The variation of the swirl number indicates a smoothening effect of swirl on turbulence. Measurements with a higher viscosity test fluid resulted in lower fluctuations as can be seen in Fig. 3. Here again the velocities are plotted as ratios of the mean tangential inlet velocity. From Fig.3 it is also evident that the fluctuations are always high in regions with high gradients of the mean velocities (see Fig.2), i.e., the largest fluctuations appear at the periphery and near to the hollow core, whilst they are damped in the region between those maxima.

PART II : SPRAY CONE INVESTIGATIONS

Experimental Set-Up

Measurements in the spray cone of real nozzles were conducted according to the arrangement as schematically illustrated in Fig.4. Water was fed from a storage vessel by a piston pump to a spill-controlled swirl presssure-jet nozzle which generated the droplets. The volume flow rate could be controlled and, in addition, the nozzle pressure was metered for both the nozzle feed and spill rates. For the experiments, a nozzle with an orifice of 1mm exit diameter was used which, at an applied pressure of approx. 10 bar, delivered a volume flow rate of 40 l/h. Different standardized units (swirl generators and nozzle chambers)

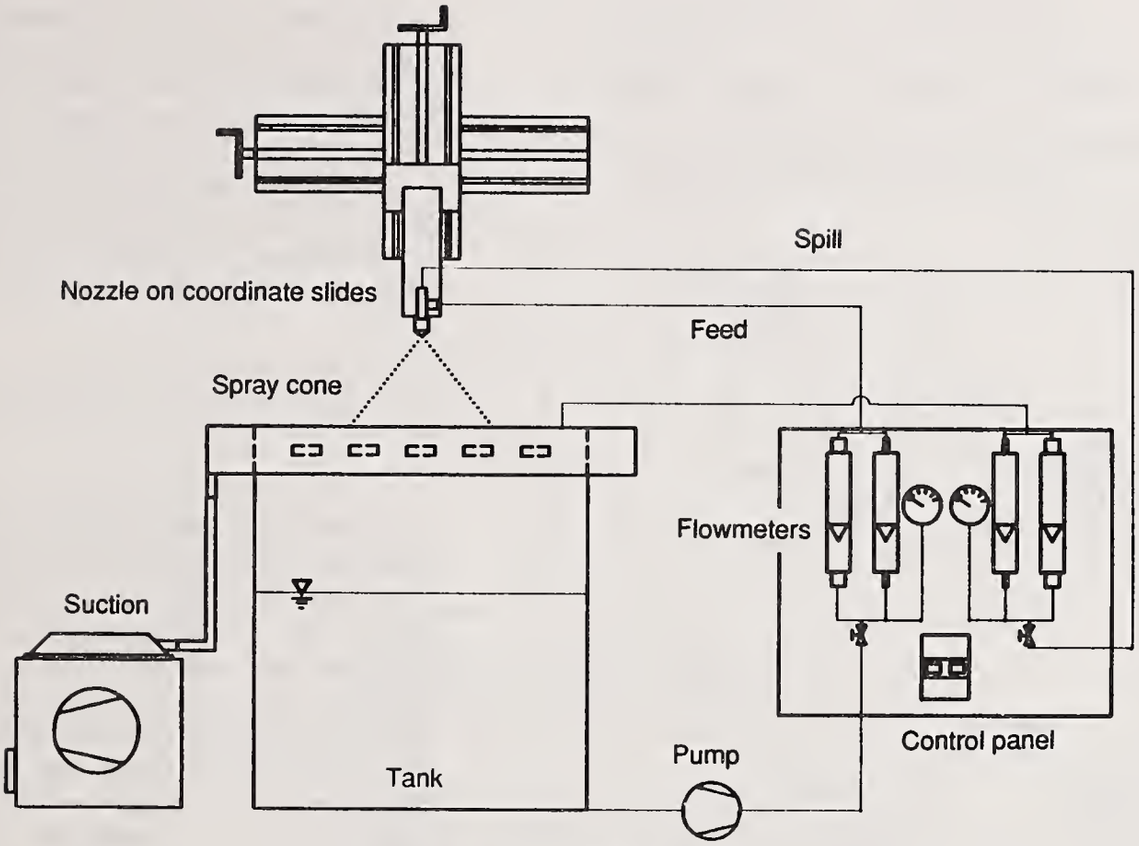

Fig. 4: Experimental set-up II

could be combined to a complete nozzle. Hence the spill:feed ratio, the swirl number and the nozzle geometry were experimental variables also in this second part of the investigation.

The atomization occurred in free atmosphere. The spray configuration was of the hollow cone type with a spray angle of approximately 80°. The spray was collected in the supply reservoir. In order to reduce the influence of secondary backflowing mist to a minimum, the surrounding air was uniformly drawn from the vessel by a suction fan. The nozzle was mounted on a 2-dimensional slide, thus allowing different spray flow sections to be probed, following a 2-dimensional coordinate system.

The optical axis of a Phase-Doppler system (PDPA) was located right above the rim of the vessel. PDPA delivers the probability density distributions of drop size (d) and drop velocity components (u,v).

Results

On the right hand side in Fig.5 drop velocity information is being presented. For three different nozzle distances, the mean values of the axial velocity and the related RMS-values are shown. The velocity is rather low in the center, then increasing to relatively high values in the main spray cone shell. This velocity maximum decreases with increasing nozzle distance, because the drops are decelerated by the surrounding air.

For detailed knowledge of the structure of the spray not only mean velocities but also RMS-values are needed which are responsible for the droplet dispersion process. There is a clear maximum of fluctuation at the inner side of the main spray cone shell, which is the region of the largest velocity gradients. In the center region the drops move slowly and exhibit low tubulence. On the left hand side of Fig.5 arithmetic mean diameter (d_{10}) and Sauter Mean Diameter (SMD) are plotted. As from the velocities, also from the drop sizes the hollow cone type of the spray becomes evident. In the center region a rather narrow size distribution exists with a SMD of about 25 μm. For comparison, the main spray cone shell exhibits a wide distribution and a SMD around 200 μm.

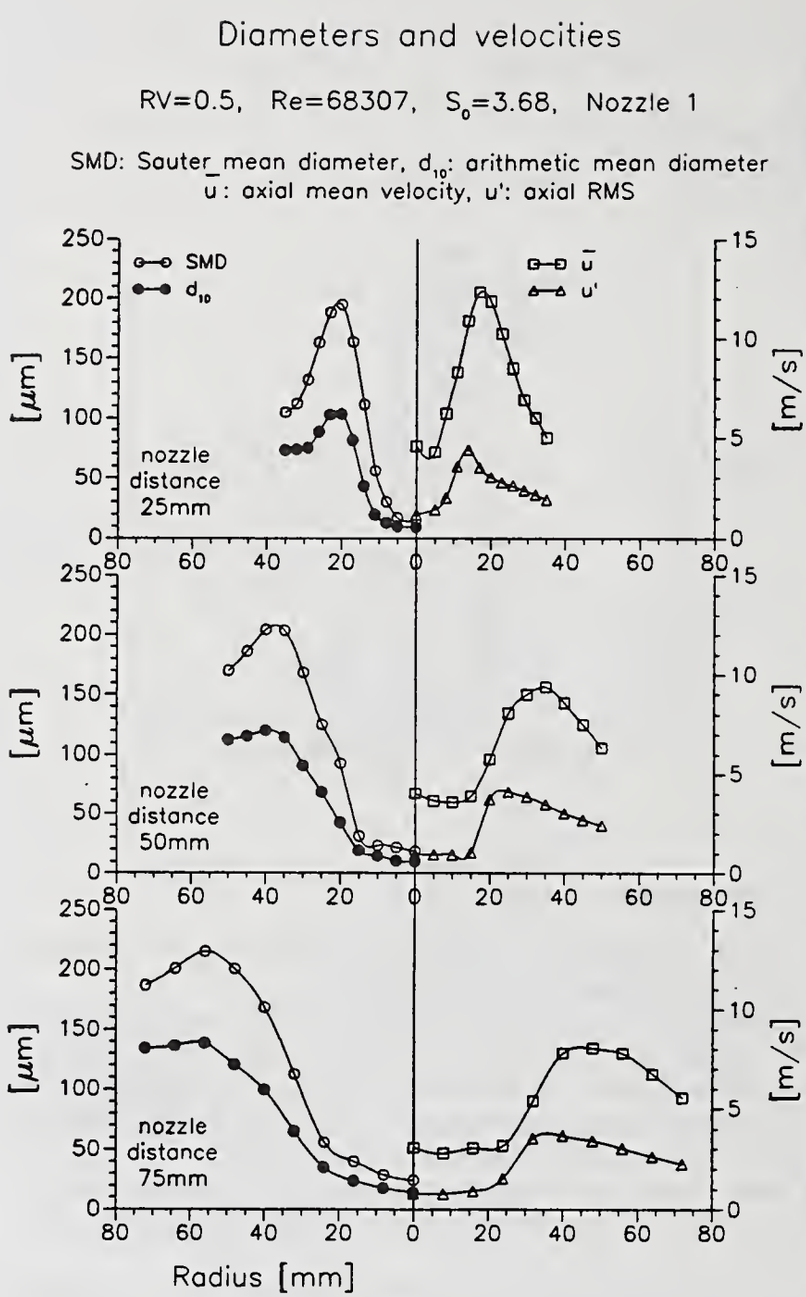

Fig. 5: Drop diameters and velocities for different nozzle distances

Another aspect can be pointed out in Fig.5. The maximum of the arithmetic mean diameter (in the spray cone shell) increases slightly with nozzle distance. The spray cone aspirates surrounding air into its center. The small drops follow the air flow without slip, leading to decreased concentration of smaller drops and, hence, increased mean drop size in the shell.

EXIT MOMENTUM AND SAUTER MEAN DIAMETER

Figure 6 compares LDV-measurements obtained for the liquid flow inside the nozzle chamber of the perspex model with drop size measurements in the spray cone. In Fig.6a reduced angular momenta (as evaluated from velocity measurements) near to the nozzle exit are plotted as functions of the spill:feed ratio RV. For the low viscosity test fluid, i.e. high Reynolds number of the swirl chamber flow, a minimum angular momentum at the nozzle exit occurs in the range of a spill:feed ratio of about 0.4, which could be expected to lead to coarser atomization in this range. Indeed, this fact is being confirmed by the spray measurements (Fig.6b). Here, the Sauter Mean Diameter (SMD) is plotted as a function of the radial position, varying the spill:feed ratio. As expected from the evaluated exit momenta, SMD values in the main spray cone shell (radial positions between 30 and 50mm) at first increase up to a maximum value at RV = 0.6, then for higher spill:feed ratios decrease again. Former measurements of drop sizes in the spray cone with a Malvern Particle Sizer showed the same trend. In Fig.6c cumulative volume distributions are plotted for different spill:feed ratios. Again the drop size at first increases with increasing spill:feed ratio up to a value of RV = 0.5 and then decreases, indicating that atomization improves for higher spill:feed ratios. This observation is important when operating spill controlled nozzles over a wide control range and will be a topic of major interest in future investigations.

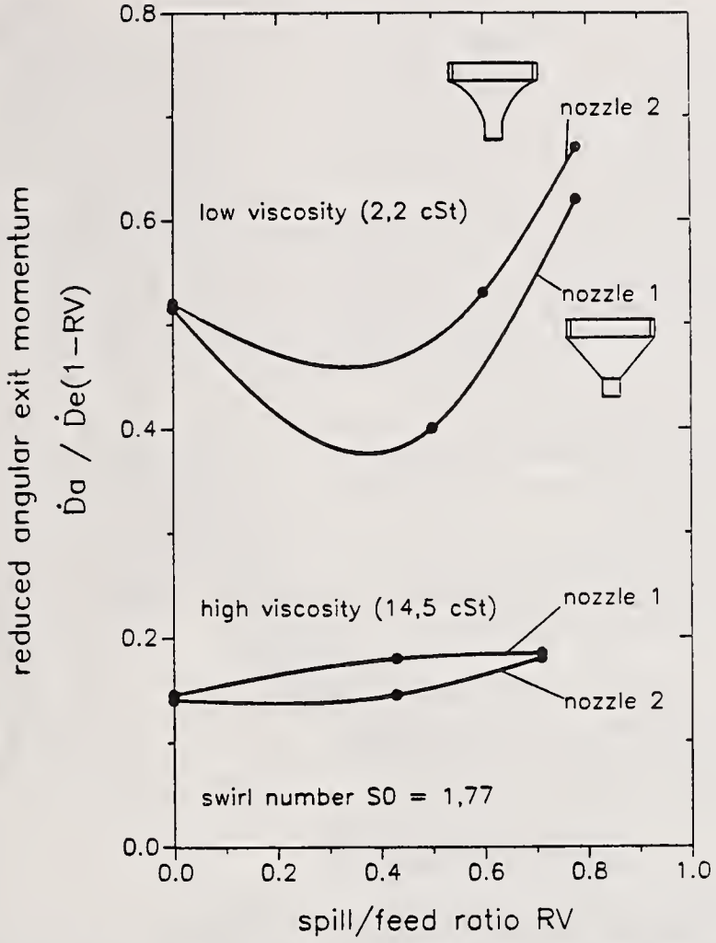

Fig. 6a: Reduced angular exit momentum over spill:feed ratio

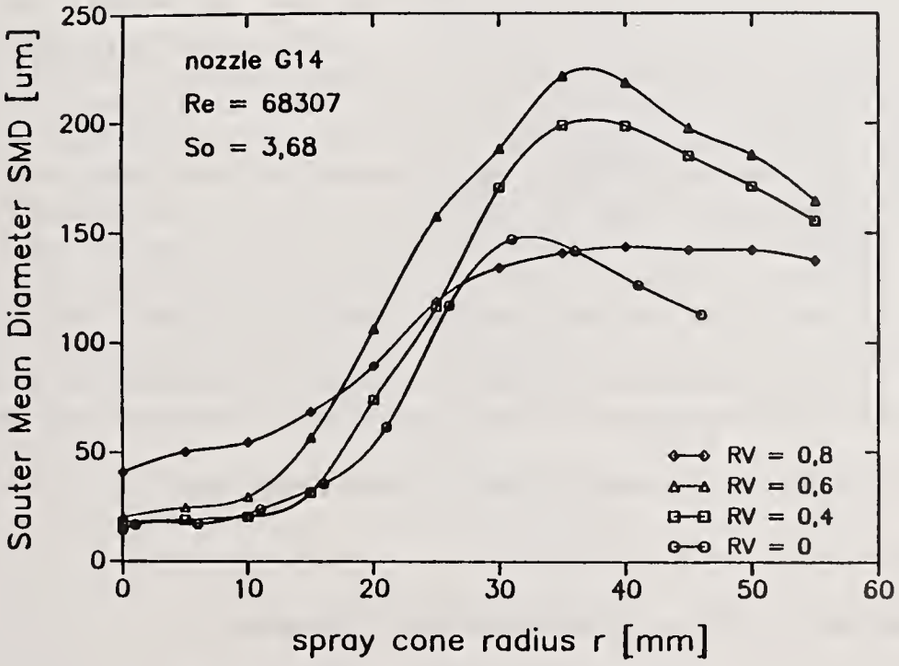

Fig. 6b: Profiles of Sauter Mean Diameter

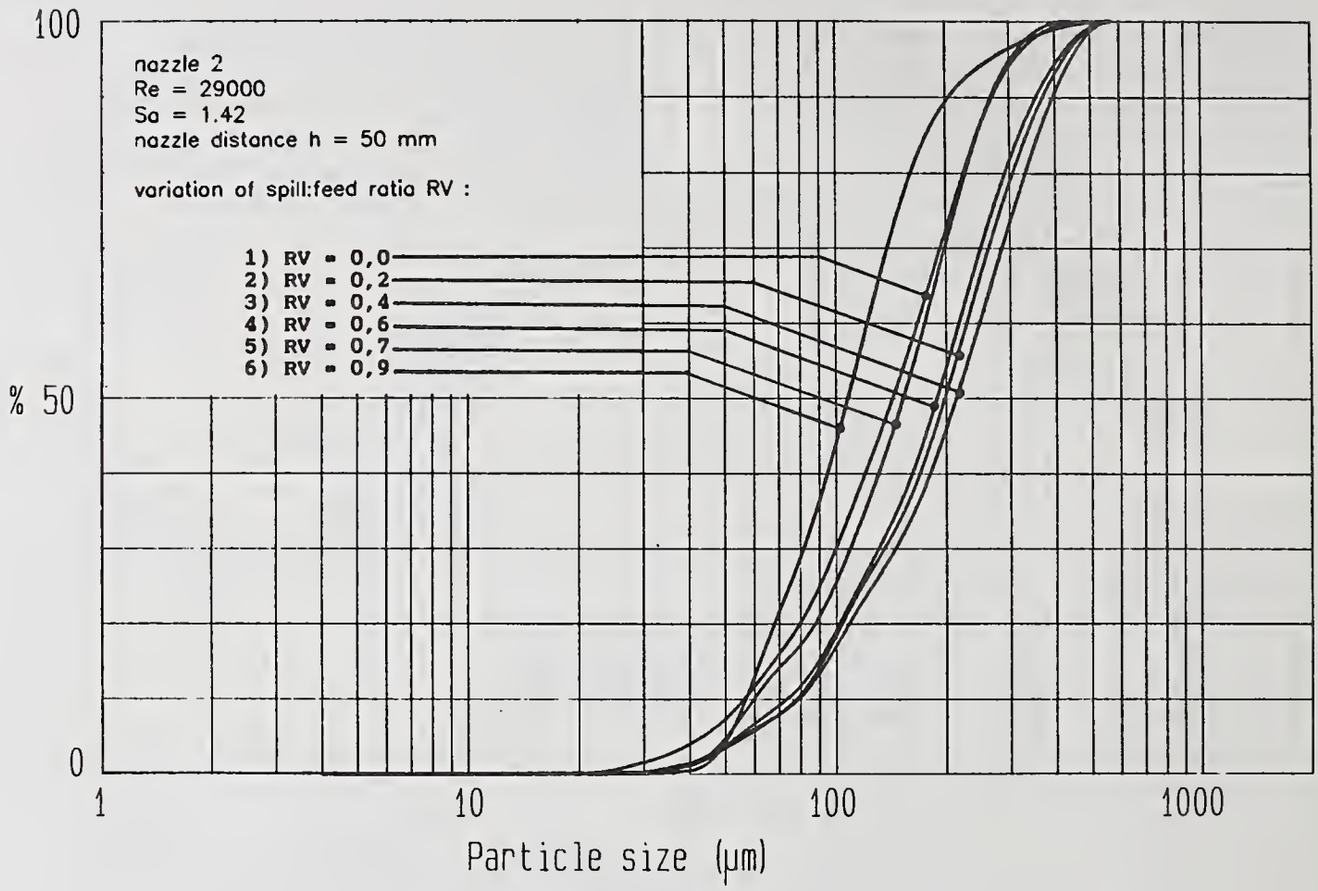

Fig. 6c: Cumulative volume distributions

ENERGY BALANCES

In this final section a simple energy balance is carried out, based on measured data from the nozzle investigations.

The energy necessary for atomization is taken from the high-pressure volume flow to the nozzle, the feed energy E_V. When operating the nozzle with spill-control, a portion of the energy flows into the spill return, the spill energy E_R. The kinetic energy in the feed and spill lines is negligible compared to the static pressure energy. Part of the remaining energy $E_V - E_R$ is converted into kinetic energy at the nozzle oriffice $E_{kin,a}$, a higher portion being lost as a result of internal fluid flow friction inside the nozzle chamber. At a nozzle distance h, a portion of $E_{kin,a}$ is expended to create the surface of the new drops E_{Ob}, other one delivers the kinetic energy of the drops E_{kin}, and a third is lost due to friction between the liquid and the surrounding air. All this energy flow rates can be estimated from measurements. For the drop energies in the spray it is necessary to integrate over the droplets of the entire spray cross section. All the equations are shown in Fig. 7 . For a nozzle distance of 50 mm, the results of the estimated energy balance can be summarized as follows; all the energy terms are being expressed as ratios of the initial energy $E_V - E_R$:

- 10-30 % of the initial static pressure energy appear as kinetic energy flux at the nozzle orifice;

- 0.1-0.4 % remain as surface energy in the spray;

- 5-25 % can be identified as kinetic energy of the droplets in the spray.

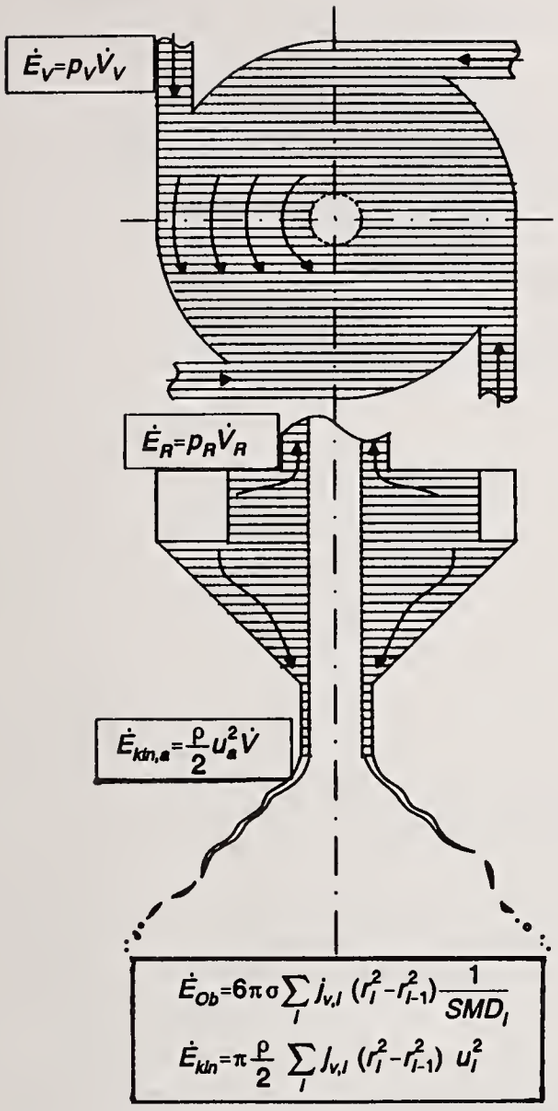

Fig. 7: Nozzle scheme and energy terms

CONCLUSIONS

The results of the first part of the investigation, as obtained from measurements inside enlarged perspex models, may be interpreted as follows:

In all cases the radial profiles of the tangential velocity resemble a Rankine vortex type distribution.

Most of the measured axial velocity profiles show two maxima, one at periphery of the chamber and the other in the vicinity of the central hollow core. For very high spill:feed ratios, a back-flow along the hollow core was evident instead.

The RMS-profiles exhibit that the velocity fluctuations are always high in regions with high gradients of the mean velocities.The variation of swirl number delivered a damping effect of swirl on the turbulence.

The second part of the study, which dealed with spray cone investigations, yielded the following results:

A hollow cone structure of the spray was clearly evident.

There were slow drops with low turbulence in the center region of the spray, whilst in the spray cone shell fast drops with high turbulence were found. Also, in the center the drops were rather small and had a narrow size distribution, but in the spray shell there were large drops with a wide size distribution.

The maximum of the arithmetic mean diameter in the spray shell increased slightly with the nozzle distance, to be explained by the fact that the spray cone aspirates surrounding air together with small droplets into its center.

From comparing calculated nozzle exit conditions (perspex model) with drop size measurements in the spray cone (real nozzle), agreement was found between a minimum of angular exit momentum and a maximum of SMD occurring in the spill:feed ratio range of about 0.5.

An estimated energy balance for the droplet mass was carried out. The calculated examples in the spray delivered a remaining surface energy between 0.1 and 0.4% only, and a remaining kinetic energy between 5 and 25% related to the initial static pressure energy.

NOMENCLATURE

A_E	total inlet area
d_0	swirl chamber diameter
d_{10}	arithmetic mean diameter
$\dot{D}_a$	angular exit momentum
$\dot{D}_e$	angular entry momentum
E_{kin}	kinetic energy at distance h
$E_{kin,a}$	kinetic energy at orifice
E_{Ob}	surface energy
E_R	spill energy
E_V	feed energy
h	nozzle distance
p_R	spill pressure
p_V	feed pressure
r_a	orifice radius
Re	Reynolds number
r_{exz}	radius of excentricity of the inlet channel
RV	spill:feed ratio
S_0	swirl number
SMD	Sauter Mean Diameter
$\dot{V}_R$	spill flow rate
$\dot{V}_V$	feed flow rate
w_0	tangential inlet velocity
w,u	tangential and axial velocity components
w',u'	tangential and axial velocity fluctuation components
ν	viscosity
ρ	density
σ	surface tension

ACKNOWLEDGEMENT

The authors wish to express their gratitude to the Deutsche Forschungsgemeinschaft (DFG) for the financial support of the investigations reported here, which have been performed in the frame of the joint research project "Sonderforschungsbereich 167/ Hochbelastete Brennräume" of the Karlsruhe University.

MULTIPLE SCATTERING AND SIZE DISTRIBUTION EFFECTS ON THE PERFORMANCE OF A LASER DIFFRACTION PARTICLE SIZER

T. Paloposki and A. Kankkunen

Helsinki University of Technology
Espoo, Finland

Abstract

The effect of multiple scattering on the performance of the Malvern Particle Sizer was studied experimentally. Two particle samples with the same volume median diameter but with different size distributions were used in the experiments. One sample could be described by a log-normal distribution function, the other by a Rosin-Rammler distribution function. The particle samples were specifically designed to simulate drop size distributions in liquid sprays.

The model independent, log-normal, and Rosin-Rammler models were used in the data analysis, and the results were compared. It was found that even when the sample concentration was low and multiple scattering did not occur, the results obtained with the log-normal and Rosin-Rammler models could be misleading, particularly in the high end of the distribution (large particles). When the log-normal test sample was used, the model independent and log-normal models gave good results, but the Rosin-Rammler model seriously underestimated the fraction of large particles. When the Rosin-Rammler test sample was used, the model independent and Rosin-Rammler models gave good results, but the log-normal model seriously overestimated the fraction of large particles.

When the sample concentration is high and multiple scattering occurs, data analysis with the model independent model is not feasible. Correction equations are available in literature for data analysis with the log-normal and Rosin-Rammler models. It was found that when the correction equations were used, both the log-normal and Rosin-Rammler models provided the mean particle size reasonably well. However, there were considerable difficulties in the high end of the distribution. This was not surprising, since the experiments with a low particle concentration had already shown that the data analysis with the log-normal and Rosin-Rammler models can produce misleading results.

Introduction

The Malvern Particle Sizer was developed by Swithenbank *et al.* [1] for the measurement of drop size distributions in liquid sprays and is commercially manufactured by Malvern Instruments Ltd. The instrument is based on the diffraction of laser light by the drops. The light energy distribution in the near-forward direction is measured with a multi-element detector and analyzed with a microcomputer. A non-linear least-squares method is used to find the best-fit drop size distribution *i.e.*, a size distribution which gives the most closely fitting light energy distribution.

Swithenbank *et al.* assumed a Rosin-Rammler distribution of drop sizes and single scattering of light by the drops. Negus and Azzopardi [2] discussed the validity of these assumptions and tested the instrument against particle samples with known size distributions and concentrations. The particle samples were made of glass spheres and suspended in water in a stirred test cell with windows for optical access. They concluded that some limitations arise from the assumption of a Rosin-Rammler size distribution and estimated the critical particle concentration above which multiple scattering problems become significant.

The assumption of a Rosin-Rammler size distribution is no longer necessary, since other models have been added to the data analysis software of the commercial instrument. The user can now choose between three different distribution functions — Rosin-Rammler, normal, and log-normal — and a model independent distribution. All three distribution functions are two-parameter functions *i.e.*, the values of two independent parameters specify the distribution. The model independent distribution is a presentation of volume fractions in 16 discrete size classes; thus, there are 15 independent parameters. Obviously, the model independent distribution is much more flexible than the two-parameter distributions. Any distribution that can be described by a two-parameter distribution function can also be described by the model independent distribution. Furthermore, bimodal distributions and some other difficult distributions can be described by the model independent distribution but not by any two-parameter distribution functions.

The two-parameter functions can still be useful in spray studies, since the drop size distributions in liquid sprays are usually unimodal. However, the normal distribution has seldom been applied in spray studies and will not be discussed here. The Rosin-Rammler and log-normal distributions have been applied more frequently and will be studied in our paper.

The multiple scattering problems have been widely investigated. A most practical solution has been presented by Felton *et al.* [3]. They presented correction equations which can be applied both to results obtained using the Rosin-Rammler model and to results obtained using the log-normal model. The correction equations were derived using a theoretical model of multiple scattering, and model predictions were compared to experimental results obtained using dense suspensions of glass beads in water. Excellent agreement was obtained. Felton *et al.* also found that multiple scattering effects were not significant for obscurations less than 50 %; obscuration is the fraction of light diffracted by the drops and is recorded in each measurement.

Felton *et al.* did not present correction equations for results obtained using the model independent model. The correction equations for results obtained using the Rosin-

TIME-BASED POLARIZATION RATIO MEASUREMENTS OF DROPLET SIZE

J.R. Zurlo, C. Presser and N. Chigier*

Chem. Sci. and Tech. Lab., National Institute of Standards and Technology, Gaithersburg, MD, U.S.A.
*Carnegie Mellon University, Pittsburgh, PA, U.S.A.

ABSTRACT

Nearly instantaneous droplet size measurements were carried out using an ensemble light scattering technique based on measurement of the polarization ratio. Measurements of droplet size were performed in a pulsed impinging diesel spray and in a steady hollow-cone spray. The measurements in the pulsed diesel spray show a change in size with time, with the largest droplets at the beginning of the spray. Measurements of droplet size and number density in the hollow-cone spray show changes in both droplet size and number density with time. A method of quantifying measurement error of average droplet size under conditions of low number density was demonstrated.

INTRODUCTION

Knowledge of the droplet size in sprays is important for spray combustion, pesticide and herbicide spraying, spray cooling, fire sprinklers and many other industrial applications. Time-based measurements of droplet size and number density are important for pulsed sprays. Not as obvious is the need for time-based measurements in "steady" sprays. High speed movies of the atomization process have shown that "steady" sprays are not uniform in time but can have clusters of droplets. This droplet clustering may have significant ramifications in combustion applications for soot production. A rapid change in spray angle, called fluttering, has been observed in airblast atomizers [1]. Quantitative measurements of droplet size and number density with time are difficult to obtain with commercially available instruments.

Techniques commonly used to determine droplet size in sprays include laser diffraction [2], phase/Doppler interferometry [3] and light-intensity deconvolution [4]. The laser diffraction particle sizer is a line-of-sight measurement with a maximum sampling rate of 45 Hz. The phase/Doppler interferometer and light intensity deconvolution instrument are single particle counters in which individual droplets are detected as they pass through the measurement volume. The phase/Doppler interferometer has a maximum sampling rate of 125,000 particles/s. The intensity deconvolution technique does not provide temporal measurements due to mechanical switching of the measurement beam that is necessary to measure the full range of droplet sizes.

One ensemble technique, which is based on measurement of the polarization ratio, has been used successfully to measure droplet size in sprays [5]. Its advantages include insensitivity to beam steering, excellent spatial resolution, rapid response time, and insensitivity to multiple scattering [6]. Its disadvantages include a dependence on the index of refraction and the need to assume a form for the size distribution. During the past several years, various approaches have been used to measure the polarization ratio. Details of these optical configurations are described elsewhere [5, 7, 8, 9].

EXPERIMENTAL SETUP

Two different configurations of the droplet sizing instrument were used in these experiments. The first arrangement consists of a randomly polarized helium-neon laser light source and two photomultiplier tubes mounted on an optical bench. Light from the laser passes through the spray and the ratio of horizontally to

vertically polarized light scattered at 105° from the forward direction is collected to determine the Sauter mean diameter of the spray. The scattered light is collimated with a lens and then passes through a focusing lens, a circular aperture (which reduces the measurement volume to approximately 1 mm^3), a narrow band pass filter and a 50/50 beam splitter cube, which produces two beams. Each beam passes through a linear polarizing filter and onto a photomultiplier tube. The polarizing filters are oriented normal to each other to provide a vertical and a horizontal component of the scattered light. The output current of each photomultiplier tube is amplified, and then measured with a microcomputer-based digital oscilloscope peripheral. The data acquisition system has four 8-bit analog-to-digital converters that allow simultaneous sampling of all channels at a rate of 500 kHz.

The pulsed spray was generated by an experimental diesel atomizer [10] impinging on a flat plate. The measurements were performed at ambient pressure and temperature. More details of the experimental setup are available in reference [11].

For measurements in the hollow-cone spray, an argon-ion laser was used as the light source. A schematic of the setup is shown in Fig. 1. Since the output of the laser is polarized, a different optical arrangement was used. The blue (488 nm) beam was used for the measurement. A polarization rotator was used to rotate the polarization of the laser beam through 45°. The beam was directed through the spray and the scattered light was collected with a lens and directed to a 50/50 beam splitter. Half of the light went through a narrow band pass filter, a horizontal polarization filter and then onto a photomultiplier tube, while the other half of the light went through a narrow band pass filter, a vertical polarization filter and then onto the other photomultiplier tube. The use of a 45° linearly polarized, or a circularly polarized laser beam is better than the use of a randomly polarized laser because of the possiblity of "polarization slipping" with a randomly polarized laser. The data acquisition system was upgraded to a 1 MHz, 12-bit system because of the wider dynamic range encountered in the steady spray.

The steady spray measurements were performed on a kerosene spray generated by a hollow-cone pressure-swirl atomizer of nominally 60° spray angle. The measurements reported in this paper were at a location 3 cm downstream and 1.5 cm off the spray centerline. This position is on the outside edge of the spray cone.

LIGHT SCATTERING CALCULATIONS

Since the form of the droplet size distribution is assumed, Mie scattering calculations can be performed to determine the polarization ratio as a function of the Sauter mean diameter (SMD). The Sauter mean diameter is commonly chosen to characterize atomization quality for many applications, and is defined as:

$$SMD = \frac{\int_0^\infty P(D) D^3 \, dD}{\int_0^\infty P(D) D^2 \, dD}, \tag{1}$$

where D is the droplet diameter and $P(D)$ is the probability distribution function. A log-normal size distribution was chosen because it is often used to represent droplet distributions in sprays. To characterize a collection of particles with a log-normal size distribution requires two parameters, the geometric mean diameter D_g, and the geometric mean standard deviation, σ_g. For all calculations σ_g was set equal to 0.3. The probability distribution function for a log-normal size distribution is expressed as:

$$P(D) = \frac{1}{\sqrt{2\pi}\sigma_g D} \exp\left[-\frac{(\ln(D/D_g))^2}{2\sigma_g^2}\right]. \tag{2}$$

The polarization ratio is defined as:

$$\gamma = \frac{Q_{hh}}{Q_{vv}}. \tag{3}$$

where Q_{vv} and Q_{hh} are two elements in the Mueller matrix. The relationship between the Mueller matrix and the Stokes parameters , $[I_v, I_h, U, V]$, is given by:

$$\begin{bmatrix} I_v \\ I_h \\ U \\ V \end{bmatrix} = \frac{1}{k^2 r^2} \begin{bmatrix} Q_{vv} & Q_{vh} & 0 & 0 \\ Q_{hv} & Q_{hh} & 0 & 0 \\ 0 & 0 & \frac{1}{2}(S_1 S_2^* + S_2 S_1^*) & -\frac{i}{2}(S_2 S_1^* - S_1 S_2^*) \\ 0 & 0 & \frac{i}{2}(S_2 S_1^* + S_1 S_2^*) & -\frac{1}{2}(S_1 S_2^* - S_2 S_1^*) \end{bmatrix} \begin{bmatrix} I_{v0} \\ I_{h0} \\ U_0 \\ V_0 \end{bmatrix}, \tag{4}$$

where $k = 2\pi/\lambda$ and r is the distance from the scattering volume. I_v is the intensity of the vertically polarized light, similarly I_h is the intensity of the horizontally polarized light. The 0 subscript on the Stokes parameters indicates incident light. S_1 and S_2, the scattering amplitudes, can be calculated using Mie scattering theory. S_1^* and S_2^* are the complex conjugates of the scattering amplitudes. The elements of the Mueller scattering matrix that are used for droplet sizing are:

$$Q_{vv} = S_1^2 \tag{5}$$

and

$$Q_{hh} = S_2^2. \tag{6}$$

Figure 2 shows the relationship between polarization ratio and Sauter mean diameter for a scattering angle of 105°, an index of refraction of 1.45 (dodecane), and a laser wavelength of 632.8 nm. Figure 2 shows the high degree of sensitivity of the polarization ratio for particle sizes less than 15 μm; for droplet sizes larger than 40 μm, there is little sensitivity.

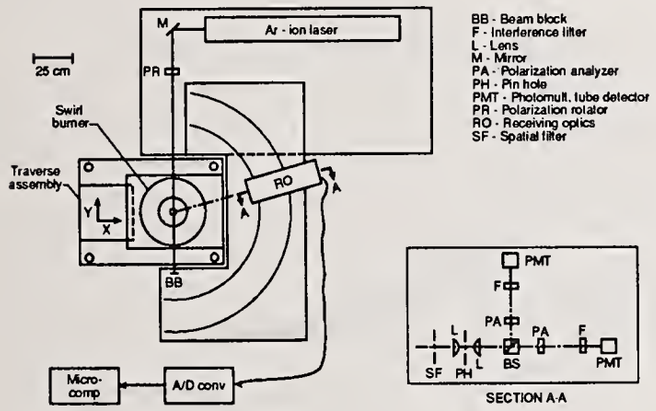

Figure 1: Schematic of the polarization ratio particle sizer used for measurements of the hollow-cone spray.

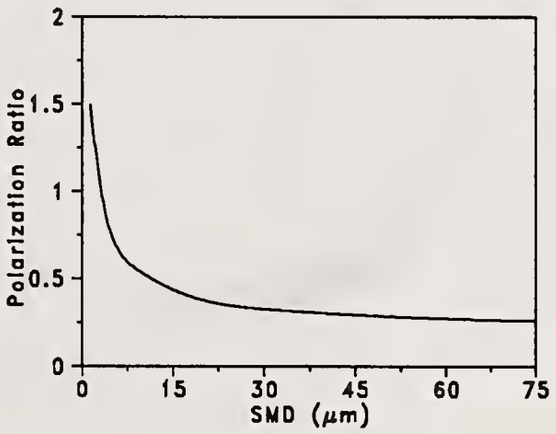

Figure 2: Calculated value of polarization ratio versus Sauter mean diameter for 105° scattering angle, an index of refraction of 1.45, and a wavelength of 632.8 nm.

Q_{vh} and Q_{hv} are zero for single scattering from an ensemble of spherical particles. The combination of the four Stokes parameters, I_v, I_h, U, V, and the Mueller matrix are useful for describing light scattering from any object. If the Mueller matrix of an object is known, then calculating the interaction of a known light source, $[I_{v0}, I_{h0}, U_0, V_0]$, with the object is a simple matter of matrix multiplication. An unpolarized light source of unit intensity has Stokes parameters of [1,1,0,0]. Use of an unpolarized incident light source allows the immediate determination of two elements of the Mueller matrix, Q_{vv} and Q_{hh} since I_v and I_h are measured. A vertically linearly polarized light source of unit intensity has Stokes parameters of [1,0,0,0]. Use of a vertically linearly polarized light source allows one to verify that one of the cross components of the Mueller matrix (Q_{hv}) is zero. Similarly, using a horizontally linearly polarized light source allows one to verify that Q_{vh} is zero.

Once the droplet size has been determined, the droplet number density can be obtained using Eq. 7.

$$N = \frac{Q_{vv}}{(\frac{\lambda}{2\pi})^2 I_v} \tag{7}$$

When taking measurements at high data acquisition rates, it is necessary to verify that sufficient numbers of droplets are in the measurement volume to ensure a representative sample. As the number of particles in the measurement volume decreases, the accuracy with which the average droplet diameter can be determined decreases. With the assumption that the droplets in the spray have a log-normal size distribution, varying size groups of droplets were generated using a random number generator. The uniform random number generator was transformed to a log-normal deviate, so that given an infinite number of random numbers, a perfect log-normal distribution would result. The Sauter mean diameter and polarization ratio were calculated directly by summing the contribution from each individual droplet in the group of droplets. As the number of droplets in each group increased, the variation in the calculated polarization ratio decreased. Figure 3 shows calculations for 200 droplets per group. Figure 4 shows calculations for 1000 droplets per group.

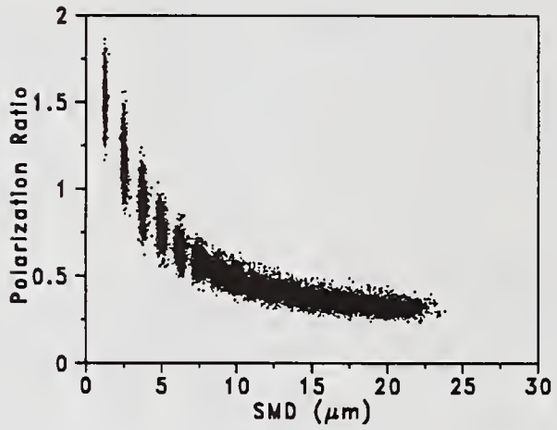

Figure 3: Polarization ratio versus Sauter mean diameter calculated using 200 droplets per group

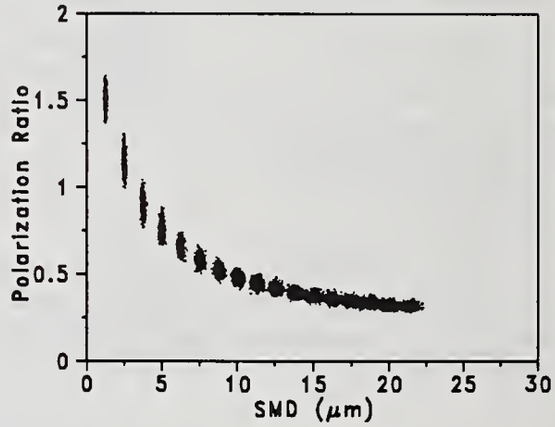

Figure 4: Polarization ratio versus Sauter mean diameter calculated using 1000 droplets per group

The standard deviation of polarization ratio for number of droplets and Sauter mean diameter was computed using the randomly generated log-normal distribution. This allows one to generate error bars on the Sauter mean diameter for a given polarization ratio and number of droplets in the measurement volume. Figure 5 shows the error bars for one standard deviation for a measurement volume that contains 1000 droplets. As expected, the measurement error for Sauter mean diameter increases as the polarization ratio decreases. Figure 6 shows the error bars for one standard deviation for a measurement volume that contains 200 droplets. The measurement error increases with decreasing number of droplets in the measurement volume. The standard deviation of polarization ratio, S, can be determined from:

$$S = \frac{367.78}{((n + 237.206) * (SMD + 5.3))}, \tag{8}$$

where n is the number of droplets in the measurement volume and SMD [μm] the Sauter mean diameter. Equation 8 is only valid for a laser wavelength of 488 nm, index of refraction of 1.45, and a scattering angle of 105°. The computations would have to be repeated for any change in the above variables.

EXPERIMENTAL RESULTS

Before accurate measurements of number density can be made, the polarization ratio droplet sizing instrument must first be calibrated. Other researchers have used scattering from propane as an absolute standard. The time-based polarization ratio measurements were not sensitive enough to detect scattering from propane so another calibration technique was needed. Latex spheres of known size suspended in distilled water provided that standard. The previous, more sensitive system [12] was used to measure the number density of latex spheres and then the latex spheres were used as a secondary calibration standard for calibrating the time-based polarization ratio measurements.

The polarization ratio particle sizer was used to make measurements of droplet size for the portion of a pulsed diesel spray that impacted on a plate. The impaction plate was wiped clean of any liquid between runs. Data was taken at a radial distance of 2.5 cm from the spray impaction centerline and a height of 7 mm above the plate. This distance is sufficiently far from the impaction zone so that the spray is moving radially outward parallel to the plate. The linear depolarization ratios were measured to verify that spherical droplets were present in the measurement location. For measurements of linear depolarization ratio, the laser light was made alternately vertically or horizontally polarized by placing a linear polarization filter in front of the laser. Measurements of both vertical and horizontal linear depolarization ratio were made at the measurement location. The vertical and horizontal linear depolarization ratios remained below 0.2 for most of the measurement time indicating that significant depolarization is not present. Figure 7 shows the Sauter mean diameter as a function of time.

The Sauter mean diameter does not remain constant with time at this position. The initial Sauter mean diameter is larger than at later times. This transient in droplet size lasts for about 0.1 ms and is attributed to the increased momentum-to-drag ratio of the larger droplets. A range of droplet sizes is produced by the impaction of the spray on the plate. Since the larger droplets have a higher momentum to drag ratio, the effect of aerodynamic drag is less pronounced and these droplets arrive first at the measurement location.

Figure 8 shows the Sauter mean diameter and number density of the hollow-cone spray as a function of time. Evidence of droplet clustering can be seen by noting the large change of number density with time. Figure 9 shows a portion of Fig. 8 with the error bars for one standard deviation of polarization ratio added. As expected, for times with high number density and small droplet size, the error bars are small and for low number density and large droplet size the error bars are larger. This illustrates a trade off between large measurement volume and high accuracy, and small measurement volume and low accuracy inherent in time-based ensemble techniques.

The evenly spaced measurements in time that this technique generates are amenable to statistical analysis. Figures 10 and 11 show autocorrelations and cross-correlations calculated from measurements in the hollow-cone spray. The autocorrelation plot can be used to look for specific frequencies in the spray. The cross-correlation plot shows that for this location in the spray there is an inverse relationship between the measured Sauter mean diameter and the measured droplet number density. It is also possible to produce power spectral density plots from the measurements. This type of information would give valuable data about the basic atomization process and useful practical information for spray nozzle designers. It is however, difficult at this time to use these preliminary results to provide quantitative information on spray structure.

CONCLUSIONS

Modifications to the polarization ratio particle sizing technique allow nearly instantaneous measurements of Sauter mean diameter and number density. Measurements were performed in a pulsed spray and in a steady hollow-cone spray. The measurements in the pulsed spray show the expected result of the larger droplets at the spray tip, followed by smaller droplets. Measurements in the steady hollow-cone spray show that there are changes in both average droplet size and number density with time. At the one measurement location there was an inverse relationship between measured Sauter mean diameter and measured droplet number density. Quantification of measurement error of average droplet size under conditions of low number density was demonstrated.

ACKNOWLEDGEMENTS

One of the authors (JRZ) would like to acknowledge the support of the Postdoctoral program at NIST, which is administered by the National Research Council.

REFERENCES

[1] Mao, C.-P., "Fluttering in Airblast Atomizer Sprays", *ILASS-Americas, Proceedings of the 2nd Annual Conference* (1988).

[2] Swithenbank, J., Beér, J.M., Taylor, D., Abbott, D., and McCreath, G., "A Laser Diagnostic Technique for the Measurement of Droplet and Particle Size Distribution", in *Experimental Diagnostics in Gas Phase Combustion Systems*, (B. Zinn, Ed.), Progress in Astronautics and Aeronautics, Vol. 53, pp. 421–447, AIAA, New York, NY (1977).

[3] Bachalo, W.D. and Houser, M.J., "Phase/Doppler Spray Analyzer for Simultaneous Measurements of Drop Size and Velocity Distributions", *Optical Engineering*, Vol. 23, No. 5, pp. 583–590, September/October (1984).

[4] Holve, D.J. and Annen, K., "Optical Particle Counting and Sizing Using Intensity Deconvolution", *Optical Engineering*, Vol. 5, No. 23, pp. 591–603, September/October (1984).

[5] Beretta, F., Cavaliere, A., and D'Alessio, A., "Drop Size and Concentration in a Spray by Sideward Laser Light Scattering Measurements", *Comb. Sci. and Tech.*, Vol. 36, pp. 19–37 (1984).

[6] Beretta, F., Cavaliere, A., and D'Alessio, A., "Experimental and Theoretical Analysis of the Angular Pattern Distribution and Polarization State of the Light Scattered by Isothermal Sprays and Oil Flames", *Combustion and Flame*, Vol. 49, pp. 183–195 (1983).

[7] Beretta, F., Cavaliere, A., and D'Alessio, A., "Ensemble Laser Light Scattering Diagnostics for the Study of Fuel Sprays in Isothermal and Burning Conditions", *Twentieth Symposium (International) on Combustion*, pp. 1249–1258. The Combustion Institute (1984).

[8] Presser, C., Gupta, A.K., Santoro, R.J., and Semerjian, H.G., "Droplet Size Measurements in a Swirling Kerosene Spray Flame by Laser Light Scattering", *ICLASS-85*, pp. VIIC/2/1–13 (1985).

[9] Hodges, J.T., Baritaud, T.A., and Heinze, T.A., "Planar Liquid and Gas Fuel and Droplet Size Visualisation in a DI Diesel Engine", SAE 910726 (1991).

[10] Sinnamon, J.F., Lancaster, D.R., and Steiner, J.C., "An Experimental and Analytical Study of Engine Fuel Spray Trajectories", SAE 800135 (1980).

[11] Zurlo, J.R. and Chigier, N., "Impinging Diesel Spray Dynamics", *Atomization and Sprays*, Vol. 1, No. 3, pp. 303–318 (1991).

[12] Presser, C., Gupta, A.K., Semerjian, H.G., and Santoro, R.J., "Application of Laser Diagnostic Techniques for the Examination of Liquid Fuel Spray Structure", *Chem. Eng. Comm.*, Vol. 90, pp. 75–102 (1990).

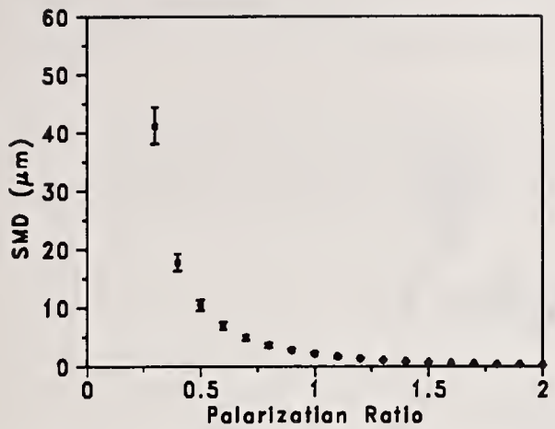

Figure 5: Error bar plot for 1000 droplets in the measurement volume.

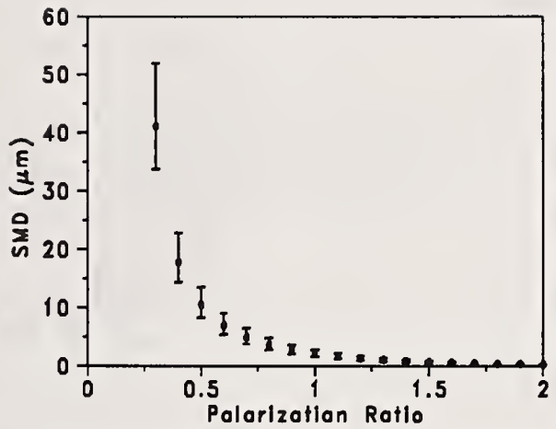

Figure 6: Error bar plot for 200 droplets in the measurement volume.

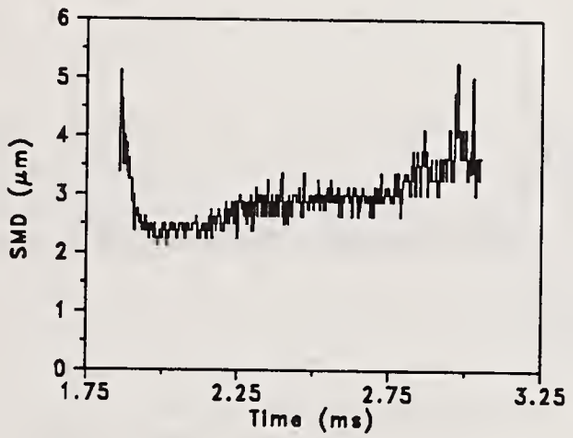

Figure 7: SMD as a function of time. Data taken at a radial distance 2.5 cm from the diesel spray centerline and a height of 7 mm above the plate.

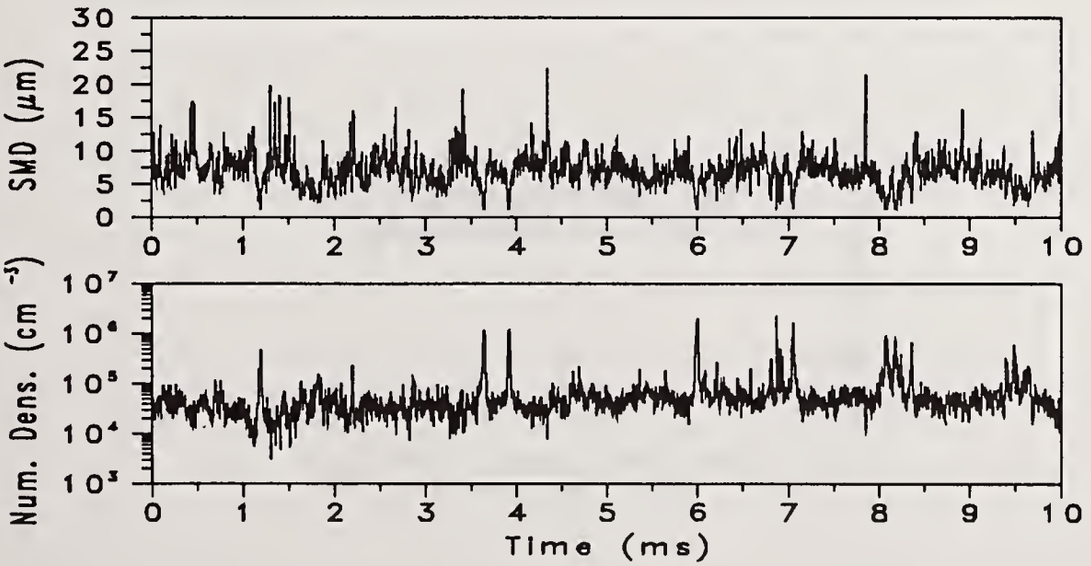

Figure 8: Sauter mean diameter and number density as a function of time for the hollow-cone spray.

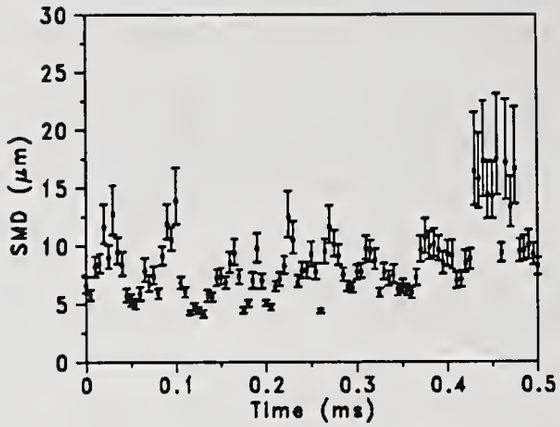

Figure 9: Sauter mean diameter and number density as a function of time for the hollow-cone spray. Error bars for one standard deviation of polarization ratio are shown.

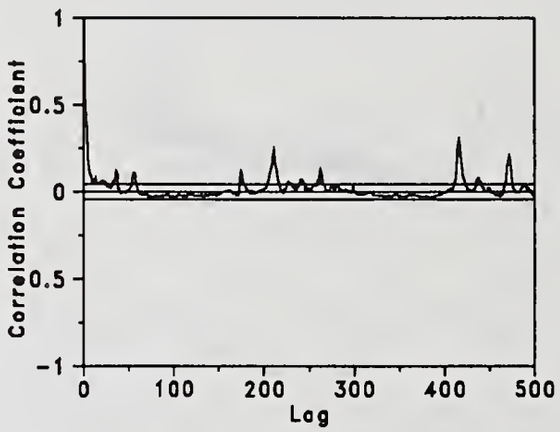

Figure 10: Autocorrelation of number density for the hollow-cone spray.

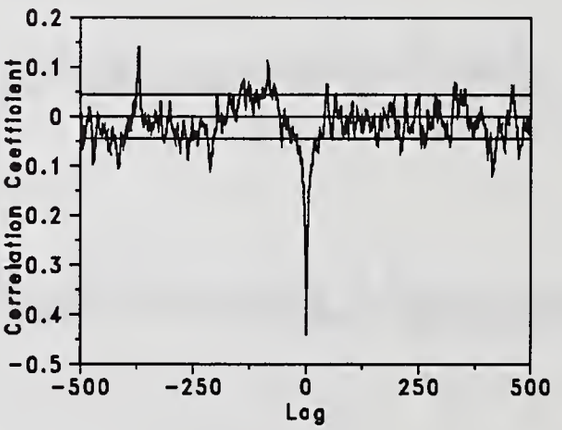

Figure 11: Cross-correlation of SMD and number density for the hollow-cone spray.

GENERATION OF SPHERICAL AND MONODISPERSE POLYMER PARTICLES BY ATOMIZATION OF MONOMERS OR DISSOLVED POLYMER PRECURSORS

T. Panagiotou and Y.A. Levendis

Department of Mechanical Engineering
Northeastern University
Boston, MA, U.S.A.

ABSTRACT

A technique to produce spherical and monodisperse particles of selected plastics is presented. Liquid precursors of either mixtures of organic monomers and initiator catalysts, or polymers dissolved in organic solvents were sprayed inside a vertical thermal reactor. The temperature range in the reactor was 400-670 K and the experiments were conducted in a nitrogen atmosphere. Atomization was achieved by an acoustically excited aerosol generator. Batches of equal size particles of two thermoplastic materials, poly(styrene) and poly(methyl methacrylate), were obtained in the range of 30-60 μm in diameter. The thermal environment, the atomization conditions, and the residence times the particles experienced in the reactor were explored using numerical techniques; residence times in the order of 10 s were estimated.

INTRODUCTION

Production of small, homogeneous polymer particles of controlled size are of technological interest to the plastics, catalyst and others industries[1]. Moreover, if the particles are produced spherical and monodispersed, they can find further applications in fundamental studies of material properties, calibration of instruments etc. Commonly, monodispersed particles have been produced from polymer colloids by emulsion or suspension polymerization. Everett and co-workers[2,3] have discussed the preparation of near spherical, 100 μm, poly(vinyl chloride) (PVC), poly(vinylidene chloride) (PVDC) and submicron poly(acrylonitrile) powders from dispersion polymerization. A similar technique was followed by Pendleton *et al.*[4] to produce submicron (0.1 μm) PVDC particles. Howard and Knutton[5] prepared large spherical carbon particles ($\approx$500 μm) from the thermal degradation of cross-linked polymeric beads, made from the suspension polymerization of mixtures of PVDC and ethylene dimethylacrylate. These materials yielded porous beads upon carbonization.

Bhanti *et al.*[6] generated poly(styrene) particles by nebulizing a polymer solution in xylene and evaporating the solvent. Subsequent size-classification and second stage atomization after resuspending the colloids in water was necessary to produce a monosized aerosol. Matijević and co-workers[7] produced fairly uniform, micron size poly(urea) particles by reacting liquid aerosol droplets of toluene diisocyanate with ethylenediamine vapor. The same aerosol technique was used for polymerization of styrene monomer droplets in vapors of the initiator trifluoromethanesulfonic

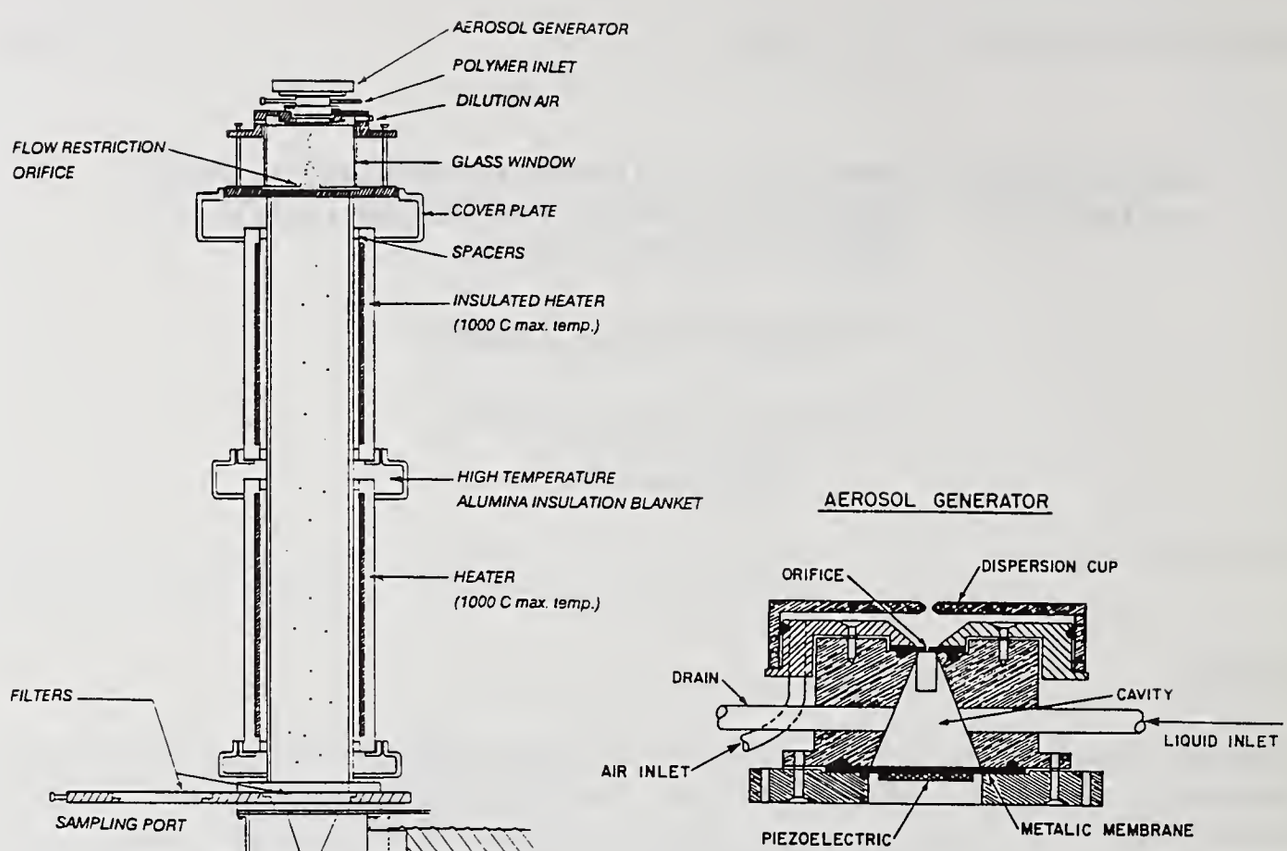

Figure 1: *Schematic of the acoustically excited aerosol generator and the two stage thermal reactor used for the production of spherical polymer particles.*

acid (TFSA)[8]. The above investigators also produced (8μm) poly(divinylbenzene) particles using the same aerosol technique[9]. These particles shrunk to porous 3-5 μm spheroid residues upon carbonization at 500°C[10].

An alternative technique was used by Levendis and Flagan[11,12] to produce monodisperse solid carbon particles (5-200 μm) to be used in combustion studies. The method utilized an aerosol generator to atomize various mixtures of poly(furfuryl alcohol) and pore-forming agents dissolved in acetone. The mixtures were sprayed inside a thermal reactor where secondary polymerization (curing) took place. The work described herein pertains to the production of poly(styrene) and poly(methyl methacrylate) particles using the above technique to either atomize solutions of these two polymers in solvents, or atomize and polymerize their liquid monomer precursors. In both cases solid polymer particles were formed in the thermal reactor. In the latter case the polymerization was conducted and completed inside the reactor. In this manner the rate of polymerization of the two thermoplastics was expedited and plastic powders were produced in a matter of seconds.

EXPERIMENTAL APPARATUS AND PROCEDURE

(A) Aerosol Generator. In order to produce spherical and monodisperse drops from a polymeric fluid an aerosol generator was constructed based on the design of Levendis and Flagan[12], shown in Fig. 1.

In this instrument a continuous flow of liquid is forced through a small orifice. Concurrently the liquid in the generator's cavity is oscillated at a high frequency using a piezoelectric transducer. The vibration creates an instability which leads to the break-up of the liquid jet into uniformly sized droplets. The size of the droplets is controlled by the size of the orifice, the oscillator frequency and the liquid feed rate. Consequently, the size of the dried particle depends on all of the above parameters in addition to the degree of dilution of the polymer (mass fraction of solvent). In the present experiments in order to produce particles of sizes in the range of 30 - 60 μm, monomers or polymers under various degrees of dilution were used in conjunction with 75 μm orifices, frequencies of 16 -18 kHz, and a flowrate of 1.6 cc/min. The piezoelectric elements used were silver electrode bimorphs (*Vernitron PZT5H* and *Piezo Kinetics PZT-550*) 1.25 cm in diameter, 0.62 mm thick. They were glued with a conductive silver epoxy (*Tra-Con*) on thin stainless steel metallic membranes 25-75 μm (thickness). These transducers were driven by a function generator at 20 V amplitude.

The pinholes were laser drilled for precision (*Melles Griot*). A high pressure syringe pump (*Harvard Apparatus 909*) was used to feed liquid polymers to the generator via (*Becton Dickinson*) plastic syringes.

(B) Thermal Reactor. A thermal reactor was constructed for the drying and curing of the aerosol droplets that were generated at the top of the reactor, where the aerosol generator was mounted, Fig. 1. This stainless steel flow reactor is 1.5 m high, 0.1 m i.d. and is externally heated in two stages by cylindrical (*Thermocraft*) heating elements. They are controlled by separate (*Omega*) temperature controllers and they supply 3800 W at the top and 3000 W at the bottom sections which provides wall temperatures up to 1000 K. The aerosol generator is placed at the top of the reactor on a special flange that incorporates provisions for introduction of dilution gas (nitrogen). This gas passes through a flow straightener and flows downwards engulfing the stream of droplets. A secondary stream of gas flows through a small orifice concentric with the aerosol jet, Fig. 1, to disperse the droplets and prevent coagulation.

A quartz observation window is mounted on the top to facilitate monitoring of the operation and uniformity of the jet. To check for monodispersivity of the droplets provisions for a small gas jet to impinge perpendicularly to the droplet stream have been made. In this manner droplets of equal size deflect at the same angle meanwhile polydisperse droplets deflect at a multitude of angles (satellites). Monodispersion can be accomplished by adjusting the flowrate and finely tuning the frequency. Theoretically, the frequency range for monodispersivity is $\frac{1}{7D_j} < f < \frac{1}{3.5D_j}$, where D_j is the orifice diameter[13]. Directly below the observation window an orifice plate has been inserted to improve the flow conditions, as discussed in a following section. At the bottom of the reactor an virtual impactor stage has been constructed to aid in the collection of dry particles and eliminate small micron-size particles formed by various mechanisms such as condensation of vapors. A sampling filter stage has also been incorporated.

Production of Polymers.

In order to produce the polymers required for this study two different techniques were employed: (i) aerosol production of dissolved polymers with subsequent evaporation of the solvent in the reactor, and (ii) aerosol production of partially polymerized precursors in a solvent with subsequent evaporation of the solvent and sequential completion of polymerization in the reactor. Both techniques can also be applicable to any other polymers that can be completely dissolved in solvents or to monomers whose polymerization can be achieved in bulk and can be readily controlled.

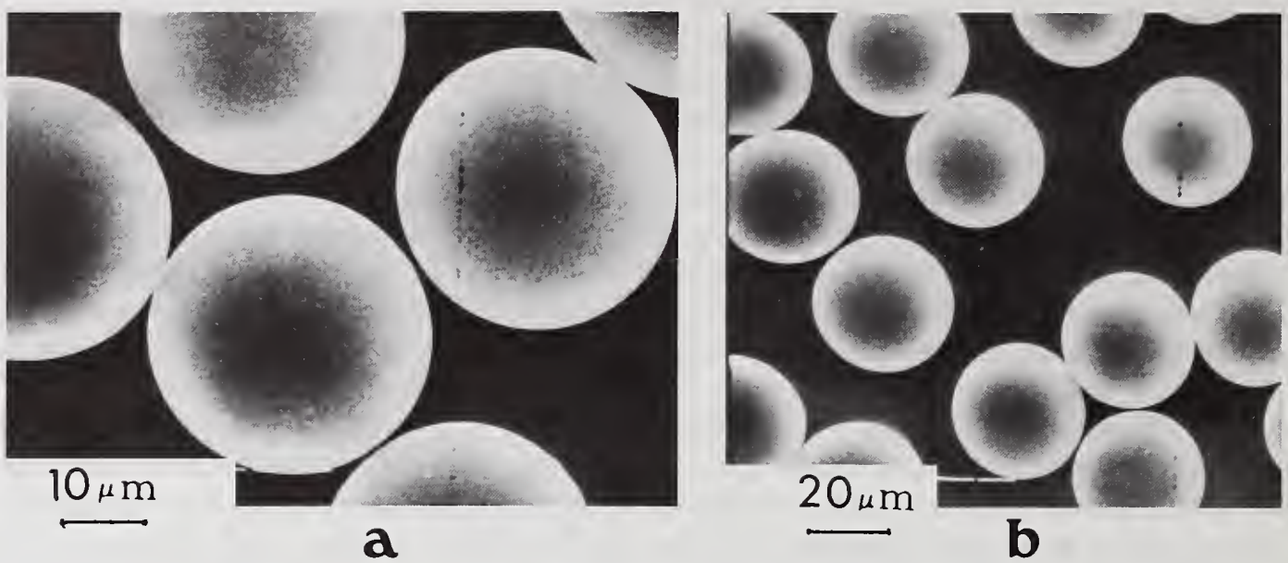

Figure 2: *SEM micrographs of polystyrene particles, (a) ×1000 and (b) ×500.*

(A) Poly(styrene). Polystyrene particles were produced with both of the above techniques:
1. An aerosol of commercially available polystyrene (*Styron 685-D, Dow Chemical*) dissolved in toluene was generated. Solutions of 1 part of polystyrene in 40 parts of toluene were used in conjunction with a 75μm orifice, a flowrate of 1.6 cc/min and an excitation frequency of 17 kHz. The gas (nitrogen) flowrates in the reactor were $\approx$ 1 lpm dispersion and 2.5 lpm dilution. The maximum wall temperature at the upper section of the thermal reactor was 300 °C and that of the lower section was 400 °C. Collected particles were smooth spheres having a diameter of $\approx$ 33μm as deduced by optical and SEM microscopy, Fig. 2 a and b. Any larger particles formed by fusion of two or three particles while still liquid (doublets, shown in the left side of Fig. 2 b, or tripplets) were separated out by subsequent sieving. Dissolution of styrene beads in toluene required a few hours at room temperature and sonication prior to atomization was necessary to achieve uniform mixing. Insufficient mixing resulted in bubble formation. Furthermore, solutions thicker than 30:1 were too viscous to handle properly and produce monodisperce particles. Extensive testing for monodispersivity of the droplets was done at the onset of each experiment using the test jet, described before. Optimum conditions for the reactor temperature and flow characteristics were determined by a combination of numerical modelling and experimental trials, with the following criteria in mind:

(i) To achieve vaporization of the solvent slowly enough to avoid formation of bubbles.

(ii) To ensure that the residual polymer phase remains in the molten state to enable formation of spherical particles.

(iii) To enable solidification of the particles, in the cooler bottom section of the reactor, before they reach the collection stage.

Overheating should be avoided since it might alter the chemical composition by pyrolyzing the polymer.
2. Production of polystyrene particles of $\approx$60 μm was achieved by generating an aerosol of partially polymerized styrene monomer. The monomer was mixed with benzoyl peroxide (2% by weight) and was heated at 83-84°C, in a nitrogen atmosphere, for 30 minutes. Subsequently, the semi-polymerized precursor was dissolved in toluene at a ratio of 1:1 and passed through the thermal reactor in nitrogen atmosphere. Production was conducted at the same conditions as before with the exception of temperature, which was optimized for the current situation. The temperature

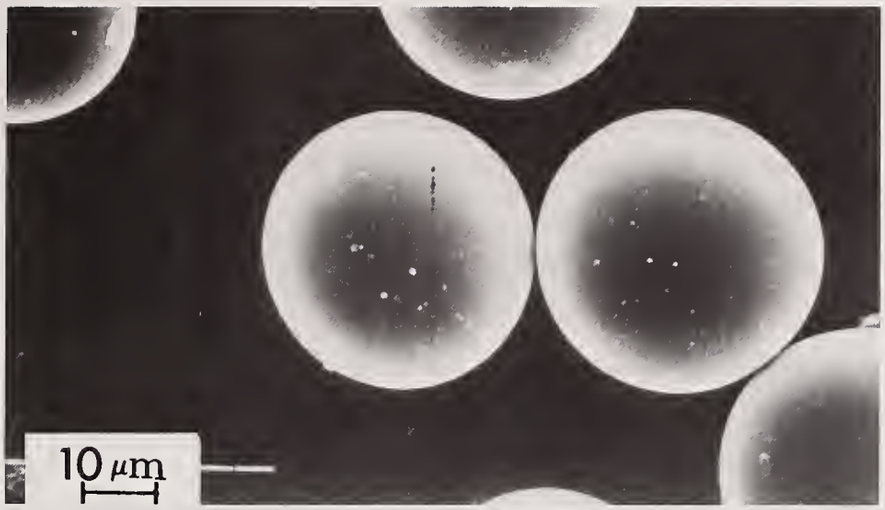

Figure 3: *SEM micrograph of poly-methyl-methacrylate particles produced in the lab from the monomer precursor (×800).*

profile in the reactor was controlled to prevent flash-vaporization of the monomer. Thus, the top section of the reactor was set at a low temperature (240°C) to provide slow initial heat-up, and the bottom section was hot enough (300°C) for the polymerization reactions to proceed to completion.

(B) Poly(methyl methacrylate). Batches of Poly(methyl methacrylate) particles of 30-60μm in diameter were produced by the above two techniques at similar conditions.

1. Solutions of 2% poly(methyl methacrylate) in acetone were atomized by the aerosol generator in conditions similar to the ones used for the poly(styrene) particles.
2. Methyl-methacrylate was pre-polymerized in bulk using benzoyl peroxide (2% by weight) as initiator. The polymerization was carried out at 75° C for 15 min resulting in a partially reacted, medium viscosity liquid. This was then dissolved in acetone at a ratio of 2:1 (acetone to polymer) and conducted to the aerosol generator. The polymerization was then completed in the thermal reactor, with wall temperatures of 260 °C and 290 °C at the top and bottom sections, respectively. Solid particles, 45μm in diameter, were collected, shown Fig. 3.

NUMERICAL SIMULATION OF THE PARTICLE HEAT TREATMENT

To model the velocity and temperature environment in the thermal reactor the "FLUENT" software package, (*Creare*, 1989) was utilized. Numerical solutions for the gas phase were obtained by simultaneously solving the continuity, momentum and energy equations. The program was used to study the effects of the reactor geometry, gas flow rates and wall temperature on the velocity and temperature profiles. Furthermore, an additional feature of this program dealt with the behavior of liquid drops introduced in the gaseous environment. Thence, the trajectory of the drops, the time required for solvent vaporization, the residence time of the solid particle, and the particle heat-up characteristics were estimated. Results so obtained were used to find the optimum reactor temperatures for droplets of the polymer-solvent mixtures investigated herein. Various droplet sizes were modelled in the range of 30-144 μm in diameter.

A brief description of the calculation with FLUENT is given in the following: A finite difference grid is set up which divides the domain of the problem into a number of computational cells. Boundary conditions are specified at the inlet and walls of the domain. The equations of continuity, momentum and energy for the gas phase are reduced to a set of simultaneous algebraic equations and an iterative scheme is

used to find the solution of the system. When the solution of the gaseous phase converges sufficiently, the introduction of droplets takes place and the mass, heat and momentun transfer between the gaseous phase and the droplets are calculated. The iterations continue until the solution converges.
Input to the model were the following:

- The geometry and the dimensions of the reactor. The overall length was 1.6 m and the inner diameter 0.1 m.
- The inlet velocities of the dispersion and the dilution gas streams. Their inlet flowrates were 1.0 lpm and 2.5 lpm respectively; the corresponding velocities were calculated to be 0.0055 m/s and 7.46 m/s.
- The wall temperature of the reactor, which was estimated by measurements taken by four thermocouples attached to the outer surface of the reactor at different heights. The temperature between the thermocouples was assumed to change linearly. The maximun and minimun wall temperatures were set according to the experimental conditions used for the generation of the various particles.
- The flow type, which was considered turbulent because of the vigorous mixing of the high velocity dispersion jet with the slow moving dilution gas. Turbulence was assumed despite a low Reynolds number, ($Re = 25$), calculated far away from the mixing zone (at mid-reactor height).
- The initial size of the droplets, as calculated from the formula[13]: $D_d = (\frac{6Q}{\pi f})^{1/6}$, where D_d is the initial droplet diameter, Q is the volumetric flowrate of liquid forming the aerosol and f is the imposed frequency. For the values of Q and f mentioned earlier, the initial droplet diameter was calculated to be 144 μm. The corresponding initial axial velocity of the droplets ($u = \frac{4Q}{\pi D_o^2}$, where D_o is the diameter of the orifice) was calculated to be 6.06 m/s. Furthermore, to investigate the behavior of drops at various radial positions in the reactor, initial radial velocity ranging from 0.1 m/s to 0.5 m/s were input. The droplets consisted of a volatile solvent (toluene or acetone) which evaporated and diffused into the reactor gaseous phase, and a solid content (2.5% by weight) which heated-up but did not evaporate, simulating the polymer. It should be noted here that the devolatization of the polymer was not taken into account in the present study.
- Finally, the physical constants of the gaseous (nitrogen) and the droplet (predominantly solvent) phases were input as a function of temperature. Since the model assumes average properties for the two constituents of the droplet, the solid particle diameter (after the vaporization stage) was overestimated because the density was biased towards that of the more abundant solvent. Corrections for the real polymer density had to be applied.

Results of the Numerical Modelling

The theoretically predicted thermal environment inside the reactor is shown in Fig. 4 for the case where the maximum wall temperatures were 400° C (673 K) and 300° C (573 K) for the upper and lower stages, respectively. The axial velocity profiles along the reactor are depicted in Fig. 4a.

Both the dispersion and the concentric dilution streams are shown with the former diffusing relatively fast in the slow moving dilution gas stream. The presence of the orifice plate situated downstream of the jet inlet, was found helpful in preventing boyant gases from rising, along the walls, to the very top of the reactor. The presence of these hot gases in close proximity to the

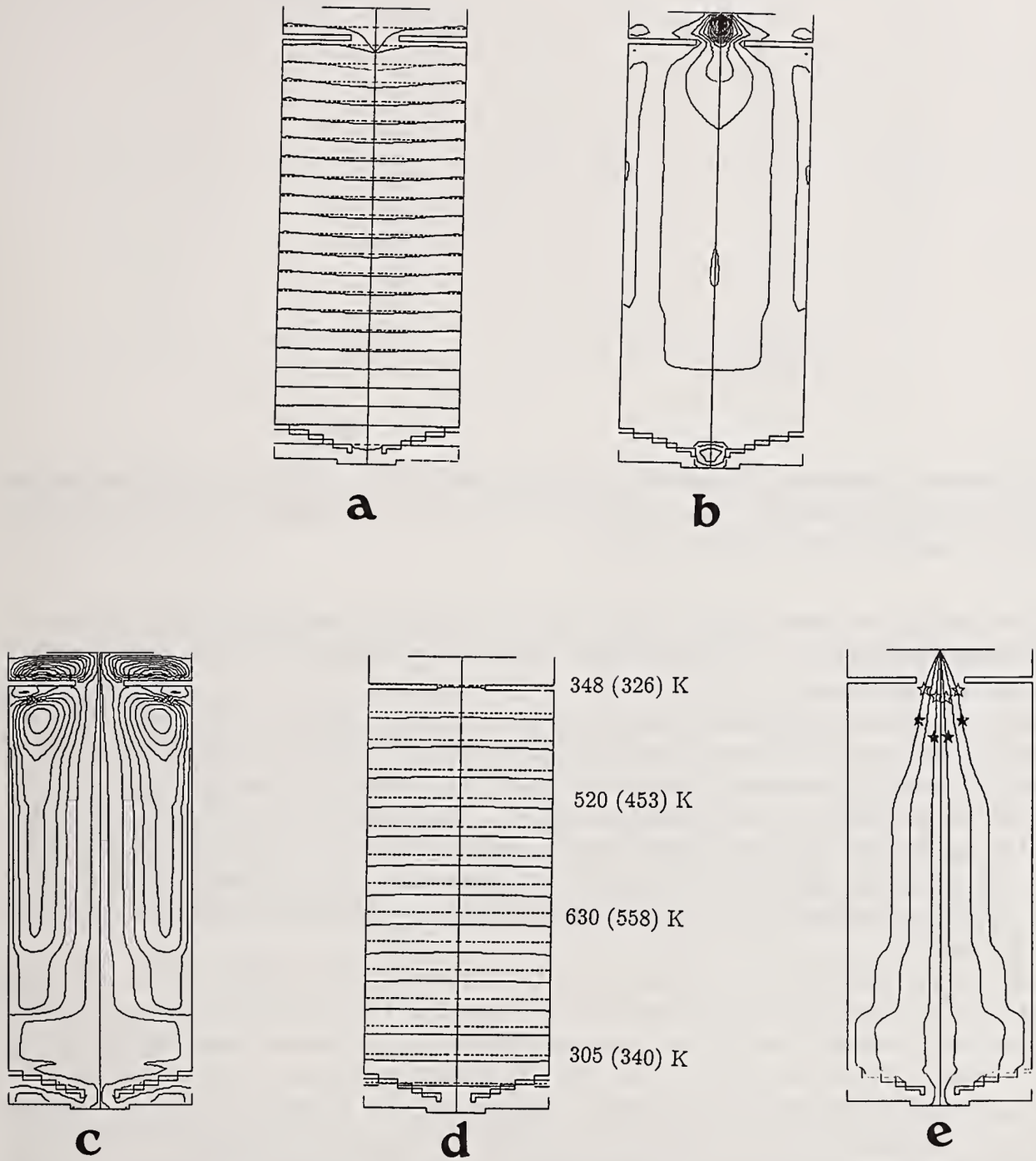

Figure 4: *Results of numerical simulation for gas flow in the thermal reactor (a) axial velocity profiles and (b) axial velocity contours (c) flow streamlines and (d) temperature profiles. Maximum wall temperatures were 400° C (673 K) and 300° C (573 K) in the upper and lower stages. Wall temperatures and centerline temperatures (in parentheses) are shown on Fig. d. (e) Results of numerical simulation for the droplet-particle phase showing tracks of equal size droplets (144 μm) having different initial radial velocities (0.1-0.5 m/s). Asterisks denote completion of solvent evaporation.*

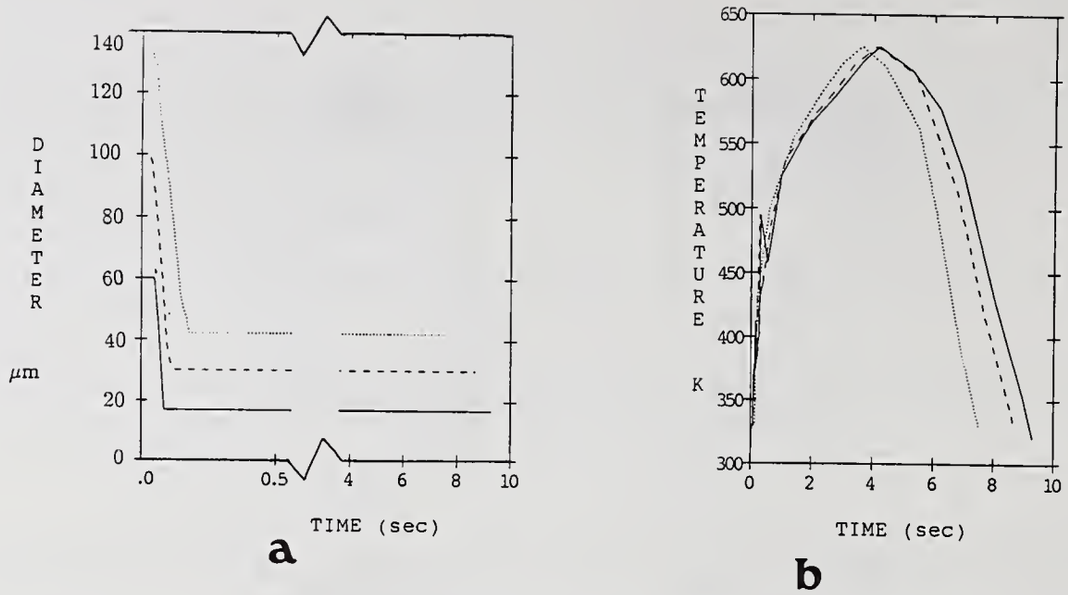

Figure 5: *Results of numerical simulation depicting (a) particle size and (b) particle temperature as a function of time for initial droplet sizes 60 (——) 100 (- - -) and 144 (.....) μm. The solvent was toluene. Conditions corresponding to Fig. 4.*

inlet of the droplets can cause rapid evaporation of the solvent and result in bubble formation, as mentioned before; moreover, as hot gases condense on the cooler surfaces of the observation window obstruct the view to the jet.

In Figs. 4b and c the contours of the axial velocities and the streamlines are shown. It can be observed that the presence of boyancy highly disturbs the flow pattern and induces circulation of gases near the walls of the reactor. Thus, in addition to the presence of the orifice plate, it was determined that application of suction at the exhaust of the reactor was necessary to control the flow field in the reactor. The temperature profiles along the reactor are shown in Fig. 4d, where it can be seen that the center-line temperature of the inlet streams is an average of 30 K below the wall. Similar temperature and velocity profiles were obtained for other experimental conditions used in this study.

Droplet trajectories are shown in Fig. 4 e. All droplets depicted in Fig. 4e had the same initial size, 144 μm, but different radial velocities (0.1-0.5 m/s). The droplets experienced an initial heat-up and evaporation period where the solvent diffused to the gaseous phase; the end of this period is marked with asterisks in Fig. 4e. Times for solvent vaporization were calculated to be $\approx$ 0.17 and $\approx$ 0.07 s (for toluene and acetone, respectively), Fig. 5a and b. It should be noted here, that according to the model used, the vaporization of most of the solvent was completed before the boiling point of toluene or acetone were reached, (383 K and 330 K) and hence, the process was diffusion controlled. Upon evaporation the particles follow the trajectories depicted in Fig. 4 a and they experience further heat-up till they reach the local gas temperature. Total residence times were calculated in the range of 7.5 to 14 seconds, depending on each particle's path. Therefore, in order to produce particles that experience the same residence time in the reactor and result in uniform properties, the particles should flow in a rather narrow stream around the reactor centerline. Furthermore, narrow streams minimize the deposition of particles on the upper surfaces of the funnel, as shown at the bottom of Fig. 4 a. Thence, even if the above arguments indicate that narrow droplet streams are desired, a certain amount of dispersion is required to avoid droplet coagulation, so a compromise must be determined experimentally. Moreover, the problem becomes more complicated since, even small instabilities of the droplet stream can initiate a rapid succession of collisions and result in a polydisperse aerosol[13].

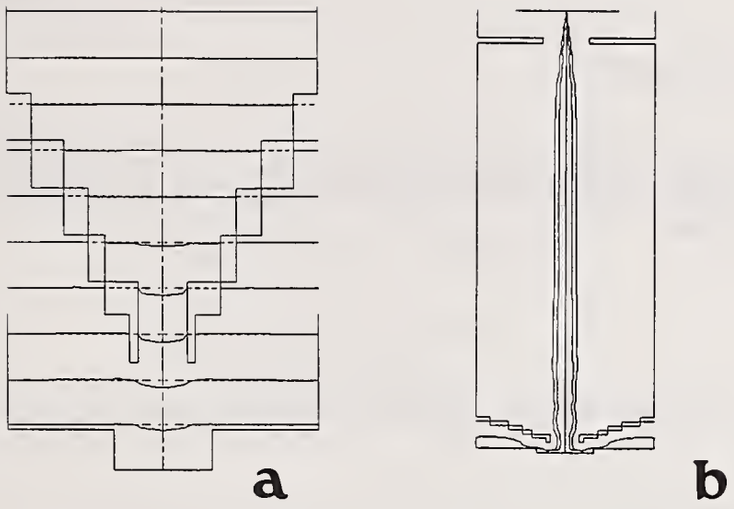

Figure 6: *Results of numerical simulation showing (a) gas velocity profiles in the virtual impactor stage of the furnace and (b) particle tracks through the reactor for two droplet (dry particle) sizes: 144 (42) and 30 (8) μm.*

To investigate the effect of size on the residence time of the particles Figs. 5a and b, are included where calculations of the variation of droplet diameter and temperature with time, respectively, are depicted for particles of diameters ranging between 60 - 144 μm, but same radial velocities. The total residence times for those particles flowing around the centerline range between 9-7 s.

Velocity profiles of the gas as it flows through the virtual impactor are shown in Fig. 6a. This particular impactor was designed to operate with a particle collection efficiency of 60% for particles having diameters bigger than 10 μm[14]. In Fig. 6b the trajectories of two particles of different sizes that flow through the reactor and pass through the impactor stage can be seen. The bigger particle, 42 μm in diameter after evaporation, is trapped in the collection stage while the smaller, 8μm, exits the reactor following the gaseous phase. Thus, any fine particles that are formed by nucleation and condensation reactions in the gas phase, escape the impactor following the exhaust stream.

SUMMARY

Spherical and monodisperse particles of poly(styrene) and poly(methyl methacrylate) in the size range of 30 to 60 μm were produced by an acoustically excited aerosol generator. The generator formed a monodisperse spray from either mixtures of polymers and their solvents, or monomers with initiator catalysts and solvents. As the spray passed through a thermal reactor in nitrogen atmosphere the solvent evaporated and solid, spherical polymer particles were formed. The above technique can be used for the production of a variety of monodisperse particles of (a) organic or inorganic solids that can dissolve and result in solutions of relatively low viscosity, or (b) polymers from their monomer precursors whose polymerization can be conducted in bulk.

The thermal treatment of the droplets was studied theoretically using numerical techniques. Results concerning the velocities and temperatures of both gas and particles, as well as the solvent evaporation and particle residence times were obtained.

ACKNOWLEDGEMENT

This research was supported by the NSF Initiation Grant #: CTS-8908652. The authors gratefully acknowledge assistance from Marina Belopolski, Jonathan Doughty in the experiments and construction of equipment.

REFERENCES

1. Sicilia, D.B. "A Most Invented Invention" Article in Invention & Technology, p.45, Spring/Summer 1990.
2. Adams, L.B., Boucher, E.A., Cooper, R.N. and Everett, D.H., "Third International Conference on Industrial Carbon and Graphite," p. 478. Soc. Chem. Ind., London, 1970.
3. Everett, D.H. and Rojas, F., Chem. Soc., Faraday Trans. 1, 84(5), 1455 (1988).
4. Pendleton, P., Vincent, B. and Hair, M.L., J. Colloid Interface Sci., 80, 512 (1981).
5. Howard, G.J. and Knutton, S., J. Appl. Polym. Sci., 19, 683 (1975).
6. Bhanti, D.P., Dua, S.K., Kotrappa, P. and Pimpal, N.S., J. Aerosol Sci., 9, 261 (1978).
7. Partch, R.E., Nakamura, K., Wolfe, K.J. and Matijević, E., J. Colloid Interface Sci., 105, 560 (1985).
8. Partch, R.E., Matijević, E., Hodgson, A. W. and Aiken, B.E., J. Polymer Sci. Polym. Chem. Ed., 21, 961 (1983).
9. Nakamura, K., Partch, R.E., and Matijević, E., J. Colloid Interface Sci., 99, 118 (1984).
10. Gangolli, S., Partch, R.E. and Matijević, J. Colloids and Surfaces, 41, 339 (1989).
11. Levendis, Y.A. and Flagan, R.C., Comb. Sci. and Tech. 53, 117 (1987).
12. Levendis, Y.A. and Flagan, R.C., Carbon, 27, 265 (1989)
13. Berglund, R.N. and Liu, B.Y.H., Environ. Sci. and Tech., 7, 147 (1973).
14. Mulholland, J.A., Yue, G.X. and Sarofim, A.F. "The Formation of Inorganic Particles During Suspension Heating of Simulated Wastes." Manuscript in Preparation (1990).
15. Biswas, P. "Impactors for Aerosol Measurements: Developments and Sampling Biases" Ph.D. Thesis, Caltech (1985).

CHARACTERISATION OF SPRAYS OF BITUMEN-IN-WATER EMULSIONS

N. Marcano and A. Williams

Department of Fuel and Energy
Leeds University
Leeds, United Kingdom

ABSTRACT

Sprays and atomisation studies of bitumen-in-water emulsion were carried out using a Delavan air assisted external mixing atomiser. A Malvern 2600 particle sizer analyser and a Dantec 58N10 phase doppler signal processor were used for measurements of the spray droplet size distribution at different air/fuel ratios. Photography were also used to study the spray break-up mechanism.

Results indicate that bitumen-in-water sprays, under the conditions covered in this study, will produce smaller droplets than predicted using correlations developed for air assisted atomisers with low viscosity liquids. Apparently the addition of bitumen particles to water produces a different spray break-up mechanism in comparison with water or medium fuel oil. This results in the formation of smaller droplets. Finally, it was demonstrated that the use of the Malvern 2600 particle sizer analyser instrument, using a Model Independent mode, was the most adequate to characterise the spray droplet size distribution for bitumen-in-water emulsions.

INTRODUCTION

The growth in energy consumption has increased the demand for substitute fuels or ways of extending existing supplies of conventional fuels. The formation of emulsions of oils with water has been considered as an alternative way of obtaining liquid fuels from bitumens [1], heavy crude oils and petroleum heavy fractions from refineries [2]. Recently a new development in the form of bitumen-in-water emulsions is being commercialised as Orimulsion [1,3]. The primary benefit of the dispersion of bitumens droplets in the water continuous medium is that the viscosity is reduced which makes easier handling and pumping and in consequence assists atomisation and combustion generally.

Although two-phase fluids, such as coal-water slurry or bitumen-in-water emulsions, have been burned successfully in industrial combustors, there is still a lack of detailed knowledge of the atomisation behaviour

particularly in the latter case. However, oil-in-water emulsions behave differently to a medium fuel oil and in some respects can parallel coal-water atomisation [4].

Efficient atomisation of the fuel is probably the most important factor in the combustion of liquid fuels. This paper reports a study of the atomisation of bitumen-in-water fuels using different techniques to provide accurate results as well as shown the strengths and limitations of each technique.

EXPERIMENTAL APPARATUS AND PROCEDURE

The liquid fuel used was a commercial bitumen-in-water emulsion (Orimulsion) supplied by INTEVEP, S.A. The mass median diameter of the bitumen particles in the emulsion was 14 μm and the other characteristics and properties are given in Refs. 1, 3 and 5.

The atomisation facility consisted mainly of a fuel tank, a gear pump and a Delavan air assisted external-mixing atomiser model SN 30610-1. Electric heating was used in the fuel tank and the line to the nozzle in order to keep the atomisation temperature between 65-68°C. Injection fuel pressures from 1.2 to 2.8 Bar and atomising air flow rates from 700 to 1400 l/hr, at ambient temperature, were used.

Droplet size measurements as a function of the air/fuel ratio were undertaken using two different techniques with different instruments: a Malvern 2600 particle sizer analyser using a 300 mm lens and Dantec 58N10 phase doppler signal processor used in a forward scatter configuration and a scattering angle of 30°. In the measurements performed with a Malvern instrument the Model Independent (MI) and Rosin-Rammler (RR) modes were used in order to compare the accuracy of fitting the data and seven hundred sweeps of the diodes were collected for each experimental measurement [6]. Additional experiments were carried out with water in order to compare them with the results obtained with the emulsion.

Direct photography using a normal camera and a strobe light and an Imacon high speed camera at a speed of 1.0×10^4 frames per second were used to study the spray break up mechanism.

RESULTS AND DISCUSSION

Choice of Droplet Size Distribution Function

Results for Orimulsion atomisation were obtained and compared with water sprays at the same atomising conditions. Each data point represents the average of 2 to 3 experiments.

In the case of bitumen-in-water emulsions there is currently no information about the best choice of drop size distribution function. Consequently both the RR and MI modes were used to find the best fit of data. The Log difference (Log diff) term is the parameter used to express the ability of the Malvern's calculated energy distributions to fit the experimental data [6]. For RR most of the computed light energy distributions generated fall in the adequate to good range (Log diff between

4.0 to 5.5), but there is a clear tendency to be excellent when the air/fuel ratio increases. The MI distribution has more strict log diff. requirements and the results are from good to excellent with log diff no higher than 4.5 in the whole range of experimental work.

Because of the good performance of the MI in fitting this data, this model was chosen to represent the data and calculate the droplet size distribution of the spray. The obscuration for all these experiments was in the range from 0.10 to 0.43, thus the measurements were not affected by multiple scattering [7].

Measurements of SMD as Function of Flow Parameter

Figure 1 shows the Sauter Mean Diameter (SMD) of the spray versus air flow rate for different atomisation pressures. Air flow rates lower than 900 l/hr, or air/fuel ratios lower than 0.27, result in a very unstable and inhomogeneous spray with consequential scattering in the results. At higher air/fuel ratios, e.g. 0.97, the spray is more homogeneous and the results are more consistent. A significant reduction in droplet size by increasing the air/fuel ratio is achieved, but there seems to be a limit to the effectiveness of increased air flow rates beyond which no further significant reduction in droplet diameter is reached. These results follow the normal tendency of all liquids sprayed, Newtonian or not. Figure 1 also shows the results obtained with the Dantec instrument. These are significantly different from the ones obtained with Malvern, even increments in the air flow rate have little effect on the SMD. Water sprays under the same conditions follow the same behaviour.

The differences between the results, in the first instance, are because two different types of sampling are employed to determine drop size distribution. The Malvern measures a line-of-sight average through the complete spray. It also registers a signal proportional to the population of drops within the sample volume during the sampling interval, i.e. the spatial average. The Dantec instrument, on the other hand, samples in a very small volume, and registers a signal proportional to the number of drops passing through the volume, i.e. temporal sampling. Generally the results obtained by spatial and temporal sampling are different because in many sprays systems the velocities are correlated with size due to variations in drag with size [8].

Secondly the extremely small sampling volume of the Dantec instrument (ca. 10^{-5} cm^3), in comparison with Malvern could also give a different measure of the average spray droplet size distribution especially if the spray is not homogeneous.

Further problems relate to the nature of the atomisation of two phase fluids. The droplets produced may consist of droplets of water, or of a single bitumen particle surrounded by water, or of a water droplet containing multiple bitumen particles. Sprays of Orimulsion show this as is presented in Fig 2. This fact introduces errors in the measurements due to different reflection or refraction patterns and variations in the particle's refractive index caused by the different types of droplets. The Dantec instrument is very sensitive to optical alignment, especially to the scattering light collection angle, and this should be chosen in such a way that just one scattering mechanism, ie. reflection or refraction, must

dominate for there to be a very smooth relationship between phase and drop size. This is determined by the polarisation of the incident light beam and the refractive index of the liquid droplet.

The Malvern's measurement technique is relatively insensitive to the particle refractive index and shape so that the particles may be absorbing or non-absorbing, spherical or irregular in shape. Furthermore, the scattered light pattern is insensitive to the particle velocity and to the position of the particle in the measurement volume. This represents an advantage for the measurements of droplet size distribution in sprays of this kind of fuel.

In general the distribution droplet size of the spray for Orimulsion presents a wide range of drop sizes and an increase in the air/fuel ratio reduces the fraction of large droplets in the spray.

Prediction of Sauter Mean Diameter in Orimulsion Sprays

A number of functions are available to describe the SMD of sprays produced by air assisted atomisers. Lefebvre presents a good survey of these correlations in his book [9]. The ones related to air assisted atomisers were used to correlate the experimental results obtained with Orimulsion.

In general, the majority of the correlations used give high SMD in comparison with the experimental ones, which is expected considering that they were developed for low viscosity single phase fluids such as kerosine, diesel, water, etc. That is the case for the Elkotb [9] equation namely:

$$SMD = A\ d_0\ Re^{-0.39}\ We^{-0.18}\ (\dot{m}_L/\dot{m}_A)^{0.29} \qquad (1)$$

Reynolds and Weber numbers are expressed as $Re = \rho_L U_R d_0/\mu_L$ and $We = \rho_L d_0 U^2_R/\sigma$. ρ_L, μ_L and σ are the density, viscosity and surface tension of the fuel respectively, d_0 the nozzle orifice diameter, U_R the air relative to liquid velocity and $\dot{m}_L$, $\dot{m}_A$ the mass flow rate for fuel and air. The constant A was found to have a value of 51 for kerosine sprays.

In an attempt to fit Orimulsion experimental data with this correlation over the whole range of experimental work, the A value was found to be a function of the air/fuel ratio according to the following:

$$A = 7.706\ (\dot{m}_A/\dot{m}_L)^{-0.438} \qquad \text{for } \dot{m}_A/\dot{m}_L < 1.687$$

and $$A = 9.824 \qquad \text{for } \dot{m}_A/\dot{m}_L > 1.687$$

Simmon's correlation [9] developed for air-assist atomisers is given in equation (2) as a function of the atomiser's characteristics. C is a constant, ρ_A is the air density and U_L, U_A the fuel and air velocity. Other terms are as defined above.

$$SMD = C \left(\frac{\rho_L^{0.25}\ \mu_L^{0.06}\ \sigma^{0.375}}{\rho_A^{0.375}} \right) \left(\frac{\dot{m}_L}{\dot{m}_L U_L + \dot{m}_A U_A} \right)^{0.55} \qquad (2)$$

The C value was found to be 802 and the experimental data fits very well with the theoretical ones, but for a very narrow range of air/fuel ratios. Figure 3 illustrates the fit of the two correlations with the experimental data.

For air-assisted atomisers the major parameter that affects the atomisation quality is the relative velocity between the liquid and the surrounding air (U_R). At a constant fuel velocity lower than the air velocity, increments in the air flow rate represent increments in the relative velocity; the size of the ligaments decrease, their life becomes shorter, and on their collapse when exposed to the high velocity air stream, much smaller droplets are former. This could be the explanation for the good fit of the Elkotb correlation, which takes into account the air relative to liquid velocity.

Mechanism of Spray Break-Up

Flat sprays were used to identify the break-up mechanism for bitumen-in-water emulsions. High speed photographs shown in Fig 4 indicate that this occurs mainly as a perforated sheet. The photographs show the behaviour near the jet and further down the spray. Small holes suddenly appear in the sheet at a distance from the orifice that varies with the viscosity of the liquid. They rapidly grow in size until the thickening rims of adjacent holes coalesce to form ligaments of irregular shape that finally break up into drops of varying size.

A reduction in the viscosity and surface tension of the emulsion, produced by a dilution in the water content has an effect on the spray break-up. Low viscosity makes the spray angle wider and easier for the appearance of holes and formation of threads, which later break up into droplets. Higher viscosity makes the sheet motion itself very much more regular and inhibits the disintegration of the rims of the sheet (Fig. 4A). Also, it resists the deformation of the ligaments into droplets so the atomisation occurs far away from the nozzle. The sheet seems to be thicker than the other one, and the spray takes longer to break up completely. This highlights the importance of spreading the liquid into a very thin sheet to achieve the finest atomisation [9].

Clark and Dombrowski [10] demonstrated that the drop size is critically dependent upon the nature of the disintegration process; where the disintegration occurs by perforations the size of the ligaments is consequently reduced, resulting in relatively smaller drop size. Thus, the water addition to the bitumen affects the break-up mechanism in such a way that the formation of smaller droplets is very much enhanced despite the high viscosity of the emulsion.

CONCLUSIONS

The atomisation of bitumen-in-water emulsions has some slight differences compared with single phase fluids such as fuel oil or water in terms of the break-up mechanism, the influence of the fluid's properties, the interaction of fuel and air and atomiser design on the spray droplet size distribution.

The main concern in making measurements with this type of fuel is the selection of the best technique and the proper control of experimental conditions which result in accurate and meaningful results in the analysis of the sprays. Accurate determinations of drop size distributions are important in attempting to relate spray characteristics to other parameters. The use of the light scattering (Malvern) technique for the characterisation of Orimulsion sprays demonstrated that the Model Independent distribution function was the best to fit the experimental data. The Rosin-Rammler model has been successfully applied to various two phase flows and sprays, but in this case, the results were acceptable only at high air/fuel ratios. Orimulsion and in general bitumen-in-water emulsion spray size distributions are best made using the Model Independent distribution function.

Results obtained with Dantec equipment are highly dependent upon the equipment measurement arrangement and the position in the spray where the sampling is done. Although this equipment is ideally suited to detailed spray modeling because of the velocity and size data obtained, two phase fluids represent a complication for this technique because consideration has to be made of the influence of the scattering angle, refractive index and refraction or reflection pattern of the sample.

ACKNOWLEDGEMENTS

We want to thank INTEVEP, S.A. Venezuela for the samples of Orimulsion and for financial support (NM). Also, we are indebted to SERC for the loan of the DANTEC phase doppler equipment and to Mr. R. Cowling and Mrs M. Kershaw for their invaluable help.

REFERENCES

1. Lees, B. "Orimulsion review of combustion and handling tests", Energy World, Vol. 179, pp. 8-10 (1990).

2. Olen, K.R., Dooher, J.P. and Woodworth, T.H. "Emulsified heavy ends. A new family of slurry fuels", Fifth International Workshop on Coal-Liquid Fuel Technology. Technical University of Nova Scotia, October (1985).

3. Hidalgo, J., Jimenez, E., Rodriguez, D., Alcantara, J., Carrizo, R., Nava, N., England, G. and Kennedy, B. "ORIMULSION™ Demonstration Test at New Brunswick, Canada: A new technological step towards bitumen commercialisation", 14th International Conference on Coal and Slurry Technology. Florida, USA. April (1989).

4. Thambimuthu, K.V., Stover, N.S.H. and Whaley, H. "The mechanism of atomization of coal-water mixtures", IChem E Symposium Series, Vol. 107, pp. 133-149 (1987).

5. Marcano, N., Pourkashanian, M. and Williams, A. "The combustion of bitumen-in-water emulsions", FUEL (to be published).

6. Meyer, P. and Chigier, N. "Drop size measurements using a Malvern 2200 particle sizer", Atomisation and Spray Technology, Vol. 2, pp. 261-298 (1986).

7. Felton, P.G., Hamidi, A.A. and Aigal, A.K. "Measurement of drop size distribution in dense sprays by laser diffraction", International Conference on Liquid Atomization and Spray Systems. London, IVA/4 (1985).

8. Dodge, L.G., Rhodes, D.J. and Reitz, R.D. "Drop size measurement techniques for sprays: Comparison of Malvern laser diffraction and aerometrics phase/doppler", Applied Optics, Vol. 26, pp. 2144-2154 (1987).

9. Lefebvre, A. Atomization and Sprays, Hemisphere Publishing Corporation, New York, NY (1989).

10. Clark, C.J. and Dombrowski, N. "An experimental study of the flow of thin liquid sheets in hot atmospheres", Journal of Fluid Mechanic, Vol. 64, pp. 167-175 (1974).

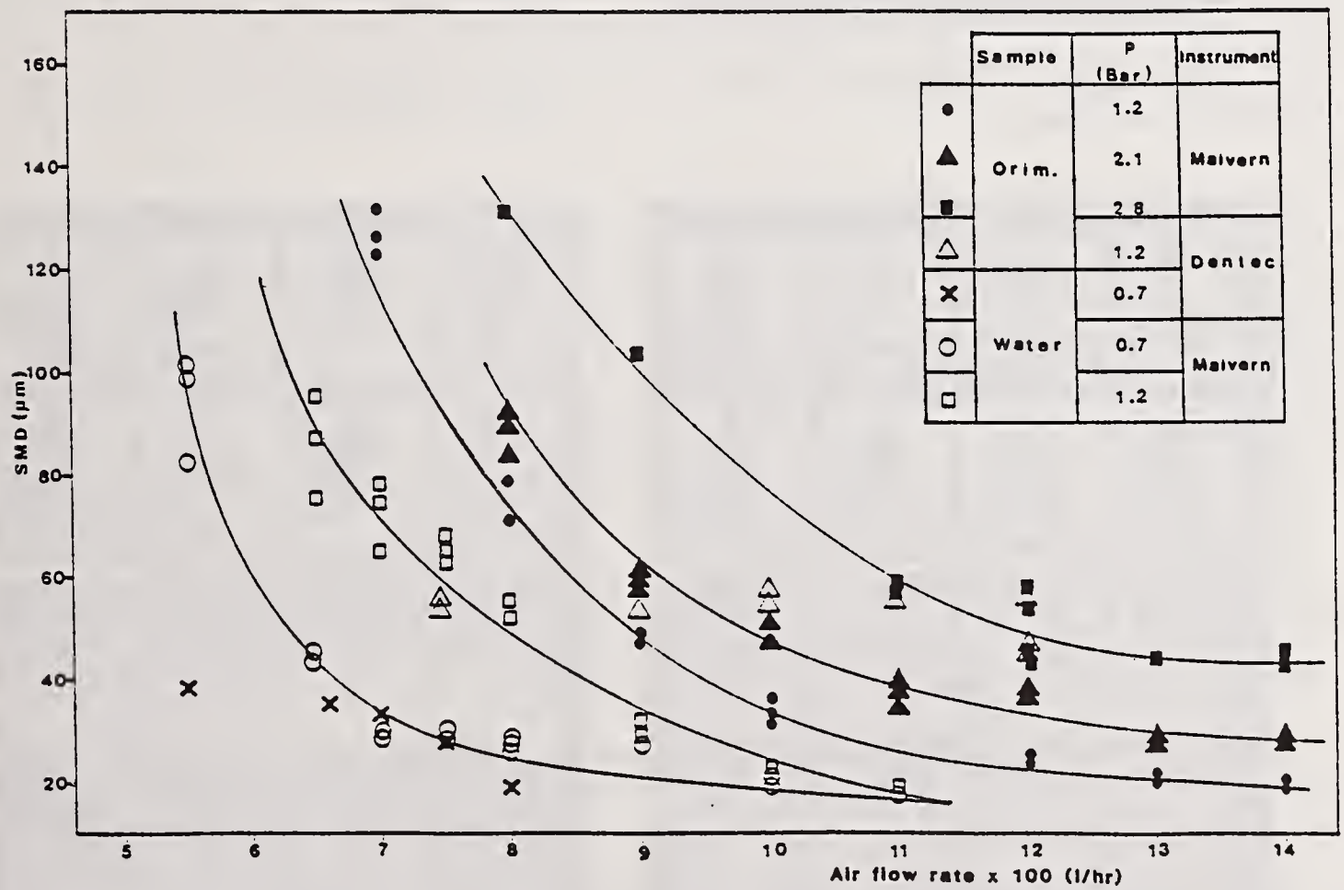

Fig. 1. Variations of the SMD with the atomising air flow rate for Orimulsion and water

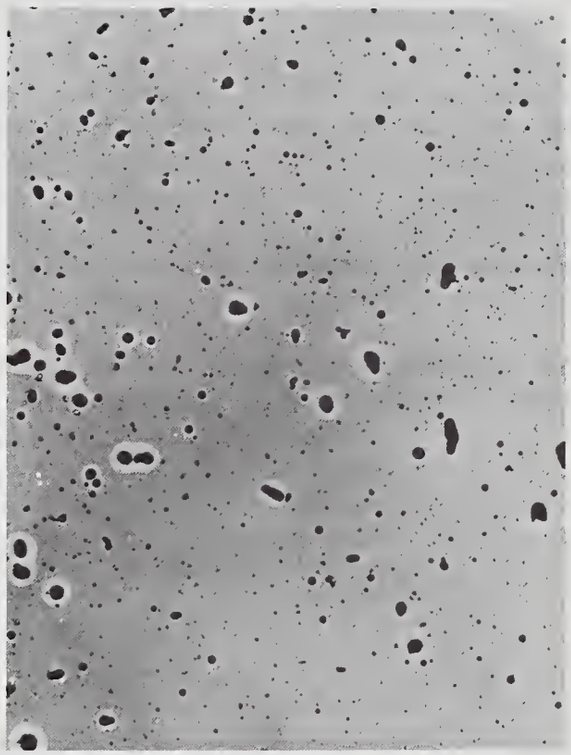

Fig. 2. Droplets collected from an Orimulsion spray.

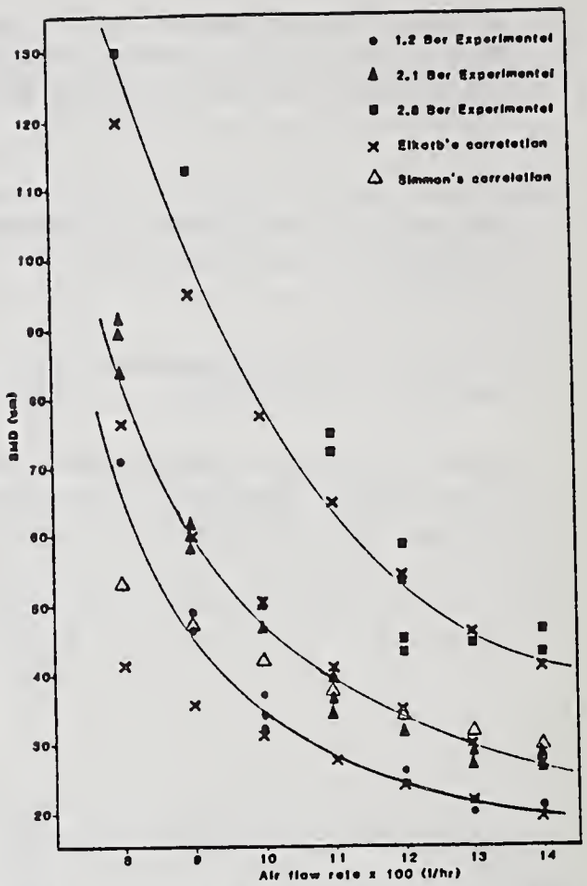

Fig. 3. Theoretical SMD using Elkotb and Simmon's correlations.

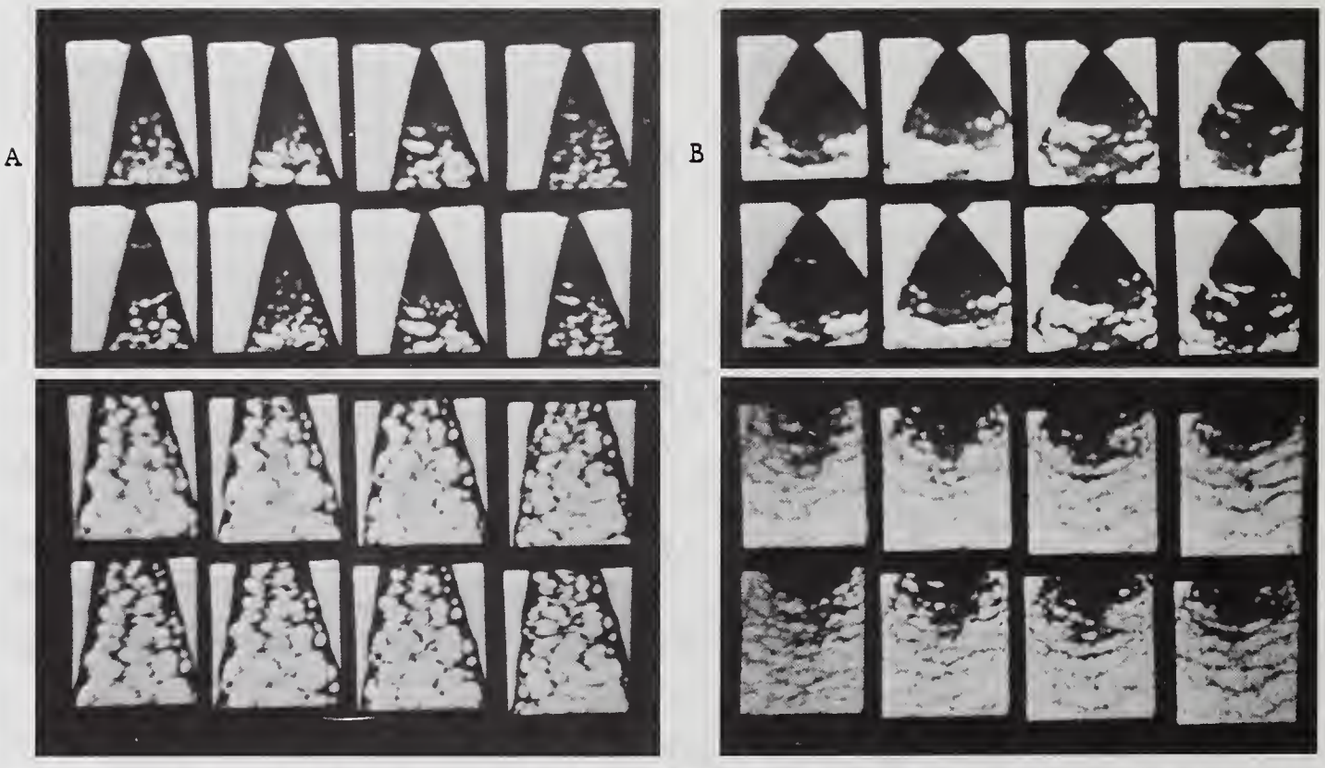

Fig. 4. High speed photographs for A: Orimulsion, B: Bitumen-in-water emulsion, 50% water. Flat spray, 3.4 bar.

THE INFLUENCE OF SPRAY PARAMETERS ON LOCAL MASS FLUXES AND DEPOSIT GROWTH RATES DURING SPRAY COMPACTION PROCESS

V. Uhlenwinkel, U. Fritsching and K. Bauckhage

University of Bremen, Verfahrenstechnik
Bremen, Germany

ABSTRACT

The spray compaction process is a relative new method to produce near-net shaped metallic preforms with better material properties and totaly new materials which are not producible by conventional methods. But there are many parameters influencing the result. Generally the aim is to predict local spray conditions in the compaction plane. Therefore a strategy is developed for the determination of local mass fluxes or deposit growth rates. It is shown, that self similar profiles exist, but they depend on melt properties. The influence of the atomization pressure is investigated, showing that the centerline value acts very different comparing water and steel atomization.

INTRODUCTION

Metal powder production by gas atomization of the melt is a well-known method. People are mainly interested in mean particle sizes and size distributions of the overall product. The equation from Lubanska /1/ is mainly used to predict particle sizes in dependence on atomization parameters, fluid properties and nozzle design. The spray compaction process (Osprey™ process /2/ /3/, also called liquid dynamic compaction or spray casting) with its aim to produce a near-net shaped, homogeneous product needs much more information to make a good specification of the process possible. Therefore the knowledge of local values for mass flux or concentration, size- and velocity distributions are necessary for input data of model calculation to predict other values of interest as cooling rates of the particles, shape of the deposit, heat transfer in the deposit, microstructure of the deposit and so on.

In this paper we try to develop a strategy to determine the local mass fluxes in the spray in dependence on some influence parameters in order to find a correlation to calculate the shape of the deposit. There are generally two methods to produce a desired shape of the deposit:

1) periodical movement of the gas atomizer ring in order to produce for instance flat products /4/
2) moving the substrate in order to produce tubes or solid discs /5/.

The following list of parameters which may affect the local mass flux points out, how complex this process can be.

I nozzle design (D, α); spray chamber design; distance from the atomizer (z)

II melt/liquid: properties of the melt (ρ_L, σ, η_L, ...); mass flow $\dot{M}_L$; initial velocity v_{Lo}; initial temperature T_{Lo}

III gas: properties of the gas (ρ_G, η_G, c_{pG} ...); mass flow $\dot{M}_G$; atomization pressure P_G; velocity v_G

The parameters listed are partly interdependent, i.e. there is a relationship between nozzle design, gas mass flow and atomization pressure. In this paper we present results showing the influence of different liquid properties, gas mass flow and atomization pressure respectively. As far as possible published results of other authors are included in our interpretation.

The first step of our strategy is to verify whether the radial profiles of the mass fluxes (or deposit growth rates) averaged by the centerline value ($\dot{m}_{L,c}$; D_c) and the half-width radius $r_{0,5}$ results in a self similar profile and if this is valid, to find an equation to determine this profile. The second step is to describe the effect of various parameters on the centerline mass flux $\dot{m}_{L,c}$ and the half-width radius $r_{0,5}$. If the mass flow of the liquid is measured and a self similar profile is known, the half-width radius can be calculated depending on the centerline mass flux.

EXPERIMENTAL SET-UP

(1) induction coil
(2) crucible
(3) insulation
(4) heater
(5) tundish
(6) melt delivery tube
(7) primary gas ring
(8) atomization gas ring
(9) deposit
(10) substrate
(11) pressure governor
(12) fan
(13) control valve
(14) N_2-tank

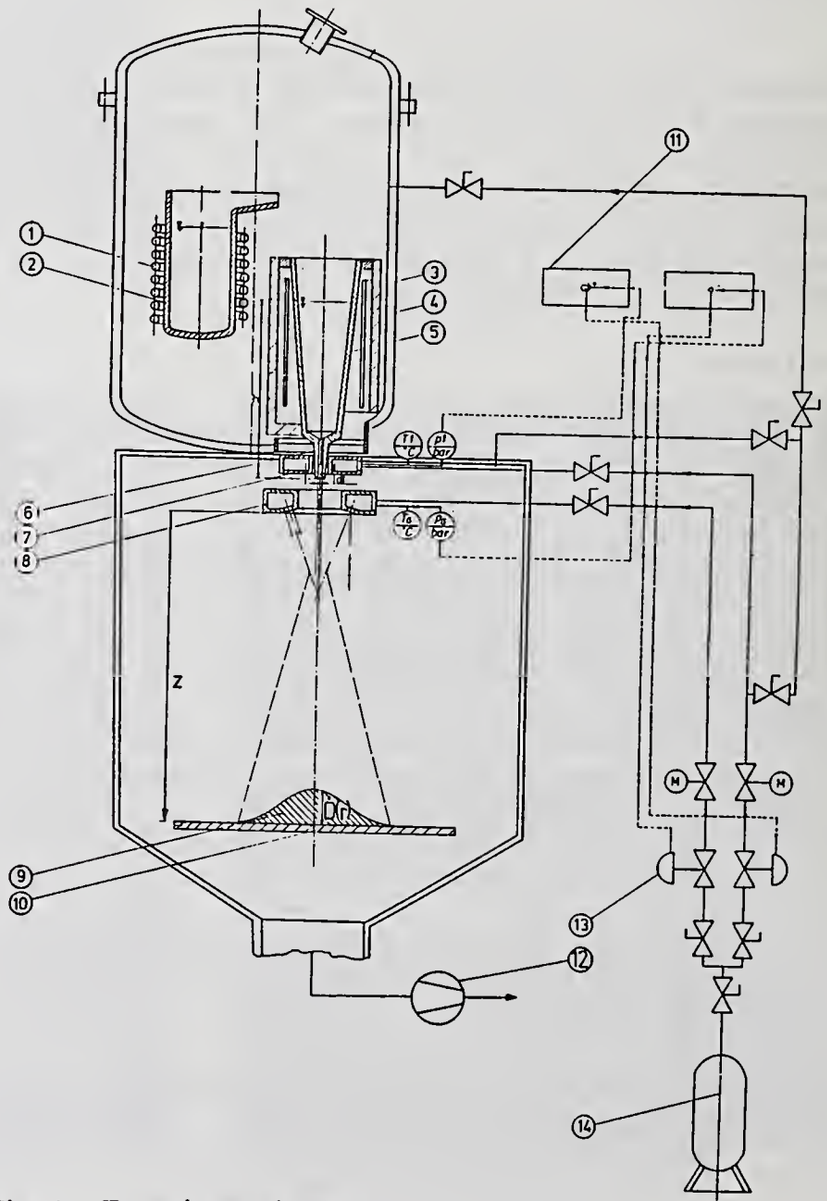

Fig. 1 Experimental set up

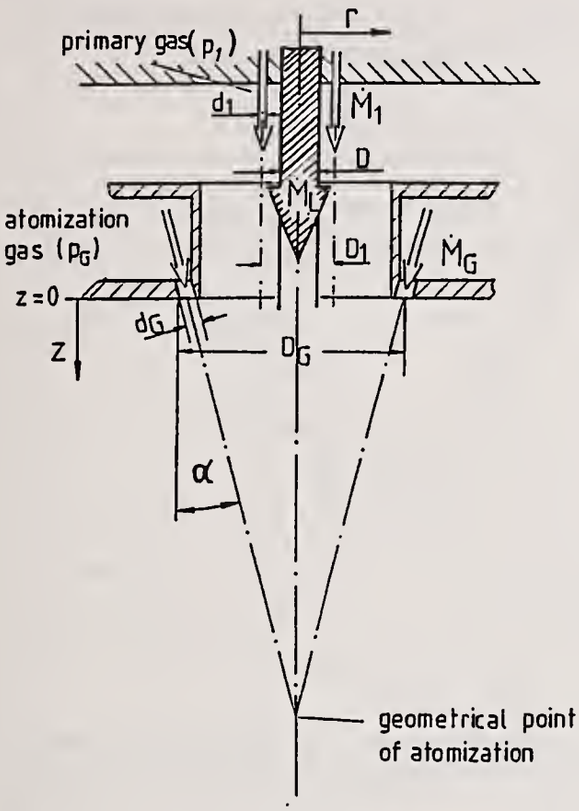

The experimental set-up for the metal atomization and compaction is shown in Fig. 1. The metal is heated by an induction coil and the melt is pulled into the pre-heated tundish when the desired melt temperature is achieved. During the experiment the height of the melt in the crucible is kept constant to guarantee a constant mass flow $\dot{M}_L$. The melt leaves the cylindrical nozzle at the bottom of the crucible and reaches the atomization zone in free fall. The particles are accelerated and meet the substrate at a distance z from the atomizer in order to compact and to build up the deposit. (A method to obtain particle probes is to collect the particles in a patternator that consists of water filled tubes).

Fig. 2 shows the design of the nozzle in use for the metal and water atomization. In general atomizers are divided into two types: free fall and confined atomizer. We use a free fall atomizer with the option to use a primary gas to protect the atomizer from back splashed melt particles.

Fig. 2 Principle sketch of the nozzle design

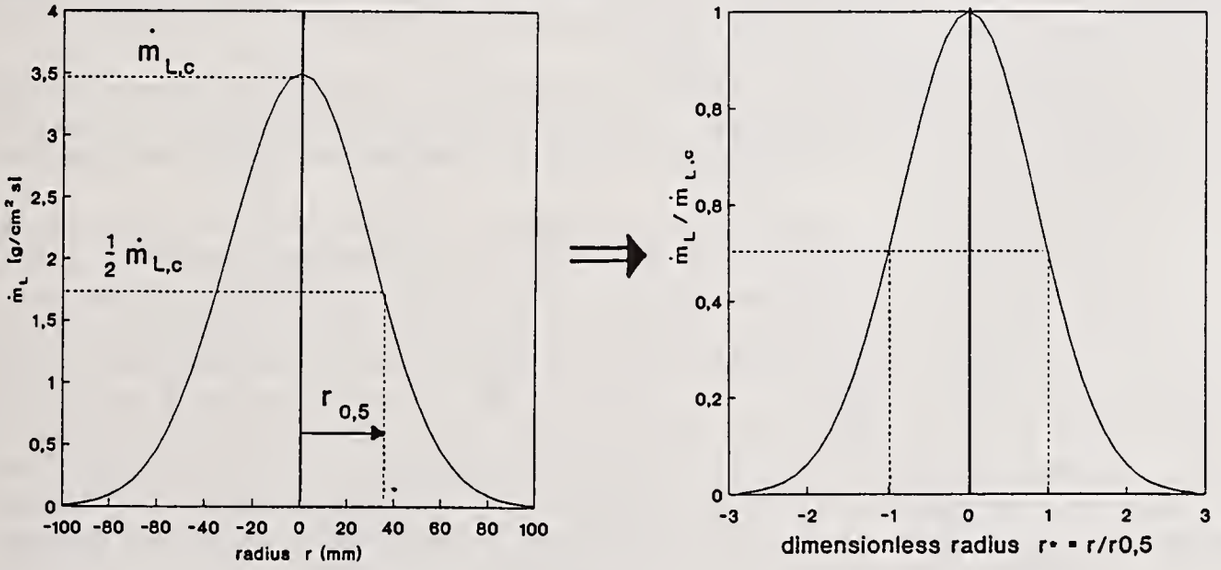

Fig. 3 Example for the generation of a dimensionless profile of the mass flux (b) from the absolute values (a)

SELF SIMILAR PROFILES

In the theory of free jets it is usual to utilize a dimensionless presentation comparing radial velocity profiles for different distances from the nozzle and parameters of influence. We use this method to proof, whether self similar profiles exist for the radial mass flux profiles using different operation and boundary conditions. Fig. 3 shows the way how to make the profiles dimensionless. Therefore the mass flux $\dot{m}_L$ is divided by the centerline (maximum)

value $\dot{m}_{L,c}$ and the radius is divided by the half-width radius $r_{0,5}$. While the half-width radius is defined by the radius where the mass flux is just half as high as the centerline value.

Tab. 1 Experimental conditions and results from various authors

author	type of atomizer	method	melt/fluid gas	$\dot{m}_{L,c}$ g/cm²/s	$\dot{D}_C$ mm/s	$r_{0,5}$ mm	z mm	P_G bar	$\dot{M}_L$ kg/h
Mathur et.al. /6/	-	deposit	Fe 20 wt % Mn N_2		5,4	18	400[1]	8,5	-
Annavarapu /7/	-	deposit	AISI 1026 N_2	4,4	5,7	28	400[1]	8,5	1080
Hartmann /11/	confined	patternator	CuSn6 N_2	0,25	-	25	400[2]	6,0	-
Liu /8/	-	calculation	89%Fe, 10%Cu, 1%C N_2	1,03 1,33 1,24	1,47 1,90 1,77	115 (d = 50 µm) 88 (d = 100 µm) 75 (d = 200 µm)	980	3,0	860
Seuren et.al. /12/	free fall	deposit	AISI 1020 N_2	0,86.. 1,46	1,09... 1,87	52... ...35	800	2,5...4,0	860
this paper	free fall	patternator	water air	4,2... ...2,3	4,2... ...2,3	32... ...49	1000	1,5...2,5	1000
this paper	free fall	patternator	AISI 1020 N_2	1,2... 2,1	1,5... 2,7	52...40	800	2,5...4,0	860

[1] from point of impingement [2] from tip of melt delivery tube

Tab. 1 summarises some results of other authors (including own results) and important parameters as they are available. The parameters can be very different for example in type of atomizer, measuring method and fluid properties.

Mathur et.al. /6/ and Annavarapu /7/ use nearly the same experimental conditions but different melts (Fe 20 wt % Mn and AISI1026) and this conducts in very different values of the half-width radius (18 mm, 28 mm). So one can assume that the properties of the melt have an influence on the spread of the spray.

The results from Liu /8/ are received from numerical calculations, assuming that monodisperse particles (50, 100 or 200 µm) are injected into the flow field (the process of atomization itself can not be taken into account). The most important boundary conditions and assumptions are reported in /9/.

The results from Liu /8/ show - as to be expected - that for the same experimental conditions, an increase of the particle diameter leads to a decrease of the half-width radius, because of a smaller dispersion of larger particles due to the turbulent fluctuations of the two-phase flow. But the absolute values of the half-width radii seem to be too high, because the value for the 50 µm particles is much higher than experimental values of the half-width radius of the one-phase jet velocity. This may be an effect of the turbulence modelling by the κ-ϵ model, which generally predicts the spread of free turbulent jets too strong /10/. All the results can only be compared using the profiles of the mass flux or deposit growth rate averaged by the centerline value in dependence on the radius averaged by the half-width radius. One can use these findings in order to check whether these results can be described by self similar profiles. Therefore we assume that the averaged profiles are a function of the type:

$$G(r^*) = \exp\left[-K_1 (r^*)^{K2}\right] \qquad (1)$$

with $G(r^*) = \dot{m}_L/\dot{m}_{L,c} = \dot{D}(r^*)/\dot{D}_C$, $r^* = r/r_{0,5}$ and K_1, K_2 = constant.

Fig. 4 shows the result of this comparison using $K_1 = \ln(2)$ and $K_2 = 2$ for equation (1). In the range of $/r^*/ < 1$ only the result from Hartmann /11/ has a strong deviation from equation (1). This may be caused by the mass flow $\dot{M}_L$, which is not constant during the experiment.

In the range $/r^*/ > 1$ the calculated values from Liu /8/ are below (d = 50 µm) or close to the curve of eq. (1), while the experimental results from Mathur /6/ and Annavarapu /7/ show a strong deviation from eq. (1) with increasing radius $/r^*/$.

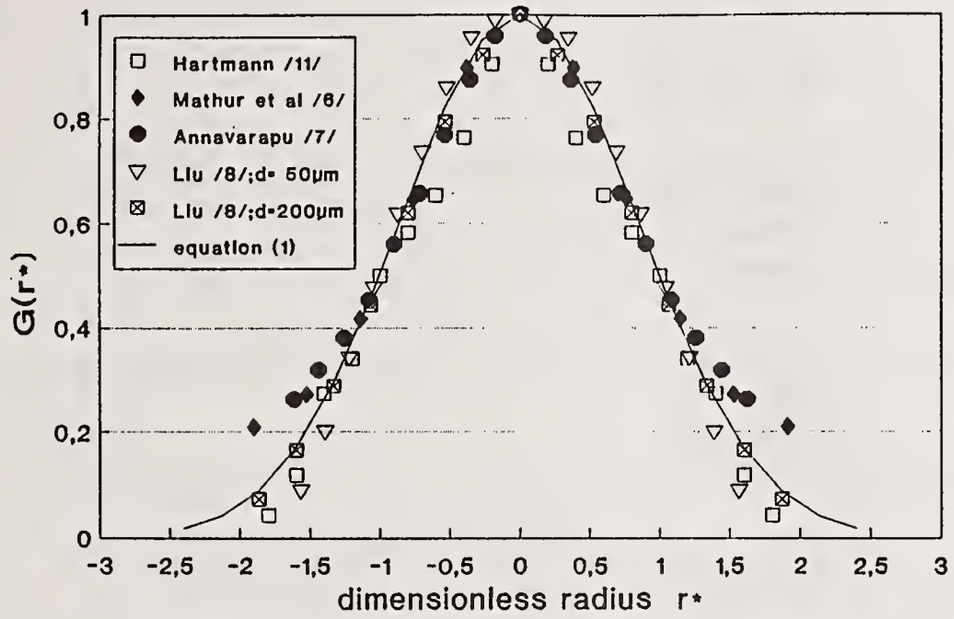

Fig. 4 Averaged profiles of mass flux or deposit growth rate comparing eq. (1) and results of other workers (compare Tab. 1)

Our results in atomizing water and steel (AISI =1020) are similar to the results from Mathur /6/ and Annavarapu /7/ in their tendency. Fig. 5 shows the averaged results from water atomization experiments for various atomization pressures, keeping constant the distance from the atomizer and the mass flow. In comparison to eq. (1) the experimental results for /r*/>1 tend to higher values.

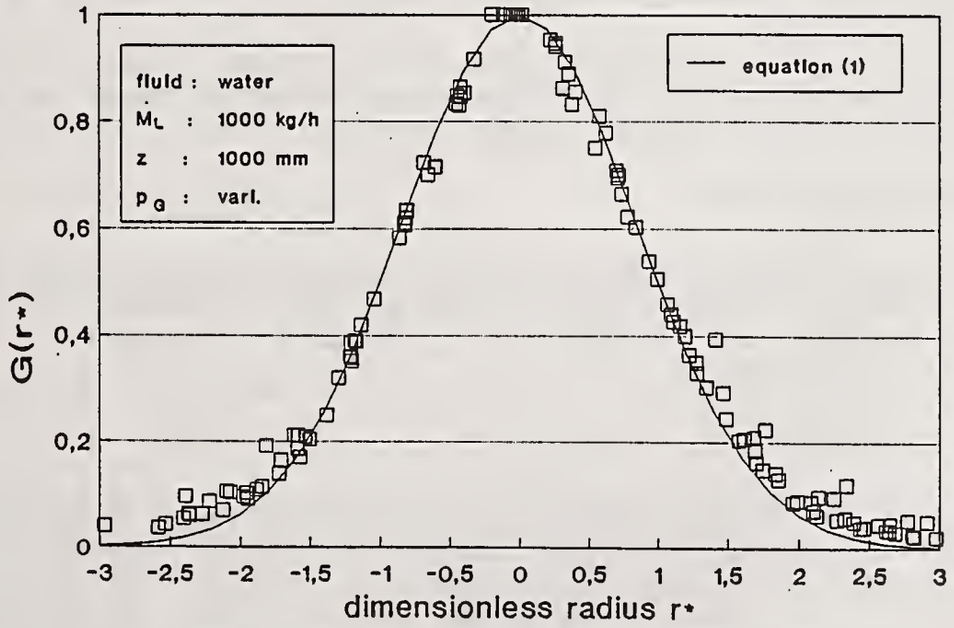

Fig. 5 Averaged profiles of mass flux from water atomization, using various atomization pressures; compared with eq. (1) (K_1 = ln (2), K_2 = 2)

In Fig. 6 averaged profiles of the mass flux are presented, using various atomization pressures, compared with equation (1). It is to be seen that the exponent K_2 = 1,4 in the range /r*/>1 fits the results by far better than the exponent K_2 = 2. Taking K_2 = 1,4 in the range /r*/>1 also the calculated mass flow (from eq. (2)) delivers much better results compared with the measured mass flow.

$$\dot{M}_L = \int_0^\infty 2\,\pi\, r\, \dot{m}_L\,(r)\, dr \qquad (2)$$

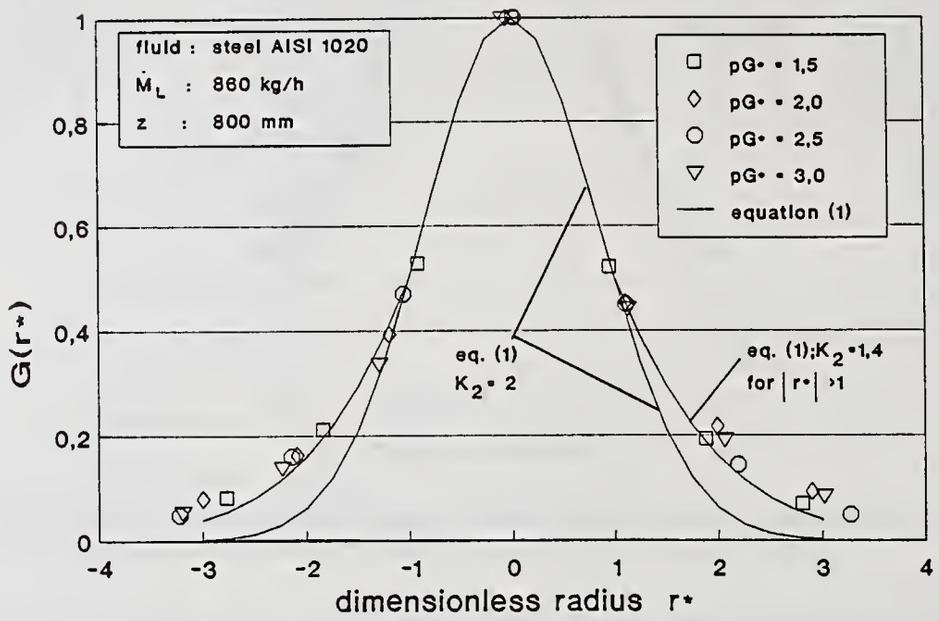

Fig. 6 Averaged profiles of mass flux (patternator result)

INFLUENCE OF PROCESS PARAMETERS ON CENTERLINE MASS FLUX (OR DEPOSIT GROWTH RATE) AND ON THE HALF-WIDTH RADIUS

If a self similar profile is found for a given fluid and nozzle system, one has to determine the averaging values (centerline value and half-width radius). We assume that the centerline mass flux $\dot{m}_{L,c}$ can be described by an equation of the type as follows:

$$\dot{m}_{L,c} = A_1 \bullet (p_G^*)^{A2} \bullet z^{A3} \bullet \dot{M}_L^{A4} \qquad (3)$$

with $p_G^* = (p_G - p_u)/p_u$ is the dimensionless atomization pressure. In the paper the influence of the atomization pressure p_G^* is investigated for water and steel atomization, keeping constant the distance from atomizer z and the mass flow $\dot{M}_L$. Therefore the parameters A and A_2 of equation (4) have to be determined.

$$\dot{m}_{L,c} = A\,[z, \dot{M}_L] \bullet (p_G^*)^{A2} \qquad (4)$$

Fig. 7a presents the centerline mass flux and the half-width radius in dependence of the atomization pressure P_G^* for water atomization. The increase of the pressure leads to a decrease of the mass flux and because of a constant mass flow to an increase of the half-width radius. For the determination of the constants A and A_2 Fig. 7b shows log ($\dot{m}_{L,c}$) in dependence of log (P_G^*) also including the linear regression with the constants A = 2.82 and A_2 = -0.55.

In the same way the results of steel atomization, using the same atomizer are evaluated in Fig. 8a/b, comparing the results from the deposit growth rate and the mass flux. These results differ because of the different experimental conditions. Three features are responsible for this difference: 1. bounce of particles from the surface of the deposit, 2. disturbance of the flow field in the vicinity of substrate and deposit respectively, 3. continuous variation of the impact location (mainly in z direction) during the growth of the deposit.

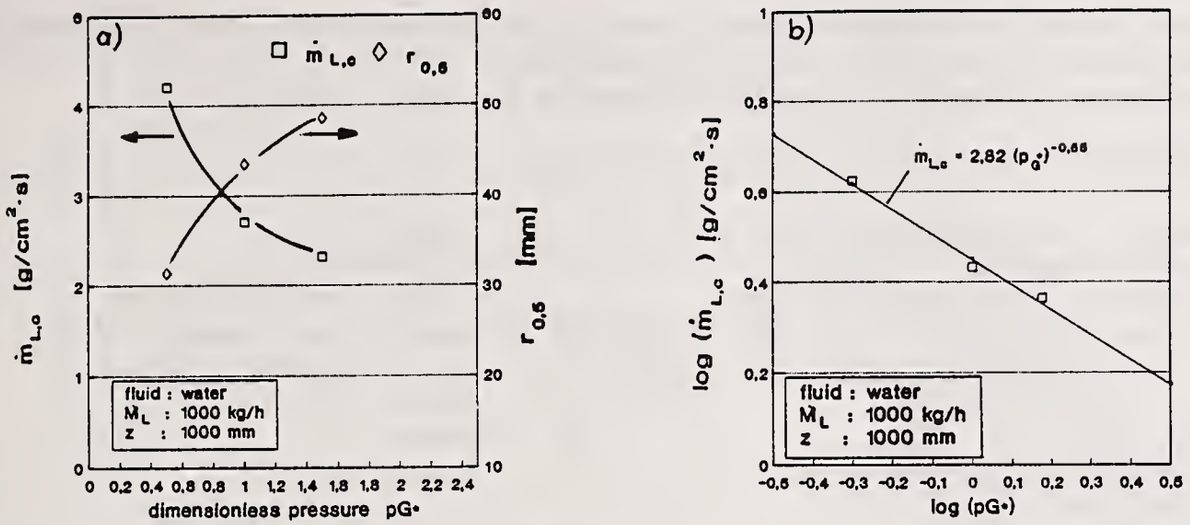

Fig. 7a/b Centerline mass flux and half-width radius in dependence on the dimensionless atomization pressure P_G^* for water atomization

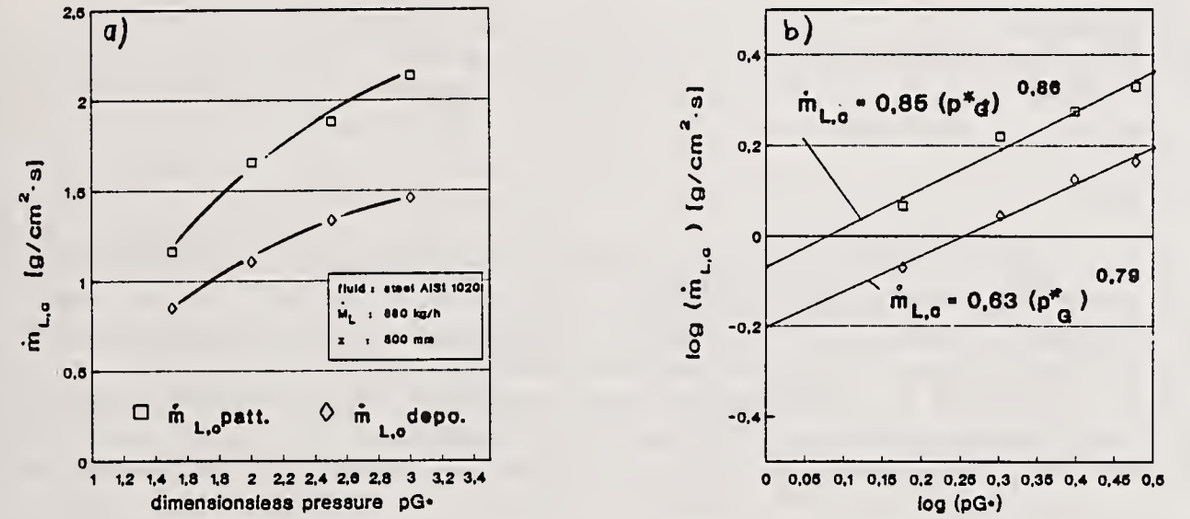

Fig. 8a/b Centerline mass flux in dependence on the dimensionless atomization pressure P_G^* for steel atomization

Looking at the influence of the atomization pressure, both results show an increase of the mass flux when increasing the atomization pressure and lead to nearly the same exponents A_2 = 0,79 (deposit growth rate) and A_2 = 0,86 (mass flux). This behaviour is generally contrary to the results from the water atomization and cannot be explained by turbulent transport mechanism of free turbulent jets. We presume that this phenomena is caused by an interdependent influence of the flow in the nozzle near field and fluid properties. A better understanding of the process in the nozzle near field is necessary to explain this behaviour, as it is partly reported in /12/.

CONCLUSIONS

The spray compaction process is affected by various numbers of parameters. Aim of this investigations is the prediction of local mass fluxes or deposit growth rates in the case of stationary atomization (static atomizer and static substrate), atomizing different fluids. It is found that self similar profiles are created, but there is a dependence on fluid properties. Fluid properties also affect the centerline value. The centerline mass flux is influenced by the

atomization pressure and leads to contrary behaviour comparing water and steel atomization. While the centerline mass flux is decreasing with higher atomization pressure in the case of water atomization, the centerline mass flux increases in the case of steel atomization.

NOMENCLATURE

c_p	specific heat capacity	v	velocity
d	particle diameter	z	axial coordinate; distance from the atomizer
$\dot{D}$	diameter of the melt delivery tube	α	angle between centerline of the atomizer holes and z-axis
$\dot{D}$	deposit growth rate	η	dynamic viscosity
$\dot{D}^*$	dimensionless deposit growth rate = $\dot{D}/\dot{D}_c$	ρ	density
G	gauss function (eq. (1))	σ	surface tension
$\dot{m}$	mass flux		
$\dot{m}^*$	dimensionless mass flux = $\dot{m}/\dot{m}_c$	**Subscripts**	
$\dot{M}$	mass flow		
p	pressure	c	centerline
p_G^*	dimensionless atomization pressure	G	gas
r	radius	L	liquid/melt
$r_{0,5}$	half-width radius	o	initial
r^*	dimensionless radius = $r/r_{0,5}$	u	ambient
T	temperature	1	primary

REFERENCES

1. Lubanska, H., "Correlation of Spray Ring Data for Gas Atomization of Liquid Metals", Journal of Metals, No.2, p.45-49 (1970).
2. Brooks, R.G.; Green, S., "Verfahren und Vorrichtung zur Herstellung von gesprühten Metallkörpern", Patent Nr. P 25 37 103.3-24, 20.8.1975.
3. Brooks, R.G. et al, "The Osprey Process. a novel method for the production of forgings", Metallurgia & Metal Forming, p.157-163 (1977).
4. Reichelt, W.; Voss-Spilker, P., "Spray deposition - a new and original shaping process for the metallurgical industry", Metallurgia, No.9, p.410-413 (1986).
5. Leatham, A.G.; Brooks, R.G.; Yaman, M., "The Osprey process for the production of spray-deposited roll, disc, tube and billet preforms", Modern Developements in Powder Metallurgy, Vol.15-17, p.157-173 (1985).
6. Mathur, P.; Apelian, D.; Lawley, A., "Analysis of Spray Deposition Process", Acta metall., Vol.37, No.2, p.429-443 (1989).
7. Annavarapu, S., "Spray casting of steel strip: Modeling and experimental studies", Ph.D. Drexel University, 1989.
8. Liu, H., "Berechnungsmodelle für die Geschwindigkeiten und die Abkühlung von Tropfen im Sprühkegel einer Stahl-Zerstäubungsanlage", Dissertation Uni. Bremen, 1990.
9. Fritsching, U.; Liu, H.; Bauckhage, K., "Numerical Modelling in the Metal Spary Compation Process" ICLASS-91, Gaithersbury Maryland, (1991).
10. Leschziner, M.A.; Rodi, W., "Calculation of Annular and Twin Parallel Jets using various Discretization Schemes and Turbulence-Model Variations", Journal of Fluids Engineering, Vol.103, No.6, p.352-360 (1981).
11. Hartmann, G.C., Die Erstarrung von Metallen im Sprühgießprozeß am Beispiel der Zinnbronze CuSn6 / Fortschritt-Berichte, Reihe 5: Grund- und Werkstoffe, Nr.195, VDI-Verlag Düsseldorf, 1990.
12. Uhlenwinkel, V. et al, "Strömungsuntersuchungen im Düsennahbereich einer Zweistoffdüse - Modelluntersuchungen für die Zerstäubung von Metallschmelzen", Chem.-Ing.-Tech., Vol.62, No.3, p.228-229 (1990).

NUMERICAL MODELLING IN THE METAL SPRAY COMPACTION PROCESS

U. Fritsching, H. Liu and K. Bauckhage

Institut für Werkstofftechnik
Bremen, Germany

ABSTRACT

Since about 20 years the producing of preformed metal products by means of the spray compaction process has become a widely known and now quite well established process. But still work has to be done to predict the correct way for the controlling of the process and the influencing of the spray product properties, here the preform. This work is in progress and is at time investigated by a variety of research groups. In this area the numerical modelling of the spray process has become an important tool in order of the understanding of the heat and mass transfer mechanisms in molten metal spraying. Following the subdivision of the spray process into three different stages, as there are (a) the atomization area, (b) the transport area, and (c) the compaction area, this paper gives some recent results of our group for the process controlling and optimization obtained by different computer calculations of the continous and two phase flow field and the related thermal conditions of the dispersed phase. Eulerian and Lagrangian calculations will be provided and compared as far as possible to measurements, especially done with the phase-Doppler method. Possible ways for the optimization of the spray nozzle design and the spray performance in terms of the mean droplet size and the mass flow ratio gas/melt will be outlined.

INTRODUCTION

The spray compaction technology for molten metals is an industrial process for the basic shaping and preforming of metals [1]. In the process, from above the melting point heated liquid metal is poured into the nozzle and is atomized by an impinging inert gas jet of high kinetic energy. The resulting spray of molten metal droplets will be compacted on the substrate surface to the desired shape, dependent on its local mass flow rate.

The application of the process covers an area of different metals like steel, copper, tin and aluminium. Also several alloys and composite materials, which are difficult or impossible to produce by conventional metallurgical processes, are in the meantime object of industrial metal spray processes. The advantages of the spray compaction process compared with conventional casting techniques are therefore

- near net shaped products
- better homogeneity and less impurities of the product
- applicable to new alloys and composites
- higher heat transfer coefficient
- contribution to micro structural refinement in the pre products.

For the scientific analysis of the spray compaction process it is useful to subdivide the total process in smaller parts, each of which is responsible for an individual aspect of the process and product optimization. The unit operation "spraying" in an industrial context can be devided into three parts [2]

- the atomization area and the liquid disintegration
- the transport process of the multiphase flow in enclosed cavities
- the droplet impingement and the formation of the product.

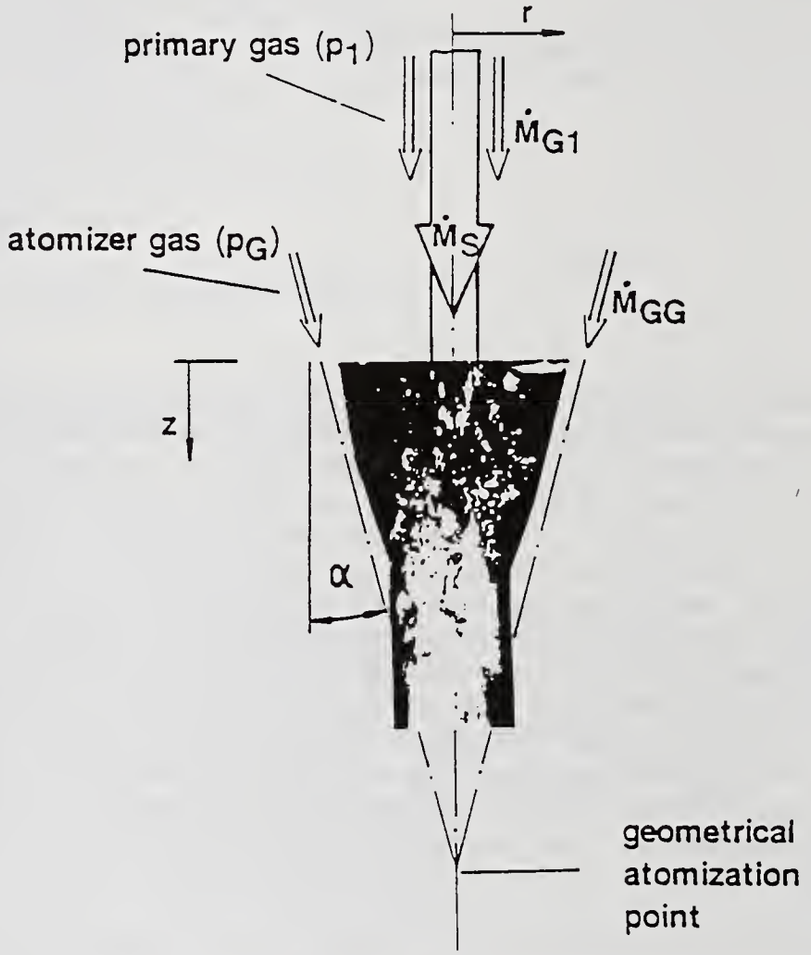

Fig. 1 Gas atomization of molten metals, principle sketch

The first area of investigations following the above list, to be reported here is the nozzle near field (Fig. 1). Particularly when atomizing sprinkling and/or solidifying fluids, special care has to be taken on to the spray nozzle design or selection and on the operation parameters of the spray process. Due to back splashing droplets which glue and assemble at the nozzle (called freezing), the atomization process will be influenced or sometimes even interrupted. In order to understand and control the flow field immediately in the atomization area, the gas flow field was numerically modelled. Gas flow recirculations in the nozzle near field will be examined and possible ways for a constructive improvement of the nozzle will be shown.

The second area of investigation is the two phase flow field of the gas jet and the dispersed metal droplets in the spray chamber. In order to enhance the understanding of the flow field and the temperature distribution of the gas as well as of individual particles in the spray chamber and to establish a control model for the regulation of the process, extensive experimental and theoretical studies are necessary. The purpose of this part of the paper is to present model calculations based on an Eulerian approach for the momentum transport and exchange for both phases under simultaneous consideration of the phase change kinetics of the dispersed

phase. This part of the study investigates the influence of the directly controllable input process parameters on the stationary turbulent flow and temperature fields in the spray chamber.

Following the area division given above the third area of investigation is the compaction area and the formation of the preform. This part will be presented as a separate paper in this conference, based primary on experimental investigations in the metal atomization and in model experiments with water as the dispersed fluid.

The three different areas of research are combined versus their initial and boundary conditions.

Method of Solution

The numerical simulation of the gas flow field in the near nozzle region is based on the approximation of the primary- and of the atomization nozzle as coaxial ring gaps. Under this assumption the system of partial differential equations describing the gas flow field are solved using the standard features of the PHOENICS code, version 1.3 [3]. This multipurpose computational fluid dynamics code is based on a finite volume discretization of the governing equations using the SIMPLEST formulation for the solution. [4]. It was assumed that the flow field can be described as to be two dimensional, using polar co-ordinates and single phased. The behaviour of the gas is described by the isentropic gas law and the turbulence modelling is based on the standard κ-ϵ model, together with log-low wall functions on all rigid walls.

The theoretical model for the two phase flow field in the spray chamber consists of the equations of continuity, momentum and energy conservation for both phases as well as of the phase change kinetic equation. The motion and temperature equations are derived by Reynolds decomposition and time averaging of the corresponding instantaneous conservation and energy equations, considering the weight and buoyancy of droplets as well as the friction between the two phases to be the volume forces in the equations of motion, and the phase change heat and the convective heat loss of the droplet-phase to be a heat source of the gas-phase and to be a heat sink of the droplet phase in the temperature equations. Closure of the time-mean equations was achieved by modelling the turbulent correlations in the equations of mean motion according to Elghobashi's method [5] and in the equations of mean temperature according to [6, 7]. The corrected κ-ϵ equations are similarly formulated. In deviation to the standard set of constants in the κ-ϵ model, the c_μ coefficient was set to 0.07, according to [7]. For a first approach the turbulent diffusivity ν_{tp} of the dispersed phase is related to the turbulent diffusivity of the gas phase ν_{tg}, according to Schönung [8] as $\nu_{tp}/\nu_{tg} \approx 0.5$ because the ratio from ν_{tp} to ν_{tg} is between 0.3 and 0.6 according to [8] for the conditions of this calculation. Similarly the extra production and dissipation of the turbulent kinetic energy, which results from the correlations of the fluctuations of gas velocity, are also treated simplified as a linear function of the droplet concentration in the corresponding terms with the same approach as described by Danon [9].

A kinetic model for the phase change has to solve two problems: to what extent the droplets can be undercooled and how quickly the phase change in the droplets occurs. On their way downwards to the substrate the smallest droplets are subject of a rapid quenching process, thus reaching the impact point as completely solidified particles. On the other hand the largest droplets don't lose so much of their heat, thus reaching the substrate as entire liquid droplets. As the microstructure of the deposit and also its porosity depend upon the temperature, the fraction of solidification and physical structure of the impacting droplets, it is essential to develop a phase change kinetic model to investigate the influence of phase change on the temperature and cooling rate of droplets. In [10] a phase change kinetic model has been derived on the base of the classical nucleation theory applying the Johnson-Mehl-Avrami transformation for solid state phase change in metals and alloys. By the combination of this model with the above mentioned temperature equation of the droplet phase, the nucleation temperature, i.e. the maximal achievable undercooling can be estimated and the temperature dependence of the phase change rate can be simulated.

The method of solution for the coupled system of partial differential equations is a modified version of the MAC-SOLA method with a second order upwind discretization [11].

The gas flow in the nozzle near field

The principal sketch of a twin-fluid atomizer for molten metal atomization is shown in Fig. 1. In order to move the atomization area away from the melt outlet, the point where the atomizer gas stream joins the melt stream has been brought downstream. In addition to that in our special case we used a coaxial primary gas stream (treated as a coaxial free jet) in order to convey the undisturbed melt stream to the atomizing point, to raise the drag of back splashing droplets and to transport these droplets downwards back to the atomization zone. The atomizing gas meets the melt stream under an angle α, generating the atomization point in some distance downwards from the nozzle. But as the photomontage from a model water nozzle shows, the atomization of water in such a nozzle nevertheless produces back splashing droplets which cannot be avoided under wrong operating conditions. One can see the movement of individual droplets upwards the atomization area. These droplets move in the inner circle vertically upwards against the main gas and melt flow direction and in the outer regions downwards.

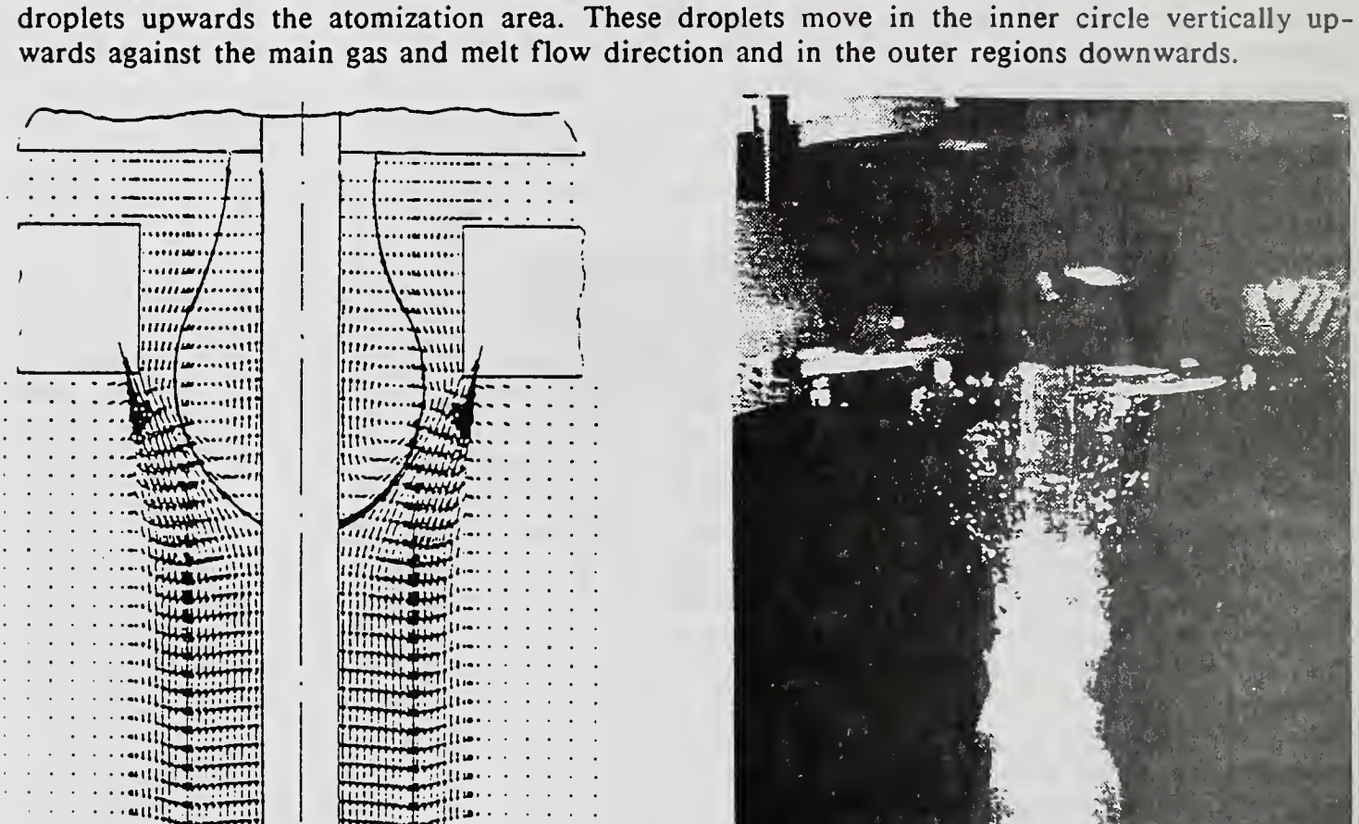

Fig. 2 Gas flow in the near nozzle region, P_G (comp) = 1.89 bar; p_G (exp) = 2 bar

Fig. 2 illustrates on the left side the result of the computation for the nozzle sketched in Fig. 1. This type of nozzle contains the typical central cylindrical flow regime of the melt stream and an atomizing coaxial jet at a lower part of the flow system. This type of melt atomization has been described in detail by [12] and [13]. The results plotted represent an atomizer pressure level of 1.89 bar absolute, which equals the velocity of the incoming atomizer gas flow to the velocity of sound, and without any primary gas application. The atomization gas flow which enter the domain under an angle of 10° contracts in the same manner as a coaxial jet, and hits the core region at a position in some distance upwards from the geometrical atomizing point. One can see a big area of a closed recirculating vortex, the border of which is marked by the solid line. The upward pointing velocity component in this vortex has a maximum value of nearly 45 $^{m}/_{s}$. Individual particles which enters this area will be accelerated upwards and some of them will hit the nozzle main body near by the fluid exit.

The comparison of this computational results with a picture of the water atomization in Fig. 2 (right side) indicates a good agreement with the behaviour of single particles beyond the atomization point, but the size of the standing vortex is underestimated in the simulation. One has to notice, that the pressure level for the atomizer gas in the experiment is a little bit different from that used in the simulation.

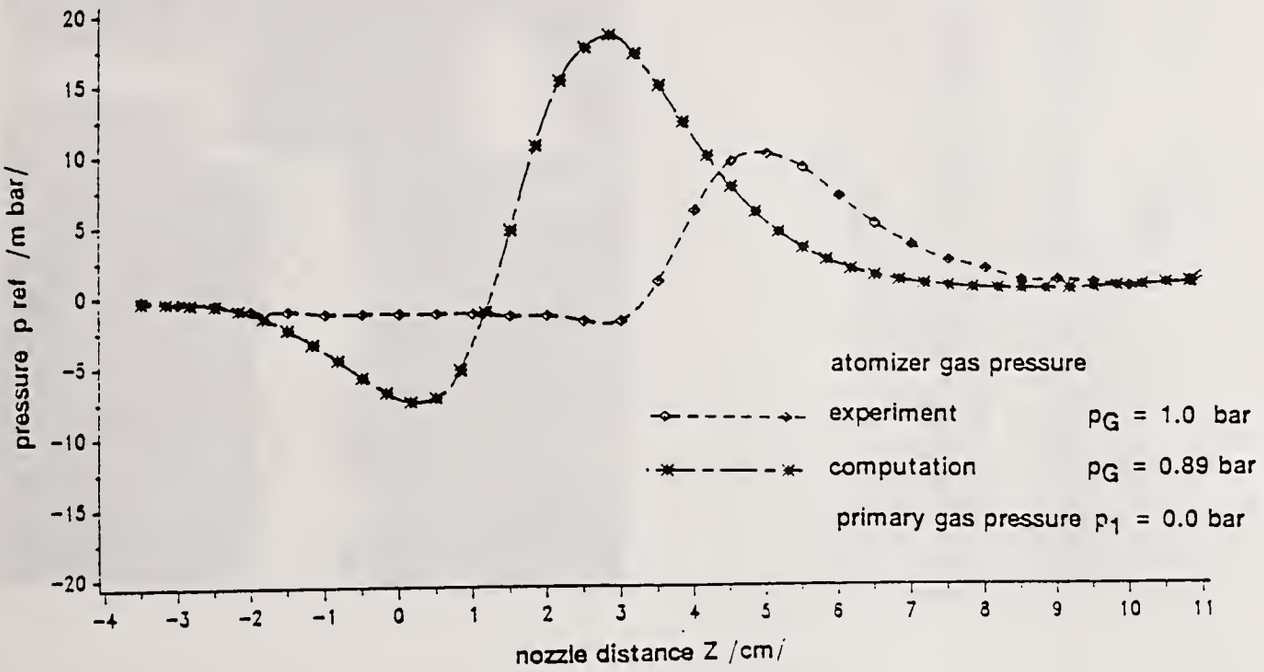

Fig. 3 Pressure on centerline - comparison computation/experiment

In Fig. 3 the comparison for the computed pressure on the core surface with pressure measurements is drawn. (Z = 0 stands for the lower edge of the atomizer gas ring) The pressure maximum, that is the main hit point of the atomizer gas stream on the core, is computed closer to the gas exit than the experimental results indicate. In combination with this failure, the angle of attack is overpredicted and therefor the radial velocity component is greater in the simulation than in the experiment, resulting in a higher value for the pressure maximum and the underpressure. This deviation is mainly affected by the use of the standard κ-ϵ model, which is known to overpredict the jet growth in the axial direction. Therefor the inner recirculation area of a coaxial jet will be underpredicted in size. The result of a constructive alteration is shown in Fig. 4 for the case of 1.89 bar pressure for the atomizing gas and 1.4 bar pressure for the primary gas. The figure indicates no vortices directly at the primary gas jet exit and the inner area of the atomizer ring. A flow field without any closed recirculating vortex occurs.

The flow field in the spray chamber

The overall flow field of the continuous and the dispersed phase are shown in Fig. 5. Because of the great velocity gradients in the flow field, the vectors are scaled square-rooted. The calculation was done for a mean droplet diameter of 100 μm and a mass flow ratio gas/melt of 0.8. The gas flow field consist of two parts. At first the gas jet which enters the spray chamber at the top. Due to the existence of the substrate the growth rate of the jet varies non linear from top to bottom of the chamber. Secondary a huge amount of gas can be observed which recirculates in the spray chamber. Therefor the velocity vectors of the dispersed phase at the edge of the spray cone are directed radially inwards in the mid part of the spray cone, half between the inlet and the substrate, because of the vertical gas entrainment from the recirculating gas into the jet. For this case no particle recirculation occurs into the spray chamber, all metal droplets will hit the substrate.

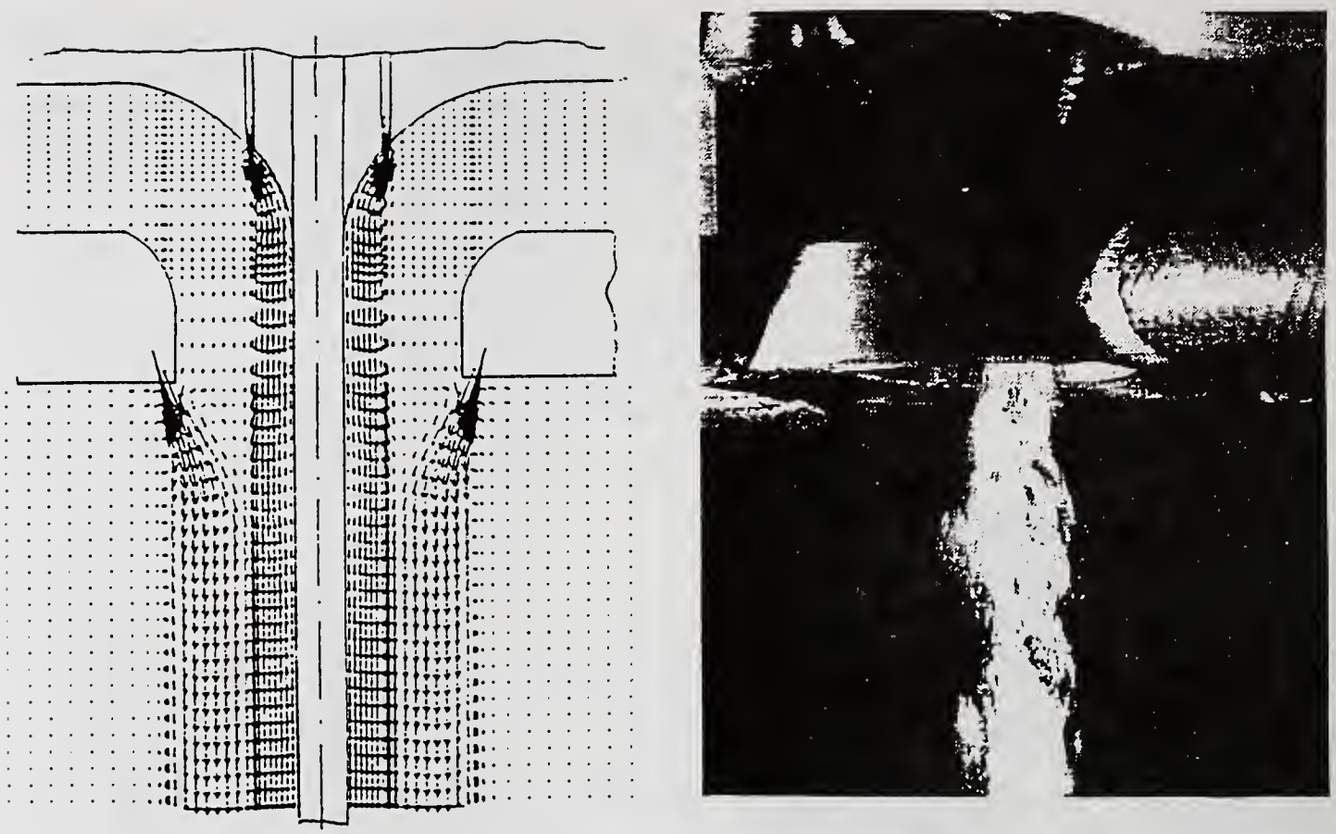

Fig. 4 Gas Flow in the near nozzle region, P_G (comp) = 1.89 bar; p_G (exp) = 2 bar

In Fig. 6 the gas and droplet velocities on the centerline of the spray cone are illustrated for three different calculations with mean droplet diameters of 50, 100 and 200 μm. The direction of the momentum transfer is reversed at some distance between 300 and 600 mm from the spray chamber inlet. While in the upper part of the chamber the droplets are accelerated by the gas jet, thereby reaching a maximum kinetic energy dependent on the drop size, further downstream the droplets are faster than the gas flow and the direction of the momentum transfer is from the disperse to the continuous phase. In this figure PDM-measured droplet velocities at z = 450 mm are shown which fit well with the calculated data.

The radial profiles of the droplet velocities, shown in Fig. 7 as a function of the mass flow ratio with values of 0.55, 0.80 and 1.08 give a non-Gaussian profile as to be expected. The width of the spray cone increases with the augmentation of the mass flow ratio. It is not yet clear, why this result does not fit the experimental observation of a narrower substrate material distribution with increasing gas pressure. But it is obvious, that the assumption of a constant mean diameter of the metal droplets with varying mass flow ratio is quite unrealistic, because the mean diameter decreases with increasing atomizing gas pressures.

CONCLUSIONS

By means of the spray compaction process for molten metals, near net shaped industrial pre-products can be manufactured with advanced properties and based on new alloys and composites. Process and product optimization can be based on the numerical modelling of the process, which must be validated and interact with model and on-line experimental works.

By dividing the process into three stages in this paper the background and results for the first two stages, the atomization area and the spay chamber, have shown that at first by the understanding of the gas flow field in the near nozzle area the geometry of the atomizer can be improved in order to prevent recirculation of droplets in this area.

The simulation of the two phase flow in the spray chamber yields a basic understanding of the transport process in the chamber and the exchange behaviour between both phases. The important parameters are the mean droplet sizes and the mass flow ratio of gas and melt.

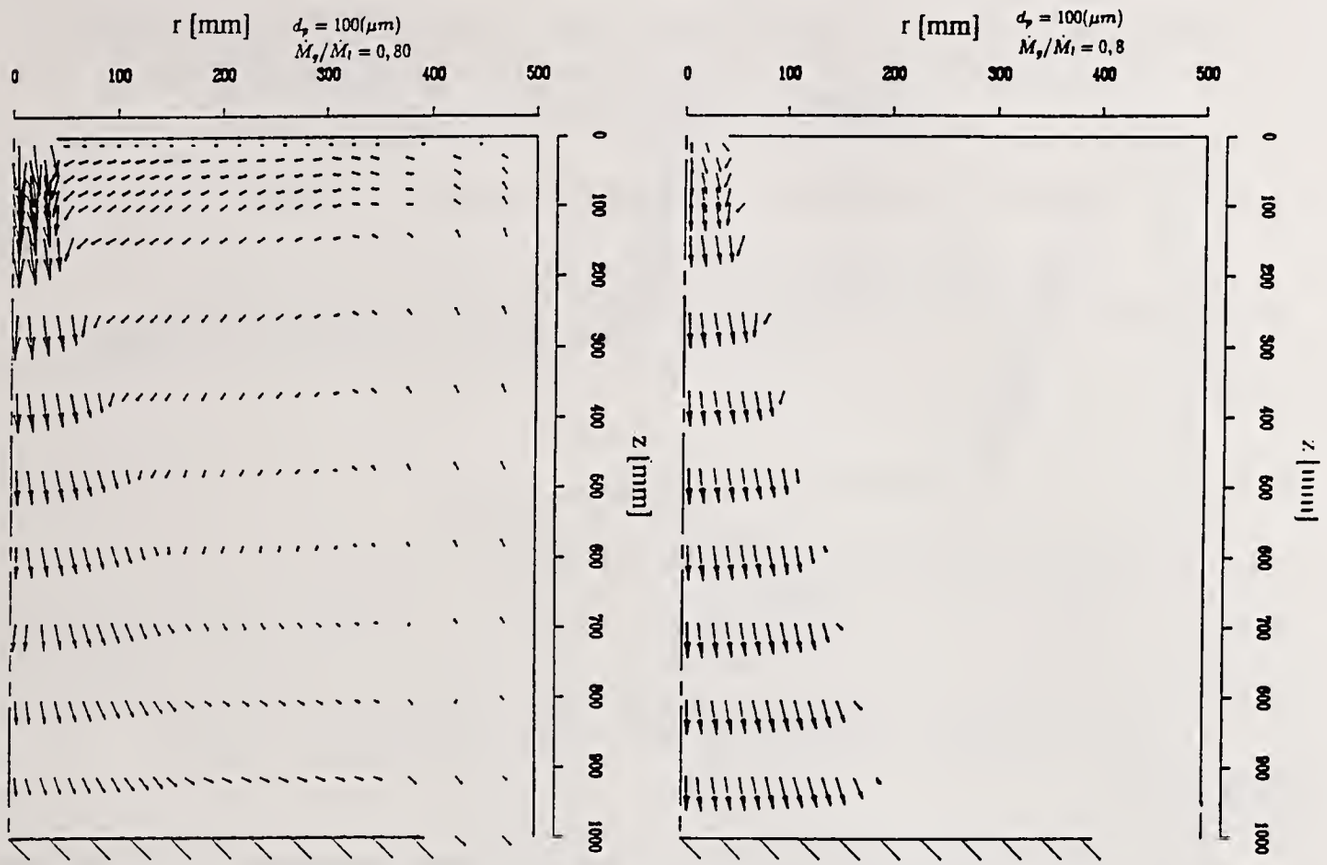

Fig. 5 Velocity vectors for continuous and dispersed phase

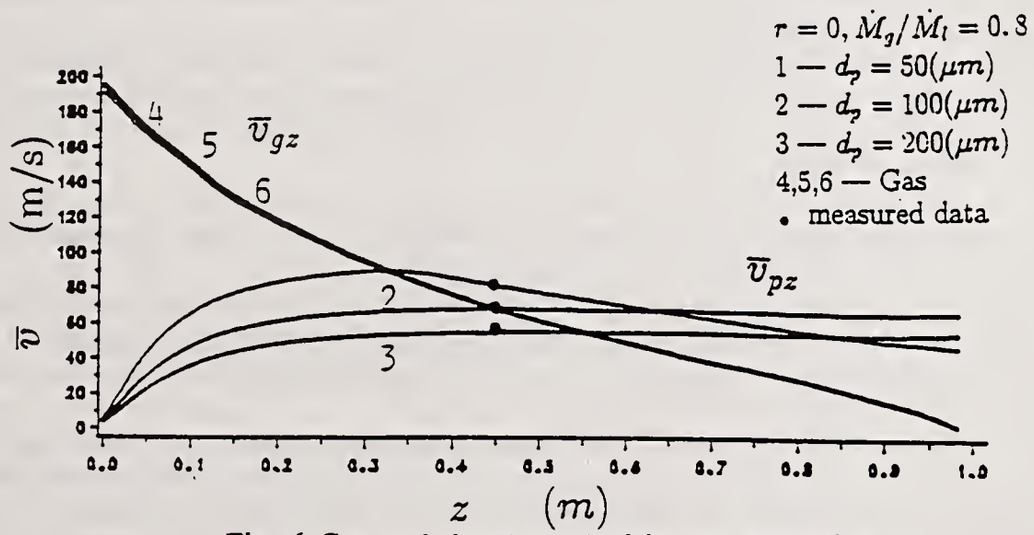

Fig. 6 Gas and droplet velocities on centerline

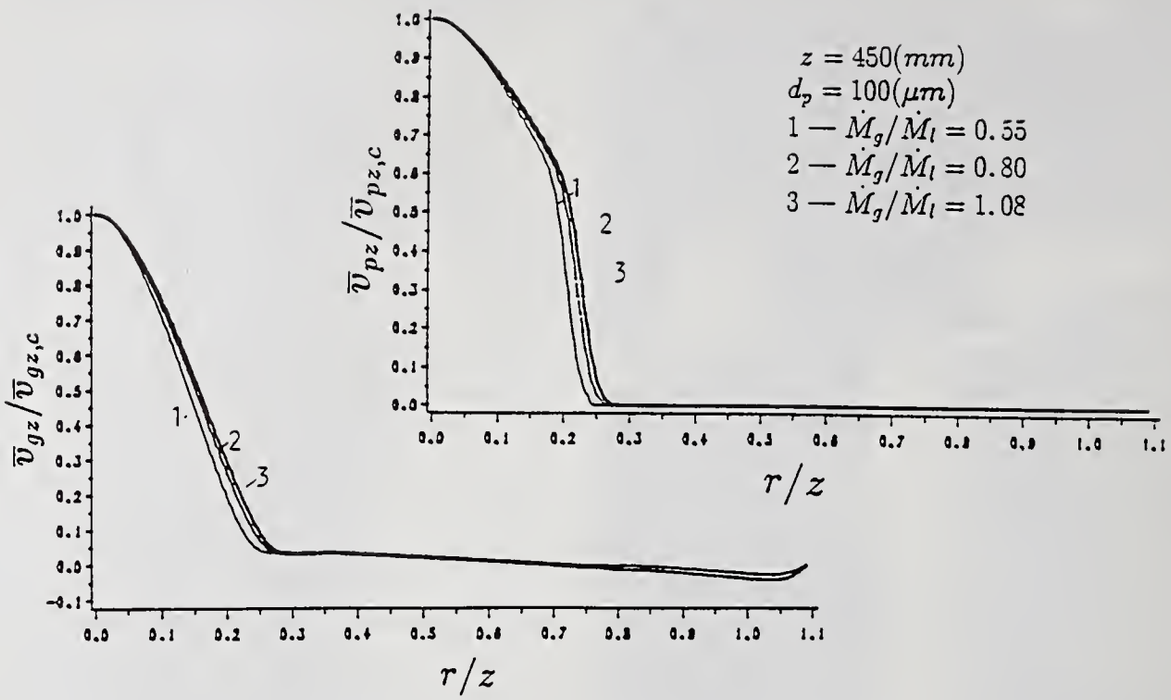

Fig. 7 Radial profiles of the gas and droplet velocities at z = 450 mm

REFERENCES

1. Apelian, D., Gillen, G. and Latham, A.: Near Net Shaped Manufacturing Via the Osprey Process, ASM Meeting, Orlando, Florida, Oct. 6-9 (1986), Proc.
2. Bauckhage K.: Das Zerstäuben als Grundverfahren, Chem.-Ing.-Tech. 62 (1990) 8; pp.613-625.
3. Rosten H.I., Spalding D.B.: The PHOENICS Reference Manual; CHAM Technical Report TR/200; London 10 (1987).
4. Patankar S.V., Spalding D.B.: A calculation procedure for heat, mass and momentum transfer in three-dimensional flows; Int. J. Heat Mass Transf. 15 (1972); pp. 1787 ff.
5. Elgobashi S.E., Abou-Arab T.W.: A two-equation turbulence model for two phase flows, Phys. Fluids 26 (1983) 4, pp. 931-938.
6. Oliver A.J.: The prediction of turbulent flow and heat transfer over backward facing steps, Computer Methods in Fluids, ed. by Morgan et al., Ondon Plymouth (1980)
7. Bradshaw P.: Turbulence, Springer-Verlag (1976).
8. Schönung, B.: Comparison of different dispersion models for particles in Lagrangian and Eulerian prediction codes, Proc. of the 2. Int. Conf. on Fluids Mechanics, China (1987).
9. Danon H. et al.: Numercial calculations of two-phases turbulent round jet, Int. J. Multiphase Flow 3 (1977), pp. 223-234.
10. Liu H.: Berechnungsmodelle für die Geschwindigkeiten und die Abkühlung von Tropfen im Sprühkegel einer Stahl-Zerstäubungsanlage, Ph.D. thesis, Univ. Bremen (1990).
11. Hirt C.W. et al.: SOLA-A Numerical Solution Algorithm for Transient Fluid Flows, LA-5852 (1975).
12. Mehrotra S.P.: Mathematical Modelling of Gas Atomization Process for Metal Powder Production; Powder Metallurgy Int.; Vol 13 No. 2 (1981) 80-84.
13. Lubanska H.: Correlation of Spray Ring Data for Gas Atomization of Liquid Metals. Journal of Metals; Feb. (1970) 45-49.

SIMULATION OF A SPRAY COMBUSTION BEHAVIOR FOR TWO KINDS OF SLURRY FUELS (Effect of Two Stage Air Introduction and Spray Characteristics on Combustion)

H. Aoki, T. Furuhata, S. Tanno, T. Miura and M. Daikoku*

Dept. of Biochemistry and Engineering, Tohoku University, Sendai, Japan
*Dept. of Mechanical Engineering, Hachinohe Technical College, Hachinohe, Japan

ABSTRACT

The effect of two stage combustion(TSC) air introduction and spray characteristics on combustion behavior was studied for two kinds of slurry fuels(pitch-water, PWM, and coal-water mixture, CWM) spray combustion system. Experiments were carried out on the isothermal flow in an acrylic duct and on the combustion flow in two different furnaces. Velocity components and fluctuations for the isothermal flow field were measured with LDA. The gas temperature, oxygen and NO concentrations in the furnace and NO and soot concentrations in the exhausted gas were measured for combustion experiments. Numerical analyses for the isothermal and combustion flow field were performed. As a result of the analysis, it was difficult to simulate the TSC isothermal air flow pattern by two-dimensional axisymmetrical analysis. For the combustion field, the NO concentration increased with the residence time of the combustion gas in the high temperature region and the soot concentration decreased with an increase of the droplet residence time in the furnace and of the oxygen concentration. For spray characteristics, the combustion efficiency was enhanced by decreasing the initial droplet velocity even if the droplet mean diameter was larger.

INTRODUCTION

A development of a high efficient combustion technology is urgently necessary to prevent the global warming and the acid rain which are caused by emission of CO_2 and of NOx and SOx, respectively. The use of low rank fuels such as pulverized coal, coke or pitch and the operation in a more severe combustion condition are required from the view point of the energy cost and the energy resources limit. The improvement of the design and operating conditions on combustion apparatus is thus needed.

One solution for these problems is to examine the combustion characteristics with the simulation method. The simulation on the liquid spray combustion system cannot be however studied enough. In this study we examine the TSC air introduction simulation method which is modeled as the axisymmetrical flow. We then study the spray combustion behavior of pitch-water mixture(PWM) and coal-water mixture(CWM) in two different furnaces and carry out the simulation of spray combustion on an axisymmetrical coordinate system using the $k-\varepsilon$ turbulence model modified with the swirling flow.

THEORY

1. Governing equations for gas phase

All time-mean transport equations in this study can be written for Cartesian geometry as;

$$\frac{\partial}{\partial x}(\rho U\phi) + \frac{1}{r}\frac{\partial}{\partial r}(r\rho V\phi) = \frac{\partial}{\partial x}\left(\Gamma_\phi \frac{\partial \phi}{\partial x}\right) + \frac{1}{r}\frac{\partial}{\partial r}\left(r\Gamma_\phi \frac{\partial \phi}{\partial r}\right) + S_\phi + Sd_\phi \qquad (1)$$

where ϕ represents the dependent variables which denote the mass(continuity), momentum(U, V, W), turbulence energy(k), eddy dissipation rate(ε), enthalpy(h), radiative heat flux(F_j, j=1,2) and mass fraction(m_i, i=soot, volatile, N_2, O_2, CO_2, CO, NO and HCN). $\Gamma\phi$ is the exchange coefficient, $S\phi$ is the source term in the gas phase and $Sd\phi$ is the source term between particle and gas phases whose coupling is estimated using the PSI cell method. We use the turbulence model modified to the swirling flow field proposed by Launder et al[1].

The flow characteristics at the wall boundary are estimated using the standard wall function model[2]. The wall temperature is given from the measurement value. The inlet conditions such as velocity components, temperatures, concentrations of gases are also given by the experimental condition.

2. Analysis of slurry droplet dynamics and reaction

2-1. Analysis of droplet dynamics

Fig.1 shows the model of the spray jet near the burner. The model of droplet dispersion is assumed that 1)the position of ejection is at the exit of the burner, and 2)droplets are already spread out in the radial direction at the tip of a core region $x=x_0$ ($x_0=6D_n$, D_n; nozzle diameter), beyond which there is no break-up or coalescence of droplets. For convenience computing the trajectories in Fig.1, let the location(x_0, r_j) be the initial point of the computation. The number fraction P_j ejected from the initial point in the total droplet numbers is expressed as;

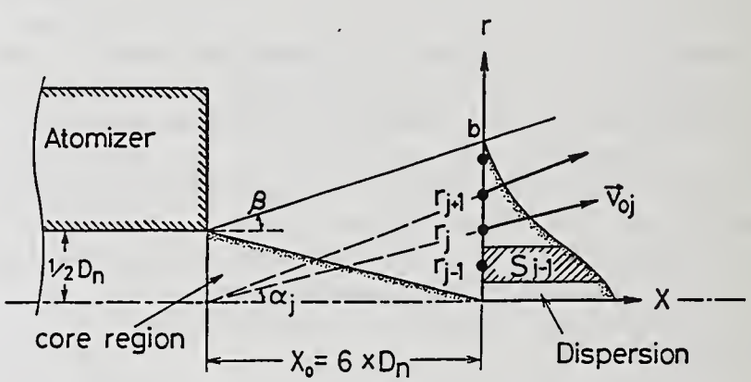

Fig.1 Spray dispersion model.

$$P_j = 2\pi S_j r_j \Delta r / M_t \qquad (2)$$

where S_j is the dispersion in the annular region between radius ($r_j - \Delta r/2$) and ($r_j + \Delta r/2$). S_j is then given by;

$$S_j = S_{max}\exp[-0.65(r_j/b)^2\{1+0.027(r_j/b)^4\}] \qquad (3)$$

which is based on the correlation for the distribution of the concentration in an axisymmetrical co-flow jet[3]. S_{max} is a normalizing constant to be determined so that S_j satisfies Eqn.(4).

$$M_l = 2\int_0^b S_j r_j dr_j \quad (4)$$

where $b(=(12\tan(\alpha)+1)D_n/2)$ is the jet radius and M_l is the liquid mass flow rate and α_j is the injection angle. If we define N as the total injected droplet number per unit time, the number rate n_{ij} of droplet having the diameter D_{pi} ejected from the core region tip is;

$$n_{ij} = P_i P_j N \quad (5)$$

where P_i is the droplet number fraction with D_{pi}, whose size is given by the logarithmic normal distribution.

2-2. Droplet reaction model The four-flux model[4] is employed to the radiative heat transfer. The gas absorption coefficient containing the soot is calculated using the mixed gray gas assumption by Hottel[5]. The formation rate of NO is calculated from both rates of thermal and fuel NO formation models which are assumed to be produced by the extended Zeldovich mechanism and the model proposed by Scott et al[6], respectively. The soot formation and its burnout in gas phase are given by the model proposed by Abbas et al[7]. The slurry droplet reaction model is shown in Fig. 2. The droplet energy equation is solved including the convective and radiative heat transfers, combustion heat release of particle and the latent heat of evaporation. The convective heat transfer rate is modified by the transfer number.

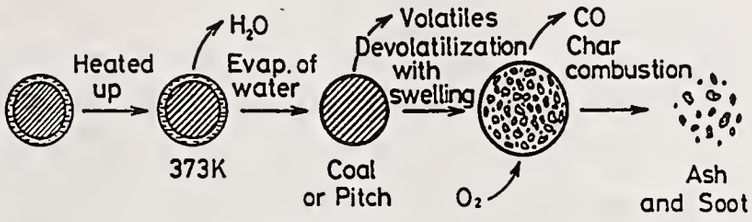

Fig. 2 Slurry droplet reaction model.

The devolatilization is computed by the single overall reaction model. The rate coefficients are given by Arrhenius expressions ($k=A\exp(-E/T)$) whose constants are quoted from another experiment for coal[8] and previously measured by a single droplet combustion experiment for pitch. Those values and experimental conditions are shown in Table 1 with the proximate and ultimate analyses of fuels.

Char burnout rate is limited by both rates of chemical reaction k_c[9] and oxygen diffusion k_d[10]. All carbons in the char are converted to CO with a heterogeneous reaction and then CO converts to CO_2 with a homogeneous reaction whose rate is controlled by the eddy dissipation model[11].

3. Numerical solution

The Lagrangian droplet equations are simultaneously integrated with Runge-Kutta-Fehlberg(RKF) method for each droplet which is divided into 7 classes in the initial ejection angle and 15 classes in the initial droplet diameter. Partial differential equations for gas phase are calculated with the method of Patankar[12].

EXPERIMENTAL APPARATUS AND CONDITION

1. Isothermal flow experiment

The acrylic duct is a 500mm I.D. x 2,000mm length geometry. Velocity components and fluctuations are measured by the two-color, three-beam type laser Doppler anemometer(DANTEC Co.) having two channel counter processors. The swirl burner is a co-axial flow type and both of primary and secondary airs flow into the duct with a tangential velocity component produced by the vanes at the burner tip. The vane angles of both air ports are fixed at 10

Table 1 Operating conditions for PWM and CWM combustion.

Species	Pitch	Coal
Proximate analysis [wt%]		
Volatile	38.9	28.37
Ash	0.22	18.03
Ultimate analysis [wt%]		
C	86.22	68.51
H	5.69	0.42
N	1.19	1.26
S	5.69	0.42
O	-	7.42
Water content [wt%]	30.0	32.0
Combustion parameters		
Devolatilization: A [s^{-1}]	3.68×10^{2}	5.50×10^{5}
E [K^{-1}]	3.30×10^{3}	9.47×10^{3}
Char combustion: A [g/cm^2s]	8710	8710
E [K^{-1}]	17980	17980
Swelling factor	3.0	1.5
Operating conditions		
Total fuel flow rate [kg/hr]	150	80
Primary air flow rate [Nm^3/hr]	102	20
Secondary air flow rate [Nm^3/hr]	1140	362
Primary air temperature [K]	283	283
Secondary air temperature [K]	423	523
Air ratio [-]	1.32	1.2

and 20 degrees whose swirl numbers are 0.12 and 0.32, respectively. The volume flow rate is fixed at 40 and 260Nm^3/hr for the primary and secondary air, respectively. TSC air flow is introduced into the duct at the axial direction x/D=0.8 to let air flow tangentially whose rate ratio to the secondary air is 30%. To estimate the accuracy of calculation in an axisymmetrical coordinate system, two different TSC air introduction methods are examined in this study, one for the practical introduction method as shown in Fig.3-(a) and another for method as modified to be an axisymmetrical coordinate system in Fig.3-(b).

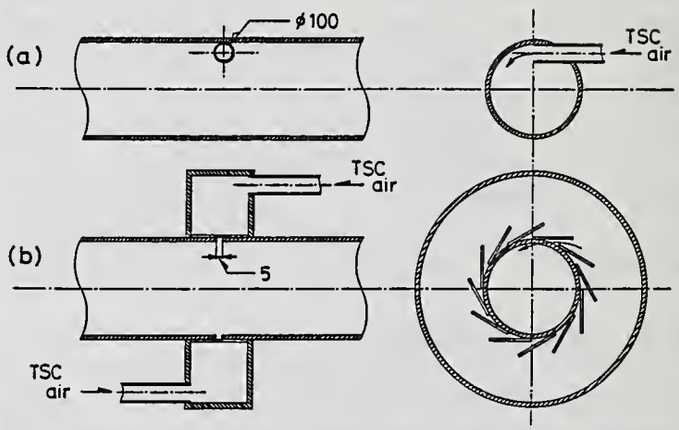

Fig.3 Experimental apparatus for isothermal flow measurement on two stage combustion air introduction.

2. PWM combustion experiment

The furnace is a 1,400mm I.D. x 5,000mm length geometry with a single burner. TSC air is introduced tangentially from the tube on the furnace side wall. The temperature and the oxygen and NO concentrations in the furnace and the NO and soot(residual carbon and soot in gas phase) concentration in the exhausted gas are measured with variations of TSC air flow rate ratio.

3. CWM combustion experiment

The furnace is a 600mm x 600mm rectangular cross section x 5,000mm length geometry with a single burner. To simplify the calculation, the furnace is modified to be a cylindrical furnace though it has a rectangular cross section. The soot(i.e. residual carbon and soot in gas phase) concentration at the furnace center line is measured using the isokinetic sampling method with variations of axial distance.

RESULT AND DISCUSSION

1. Application of TSC air introduction model

As the TSC air is usually introduced into the furnace from one or more inlet ports, it is necessary to calculate as a three-dimensional cylindrical coordinate system. However, it takes more CPU time and memory in the calculation than the two dimensional analysis. We then examine the applicability of the two-dimensional analysis to the usual TSC system.

Fig.4 shows the axial and tangential velocity profiles in the duct where the solid point, solid line and dotted line correspond to results of the measurement (method (b) shown in Fig.3) and the predictions with and without TSC air, respectively. Both measured and calculated results with TSC air are in good agreement at two different axial distances.

Fig.5 shows experimental results at two different axial distances. Measured velocity components, solid circle marks (a), tend to have non-axisymmetric velocity profiles compared with the solid line (b). It is thus necessary to apply the three-dimensional analysis to the usual TSC process flow into the furnace from one tube.

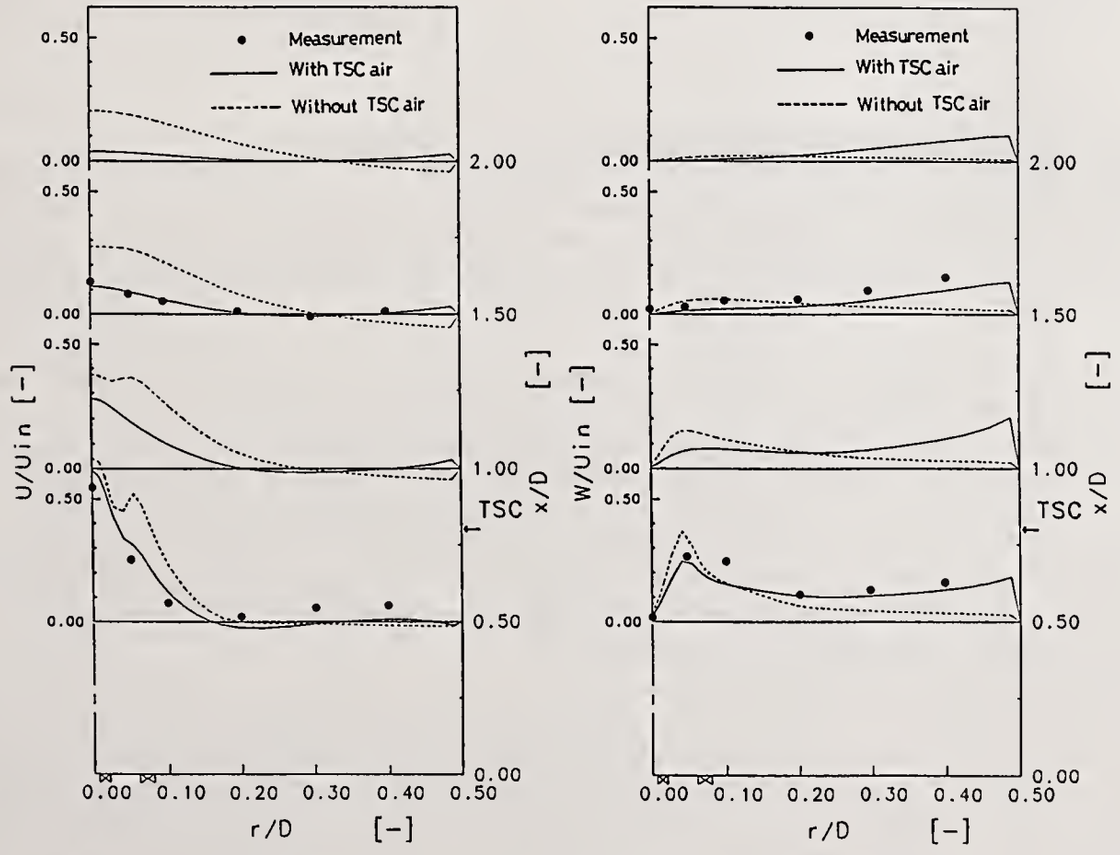

Fig.4 Measured and predicted velocity profiles in the duct for the introduction method (b).

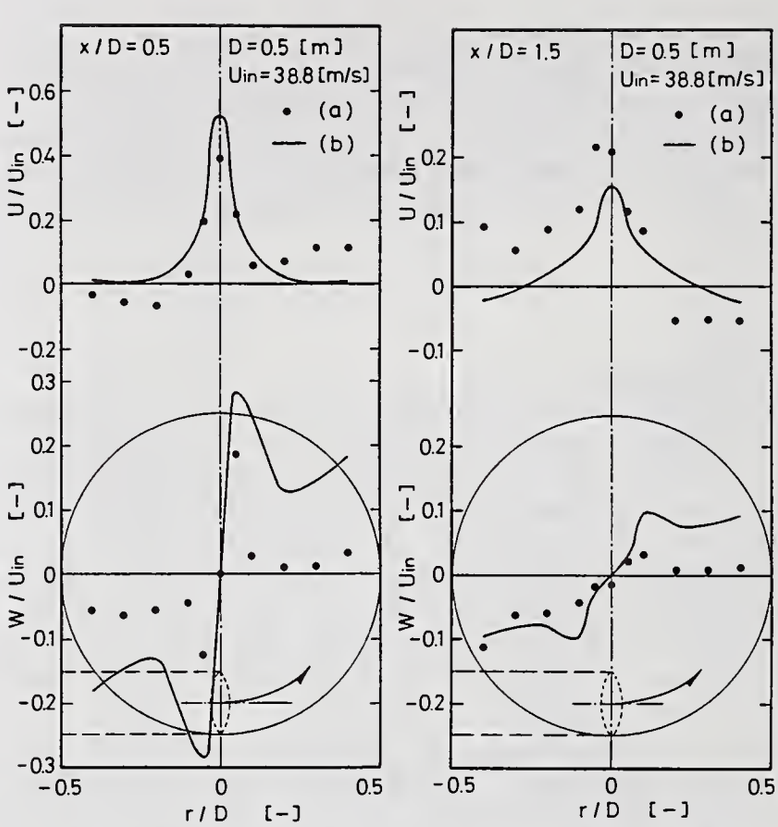

Fig. 5 Measured velocity profiles in the duct for the two different introduction methods.

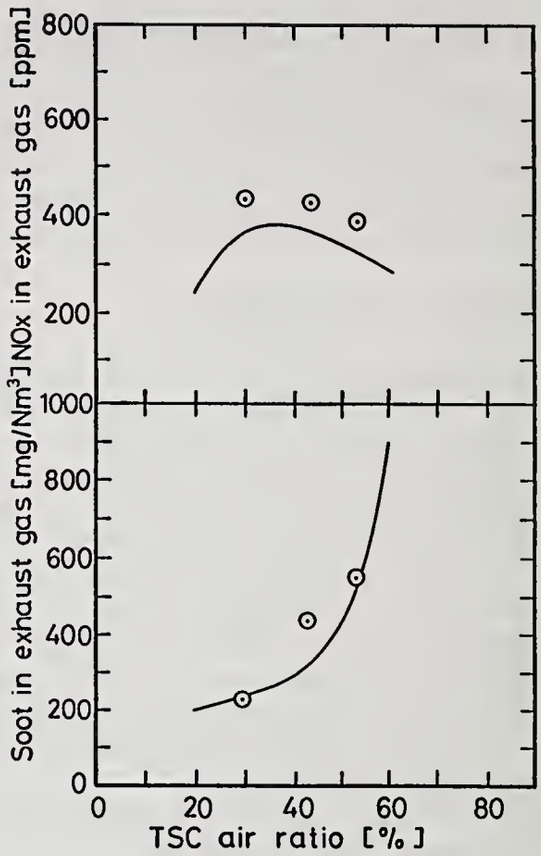

Fig. 6 Effect of TSC air flow rate ratio on NO and soot concentration in the exhausted gas.

2. Effect of two stage air flow rate ratio on combustion

Fig. 6 shows the effect of TSC air flow rate ratio to the total combustion air flow rate on NO and soot concentrations in the exhausted gas. Predicted results are in good agreement with experimental results in both NO and soot concentrations. The predicted NO concentration takes the maximum at 30% in TSC air ratio and the predicted soot concentration increases with TSC air ratio.

To confirm numerically this tendency, the gas temperature and oxygen concentration at the center line of the furnace, the droplet weight and NO concentration which is integrated over each cross section of the furnace are shown in Fig. 7. In the case of a small TSC air ratio, NO is produced downstream in the furnace as the residence time of combustion gas is short. On the contrary, in the case of a large TSC air ratio, the gas temperature decreases with an increase of the TSC air inflow rate and then the NO concentration in the exhausted gas decreases, though NO concentration increases in the high temperature region near the burner.

Soot production rate in exhausted gas nearly equals to the droplet weight since most of the soot (about 90%) are derived from residual carbon. In the case of small TSC air ratio, the oxygen near the center line of the furnace does not steeply decrease and the high temperature region is formed as the residence time of combustion gas and droplets is short, and the combustion gas is mixing well. With an increase of TSC air ratio, there is little oxygen content near the center line of the furnace, though the combustion delay time is short.

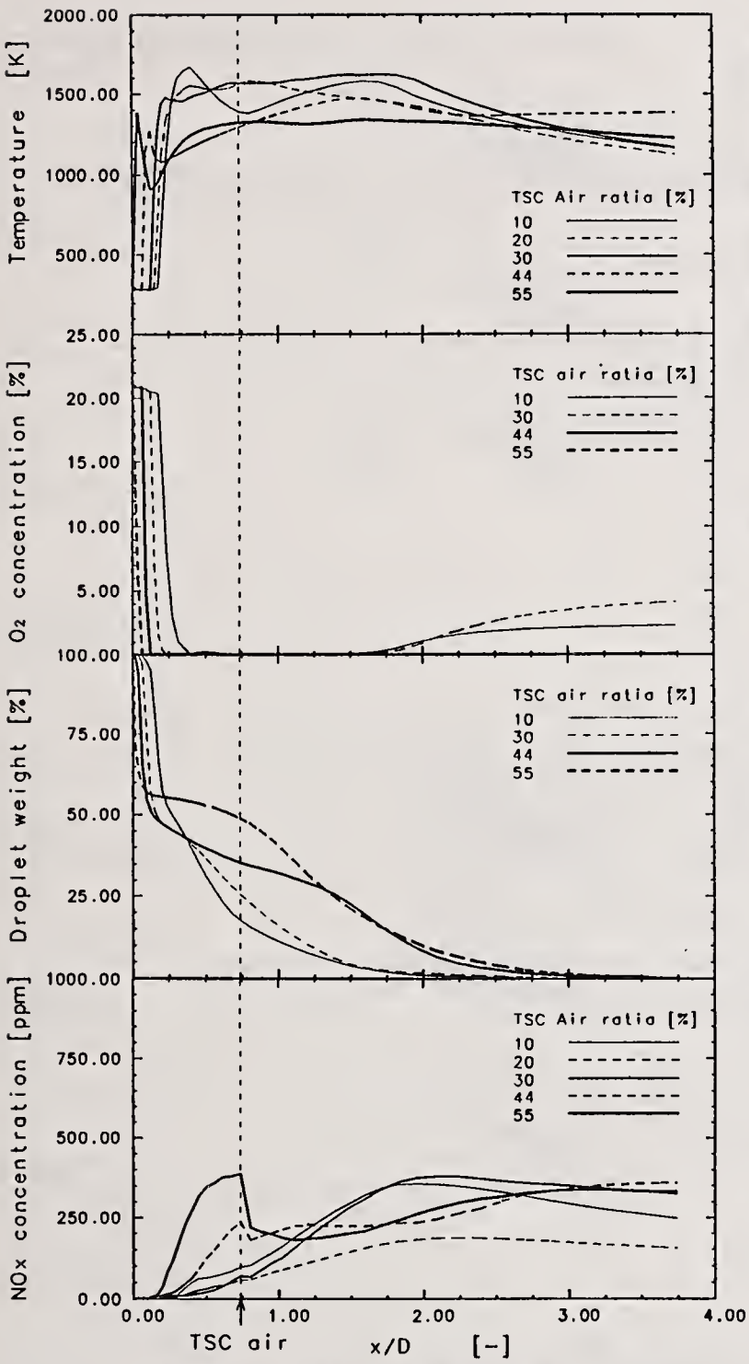

Fig. 7 Predicted gas temperature, oxygen concentration, droplet weight and NO concentration (gas temperature and oxygen concentration are shown at the center line, droplet weight and NO concentration are integrated over each radial plane.

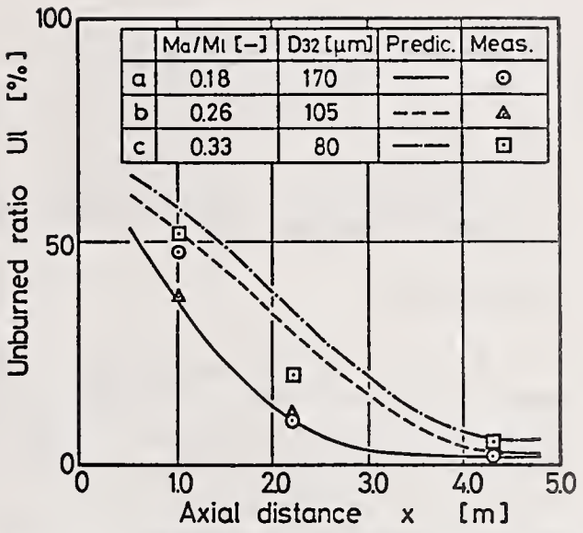

Fig. 8 Comparison of predicted and measured unburned ratio in the exhausted gas with variations of M_a/M_l.

3. Effect of spray characteristics on combustion

Fig. 8 shows the predicted and experimental unburned ratio at the furnace center line with variations of M_a/M_l. Both predicted and experimental results show that the unburned ratio is the largest in the case of the maximum M_a/M_l (initial droplet velocity is the highest) though the SMD is the smallest.

Fig. 9 shows the predicted temperature distribution in the furnace with variations of M_a/M_l. In the case of small M_a/M_l (initial droplet velocity is the lowest), the increase of gas temperature delays, however the droplet weight decreases and the high temperature region expands down-stream because of long residence time of droplets though droplets flow densely near the center line of the furnace. In the case of large M_a/M_l, the gas temperature decreases toward the down-stream due to short residence time of droplets though the high temperature region is formed near the burner.

Fig. 10 shows the predicted oxygen concentration distribution in the furnace with variations of M_a/M_l. In the case of small M_a/M_l, the combustion air is recirculated by the large recirculation flow zone which promotes the reaction of droplets and inflammable gas with oxygen. As M_a/M_l increases, the zone of low oxygen concentration expands down-stream so that the droplet and

inflammable gas continue reacting even in the outlet of the furnace. The combustion efficiency can be thus enhanced by decreasing the initial droplet velocity even if the droplet is larger.

CONCLUSIONS

A theoretical model for spray combustion of PWM and CWM on an axisymmetrical coordinate system has been described and effects of two-stage air flow rate ratio and spray characteristics on combustion behavior are studied. Summary is;

(1)It is necessary to apply the three dimensional analysis to the usual TSC process flow into the furnace from one tube.

(2)NO formation rate is mainly influenced by the combustion gas residence time in the high temperature region and the soot is mainly influenced by the gas temperature and oxygen concentration.

(3)The combustion efficiency is enhanced by decreasing the initial droplet velocity even if the droplet is larger.

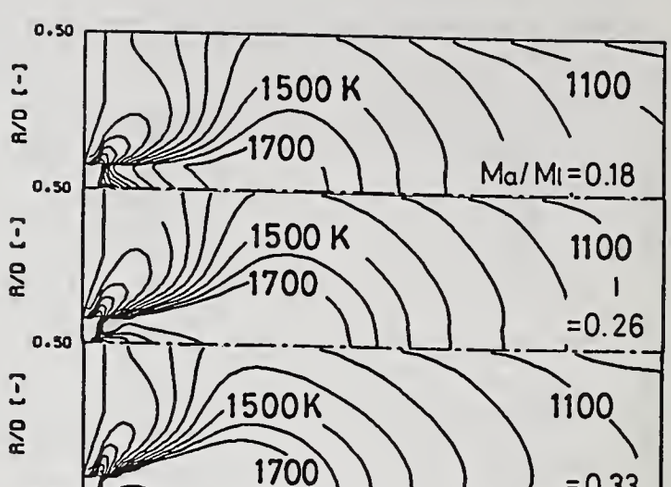

Fig.9 Predicted gas temperature distributions in the furnace with variations of M_a/M_i.

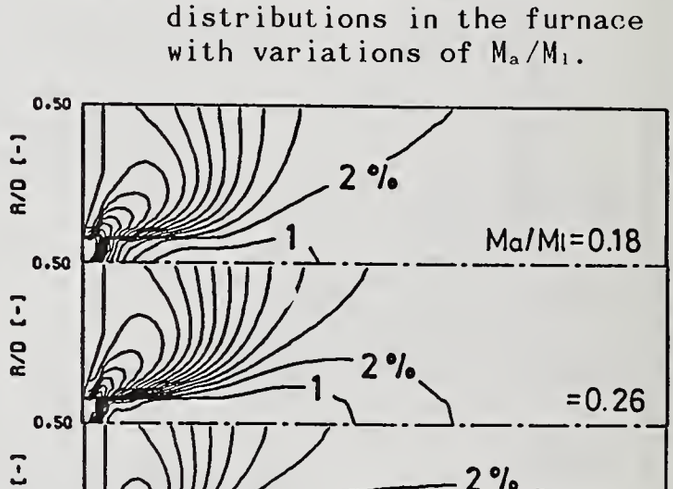

Fig.10 Predicted oxygen concentration distributions in the furnace with variations of M_a/M_i.

REFERENCES

1) Launder, B. E., C. H. Priddin and B. I. Sharma: J. Fluids Eng., 99, pp. 231-239 (1977).
2) Launder, B. E. and D. B. Spalding: Comp. Methods in Appl. Mech. and Eng., 3, pp. 269-289 (1974).
3) Rajaratnam, N.: "Turbulent Jets", Elsevier Sci. Pub. Co. (1976)
4) Gosman, A. D. and F. C. Lockwood: 14th Symp. (Int.) on Comb., pp. 661-671 (1973).
5) Hottel, H. C.: "Section in Heat Transmission", McGraw-Hill (1954).
6) Scott, C. H., L. D. Smoot and P. J. Smith: 20th Symp. (Int.) on Comb., pp. 1391-1400 (1984).
7) Abbas, A. S. and F. C. Lockwood: J. Instit. of Energy, 58, pp. 112-115 (1985).
8) Goldberg, P. M. and Essenhigh, R. H.: 17th Symp. (Int.) on Comb., pp. 145-154 (1978).
9) Field, M. A.: Comb. Flame, 13, pp. 237-252 (1969).
10) Mulcahy, M. F. R. and I. W. Smith: Rev. Pure and Appl. Chem., 19, pp. 81-108 (1969).
11) Magnussen, B. F. and B. H. Hjertager: 16th Symp. (Int.) on Comb., pp. 719-729 (1976).
12) Patankar, S. V.: "Numerical Heat transfer and Fluid Flow", Hemisphere Pub. Co. (1980).

CRYOGENIC LIQUID-JET BREAKUP IN TWO-FLUID ATOMIZERS

R.D. Ingebo

National Aeronautics and Space Administration
Lewis Research Center
Cleveland, OH, U.S.A.

ABSTRACT

A two-fluid atomizer was used to study the breakup of liquid-nitrogen jets in nitrogen, argon and helium atomizing-gas flows. A scattered-light scanner particle sizing instrument previously developed at NASA Lewis Research Center was further developed and used to determine characteristic drop diameters for the cryogenic sprays. In the breakup regime of aerodynamic-stripping, i.e., sonic-velocity conditions, the following correlation of the reciprocal Sauter mean diameter, D_{32}^{-1} , with the atomizing-gas flowrate, W_g, was obtained: $D_{32}^{-1} = k_c W_g^{1.33}$, where k_c is a proportionality constant evaluated for each atomizing gas. Values of k_c = 120, 220 and 1100 were obtained for argon, notrogen and helium gasflows respectively. The reciprocal Sauter mean diameter D_{32}^{-1} and gas flowrate, W_g, have the units of cm^{-1} and g/sec, respectively.

In the regime of capillary-wave breakup, or subsonic conditions, it was found that; $D_{32}^{-1} = k_g W_g^{0.75}$, where k_g = 270, 390 and 880 for argon, nitrogen and helium gasflows, respectively.

INTRODUCTION

The drop size of disintegrating liquid jets in low velocity airflow is controlled primarily by a capillary-wave mechanism and characteristic particle size is generally relatively large. However when a liquid jet is injected into high velocity or sonic flows, an aerodynamic stripping mechanism occurs in which the jet is disintegrated into a large number of small liquid particles, thereby producing a large liquid surface area. In this case, disintegration occurs before waves have time to form on the liquid-jet surface. The emphasis of the present study was on the mechanism of aerodynamic-stripping, in which two-fluid nozzles were used to impact liquid-nitrogen jets with argon, nitrogen and helium atomizing-gas flows.

Cryogenic liquid-jets with atomizing-gas flows injected into rocket combustors are quickly disintegrated into small-droplet sprays. In order to calculate vaporization or burning rates, it is necessary to characterize the spray in terms of drop size distribution and mean drop size such as the Sauter mean diameter. Once characteristic drop sizes are known, mathematical expressions can be derived to adequately describe a two-fluid atomization process in which

various liquid propellants and atomizing-gas combinations are used to enhance spray combustion and yield high combustor performance over a wide range of operating conditions.

Knowledge of the characteristic size of drops in sprays are also needed in experimental studies of fuel-spray combustion in diesel and other internal combustion engines and gas turbine combustors. In addition, knowledge of water sprays is needed to study the formation of ice on airfoils in icing wind tunnel experiments. In the task of characterizing sprays, detailed knowledge of the mechanics of liquid-jet disintegration is especially needed at the point of initial spray formation close to the atomizer orifice. This is especially true in the study of highly volatile cryogenic liquids. From this knowledge, accurate initial conditions can be established for modeling a fuel spray combustion process or modelling the process of ice formation on airfoils.

Numerous investigators have obtained experimental drop size data and correlated it with relative velocity, i.e., gas velocity relative to liquid velocity and also with liquid properties, as given in Refs. 1 to 7. Some of the correlations do not agree very well with atomization theory; which is generally attributed to the fact that measurement techniques and drop sizing instruments have yet to be developed and standardized to the extent that good agreement might be expected. The fluid property having the greatest effect on the drop size of sprays produced with two-fluid nozzles is the gas velocity. Although numerous investigators have studied this phenomena, the effect of gas mass flux on the drop size of cryogenic sprays has not been established in the spray literature. Therefore, the main objective of the present study was to determine the effect of atomizing-gas mass flux on liquid-nitrogen spray characteristics.

Prior to the present study, an investigation of water sprays was made with two-fluid nozzles and good agreement of experimental results with atomization theory was obtained, as discussed in Ref. 1. It was found that the Sauter mean diameter, D_{32}, could be correlated with nitrogen gas flowrate, W_n, raised to the -1.33 power, which agrees well with theoretical expressions for liquid jet breakup in high velocity gasflow. As a continuation of this study, the present investigation was initiated to extend experimental conditions to include cryogenic liquid-jet breakup in helium, argon, and nitrogen gas flows.

Two-phase flow in which transfer of momentum from low velocity and sonic gasflows to the surface of liquid-nitrogen jets was experimentally investigated by using three different atomizing gases to produce clouds of liquid-nitrogen droplets. Tests were conducted in the capillary-wave and aerodynamic-stripping regimes of disintegrating liquid jets. A scattered-light scanning instrument developed at NASA Lewis Research Center was used to measure characteristic drop diameters of the cryogenic-liquid sprays. By correcting for gas turbulence and thermal gradient effects on measurements, reproducible data was obtained with the scattered-light scanner. To avoid the loss of small liquid-nitrogen droplets due to their high vaporization rate, measurements were taken close to the nozzle orifice. The entire spray cross section was sampled with a 4.4 by 1.9 cm rectangular laser beam, at an axial distance of 1.3 cm downstream of the atomizer.

APPARATUS AND PROCEDURE

A two-fluid nozzle was mounted in the test section as shown in Fig. 1, which also shows the optical path of the scattered-light scanner. Air supplied at ambient temperature, 293 K, passed through the 15.24 cm inside diameter test section and exhausted to the atmosphere. The test section was 1 m in length

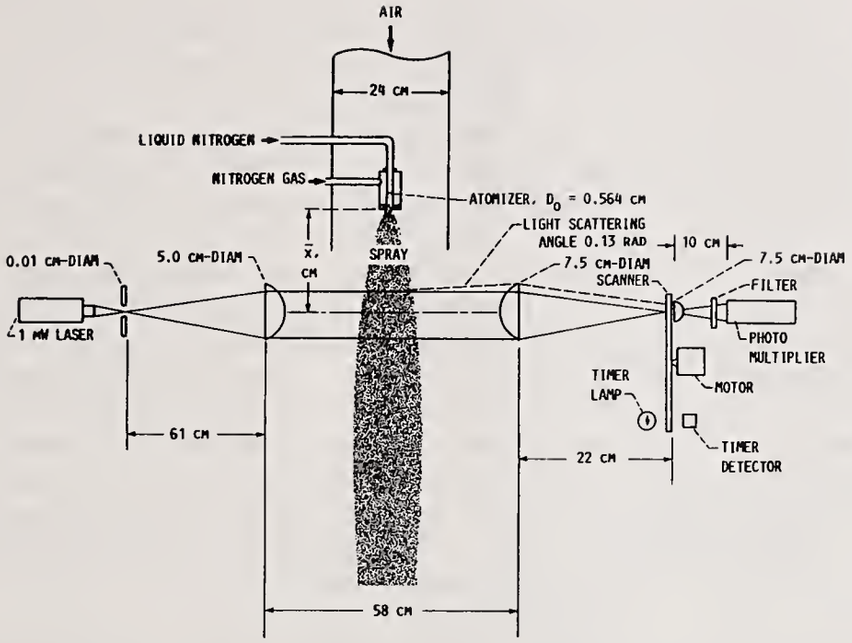

Fig. 1 Atmospheric pressure test section and optical path of scattered-light scanner.

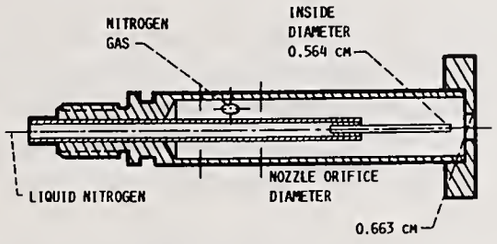

Fig. 2 Diagram of pneumatic two-fluid atomizer.

and a 5.08 cm diameter orifice was used to measure the air flowrate in the test section. A flow of dry air at a velocity of 5 m/sec was maintained in the test section to aid in transporting small droplets through the laser beam. This prevented ambient humid air from contacting the spray and thereby avoided the formation of ice particles in the laser beam.

A detailed diagram of the two-fluid nozzle is shown in Fig. 2. It was mounted in the center of the test section and operated over pressure ranges of 0.2 to 1.0 MPa for both liquid nitrogen and the atomizing gases. Liquid nitrogen sprays were injected downstream into the airflow just upstream of the duct exit. The spray was sampled at a distance of 1.3 cm downstream of the atomizer orifice with a 4.4 by 1.9 cm rectangular laser beam produced by the 0.01 cm diam aperture shown in Fig. 1.

Liquid nitrogen, LN_2, at a temperature of 77 K measured with an I.C. thermocouple, was axially injected into the airstream at a flowrate of 27.5 g/sec, as indicated by a turbine flow meter. The atomizing gas was then turned on to break up the LN_2 jet and weight flow rate was measured with a 0.51 cm diameter sharp-edge orifice. After the air, atomizing-gas and LN_2 flow rates were set, characteristic drop diameters were determined from measurements made with the scattered-light scanner.

The optical system of the scattered-light scanner is shown in Fig. 1. The instrument measures scattered-light as a function of scattering angle by repeatedly sweeping a variable-length slit in the focal plane of the collecting lens. The data obtained is scattered-light energy as a function of the scattering angle relative to the laser-beam axis. This method of particle size measurement is similar to that given in Ref. 8 and it is described in detail in Ref. 9. Calibration was accomplished with five sets of monosized polystyrene spheres having diameters of 8, 12, 25, 50 and 100 μm. Since the sprays were sampled very close to the atomizer orifice, they contained a relatively high number of very small drops. As a result, the light-scattering measurements required correction for multiple scattering as described in Refs. 9 and 10 for the case of high concentrations of droplets. Drop size measurements were also corrected as described in Ref. 9 to include Mie scattering theory when very small characteristic droplet diameters, i.e., <10 μm, were measured.

Atomizing-gas temperatures were approximately 293 K and surface temperatures of the liquid-nitrogen jets were always near the boiling point of liquid-nitrogen, i.e., approximately 77 K. This created large temperature gradients that deflected the laser beam and caused beam steering to occur. However, by carefully adjusting the laser beam away from the slit in the scattered-light scanner optical system, the effect of beam steering on measurements was negligible.

EXPERIMENTAL RESULTS

As shown in Fig. 1, the entire spray cross section was sampled at an axial distance of $\bar{x}$ = 1.3 cm downstream of the two-fluid atomizer orifice. Values of the Sauter mean diameter, D_{32}, and reciprocal SMD, D_{32}^{-1}, are plotted against atomizing-gas flowrate as shown in Fig. 3. Tests were conducted over a relatively wide range of atomizing-gas flowrates that included both subsonic and sonic gas-velocity conditions.

At relatively low or subsonic atomizing-gas flow conditions, breakup of the LN_2 jets occurred primarily in the capillary-wave regime of atomization

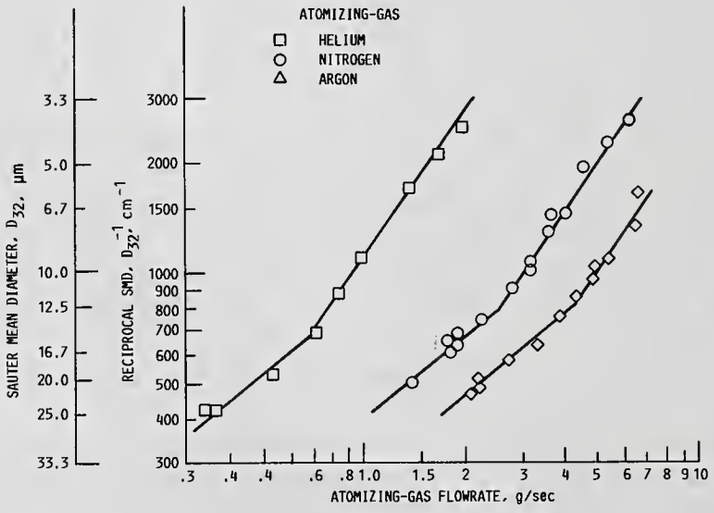

Fig. 3 Correlation of Sauter mean diameter with atomizing-gas flowrate.

Table 1 Proportionality constant, k, and gas flowrate exponent, x, for correlating expression:

$$D_{32}^{-1} = k\, W_g^x$$

Breakup regime	Argon	Nitrogen	Helium
Capillary-wave:			
k_g, constant	270	390	880
x, exponent	0.75	0.75	0.75
Aerodynamic-stripping:			
k_c, constant	120	220	1100
x, exponent	1.33	1.33	1.33

and the following general correlation of D_{32}^{-1} with gas flowrate, W_g, was obtained:

$$D_{32}^{-1} = k_g W_g^{0.75}$$

where the reciprocal SMD and gas flowrate are expressed as cm^{-1} and g/sec, respectively. The correlating constant k_g = 270, 390 and 880 when argon, nitrogen and helium, respectively, were used to atomize the LN_2 jets. The exponent 0.75 for W_g is approximately 10 percent higher than the 2/3 exponent given for gas velocity in the theoretical expression reported in Ref. 11.

In regime of aerodynamic-stripping or sonic-velocity atomizing-gas flow conditions, the following expression was obtained:

$$D_{32}^{-1} = k_c W_g^{1.33}$$

where the correlating constant k_c = 110, 220 and 1100 when argon, nitrogen and helium, respectively were used as atomizing gases. The exponent 1.33 for W_g is the same at the 4/3 exponent given for gas velocity in Ref. 11. Thus, good agreement with atomization theory was obtained in the regime of aerodynamic stripping conditions.

Transition from the regime of capillary-wave breakup to that of aerodynamic-stripping occurred at values of D_{32}^{-1} = 700 cm^{-1} or D_{32} = 15 μm, approximately, for the atomizing gases used in the present study. Values of k_c and k_g are given in Table 1.

CONCLUDING REMARKS

The fluid mechanics of liquid-nitrogen jet breakup is much more difficult to study than the atomization of fuel or water jets. This is primarily due to the fact that surface temperatures of the liquid-nitrogen jets used in the present study were always near the boiling point of liquid nitrogen, i.e., approximately 77 K. Since the atomizing gases were at room temperature, approximately 293 K, this created large temperature gradients that deflected the laser beam and caused beam steering to occur as characteristic drop diameter was measured with the scattered-light scanner. This problem was minimized in the present investigation by moving the laser beam away from the slit in the scattered-light scanner optical system.

REFERENCES

1. Ingebo, R.D., "Experimental and Theoretical Effects of Nitrogen Gas Flow-rate on Liquid-Jet Atomization," Journal of Propulsion and Power, Vol. 4, No. 6, Nov.-Dec., 1988, pp. 406-411.

2. Kim, K.Y. and Marshall, W.R., Jr., "Drop Size Distributions from Pneumatic Atomizers," AIChE Journal, Vol. 17, No. 3, May 1971, pp. 575-584.

3. Lorenzetto, G.E. and Lefebvre, A.H., "Measurements of Drop Size on a Plain Jet Airblast Atomizer," AIAA Journal, Vol. 15, No. 7, July 1977, pp. 1006-1010.

4. Nukiyama, S. and Tanasawa, Y., "Experiments on the Atomization of Liquids by Means of a Air Stream, Parts III-IV," Transactions of the Society of Mechanical Engineers, Japan, Vol. 5, No. 18, Feb. 1939, pp. 63-75.

5. Weiss, M.A. and Worsham, C.H., "Atomization in High Velocity Airstreams," American Rocket Society Journal, Vol. 29, No. 4, Apr. 1959, pp. 252-259.

6. Wolf, H.E. and Andersen, W.H., "Aerodynamic Break-up of Liquid Drops," Proceedings of the 5th International Shock Tube Symposium, Z.I. Slawasky, J.F. Moultin, Jr., and W.S. Filler, eds., Naval Ordnance Lab., White Oak, MD, 1965, pp. 1145-1169. (Avail. NTIS, AD-638011.)

7. Ingebo, R.D., "Fuel Spray Simulation With Two-Fluid Nozzles," AIAA Paper 89-0053, July 1989 (also, NASA TM-101367, 1988).

8. Swithenbank, J., Beer, J.M., Taylor, D.S., Abbot, D., and McCreath, G.C., "A Laser Diagnostic Technique for the Measurement of Droplet and Particle Size Distribution," in Experimental Diagnostics in Gas Phase Combustion Systems," B.T. Zinn and G.T. Boulman, eds., Progress in Astronautics and Aeronautics, Vol. 53, AIAA, New York, 1977, pp. 421-447.

9. Buchele, D.R., "Particle Sizing by Weighted Measurements of Scattered Light," NASA TM-100968.

10. Felton, P.G., Hamidi, A.A., and Aigail, A.K., "Measurement of Drop Size Distribution in Dense Sprays by Laser Diffraction," in ICLASS-85; Proceedings of the Third International Conference on Liquid Atomisation and Spray Systems, P. Eisenklam and A. Yule, eds., Institute of Energy, London, 1985, Vol. 2, pp. IVA/4/1-IVA/4/11.

11. Adelberg, M., "Mean Drop Size Resulting from the Injection of a Liquid Jet Into a High-Speed Gas Stream," AIAA Journal, Vol. 6, June 1968, p. 1143-1147.

EFFECT OF AIR SWIRLERS ON ATOMIZATION AND SPRAY FLAME STABILITY

C.-P. Mao

Delavan Inc.
West Des Moines, IA, U.S.A.

ABSTRACT

This study investigated the effect of outer air swirlers on atomization and stability performance of spray flames. In airblast atomizers, the outer swirler controls the air effective area and spray angle. Thirteen different air swirlers were used to examine the importance of air effective area and spray angle. It was found that a wider spray angle produced smaller mean drop sizes and better stability. For a given spray angle, an increase in air effective area resulted in further improvement in spray quality and stability limits. However, spray angle had a more significant effect on stability performance than the air effective area.

INTRODUCTION

The advantages of swirl flow in gas turbine engine systems have long been recognized. The proper use of swirling flow in combustors provides better fuel/air mixing, improves combustion efficiency, stabilizes the spray flame, and reduces pollutant emissions.

The flow characteristics produced by swirler systems in combustors have been studied by many researchers. Gupta et al [1] summarized various aspects and applications of swirl aerodynamics. However, there is insufficient information about the effect of air swirlers used in the fuel injectors on atomization and spray flames.

In advanced gas turbine engines, the fuel injectors are required to operate over a wide range of conditions. Their performance is especially critical for aircraft engines which must function in harsh and abnormal environments. Air swirler design can play a very important role in determining the performance of fuel injectors. Several investigators [2-4] have reported the effect of airblast nozzle swirlers on atomization. Mao [2] concluded that they have a significant effect on mean drop size and spray angle. Generally, a wider spray angle is associated with finer droplets. In a later study [5], it was found that the air swirler design in atomizers can also have a significant impact on spray flame stability.

Turbine combustors often encounter flame-out problems during engine acceleration because of the rich mixture produced by the fuel injectors. Therefore, one of the primary requirements in aircraft engines is to ensure that spray flames can be sustained over a wide range of fuel and air flows. The air swirler helps control the structure of the spray flame. It was noted that an optimized swirler not only provides good flame stability, but also improves performance during ignition and altitude relight conditions.

The present study examines the effect of air swirler design on atomization and spray flame stability. The structure of the sprays produced by different swirlers will be analyzed to determine its influence on the flame.

TEST METHODS

A conventional method [6] of evaluating spray flame stability is to gradually increase or reduce the fuel flowrate at a fixed air flow condition to establish the flame extinction limits. This process is repeated at increasing levels of air flow, until the complete stability loop can be determined.

Our study selected a slightly different approach. The air flow was gradually increased or decreased at a fixed fuel flow condition to determine the lean and rich limits. The process was then repeated at several different fuel flowrates. This approach was chosen simply because our experimental setup allowed us to change the air flow more easily than the fuel flow.

A prefilming airblast atomizer was selected for our study. The fuel sheet produced by the atomizer was sandwiched between a non-rotating central air jet and a swirling outer air stream. The outer swirler and the air gap were the primary design variables of interest. There are a number of parameters which designers can manipulate to provide different swirl flow characteristics. For a typical air swirler with helical vanes, these parameters include vane angle, slot depth and cutter width. By varying these design parameters, wide ranges of spray angle and air effective area could be attained.

Since the air effective area and the spray angle are two of the primary dependent variables in the swirler design for a given nozzle envelope, it was only necessary to vary the air gap and the slot dimensions in the outer swirler. Table I summarizes the swirler parameters.

During the study, photos were taken to measure the spray angles. An Aerometrics Phase/Doppler Particle Analyzer was used to make detailed measurements of drop size and velocity. Combustion tests were also conducted to determine the stability limits of the spray flames.

RESULTS AND DISCUSSION

Effect of Outer Swirlers on Air Effective Area and Spray Angle.

Air flowrate measurements were made for all swirlers to find their effective areas. The air pressure drop across the nozzle was varied within the range between 1.2 and 55 kPa. Spray angle measurements were obtained at fuel pressures of 69, 138 and 276 kPa.

From Table I, we can perceive systematic variations in the air effective area, CdA, and the spray cone angle when the air gap and the slot dimensions are changed. For the same swirler slot width and depth, the effective area and spray angle increased with an increase in the air gap. It also appears that, for a fixed air gap, a smaller slot dimension would generally produce a smaller CdA and a wider spray angle.

Both the air effective area and spray angle play a very important role in determining the spray structure in the combustors. From an aerodynamic standpoint, they not only affects fuel atomization, but also control the characteristics of the spray flames.

Effect of CdA and Spray Angle on Spray Structure

An Aerometrics Phase/Doppler Particle Analyzer was used to make detailed measurements in sprays. This unit was recalibrated using a single-drop generator to obtain new separation distances between the three detectors in the instrument. The original distances specified by Aerometrics were found inappropriate for drops larger than 200 microns.

The primary parameters used for examining the structural differences in sprays included distributions of drop Sauter mean diameter (SMD), axial velocity, and volume flux. All measurements were made at a 5-cm distance downstream from the nozzle face. The nozzle was traversed in 0.5-cm increments from one boundary to the other along the major diameter. The radial distributions of the parameters were then plotted.

For a given swirler, the spray structure gradually changed as the flow operating conditions were varied. Using Swirler No. ll, the effect of increasing the fuel flowrate on SMD and axial velocity at a fixed air pressure drop of 6.9 kPa is shown in Figs. 1-2.

In airblast atomizers, it is typical that the SMD increases and the spray angle decreases with an increase in the fuel pressure when the air flow is maintained at a constant value. The increase in fuel pressure reduces the relative velocity between the liquid and air phases. Hence, atomization becomes poorer and drop size increases. Meanwhile, the higher fuel flow also increases the mean axial velocity of the drops, resulting in a narrower spray angle.

Shown in Fig. 2, there was a significant change in the velocity profile as the fuel pressure increased from 69 to 276 kPa. At 276 kPa, the droplets located in the center core of the spray had the maximum axial velocity. However, at 69 and 138 kPa, the velocity profiles were characterized by a double peak. Two apparent maximum velocities appeared at the center area of the sprays. It is very common in a swirling flow that the velocity profile undergoes a transition from a double-peak to a single-peak mode as the fuel flow increases. This is primarily associated with the change of spray angle and relative magnitude between axial and swirling velocities. This type of structural change has a serious impact on spray flames. The next section will discuss what type of spray structure is most beneficial in engine combustors.

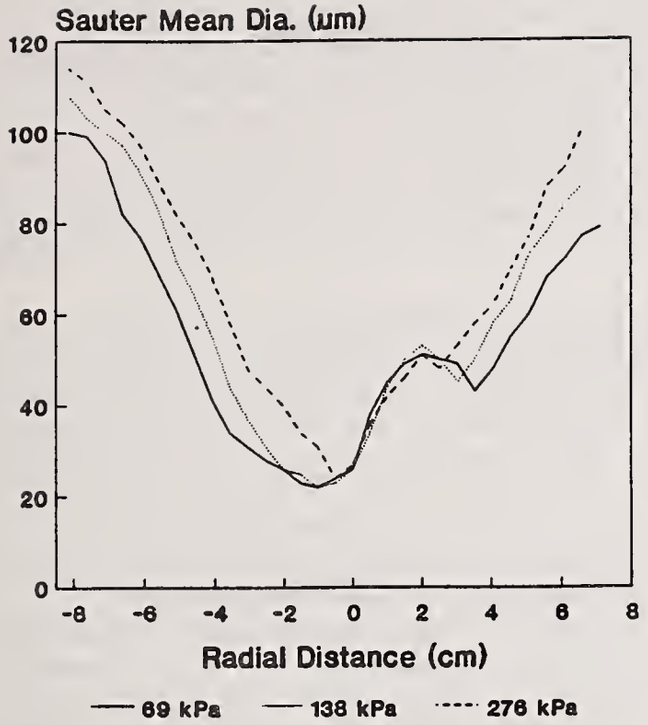

Fig. 1 Effect of increasing fuel flowrate on the radial distribution of Sauter mean diameters for air swirler No. 11. Air pressure drop was at 6.9 kPa.

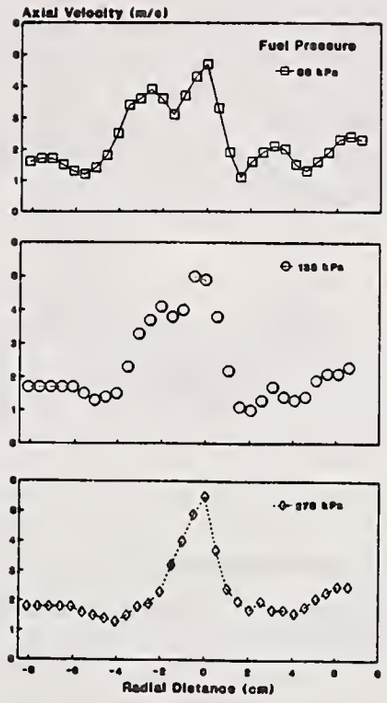

Fig. 2 Effect of increasing fuel flowrate on drop axial velocity distribution for air swirler No. 11. Air pressure drop was at 6.9 kPa.

To observe the effect of spray angle on spray structure, it is necessary to maintain a constant air effective area (CdA). Swirlers 4, 7 and 13 were selected for a comparative study. These three swirlers have about the same CdA (17.4 mm^2), but different spray angles.

Fig. 3 shows a comparison of the radial SMD and drop axial velocity distributions for the three swirlers at a fuel pressure of 276 kPa and an air pressure of 6.9 kPa. At the same CdA and radial distance, the SMD decreased with an increase in spray angle. Swirler No. 13 had the widest spray angle (124°), and the smallest mean drop size at most of the sampling locations.

The shape of the velocity profile changed from a double-peak to a single-peak mode as the spray angle decreased. With the same CdA, it was surprising to note that the maximum drop velocity could be tripled by reducing the spray angle from 124° to 81°. This clearly demonstrates that the design of the outer air swirler can control the spray structure.

It was also of interest to examine the effect of the air effective area, CdA, on spray structure when the spray angle remained constant. Swirlers 5 and 12 were selected for comparison. These two swirlers produced about the same spray angle at a fuel pressure of 276 kPa and air pressure of 6.9 kPa. Swirlers 5 and 12 have effective areas of 18.7 and 14.8 square mm, respectively.

Fig. 4 shows the radial distributions of SMD and axial velocity for the two swirlers. The increase in the effective area had a very minimal effect on the mean drop size and only increased the velocity in the center area. The shape of the velocity profile remained about the same, primarily because the spray angle did not change. In some other cases, (e.g., Swirlers 3 and 11), similar results were observed.

For a given air swirler design, Fig. 5 demonstrates the effect of the air gap on spray drop size and velocity. Swirlers No. 1, 2 and 3 were chosen to examine this effect. For the same slot dimension, a larger air gap increased both CdA and the spray angle. As indicated in Fig. 5, a larger gap produced a wider spray angle and a smaller mean drop size.

The drop velocity was affected differently by the air effective area and spray angle. Although an increase in CdA generally increased the drop velocity, an increase in the spray angle reduced the velocity. In Fig. 5, the spray angle seems to have a dominant effect on the velocity profile. A wider spray angle produced a double-peak velocity profile, whereas a narrow spray angle produced a single-peak velocity profile.

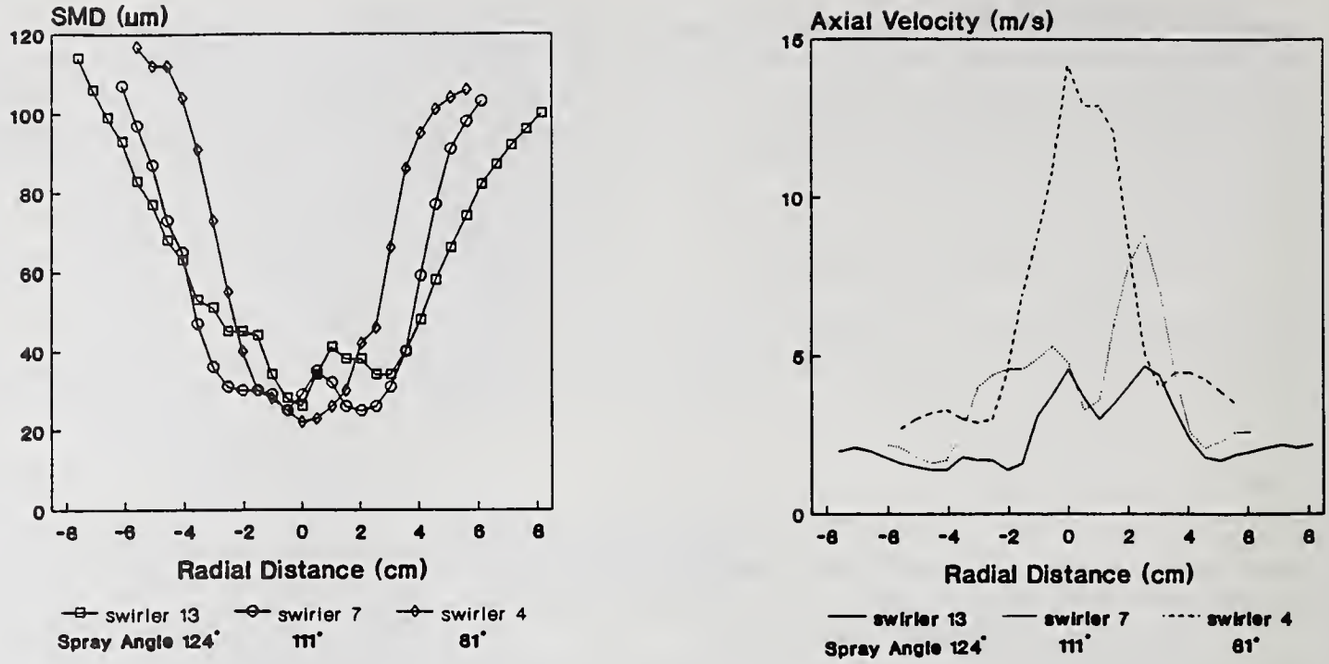

Fig. 3 Effect of spray angle on radial SMD and drop mean axial velocity distributions as the spray angle increases. All swirlers have the same CdA.

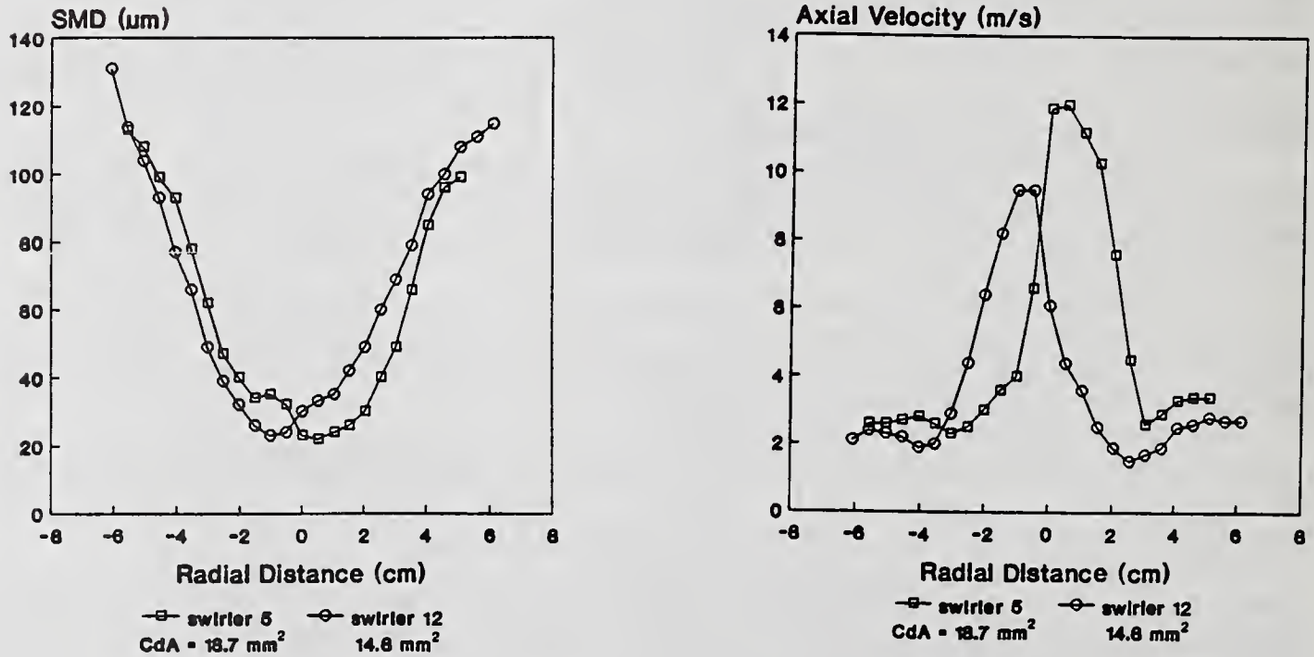

Fig. 4 Effect of air effective area CdA on the radial SMD and drop axial velocity distributions. Spray angle maintained the same value.

As the air gap increased, the shape of the velocity profile shifted from a single-peak to a double-peak mode, and the maximum velocity decreased. It will be demonstrated later that a double-peak velocity profile is desirable in combustors. This type of spray structure can sustain the flame over a wider range of air flows.

After comparing all of the swirler designs, an important result was derived from the spray structure measurements. That is, the structure appears to be the same if the air effective area and spray angle remain constant. What remains to be examined is whether quality of the combustion will also be similar? It will also be of great interest to determine whether the spray angle or the CdA plays the greater role in affecting the stability spray flames.

Effect of Spray Angle and Air Effective Area on Spray Flame Stability

One of the primary goals of the present study was to optimize the air swirler designs for better stability performance. From the preceding analysis, spray angle and air effective area appeared to be the significant variables. For a given CdA and spray angle, however, the spray structure seemed to be independent of the air swirler dimensions. Therefore, the flame stability study will be focused on CdA and spray angle rather than dimensional differences.

Flame stability was evaluated from the lean and rich limits observed for several different fuel flowrates. As in the spray structure analysis, spray angle and CdA were varied.

The rich and lean limits were determined for each swirler using the test method described earlier. At a fixed fuel pressure, the rich limit was determined by reducing air flow to the extent when flame extinguishes. Because the air flowrates were uncertain near the lean limits, the extinction criterion was that the spray flame has to stay alight for at least one minute. The air flow was further increased until it met the above criterion to find the actual lean limit. After establishing the limits, the results were plotted as fuel/air ratio vs. air flowrate.

At a fixed fuel flow, an increase of air flow will typically reduce the spray angle and push the flame front away from the nozzle face. Because the flame is confined within the spray boundary, blow-out ultimately occurs when the flow velocity exceeds the flame speed.

Fig. 6 shows typical flame stability ranges at several fuel flow conditions. As the fuel pressure increased, there was a greater separation between the rich and lean limits. This indicates that fuel nozzles may operate over a wider range of air flows without flame-out problems at higher flowrates. For all swirlers, the lean limits vary significantly, depending upon the spray angle and CdA. However, the rich limits do not vary significantly.

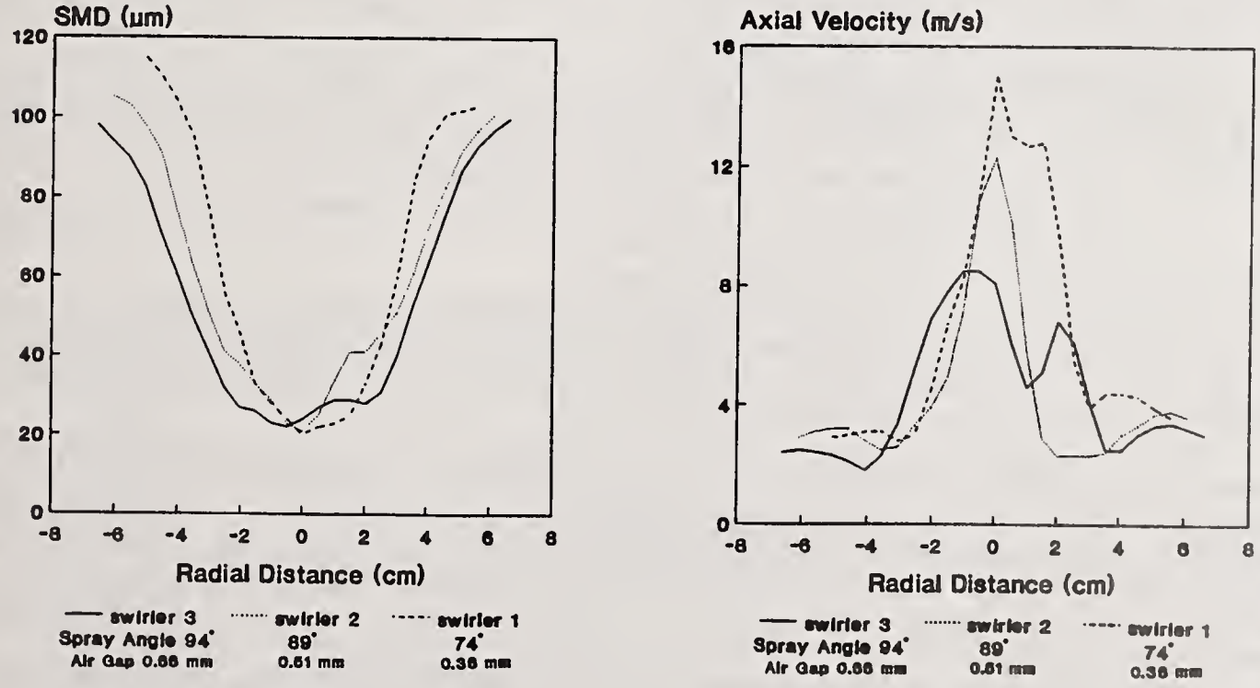

Fig. 5 Effect of increasing air gap on radial SMD and drop axial velocity distributions. Fuel pressure was 276 kPa and air pressure was 6.9 kPa.

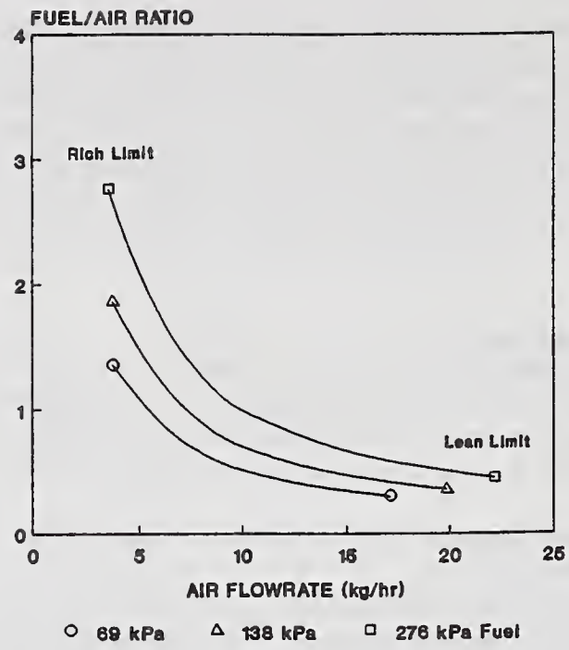

Fig. 6 Spray flame stability limits for air swirler No. 8 at a fixed fuel flowrate of 69, 138 and 276 kPa.

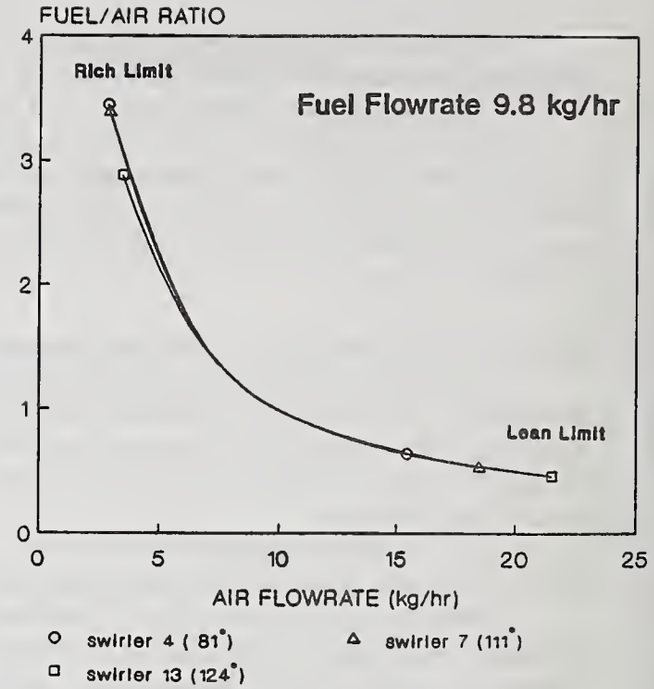

Fig. 7 Comparison of flame stability limits at increasing spray angle under the same air effective area.

It would be desirable to determine those spray characteristics which will produce a stable flame over a wide range of air flow conditions.

The range of air flowrates required for good flame stability will be determined for several different spray angles. Fig. 7 shows a comparison of stability limits for several swirlers at a fixed CdA. At the same fuel flow rate, the swirler that produced the widest spray angle showed the widest range of stability limits. That is, the spray flame sustained without extinction over the widest range of air flow conditions. Swirler 13 had the widest spray angle and the best performance in flame stability.

The above results can be easily explained using the spray structure shown in Fig. 3. Because of its wide spray angle, Swirler No. 13 produced the smallest mean drop size. In addition, its velocity profile showed a favorable double peak where the low velocity drops reside in the center core of the spray. This type of velocity profile favors a central recirculation zone for anchoring the spray flames.

On the other hand, Swirler No. 4 had a very narrow spray angle. Its velocity profile is characterized by a single-peak where the maximum velocity is located near the center of the spray. This maximum velocity can easily exceed the speed of the flame and cause its extinction.

The importance of the air effective area on the performance of combustors has long been recognized by engine manufacturers. Because variations in CdA are usually associated with changes in spray angle, it is difficult to identify which parameter is more important. Hence, the effect of CdA was examined using air swirlers that produced the same spray angle.

In the following case, Swirlers No. 5 and 12 were compared in Fig. 8. The data indicate that the air flowrate range required for a stable flame is slightly wider for the swirler with higher CdA. This result seems to contradict what is assumed by many engine designers; namely, that a lower CdA will produce better performance from the standpoint of flame stability limits. In fact, for a fixed spray angle, a decrease of CdA further reduced the range of stability limits. Hence, the observed performance may actually be due to the wider spray cone angle. As indicated in Table I, for a given air gap, a reduction of CdA resulted in an increase in spray angle.

According to Fig. 4, the primary characteristics of the spray structure for swirlers 5 and 12 are similar because the spray angle was about the same. The effect of a larger CdA was a higher average drop velocity and a slightly reduced mean drop size. The improvement in stability limits is probably caused by the reduction in drop size rather than the increased drop velocity. In addition, the local fuel concentrations have increased so as to favor the sustention of flames.

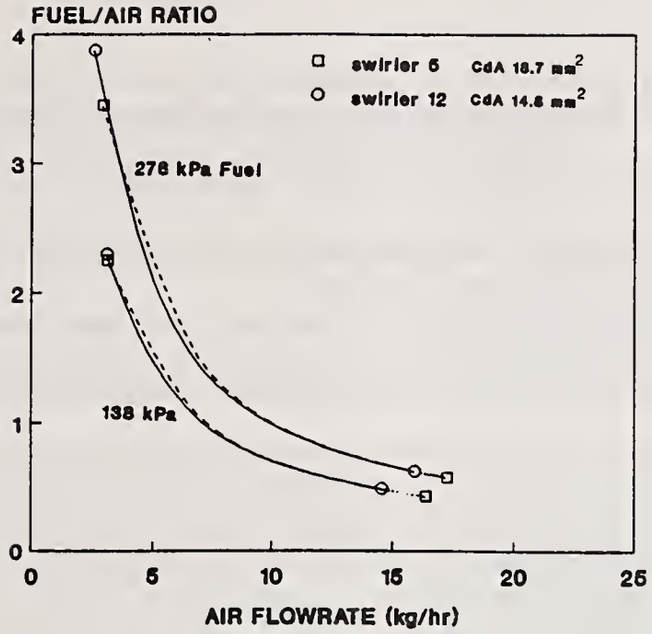

Fig. 8 Comparison of flame stability limits by increasing CdA at several fuel flow conditions under the same spray angle.

The above results indicate that the spray angle has a significant effect on the stability limits of the flame. An increase in spray angle and CdA would result in improved stability. However, these two parameters have a contrary effect on drop velocity. That is, an increase in spray angle decreases drop velocity but an increase in CdA increases velocity.

In terms of spray structure, a wide spray angle provides a favorable velocity profile characterized by a double-peak mode. A higher CdA produces smaller drops but an unfavorable drop velocity profile. In addition to drop size and velocity, it is also important to take into account the volume flux distribution. A higher volume flux generally extends the range of flame stability limits.

SUMMARY

The following major conclusions can be drawn from this study:

1. The air swirler design affects the air effective area (CdA) and the spray angle. These two parameters determine the structure and stability of the spray flames.
2. For any given CdA and spray angle, the air swirler design has little effect on spray structure and flame stability.
3. A wide spray angle appears to allow the spray flame to stay alight over a wider range of air flow conditions.
4. The air effective area has a less significant effect on spray flame stability limits than that of the spray angle. However, for a given spray angle, an increase in CdA will result in a further improvement in stability limits.
5. Although smaller drops and low velocity produce a more stable flame, the local drop concentration also plays important role in determining the stability limits. A higher drop concentration means a more stable flame.

REFERENCES

1. Gupta, A. K., Lilly, D. G. and Syred, N., Swirl Flows, Abacus Press, 1984.
2. Mao, Chien-Pei, "Effect of Air and Fuel Swirlers on Atomization", Delavan Inc, Technical Report 562, August 1990.
3. Martin, C. A., "Air Flow Performance of Air Swirlers for Gas Turbine Fuel Nozzles", ASME Paper No. 88-GT-108, 1998.
4. Martin, C. A., "Leading Edge Vortex Generation and Its Application to Twin Fluid Atomization Nozzles", Ph.D. Thesis, University of Detroit, 1982.
5. Mao, Chien-Pei, "Effect of Air Swirlers on Atomization and Spray Flame Stability", Delavan Inc, Technical Report 563, September 1990.
6. Lefebvre, A. H., Gas Turbine Combustion, Hemisphere Publishing Corporation, 1983.

TABLE I

A SUMMARY OF AIR SWIRLER PARAMETERS

Swirler	Air Gap (mm)	Slot Width (mm)	Slot Depth (mm)	CdA (mm^2)	Spray Angle* (Degree)
1	.36	2.39	1.27	17.4	74
2	.51	2.39	1.27	20.0	89
3	.66	2.39	1.27	20.6	97
4	.36	2.39	1.09	17.4	81
5	.48	2.39	1.09	18.7	89
6	.36	2.39	0.86	16.1	106
7	.46	2.39	0.86	17.4	111
8	.64	2.39	0.86	18.1	128
9	.51	1.98	1.27	18.7	103
10	.66	1.98	1.27	20.6	116
11	.51	1.98	1.09	18.1	97
12	.36	1.57	1.09	14.8	102
13	.53	1.57	1.09	17.4	124

All swirlers have twelve vanes with a 45° vane angle

* Spray angle was measured at air ΔP of 6.9 kPa and fuel pressure of 276 kPa

EFFECT OF DODECANOL CONTENT ON THE COMBUSTION OF METHANOL SPRAY FLAMES

C. Presser*, A.K. Gupta†, C.T. Avedisian‡ and H.G. Semerjian*

*Chem. Sci. and Tech. Lab, National Institute of Standards and Technology, Gaithersburg, MD, U.S.A.
†Dept. of Mechanical Engineering, University of Maryland, College Park, MD, U.S.A.
‡Sibley School of Mechanical and Aerospace Engineering, Cornell University, Ithaca, NY, U.S.A.

ABSTRACT

The structure of a swirl-stabilized spray flame, fueled by methanol and two methanol/dodecanol mixtures, has been examined. The main objective of this study was to obtain evidence of the occurrence of microexplosions in spray flames. Measurement of droplet size and velocity distributions were carried out under burning conditions using a single-component phase/Doppler interferometry system. Initially, experiments were carried out with methanol and 50/50 methanol/dodecanol mixture spray flames. Some evidence was found to indicate the occurrence of microexplosions in the mixture flame. In this study, it was observed that the occurrence of microexplosions is reduced for 75/25 methanol/dodecanol mixture flames. These results indicate that the tendency for microexplosions to occur appears to strengthen with higher dodecanol content.

1. INTRODUCTION

An investigation of the combustion of methanol/dodecanol mixtures offers the possibility of examining the phenomenon of microexplosions. Microexplosions or disruptive burning is the process whereby a droplet literally explodes during its combustion into smaller droplets due to internal bubble formation [1,2]. Microexplosions of particular mixtures of methanol and dodecanol are thought to occur because of large difference in volatility of the two fuels and preferential vaporization of the two components of the miscible mixture. An equivolume mixture of methanol and 1-dodecanol has been used in studies of burning single droplets. Wang and Law [1] have shown that, for monodispersed droplet streams, microexplosions occur in a 50/50 mixture (by volume) of methanol and 1-dodecanol. Recent evidence by Yang et al. [2] has indicated that microexplosions for this mixture were not observed for stationary isolated and unsupported droplets under spherically symmetric burning conditions; however, microexplosions were observed for mixtures more diluted by methanol (in particular, 75/25 methanol/dodecanol mixtures). These results have suggested that in a convective flow environment the internal liquid circulation (resulting in concentration gradients [3]) may distribute the mixture components within the droplet in a manner favorable to creating the necessary superheat conditions for microexplosions. Properties that may influence the tendency for microexplosions to occur (e.g., droplet mixture composition, residence time, temperature, etc.), of course, require further examination. The motivation of this work was therefore to determine the extent to which microexplosions occur in 75/25 methanol/dodecanol mixture flames.

In previous investigations [4,5], a comparative study of methanol and 50/50 methanol/dodecanol mixture spray flames was carried out. Spatially resolved information on droplet size and velocity distributions was obtained using a phase/Doppler interferometry system [6]. Some evidence for the occurrence of microexplosions was found in the methanol/dodecanol mixture flame. This evidence was in the form of a sudden decrease in droplet size and velocity, and an increase in number density when compared with the methanol flame or with data obtained at different spatial positions of the mixture flame. In addition, photographic evidence in the form of particle streaks in random directions was observed which was also suggestive of the presence of microexplosions.

2. EXPERIMENTAL ARRANGEMENT

Experiments were carried out in a spray combustion facility which was designed to simulate practical combustion systems. The facility includes a swirl burner with a moveable 12-vane swirl cascade; the vanes are rotated simultaneously to impart the desired degree of swirl intensity to the coflowing combustion air stream. The spray facility permits examination of the effects of combustion air swirl, atomizer design, fuel type, and air preheat on spray structure and combustion characteristics. The swirl strength introduced to the combustion air is given in terms of the swirl number, S, which is determined according to the theory outlined in Ref. [7]. Experiments were carried out for S = 0.53 under burning conditions.

A simplex pressure-jet nozzle is located along the centerline of the burner. The fuel nozzle was operated at total air and fuel flow rates of 64.3 kg/hr and 3.2 kg/hr, respectively. The spray is injected vertically upwards from the nozzle, located at the burner exit. The pressure-jet nozzle provides a nominal 60° hollow-cone spray. A stepper-motor-driven three-dimensional traversing arrangement is used to translate the burner assembly in the vertical (Z) and both horizontal (X and Y) directions. All optical diagnostics are fixed in position about the burner assembly so that the burner can translate independently of the optical equipment. This arrangement permits precise alignment of the measurement volume within the spray (see Fig. 1). Measurement of radial profiles of the spray flame properties, e.g., droplet size and velocity distributions, can then be carried out at different axial positions. Further details on the experimental arrangement are given elsewhere [8].

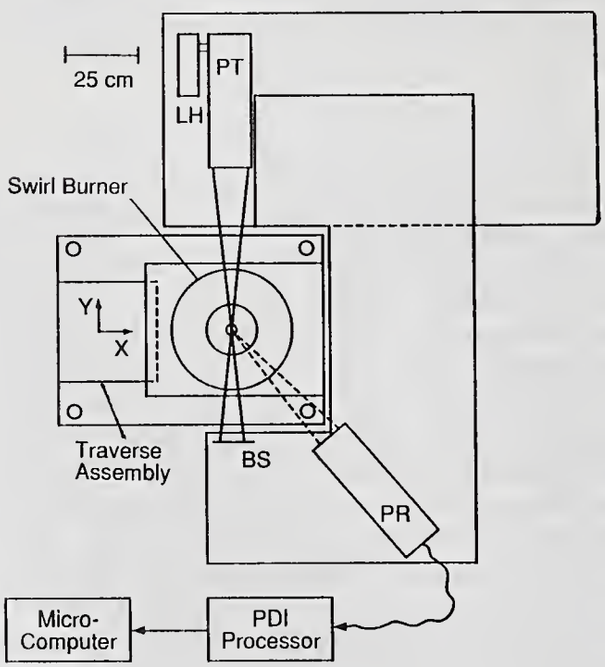

Fig. 1. Schematic of experimental spray combustion facility. BS - Beam stop; LH - He-Ne laser; PR - PDI receiving optics; PT - PDI transmitting optics.

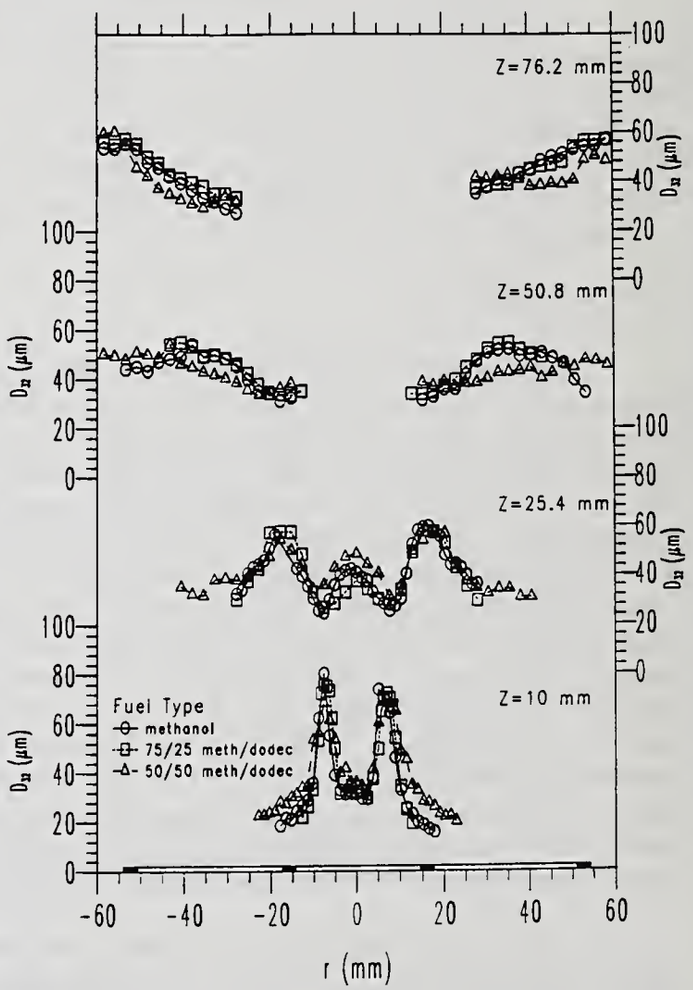

Fig. 2. Variation of droplet Sauter mean diameter (D_{32}) with radial position (r) at different axial positions (Z) for the methanol and two methanol/dodecanol mixture flames.

Droplet size and velocity distributions were measured using a single-channel phase/Doppler interferometer [6]. The instrument provides in-situ nonintrusive measurements at different positions within the spray. For these experiments, an off-axis light collection system was used, with the optics positioned at a scattering angle of 30° (see Fig. 1). The focal length of the transmitting and receiving optics was 495 and 500 mm, respectively. A 10 mW He-Ne laser, operating at a wavelength of 632.8 nm, provided the light source for the methanol and 50/50 methanol/dodecanol mixture flames. An upgraded system, incorporating a 4W cw Ar-ion laser and operating at a wavelength of 514.5 nm, was used for the 75/25 mixture flame. The laser was operated at 400 mW for the measurements presented in this paper. The signal data rate was kept at a relatively low value (approximately 200 Hz) by adjusting the supply voltage to the scattered light detector. Data were also acquired by optimizing the system gain to detect the maximum number of droplets without saturating the photomultiplier tube (PMT) detectors and thus affecting the signal-to-noise level. This was accomplished by setting the PMT voltage (for a specified laser beam intensity) at a level commensurate with the maximum value of volume flux [9,10]. This value generally corresponded to the instrument operating procedures recommended by the manufacturer.

3. RESULTS AND DISCUSSION

3.1 Droplet Mean Diameter, Number Density and Velocity

In this study, data for a 75/25 methanol/dodecanol mixture flame were obtained since recent single droplet experiments under spherically symmetric burning conditions have indicated an enhanced tendency for the occurrence of microexplosions. The Sauter mean diameter (D_{32}) and number density (N) are presented in Figs. 2 and 3 for methanol and the two methanol/dodecanol mixture flames, described earlier, at axial positions of Z = 10, 25.4, 50.8 and 76.2 mm. The solid boxes along the abscissa indicate the position of the burner passage walls, with the fuel nozzle located at the centerline. Limited data are presented for Z = 50.8 and 76.2 mm because of the very low data rate in the central region of the spray flame. The variation of D_{32} with spatial position is typical of hollow-cone pressure-atomized spray flames. The droplets near the spray boundary (defined by the peaks in the D_{32} distributions) are larger than those near the spray centerline in the upstream portion of the spray. The profiles become more uniform with increasing axial position. At Z = 10 mm the values of D_{32} are similar for all three flames near the spray boundary and toward the center of the spray. At upstream positions, microexplosions are not expected to occur since the droplets have not experienced the necessary period of rapid heating (i.e., sufficient residence time in a high temperature environment). Further downstream (at $Z \geq 50.8$ mm), the droplet mean diameter for the 50/50 mixture flame becomes significantly smaller near the spray boundary than the methanol flame; as discussed earlier, the reduced size for the 50/50 mixture flame is indicative of the occurrence of microexplosions. The droplet mean size and number density (see Fig. 3) for the 75/25 mixture flame remain similar to that of methanol. These results suggest that there is little or no evidence of the presence of microexplosions for the 75/25 mixture flame.

Radial profiles of droplet mean axial velocity (U) for the methanol and two mixture flames are presented in Fig. 4 at Z = 10, 25.4, 50.8 and 76.2 mm. The mean velocity profiles are also indicative of the overall structure of hollow-cone spray flames, viz., the highest droplet velocities are found near the spray boundary. The results indicate that the value of U decreases with higher dodecanol content near the spray boundary. This trend may be expected since denser fuels will create larger droplets with lower velocities for a given initial droplet momentum. However, since the droplet mean size decreases in regions where microexplosions are expected to occur, the decrease in droplet velocity may be attributed to rapid droplet entrainment into the air flow field and subsequent deceleration. These trends may be further substantiated by examining changes in the size and velocity distributions, and size/velocity correlations with spatial position, as discussed in the next section.

3.2 Size and Velocity Distributions

The droplet size and velocity distributions have been found to vary significantly with spatial position in the investigated spray flames. A typical set of size and velocity distributions, and velocity/size correlations obtained for the three spray flames is presented in Fig. 5 at a radial position (r) of 33.0 mm and an axial position (Z) of 50.8 mm. This radial position was chosen since it represents a position where the occurrence of microexplosions is expected (see Figs. 2-4). The solid bars of the distributions represent the measured data on a flux (or temporal) basis, while the open bars represent the data corrected for variations in the effective measurement volume [6]. Also note the change in axes scales between distributions. The results indicate that the size distributions for the methanol and 50/50 methanol/dodecanol mixture flames generally remain monomodal (see Figs. 5A and 5C); however, a

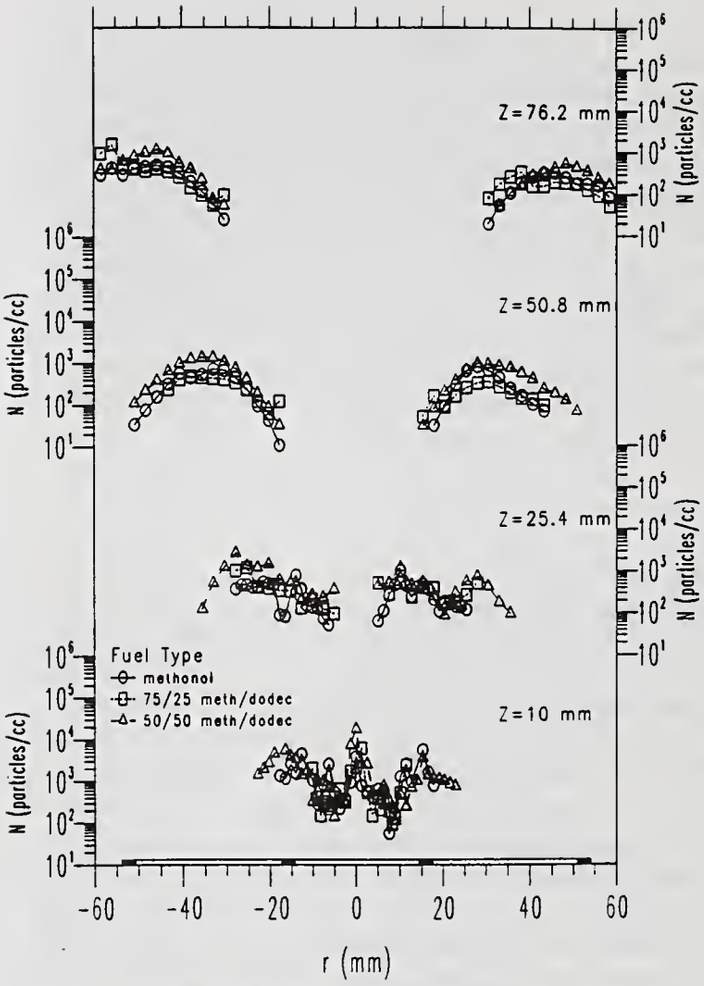

Fig. 3. Variation of droplet number density (N) with radial position (r) at different axial positions (Z) for the methanol and two methanol/dodecanol mixture flames.

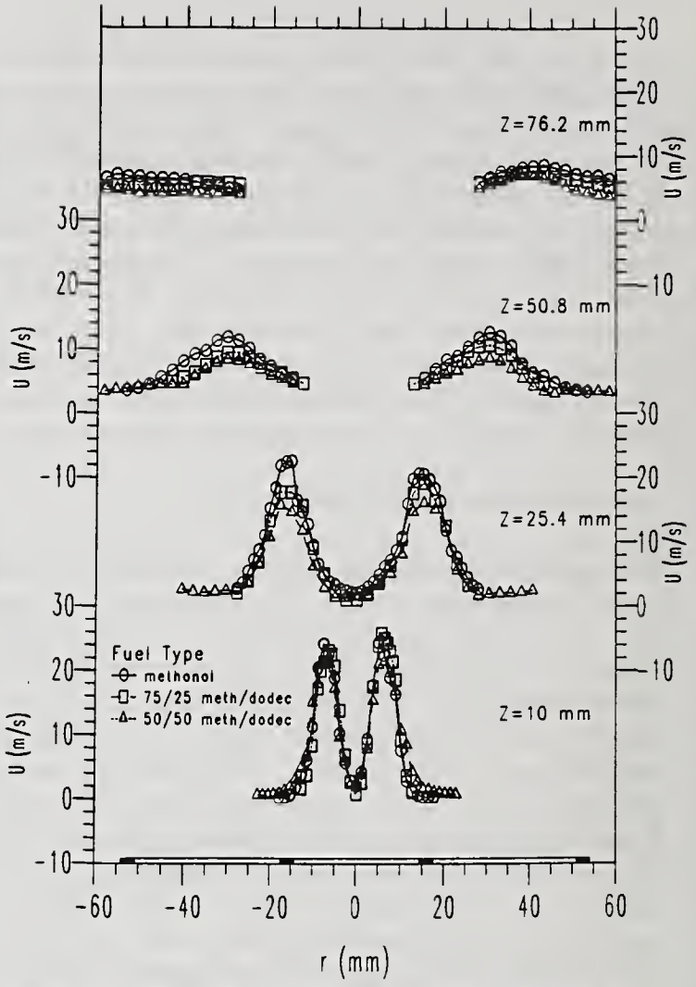

Fig. 4. Variation of droplet mean axial velocity (U) with radial position (r) at different axial positions (Z) for the methanol and two methanol/dodecanol mixture flames.

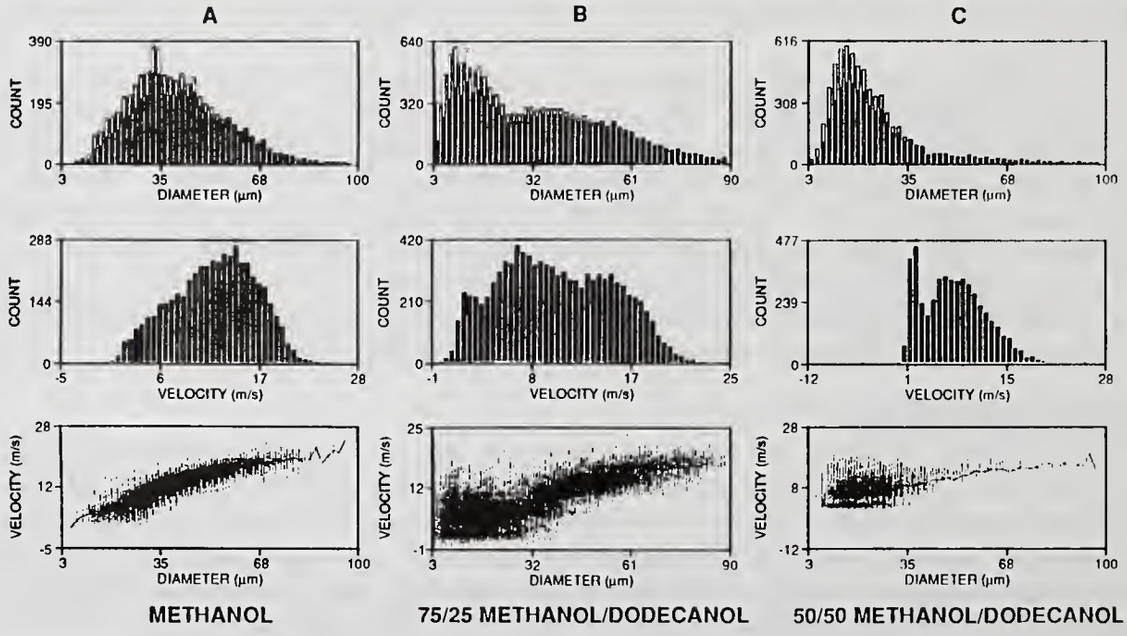

Fig. 5. Distribution of droplet size, velocity and velocity/diameter correlations for the a) methanol, b) 75/25 methanol/dodecanol and c) 50/50 methanol/dodecanol flames at r = 33.0 mm and Z = 50.8 mm.

significant increase is observed in the number of detected smaller droplets and a decrease in the larger sizes for the mixture. The 75/25 mixture flame appears to be an intermediate case, i.e., a bimodal distribution that corresponds to a combination of the other two flames (see Fig. 5B).

The velocity distributions for the methanol and 50/50 mixture flames indicate a dramatic increase in the number of lower velocity droplets for the mixture. The bimodal velocity distribution for the 50/50 mixture flame (see Fig. 5C) may result from a combination of faster-moving larger droplets originating from the nozzle and slower-moving smaller droplets which form during microexplosions. The velocity/size correlation indicates the presence of two separate regions, with the formation of the lower velocity region as a result of microexplosions. Further details are presented in Refs. [4] and [5]. Again, the 75/25 mixture flame appears to be a combination of the methanol and 50/50 mixture flames, resulting in a trimodal velocity distribution (see Fig. 5B). The velocity/size correlation shows the initial formation of this second lower velocity region. These trends are also present at Z = 76.2 mm. The results indicate that the 75/25 methanol/dodecanol mixture flame does not appear to be a mixture which enhances microexplosions but an intermediate case, perhaps indicating incipient formation of microexplosions. Evidence for the occurrence of microexplosions appears to be strengthened with higher dodecanol content; the optimum quantity of dodecanol remains to be determined. Other properties to consider in future studies include examination of mixture composition (volatility of the mixture components), residence time, and temperature (air and fuel preheating).

3.3 Effect of System Gain

Spray flames generally contain a wide range of droplet sizes, ranging from submicron droplets to droplet diameters of several hundred microns. Detection of all droplets encountered in the probe volume of the phase/Doppler interferometer can be a formidable task in dense regions of the spray. To optimize detection of droplets in these regions the system gain has to be set such that the PMT detectors are not saturated by the larger droplets and remain sensitive enough to detect the smaller sizes. Alternatively, multiple measurements must be recorded and combined during postprocessing of the data to determine the appropriate statistics.

The system gain of the phase/Doppler system can be affected by the PMT voltage setting, laser power and other parameters. It is therefore of interest to determine how the system gain influences the aforementioned results, especially as regards the occurrence of microexplosions. Data were recorded at two different operating conditions of the phase/Doppler instrument. In the first case, the data rate was kept low at approximately 200 Hz in order to keep the sample duration time relatively constant across the entire radial profile. The results presented in Figs. 2-4 were recorded for this condition. In the second case, the PMT voltage was changed to optimize detection of the droplets as recommended by McDonell and Samuelsen; this meant adjusting the PMT voltage at each point to achieve maximum volume flux [9]. This criterion appeared to parallel in most regions of spray flames the procedures recommended by the manufacturer (i.e., when the PMT detectors begin to saturate).

Figures 6-8 present the results obtained for droplet mean size, number density and velocity, respectively, at Z = 10, 25.4 and 76.2 mm. Data were recorded in the 75/25 mixture flame for the two above-mentioned instrument operating conditions. The results indicate that, at $Z \leq 25.4$ mm, there is a significant difference in the values of D_{32}, N and U measured across the profiles. This is to be expected since the "optimum gain" case detects more smaller droplets (resulting in a strong signal with a high data rate); the threshold level for the "low data rate" case is too high to detect smaller droplets. For example, Fig. 9 presents the size and velocity distributions at r = 15.2 mm and Z = 25.4 mm for the two cases. The optimum gain case (see Fig 9B) shows the detection of many smaller droplets and development of a second lower-velocity peak in the distribution as compared to the low data rate case (see Fig. 9A). As a result, the mean value for D_{32} decreases from 58.5 to 46.3 μm, U decreases from 19.3 to 14.2 m/s, and N increases from 4.2×10^2 to 2.2×10^3 particles/cc for the optimum gain setting. At $Z \geq 50.8$ mm, the results indicate negligible difference between the two readings. This is as expected because of droplet vaporization and dispersion with increasing axial position. The measurement therefore requires a high PMT voltage to maintain a low data rate, i.e., the two instrument settings are essentially the same at downstream positions. The importance of these findings is that at Z = 50.8 and 76.2 mm, where possible evidence for microexplosions has been found, the instrument system gain has negligible influence upon the measured trends.

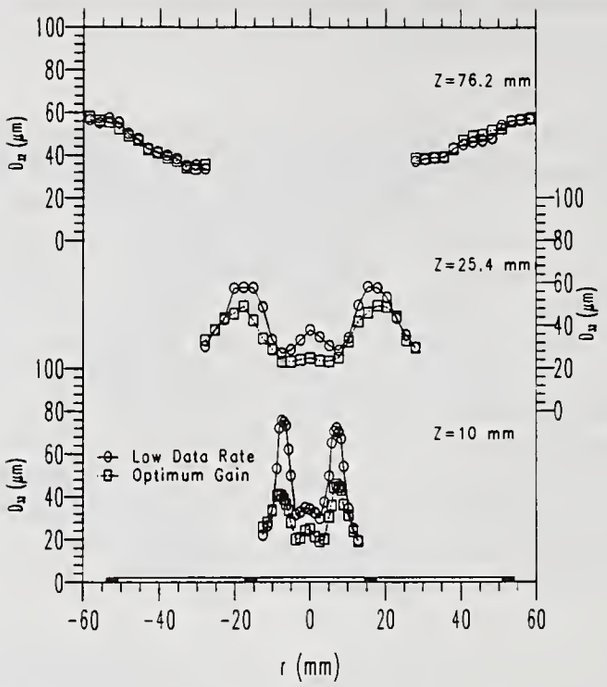

Fig. 6. Variation of droplet Sauter mean diameter (D_{32}) with radial position (r) at different axial positions (Z) at two different instrument operating conditions for the 75/25 methanol/dodecanol mixture flame.

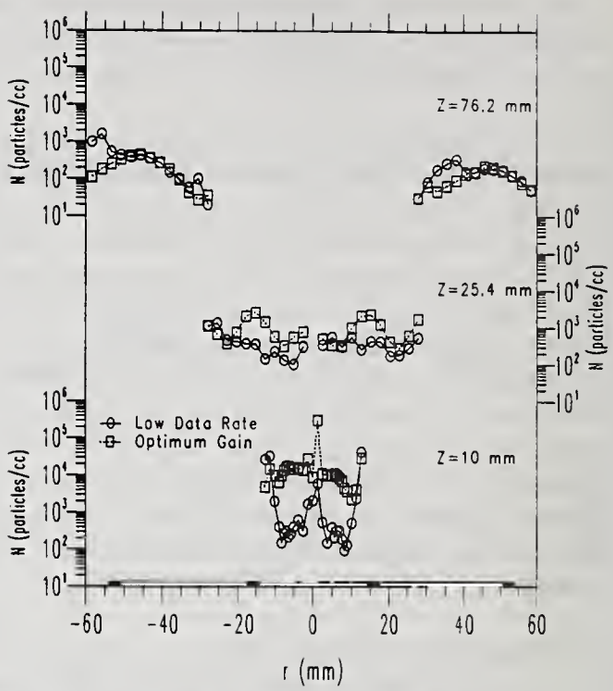

Fig. 7. Variation of droplet number density (N) with radial position (r) at different axial positions (Z) at two different instrument operating conditions for the 75/25 methanol/dodecanol mixture flame.

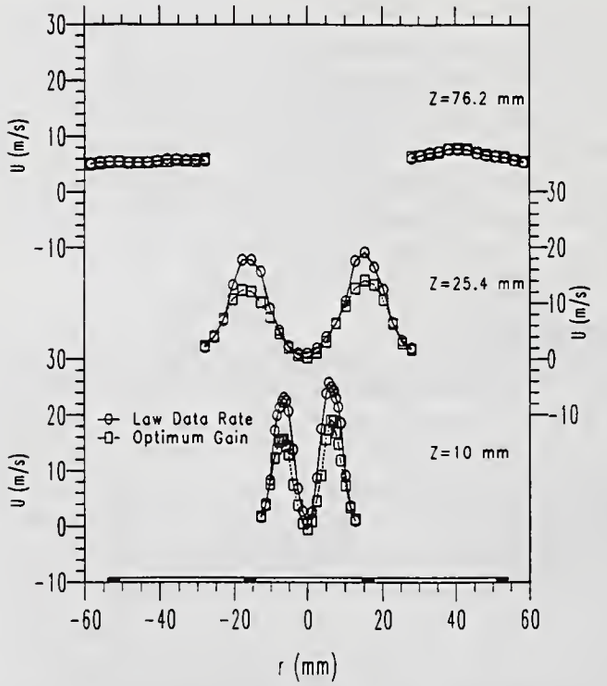

Fig. 8. Variation of droplet mean axial velocity (U) with radial position (r) at different axial positions (Z) at two different instrument operating conditions for the 75/25 methanol/dodecanol mixture flame.

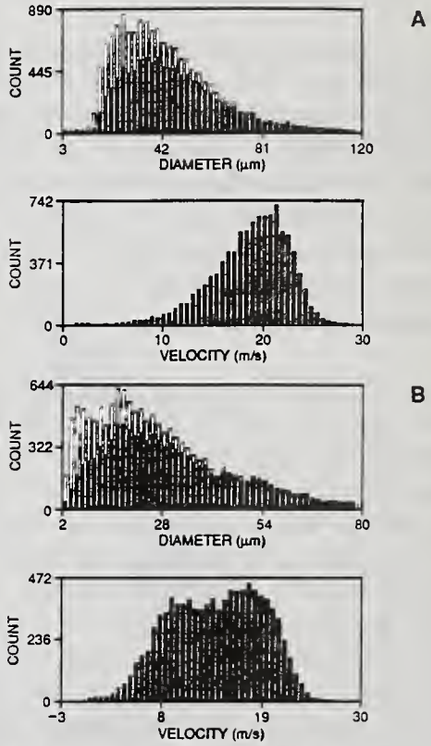

Fig. 9. Distribution of droplet size and velocity for the a) low data rate and b) optimum gain operating conditions of the phase/Doppler system with the 75/25 methanol/dodecanol mixture flame at r = 15.2 mm and Z = 25.4 mm.

The change in the mean droplet properties (i.e., D_{32}, N and U) with axial position is, in general, dependent upon the instrument operating conditions. For the low data rate case, the maximum value of D_{32} decreases with axial position (see Fig. 6). This can be attributed to detection of primarily larger droplets as they undergo vaporization. This trend is contrary to that indicated by the optimum gain case (since the rapid vaporization of the smaller droplets tends to increase the mean diameter) and to observations generally reported in the literature for nonburning sprays [8]. The maximum mean velocity decreases with axial position for both cases. The maximum number density decreases with axial position for the optimum gain case (as expected) and remains relatively unchanged for the low data rate case. The importance of these trends is that at downstream positions there are primarily larger vaporizing droplets. If there is a sudden abundance of smaller droplets, it may then be attributed to microexplosions.

It is also important to ascertain that the laser power did not influence the results since two different phase/Doppler systems (with lasers of different power) were used. Figure 10 presents the effect of PMT voltage upon the droplet mean axial velocity at four different laser beam intensities of 10, 125, 200 and 400 mW. The data were acquired for the 75/25 mixture flame at r = 0 and Z = 10 mm. The results indicate that the PMT voltage has a significant effect upon the values of U for a preset laser power. This effect is the same for the droplet mean size and number density. It is also observed that the number density (and volume flux) does not reach a maximum value at each measured position (see Fig. 10). A maximum value is generally achieved in regions near the spray boundary where the data rate is high. When no maximum value is found the PMT voltage is set according to the recommended procedures of the manufacturer. Figure 10 indicates that as the laser power increases, lower PMT voltages are required to maintain a particular value of droplet mean velocity (or size). The use of two different lasers with the phase/Doppler system therefore should have negligible influence on the results, provided the detector voltage is appropriately adjusted.

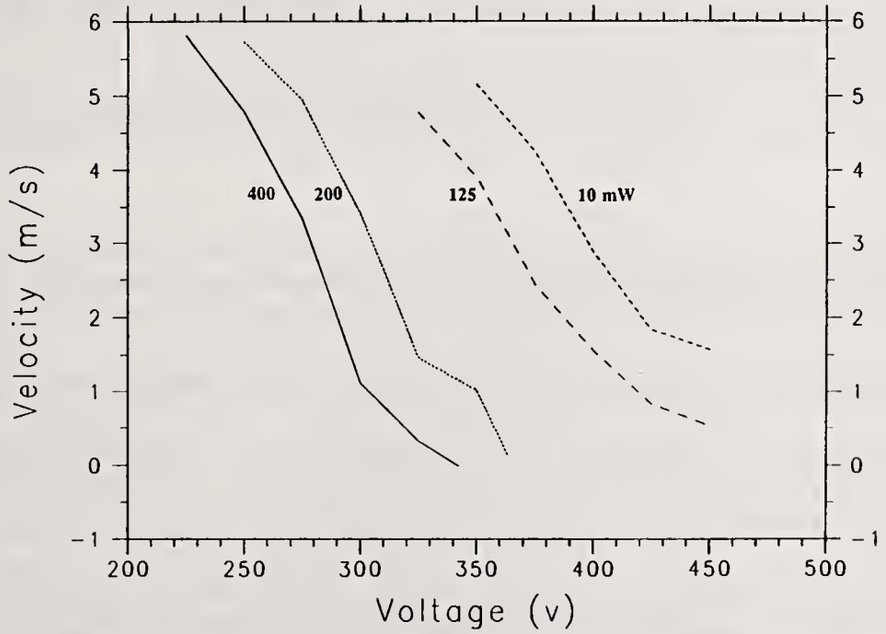

Fig. 10. Variation of mean droplet velocity with PMT voltage at different laser powers for the 75/25 methanol/dodecanol mixture flame at r = 0 and Z = 10 mm.

4. SUMMARY

Measurement of droplet mean size, velocity and number density have been obtained using a phase/Doppler interferometry system. The measurements were carried out in a methanol and two methanol/dodecanol mixture flames. The study focused on detection of microexplosions in methanol/dodecanol mixture flames. The results obtained in these three flames indicate that the tendency for microexplosions is strengthened with higher dodecanol content. The effect of system gain (i.e., PMT voltage and laser power) on the measurements has been found to influence dense regions of spray flames, but has a negligible effect at downstream positions where microexplosions are expected to occur.

ACKNOWLEDGEMENTS

The authors would like to acknowledge the support of this work by the U.S. Department of Energy, Conservation and Renewable Energy, Office of Industrial Processes, Advanced Industrial Concepts Division. Messrs. Marvin Gunn and John Larson are the project monitors. One of the authors (CTA) would like to acknowledge the support of the New York State Center for Hazardous Waste Management (Dr. Ralph R. Rumer, project manager). The technical support provided by Mr. J.D. Allen is also gratefully acknowledged.

REFERENCES

1. Wang., C.H. and Law, C.K., "Microexplosion of Fuel Droplets Under High Pressure," Combustion and Flame, Vol 59, pp. 53-62 (1985).

2. Yang, J.C., Jackson, G.S. and Avedisian, C.T., "Combustion of Unsupported Methanol/Dodecanol Mixture Droplets at Low Gravity", Twenty-Third Symp. (Int'l) on Combustion, The Combustion Institute, Orleans, France (1990).

3. Lara-Urbaneja, P. and Sirignano, W.A., "Theory of Transient Multicomponent Droplet Vaporization in a Convective Field", Eighteenth Symp. (Int'l) on Combustion, pp. 1365-1374, The Combustion Institute, Pittsburgh, PA (1981).

4. Presser, C., Gupta, A.K., Avedisian, C.T. and Semerjian, H.G., "Combustion of Methanol and Methanol/Dodecanol Spray Flames", AIAA 90-2446, AIAA/SAE/ASME/ASEE 26th Joint Propulsion Conf., Orlando, FL (1990).

5. Presser, C., Gupta, A.K., Avedisian, C.T. and Semerjian, H.G., "Fuel Property Effects on the Structure of Spray Flames", Twenty-Third Symp. (Int'l) on Combustion, The Combustion Institute, Orleans, France (1990).

6. Bachalo, W.D., Houser, M.J. and Smith, J.N., "Behavior of Sprays Produced by Pressure Atomizers as Measured Using a Phase/Doppler Instrument", Atomization and Spray Technology, Vol 3, pp. 53-72 (1987).

7. Gupta, A.K., Lilley, D.G. and Syred, N., Swirl Flows, Abacus, Tunbridge Wells, England (1984).

8. Presser, C., Gupta, A.K., Semerjian, H.G., and Santoro, R.J., " Application of Laser Diagnostic Techniques for the Examination of Liquid Fuel Spray Structure", Chemical Engineering Communications, Vol 90, pp. 75-102 (1990).

9. McDonell, V.G. and Samuelsen, S., "Sensitivity Assessment of a Phase-Doppler Interferometer to User-Controlled Settings", in Liquid Particle Size Measurement Techniques: 2nd Volume (E.D. Hirleman, W.D. Bachalo, and P.G. Felton, Eds.), ASTM STP 1083, pp. 170-189, American Society for Testing and Materials, Philadelphia, PA (1990).

10. Chao, J., Hwang, K. and Lee, T., "Sensitivity of User Parameter Settings of Phase Doppler Particle Analyzer in Combusting Spray", AIAA 90-1553, AIAA 21st Fluid Dynamics, Plasma Dynamics and Lasers Conf., Seattle, WA (1990).

SPRAY CHARACTERIZATION IN AXISYMMETRIC, SWIRLING COMBUSTOR FLOWS

M.J. Ward, J.A. Bossard, R.E. Peck, and E.D. Hirleman

Department of Mechanical and Aerospace Engineering
Arizona State University
Tempe, AZ, U.S.A.

ABSTRACT

Droplet size and velocity characteristics of burning fuel sprays in a laboratory combustor have been measured with a single-component Phase-Doppler Particle Analyzer. Tests were conducted to investigate the effects of inlet velocity, fuel flow, swirl quantities, and nozzle air-assist on the spray dynamic processes. The results indicate that the air-assist atomizer produced hollow-cone sprays having a Sauter mean diameter (SMD) of about 20-25μm. The atomization improved (smaller SMD) with increased air-assist flow or decreased fuel flow. Increasing swirl was found to centrifuge the larger droplets comprising most of the liquid volume flux further away from the centerline. In certain cases these droplets could escape the recirculation zone and impinge the combustor wall causing poor combustion efficiency. Size-segregated velocity measurements revealed areas of recirculation and further showed the droplet acceleration due to the accompanying heat release.

INTRODUCTION

The development of advanced gas-turbine engines is always striving to improve combustion stability, efficiency, and emissions. Because the fuel spray distribution strongly affects combustor performance, knowledge of spray dynamics in reacting flows is a prerequisite to design improvements. Combustion-chamber design and performance evaluation has heretofore been accomplished by component testing. The advent of advanced optical diagnostic methods permits engineers to study non-intrusively spray characteristics such as droplet size and velocity.

During the 1960's and 1970's research began on the application of lasers for combustion diagnostics. The advantages of using laser-based methods are that they are non-intrusive and enable real-time data acquisition and processing. Bachalo and Houser [1] developed the Phase Doppler Particle Analyzer (PDPA) for measuring simultaneously the drop size and velocity of spherical particles. The instrument utilizes an optical system resembling a conventional laser-Doppler velocimeter (LDV) except that three detectors are located at selected spacings behind a receiver aperture. Droplets passing through the intersection of two laser beams scatter light which produces a far field interference fringe pattern. The spacing between these fringes is proportional to the drop diameter. The PDPA obtains measurements of this fringe spacing image with the use of a photomultiplier tube, which converts the scattered light into an electronic signal. The fringes move past the detectors at the Doppler difference frequency and produce identical signals but with a phase shift proportional to the fringe spacing.

McDonell *et al.* [2] made measurements with a phase-Doppler instrument in an isothermal chamber (non-reacting fuel), and a swirl-stabilized combustor. As expected, they found significant differences in the drop size from reacting to non-reacting flow. McDonell and Samuelsen [3] investigated symmetry of an air-blast atomizer using a two-component instrument. They measured velocities in both the axial and azimuthal directions inside a combustion chamber. Breña de la Rosa *et al.* [4] studied the effect of swirl on the dynamic behavior of drops and on the velocity and turbulence fields of an isothermal spray using a two-component phase-Doppler particle analyzer (PDPA). Recently, Hardalupas *et al.* [5], used a similar technique to study spray characteristics of unconfined swirl-stabilized flames.

The purpose of the present study is to apply the PDPA to obtain some basic data on droplet ballistics in complex flows found in practical gas-turbine combustors. This information can then be used to clarify the relevant spray combustion processes and assist in the development of computational tools for combustor design.

EXPERIMENTAL

The continuous-combustion test facility, shown schematically in Fig. 1, was used to conduct the present experiments. The combustor consists of a 78-mm dia. x 350-mm long stainless-steel, flanged pipe with 305mm x 25mm x 5mm quartz glass side-panels for optical access. A Delavan siphon-type nozzle (P/N 30609-2) was used for on-axis fuel injection into a co-flowing air stream (up to 0.2kg/s) entering at atmospheric pressure and 300K. Two 51-mm o.d. x 24-mm i.d. vane-type swirlers (60°; 45°) or a 38-mm o.d. disk were mounted to the nozzle for flame stabilization.

Particle diagnostics included an Aerometrics PDPA system consisting of a transmitter Model XMT-1100-4S with a 10mW He-Ne laser, motor controller Model MCB-7100-1, receiver Model RCV-2100, signal processor Model PDP-3100, and data management system Model DMS-4000-5 including a Compaq 386 computer. Instrument accuracy was assessed in an earlier study [6] where the results for two different PDPA optical configurations were found to be within a total experimental uncertainty of 3.5% in sizing monodisperse droplets. In order to measure the axial component of velocity, which coincides with the horizontal spray axis, the transmitter and receiver are each mounted at 15° on a movable optical table that enables mapping the flowfield. The PDPA configuration used throughout these experiments used a 300-mm collimating lens and 500-mm transmitting lens, with three tracks providing the following size ranges: 0.9 to 127.8 μm, 2.7 to 258 μm, and 3.8 to 520 μm. The velocity ranges were first chosen so that there were no velocity over rejections; then the velocity offset was increased to eliminate the velocity under rejections.

In some earlier work [6] it was found that the SMD increased dramatically as the PMT voltage is reduced. The explanation was that the larger drops are seen at the lower voltage settings while it becomes increasingly more difficult to detect the small drops. Figure 2 shows the SMD's versus PMT voltage with maximum diameters of 100-150 μm, 250 μm, and 520 μm. The 100-150 μm case found the SMD decreasing to about 13 μm at 400V then increasing to 32 μm at 600V showing that the larger the PMT voltage, the larger the mean diameters. This discrepancy may be caused by the presence of non-spherical droplets or possibly due to detection of stray light reflected by small droplets on the edge of the measurement volume at higher voltage settings. These results suggest that measurements within 10 mm of the nozzle exit are subject to increasing uncertainty, apparently due to droplet nonsphericity or multiple scattering, that the PMT voltage will effect the results of all measurements, and that the data acquisition process must include adjustments for the on-line indications of out-of-range size and velocity measurements.

RESULTS AND DISCUSSION

This study is designed to determine the structure of burning fuel sprays in a laboratory combustor. Experiments were conducted for various inlet air velocities (3-17 m/s), heat inputs, swirl numbers (0.77 and 1.33), and atomizer air flow. The combustor was operated on Jet-A fuel at equivalence ratios ranging from 0.04-0.20. The test matrix is presented in Table 1. All valid measurements along a radius are reported at four axial stations. The PMT voltage was initially set at 400V and the size range at Dmax of 125 μm. Minor adjustments to these settings were made during the course of the test as needed.

Effect of Fuel Flow

Figure 3 shows the Sauter mean diameter (D_{32}) as a function of the radial and axial locations for cases 1 and 2 with two different fuel flow rates (equivalence ratios). The higher fuel flow rate produced larger SMD's indicating reduced atomization effectiveness at constant air-assist flow. At 20.32 mm from the atomizer tip, the higher equivalence ratio droplet SMD's are larger near the center of the combustor then become smaller than the SMD for the low equivalence ratio spray further from the centerline of the combustor. Because the higher fuel flow has higher flame temperatures the smaller droplets are consumed faster. The peaks in the curves are indicative of the rapid consumption of smaller droplets in the flame zone.

Figure 4 presents size-specific droplet velocity profiles. The lower equivalence ratio spray has a wider recirculation zone, the extent of which is determined partly by the relative momentum of the liquid jet and the surrounding swirling air. At the centerline and near the wall all drops have about the same velocity. In the swirl region the centrifuge effect separates the particles according to size with the larger droplets having a greater velocity at a given radius.

Similar trends to the above were observed when varying the atomizer air flow (cases 2 and 5). Higher nozzle air flows produced finer droplets with higher velocities and a wider recirculation zone.

Effect of Swirl

Cases 1 and 3 are identical operating conditions but the aerodynamics were changed by using different swirlers. Case 1 was run with a 60° swirler (S=1.33); case 3 with a 45° swirler (S=0.77). Figure 5 shows the effect of swirl number on the Sauter mean diameter. The 60° swirler produces a larger circumferential velocity component which tends to bend the spray away from the centerline. There is a local peak of 20-30 μm SMD in the radial profile between radial locations of 5-10 mm for both swirlers. At large radii, the 60° swirler yields larger SMD's. The SMD gradually increases at increasing axial distance from the nozzle due to preferential consumption of smaller droplets. Figure 6 shows the particle velocities for droplets within 5 and 30 μm size bands. The results show that the recirculation zone is much stronger with the 60° swirler.

Reacting and Non-reacting measurements

The Sauter mean diameters measured as a function of axial and radial locations are shown in Fig. 7. The SMD for the non-reacting spray (Case 6b) stays nearly constant at about 25-30 μm at most measurement locations, but shows a slight tendency to increase near the spray periphery. The SMD measured in the reacting flow (Case 6a) condition is about the same but the spray boundaries are much narrower, the non-reacting case having the larger droplets. Because the small droplets are being consumed during reaction, the effect is to raise the SMD.

The mean axial velocity of the 5 and 30 μm droplets are shown versus radial location in Fig. 8. The reacting flow is accelerating faster than the non-reacting flow due to the heat release from combustion. The 5 μm droplets show much wider velocity fluctuations and give a better indication of the gas-phase velocity distribution. The reacting case shows an expanded recirculation zone extending from 10 mm to 16 mm. Near the combustor wall both the 5 and 30 μm droplets approach the average main stream velocity (8 m/s) for these cases. The non-reacting case remains fairly flat at the more distant radial locations. The 5 μm droplets are slower at the centerline reflecting the effect of the recirculation and their velocity increases as the drops move further out from the centerline.

The volume flux measurements are shown in Fig. 9. The non-reacting case had a larger volume flux at all locations as would be expected, since the reacting droplets are being consumed and therefore are not being measured. The data indicates that about 80% of the incoming liquid (spray) is already consumed at the 20.32 mm axial location. This trend must be considered when evaluating the size and velocity measurements previously discussed. The number density is reduced for the reacting spray, therefore the SMD and velocity measurements represent fewer droplets. The reacting flow measurements are detecting only large droplets that pass through the reaction zone. Non-reacting droplet data at the 50.8-mm axial location are quite scattered. The integrated liquid volume flux for the non-reacting case compares favorably to the measured fuel flowrate at axial stations beyond one pipe radius downstream of the nozzle exit.

CONCLUSIONS

A Phase Doppler Particle Analyzer has been used to obtain real-time, point-by-point data on droplet size, velocity and liquid volume flux in a confined, turbulent spray flame. The Sauter mean diameter for these hollow-cone sprays produced by an air-assist atomizer was typically 20-25 μm. The effect of increased swirl air was to shift the volume flux radially outward. Increased fuel flow or decreased atomizer air flow produced sprays having larger droplets. The velocity data was grouped by droplet size and the small (5 μm) droplets were found to track the gas velocity even in reverse flow regions while the larger droplets were centrifuged away from the centerline for the swirling flow conditions. The volume flux measurements in the non-reacting spray were integrated and compared to the fuel flow in the system. At one pipe radius downstream of the nozzle, the measured mass flows were within 9% of the known fuel input.

The Phase Doppler Particle Analyzer is a useful tool for spray diagnostics in reacting and non-reacting flows. Measurements too close to the nozzle exit introduced errors in the droplet size and volume flux due to the high number density of droplets, and possibly from measuring the break-up of the fuel ligaments which are non-spherical. The instrument output was sensitive to the User settings, and a procedure to determine the appropriate values was developed and used throughout the experiments.

Acknowledgments

This research is sponsored in part by a grant from the Allied-Signal Aerospace Company (Garrett Engine Div./Auxiliary Power Div.). MJW was also the recipient of a Garrett Fellowship to support graduate studies. Thanks are also extended to Tony Bruner, Steve Kenney, Eric Krinke, Makarand Kulkarni, Keith Parsons, and Steve Thomas for their assistance in hardware design, instrumentation and software development, and data acquisition.

REFERENCES

1. Bachalo, W.D., Houser, M.J., "Phase/Doppler Spray Analyzer for Simultaneous Measurements of Drop Size and Velocity Distributions", Optical Engineering , Vol. 23, pp. 583-590 (1984).

2. McDonell, V.G., Wood, C.P., and Samuelsen, G.S., "A Comparison of Spatially-Resolved Drop Size and Drop Velocity Measurements in an Isothermal Chamber and a Swirl-Stabilized Combustor", *Twenty-First Symposium (International) on Combustion*, pp. 685-694, The Combustion Institute, Pittsburgh, (1986).

3. McDonell, V.G., Samuelsen, G.S., "Influence of the Continuous and Dispersed Phases on the Symmetry of a Gas Turbine Air-Blast Atomizer", ASME Paper No. 89-GT-303, presented at the Gas Turbine and Aeroengine Congress and Exposition, Toronto, Ontario, Canada, (1989).

4. Breña de la Rosa, A., Wang, G., and Bachalo, W.D., "The Effect of Swirl on the Velocity and Turbulence Fields of a Liquid Spray," ASME Paper No. 90-GT-32, presented at the Gas Turbine and Aeroengine Congress and Exposition, Brussels, Belgium, (1990).

5. Hardalupas, Y., Taylor, A.M.K.P., and Whitelaw, J.H., "Velocity and Size Characteristics of Liquid-Fuelled Flames Stabilized by a Swirl Burner", Proc. R. Soc. Lond. A, Vol. 428, pp. 129-155 (1990).

6. Parsons, K.D., "Characterization of the Performance of the Aerometrics Phase Doppler Particle Analyzer", M.S. Thesis, Arizona State University, Tempe (1990).

Table 1 Test Matrix

Case No.	Avg. Inlet Air Velocity [m/sec]	Equivalence Ratio, Φ	Swirl Angle [degrees]	Air flow in Atomizer [kg/sec]x10^3	Comments
1	2.9	0.14	60	0.37	
2	2.9	0.20	60	0.37	
3	2.9	0.14	45	0.37	
4	8.0	0.05	60	0.47	
5	2.9	0.19	60	0.47	
6	2.9	0.16	0	0.25	
6a	8.0	0.04	0	0.30	reacting
6b	8.0	0.04	0	0.30	non-react.

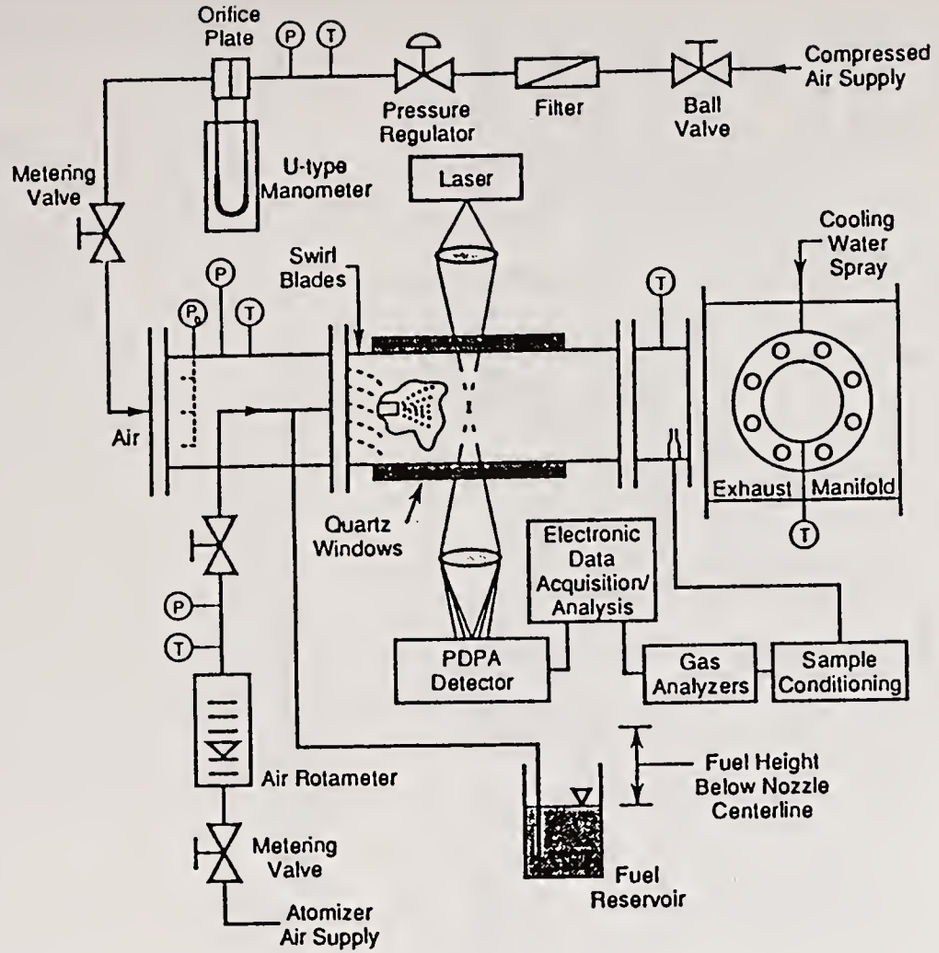

Fig. 1 Schematic of spray combustion test facility

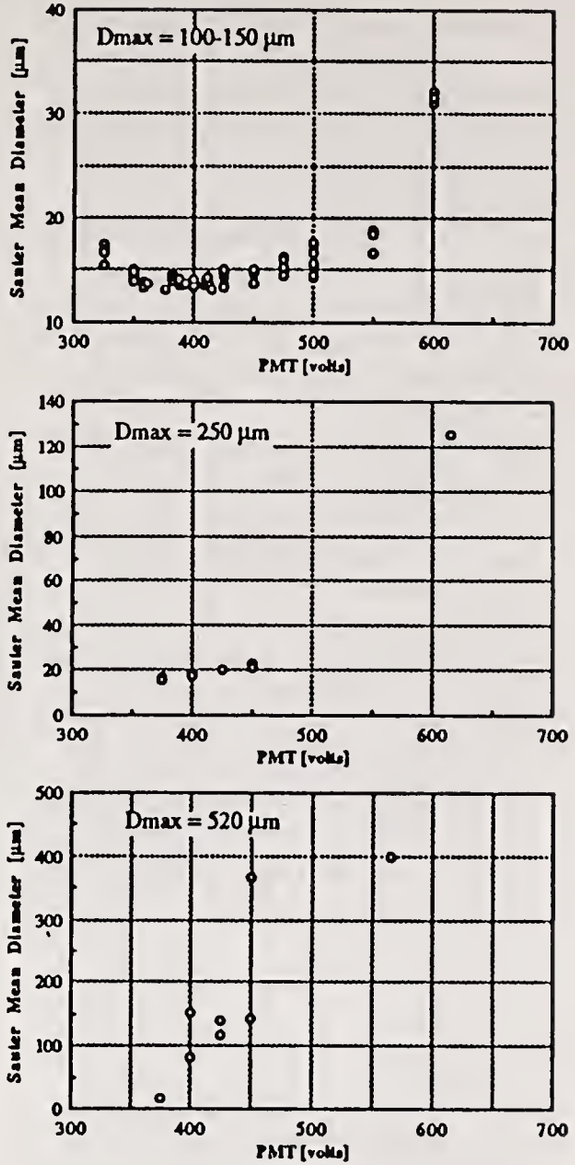

Fig. 2 SMD versus PMT voltage with Dmax = 100-150, 250, and 520 µm at 10.16 mm axial and 11.36 mm radial distance from atomizer tip

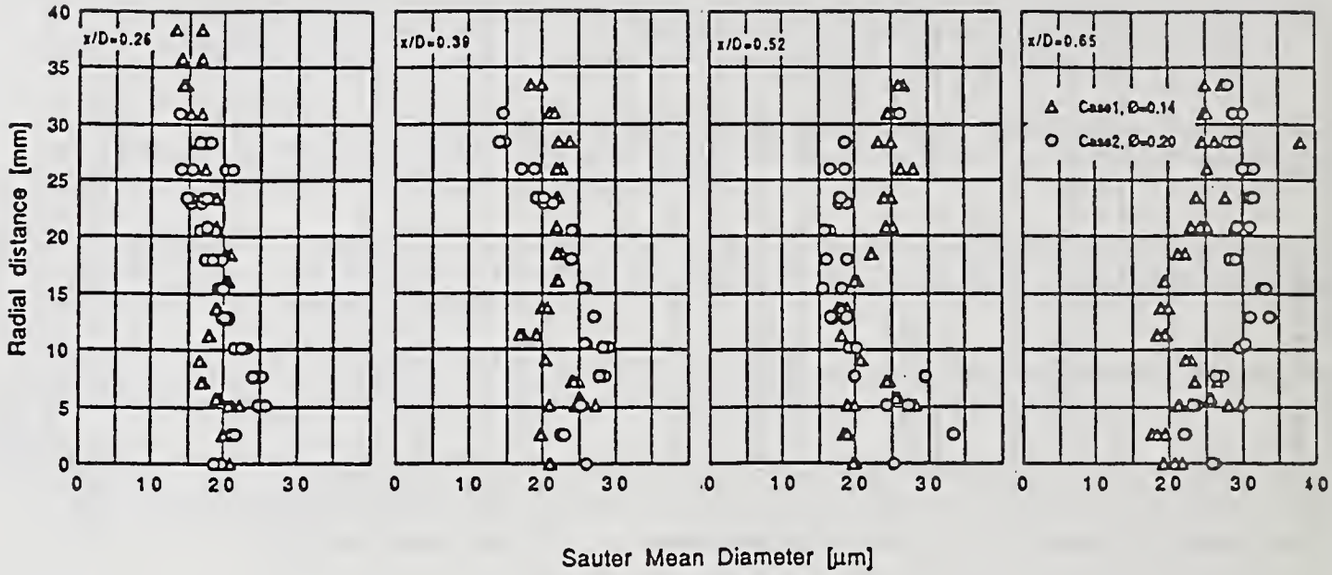

Fig. 3 Effect of fuel flow on SMD

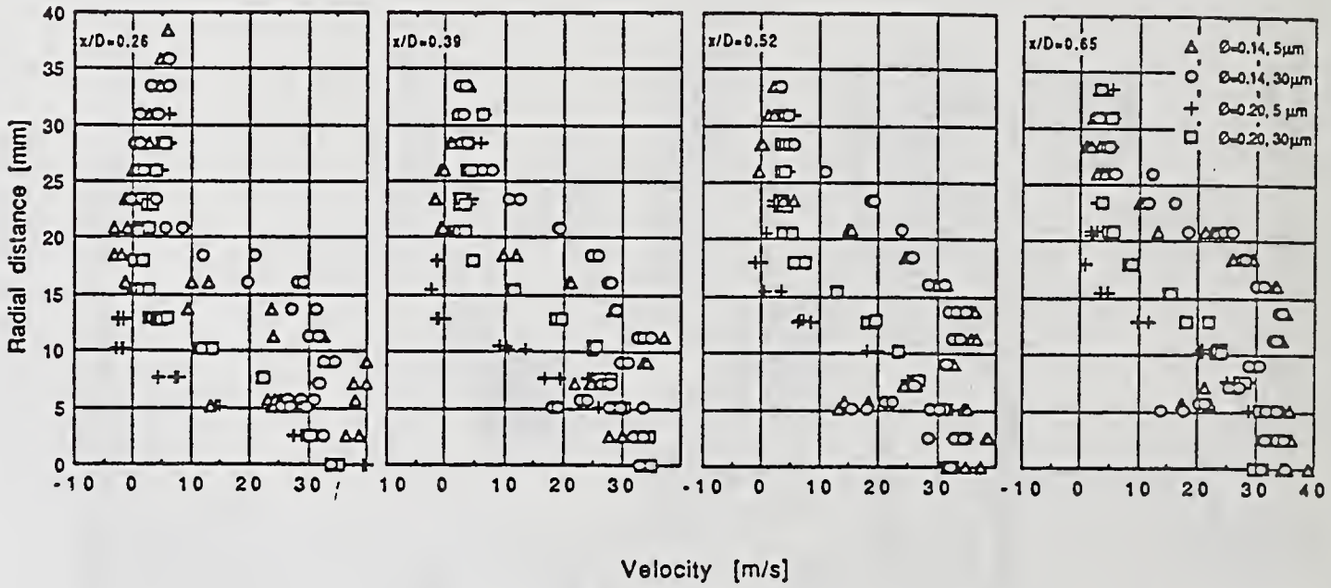

Fig. 4 Effect of fuel flow on droplet velocities

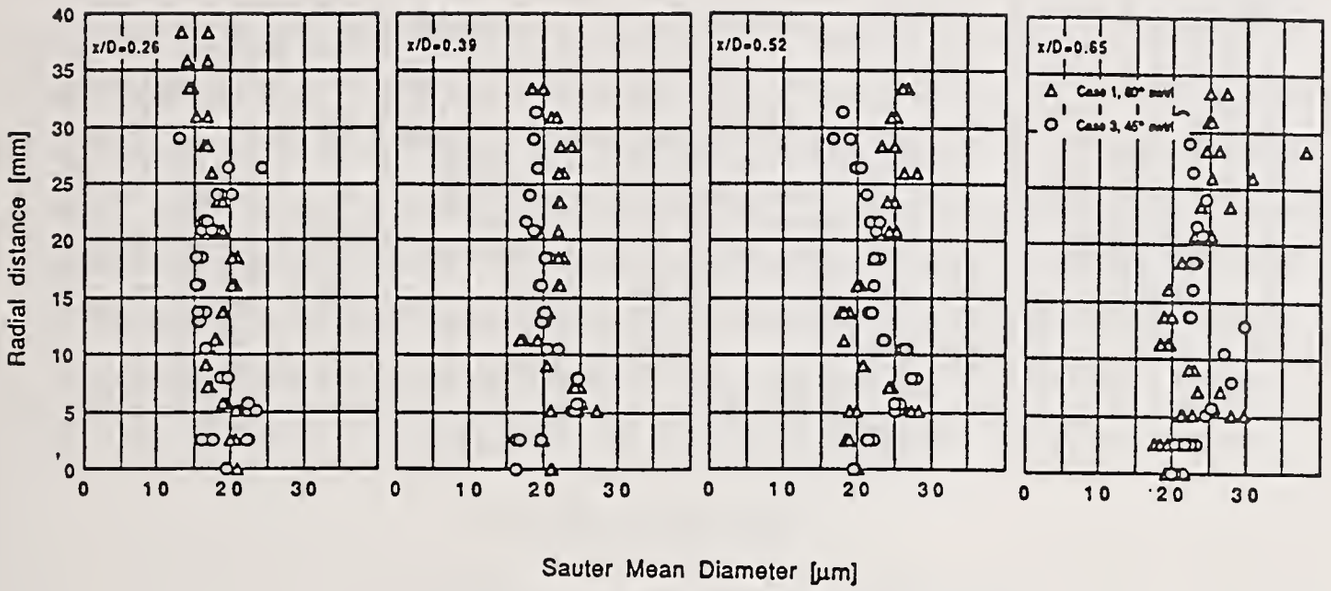

Fig. 5 Effect of swirl on SMD

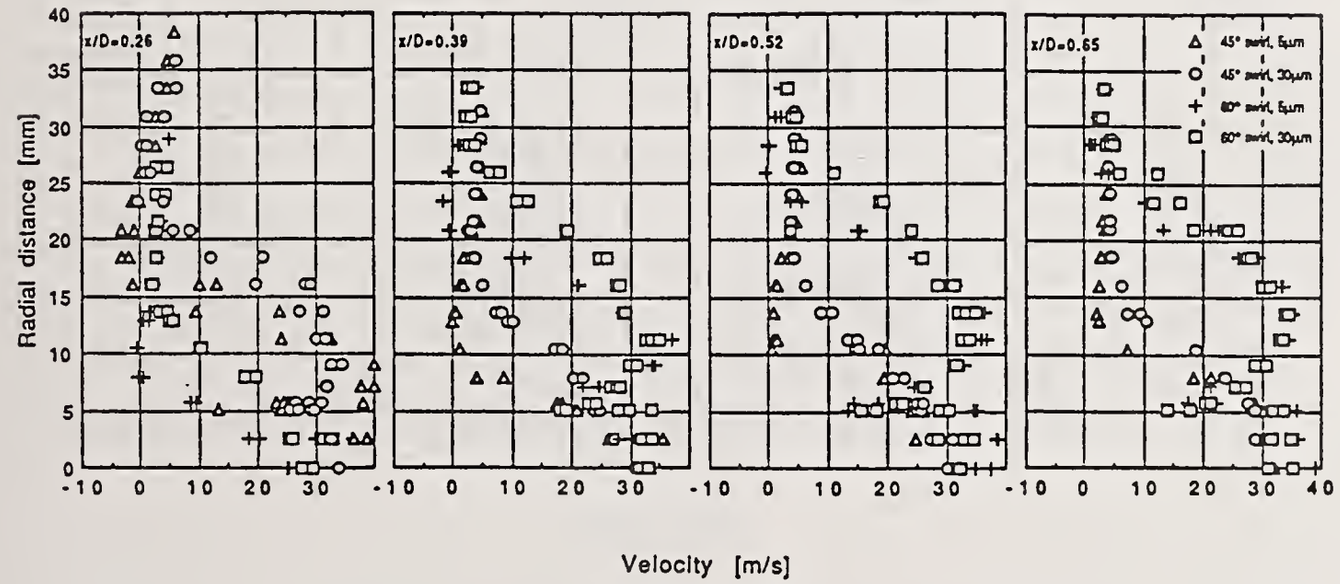

Fig. 6 Effect of swirl on droplet velocities

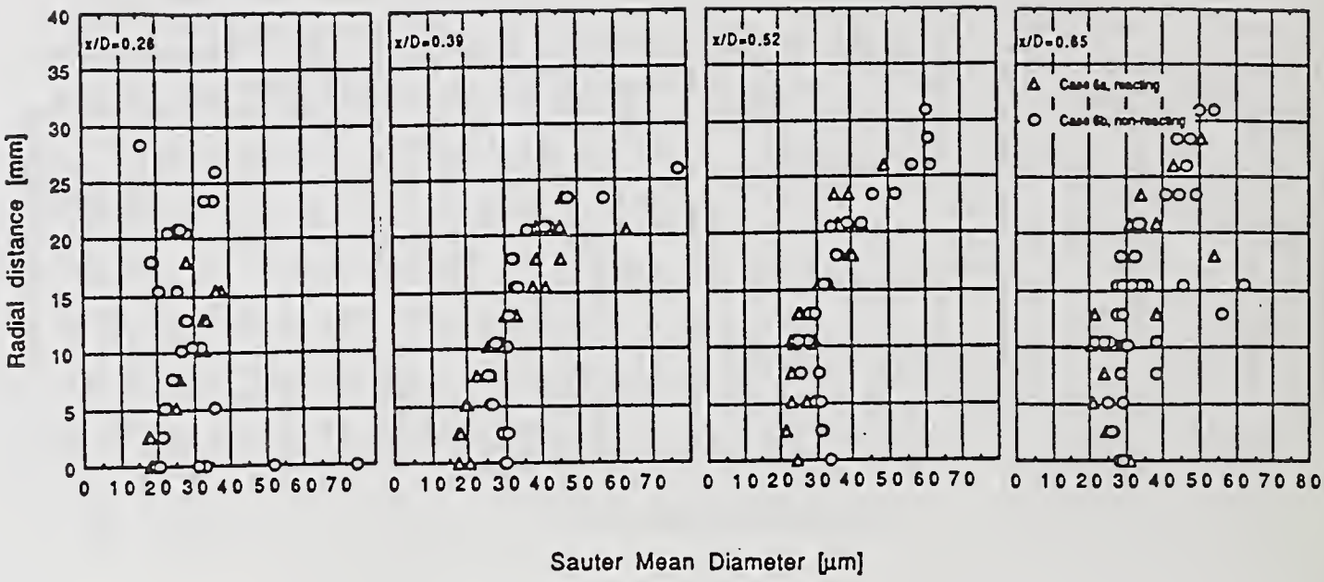

Fig. 7 Effect of combustion reaction on SMD

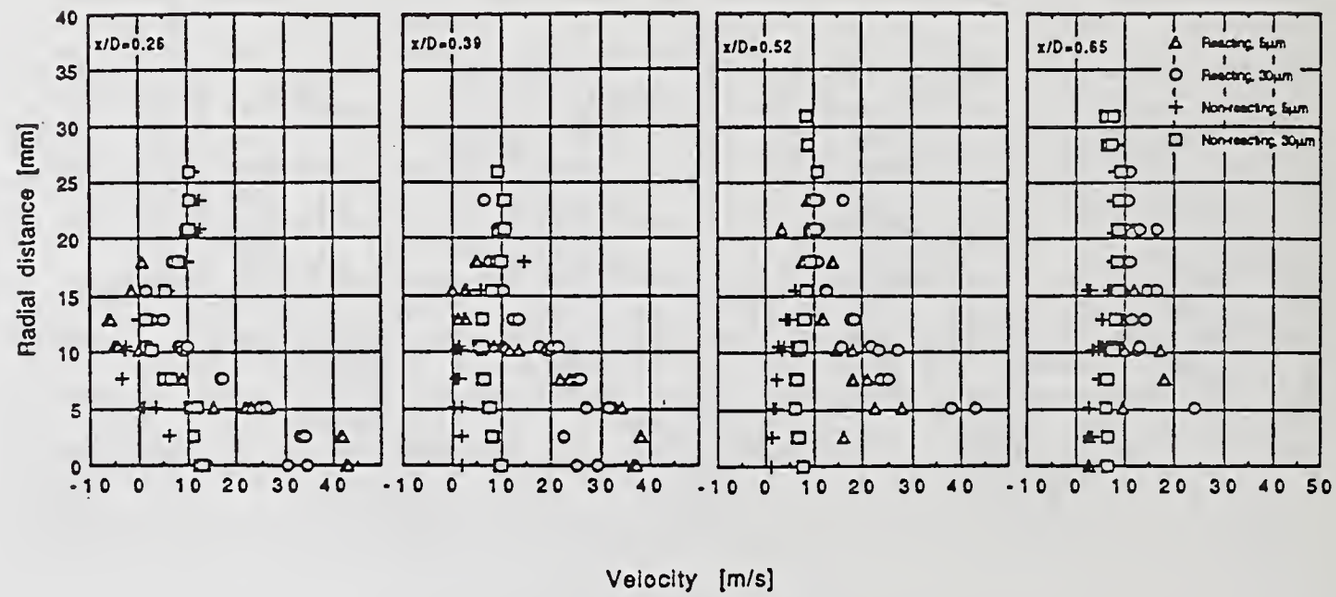

Fig. 8 Effect of combustion reaction on droplet velocities

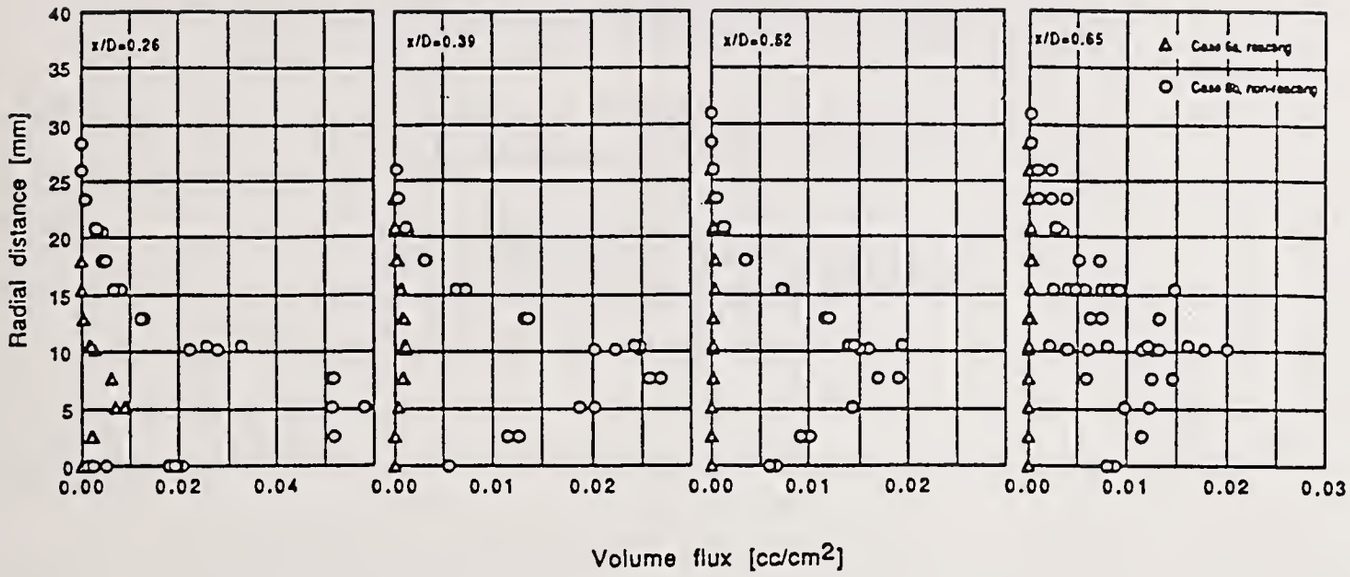

Fig. 9 Effect of combustion reaction on volume flux

SPARK-IGNITED SPHERICAL FLAMES PROPAGATING IN A SUSPENDED DROPLET CLOUD

K. Nakabe*, Y. Mizutani*, F. Akamatsu*, M. Fuchihata† and S.H. El-Emam‡

*Faculty of Engineering, Osaka University, Osaka, Japan
†Mazda Motor Corporation, Hiroshima, Japan
‡Mansoura University, El-Mansoura, Egypt

ABSTRACT

A droplet suspension of liquid fuel produced by an ultrasonic atomizer was spark-ignited and the flame ball propagating outwards was observed in detail in order to elucidate the mechanism of flame propagation and the complicated group structure of spray flames. The chemiluminescence of OH radicals and the flame luminosity in C_2-radical emission band were monitored at a fixed point during the passage of a flame front. The flame structure was visualized by processing the flame images taken by a water-cooled CCD camera system which had an extremely high sensitivity, a wide dynamic range and a sufficiently wide spectral range between 200 nm and 1000 nm in wavelength. In addition, the statistical behavior of the luminous flame contour was visualized by processing the images taken from the successive frames of high-speed photography. It was found that a nonluminous flame was propagating continuously through a gas-phase mixture followed by a luminous flame frequently having a discontinuous geometry. Due to the inherent spatial nonuniformity of the droplet cloud, a number of small-scaled droplet clusters burning brightly in diffusion combustion mode were observed behind the flame front propagating in premixed combustion mode. This fact implies that the group structure of a spray flame is not simple but complex.

INTRODUCTION

The process of flame propagation in a liquid-fuel spray is apparently statistical and discontinuous as far as the behavior of the luminous portions of a flame is observed by a photographic method, in paticular, by high-speed photography [1 - 4]. The mechanism of flame propagation, however, should be elucidated not only from the behavior of luminous portions of the flame but also from the one of nonluminous portions. The authors have found that the instantaneous images of a spray flame at the OH-radical emission band (corresponding to the nonluminous portions) and at the C_2-radical emission band (corresponding to the luminous portions) are significantly different in shape from each other [3,5], and have successfully developed a technique to determine the burning velocity of a spray from the time-averaged image of OH-chemiluminescence [3]. Unfortunately, no information has been obtained on the detailed dynamic behavior of the nonluminous portions of a spray flame. In

addition, the authors previously observed the detailed structure of spray flames using an optical technique [6], and found that a spray flame had a group structure, not simple one but complex one.

In the present study, a flame ball propagating outwards through a droplet suspension was selected as the object of optical observation for the elucidation both of the mechanism of flame propagation and of the complex group structure of spray flames, in expectation of the easiness of detailed observation due to its slow movement. In this case, the instantaneous image of a flame ball gives us some information on the detailed structure of the flame at least in the initial stage of its growth.

A droplet suspension of liquid fuel produced by an ultrasonic atomizer was spark-ignited and the flame ball propagating outwards was observed in detail. The chemiluminescence of OH radicals and the flame luminosity in C_2-radical emission band were monitored at a fixed point during the passage of the flame front. The flame structure was visualized by processing the flame images taken by a water-cooled CCD camera system which had an extremely high sensitivity, a wide dynamic range and a sufficiently wide spectral range between 200 nm and 1000 nm in wavelength. In addition, the statistical behavior of the luminous flame contour was visualized by processing the images taken from the successive frames of high-speed photography.

It was found that a nonluminous flame was propagating continuously through a gas-phase mixture followed by a luminous flame having a ragged discontinuous geometry. Due to the inherent spatial nonuniformity of a droplet cloud, a number of small-scaled droplet clusters burning brightly in diffusion combustion mode were observed behind the flame front propagating in premixed combustion mode. This fact implies that the group structure of a spray flame is not simple but always complex.

EXPERIMENTAL APPARATUS AND PROCEDURE

The experimental apparatus is shown in Fig.1. A kerosene spray was produced using an ultrasonic atomizer (the resonance frequency: 18.5 kHz) installed at the top center of a vertical square duct of 280 mm x 280 mm and was made to fall down freely and to mix with the air induced through the top end around the atomizer. The Sauter mean diameter of spray droplets varied from 57 μm to 66 μm as the fuel injection rate was varied from 2.13 cm^3/min to 4.44 cm^3/min. A spark gap of 4.0 mm wide was located at 400 mm directly below the atomizer tip, and the spray was ignited by an intermittent spark of ca. 2 ms duration.

The optical system for flame imaging is also shown in Fig.1. After the preset delay period from the start of discharge, the mechanical iris shutter S was opened for 1 ms by the timing circuit TC. The

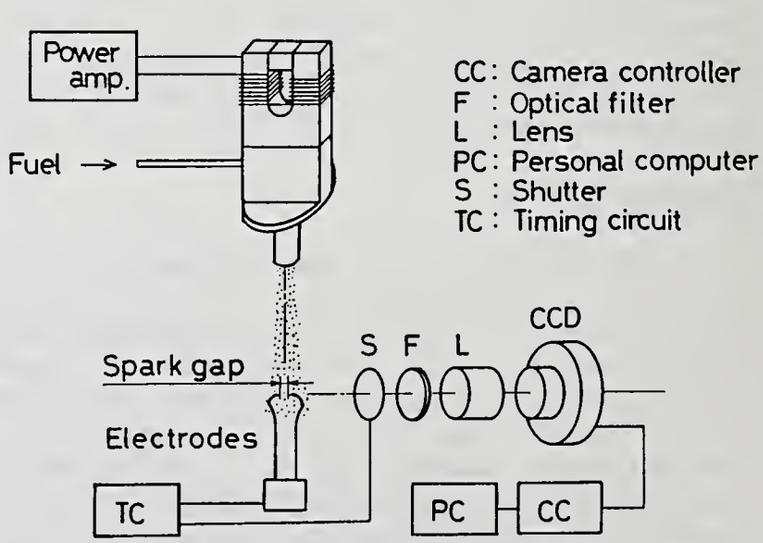

Fig.1 Experimental apparatus and CCD camera system.

flame image was focused onto a CCD array by a UV Nikkor lens L after passing through an exchangeable interference filter F (being removed in the present study). The CCD camera system (Photometrics, CH220, CE200, CC200) was of water-cooled high-sensitivity type, having an extremely wide spectral range from 200 nm to 1000 nm in wavelength and a sufficiently wide dynamic range of 14 bits. The range of sight was confined to 55 mm(H) x 80 mm(W) by the quartz window installed in the duct wall.

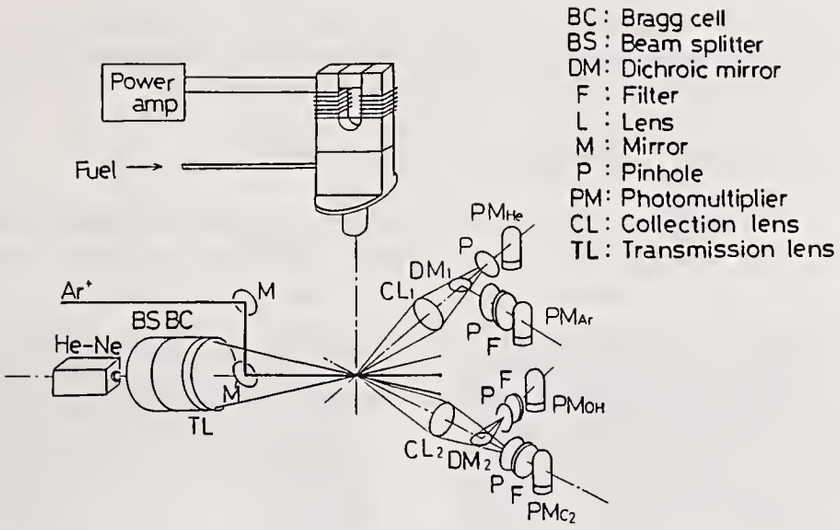

Fig.2 Optical system for point monitoring.

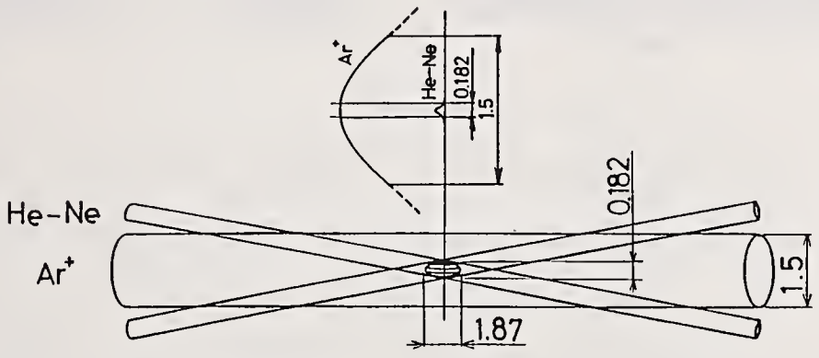

Fig.3 Arrangement of laser beams.

The optical system for local continuous monitoring of the velocity and diameter of droplets and the light emissions in OH- and C_2-radical emission bands is shown in Fig.2. The LDA with a He-Ne laser was of dual-beam, off-axis forward-scattering type, the offset angle of which was 5 degrees. The light of a He-Ne laser scattered by droplets was transmitted through a dichroic mirror DM_1, detected by a photomultiplier PM_{He}, and converted into the droplet velocity signal by a counter-type signal processor. The light of an Ar^+ laser scattered by the same droplets, on the other hand, was reflected by DM_1, detected by a photomultiplier PM_{Ar}, and converted into the droplet diameter signal by a low-pass filter and a root circuit.

As illustrated in Fig.3, the control volume of the He-Ne LDA was a pseudo-ellipsoid of 0.182 mm diam. and 1.87 mm long. The beam from the Ar^+ laser was once expanded up to 7 mm diam. and made to pass through a pinhole of 1.5 mm diam. to realize a uniform intensity distribution. The axis of the Ar^+ laser beam was made coincident with the major axis of the pseudo-ellipsoid. If, therefore, only the scattered signals of the Ar^+ laser coincident with the velocity signal were picked up, the diameters and velocities of droplets could be obtained simultaneously.

The light emitted by the flame in the direction at 5 degrees from the beam axis was collected by a quartz lens CL_2. The range of sight was a pseudo-cylinder of 0.1 mm throat diameter with apex angle of 2 x 3.6 degrees. OH-chemiluminescence signal was reflected by a dichroic mirror DM_2 and detected by a photomultiplier PM_{OH} through an optical interference filter F_{OH}, the peak wavelength and half-value width of which were 308.5 nm and 18.0 nm, respectively, whereas the light emission in C_2-band was transmitted by DM_2 and detected by PM_{C2} through an interference filter F_{C2}, the peak wavelength and

half-value width of which were 516.9 nm and 0.9 nm, respectively. The latter signal was biased by the solid emission from soot having a continuous spectrum.

EXPERIMENTAL RESULTS AND DISCUSSIONS

Figure 4 shows the distributions of mean diameter (SMD) $\overline{d}$, mean velocity $\overline{U}$ and velocity fluctuation (RMS) u' of the droplets passing through the horizontal cross section at the spark gap for the injection rates of liquid fuel of (a) 4.44 cm^3/min and (b) 2.13 cm^3/min, where r denotes the radial distance from the axis of the atomizer. Both the mean diameter and the mean velocity are high around the axis decreasing outwards, whereas the velocity

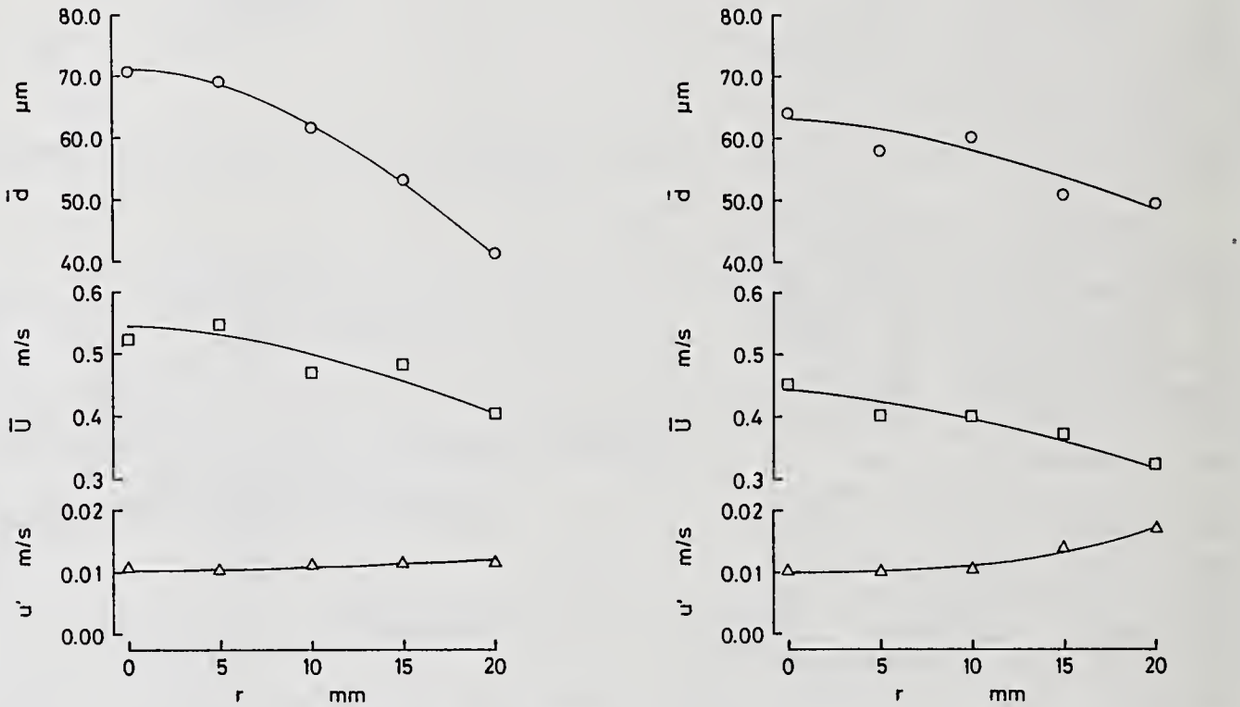

(a) Injection rate of 4.44 cm^3/min. (b) Injection rate of 2.13 cm^3/min.

Fig.4 Distributions of Sauter mean diameter, mean velocity and velocity fluctuation of droplets.

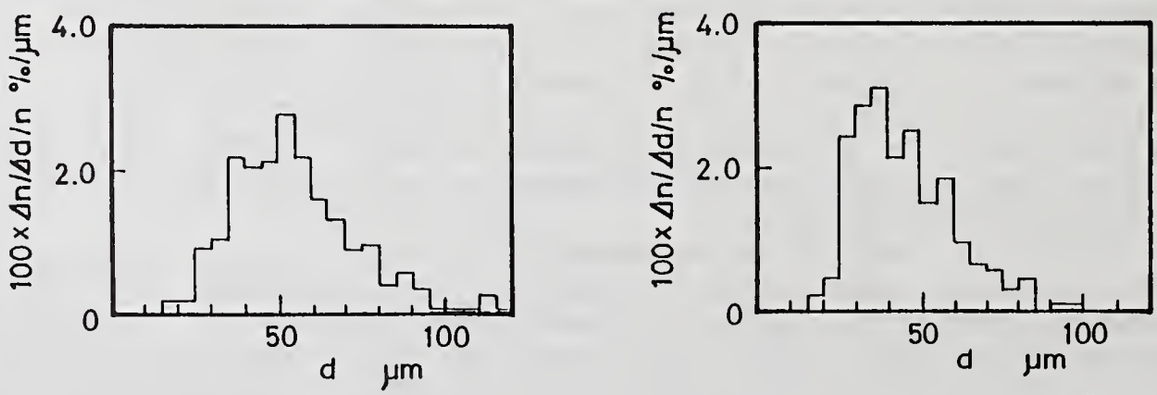

(a) Injection rate of 4.44 cm^3/min. (b) Injection rate of 2.13 cm^3/min.

Fig.5 Size distribution of droplets at spark-gap position.

Table 1 Properties of droplet clouds*

Injection rate cm^3/min	Sauter mean diameter μm	Population density particles/cm^3	Average interval mm
4.44	65.2	653.5	1.43
2.13	57.0	385.0	1.71

* Measured at the position of spark gap.

fluctuation is as low as ca. 2 % around the axis slightly increasing outwards.

Typical examples of the size distribution of droplets are shown in Fig.5, where $\Delta n/\Delta d/n$ denotes the number fraction of droplets in a unit size span (1 μm). It is noticed that the size range is rather narrow and the mass fraction of the droplets smaller than 30 μm is extremely small. This is the characteristic of ultrasonic atomizers. The properties of the droplet clouds are shown in Table 1.

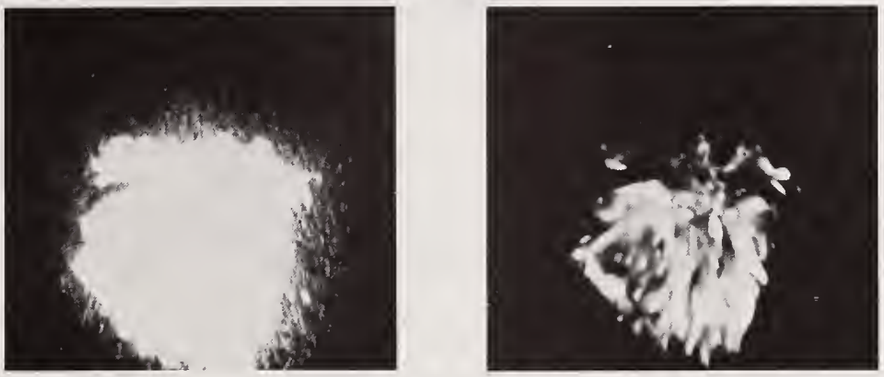

(a) Low-contrast image. (b) High-contrast image.

Fig.6 Two aspects of a flame ball with different tones.

Typical examples of flame image taken by the CCD camera system are shown in Fig.6. (a) and (b) are the images of the same flame ball, but the tone (the contrast between light and shade) has been changed on displaying. Due to the extremely wide dynamic and spectral ranges of this camera system, the image changes its appearance completely as the displaying tone is changed. The peripheral flame front burning in premixed combustion mode with intense OH-radical chemiluminescence is visualized in Fig.6(a). The contour is slightly vague but continuous. Droplets illuminated by the luminous flame are seen around the vapor flame front. A number of droplet clusters various in size and luminously burning in diffusion combustion mode are involved within the closed contour of the continuous vapor flame front as seen in Fig.6(b), where the horizontal dark zones seen on both sides in the upper portion of the flame ball are the electrodes. The interval between the vapor flame front and the luminous flame zone is considerably shorter in the upper portion of the flame ball, where droplets are falling into the flame ball, than in the lower portion.

Then, the light emission signals in OH- and C_2-radical emission bands were monitored at 25 mm below the spark gap while the bottom of the flame front was passing by the position. Typical examples of the signal patterns are shown in Fig.7 for fuel injection rates of (a) 4.44 cm^3/min and (b) 2.13cm^3/min. The emission in OH-radical band is almost pure chemiluminescence of OH radicals, whereas the major fraction of the emission in C_2-radical band is the solid emission from soot with a continuous spectrum and the chemiluminescence of C_2 radicals is almost hidden behind the background noise.

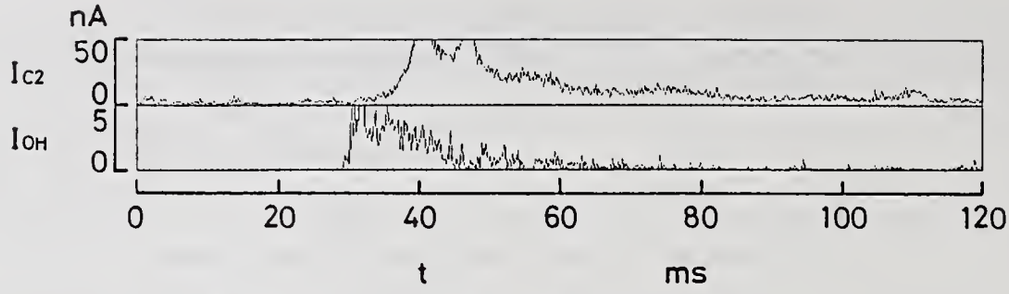

(a) Injection rate of 4.44 cm^3/min.

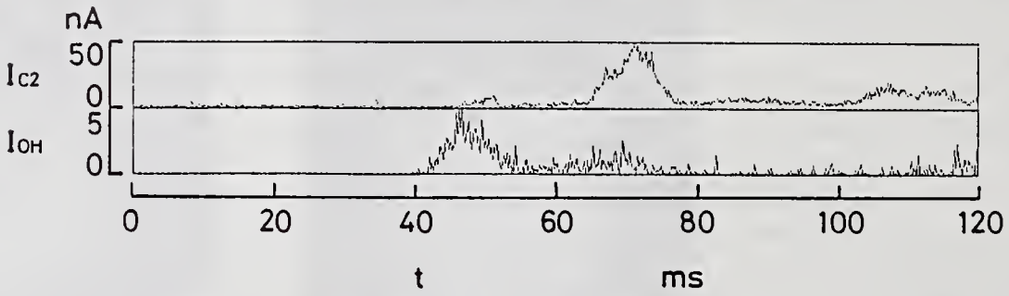

(b) Injection rate of 2.13 cm^3/min.

Fig.7 Typical light emission signal patterns.

As compared the emission signals in OH- and C_2-radical bands with each other, the interval between the rise-up points of both signals is a few milliseconds regardless of the fuel injection rate. Peaks appear in the C_2-band signal intermittently whereas the OH-band signal has usually a single peak gradually descending thereafter. This fact implies that a nonluminous flame propagates downwards in the forefront and that droplet clusters burn behind the front in diffusion combustion mode with soot formation. No nonluminous flame burning in premixed combustion mode exists in the central region of the flame ball with some exceptions. This is coincident with the appearances of flame image shown in Fig.6.

Finally, the statistical behavior of the luminous flame burning in diffusion combustion mode was observed by high-speed photography combined with image processing. For that purpose, the images taken from a few successive frames were binarized with the threshold adjusted at the luminous flame contour level.

Typical examples of the binarized images are shown in Fig.8 for fuel injection rates of (a) 4.44 cm^3/min and (b) 2.13 cm^3/min, where bold and fine solid curves represent the flame contours at 40 ms and 46 ms, respectively, after the start of discharge. The luminous flame expands principally downwards due to the movement of droplets and air. Here, the indicated portions of 11 mm x 15 mm, where the typical behavior of luminous flame was observed, were cut out from Fig.8, and the movement of luminous flame contour was observed from frame to frame as partially shown in Fig.9.

In case of a large fuel injection rate shown in Fig.9(a), the luminous flame contour is rather continuous and smooth and it moves slowly. In case of a small fuel injection rate shown in Fig.9(b), on the other hand, the contour is discontinuous and ragged, and it moves rapidly and discontinuously. The difference between the both cases may be ascribed to the difference in the population density of droplets (see Table 1). Some investigators observed similar phenomena [2], and called it "relay type flame propagation". It has

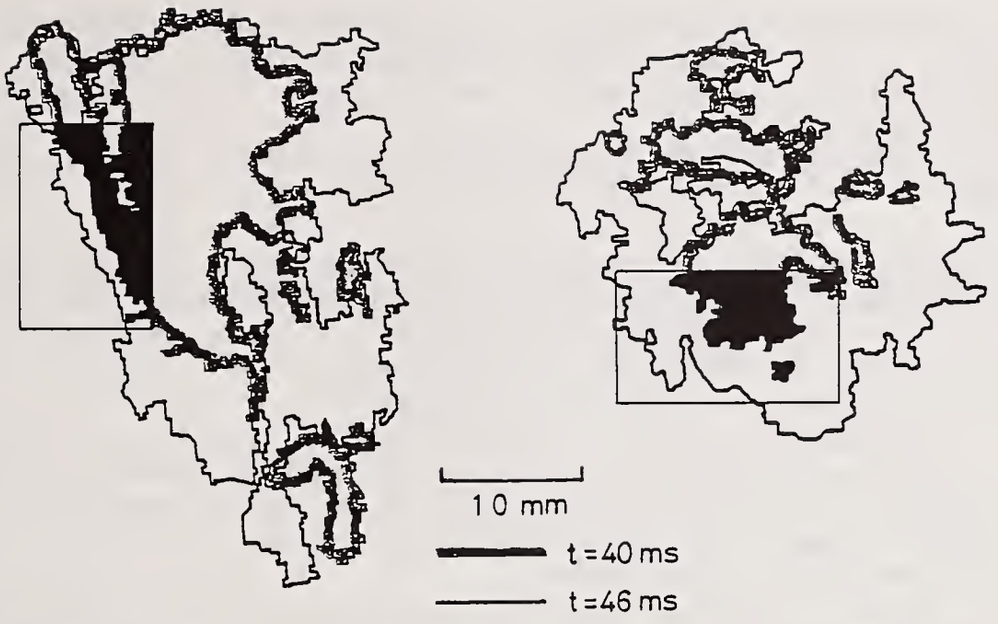

(a) Injection rate of 4.44 cm^3/min. (b) Injection rate of 2.13 cm^3/min.

Fig.8 Binarized flame images and their movements.

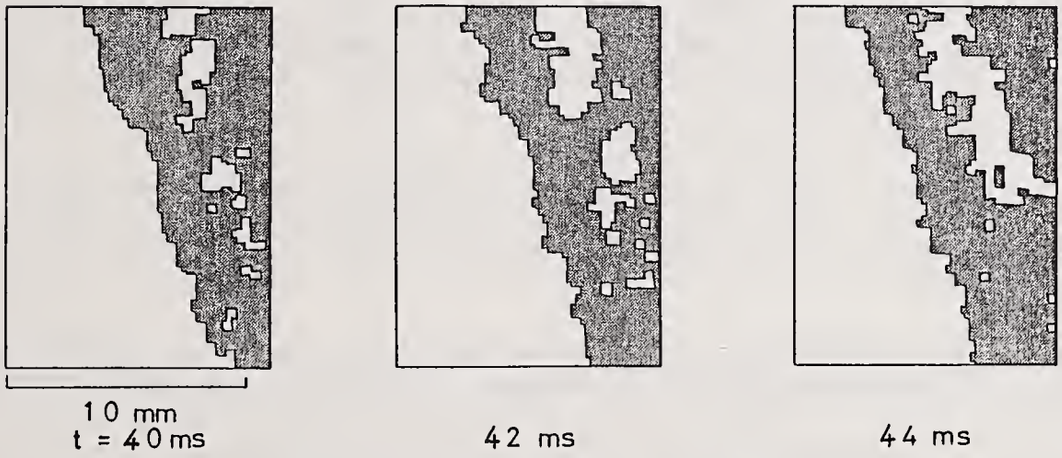

(a) Injection rate of 4.44 cm^3/min.

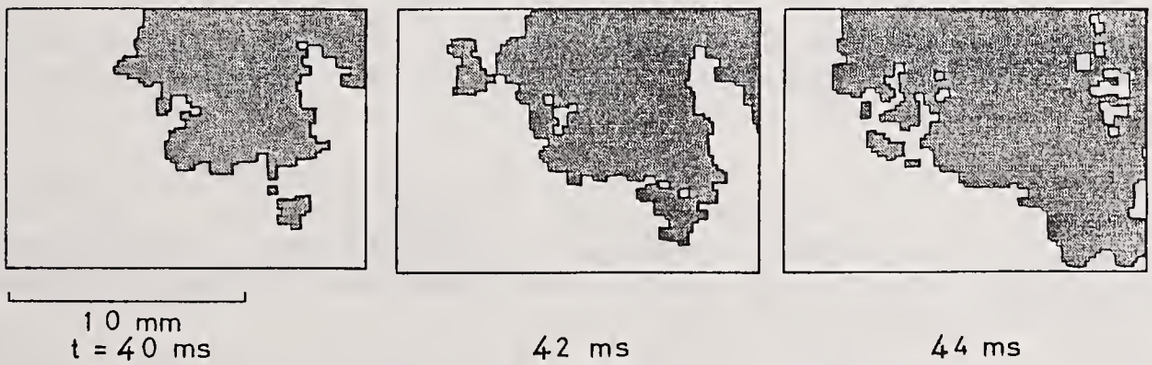

(b) Injection rate of 2.13 cm^3/min.

Fig.9 Successive frames of a luminous flame image.

been found, however, by the present and previous studies [5] of the authors, that this is not real flame propagation but it is only the random/discontinuous expansion of the luminous flame zone behind the nonluminous flame front.

CONCLUSIONS

A droplet suspension of liquid fuel produced by an ultrasonic atomizer was spark-ignited and the flame ball propagating outwards was observed in detail in order to elucidate the mechanism of flame propagation and the complicated group structure of spray flames. The results obtained are summarized as follows:

(1) A nonluminous flame front burning in premixed combustion mode propagated continuously through the vapor-air mixture formed in front of the flame followed by a luminous flame burning in diffusion combustion mode. The time interval between the passages of both flames was a few milliseconds regardless of the fuel injection rate.

(2) A number of droplet clusters various in size and luminously burning in diffusion combustion mode were involved within the closed contour of the continuous vapor flame front. No nonluminous flame burning in premixed combustion mode existed in the central region of the flame ball with some exceptions.

(3) The apparent relay transfer mechanism of luminous flame contour was not a real flame propagation but it was only the random/discontinuous expansion of the luminous flame zone behind the nonluminous flame front.

(4) The group structure of a spray flame is not simple but complex.

REFERENCES

1. Polymeropoulos, C.E. and Das, S., "The Effect of Droplet Size on the Burning Velocity of Kerosene-Air Sprays", Combustion & Flame, Vol. 25, pp. 247-257 (1975).

2. Ashgriz, N. and Yao, S.C., "Combustion Studies in Fuel Rich Idealized Sprays", PhysicoChemical Hydrodynamics, Vol. 8, pp. 335-347 (1987).

3. Nakabe, K, Mizutani, Y., Hirao, T. and Tanimura, S., "Burning Characteristics of Premixed Sprays and Gas-Liquid Coburning Mixtures, Combustion & Flame, Vol. 74, pp. 39-51 (1988).

4. Queiroz, M. and Yao, S.-C., "A Parametric Exploration of the Dynamic Behavior of Flame Propagation in Planar Sprays, Combustion & Flame, Vol. 76, pp. 351-368 (1989).

5. Nakabe, K., Mizutani, Y., Akamatsu, F. and Fujioka, H., "Simultaneous Visualization of Droplet Clusters, Chemiluminescence and Spectral Luminosity in Spray Flames", ASME-JSME Thermal Engineering Joint Conference, Vol. 5, pp. 71-78, The American Society of Mechanical Engineers, New York, N.Y. (1991).

6. Nakabe, K., Mizutani, Y., Hirao, T. and Fujioka, H., "An Experimental Study on Detailed Flame Structure of Liquid Fuel Sprays with and without Gaseous Fuel", to be published in Combustion & Flame.

SOME STUDIES ON FLAME INTERFERENCE EFFECTS OF BURNING METHANOL DROPLETS

B. Roy, R. Chandrasekhar, S. Bhattacharyya and A.K. Ghosh

Department of Aerospace Engineering
Indian Institute of Technology
Kharagpur, India

ABSTRACT

The present study deals with experimental investigations on flame interference effects involving two burning droplets placed at different interdrop distances. The two drops of identical diameter have been simulated by a porous sphere technique with independent fuel feed control. Provision was also made to rotate one of the spheres about its horizontal axis up to 120 rpm for studies on drop rotation effects. The data generated have been compared with those obtained from single non-rotating droplet combustion experiments under identical conditions. The experimental measurements include fuel consumption rates, flame height, flame temperature and composition. The results do reveal some effects of flame interference on burning behaviour of droplets.

INTRODUCTION

Drop rotation and flame interference effects seem to have received little attention in the numerous studies carried out so far on droplet combustion (Ref. 1) While drop rotation has been discussed in Ref. 2, some limited studies on interference effects have been reported in Refs. 3, 4 and 5.

The porous sphere technique has been used in the present study with methanol as fuel to study drop rotation and flame interference effects. This study considers interference effects on flame height, flame temperature and composition in addition to the burning rate. In earlier studies, attention was mostly devoted to interference effects on burning rate.

EXPERIMENTAL SET-UP AND MEASUREMENTS

The experimental facility is based on the well-known porous sphere technique used by several investigators earlier (e.g., Ref. 6) and need not be discussed in detail. Only some specific aspects of the facility will be stressed. The consumption rate for a stable flame has been measured as volumetric rate in cc/sec. instead of mass consumption rate. For flame interference experiments, two identical spheres of 6 mm diameter with independent feed control have been used with a provision to vary interdrop distance (IDD). IDD is the distance between the centres of the two spheres and expressed in terms

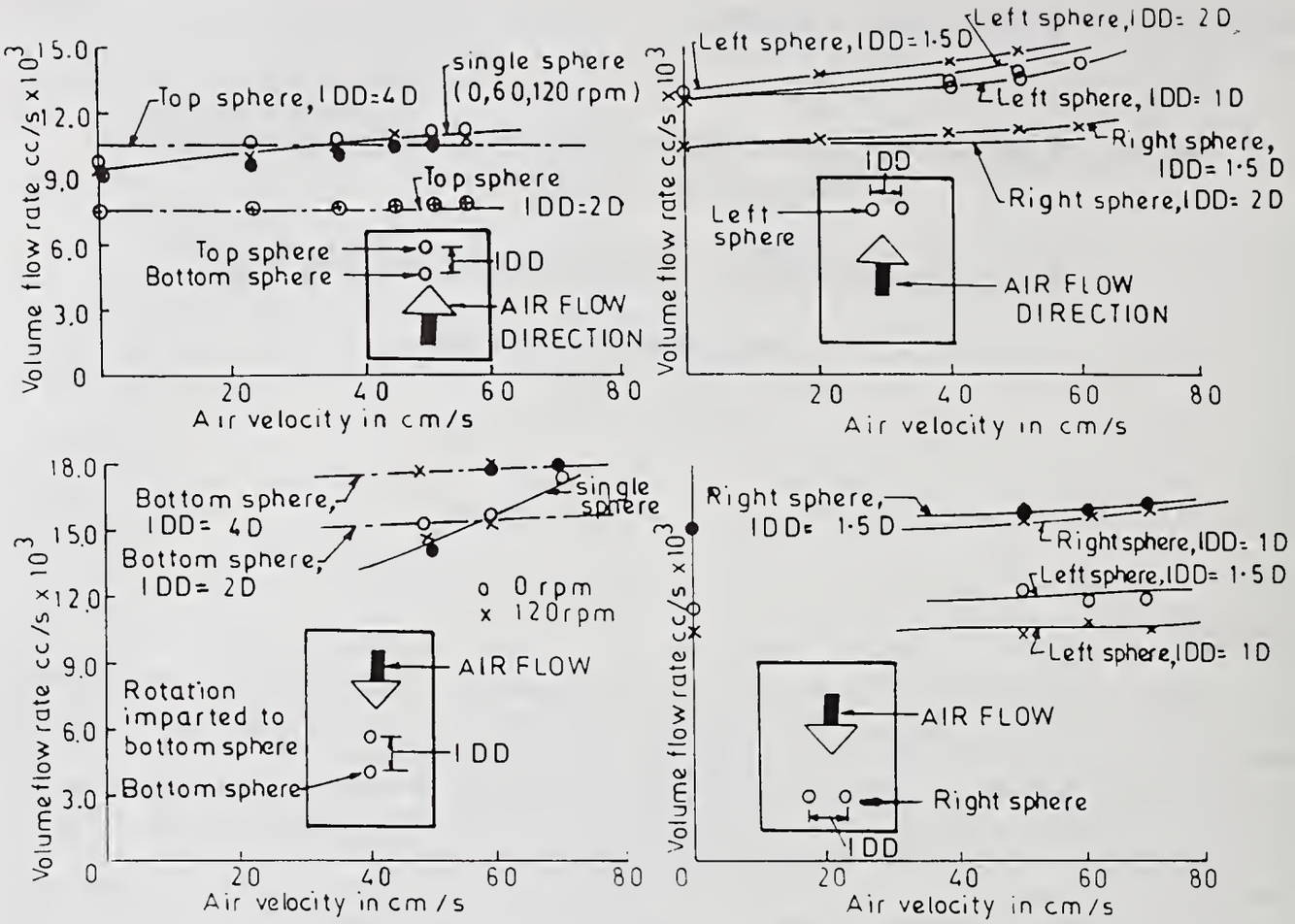

Fig. 1(a). Methanol consumption rates vs. air velocity for different flame configurations.

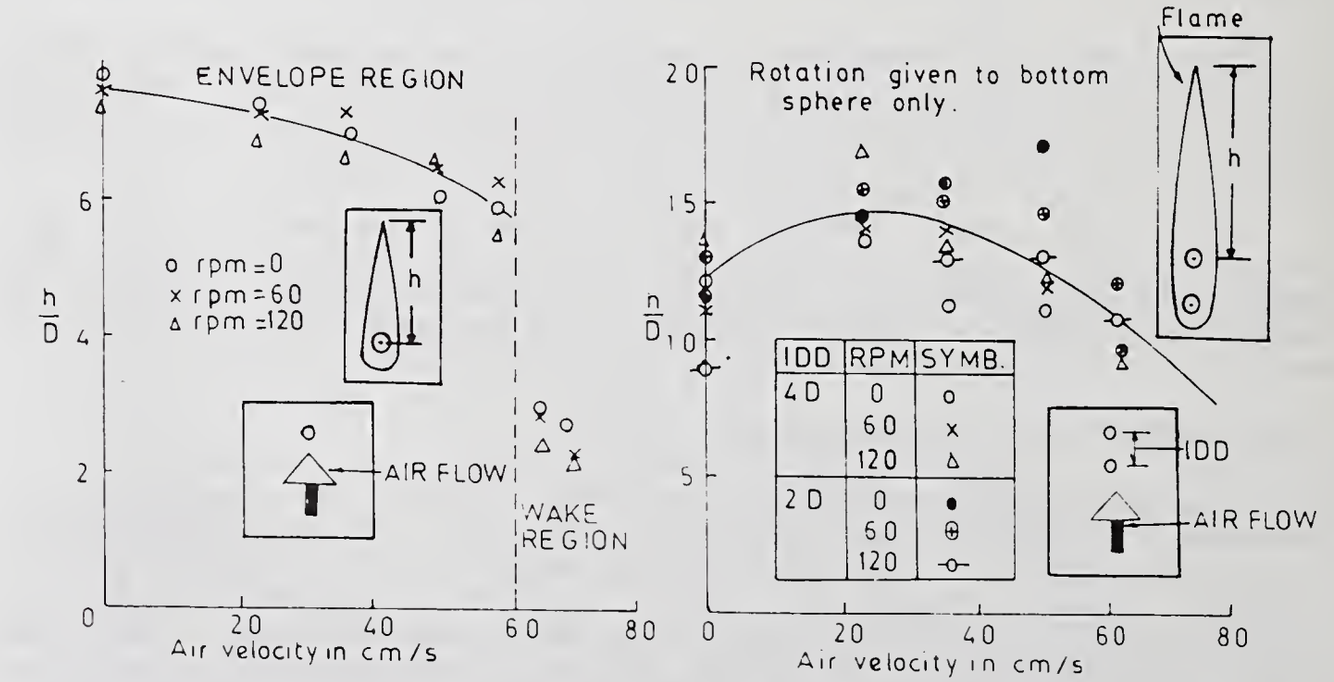

Fig. 1(b). Nondimensional flame height vs. air velocity for methanol flames.

of sphere diameter. Sphere rotation was imparted with a separate motor pulley arrangement up to a speed of 120 rpm. A Pt-Pt+10%Rh thermocouple of 0.4 mm diameter has been used to measure flame temperature. The bead was coated with SiO_2 to minimize catalytic effect and usual conduction and radiation corrections were applied. Gas samples have been drawn from the flame by means of a gas tight syringe and introduced into a dual column chromatograph with a microprocessor controlled integrator which recorded the flame composition. Molecular sieve 5A and Porapak-N were used as the column material and helium was the carrier gas. The flame height has been measured from flame photographs taken with a Nikkon camera with close-up arrangements.

RESULTS AND DISCUSSION

Burning rate: Figure 1(a) shows the measured burning rate plotted against air velocity. The principal observations are: (a) There is an increase in fuel consumption rate with increasing air velocity. (b) Drop rotation up to 120 rpm does not appear to affect consumption rate significantly. (c) For vertical arrangement (one drop placed above the other) in upward air flow, IDD=4D produces a burning rate comparable with that of a single drop whereas IDD=2D produces a burning rate less than that of a single drop. (d) For the same arrangement in downward air flow, flame interference increases burning rate for IDD=4D. But for IDD=2D, flame interference increases burning rate below an air velocity of 59 cm/s and decreases the rate above 59 cm/s. (e) For drops in tandem arrangement, the left drop has a slightly higher burning rate than the right one. The reverse trend is observed for downward airflow.

Flame height: Figure 1(b) shows non-dimensional flame height vs. air velocity. It is observed that: (a) Flame height decreases with air velocity until a critical point is reached where the envelope flame changes over to a wake flame. (b) There is a slight reduction in flame height with rotational speed as compared with a non-rotating drop. (c) For flame interference experiments, the flame height seems to reach a peak at an air velocity of 20 cm/s.

Temperature profiles : Figures 2a and 2b show axial and radial temperature profiles in upward airflow. The following observations are noted: (a) Compared with a single drop, axial profiles are flatter for double drop studies. (b) Flame interference produces slightly higher maximum axial temperature. (c) Drop in temperature after reaching the maximum value is slower for double drop experiments. (d) Increasing IDD produces flatter axial temperature profiles. (e) The point of maximum axial temperature shifts downstream for interference experiments. (f) The maximum radial temperature for a double drop is higher than a single drop. (g) The rise in radial temperature is rapid in the case of a single drop when compared with interference studies.

Figure 3 shows some typical temperature profiles for downward airflow. The main observations are: (a) Comparing Figs. 3b and 3c, it is seen that the main effect of drop rotation seems to make temperature profiles a little broader with no appreciable difference in maximum temperature. (b) In general, radial temperature profiles show peaks at the interface between the flame boundary and ambient air. (c) Comparing Figs. 3a and 3d, the shape of a single drop profile is different from that of a double drop. (d) Comparing Figs. 3c and 3f, the effect of increasing air velocity seems to make the radial temperature profiles somewhat steeper with a slight increase in maximum temperature.

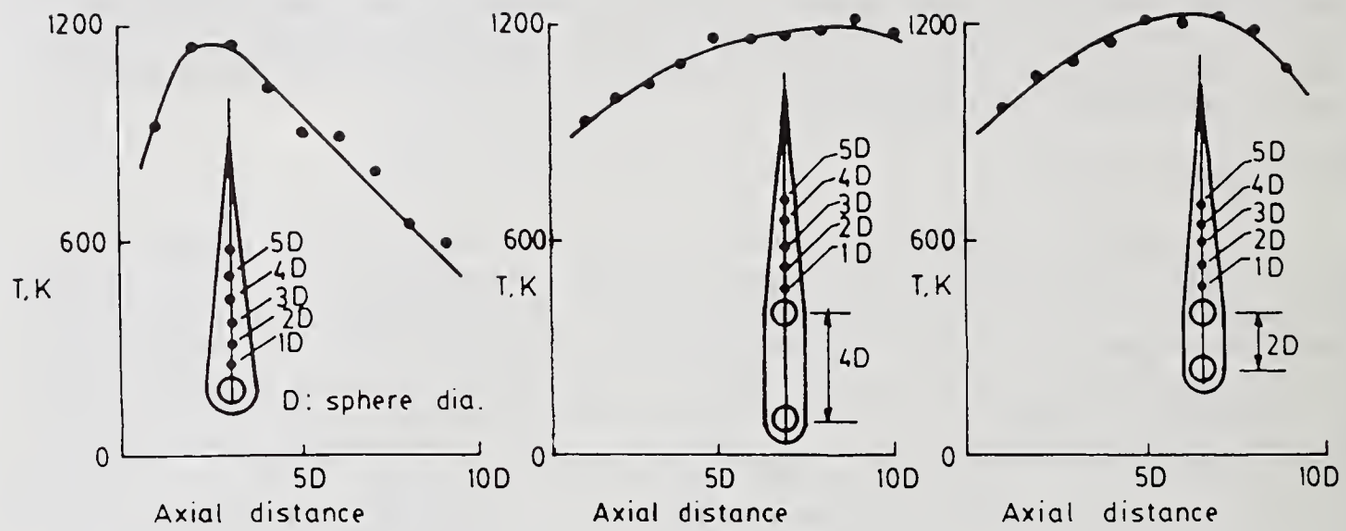

Fig. 2(a). Axial temperature profile for methanol droplets in upward air flow.

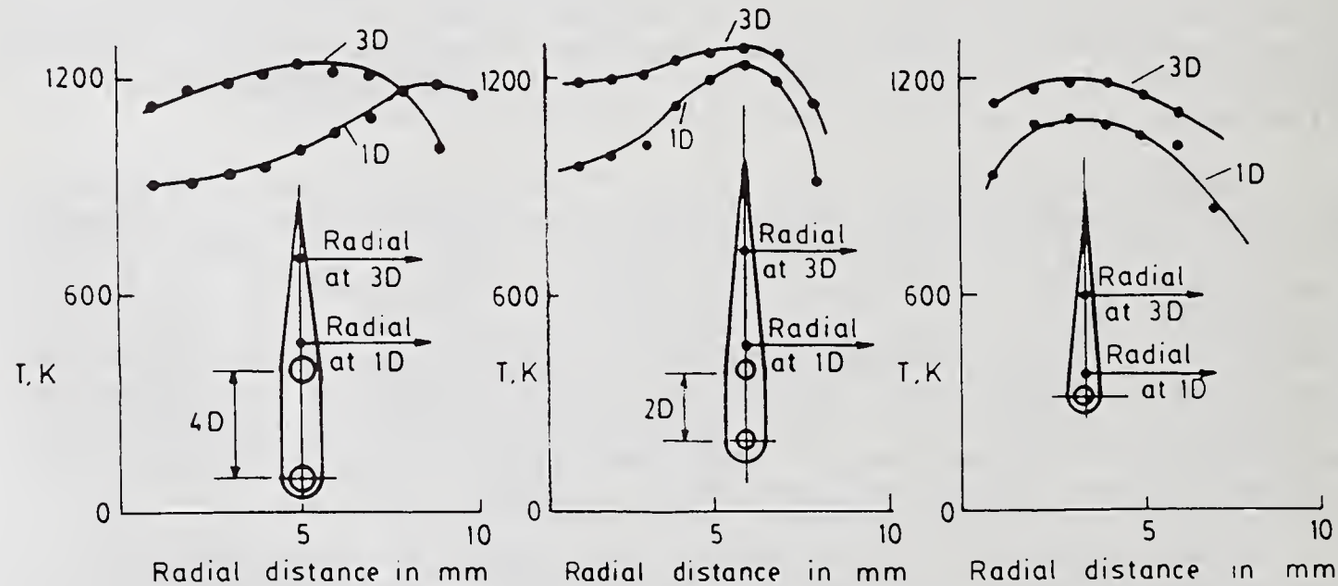

Fig. 2(b). Radial temperature profile for methanol droplets in upward air flow. (Radial distance is measured from the central axis).

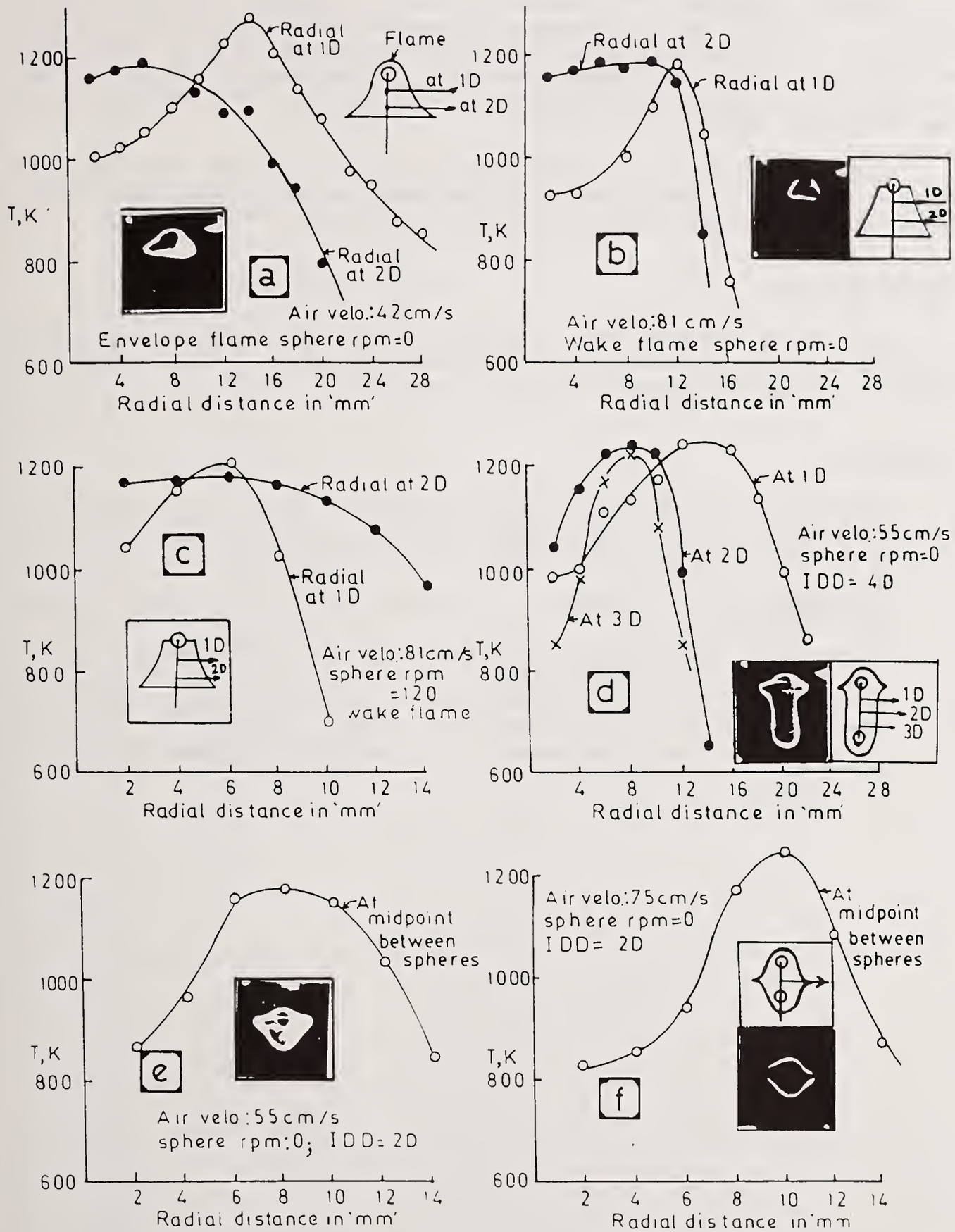

Fig. 3. Typical radial temperature profiles for methanol in downward air flow. Inset photo shows flame configuration.

Flame composition: The composition data for upward airflow are shown in Table 1. It shows that the principal components are O_2, N_2, CO, CO_2 and fuel vapour. The fuel decomposes into CO and H_2 due to pyrolysis (Ref .7). CO finally gets oxidized to CO_2. Fuel vapour concentration is maximum near the drop surface and progressively diminishes downstream. This trend does not appear to change due to flame interference.

Table 2 shows flame composition data for downward airflow. Again near the drop surface, fuel concentration is high and decreases downstream progressively. Again CO is the principal pyrolysed product which gets oxidized to CO_2.

ACKNOWLEDGEMENT

One of the authors (AKG) gratefully acknowledges financial assistance received from the Aeronautics Research and Development Board, Ministry of Defence, for part of the work reported in this paper.

REFERENCES

1. Williams, A., Oxidation and Combustion Review, Vol. 3, pp. 1 (1968).
2. Natarajan R., Can. J. Chem. Engg., Vol. 52, pp. 834 (1974).
3. Rex, J.F., Fuhs, A.E. and Penner, S.S., Jet Propulsion, Vol. 26, pp. 174 (1956).
4. Nuruzzaman, A.S.M., Headley, A.B. and Beer, J., J. Inst. Fuel, Vol. 39, pp. 248 (1966).
5. Brzustowski, T.A., Twardus, E.M., Woiceiki, S. and Sobiesiak, A., AIAA J. Vol. 17, No. 11, pp. 1234 (1974).
6. Gollahalli, S.R. and Brzustowski, T.A., Fourteenth Symp. (Intl.) on Combustion, pp. 1333, The Combustion Institute, Pittsburg, PA (1973).
7. Gollahalli, S.R. and Brzustowski, T.A., Combustion and Flame, Vol. 22, pp. 313 (1974).

Table 1. Flame composition in mole fraction for methanol in upward air flow.

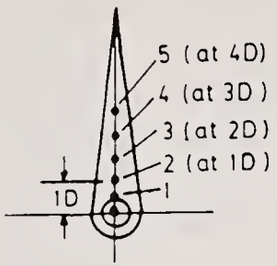

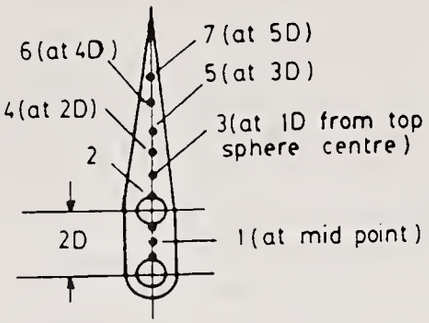

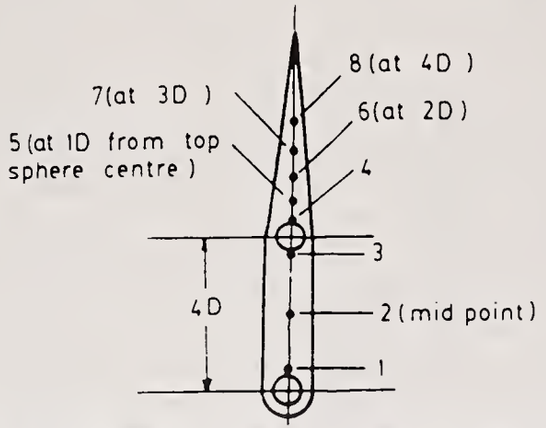

pos. / comp.	1	2	3	4	5	1	2	3	4	5	6	7	1	2	3	4	5	6	7	8
O_2	0·0118	0·0118	0·0124	0·0118	0·0106	0·0121	0·0124	0·0116	0·0113	0·0096	0·0119	0·0112	0·0134	0·0128	0·0122	0·0131	0·0115	0·0112	0·0146	0·0217
N_2	0·5822	0·5888	0·5925	0·6278	0·6538	0·5669	0·5667	0·5677	0·5788	0·6009	0·6135	0·6442	0·5983	0·5940	0·5951	0·5917	0·5786	0·6037	0·6329	0·6822
H_2	0·001	0·002	0·001	0·001	0·001	0·0011	0·0017	0·0009	0·0011	0·001	0·0011	0·0013	0·0012	0·0012	0·0011	0·0014	0·0017	0·0017	0·0014	0·0008
CO	0·122	0·1206	0·1418	0·129	0·118	0·1308	0·1317	0·1292	0·1339	0·1451	0·1481	0·1449	0·1371	0·1463	0·1592	0·1023	0·1189	0·1280	0·1279	0·0743
CO_2	0·1265	0·1360	0·1304	0·152	0·1803	0·1160	0·1217	0·1273	0·1352	0·1411	0·1558	0·1742	0·1175	0·1291	0·1329	0·1260	0·1363	0·1467	0·1631	0·1946
CH_3OH	0·1563	0·1412	0·1218	0·0787	0·0367	0·1730	0·166	0·1631	0·1397	0·1026	0·0698	0·0244	0·1326	0·1165	0·0992	0·1654	0·1530	0·1087	0·0602	0·0266

Table 2. Flame composition (in mole percent) for methanol in downward air flow for single and double droplet experiments.

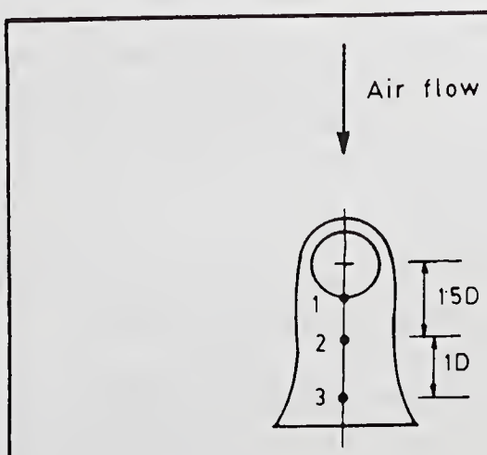

D = Sphere diameter

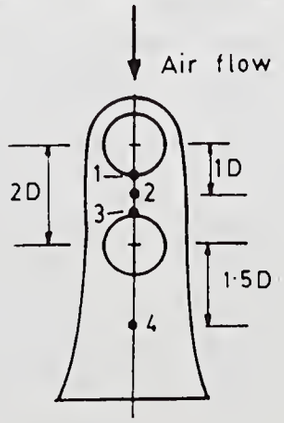

Double drop , 1DD = 2D

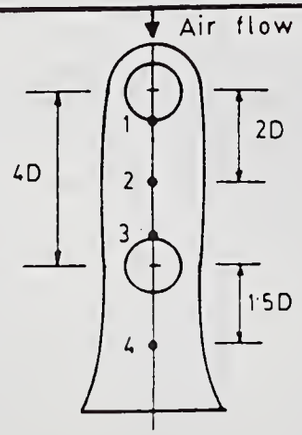

Double drop , 1DD = 4D

comp. / pos.	O_2	N_2	H_2	CO	CO_2	CH_3OH	O_2	N_2	H_2	CO	CO_2	CH_3OH	O_2	N_2	H_2	CO	CO_2	CH_3OH
1	1·03	56·73	0·13	14·61	13·27	14·23	1·23	61·64	0·14	9·27	14·47	13·23	1·00	65·32	0·09	7·59	14·33	11·69
2	1·18	57·91	0·12	12·32	14·85	13·61	1·44	59·79	0·15	15·61	14·65	8·35	1·50	67·44	0·12	8·92	14·35	7·69
3	1·59	70·67	0·12	5·08	16·60	5·91	1·07	57·66	0·13	15·65	13·80	11·69	1·06	65·61	0·11	10·52	14·08	8·20
4							1·47	65·80	0·14	10·19	13·88	8·48	1·12	71·99	0·11	8·27	14·18	4·33

ATOMIZATION AND COMBUSTION OF LIQUID FUELS IN COUNTER-FLOW

B.N. Raghunandan, G. Jagannath and D.S. Mehra

Department of Aerospace Engineering
Indian Institute of Science
Bangalore, India

ABSTRACT

Counter-flow configurations have certain inherent advantages over the normal co-flowing types like flame-holding capability and compactness of the combustion chamber. The study aims to generate some basic data on the flame-holding capability of pressure as well as air assisted jets in the counter-flow mode. It is shown that even in cold flow, the opposing air stream exerts a considerable influence on the atomization from a pressure jet. The trends of stability boundaries in both the cases are similar to each other and to gaseous fuel jets. Within the acceptable range of fuel penetration levels, a finer spray provides better quality of combustion, but has a narrower stability bounds than a coarse spray.

INTRODUCTION

There are many recent developments in burner configurations both in aeroengine field and in industrial applications where the injection of liquid fuel is not necessarily at the head-end as in conventional burners. In such non-coflowing configurations, an obvious advantage is that the fuel finds a longer residence time in the combustion chamber [1]. In addition to making the chamber more compact, this mode is envisaged to accommodate a coarse spray as would result in off-design conditions. Even from the point of view of safety of igniter, the counter-flowing system offers some advantages. The flame after ignition can be easily manipulated to anchor away from the igniter which remains in a cooler air stream [2].

Burners, in general, contain either a swirl flow or a bluff body for the purpose of flame stabilization. The ability of the counter-flowing jets to act as aerodynamic flame holders has been a subject of investigation since long [3,4]. The studies so far have been restricted to gaseous fuels only whereas it is more relevant to determine such blow-off characteristics for liquid fuel sprays which are more commonly used in practical burners. Even basic information like stability of jet flames of liquid

fuel in counter-flow configuration does not seem to be available. Towards this objective of generating some basic data and understanding, this study on the combustion stability of liquid fuel jets- both pressure jets as well as air-assisted jets in a counter-flow of air has been undertaken. Some of the interesting observations on atomization in cold-flow conditions are expected to find industrial applications.

EXPERIMENTAL

Experiments have been conducted in a combustion tunnel as shown in Fig. 1. The air from a centrifugal blower is channelled through a control valve, flow straightner and metering instrument into a settling chamber. A nozzle of high contraction ratio (18:1) and having an exit section of 200mm x 200 mm provides a uniform outlet. While some of the initial experiments were conducted in a test section attached to the nozzle-exit later ones have been conducted without any confinement. However, a large shroud had been used for the sake of safety when the flame sizes were too big for a laboratory experiment. The water-head measured at the venturimeter is calibrated against the velocity in the test zone.

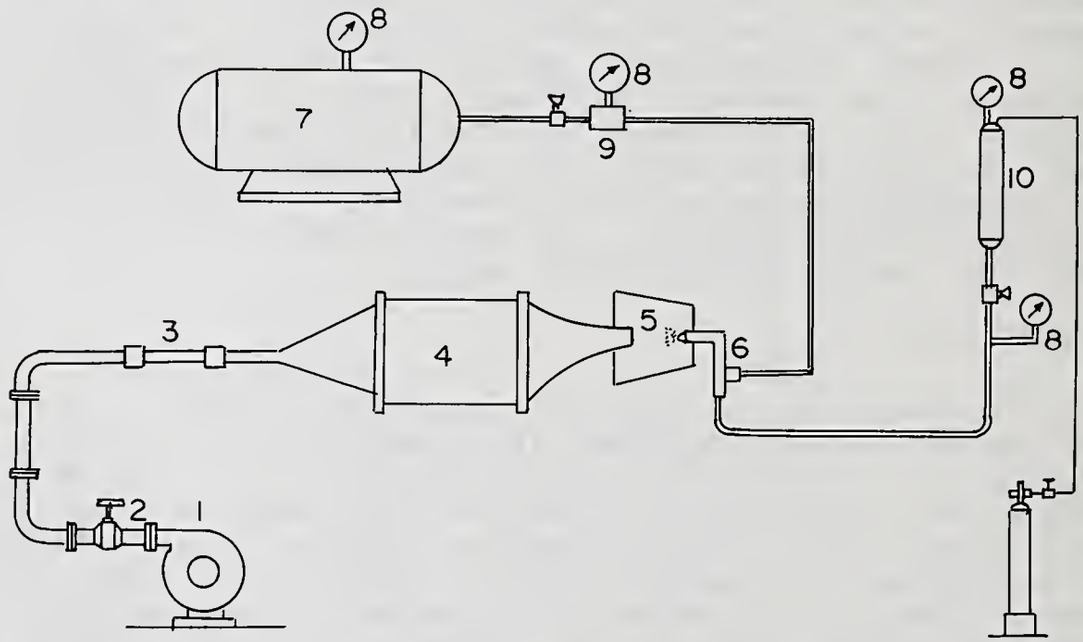

Fig.1 Schematic of the experimental set up: (1. Blower 2. Control valve 3. Venturimeter 4.Settling chamber 5. Test Section 6. Atomizer 7. Pressure bottle 8. Pressure gauge 9. Orifice meter 10. Fuel Tank)

The fuel injection line consists of a tank, pressurising system and finally the atomizer. While this suffices for a pressure jet, an additional high pressure air attachment is necessary (Fig. 1) for the studies with air-assisted atomizer. The atomizing air flow rate is measured with a choked-orifice meter. The liquid fuel (kerosine) flow rate is obtained by direct calibration of the flow against pressure drop. While checking the flow rates in the presence of counter-flow, a slight

variation has been adopted namely one of discharging a known amount of fuel over a measured time period. The details of the atomizer characteristics are included in the following section.

RESULTS AND DISCUSSION

Pressure Atomizer:

The pressure atomizers employed are all conventional swirl chamber type with wide range of swirl parameter, A[1] from 3 to 12. In terms of the parameter $A_p/d_s d_o$ (see Ref 1), this corresponds to a range of 0.08 to 0.35. Out of the several variations tried, three representative ones are described below.

Table 1 Pressure Jet Characteristics

Parameter	PJ-1	PJ-2	PJ-3
Orifice diameter (mm)	0.8	0.8	0.8
Swirl Parameter, A*	3.0	6.0	12.0
Coefficient of Discharge C_d**	0.55	0.28	0.175
Cone Angle (Degrees) in Quiescent surroundings	45-50	50-55	45-50
Penetration	High	Low	Low
Spray	Coarse	Very good	Good
Effect of counter-flow	Unaffected	Significant	Significant

* $A = A_o d_c / A_t d_o$

** Nearly independent of Δp and counter-flow velocity (within 5%)

Table 1 describes some of the major characteristics of the pressure jets PJ-1, PJ-2 and PJ-3. The case PJ-1 and similar ones having high C_d values tend to produce high penetrations both due to coarse particle sizes and high axial component of the velocity. Since such large penetrations annul the advantage of compactness and also that in the present experimental set up pose some hazard by way of fuel entering the settling chamber, they are considered unsuitable. However, some tests were conducted to determine if the counter-flowing air alters the spray characteristics. But no favourable changes were observed in the experimental range of velocity.

The injectors PJ-2 and PJ-3 with relatively low cone angle, finer spray and low penetration have been tested for their behaviour in the presence of counter-flowing air. With the air velocity, though the C_d values are not altered much (within about 3%), the cone angle variation shows an interesting trend. As seen in Fig. 2, for both types, the cone angle initially shows a very weak increasing trend with air velocity followed by a sudden increase in slope. In this expanded state, the atomization level

---

[1] $A = A_o d_s / A_p d_o$ where d_o and A_o are diameter and area of the orifice and d_s the diameter and A_p inlet area of swirl chamber.

becomes much finer even for those cases which can otherwise be termed as poor sprays. This trend can be seen for all the values of pressure-drops studied.

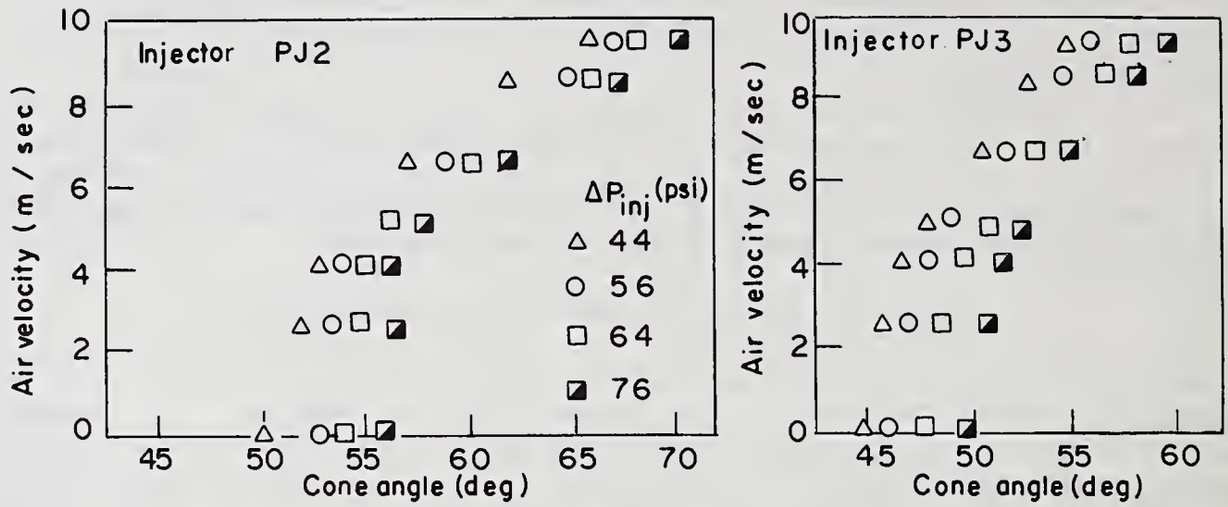

Fig. 2 Injector characteristics with counter-flow (cold flow)

Further experimentation to understand the transition process lead to the observation that there is a transition region (see Fig. 3) where the variation of cone angle is not really monotonic, but involves some oscillations. The cone at the exit of the orifice fluctuates between the normal state and the expanded state aperiodically. Though this can be attributed to the influence of counter-flow on the air-core formation and its size in the vicinity of the orifices, it warrants further work to ascertain the exact mechanism.

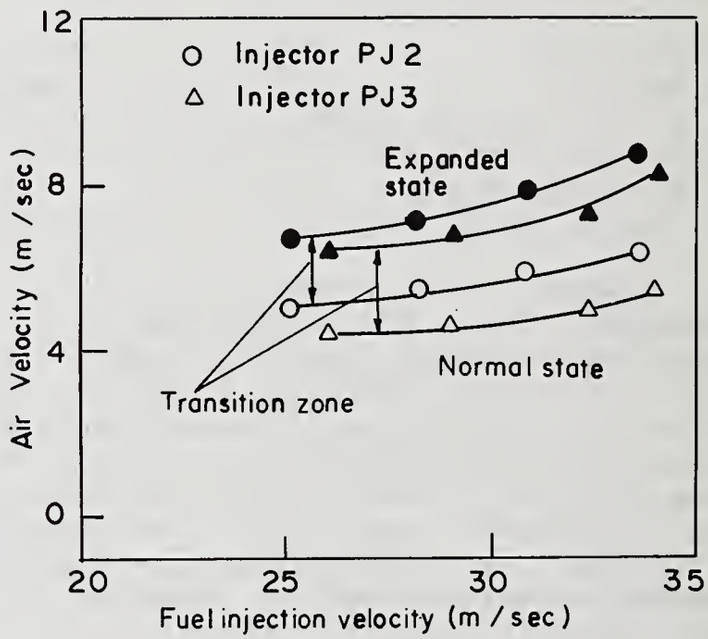

Fig. 3 Transition in cold flow

The blow-off characteristics of the flame generated by counter-flowing system is shown in Fig. 4. Extinction of the flame occurs for both PJ2 and PJ3 at air velocities slightly higher than that causing complete transition described above. Interestingly, at a given fuel injection velocity, the counter-flow air velocity for blow-off is in the same range as for gaseous fuels (see Ref 2) though the actual fuel mass flow rates in the present case are very much higher. Like with the gaseous fuels, even in the present set of experiments, the onset of

extinction is marked by the formation of a dark zone along the axis of the injector.

Air-assisted Atomizer:

At the outset, it may be noted that this type of atomizers provide cooling to the injector inside the enveloping flame and at the same time, provide air for combustion in the vicinity of the jet orifice. The atomizer consists of a fuel nozzle concentric with which is an annular passage for atomizing air [see Ref 5 for details]. The atomizer has the provision of moving the fuel orifice relative to the atomizing air outlet in such a way that the same unit can be made to act either as an internal mixing type or as an external mixing type.

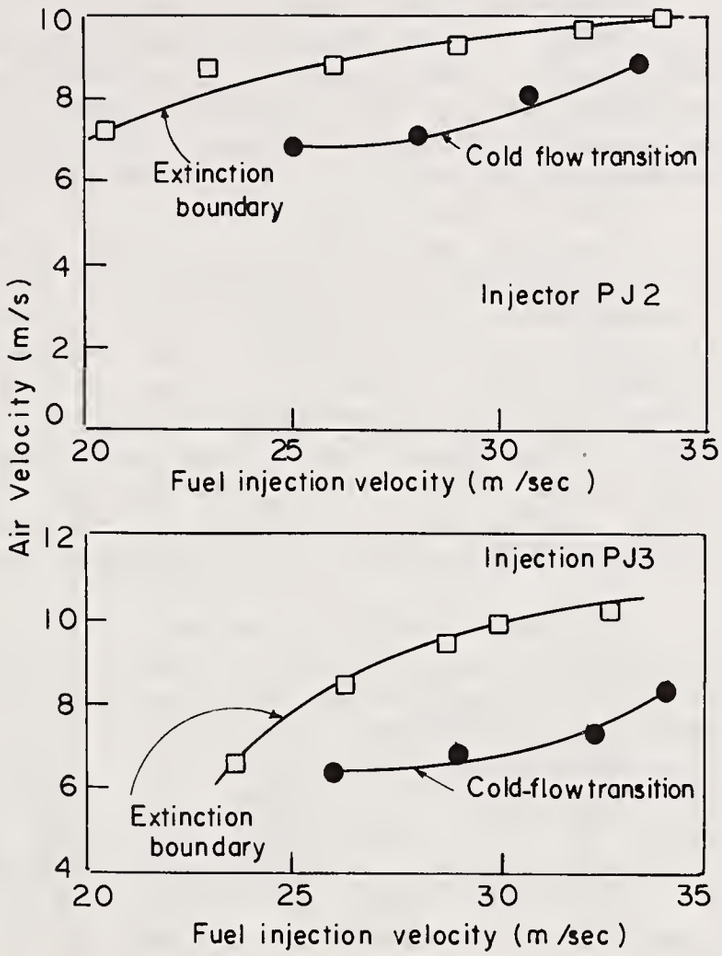

Fig. 4 Combustion stability characteristics (Pressure Atomizer).

Three of the representative atomizer configurations are described in Table 2. Like in pressure jets, here also narrower cone angles show greater ability of flame holding and hence are adopted for the experiments. Cold flow tests have shown that the experimental injector yields fine spray in external mixing position, but in a rather coarse spray when the fuel orifice is retracted deeper into the air nozzle. As is to be expected, the

Table 2 Some Characteristics of Air-assisted Jets

Parameter	AJ-1	AJ-2	AJ-3
Fuel Orifice(mm)	0.4	0.4	0.4
Air Nozzle dia (mm)	3.0	3.0	4.5
Configuration (relative position of the orifices)	In-plane ext.mixing	Internal mixing	External mixing
Spray	Fine	Coarse	Finer than AJ-1
Cone angle (deg)	12-19	7-10	12-14

fineness of the spray improves as the ratio of atomiser air flow (m_a) to fuel flow (m_f) is increased.

Unlike the case of pressure jets, here the counter-flowing air does not seem to alter the spray in the vicinity of the injector, i.e., the cone angle does not get affected. This is perhaps due to the fact that the atomizing air velocity has to be necessarily very large (~ 50 m/sec) and also there is no low-pressure air core in this type of atomizer.

Combustion of this type of spray yields a flame which has a hollow conical region which is blue in colour and at the far end a mush-room like flange. The conical region is due to combustion of fuel in the presence of atomizing air. With increasing counter-flow velocity, the flange bends towards the injector before being blown off. Increasing atomizing air flow tends to shift the flame away from the injector and at a given counter-flow velocity, the flame can be blown-out with atomizing air alone although the atomizer air-fuel ratios are well within the values used in such air-assisted atomizers [6].

In this configuration, the atomizing air flow is an additional parameter in the stability diagram. The data of blow-off as obtained in the experiment are shown in Fig. 5 for two different configurations AJ-1 and AJ-3. For the case of AJ-2 also one gets similar plots with the curves shifted towards higher counter-flow air velocity, but the flame tends to be sooty due to coarseness of the drops. The nature of curves hint at a possible explanation for extinction in terms of the effective equivalence ratio at the critical zone around the stagnation point much as the one invoked by Schaffer and Cambell [4] in their work on flame holding. But a precise description in terms of accurate numbers has so far proved elusive.

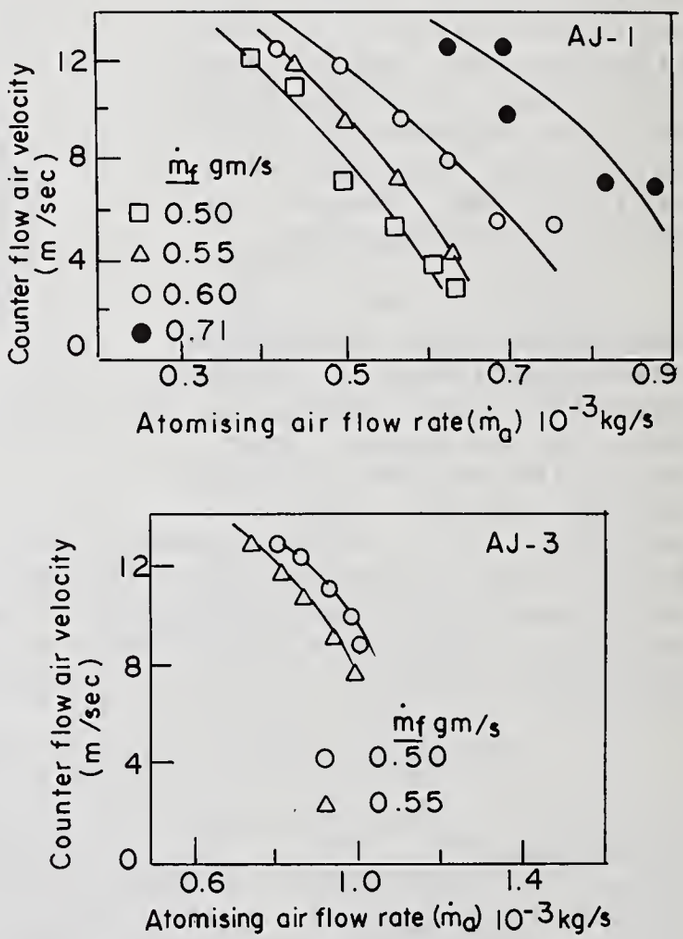

Fig. 5 Combustion stability plots for air-assisted jet in counter-flow.

Shown in Fig. 6 is the stability plot for AJ-1 redrawn from the data in the

previous figure. On this plane with (m_f/m_a) as a variable the different curves merge into a narrow band. Identical behaviour is observed with the fine spray of AJ-3, but for AJ-2 substantial dispersion exists. Noting that such a merging is obtained for a range of both m_f and m_a, one can view the abscissa as the fuel flow variation at a constant atomizer air flow rate. From this point of view the trend in Fig. 6 is comparable with that of pressure atomizer in Fig.4. This argument suggests that the mechanism of extinction may be common to both the cases discussed here and to the gaseous counter flow system described in Ref. 2.

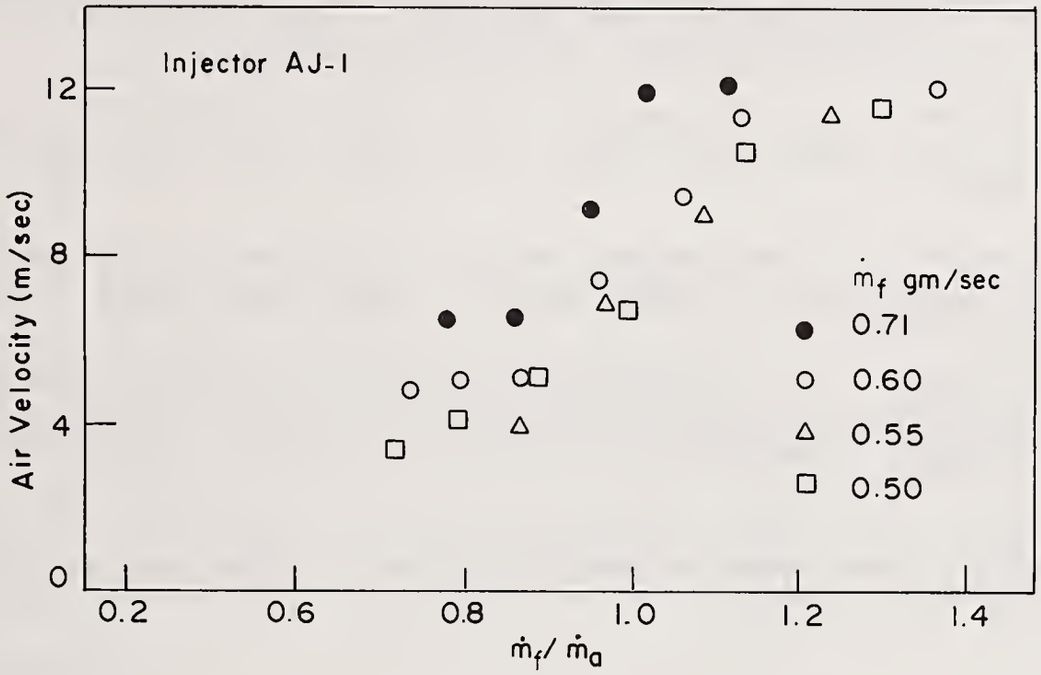

Fig. 6 Flame-holding ability of air-assisted jet

CONCLUDING REMARKS

The atomization from a pressure jet is considerably influenced by the presence of a counter-flowing air stream. An air-assisted fuel jet however is quite resistant to the counter-flow. Fuel sprays of either type can act as flame-holders over a range of air velocities without any swirl motion. One can expect the stability to improve if recirculation is also imposed. Coarse sprays tend to have higher penetration and accommodate higher counter-flow velocity than the fine-sprays. The combustion stability characteristics of both the types of jets are similar and seem to share some features with the gaseous fuel jets. Unlike the co-flowing streams where the flame anchoring is governed by the processes near the fuel outlet, in these flames the region around the stagnation point is critical. This is despite the fact that the sprays fan out leaving low fuel concentrations along the axis.

ACKNOWLEDGEMENTS

The authors thank Mr. S. Nagaraj for his ready services in photography.

REFERENCES

1. Lefebvre, A.H., Gas Turbine Combustion, Hemisphere, Washington (1983).

2. Raghunandan, B.N., Gopakumar, B.R. and Jagannath, G., "Arc Ignition of Gaseous Fuel Jets in a Counter-flow of Air", Jl. Inst. Energy, Vol. 60, pp 132-137 (1987).

3. Schaffer, A. and Cambel, A.B., "The Effect of an Opposing Jet on Flame Stability", Jet Prop., Vol. 25, pp 284-287 (1955).

4. Schaffer, A. and Cambel, A.B., "Continued Investigations of the Opposing Jet Flame holder", Jet Prop., Vol. 26, pp 576-578 (1956).

5. Jagannath, G., "Combustion Stability Studies of Plain-jet Atomizer in a Counter-flowing Air Stream", ME Thesis, KREC Surathkal (1988).

6. Rizk, N.K. and Lefebvre, A.H., " Influence of Atomizer Design Features on Mean Drop Size", AIAA Jl., Vol. 21, pp 1139-1142 (1983).

SIMILARITY BETWEEN THE BREAK-UP LENGTHS OF A HIGH SPEED LIQUID JET IN ATMOSPHERIC AND PRESSURIZED CONDITIONS

M. Arai*, M. Shimizu† and H. Hiroyasu‡

* Dept. of Mechanical Systems Engineering, Gunma University, Kiryu, Gunma, Japan
† Dept. of Mechanical Engineering, Kinki University, Osaka, Japan
‡ Dept. of Mechanical Engineering, University of Hiroshima, Hiroshima, Japan

ABSTRACT

It is well known that the break-up length of a high speed jet such as a diesel spray is greatly affected by a structure of an injection nozzle. In this paper, to reveal the relationship between the break-up length and the structure, an internal flow in a transparent nozzle of 3 mm diameter was observed. The breakup lengths of jets injected through nozzles of diameters 0.3 mm and 3 mm, were measured by an electric resistance method. They were compared and suitable nozzle structures were selected to keep phenomenological analogies of break-up lengths in nozzles of different scales and in different surrounding conditions. Similarities of the break-up lengths in atmospheric and pressurized conditions were discussed about an internal flow effect on the break-up mechanism. A reattachment point of a separated flow in a nozzle was investigated as a characteristic of the internal flow. The behavior of break-up length in the spray flow region could be explained by a movement of this point.

INTRODUCTION

The main causes for the disintegration of a high speed liquid jet have been suggested by vibration of an injection pressure[1)], velocity distribution in a nozzle[2)], injection velocity[3)], internal and shear forces between a jet and gaseous environment[4,5)]. However, disintegration mechanisms just after a nozzle exit are not well understood, although several studies[2,5,6)] have attempted to explain them. Liquid turbulence, cavitation and aerodynamic interaction between the jet and surroundings are thought to be important factors[7)].

The disintegration of the jet is also affected by physical properties of the injected liquid, structure of the nozzle, injection velocity and ambient gas pressure or density. It have been already suggested in previous studies[8-12)] that there is a strong dependence between the break-up length and an interfacial force due to the gaseous environment. Therefore, as a further study of the break-up length, the effect of the internal flow in a nozzle on the break-up length was investigated and discussed in this study. The break-up mechanism of the liquid jet injected in a pressurized surroundings was discussed by a phenimenological analogy of the break-up lengths of the jets in atmospheric and pressurized surroundings.

EXPERIMENTAL APPARATUS AND METHOD

The apparatus shown in Fig. 1 was constructed to study the break-up phenomena of a high speed jet in a high pressure surroundings. The apparatus consisted of a spray chamber, a liquid injection system, an injection nozzle and a wire net detector for measuring a break-up length.

Water was continuously injected by the injection system into the spray chamber. The injection velocity of a jet was calculated as the sectional average velocity in the nozzle. The Reynolds number Re of the jet was

calculated with kinematic viscosity of water, nozzle diameter and this velocity. An electrical circuit was used to determine the break-up length. Definitions of the break-up length and spray angle were reported with measurement methods in the previous papers[8,9].

A fundamental structure of a nozzle used in this investigation is also shown in the figure. It had a long inlet pipe to obtain a smooth inlet flow to the nozzle. The entrance of the nozzle was made in a sharp edge, so that a constricted flow was easily generated at the entrance. Hole diameter D, length L and inlet pipe diameter D_0 specified a structure of the nozzle. Length-to-diameter ratio L/D and sectional area ratio of the hole diameter to the inlet pipe diameter, $M = (D/D_0)^2$ were the non-dimensional parameters used to represent the structure.

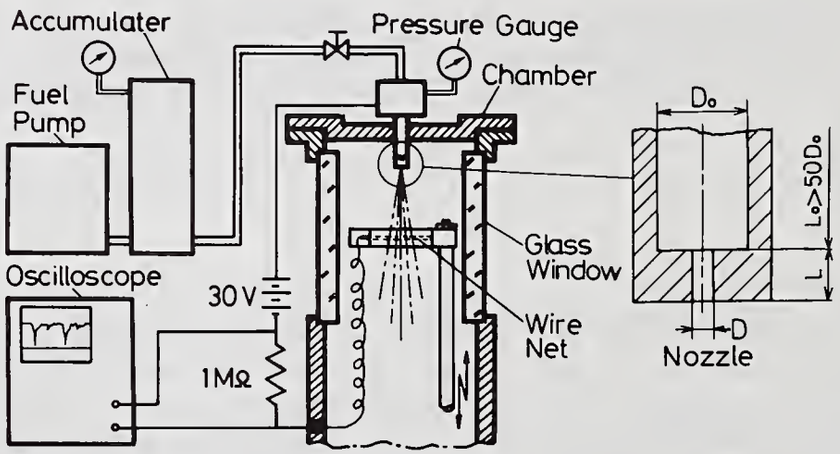

Fig. 1 Experimental apparatus and nozzle

BREAK-UP LENGTHS IN VARIOUS LIQUID JETS

The disintegrating behavior and break-up length of a high speed liquid jet are frequently a technical matter of great importance for diesel injection nozzle performance. Therefore, a hole diameter 0.3 mm of a nozzle and an ambient pressure 3.0 MPa into which a jet was injected were selected to reproduce a spray in a combustion chamber of a diesel engine.

Effects of the length-to-diameter ratio L/D on the break-up length are summarized in Fig. 2. Since the ambient pressure was high enough to produce a strong interfacial force between the jet and surroundings, fine atomization could be observed when an injection velocity was higher than 70 m/s and this was termed spray. The break-up length in this region decreased with an increase in the injection velocity. For the cases of L/D = 4 and 10, it passed through a minimum, and then reached an almost constant value. When the L/D ratio was 1 or far larger than 10, there was no minimum point of the break-up length in the spray region.

When the ambient pressure was reduced from 3.0 MPa to 0.1 MPa, the break-up length was extended as shown in Fig. 3. Further, a kind of hysteresis appeared in a low velocity region. If the velocity increased from lower value than where two possible break-up lengths existed, the actual break-up length was the shorter of the two. However, if the velocity decreased from the higher value, it was the longer break-up length produced by the separated flow issuing from the nozzle[12]. This phenomena was more evident in the break-up length produced by 3.0 mm diameter nozzle, that is also shown in the figure. From the behavior described above, it is concluded that no analogy in the break-up length could be maintained between the 0.3 mm and 3.0 mm nozzles, using in the different pressures.

The sectional area ratio $M = (D/D_0)^2$ could sometimes affect the break-up length. Figure 4 shows this effect on the break-up lengths of jets injected by 3.0 mm nozzles into atmospheric environment. The hysteresis mentioned above was only observed with the nozzle which had 0.0036 as the value of M. The break-up lengths in the spray region that is shown in higher velocity than 10 m/s, were different corresponding the values of M.

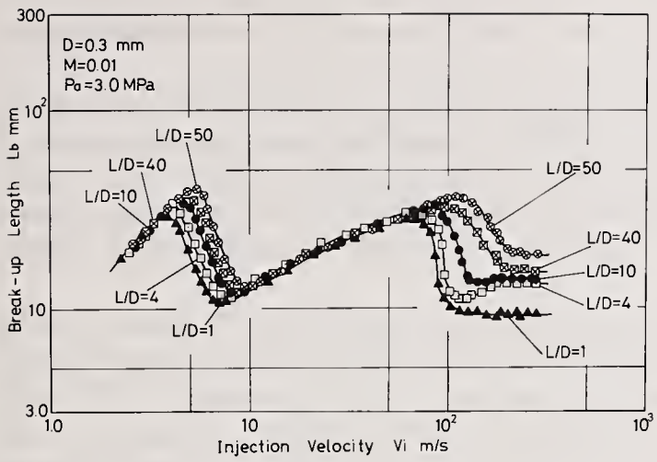

Fig. 2 Effect of L/D on the break-up length in 3.0 MPa surroundings

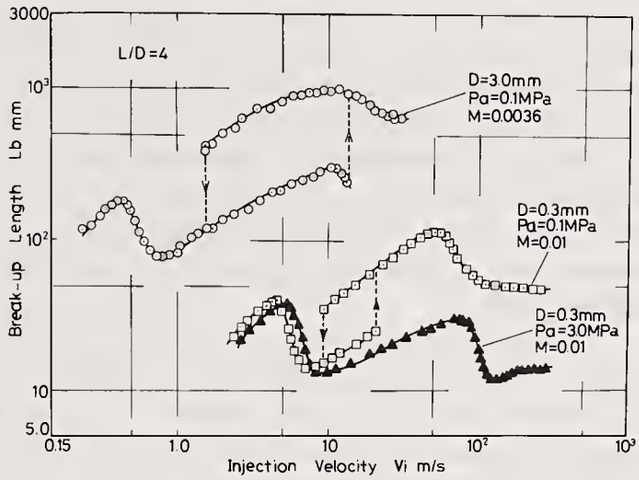

Fig. 3 Effect of the hole diameter on the break-up length

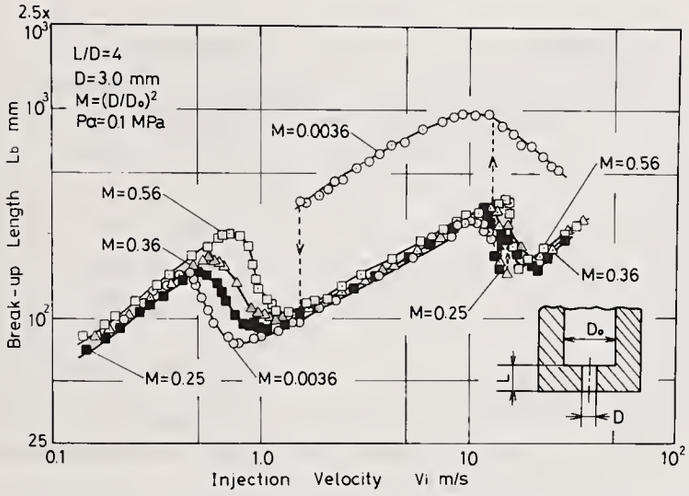

Fig. 4 Effect of sectional area ratio of the inlet pipe on the break-up length

ANALOGY OF THE BREAK-UP LENGTHS IN DIFFERENT PRESSURE SURROUNDINGS

Figure 5 illustrates the two different forms of the break-up behavior recognized in Fig. 2 as a function of the injection velocity. The spray region was divided into two different sub-regions, such as the pseudo spray and the complete spray which are shown by E, G and F. In this study, a new analogical method was introduced to explain the break-up behaviors in the E - F and E - G - F processes, using an internal flow structure in a nozzle injecting into atmospheric surroundings.

As mentioned before, the break-up length was greatly affected by D, L/D and M of a nozzle as well as the velocity and the pressure of the surroundings. Thus, the L/D and M of a transparent nozzle of 3.0 mm diameter at the atmospheric condition, could be selected to produce similar behavior in break-up length that produced by a 0.3 mm diameter nozzle in a pressure of 3.0 MPa.

Figure 6 shows the comparison of the non-dimensional break-up length L_b/D with Reynolds number under the conditions of high and atmospheric pressures. The horizontal axis indicates the Reynolds number because the injection velocities and the nozzle diameters were different. In general, when the nozzles of different diameter were used in different pressure surroundings, the behavior of the break-up lengths were different owing to

different break-up mechanisms. However if a suitable value of the sectional area ratio M and the length-to-hole diameter ratio L/D of a nozzle were selected. The same behavior of the break-up length with Reynolds number could be approximately obtained as shown in this figure.

In the case of the nozzle in which a minimum break-up length was produced within the pseudo spray region in 3.0 MPa surroundings, 10 times larger nozzle that had different M but had the same break-up behavior in atmospheric surroundings could be found out as shown in Fig. 7. The Reynolds numbers were different where the non-dimensional break-up length L_b/D indicated the minimum in the pseudo spray region. However, the trends of the break-up lengths were similar to each other if the difference in the Reynolds numbers was discounted.

The reason why this analogy was attained could be explained by discharge coefficients shown in these figures. The decreasing tendency of the discharge coefficient meant an increasing tendency of a drag force that produced turbulence in the nozzle. The rapid decreases appearing in Fig. 6 at $Re = 4 \times 10^4$ to 10^5 produced the pseudo sprays in both nozzles, so that the analogy of the break-up length was obtained by the analogy of the internal flow in the nozzles. Table 1 shows the summarized specifications of the nozzles used in Figs. 6 and 7. The break-up behavior of the jet injected by Nozzle-c into atmospheric surroundings was similar to that of Nozzle-a in 3.0 MPa surroundings, and the break-up length of Nozzle-d consists with that of Nozzle-b. Further investigation on the relationship between internal flow and break-up length was therefore carried out under atmospheric conditions using transparent nozzles specified by Nozzle-c and -d.

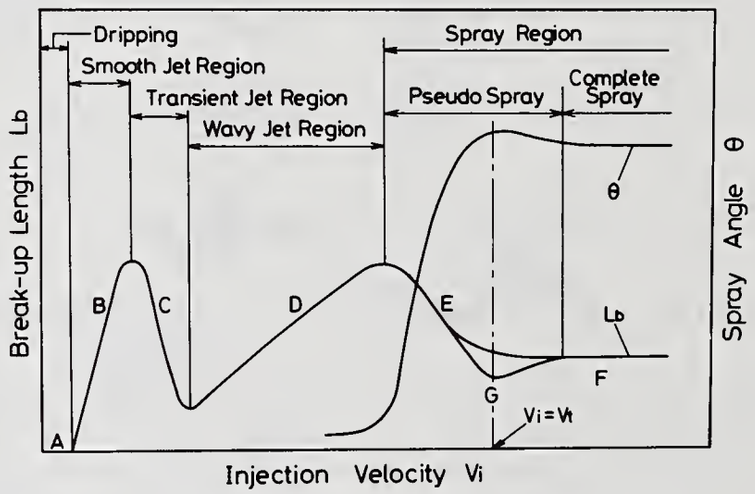

Fig. 5 General behavior of the break-up length of a jet in a high pressure surroundings

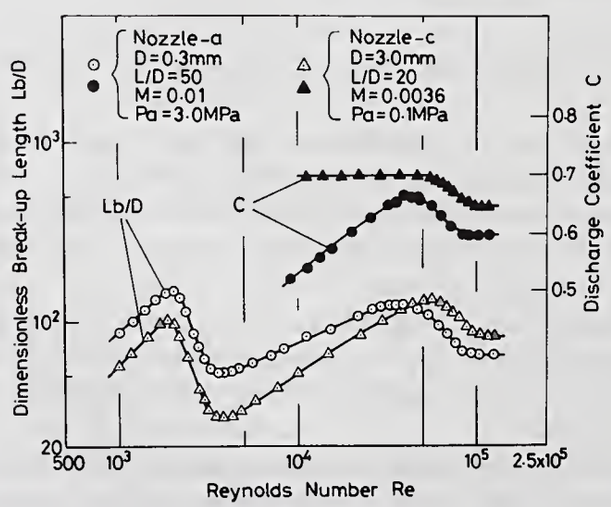

Fig. 6 Analogy of the break-up lengths and discharge coefficients between Nozzle-a and Nozzle-c

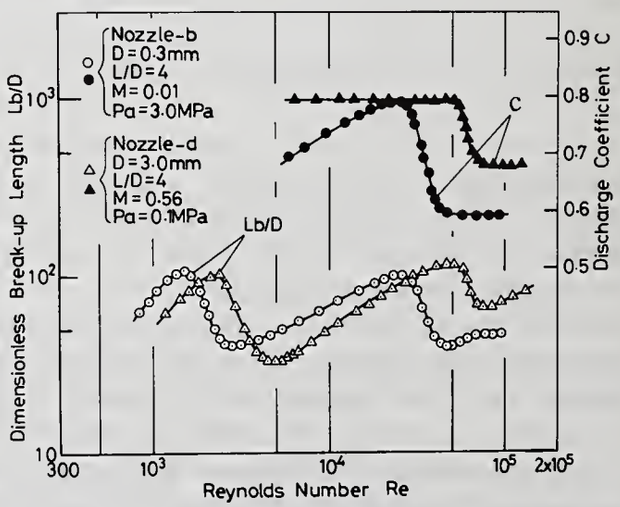

Fig. 7 Analogy of the break-up lengths and discharge coefficients between Nozzle-b and Nozzle-d

Table 1 Specifications of nozzles

Nozzle	D (mm)	L (mm)	L/D	D_o (mm)	$M=(D/D_o)^2$	Comments
a	0.3	15.0	50	3.0	0.01	E-F in 3.0 MPa.
b	0.3	1.2	4	3.0	0.01	E-G-F in 3.0 MPa, Analogous to a diesel nozzle.
c	3.0	60.0	20	50.0	0.0036	E-F in 0.1 MPa, Analogous to nozzle-a.
d	3.0	12.0	4	4.0	0.56	E-G-F in 0.1 MPa, Analogous to nozzle-b.

CORRELATION OF BREAK-UP LENGTH AND SPRAY ANGLE WITH AN INTERNAL FLOW IN A NOZZLE

Photographs of the internal flows of Nozzle-c and the jets under conditions specified in Fig. 6 are shown in Fig. 8. As the injection velocity increased from the pseudo spray at 13.5 m/s ($Re = 5\times10^4$) to the complete spray at 27.0 m/s ($Re = 10^5$), a constriction flow and a cavitation with bubbles were simultaneously produced at the entrance of the nozzle. Also a separated flow made by this constriction reattached the nozzle wall. With an increase in the velocity, the reattachment point of the separated flow moved toward the nozzle exit.

While velocity remained above 21.4 m/s ($Re = 8\times10^4$), the reattachment point moved up-and-down at the vicinity of the nozzle exit. With the internal flow phenomena described above, the disintegration of the issuing jet was promoted and the break-up length and the discharge coefficient smoothly decreased by increasing the Reynolds number as shown in Fig. 6.

Photographs of the internal flows in Nozzle-d and the jets in atmospheric surroundings are shown in Fig. 9. With the velocity increase from 12.0 m/s (Re = 45,000), a constricted flow and a cavitation with bubbles were produced as in the previous photographs. However, when the velocity increased above 16.6 m/s (Re = 61,000), the reattachment point moved upstream. The break-up length decreased and the spray angle increased with a downward movement of this point. Also the 16.6 m/s velocity that produced the minimum break-up length in the pseudo spray region consisted with the velocity where the point was nearest to the exit.

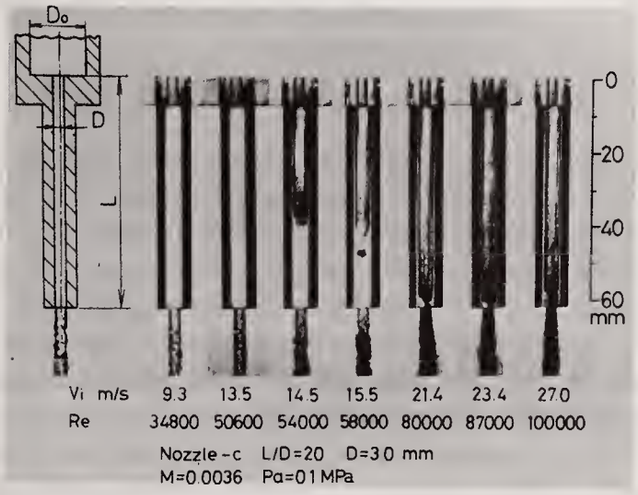

Fig. 8 Internal flows and jets produced by Nozzle-c

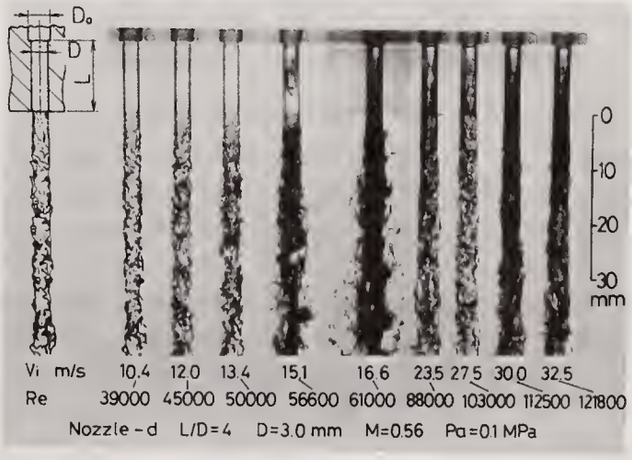

Fig. 9 Internal flows and jets produced by Nozzle-d

The reattachment point was measured from the photographs and expressed by a distance l from the entrance of the nozzle. Figure 10 shows the correlation of the break-up length L_b and the spray angle θ of the jets produced by Nozzle-c, connecting with the reattachment distance l. This result corresponded to the break-up length smoothly changing from E to F, as shown in Fig. 5. Further it was considered to be a simulation of the internal flow in Nozzle-a, as used in 3.0 MPa surroundings according the analogy of the internal flows in the nozzles. In the pseudo spray region, as the injection velocity increased from 12.5 m/s, the reattachment distance l increased and moved toward the nozzle exit. In the complete spray region of the injection velocity above 19 m/s, this point moved up-and-down near the nozzle exit. Accompanying these phenomena in a nozzle, the break-up length decreased and the spray angle θ reached a maximum at around 22 m/s.

The same trend in results concerning Nozzle-d are shown in Fig. 11. In this case, the behavior of the break-up length shown by the E - G - F curve in Fig. 5 was presented by the analogy between Nozzle-b and -d. With an increase in the velocity, the reattachment distance l increased and approached the exit at 18.0 m/s in the pseudo spray region. Furthermore, the injection velocity increased, the recovery of the constricted flow in the nozzle was promoted and the reattachment distance was decreased. However, the reattachment point moved up-and-down at the location a little upstream from the exit. Accompanying the internal phenomena at the injection velocity of 18.0 m/s, the spray angle θ reached the maximum and the break-up length L_b became the minimum.

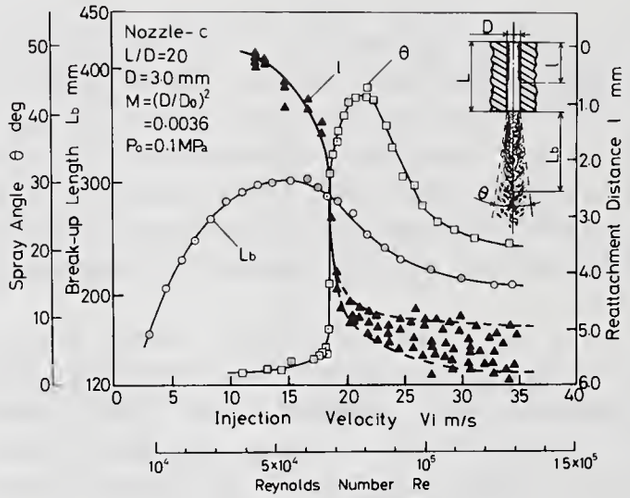

Fig. 10 Break-up length, spray angle and reattachment distance obtained by Nozzle-c as functions of the injection velocity

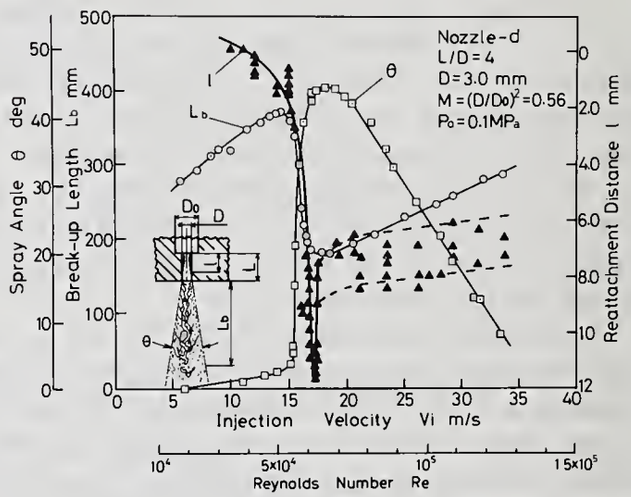

Fig. 11 Break-up length, spray angle and reattachment distance obtained by Nozzle-d as functions of the injection velocity

Figure 12 shows the results in which Fig. 10 was rewritten by using the non-dimensional reattachment distance l/L. As the l/L increased by increasing the injection velocity, the break-up length decreased. The spray angle reached the maximum value at around l/L = 0.75. The L_b/D and θ had tendencies to be reduced by the effects of an up-and-down vibration of the reattachment point (its range is shown by arrows in the figure).

The relation between the l/L and the break-up behavior when the minimum break-up length appeared in the pseudo spray region is shown in Fig. 13. The results in the pseudo spray are represented by open symbols and solid symbols show the complete spray. As l/L increased, L_b/D decreased and θ increased in the pseudo spray region. Further increase of l/L, the spray angle reached the maximum and L_b/D became the minimum at l/L = 0.95. In the complete spray region, l/L was decreased by an increase of the velocity. It remained in the range of 0.5 to 0.65 but was unstable. The L_b/D increased and the spray angle decreased by an unstable effect of an up-and-down vibration on the reattachment point. It could be considered that this form of the disintegration might appeared in the increasing behavior of the break-up length shown by G - F curve in Fig. 5.

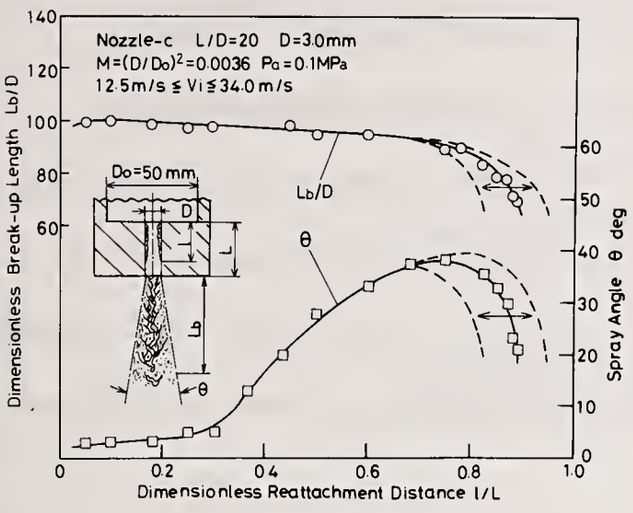

Fig. 12 Break-up length and spray angle as functions of reattachment distance (Nozzle-c)

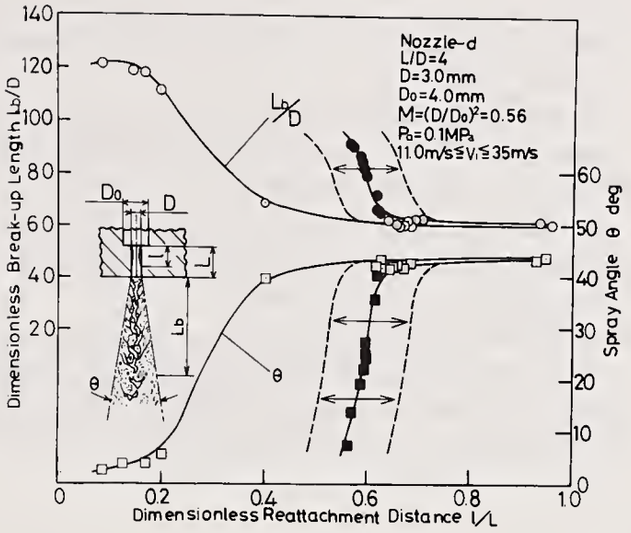

Fig. 13 Break-up length and spray angle as functions of reattachment distance (Nozzle-d)

CONCLUSIONS

In order to explain the disintegrating mechanisms of a high speed liquid jet under high pressure environment, the correlation of the internal flow in a nozzle and the break-up length was investigated and following results were obtained.

(1) A spray which shows the analogical behavior in break-up length of a jet in high pressure surroundings could be reproduced by selecting the suitable sectional area ratio and length-to-hole diameter of a nozzle under an atmospheric pressure condition.

(2) Concerning the observations of the liquid flows in the nozzle, if the separated flow and cavitation occurred, the jet could be broken up to the spray.

(3) The closer a reattachment point of the internal flow in a nozzle approached the nozzle exit, the shorter the break-up length and the larger the spray angle become.

(4) The reattachment point of the liquid flow oscillated in the vicinity of the nozzle exit when the break-up length reached the minimum in the pseudo spray region.

(5) From the results described above, it is concluded that if a large disturbance contains in an issuing jet, it may be atomized and broken-up to a spray very quickly.

REFERENCES

1) Bregwere,W., "Flow pattern in Diesel Nozzle Spray Holes", Proc. Inst. Mech, Engirs., 173 (1959), 655.
2) Rupe,S.H., "On the dynamic characteristics of fuel liquid jet and a partial correlation with orifice geometry", JPL Tech. Rept., 32 (1962), 207.
3) Lee, D.W., " the effect of nozzle design and operating conditions on the atomization and distribution of fuel sprays", NACA Tech. Rept., No.425 (1932), 565.
4) Tanasawa, Y., High speed diesel engines I, "Fuel systems and spray combustion", Sankaido (in Japanese), (1956), 87.
5) Ruiz, F. and Chigier, N. " Mechanism of high speed atomization", Proc. 3rd ICLASS, Vol. 1 (1985), VIB/3/1.
6) Schweizwer,P.H., "Mechanism of disintegration of liquid jet", J. Appl. Phys. Vol.8, (1938).513.

6) Schweizwer,P.H., "Mechanism of disintegration of liquid jet", J. Appl. Phys. Vol.8, (1938).513.
7) Reitz, R.D. and Bracco,F.V. "Mechanism of atomization of a liquid jet", Phys Fluids Vol.25 No.10 (1980),1730.
8) Hiroyasu,H., Shimizu, M. and Arai, M.," The break-up of high speed jet in a high pressure gaseous atmosphere" Proc. 2nd ICLASS (1982), 69.
9) Arai,M., Tabata,M.,Hiroyasu,H. and Shimizu, M., "Disintegrating process and spray characterization of fuel jet injected by a diesel nozzle", SAE Paper No. 840275 (1984).
10) Arai,M. Shimizu,M. and Hiroyasu,H. " Break-up length and spray angle of a high speed jet" Proc. 3rd ICLASS, Vol.1 (1985), IB/4/1.
11) Simizu,M. Arai,M. and Hiroyasu,H. "Effects of ambient pressure on break-up length in high speed jets", 14th Conf. on Liquid Atomization and Spray systems in Japan (1986),1.
12) Arai,M., Shimizu,M. and Hiroyasu,H. "Break-up length and spray formation mechanisms of a high speed liquid jet" Proc. 4th ICLASS, (1988), 177.

EFFECT OF NOZZLE CONFIGURATION ON THE ATOMIZATION OF STEADY SPRAY

T. Karasawa*, M. Tanaka*, K. Abe†, S. Shiga* and T. Kurabayashi‡

*Dept. of Mechanical Engineering, Gunma University, Kiryu, Gunma, Japan
†Fuji Heavy Industry, Ohta, Gunma, Japan
‡Hiroshima Institute of Technology, Hiroshima, Japan

ABSTRACT

The purpose of this study is to obtain the relationship between spray size and the nozzle hole configuration represented by L/D and the shape of flow inlet in steady spray under the condition of diesel injection pressure. The spray size is apparently affected by the entrance shape. However, it is not substantial, because the effect disappears by correcting the injection velocity using the nominal value which can be calculated on the basis of the discharge coefficient of the nozzle. The droplet size increases with increasing the value of L/D. This behaviour is considered to be caused by the recovery of the separated flow at the inlet edge, which is suggested by the observation of photographs. The nozzle diameter also has much influence on the spray size, where a characteristic affecting behaviour is recognized.

1. INTRODUCTION

Even the spray formation without combustion has not fully understood because of the complexity of the phenomenon. Spray formation behaviour of an intermittent spray has been being studied by several researchers including the authors.[1]-[4] However, less studies of steady spray can be found out, although it is fairly important to reveal the very basic feature of spray. In this field, studies of Tabata et al[5] and Shimizu et al[6]-[8] should be cited. Tabata measured the spray size in rather wide range of the injection pressure, and Shimizu proposed a concept of a new parameter of break-up length to characterize the steady spray. However, there is little study aiming at systematically clarifying the relationship between the nozzle configuration and the spray size. In terms of the break-up length, Shimizu et al[6] showed that the best atomization can be realized when the nozzle depth to diameter ratio (L/D) is around 5. It also refers to the recovery of the separated flow at the edge of nozzle inlet as the mechanism of L/D effect, although it has not been verified clearly yet.

On the basis of this background, an experimental study was carried out to reveal how much we have the responsibility of nozzle configuration for the droplet size of steady spray. Several interesting aspects of the configuration effect could be obtained, and a possible mechanism to explain those effects could be proposed on the basis of several verification experiments.

2. EXPERIMENTAL APPARATUS AND PROCEDURE

A schematic of experimental apparatus is shown in Fig. 1. Water was used as a tested liquid. It is contained in a flexible bag(No.4).

Most data were obtained by a phase doppler system (Aerometrics Co., PDPA) and were checked by the measurement of a sampling technique, immersion sampling method having a mechanical shutter.

As the parameters to represent the nozzle configuration, two sets of variables were chosen, which are seemed to have major effect on the atomization; nozzle depth to diameter ratio (L/D) and the shape of flow inlet. Three kinds of the shape of the nozzle inlet were applied form a viewpoint of flow separation, straight type (S-type), round type (R-type) and C-type, which are shown in Fig. 2. The naming procedure is shown in Table I.

The liquid was injected downward into an atmospheric condition. The sampling point for the immersion method is 1500 mm downstream of the nozzle along the spray axis which was determined by a preliminary optimization test. The measuring points for the optical technique were 1000 mm or 1500 mm downstream of the nozzle along the spray axis which were also determined by an optimization test.

3. RESULTS AND DISCUSSION

3-1. Effect of Nozzle Depth to Diameter Ratio (L/D) on Atomization

In Fig. 3, the droplet diameter variation of S-type nozzle with L/D is shown at three mean injection velocities. The droplet size increases with increasing the value of L/D in every injection velocity. In Fig. 4 of R-type nozzle, it can be seen at least that the variation of the size with L/D is not so large comparing with that of Fig. 3, and that there is no clear increasing tendency of SMD. Thus, the characteristic feature of S-type nozzle is related to the difference of the configuration of the flow inlet.

The inlet flow of S-type will be easily separated at the edge, while it should be much harder to occur for R-type. Then, the flow separation can be assumed to have some role to realize the characteristics of S-type nozzle, which was suggested in the previous study[6] on the break-up length measurement. Because of the separation, the effective area for flow coming is reduced, and the flow is free from the wall effect. Then, the velocity can reach the nearly ideal velocity of potential flow, which leads to the atomization improvement. When the L/D is greater than that particular value, the separation will be recovered and the flow will be again attached to the wall. The velocity will be decreased by the wall effect, and then the atomization effect of the flow separation tends to disappear. In Fig. 5, the droplet size of S-type at 1000 mm downstream of the nozzle is shown, where the exactly similar tendency to the 1500 mm measurement can be recognized.

3-2. Verification of the Separation Effect

In order to verify the separation effect suggested above, discharge coefficients for several conditions were measured and shown in Fig. 6. The solid line without a point is obtained by the calculation based on the Blasius' empirical formula of turbulent pipe flow[9]. The variation of the discharge coefficient of R-type nozzle with L/D is quite similar to the developed turbulent flow. Then, the flow is considered to be governed by the turbulent boundary layer. In contrast to this, the coefficient of S-type nozzle does not vary at all over the whole range of L/D. This is an indication of the occurrence of separation, and is not the indication of the separation recovery, because the discharge coefficient would have an increase with increasing L/D from a certain value of L/D if the recovery could have occurred. In any way, the recovery should occur in this case, because even

the separation of back step can be recovered at the downstream distance of around 7 times as much as the step height. This may be caused by the velocity distribution within the hole, i.e., the velocity distribution of the separation point will be conserved to some extent for a while[10]. In addition, the fully developed turbulent boundary layer of pipe flow is said to be realized at 25 to 40 of L/D (originally called as "inlet length"), which coincides with our results[11].

Further indication of the recovery occurrence is shown in the photographic observation. In less than L/D of 4, the spray surface of S-type looks quite smooth, while the other conditions including the spray of R-type do not show this distinguished feature.

3-3. Factors Determining the Atomization

The droplet size dependence on the mean injection velocity is shown in Fig. 7 for every kind of inlet shape. The size decreases exponentially with the increase of the mean injection velocity, which may be qualitatively consistent with the result of a previous study[1],[5]. It is also clear that the size is smallest for S-type nozzle, largest for R-type and intermediate for C-type. Then, it can be seen apparently that the S-type nozzle has the best configuration in terms of the atomization. However, we need much more injection pressure for S-type nozzle than for R-type to get the same mean injection velocity. It is due to the difference of the discharge coefficient.

Figure 8 shows the droplet size dependence on the corrected injection velocity which is obtained by the following relationship.

$$V_c = V_m / C_d .$$

Here, V_c : corrected injection velocity
V_m : mean injection velocity
C_d : discharge coefficient.

This correction implicitly assumes that the discharge coefficient is mainly determined by the flow separation, i.e., the decrease of the effective sectional flow area. The variation of droplet size with the nozzle configuration almost disappears, and the dependence of every kind of nozzle can be approximately represented by a unique line. Thus, when the corrected injection velocity is used, that may be the nominal injection velocity at the nozzle exit, the droplet size is not affected by the nozzle configuration. In the other words, atomization is not determined by the nozzle configuration but by the actual injection velocity.

Further verification of the above mechanism can be made more accurately as shown in Figs. 9 and 10. Usually, rather precise mechanical processing is necessary to get the reproducible value of discharge coefficient. Then, most nozzles used in this study is made by an electric discharge method. When a simple processing like drilling is used, pretty much variation of the discharge coefficient is not avoidable. This variation can be seen in Fig. 9. Four nozzles are used numbered from 1 to 4 and made by a simple processing. Although the droplet size dependence of a particular nozzle on the mean injection velocity is precisely expressed by an exponential curve, the dependence varies much in every nozzle. When the corrected injection velocity is used by the discharge coefficient, that dependence can be exactly expressed by a unique line as shown in Fig. 10. Thus, the previous mechanism of the importance of the nominal injection velocity is well supported by this result.

4. CONCLUSIONS

(1) The droplet size increases with the increase of L/D for straight type nozzle, which is caused by the flow separation at the inlet edge and the separation recovery downstream of the separation point.
(2) Above mechanism can be verified by a comparison study between nozzles of S-type, C-type and R-type, measurement of discharge coefficient and photographic observation.
(3) Atomization is determined by the flow velocity at the nozzle exit, which can be shown by the correction of the droplet size dependence on the injection velocity using the discharge coefficient.

REFERENCES

(1) Shiga, S. et al, Proc. ICLASS-88, (1988), 397.
(2) Takahashi, H. et al, Trans. JSME ser. B, 56-526, (1990), 1837, (in Japanese).
(3) Varde, K. S. and Popa, D. M., SAE Paper, 83448(1983).
(4) Hiroyasu, H. and Arai, M., Trans. JSME, No. 21, (1980), 5, (in Japanese).
(5) Tabata, M., et al, Proc. ICLASS-85, (1985), II/1/1.
(6) Shimizu, et al, Trans. JSME ser. B, 49-448, (1983), 2886, (in Japanese).
(7) Shimizu, et al, Trans. JSME ser. B, 51-461, (1985), 257, (in Japanese).
(8) Shimizu, et al, Trans. JSME ser. B, 54-504, (1988), 2236, (in Japanese).
(9) Schlichting, H., Boundary-Layer Theory 7th ed., McGraw-Hill Co., (1979), 597.
(10) Private communication with Dr. N. Fujisawa, associate professor of fluid dynamics laboratory in Gunma University.
(11) Schlichting, H., Boundary-Layer Theory, 7th ed., (1979), Chapter XX, McGRAW-HILL BOOK Co.

ACKNOWLEDGEMENT

The particle sizing system of PDPA is supplied by CENTER FOR COOPERATIVE RESEARCH GUNMA UNIVERSITY. Apparatus for experiment is partly supplied by ZEXEL Co. Ltd. The authors acknowledge Mr. Hisao NAKAMURA, Yasuo NAKAJIMA and Koichi HASHIMOTO for their help with the experiment.

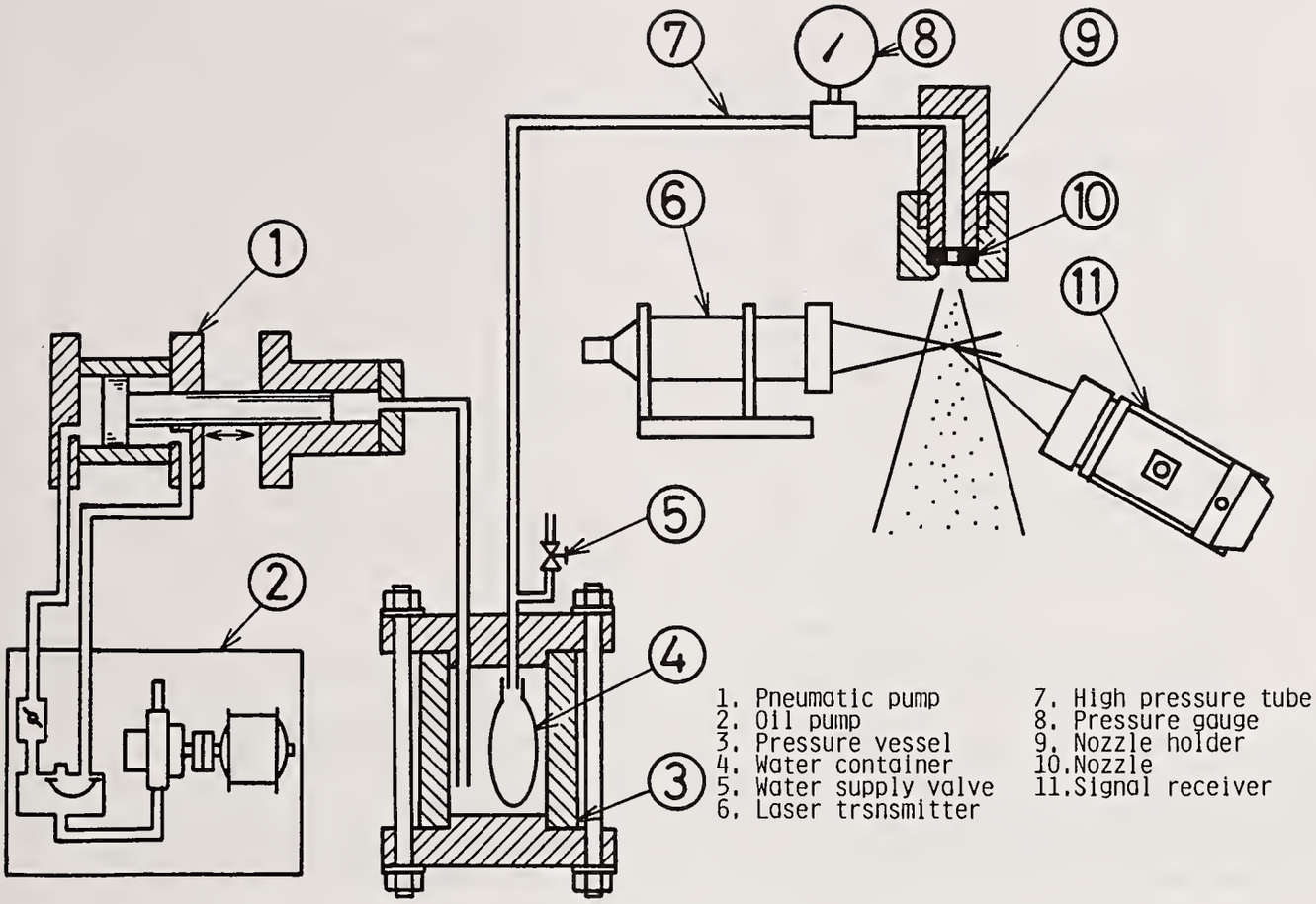

Fig. 1. Schematic of experimental apparatus.

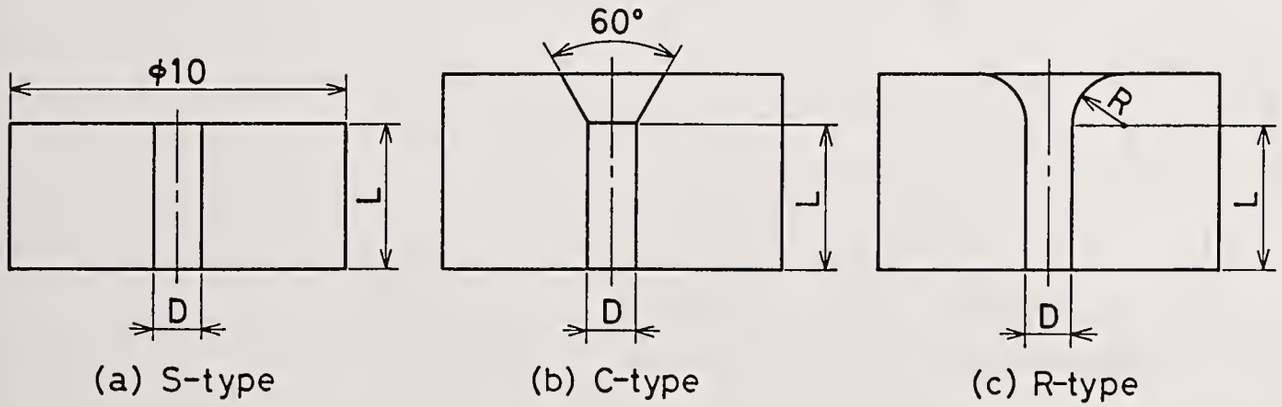

Fig. 2. Configuration of nozzle.

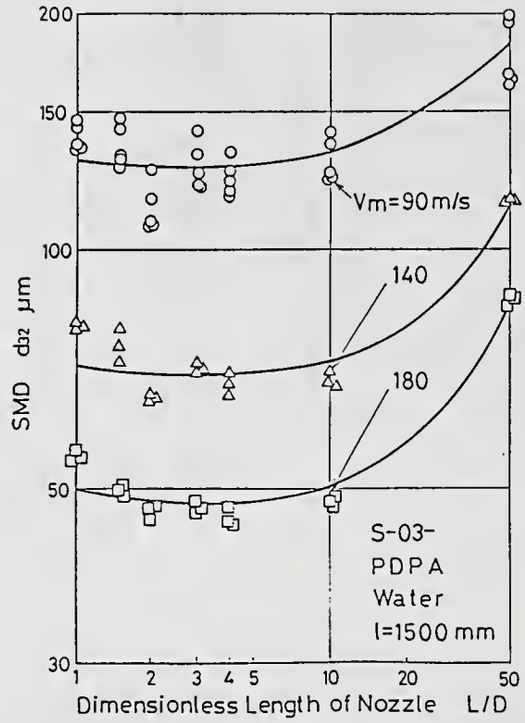

Fig. 3. Variation of droplet size with the dimensionless length of nozzle(L/D), S-type nozzle, measuring point; 1500 mm downstream of the nozzle.

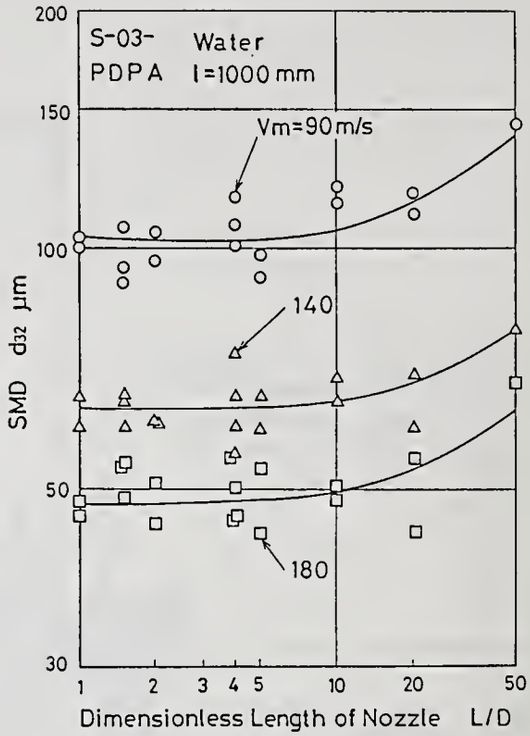

Fig. 5. Variation of droplet size with the dimensionless length of nozzle(L/D), S-type nozzle, measuring point; 1000 mm downstream of the nozzle.

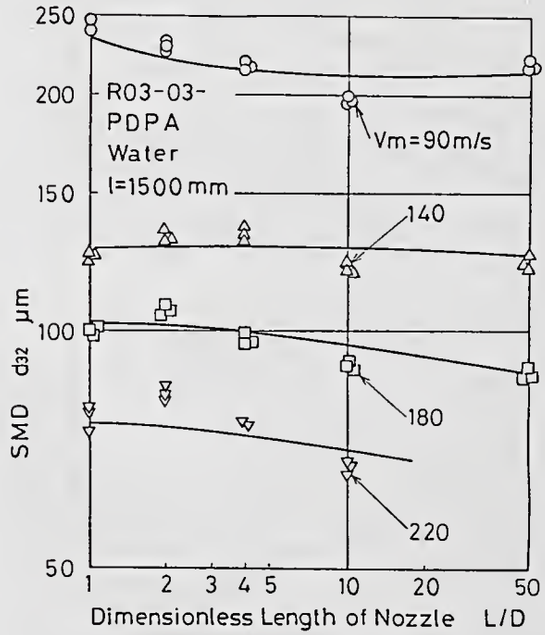

Fig. 4. Variation of droplet size with the dimensionless length of nozzle(L/D), R-type nozzle.

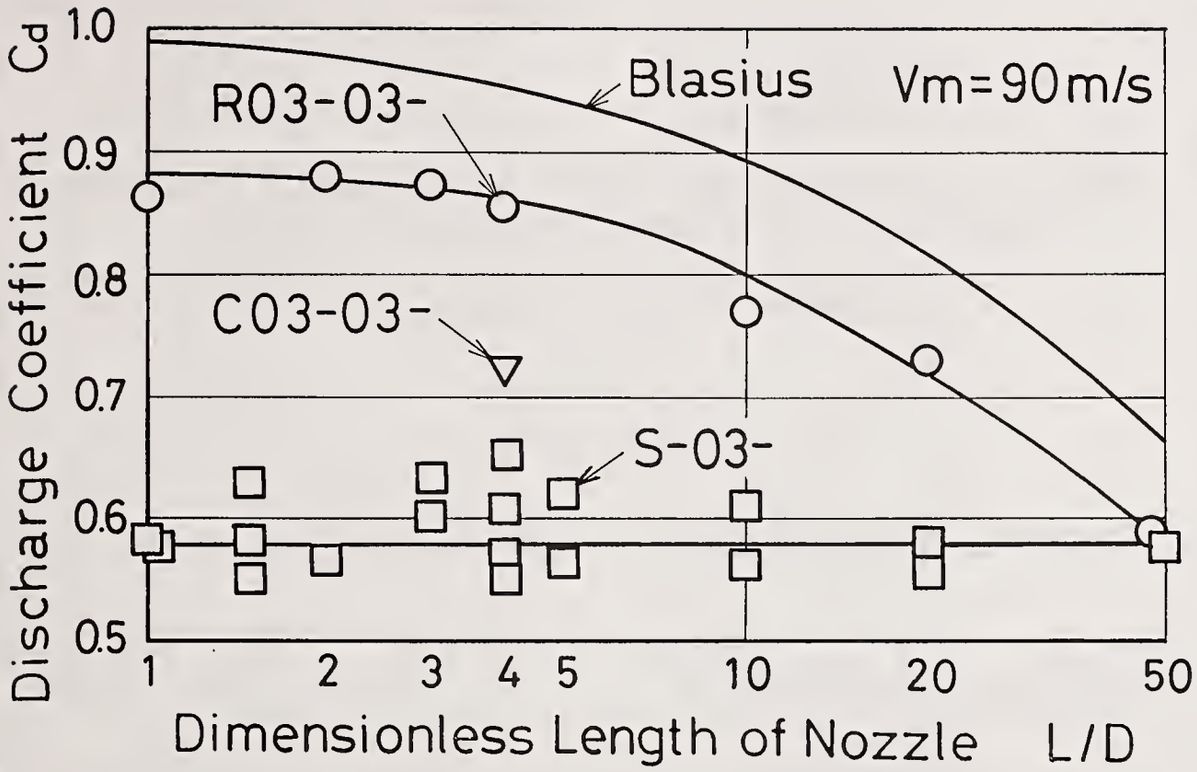

Fig. 6. Variation of discharge coefficient with the dimensionless length of nozzle (L/D).

Table I. Naming procedure of nozzles.

Shape of entrance	Hole diameter	L/D	Lot number
"Straight"	"0.3mm"	"4"	"3"
S -	03 -	04 -	3

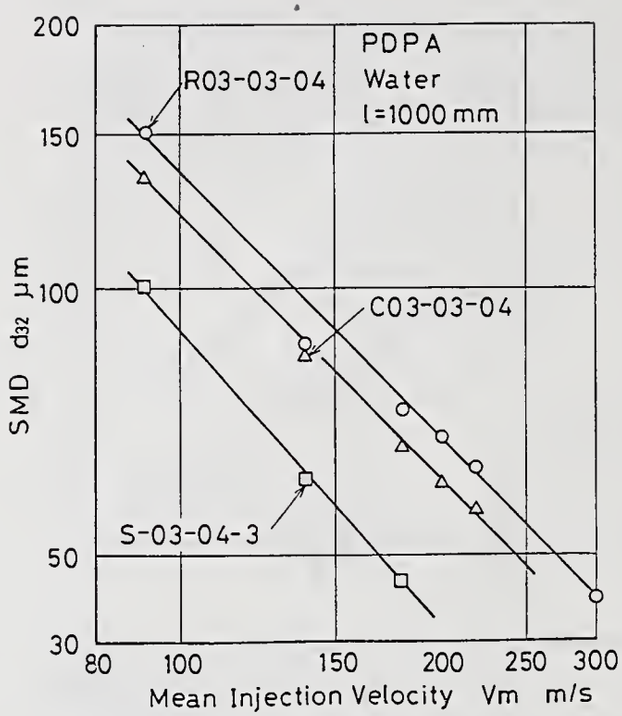

Fig. 7. Variation of droplet size with the mean injection velocity, L/D = 4.

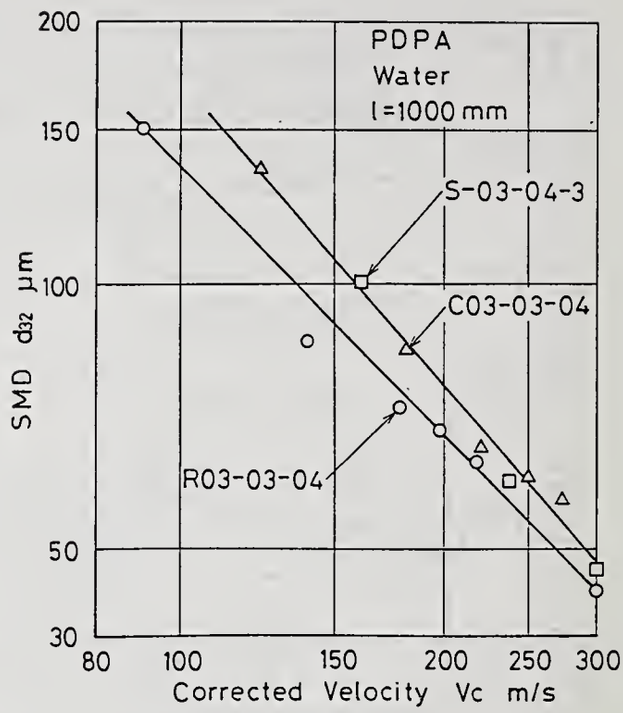

Fig. 8. Variation of droplet size with the corrected injection velocity, L/D=4.

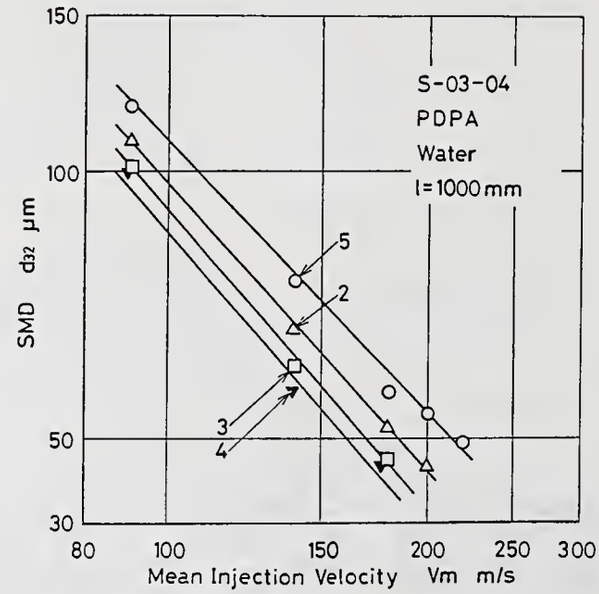

Fig. 9. Droplet size dependence on the mean injection velocity, showing the variation of individual nozzle having the same specifications.

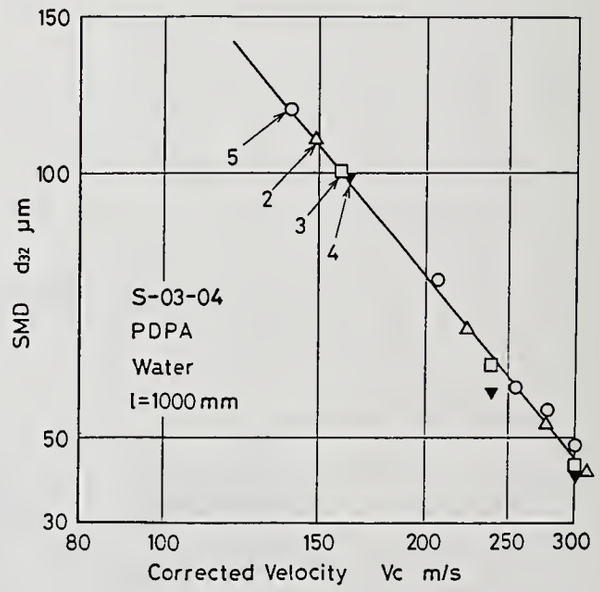

Fig. 10. Droplet size dependence on the corrected injection velocity, variation of individual nozzle disappears and every dependence can be expressed by a unique line.

A STUDY ON SPRAY FLOW ISSUED FROM PLAIN JET ATOMIZER USING PHASE/DOPPLER PARTICLE ANALYZER

T. Inamura, N. Nagai and T. Hirai

Faculty of Engineering
Tohoku University
Sendai, Japan

ABSTRACT

Twin-fluid atomizer has been widely used in combustors, for instance spark ignition engines, gas turbine, rocket engine and industrial furnaces, because of its high performance and simple structure. The spray characteristics, such as the drop size, the drop velocity, the number density and the mass flux, become increasingly important in the design of combustors and in testifying numerical simulation of spray flow in the combustor. In spite of their importance, it was difficult to measure these characteristics locally and simultaneously by the conventional method. On the other hand, recently laser diagnostics technique has been developed rapidly. In particular, phase/Doppler particle analyzer system has been popular, and the results are discussed by some researchers comparing to the conventional method. This study aims to clarify the spray characteristics of twin-fluid atomizer and to offer the data for combustor design and the numerical simulation of a spray flow. In this report, spatial mean drop size distribution, spatial drop velocity distribution and the relationship of the drop size and the velocity were measured by phase/Doppler particle analyzer. And the empirical equations of spatial drop velocity distribution were deduced.

INTRODUCTION

Local and simultaneous data of spray characteristics, for example the drop size, the drop velocity, the number density of droplets and the local mass flux of droplets are very important for the design of combustors. However, it has been very difficult for the conventional method to obtain these local and simultaneous data of the spray characteristics. And the designs of combustors were generally conducted by trial and error.

Recently the numerical simulation of a spray flow becomes popular in a combustion field [1], and it has a potentiality to be applied to the design of the combustor. In that case the accurate measurements of spray characteristics are required to validate the numerical predictions.

On the other hand, the twin-fluid atomizers have been very popular in the industrial combustors [2], because of their high performances and the flexibility of a design. Recently the airblast atomizer has been used for the jet engine combustors instead of the pressure atomizers to decrease soot emission [3], since the mixing between fuel spray and combustion air can be improved by the twin-fluid atomizers.

The plain jet atomizer, which is one of the twin-fluid atomizer has simple structure and high performances. So it has been applied to the combustor of the rocket [4], which needs high reliability. This type of atomizer has simple structure and simple spray flow and it seems to be suitable for the validation of numerical prediction. The present study is directed to clarify the spray characteristics and to deduce the empirical equations of those of twin-fluid atomizers. In present report, the plain jet atomizer was selected as the twin-fluid atomizer because of its simple spray flow. The spatial

drop size distribution, spatial drop velocity distribution and the relationship between drop size and drop velocity were measured by phase/Doppler particle analyzer [5]. And the empirical equations of drop velocity distribution were deduced.

APPARATUS AND PROCEDURES

Figure 1 shows the experimental apparatus. The atomizing air is supplied from the compressor 1 to the atomizer 11. Its flow rate is adjusted by valves 2,3,5 and metered by orifice flow meter 4. And its pressure and the temperature are measured by pressure gauge and the thermocouple. The atomized liquid is supplied from pressure vessel 7 to the atomizer. Its flow rate is adjusted by valves 8,10 and metered by the orifice flow meter 9. Phase/Doppler particle analyzer 12 ~ 16, manufactured by Dantec Inc. was used to measure local drop size and drop velocity simultaneously. The atomizer was mounted vertically in a open chamber and the spray was pulled through the chamber by exhaust fan. And it is certified that the exhaust fan scarcely affects the drop velocity at test section.

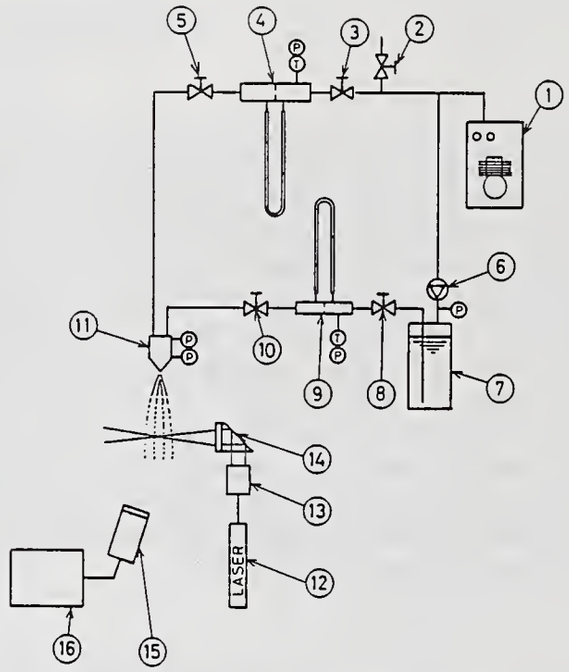

Fig.1 Experimental apparatus

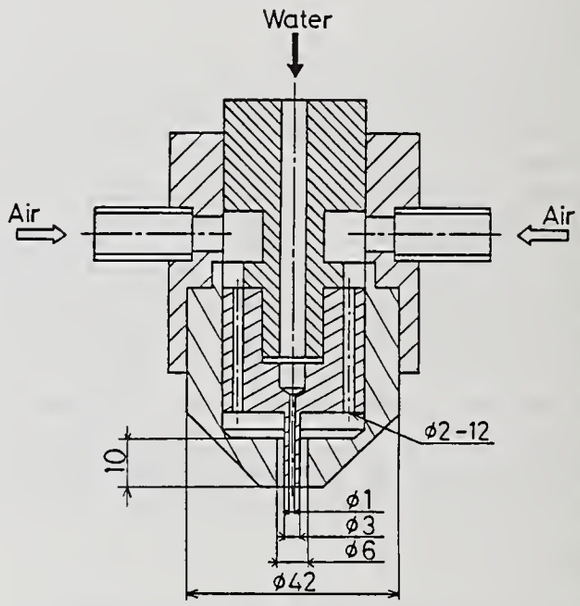

Fig.2 Structure of the plain jet atomizer

The structure of plain jet atomizer is shown in Fig.2. The structure of twin-fluid atomizer is rich in variety and this is one of the advantages of twin-fluid atomizer. In this report the simple structure was selected because of the purpose of this report mentioned above. The injection velocity of the atomizing air was measured by hot wire anemometer at 1 mm downstream of the nozzle exit.

The ranges of operating conditions were, V_{ai}=147 ~ 178 m/s(W_a=3.5 ~ 4.5 g/s), V_f=0.6 ~ 1.9 m/s(W_f=0.5 ~ 1.5 g/s). Tap water was used as the atomized liquid.

RESULTS AND DISCUSSIONS

Disintegration Phenomena

Figure 3 is the magnified picture back-lighted by microflash in the vicinity of atomizer exit, and the side-lighted streak picture of spray flow. The nozzle of 2 mm in innner diameter was used only for taking the photograph to make the observation of disintegration phenomena easy. Figure 3(a) and (b) are in the case of low speed airflow. In the microflash photograph (a), the liquid column is scarcely disturbed until one moves about 1.5 mm downstream of the atomizer exit. In this region the liquid column seems not to be in contact with atomizing air stream. At 1.5 mm

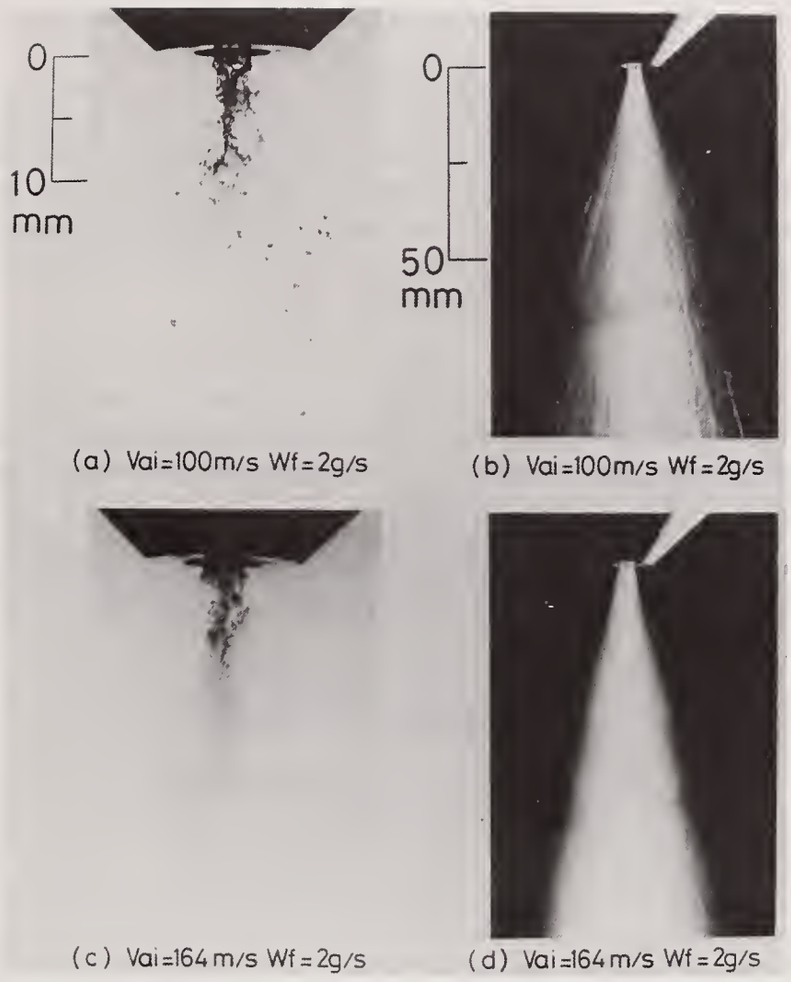

Fig.3 Disintegration phenomena and spray flow

downstream the liquid column is suddenly disturbed by air stream, and then liquid jet gets thin gradually. This is due to the acceleration of liquid jet and the disintegration by air stream. At 15 ~ 20 mm downstream the liquid column is completely disintegrated into droplets. By the observation with the eye the tip of the liquid column vibrates right and left. And the large drops scatter to the surrounding just after the atomization. By above observation it is deduced that under low air speed condition the dispersion of the drops is controlled by the vibration of the liquid column, since under low air velocity large drops are produced and a large particle maintains its initial velocity for long time due to its large mass and low surrounding air velocity.

On the other hand in the streak photograph (b), the trajectories of the drops spread straight from the point at about 2 mm below from atomizer exit. This point is almost coincident with the point where the liquid column comes in contact with the air stream shown in Fig.3(a). This means that the dispersion of drops toward the surrounding starts at just disintegration point. The spray angle is about 40 degree.

Figure 3(c) and (d) are in the case of high speed air flow. In the microflash photograph (c), there exists no undisturbed liquid column. The liquid column is disturbed just below the atomizer exit. And at 2 mm downstream the liquid column is completely disintegrated into drops. The liquid column is disintegrated into large particles first, and then it is atomized again into further fine particles. At 20 mm below the atomization seems to complete. The break-up length which indicates the distance from the atomizer exit to the point where the liquid column is completely disintegrated into drops is the function of liquid flow rate and the atomizing air velocity. In particular, it decreases greatly with increase in the air velocity.

In the streak photograph (d), the contour of the spray spreads first. The point where the spray contour spreads is almost coincident with the point where the atomization starts. Then the spray contour deflates and starts to spread again at about 10 mm downstream. This point where the spray contour spreads again is almost coincident with the point where the drops disintegrate again into further fine drops. The spray dispersion starts after fine spray drops are produced. From these considerations it is deduced that under high speed air condition the spray dispersion is almost controlled by the disturbances of a air flow, since under high air velocity condition small particles are produced and a small particle follows a air flow immediately due to its small mass. Under this injection conditions the spray angle is about 30 degree. The spray angle decreases as liquid flow rate decreases and as atomizing air velocity increases.

Phase/Doppler Particle Analyzer

Figure 4 compares drop size distribution measured by phase/Doppler particle analyzer (PDA) to that measured by the liquid immersion method. The measuring point is placed at 200 mm downstream of nozzle exit and at the center of the spray. The slide shutter was used for liquid immersion method. The drop size distribution measured by liquid immersion method almost agrees with the result obtained by PDA. However, by the detailed observation the result obtained by PDA shows less small particles and more large particles. The Sauter's mean diameter measured by liquid immersion method is 27.2 μm and that measured by PDA is 29.8 μm. By our further investigations

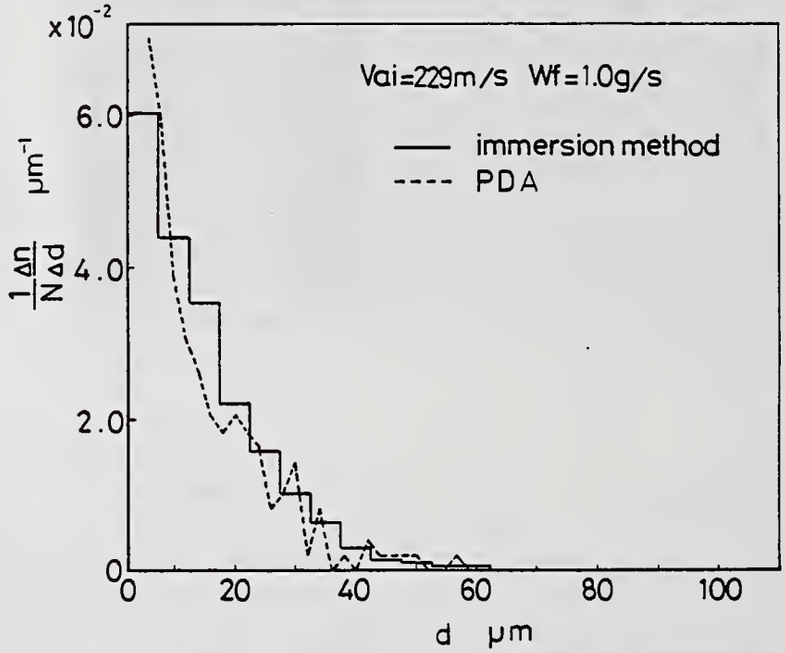

Fig.4 The comparison of drop size distributions

about the accuracy of PDA, the measuring results are influenced by three operating factors. First one is the power of laser source. Second is the input voltage of photomultiplier and last one is the threshold which determines whether or not the particle is spherical. High power of laser source results in smaller drop size, high voltage of photomultiplier results in smaller drop size and severe threshold results in smaller drop size. The optimal three operating factors were determined by the comparison of drop size distribution by PDA and by liquid immersion method and were kept constant during the measurement. Further discussions about the accuracy of PDA are published in other papers [6,7].

Radial Mean Diameter Distribution

Figure 5 shows the influences of the vertical distance from the nozzle exit on the radial Sauter's mean diameter distribution. Near the nozzle exit, mean diameter decreases gradually as radial distance from the center axis increases. At a short distance from the nozzle exit, mean

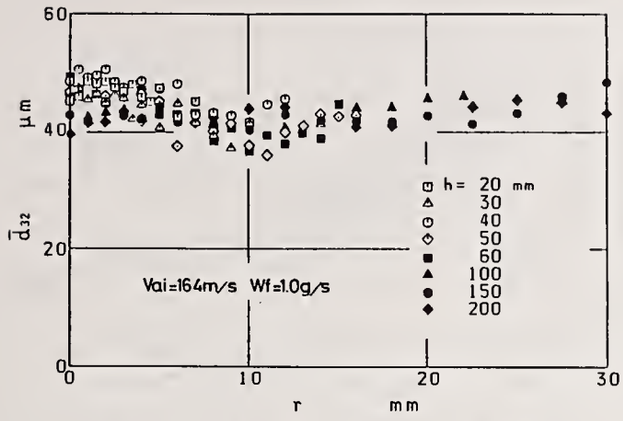

Fig.5 The influences of vertical distance on radial mean diameter distribution

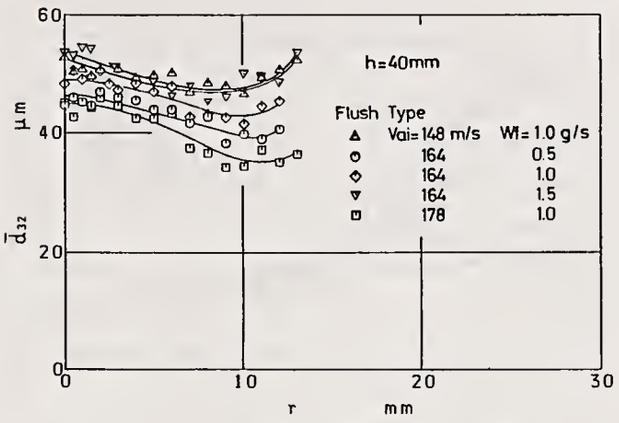

Fig.6 The influences of injection conditions on radial mean diameter distribution

diameter decreases first and then increases gradually with increasing the radial distance. With increasing the vertical distance from the nozzle exit the mean diameter at the center line decreases, however, at the edge of the spray the mean diameter is almost constant. At the downstream, the mean diameter is almost constant until r=10 mm, then it increases gradually with increasing radial distance.

As mentioned above, the mean diameter at the center decreases with increase in the vertical distance. On the other hand at the edge of the spray the mean diameter scarcely changes. The reason of this trend seems as follows. In the vicinity of nozzle exit, the mean diameter at the center line is larger than that at the edge due to the remained liquid column at the center. Further downstream the small particles are remained at the center because of their small momenta and the larger particles disperse to the edge against the air stream. Consequentially the small particle increases at the center and the mean diameter decreases. At the edge of the spray, as there are many larger particles the mean diameter is almost constant.

Figure 6 shows the dependences of radial mean diameter distribution on the injection conditions. The measuring point is placed at 40 mm downstream from the nozzle exit. Under every injection condition the mean drop size decreases first and then increases. The mean diameter decreases over the whole radial distance as liquid flow rate decreases and as air velocity increases. The decrease of mean diameter is larger at the edge of the spray rather than at the center. At the edge of the spray there are many particles produced by the shear force of the air stream on the surface of liquid column. And the drop sizes of the particles produced by the shear force on the surface of liquid column are greatly influenced by the air velocity and the shear force.

Radial Drop Velocity Distribution

The dependences of radial drop velocity profile of 1 μm($\pm$ 0.5 μm) drops on the vertical distance from the nozzle exit are shown in Fig.7. Figure 8 shows that of 60 μm($\pm$ 0.5 μm) drops. Near the nozzle exit($h \leq 40$ mm) the velocities of large particles at the center line are smaller than those of small particles. By further investigations, at the edge of the spray the velocities of small particles are smaller. This trend indicates that the center part of the spray is the region in which the drops are accelerated by the air stream and the surrounding of the spray is drop decelerating region. Because the small particles are greatly influenced by the air stream due to those small momenta.

On the other hand further downstream, the velocities of small particles are smaller than those of large particles over the whole radial distance. This trend means that further downstream the drop velocities are larger than the air velocity over the whole radial distance.

Figure 9 shows the drop velocity at the center as a function of the vertical distance for various drop sizes. The velocity changes of small particles are larger than those of large particles. This trend indicates that small particles can be easily accelerated and decelerated because of their small momenta. The drop velocities for all drop sizes have a maximum velocity at about h=50 mm. This

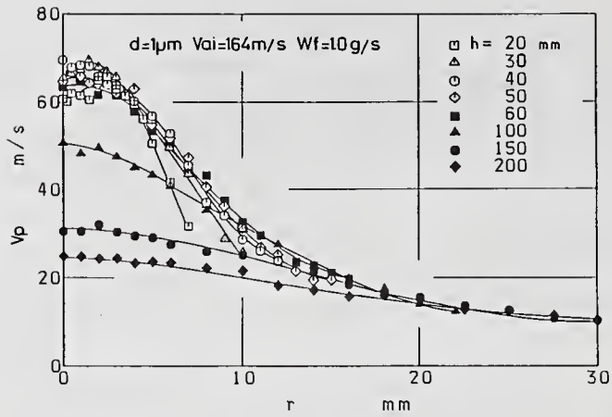

Fig.7 The dependences of radial drop velocity profile on vertical distance (d=1 μm)

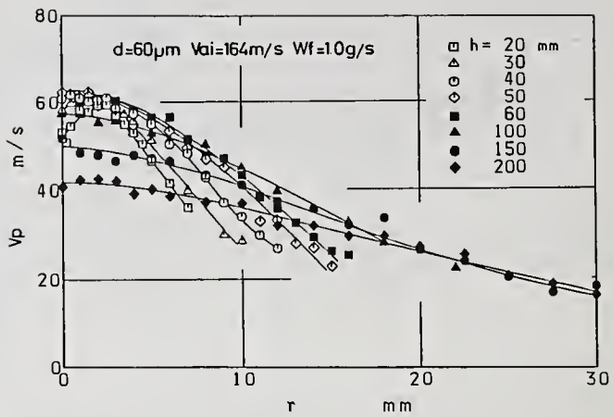

Fig.8 The dependences of radial drop velocity profile on vertical distance (d=60 μm)

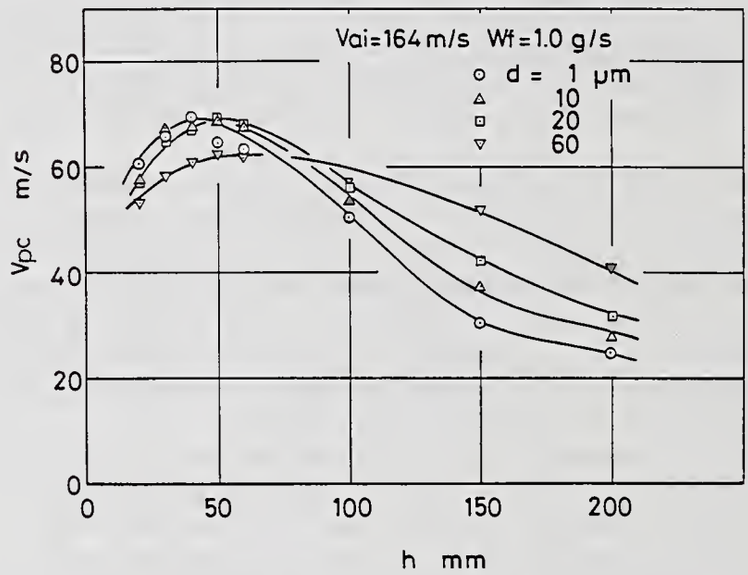

Fig.9 The variation of drop velocity at the center with the vertical distance

means that at the center the region within 50 mm downstream of the nozzle exit is drop accelerated region, whereas the region more than 50 mm downstream is drop decelerated region.

Figure 10 shows the validity of the dimensionless empirical equation of radial drop velocity profile of 1 μm($\pm$0.5 μm) drops. And Fig.11 shows that for 60 μm($\pm$0.5 μm) drops. The axis of abscissa is the radial distance made dimensionless by half the width of the radial drop velocity profile at half the drop velocity on the center line, and the vertical axis is the drop velocity made dimensionless by respective drop velocities on the center line. The broken lines indicate the following empirical equation deduced by Yatsuyanagi [8] for the air velocity distribution of gas liquid two-phase flow:

$$\frac{V_p}{V_{pc}} = \left\{ 1 - \left(\frac{r}{2.267 \cdot \bar{r}_{pv}} \right)^{1.5} \right\}^2 \tag{1}$$

The experimental results of drop velocities are almost represented by the broken line for all drop sizes. However, at the edge of the spray($r/\bar{r}_{pv} \geq 1.3$) there exists the trend that the experimental results are slightly larger than those of eqn.(1) for all drop sizes.

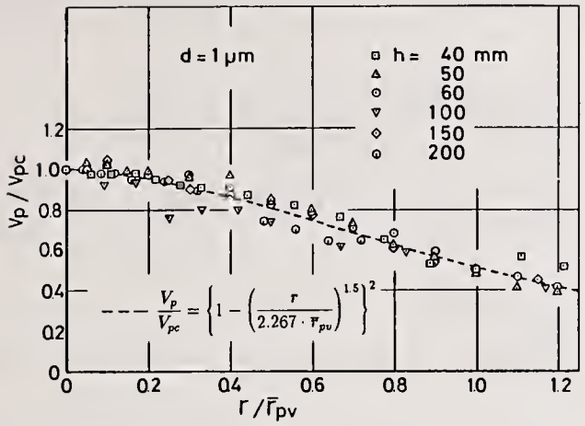

Fig.10 The comparison of radial drop velocity profile (d=1 μm)

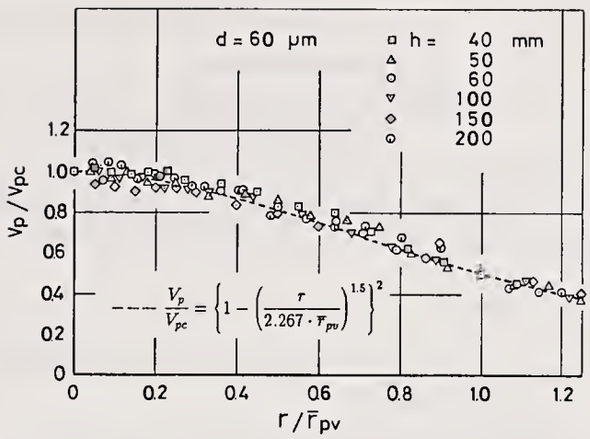

Fig.11 The comparison of radial drop velocity profile (d=60 μm)

CONCLUSIONS

In order to clarify the spray characteristics issued from the plain jet atomizer, the spray characteristics, that is spatial drop size distribution, spatial drop velocity distribution and the relationship between drop size and drop velocity were measured by phase/Doppler particle analyzer. The disintegration phenomena were observed by the microflash pictures and the streak pictures. Consequently the following results were obtained:

1. Under low air speed condition the dispersion of the drops is controlled by the vibration of the liquid column, whereas under high air speed condition the dispersion is controlled by the disturbances of a air flow.
2. Both of the break-up length and the spray angle decrease with increasing atomizing air velocity and with decreasing the atomized liquid flow rate.
3. In the vicinity of the nozzle the drop size decreases with increase in radial distance, whereas further downstream the drop size increases. And at the center of the spray the drop size slightly decreases as one moves downstream, whereas at the edge of the spray the drop size is almost constant.
4. In the vicinity of nozzle exit there exists the drop accelerating region. In this region the smaller the particle, the larger its velocity is. On the other hand further downstream there exists the drop decelerating region. In this region the larger the particle, the larger its velocity is.
5. The spatial drop velocity profiles can be represented by the empirical equation (1) for all drop sizes.

NOMENCLATURE

- d : drop diameter
- $\bar{d}_{32}$: Sauter's mean diameter
- h : vertical distance from the nozzle exit
- n : the number of drops
- N : total number of drops
- r : radial distance
- $\bar{r}_{pv}$: half the width of the radial drop velocity profile at half the drop velocity at the center
- V_{ai} : injection velocity of the atomizing air
- V_f : liquid injection velocity
- V_p : mean drop velocity

V_{pc} : mean drop velocity on the center line
W_a : air mass flow rate
W_f : liquid mass flow rate

ACKNOWLEDGEMENTS

The authors would like to thank Mr. T. Mori, Mr. Y. S. Kim and Mr. H. Okuyama of Tohoku University for their help in the experiments.

REFERENCES

1. Faeth, G. M., "Evaporation and Combustion of Sprays", Prog. Energy Combust. Sci., Vol.9, pp.1-76 (1983).
2. JSME, RC–82 Report (Chairman, Nagai, N.) (1990) (in Japanese).
3. Sato, Y., "Current Design Status and Design Trend of Fuel Injectors for Jet Engines", Journal J.S.A.S.S., Vol.34, No.393, pp.519-530 (1986) (in Japanese).
4. Yatsuyanagi, N., "A Study on a Spray Flow Issued from Plain Jet Air Blast Atomizer (3rd Rep.)", Trans. J.S.M.E., Ser.B, Vol.51, No.471, pp.3599-3607 (1985) (in Japanese).
5. Bachalo, W. D., Hess, C. F. and Hartwell, C. A., "An Instrument for Spray Droplet Size and Velocity Measurements", J. Eng. Power, Vol.102, pp.798-806 (1980).
6. Dodge, L. G. and Reitz, R. D., "Comparison of Drop-Size Measurement Techniques in Fuel Sprays: Malvern Laser-Diffraction and Aerometrics Phase/Doppler", GMR–5382, General Motors Res. Rep., (1986).
7. Yoshizu, F., Arai, M. and Nakayama, M., "Correlation between Measured Particle Size Using Laser Diffraction and Phase Doppler Velocimeter Measurement Systems", Proc. J.S.M.E. Meeting, No.900-59(B), pp.509-511 (1990) (in Japanese).
8. Yatsuyanagi, N., "A Study on a Spray Flow Issued from Plain Jet Air Blast Atomizer (1st Rep.)", Trans. J.S.M.E., Ser.B, Vol.51, No.466, pp.1857-1866 (1985) (in Japanese).

SPRAY CHARACTERISTICS OF A PILOT INJECTION SYSTEM OPERATING IN AN IDLING D.I. DIESEL ENGINE

F. Yoshizu and M. Nakayama

Department of Mechanical Engineering
Gunma University
Kiryu, Gunma, Japan

ABSTRACT

A new Diesel injector has been developed, utilizing pilot injection to control the injection rate. It offers many advantages for use in small to medium DI diesel engines, such as: control of initial spray tip penetration, good atomization, and small droplet size. This paper presents the spray characterization of this injector at idle conditions, including time-dependent spray penetration, mean particle diameter, local mean particle diameter on radius direction, emissions and combustion noise.

INTRODUCTION

Many current designs of high speed direct injection (HSDI) Diesel injector systems are of the initial throttle injection type that use a smaller orifice in the vicinity of the needle valve. The purpose of this narrower opening is to reduce both the emissions and combustion noise. Typical of throttle injection nozzles, are the two spring type detailed by Greeves and Wang[1], and by Kageyama[2] where the needle may be stopped in the middle of the lift process. The results from this study showed that emissions of HC and NOx were reduced, with CO and smoke emissions remaining unchanged. The combustion noise was also reduced without any change in fuel consumption. The main reason for these improvements was a reduction in the amount fuel induced during the onset of the injection process, allowing better precombustion control[3]. In addition to this the amount of unburnt fuel colliding with the cylinder walls was reduced. However both throttle and two-spring type injectors result in increased HC emissions at set NOx emissions levels. This problem being most prevalent at starting and continuous idling operating conditions. An injection nozzle offering a solution to this problem would therefore have to reduce HC emissions (at constant NOx levels) while simultaneously offering reduced idling combustion noise. This paper therefore details the preliminary design of a novel pilot injector system not using the throttle nozzle principle. To allow both the emissions and combustion noise to be reduced, it was thought that the use of a pilot injection system would be beneficial. At first the atomization characteristics of this nozzle were investigated at atmospheric conditions, with subsequent tests carried out in a small DI engine allowing both emissions and noise tests to be carried out.

INJECTOR SYSTEM DESIGN CONCEPT

It is known that the main factor causing HC emissions at idling conditions is the complete throttling of the entire injection period. The result of this process is a larger pressure difference between the chamber and nozzle, leading to an increase in the average size of spray droplet diameter. The purpose of the pilot injection system was to control the average droplet size, while retaining the spray penetration characteristics of throttle type injectors, which are known to be satisfactory.

The important operating features were listed as follows:

(1) Short spray penetration at ignition delay.
(2) Small mean spray droplet size.
(3) Stratified spray droplet size distribution on radial direction from center to outside.
(4) Stability of injection from idling to maximum speed and maximum load.
(5) Stability of initial injection characteristics for required operating lifetime.
(6) Easy setting and maintenance free operation.

In order to satisfy these requirements, the main design characteristics of the new injector were as follows.

(1) Correct pilot injection characteristics.
(2) Main opening pressure higher than pilot opening pressure.
(3) Easily adjusted distance between pilot and main injection.
(4) Constant pilot injection quantity.
(5) Use of conventional nozzle types.

EXPERIMENTAL SYSTEMS

Description of Injection Systems

The types of nozzle used in this investigation are shown in Fig.1.1-1.4, Figs.1.1-1.2 show a single spring injector in which two nozzle types (Standard and throttle type) were used. The nozzle shown in Fig.1.2 has a clearance between the tip of the needle valve and the nozzle body. Fig.1.3 shows a two spring injector, in which the pre-lift value of the first spring, when used with a standard nozzle, gives the flow characteristics shown in Fig.2. This figure also compares the features of the throttle nozzle. It can be seen that at the pre-lift value of the two spring injector(0.04mm), the volume flow rate of both nozzles is the same.

The new injector design is shown in Fig.1.4. The system uses a standard nozzle design, with a single stage lift arrangement. However in addition to the standard fuel path leading to the nozzle area, there is a second fuel line leading to a Dodge Plunger* assembly.

---

* A valve system allowing leakage past the plunger to force an early valve closure thus allowing Pilot injection.

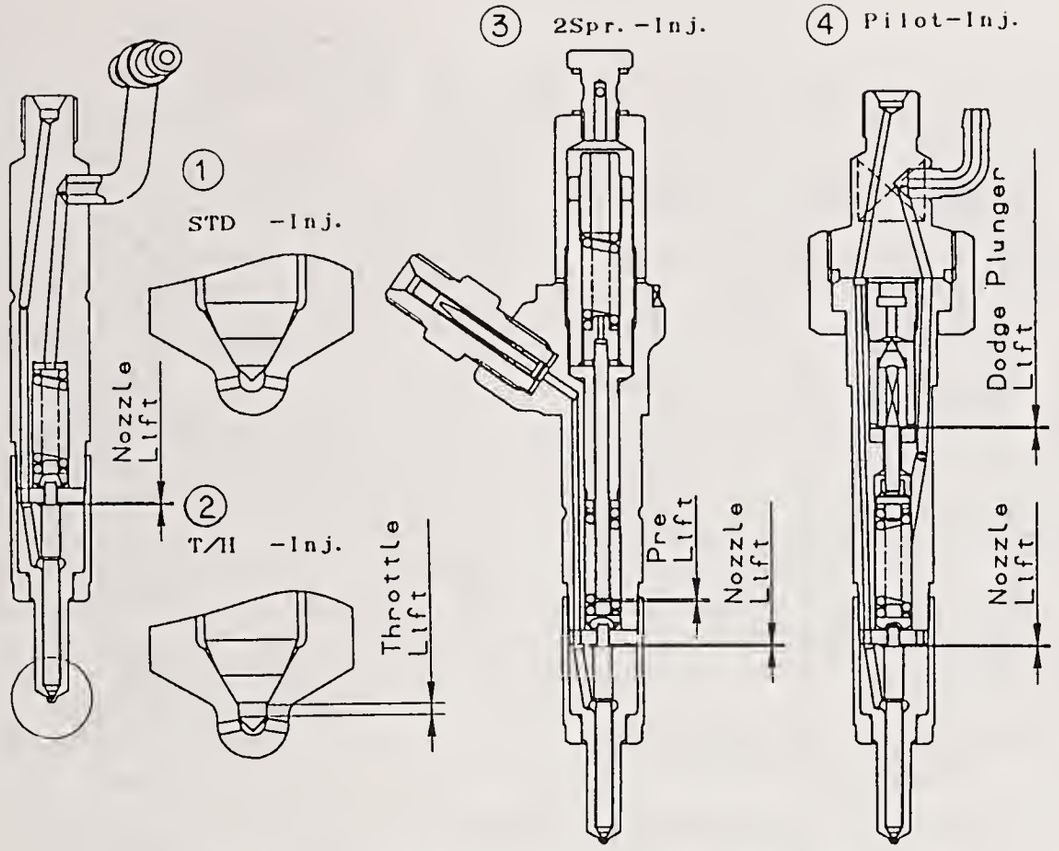

Fig. 1 Details of injection systems

The relationship between the pressurized area of the Dodge plunger and the nozzle was selected according to the following relationship:

$$A_{DPS} < (A_N - A_{NS}) < A_{DP} \quad \ldots\ldots\ldots\ldots (1)$$

Where:

A_{DPS} - Dodge Plunger seat area
A_{DP} - Dodge Plunger cross section area
A_{NS} - Nozzle seat area
A_N - Needle cross section area

Before the start of injection the pressure/area relationship is stable according to the relationship - $A_{DPS}<A_N-A_{NS}$. At the start of an injection cycle the needle valve lifts and subsequently, when the opening pressure of the Dodge Plunger is reached it also lifts. The movement of the Dodge Plunger creates a drop in the line pressure due to the dead volume in the the Plunger. At this time a new pressure/area relationship is created - $A_N<A_{DP}$ - signifying the end of the pilot injection process, this is also accompanied by the close of the needle valve. The fuel line pressure then increases producing a second lift in the needle valve, with the Dodge Plunger remaining open from the previous line pressure increase. This process begins the main injection.

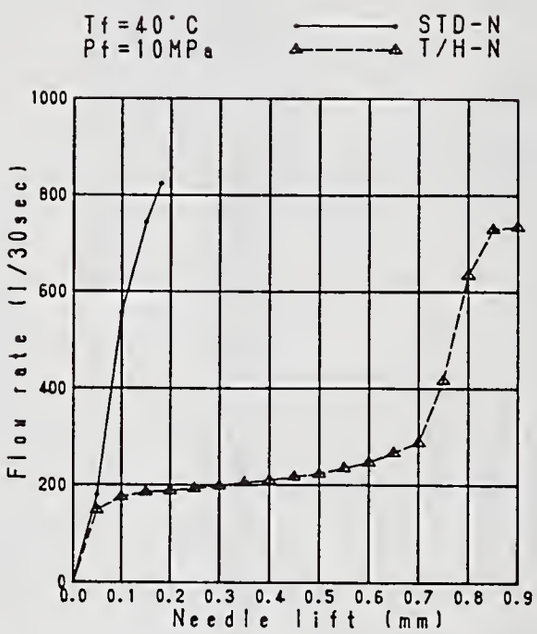

Fig. 2 Standard and throttle nozzle flow characteristics

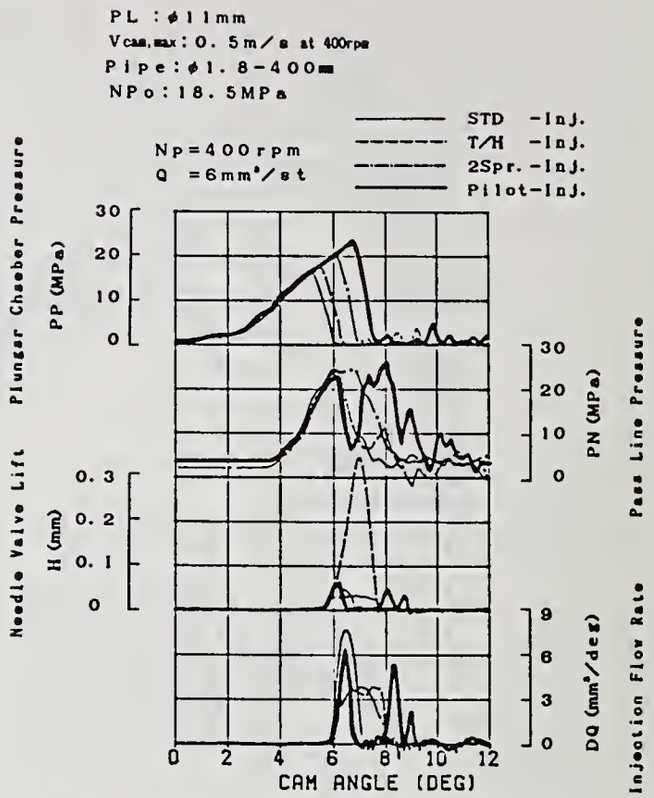

Fig. 3 Injection system characteristics

When the line pressure begins to drop, signifying the end of the injection process, the needle valve closes first. This is followed by the closure of the Dodge Plunger when the line pressure has fallen to the respective value.

The Dodge Plunger used in this investigation had a cross sectional diameter of 6mm, with a seat diameter of 3.3mm. The plunger lift was set to 0.65mm. The injection nozzles used were of the 5 hole type, with a orifice diameter of 0.25mm. The primary opening pressure was set at 18.5MPa. At idle operating conditions the delivery pump speed was 400rpm, with an engine speed of 800rpm. The injected volume of the fuel was 6mm^3/st. at no load conditions. These test conditions were kept constant for all the nozzles throughout the test procedure. Fig.3 shows the fuel injection pump plunger chamber pressure (PP/MPa), path line pressure (PN/MPa), needle valve lift (H/mm), and injection rate (DQ/mm^{3}deg^{-1}).

Measurement of Spray Particles

Two different optical methods were used to measure the size of the spray particles, a laser diffraction method (MALVERN 2600 PARTICLE SIZER) and a Phase Doppler method (AEROMETRICS PDPA-100). The MALVERN system performed a time dependent measurement of particles within the laser beam volume, whereas the AEROMETRICS system measured the local mean particle diameter on a radial direction. The operating principle of both these systems is detailed in references (4 & 5) and (6) respectively, only the test results will be reported here.

DISCUSSION OF RESULTS

Spray Shape

Flash photographs of the sprays are shown in Fig.4 at varying time periods after the start of injection. The standard injector shows both wide spray angles and long penetration, however the throttle and two-spring injector arrangement (both throttle type systems) show shorter penetration with smaller spray angles. The new injector type (Pilot Injection) results in both penetration and spray width values between the standard and throttle type systems. The actual mean numerical values are shown in comparison in Fig.5.

The similarity between the Standard injector and the new type at the smallest time delay (0.5deg.) can been seen. However after the reduction in the fuel line pressure in the Pilot System (due to the motion of the Dodge Plunger) the reduction in the spray penetration can been seen. Also as the time lapse after injection increases (1.5-2deg.) the termination of the pilot injection process in the new injector can be clearly seen. When compared to the standard nozzle this termination process allows the air in the vicinity of the new nozzle to mix thoroughly with the pilot fuel injection.

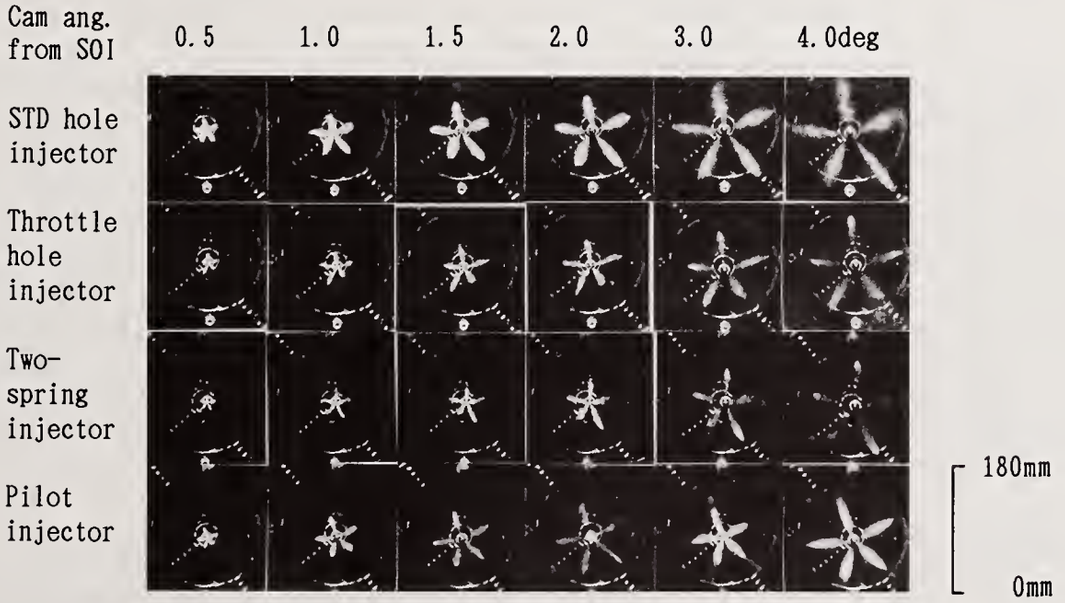

Fig. 4 Injection spray photographs

Time Dependence of Spray Characteristics

Fig.6 shows the Sauter Mean Diameter as produced by the MALVERN diffraction system. The actual figure (D32) is an average produced along the length of the laser beam's intersection, with the spray cone at a set period after the start of injection. The position of the laser beam (diameter 9mm) was set at a constant separation (80mm) away from the tip of the nozzle.

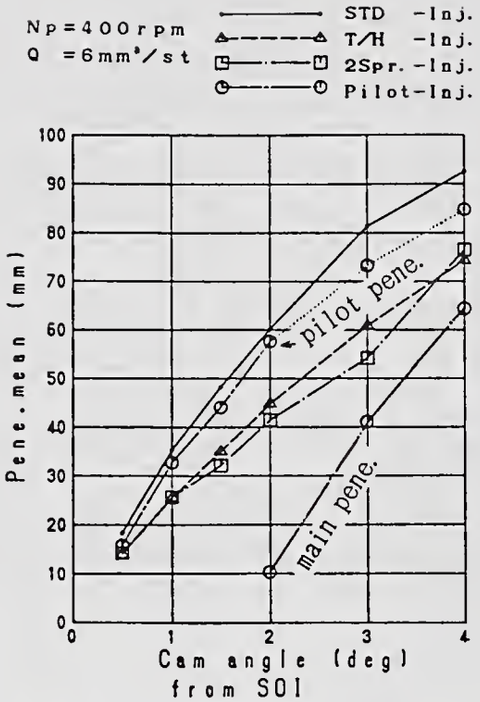

Fig. 5 Injection spray penetration

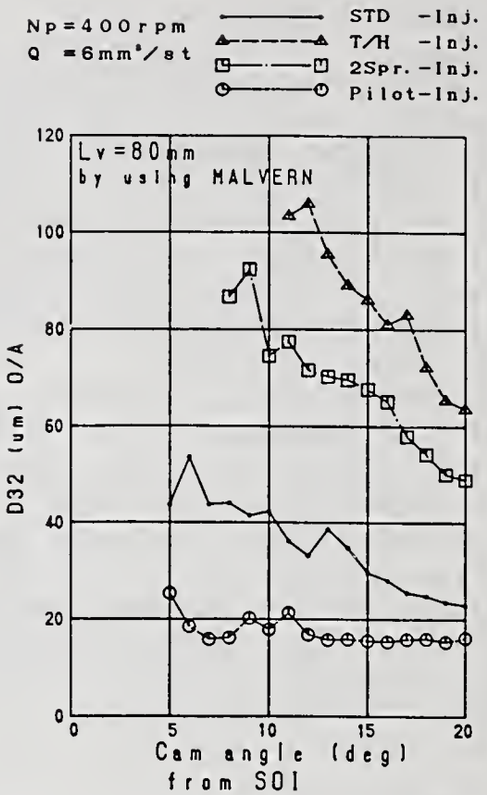

Fig. 6 Sauter mean diameter (MALVERN)

The time dependence of the Sauter mean diameter for all four nozzles systems shows similar characteristics, with large initial mean diameters, gradually decreasing with time. However if the actual mean diameters of each injector are compared, both the two-spring and throttle hole systems produce particles with a mean diameter too large for efficient operation at idling conditions. The standard nozzle does approach the mean size distribution of the Pilot system late in the injection process, but a comparison of the early mean diameters (5deg. after injection) reveals a large difference between the two. The Pilot system also produces a smaller size distribution much earlier in the injection process (10deg. after injection).

Positional Dependence of Spray Characteristics

The AEROMETRICS PDPA system was used to investigate the characteristics of the spray using single point measurements as opposed to the beam integration of the MALVERN system. The position of a single set of measurements, taken on a radius from the center line of the jet, was again set at 80mm separation from the nozzle exit. The distance between each measurement point was 5mm.

Fig.7 shows the results given by the PDPA for both Sauter mean diameters. A comparison with Fig.6 shows that the results from this system and the MALVERN 2600 (Fig. 6) give approximately the same particle size results at the jet center line. It is known that the calculation routine for the evaluation of mean particle diameter in the MALVERN system can under estimate the

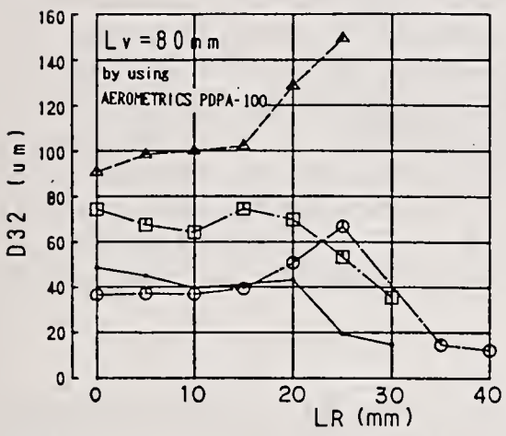

FIG. 7 Sauter mean diameter (AEROMETRICS PDPA)

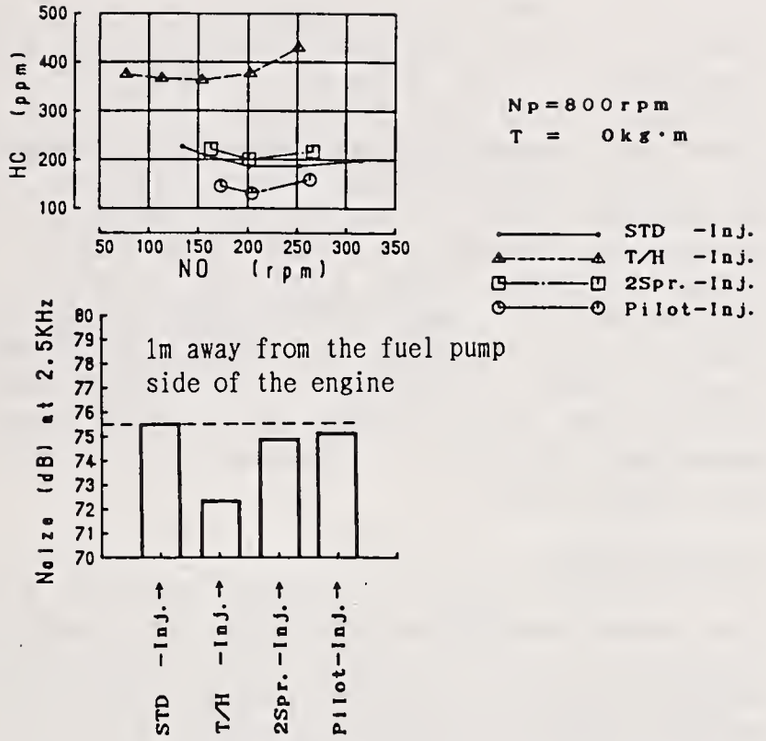

FIG. 8 Engine emission and noise characteristics

true particle size. The absolute use of the ROSIN-RAMMLER curve fit excludes, in some cases, large diameter particles. This possible inaccuracy only occurs in lower mean diameter distributions, where a small percentage of larger particles is known to exist.

The size distribution of the Throttle hole injector is different from the other systems tested, showing a large overall mean diameter. The Two-spring injector also shows an overall large size distribution. The Standard system gives a relatively small particle size distribution. The Pilot injector however shows small particle sizes at the outer edge of the jet, which change to a larger mean size at L=25mm. The size distribution of the Pilot jet is therefore termed as stratified. The change in distribution of this jet is thought to result from the interaction on the main and pilot jet fuel volumes. At the time of the main injection the velocity and momentum of the main jet exceed that of the pilot injection. The main jet therefore collides with the previously injected fuel forcing it to the outside of the jet arssea.

Emissions and Combustion Noise Tests

The engine used for this series of tests was a four cylinder turbocharged type with a bore/stroke ratio of 93/102. The boost pressure limit was set to 0.7bar, however this limit was not encountered at idling conditions. The swept volume was 2771cc, with a compression ratio of 17.5. The four injectors were all tested with reference to NO and HC emissions. The combustion noise was also measured in the 2.5KHz range 1 meter away from the fuel pump side of the engine.

The results are shown in Fig.8. At constant NO levels the Throttle hole injector produced very high HC emissions when compared to the remaining three injectors. The cause of this is thought to be the high mean particle diameter, shown in Fig. 7 , leading to very slow combustion rates, and low noise levels (Fig. 8). Among these injectors the Pilot system produced the lowest HC emission levels. The noise level of the standard nozzle is shown to be the highest. Again reference to the mean particle diameter (Fig. 7) shows this injector to have a small mean particle size. The result of this is a high rate of combustion. The relatively high level of noise produced by the Pilot system is thought to result from a high rate of combustion in the outside, and center of the jet only. These areas are shown in Fig.7 to have the small mean particle size necessary to produce this relatively high rate of combustion.

CONCLUSIONS

A new Diesel injector system has been designed. The system has been tested at atmospheric conditions with reference to spray formation and particle size characteristics. The system has also been tested at engine idling operating conditions to assess both emissions and noise levels.

The main conclusions were as follows:

(1) Good controllability of spray tip penetration.
(2) Increased air/fuel mixing during pilot injection.
(3) Lower mean spray particle diameter.
(4) Lower particle diameter in spray center.
(5) Stratified spray diameter distribution.

It must be noted that the particle size and spray analysis was performed at atmospheric conditions, so a direct comparison of the injector system's performance within an engine, concerning the emissions and noise levels, is not strictly valid. The next step in this research is therefore to repeat the characterization of the injection system in an environment equivalent to an operating engine.

REFERENCES

1) Greeves, G., Wang, C.H.T., "Two stage lift injection and HSDI combustion", SAE 905025 (1990).
2) Kageyama, K., "Injection characteristics of two spring Diesel injector", JSAE New Diesel Engine Symposium Tokyo (1983).
3) Gill, A.P., "Design choices for 1990's low emission Diesel engines", SAE 880350 (1988).
4) Swithenbank, J., Beer, J.M., Taylor, D.S., Abbot, D. and McCreath, G.C., "A laser diagnostic technique for the measurement of droplet and particle size distribution", AIAA No. 76-69 (1976).
5) Nakayama, M., "Principles of laser diffraction theory and its application to particle sizing", Japan Automotive Research Institute. (JARI) (1989) Vol. 2.
6) Bachalo, W.D. and Houser, M.J., "Phase Doppler spray analyser for simultaneous measurements of drop size and velocity distribution", Optical Engineering Sept/Oct (1984) Vol. 23, No. 5/583.

A FEW USEFUL RELATIONS FOR CAVITATING ORIFICES

F. Ruiz

Department of Mechanical and Aerospace Engineering
Illinois Institute of Technology
Chicago, IL, U.S.A.

ABSTRACT

Elementary Fluid Mechanics is used to show the relationships between the several cavitation parameters for plain orifice atomizers that have been proposed over the years. Cavitation makes the orifice flow behave in a way analogous to that of a compressible flow through a nozzle. With some simplifying assumptions, it is possible to estimate the order of magnitude of the energy disappearing from the main flow and going into turbulence. A criterion for cavitation inception in orifices is given, as well as an equation for the discharge coefficient of the fully reattaching, non-cavitating flow.

INTRODUCTION

When the injection pressure is sufficiently high, or the back pressure sufficiently low, the liquid injected through an orifice will form a cavitation bubble, surrounding a detached liquid flow or "vena contracta". This phenomenon has been known for a long time [1], and has even been the basis of certain devices [2]. Since the studies of Bergwerk [3] were published, orifice cavitation has been considered a likely candidate to explain the phenomenon of liquid atomization. Later experiments [4, 5] have also found evidence of cavitation for the conditions that promote good atomization.

The appearance of cavitation is also linked to a drop of the discharge coefficient [3, 4, 6, 7]. Indeed, when cavitation appears, a subsequent drop of the back pressure will not increase the flow, that has become choked at the cavitation region. There is an analogy between this choking and the choking of a compressible flow.

Despite the obvious importance of long-orifice cavitation, studies have been infrequent. A major obstacle found in searching though the literature is the fact that different cavitation parameters are used by different authors. The intent of this communication is to show the relationships between them, and to formulate some useful expressions.

DEFINITIONS OF CAVITATION PARAMETER

Using the variables shown in Fig. 1, three main parameters have been proposed:

1. Knapp, Daily and Hammitt [8], and the main body of researchers in cavitation, prefer the parameter:

$$\sigma = \frac{P_\infty - P_v}{\frac{1}{2}\rho V_\infty^2} \tag{1}$$

where P_∞, V_∞ are the unperturbed or characteristic values of the pressure and velocity, respectively, and P_v is the apparent vapor pressure (which includes the pressure of the gases dissolved in the liquid). For the particular case of orifice cavitation, the parameter used is:

$$\sigma = \frac{P_2 - P_v}{\frac{1}{2}\rho V^2} \tag{2}$$

using the downstream pressure P_2, and the average flow velocity, V. When $P_2 = P_v$, $\sigma = 0$, and the cavitation must extend all the way from the inlet to the outlet, which constitutes the so-called "flip" condition. The flow does not reattach to the orifice wall. Flip usually occurs below some value of σ, larger than zero. For $\sigma = 0$, the pressure throughout the orifice is the vapor pressure, and the liquid is atomized by flashing, if discharged after the orifice.

2. Bergwerk [3] preferred to use the parameter:

$$K = \frac{P_1 - P_2}{P_2 - P_v} \tag{3}$$

Using a variation of this parameter (assuming $P_v \approx 0$), he found a relation between the cavitation parameter and the length of the cavity, before reattachment occurs. He also correlated the discharge coefficient against this parameter and the Reynolds number. The same parameter was used by Spikes and Pennington [7].

3. Hall [9] and, later, Nurick [4], used the parameter:

$$K' = \frac{P_1 - P_2}{P_1 - P_v} \tag{4}$$

and found that, by just applying this definition and that of discharge coefficient, C_d, and the continuity equation, one could deduce:

$$\frac{C_c^2}{C_d^2} = K' \tag{5}$$

where C_c is the contraction coefficient, ratio of the narrowest cross-section of the "vena contracta", to the orifice cross-section. This relation, although very simplified (it does not include Reynolds number effects), yields a good approximate value of the discharge coefficient of a cavitating orifice, as shown by Nurick [4].

These three numbers are related to each other. It is easy to see that:

$$\frac{1}{K} = \frac{P_2 - P_v}{P_1 - P_2} = \frac{P_1 - P_v}{P_1 - P_2} - 1 = \frac{1}{K'} - 1 \qquad (6)$$

and also:

$$1 - C_c^2\sigma = 1 - \frac{P_2 - P_v}{\frac{1}{2}\rho(V/C_c)^2} = 1 - \frac{P_2 - P_v}{\frac{1}{2}\rho V_v^2} \qquad (7)$$

where V_v is the average velocity at the vena contracta. Now, from Bernoulli:

$$P_1 - P_v = \frac{1}{2}\rho V_v^2 \qquad (8)$$

so:

$$1 - C_c^2\sigma = 1 - \frac{P_2 - P_v}{P_1 - P_v} = \frac{P_1 - P_2}{P_1 - P_v} = K' \qquad (9)$$

In other words:

$$K' = 1 - C_c^2\sigma = \frac{1}{\frac{1}{K} + 1} \qquad (10)$$

Similar equations for the discharge coefficient can be obtained by substituting this result into equation (5).

ENERGY LOSS IN REATTACHMENT

It was mentioned above that there is a similarity between the flow in a cavitating orifice, and the choked compressible flow through a nozzle [1, 2]. Figure 2 illustrates the analogy, by representing the evolution of the flow, as the downstream pressure, P_2, is decreased.

In the compressible case, the flow rate continually increases until critical conditions (M = 1) are reached at the throat, at which point the condition at the throat cannot change further, since M = 1 must occur at the narrowest section. In the orifice case, the flow rate also increases as P_2 decreases, until the pressure at the narrowest point of the vena contracts is equal to the apparent vapor pressure, P_v. A further decrease of P_2 does not increase the flow, because the pressure at the vena contracta cannot be smaller than P_v.

In the compressible case, if P_2 drops below the critical value, a region of supersonic flow appears downstream from the throat. This region ends in a shock wave, which suddenly raises the static pressure. After this, the flow is subsonic. In the orifice case, when P_2 drops below the critical value, a cavitation bubble surrounds the vena contracta. The liquid eventually reattaches to the wall, within a short distance. This reattachment process raises the pressure and, as we shall see later, is accompanied by energy degradation, like in a shock wave. After reattachment, there are no cavitation bubbles.

If P_2 is lowered sufficiently, in the compressible case, the shock wave will move out of the nozzle, until all the flow downstream from the throat is supersonic. Similarly, a lower value of P_2 exists, for which the cavitation region (which grows as P_2 decreases) reaches the end of the orifice. At this

point the liquid totally clears the orifice walls, without reattachment: it is the condition known as hydraulic flip.

The normal cavitating orifice flow is, thus, not unlike the compressible flow in a convergent-divergent nozzle, with a shock wave in the divergent part. The energy lost in the reattachment of the flow is partly transformed into strong turbulent fluctuations. If the liquid is injected into air, these fluctuations are responsible, to a large extent, for its atomization into fine droplets. It is possible to correlate jet atomization characteristics with the intensity of cavitation [5, 10]. The energy lost by the mean flow in the reattachment can be evaluated in the following manner:

Assume that the flow up to the vena contracta is inviscid and that the Bernoulli equation is applicable, then:

$$P_1 - P_v = \frac{1}{2} \rho V_v^2 \tag{11}$$

The average speed at the vena contracta, V_v, is equal, by continuity, to:

$$V_v = \frac{V}{C_c} \tag{12}$$

Now, the pressure head loss at reattachment, assuming that the reattachment has been completed, and the velocity profile has been able to relax to a nearly uniform shape, is:

$$\Delta h = P_1 - (P_2 + \frac{1}{2} \rho V^2) \tag{13}$$

so:

$$\Delta h = \frac{1}{2} \rho V_v^2 + P_v - P_2 + \frac{1}{2} \rho V^2 = \frac{1}{2} \rho V^2 (1/C_c^2 - 1) - (P_2 - P_v) \tag{14}$$

and, from the definition of the parameter σ:

$$P_2 - P_v = \sigma \frac{1}{2} \rho V^2 \tag{15}$$

so:

$$\Delta h = \frac{1}{2} \rho V^2 (1/C_c^2 - 1 - \sigma) \tag{16}$$

or, using the other parameters:

$$\Delta h = \frac{1}{2} \rho V^2 (\frac{K'}{C_c^2} - 1) = \frac{1}{2} \rho V^2 (\frac{K}{1 + K} \frac{1}{C_c^2} - 1) \tag{17}$$

When there is no cavitation, there is still a loss associated with flow reattachment, although the separation bubble is filled with liquid, not with a vapor. To find this value, one only needs to apply the momentum equation from the section of the vena contracta, to a section after the reattachment:

$$P_2 - P_v = \rho V (V_v - V) \tag{18}$$

Then:

$$P_2 - P_v = \rho V^2 (1/C_c - 1) \tag{19}$$

Using this relationship, instead of (15) we obtain, finally:

$$\Delta h_{nc} = \frac{1}{2} \rho V^2 (1/C_c - 1)^2 \tag{20}$$

which is, of course, independent of any cavitation parameter.

CRITICAL CAVITATION PARAMETER

Equations (15) and (18) also yield, by comparison, the condition for cavitation inception, for which both are valid (there is no sudden jump in head loss when cavitation starts). One obtains:

$$\sigma < \sigma_{crit} = 2(1/C_c - 1) \tag{21}$$

which, for the other cavitation parameters, becomes:

$$K > K_{crit} = \frac{1}{2} \frac{1}{C_c(1 - C_c)} - 1 \tag{22}$$

$$K' > K'_{crit} = C_c^2 + (1 - C_c)^2 \tag{23}$$

For a sharp-inlet orifice, for which $C_c = \pi/(\pi+2) = 0.611$, the critical values are:

$\sigma_{crit} = 1.273$ $\quad$ $K_{crit} = 1.103$ $\quad$ $K'_{crit} = 0.525$

This is, of course, just a simplification. Since the pressure at reattachment is actually larger than P_2, we should expect that the actual σ_{crit} will be smaller than the value given above, and K_{crit} and K'_{crit} larger. The pressure variation from reattachment to the outlet can be approximated by:

$$\Delta P = \frac{1}{2} \rho V^2 \, f \frac{L}{D} \tag{24}$$

where the friction coefficient, f, for the strongly turbulent flow after reattachment, can be assumed, as a first approximation, to be independent of the Reynolds number. An appropriate value is f = 0.04, which is the maximum attainable in a smooth-walled pipe, for transitional flow. Then:

$$\sigma_{crit} = 2(1/C_c - 1) - 0.04 \, L/D \tag{25}$$

and the values of K_{crit}, K'_{crit} would be obtained by the relations in (10), that is:

$$K'_{crit} = C_c^2 + (1 - C_c)^2 + 0.04 \, C_c^2 \, L/D \tag{26}$$

$$\frac{1}{K_{crit}} = \frac{1}{C_c^2 + (1 - C_c)^2 + 0.04\ C_c^2\ L/D} - 1 \qquad (27)$$

A similar equation by Hall [9] for the prediction of K_{crit} gave, instead, a prediction of the K for hydraulic flip as reported by Bergwerk [3](observe in reference [3] that the data that Hall erroneously took as inception, correspond rather to the definition of flip). That equation predicted considerably larger values of K_{crit}, because it was based on unusually small values of the discharge coefficient, C_d.

Critical Discharge Coefficient

Equation (5) is valid at the limit of cavitation conditions, when cavitation is barely occurring. In this condition, one can substitute the critical value of the cavitation parameter, discussed above:

$$C_d^2 = \frac{1}{(1/C_c - 1)^2 + 1 + 0.04\ L/D} \qquad (28)$$

For the particular case of sharp-edged orifices, ($C_c = 0.611$), one obtains:

$$C_d = (1.4 + 0.04\ L/D)^{-1/2} \qquad (29)$$

A relation of this type had been hinted by Sadek [11]. This equation can also be used to estimate C_d in non-cavitating orifices, at high Reynolds number. Figure 3 represents a comparison of this estimation with experimental data, from different sources (non-cavitating), after Lichtarowicz et al. [12].

ACKNOWLEDGMENT

The author wishes to express his thanks to the National Science Foundation which, under Grant No. CTS-9010479 is supporting this research.

REFERENCES

[1] Ackeret, J., "Experimental and Theoretical Investigations of Cavitation in Water". NACA Technical Memo. No. 1073. 1930.
[2] Randall, L.N., "Rocket Applications of the Cavitating Venturi". ARS Journal, Jan-Feb 1952, pp. 28-31.
[3] Bergwerk, W., "Flow Pattern in Diesel Nozzle Spray Holes". Proceedings of the Institution of Mechanical Engineers, vol. 173, pp. 655-660. 1959.
[4] Nurick, W.H., "Orifice Cavitation and its Effect on Spray Mixing". Journal of Fluids Engineering, vol. 98, pp. 681-687. 1976.
[5] Arai, M., Shimizu, M., and Hiroyasu, H., "Break-up Length and Spray Angle of High-Speed Jet". Proceedings of ICLASS-85, p. IB/4/1. The Institute of Energy. London, 1985.
[6] Kling, R., and Leboeuf, R., "Flow through Nozzles in Rocket Motors". The Engineers Digest, vol. 14, pp. 461-463. 1953.
[7] Spikes, R.H., and Pennington, G.A., "Discharge Coefficients of Small Submerged Orifices". Proceedings of the Institution of Mechanical Engineers, vol. 173, pp. 661-664. 1959.

[8] Knapp, R.T., Daily, J.W., and Hammitt, F.G., "Cavitation". McGraw-Hill. 1970.
[9] Hall, G.W., "Analytical Determination of the Discharge Characteristics of Cylindrical-Tube Orifices". Journal of Mechanical Engineering Science, vol. 5, pp. 91-97. 1963.
[10] Ruiz, F., "Experimental and Theoretical Analysis of High Speed Atomization, and its Application to Diesel Fuel Injection". Ph.D. Thesis. Carnegie-Mellon University, Pittsburgh. 1987.
[11] Sadek, R. comment to [3] and [4]. Proceedings of the Institution of Mechanical Engineers, vol. 173, p. 671. 1959.
[12] Lichtarowicz, A., Duggins, R.K., and Markland, E., "Discharge Coefficients for Incompressible Non-Cavitating Flow through Long Orifices". Journal of Mechanical Engineering Science, vol. 7, pp. 210-219. 1965.

NOMENCLATURE

C_c	contraction coefficient
C_d	discharge coefficient
D	orifice diameter
f	friction factor
Δh	pressure head loss
K	Bergwerk's cavitation parameter
K'	Hall's cavitation parameter
L	orifice length
M	Mach number
P	pressure
V	velocity
ρ	density
σ	standard cavitation parameter
subscripts:	
1	before the orifice
2	after complete reattachment and velocity profile relaxation
crit	at cavitation inception conditions
v	at the narrowest section of the cavitating vena contracta

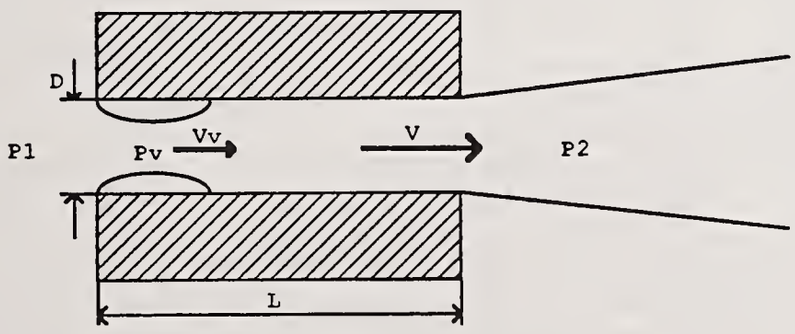

Fig. 1 Schematic representation of cavitating orifice flow

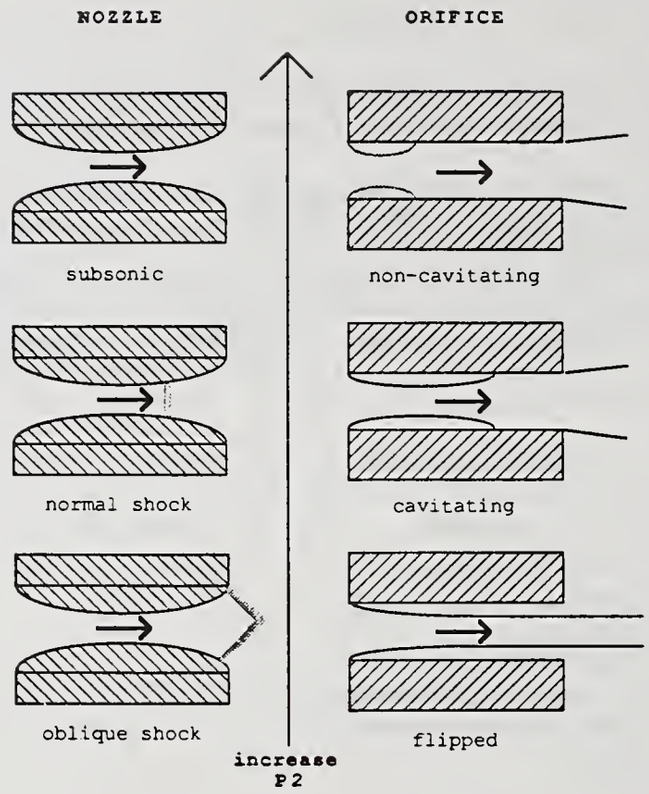

Fig. 2 Analogy between nozzle flow and cavitating orifice

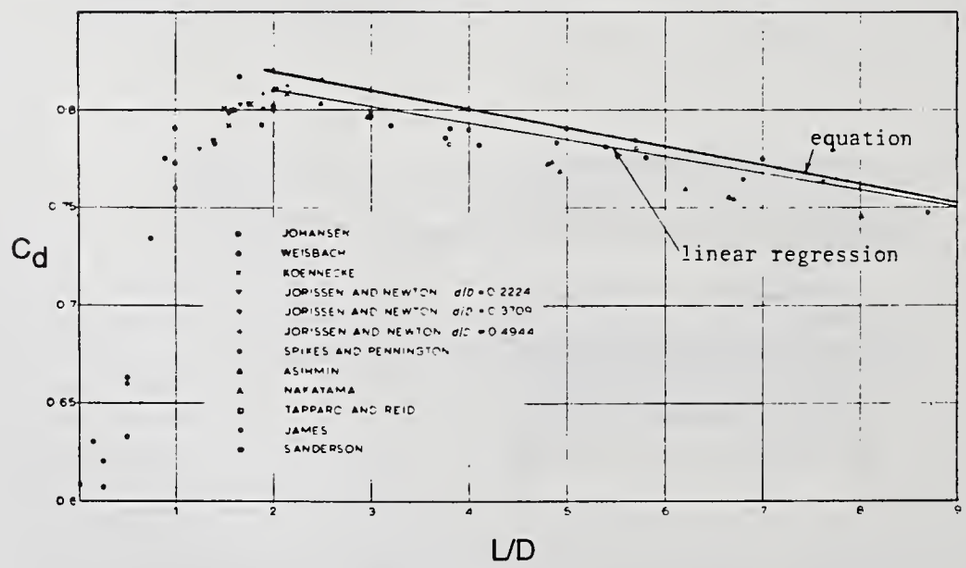

Fig. 3 Comparison between predictions of eq. (29) and experimental values of C_d (adapted from Lichtarowicz et al. [12])

HOLOGRAPHIC DIAGNOSTICS FOR DIESEL SPRAY RESEARCH

Z. Huang, L.-F. Zhang and B.-Z. Li

Power Machinery Engineering Dept.
Shanghai Jiao Tong University
Shanghai, P.R. China

ABSTRACT

This paper presents results of studies of the feasibility of applying laser holography to Diesel spray research. A laser holographic and data processing system for Diesel spray is described. The holographic methods investigated include in-line, off-axis holography, laser shadowgraphy and their capability for recording Diesel spray events is demonstrated. The concerning problems in Diesel spray research including droplet size measurement in dense fuel spray, fuel concentration analysis, two and three dimensional spray visualization are explored and discussed.

1. INTRODUCTION

Pulsed laser holography with it's ability to freeze three dimensions dynamic test volume with high resolution, which has hitherto never been possible by any other techniques, has become a powerful tool in the diagnostics of fluid and particle flow field.[1] There have been some examples of using holography techniques to measure fuel droplet of Diesel spray, with varying degrees of success.[2,3,4] But the application of laser holography to highly dense Diesel spray is still uncertain. In other hand, laser holography has great potentialities of providing new and valuable insights into physics of Diesel spray formation and structure, its application remains to develope. In this paper, an investigation on laser holographic methods for Diesel spray research was conducted. The concerning problems in Diesel spray research including droplet size measurement in dense fuel spray, fuel concentration analysis, two and three dimensional spray visualization, ect. were explored and discussed. Based on investigation, information on disintegrating process, droplet distribution and fuel-air mixture formation in Diesel spray from holographic visualization is useful to clarify the mechanism of atomization and will greatly help to promote combustion research.

2. EXPERIMENTAL TECHNIQUE AND APPARATUS

Holography is a two-step image-forming technique for recording and reconstructing the light waves.[5] Application of the pulsed laser holography enables a record of a high velocity transient fuel spray to be frozen in time.

This recording can subsequently be reconstructed into the original three-dimensional form and analyzed at leisure without the deterioration of the sample. In this work, a laser holographic and data processing system for Diesel spray has been set up. The Diesel spray is injected into the various ambient gas density from hole type nozzle. To maintain clean window, an electronically controlled injection device enables single injection of fuel to be achieved with good repeatability. The system controller receives signals from the needle lift transducer and triggers the pulse laser at the fixed time to synchronize emission of the laser and fuel injection.

The layout of the recording system is shown schematically in Fig.1. The ruby laser is Q-switched with a Pockels cell and emits a 30 nanosecond light pulse. the optical wedge is used to produce two beams, which are expanded and collimated to the size of the quartz glass window. One is led into the vessel to be transmitted through the spray as object beam. The other one is led to the holographic film as reference beam combined with the object beam. All the optical components and the vessel are arranged on a massive isolated table. This off-axis layout could be easily changed into in-line layout by removing the reference beam.

The reconstruction and data processing system is shown in Fig.2. A coherent plane wave provided by a helium-neon gas laser illuminates the hologram

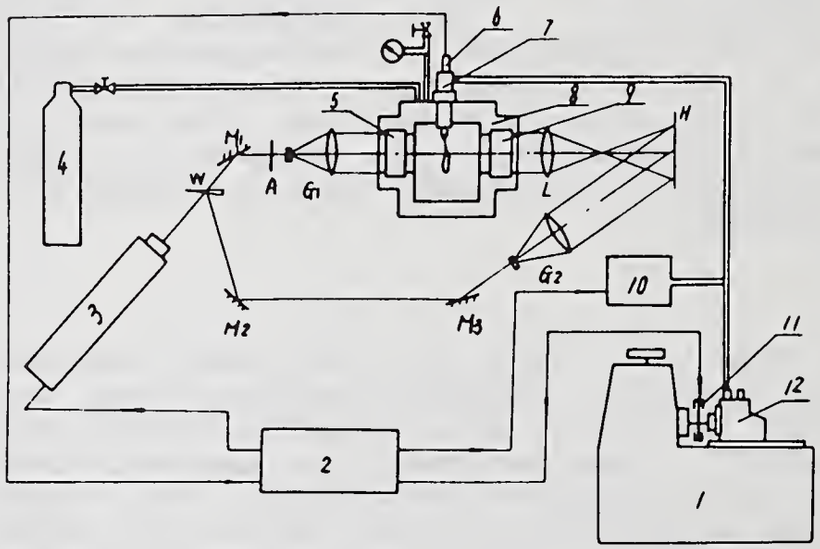

1. Fuel pump rig
2. System controller
3. Pulse ruby laser
4. Air bottle
5. Quartz window
6. Transducer
7. Fuel injector
8. Pressure vessel
9. Quartz window
10. Auxiliary injector
11. Angle markers
12. Injection pump

Fig.1 Schematic of holographic system.

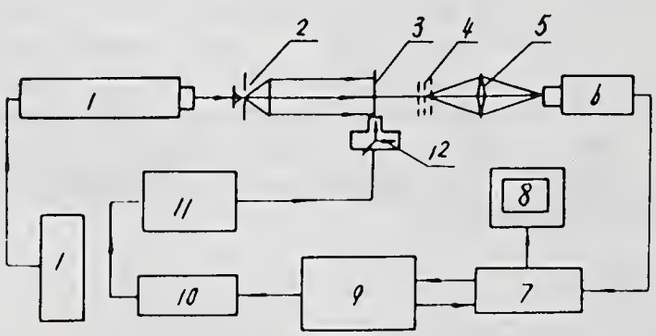

1. He-Ne laser
2. Spatial filter/EC
3. Hologram
4. Reconstructed image
5. Imaging lens
6. TV camera
7. Pcvision plate
8. Monitor
9. Computer
10. D/A circuit
11. Step-motor power
12. 3-D carriage

Fig.2 Schematic of reconstruction and data processing system.

which is transported on a three-dimensional motor-driven carriage controlled by computer to reconstruct the spray field. The reconstructed real images are magnified and relayed into the TV camera by image lens. The system transforms the video signal into digital signal and provides a image of matrix of 512*512 elements which is quantized linearly with 256 brightness levels from 0 to 255. The digital image is processed by computer with the threasholding and infocus discrimination techniques to open data source for studying the spray field.[6]

3. DROPLET SIZE MEASUREMENT

The droplet size and distribution of Diesel spray have great effect on the spray evaporation, fuel-air mixture formation and combustion. Holography is the most attractive and only known method by which high resolution images of individual particles in dynamic Diesel spray can be produced.

In-line far-field holography has the advantage of simplicity and should be explored first when holographic techniques is applied to Diesel spray. The theory of far-field holography has been well developed.[7,8] Here we will discuss some special consideration in Diesel spray including droplet density, depth of the field and their limit on far-field holography.

The in-line holography is the recorded interference pattern between the light diffracted by the object and a collinear background wave. The necessary condition is that, first, the location of particles to be recorded must satisfy far-field condition, second, the particle density to be measured must be such that a significant amount of light could pass through the field without modulation so as to serve as an effective reference beam. In order to make good quality holograms of Diesel spray, an experiment was designed and conducted to test the effect of particle density on the quality of reconstructed image. Samples of glass spheres of size 50-150 μm and with SMD = 110 μm were used. Holograms of various particle density were made. The quality of the image including shape feature, focusing and particle intensity distribution were examined in the reconstruction and data processing system. Fig.3 is a example of reconstructed image with 1 mm depth of particle field. The hologram of particle density equal to 8 particles/mm^3 is seen to be good, while those of 48 particles/mm^3 would be considered as marginal. Whereas those of 96 particles/mm^3 are bad. In that case, light passes through the field was badly deteriorated, contributing to noisy hologram and degradation of the recon-

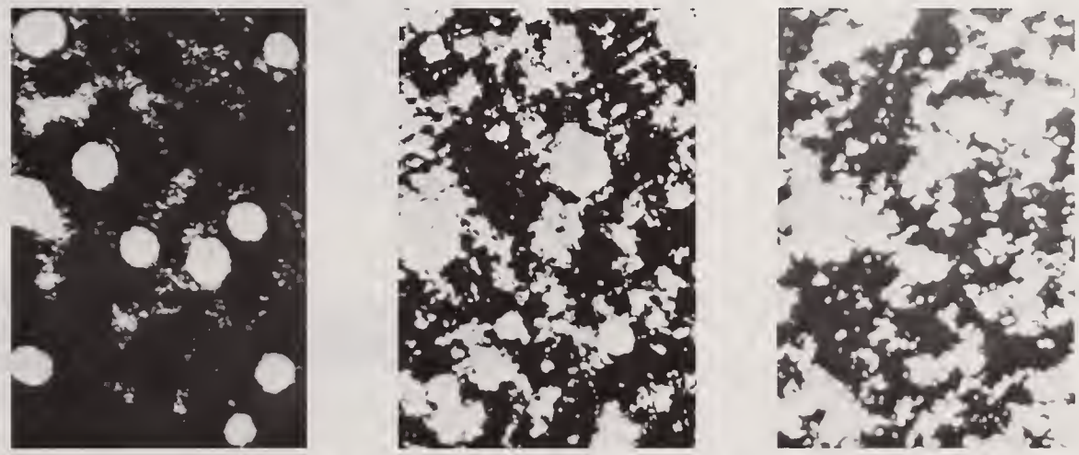

(a) (b) (c)

Fig.3 Effect of particle field density on quality of the image
(a) 8 (b) 48 (c) 96 particles/mm^3

structed image. Particles can't be resolved individually.

Based on experimental results, according to the 80% fraction of transmitted light criterion,[9] the effects of various monodisperse particle diameters, particle density and depth of the field on in-line far-field holography were calculated. In combination with far-field condition, the limit on the holography is then found to be:

$$n \leq 254 \cdot 10^3/(d^2 \cdot l) \tag{1}$$

$$d^2/\lambda \leq Z \leq 100\ d^2/\lambda \tag{2}$$

$$l \leq (100d_{min}^2 - d_{max}^2)/\lambda \tag{3}$$

Where l is depth of particle field, d the diameter of particle, n the particle density, Z the far-field distance and λ the wavelength of light used. In practice, size distribution has to be considered in Diesel spray. In that case, d in Eq.(1) could be replaced by SMD of the spray field. Fig.4 illustrates the relationship between particle density, particle size and depth of the field. It is seen that the smaller the particle size, the shorter the depth of the field to be measured. On the other hand, the large the particle size, the more stringent the requirements for particle density. Therefore, particle density and depth of the field are of vital importance to feasibility of holographic technique and quality of reconstructed image.

The off-axis holography, in which the reference beam is added separately, thus could make a good reference wave and easily control the O/R ratio. It will handle the case with higher particle density and produce higher quality image than in-line holography. But off-axis holography is also restricted by particle density because of multiple scattering and shadowing effects in the object field.

The Diesel spray is very dense and its droplet density goes far beyond the density limit established above. In other hand, Diesel droplet size is very small and depth of the field is relatively large. Light passes through

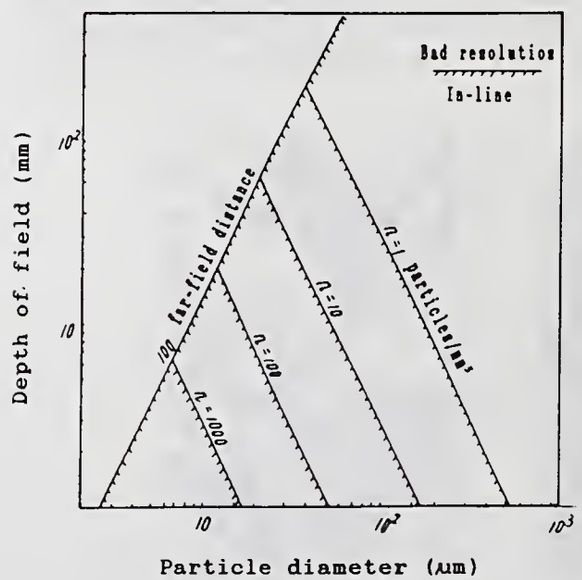

Fig.4 The limit on in-line far-field holography.

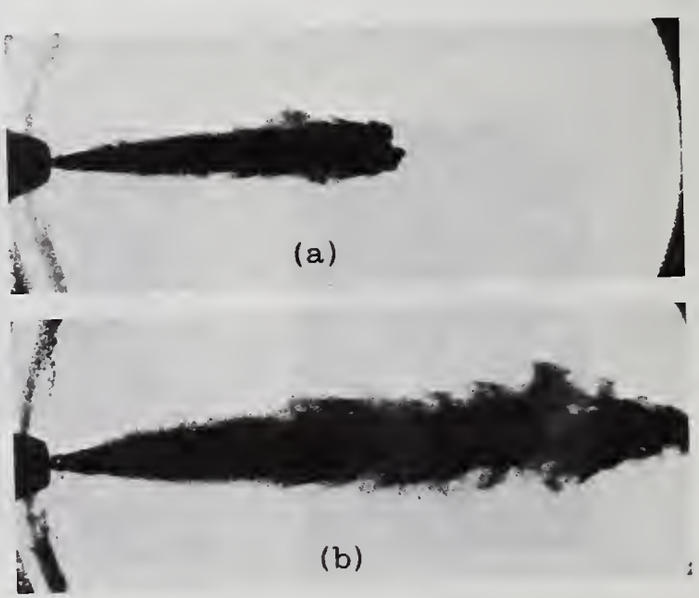

Fig.5 Laser shadowgraphy of Diesel spray (a) 0.35 (b) 0.95 ms after injection.

the spray field was badly deteriorated due to multiple scattering and shadowing effects. The recording can then be classed as a good coherent shadowgraphy, but with very poor hologram characteristics. Fig.5 illustrates the character of such recording. Therefore in-line holography can't be used to measure droplet size and distribution of such dense spray field directly. It is found that the technique may be recoverable with the use of sampling method, which means that some special measures are to be taken to purposely decrease density and depth of the field to be measured.

In this work, Diesel spray was measured by sampling a slice of the spray, as shown in Fig.6. It is worthwhile to note that the sampling slot and position must be elaborately designed to make sure of disturbing the atomization process and flow of spray field as less as possible and producing representative spray sample. [10] The image lens provide a enlarged image of the spray close to the holographic film to relax far-field condition and depth limit. Fig.7 is the fuel droplet images taken of 2-mm slice of Diesel spray, in which both in-focus and out of focus droplets can be observed. The data of holograms were analysed by the computer data processing system and droplet size distribution is presented in Fig.8.

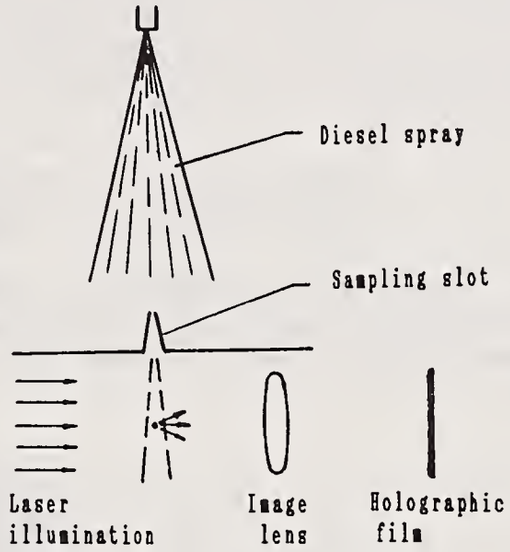

Fig.6 Schematic of sampling method.

Fig.7 Reconstructed image of fuel droplet in Diesel spray.

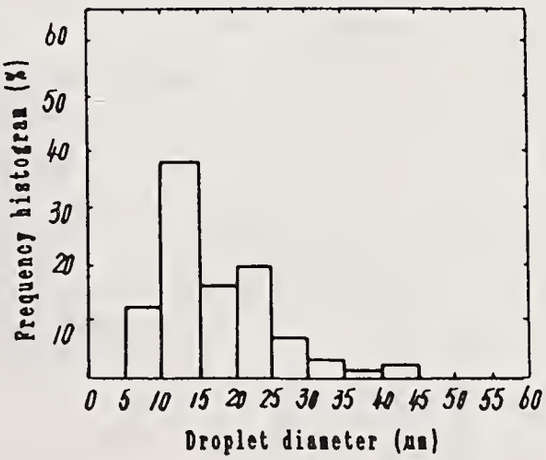

Fig.8 Droplet size distribution.

4. SPRAY FIELD VISUALIZATION

The understanding of the physics of Diesel spray formation and structure is very important indeed in producing more effective and clean engine. The technique of holography enables a way of direct visualization of the process.

As mentioned above, although the in-line holography can not yet be used

for droplet size measurement in dense Diesel spray directly, it can nevertheless produce high quality shadowgraphy of Diesel spray by virtue of "freezing" effect of pulsed laser and high resolution of holographic film, as shown in Fig.5. Even without reconstruction, laser shadowgraphy could well define the spray shape and structure in two dimensions, which has never been possible by conventional imagery.

In particular, by analysing the image of such recordings with the help of digital image processing technique, the distribution of light intensity transmissivity t(y) in Diesel spray shadowgraphy could be obtained, as shown in Fig.9. According to the light extinction theory, assuming that the spray is of axial symmetry, the optical thickness of the particle field is thin. The following fuel concentration C(r) of nonevaporating Diesel spray is found to be:[11]

$$\int_y^R \frac{C(r)\cdot r\cdot dr}{(r^2-y^2)^{0.5}} = \frac{0.767\cdot \rho_f \cdot D_{32}\cdot \lg\{t(y)\}}{\bar{\eta}_{ext}\cdot k} \qquad (4)$$

where R is the radius of spray cross section to be measured, r the radial distance, ρ_f the density of Diesel fuel, $\bar{\eta}_{ext}$ the extinction coefficient, in general which lies very near to value of 2.0 [3] and k the film constant. D_{32}

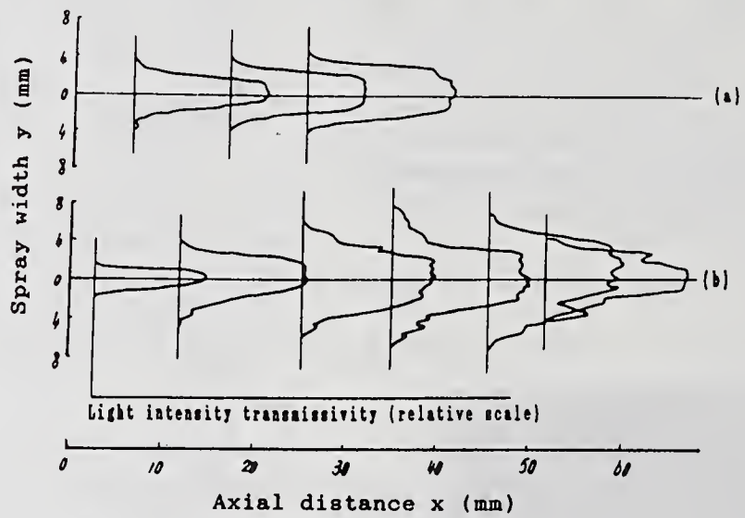

Fig.9 Distribution of light intensity transmissivity of Diesel spray.

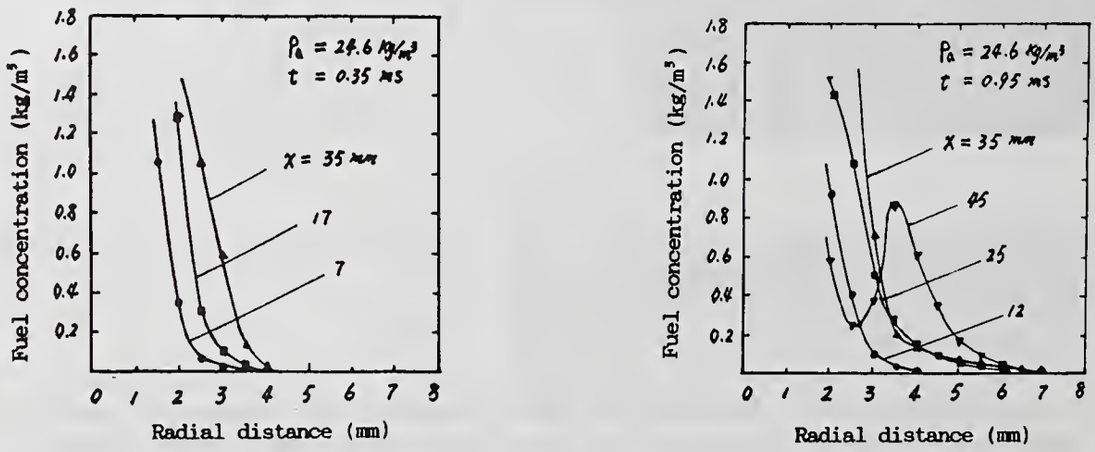

Fig.10 Fuel concentration of non-evaporating Diesel spray.
x is the axial distance.

is the sauter mean diameter of the droplets which is measured by in-line holography in this work.

By means of symmetrizing treatment and numerical method, the temporal and spatial development of fuel concentration is given in Fig.10. It is seen that at different time and section, the the distribution of fuel concentration is different. It is worth noticing that (1) although this method is only suitable for non-evaporating Diesel spray, on these grounds one could well predict fuel-air mixture formation and distribution of Diesel spray in the working cylinder. (2) this method can not be uesd to calculate the fuel concentration in core region of the spray because of incomplete break up and large optical thickness.

Off-axis holography, in which the far-field condition (in in-line holography) does not set any limit to it since the reconstructed images are separated angularly, is particularly useful in spray visualization. In this work, the off-axis holography with direct illumination of object field has been successfully used to record and study Diesel spray formation and structure. New atomization phenomenon, such as wavelike, perforated dendroid, fragmental and ligamentous fuel inner structure were discovered. Fig.11 presents example of reconstructed images. By scanning through the images of such recordings in data processing system, one can not only observe clearly the process of fuel injection and atomization, but also determine the size and shape of fuel droplets.

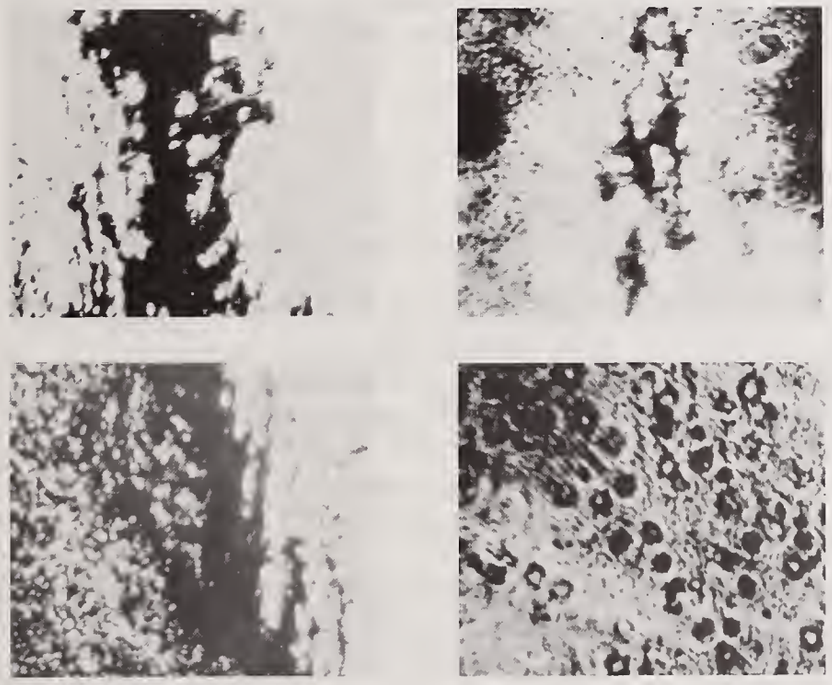

Fig.11 Reconstructed image of spray inner structure.

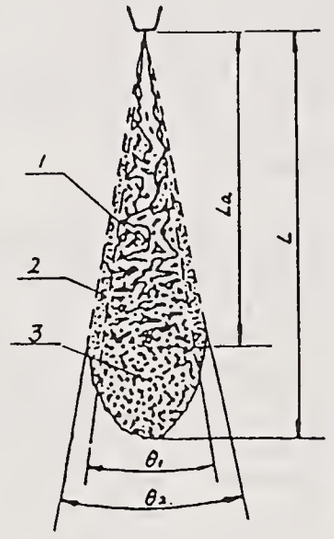

1. Core region
2. Spray mantle
3. Postatomization region

Fig.12 The shape and structure of Diesel spray.

Based on observation, it is found that the atomization of Diesel spray usually exhibits three modes, that is, wave, dendritic, and chaotic disintegration.[12] The shape and structure of Diesel spray could be classified into core region, postatomization region and spray mantle, as shown in Fig.12.

To enhance the understanding of the evaporating spray field, holography interferometry has also be applied in this work. Theoretically, this technique will allow one to visualize not only the movement of spray but also the development of density gradient existing in the spray field. However, it is found that from the practical standpoint the value of such recording is uncer-

tain at this time because the spray field are so complex that interferometic fringes are extremely difficult to interpret.

5. CONCLUSION

This investigation has demonstrated that the laser holography has great capability for providing new and valuable insights into the physics of Diesel spray formation and structure. Based on investigation, the following conclusions can be made.

1. In-line holography is useful for the measurement of the particle field, but suffers particle density limit and tedious data reduction. But the technique may quite be of use with the aid of the sampling method. In this work, a density and depth limit that can be applied to in-line holographic recording is established and a computer-aided data processing system has been developed which could make the technique more effective and attractive.

2. Laser shadowgraphy, without reconstruction, could well define spray shape and structure in two dimensions. Particularly with the help of digital image processing technique, it can provide information on fuel concentration of non-evaporating Diesel spray.

3. Off-axis holography is best suited for spray field visualization. In this work, the inner structure of Diesel spray was firstly visualized and new atomization phenomenon were discovered by means of off-axis holography with direct illumination. Information on disintegrating process, droplet formation, shape and structure of Diesel spray from the holographic visualization will greatly help to advance these studies.

REFERENCE

1. Lee,Y.J.and Kim,J.H.: "A Review of Holography Application in Multiphase Flow Visualization Study" Journal of Fluids Engineering. Vol.108, Sep. pp.279(1986)
2. Trolinger,J.D. and Bentley,H.T. et,al: "Application of Electro-optical Techniques in Diesel Engine Research" SAE 740125. pp.633
3. Isao Shimizu et,al: "A Light Scattering and Holographic Technique for Determine Droplet Size and Volume Density Distribution in Diesel Fuel Sprays" SAE 820355. pp.155
4. Keiya Nishida and Hiroyuki Hiroyasu et,al: "Holographic Measurement of Evaporating Diesel Spray at High Pressure and Temperature" JSME International Joural. Vol.107, pp.30(1987)
5. Collier,R.J.: Optical Holography. Academic Press. 1971
6. Xiao Bo, Xia Xiao-mei, Huang Zhen et,al: "Data Processing on Particle Field Hologram." Paper presented at the 4th China ICE Diagnostics and Measuerment Meeting. April,1988
7. Siliverman,B.A., Thompson,B.J. et,al: "A Laser Fog Disdrometer" Journal of Applied Meteorology. 3, 792(1964)
8. Cartwright,S.L., et, al: "Particle Sizing Using Far-field Holography" Optical Engineering. Vol.19, NO.5, pp.727 (1980)
9. Trolinger,J.D.: "Particle Field Diagnostics by Holography." AIAA-80-0018
10. Huang Zhen: "In-line Holography for Analysis of Dynamic Particle Field." Thesis of Shanghai Jiao Tong University. 1990.
11. Huang Zhen, Zhang Lian-fang: "Measurement of Fuel Concentration in Non-evaporating Diesel Spray" Science & Technology of SJTU. No.57, pp.57(1990)
12. Huang Zhen, Zhang Lian-fang: "The Laser Holographic Study on Fuel Atomization of Diesel Spray" International Symposium on COMODIA '90 pp.303-308 (1990)

RESULTS OF THE ASTM INTERLABORATORY STUDY ON CALIBRATION VERIFICATION OF LASER DIFFRACTION PARTICLE SIZING INSTRUMENTS USING PHOTOMASK RETICLES

E.D. Hirleman*, P.G. Felton† and J. Kennedy‡

* Mechanical and Aerospace Engineering Dept., Arizona State University, Tempe, AZ, U.S.A.
† Dept. of Mechanical and Aerospace Engineering, Princeton University, Princeton, NJ, U.S.A.
‡ United Technologies Research Center, East Hartford, CT, U.S.A.

ABSTRACT

The results of the Interlaboratory Study (ILS) supporting the proposed ASTM Standard Test Method for Calibration Verification of Laser Diffraction Particle Sizing Instruments using Photomask Reticles are presented. The study was limited to the class of instruments known as laser diffraction particle sizing instruments which analyze the near-forward light scattering signature of ensembles of particles and measure properties of the particle size distribution. The standard materials used in the ILS, termed photomask reticles, consist of a quartz substrate with a 2-D photo-etched array of randomly-positioned circular disks of chrome thin film. The reticles represent an orthogonal projection of the cross-sections of the spherical particles in a specified 3-D reference population. The near-forward optical scattering properties of the ensemble of circular chrome disks approximate that of the corresponding reference particle population. Values for statistical parameters of the size distribution of the reference population can be directly related to measurements obtained using optical microscopy and are therefore traceable to the standard meter. The participants in the ILS represented thirteen laboratories using twenty-one different instruments of nine different models produced by four different instrument manufacturing companies. Each lab was asked to obtain four test results on two nominally identical photomask reticles for three different receiving lenses. ILS results on precision for the volume median diameter $D_{v0.5}$ for three lenses indicated a within-lab repeatability of about 1% (2.8σ) and a between-lab reproducibility of about 10% (2.8σ). Results for $D_{v0.1}$ and $D_{v0.9}$ showed greater variabilities by factors ranging approximately from 2 to 5. Bias between the mean of the ILS test results for all lenses and the corresponding image-analysis reference values was approximately -8% for $D_{v0.1}$, -6% for $D_{v0.5}$, and +6% for $D_{v0.9}$. The bias values were not statistically significant at 95% confidence in light of the observed reproducibility and the uncertainty limits on the reference values.

INTRODUCTION

Since the mid-1970's ASTM Subcommittee E29.04 has been addressing standards related to the measurement of liquid particle sizes. Since there exists a large variety of techniques and instruments for the sizing of particles and droplets in fluid suspension, work on the comparison of the results provided by these various instruments has been ongoing. The earliest interlaboratory comparisons of data on, for example, reference liquid sprays showed significant variability (greater than 100% differences in measured mean drop size diameters in some cases). More recent results from an interlaboratory study have also shown significant (albeit not as severe) discrepancies within and between the various instrument types as reported by Dodge [1].

In that context, it is important to isolate the factors causing the observed variability in order to better understand the results and the implications of the results. Two primary probable causes for the variability are: 1) difficulties associated with creating a reproducible liquid spray with the reference spray nozzle; and 2) fundamental differences in the sampling and performance characteristics of the various types of instruments used in the study. This ILS and the associated Standard minimize the possible influence of these two factors by: 1) using a stable artifact to simulate the liquid spray; and 2) considering only one type of liquid particle sizing instrument, i.e. those commonly known as laser diffraction instruments.

The reference material used in this ILS, a photomask reticle, represents a 2-D projection of a 3-D particle population. The reticle is comprised of about 10^4 randomly positioned circular discs of chrome thin film deposited on a transparent optical substrate. Further details on the reference material are discussed below. The potential usefulness of the photomask reticle in calibration verification was confirmed by an informal study of the

performance of laser diffraction instruments manufactured by Malvern Instruments Ltd. as reported by Hirleman and Dodge [2]. That study generated sufficient interest to pursue development of an ASTM Standard Test Method specifying the procedure and a quantitative assessment of the expected within-lab repeatability, between-lab reproducibility, and bias errors which would be associated with the use of photomask reticles as a reference standard for laser diffraction instruments. The ILS (round-robin) discussed in this paper provided the data on precision and bias errors included in the proposed Standard Test Method. A discussion of the ILS including reference material, participants, procedure, and results are presented below.

REFERENCE MATERIAL

The ideal calibration test samples for laser diffraction particle sizing instruments would be comprised of the actual particle or droplet material of interest in the actual environment of interest with a size distribution closely approximating that encountered in practice. Unfortunately the use of such calibration test samples is not currently feasible because multi-phase mixtures may undergo changes during a test and because actual samples (e.g. a spray) are not easily collected and stabilized for long periods of time. A photomask reticle is an artifact designed to simulate the optical-scattering properties of a 3-dimensional constellation of particles or droplets. A reticle depicts the orthogonal projection, onto a plane, of the geometric cross-sections of all particles in the simulated 3-dimensional particle constellation. In other words, a reticle is equivalent to the 2-D image of the 3-D particle field which would be obtained with an infinite-depth-of-field imaging system in the absence of diffraction. In addition to representing a 2-D rendering of a 3-D particle cloud, a photomask reticle also simulates the near-forward scattering properties of the same 3-D particle cloud. It is this latter property of a reticle which makes it useful as a standard for laser diffraction particle sizing instruments.

One problem with using a reticle to simulate a 3-D constellation of particles is that of nonuniqueness, i.e. since all information concerning the position of any particle along an axis parallel to the orthogonal projection is lost there are an infinite number of ways in which a given population of particles can be distributed in 3-D space and still produce the same 2-D projection. Unfortunately the near-forward scattering properties of the constellation of a given population of particles will also, in general, depend on the exact positions of the particles. As an example, consider two particles positioned such that they are intersected by the same line-of-sight (i.e. if the z-axis is parallel to the line of sight and normal to the reticle plane, then both particles encompass some common x and y coordinates). If these two particles were very close, say within a few diameters, then the particles would not scatter light independently as each would influence the scattering process of the other. In that case single-scattering models for isolated particles would not adequately predict the interactive or multiple scattering by these adjacent particles. From a geometric optics point-of-view, one particle would fall within the shadow of the other and the light scattering properties of the doublet would not simply be a superposition of the scattering signatures which would be produced by the two particles if they were isolated.

Now the shadow produced by a spherical particle illuminated by a planar light beam does not actually extend to infinity, but rather disappears some distance behind the particle due to diffraction. The length of the shadow is approximately D^2/λ where D is the particle diameter and λ is wavelength. After this distance the local disturbance to the planar incident light beam is dissipated, and in some sense diffraction effects work to reconstitute a wave which is again approximately planar. If a particle was encountered after this distance, even if it was located in the line-of-sight, the light scattering process would occur basically independently of the presence of the first particle. However, on a reticle the images of these two particles would be overlapped regardless of the interparticle spacing, and it is therefore clear that a photomask reticle will not be able to perfectly match the light scattering characteristics of all possible 3-D particle constellations which it may be representing.

The photomask reticles used in this ILS consist of a two-dimensional array of thin, opaque circular discs (termed particle artifacts) deposited on a transparent substrate. The substrates of the two samples used in this ILS, RR-50-3.0-0.08-102 serial numbers 246 and 247, were Schlieren-grade quartz 6.25 x 6.25 x 0.635 cm thick with a narrowband anti-reflection coating for operation at 0.6328 nm. The chrome particle artifacts were randomly positioned within an 8 mm diameter sample area centered in the 6.25 cm square substrate. The 23 primary particle sizes used in the discrete size distribution were approximately uniformly spaced in a geometric progression of diameters from 4 to 91 μm. The *reference population* represented by the reticle contained a total of 10,441 particles distributed over the 23 primary sizes and approximated a Rosin-Rammler particle size distribution of nominal parameters X = 50 μm and N = 3.0. This specific particle population, if distributed within a cylinder of 8 mm diameter and arbitrary length, would result in a projected area of covering nominally 8% of the cylinder cross-section. Hence the reticle, which represents a projection of the population, also has nominally 8% of the 8 mm diameter sample area covered with particle artifacts. Further details of the size distribution of the particle artifacts on the reticle are available elsewhere [5].

Since the photomask reticle is used as a reference material for particle sizing instruments based on near-forward light scattering, the degree to which the reticle can approximate the near-forward scattering properties of the reference particle population is crucial. In regimes where the diffraction approximation to light scattering is very accurate, i.e. for near-forward angles and particles large compared to the wavelength, the scattering signature produced by the projection of a particle (an opaque circular disc on the reticle) is very close to that produced by the

corresponding spherical particle *independent of the particle chemical composition.* Further, the properties of the reference particle population and of the near-forward scattering properties thereof can be estimated from an independent characterization (using optical microscopy) of the number, positions, and sizes of the discs on the reticle.

REFERENCE VALUES

A complete description of a particle population requires a large amount of information including the size, positions, and chemical composition of each of the constituents. In order to reduce this information to a manageable level, statistical parameters (e.g mean diameters and moments) of the particle size distribution are often used. Two important examples of statistical parameters, the volume median diameter $D_{v0.5}$ and the relative span $(D_{v0.9} - D_{v0.1})/D_{v0.5}$ as defined in E799-87, were used in this study. These representative parameters are quite important in many applications and are measured by most if not all laser diffraction instruments.

A standard test method can be used to characterize the performance of an instrument in either a relative (precision error) or absolute (bias error plus precision error) sense. For a relative measurement, it is the repeatability of the instrument which is under study and the stability of the reference material which must be confirmed. For absolute measurements, the true values (and associated uncertainties) of the representative diameters to be measured must also be known. The true values of volume parameters such as $D_{v0.x}$ for a photomask reticle are those that apply to the reference particle population for which the reticle is a simulation. However, since the reference particle population is an imaginary entity, we must estimate these true values using measurements on the photomask reticle combined with information on the design of the reticle. Estimates of these true values can be established using optical or scanning electron microscope measurements of the diameters of the particle artifacts on the reticle combined with design information and standard mathematical procedures (E799-87). The values so established are termed *image-analysis reference values* and are used as the accepted reference values in this study. The image-analysis reference values are fundamental in that they are defined independent of scattering or diffraction and can be traceable to a NIST length standard. The stability of $D_{v0.5}$, the relative span, and all other statistical parameters representative of the particle artifact size distribution for a reticle and the ability to produce nearly identical replicate copies contribute to the usefulness of a reticle as a reference material.

Several factors complicate the determination of image-analysis reference values for photomask reticles. First, there is a problem associated with the rather large number of particles (10,441) in the reference population. The most straightforward approach to determining image-analysis reference values involves measuring the size of each of the numerous particle artifacts on the reticle. However, this is a very large number of measurements if accuracy to some fraction of a micrometer is desired, and acceptable levels of uncertainty can be obtained with fewer measurements. A second complication involves the fact that some of the particles fall within the same line-of-sight (i.e. the projections of these particles on the reticle are overlapped). The image-analysis reference values of interest are parameters of the *volume* distribution of the reference particle population, and there is obviously some ambiguity associated with estimating the volume of a particle from its 2-D projection. If the particles are assumed to be spherical and not in the same line-of-sight the uncertainty is small, but overlapping images complicates the determination.

While a simulation of a "real" particle population would require a continuous distribution of particle sizes, the photomask reticles used in this ILS have multiple replications of only a limited number (23) of primary particle sizes. This facilitates basing calculated image-analysis reference values on measurements of the sizes of only a representative subset of the particle artifacts. The image-analysis reference values reported in Table II are based on measurements of the maximum chord (in the x-direction) of several hundred of the 10,441 possible particle projections. The sizes of particle artifact projections that were not measured were determined statistically assuming that the within-primary-size distribution (due, for example, to manufacturing variability) of the measured particle artifacts is representative of all artifacts of that primary size.

Overlapped (Noncircular) Particle Artifact Projections

The particle artifact images on the photomask reticles used in this study contain overlapped images. For this reason, some additional uncertainty is introduced in determining the image-analysis reference values. Four methods to account for these overlapped particles in determining reference values for the $D_{v0.x}$ are considered. The first is effectively the theoretical value, and the others attempt to account for the change in the apparent population caused by loss of information due to projecting the particles onto the reticle plane.

Reference Population. In the first approach the overlapped images are neglected, and properties of the originally-specified particle population used. In this approach, small particles which fall completely within the boundary of the projection of a larger particle and are still counted even though they would be invisible on the reticle. Overlapped particles are therefore treated as if the 3-D constellation of the population had very large interparticle spacings and all particles contribute independently to the light scattering signature with equal weighting. If the 3-D constellation were such that no portions of any particles fell within a common line-of-sight, the reference population values would be used.

Parsed analysis. In this approach partially-overlapped projections of spherical particles are counted (number basis) as a fraction of a particle. Only the smaller of an overlapping pair of circular discs is reduced to a fractional count, and the fraction is equal to the ratio of the nonoverlapped area (area not occluded) to the total area of a isolated circular projection of the same primary size. For the reticles used in the ILS, this results in a number distribution consisting of non-integer effective numbers of the 23 discrete primary sizes.

A parsed analysis would provide an exact representation of what a laser diffraction instrument would "see" if nonoverlapped portions of the smaller (daughter) particle artifacts scattered with the same *relative* angular scattering signature as an isolated (nonoverlapped) circular disc but with the total scattering reduced by an amount proportional to the fraction of the disc area which is contained in the overlapped region. This would also imply independent scattering by the mother (larger) particle and the non-occluded portion of the smaller particle of an overlapped pair.

Equivalent Volume of Planar Spherical-Particle Multiplet. This method assumes that: 1) the partial circles comprising a multiplet (overlapped) image are 2-D projections of intersecting spheres of the same diameter, and 2) the centers of the spheres of the multiplet are coplanar in a plane normal to the line-of-sight (e.g. in the plane of the reticle). A resulting volume-equivalent diameter, necessarily larger than that of any of the primary singlets, is thereby assigned to each overlapping multiplet. This volume-equivalent diameter D_{ve} is assigned such that the total apparent volume of the intersecting particles equals $\pi D_{ve}^3/6$.

Area-equivalent weighting. This method also assumes that overlapping particle projections are due to a multiplet particle made up of intersecting singlets. Regions where projections of two or more particle artifacts are overlapped are assumed to represent one spherical particle of the area-equivalent diameter D_{ae} such that the total projected area of the overlapped particles equals $\pi D_{ae}^2/4$. The equivalent volume of the multiplet then equals $\pi D_{ae}^3/6$. In other words, two or more interconnected, overlapped particles are assumed to scatter as one particle of the area-equivalent diameter.

Values for the various estimates of the reference values for the reticles used in the ILS are given in Table II. Size values based on the reference population are the smallest, and the area-equivalent analysis gives the largest values for $D_{V0.x}$. The differences between weighting approaches is greatest at large volume fractions where the D^3 effect has the greatest influence. The area-equivalent weighting adds considerable apparent volume to each overlapped multiplet due to the volume-of-rotation effect (the differences are not so great when considering $D_{A0.x}$). The planar spherical-particle multiplet approach to generate an apparent volume gives smaller volumes and thereby lower values for $D_{V0.x}$.

The four values in Table II are based on reasonable models and should certainly bound the "best" value. For that reason the values were averaged to arrive at the image-analysis reference values. The uncertainty limits in Table II contain two bias components: 1) bias in the measuring equipment used to size the particle artifacts, and 2) one standard deviation of the values obtained from the four methods. An estimate of the resulting overall bias limits was obtained by summing in quadrature the two components according to Abernathy and Thompson [7]. The bias limits were added [7] to 95% confidence precision error limits due to sizing a limited sample of the particle artifacts to arrive at the total uncertainty limits in Table II.

PARTICIPANTS

Participation in the ILS was open to any laboratory or individual with a laser diffraction particle sizing instrument available. The ILS was announced publicly in a monthly ASTM publication and in various technical forums where interested parties were involved. Eleven laboratories representing twenty-two instruments participated in the ILS which ran for a little over two years beginning in March 1988. A list of the instruments used by the participants along with the laboratory identifier codes used in this report are shown in Table I. A list of the individual participants, not identified with the particular instruments, can be found in the acknowledgements.

PROCEDURE

The overall procedure followed in the ILS was based on the ASTM Standard for Interlaboratory Studies, E691-87. A document specifying the protocol to be followed was sent to each participant along with the most recent version of the draft Standard Test Method for Calibration Verification of Laser Diffraction Particle Sizing Instruments using Photomask Reticles (Draft STM). The ILS Protocol specified: the preferred options in cases where the Draft STM allowed for user choices; the conditions of the tests to be run including the laser diffraction receiving lens focal lengths (63, 100, and 300 mm); the number of test results required for each sample/instrument configuration (4); the number of samples to be analyzed (2); and the data reporting forms. The Draft STM specified the procedure to be used in obtaining a single test result including: methods for presenting the photomask reticle to the instrument; methods for minimizing reflections; acquisition of background and signal measurements signatures; and finally the test results to be reported which included $D_{v0.1}$, $D_{v0.5}$, $D_{v0.9}$ and volume span as defined in ASTM E799-87. For further details the reader is referred to the Standard Test Method document which is available from ASTM [3]. An ASTM Research Report which provides further details on the procedure is available [4].

ILS RESULTS

The objective of an ILS is to provide data to support precision and bias statements for a Standard Test Method. The results of the ILS in terms of precision are summarized in Table III. The statistical parameters tabulated correspond to those specified in E691-87. Each row of results corresponds to the data for all instruments for all lens focal lengths and the indicated test results. The repeatability (within-lab) limits r indicate the range (95% confidence) of measured results which could be expected from measurements of a single reticle repeated over short time intervals by a single operator with a single instrument. The reproducibility (between-lab) limits R indicate the range (95% confidence) of measured results which could be expected from measurements on a single reticle in different labs using different instruments and possibly different focal lengths. The results indicate very good within-lab repeatability for $D_{V0.5}$ (<1%) as would be expected since this parameter is least sensitive to noise sources. The repeatability is somewhat worse for $D_{V0.1}$ and $D_{V0.9}$ which fall on the tails of the size distribution. The reproducibility limits are considerably larger as would be expected due to differences in instrument design.

The apparent bias of the test method is obtained by subtracting the mean of the series of test results obtained in the ILS from the reference value. The apparent bias terms for each of the 3 complete cases are shown in Table IV. The apparent bias errors are about -6% for $D_{V0.1}$ and $D_{V0.5}$ and +6% for $D_{V0.9}$. However, it should also be noted that these bias estimates are not significant (95% confidence) given the very large reproducibility limits in Table III.

Another method for visualizing results of interlaboratory studies on which two nominally identical samples are used is the Youden plot [6]. In this ILS two test samples were used, photomask reticles RR-50-3.0-0.08-102 serial number 246 and 247. Since the data obtained for the two nominally identical reticles were independent, plotting the measured results against each other as shown in Figs. 1 and 2 is of interest. Data spread along the 45 deg. line (lower left to upper right) in the plots indicates between-lab variability, and data spread normal to that line indicates within-lab variability. In standard ASTM terms, the spread *along* the 45-degree line is related to the *reproducibility* of the Test Method, and spread *normal* to the line is indicative of *repeatability*. Ideally, the data would fall in a circular pattern, indicating a good balance between instrument-to-instrument variability and the repeatability limits of the test method. The ellipticities of the data shown in Figs. 1 and 2 range from about 3.0 to 5.0 indicating relatively poor between-instrument reproducibility.

CONCLUSIONS

An ILS was successfully carried out to quantify the precision and bias errors associated with calibration verification of laser diffraction particle sizing instruments using photomask reticles. The within-lab repeatability was observed to be quite good, on the order of 1% (2.8σ) for $D_{V0.5}$, confirming the applicability of the test method for laser diffraction instrument performance verification on a relative basis. The between-lab, between-lens reproducibilities were about 10% for the best possible parameter, $D_{V0.5}$, and were about 20% and 35% for $D_{V0.1}$ and $D_{V0.9}$ respectively. These values are rather high given the levels of accuracy desired for some particle size measurement applications. However, the bewteen-lab reproducibility was somewhat better for certain instrument configurations, and ultimately the method might operate at several percent reproducibility.

ACKNOWLEDGEMENTS

The ILS was directed by a Task Group consisting of E29.04 members, who assisted in preparation of the Standard and monitoring results. The Task Group was comprised of Dr. Phil Felton, Princeton University, Dr. E. Dan Hirleman, Arizona State University, and Dr. Jan Kennedy, United Technology Research Center. Dr. Charles Martin, originally affiliated with Parker Hannifin Co. and presently with Goodyear Aerospace, was a member of the Task Group during the first year of the ILS. Mr. Lee Dodge, Southwest Research Institute, provided much-appreciated assistance during the study. The capable leadership of the Chairman of E29.04, Dr. Julian Tishkoff, has been instrumental to the success of the group and is acknowledged.

Finally, the author wishes to acknowledge the participants and sponsoring laboratories who participated in the ILS: Dr. T. Allen, E. I. Dupont, Mr. F. Biancaniello, National Institute of Standards and Technology, Mr. C. Fagan, Parker Hannifin Corp., Dr. P. Felton, Princeton University, Mr. R. Gourley, The Munhall Co., Dr. D. Holve, Insitec Inc., Mr. E. Hovenac, NASA Lewis Research Center, Mr. C. Hughes, Malvern Instruments USA, Dr. R. Ingebo, NASA Lewis Research Center, Dr. J. Kennedy, United Technologies Research Center, Mr. S. Kenney, Arizona State University, Mr. J. Melvin, Parker Hannifin Corp., Mr. S. Miller, University of Texas, Dr. S. Ridder, National Institute of Standards and Technology, Mr. J. Sager, Textron, Prof. P. Sojka, Purdue University, and Mr. R. Williams, Garret Auxiliary Power Division, Allied-Signal.

REFERENCES

1. Dodge, L., "Comparison of Performance of Drop-sizing Instruments", *Applied Optics*, V. 26, pp. 1328-1341, 1987.
2. Hirleman, E. D. and Dodge, L., "performance of Laser Diffraction Drop Size Analyzers", paper 85-64, *ICLASS 85 Conference Proceedings*, The Institute of Energy, London, 1985
3. Standard Test Method for Calibration Verification of Laser Diffraction Particle Sizing Instruments using Photomask Reticles, available from the American Society of Testing Materials, 1916 Race Street, Philadelphia, PA, 19103.
4. Report on the Interlaboratory Study supporting the Standard Test Method for Calibration Verification of Laser Diffraction Particle Sizing Instruments using Photomask Reticles, Research Report, available from the American Society of Testing Materials, 1916 Race Street, Philadelphia, PA, 19103.
5. Hirleman, E. D., Oechsle, V. and Chigier, N. A., "Response Characteristics of Laser Diffraction Particle Sizing Systems: Optical Sample Volume and Lens Effects," *Optical Engineering*, V. 23, pp. 610-619 (1984).
6. Youden, W. J., "Graphical Diagrams of Interlaboratory Test Results", *Journal of Industrial Quality Control*, V. 15, pp. 133-137, 1959.
7. Abernathy, R. B. and Thompson, J. W. "Measurement Uncertainty Handbook", Instrument Society of America, Research Triangle Park, NC, 1980.

Table I. Instruments used by Participants in the ILS

Lab ID	Diffraction Instrument Supplier	Instrument Model	Software Version
1	Sympatec[1]	Helos	-
2	Malvern	2600HSD	VF.5
3	Malvern	2600HSD	M5.4
4	Malvern	2600C	M3.1
5	Malvern	2600C	-
6	Malvern	3600Ec	M3.0
7	Malvern	2600C	6.10
8	Malvern	3600E	M5.4
9	Malvern	2600	VF.3
10	Malvern[3]	2600HSD	In-house[4]
11	Malvern	Mastersizer	-
12	Malvern	3600	M3.0
13	Insitec	EPCS-P	In-house[5]
14	Sympatec[2]	Helos	-
15	Malvern	2600HSD	M5.4
16	Malvern	3600E	M5.4
17	Malvern	2600	M3.1
18	Malvern	2600HSD	VF.6
19	Insitec[6]	EPCS-P	1.1
20	Malvern	3600E	M5.4
21	Munhall Co.	PSA-32	1.90

[1] The Sympatec Helos instrument referenced here used focal lengths of 100 and 200mm. The 200 mm data obtained here were grouped with the 300mm data from other instruments (see note 2 below).

[2] The Sympatec Helos instrument referenced here used a focal length of 500 mm, but the data were grouped for analysis along with the 300 mm data (see note 1 above).

[3] Two test results taken with an in-house diffraction instrument are included with data from this lab. For the other test results the scattering signature was obtained with a Malvern 2600HSD and in-house inversion software was used to obtain the reported size distribution.

[4] In-house means the instrument or software was developed for internal use by the laboratory and is not commercially available.

[5] The data from this lab were obtained using the Insitec EPCS-P detector but with in-house receiving optics and inversion software.

[6] The Insitec EPCS-P instrument used a receiving lens of 58 mm focal length, but the data were grouped with the 63 mm results for analysis.

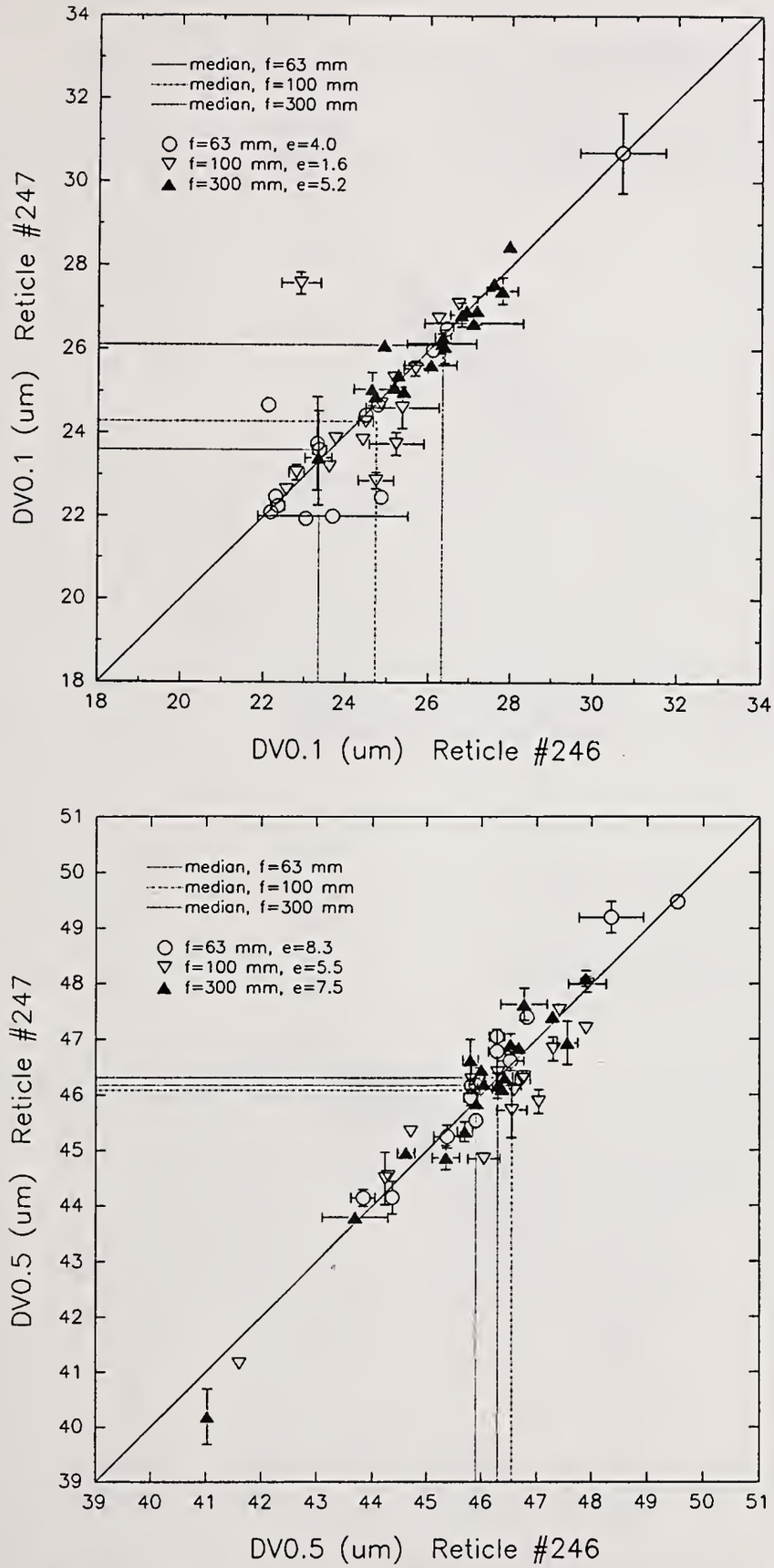

Figure 1. Plot of the final ILS test results for $D_{v0.1}$ and $D_{v0.5}$. The symbols indicate the mean of the data for the four repeated measurements for each reticle/lens combination in each lab. The error bars indicate one standard deviation of these four test results. The dashed lines indicate the median of the data for the three different lenses, and the ellipticity of the data for each lens are shown in the legend.

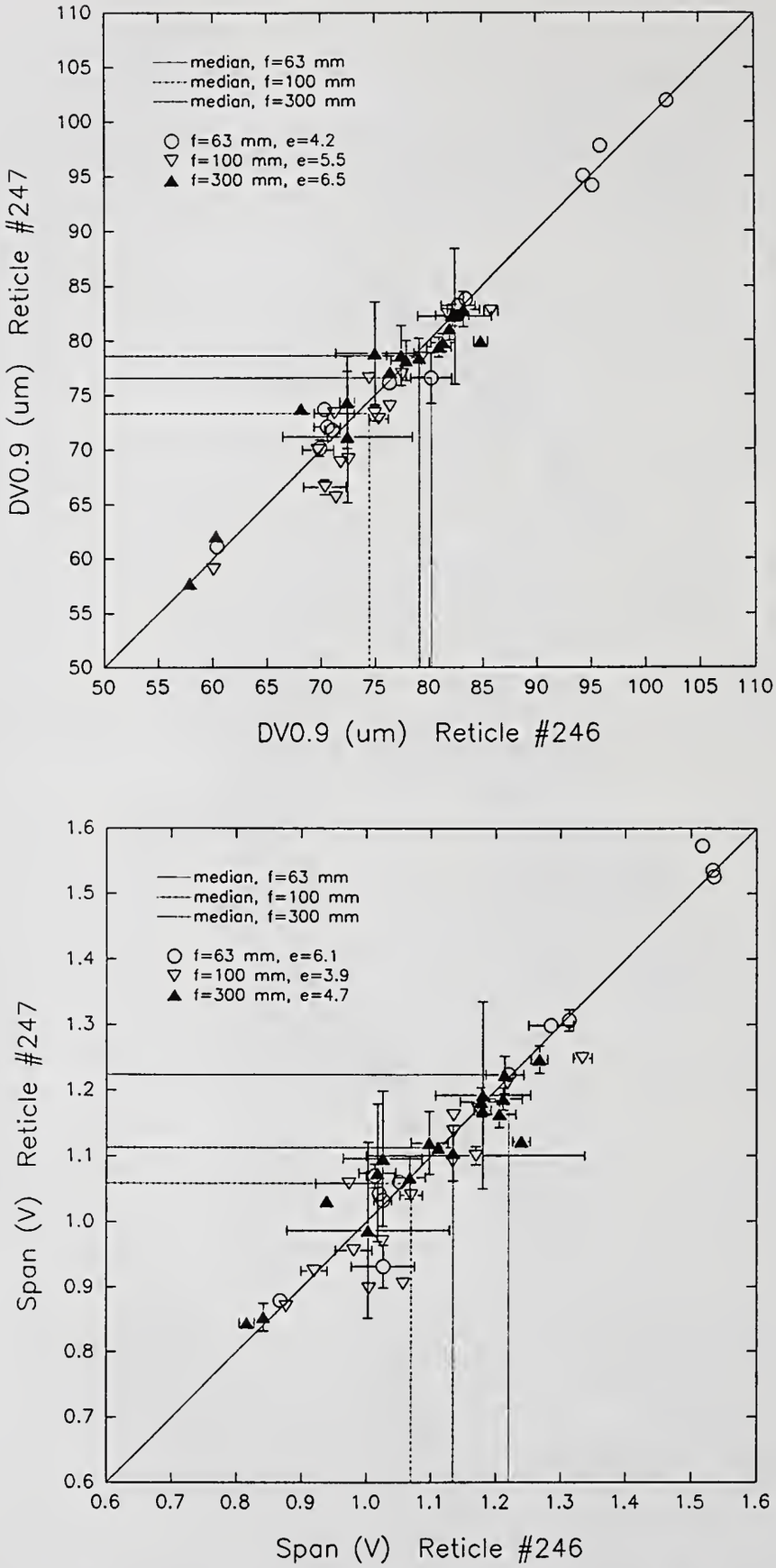

Figure 2. Plot of the final ILS test results for $D_{v0.9}$ and relative span (volume basis). The symbols indicate the mean of the data for the four repeated measurements for each reticle/lens combination in each lab. The error bars indicate one standard deviation of these four test results. The dashed lines indicate the median of the data for the three different lenses, and the ellipticity of the data for each lens are shown in the legend.

Table II. Image-analysis Reference Value for Reticles used in the ILS.

Test Result	Reticle Serial #	Reference Population Value (μm)	Parsed Number Value (μm)	Volume Equiv. Sphere Multiplet Value (μm)	Area Equivalent Value (μm)	Image-analysis Reference Value[1] (μm)
$D_{V0.1}$	246	25.74	26.16	26.39	29.63	27.0 ± 2.3
$D_{V0.1}$	247	25.82	26.24	26.46	29.60	27.0 ± 2.4
$D_{V0.5}$	246	47.54	47.95	49.80	51.38	49.2 ± 2.3
$D_{V0.5}$	247	47.26	47.66	49.41	51.26	48.9 ± 2.7
$D_{V0.9}$	246	69.15	69.40	72.78	78.52	72.5 ± 5.1
$D_{V0.9}$	247	69.33	69.57	72.77	78.75	72.6 ± 6.3

[1]The image-analysis reference value is taken as the mean of the four estimates. The uncertainty limits for the image-analysis reference values represent 95% confidence intervals based on estimates of precision and bias error in assigning the values.

Table III. Precision Statistics for the Test Method (all focal lengths grouped).

Test Result	Reticle Serial #	Mean of ILS Results X (μm)	Within-lab Repeatability Limit r[1] (μm)	Between-lab Reproducibility Limit R[1] (μm)	Rel. Within-lab Repeatability Limit r/X (%)	Rel. Between-lab Reproducibility Limit R/X (%)
$D_{V0.1}$	246	25.09	± 1.25	± 5.18	± 5.0	± 20.7
$D_{V0.1}$	247	25.04	± 0.91	± 5.37	± 3.7	± 21.5
$D_{V0.5}$	246	46.05	± 0.56	± 4.26	± 1.2	± 9.3
$D_{V0.5}$	247	46.05	± 0.59	± 4.57	± 1.3	± 10.0
$D_{V0.9}$	246	77.47	± 3.95	± 26.50	± 5.1	± 34.2
$D_{V0.9}$	247	77.33	± 6.80	± 29.18	± 8.8	± 37.7

[1]The precision indices r and R, defined in E691-87, are 2.83 times the repeatability (within-lab) and reproducibility (between-lab) standard deviations, respectively.

Table IV. Bias of the Test Method (all focal lengths grouped).

		ILS Results		Image-analysis		Bias Estimates	
Test Result	Reticle Serial #	Mean Value (μm)	Reproducibility Limit R (μm)	Reference Value (μm)	Uncertainty Limits[1] (μm)	Measured Bias (μm)	Statistically Significant?
$D_{V0.1}$	246	25.09	± 5.18	27.0	± 2.3	-1.9	No
$D_{V0.1}$	247	25.04	± 5.37	27.0	± 2.4	-2.0	No
$D_{V0.5}$	246	46.05	± 4.26	49.2	± 2.3	-3.1	No
$D_{V0.5}$	247	46.04	± 4.57	48.9	± 2.7	-2.8	No
$D_{V0.9}$	246	77.47	± 26.50	72.5	± 5.1	5.0	No
$D_{V0.9}$	247	77.33	± 29.18	72.6	± 6.3	4.7	No

[1]The uncertainty limits for the image-analysis reference values represent 95% confidence intervals based on estimates of precision and bias error in assigning the values. The statistical significance indication also is for 95% confidence.

CORRECTING MALVERN PARTICLE SIZE MEASUREMENTS FOR PHASE DISTORTION

R.A. Pietsch, P.E. Sojka and G.B. King

Thermal Sciences and Propulsion Center
School of Mechanical Engineering
Purdue University
West Lafayette, IN, U.S.A.

1 ABSTRACT

The two effects of phase distortion on particle size measurements made with a Malvern Spray Analyzer are identified as beam spread and a shift of the Airy pattern extrema to higher spatial frequencies. Beam spread is shown to be present regardless of the laser beam coherence length (l_c), while the Airy pattern shift occurs only when the size of the particle being sampled exceeds l_c. A correction scheme that removes the effects of phase distortion when possible is outlined, and then evaluated by comparing phase distorted particle size information with its undistorted counterpart. The enhanced agreement indicates the proposed technique successfully removes the effects of phase distortion when possible. Finally, guidelines are provided for determining when phase distortion is present.

2 INTRODUCTION

The quality of atomization cannot be ignored when considering the performance of any liquid fueled combustion system. Information about both the mean particle size and distribution of particle sizes is important to the combustion engineer in his search for more efficient combustor designs and alternative fuels. A popular optical method of collecting this size information utilizes Fraunhofer diffraction of a laser beam as it passes through a spray. Currently, measurement systems based on Fraunhofer diffraction are commercially available; the Malvern Spray Analyzer is one such system. Unfortunately, recent studies of particle sizing in high temperature turbulent environments have shown that this type of instrument, in its current form, is incapable of accurately measuring the scattered light profile and yielding the desired particle size data [1,2]. The inaccuracies noted in References 1 and 2 result from optical perturbations present in the system being studied.

The primary perturbing optical effects associated with laser beam propagation in a high temperature turbulent environment are known as beam wander and phase distortion. Beam wander occurs when the laser beam encounters an index of refraction gradient and is displaced, or steered, from its normal path of propagation. Phase distortion occurs when different points on the same laser beam wavefront vary in phase after passing through an index of refraction gradient.

The effects of beam wander were studied in detail by Miles et al [2] and a technique was developed to successfully compensate for this phenomenon. Miles et al also suggested that any errors remaining in the particle distribution measurements after correcting for beam wander were due to phase distortion. Support for their hypothesis was provided by performing a Young's double slit experiment at various temperatures to measure Michelson's visibility, arguing that Michelson's visibility was equivalent to the complex degree of coherence between two points on the laser beam, and then noting that the observed decrease in coherence length was indicative of an increase in the level of phase distortion.

Leader [3] studied phase distortion, concentrating on how it affects laser beam propagation through weakly and strongly turbulent atmospheres. He discovered that as the turbulence

became stronger, phase distortion's effects were dominant over those of beam wander. Leader also noted that as phase distortion increased, the ability to focus the beam to a given spot size decreased. Additionally, the unfocused beam's diameter, known as the beam spread, was seen to increase log-normally as phase distortion increased.

This increase in beam diameter is an important issue since some of the incident beam's energy will emerge from a spray as unscattered light. In many diffraction based instruments, this unscattered energy is removed from the particle diffraction profile by measuring the background light intensity incident on the photodiode. Leader's work therefor suggests that a background light intensity reading for a phase distorted beam will have a greater intensity at lower spatial frequencies than for an undistorted beam.

Two conclusions can be drawn from the work of Miles et al and Leader. First, the effects of phase distortion become more pronounced as the turbulence within a system increases. Second, since the amount of beam spread, and thus additional background intensity, is dependent on the flow conditions, a separate background intensity reading should be taken at each temperature or flow velocity being investigated in order to eliminate this effect of phase distortion.

Two issues, however, remain to be addressed. First, how is a researcher to know when the effects of phase distortion are important, and second, are there any further effects of phase distortion that must be eliminated or compensated for.

The goal of the this work then is twofold: to develop a technique that eliminates the errors resulting from phase distortion whenever possible and to outline a procedure that will aid users in determining when the effects of phase distortion are present. The next section provides a summary of the theory needed to accomplish these objectives.

3 THEORY

In order to develop a correction scheme to remove the effects of phase distortion on optical particle sizing with the Malvern instrument, it is first necessary to determine if phase distortion is present and, if so, to describe its impact. Phase distortion is present if the medium of interest reduces the spatial coherence length of a laser beam passing through it. Its effect on Malvern particle size measurements depends on the relative size of the perturbed laser beam's spatial coherence length and the diameter of the largest particle to be sampled.

A level of phase distortion such that the spatial coherence length of a beam passing through the medium is less than the diameter of the largest particle in a spray indicates that all particles are not illuminated coherently. Fraunhofer diffraction by apertures illuminated using partially incoherent light was studied by Shore et al [4] who showed that a gradual loss in the intensity contrast of the diffraction signature occurs as the coherence length decreases. Furthermore, when the coherence length approaches zero, the diffraction maxima and minima shift to higher spatial frequencies. This indicates that more light would be incident on the Malvern detector array at larger radii, thus skewing the particle size distribution to smaller diameters.

Phase distortion on this level can be detected by employing a calibrated aperture. Specifically, a pinhole may be introduced into the phase distorting media and its intensity profile obtained using the Malvern receiver. If the diffraction maxima and minima of the resultant Airy pattern are shifted to higher spatial frequencies, the particle size measurements cannot be corrected. Consequently, a series of calibrated apertures is inserted into the flow with the smallest pinhole exhibiting no shift in its diffraction extrema, for a given flow condition, indicating the largest particle that can be accurately sized. A correction scheme was developed for this case.

When no shift in the position of the diffraction extrema occurs for any particle, the complex degree of coherence, γ, is used to describe the optical perturbations. By examining the scattering geometry illustrated in Figure 1, and following the notation from Hecht and Zajac [5], the complex degree of coherence may be derived in the following fashion.

Consider two identical apertures or particles as the source of the diffracted radiation. If they are located at a distant plane along the path of propagation, the electromagnetic fields can be combined as:

$$E_P(t) = \bar{K}_1 E_1(t - t_1) + \bar{K}_2 E_2(t - t_2) \qquad (1)$$

where $t_1 = r_1/c$ and $t_2 = r_2/c$. The $\bar{K}$ factors depend on the size and location of the scatterers relative to the point P and also account for absorption, diffraction and other physical effects. Defining $\tau = t_2 - t_1$ allows the time origin to be shifted and the $\bar{K}$ factors to be removed with the result that the mutual coherence function can be defined as

$$\Gamma_{12}(\tau) = < E_1(\tau + t) E_2^*(t) > \tag{2}$$

Normalizing the mutual coherence function by the magnitude of the two sources gives the complex degree of coherence

$$\gamma_{12}(\tau) = \frac{< E_1(\tau + t) E_2^*(t) >}{(< |E_1|^2 >< |E_2|^2 >)^{1/2}} \tag{3}$$

The magnitude of $\gamma_{12}(t)$ is between 0 and 1. If it is equal to unity the field at P is the result of two coherent waves out of phase by some quantifiable amount while if the magnitude is zero then the two waves are said to be incoherent. Any value of $\gamma_{12}(t)$ between these two extremes defines partial coherence.

Thompson [6] studied diffraction and interference from multiple apertures and arrays by looking at the generalized interference law:

$$I_R = \sum_{n=1}^{N} \sum_{m=1}^{N} (I_n I_m)^{1/2} |\gamma_{nm}(0)| \cos(\beta_{nm}(0) + \delta_{nm}) \tag{4}$$

where I_n and I_m are the intensities produced by each beam individually, $|\gamma_{nm}|$ is the modulus of the complex degree of coherence between apertures n and m, and

$$\beta_{nm}(\Delta) = 2\pi\bar{\nu}\Delta + arg(\gamma_{nm}(\Delta)) \tag{5}$$

$$\delta_{nm} = (2\pi/\bar{\lambda})(r_m - r_n) \tag{6}$$

Here r_m and r_n are the path lengths from the two source points to the observation point, Δ is the path difference divided by the speed of light, $\bar{\nu}$ is the mean frequency, and $\bar{\lambda}$ is the mean wavelength of the laser beam. It is important to note that

$$|\gamma_{nm}(0)| = 1, \qquad n = m$$

$$|\gamma_{nm}(0)| = |\gamma_{mn}(0)|$$

For a circular source illuminating a regular array of circular apertures, only nearest neighbor apertures along the array directions can be arranged to be incoherent with respect to each other. That is, for a regular array, $\gamma_{n,n+1}(0) = 0$ is a possible occurrence. However, because the spacing of the Airy ring minima is not constant, some degree of coherence between an aperture and its non-nearest neighbors will always exist. This implies that unless the coherence length is much less than the spacing of the array, no difference will be seen in the resulting diffraction pattern.

This observation is important to the operation of particle sizing instruments based on forward light scattering since it suggests that if phase distortion produces a beam whose coherence length is greater than the diameter of the largest particle to be sampled then the shape of the diffraction profile will be the same as for the unperturbed case.

Thompson also investigated diffraction from irregular arrays using lycopodium powder. Of specific interest were the diffraction profiles that resulted from using illumination whose coherence length ranged from several thousand to only a few particle diameters. The results showed no loss in fringe contrast with a drop in coherence length, as perhaps might have been predicted from the work of Shore et al. The only difference was a "smoothing" of the intensity profiles as the coherence length decreased since the values of γ_{nm} contribute less to the sum in Eqn (4).

In summary, the level of phase distortion can be determined by sampling the Airy patterns produced by a series of calibrated apertures. The minimum size aperture yielding a pattern not

shifted to higher spatial frequencies must be greater than the largest particle to be sized or the measurements cannot be corrected. If this condition holds, the work of Thompson shows that the phase distorted diffraction profile will not differ from the undistorted profile. Furthermore, under these conditions the only effect of phase distortion that need concern the user of a Fraunhofer diffraction based particle sizing instrument is beam spread. Fortunately, this spread, which will appear as undiffracted light in the energy profile, can be removed by acquiring the instrument's background signal under the conditions that lead to phase distortion and then processing the particle scattering data using the standard software. A demonstration of this technique is provided in Section 5.

4 EXPERIMENTAL APPARATUS

A Malvern 2600HSD diffraction based particle sizing instrument was employed in this investigation since the Malvern serves as a sort of default standard in diffraction based systems and Malverns have been used extensively in industry and research applications by many individuals and groups. A high temperature flow tunnel was used to generate the desired optical perturbations. It has been described in detail by Miles [7].

In order to isolate the effects of phase distortion on the particle diffraction profile, it was first necessary to remove the effects of beam wander. This was accomplished by utilizing the conditional sampling hardware developed by Miles et al [2]. This hardware was added to the optical train developed to study phase distortion and is denoted by the extension ".BW" in Figure 2. It includes a 4% reflection beam splitter, a focusing lens (250 mm focal length), a four-quadrant photodetector, and electronic circuitry used to compare the laser beam's wandered position to that of the ambient situation. If the wandered beam's position is within an acceptable window, the conditional circuitry triggers the Malvern receiver to collect the diffraction profile information.

In order to ensure that a repeatable particle size distribution could be obtained throughout the course of the experiments, a standard reticle was employed [8]. It had best-fit Rosin-Rammler parameters of N = 3.20, $\overline{X}$ = 52.8 μm, and SMD (Sauter mean diameter) = 40.27 μm.

Several issues had to be considered when observing the effects of phase distortion on the unscattered laser beam, on the diffraction pattern from the reticle, and on the diffraction pattern from the calibrated apertures. The ability to reproduce the same diffraction pattern from either a calibrated aperture or the reticle was limited by the ability to reproduce their exact physical location within the optical train. The repeatability of such a task was determined through trial and error to be low, regardless of the positioning method employed. In order to observe each of the above profiles individually, without having to reposition the reticle or calibrated aperture, the experimental apparatus shown in Figure 2 was utilized.

The optical hardware illustrated in Figure 2 consists of a 10 mW HeNe laser whose beam is spatially filtered and collimated to a diameter of 4.5 mm, plus two Mach-Zehnder interferometers in series that sample and redirect the laser beam and the diffraction profiles resulting from the reticle and calibrated aperture. As shown in Figure 2, the calibration aperture and reticle are permanently positioned in separate arms of the interferometers, thus guaranteeing that their diffraction profiles are reproducible. The interferometer arrangement also allows for observation of the effects of phase distortion on the undiffracted laser beam by adjusting the iris diaphragms to block off both the reticle and aperture. As a result, the user can observe each of the relevant intensity profiles individually without having to reposition the reticle or calibrated aperture between runs.

Experimental data obtained using the apparatus presented in Figure 2 are introduced in the next section and indicate the effects of phase distortion on the standard instrument's performance, plus the enhanced agreement that results from correcting particle size data for phase distortion.

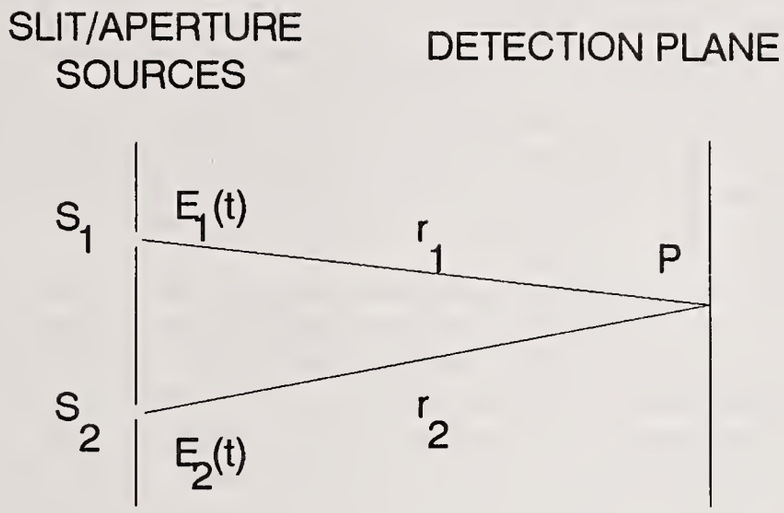

Figure 1. Scattering geometry for two identical apertures.

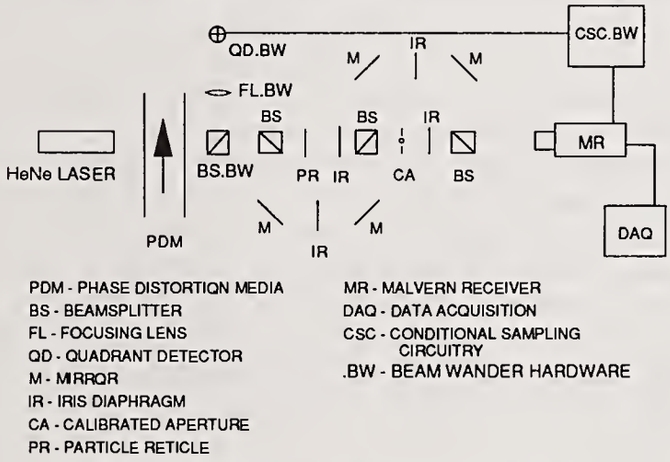

Figure 2. Experimental apparatus.

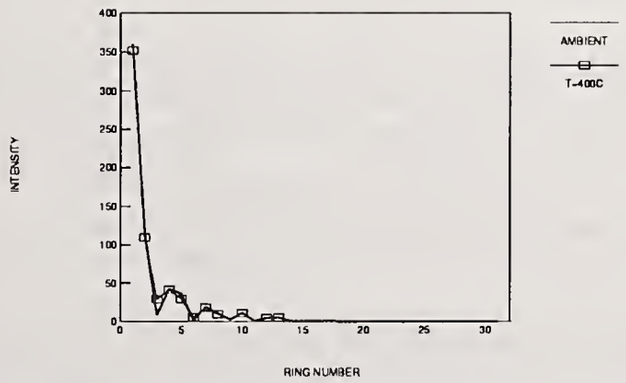

Figure 3. Fraunhofer diffraction profiles for a 600 μm diameter pinhole.

5 RESULTS

Data acquisition commenced by placing the calibrated aperture and reticle in their respective interferometer arms, centering the Malvern photodiode array on the laser beam, and aligning the beam wander conditional sampling hardware. Three sets of ambient background, calibrated aperture diffraction profile, and particle diffraction profile data were then collected by shutting the appropriate iris diaphragms. At this point, the blower supplying air to the test section was started and an air velocity of 25 m/s was established in the test section. The air temperature was adjusted to 200, 400 and then 600 C with one background profile, three calibrated aperture diffraction profiles, and three particle diffraction profiles obtained at each temperature. The entire process was performed once a day for three days for a total of nine data points at ambient and each of the elevated temperatures.

As mentioned previously, the calibration aperture serves as a users' guide to recognize when phase distortion is present and indicates the largest particle diameter that can be sized without phase distortion affecting the light intensity profile. Sample intensity profiles for a phase distorted and non-phase distorted aperture (circular pinhole, d = 600 μm) are shown in Figure 3. The agreement between the two profiles indicates no shift in the maxima or minima and therefor a coherence length greater than 600 μm. Consequently, all particles up to the 564 μm limit measurable using the Malvern's 300 mm focal length lens will be coherently illuminated and the only effect that need be considered is beam spread.

A sample phase distorted diffraction profile from the reticle appears in Figure 4. Compared to a non-phase distorted profile, the perturbed profile reveals large intensity variations at lower spatial frequencies, i.e. in the innermost photodiode rings, due to beam spread. However, at larger spatial frequencies no intensity variation is observable supporting the conclusion that the spatial coherence length was larger than the largest particle in the distribution. Figure 5 shows the background readings corresponding to each of the profiles in Figure 4. By subtracting the background taken under phase distorting conditions from the phase distorted particle profile, a corrected diffraction profile is generated and used to determine the particle size distribution. An example profile appears in Figure 6; comparing it to the light intensity profile of Figure 4 clearly demonstrates the improvement achieved when using the correction procedure outlined above. This improvement is also apparent from the Malvern calculated Rosin-Rammler size distribution parameters for the uncorrected and corrected profiles, as shown in Tables 1 and 2. Uncertainties in these tables are reported as one standard deviation. Note that the discrepancies between the ambient and 200, 400 and 600 C corrected values for $\overline{X}$, N and SMD are within the sum of their standard deviations, with the exception of the 600 C value for N. In contrast, the discrepancies between the ambient and uncorrected 400 and 600 C values for $\overline{X}$, N and SMD are at best one standard deviation and most often greater than 2σ.

6 SUMMARY

The two effects of phase distortion on the diffraction pattern produced by a particle, beam spread and a shift of the Airy pattern extrema to higher spatial frequencies, have been noted. Beam spread is present regardless of the laser beam coherence length (l_c), while the Airy pattern shift occurs only when the size of the particle being sampled exceeds l_c. A procedure to determine the coherence length under phase distorting conditions was described and a correction scheme was developed to remove the effects of phase distortion when all particles have diameters less than l_c.

The correction scheme is straightforward, requiring only that the Malvern's background signal be acquired under the same phase distorting conditions as the particle diffraction profile. The data may then be processed using the standard Malvern software.

The correction technique was evaluated by comparing phase distorted diffraction profiles and background intensities with their undistorted counterparts that were collected under identical flow conditions. Results showed that phase distorted intensity profiles yielded particle distribution parameters that were as much as 9% in error. Parameters calculated from corrected intensity

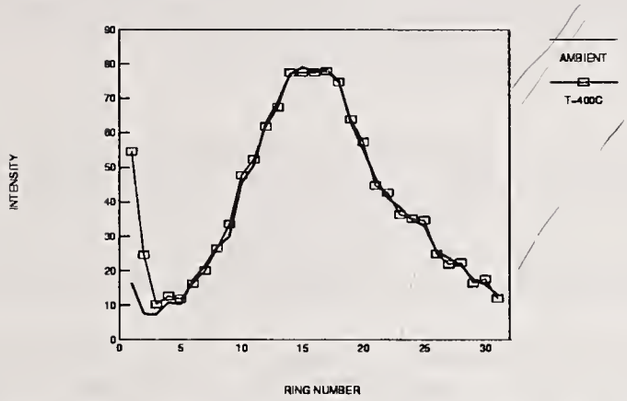

Figure 4. Fraunhofer diffraction profiles for the reticle.

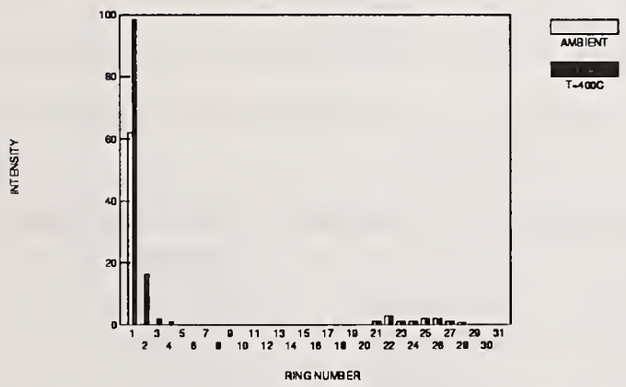

Figure 5. Ambient and high temperature backgrounds.

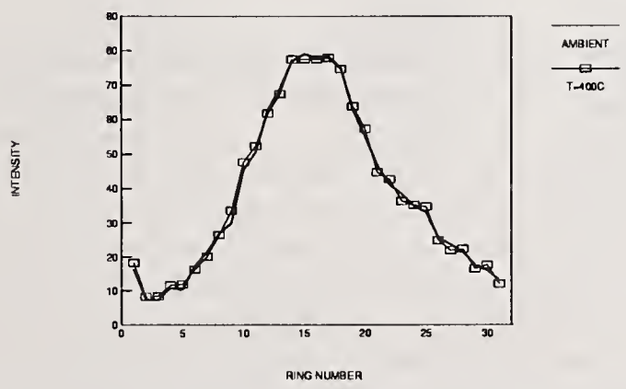

Figure 6. Fraunhofer diffraction profile corrected for phase distortion.

profiles, however, were within 2 % of those obtained under ambient conditions. This indicates the proposed technique successfully removes the effects of phase distortion when possible.

We thank E.D. Hirleman (Arizona State University) for several helpful discussions and B.H. Miles (US Army Waterways Experiment Station) for providing comments on an early version of this manuscript.

REFERENCES

1. Roesler, T.C., Lefebvre, A.H. and Sojka, P.E., "Fuel Atomization at High Ambient Temperatures," Central States Section/Combustion Institute paper 86-6D1, NASA-LeRC, Cleveland, OH (1986).
2. Miles, B.H., Sojka, P.E. and King, G.B., "Malvern Particle Size Measurements in Media with Time Varying Index of Refraction Gradients," Applied Optics, Vol. 29, No. 31, pp. 4563-4573 (1990).
3. Leader, J.C., "Beam Properties of Partially Coherent Curved Beam Waves in the Turbulent Atmosphere," Journal Optical Society America Vol. 70, pp. 682-688 (1980).
4. Shore, A., Thompson, B.J. and Whitney, R.E., "Diffraction by Apertures Illuminated with Partially Coherent Light," Journal Optical Society America, Vol. 56, 733 (1966).
5. Hecht, E. and Zajac, A., *Optics*, Addison-Wesley, Reading MA, (1979).
6. Thompson, B.J., "Multiple-Beam Interference with Partially Coherent Light," Journal Optical Society America, Vol. 56, pp. 1157-1161 (1966).
7. Miles, B.H., "Optical Particle Sizing in a High Temperature Environment," M.S. Thesis, Purdue University (1988).
8. Hirleman, E.D., "On Line Calibration Techniques for Laser Diffraction Particle Sizing Instruments," ASME Paper No. 83-GT-232.

Table I. Particle Size Distribution Parameters for Uncorrected Data

Temperature, C	$\overline{X}$, μm	N	SMD, μm
20	52.34±0.18	3.40±0.03	41.97±0.04
200	52.86±0.07	3.39±0.00	42.33±0.57
400	54.99±0.73	3.24±0.06	43.47±0.33
600	56.25±0.32	3.17±0.17	44.15±0.48

Table II. Particle Size Distribution Parameters for Corrected Data

Temperature, C	$\overline{X}$, μm	N	SMD, μm
20	52.34±0.18	3.40±0.03	41.97±0.04
200	52.45±0.00	3.39±0.00	42.00±0.00
400	52.03±0.70	3.35±0.07	41.53±0.49
600	51.85±1.05	3.55±0.08	42.03±0.61

A COAXIAL-BEAM DROP SIZING INSTRUMENT FOR DENSE SPRAYS

W.M. Grissom

Physics Department
Morehouse College
Atlanta, GA, U.S.A.

ABSTRACT

A low-cost instrument has been developed to measure drop size and speed in dense sprays. The instrument uses two coaxial laser beams of different colors. The smaller locater beam defines the center of the larger main beam and triggers a measurement only when a drop passes through the center of the main beam. Light scattered perpendicular to the beam is focused through a double slit imaging system which avoids partial obscuration of the image. A vibrating glass tube produces a uniform drop stream for calibration. A simple "scattering tomography" analysis accounts for beam attenuation. Fluctuations in beam intensity are also considered. Data in a spray nozzle are reported. Both the diameter and speed histograms are best fit by a log-normal function.

INTRODUCTION

A review of most drop sizing techniques up to 1978 is given by Azzopardi [1]. Since then the Polarization Ratio [2,3], Phase Doppler [4], and Pulse Intensity [5-7] techniques have been developed. The present instrument is of the latter type.

The Pulse Intensity techniques determine the drop size by measuring the scattered pulse as a drop crosses a laser beam. This gives a robust signal with simple optics. The main problem is that the scattered intensity depends upon the path the drop follows across the beam. Since the laser beam normally has a Gaussian intensity distribution, a drop passing far from the beam center gives a smaller pulse height than if it passed through the center. This problem is termed "Gaussian ambiguity".

An obvious solution to the Gaussian ambiguity problem is to generate a beam with a uniform ("tophat") profile, but this has proven difficult [8]. Instead, several researchers [5,6] developed deconvolution algorithms to analytically correct for the ambiguity. Another obvious solution is to accept a Gaussian beam, but define the center of the beam such that measurements are triggered only when a drop passes through the center.

Hess [7] used a laser velocimeter to define the beam center. Since the velocimeter signal is weak, forward scattered light was collected by viewing the beam at an oblique angle, greatly increasing the probe volume size. Since the velocimeter probe volume must be about 4 times wider than the drop to give a good visibility signal and the main beam must be about 5 times wider than the velocimeter probe volume, the minimum average drop spacing is about 20 drop diameters, which is fairly sparse.

EXPERIMENTAL APPARATUS

The optical arrangement is shown in Figure 1. A small yellow beam (He-Ne, 594 nm) defines the center of a coaxial red beam (He-Ne, 633 nm). The red main beam is about 5 times larger than the yellow locater beam at the probe volume. A similar coaxial arrangement was reported by Wang and Hencken [9]. Light scattered at 90° is imaged onto the main slit. The slit width, together with the beam diameter defines the size of the probe volume. The two colors are separated by an edge filter. The red light, from the main beam, is reflected into a photomultiplier. The yellow light, from the locater beam, is re-imaged onto the "locater slit".

The locater slit views only the center of the main slit, ignoring drops which are partially obscured by the edges of the main slit. The locater photomultiplier triggers a measurement only when a drop passes through the center of the main beam and is centered in the view of the main slit. Umhauer [10] reported a similar two slit imaging system, with the slits in parallel.

A locater pulse triggers storage of a main photomultiplier pulse with a Rapid Systems R2000 digital O-scope. The digitized pulse is fit to a Gaussian curve by a logarithmic transform to a parabola and linear regression. About 50 samples per pulse are needed to average over ripples on the pulse. The pulse peak determines the drop diameter and the width determines the speed transverse to the beam. Checks on the fitting error help eliminate drop coincidences in the probe volume. Since both size and speed are obtained, either a flux or spatial drop size distribution can be generated and speed-size correlations can be obtained.

Since the pulse amplitude is approximately proportional to the square of the drop diameter, care must be taken to provide a wide dynamic range. Previous researchers used logarithmic amplifiers. Instead, the programmable gain feature of the digitizer is used. Measurements are made at three gain ranges. The processing rate is usually slower than the data rate. To avoid bias against the busier ranges, a set of pulses is digitized and the elapsed time recorded. The pulses are then processed and the histogram bins incremented inverse to the digitization time.

The transmitted beam is focused onto a pinhole in front of a phototube. A 4 axis positioning system controlled by a Precision Micro Control DCX-8 board allows translations in the scattering plane and rotations about the spray and collection axes. A vacuum collects the spray drops, allowing operation with the spray pointing upward.

CALIBRATION

A glass pipet is drawn to a small diameter and cleaved. A laminar jet of liquid is forced from the pipet while vibrated by a speaker. At certain frequencies the jet breaks into a stream of uniform drops. Sakai [12] gave a detailed report on the phenomenon. A time trace is shown in Figure 2. The drops almost overlap in the main beam. The ripples in the main pulses are due to noise in the beam profile. Reducing the beam diameter

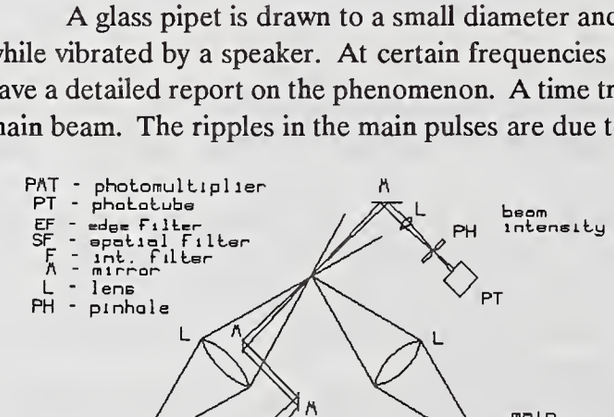

Fig. 1 Optical arrangement

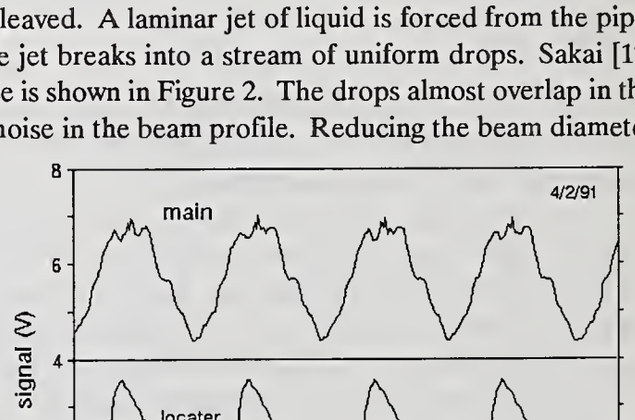

Fig. 2 Photomultiplier signals with uniform 230 umD drops, 700 umD main beam, 200 umD locater beam

yields smoother pulses. The spatial filter partially obscures the main beam, resulting in steeper edges than a true Gaussian pulse, which is advantageous in decreasing overlap of adjacent pulses.

Knowing the frequency and flow rate, the drop diameter is easily calculated. The calculated size has been verified using a microscope, with stroboscopic illumination. Photographing the drop stream and measuring the drop spacing allows calculation of the speed. Comparing this with the e^{-2} pulse width (temporal) allows calculation of the e^{-2} beam width, which is the calibration constant for speed.

Since the drops follow a very defined path through the beam, the drop stream must be scanned back and forth across the beam to test the instrument's resolution. The resulting histograms are shown in Figure 3. Equally narrow histograms are obtained for scans along the laser beam. Disabling the locater beam gives the histograms shown in Figure 4, displaying the "Gaussian ambiguity". It appears difficult to deconvolve the diameter histogram to appear as that in Figure 3, as suggested by Holve and Self [5] and Mizutani [6]. The speed histogram is less affected. Theoretically, with a Gaussian beam, it should be unaffected [5]. However, in practice the degradation is severe.

Scanning the drop stream across the laser beam also allows determination of the size of the locater probe volume, by noting the limits over which the locater beam is triggered. Wang and Hencken [9] found that large drops are more likely to trigger a measurement. However, testing with drops from 163 to 279 μmD, using a locater beam about 200 μmD and locater slit 500 μm wide, showed no difference in probe volume size. Therefore no correction is made for size bias. The likely explanation is that most of the light scattered at 90° is due to total internal reflection from a small region on the back of the drop, so that the effective scattering area of a drop is much smaller than the actual cross section.

Calibration results are shown in Figure 5. Ideally, the drop diameter should be proportional to the square root of the normalized scattered intensity, however a slight curvature is apparent as the drops increase in size. An explanation results by averaging the beam intensity over the drop cross section, giving the fit shown in Figure 5. The best fit occurs by assuming a main beam diameter (D) of 700 μmD, although the curvature is so slight that a much larger value would make little difference. The beam diameter estimated by eye was 550 μmD, while the speed calibrations determined 578±63 μmD. The difference is again attributed to the effective scattering diameter being smaller than the actual diameter.

For drops smaller than about 10 μmD, the light collection cone is not large enough to average over the Mie interference pattern and the calibration curve becomes multivalued. However, few drops this small exist in the sprays tested. Calibration streams smaller than 150 μmD can be generated, but the drops overlap in the probe volume, so that the lower end of the calibration curve has not been verified. One solution is to decrease the number density by electrostatically deflecting away every other drop [13].

Calibrations using 8 different liquids suggest a linear relation between the apparent diameter increase and the refractive index relative to water, as shown in Figure 6. The incident light was polarized perpendicular (vertical) to the scattering plane. For most low molecular weight liquids the correction is fairly small.

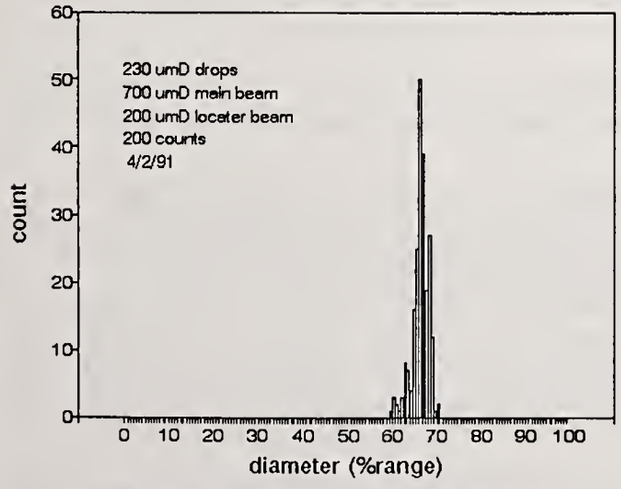

Fig. 3 a) Diameter histogram with drops scanned across beam

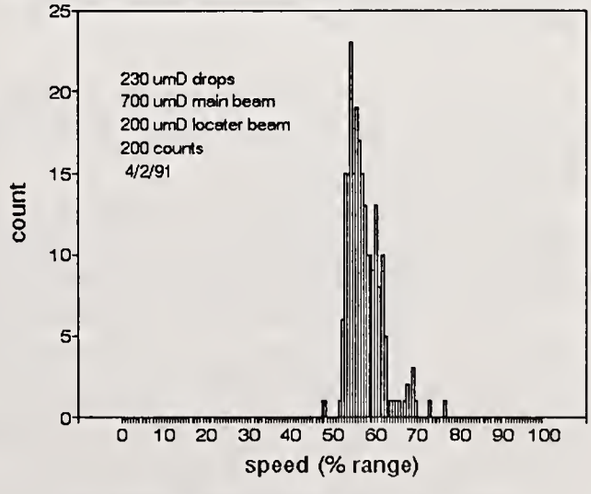

Fig. 3 b) Speed histogram with drops scanned across beam

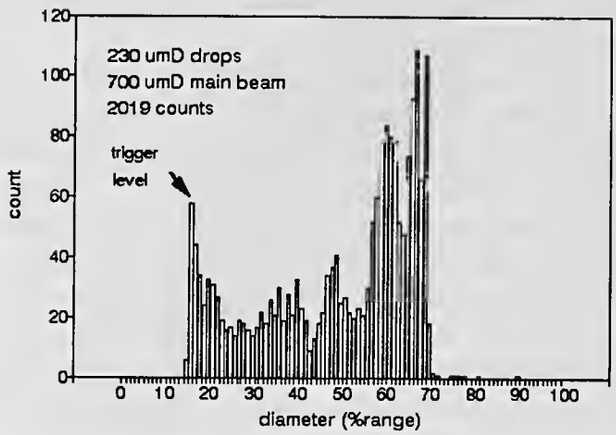

Fig. 4 a) Diameter histogram without locater beam

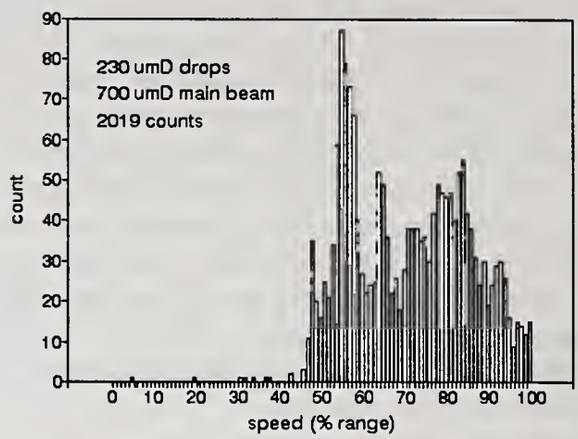

Fig. 4 b) Speed histogram without locater beam

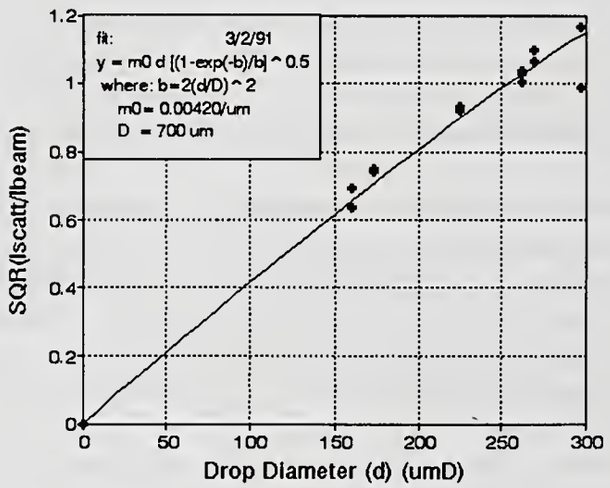

Fig. 5 Diameter calibration

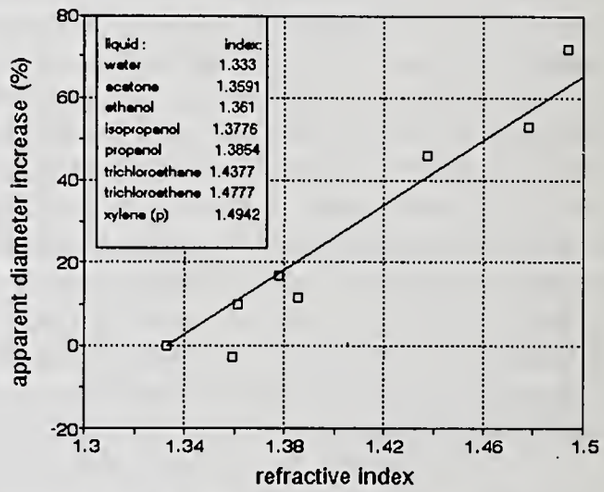

Fig. 6 Effect of refractive index on drop size , rel. to H2O

By averaging over the beam area, a large drop gives a slightly wider pulse as it crosses the beam than a small drop. The resulting pulse is still essentially Gaussian. Numerical integration predicts a fractional increase in pulse width of $0.539(d/D)^{2.3\,4\,6}$, where d is the effective scattering diameter. The present scatter in the speed calibrations (±11%) preclude verifying this prediction.

BEAM ATTENUATION

In a dense spray the laser beam is attenuated in traveling to the probe volume and the scattered light suffers attenuation in exiting the spray. These attenuations cause the drop pulses to appear smaller than normal and must be corrected.

The transmittance to the probe volume is found by passing the beam from the left and right, in turn: $t_\ell = [(t_\ell / t_r)T]^{1/2}$, where t_ℓ and t_r are the transmittances for the beam from the left and right, respectively, and T is the total transmittance. A linear "absorption" law (actually scattering) is assumed, i.e. $T = t_\ell\, t_r$.

The pulse height histograms appear similar in each case, with the abscissas simply scaled by the ratio of the beam intensities. The ratio t_ℓ / t_r is thus found by ratioing the peak values of the two histograms. The collected light transmittance is the same fraction in each case, so that the ratio is unaffected. It is not actually necessary to pass a beam from the right. The same geometry results by rotating the spray 180° about the collection axis, i.e. so that the spray points upward.

This analysis has general application to any problem where the attenuation is due partially to scattering, and the "absorptivity" at every point in a cross section is desired, for example in studying soot generation. The

"absorptivity" at every point along a line through the region can be found by differentiating the transmittances along the line. This analysis is best termed "scattering tomography".

The transmittance along the collection path can be found by rotating the spray 90° about the spray axis, as shown in Figure 7, making the former collection path (t_3) align with the beam, allowing its transmittance to be determined. Denote the peak of the measured pulse height histogram by $P_{k\theta}$, where $k=\ell$ or r for the beam from the left or right, respectively, and $\theta = 0°$ or 90° for the spray at the original orientation or rotated 90° about the vertical, respectively. t_i denotes the transmissivity along the four paths shown and T_1 and T_2 are the transmittances along the two perpendicular paths across the spray. The corrected pulse height peak is found as: $P = P_{\ell 0°}/(t_1 t_3)$. Expressing t_1 and t_3 with the scattering tomography analysis above eventually results in an identity (note $T_1 = t_1 t_2$ and $T_2 = t_3 t_4$):

$$P = \left[\frac{t_1 t_2 t_3 t_4 \; PP}{T_1 \; T_2}\right]^{\frac{1}{2}}$$

Referring to Figure 7, the possibilities for the numerator are:

$$(t_1 t_3 P)(t_2 t_4 P) = P_{\ell 0°} P_{\ell 180°}, P_{\ell 0°} P_{r270°}, P_{r90°} P_{\ell 180°}, \text{ or } P_{r90°} P_{r270°}$$
$$(t_1 t_4 P)(t_2 t_3 P) = P_{\ell 90°} P_{r0°}, P_{\ell 90°} P_{\ell 270°}, P_{r180°} P_{r0°}, \text{ or } P_{r180°} P_{\ell 270°}$$

These are summarized as two procedures: (1) after the first measurement, rotate the spray 180° about the spray axis, or (2) after the first measurement, rotate the spray 90° about the spray axis and 180° about the collection axis (to pass beam from right). The first procedure is more convenient since the spray remains pointing downward. It is interesting that including the collection attenuation leads to a simpler procedure than considering the input attenuation alone. Beretta [2] states the same result for the case of an axially symmetric spray. As seen here, the result is not restricted to axial symmetry.

A related problem is that the beam attenuation is not constant, due to statistical fluctuations in the number of drops along the path to the probe volume. The collected light also fluctuates, but it is not significant due to the large collection cone.

A drop scatters most of the light incident upon its cross-sectional area out of the beam. An equal amount of light is diffracted, but most of it remains within the confines of the beam. Scattering causes localized shadows in the beam profile, giving ripples on the pulses. However, the Gaussian fitting largely negates the ripples, so that only temporal fluctuations in the spatially averaged intensity need be considered.

Assuming a uniform beam intensity and a mono-disperse spray, the fraction of beam energy scattered by a single drop is $(d/D)^2$. The total fraction attenuated is: $A = 1\text{-}\exp[-N(d/D)^2]$, where N is the number of drops in the beam. According to Poisson statistics, the attenuated fraction fluctuates by an rms fraction $A/\sqrt{N}$, so the rms beam intensity fluctuation is:

$$I_{rms}/I = (d/D)\, A[-\ln(1-A)]^{-\frac{1}{2}}$$

For both very low and very high attenuations there is little fractional intensity fluctuation. The maximum fluctuation occurs at an attenuation of 71.5%, in which case $I_{rms}/I = 0.638(d/D)$. Given the square root relation, the corresponding diameter fluctuations are half this. It is desirable to converge the main beam as it approaches the probe volume, so that its average diameter through the spray is increased, decreasing the fluctuations.

Hess [11] measured intensity fluctuations of +/-14%, at a beam attenuation of 10.7%. The beam diameter was about 600 μmD at the probe volume, and somewhat larger in the spray. Since the attenuating drops were far upstream, a factor of 2 should be added to account for diffraction. The analysis would then predict an rms fluctuation of $\sqrt{2}(d/D)(0.318)$. The average drop size in the spray was not stated. To agree with the above analysis, the drops would have to have been an average of 187 μm in diameter.

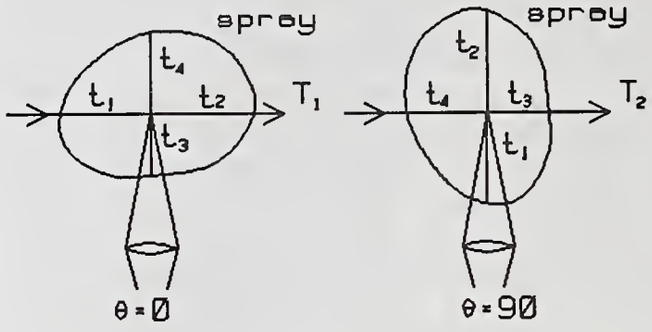

Fig. 7. Input and collection attenuation

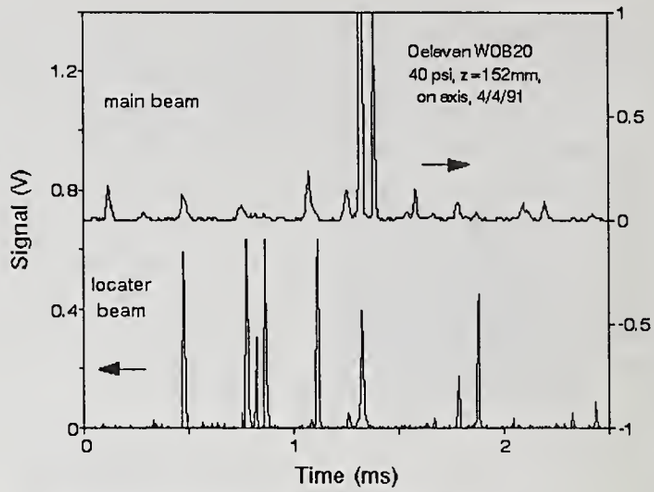

Fig. 8 Photomultiplier signals in spray

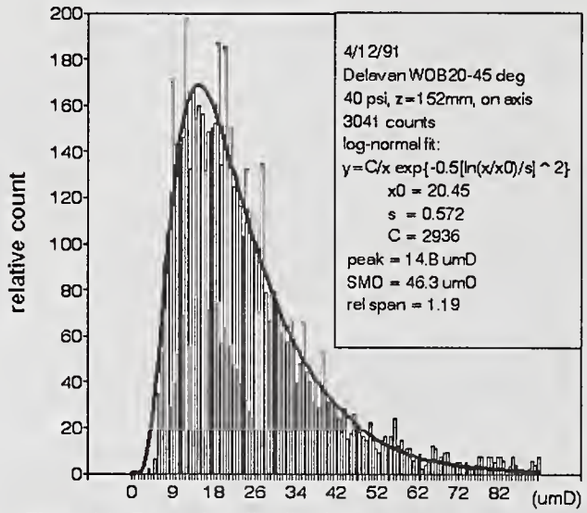

Fig. 9 (a) Drop size distribution in spray

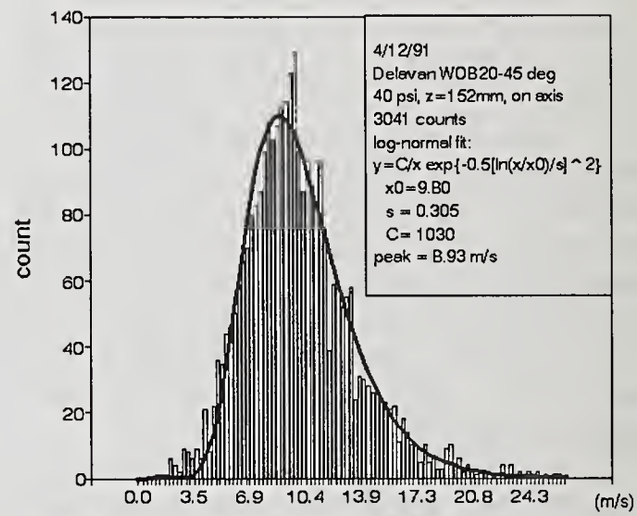

Fig. 9 (b) Speed distribution in spray

EXPERIMENTAL RESULTS

Measurements in a Delavan WDB20-45° nozzle spraying water at 276 kPa, 685 cc/min, 152 mm from the nozzle on the centerline, are shown in Figures 8 and 9. Similar shaped drop size distributions have been reported [6,14,15].

To insure that the rapid cutoff on the low side of the drop size histogram was not due to instrument sensitivity, the time traces were monitored. The smallest drops detected had locater pulses well above the trigger threshold, so that drops smaller than the 5 μmD limit in Figure 9a could have been detected. The limiting drop size is probably due to the limited kinetic energy available to atomize the liquid.

The log-normal function gives the best fit to both the diameter and speed histograms, as shown in Figure 9:

$$f(x) = (C/x)\exp\{-\tfrac{1}{2}[\ln(x/x0)/s]^2\} \quad ; \quad \text{normalize: } C = 1/[s(2\pi)^{1/2}]$$

The parameters x0 and s control the peak and width of the distribution. An upper limit modification to the log-normal function has been suggested [16], however, the addition of a third parameter confuses the data analysis. Such a limit is better added at the modeling stage.

The Nukiyama-Tanasawa (N-T) function has also been used:

$$f(x) = C\,x^m \exp[-(x/x0)^p] \quad ; \quad \text{normalize: } C = p/\{x0\,\hat{}\,(m+1)\,\Gamma[(m+1)/p]\}$$

where $\Gamma()$ is the gamma function. When exponent m is restricted to (p-1) it is termed the Weibull function [17]. One difficulty is that the N-T function does not maintain a similar shape. For wide distributions it is skewed left, appearing similar to the log-normal function, whereas for narrow distributions it becomes skewed right. Also, if $m < 0$ it predicts an infinite number of drops as the diameter approaches zero.

Another popular function is the Rosin-Rammler, usually expressed as a cummulative volume fraction:

$$F_V(x) = 1\text{-}\exp[-(x/x0)^p]$$

however,

$$F_V(x) = \frac{\pi}{6}\int_0^x x^3 f(x)dx$$

so that it is seen to be simply the Nukiyama-Tanasawa function with $m = p-4$, a fact noted by Bevans [18].

For application to combustion models, an efficient procedure should exist to generate random variates from the selected distribution function. When the cumulative distribution function (cdf) can be analytically inverted, random variates are generated simply as $X = F^{-1}(R)$, where $F^{-1}()$ is the inverse cdf and R is a random number from 0 to 1 [19]. Examples are the exponential function, used in Los Alamos' KIVA code [20], and the Weibull function. The log-normal cdf cannot be inverted, however efficient methods exist for generating random variates from it [19, p 132].

The Delavan nozzle used was the subject of a "round-robin" test, using 6 different drop sizing instruments [21]. At the test conditions of Figure 9a they reported Sauter Mean Diameters (SMD) from 65 to 180 μmD and "relative spans" from 0.95 to 1.7. The present data gives an SMD of 46.3 μmD and 1.19 relative span. However, the SMD is a poor basis for comparing distributions from single particle counters since it is overly sensitive to the tail, where the counts are very low.

The beam attenuation through the center of the spray was 19.4%, with an rms fluctuation of 2.42%. The previous attenuation analysis calculates an equivalent monodisperse drop size of 16.4 μmD, for the 400 μmD (minimum) main beam, which is close to the peak value of 14.8 μmD in Figure 9a. Doubling the pressure to 552 kPa hardly changed the peak diameter (15.8 μmD) but narrowed the distribution (SMD = 36.3 μmD), while the peak velocity increased from 8.93 m/s to 11.0 m/s.

CONCLUSIONS

A low-cost instrument has been developed to allow drop size and speed measurements in dense sprays. The design overcomes previous difficulties with Pulse Intensity methods. A simple "scattering tomography" analysis accounts for beam attenuation through the spray. Drop size and speed distributions in the Delavan spray are best fit by a log-normal distribution.

ACKNOWLEDGEMENTS

The research followed a 1986 UES/AFOSR Summer Faculty Research Program (SFRP) tenure at the Air Force Phillips Lab and a 1988 SFRP tenure at Arnold Engineering Development Center. Michael Powell at the Phillips Lab assisted with the initial design and Chad Limbaugh at Arnold Engineering supported tests in a model rocket injector. Research sponsored by the Air Force Office of Scientific Research, under Contract F49620-88-C-0053.

REFERENCES

1. Azzopardi, B.J., "Measurement of Drop Sizes", Int. Journal of Heat and Mass Transfer, Vol 22, pp. 1245-1279 (1979).
2. Beretta, F., Cavaliere, A., and D'Alessio, A., "Drop Size and Concentration in a Spray by Sideward Laser Light Scattering Measurements", Combustion Science and Technology, Vol 36, pp 19-37 (1984).
3. Presser, C., Santoro, R.J., and Semerjian, H.G., "Velocity and Droplet Size Measurements in a Fuel Spray", AIAA 24th Aerospace Sciences Meeting, AIAA-86-0297, (Jan 1986).
4. Bachalo, W.D. and Houser, M.D., "Phase/Doppler Spray Analyzer for Simultaneous Measurements of Drop Size and Velocity Distributions", Optical Engineering, Vol 23, no 5, pp 583-590, (Sept/Oct 1984).
5. Holve, D. and S.A. Self, "Optical Particle Sizing for in situ Measurements, Part II", Applied Optics 18, p. 1646 (1979)
6. Mizutani, Y., Kodama, H., and Miyasaka, K., "Doppler-Mie Combination Technique for Determination of Size-Velocity Correlation of Spray Droplets", Combustion and Flame, Vol 44, pp 85-95 (1982).
7. Hess, C.F. "Nonintrusive Optical Single-Particle Counter for measuring the Size and Velocity of Droplets in a Spray", Applied Optics, Vol. 23, no 23, pp 4375-4382 (Dec 1984).
8. Eauret, P.R. et al, "Measurement of Drop Size and Velocity in Vaporizing Sprays, in Proceedings, Second Int'l Conference on Liquid Atomization and Spray Systems, Madison, Wisconsin, p 261 (June 1982).
9. Wang, J.C.F. and Hencken, K.R., "In situ Particle Size Measurements using a Two-Color Laser Scattering Technique", Applied Optics, Vol 25, no 5, pp 653-657 (March 1986).
10. Umhauer, H., "Particle Size Dist. Analysis by Scattering Light Meas. using an Optically Defined Measurement Volume", Journal of Aerosol Science, Vol 14, no 6, p 765 (1983).
11. Hess, C.F., "An Instrument to Measure the Size and Velocity of Particles in Particle Laden Flows", 21st Joint Propulsion Conference, Moterey, California, AIAA-85-1443 (July 1985).
12. Sakai, T., Sadakata, M., Saito, M., et al, "Uniform Size Droplets by Longitudinal Vibration of Newtonian and non-Newtonian Fluids", Second Int'l Conference on Liquid Atomization and Spray Systems, Madison, Wisconsin, pp 37-45 (June 1982).
13. Keng, Weaver, and Orr. "A Study of Vibrating Capillary Atomizers", Georgia Institute of Technology Engineering Experiment Station Report, Grant B-279 (April 1967).
14. Bolle, L. and Moureau, J.C., "Spray Cooling of Hot Surfaces" in Multiphase Science and Technology, Vol 1, (G.F. Hewitt, J.M. Delhaye, and N. Zuber, Eds.), pp. 1-10, Hemisphere Publ., Washington (1982).
15. Hiroyasu, H., Kadota, T., and M. Arai, "Supplementary Comments: Fuel Spray Characterization in Diesel Engines" in Combustion Modeling in Reciprocating Engines (Mattavi, J.N. and Ammna, C.A., Eds.), pp. 369-405, Plenum Press, N.Y. (1980).
16. Dobbins, R.A. "Light Scattering and Transmission Prop. of Sprays", Phd. Thesis, Princeton Univ. (1960).
17. Derman, C., Gleser, L., and Olkin, I., A Guide to Probability Theory and Applications, Holt, Rinehart, and Winston (1973).
18. Bevans, R.S., "Mathematical Expressions for Drop Size Distributions in Sprays", Conference on Fuel Sprays, Univ. of Michigan (March 1949).
19. Dagpunar, J. Principles of Random Variate Generation, Clarendon Press (1988).
20. Amsden, A.A., J.D. Ramshaw, et al. "KIVA: A Computer Program for 2 and 3 - Dimensional Fluid Flows with Chemical Reactions and Fuel Sprays", Los Alamos National Laboratory Report LA-10245-MS (Feb 1985).
21. Dodge, L.G., "Comparison of Drop-Size Measurements for Similar Atomizers", Special Report No. SwRI-8858/2, Office of Naval Reseach, (December 1986).

MEASUREMENT OF DROPLET SIZES BY LIQUID NITROGEN FREEZING METHOD

T. Karasawa*, S. Shiga* and T. Kurabayashi†

*Dept. of Mechanical Engineering, Gunma University, Kiryu, Gunma, Japan
†Hiroshima Institute of Technology, Hiroshima, Japan

ABSTRACT

A liquid nitrogen freezing method for accurate measurement of droplet sizes has been developed since 1971 and recently the final setup has been completed through the efforts for overcoming some problems and difficulties. Droplet sizes of water spray are measured by both the freezing method and the immersion sampling method and the results are compared. It is revealed that the number of droplets caught in the freezing method is several times as much as that of the immersion sampling method. The reason of the decrease of droplets number in the immersion sampling method is considered to be caused by the disappearing of smaller droplets due to evaporation. Therefore the Sauter mean diameter obtained by the immersion sampling method tends to be larger than that by the freezing method. Through the comparison experiment with immersion sampling method, it has been revealed the present apparatus can afford highly accurate value of droplet sizes.

INTRODUCTION

It is strongly desired to obtain accurate droplet sizes in the fields of liquid atomization technique. While various measuring methods have been used, few of them seems to be able to afford the reliable value of droplet sizes due to individual shortcoming essential to each method. The freezing method, in which liquid droplets are solidified by low temperature atmosphere possesses several advantages to obtain their accurate sizes. Since the first study on this method by Longwell(1) in 1943, several works in this field have been made by different investigators (2)-(7). In recent ten years, however, no successful results has reported.

The authors started the research on this freezing method in 1971. A cylindrical freezing chamber is air-proved to avoid generation of cloud in the chamber. Liquid nitrogen fed into the double wall space of the chamber vaporizes and forms cooling atmosphere. Liquid to be tested is injected downward through a nozzle and its frozen droplets fall onto a photographic film set on a bottom plate of the chamber. In order to avoid the severe problems of frosting and optical difficulty, a simple photographic technique called photogram is employed to get shadows of the droplets. In 1978, at the

first ICLASS, history of development of the research from the first trial setup to the sixth setup was reported and availability of this method for accurate measurement was suggested on the basis of the experimental results.

In 1979 and 1980, remarkable improvements had been made in the method and the seventh trial setup was designed and developed. Prior to the construction of this device, distance neccessary for droplets to freeze was theoretically estimated and evaporation of droplets were also calculated. The most important improvement in the setup was employment of 100 feet long film in a film suply system, which enables to obtain a significantly increased number of data in one series of experiment using liquid nitrogen filled in a 150 liter Dewer tank. The film suply system was also newly designed to protect the film against sudden exposure to the atmosphere with large temperature difference from room to freezing chamber, to avoid the temperature shock which deteriorates film emulsion. Using the setup, adequate exposure time to compensate the decrease of light sensitibity of the film emulsion due to lowered temperature, and adequate axial temperature gradient in the test chamber to form spherical frozen particles were searched experimentally. All these results were already reported (8).

Through further improvement made in recent years, the final setup has been completed for accurate measurement of droplet sizes. In this paper procedure of the improvements is described at first, and the accuracy of the freezing method is examined by comparing the droplet sizes obtained by this method with those by the another method. This time, the immersion sampling method is chosen as a representative of the other methods, which is widely used at present and is often employed as a standard method when comparison is required.

EXPERIMENTAL SETUP AND PROCEDURE

The arrangement of experimental devices is shown in Fig.1. The freezing chamber (32) is composed of a double wall type cylinder and a top and bottom end plates to keep airtight for avoiding generation of fog in the chamber. The inside of the chamber is kept dark. A length of 2 meter of the chamber was determined considering the analytical result mentioned above, and the inner diameter is 600 mm. The cylinder walls are made of 0.5 mm stainless steel plate. The thickness of the previous body wall was 1.0 or 1.2 mm, and this reducton of the wall thickness produced decreased heat capacity of the body, nitrogen consumption economy and easy control of ambient gas temperature. Liquid nitrogen in the Dewer tank (14) is poured into the gap between the inner and outer walls of the chamber cylinder and the evaporated nitrogen forms freezing atmosphere in the chamber. The amount of nitrogen supplied is measured by using a spring balance (13). The chamber is thermally insulated by foamed polystyrene with a thickness of 150 mm. Distribution of temperature in the freezing chamber is measured by thermocouples (29) set at seven heights, which can be moved radially by rotating a support bar (30). Thermocouples are also inserted in other parts, injection nozzle (5), film boxes (17) and (28), etc.. All of these sixteen thermocouples are connected to a data-logger(1) and their measurement time is controled by a micro computor.

When the temperature distribution in the chamber achieves required profile, a new part of a 35 mm roll type long film is pulled out from the film box (28) through the temperature buffer (25) at adequate speed for avoiding heat shock, and is set on a film guide (23). On the guide the spread film forms a collective area of frozen particles with a width of 24 mm and a length of 600 mm. These operations are made automatically by a rolling system

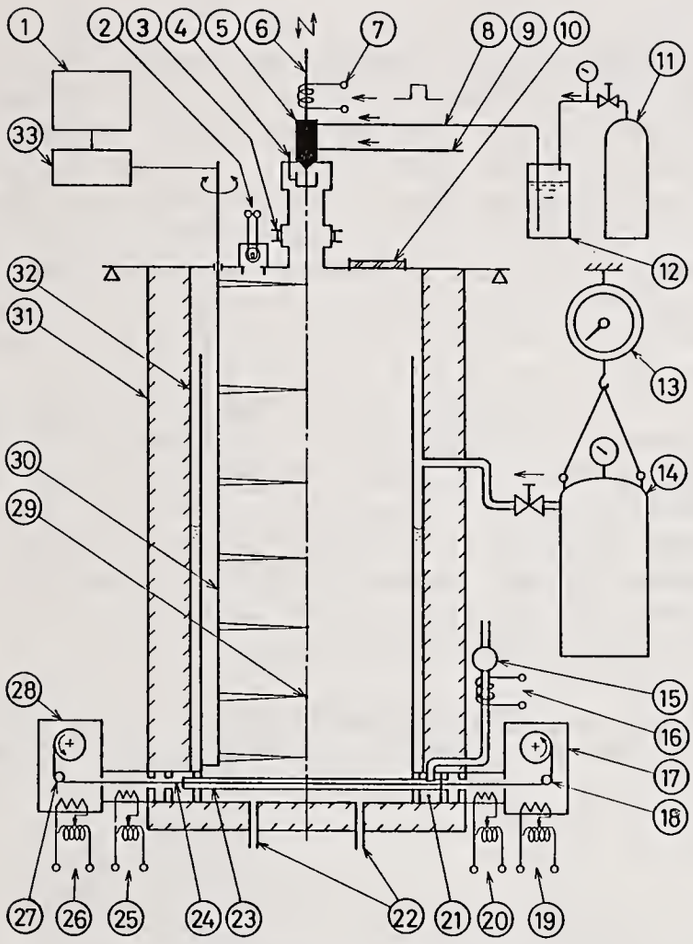

Fig.1 The eighth apparatus

consisted of a photo-detect counter (27), an inverter motor and an electronic control circuit. Liquid to be tested is then injected downward into the freezing chamber. When the smallest frozen particles are considered to reach the film completely, shadows of the frozen particles are recorded on the film by the technique called photogram, at which direct exposure is made to the light from the bulb (2) for adequate duration determined depending on the coldness of the film. As soon as the exposure is finished, the exposed part of the film is rolled up into the film box (17), and the frozen particles on the film are replaced by a suction unit (15). The photogramed particles are printed with magnification of 20 and then measured.

Since the experiments for comparison of the two methods have to be carried out under the same conditions as far as possible, the chamber of the freezing method is also used to carry out the experiment of immersion sampling method and the sampling cells are placed at the same position as that of the film supply system in the freezing method. All the experiments are carried out on water spray injected through a hole nozzle with 0.3 mm diameter. Injection pressure is changed in four steps, i.e. 12, 10, 8 and 6 MPa, and the injection period is changed also in four steps, i.e. 150, 90, 40 and 30 millisecond. The injection period of 90 ms is set as a standard injection period. The quantities of water injected are chosen as small enough not to cause the coalescence of droplets at the immersion liquid surface and large enough to offer reasonable number of particles.

RESULTS AND DISCUSSIONS

Influence of Exposure Time to Low Temperature Atmosphere on its Negative

It is known that the application of sudden change of temperature to the film sometimes causes unevenness in density and spots or patches with irregular shape on its negative. However the details of these phenomena have not been clear. Therefore the following tests were carried out. The elapsed time from the setting of a film in alow temperature atmosphere of -100 C to the light exposure was changed as 0, 30 and 60 minutes, and then the film was developed. The result showed that the negative without elapsed time is normal, but a lot of fine spots appeared on the negative with 30 minutes elapsed time and the number of the spots increase in the case of 60 minutes. However since the contour of the spot is not clear, while that of the shadow of the frozen particle is quite clear regardless of its size, both the spots and the particles can be easily distinguished. Therefore, it is considered that the elapsed time of 30 minutes which generates relatively small number of the spots does not affect on the result of measurement. To avoid these undesiarable phenomena, in the present experiments the film is introduced into the chamber immediately before the liquid injection and rolled up into the film box as soon as the exposure is finished.

Comparison of the Number of Droplets Captured

In Fig.2 radial profiles of number density of droplet caught in the freezing

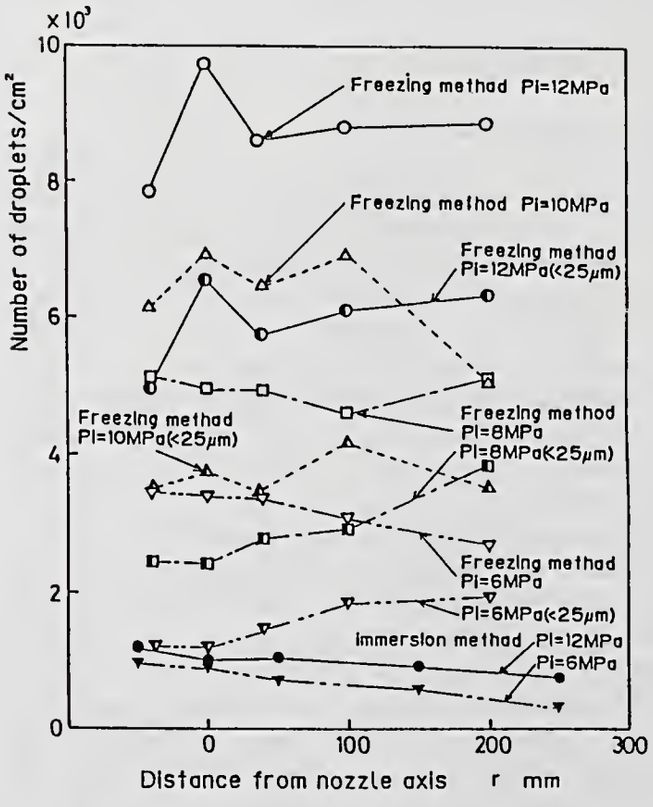

Fig.2 Variation of the number of droplets caught by both the freezing method and immersion method

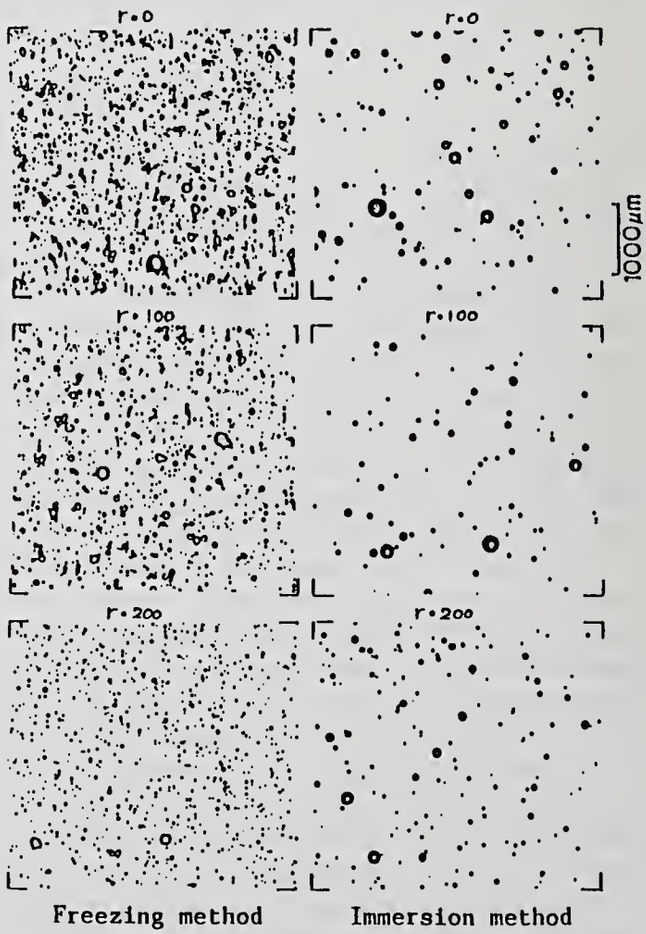

Fig.3 Photographs of droplets

method is compared with those in the immersion sampling method for four injection pressure levels. Some representative photographs of droplets in the two methods are shown in Fig.3. The figure shows that the number of droplets caught in the freezing method is nine times as much as that in the immersion sampling method, and more than half of the number is occupied by the fine droplets smaller than 25 micrometer. These facts are caused by evaporation of the droplets during their flights in the ambient gas, and the increased evaporation rate as the diameter becomes small (8). In the freezing method droplets are prevented from evaporation due to the extremely low temperature atmosphere and almost all droplets can remain and are captured. Fig.2 also shows the same tendency as above.

Comparison of Sauter Mean Diameter in Two Methods

Fig.4 shows the radial distributions of local Sauter mean diameter obtained by freezing method and immersion sampling method. In Fig.4(a) it is shown that the Sauter mean diameters by the immersion sampling method are much larger than those by the freezing method over whole range of radial derection. A similar tendency was observed in the case of injection pressure of 10 MPa. The reason of these facts is that in the immersion sampling method the number of finer droplets is decreased by evaporation as mentioned above. Radial profiles of the mean diameter in (a) are more gentle than those in (b) and (c). This tendency may be caused by the fact that in the high pressure injection the size of droplets becomes smaller even at the center of the spray, and the ralatively larger droplets in the vicinity of spray axis are apt to be shifted toward periphery due to the high injection velocity.

In figure (b) in the case of injection pressure of 8 MPa, Sauter mean diameters by the two methods come to nearly the same at the vicinity of spray center. This is caused by that although the number of droplets obtained by the freezing method is larger than that of the immersion sampling method, the total number of droplets generated decreases and the number of large droplets over a diameter of 200 micrometer becomes to increase as the injection pressure decreases.

In figure (c) Sauter mean diameters by the immersion sampling method becomes larger again than those by the freezing method. As the injection pressure decreases the dispersion of spray becomes weak and the sizes of droplets increase. These tendencies bring larger possibility of coalescence of droplets when they are captured by immersion liquid. This fact shifts the value of mean diameter near the spray center. In the periphery of spray the mean diameters are shifted down nearly to the values of freezing method. In this region the increase of mean diameter due to the evaporation of fine droplets becomes small, the number of fine droplets decreases under the lower injection pressure.

Comparison of Size Distribution

In Fig.5 number distributions of droplets obtained by the freezing method are compared with those by the immersion sampling method. Difference is seen in the region of fine droplet under the condition of high injection pressure.

Influence of Injection Period on Sauter Mean Diameter

Injected liquid quantity was changed by changing the injection period to reveal their influence on Sauter mean diameter, and the results are shown in Fig.6. As seen in Fig.6(a) the mean diameter by the freezing method with injection periods of 30 and 40 millisecond is larger than those with 90 and 150 millisecond. This may be caused by the relatively longer transient period

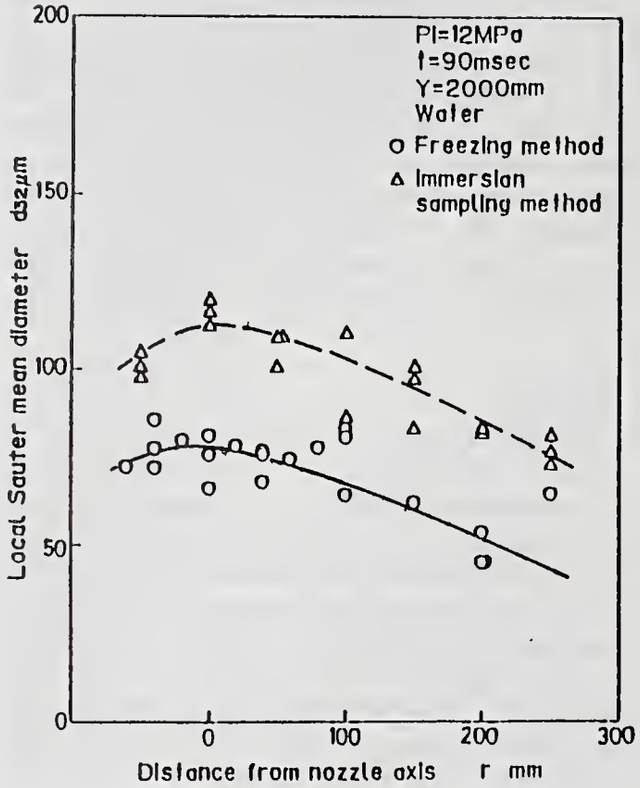

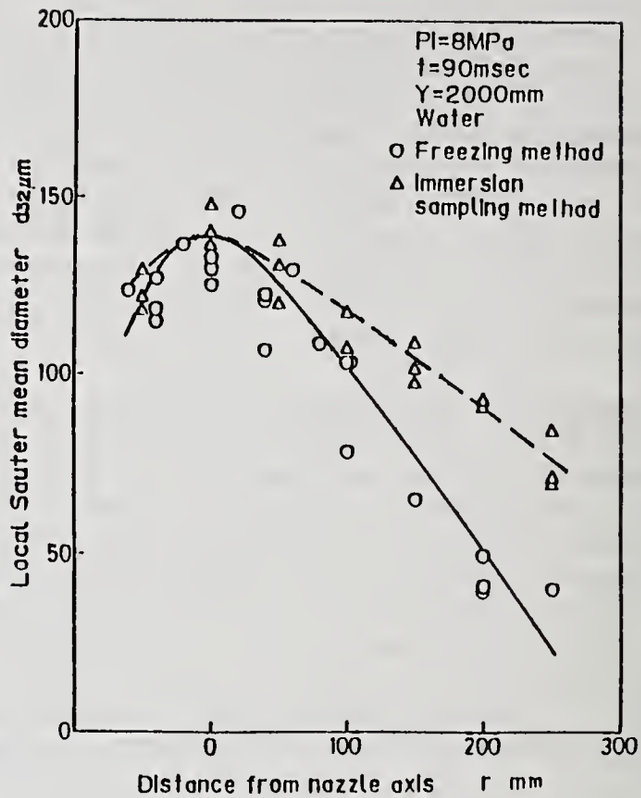

Fig.4 Comparison of local SMD by freezing method with that by immersion method

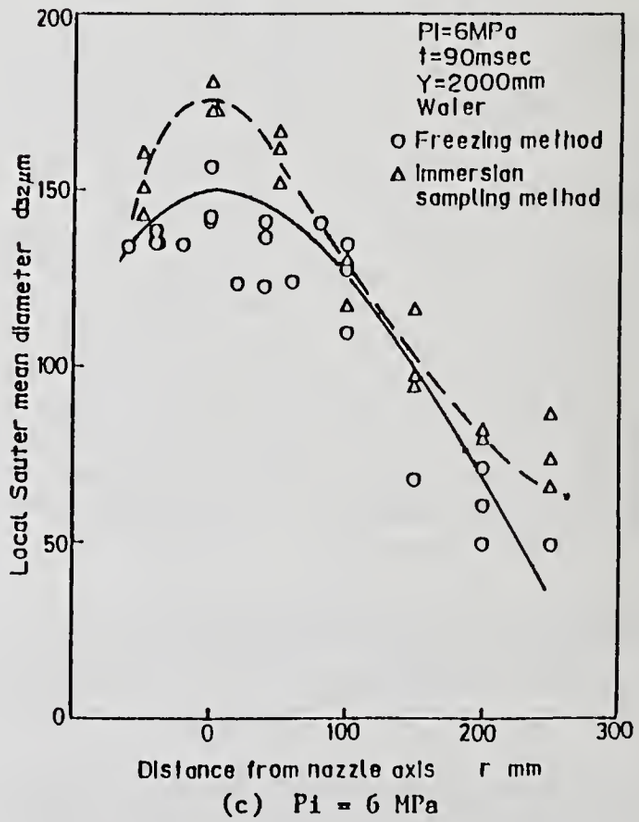

of nozzle needle motion in the case of shorter injection period where insufficient atomization occurs. In the immersion sampling method these differences are not recognized. Based on this result, it can be said that the freezing method is more sensible than the immersion sampling method.

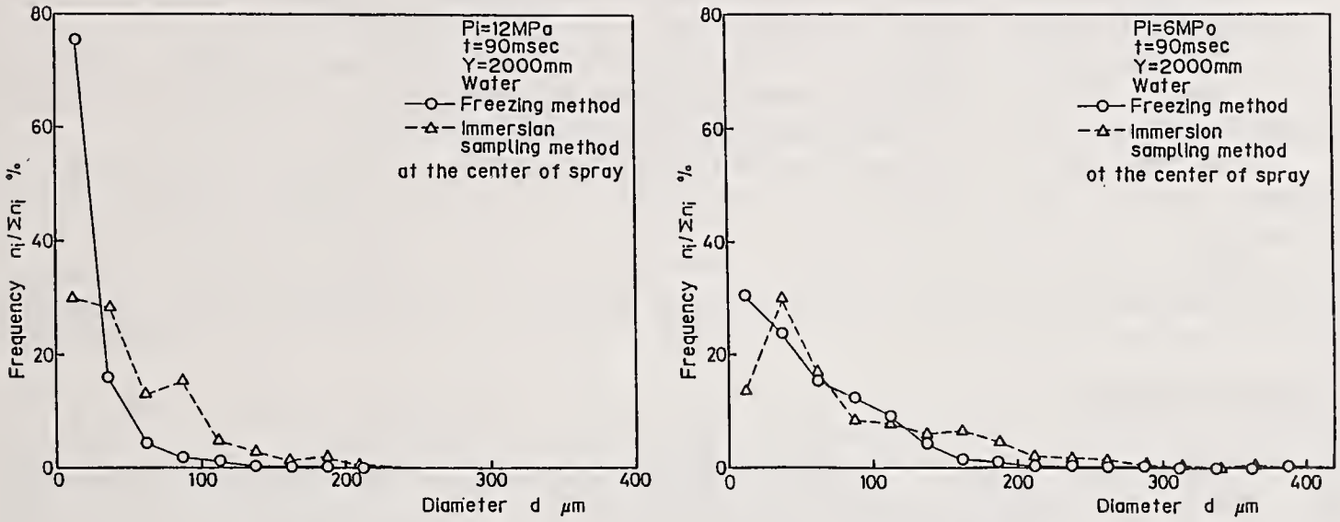

(a) Pi = 6 MPa (b) Pi = 12 MPa

Fig.5 Distribution of droplet size

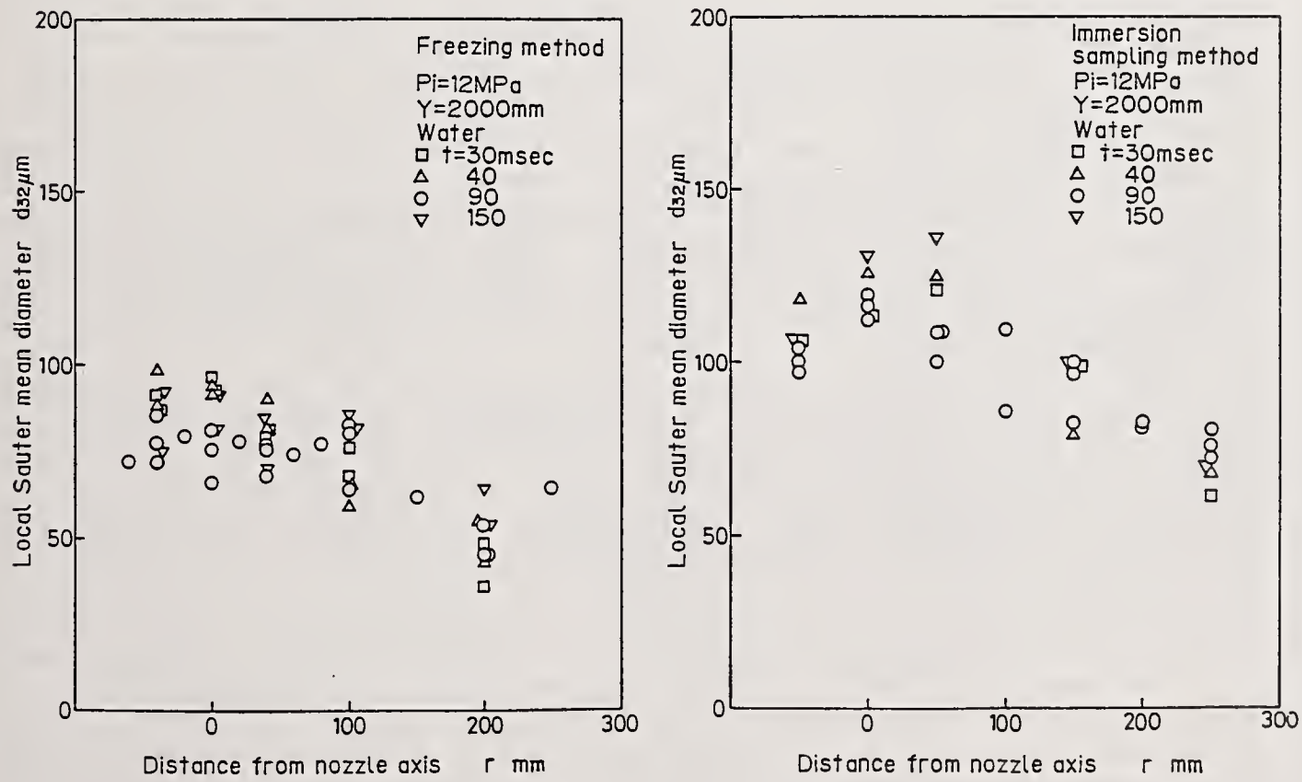

(a) Freezing method (b) Immersion method

Fig.6 Influence of injection period on local SMD

CONCLUSIONS

A new apparatus for accurate measurement of spray droplet sizes based on the liquid nitrogen freezing method has been constructed after the constructions of seven trial setups. Using this apparatus comparison tests with the immersion sampling method were carried out and the results are summerized as:

In the present apparatus improvements were made on some points for more reliable measurement, easy operation and nitrogen economy.

The immersion sampling method presents larger mean droplet diameter mainly due to disappearing of fine droplets by evaporation and coalescence of droplets occurs when they are captured by immersion liquid.

In the freezing method the evaporation and coalescence of droplets are almost avoided and, therefore, the method can afford highly accurate spray diameter.

Since the freezing method is based on a quite simple principle and has little possibility of error, the present setup is considered to be a standard measuring apparatus.

ACKNOWLEDGMENTS

The authors wish to thank Mr. Hisao Nakamura for his enthusiastic helps for constructions and tests of the apparatus.

This work was partly supported by the Tanikawa Foundation, Osaka, Japan.

REFERENCES

1 Longwell J P, Doctorial dissertation, Massachusetts Institute of Technology, 1943.

2 Taylor E H and Harman D B, 'Measuring Drop Sizes in Sprays', Industrial and Engineering Chemistry, Vol.46, No.7, pp.1455-1457, July 1954.

3 Tanasawa Y, 'Automobile Engines, Lecture', Toyota Gijutu, Vol.5, No.7, pp.24-34, 1952.

4 Joyce J R, 'The Atomization of Liquid Fuels for Combustion', Inst. Fuels J., Vol.22, No.124, pp.150-156, 1949.

5 Nelson P A and Stevens W F, 'Size Distribution of Droplets from Centrifugal Spray Nozzles', J. Am. Inst. Chem. Eng., Vol.7, No.1, pp.80-86, Mar. 1961.

6 Street P J and Danaford V E J, 'A Technique for Determining Droplet Size Distributions Using Liquid Nitrogen', J. Inst. Petroleum, Vol.54, No.536, pp.241-242, Aug. 1968.

7 Rao K V L, 'Liquid Nitrogen Cooled Sampling Probe for the Measurement of Spray Drop Size Distribution in Moving Liquid-Air Sprays', Proc. 1st ICLASS, Tokyo, pp.293-300, Aug. 1978.

8 Karasawa T, Kaeriyama H and Kurabayashi T, 'Freezing Method by Liquid Nitrogen for Measuring Spray Droplet Sizes', J. of the Fuel Society of Japan, Vol.62, No.679, pp.901-912, Nov. 1983.

LDV AND PDA ANALYSIS OF SPRAY-WALL INTERACTION

G. Brunello*, S. Callera*, A. Coghe†, G.E. Cossali† and F. Gamma‡

*CNPM-CNR, Peschiera Borromeo (MI), Italy
†Politecnico di Milano, Milano, Italy
‡Università "La Sapienza", Roma, Italy

ABSTRACT

A diesel spray impacting on a wall in a close chamber, under ambient air conditions, has been analysed by means of Laser Doppler Velocimetry (LDV) and Phase Doppler Anemometry (PDA) in order to measure droplet size and velocity in regions close to the wall. Spray behaviour has been characterized in terms of different injection periods and different spatial regions, and proper data analysis allowed to identify the main features of the droplet-wall interaction phenomenon.

INTRODUCTION

Recent theoretical predictions, experimental observations and engine tests [1] evidenced that the interaction of a diesel sprays with the piston wall might be beneficial to engine combustion because of the influence on fuel vaporization and heterogeneous mixture formation processes. Many experiments have been performed in the past by different groups [2,3,4,5] to investigate the spray-wall interaction, generally using high-speed photography, and the first submodel developed to describe the spray-wall interaction process has been presented very recently [6]. Spray-wall interaction characteristics seem to be controlled mainly by the drop Weber number although other parameters as wall temperature, fuel boiling temperature, drop impinging angle, swirl intensity, air density and temperature, Leidenfrost temperature, wall surface roughness have also been proven to be important. Analysis of spray-wall interaction is furthermore complicated, due to the interaction of spray droplets with entrained air flow [7], which makes unrealistic to extrapolate data obtained in experiments with single droplets. Development and validation of a spray impingement model requires a large amount of experimental data on the droplets of a real spray, like size and velocity in the region close to the wall. The present research work was aimed to a detailed analysis of the spray wall impingement process, by using the Phase Doppler Anemometer (PDA) to obtain simultaneous measurements of spray drop size and velocity in the close proximity of the wall.

EXPERIMENTAL SET-UP

The experiment was performed in a closed cylindrical chamber (89 mm i.d.,300 mm height) equipped with two glass windows positioned to allow the use of the PDA in the 70 deg forward scattering configuration to reduce the effective probe volume dimensions (about 1mm in length and o.15 mm diameter) and the sensitivity of the phase shift to refractive index of the drops [9]. A standard diesel injector (Bosch single hole nozzle, 0.25 mm diameter) injecting at 45 deg with respect to the nozzle axis, was mounted off-axis on the top wall of the chamber.The injector was fed by a Bosch high-pressure pump driven at 500 rpm by an electrical motor and diesel oil was used as fuel. The impact wall, an aluminium disc (50 mm diameter) with a polished surface, was centred on the chamber axis and positioned at a distance of 20 mm from the nozzle tip. (see fig.1). The impingement distance (L) and the impingement angle (45 deg) were kept constant. The nozzle opening pressure was fixed at 20 MPa and the injection pressure history is shown in Fig.2. Operating experience indicated that the injection system provides very reproducible pressure time histories. The ambient gas was air at room temperature and pressure. The operating conditions of the experiment are summarized in Table 1.

Table 1 - Operating conditions

Nozzle diameter, d	(mm)	0.25
Max. fuel inj. pressure	(MPa)	70
Pump speed	(RPM)	500
Volume of fuel injected	(mm^3/inj)	36
Duration of injection	(ms)	3.4

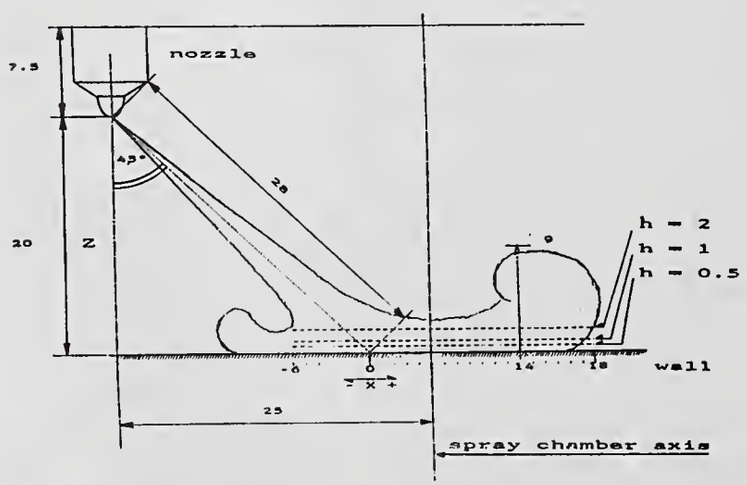

Fig.1 Schematic of the impingement experiment (all dimensions in mm).

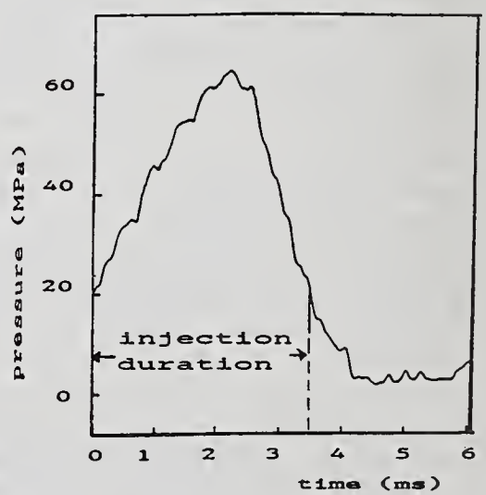

Fig.2 The liquid injection pressure.

Drop size and velocity were measured by the Phase Doppler Anemometer (Dantec PDA); the light source was an Argon-ion laser (5 W nominal power) and the transmitting optics comprised a 40 MHz Bragg cell for frequency shifting and directional sensitivity and a front lens of 300 mm focal length. The receiving optics was the 57X10 Dantec unit equipped with three preamplified photomultipliers. The covariance processor of the PDA instrument was capable of 1 μs time resolution in data acquisition and the data transfer rate, to a PC, was higher than 100 kHz. The frequency bandwidth (36 MHz) and the optical configuration of the transmitting optics defined a measurable velocity range from -25 to 125 m/s and a measurable size range from 2 to 80μm which resulted the most appropriate in the present case. Normal and tangential velocity components were measured at the same point at different times and drop size was measured together with the velocity component normal to the flat plate.
Measurements were performed at several locations on three lines at distances of 0.5, 1 and 2 mm from the surface (see Fig.1), laying on the symmetry plane normal to the wall. The investigated region extended from the impingement area to the boundary of the impact disc, in the downstream direction. Data acquisition, triggered by the needle lift opening at 20 MPa, covered a period of 5 ms for each injection and 5,000 to 10,000 data were collected over many consecutive injections for each measurement point. An encoder pulse with 1 μs resolution allowed a subsequent reconstruction of the size and velocity time history of each individual injection and also the application of time-ensemble averaging procedures.

RESULTS AND DISCUSSION

A typical result for the drop size and two velocity components, measured downstream the nominal spray impinging location, is shown in Fig.3, where all the individual measurements collected over a large number of injections are reported versus time, the origin, t = 0, being defined by the 20 MPa triggering level on the injection pressure trace. As in free sprays [8] three main periods are distinguishable: the first period with strong unsteadiness due to the passage of the spray head, a main period where most of the fuel is injected, and a late period characterized by the trailing edge, where the smaller droplets, left behind by the passage of the previous structures, and the bigger ones, generated during the late injection at low pressure, are travelling together at low velocity. Close to the surface (h=0.5 mm in Fig.3), after the tip arrival, tangential velocity stabilizes, with high rms, around a value larger than the tip velocity and than decays after completion of injection. The corresponding normal (i.e. perpendicular to the wall) velocity component shows that only droplets traversing the control volume with negative velocities (i.e. back from the wall) were detected (Fig.3). The size distribution shows an upper bound of approximately 30 μm and few data at higher values. At the same location (X = 6 mm) and larger distance from

the wall (h=2 mm) the tangential component (Fig.4) shows a transient behaviour in correspondence of the early and late injection periods, while the velocity of a large fraction of droplets is almost zero during the main injection period, suggesting that the wall spray does not extend beyond 2 mm from the wall. At the same point, it appears clearly the coexistence of droplets traversing the control volume with positive and negative normal velocity components (fig. 4). Comparison with Fig.3 shows that the droplet sizes appear lower at h = 2 mm, during the main injection period.

The relative steadyness of normal and tangential velocity components during the main injection period, although the variability is high, suggested the following data analysis: tangential velocities were ensemble averaged over a period from 1.5 to 2.5 ms after injection start (AIS) and the results plotted versus distance from the wall, at X = 14 mm, and the same was done with the size data. The results (Figs.5 and 6) show that the maximum mean velocity and mean diameter were reached both at the closest distance from the wall with a steep gradient, suggesting that the most of the tangential droplet momentum remains concentrated close to wall during the main injection period.

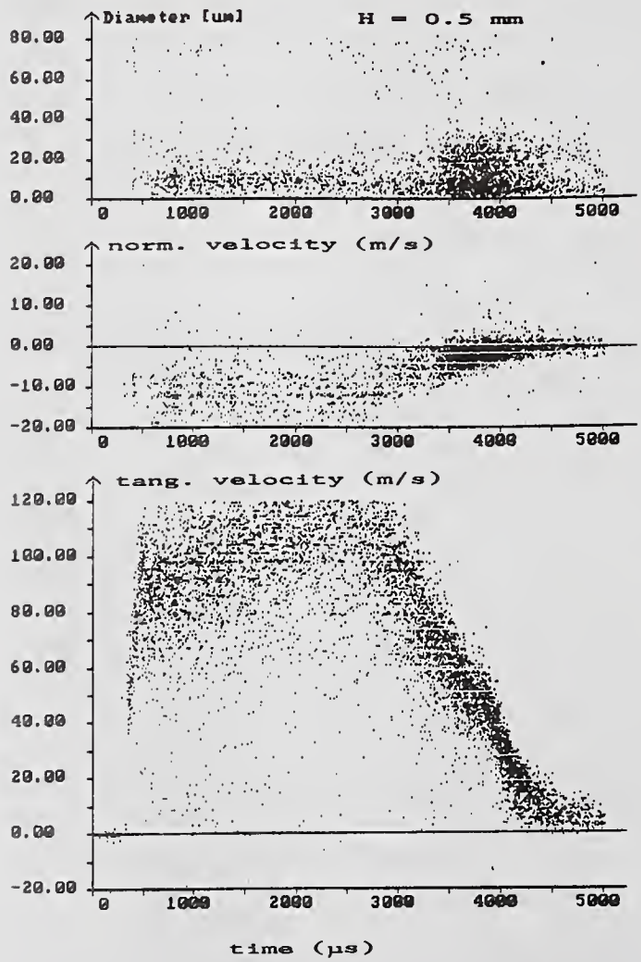

Fig.3 Time evolution of drop size and velocity at X = 6 mm.

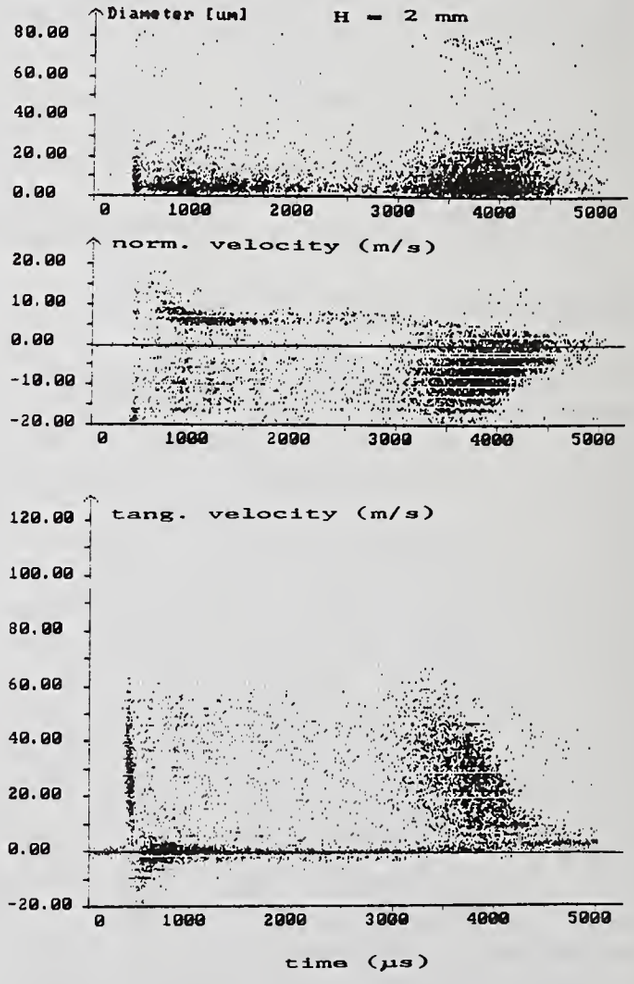

Fig.4 Time evolution of drop size and velocity at X = 6 mm.

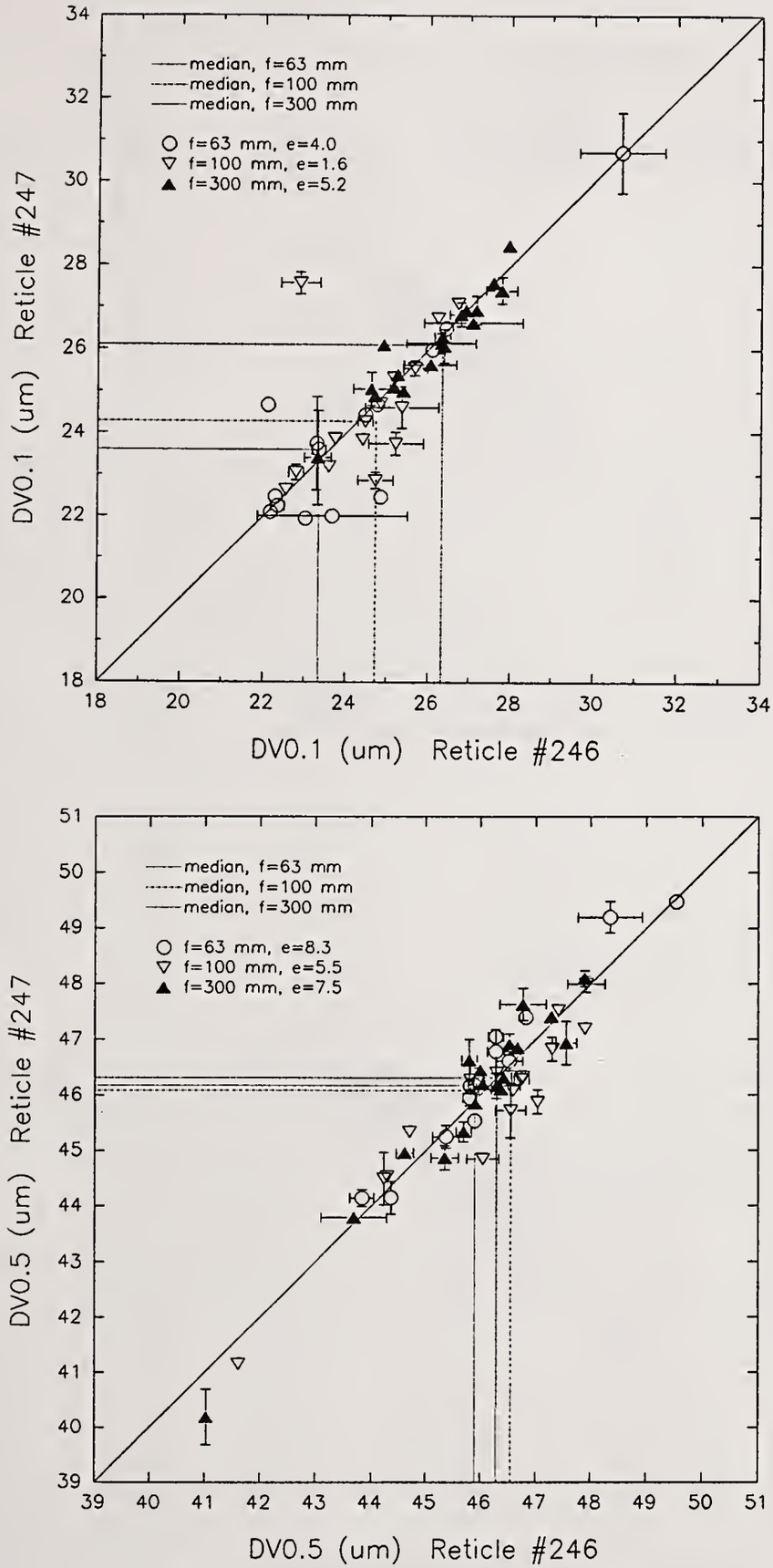

Figure 1. Plot of the final ILS test results for $D_{v0.1}$ and $D_{v0.5}$. The symbols indicate the mean of the data for the four repeated measurements for each reticle/lens combination in each lab. The error bars indicate one standard deviation of these four test results. The dashed lines indicate the median of the data for the three different lenses, and the ellipticity of the data for each lens are shown in the legend.

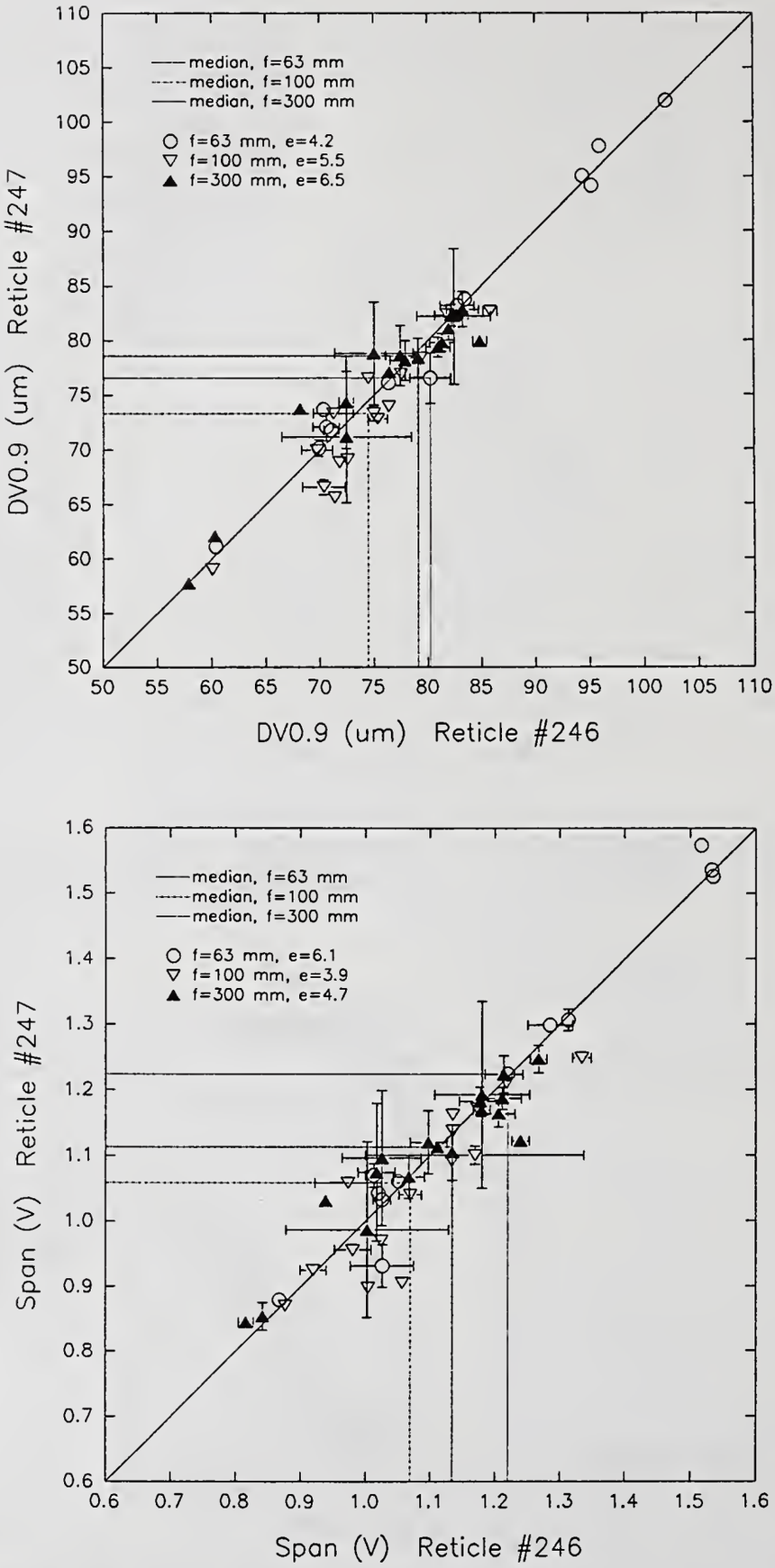

Figure 2. Plot of the final ILS test results for $D_{v0.9}$ and relative span (volume basis). The symbols indicate the mean of the data for the four repeated measurements for each reticle/lens combination in each lab. The error bars indicate one standard deviation of these four test results. The dashed lines indicate the median of the data for the three different lenses, and the ellipticity of the data for each lens are shown in the legend.

Table II. Image-analysis Reference Value for Reticles used in the ILS.

Test Result	Reticle Serial #	Reference Population Value (μm)	Parsed Number Value (μm)	Volume Equiv. Sphere Multiplet Value (μm)	Area Equivalent Value (μm)	Image-analysis Reference Value[1] (μm)
$D_{V0.1}$	246	25.74	26.16	26.39	29.63	27.0 ± 2.3
$D_{V0.1}$	247	25.82	26.24	26.46	29.60	27.0 ± 2.4
$D_{V0.5}$	246	47.54	47.95	49.80	51.38	49.2 ± 2.3
$D_{V0.5}$	247	47.26	47.66	49.41	51.26	48.9 ± 2.7
$D_{V0.9}$	246	69.15	69.40	72.78	78.52	72.5 ± 5.1
$D_{V0.9}$	247	69.33	69.57	72.77	78.75	72.6 ± 6.3

[1]The image-analysis reference value is taken as the mean of the four estimates. The uncertainty limits for the image-analysis reference values represent 95% confidence intervals based on estimates of precision and bias error in assigning the values.

Table III. Precision Statistics for the Test Method (all focal lengths grouped).

Test Result	Reticle Serial #	Mean of ILS Results X (μm)	Within-lab Repeatability Limit r[1] (μm)	Between-lab Reproducibility Limit R[1] (μm)	Rel. Within-lab Repeatability Limit r/X (%)	Rel. Between-lab Reproducibility Limit R/X (%)
$D_{V0.1}$	246	25.09	± 1.25	± 5.18	± 5.0	± 20.7
$D_{V0.1}$	247	25.04	± 0.91	± 5.37	± 3.7	± 21.5
$D_{V0.5}$	246	46.05	± 0.56	± 4.26	± 1.2	± 9.3
$D_{V0.5}$	247	46.05	± 0.59	± 4.57	± 1.3	± 10.0
$D_{V0.9}$	246	77.47	± 3.95	± 26.50	± 5.1	± 34.2
$D_{V0.9}$	247	77.33	± 6.80	± 29.18	± 8.8	± 37.7

[1]The precision indices r and R, defined in E691-87, are 2.83 times the repeatability (within-lab) and reproducibility (between-lab) standard deviations, respectively.

Table IV. Bias of the Test Method (all focal lengths grouped).

		ILS Results		Image-analysis		Bias Estimates	
Test Result	Reticle Serial #	Mean Value (μm)	Reproducibility Limit R (μm)	Reference Value (μm)	Uncertainty Limits[1] (μm)	Measured Bias (μm)	Statistically Significant?
$D_{V0.1}$	246	25.09	± 5.18	27.0	± 2.3	-1.9	No
$D_{V0.1}$	247	25.04	± 5.37	27.0	± 2.4	-2.0	No
$D_{V0.5}$	246	46.05	± 4.26	49.2	± 2.3	-3.1	No
$D_{V0.5}$	247	46.04	± 4.57	48.9	± 2.7	-2.8	No
$D_{V0.9}$	246	77.47	± 26.50	72.5	± 5.1	5.0	No
$D_{V0.9}$	247	77.33	± 29.18	72.6	± 6.3	4.7	No

[1]The uncertainty limits for the image-analysis reference values represent 95% confidence intervals based on estimates of precision and bias error in assigning the values. The statistical significance indication also is for 95% confidence.

CORRECTING MALVERN PARTICLE SIZE MEASUREMENTS FOR PHASE DISTORTION

R.A. Pietsch, P.E. Sojka and G.B. King

Thermal Sciences and Propulsion Center
School of Mechanical Engineering
Purdue University
West Lafayette, IN, U.S.A.

1 ABSTRACT

The two effects of phase distortion on particle size measurements made with a Malvern Spray Analyzer are identified as beam spread and a shift of the Airy pattern extrema to higher spatial frequencies. Beam spread is shown to be present regardless of the laser beam coherence length (l_c), while the Airy pattern shift occurs only when the size of the particle being sampled exceeds l_c. A correction scheme that removes the effects of phase distortion when possible is outlined, and then evaluated by comparing phase distorted particle size information with its undistorted counterpart. The enhanced agreement indicates the proposed technique successfully removes the effects of phase distortion when possible. Finally, guidelines are provided for determining when phase distortion is present.

2 INTRODUCTION

The quality of atomization cannot be ignored when considering the performance of any liquid fueled combustion system. Information about both the mean particle size and distribution of particle sizes is important to the combustion engineer in his search for more efficient combustor designs and alternative fuels. A popular optical method of collecting this size information utilizes Fraunhofer diffraction of a laser beam as it passes through a spray. Currently, measurement systems based on Fraunhofer diffraction are commercially available; the Malvern Spray Analyzer is one such system. Unfortunately, recent studies of particle sizing in high temperature turbulent environments have shown that this type of instrument, in its current form, is incapable of accurately measuring the scattered light profile and yielding the desired particle size data [1,2]. The inaccuracies noted in References 1 and 2 result from optical perturbations present in the system being studied.

The primary perturbing optical effects associated with laser beam propagation in a high temperature turbulent environment are known as beam wander and phase distortion. Beam wander occurs when the laser beam encounters an index of refraction gradient and is displaced, or steered, from its normal path of propagation. Phase distortion occurs when different points on the same laser beam wavefront vary in phase after passing through an index of refraction gradient.

The effects of beam wander were studied in detail by Miles et al [2] and a technique was developed to successfully compensate for this phenomenon. Miles et al also suggested that any errors remaining in the particle distribution measurements after correcting for beam wander were due to phase distortion. Support for their hypothesis was provided by performing a Young's double slit experiment at various temperatures to measure Michelson's visibility, arguing that Michelson's visibility was equivalent to the complex degree of coherence between two points on the laser beam, and then noting that the observed decrease in coherence length was indicative of an increase in the level of phase distortion.

Leader [3] studied phase distortion, concentrating on how it affects laser beam propagation through weakly and strongly turbulent atmospheres. He discovered that as the turbulence

became stronger, phase distortion's effects were dominant over those of beam wander. Leader also noted that as phase distortion increased, the ability to focus the beam to a given spot size decreased. Additionally, the unfocused beam's diameter, known as the beam spread, was seen to increase log-normally as phase distortion increased.

This increase in beam diameter is an important issue since some of the incident beam's energy will emerge from a spray as unscattered light. In many diffraction based instruments, this unscattered energy is removed from the particle diffraction profile by measuring the background light intensity incident on the photodiode. Leader's work therefor suggests that a background light intensity reading for a phase distorted beam will have a greater intensity at lower spatial frequencies than for an undistorted beam.

Two conclusions can be drawn from the work of Miles et al and Leader. First, the effects of phase distortion become more pronounced as the turbulence within a system increases. Second, since the amount of beam spread, and thus additional background intensity, is dependent on the flow conditions, a separate background intensity reading should be taken at each temperature or flow velocity being investigated in order to eliminate this effect of phase distortion.

Two issues, however, remain to be addressed. First, how is a researcher to know when the effects of phase distortion are important, and second, are there any further effects of phase distortion that must be eliminated or compensated for.

The goal of the this work then is twofold: to develop a technique that eliminates the errors resulting from phase distortion whenever possible and to outline a procedure that will aid users in determining when the effects of phase distortion are present. The next section provides a summary of the theory needed to accomplish these objectives.

3 THEORY

In order to develop a correction scheme to remove the effects of phase distortion on optical particle sizing with the Malvern instrument, it is first necessary to determine if phase distortion is present and, if so, to describe its impact. Phase distortion is present if the medium of interest reduces the spatial coherence length of a laser beam passing through it. Its effect on Malvern particle size measurements depends on the relative size of the perturbed laser beam's spatial coherence length and the diameter of the largest particle to be sampled.

A level of phase distortion such that the spatial coherence length of a beam passing through the medium is less than the diameter of the largest particle in a spray indicates that all particles are not illuminated coherently. Fraunhofer diffraction by apertures illuminated using partially incoherent light was studied by Shore et al [4] who showed that a gradual loss in the intensity contrast of the diffraction signature occurs as the coherence length decreases. Furthermore, when the coherence length approaches zero, the diffraction maxima and minima shift to higher spatial frequencies. This indicates that more light would be incident on the Malvern detector array at larger radii, thus skewing the particle size distribution to smaller diameters.

Phase distortion on this level can be detected by employing a calibrated aperture. Specifically, a pinhole may be introduced into the phase distorting media and its intensity profile obtained using the Malvern receiver. If the diffraction maxima and minima of the resultant Airy pattern are shifted to higher spatial frequencies, the particle size measurements cannot be corrected. Consequently, a series of calibrated apertures is inserted into the flow with the smallest pinhole exhibiting no shift in its diffraction extrema, for a given flow condition, indicating the largest particle that can be accurately sized. A correction scheme was developed for this case.

When no shift in the position of the diffraction extrema occurs for any particle, the complex degree of coherence, γ, is used to describe the optical perturbations. By examining the scattering geometry illustrated in Figure 1, and following the notation from Hecht and Zajac [5], the complex degree of coherence may be derived in the following fashion.

Consider two identical apertures or particles as the source of the diffracted radiation. If they are located at a distant plane along the path of propagation, the electromagnetic fields can be combined as:

$$E_P(t) = \bar{K}_1 E_1(t - t_1) + \bar{K}_2 E_2(t - t_2) \tag{1}$$

where $t_1 = r_1/c$ and $t_2 = r_2/c$. The $\tilde{K}$ factors depend on the size and location of the scatterers relative to the point P and also account for absorption, diffraction and other physical effects. Defining $\tau = t_2 - t_1$ allows the time origin to be shifted and the $\tilde{K}$ factors to be removed with the result that the mutual coherence function can be defined as

$$\Gamma_{12}(\tau) = < E_1(\tau + t) E_2^*(t) > \tag{2}$$

Normalizing the mutual coherence function by the magnitude of the two sources gives the complex degree of coherence

$$\gamma_{12}(\tau) = \frac{< E_1(\tau + t) E_2^*(t) >}{(< |E_1|^2 >< |E_2|^2 >)^{1/2}} \tag{3}$$

The magnitude of $\gamma_{12}(t)$ is between 0 and 1. If it is equal to unity the field at P is the result of two coherent waves out of phase by some quantifiable amount while if the magnitude is zero then the two waves are said to be incoherent. Any value of $\gamma_{12}(t)$ between these two extremes defines partial coherence.

Thompson [6] studied diffraction and interference from multiple apertures and arrays by looking at the generalized interference law:

$$I_R = \sum_{n=1}^{N} \sum_{m=1}^{N} (I_n I_m)^{1/2} |\gamma_{nm}(0)| \cos(\beta_{nm}(0) + \delta_{nm}) \tag{4}$$

where I_n and I_m are the intensities produced by each beam individually, $|\gamma_{nm}|$ is the modulus of the complex degree of coherence between apertures n and m, and

$$\beta_{nm}(\Delta) = 2\pi\bar{\nu}\Delta + arg(\gamma_{nm}(\Delta)) \tag{5}$$

$$\delta_{nm} = (2\pi/\bar{\lambda})(r_m - r_n) \tag{6}$$

Here r_m and r_n are the path lengths from the two source points to the observation point, Δ is the path difference divided by the speed of light, $\bar{\nu}$ is the mean frequency, and $\bar{\lambda}$ is the mean wavelength of the laser beam. It is important to note that

$$|\gamma_{nm}(0)| = 1, \qquad n = m$$

$$|\gamma_{nm}(0)| = |\gamma_{mn}(0)|$$

For a circular source illuminating a regular array of circular apertures, only nearest neighbor apertures along the array directions can be arranged to be incoherent with respect to each other. That is, for a regular array, $\gamma_{n,n+1}(0) = 0$ is a possible occurrence. However, because the spacing of the Airy ring minima is not constant, some degree of coherence between an aperture and its non-nearest neighbors will always exist. This implies that unless the coherence length is much less than the spacing of the array, no difference will be seen in the resulting diffraction pattern.

This observation is important to the operation of particle sizing instruments based on forward light scattering since it suggests that if phase distortion produces a beam whose coherence length is greater than the diameter of the largest particle to be sampled then the shape of the diffraction profile will be the same as for the unperturbed case.

Thompson also investigated diffraction from irregular arrays using lycopodium powder. Of specific interest were the diffraction profiles that resulted from using illumination whose coherence length ranged from several thousand to only a few particle diameters. The results showed no loss in fringe contrast with a drop in coherence length, as perhaps might have been predicted from the work of Shore et al. The only difference was a "smoothing" of the intensity profiles as the coherence length decreased since the values of γ_{nm} contribute less to the sum in Eqn (4).

In summary, the level of phase distortion can be determined by sampling the Airy patterns produced by a series of calibrated apertures. The minimum size aperture yielding a pattern not

shifted to higher spatial frequencies must be greater than the largest particle to be sized or the measurements cannot be corrected. If this condition holds, the work of Thompson shows that the phase distorted diffraction profile will not differ from the undistorted profile. Furthermore, under these conditions the only effect of phase distortion that need concern the user of a Fraunhofer diffraction based particle sizing instrument is beam spread. Fortunately, this spread, which will appear as undiffracted light in the energy profile, can be removed by acquiring the instrument's background signal under the conditions that lead to phase distortion and then processing the particle scattering data using the standard software. A demonstration of this technique is provided in Section 5.

4 EXPERIMENTAL APPARATUS

A Malvern 2600HSD diffraction based particle sizing instrument was employed in this investigation since the Malvern serves as a sort of default standard in diffraction based systems and Malverns have been used extensively in industry and research applications by many individuals and groups. A high temperature flow tunnel was used to generate the desired optical perturbations. It has been described in detail by Miles [7].

In order to isolate the effects of phase distortion on the particle diffraction profile, it was first necessary to remove the effects of beam wander. This was accomplished by utilizing the conditional sampling hardware developed by Miles et al [2]. This hardware was added to the optical train developed to study phase distortion and is denoted by the extension ".BW" in Figure 2. It includes a 4% reflection beam splitter, a focusing lens (250 mm focal length), a four-quadrant photodetector, and electronic circuitry used to compare the laser beam's wandered position to that of the ambient situation. If the wandered beam's position is within an acceptable window, the conditional circuitry triggers the Malvern receiver to collect the diffraction profile information.

In order to ensure that a repeatable particle size distribution could be obtained throughout the course of the experiments, a standard reticle was employed [8]. It had best-fit Rosin-Rammler parameters of N = 3.20, $\overline{X}$ = 52.8 μm, and SMD (Sauter mean diameter) = 40.27 μm.

Several issues had to be considered when observing the effects of phase distortion on the unscattered laser beam, on the diffraction pattern from the reticle, and on the diffraction pattern from the calibrated apertures. The ability to reproduce the same diffraction pattern from either a calibrated aperture or the reticle was limited by the ability to reproduce their exact physical location within the optical train. The repeatability of such a task was determined through trial and error to be low, regardless of the positioning method employed. In order to observe each of the above profiles individually, without having to reposition the reticle or calibrated aperture, the experimental apparatus shown in Figure 2 was utilized.

The optical hardware illustrated in Figure 2 consists of a 10 mW HeNe laser whose beam is spatially filtered and collimated to a diameter of 4.5 mm, plus two Mach-Zehnder interferometers in series that sample and redirect the laser beam and the diffraction profiles resulting from the reticle and calibrated aperture. As shown in Figure 2, the calibration aperture and reticle are permanently positioned in separate arms of the interferometers, thus guaranteeing that their diffraction profiles are reproducible. The interferometer arrangement also allows for observation of the effects of phase distortion on the undiffracted laser beam by adjusting the iris diaphragms to block off both the reticle and aperture. As a result, the user can observe each of the relevant intensity profiles individually without having to reposition the reticle or calibrated aperture between runs.

Experimental data obtained using the apparatus presented in Figure 2 are introduced in the next section and indicate the effects of phase distortion on the standard instrument's performance, plus the enhanced agreement that results from correcting particle size data for phase distortion.

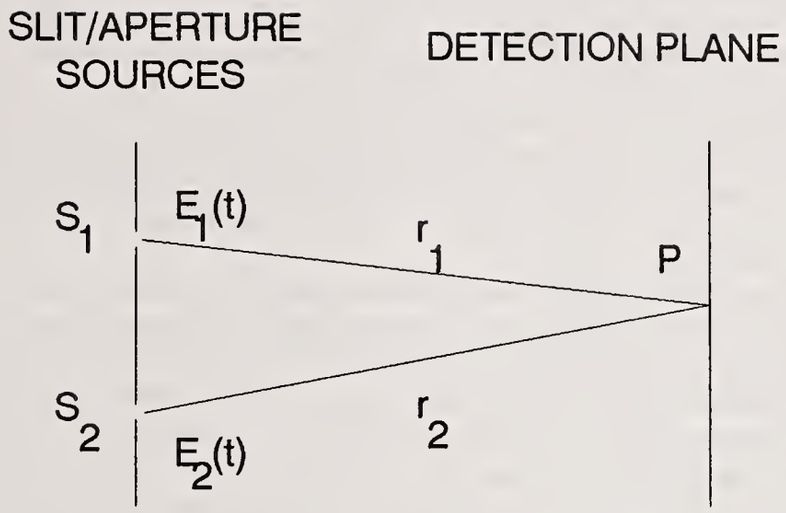

Figure 1. Scattering geometry for two identical apertures.

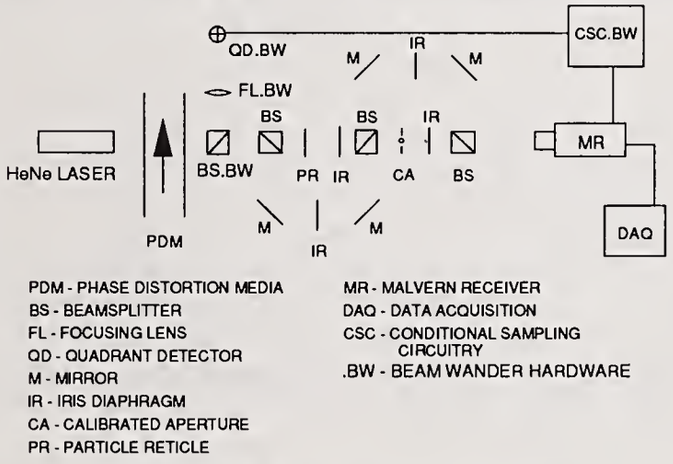

Figure 2. Experimental apparatus.

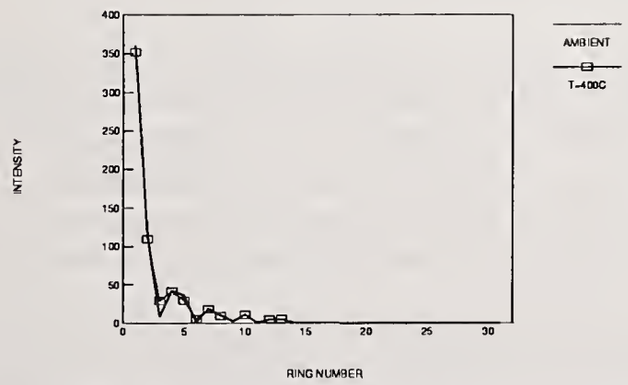

Figure 3. Fraunhofer diffraction profiles for a 600 μm diameter pinhole.

5 RESULTS

Data acquisition commenced by placing the calibrated aperture and reticle in their respective interferometer arms, centering the Malvern photodiode array on the laser beam, and aligning the beam wander conditional sampling hardware. Three sets of ambient background, calibrated aperture diffraction profile, and particle diffraction profile data were then collected by shutting the appropriate iris diaphragms. At this point, the blower supplying air to the test section was started and an air velocity of 25 m/s was established in the test section. The air temperature was adjusted to 200, 400 and then 600 C with one background profile, three calibrated aperture diffraction profiles, and three particle diffraction profiles obtained at each temperature. The entire process was performed once a day for three days for a total of nine data points at ambient and each of the elevated temperatures.

As mentioned previously, the calibration aperture serves as a users' guide to recognize when phase distortion is present and indicates the largest particle diameter that can be sized without phase distortion affecting the light intensity profile. Sample intensity profiles for a phase distorted and non-phase distorted aperture (circular pinhole, d = 600 μm) are shown in Figure 3. The agreement between the two profiles indicates no shift in the maxima or minima and therefor a coherence length greater than 600 μm. Consequently, all particles up to the 564 μm limit measurable using the Malvern's 300 mm focal length lens will be coherently illuminated and the only effect that need be considered is beam spread.

A sample phase distorted diffraction profile from the reticle appears in Figure 4. Compared to a non-phase distorted profile, the perturbed profile reveals large intensity variations at lower spatial frequencies, i.e. in the innermost photodiode rings, due to beam spread. However, at larger spatial frequencies no intensity variation is observable supporting the conclusion that the spatial coherence length was larger than the largest particle in the distribution. Figure 5 shows the background readings corresponding to each of the profiles in Figure 4. By subtracting the background taken under phase distorting conditions from the phase distorted particle profile, a corrected diffraction profile is generated and used to determine the particle size distribution. An example profile appears in Figure 6; comparing it to the light intensity profile of Figure 4 clearly demonstrates the improvement achieved when using the correction procedure outlined above. This improvement is also apparent from the Malvern calculated Rosin-Rammler size distribution parameters for the uncorrected and corrected profiles, as shown in Tables 1 and 2. Uncertainties in these tables are reported as one standard deviation. Note that the discrepancies between the ambient and 200, 400 and 600 C corrected values for $\overline{X}$, N and SMD are within the sum of their standard deviations, with the exception of the 600 C value for N. In contrast, the discrepancies between the ambient and uncorrected 400 and 600 C values for $\overline{X}$, N and SMD are at best one standard deviation and most often greater than 2σ.

6 SUMMARY

The two effects of phase distortion on the diffraction pattern produced by a particle, beam spread and a shift of the Airy pattern extrema to higher spatial frequencies, have been noted. Beam spread is present regardless of the laser beam coherence length (l_c), while the Airy pattern shift occurs only when the size of the particle being sampled exceeds l_c. A procedure to determine the coherence length under phase distorting conditions was described and a correction scheme was developed to remove the effects of phase distortion when all particles have diameters less than l_c.

The correction scheme is straightforward, requiring only that the Malvern's background signal be acquired under the same phase distorting conditions as the particle diffraction profile. The data may then be processed using the standard Malvern software.

The correction technique was evaluated by comparing phase distorted diffraction profiles and background intensities with their undistorted counterparts that were collected under identical flow conditions. Results showed that phase distorted intensity profiles yielded particle distribution parameters that were as much as 9% in error. Parameters calculated from corrected intensity

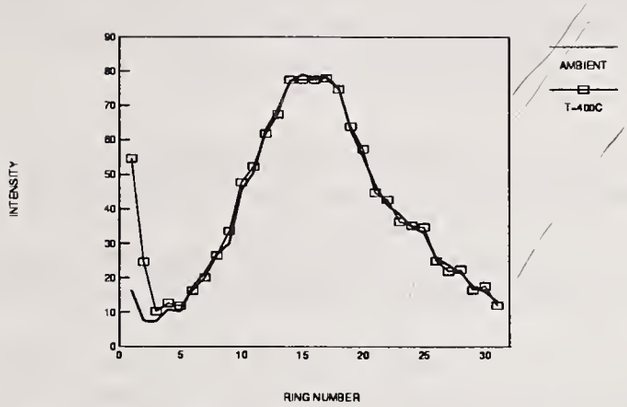

Figure 4. Fraunhofer diffraction profiles for the reticle.

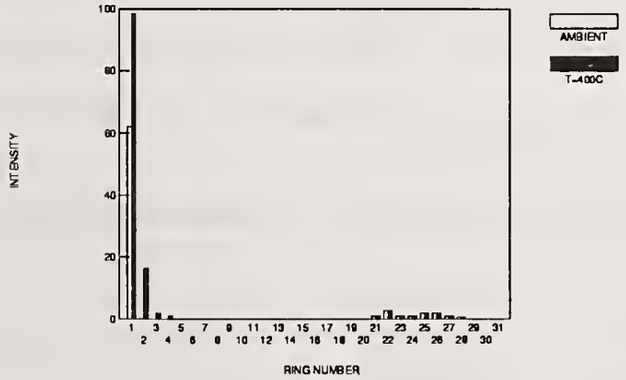

Figure 5. Ambient and high temperature backgrounds.

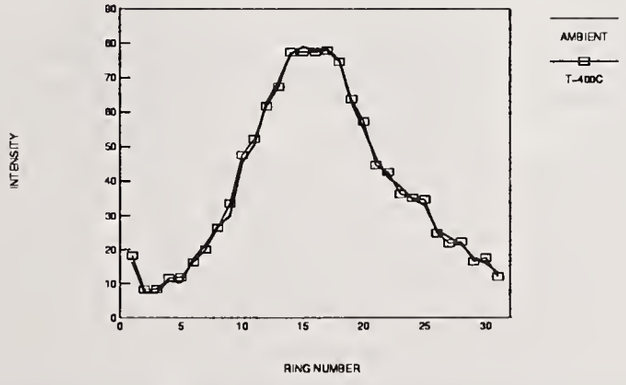

Figure 6. Fraunhofer diffraction profile corrected for phase distortion.

profiles, however, were within 2 % of those obtained under ambient conditions. This indicates the proposed technique successfully removes the effects of phase distortion when possible.

We thank E.D. Hirleman (Arizona State University) for several helpful discussions and B.H. Miles (US Army Waterways Experiment Station) for providing comments on an early version of this manuscript.

REFERENCES

1. Roesler, T.C., Lefebvre, A.H. and Sojka, P.E., "Fuel Atomization at High Ambient Temperatures," Central States Section/Combustion Institute paper 86-6D1, NASA-LeRC, Cleveland, OH (1986).
2. Miles, B.H., Sojka, P.E. and King, G.B., "Malvern Particle Size Measurements in Media with Time Varying Index of Refraction Gradients," Applied Optics, Vol. 29, No. 31, pp. 4563-4573 (1990).
3. Leader, J.C., "Beam Properties of Partially Coherent Curved Beam Waves in the Turbulent Atmosphere," Journal Optical Society America Vol. 70, pp. 682-688 (1980).
4. Shore, A., Thompson, B.J. and Whitney, R.E., "Diffraction by Apertures Illuminated with Partially Coherent Light," Journal Optical Society America, Vol. 56, 733 (1966).
5. Hecht, E. and Zajac, A., *Optics*, Addison-Wesley, Reading MA, (1979).
6. Thompson, B.J., "Multiple-Beam Interference with Partially Coherent Light," Journal Optical Society America, Vol. 56, pp. 1157-1161 (1966).
7. Miles, B.H., "Optical Particle Sizing in a High Temperature Environment," M.S. Thesis, Purdue University (1988).
8. Hirleman, E.D., "On Line Calibration Techniques for Laser Diffraction Particle Sizing Instruments," ASME Paper No. 83-GT-232.

Table I. Particle Size Distribution Parameters for Uncorrected Data

Temperature, C	$\overline{X}$, μm	N	SMD, μm
20	52.34±0.18	3.40±0.03	41.97±0.04
200	52.86±0.07	3.39±0.00	42.33±0.57
400	54.99±0.73	3.24±0.06	43.47±0.33
600	56.25±0.32	3.17±0.17	44.15±0.48

Table II. Particle Size Distribution Parameters for Corrected Data

Temperature, C	$\overline{X}$, μm	N	SMD, μm
20	52.34±0.18	3.40±0.03	41.97±0.04
200	52.45±0.00	3.39±0.00	42.00±0.00
400	52.03±0.70	3.35±0.07	41.53±0.49
600	51.85±1.05	3.55±0.08	42.03±0.61

A COAXIAL-BEAM DROP SIZING INSTRUMENT FOR DENSE SPRAYS

W.M. Grissom

Physics Department
Morehouse College
Atlanta, GA, U.S.A.

ABSTRACT

A low-cost instrument has been developed to measure drop size and speed in dense sprays. The instrument uses two coaxial laser beams of different colors. The smaller locater beam defines the center of the larger main beam and triggers a measurement only when a drop passes through the center of the main beam. Light scattered perpendicular to the beam is focused through a double slit imaging system which avoids partial obscuration of the image. A vibrating glass tube produces a uniform drop stream for calibration. A simple "scattering tomography" analysis accounts for beam attenuation. Fluctuations in beam intensity are also considered. Data in a spray nozzle are reported. Both the diameter and speed histograms are best fit by a log-normal function.

INTRODUCTION

A review of most drop sizing techniques up to 1978 is given by Azzopardi [1]. Since then the Polarization Ratio [2,3], Phase Doppler [4], and Pulse Intensity [5-7] techniques have been developed. The present instrument is of the latter type.

The Pulse Intensity techniques determine the drop size by measuring the scattered pulse as a drop crosses a laser beam. This gives a robust signal with simple optics. The main problem is that the scattered intensity depends upon the path the drop follows across the beam. Since the laser beam normally has a Gaussian intensity distribution, a drop passing far from the beam center gives a smaller pulse height than if it passed through the center. This problem is termed "Gaussian ambiguity".

An obvious solution to the Gaussian ambiguity problem is to generate a beam with a uniform ("tophat") profile, but this has proven difficult [8]. Instead, several researchers [5,6] developed deconvolution algorithms to analytically correct for the ambiguity. Another obvious solution is to accept a Gaussian beam, but define the center of the beam such that measurements are triggered only when a drop passes through the center.

Hess [7] used a laser velocimeter to define the beam center. Since the velocimeter signal is weak, forward scattered light was collected by viewing the beam at an oblique angle, greatly increasing the probe volume size. Since the velocimeter probe volume must be about 4 times wider than the drop to give a good visibility signal and the main beam must be about 5 times wider than the velocimeter probe volume, the minimum average drop spacing is about 20 drop diameters, which is fairly sparse.

EXPERIMENTAL APPARATUS

The optical arrangement is shown in Figure 1. A small yellow beam (He-Ne, 594 nm) defines the center of a coaxial red beam (He-Ne, 633 nm). The red main beam is about 5 times larger than the yellow locater beam at the probe volume. A similar coaxial arrangement was reported by Wang and Hencken [9]. Light scattered at 90° is imaged onto the main slit. The slit width, together with the beam diameter defines the size of the probe volume. The two colors are separated by an edge filter. The red light, from the main beam, is reflected into a photomultiplier. The yellow light, from the locater beam, is re-imaged onto the "locater slit".

The locater slit views only the center of the main slit, ignoring drops which are partially obscured by the edges of the main slit. The locater photomultiplier triggers a measurement only when a drop passes through the center of the main beam and is centered in the view of the main slit. Umhauer [10] reported a similar two slit imaging system, with the slits in parallel.

A locater pulse triggers storage of a main photomultiplier pulse with a Rapid Systems R2000 digital O-scope. The digitized pulse is fit to a Gaussian curve by a logarithmic transform to a parabola and linear regression. About 50 samples per pulse are needed to average over ripples on the pulse. The pulse peak determines the drop diameter and the width determines the speed transverse to the beam. Checks on the fitting error help eliminate drop coincidences in the probe volume. Since both size and speed are obtained, either a flux or spatial drop size distribution can be generated and speed-size correlations can be obtained.

Since the pulse amplitude is approximately proportional to the square of the drop diameter, care must be taken to provide a wide dynamic range. Previous researchers used logarithmic amplifiers. Instead, the programmable gain feature of the digitizer is used. Measurements are made at three gain ranges. The processing rate is usually slower than the data rate. To avoid bias against the busier ranges, a set of pulses is digitized and the elapsed time recorded. The pulses are then processed and the histogram bins incremented inverse to the digitization time.

The transmitted beam is focused onto a pinhole in front of a phototube. A 4 axis positioning system controlled by a Precision Micro Control DCX-8 board allows translations in the scattering plane and rotations about the spray and collection axes. A vacuum collects the spray drops, allowing operation with the spray pointing upward.

CALIBRATION

A glass pipet is drawn to a small diameter and cleaved. A laminar jet of liquid is forced from the pipet while vibrated by a speaker. At certain frequencies the jet breaks into a stream of uniform drops. Sakai [12] gave a detailed report on the phenomenon. A time trace is shown in Figure 2. The drops almost overlap in the main beam. The ripples in the main pulses are due to noise in the beam profile. Reducing the beam diameter

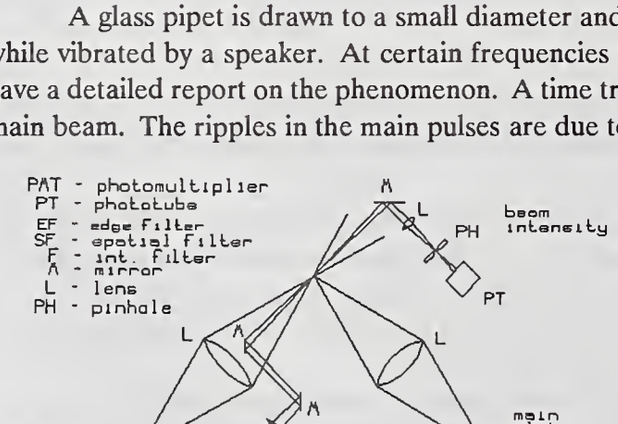

Fig. 1 Optical arrangement

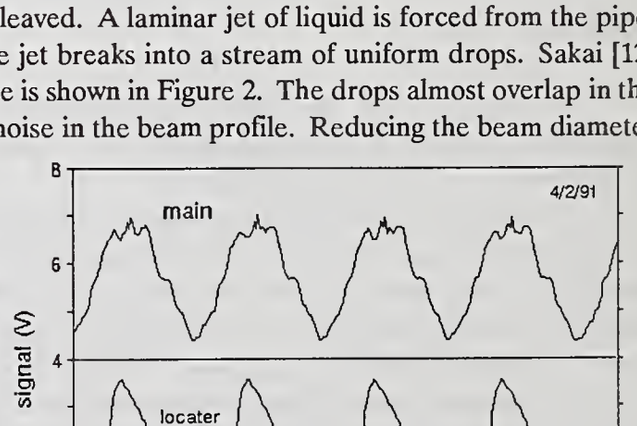

Fig. 2 Photomultiplier signals with uniform 230 umD drops, 700 umD main beam, 200 umD locater beam

yields smoother pulses. The spatial filter partially obscures the main beam, resulting in steeper edges than a true Gaussian pulse, which is advantageous in decreasing overlap of adjacent pulses.

Knowing the frequency and flow rate, the drop diameter is easily calculated. The calculated size has been verified using a microscope, with stroboscopic illumination. Photographing the drop stream and measuring the drop spacing allows calculation of the speed. Comparing this with the e^{-2} pulse width (temporal) allows calculation of the e^{-2} beam width, which is the calibration constant for speed.

Since the drops follow a very defined path through the beam, the drop stream must be scanned back and forth across the beam to test the instrument's resolution. The resulting histograms are shown in Figure 3. Equally narrow histograms are obtained for scans along the laser beam. Disabling the locater beam gives the histograms shown in Figure 4, displaying the "Gaussian ambiguity". It appears difficult to deconvolve the diameter histogram to appear as that in Figure 3, as suggested by Holve and Self [5] and Mizutani [6]. The speed histogram is less affected. Theoretically, with a Gaussian beam, it should be unaffected [5]. However, in practice the degradation is severe.

Scanning the drop stream across the laser beam also allows determination of the size of the locater probe volume, by noting the limits over which the locater beam is triggered. Wang and Hencken [9] found that large drops are more likely to trigger a measurement. However, testing with drops from 163 to 279 μmD, using a locater beam about 200 μmD and locater slit 500 μm wide, showed no difference in probe volume size. Therefore no correction is made for size bias. The likely explanation is that most of the light scattered at 90° is due to total internal reflection from a small region on the back of the drop, so that the effective scattering area of a drop is much smaller than the actual cross section.

Calibration results are shown in Figure 5. Ideally, the drop diameter should be proportional to the square root of the normalized scattered intensity, however a slight curvature is apparent as the drops increase in size. An explanation results by averaging the beam intensity over the drop cross section, giving the fit shown in Figure 5. The best fit occurs by assuming a main beam diameter (D) of 700 μmD, although the curvature is so slight that a much larger value would make little difference. The beam diameter estimated by eye was 550 μmD, while the speed calibrations determined 578±63 μmD. The difference is again attributed to the effective scattering diameter being smaller than the actual diameter.

For drops smaller than about 10 μmD, the light collection cone is not large enough to average over the Mie interference pattern and the calibration curve becomes multivalued. However, few drops this small exist in the sprays tested. Calibration streams smaller than 150 μmD can be generated, but the drops overlap in the probe volume, so that the lower end of the calibration curve has not been verified. One solution is to decrease the number density by electrostatically deflecting away every other drop [13].

Calibrations using 8 different liquids suggest a linear relation between the apparent diameter increase and the refractive index relative to water, as shown in Figure 6. The incident light was polarized perpendicular (vertical) to the scattering plane. For most low molecular weight liquids the correction is fairly small.

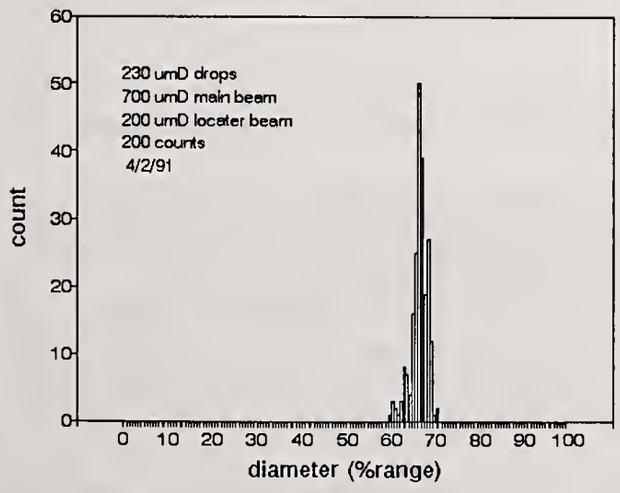

Fig. 3 a) Diameter histogram with drops scanned across beam

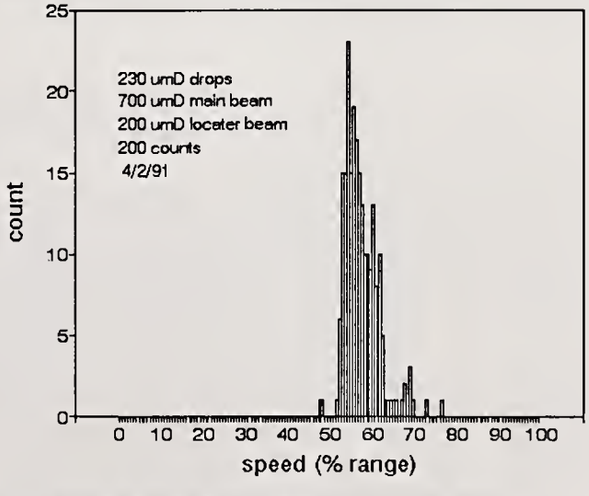

Fig. 3 b) Speed histogram with drops scanned across beam

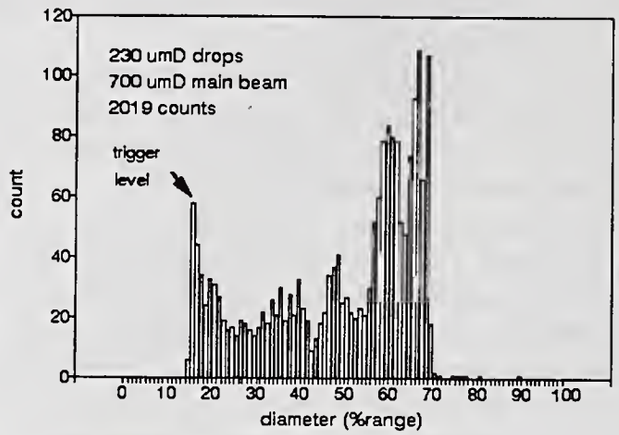

Fig. 4 a) Diameter histogram without locater beam

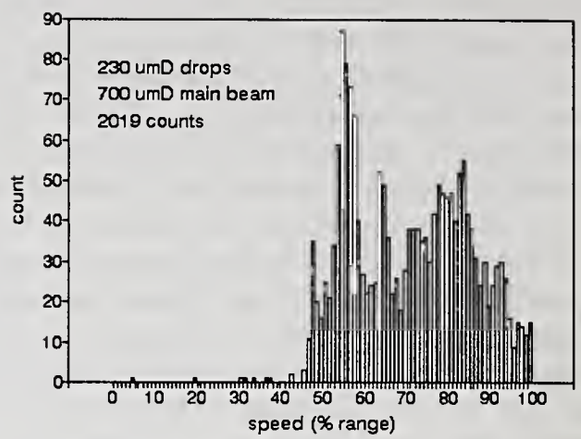

Fig. 4 b) Speed histogram without locater beam

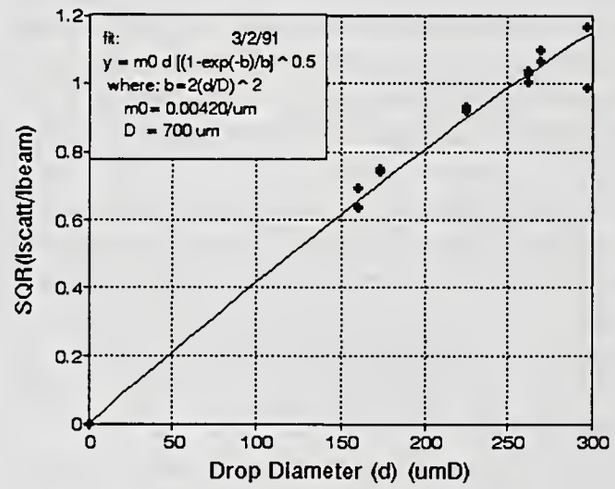

Fig. 5 Diameter calibration

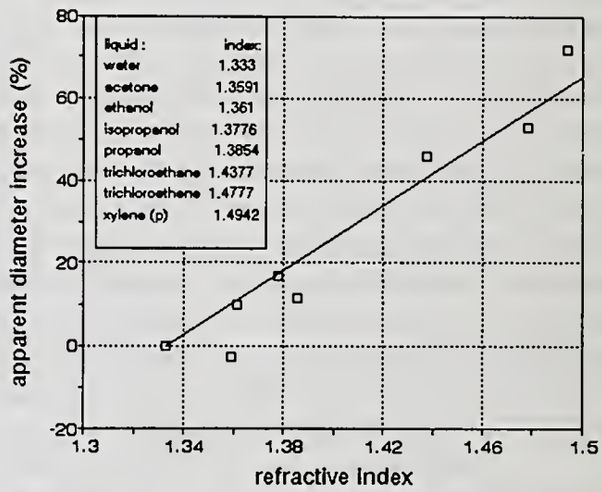

Fig. 6 Effect of refractive index on drop size , rel. to H2O

By averaging over the beam area, a large drop gives a slightly wider pulse as it crosses the beam than a small drop. The resulting pulse is still essentially Gaussian. Numerical integration predicts a fractional increase in pulse width of $0.539(d/D)^{2.3\,4\,6}$, where d is the effective scattering diameter. The present scatter in the speed calibrations (±11%) preclude verifying this prediction.

BEAM ATTENUATION

In a dense spray the laser beam is attenuated in traveling to the probe volume and the scattered light suffers attenuation in exiting the spray. These attenuations cause the drop pulses to appear smaller than normal and must be corrected.

The transmittance to the probe volume is found by passing the beam from the left and right, in turn: $t_\ell = [(t_\ell / t_r)T]^{1/2}$, where t_ℓ and t_r are the transmittances for the beam from the left and right, respectively, and T is the total transmittance. A linear "absorption" law (actually scattering) is assumed, i.e. $T = t_\ell\, t_r$.

The pulse height histograms appear similar in each case, with the abscissas simply scaled by the ratio of the beam intensities. The ratio t_ℓ / t_r is thus found by ratioing the peak values of the two histograms. The collected light transmittance is the same fraction in each case, so that the ratio is unaffected. It is not actually necessary to pass a beam from the right. The same geometry results by rotating the spray 180° about the collection axis, i.e. so that the spray points upward.

This analysis has general application to any problem where the attenuation is due partially to scattering, and the "absorptivity" at every point in a cross section is desired, for example in studying soot generation. The

"absorptivity" at every point along a line through the region can be found by differentiating the transmittances along the line. This analysis is best termed "scattering tomography".

The transmittance along the collection path can be found by rotating the spray 90° about the spray axis, as shown in Figure 7, making the former collection path (t_3) align with the beam, allowing its transmittance to be determined. Denote the peak of the measured pulse height histogram by $P_{k\theta}$, where $k = \ell$ or r for the beam from the left or right, respectively, and $\theta = 0°$ or 90° for the spray at the original orientation or rotated 90° about the vertical, respectively. t_i denotes the transmissivity along the four paths shown and T_1 and T_2 are the transmittances along the two perpendicular paths across the spray. The corrected pulse height peak is found as: $P = P_{\ell 0°}/(t_1 t_3)$. Expressing t_1 and t_3 with the scattering tomography analysis above eventually results in an identity (note $T_1 = t_1 t_2$ and $T_2 = t_3 t_4$):

$$P = \left[\frac{t_1 t_2 t_3 t_4 \; PP}{T_1 \; T_2}\right]^{\frac{1}{2}}$$

Referring to Figure 7, the possibilities for the numerator are:

$$(t_1 t_3 P)(t_2 t_4 P) = P_{\ell 0°} P_{\ell 180°}, P_{\ell 0°} P_{r270°}, P_{r90°} P_{\ell 180°}, \text{ or } P_{r90°} P_{r270°}$$
$$(t_1 t_4 P)(t_2 t_3 P) = P_{\ell 90°} P_{r0°}, P_{\ell 90°} P_{\ell 270°}, P_{r180°} P_{r0°}, \text{ or } P_{r180°} P_{\ell 270°}$$

These are summarized as two procedures: (1) after the first measurement, rotate the spray 180° about the spray axis, or (2) after the first measurement, rotate the spray 90° about the spray axis and 180° about the collection axis (to pass beam from right). The first procedure is more convenient since the spray remains pointing downward. It is interesting that including the collection attenuation leads to a simpler procedure than considering the input attenuation alone. Beretta [2] states the same result for the case of an axially symmetric spray. As seen here, the result is not restricted to axial symmetry.

A related problem is that the beam attenuation is not constant, due to statistical fluctuations in the number of drops along the path to the probe volume. The collected light also fluctuates, but it is not significant due to the large collection cone.

A drop scatters most of the light incident upon its cross-sectional area out of the beam. An equal amount of light is diffracted, but most of it remains within the confines of the beam. Scattering causes localized shadows in the beam profile, giving ripples on the pulses. However, the Gaussian fitting largely negates the ripples, so that only temporal fluctuations in the spatially averaged intensity need be considered.

Assuming a uniform beam intensity and a mono-disperse spray, the fraction of beam energy scattered by a single drop is $(d/D)^2$. The total fraction attenuated is: $A = 1\text{-}\exp[-N(d/D)^2]$, where N is the number of drops in the beam. According to Poisson statistics, the attenuated fraction fluctuates by an rms fraction $A/\sqrt{N}$, so the rms beam intensity fluctuation is:

$$I_{rms}/I = (d/D)\, A[-\ln(1-A)]^{-\frac{1}{2}}$$

For both very low and very high attenuations there is little fractional intensity fluctuation. The maximum fluctuation occurs at an attenuation of 71.5%, in which case $I_{rms}/I = 0.638(d/D)$. Given the square root relation, the corresponding diameter fluctuations are half this. It is desirable to converge the main beam as it approaches the probe volume, so that its average diameter through the spray is increased, decreasing the fluctuations.

Hess [11] measured intensity fluctuations of +/-14%, at a beam attenuation of 10.7%. The beam diameter was about 600 μmD at the probe volume, and somewhat larger in the spray. Since the attenuating drops were far upstream, a factor of 2 should be added to account for diffraction. The analysis would then predict an rms fluctuation of $\sqrt{2}(d/D)(0.318)$. The average drop size in the spray was not stated. To agree with the above analysis, the drops would have to have been an average of 187 μm in diameter.

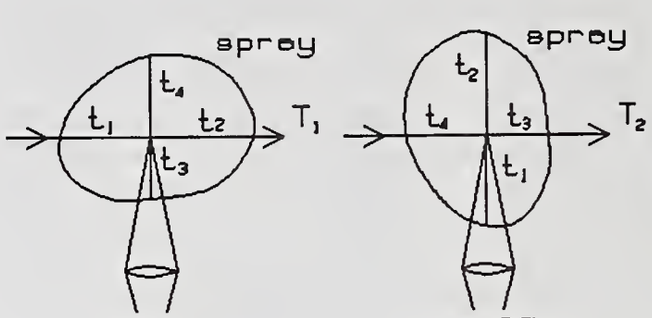

Fig. 7. Input and collection attenuation

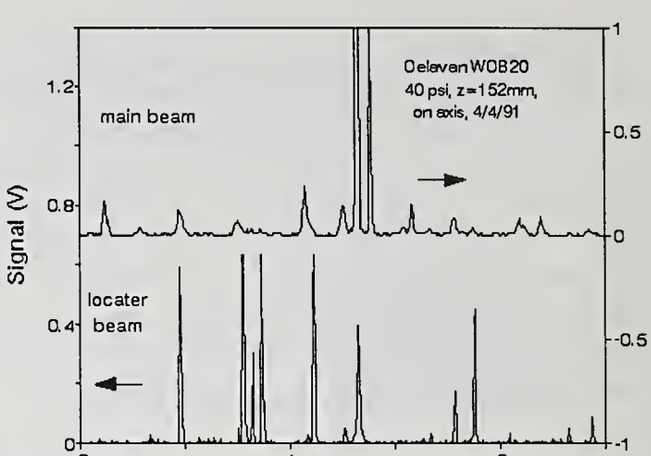

Fig. 8 Photomultiplier signals in spray

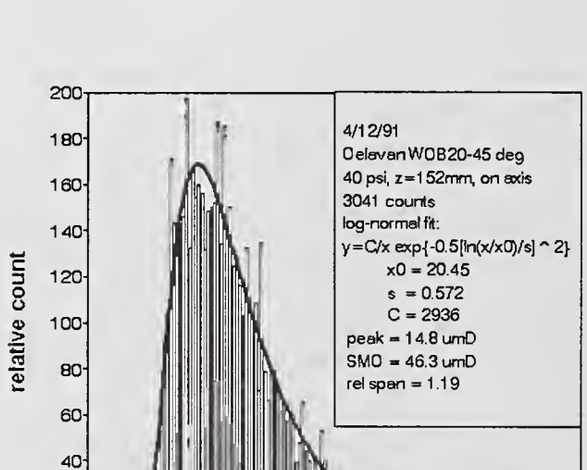

Fig. 9 (a) Drop size distribution in spray

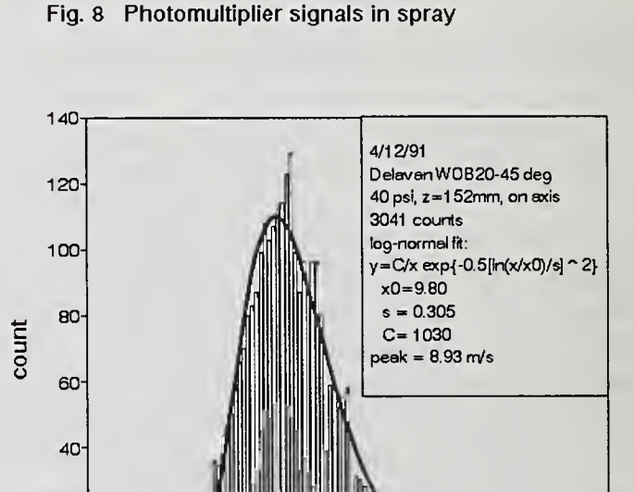

Fig. 9 (b) Speed distribution in spray

EXPERIMENTAL RESULTS

Measurements in a Delavan WDB20-45° nozzle spraying water at 276 kPa, 685 cc/min, 152 mm from the nozzle on the centerline, are shown in Figures 8 and 9. Similar shaped drop size distributions have been reported [6,14,15].

To insure that the rapid cutoff on the low side of the drop size histogram was not due to instrument sensitivity, the time traces were monitored. The smallest drops detected had locater pulses well above the trigger threshold, so that drops smaller than the 5 μmD limit in Figure 9a could have been detected. The limiting drop size is probably due to the limited kinetic energy available to atomize the liquid.

The log-normal function gives the best fit to both the diameter and speed histograms, as shown in Figure 9:

$$f(x) = (C/x)\exp\{-\tfrac{1}{2}[\ln(x/x0)/s]^2\} \quad ; \quad \text{normalize: } C = 1/[s(2\pi)^{1/2}]$$

The parameters x0 and s control the peak and width of the distribution. An upper limit modification to the log-normal function has been suggested [16], however, the addition of a third parameter confuses the data analysis. Such a limit is better added at the modeling stage.

The Nukiyama-Tanasawa (N-T) function has also been used:

$$f(x) = C\, x^m \exp[-(x/x0)^p] \quad ; \quad \text{normalize: } C = p/\{x0\,\hat{}\,(m+1)\,\Gamma[(m+1)/p]\}$$

where $\Gamma()$ is the gamma function. When exponent m is restricted to (p-1) it is termed the Weibull function [17]. One difficulty is that the N-T function does not maintain a similar shape. For wide distributions it is skewed left, appearing similar to the log-normal function, whereas for narrow distributions it becomes skewed right. Also, if $m < 0$ it predicts an infinite number of drops as the diameter approaches zero.

Another popular function is the Rosin-Rammler, usually expressed as a cummulative volume fraction:

$$F_V(x) = 1\text{-}\exp[-(x/x0)^p]$$

however,

$$F_V(x) = \frac{\pi}{6}\int_0^x x^3 f(x)dx$$

so that it is seen to be simply the Nukiyama-Tanasawa function with $m = p-4$, a fact noted by Bevans [18].

For application to combustion models, an efficient procedure should exist to generate random variates from the selected distribution function. When the cumulative distribution function (cdf) can be analytically inverted, random variates are generated simply as $X = F^{-1}(R)$, where $F^{-1}()$ is the inverse cdf and R is a random number from 0 to 1 [19]. Examples are the exponential function, used in Los Alamos' KIVA code [20], and the Weibull function. The log-normal cdf cannot be inverted, however efficient methods exist for generating random variates from it [19, p 132].

The Delavan nozzle used was the subject of a "round-robin" test, using 6 different drop sizing instruments [21]. At the test conditions of Figure 9a they reported Sauter Mean Diameters (SMD) from 65 to 180 μmD and "relative spans" from 0.95 to 1.7. The present data gives an SMD of 46.3 μmD and 1.19 relative span. However, the SMD is a poor basis for comparing distributions from single particle counters since it is overly sensitive to the tail, where the counts are very low.

The beam attenuation through the center of the spray was 19.4%, with an rms fluctuation of 2.42%. The previous attenuation analysis calculates an equivalent monodisperse drop size of 16.4 μmD, for the 400 μmD (minimum) main beam, which is close to the peak value of 14.8 μmD in Figure 9a. Doubling the pressure to 552 kPa hardly changed the peak diameter (15.8 μmD) but narrowed the distribution (SMD = 36.3 μmD), while the peak velocity increased from 8.93 m/s to 11.0 m/s.

CONCLUSIONS

A low-cost instrument has been developed to allow drop size and speed measurements in dense sprays. The design overcomes previous difficulties with Pulse Intensity methods. A simple "scattering tomography" analysis accounts for beam attenuation through the spray. Drop size and speed distributions in the Delavan spray are best fit by a log-normal distribution.

ACKNOWLEDGEMENTS

The research followed a 1986 UES/AFOSR Summer Faculty Research Program (SFRP) tenure at the Air Force Phillips Lab and a 1988 SFRP tenure at Arnold Engineering Development Center. Michael Powell at the Phillips Lab assisted with the initial design and Chad Limbaugh at Arnold Engineering supported tests in a model rocket injector. Research sponsored by the Air Force Office of Scientific Research, under Contract F49620-88-C-0053.

REFERENCES

1. Azzopardi, B.J., "Measurement of Drop Sizes", Int. Journal of Heat and Mass Transfer, Vol 22, pp. 1245-1279 (1979).
2. Beretta, F., Cavaliere, A., and D'Alessio, A., "Drop Size and Concentration in a Spray by Sideward Laser Light Scattering Measurements", Combustion Science and Technology, Vol 36, pp 19-37 (1984).
3. Presser, C., Santoro, R.J., and Semerjian, H.G., "Velocity and Droplet Size Measurements in a Fuel Spray", AIAA 24th Aerospace Sciences Meeting, AIAA-86-0297, (Jan 1986).
4. Bachalo, W.D. and Houser, M.D., "Phase/Doppler Spray Analyzer for Simultaneous Measurements of Drop Size and Velocity Distributions", Optical Engineering, Vol 23, no 5, pp 583-590, (Sept/Oct 1984).
5. Holve, D. and S.A. Self, "Optical Particle Sizing for in situ Measurements, Part II", Applied Optics 18, p. 1646 (1979)
6. Mizutani, Y., Kodama, H., and Miyasaka, K., "Doppler-Mie Combination Technique for Determination of Size-Velocity Correlation of Spray Droplets", Combustion and Flame, Vol 44, pp 85-95 (1982).
7. Hess, C.F. "Nonintrusive Optical Single-Particle Counter for measuring the Size and Velocity of Droplets in a Spray", Applied Optics, Vol. 23, no 23, pp 4375-4382 (Dec 1984).
8. Eauret, P.R. et al, "Measurement of Drop Size and Velocity in Vaporizing Sprays, in Proceedings, Second Int'l Conference on Liquid Atomization and Spray Systems, Madison, Wisconsin, p 261 (June 1982).
9. Wang, J.C.F. and Hencken, K.R., "In situ Particle Size Measurements using a Two-Color Laser Scattering Technique", Applied Optics, Vol 25, no 5, pp 653-657 (March 1986).
10. Umhauer, H., "Particle Size Dist. Analysis by Scattering Light Meas. using an Optically Defined Measurement Volume", Journal of Aerosol Science, Vol 14, no 6, p 765 (1983).
11. Hess, C.F., "An Instrument to Measure the Size and Velocity of Particles in Particle Laden Flows", 21st Joint Propulsion Conference, Moterey, California, AIAA-85-1443 (July 1985).
12. Sakai, T., Sadakata, M., Saito, M., et al, "Uniform Size Droplets by Longitudinal Vibration of Newtonian and non-Newtonian Fluids", Second Int'l Conference on Liquid Atomization and Spray Systems, Madison, Wisconsin, pp 37-45 (June 1982).
13. Keng, Weaver, and Orr. "A Study of Vibrating Capillary Atomizers", Georgia Institute of Technology Engineering Experiment Station Report, Grant B-279 (April 1967).
14. Bolle, L. and Moureau, J.C., "Spray Cooling of Hot Surfaces" in Multiphase Science and Technology, Vol 1, (G.F. Hewitt, J.M. Delhaye, and N. Zuber, Eds.), pp. 1-10, Hemisphere Publ., Washington (1982).
15. Hiroyasu, H., Kadota, T., and M. Arai, "Supplementary Comments: Fuel Spray Characterization in Diesel Engines" in Combustion Modeling in Reciprocating Engines (Mattavi, J.N. and Ammna, C.A., Eds.), pp. 369-405, Plenum Press, N.Y. (1980).
16. Dobbins, R.A. "Light Scattering and Transmission Prop. of Sprays", Phd. Thesis, Princeton Univ. (1960).
17. Derman, C., Gleser, L., and Olkin, I., A Guide to Probability Theory and Applications, Holt, Rinehart, and Winston (1973).
18. Bevans, R.S., "Mathematical Expressions for Drop Size Distributions in Sprays", Conference on Fuel Sprays, Univ. of Michigan (March 1949).
19. Dagpunar, J. Principles of Random Variate Generation, Clarendon Press (1988).
20. Amsden, A.A., J.D. Ramshaw, et al. "KIVA: A Computer Program for 2 and 3 - Dimensional Fluid Flows with Chemical Reactions and Fuel Sprays", Los Alamos National Laboratory Report LA-10245-MS (Feb 1985).
21. Dodge, L.G., "Comparison of Drop-Size Measurements for Similar Atomizers", Special Report No. SwRI-8858/2, Office of Naval Reseach, (December 1986).

MEASUREMENT OF DROPLET SIZES BY LIQUID NITROGEN FREEZING METHOD

T. Karasawa*, S. Shiga* and T. Kurabayashi†

*Dept. of Mechanical Engineering, Gunma University, Kiryu, Gunma, Japan
†Hiroshima Institute of Technology, Hiroshima, Japan

ABSTRACT

A liquid nitrogen freezing method for accurate measurement of droplet sizes has been developed since 1971 and recently the final setup has been completed through the efforts for overcoming some problems and difficulties. Droplet sizes of water spray are measured by both the freezing method and the immersion sampling method and the results are compared. It is revealed that the number of droplets caught in the freezing method is several times as much as that of the immersion sampling method. The reason of the decrease of droplets number in the immersion sampling method is considered to be caused by the disappearing of smaller droplets due to evaporation. Therefore the Sauter mean diameter obtained by the immersion sampling method tends to be larger than that by the freezing method. Through the comparison experiment with immersion sampling method, it has been revealed the present apparatus can afford highly accurate value of droplet sizes.

INTRODUCTION

It is strongly desired to obtain accurate droplet sizes in the fields of liquid atomization technique. While various measuring methods have been used, few of them seems to be able to afford the reliable value of droplet sizes due to individual shortcoming essential to each method. The freezing method, in which liquid droplets are solidified by low temperature atmosphere possesses several advantages to obtain their accurate sizes. Since the first study on this method by Longwell(1) in 1943, several works in this field have been made by different investigators (2)-(7). In recent ten years, however, no successful results has reported.

The authors started the research on this freezing method in 1971. A cylindrical freezing chamber is air-proved to avoid generation of cloud in the chamber. Liquid nitrogen fed into the double wall space of the chamber vaporizes and forms cooling atmosphere. Liquid to be tested is injected downward through a nozzle and its frozen droplets fall onto a photographic film set on a bottom plate of the chamber. In order to avoid the severe problems of frosting and optical difficulty, a simple photographic technique called photogram is employed to get shadows of the droplets. In 1978, at the

first ICLASS, history of development of the research from the first trial setup to the sixth setup was reported and availability of this method for accurate measurement was suggested on the basis of the experimental results.

In 1979 and 1980, remarkable improvements had been made in the method and the seventh trial setup was designed and developed. Prior to the construction of this device, distance neccessary for droplets to freeze was theoretically estimated and evaporation of droplets were also calculated. The most important improvement in the setup was employment of 100 feet long film in a film suply system, which enables to obtain a significantly increased number of data in one series of experiment using liquid nitrogen filled in a 150 liter Dewer tank. The film suply system was also newly designed to protect the film against sudden exposure to the atmosphere with large temperature difference from room to freezing chamber, to avoid the temperature shock which deteriorates film emulsion. Using the setup, adequate exposure time to compensate the decrease of light sensitibity of the film emulsion due to lowered temperature, and adequate axial temperature gradient in the test chamber to form spherical frozen particles were searched experimentally. All these results were already reported (8).

Through further improvement made in recent years, the final setup has been completed for accurate measurement of droplet sizes. In this paper procedure of the improvements is described at first, and the accuracy of the freezing method is examined by comparing the droplet sizes obtained by this method with those by the another method. This time, the immersion sampling method is chosen as a representative of the other methods, which is widely used at present and is often employed as a standard method when comparison is required.

EXPERIMENTAL SETUP AND PROCEDURE

The arrangement of experimental devices is shown in Fig.1. The freezing chamber (32) is composed of a double wall type cylinder and a top and bottom end plates to keep airtight for avoiding generation of fog in the chamber. The inside of the chamber is kept dark. A length of 2 meter of the chamber was determined considering the analytical result mentioned above, and the inner diameter is 600 mm. The cylinder walls are made of 0.5 mm stainless steel plate. The thickness of the previous body wall was 1.0 or 1.2 mm, and this reducton of the wall thickness produced decreased heat capacity of the body, nitrogen consumption economy and easy control of ambient gas temperature. Liquid nitrogen in the Dewer tank (14) is poured into the gap between the inner and outer walls of the chamber cylinder and the evaporated nitrogen forms freezing atmosphere in the chamber. The amount of nitrogen supplied is measured by using a spring balance (13). The chamber is thermally insulated by foamed polystyrene with a thickness of 150 mm. Distribution of temperature in the freezing chamber is measured by thermocouples (29) set at seven heights, which can be moved radially by rotating a support bar (30). Thermocouples are also inserted in other parts, injection nozzle (5), film boxes (17) and (28), etc.. All of these sixteen thermocouples are connected to a data-logger(1) and their measurement time is controled by a micro computor.

When the temperature distribution in the chamber achieves required profile, a new part of a 35 mm roll type long film is pulled out from the film box (28) through the temperature buffer (25) at adequate speed for avoiding heat shock, and is set on a film guide (23). On the guide the spread film forms a collective area of frozen particles with a width of 24 mm and a length of 600 mm. These operations are made automatically by a rolling system

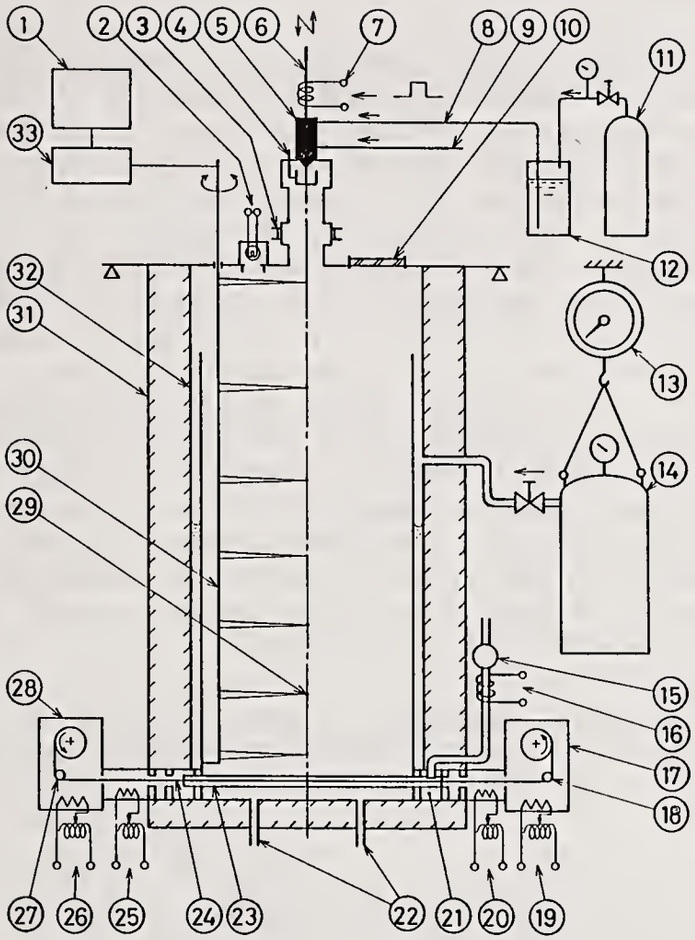

Fig.1 The eighth apparatus

consisted of a photo-detect counter (27), an inverter motor and an electronic control circuit. Liquid to be tested is then injected downward into the freezing chamber. When the smallest frozen particles are considered to reach the film completely, shadows of the frozen particles are recorded on the film by the technique called photogram, at which direct exposure is made to the light from the bulb (2) for adequate duration determined depending on the coldness of the film. As soon as the exposure is finished, the exposed part of the film is rolled up into the film box (17), and the frozen particles on the film are replaced by a suction unit (15). The photogramed particles are printed with magnification of 20 and then measured.

Since the experiments for comparison of the two methods have to be carried out under the same conditions as far as possible, the chamber of the freezing method is also used to carry out the experiment of immersion sampling method and the sampling cells are placed at the same position as that of the film supply system in the freezing method. All the experiments are carried out on water spray injected through a hole nozzle with 0.3 mm diameter. Injection pressure is changed in four steps, i.e. 12, 10, 8 and 6 MPa, and the injection period is changed also in four steps, i.e. 150, 90, 40 and 30 millisecond. The injection period of 90 ms is set as a standard injection period. The quantities of water injected are chosen as small enough not to cause the coalescence of droplets at the immersion liquid surface and large enough to offer reasonable number of particles.

RESULTS AND DISCUSSIONS

Influence of Exposure Time to Low Temperature Atmosphere on its Negative

It is known that the application of sudden change of temperature to the film sometimes causes unevenness in density and spots or patches with irregular shape on its negative. However the details of these phenomena have not been clear. Therefore the following tests were carried out. The elapsed time from the setting of a film in alow temperature atmosphere of -100 C to the light exposure was changed as 0, 30 and 60 minutes, and then the film was developed. The result showed that the negative without elapsed time is normal, but a lot of fine spots appeared on the negative with 30 minutes elapsed time and the number of the spots increase in the case of 60 minutes. However since the contour of the spot is not clear, while that of the shadow of the frozen particle is quite clear regardless of its size, both the spots and the particles can be easily distinguished. Therefore, it is considered that the elapsed time of 30 minutes which generates relatively small number of the spots does not affect on the result of measurement. To avoid these undesiarable phenomena, in the present experiments the film is introduced into the chamber immediately before the liquid injection and rolled up into the film box as soon as the exposure is finished.

Comparison of the Number of Droplets Captured

In Fig.2 radial profiles of number density of droplet caught in the freezing

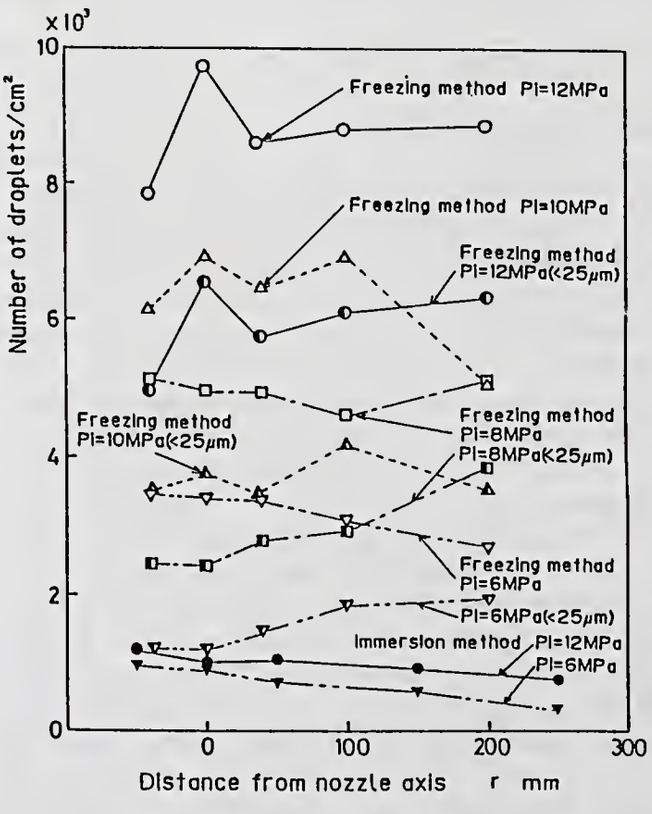

Fig.2 Variation of the number of droplets caught by both the freezing method and immersion method

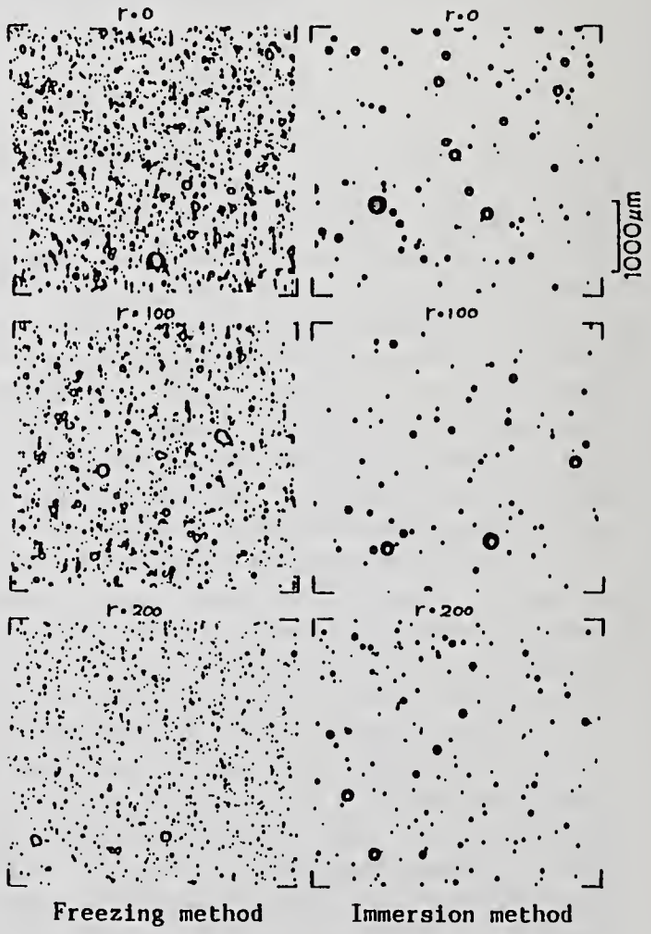

Fig.3 Photographs of droplets

method is compared with those in the immersion sampling method for four injection pressure levels. Some representative photographs of droplets in the two methods are shown in Fig.3. The figure shows that the number of droplets caught in the freezing method is nine times as much as that in the immersion sampling method, and more than half of the number is occupied by the fine droplets smaller than 25 micrometer. These facts are caused by evaporation of the droplets during their flights in the ambient gas, and the increased evaporation rate as the diameter becomes small (8). In the freezing method droplets are prevented from evaporation due to the extremely low temperature atmosphere and almost all droplets can remain and are captured. Fig.2 also shows the same tendency as above.

Comparison of Sauter Mean Diameter in Two Methods

Fig.4 shows the radial distributions of local Sauter mean diameter obtained by freezing method and immersion sampling method. In Fig.4(a) it is shown that the Sauter mean diameters by the immersion sampling method are much larger than those by the freezing method over whole range of radial derection. A similar tendency was observed in the case of injection pressure of 10 MPa. The reason of these facts is that in the immersion sampling method the number of finer droplets is decreased by evaporation as mentioned above. Radial profiles of the mean diameter in (a) are more gentle than those in (b) and (c). This tendency may be caused by the fact that in the high pressure injection the size of droplets becomes smaller even at the center of the spray, and the ralatively larger droplets in the vicinity of spray axis are apt to be shifted toward periphery due to the high injection velocity.

In figure (b) in the case of injection pressure of 8 MPa, Sauter mean diameters by the two methods come to nearly the same at the vicinity of spray center. This is caused by that although the number of droplets obtained by the freezing method is larger than that of the immersion sampling method, the total number of droplets generated decreases and the number of large droplets over a diameter of 200 micrometer becomes to increase as the injection pressure decreases.

In figure (c) Sauter mean diameters by the immersion sampling method becomes larger again than those by the freezing method. As the injection pressure decreases the dispersion of spray becomes weak and the sizes of droplets increase. These tendencies bring larger possibility of coalescence of droplets when they are captured by immersion liquid. This fact shifts the value of mean diameter near the spray center. In the periphery of spray the mean diameters are shifted down nearly to the values of freezing method. In this region the increase of mean diameter due to the evaporation of fine droplets becomes small, the number of fine droplets decreases under the lower injection pressure.

Comparison of Size Distribution

In Fig.5 number distributions of droplets obtained by the freezing method are compared with those by the immersion sampling method. Difference is seen in the region of fine droplet under the condition of high injection pressure.

Influence of Injection Period on Sauter Mean Diameter

Injected liquid quantity was changed by changing the injection period to reveal their influence on Sauter mean diameter, and the results are shown in Fig.6. As seen in Fig.6(a) the mean diameter by the freezing method with injection periods of 30 and 70 millisecond is larger than those with 90 and 150 millisecond. This may be caused by the relatively longer transient period

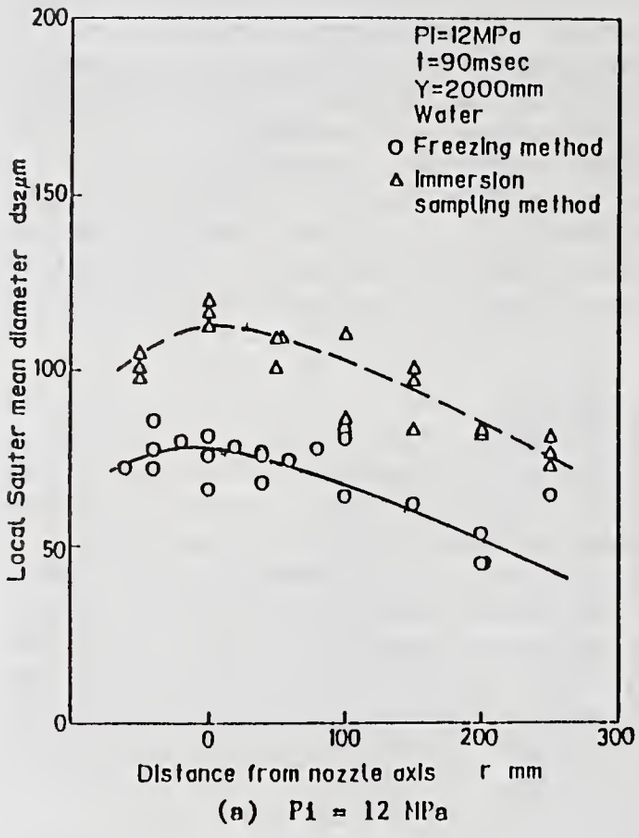

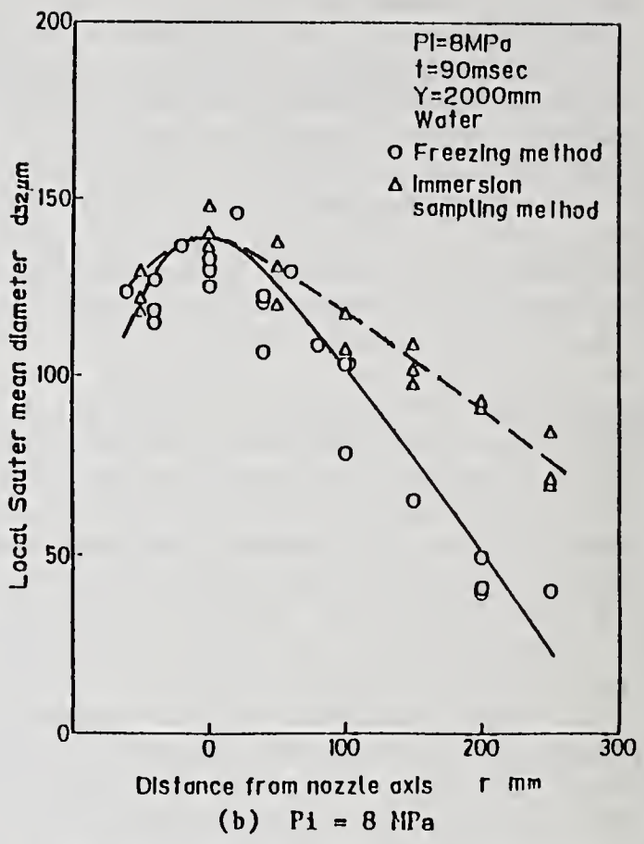

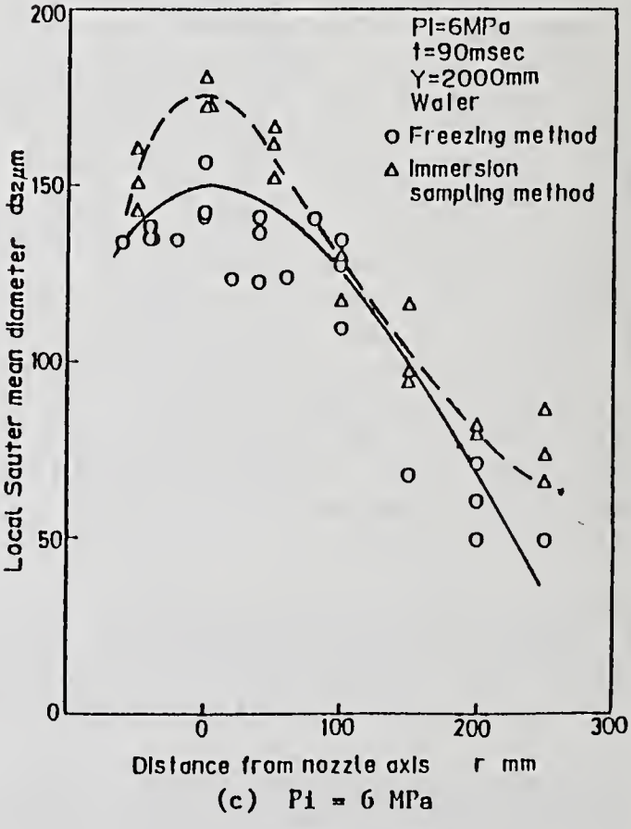

Fig.4 Comparison of local SMD by freezing method with that by immersion method

of nozzle needle motion in the case of shorter injection period where insufficient atomization occurs. In the immersion sampling method these differences are not recognized. Based on this result, it can be said that the freezing method is more sensible than the immersion sampling method.

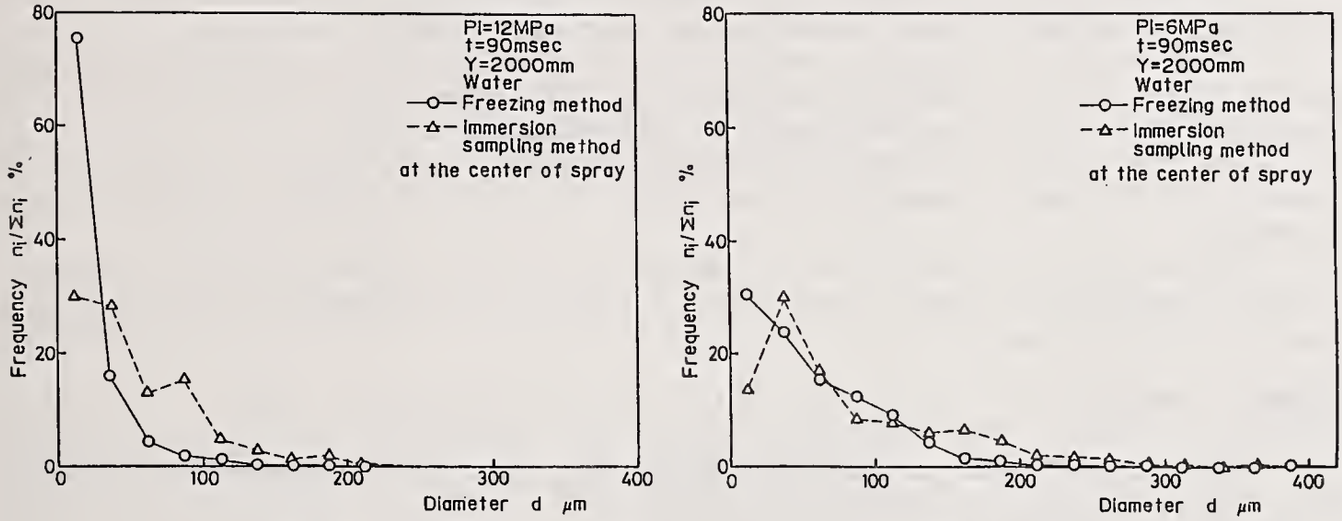

(a) Pi = 6 MPa (b) Pi = 12 MPa

Fig.5 Distribution of droplet size

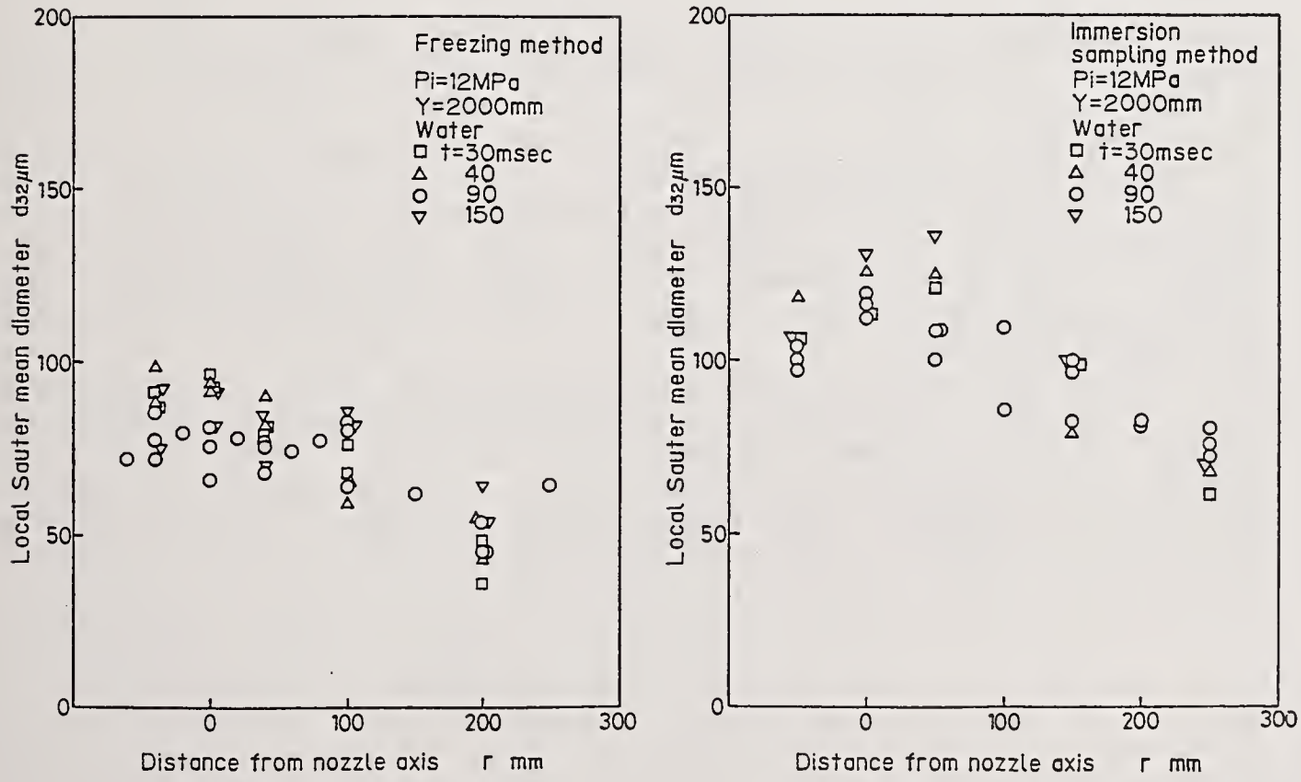

(a) Freezing method (b) Immersion method

Fig.6 Influence of injection period on local SMD

CONCLUSIONS

A new apparatus for accurate measurement of spray droplet sizes based on the liquid nitrogen freezing method has been constructed after the constructions of seven trial setups. Using this apparatus comparison tests with the immersion sampling method were carried out and the results are summerized as:

In the present apparatus improvements were made on some points for more reliable measurement, easy operation and nitrogen economy.

The immersion sampling method presents larger mean droplet diameter mainly due to disappearing of fine droplets by evaporation and coalescence of droplets occurs when they are captured by immersion liquid.

In the freezing method the evaporation and coalescence of droplets are almost avoided and, therefore, the method can afford highly accurate spray diameter.

Since the freezing method is based on a quite simple principle and has little possibility of error, the present setup is considered to be a standard measuring apparatus.

ACKNOWLEDGMENTS

The authors wish to thank Mr. Hisao Nakamura for his enthusiastic helps for constructions and tests of the apparatus.

This work was partly supported by the Tanikawa Foundation, Osaka, Japan.

REFERENCES

1 Longwell J P, Doctorial dissertation, Massachusetts Institute of Technology, 1943.

2 Taylor E H and Harman D B, 'Measuring Drop Sizes in Sprays', Industrial and Engineering Chemistry, Vol.46, No.7, pp.1455-1457, July 1954.

3 Tanasawa Y, 'Automobile Engines, Lecture', Toyota Gijutu, Vol.5, No.7, pp.24-34, 1952.

4 Joyce J R, 'The Atomization of Liquid Fuels for Combustion', Inst. Fuels J., Vol.22, No.124, pp.150-156, 1949.

5 Nelson P A and Stevens W F, 'Size Distribution of Droplets from Centrifugal Spray Nozzles', J. Am. Inst. Chem. Eng., Vol.7, No.1, pp.80-86, Mar. 1961.

6 Street P J and Danaford V E J, 'A Technique for Determining Droplet Size Distributions Using Liquid Nitrogen', J. Inst. Petroleum, Vol.54, No.536, pp.241-242, Aug. 1968.

7 Rao K V L, 'Liquid Nitrogen Cooled Sampling Probe for the Measurement of Spray Drop Size Distribution in Moving Liquid-Air Sprays', Proc. 1st ICLASS, Tokyo, pp.293-300, Aug. 1978.

8 Karasawa T, Kaeriyama H and Kurabayashi T, 'Freezing Method by Liquid Nitrogen for Measuring Spray Droplet Sizes', J. of the Fuel Society of Japan, Vol.62, No.679, pp.901-912, Nov. 1983.

LDV AND PDA ANALYSIS OF SPRAY-WALL INTERACTION

G. Brunello*, S. Callera*, A. Coghe†, G.E. Cossali† and F. Gamma‡

*CNPM-CNR, Peschiera Borromeo (MI), Italy
†Politecnico di Milano, Milano, Italy
‡Università "La Sapienza", Roma, Italy

ABSTRACT

A diesel spray impacting on a wall in a close chamber, under ambient air conditions, has been analysed by means of Laser Doppler Velocimetry (LDV) and Phase Doppler Anemometry (PDA) in order to measure droplet size and velocity in regions close to the wall. Spray behaviour has been characterized in terms of different injection periods and different spatial regions, and proper data analysis allowed to identify the main features of the droplet-wall interaction phenomenon.

INTRODUCTION

Recent theoretical predictions, experimental observations and engine tests [1] evidenced that the interaction of a diesel sprays with the piston wall might be beneficial to engine combustion because of the influence on fuel vaporization and heterogeneous mixture formation processes. Many experiments have been performed in the past by different groups [2,3,4,5] to investigate the spray-wall interaction, generally using high-speed photography, and the first submodel developed to describe the spray-wall interaction process has been presented very recently [6]. Spray-wall interaction characteristics seem to be controlled mainly by the drop Weber number although other parameters as wall temperature, fuel boiling temperature, drop impinging angle, swirl intensity, air density and temperature, Leidenfrost temperature, wall surface roughness have also been proven to be important. Analysis of spray-wall interaction is furthermore complicated, due to the interaction of spray droplets with entrained air flow [7], which makes unrealistic to extrapolate data obtained in experiments with single droplets.
Development and validation of a spray impingement model requires a large amount of experimental data on the droplets of a real spray, like size and velocity in the region close to the wall. The present research work was aimed to a detailed analysis of the spray wall impingement process, by using the Phase Doppler Anemometer (PDA) to obtain simultaneous measurements of spray drop size and velocity in the close proximity of the wall.

EXPERIMENTAL SET-UP

The experiment was performed in a closed cylindrical chamber (89 mm i.d.,300 mm height) equipped with two glass windows positioned to allow the use of the PDA in the 70 deg forward scattering configuration to reduce the effective probe volume dimensions (about 1mm in length and o.15 mm diameter) and the sensitivity of the phase shift to refractive index of the drops [9]. A standard diesel injector (Bosch single hole nozzle, 0.25 mm diameter) injecting at 45 deg with respect to the nozzle axis, was mounted off-axis on the top wall of the chamber.The injector was fed by a Bosch high-pressure pump driven at 500 rpm by an electrical motor and diesel oil was used as fuel. The impact wall, an aluminium disc (50 mm diameter) with a polished surface, was centred on the chamber axis and positioned at a distance of 20 mm from the nozzle tip. (see fig.1). The impingement distance (L) and the impingement angle (45 deg) were kept constant. The nozzle opening pressure was fixed at 20 MPa and the injection pressure history is shown in Fig.2. Operating experience indicated that the injection system provides very reproducible pressure time histories. The ambient gas was air at room temperature and pressure. The operating conditions of the experiment are summarized in Table 1.

Table 1 - Operating conditions

Nozzle diameter, d	(mm)	0.25
Max. fuel inj. pressure	(MPa)	70
Pump speed	(RPM)	500
Volume of fuel injected	(mm^3/inj)	36
Duration of injection	(ms)	3.4

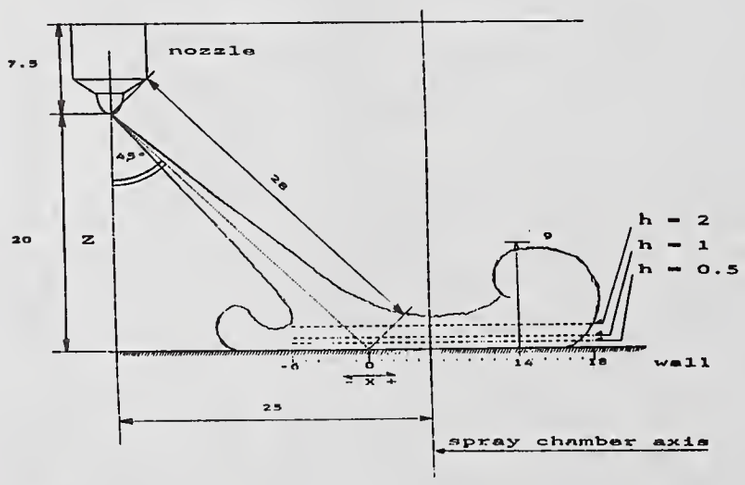

Fig.1 Schematic of the impingement experiment (all dimensions in mm).

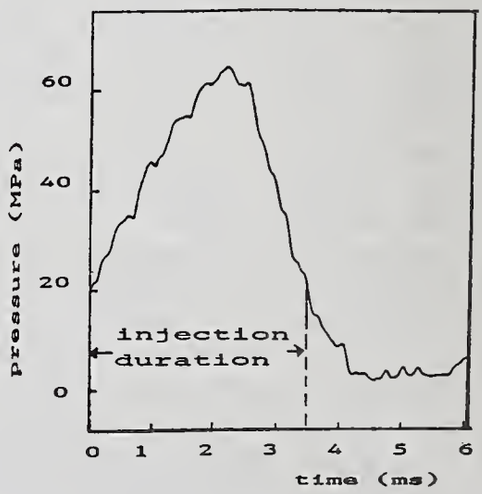

Fig.2 The liquid injection pressure.

Drop size and velocity were measured by the Phase Doppler Anemometer (Dantec PDA); the light source was an Argon-ion laser (5 W nominal power) and the transmitting optics comprised a 40 MHz Bragg cell for frequency shifting and directional sensitivity and a front lens of 300 mm focal length. The receiving optics was the 57X10 Dantec unit equipped with three preamplified photomultipliers. The covariance processor of the PDA instrument was capable of 1 μs time resolution in data acquisition and the data transfer rate, to a PC, was higher than 100 kHz. The frequency bandwidth (36 MHz) and the optical configuration of the transmitting optics defined a measurable velocity range from -25 to 125 m/s and a measurable size range from 2 to 80μm which resulted the most appropriate in the present case. Normal and tangential velocity components were measured at the same point at different times and drop size was measured together with the velocity component normal to the flat plate.
Measurements were performed at several locations on three lines at distances of 0.5, 1 and 2 mm from the surface (see Fig.1), laying on the symmetry plane normal to the wall. The investigated region extended from the impingement area to the boundary of the impact disc, in the downstream direction. Data acquisition, triggered by the needle lift opening at 20 MPa, covered a period of 5 ms for each injection and 5,000 to 10,000 data were collected over many consecutive injections for each measurement point. An encoder pulse with 1 μs resolution allowed a subsequent reconstruction of the size and velocity time history of each individual injection and also the application of time-ensemble averaging procedures.

RESULTS AND DISCUSSION

A typical result for the drop size and two velocity components, measured downstream the nominal spray impinging location, is shown in Fig.3, where all the individual measurements collected over a large number of injections are reported versus time, the origin, t = 0, being defined by the 20 MPa triggering level on the injection pressure trace. As in free sprays [8] three main periods are distinguishable: the first period with strong unsteadiness due to the passage of the spray head, a main period where most of the fuel is injected, and a late period characterized by the trailing edge, where the smaller droplets, left behind by the passage of the previous structures, and the bigger ones, generated during the late injection at low pressure, are travelling together at low velocity. Close to the surface (h=0.5 mm in Fig.3), after the tip arrival, tangential velocity stabilizes, with high rms, around a value larger than the tip velocity and than decays after completion of injection. The corresponding normal (i.e. perpendicular to the wall) velocity component shows that only droplets traversing the control volume with negative velocities (i.e. back from the wall) were detected (Fig.3). The size distribution shows an upper bound of approximately 30 μm and few data at higher values. At the same location (X = 6 mm) and larger distance from

the wall (h=2 mm) the tangential component (Fig.4) shows a transient behaviour in correspondence of the early and late injection periods, while the velocity of a large fraction of droplets is almost zero during the main injection period, suggesting that the wall spray does not extend beyond 2 mm from the wall. At the same point, it appears clearly the coexistence of droplets traversing the control volume with positive and negative normal velocity components (fig. 4). Comparison with Fig.3 shows that the droplet sizes appear lower at h = 2 mm, during the main injection period.

The relative steadyness of normal and tangential velocity components during the main injection period, although the variability is high, suggested the following data analysis: tangential velocities were ensemble averaged over a period from 1.5 to 2.5 ms after injection start (AIS) and the results plotted versus distance from the wall, at X = 14 mm, and the same was done with the size data. The results (Figs.5 and 6) show that the maximum mean velocity and mean diameter were reached both at the closest distance from the wall with a steep gradient, suggesting that the most of the tangential droplet momentum remains concentrated close to wall during the main injection period.

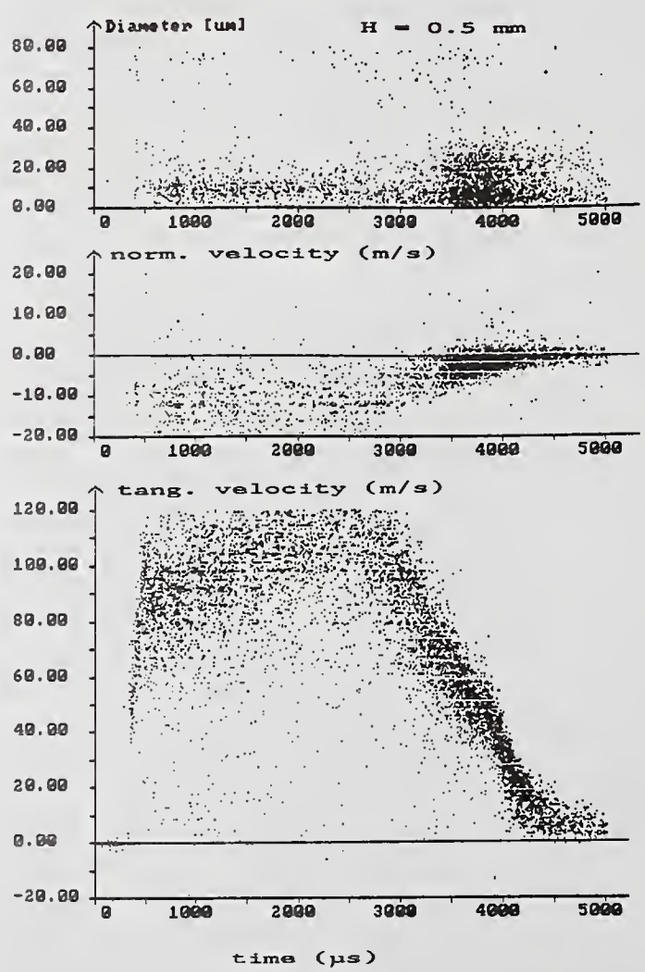

Fig.3 Time evolution of drop size and velocity at X = 6 mm.

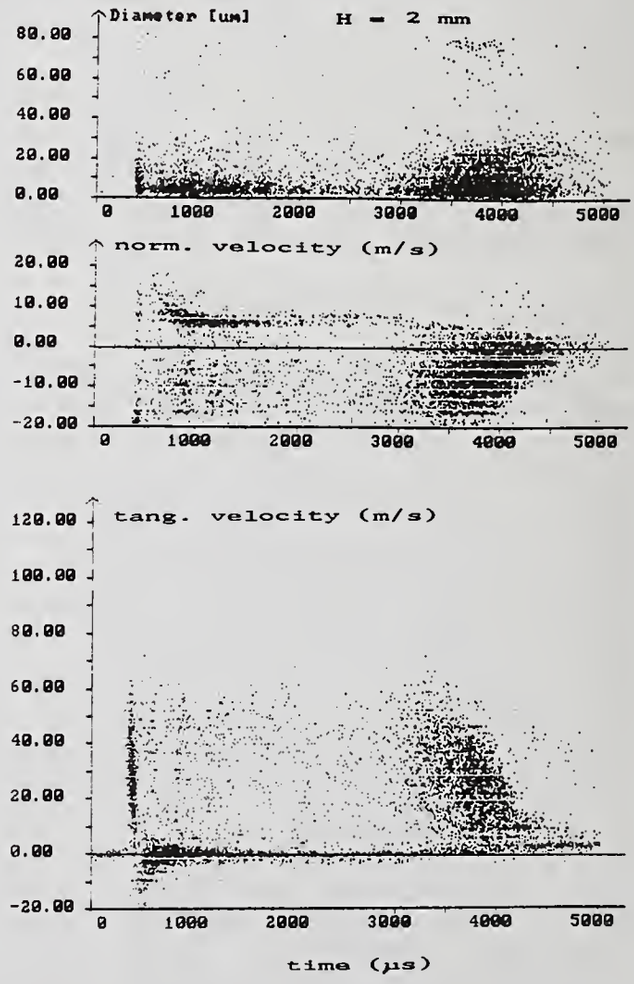

Fig.4 Time evolution of drop size and velocity at X = 6 mm.

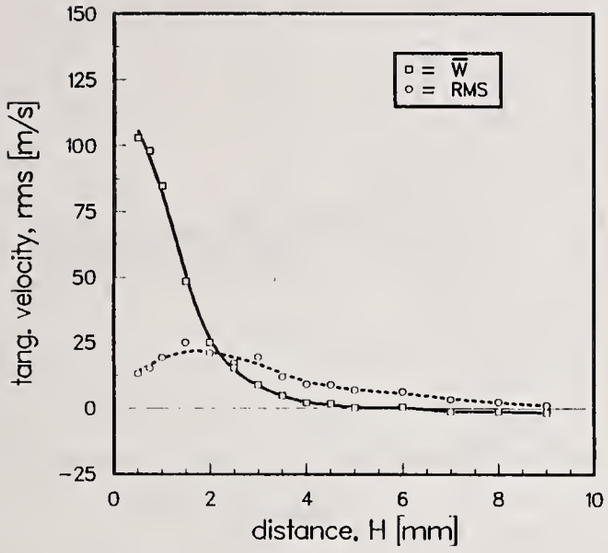

Fig. 5

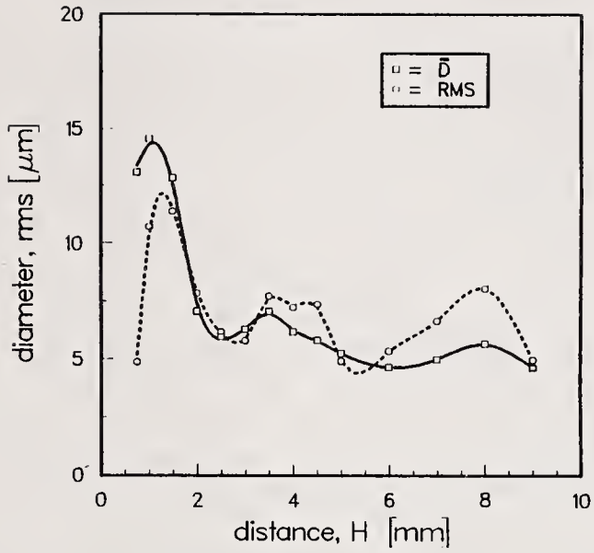

Fig. 6

The time evolution of the droplet velocity vector at larger distances from the wall allows to get insights of the air entrainment process. Each velocity component has been ensemble averaged over time windows of 10 μs and the results at X = 14 mm and h = 3.5 mm are presented in Fig.7. At the very beginning of the spray passage the velocity vector is almost parallel to the wall, slightly upward tilted, then , after performing a complete revolution, it reachs the downward orientation, at 1 ms AIS, with magnitude reduced to few m/s, and it maintains such orientation during all the main injection period, indicating the existence of entrainment by the wall spray. At lower distances from the wall the velocity vector slightly oscillates up and down around the parallel orientation, particularly during the early period. The presence of periodic oscillations of the normal velocity component was clearly identified at h = 2.5mm on the ensemble averaged time history, just after the tip passage, as shown in Fig. 8. It is remarkable the coherence of this structure which reproduces itself almost in phase over a large number of injections, with a characteristic period of about 0.25 ms which corresponds to a frequency of 4 kHz.

The tip arrival time at any location downstream the impact nominal point (X = 0) can be detected from the tangential and/or normal velocity histories, as the time at which the first high velocity is measured. The results are reported in Fig.9 as penetration versus time for two distances from the wall: h = 0.5 and 2 mm, from wich the mean tip velocity was deduced. Comparison with the results obtained on the free spray [8] shows a decrease of the tip velocity to about 50% of the free spray value. The spray front is not normal to the wall as it stems by the fact that at 0.5 mm the leading droplets reach the measurement location systematically before the corresponding droplets at 2 mm. The measured time delay is independent of location, suggesting that the front shape does not change with distance from the impingement location and implying a wall/front angle of about 30 deg.

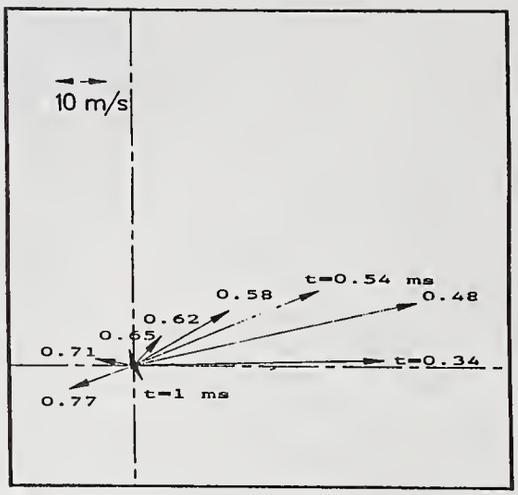

Fig. 7

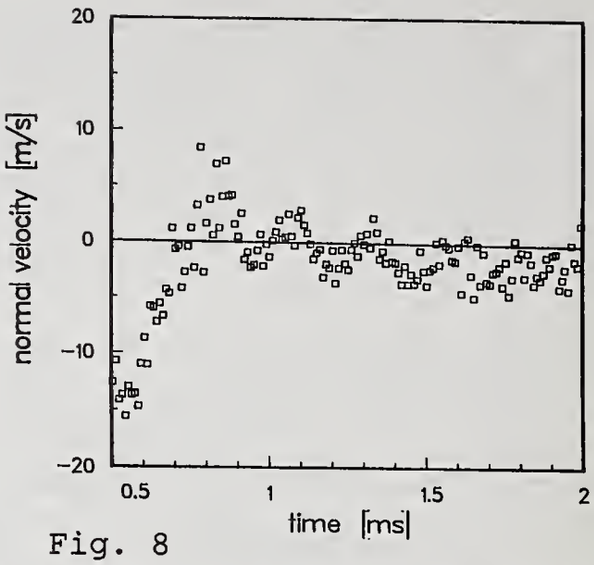

Fig. 8

The analysis of all velocity probability distribution functions (PDF), for both the normal and tangential velocity components, revealed the presence, in many cases, of bimodal distributions, indicating the coexistence of two droplet populations. Although it was easy to identify the two groups of droplets, characterized by opposite signs of the normal velocity component, as the impinging and reflected ones, it was puzzling to which of the two populations were associated the two peaks in the tangential component pdf, as the two velocity components were measured separately and thus no correspondence between individual data exists. Anyway, an attempt was made to reconstruct the velocity profiles along the X orientation, by using the ensemble averages of each population, for both components, and typical results are shown in Figs.10, for the time window of 0.2 ms after tip arrival.
It can be noticed that one of the two curves representing the tangential component shows a similar profile and peaks at the same location where the normal velocity profile of the impacting

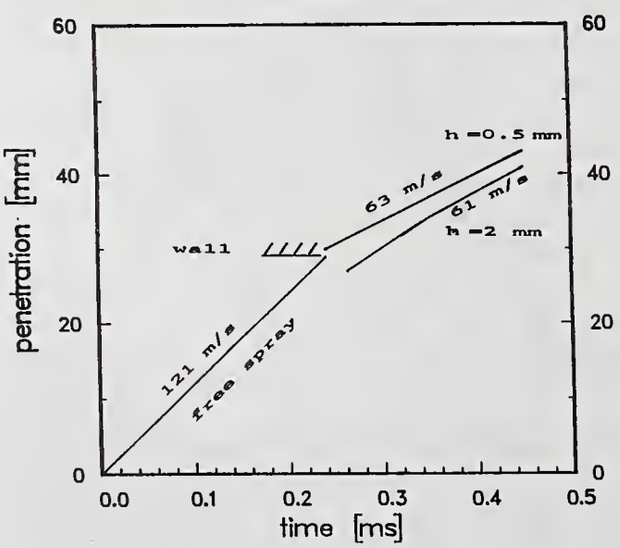

Fig. 9

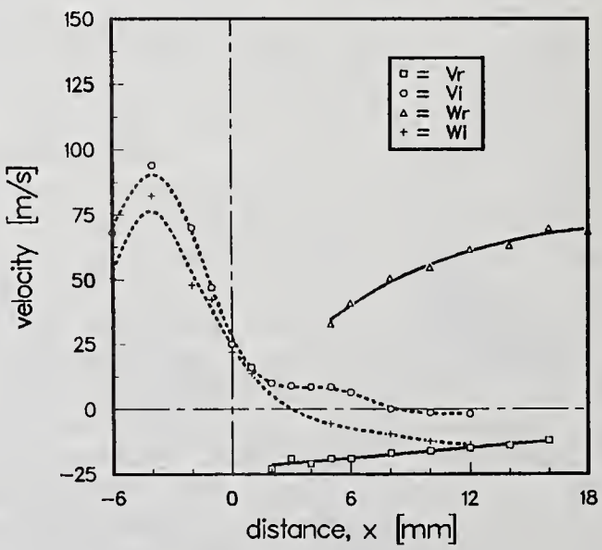

Fig. 10

droplets peaks too. This must be considered as sufficient to regard such part of the tangential velocity profile as relative to the impinging droplets. In fact, due to the 45 deg spray impact angle, the normal and tangential drop velocity components should be of comparable magnitude inside the impingement region ($-6 < X < +2$). Downstream, in the wall region, the normal component is only negative and the tangential velocity reaches the extreme values. In the transition region, incoming droplets whose tangential velocity rapidly decreases, coexist with reflected or deflected droplets whose tangential velocity component rapidly increases toward the high values, characteristic of the wall spray. It must be stressed that the measurements in the impingement region ($-6 < X < +2$) resulted more difficult and in some cases, especially during the main injection period, actually impossible, due to the higher drop number density. Fig.11 shows a vectorial plots of the droplet flow field, based on the same data of Fig. 10 , from which the characteristics of each wall region and droplet population might be better understood.

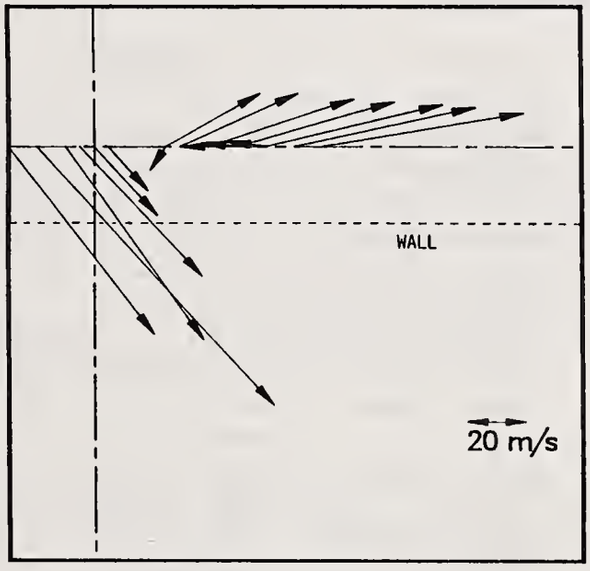

Fig. 11 Vectorial plot of the droplet flow field 2 mm from the impact wall (same data of figure 10).

CONCLUSIONS

The experimental study of a diesel spray impinging at 45 deg on a flat surface under ambient gas conditions revealed the following:

1) The time behaviour of the wall spray strongly resembles that of a free spray; three different periods may be recognised: i) an early period lasting about 0.2 ms, characterised by the passage of the spray head and by high velocity unsteadiness; ii) a main period lasting about 70% of the injection duration, characterised by an almost steady spray, although the variability is high; iii) the late period, characterised by the presence of low velocity droplets.

2) The wall region my be subdivided into three regions with different characteristics: a) the impingement region characterized by still high normal velocity component and high droplet density; b) the wall spray region characterized by high tangential velocity component and comparatively low normal component, where the droplet density is lower and allows direct measurements of drop size and velocity; c) a transition region

in between, with characteristics of both of the previously mentioned regions.
3) Estimated tip velocity is about 50% of that of the impinging free spray; the spray front appears to move with an angle of about 30 deg respect to the wall, and such value is not changing with distance from the impingement location.
4) Droplet tangential momentum remains concentrated close to the wall, the maximum mean tangential velocity as well as the maximum mean droplet size were found at 0.5 - 1 mm from the wall.
5) Double peak PDFs, found at many measurement locations, suggest the existence of two droplet populations characterized by different trajectories. The data analysis here reported suggests that such populations represent impinging and reflected droplets, the latter probably coming from the impact of the former on the wall.

REFERENCES

[1] Binder K. and Pfeffer V.; "New results of research into mixture formation in the D.I. Diesel engine"; Intn. Symp. COMODIA 90, Kyoto, Japan, September 1990.
[2] Katsura N. et al.; "Characteristics of a Diesel spray impinging on a flat wall"; SAE Paper No.890264, 1989.
[3] Fujimoto H. et al.; "Characteristics of a Diesel spray impinging on a flat wall"; Intn. Symp. COMODIA 90, Kyoto, Japan, September 1990.
[4] Hiroyasu H. et al.; "Computed tomographic study on internal structure of a Diesel spray impinging on a flat wall"; Intn. Symp. COMODIA 90, Kyoto, Japan, September 1990.
[5] Coghe, A. , Cossali, G. , Gamma, F.; "LDV Analysis of Spray-Wall interaction"; 6th Annual Conf. ILASS-Europe, Pisa, 1990
[6] Naber J.D. and Reitz R.D.; "Modeling Engine Spray/Wall Impingement"; SAE Paper No.880107, 1988.
[7] Cossali G.E., Brunello G., Coghe A.; "LDV characterization of air entrainment in transient diesel sprays"; SAE paper 910178, Detroit 1991.
[8] Brunello G. et al.; "Simultaneous evaluation of tip and drop velocities in unsteady Diesel sprays"; Workshop on Fluid Dynamics and Combustion in Reciprocating Engines, CNR-Istituto Motori, Capri, Italy, April 1990.
[9] Pitcher G., Wigley G. and Saffman M.; "Sensitivity of dropsize measurement by Phase Doppler Anemometry to refractive index changes in combusting fuel sprays"; Fifth Intn. Symp. on Application of Laser Techniques to Fluid Mechanics, Lisbon, July 1990.
[10] Matsuoka S.; "Combustion in the Diesel Engine"; in : "Internal Combustion Engineering, Science and Technology" Ed. J.H. Weaving, Elsevier Applied Science, London 1990.

Support for this work was provided by the Commission of the European Cummunities, under Program "Joule" (Contract N.JOUE-0012-D (AM)).

APPLICATION OF POISSON STATISTICS TO THE PROBLEM OF SIZE AND VOLUME FLUX MEASUREMENT BY PHASE-DOPPLER ANEMOMETRY

C.F. Edwards and K.D. Marx

Combustion Research Facility
Sandia National Laboratories
Livermore, CA, U.S.A.

ABSTRACT

This paper outlines the effects of Poisson particle statistics on the ability of a "single-particle" diagnostic to make accurate size and volume flux measurements. Although the analysis presented is quite general, a simplified flowfield and probe volume have been used to illustrate its consequences. Even this simple example suffices to show that the action of the Poisson filters places restrictions on the quality of measurements by techniques such as phase-Doppler anemometry. The keys to the filters are the expected values of the number of particles in the probe volume and the number of particles entering the probe region during the residence time of a preceding particle. Only if these values are kept below order 10^{-2} can the measured joint distribution function and particle rate be assumed to reflect the true distribution and rate of the flow.

INTRODUCTION

Phase-Doppler Anemometry is a technique via which both the size and velocity of a spherical particle may be determined with good accuracy, high speed and good spatial resolution. Because of this capability it is possible to compute particle size distributions, size-velocity correlations and even liquid volume flux rate for spray applications. However, some controversy has arisen recently regarding its ability to provide accurate volume flux measurements in test flows designed specifically for that purpose. In other flows which are of more practical interest, there is no way to know how accurate the measured volume flux is, so this unknown must be carried as a caveat with the data set when it is used.

This issue was brought clearly into focus at a recent ILASS-Americas meeting in Hartford, CT. At this meeting a paper was presented by Dr. L. Dodge and co-workers at Southwest Research Institute which showed a potential underaccounting of the liquid volume flux in a test spray. Other papers were presented which reported data for liquid volume flux, but which were unable to quantify the bands of uncertainty associated with the data.

During the discussion of these papers, Prof. D. Senser of Purdue University suggested that the major difficulty might simply be a result of the requirement that there be only a single particle in the probe volume. He also noted that in flows where a strong size-velocity correlation exists, errors might be introduced into the measured size distribution function.

This paper investigates the potential for accuracy in such measurements in light of Prof. Senser's suggestion. It outlines the sampling process of an ideal phase-Doppler system in terms of the Poisson statistics of particles in the probe volume. The results show that even for an ideal processor, Poisson statistics impose severe constraints on the ability of any "single particle" diagnostic to accurately measure size and volume flux.

Since the need for brevity precludes our giving a systematic derivation of the analysis along with examples of the concomitant effects, we attempt here to provide only the backbone of the analysis and a single illustration in a simplified flowfield. The reader who is interested in a more systematic exposition, evaluation of assumptions, and illustration of effects, should contact the authors to obtain a copy of the full manuscript [1].

AN IDEAL PHASE-DOPPLER SYSTEM

Consider the flow of particles through the probe volume of an ideal phase-Doppler system. The system which we postulate is not connected with any hardware, but is a region of space in which particles of any size are detected with perfect accuracy and in which they exist only as points (infinitesimal spatial extent). Since the idealized particles are of infinitesimal spatial extent, no two can occupy the same position at the same time and no interactions between particles are possible (e.g., collisions).

Anticipating that the probe volume of an actual phase-Doppler system is a function of the particle size, the probe volume considered here is formed by combining probe volumes of various sizes, $\Delta V(\phi)$, corresponding to each particle diameter ϕ. Each of the probe volumes senses only those particles which are of size ϕ associated with it. The probe volumes may be of arbitrary shape but all are subject to the constraint that ΔV cannot be reentrant. All of the probe volumes are assumed to be sufficiently small that the particle statistics are constant over the dimensions of the composite probe volume and the velocity and size of a particle are constant during its transit through the composite probe volume. Each of the component probe volumes has associated with it an area, $A_p(\mathbf{v},\phi)$, which is its cross sectional area projected in the direction of a particle traveling with vector velocity $\mathbf{v}$.

The question to be answered then is a simple one. Given a known flux of particles through this region and the restriction that there must be only one particle sensed in the composite probe volume at a given time for a measurement to be considered valid, what will be the relationship between the validated and true fluxes through the region?

The answer to this question is that the validated flux of particles will reflect the true flux but only after having passed through two stages of filters. Since the characteristics of these filters are specified by spatial and temporal Poisson processes, we will refer to these as Poisson filters.

The first stage filter (Fig. 1a) is formed by a spatial Poisson process. Since a particle can only be measured if it is the only one in the probe volume, then at the instant of entry of any particle into the probe volume there must be sufficient interparticle separation that the previous particle has already left the probe volume. If the separation is not sufficient, the particle will be invalidated.

Consider a flow with only a single class of monodisperse particles of size ϕ, traveling through the probe volume. Denote this class of particles by the subscript i. Since all particles within class i are the same size, then the composite probe volume is the same as the component probe volume and is given by $\Delta V_i = \Delta V(\phi_i)$. The probability that a particle in this class will pass through the spatial filter is the same as the probability that the interparticle volume, $\hat{V}_i$, is greater than the probe volume, ΔV_i. If the probability distribution of interparticle volume for this class is denoted by $p_{xi}(\hat{V}_i)$ (normalized to unity), then the probability of passage through the spatial filter is given by

$$P_{xi} = P(\hat{V}_i > \Delta V_i) = 1 - P(\hat{V}_i \le \Delta V_i) = 1 - \int_0^{\Delta V_i} p_{xi}(\hat{V}_i) d\hat{V}_i \qquad (1)$$

Once a particle has passed through the spatial Poisson filter — that is, it has an empty probe volume at the time of its entrance — the particle must still pass through another Poisson filter before it can be validated. This filter corresponds to the particle being able to exit the probe volume before another particle enters and thereby invalidates it (Fig. 1b). It is apparent that the probability that the particle will be able to do this will depend both upon its residence time in the probe volume and upon the distribution of interparticle arrival times at the probe volume.

If the residence time of a particle in the probe volume is denoted by τ, and the probability distribution of interparticle arrival times at the probe volume for class i is denoted by $p_{ti}(\hat{t}_i)$ (normalized to unity), then the probability of passage through this temporal filter for a flow with a single class i is given by

$$P_{ti} = P(\hat{t}_i > \tau) = 1 - P(\hat{t}_i \le \tau) = 1 - \int_0^{\tau} p_{ti}(\hat{t}_i) d\hat{t}_i \qquad (2)$$

In order to complete this description we need expressions for the distribution functions $p_{xi}(\hat{V}_i)$ and $p_{ti}(\hat{t}_i)$. These expressions may be found by application of Poisson statistics to our point particle flux. The interparticle time distribution for a continuous, homogeneous Poisson process is given by Snyder [2] as

$$p_{ti}(\hat{t}_i) = \lambda_{ti} e^{-\lambda_{ti} \hat{t}_i} \tag{3}$$

In a similar fashion, the interparticle volume distribution for a continuous, homogeneous process is given by

$$p_{xi}(\hat{V}_i) = \lambda_{xi} e^{-\lambda_{xi} \hat{V}_i} \tag{4}$$

where λ_{ti} and λ_{xi} are the temporal and spatial process intensities. Note that, by definition, λ_{xi} is the mean number of particles per unit volume, or number density ρ_i, of the ith class of the spray.

Substituting the Poisson expressions for interparticle time and volume into the expressions for the spatial and temporal filters yields the probability of measurement of a given single particle of class i with residence time τ. What is required, however, is the response of the ideal phase-Doppler system to a distribution of droplets (classes) within the spray. This may be accomplished by introducing a particle distribution function in the two quantities measured by the phase-Doppler instrument: velocity and size. This distribution function may be cast in either spatial (particles per unit volume) or temporal (particles per unit area per unit time) terms. Both formulations have advantages and disadvantages. However, since the phase-Doppler instrument is temporally-based (measuring particle flow through the probe volume) we will adopt the temporal distribution function in the following discussion.

Consider the true particle flux through the probe volume. The number of particles entering the probe volume per unit time in the phase space element $dv\, d\phi$ may be written as

$$\lambda_t'' A_p(v,\phi) f_t(v,\phi) d\phi dv \tag{5}$$

where λ_t'' is the composite flux rate, $f_t(v,\phi)$ is the temporal joint distribution function in size and velocity (normalized to unity), and dv and $d\phi$ are differential elements of phase space centered about the velocity v and size ϕ.

Correspondence between the temporal and spatial approaches gives the number density in terms of temporal variables as

$$\rho = \lambda_t'' / \bar{S}_x \tag{6}$$

where $\bar{S}_x$ is the spatial mean particle speed.

Composite probabilities P_x and P_t may be formed in terms of this distribution function by letting each class i comprise the population of particles within a differential element $d\phi$ wide, centered about particle size ϕ_i, and noting that the probabilities of each class are independent. Under these conditions, the composite probabilities are given by the products of the component probabilities, and sums over classes become integrals over the distribution functions:

$$P_x = \prod_i P_{xi} = \prod_i e^{-\lambda_{xi} \Delta V_i} = e^{-\sum_i \rho_i \Delta V_i} = e^{-\rho \overline{\Delta V}_x} \tag{7}$$

$$P_t = \prod_i P_{ti} = \prod_i e^{-\lambda_{ti} \tau} = e^{-\sum_i \lambda_{ti} \tau} = e^{-\lambda_t'' \overline{A}_{pt} \tau} \tag{8}$$

where the spatial mean probe volume $\overline{\Delta V}_x$ and temporal mean probe area $\overline{A}_{pt}$ are given by

$$\overline{\Delta V}_x = \int_{\phi} \Delta V(\phi) \tilde{f}_x(\phi) d\phi = \bar{S}_x \int_{\phi} \int_{v} \frac{\Delta V(\phi)}{|v|} f_t(v,\phi) dv d\phi \tag{9}$$

$$\overline{A_{pt}} = \int_{\phi} \int_{v} A_p(v,\phi) f_t(v,\phi) dv d\phi \tag{10}$$

and $\tilde{f}_x(\phi)$ is the spatial size distribution function.

Note that the spatial filter probability does not depend upon the size or velocity class of the particle being considered but only on the composite characteristics of the particle flow. As such, this filter rejects particles uniformly over the size/velocity space of the particle flux, and therefore introduces no bias into the "measured" size/velocity distribution.

This is not true of the temporal filter, however. In this case the filter probability depends upon the residence time of the particle under consideration. Since the residence time is correlated inversely with the particle velocity and directly with the probe volume depth, the temporal filter will preferentially suppress the populations of particles with low velocities or large component probe volumes and will therefore introduce a bias into the measured distribution function.

Armed with the expressions for P_x and P_t, we can now return to consideration of the relationship between the flux of particles which is measured by our ideal system and the true flux of particles. Combining the expression for the true flux with the expression for P_x and substituting for ρ in terms of temporal variables, the number of particles passing through the spatial filter per unit time in $dv\ d\phi$ is given by

$$\lambda_t'' A_p(v,\phi) e^{-\lambda_t'' \overline{\Delta V}_x / \bar{S}_x} f_t(v,\phi) d\phi dv \tag{11}$$

These are the particles which are eligible for measurement if they can pass through the temporal filter. The function P_t gives the probability of passage through the temporal filter as a function of particle residence time in the probe volume. As noted previously, this residence time will certainly depend upon the velocity and may also depend upon the particle size. However, specification of particle velocity and size alone is not sufficient to determine particle residence time. This is because particles with identical size and velocity but traveling through different parts of the probe volume will yield different residence times since the depth of the probe volume is not constant but is a function of the position where the particle enters.

In order to account for this distribution of residence times among the particles that populate $dv\ d\phi$, we introduce an auxiliary distribution function of residence time, $g(\tau; v,\phi)$, with parametric dependence upon v and ϕ, and normalized to unity. This distribution is used, in effect, to spread the distribution function $f_t(v,\phi)$ into a new dimension τ.

Combining this with P_t gives the number of particles per unit time which pass through the composite Poisson filter in dv about v, $d\phi$ about ϕ, and $d\tau$ about τ

$$\lambda_t'' A_p(v,\phi) e^{-\lambda_t'' \overline{\Delta V}_x / \bar{S}_x} e^{-\lambda_t'' \overline{A_{pt}}\ \tau}\ g(\tau; v,\phi) f_t(v,\phi) d\phi dv d\tau \tag{12}$$

But we are only interested in the distribution of particles over size/velocity space. This may be recovered by integrating over the particle residence time, which gives the number of particles passing through the composite filter per unit time in $dv\ d\phi$ as

$$\lambda_t'' A_p(v,\phi) e^{-\lambda_t'' \overline{\Delta V}_x / \bar{S}_x} f_t(v,\phi) d\phi dv \int_{\tau} e^{-\lambda_t'' \overline{A_{pt}}\ \tau}\ g(\tau; v,\phi) d\tau \tag{13}$$

For an ideal phase-Doppler system, subject only to the single particle constraint, this is the measured number of particles per unit time in $dv\ d\phi$, which can be expressed as

$$\lambda_{tm} f_{tm}(v,\phi) d\phi dv \tag{14}$$

where λ_{tm} is the measured particle rate and $f_{tm}(v,\phi)$ is the measured joint distribution function with unit normalization. The relationship between the measured and true distributions is then given by

$$f_{tm}(v,\phi) = \frac{\lambda_t'' A_p(v,\phi)}{\lambda_{tm}} e^{-\lambda_t'' \overline{\Delta V}_x / \bar{S}_x} f_t(v,\phi) \int_\tau e^{-\lambda_t'' \overline{A_{pt}}\ \tau} g(\tau; v,\phi) d\tau \tag{15}$$

For convenience, we will return to using the notation P_x for the spatial filter probability and we introduce the mean temporal filter probability for a particle of velocity v and size ϕ as

$$\bar{P}_t(v,\phi) = \int_\tau e^{-\lambda_t'' \overline{A_{pt}}\ \tau} g(\tau; v,\phi) d\tau \tag{16}$$

The relationship between the measured particle rate and the true flux rate may be determined by integrating over v and ϕ and using the normalization constraint on $f_{tm}(v,\phi)$:

$$\lambda_{tm} = \lambda_t'' P_x \int_\phi \int_v A_p(v,\phi) \bar{P}_t(v,\phi) f_t(v,\phi) dv d\phi \tag{17}$$

The relationship between the measured and true distribution functions can best be expressed in terms of an efficiency for each distribution. We define the Poisson efficiency as the number of particles measured per unit time in some element of phase space divided by the true number of particles that passed through the probe volume per unit time in that same element. Using this definition, the joint distribution efficiency is given by

$$\eta(v,\phi) = \frac{\lambda_{tm} f_{tm}(v,\phi)}{\lambda_t'' A_p(v,\phi) f_t(v,\phi)} = P_x \bar{P}_t(v,\phi) \tag{18}$$

Similar efficiencies can be defined for the size distribution and velocity distribution by considering the number of particles measured, divided by the true number of particles. We denote the size and velocity efficiencies by $\eta(\phi)$ and $\eta(v)$ respectively.

ILLUSTRATION OF THE FILTER EFFECTS IN A UNIDIRECTIONAL FLOW

The effect of the Poisson filters on the data measured by an ideal phase-Doppler system may be illustrated by considering a simplified system consisting of a unidirectional flow of particles through a constant-depth probe volume of arbitrary cross section with area A_p , and depth L in the flow direction. The probe volume is the same for particles of all sizes so that $\overline{\Delta V}_x(\phi) = \Delta V = L A_p$. Under these conditions, the residence time of the particle is a function of velocity only and is given by $\tau = L / v$. The spatial and mean temporal probabilities for this simplified system may then be written as

$$P_x = e^{-\rho \Delta V}, \qquad \bar{P}_t(v,\phi) = \bar{P}_t(v) = e^{-\lambda_t L / v} \tag{19,20}$$

where $\lambda_t = \lambda_t'' A_p$.

It is apparent that the probability of passage through the spatial filter depends only on the total number density of the flow and the probe volume. In fact, it is the product of these two, i.e., the expected value of the number of particles in the probe volume, that determines the filter probability. In a similar fashion, the temporal filter depends upon the expected value of the number of particles in the probe volume during residence time τ. Since both expressions have the same functional form, the effects of both filters may be summarized on a single plot as a function of either expected value.

Figure 2 shows the probability of rejection (1 - P_x or 1 - $\bar{P}_t$) as a function of either expected value. This figure shows that for values as low as 10^{-1}, a 10% rejection rate occurs, while for values just over 2, greater than 90% rejection will result. Only if the expected value is kept below ~10^{-2} can the results be assumed to be unaffected.

The joint distribution efficiency of our simplified flow is given by the product of the spatial and temporal filter probabilities (one minus the values in Fig. 2). The size and velocity distribution efficiencies, however, depend upon integrals of the single-particle temporal filter probability over some prescribed joint distribution function $f_t(v,\phi)$. In order to illustrate these efficiencies, we use a joint distribution function representative of the data measured in the decelerating flowfield of a kerosene spray flame [3].

Figure 3a gives the measured size/velocity correlation of the spray and Fig. 3b shows the impact of the temporal Poisson filter. In a decelerating flowfield like this, one expects to find that particles up to some maximum size will follow the gas phase behavior. Above this size droplets remain ballistic to the flow, increasingly so with size. As shown in the figure, droplets of 10 μm and below are equilibrated with the gas phase while those above 10 μm have excess velocities. The dashed lines in the figure give the mean velocity +/- the RMS, to indicate the width of the velocity distribution. (Note that for the measured data, the RMS is essentially independent of size at this location.)

Figure 3b shows the size distribution efficiency $\eta(\phi)$ for various particle flux rates. Since the true number density of the flow is not known, P_x has been set equal to one. In this case, $\eta(\phi)$ shows only the effect of the temporal filter on the measured flow. These results were obtained by assigning a Gaussian velocity distribution (clipped at three standard deviations) with mean and RMS as shown in Fig. 3a, and computing $\eta(\phi)$ for flow through the 200 μm probe volume depth. The results show that for particle flux rates of the order 10^3 /s and below, there is little effect of the filter (a few percent at low velocities). At 10^4 /s, however, more than 10% of the high velocity component of the spray is rejected, and 20% of the equilibrated spray is lost. When the particle flux is increased to 10^5 /s, almost 70% of the high velocity spray is lost, and more than 85% of the equilibrated spray is not accounted for. The dashed line in the figure indicates the filter behavior for the experimentally measured particle rate of 3700 /s. Even at this low rate almost 10% of the spray is lost to the temporal Poisson filter.

It should be noted that high particle flux rate is not the only condition under which the temporal Poisson filter can have a substantial impact on measured data. An alternative case of practical interest is that of intermediate flux rate but long particle residence time. This may be achieved by considering the same decelerating flow system depicted in Fig. 3, but with a much lower carrier velocity.

The data shown in Fig. 3 were taken for an air-assist atomizer with mass-based atomizing-air to fuel ratio of one. The result of this high atomizing air flowrate is that the carrier stream for this flow achieves a significant velocity (~10 m/s) even as the spray decelerates. Instead, consider the case where there is no initial carrier stream, but the spray is into quiescent air. This may be simulated by reducing the velocity of the equilibrated particles (ϕ < 10 μm) from 10 m/s, as shown in Fig. 3a, to ~1 m/s, and then allowing the velocity to increase linearly to 20 m/s at 40 μm. The result of passing a spray with this characteristic through the temporal Poisson filter is shown in Fig. 4. Even at a very low particle flux rate (10^3 /s) a substantial amount of the low velocity component of the spray is lost. At 10^4 /s, while high velocity particles have just started to be affected, low velocity particles have already experienced an order of magnitude loss in numbers through the filter. For the highest flux case shown (10^5 /s), 2/3 of the highest velocity particles are rejected, while the low velocity particles are virtually eliminated.

As mentioned in the introduction, the original motivation for investigating the effects of the single-particle measurement constraint was the controversy surrounding the ability of phase-Doppler instruments to measure volume flux. Although there are many more effects which need to be considered in order to perform a complete analysis of the volume flux problem (e.g., probe volume corrections, etc.), the consideration of the Poisson filter effect provides a baseline analysis since no real system can out-perform the ideal system constructed here.

The effect of the first stage of the Poisson filter (spatial) on the measured size distribution and volume flux is easy to see. Since all classes of particles are individually, as well as collectively, Poisson distributed in space, the first stage filter exhibits no preference for any particular marked class. Particles rejected by this filter are therefore distributed in the same proportion as the true size/velocity distribution and as a result, no bias is imparted to the measured distributions. Similarly,

the loss of liquid volume flux is spread proportionately over the true distribution. The result is that when X% of the spray is lost in the filter, X% of the volume flux is also lost.

The effect of the second stage filter (temporal) on the measured size distribution and volume flux must be computed for each individual case. The curves of Figs. 5 and 6 show the size distributions for the two cases previously discussed. These were computed using the measured size distribution from the kerosene spray flame and the size distribution efficiency of Figs. 3b and 4. Note that in the case with the higher carrier velocity (Fig. 5), there is little effect until the particle rate approaches 10^5 /s, while in the more severe case (Fig. 6), significant bias begins to appear even at 10^3 /s.

Also shown in these figures is the fraction of the liquid volume flux that passes through the temporal filter. It is apparent that even in the milder of the two cases, a significant fraction of the volume flux may be lost. Note that if the loss through the spatial filter were also included, these values would be reduced further.

SUMMARY

In this paper we have outlined the effects of Poisson particle statistics on the ability of a "single-particle" diagnostic to make accurate size and volume flux measurements. Although the analysis presented is quite general, a simplified flowfield and probe volume have been used to illustrate its consequences. Even this simple example suffices to show that the action of the Poisson filters places restrictions (possibly severe) on the quality of measurements by techniques such as phase-Doppler anemometry. The keys to the filters are the expected values of the number of particles in the probe volume $\rho\overline{\Delta V_x}$, and the number of particles entering the probe region during residence time τ, which is given by $\lambda_t'' \overline{A_{pt}} \tau$. Only if these values are kept below order 10^{-2} can the measured joint distribution function and particle rate be assumed to reflect the true distribution and rate of the flow.

ACKNOWLEDGEMENT

This work was performed at the Combustion Research Facility, Sandia National Laboratories, and was supported by the U.S. Department of Energy, Office of Industrial Processes, Advanced Industrial Concepts Division.

REFERENCES

1. Edwards, C. F. and Marx, K. D.: manuscript in preparation, to be submitted to Atomization and Sprays, (1991).
2. Snyder, D. L.: Random Point Processes, Wiley, (1975).
3. Edwards, C. F., Rudoff, R. C., and Bachalo, W. D.: "Measurement of Correlated Droplet Size and Velocity Statistics, Size Distributions, and Volume Flux in a Steady Spray Flame," Proceedings of the Fifth International Symposium on the Applications of Laser Techniques to Fluid Mechanics, Lisbon, Portugal, (1990).

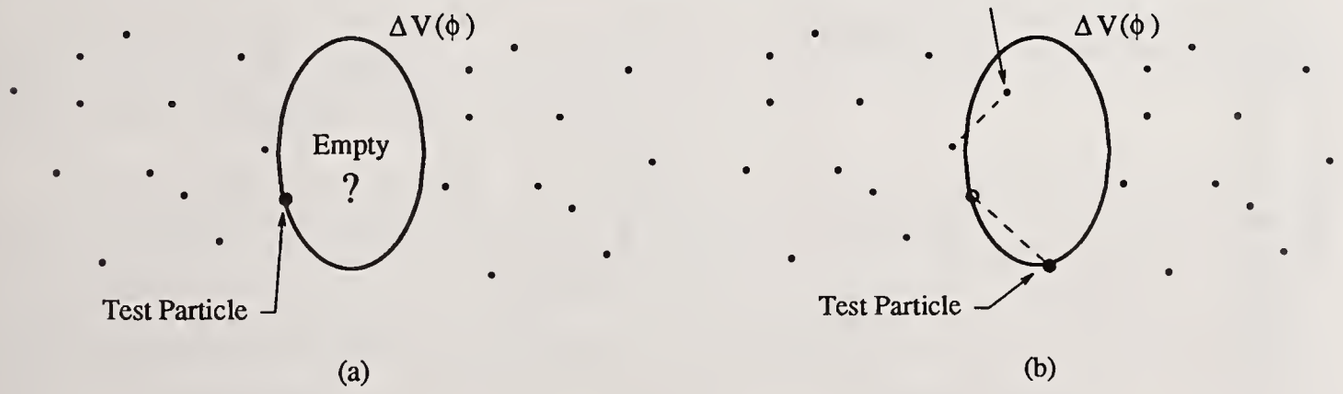

Fig. 1 Illustration of the spatial (a) and temporal (b) Poisson filter processes.

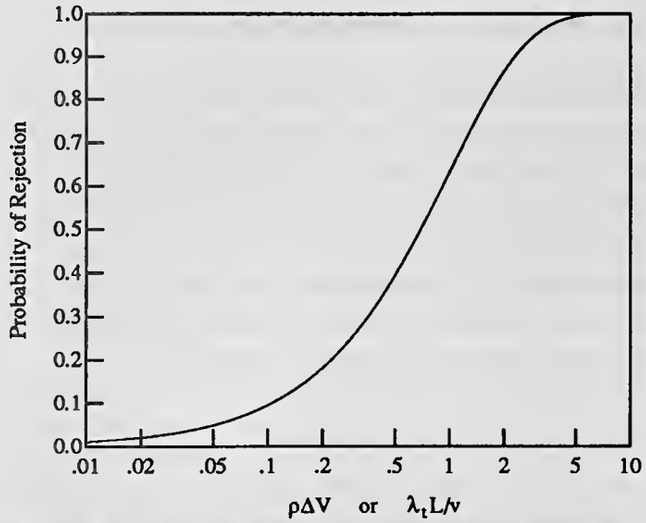

Fig. 2 Probability of rejection by the spatial or temporal filters vs. expected number of particles in the probe volume.

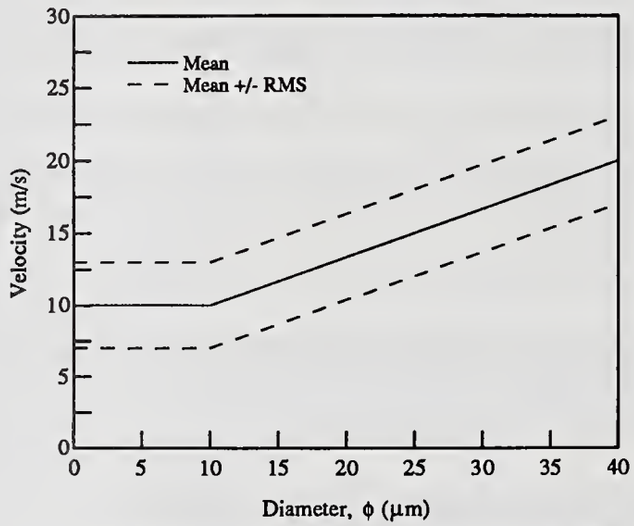

Fig. 3a Size/velocity correlation used to illustrate the effect of the Poisson filters.

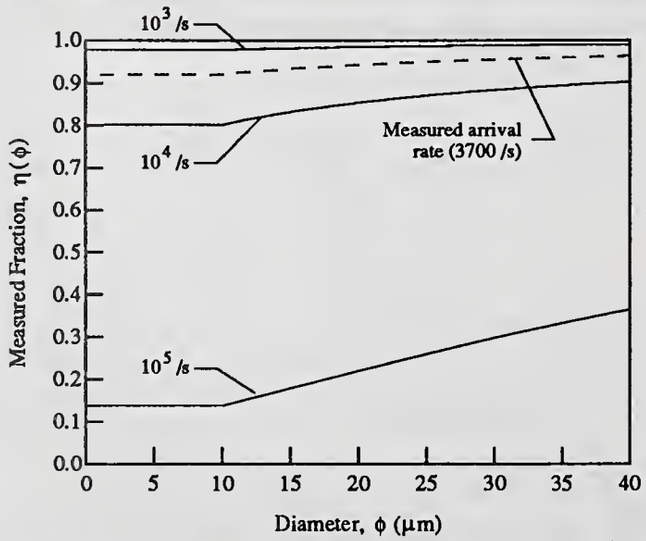

Fig. 3b Measured fraction as a function of particle size for the size/velocity correlation of Fig. 3a.

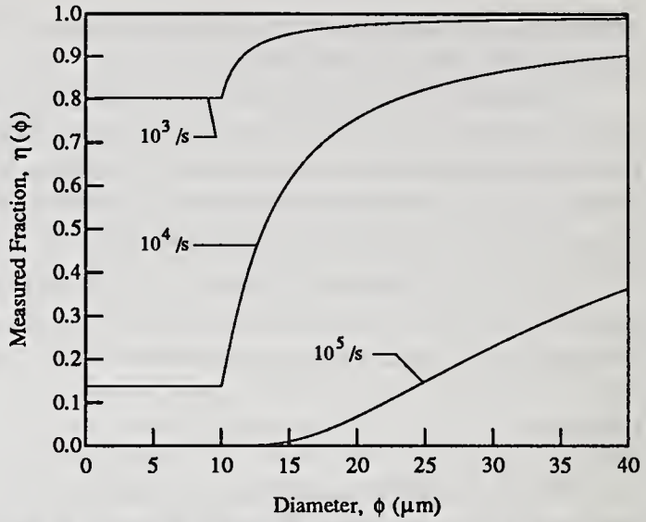

Fig. 4 Measured fraction as a function of particle size for the reduced carrier velocity case.

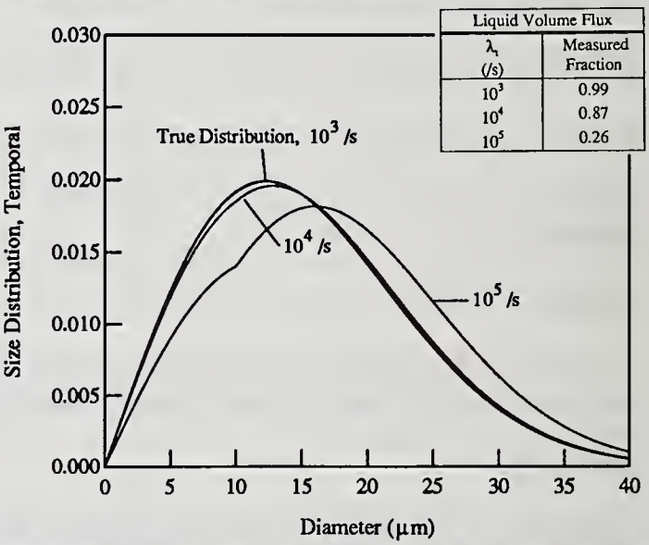

Fig. 5 Measured and true size distribution functions for the size/velocity correlation of Fig. 3a.

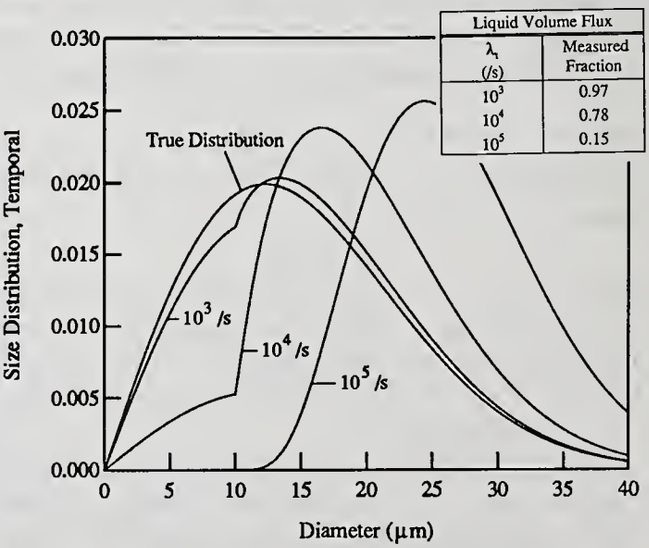

Fig. 6 Measured and true size distribution functions for the reduced carrier velocity case.

CLASSIFICATION OF ROUND LIQUID JET DISINTEGRATION IN COAXIAL AIR STREAMS

Z. Faragó[*] and N. Chigier[†]

[*]DLR, German Aerospace Research Establishment, Hardthausen, Germany
[†]Mechanical Engineering Dept., Carnegie Mellon University, Pittsburgh, PA, U.S.A.

ABSTRACT

From an analysis of over one thousand high speed spark photographs, the modes of round liquid jet disintegration in a coaxial air stream were classified over a liquid Reynolds number range of 200 to 20,000 and over an aerodynamic Weber number range of 0.001 to 600. The observed disintegration modes are compared to the modes of spherical water drop and thin water sheet disruption in an air stream.

INTRODUCTION

In order to understand the basic mechanisms of free liquid jet disruption in a gas stream, experiments on different types of research atomizers have recently been carried out at Carnegie Mellon University. Mansour and Chigier [1] examined the disintegration of a two-dimensional liquid sheet between two parallel gas streams. Parametric experiments on coaxial airblast jet atomization were carried out by Faragó and Chigier [2] in which the aerodynamic Weber number was varied over a range of six orders of magnitude, while the Reynolds number was varied over a range of two orders of magnitude. Using these experiments, intact liquid lengths of coaxial atomizers were measured by Eroglu et al. [3].

After a thorough analysis of more than 1600 photographs of the author's experiments, a new chart of morphological classification of the disintegration of round liquid jets was developed and is presented in this paper. Different modes of liquid jet and spherical liquid drop disruption observed by other investigators are compared with the present results.

The classifications of the modes of jet disruption developed by Ohnesorge [4], Miesse [5] and Reitz [6] show the modes of atomization as a function of the Reynolds and Ohnesorge numbers. However, these representations do not include the relative velocity between the gas and the liquid stream for twin fluid atomizers. Other investigators like Wolfe [7] or Buschulte [8,9] used the aerodynamic Weber number as a single variable for their presentations. Kennedy [10] presented his experiments on the disintegration of spherical water drops in an air stream as a function of the air velocity and the nondimensional number of $We_a/Re_w^{0.5}$. Dimensional analysis of disintegration of liquid jets in quiescent air, in parallel gas flow and of spherical drops in a gas stream shows that at least four independent non-dimensional groups are needed to guarantee the similarity between different experiments (Faragó [11]). The analysis presented in this paper shows that jet

disintegration modes are a function of only two parameters: the liquid Reynolds number and the aerodynamic Weber number. This presentation is limited to the aerodynamic atomization of liquid with water and air both at ambient pressure and temperature.

EXPERIMENTAL PROCEDURE

The nozzle exit dimensions are shown in Fig. 1. The atomizer consists of a central water jet surrounded by a coaxial air jet. Both water and air mass flows can be varied by changing their supply pressures. Water is stored in a pressurized tank with a capacity of 10 liters. The driving force for the water supply is pressurized air. The highest water pressure which could be achieved was 620 kPa. This water supply provides a flow, free of pulsations and vibrations, with a maximum emerging jet velocity of about 20 m/s. The inlet pressure of the atomizing air could be varied from zero to 25 kPa, the latter providing an air velocity of about 180 m/s. The atomizer and the exhaust system were connected to the same three-directional (z-r-phi) positioner so that the axial distance between the nozzle exit and the exhaust inlet always remained the same (120 mm). The accuracy of the positioner is 10 micrometer in the axial (z) and the radial (r) directions and 0.1 degree in the phi-direction. When the exit velocity of the atomizing air was kept at zero for experiments on emerging round liquid jets in the "quiescent" air, the exhaust system generated an environmental air velocity of about 0.5 m/s.

Photographs of jet disintegration and spray formation were taken with a Canon F1 camera using a f=200 mm macro lens. Different extension tubes and bellows were attached to the camera while taking photographs. An Electro-Optics EG&G 549 microflash was used to provide a 0.5 microsecond flash duration and 5 x 10^7 beam candlepower light intensity.

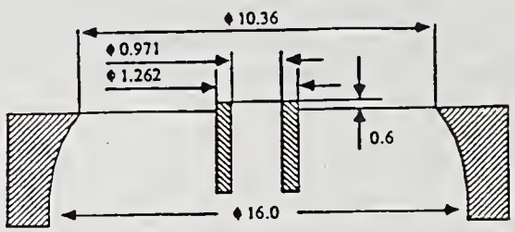

Fig. 1 Sketch of the nozzle exit

EXPERIMENTAL RESULTS AND DISCUSSION

The water flow rate was changed from 0.65 to 52 kg/h, corresponding to a velocity range of 0.24 to 19.6 m/s and a Reynolds number range of 240 to 18,960. The air flow rate was varied from quiescent conditions to 68 kg/h maximum. The maximum air flow condition corresponds to an air velocity of 183 m/s and an air Reynolds number of 104,400. For the coaxial airblast jet atomization, the lowest air mass flow rate was 8.5 kg/h with the corresponding air velocity and Reynolds number of 22.9 m/s and 13,065 respectively. For aerodynamic atomization, the highest aerodynamic Weber number was achieved by a low emerging water velocity of 0.95 m/s combined with the maximum air exit velocity of 183 m/s. Correspondingly, the maximum aerodynamic Weber number was 550. The lowest Weber number for coaxial airblast jet atomization was 0.4 corresponding to an air and water exit velocity of 18.2 and 22.9 m/s respectively. An ambient air velocity of 0.5 m/s was imposed by the exhaust system even when there was no air flow from the atomizer. The lowest Weber numbers were achieved by emerging water jets into the quiescent air. For the water velocity of 0.24 m/s, the corresponding Weber number was 0.001.

Detailed analysis of the photographs shows that jet disintegration can be divided into three categories:

1) Rayleigh breakup. The dominant criteria for assigning jet disintegration for this category were: i) the mean drop diameter is of the order of the jet diameter; the maximum drop diameter is about twice the jet diameter. ii) The liquid jet disintegrates to drops without any liquid membrane or liquid fiber ligament formation. This mechanism can be divided into two

subgroups such as:
1a) Axisymmetric Rayleigh breakup
1b) Non-axisymmetric Rayleigh breakup.

2) Jet disintegration via membrane type ligaments. The round jet develops into a thin liquid sheet (membrane) which forms Kelvin-Helmholtz waves and breaks into drops as described by Crapper, Dombrowski et al. [12]. Jet disintegration is completed within one or two wave lengths. The diameter of the drops is considerably smaller than the diameter of the jet.

3) Jet disintegration via fiber type ligaments. Fibers are formed, peel off the jet, and the fibers break into drops via the Rayleigh mechanism. The liquid core is accelerated and develops waves. It may break into drops via the non-axisymmetric Rayleigh mechanism, or it may break into ligaments. The ligaments may then break into smaller drops or ligaments by one of the three disintegration modes. The completion of jet disintegration needs many wave lengths. The drop diameter is an order of magnitude smaller than the diameter of the jet.

All three categories can be divided into two sub-modes:

A) Pulsating jet disruption as the normal sub-mode of atomization
B) Super-pulsating jet disruption which is connected to an extremely high periodical change between low and high density regions in the spray.

More photographs and more details of this experiment are presented in reference 15.

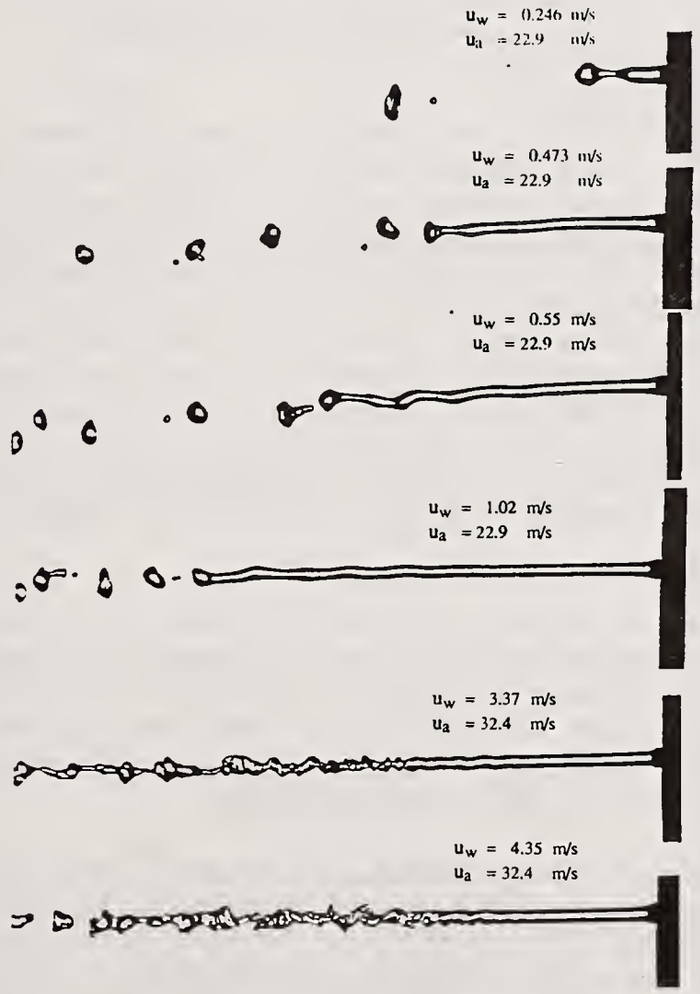

Fig. 2 Disintegration of water jet in a coaxial air stream

Axisymmetric Rayleigh Breakup

Studies of axisymmetric Rayleigh jet disintegration for water emerging into quiescent air were made for Ohnesorge number 0.0037. According to Reitz's classification, the first-wind-induced disintegration mechanism should appear at the liquid Reynolds number of $Re_w = 1500$. The second wind induced disintegration mode should begin at $Re_w = 5000$. In contrast to Reitz's classification, no significant change in the Rayleigh breakup from the first to the second wind induced region was observed. The present experiments show the well known dependence of the intact liquid length on the jet velocity which, for the first time, was described by Haenlein [13] at similar experimental conditions.

The influence of gravity on the initially horizontal jet was clearly seen at low exit velocities. Nevertheless, the shape of the jet, the ligaments and the drops were nearly axisymmetric for the whole flow range. The influence of gravity on the jet flow direction is highly reduced for a horizontal water jet with a coaxial air stream, as can be seen in Fig. 2. Though this disintegration mode is classified as the axisymmetric Rayleigh mechanism, the disintegrating jet may begin to show a very slight tendency to form a helical axis. Nevertheless, the jet, the ligaments and the drops are still nearly axisymmetric around this slightly helical axis. The jets with the corkscrew shape before the jet disruption shown in Fig. 2 are typical examples of the first wind-induced disintegration according to Reitz's classification. They are still assigned to the axisymmetric Rayleigh mechanism in this presentation. The boundary between the axisymmetric and non-axisymmetric Rayleigh type jet disintegration modes is poorly defined.

Non-Axisymmetric Rayleigh Breakup

The non-axisymmetric Rayleigh mode of jet breakup forms the boundary between the classical Rayleigh breakup and the membrane-type breakup. Figure 3 shows photographs of this jet disintegration. The liquid jet first accelerates rapidly in the high speed gas stream. Accordingly, it's diameter is significantly reduced. The direction of the thin capillary liquid jet is influenced by the interaction between the liquid jet and the turbulent structures of the surrounding air stream. The wave formation on the round liquid jet may be caused by both the Kelvin-Helmholz instability and the liquid-gas interaction. The aerodynamic forces reduce the jet diameter, but the breakup itself may be due to the Rayleigh mechanism. The whole jet breaks into drops without intermediate membrane formation or fibers peeling off. This mode of jet disintegration may also be the final step of the membrane type and the fiber type atomization. To understand this mechanism of round liquid jet breakup, a combination is needed of the description of the jet deformation by aerodynamic forces and the instability analysis of the deformed round liquid jet.

Membrane Type Breakup

The dominant criteria for the membrane type breakup are: The whole round jet forms a thin sheet (membrane) before breaking into drops. The liquid matter accumulates at the edge of the thin sheet, forming a round liquid frame. The diameter of the round frame is smaller than the diameter of the emerging intact liquid jet. The liquid frame breaks into drops via the non-axisymmetric Rayleigh mechanism. The mean drop diameter is one order smaller than the jet diameter. The maximum drop diameter is also smaller than the jet diameter.

Figure 4 shows photographs demonstrating this type of liquid jet disintegration. The morphology of the membrane type disintegration of round jets is very similar to that of thin liquid sheets, previously described by Dombrowski and Mansour, among others. The very similar disintegration mode of spherical liquid drops in an air stream is known in the literature as "umbrella", "bag" or "hat" - type disintegration presented by Lane [14], Wolfe [7], Kennedy [10] and others.

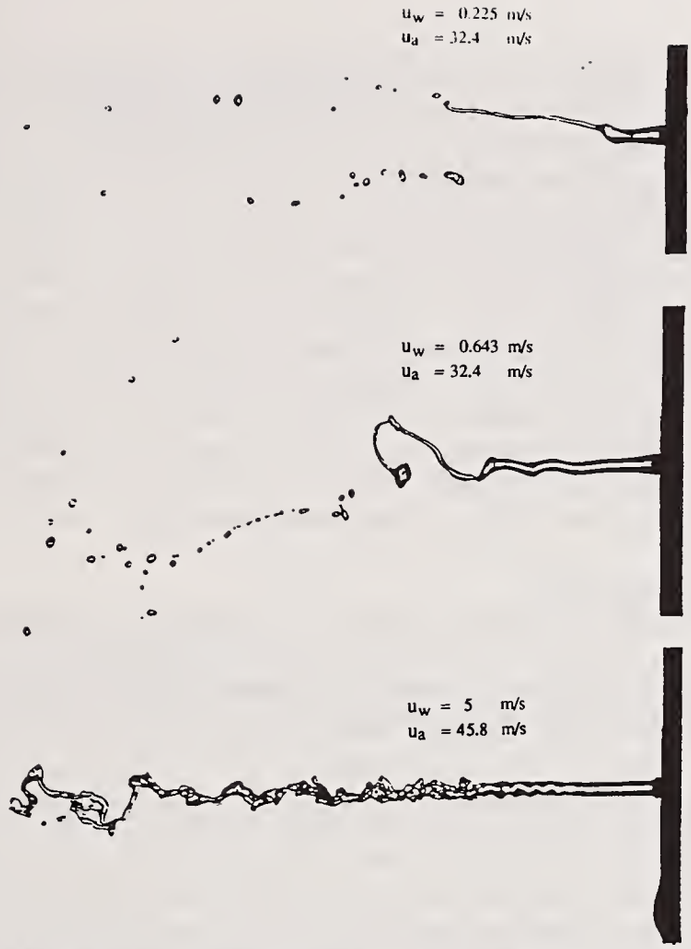

Fig. 3 Non-axisymmetric rayleigh breakup of water jet in a coaxial air stream

Fig. 4 Membrane type breakup of water jet in a coaxial air stream

Fiber Type Breakup

For many applications, such as the atomization of liquid oxygen in the space shuttle main engine, the fiber type liquid jet breakup is the most important mode of liquid atomization. The atomization begins with the formation of fibers and their peeling off the main liquid core. The fibers break into droplets by the non-axisymmetric Rayleigh jet disintegration mode. In this stage of the atomization, very small drops are produced. The diameter of those droplets is a few orders of magnitude smaller than the diameter of the emerging liquid jet. Further downstream, the main liquid core becomes wavy and breaks into ligaments. The length of these ligaments is about two to five times the initial jet diameter. From the ligaments, new fibers are peeled off. The diameter of the newly formed fibers increases with increasing axial distance from the nozzle exit. Even further downstream, the ligaments form clouds of drops and liquid fibers, which leads to a periodic change from high to low density spray. Generally, the size of the drops generated further downstream is bigger than those formed closer to the nozzle exit. For calculation of drop size, breakup time, and axial distance to complete the atomization, measurements need to be made of the velocity field of the ligaments and of the surrounding gas stream.

Pulsating Disintegration Sub-Mode

All the photographs in Figs. 2 through 4 show the pulsating jet disintegration sub-mode which can be considered as the "normal" sub-mode of jet disintegration. As can be seen in all the photographs, the ligament and drop formation is connected to unstable wave formation of the disintegrating liquid jet. Therefore, atomization is always a pulsating process.

Super-Pulsating Disintegration Sub-Mode

For air velocities of 183 m/s and liquid velocities between 1 and 6 m/s, photographs show the "super-pulsating" jet disintegration sub-mode. This type of jet disruption appears when a low liquid mass flow rate is associated with a very high flow rate of the atomizing gas. Reducing the liquid flow rate which induces the change from a continuous liquid flow (in the quiescent air) to dripping flow conditions can be considered an analogy to the change from the pulsating to the super-pulsating sub-mode of airblast atomization. The intact liquid length is extremely short for this sub-mode. In some cases, it amounts only to one or two jet diameters. Generally, the periodic change of liquid flow rate, drop size and number density is significantly higher for the super-pulsating sub-mode than for the "normal" pulsating sub-mode. When the air mass flow rate increases, the corresponding liquid mass flow also increases at which point the super-pulsating sub-mode changes to the normal pulsating conditions. Although the boundary between the two sub-modes is not clearly defined, the tendency is clear and obvious. In the transient region from the normal-pulsating to the super-pulsating sub-modes, the jet disintegration shows either the morphology corresponding to the normal-pulsating mode or the shape of the super-pulsating disruption. Especially at very low liquid flow rates, the spray pulsation, which is defined as the ratio in number density or in liquid flow rate between the dense and the diluted spray, is extremely high.

Classification of Jet Disintegration Modes

Figure 5 shows a plot of the different jet disintegration modes described above as a function of the aerodynamic Weber number and the liquid Reynolds number at the nozzle exit. For each experimental point in Fig. 5, four to ten photographs were analyzed. If one of the photographs demonstrated different disintegration modes than the others at the same flow condition, both observed modes were overlapped in Fig. 5. This case often occurred at the transition range between two disintegration modes.

According to this chart, the axisymmetric Rayleigh type disintegration is the dominant mode of jet disruption for the aerodynamic Weber number range of about $We < 15$. In the range of about $15 < We < 25$, the non-axisymmetric disintegration mode is the most typical. However, at the transition from the axisymmetric to the non-axisymmetric disintegration mode, the corresponding Weber number slightly increases with the increasing Reynolds number. The membrane type jet disintegration appears in the aerodynamic Weber number range of about $25 < We < 70$. This range

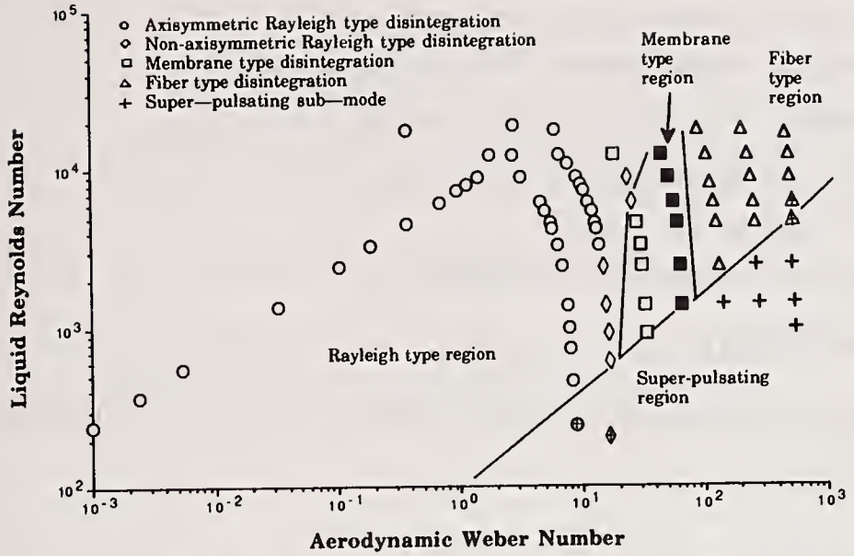

Fig. 5 Modes of liquid water jet disintegration in a coaxial air stream

seems to reduce with the increasing liquid Reynolds number. At higher Weber numbers, the round jet disintegrates by the fiber type disruption mode. If the ratio of the Reynolds number to the square root of the Weber number is lower than about Re_w / SQRT (We_a) < 100, the super-pulsating sub-mode dominates for the jet disintegration.

CONCLUSION

The photographic studies show similarities between the disintegration modes of round water jets in a coaxial air stream and the disintegration of water drops in an air stream previously investigated by Lane [14], Wolfe [7], Kennedy et al. [10]. At similar aerodynamic Weber numbers, the disintegration modes are also similar. Additionally, the disintegration of thin water sheets, previously examined by Dombrowski [12], Mansour [1] and others, shows similar events at similar Weber numbers. A comparison of the classification of round liquid jet disintegration modes shows some disagreement with the first and second wind induced atomization classification presented by Ohnesorge [4], Reitz [6], and others.

For technical applications, the most important mode of atomization is the "fiber-type" jet disintegration. Spark light photographs show high pulsation for this mode of atomization, especially for the flow condition corresponding to Re_w / SQRT (We_a) < 100. For the fiber type atomization, the greatest amount of liquid is atomized in the secondary atomization region. Here too, the biggest drops are generated. However, most theoretical studies deal only with the onset of the instabilities and the primary atomization region based on wave instabilities at the axisymmetric intact liquid surface. For calculations in the critical and most important secondary atomization region, detailed measurements are needed of ligament size, ligament velocities, and relative velocities.

NOMENCLATURE

d_i	coaxial tube inner diameter [m]
d_h	air gap hydraulic diameter [m]
Oh	Ohnesorge Number, $Oh = We_m^{0.5} / Re_w$
Re_a	Reynolds Number of air, $Re_a = u_a (d_h/\nu_a)$
Re_w	Reynolds Number of water, $Re_w = u_w (d_i/\nu_w)$
u_a & u_w	air and water mean velocity [m/s]

u_r relative velocity between gas and liquid [m/s]

We_a aerodynamic Weber Number, $We_a = u_r^2 \rho_a d_i/\sigma_w$

We_m mechanical Weber Number, $We_m = u_w^2 \rho_w d_i/\sigma_w$

ρ_a & ρ_w air and water density [kg/m^3]

σ_w water surface tension [kg/s^2]

ν_a & ν_w air and water kinematic viscosity [m^2/s]

ACKNOWLEDGEMENT

The authors wish to acknowledge financial support from NASA Marshall Space Center, grant number NAG8-126.

REFERENCES

1. Mansour, A., Chigier, N., Physics of Fluids, Vol. 2, No. 5, 1990.

2. Faragó, Z., Chigier, N., ASME Paper No. 90-GT-81, International Gas Turbine and Aeroengine Congress, Brussels, Belgium, June 1990.

3. Eroglu, H., Chigier, N. and Faragó, Z., Physics of Fluids A to be published, 1991.

4. Ohnesorge, W.V., Z.V.D.I., Vol. 81, No. 16, 1937.

5. Miesse, C.C., Ind. Eng. Chem., Vol. 49, No. 9, 1955.

6. Reitz, R.D., Ph.D. thesis, Princeton University, 1978.

7. Wolfe, H.E., Unclassified AD473340, U.S. Defense Documentation Center, Cameron Station, Alexandria, VA, 1964.

8. Buschulte, W., DLR-FB 73-79, 1973.

9. Buschulte, W., ISABE, 9th Int. Symp. of Air Breathing Engines, Athens, 1989.

10. Kennedy, J.B., Roberts, J., ILASS-Americas, 4th Annual Conference, Hartford, CT, May 1990.

11. Faragó, Z., Chigier, N., ILASS-Americas, 4th Annual Conference, Hartford, CT, May 1990.

12. Crapper, G.D., Dombrowski, N., Jepson, W.P., and Pyott, G.A.D., cited in An Album of Fluid Motion, Parabolic Press, Stanford, CA, 1982.

13. Haenlein, A. ,Forsch. Geb. Ingenieurwesens A, Vol. 2, No. 4, 1931.

14. Lane, W.R., Ind. Eng. Chem., Vol. 43, 1951.

15. Faragó, Z. and Chigier, N., Atomization and Sprays, Vol. 2, 1992.

EXPERIMENTAL INVESTIGATION OF TWO-PHASE FLOW IN THE NEAR FIELD OF AN AIRBLAST ATOMIZER

P. Hebrard, P. Trichet and X. Bardey*

ONERA/CERT/DERMES, Toulouse, France
*SNECMA, Centre de Villaroche, Moissy Cramayel, France

ABSTRACT

A detailed study of the two-phase flow produced by a gas turbine airblast atomizer is performed. Two-component Phase Doppler Interferometry is utilized to characterize the two-phase flow fields produced by the atomizer: continuous and dispersed phases. Measurements of the mean axial and transverse velocities for each phase are conducted. In addition, the droplet size distribution and the volume flux are measured. The results demonstrate the influence that the spray has on the gas flow and also the swirl influence on the drop size distribution.

INTRODUCTION

The spray behavior of an atomizer has a direct effect on the combustor performance. Detailed measurements of both continuous and dispersed phases in liquid fuel sprays are essential for a good understanding of the physical processes of fuel-air mixing and transport phenomena. The present work addresses these questions by utilizing recently developed diagnostic techniques which provide nonintrusive measurements of droplet size distribution, droplet velocity, droplet mass flux and dilute phase velocity inside a small measuring volume in the flow field. In addition, the experimental data obtained are to be utilized as a data base for the development and validation of numerical codes [1].

The approach taken in this study is to apply nonintrusive diagnostic techniques to characterize an airblast atomizer under nonreacting conditions. Measurements are obtained at three axial sections 4.5, 16.4 and 36.4 mm downstream of the atomizer and include mean axial and transverse velocities of the gas phase within the isothermal spray, mean axial and transverse droplet velocities, local drop size distribution and volume flux.

EXPERIMENTS

Atomizer

The atomizer utilized in the present study is shown in Fig. 1a. The atomizer is of the airblast type and is designed for use in gas turbine engines.

Test Conditions

The operating conditions selected for the present study are a baseline case corresponding to a "cruise" operating level: the fuel flowrate is 4.1 g/s, and the pressure drop through the atomizer is 4 %. Water is employed as fuel simulation fluid in the present study.

a) Airblast Atomizer

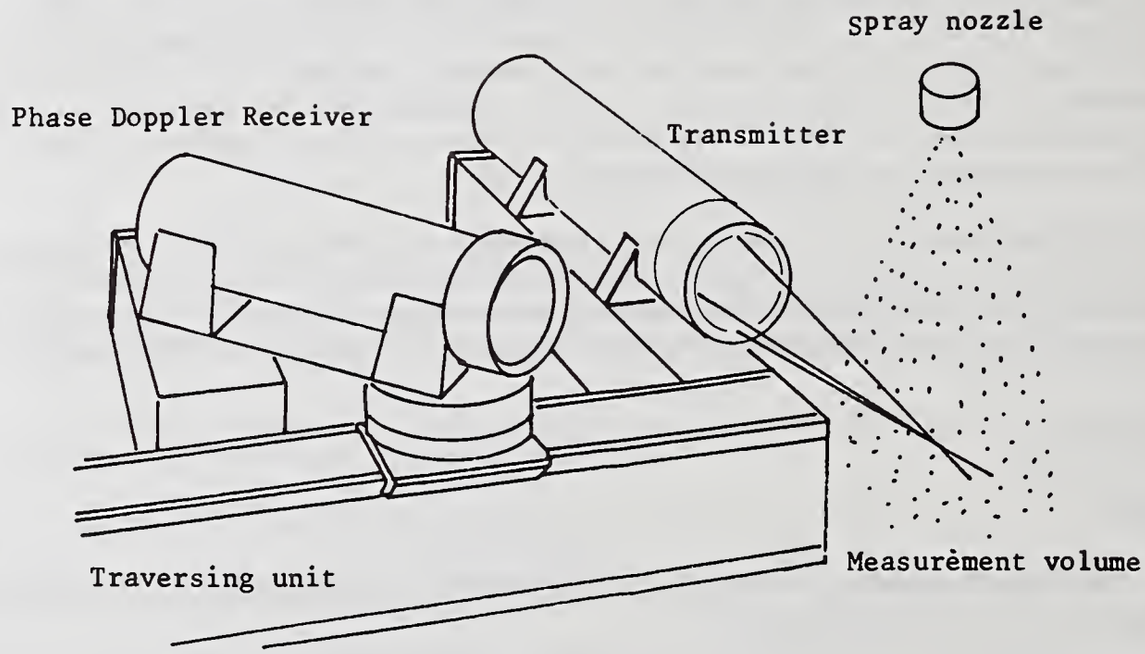

b) Schematic of the spray test rig

Figure 1 Experimental set up for spray analysis

Facility

The atomizer is mounted in an adapter (airbox) which provides both fuel and atomizing air. The particular configuration and orientation employed in this study are presented in Fig. lb.

Diagnostics

The anemometer used in this study is a two-components dual-beam Phase Doppler Particle Analyzer (Aerometrics PDPA System 200) [2]. Two orthogonal probe volumes are provided by separating the 488.0 nm and 514.5 nm lines from an Argon laser. Data acquisition, processing and storage are conducted on a Compaq deskpro 386/20 e Computer.

The PDPA provides spatially and temporally resolved measurements of drop size (D_{10}, D_{20}, D_{30}, D_{32}) velocity (mean, rms), correlations (size-velocity, velocity-velocity) and volume distributions. In addition, the instrument is used to discriminate the two phases in the spray [3]. By optimizing the sensitivity of the instrument to small particles and extracting particles which are small enough to track the flow, the continuous phase velocity can be measured.

Measurements are made across three axial planes: 4.5, 16.4 and 36.4 mm. For each of these planes, data are collected at each point of a grid (see Fig. 2b). Through most of the spay, 4000 data points are collected for each location - Exceptions were made when the data rate was very low: in these regions, the flow was sampled for a minimum of 1000 seconds.

RESULTS AND DISCUSSION

Droplet Size Distribution

Surface plots showing the local variation of Sauter mean diameter SMD = D_{32} for each of the three cross sections are shown in Fig. 3. Close to the nozzle, the droplet size distribution exhibits a dome shaped repartition. The inner and outer air flows of the airblast atomizer produce a near uniform drop size distribution, but the air jets issuing from the cup holes produce a secondary atomization attested by the near circular depression. Some large drops are observed in the core evidencing the fact that large drops are generated by the inner swirling air.

Further downstream, the distribution broadens as one moves along the spray. The swirling flow recirculates the small drops back within the central region of the flow. Large indentations on the boundary of the spray are due to the cup hole jets. At the lower section, the size distribution is more uniform on the periphery of the spray. The spray cone angle is widened by the swirl effect and small drops are in the inner core. These size distributions are characteristic of sprays with swirl [4].

Droplet Velocity

Surface plots showing the local variation of droplet mean velocity for each of the three cross sections are presented in Fig. 4 (axial velocities) and Fig. 5 (transverse velocities). Close to the nozzle, the axial velocity distribution exhibits two concentric maxima; these peaks are due to the inner and outer swirling air. Further downsteam, these two distributions merge to form an unique axial flow field. At the lower position the velocity distribution widens. Between the three cross sections, we can note increasing velocities indicating droplet acceleration. In the core of the swirling flow, a size-velocity correlation exists.

Transverse velocity distributions shown in Fig. 5 indicate that, close to the nozzle, there are two swirling flows; the near circular dip is due to the cup hole jets. Along the $y = 0$ axis, we have a diametral evolution of tangential velocity and along $x = 0$ we have the radial velocity. Further downstream, the huge swirl flow occupies the core of the spray and on the outer edge of the spray, the transverse velocity is nearly

a) Spray visualization by laser light sheet

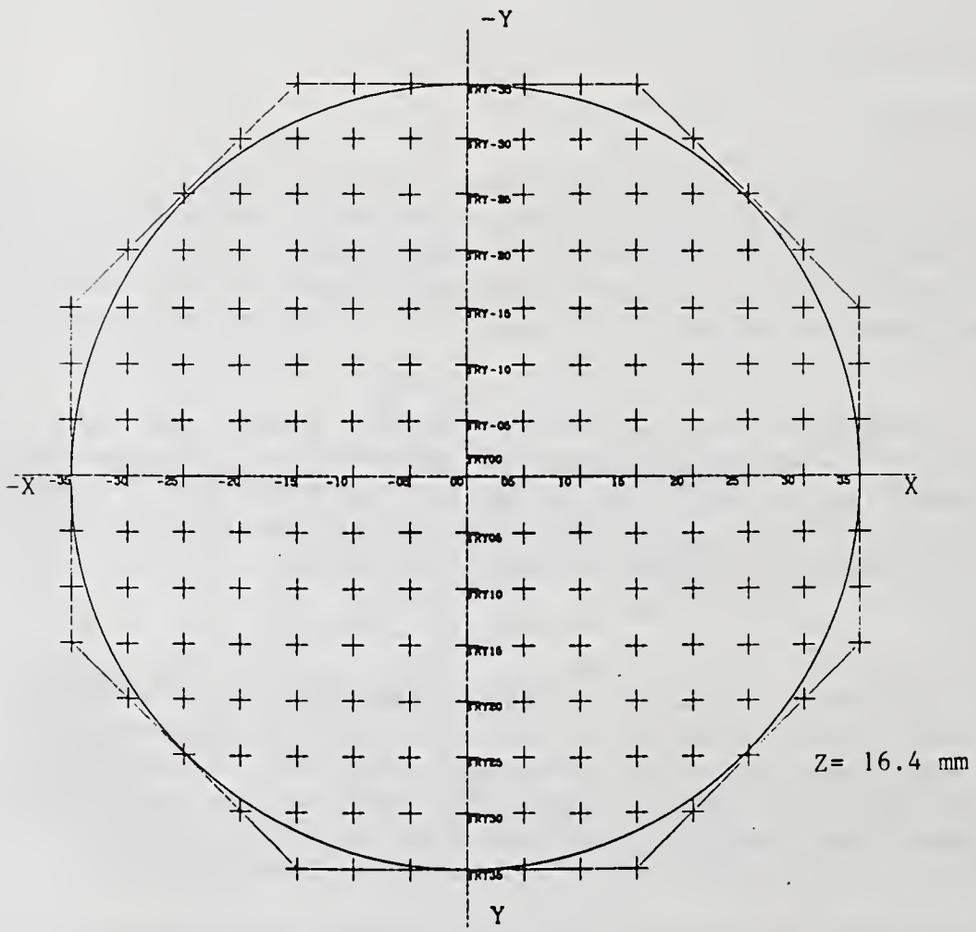

b) Net of measurement locations (grid size 5mmX5mm)

Figure 2 Shape of spray area in the spray cone

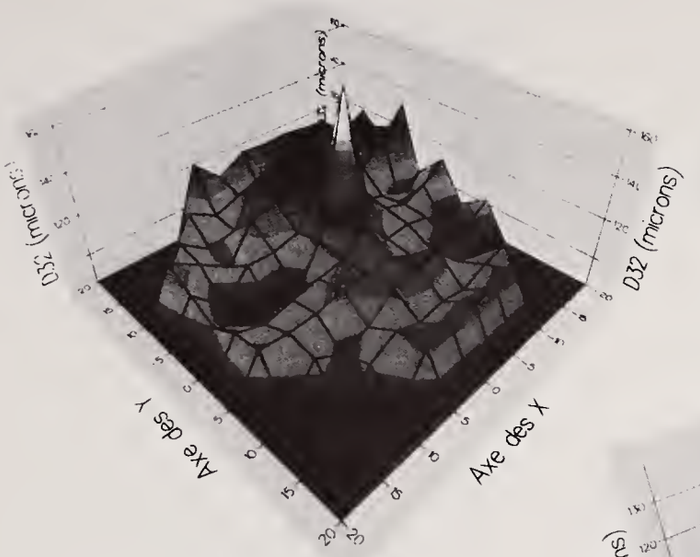

Z= 4.5 mm

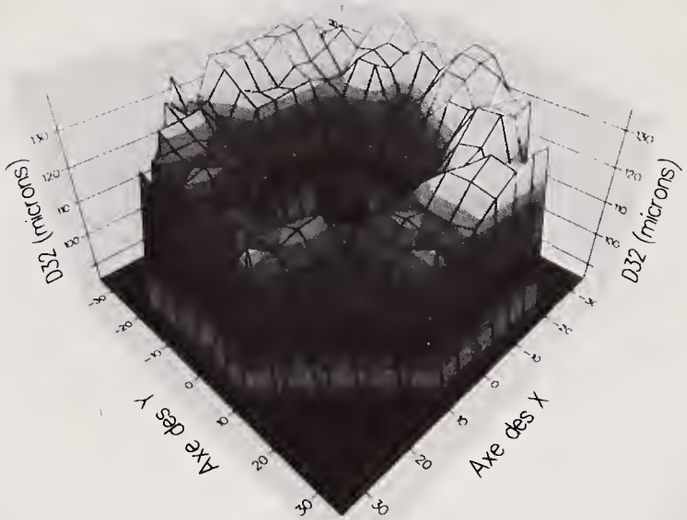

Z= 16.4 mm

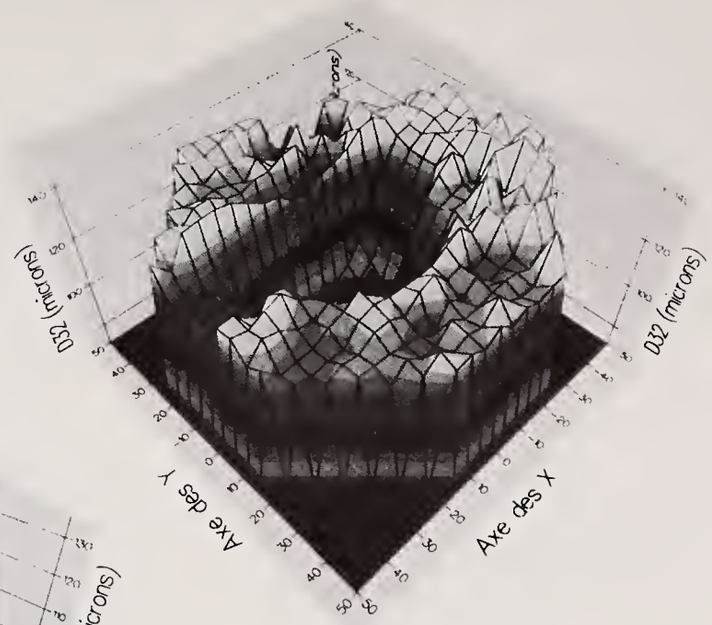

Z= 36.4 mm

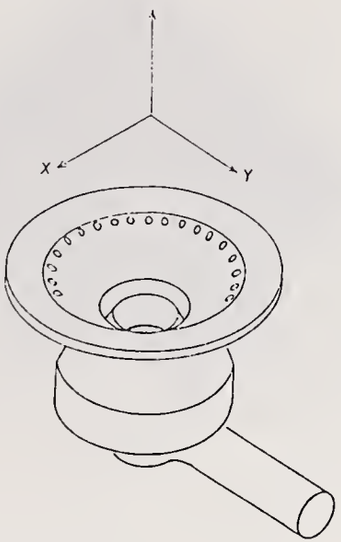

Figure 3 SMD as a function of X and Y positionsfor cross sections located at 4.5,16.4 and 36.4 mm downstream of the atomizer (X and Y are given in mm)

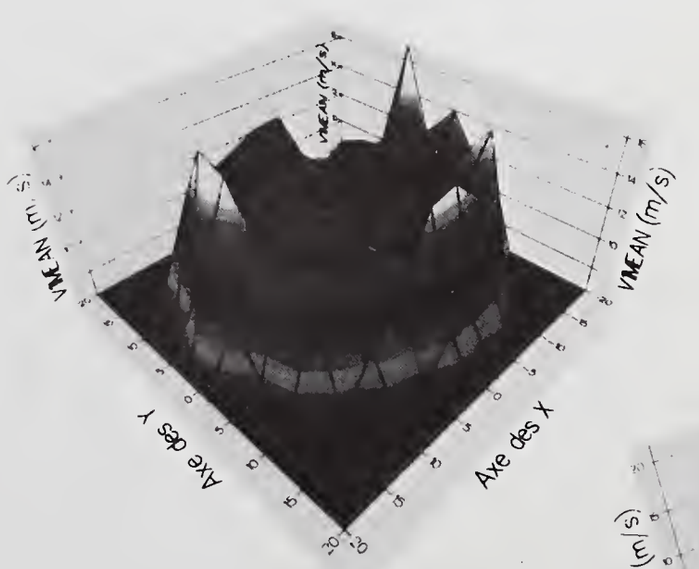

Z= 4.5 mm

Z= 16.4 mm

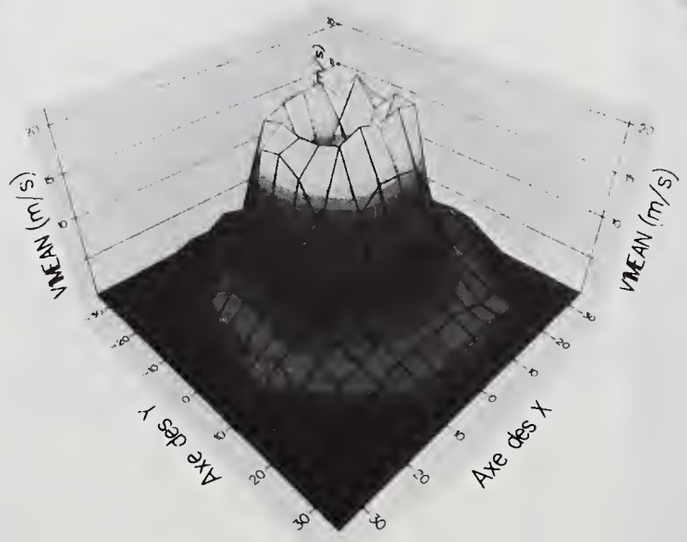

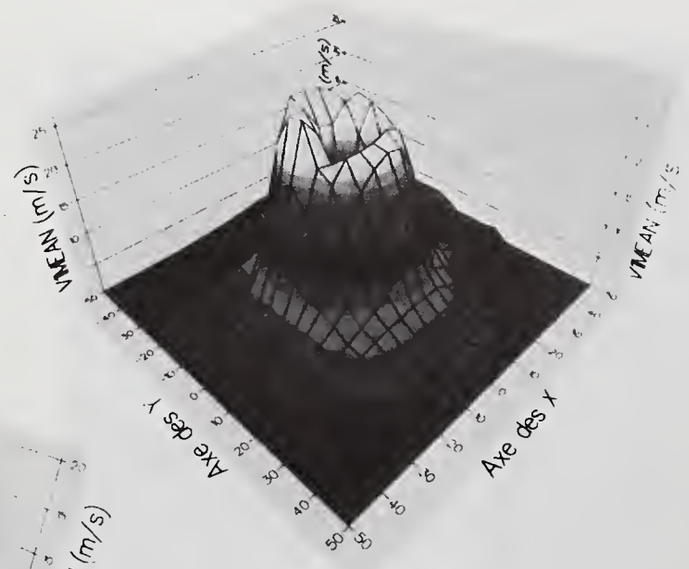

Z= 36.4 mm

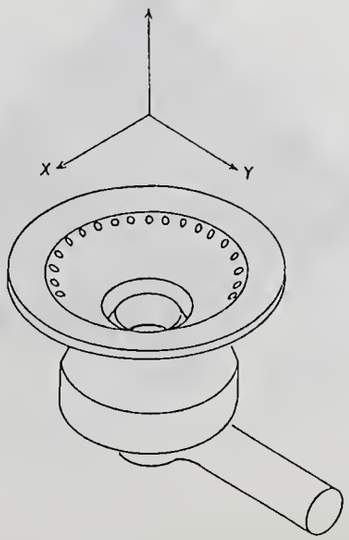

Figure 4 Droplet mean axial velocity as a function of X and Y positions for cross sections located at 4.5,16.4 and 36.4mm downstream of the atomizer (X and Y are given in mm)

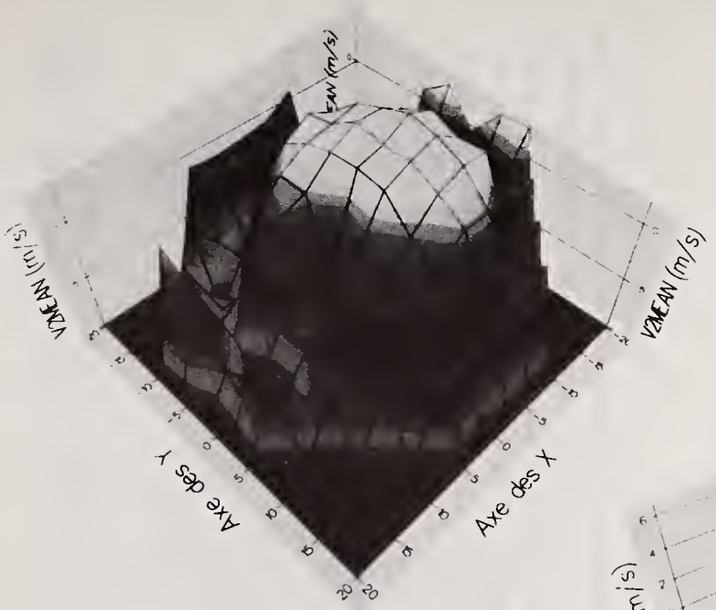

Z= 4.5 mm

Z= 16.4 mm

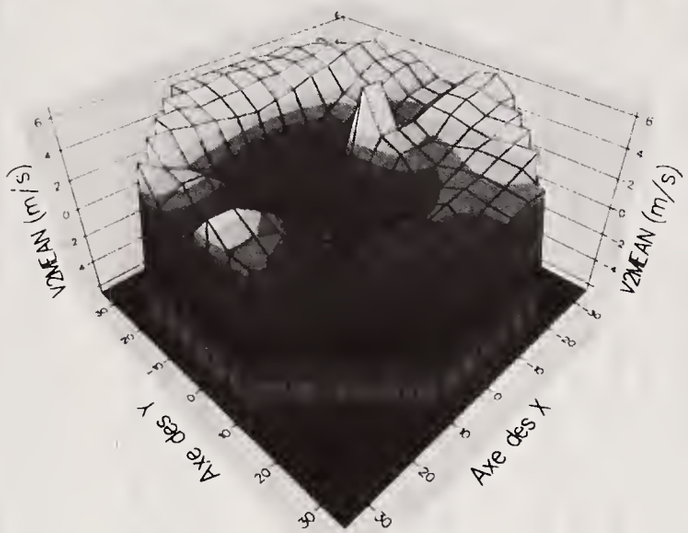

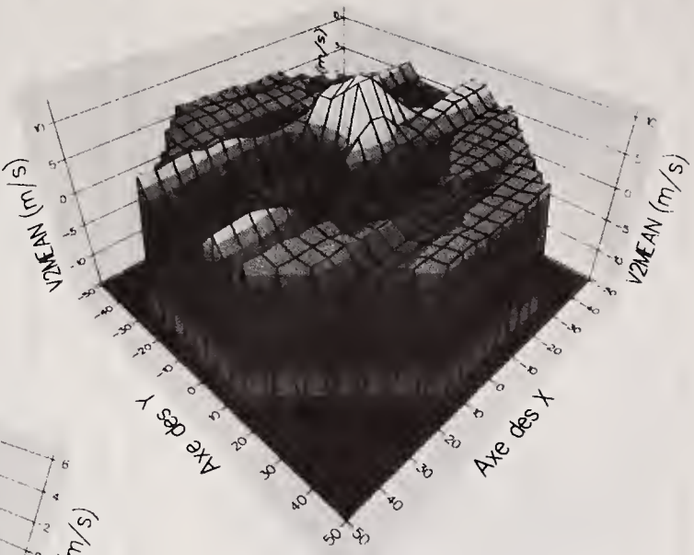

Z= 36.4 mm

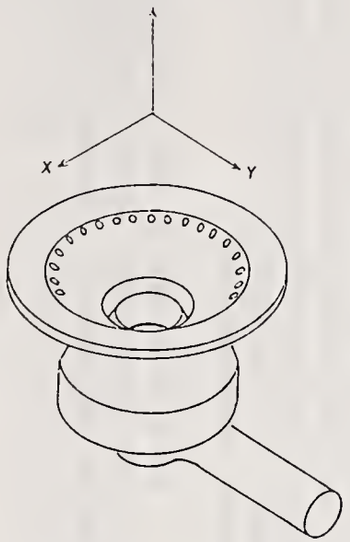

Figure 5 Droplet mean transverse velocity as a function of X and Y positions for cross sections located at 4.5,16.4 and 36.4mm downstream of the atomizer (X and Y are given in mm)

constant. At the lower position, we find a widening of the velocity distribution, and the swirling core is still present. As for the axial velocity, the transverse velocity increases downstream. However, contrary to the axial velocity, the transverse velocities demonstrate no significant dependence upon size, indicating little momentum transfer between phases in this velocity component.

Droplet Volume Flux

The phase Doppler instrument can also be used to measure the volume flux of the fuel. It calculates the cross section of the measurement volume and utilizes size and velocity measurements to obtain the local volume flux [5]. Surface plots showing the local variation of volume flux for each of the three cross sections are shown in Fig. 6. Nozzles generally display asymmetries [6]. The swirl component of the flow produces a rotation of this asymmetry in a "cork screw" manner in and out of the measurement planes. The swirling air has the effect of widening the spray cone angle, showing low concentration of drops in the core.

Continuous Phase in the Presence of the Spray

The PDPA has been used to discriminate the gas and dispersed phases of the flow. Comparisons have been made between the two phases, for the cross section located at 16.4 mm downstream of the atomizer (data not shown). There are several interesting points which can be pointed out. The axial gas velocity is found to be slightly higher than the drop velocity. The outside boundary of the spray presents indentations, proof of the cup hole jets' interactions. On the transverse velocity, many peaks have been observed which can be attributed to the same cause. Only at the lowest position, we find negative values on the axis for the gas velocity, indicating a recirculating flow.

Figure 7 presents a diametral scan of the mean axial continuous phase velocities. We can note that the presence of the spray seems to reduce the width of the profile and also that, in this section, the reverse flow near the axis cannot be measured.

CONCLUSION

Several measurements have been made throughout each of three cross sections in an airblast atomizer spray. These results are presented as surface plots showing how the liquid volume flux, SMD and velocities vary with position within each of these cross sections, corresponding to 4.5, 16.4 and 36.4 mm downstream of the nozzle orifice.

This study demonstrates that substantial information can be extracted from the complex environment of a spray, using non intrusive techniques. For the present atomizer and operating conditions it is observed that: a) the conditions near the atomizer differ greatly from the conditions further downstream; b) the distributions of size, velocity and volume flux are strongly influenced by the dynamics imposed by the swirling field; c) the presence of fuel spray injection substantially changes the character of the flow field in the near field of the atomizer; and d) between the three cross sections, the drop velocity increases with increasing axial distance, indicating a momentum change.

Future work will be extended to the third velocity component, then leading to insight into : velocity of selected size groups, estimated droplet flight path, momentum transfer from the gas to the drops, assessment of droplet drag coefficients, and turbulence damping by the drop. These additional data are necessary for further development and verification of two-phase flow numerical codes.

ACKNOWLEDGEMENTS

This work was supported by a SNECMA contract. We would like to thank Dr P. MILLAN for his expert technical assistance. The participation of J. FORNE in the collection of data and development of data reduction software is appreciated.

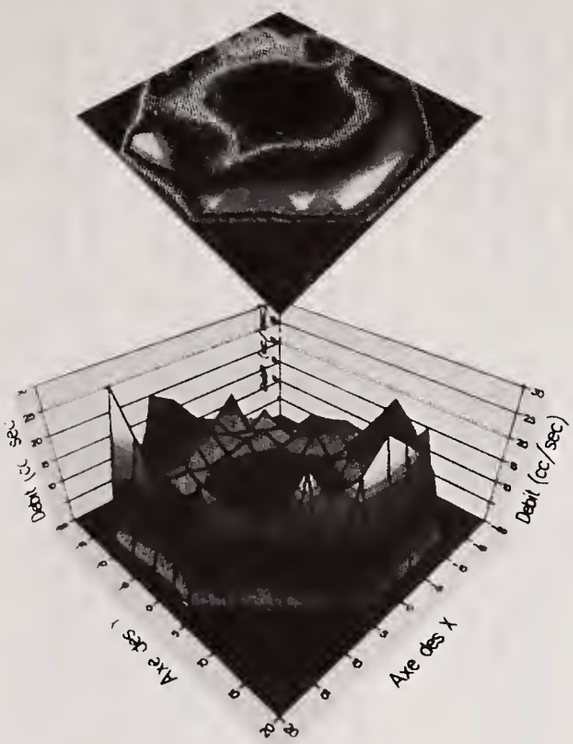

Z= 4.5 mm

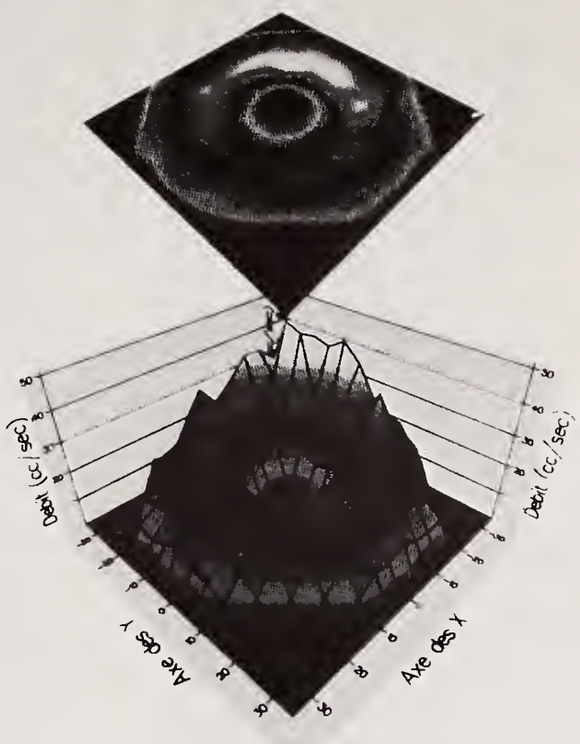

Z= 16.4 mm

Z= 36.4 mm

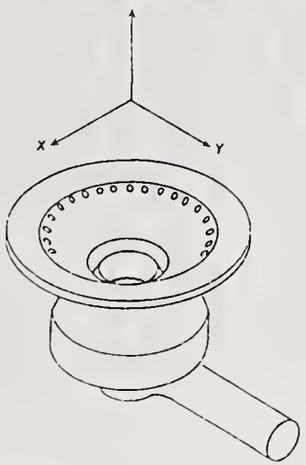

Figure 6 Droplet volume flux as a function of X and Y positions for cross sections located at 4.5,16.4 and 36.4 downstream of the atomizer
(X and Y in mm and multiply values by 10^{-6})

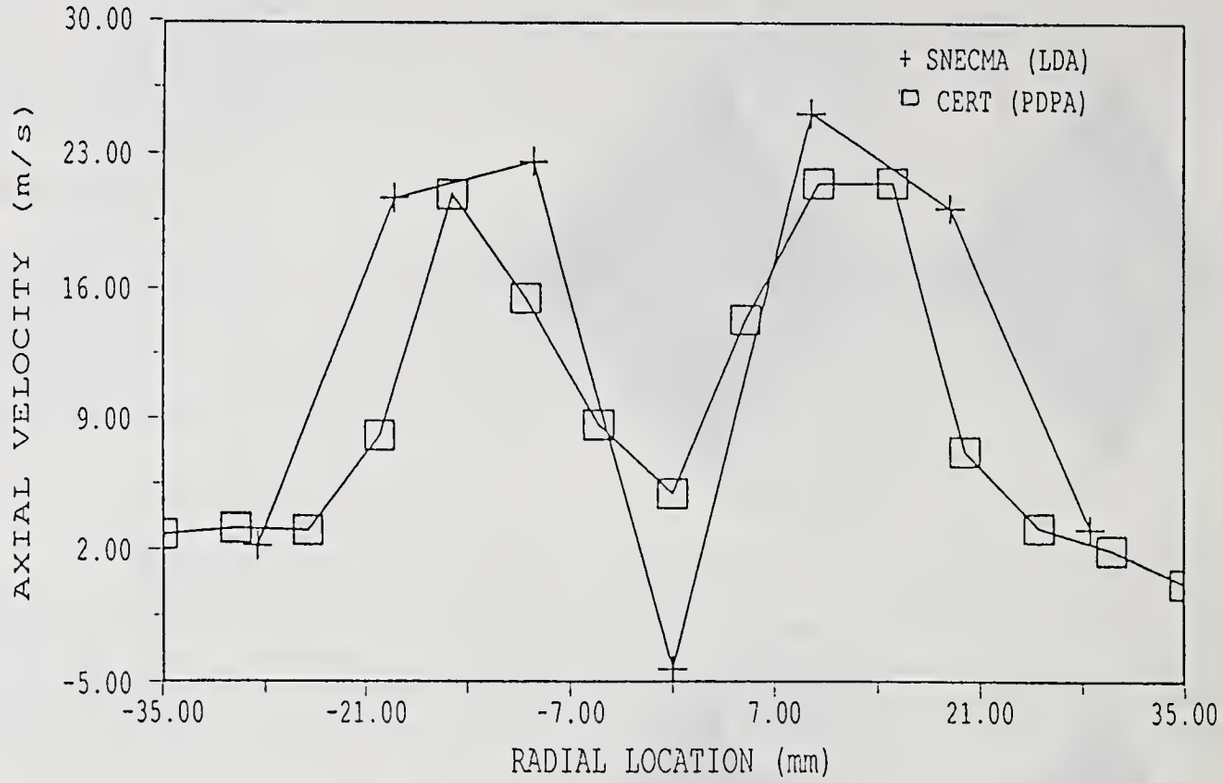

Figure 7 Continuous phase mean velocities,downstream location: 16.4 mm.
SNECMA LDA results: without spray
CERT PDPA results: with isothermal spray

REFERENCES

1. Hebrard, P., Lavergne, G., Trichet, P., "Experimental Study of Boundary Conditions for Spray Systems in Combustion Chambers", Sixth Annual Conference ILASS Europe, Pise, Italy (July 1990).
2. Bachalo, W.D., Houser, M.J., "Development of the Phase/Doppler Spray Analyzer for Liquid Drop Size and Velocity Characterizations", AIAA/SAE/ASME Twentieth Joint Propulsion Conference, Cincinnati, Ohio (June 1984).
3. Mc Donnell, V.G., Samuelsen, G.S., "Application of two Component Phase Doppler Interferometry to the Measurement of Particle Size, Mass Flux, and Velocities in two phase-flows". Twenty second Symposium on Combustion, pp. 1961-1971, The Combustion Institute, Pittsburgh, PA (1988).
4. Brena de Ia Rosa, A., Bachalo. W.D., Rudoff, RC.. "Spray Characterization and Turbulence Properties in an Isothermal Spray with Swirl". ASME paper 89 GT 273, Gas Turbine and Aero Engine Congress, Toronto, Canada (June 1989).
5. Bachalo. W.S., Rudoff, R.C., Brena de Ia Rosa, A., "Mass Flux Measurements of a High Number Density Spray System using the Phase Doppler Particle Analyzer", AIAA 88-236, AIAA Twenty Sixth Aerospace Science Meeting, Reno, Nevada (January 1988).
6. Rosfjord, T.J., Russsell, S., "Influences on Fuel Spray Circumferential Uniformity", AIAA/SAE/ASME/ASEE Twenty-third Joint Propulsion Conference, San Diego, CA (July 1987).

LIQUID SHEET INSTABILITY IN A COFLOWING AIR STREAM

H. Eroglu and N. Chigier

Mechanical Engineering Department
Carnegie Mellon University
Pittsburgh, PA, U.S.A.

ABSTRACT

Wave characteristics of a liquid sheet injected from a two-dimensional airblast atomizer were investigated using high speed photography and frequency measurements. Photography was used to determine the spatial wave amplitude growth rates and average wavelengths. Wave frequencies were measured by means of a laser beam attenuation technique. Wave propagation speeds were calculated from the measured average wavelengths and frequencies. The effects of liquid viscosity and surface tension on the frequencies were investigated by mixing glycerine and Triton X-100 respectively with water. The average wavelengths decreased with both liquid mass flow rate and air velocity. However, the dominant frequency increased with these parameters. The spatial wave amplitude growth rate decreased with liquid mass flow rate and increased with air velocity.

INTRODUCTION

Study of the disintegration of a thin liquid sheet in a coflowing air stream can help in the understanding of the basic mechanisms of atomization in practical systems without the added complexity of a three-dimensional configuration.

Liquid sheet disintegration has been studied previously by several researchers [1-5]. More recently, computational methods have been developed. Among the recent computational methods, Lin and Lian [6] studied the instability of a viscous liquid jet in a gas, using a linear model. They assumed that the disturbances on the sheet surface grow spatially, but they did not consider the temporal growth rates.

Among the recent experimental investigations of liquid sheet instability, Lee and Yang [7] measured sheet thickness variations both as a function of time and distance in the flow direction. They performed their experiments on liquid films bounded by a solid surface at one side and a high velocity air flow on the other. As a result, the liquid surface waves were found to be influenced considerably by the air velocity. Arai and Hashimoto [8] investigated the disintegration of a thin liquid sheet in a co-current air stream. The liquid sheet vibration and breakup frequencies were observed to be equal to each other. The wave frequency and amplitude were correlated with Weber and Reynolds numbers. Their frequency measurements revealed that the wave frequency increases with liquid and air velocities. Mansour and Chigier [9] studied the instability of a liquid sheet issuing from a two-dimensional airblast atomizer. They reported that the liquid sheet vibrates in the sinuous mode at low liquid velocities, and dilational waves are dominant at high liquid

velocities. At intermediate liquid sheet velocities, both sinuous and dilational modes are superimposed on the liquid sheet.

This paper describes the wave characteristics in terms of average wavelengths, spatial amplitude growth rates, wave frequencies and propagation speeds for the same two-dimensional airblast atomizer used in reference [9]. The effects of liquid viscosity and surface tension on the wave frequencies are also investigated.

EXPERIMENTAL TECHNIQUE

Figure 1 shows the two-dimensional airblast atomizer. The liquid sheet emerges from a central slit which is 0.254 mm wide and has an aspect ratio of 120:1. The air streams have a convergence angle of about 48 degrees and impinge on both sides of the liquid sheet. The slit width for the discharging air streams is 1.45 mm. The two-dimensional atomizer was mounted on an XY positioner with an accuracy of 1 mm in all directions. The liquid and air supply systems provide a maximum liquid flow rate of 2270 kg/h and air pressure of 600 kPa.

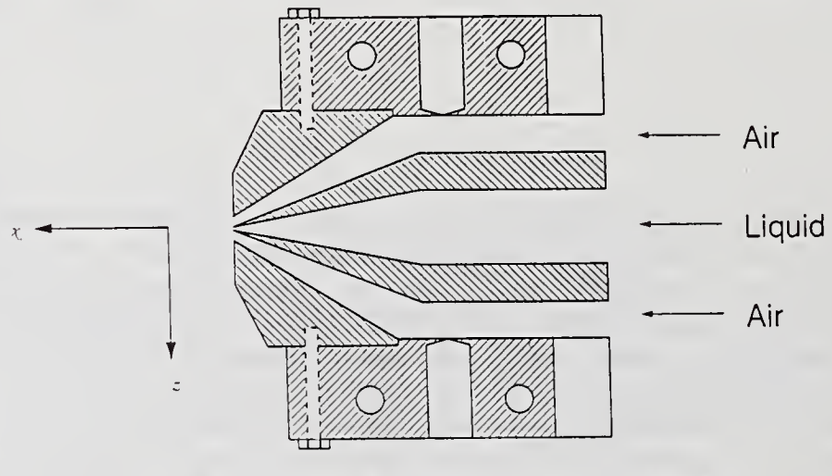

Fig. 1 2-Dimensional Airblast Atomizer

A 4x5 inch plate camera was used with bellows extensions. This camera provides a narrow depth of field and up to three times magnification of the disintegrating liquid on the film plane. An EG&G 549 microflash was used with a 0.5 μs pulse duration. A back lighting technique was found to be the most effective lighting arrangement for obtaining high contrast images. Four to seven photographs of the liquid sheet were taken at each flow condition for determining average values of wave amplitudes and lengths. The accuracy of these average values is estimated to be within 10%.

Figure 2 shows the optical configuration for the frequency measurements. An Aerotech model LS2P Helium-Neon laser with 2 mW output power is used as the light source. The oscillating liquid sheet is positioned such that the line of the laser beam coincides with the y direction of Fig. 2. The photodiode generates a current proportional to the incident light intensity which varies as the liquid sheet crossed the laser light and causes its attenuation. The current from the photodiode is converted into voltage by way of a simple operational amplifier feedback circuit. This voltage is fed into a Nicolet digital oscilloscope to visualize the waveform. The analog voltage is also transferred to an IBM PC/XT computer at the rate of 20 kHz via an analog-to-digital converter. Fast Fourier transform analysis is applied to the data in order to determine the dominant frequencies. Dominant frequencies are finally displayed in the frequency domain as shown in Fig. 3. The best signal quality was obtained when the laser beam was positioned close to the wave crests as suggested by Mansour and Chigier [9]. The uncertainty of the frequency measurements at low liquid flow rates was about 3% for a 95% confidence level. However, it increased to 15% at very high flow rates, due to the broadening of the frequency band widths. The experiments at high liquid flow rates were repeated four or five times, and the frequencies were averaged.

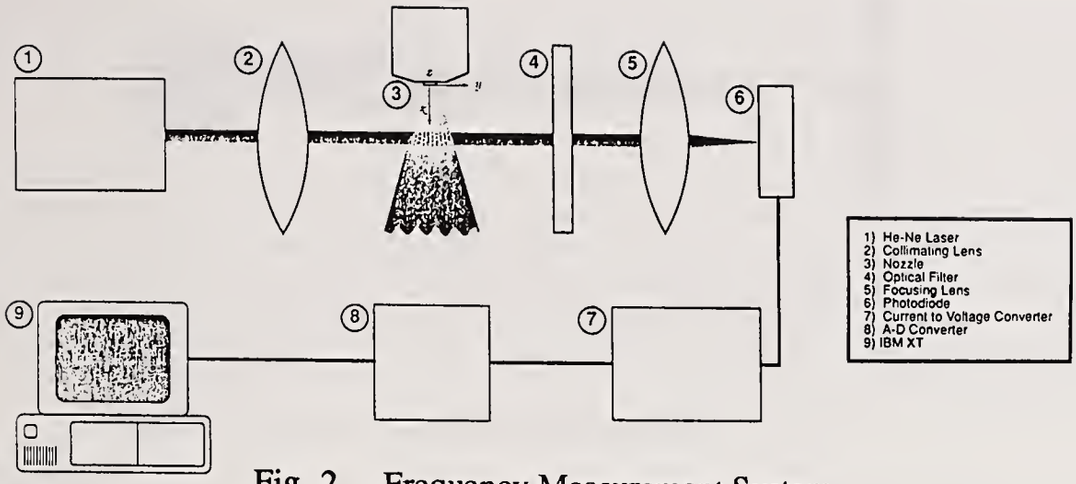

Fig. 2 Frequency Measurement System

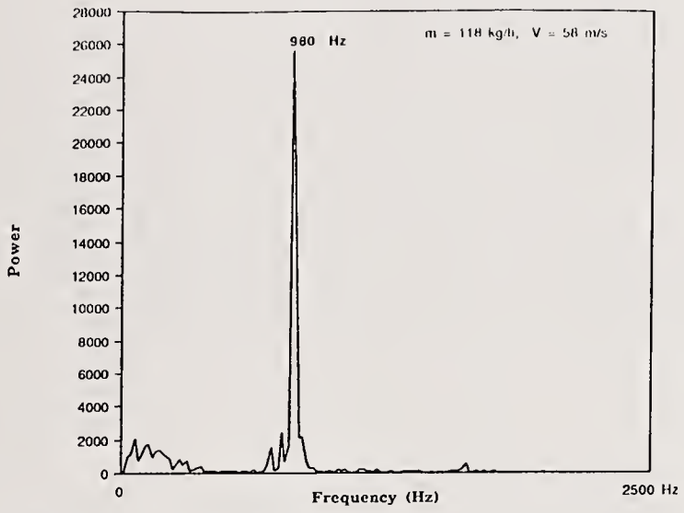

Fig. 3 Typical Spectral Power Density at $\dot{m}_\ell$ = 118 kg/h, V_{air} = 58 m/s

RESULTS AND DISCUSSION

The wave amplitudes and lengths were measured from the photographs over an air velocity range of 17.73 - 74.67 m/s and up to a maximum liquid mass flow rate of 450 kg/h. The wave frequencies were measured using a laser beam attenuation technique. Wave propagation speeds were calculated from the measured wavelengths and frequencies. Finally, the effects of liquid viscosity (3-12 cps) and surface tension (32-55 dynes/cm) on the sheet wave frequencies were investigated using solutions of glycerine and Triton X-100 respectively with water.

Wave Amplitudes and Lengths

Figure 4 shows the spatial wave growth for a liquid sheet of mass flow rate 81.76 kg/h, at an air velocity of 17.73 m/s. Although both sinuous and dilational waves are superimposed on the liquid sheet, the growth of the sinuous wave in the downstream flow direction is much larger. The higher growth rate of sinuous waves was also reported by Hagerty and Shea [3]. Wave amplitudes were obtained by measuring the distances from the sheet centerline to the crests of the major disturbances as shown in Fig. 4. Figure 5 illustrates the variation of wave amplitude with the distance from the nozzle exit. In this figure, the wave amplitude is normalized by the slit width (t) for the emerging liquid sheet. Although the variation in Fig. 5 is approximately linear, exponential or other higher order variations were also observed in some of the photographs. Since the slope of the linear amplitude variation is constant, it was possible to define a constant spatial amplitude growth rate for this pair of liquid and air flow conditions. The rate of increase of wave

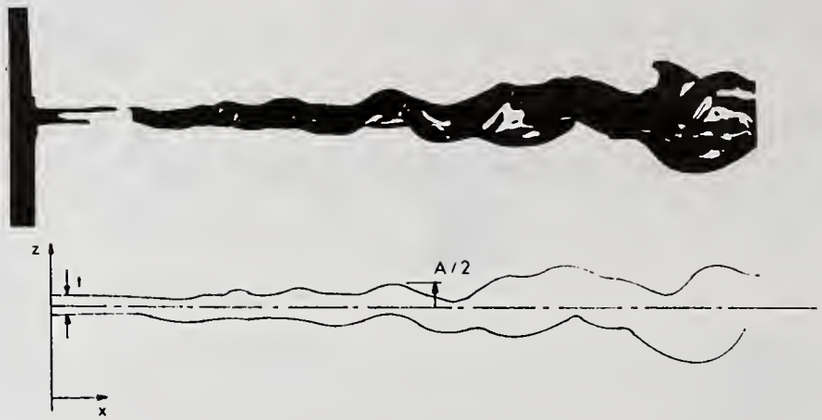

Fig. 4 Amplitude Measurements from a Photograph

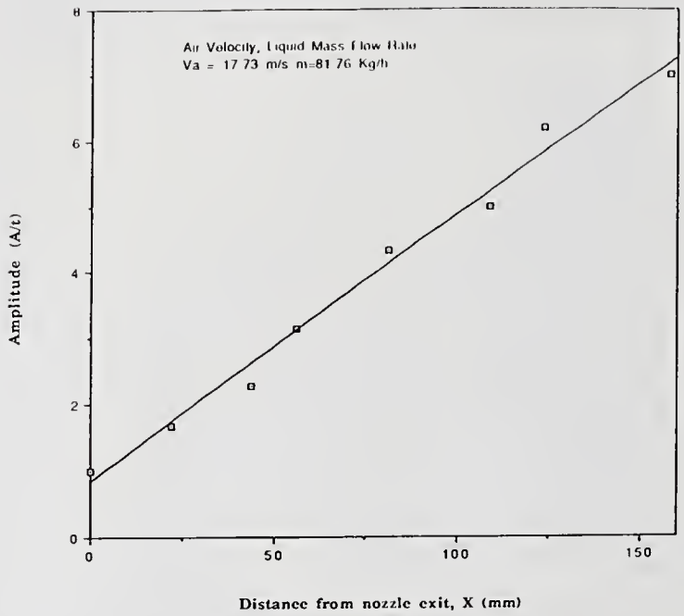

Fig. 5 Variation of Wave Amplitude along the Jet Axis (V_{air} = 17.73 m/s, $\dot{m}_\ell$ = 81.76 kg/h)

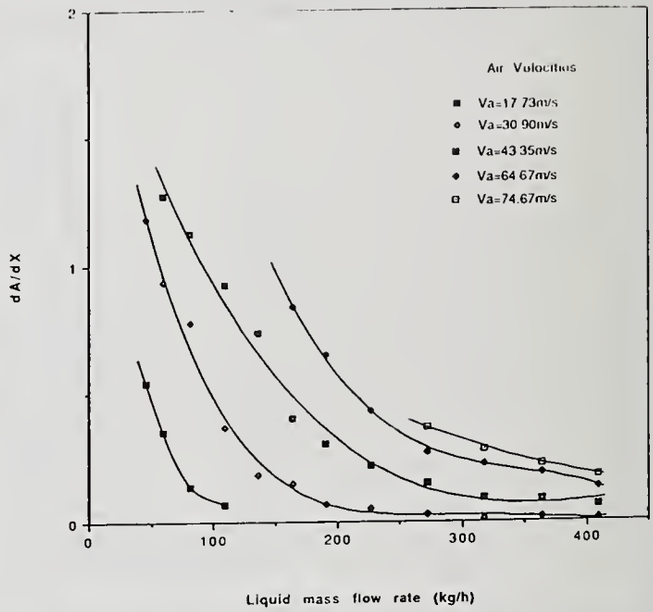

Fig. 6 Variation of Average Wave Growth Rate with Liquid Mass Flow Rate (V_{air} = 17.73, 30.90, 43.35, 64.67, 74.67 m/s)

amplitude with distance downstream is plotted as a function of increase in liquid mass flow rate and air velocity in Fig. 6. This figure shows that the spatial amplitude growth rate decreases with liquid mass flow rate and increases with air velocity. High spatial amplitude growth rates occur when the liquid inertia is low at low liquid flow rates. At that time, the specific energy of air per unit volume of liquid is high, and this energy is sufficient to cause sinuous wave formation with rapid amplitude growth. The relative velocity between the air and the liquid increases with decreasing liquid mass flow rate when the air velocity remains unchanged. The disturbances are known to be amplified faster when the aerodynamic force increases at the air-liquid interface due to higher relative velocities [10]. Figure 6 also illustrates that the spatial amplitude growth rate increases with air velocity when the liquid mass flow rate is kept constant. At very high liquid flow rates, dilational surface waves were observed on the liquid sheet surface with insignificant amplitude growth. The specific energy of air per unit volume of liquid at these test conditions was not enough to cause any sinusoidal oscillations, especially at low air discharge velocities. At intermediate liquid mass flow rates, both sinuous and dilational waves were superimposed. With increasing downstream distance, the sinuous waves grew faster. As a result, more gradual variation of spatial amplitude growth rates occurred at the intermediate liquid mass flow rates.

The disturbances on the liquid-air interface were found to be rather irregularly spaced. The spacings between the crests of the waves were measured using the same method as that of Eroglu

and Chigier [11] for the round jets from airblast coaxial atomizers. These distances were accepted as the wavelengths. Since the wavelengths vary in the axial (x) direction, average wavelengths were calculated and normalized with respect to the central slit width (t) for the liquid phase. The normalized average wavelengths were plotted as a function of liquid mass flow rate at four different air velocities as shown in Fig. 7. Average wavelengths were found to decrease with increasing liquid mass flow rate and air velocity. This decrease is more pronounced at lower liquid mass flow rates, where the liquid sheet develops predominantly sinuous waves with large wavelengths. The more gradual decrease or negligible change of wavelengths at high liquid mass flow rates occurs when the dilational waves are the dominant disturbances. The dilational wave development is usually accompanied by turbulent fluctuations in the liquid sheet. It seems that the small scale turbulent structures inside the liquid sheet control the initial phase of the wave development at high liquid mass flow rates and cause short wavelength surface disturbances to develop.

Wave Frequencies

A preliminary survey was performed in order to determine the optimum location for measurement of the wave frequencies in the downstream flow direction (x) of the liquid sheet. Figure 8 shows the result of this survey at the liquid mass flow rate of 56.78 kg/h, and air velocity of 26 m/s. The dominant wave frequency was measured as 400 Hz at this pair of flow conditions and did not change along the downstream flow direction. However, it was interesting to notice that the maximum spectral power density (spd) first increased to a maximum at about 7 mm distance from the nozzle exit and then started decreasing. A comparison of Fig. 8 with the photographs taken at similar flow conditions indicated that the peak of the curve corresponds to the position of maximum wave amplitude before the start of sheet disintegration. The maximum spd continued decreasing in the downstream flow direction until the disintegration was completed. The initial increase of maximum spd at upstream locations is a direct result of the emergence of a

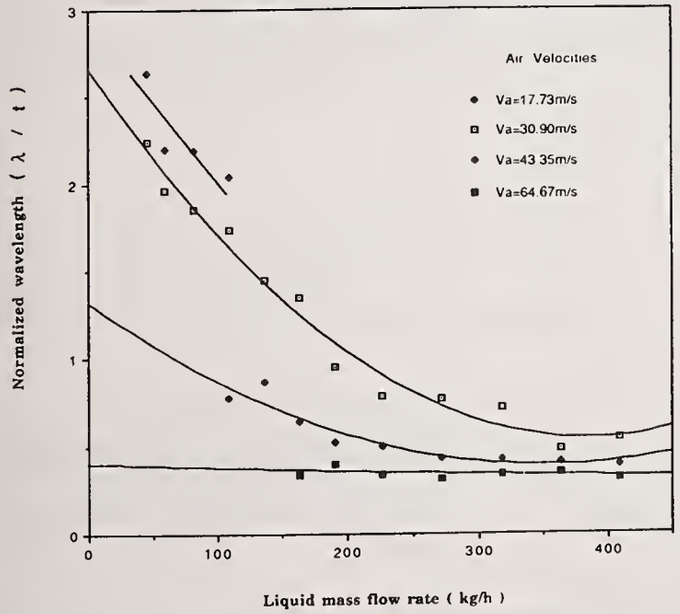

Fig. 7 Variation of Normalized Average Wavelength with Liquid Mas Flow Rate (V_{air} = 17.73, 30,90, 43.35, 64.67 m/s)

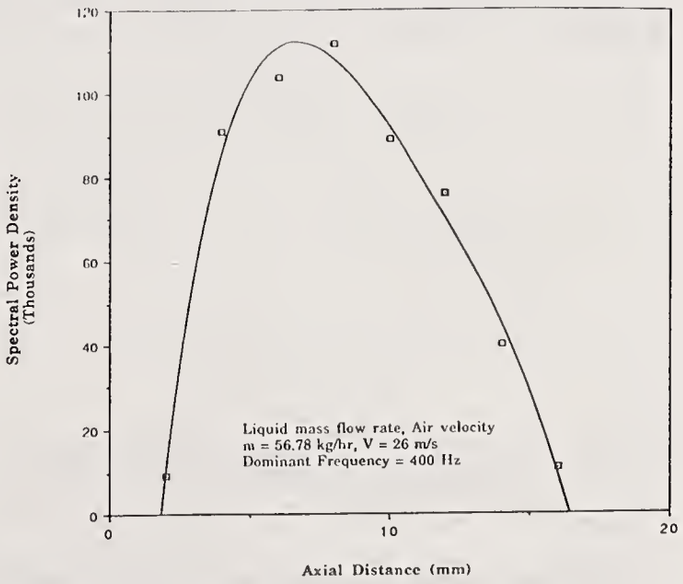

Fig. 8 Spectral Power Density Variation along the Jet Axis (V_{air} = 26 m/s, $\dot{m}_\ell$ = 56.78 kg/h, f = 400 Hz)

dominant frequency, and the disappearance of the secondary modes. Since the wave frequency does not change in the x direction, the optimum measurement location is selected for signal clarity.

Figure 9 shows the oscillation frequencies of the liquid sheet as a function of liquid mass flow rate at six different air velocities. In general, the wave frequency increases with liquid mass flow rate and air velocity. This behavior is consistent with the results of Lee and Yang [7] and Arai and

Hashimoto [8] on the liquid sheet instability with co-current air flow. Further analysis of Fig. 9 and the frequency jumps separating the regions A, B, and C for the different oscillation modes are explained in detail by Mansour and Chigier [9].

The results presented in this paper were obtained from the instantaneous photographs and frequency measurements from points in a fixed (Eulerian) reference frame for a naturally vibrating liquid sheet in a coflowing air stream. The photographic results gave average wavelengths and spatial amplitude growth rates although it was not possible to identify the amplitude growth corresponding to an optimum wavelength within a band of several wavelengths. The frequency measurements in a fixed (Eulerian) reference frame provided the number of waves passing through a point per second. Since it is very difficult to measure the temporal amplitude growth rates in a moving (Lagrangian) reference frame with the same velocity as the liquid sheet velocity, this study only provides information for the analysis of spatial instability.

Wave Propagation Speed

The wave propagation speeds were calculated by taking the product of average wavelengths and the wave frequencies. Figure 10 shows the variation of wave propagation speed with liquid sheet velocity at three different air velocities (30.90, 43.35, 64.67 m/s). Values are less than 1 m/s for liquid sheet velocities lower than 15 m/s. The wave propagation speed seems to be insensitive to both liquid and air velocity variations. This behavior is consistent with the wavelength decrease shown in Fig. 7 and the corresponding frequency increase shown in Fig. 9.

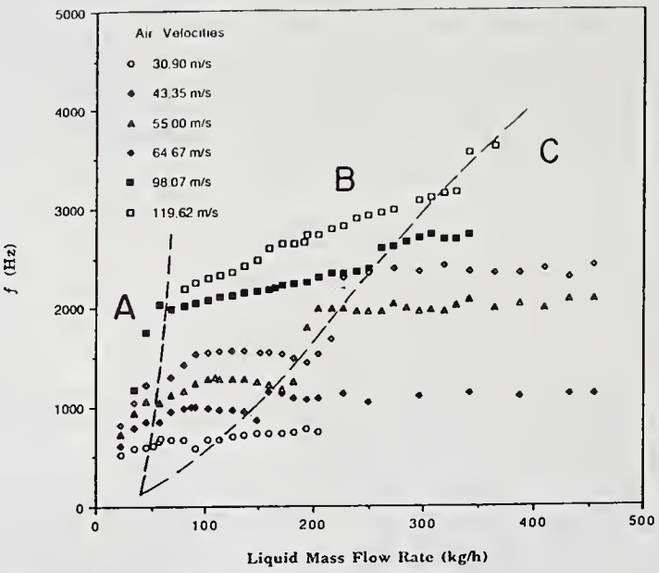

Fig. 9 Liquid Sheet Wave Frequency versus Liquid Mass Flow Rate, [9] (V_{air} = 30.50, 43.35, 55.0, 64.67, 98.07, 119.62 m/s)

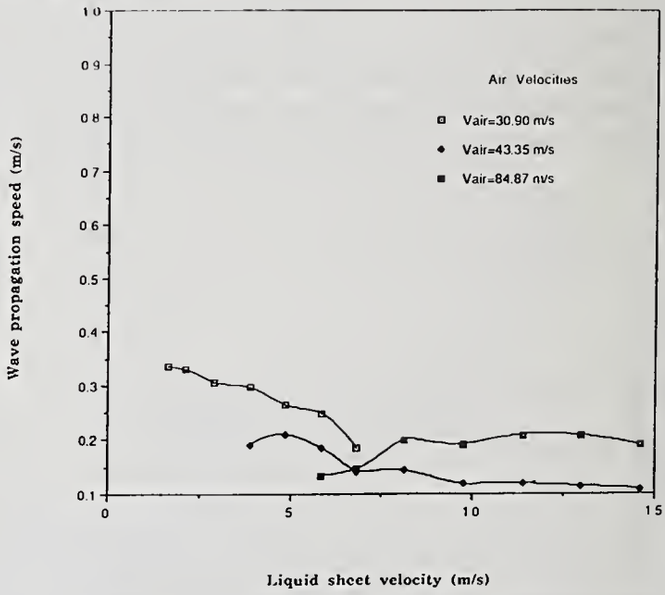

Fig. 10 Wave Propagation Speed versus Liquid Sheet Velocity (V_{air} = 30.90, 43.35, 64.67 m/s)

Effects of Liquid Viscosity and Surface Tension

The viscosity of the liquid phase was varied by adding 96% pure glycerine obtained from Dow Chemical Company into water at several volume percentages. The volume percentages of glycerine-water solutions were 66, 60, 40 and 0% respectively. The corresponding liquid viscosities changed from a maximum of 12 centipoise (66% glycerine) to a 3 centipoise (pure water) as measured by using a Brookfield viscometer.

The results of this investigation are shown in Fig. 11. The graphs show that the dominant wave frequencies decrease with viscosity. This decrease is more pronounced at higher liquid mass flow rates and air velocities. Such a result is expected since the viscosity is generally accepted to dampen the wave motion and give rise to increases in the wavelengths which are normally associated with frequency decrease.

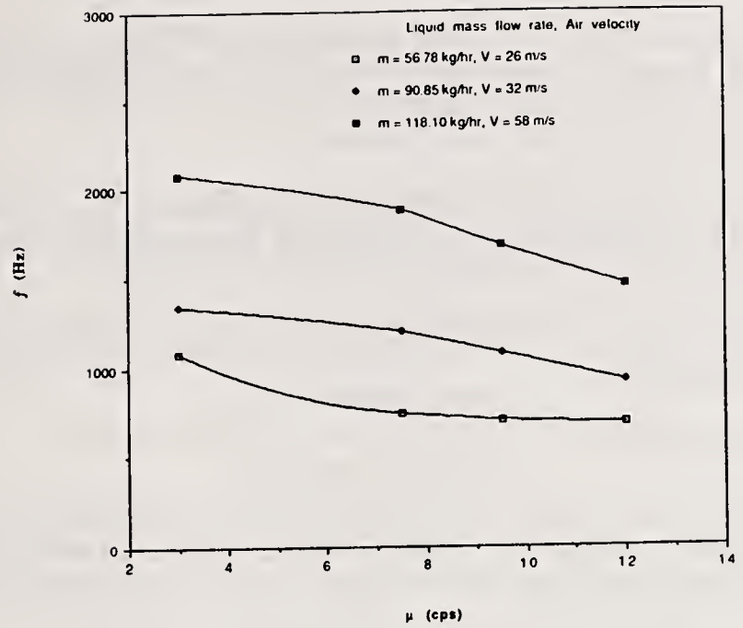

Fig. 11 Effect of Viscosity Variation on Liquid Sheet Wave Frequency

Triton X-100 non-ionic surfactant was added to water in order to vary its surface tension. The surface tension values of the liquid were obtained using the Du Novy ring method for different amounts of surfactant addition. The frequency measurements were made for the surface tension values 55, 50, 43, 41, 36 and 32 dynes/cm. The same liquid and air flow conditions as those for the viscosity investigation were selected. Frequency measurement uncertainties are estimated to be less than 5% for a 95% confidence level. The frequency measurement results shown in Fig. 12 indicate that the effect of surface tension on the dominant wave frequencies is insignificant for the tested liquid and air flow conditions.

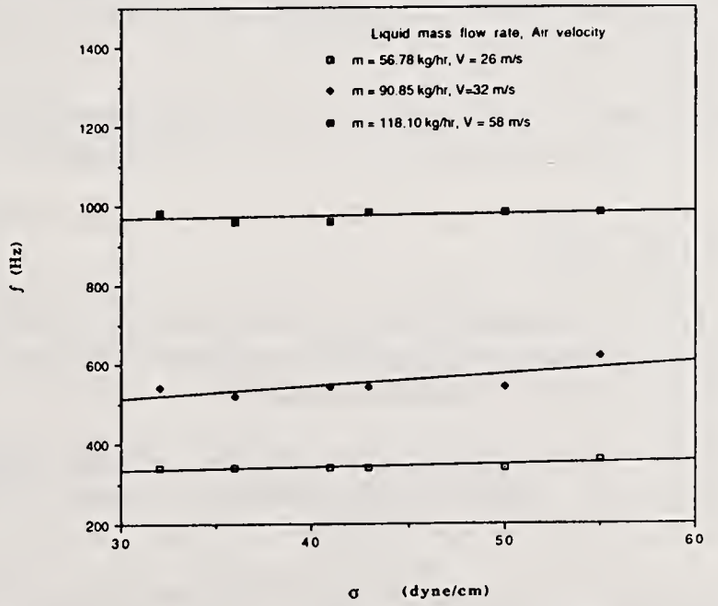

Fig. 12 Effect of Surface Tension on Liquid Sheet Wave Frequency

CONCLUSIONS

Wave characteristics of a liquid sheet with impinging air streams on the two opposite interfaces were investigated by means of high speed photography and frequency measurements.

Spatial amplitude growth rates were found to decrease with liquid mass flow rate and increase with air velocity. Average wavelengths decreased with increasing liquid mass flow rate and air velocity. Small scale turbulent structures in the liquid sheet are probably responsible for the short wavelengths encountered at high liquid mass flow rates.

The dominant wave frequency of the vibrating liquid sheet increased with both liquid mass flow rate and air velocity. It decreased with increasing viscosity. The frequency appears to be insensitive to the variation of surface tension from 32 to 55 dynes/cm.

The wave propagation velocity was in general less than 1 m/s, and there was little change with liquid and air velocity variations.

ACKNOWLEDGEMENTS

The authors would like to thank Mr. Eric Dion for performing some of the frequency measurements. The financial support from NASA Marshall Space Center (grant No. NAG8-126), and the atomizer from Parker Hannifin Corporation are gratefully acknowledged.

REFERENCES

1. York J.L., Stubbs, H.F. and Tek, M.R., "The Mechanism of Disintegration of Liquid Sheets", Trans. ASME, Vol. 75, pp. 1279-1286, 1953.

2. Squire, H.B., "Investigation of the Instability of a Moving Liquid Film", Br. J. Appl. Phys., Vol. 4, pp. 167-169, 1953.

3. Hagerty, W.W. and Shea, J.F., "A Study of the Stability of Plane Fluid Sheets", J. Appl. Mech., Vol. 22, No. 4, pp. 509-514, 1955.

4. Dombrowski, N. and Johns, W.R., "The Aerodynamic Instability and Disintegration of Viscous Liquid Sheets", Chem. Eng. Sci., Vol. 18, pp. 203-214, 1963.

5. Fraser, R.P., Dombrowski, N. and Routley, J.H., "The Atomization of a Liquid Sheet by an Impinging Air Stream", Chem. Eng. Sci., Vol. 18, pp. 339-353, 1963.

6. Lin, S.P. and Lian, Z.W., "Mechanisms of the Breakup of Liquid Jets", AIAA Journal, Vol. 28, No. 1, pp. 120-126, 1990.

7. Lee, G.Y. and Yang, O.Y., "Mechanism for the Disintegration of Liquid Film Surface Waves by a Parallel air Flow", proceedings of the 4th International Conference on Liquid Atomization and Spray Systems, pp. 193-199, Sendai, Japan, 1988.

8. Arai, T. and Hashimoto, H., "Disintegration of a Thin Liquid Sheet in a Cocurrent Gas Stream", proceedings of the 3rd International Conference on Liquid Atomization and Spray Systems, London, pp. VIB/1/1 - VIB/1/7, 1985.

9. Mansour, A. and Chigier, N., "Dynamic Similarity Between Liquid Sheets and Hard Spring Systems",. submitted to Physics of Fluids, 1990.

10. Lefebvre, A.H., Atomization and Sprays, Hemisphere Publishing Company, New York, 1989.

11. Eroglu, H. and Chigier, N., "Wave Characteristics of Liquid Jets from Airblast Coaxial Atomizers" submitted to Atomization and Sprays, 1990.

SPRAY GAS-PHASE INTERACTION DOWNSTREAM OF A CO-AXIAL COUNTER-SWIRLING DOME SWIRL CUP

H.Y. Wang, W. Sowa, V.G. McDonell and G.S. Samuelsen

UCI Combustion Laboratory
Dept. of Mechanical and Environmental Engineering
University of California
Irvine, CA, U.S.A.

ABSTRACT

The flow field downstream of a 3x scale GE CFM56 combustor swirl cup is characterized with and without the presence of a spray by using phase Doppler interferometry. The gas-phase mean axial velocities reveal a closed, on-axis recirculation zone in each case. For the case without the spray, the recirculation zone is comparatively larger. Anisotropic turbulence persists within the regions where the measurements were conducted. Velocity statistics are determined for the single-phase (gas phase in absence of spray), the continuous-phase (gas phase in presence of spray), and the discrete-phase (liquid phase in presence of spray). Differences between the cases are revealed and discussed. Overall, the effect of the spray on the gas-phase mean velocity is relatively small and can, in the present case, be reasonably neglected in modeling the flow.

INTRODUCTION

Co-axial, counter-swirling air streams have been investigated to understand differences in combustion characteristics relative to co-swirl combustion [1,2,3,4]. Isothermal, co-axial, counter-swirling systems, for example, have been studied by several investigators [2,3,4] who suggest that co-swirl does not produce a recirculation zone. Other investigators find that a recirculation zone exists for both co-swirl and counter-swirl [5,6]. The different conclusions are attributed to different swirl number and other factors (e.g., the method employed to generate swirl since the swirl number is not the only parameter that characterizes swirling flow).

Droplet laden swirling flows are not well understood. Some efforts have been conducted to characterize sprays with different primary air swirling conditions [7,8,9,10], but none investigate the effect of a spray on the gas-phase flow field. In the research reported herein, a complex flow field generated by a practical hardware is characterized for both the single-phase and the two-phase flow, and the effect of the spray on the gas-phase is identified.

The purpose of this paper is to establish the effect of the spray on the gas-phase flow field for a liquid spray injected into a swirl cup air stream.

EXPERIMENT

Facilities

The 3x model combustor swirl cup is shown schematically in Fig. 1. A 90^{o} cone-angle simplex nozzle is mounted in the center of the swirl cup. The venturi separates the primary and secondary swirlers. The primary swirl stream rotates clockwise looking from the top of the nozzle, while the secondary swirl stream rotates counterclockwise.

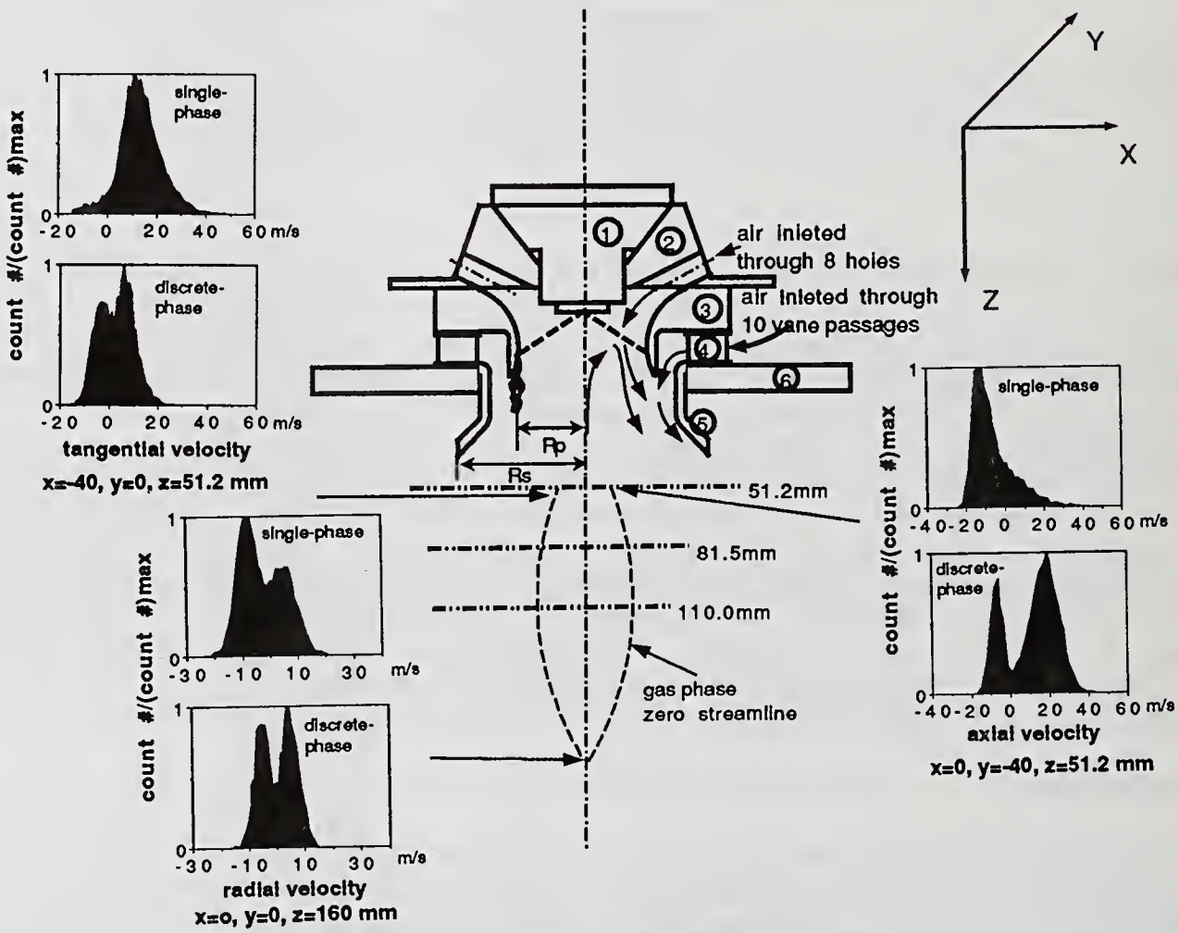

Fig. 1 Swirl cup and velocity histograms
(1) Simulated fuel nozzle
(2) Primary swirler component
(3) Primary venturi
(4) Secondary swirler component
(5) Conical sleeve

The swirl cup was cemented onto an aluminium plate to provide symmetric boundary conditions to the flow field. The aluminum plate, in turn, was fastened to a PVC cylindrical plenum. A 0.006 m cell-diameter polycarbonate honeycomb (0.106 m thick) was placed 0.051 m above the top of the swirl cup to provide a uniform velocity profile at the entrance plane to the swirlers. Water was used to simulate the fuel.

A two-component phase Doppler interferometer (Aerometrics PDPA Model 3100-s) was used to measure (1) the single-phase velocities, (2) the continuous-phase velocities in the presence of the spray, and (3) the size and velocities of the discrete-phase. Table 1 provides details of the configuration used in the present study. A TSI Model No. 3906 six-jet atomizer was used as a seed generator. A 10% salt solution was used to provide adequate seed yielding a satisfactory signal at a laser power of 1.0 W. In the presence of the spray, the continuous-phase and discrete-phase velocities were measured separately. The continuous-phase velocities measured in the presence of spray were determined by isolating the statistics to droplets ranging in diameter from 2.44-4.14 μm, which was the smallest size class detected by the PDPA. These droplets were assumed to follow the gas-phase.

TABLE 1. Characteristics of PDPA 3100-S

Transmitter	
0.5145μm line (U, D)[2]	
Fringe Spacing	9.88 μm
Waist	187.17 μm
0.4880μm line (V or W)[2]	
Fringe Spacing	9.84 μm
Waist	177.53 μm
Receiver	
1000 mm f/9.3 Collection Lens	
238 mm Focusing Lens	
100 μm Spatial Filter	
30° Off-Axis Forward Collection Angle	

[2]U, V, W and D are axial, radial, tangential velocity and droplet diameter respectively.

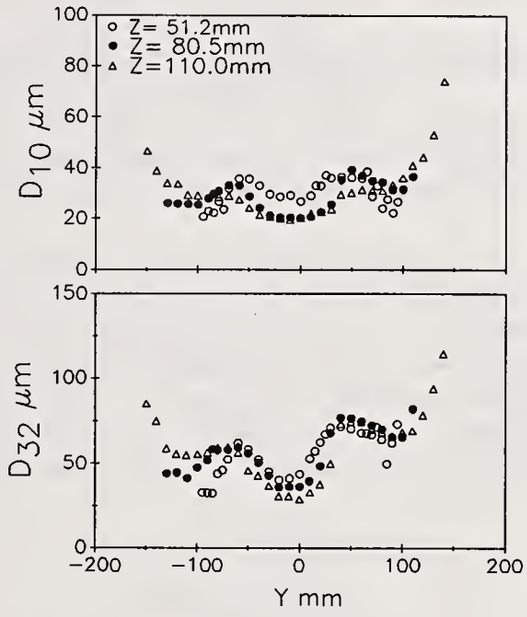

Fig. 2 Droplet size profiles

Test Conditions And Test Locations

Both the two-phase tests and the single-phase tests were conducted at an air flow rate 0.154 kg/s. The liquid flow rate was 0.010 kg/s for the two-phase tests. The pressure drop across the nozzle discharge was 827 kPa. For the same air flow rate at the exit plane of primary cup, the swirl number was 0.47 for the primary cup and -0.55 for the secondary cup [6]. Measurements were conducted at three axial locations (Z/R_p = 1.75, 2.75 and 3.75 where the radius of the exit plane of the primary swirler cup, R_p, is 0.029 m and the origin is the exit plane of the primary cup). In addition, data were acquired along the center line to study the change in the length of the recirculation zone.

DISCUSSION OF RESULTS

The results are divided into two groups: discrete-phase and gas-phase measurements in the presence (continuous-phase) and absence (single-phase) of the spray.

Discrete-Phase Results

One feature of the swirl cup design is to provide uniform and fine droplets. A portion of the droplets issue from the nozzle and convect downstream directly and a portion impinge onto the inner surface of the primary swirl component to form a liquid film which is then atomized due to the strong shearing of the primary and secondary air streams at the edge of the primary cup. Fig. 2 shows the length mean diameter D_{10} and the Sauter mean diameter D_{32}. These distributions indicate the presence of small droplets along the centerline. At the periphery of the spray, D_{10} and D_{32} increase sharply. This is attributed to (1) larger droplets from the atomizer that have sufficient radial momentum to penetrate through the swirling air streams, and (2) the breakup of liquid film at the edge of swirl cup that can produce large droplets with a substantial radial momentum.

Continuous-Phase and Single-Phase Results

In this section, the gas-phase is compared with and without the spray. In particular, the continuous-phase flow field in the two-phase test is compared to the single-phase test. Both mean and fluctuating components are considered for the axial, radial, and tangential components.

Mean Velocity Comparison. As shown in Fig. 3, the continuous-phase axial velocities are generally similar to those of the single-phase with one notable exception. In the recirculation zone, the continuous-phase axial velocities are less negative indicating a recirculation zone of reduced strength. The axial momentum transfer from the discrete-phase to the continuous-phase is likely responsible in the recirculation region as droplets propelled downstream oppose the reverse flow of the continuous-phase.

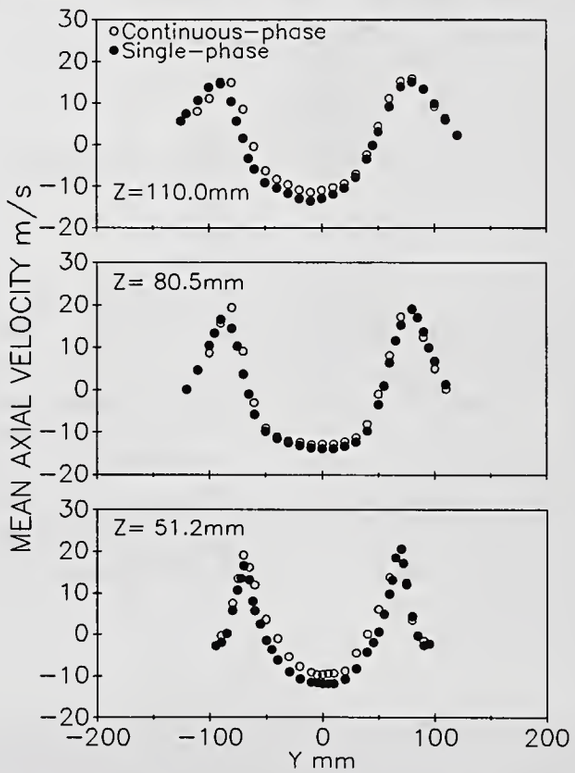

Fig. 3 Gas-phase mean axial velocity

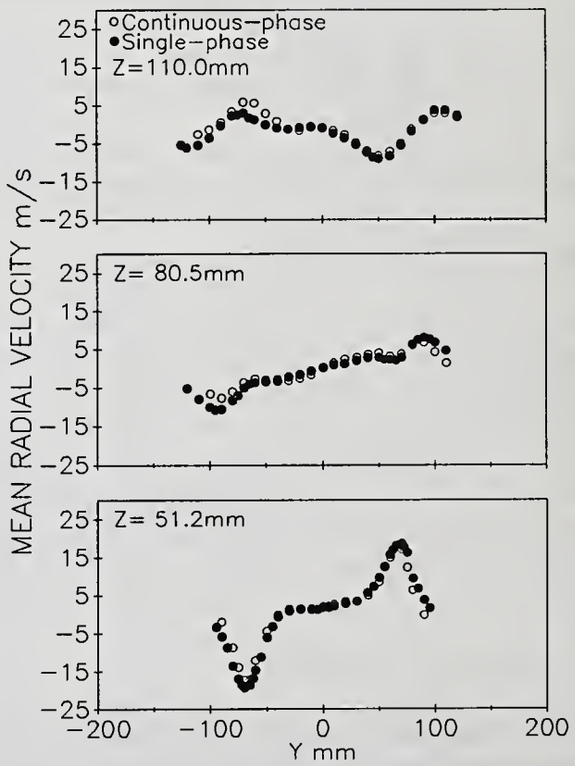

Fig. 4 Gas-phase mean radial velocity

The radial velocity data in Fig. 4 also reveal similar behavior between the continuous-phase and single-phase.

Fig. 5 presents the comparison of mean tangential velocities at two axial locations. The single-phase shows generally higher mean tangential velocity. In the two-phase flow, most of the droplets that issue from the nozzle, unlike the continuous-phase, do not have initial tangential velocity. Their tangential velocity increases due to (1) the tangential momentum transfer from the continuous-phase to the discrete-phase, and (2) the liquid film breakup at the edge of the primary swirl cup. Therefore, the continuous-phase tangential momentum is suppressed relative to the single-phase case.

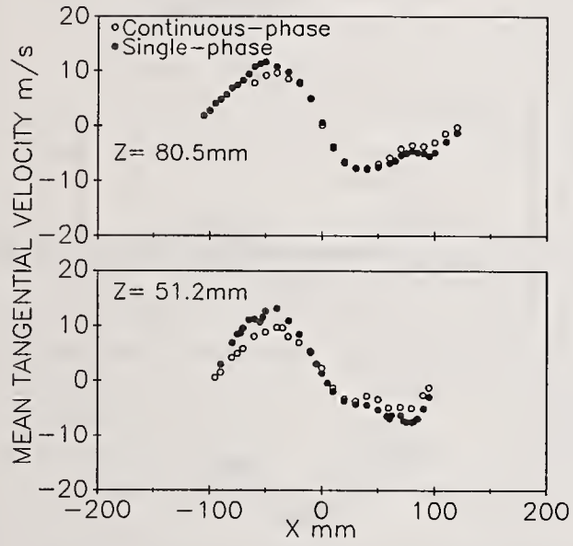

Fig. 5 Gas-phase mean tangential velocity

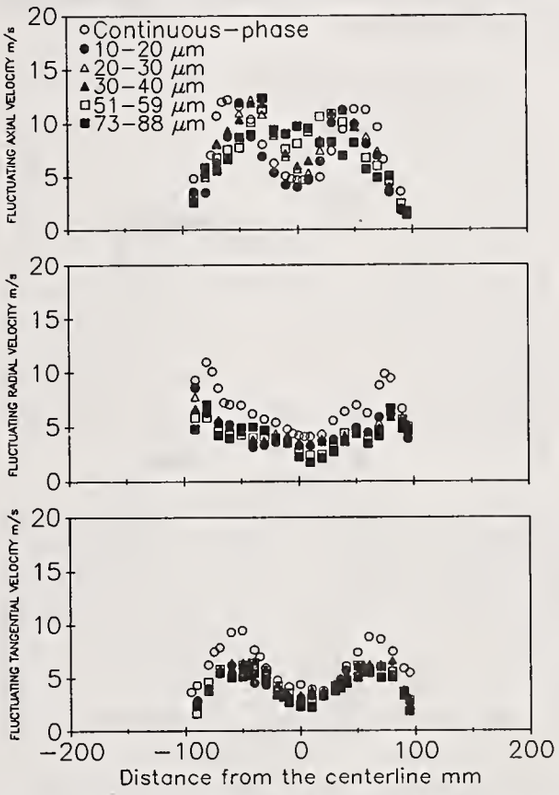

Fig. 6 Rms of discrete-phase velocities

Fluctuating Velocity Comparison. To aid in interpretation of the fluctuating velocity results, the profiles of the fluctuating velocity components of the continuous-phase are presented in Fig. 6 along with the "fluctuating velocities" of various size classes at axial location z = 51.2 mm. Note that the relative fluctuating velocity differences between the continuous- and discrete-phase change radially.

Fluctuating gas-phase axial velocities are compared in Fig. 7. At the first axial location, note the higher magnitude for the continuous phase within the recirculation zone. This is attributed to the relative magnitude of the fluctuating velocities between the continuous-phase and large droplets (over 30 μm) as shown in Fig. 6. The continuous-phase velocity fluctuations are enhanced when the velocity "fluctuation" of the large droplets is greater than that of the continuous-phase. The greater velocity fluctuation of the large droplets results from a variation in their ballistic injection instead of the turbulent fluctuation in the common sense and is more dominant, as shown, close to the injection place.

The radial and tangential velocity fluctuations for the continuous phase are consistently lower than the corresponding single-phase measurements. Again, the continuous-phase radial and tangential velocity fluctuations are consistently greater than those of the large droplets and thus dampened (Fig. 6).

For the single-phase case, the fluctuating radial velocity reveals a two-peak distribution at the axial location Z = 51.2 mm (close to the exit plane of the swirl cup) (Fig. 8). The double peak distribution is suppressed for the two-phase case. This is attributed to a momentum exchange between the gas-phase and the droplets, which have a single peak distribution and dampen the two-peak structure. Within the recirculation zone, both cases show a similar behavior.

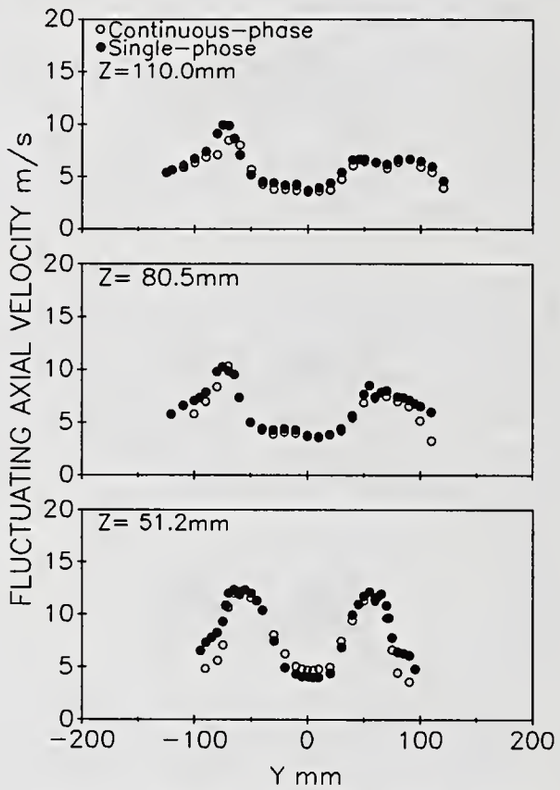

Fig. 7 Rms of gas-phase axial velocity

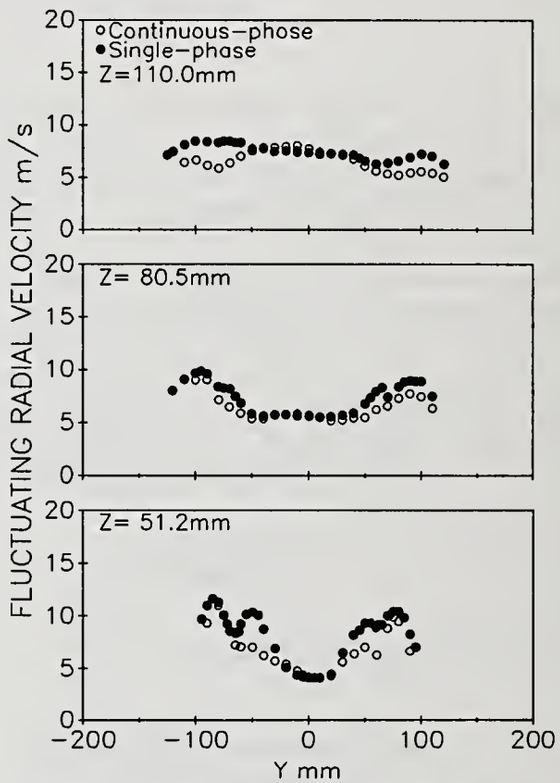

Fig. 8 Rms of gas-phase radial velocity

The greatest differences in gas-phase tangential velocity fluctuation between the single-phase and continuous-phase is observed in and near the shear layer (Fig. 9). This corresponds to the location at which the greatest difference in tangential velocity fluctuation between the continuous-phase and large droplets (over 30 μm) occurs (Fig. 6). The degree of this difference decreases as flow develops downstream due to mixing and entrainment.

Distribution along the Centerline. The mean and fluctuating gas-phase axial velocity distributions along the centerline are presented in Fig. 10. The recirculation zone closes closer to the inlet plane in the two-phase case. Moreover, differences in the mean axial velocity between the single-phase and the continuous-phase decreases downstream and coincides well with the decrease in mean axial velocity difference between the continuous-phase and the larger droplets [11]. This supports again the arguments used to interpret the mean and fluctuating velocity differences between the single-phase and the

continuous-phase. The greatest fluctuation is observed at about Z = 160 mm near the stagnation point of the recirculation zone.

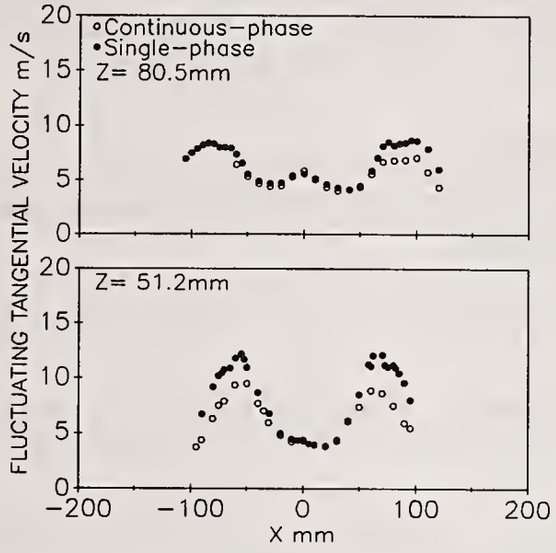

Fig. 9 Rms of gas-phase tangential velocity

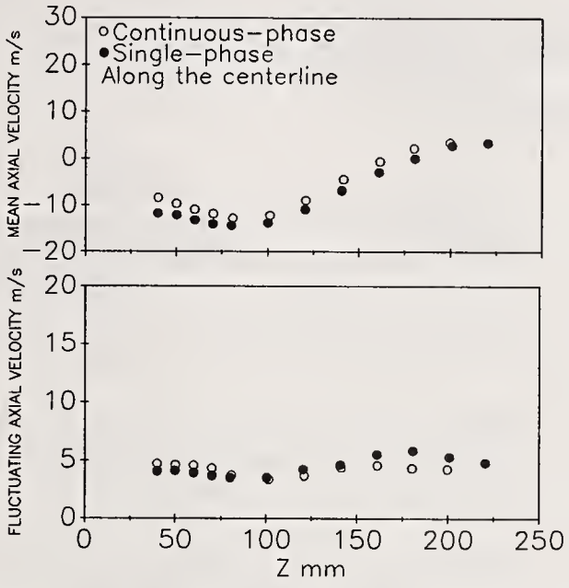

Fig. 10 Mean and fluctuating gas-phase axial velocity along the centerline

Single-Phase and Discrete-Phase Results

Both the single-phase and the discrete-phase histograms are shown respectively in Figure 1 for the axial velocity in the shear layer, the tangential velocity in the shear layer, and the radial velocity around the stagnation point. Velocity bimodal distributions are evident for the discrete-phase at these locations, which reflects the flow field characteristics superimposed on the gas-phase that are not present in the single-phase case. The well defined bimodal velocity distributions of the discrete-phase can be associated with either significant size-velocity correlations, or intermittent flow field characteristics, or both. This behavior which is pronounced in discrete-phase measurements is negligible or relatively insignificant in the single-phase case. As a result, the two-phase flow field in this practical hardware is both intriguing and complex.

CONCLUSIONS

(1) The differences in mean and fluctuating velocities between the single-phase and the continuous-phase correlate with differences in mean and fluctuating velocities between the continuous-phase and the larger droplets (over 30 μm).

(2) The turbulent fluctuations for both the continuous-phase and the single-phase are anisotropic. The effect of the spray on the gas-phase mean velocities is surprisingly small in this complex, two-phase flow.

(3) The two-phase case reveals a more intermittent behavior than the single-phase case at selected locations in the flow field such as in the shear layer and at the stagnation point of the on-axis recirculation zone.

(4) The two-phase flow field and phase interaction in a practical hardware can be complex. Intermittency, for example, plays an important role and suggests, for example, the need for detailed transient analyses.

ACKNOWLEDGEMENTS

The authors acknowledge the financial support from GE Aircraft Engines, and the assistance of C.T. Brown with testing protocol and H.D. Crum with facility development.

REFERENCES

1. Yetter, R.A. and Gouldin, F.C., "Exhaust Gas Emissions of a Vortex Breakdown Stabilized Combustor", Fall Meeting of the Western States Section of the Combustion Institute (1976).

2. Vu, B.T. and Gouldin, F.C., "Flow Measurements in a Model Swirl Flow", AIAA Journal, Vol. 20, pp. 652-659 (1982).

3. Habib, M.A. and Whitelaw, J.H., "Velocity Characteristics of Confined Coaxial Jets with and without Swirl", Journal of Fluid Engineering, Vol. 102, pp. 47-53 (1980).

4. Gouldin, F.C., Depsky, J. and Lee, S.L., "Velocity Field Characteristics of a Swirling Flow Combustor", AIAA Paper 83-0314 (1983).

5. Samimy, M. and Langenfeld, C.A., "Experimental Study of Isothermal Swirling Flow in a Dump Combustor", AIAA Journal, Vol. 26, No.12, pp. 1442-1449 (1988).

6. Mehta, J.M., Shin, H.W. and Wisler, D.C., "Mean Velocity and Turbulent Flow Field Characteristics inside an Advanced Combustor Swirl Cup", AIAA Paper 89-0215 (1989).

7. Cameron, C.D., Brouwer, J. and Samuelsen, G.S., "A Comparison of Spray Characterization in an Isothermal Chamber and in a Model Gas Turbine Can Combustor", Second Int'l Conference on Liquid Atomization and Spray System, pp. 145-152, Sendai, Japan (1988).

8. McDonell, V.G., Wood, G.P. and Samuelsen, G.S., "A Comparison of Spatially Resolved Drop Size and Drop Velocity Measurements in an Isothermal Chamber and a Swirl Stabilized Combustor", Twenty-First Symp. (Int'l) on Combustion, pp. 685-694, The Combustion Institute, Munich, West Germany (1986).

9. De la Rosa, A.B., Bachalo, W.P. and Rudoff, R.C., "Spray Characterization and Turbulence Properties in an Isothermal Spray with Swirl," ASME Journal of Engineering For Gas Turbines and Power, Vol. 112, pp. 60-66 (1990).

10. Sankar, S.V., De la Rosa, A.B., Isakovic, A. and Bachalo, W.D., "A Technique for Studying Mixing in Swirl Combustor," Sixth Int'l Sypm. on Laser Anemometry Application to Fluid Mechanics, Lisbon, Portugal (1990).

11. Wang, H.Y., Sowa, W., McDonell, V.G. and Samuelsen, G.S., "Swirl Cup Continuous and Discrete Phase Measurements in a 3x Scale Module", Report UCI-ARTR-90-11-A, Combustion Laboratory, Univ. of Cal., Irvine (1990).

AIR BLAST ATOMIZATION: INSTABILITY OF AN ANNULAR LIQUID SHEET SURROUNDED BY TWO AIR FLOWS OF DIFFERENT VELOCITIES

P. Camatte and M. Ledoux

URA CNRS 230/CORIA - University of Rouen
Mont Saint Aignan, France

ABSTRACT

Air blast atomization of a flat or annular sheet is studied under the influence of internal and external air flows of two different velocities. Non dimensional results are presented. Asymptotic cases of high velocity atomizations, high thickness and high radius sheet are derived. First experiments are also presented.

INTRODUCTION

Air blast atomization is of a wide use, especially in aircraft engines where air is provided in excess by the compressor. In many aircraft atomizers an annular liquid fuel sheet is disintegrated by to coflowing air flows, one internal the other external. These air flows are generally swirling and at two different relative velocities with liquid flow.

Modelisation of such an atomizer involves two problems : 1)-instability of the annular sheet. 2)-breaking and restructuration into drops. The present paper deals with the first problem, i.e. the instability of an annular sheet surrounded by two coaxial air flows.

Few studies of this problem are found in the litterature [1] [2] [3] [4] [5] all with the same velocity on both sides of the sheet. An analysis is given here in the case of different velocities of internal and external air flows.

Linear analysis as given here is criticable in nature since break-up processes are far from linearity. Nevertheless linear analysis has been previously usued with success in designing pressure swirl atomizers [4]. It has also to be pointed out that non linear theory (weakly non linear or based on wortex sheet analysis) need results of linear calculations to be achieved. Furthermore interesting qualitative information can be drawn from linear analysis.

ANALYSIS

The flow is shown on Fig.1 in stable configuration. Both liquid and gases are non-viscous (which can be accepted for low viscosity fluids as water or kerosene). Two linear analyses of stability are given : 1)-for a flat sheet (asymptotic case for $a \to \infty$) 2)-for the real case (a finite). Notations are defined on Fig.1.

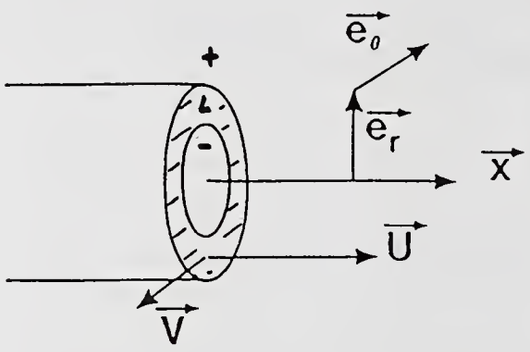

Fig.1 The stable flow

General features

Both analyses are based on the same physical grounds. Time varying velocity field is decomposed into stable and instable part. In each flow this last part derives from a potential (φ^+, φ^- and φ_L) η (x,t,θ) is the deviation of the surface from stable shape.

Potentials are searched under the separate form $R\,T(\theta)e^{iwt}$ $R=R(y)$ in case 1 (plane) or $R=R(r)$ in case 2 (annular sheet). From following interface conditions η will be found of the form :

$$\eta = \eta_o \exp i(kx + n\theta - \omega t) \qquad (2.1)$$

k is the axial wavenumber : $k = 2\pi/\lambda$
n is the azimuthal wavenumber
ω is a complex pulsation $\omega = \omega_r + i\omega_i$
ω_r is related to axial propagation velocity c $\omega_r = kc$
ω_i when positive leads to instability $\alpha\ e^{\omega_i t}$
η_o is the initial amplitude at each side of the sheet ; one finds then two values η_o^+ and η_o^-.

Continuity (2.2) and impulsion equation (2.3) under linearized form are written :

$$\Delta\varphi^+ = 0 \ ; \ \Delta\varphi^- = 0 \ ; \ \Delta\varphi_L = 0 \qquad (2.2)$$

$$\frac{\partial u}{\partial t} + U\frac{\partial u}{\partial x} + \frac{V}{r}\frac{\partial u}{\partial \theta} = -\frac{1}{\rho}\frac{\partial p}{\partial x} \qquad (2.3)$$

in each fluid (In case 1, $V \equiv 0$)

Condition at the interface give :

$$\frac{\partial \varphi}{\partial r} = \frac{\partial \eta}{\partial t} + U\frac{\partial \eta}{\partial x} + \frac{V}{r}\frac{\partial \eta}{\partial \theta} \qquad (2.4)$$

in each fluid at each interface.

Surface tension gives :

$$\rho_L - \rho_{gas} = \pm \sigma \frac{\partial^2 \eta}{\partial x^2} \qquad (2.5)$$

at each interface, under non linearized form.

Results will be shown here under non dimensionalized forms. U_M is the average velocity of the two air flows $U_M = (U^+ + U^-)/2$.

ΔU is the difference between the two air flows $\Delta U = U^+ + U^-$ ($\Delta U = 0$ leads to $U_M = U^+ = U^-$).

One introduces k_c which is the maximum value of k leading to instability in the case of symetrical plane sheet (Squire problem)

$$k_c = \frac{\rho_G \, U_M^2}{\sigma}$$

So $\tilde{h} = k_c h$, $\tilde{k} = k/k_c$, $\tilde{\rho} = \frac{\rho_G}{\rho_L}$, $\tilde{\Delta U} = \frac{\Delta \tilde{U}}{U_M}$, $\tilde{\omega} = \frac{\omega}{k_c \, U_M}$

By combining equations (2.2) to (2.5) a system of the following form is found for η_o^+ and η_o^- :

$$\begin{aligned} F\eta_o^+ + G\eta_o^- &= 0 \\ G'\eta_o^+ + F'\eta_o^- &= 0 \end{aligned} \qquad (2.6)$$

F,G,F',G' are depending on the system studied. Detailed calculations can be obtained from the authors. (2.6) shows that :

-The determinant FF'- GG' must be zero.

- η_o^+ and η_o^- cannot be independant. Their value can be arbitrary but their ratio η_o^+ / η_o^- can be calculated from - G/F or - F'/G'.

FF' - GG' gives a dispersion equations of the form :

$$H_4 \tilde{\omega}^4 + H_3 \tilde{\omega}^3 + H_2 \tilde{\omega}^2 + H_1 \tilde{\omega} + H_o = 0 \qquad (2.7)$$

where coefficients are function of k and n.

Case 1 : The flat sheet

a) U^+, U^-, U_L are parallel flows. The dispersion equation (2.7) has the form :

$$\left[-\omega^2 \coth 2kh - \tilde{\rho}(kU^+ - \omega)^2 + \frac{\sigma k^3}{\sigma_L}\right] \left[-\omega^2 \coth 2kh - \tilde{\rho}(kU^- - \omega)^2 + \frac{\sigma k^3}{\rho_L}\right] - \frac{\omega^4}{\mathrm{sh}^2 2kh} \qquad (2.8)$$

The ratio between amplitudes on two sides is :

$$\frac{\eta_o^+}{\eta_o^-} = \frac{-\omega^2}{\mathrm{sh}\ 2kh \left[-\omega^2 \coth 2kh - \tilde{\rho}(kU^+ - \omega)^2 + \frac{\sigma k^3}{\rho_L}\right]}$$

$$= \frac{\text{sh}(2kh)\left[-\omega^2 \coth 2kh - \tilde{\rho}(kU^- - \omega)^2 + \frac{\sigma k^3}{\rho_L}\right]}{-\omega^2} \qquad (2.9)$$

These equations are interesting not only as an asymptotic result ($a \to \infty$) of case 2, but also the equations allow visible simplifications in the asymptotic case $kh \to \infty$.

b) Asymptotic case $kh \to \infty$

This case corresponds either to great velocities U^+ and U^- (small λ, great k) or to a very thick sheets (h great).

In both cases $kh \to \infty$, sh $2kh \to \infty$ and term $\frac{\omega^4}{\text{sh}^2 2kh}$ vanishes.

(2.8) is then factorizing in two equations of degree two which can be recognized as Kelvin-Helmholtz equations for simple interfaces. So each interface is atomized independently. η_0^+ / η_0^- has then no definite values.

c) $U^+ = U^- = U$. This is the problem of Squire [6] . The equation is factorized into two new equations of degree two, of the form :

$$A\,\omega^2 + \tilde{\rho}\,(kU - \omega)^2 - \frac{\sigma k^3}{\rho_L} = 0$$

where A = tank kh or coth kh. These two values of A correspond respectively to values of η_0^+ / η_0^- equal +1 (antisymetric perturbations) or -1 (symetric case). This corresponds to the problem analyzed by Hagerty and Shea [7].

Corresponding solutions are shown on figures 2 and 3. It can be seen that for increasing h solutions are asymptotic to a unique curve, which is in fact the Kelvin Helmholtz solution. This is achieved for h of order 10.

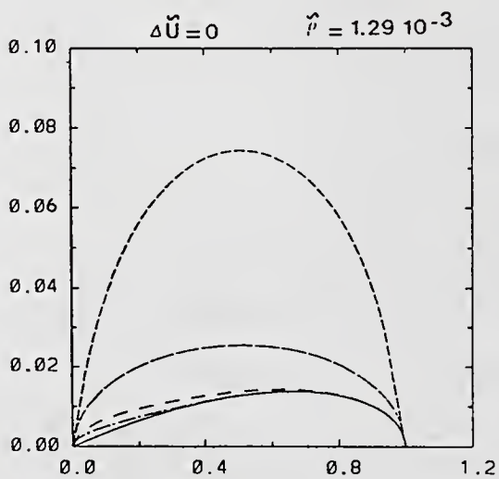

Fig. 2 First solution
Growth rate versus wave number

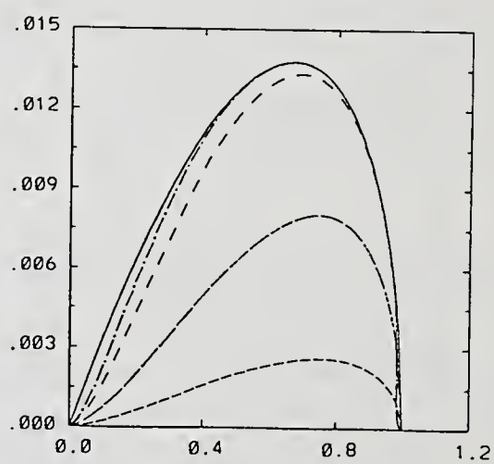

Fig. 3 Second solution
Growth rate versus wave number

d) Case when $U^+ \neq U^-$

Solutions are presented on Fig.4 and 5. Two different solutions

giving $\omega_i > 0$ are found. So the shape of the sheet have to be considered as the sum of those two solutions. Some features have to be remarked.

-For thick sheets (h greater than 5) the ratio η_0^+ / η_0^- (or inverse) becomes very great. The perturbation from one side has a very low influence on the other side (very low "penetration"). In this case the values of η_0^+ / η_0^- found here only give a qualitative indication since the non-linearity is not represented. In fact solutions are asymptotic to Kelvin-Helmholtz theory for each interface.

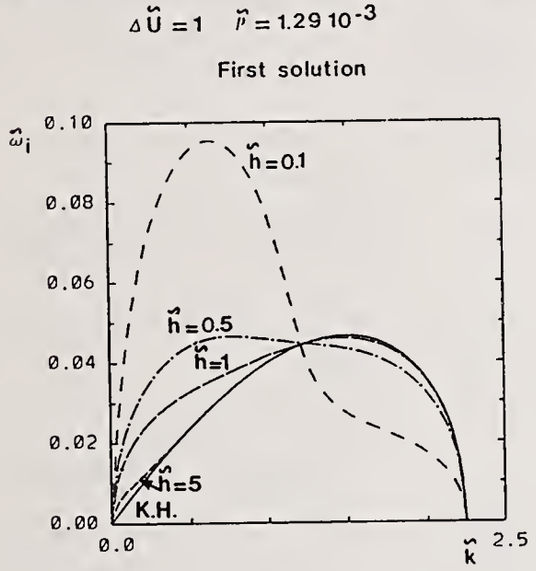

Fig. 4.a Growth rate versus wave number

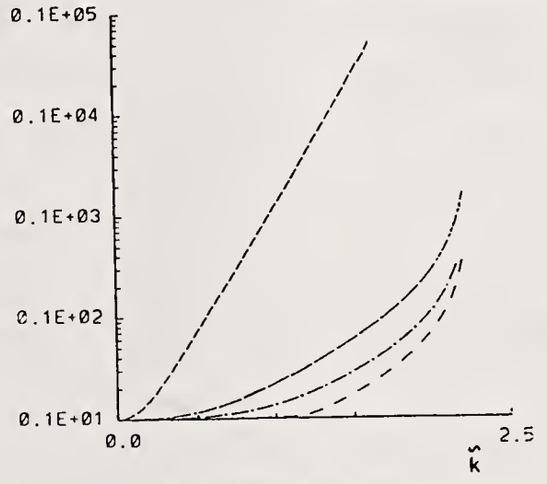

Fig. 4.b Amplitude ratio versus wave number

-For very small $\tilde{h}$, amplitude ratio is practically equal to 1 (or negative for the second solution) (see h = 0.1 on fig. 3-4). That is not surprising since it is the case particularly of this sheets. Furthermore, one solution is predominant.

-In intermediate cases (e.g. $\tilde{h}$ = 1-5) η_0^+ / η_0^- can be significally different from 1 or -1. $\tilde{\omega}_i$ terms are still very different. Generally one solution can be then be considered as predominant from the point of view of atomization (see fig. 3-4). In this case it is to be noticed that diagrams are resolutly different from Kelvin-Helmholtz results (h << 1).

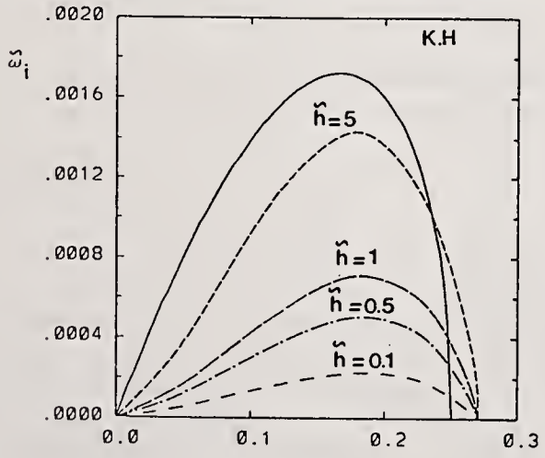

Fig. 5.a Growth rate versus wave number $\tilde{h}$

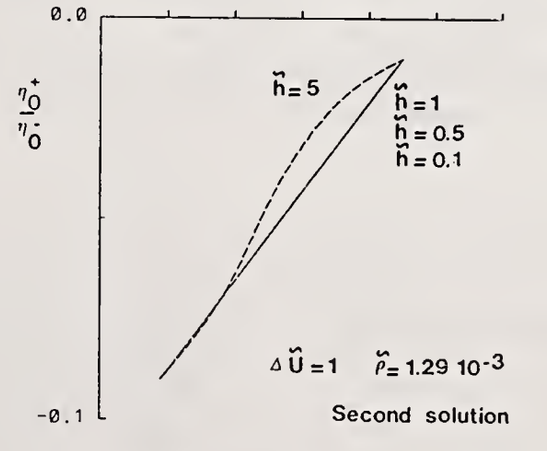

Fig. 5.b Amplitude ratio versus wave number

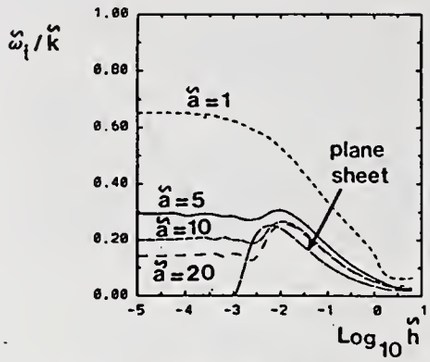

Fig. 6.a Growth velocity for the maximum growth rate versus $\tilde{h}$

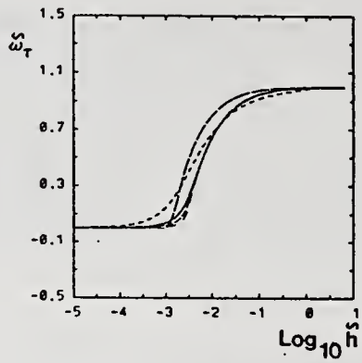

Fig. 6.b Wave velocity for the maximum growth rate versus $\tilde{h}$

$\Delta\tilde{U}=0 \qquad \tilde{\rho}=1.29\,10^{-3}$

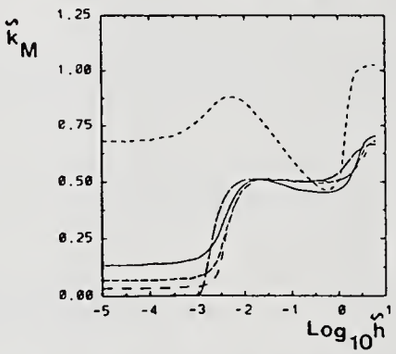

Fig. 6.c Wave number for the maximum growth rate versus $\tilde{h}$

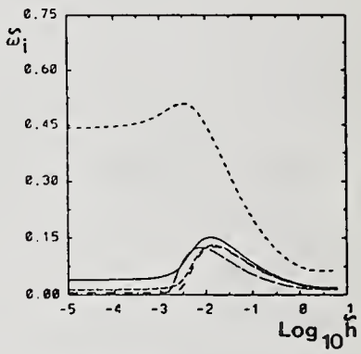

Fig. 6.d Maximum growth rate versus $\tilde{h}$

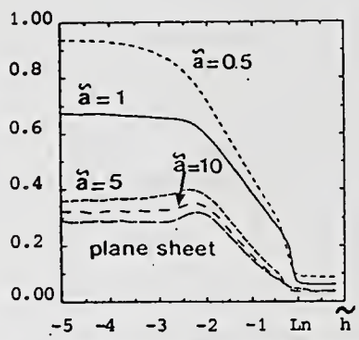

Fig. 7 a Growth velocity for the maximum growth rate versus $\tilde{h}$

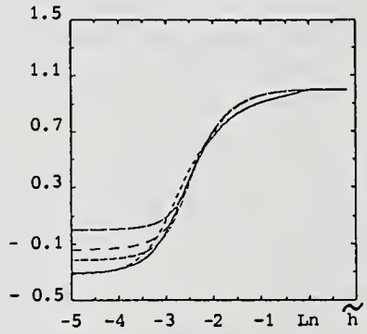

Fig. 7.b Wave velocity for the maximum growth.rate versus $\tilde{h}$

$\Delta\tilde{U}=1 \qquad \tilde{\rho}=1.29\,10^{-3}$

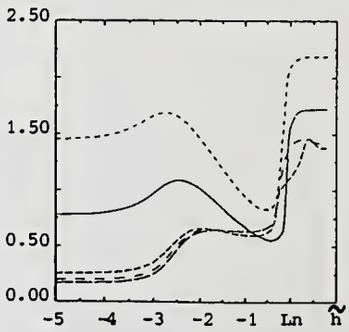

Fig. 7.c Wave number for the maximum growth rate versus $\tilde{h}$

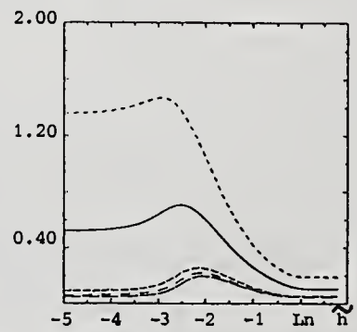

Fig. 7.d Maximum growth rate versus $\tilde{h}$

Annular sheet

A new parameter is now involved, the radius a. It will appear non-dimensionally as $a = k_c$. No place can be found here to show the analytic forms of the results but some calculated values are shown for two specific cases : $\Delta U = 0$ and $\Delta U = 1$.

It is to be remarked that results presented here do not involve the hypothesis of very thin sheet ($h << a$) which was accepted in previous papers ([1] [2] [3] [5]). It has been shown by the authors [8] that this hypothesis could not stand when $h/a > 10^{-5}$ [8].
Two solutions are also found. As an example the solution of greated $\tilde{\omega}_i$ is shown on figures 6 and 7. Some features can be observed.

1)-Case $\tilde{\Delta U} = 0$ (fig. 6)

- ω_r has a jump around $\tilde{h}$ equal $10^{-2.5}$ $\tilde{\omega}_r$ is proportional to c and the corresponding values of c are that of the gas (small $\tilde{h}$) or that of the liquid (high h).
- ω_i is very small at lower $\tilde{h}$. There is a very small velocity difference between the wave and the gas.
- ω_i is small at higher h. The inertia of the sheet becomes important.
- For $\tilde{a}>10$ solution become asymptotic to the solution relative to the flat sheet. This give a criteria to adopt then a simpler analysis (case 1).

2)-Case $\tilde{\Delta U} = 1$ (fig.7). The distinction between aerodynamical (low $\tilde{h}$) and inertial domains (high h) is found again on ω_r curves.

When $\tilde{a}$ increases ($\tilde{a}>10$) the analysis relative to fat sheet is valid again.

Although no results are presented here, our model can also deal with swirling flows.

EXPERIMENTS

In order to validate some of these results, a generator of cylindrical shet has been built. No place is found here to describe it but some characteristics are given :
-thickness h = 300μm -radius a = 2,55mm -velocity of liquid = 2-4m/s
-velocity of internal air flow U^- = 0-40m/s.

Photography and acoustic frequency measurements are used. Experiments are in advance now to study effects of swirl and external flows.

CONCLUSION

A new model of the instability of flat and annular sheet surrounded by air flows of different velocities has been presented here. It has been shown that two different perturbations where running along the sheet, both with different amplitudes on each side. Asymptotic cases show that, for high thicknesses or high velocities, the atomization (Kelvin-Helmholtz) theory was valid. A criteria ($a \sim 10$) is given for identifying an annular sheet of great radius to a flat sheet. A first experimental validation is presented.

This work was executed under CEE BRITE-EURAM contracts as associated partner with Society SNECMA.

Nomenclature

a radius of annular sheet
h thickness of the sheet
k wavenumber ($=2\pi/\lambda$)
η perturbation of interface
ω complex pulsation
σ surface tension
ρ density (L liquid, +, - gas)
subscript ~ indicate non dimensionalized numbers

BIBLIOGRAPHY

[1] G.D. Crapper, N. Dombrowski and G.A.D. Pyott, "Kelvin-Helmholtz wave growth on cylindrical sheets". J. Fluid Mech., vol.68 (1975).
[2] Martinon, "Instabilités d'une nappe liquide cylindrique en présence de deux écoulements gazeux". Journal de Mécanique Théorique et Appliquée, vol.2 (1983).
[3] Guillié , "Etude expérimentale et théorique de l'injection aérodynamique. Thèse de 3ème cycle à l'Ecole Nationale des Mines de Paris (1987).
[4] CH. Dumouchel , "Problèmes liés à la conception d'un pulvérisateur mécanique hydrodynamique de chambre et instabilité de nappe". Thèse de l'Université de Rouen (1989).
[5] Meyer J., Weihs D., J. Fluids Mech, vol.179, p. 531-545 (1987).
[6] Squire, Brit. Journ. of Appl. Phys., vol.4 (1953).
[7] Hagerty and Shea, "A study of the stability of plane fluid sheets". Journal of Applied Mechanics, vol.22 (1955).
[8] PH. Camatte, in ILASS (1989) proceedings, Pisa.
[9] Kendall, "Experiments on annular liquid jet instability and on the formation of liquid shells".Phys. of Fluids, vol.29 (1986).

LIQUID JET INSTABILITY IN COAXIAL AIR FLOW

H. Eroglu and N. Chigier

Mechanical Engineering Department
Carnegie Mellon University
Pittsburgh, PA, U.S.A.

ABSTRACT

Wave characteristics of liquid jets issuing from airblast coaxial atomizers have been investigated. The wavelengths on the liquid jet surface were measured from high magnification micro-photographs over a liquid jet velocity range of 1.1 - 18.2 m/s and for the air velocities 45.8, 56.12, 64.8 and 91.64 m/s. The wave frequencies were measured using a laser beam attenuation technique. Both dilational and sinuous waves were observed. The wavelengths generally increased in the downstream axial direction. Average wavelengths decreased with liquid and air velocities, however, the average jet surface oscillation frequencies were found to increase with these velocities. Wave propagation velocities were found to have much lower magnitudes than the liquid jet velocity for all air velocities, and were insensitive to the variation of these velocities.

INTRODUCTION

The disintegration of liquid sheets and jets has been studied by many investigators. Comprehensive reviews of disintegration mechanisms are reported by McCarthy and Molloy [1], Reitz and Bracco [2], and Lefebvre [3]. The disintegration of low viscosity liquid jets issuing at sufficiently high velocities from a nozzle was analyzed by Levich [4]. According to this analysis, both long and short length (as compared to the jet radius) waves appear on the jet surface under the effect of infinitely small disturbances. Because of the dynamic influence of air, both the long and the short wavelengths become unstable and lead to the generation of a wide range of drop sizes.

Recent theoretical research has concentrated on the development of computational models [5-7] for analysis of the disintegration of liquid sheets and jets. However, the number of experimental investigations providing data on the wave characteristics of liquid sheets and jets is very limited.

Among the recent experimental studies, Arai and Hashimoto [8] investigated the disintegration of a thin liquid sheet in a co-current air stream. The vibration frequency of the liquid sheet was measured using an electro-optical displacement device. The breakup frequency was obtained by means of a stroboscope. The liquid sheet vibration frequency was found to be equal to the breakup frequency. The liquid sheet vibration frequency was shown to be a function of Weber and Reynolds numbers. These results also showed that the disintegration of the thin liquid sheet depends on the wave motion of the liquid sheet. Therefore, the mean droplet diameter resulting from the disintegration was correlated to the frequency of the vibrating liquid sheet.

Mansour and Chigier [9] studied the aerodynamic instability of liquid sheets issuing from a two-dimensional air-assisted atomizer. Still microphotography was used to determine the global structure of the sprays, and a laser light attenuation technique was employed to measure the oscillation frequencies. The measured vibrational frequencies were correlated with the resulting spray angle. It was shown that the liquid sheet oscillations are dynamically similar to those in hard spring systems. At low liquid flow rates, the sinuous breakup was found to be the dominant mode. At high liquid flow rates, the oscillations were of the dilational type. At intermediate liquid flow rates, both the sinuous and the dilational modes were superimposed on the liquid sheet.

This paper presents the results of the wavelength and frequency measurements for liquid jets issuing from airblast coaxial atomizers.

EXPERIMENTAL CONFIGURATION

The atomizer consists of a central water jet surrounded by a coaxial air jet. Both water and air supply pressures and mass flow rates can be varied. The house air supply provides a maximum inlet pressure of 25 kPa for the atomizing air. Water is supplied from a tank with 10 liter capacity and is pressurized with house air. This water supply provides a pulsation and vibration free water flow and a maximum water pressure of 600 kPa if no air is used to assist the atomization. When the maximum air flow rate is used for the atomization, the maximum possible water supply pressure is reduced to 500 kPa.

The test atomizer and the exhaust system were connected to the same three-directional (z-r-phi) positioner so that the axial distance between the nozzle exit and the exhaust inlet always remained the same (120 mm). The accuracy of the positioner is 0.01 mm in the axial (z) and radial (r) directions and 0.1 degree in the phi direction.

The test nozzle has provisions for the accurate positioning of the central tube with respect to the outer tube. A screen is used in order to reduce turbulence and also serves as a flow straightener. The converging section of the outer tube provides a plug flow air velocity profile at the nozzle exit. Figure 1 shows the nozzle exit geometry; the dimensions are in millimeters.

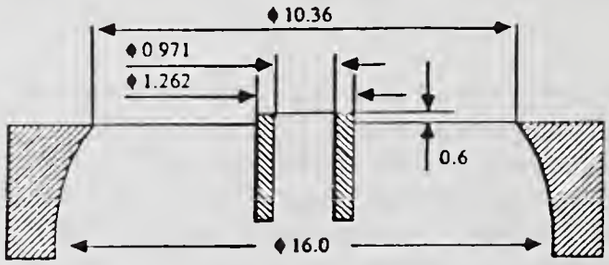

Fig. 1 Enlarged sketch of the nozzle exit

Photographs of the sprays were taken using a Canon F1 camera with a f = 200 mm macro lens. Different extension tubes and bellows were attached to the camera. An Electro-Optics EG&G 549 microflash was used to provide a 0.5 μs flash duration and 5 x 10^7 beam candlepower light intensity. More than 1500 photographs were taken at various air and water flow conditions. The description of the photographs was previously reported by Farago and Chigier [10].

The schematic of the frequency measurement system is shown in Fig. 2. This system utilizes the attenuation of a collimated laser beam passing through the liquid jet in the transverse direction (y-direction). The intensity of the laser beam is measured using a photodiode which generates a current proportional to the incident radiation. This current is converted to a voltage in the range of 0 - 1.5 volts. A Tektronix T912 storage oscilloscope is used to visualize the signal. The wave form is then transferred to an IBM PC/XT for data analysis and storage. An FFT routine is used to transform the wave form from the time domain to the frequency domain. The power spectra of oscillations are then displayed in the graphics form.

Initially, the axial location of the laser beam was brought close to the nozzle exit. Then, the axial position of the beam with respect to the nozzle was varied until a clear wave form was obtained on the oscilloscope screen. The actual waves on the surface of the jet were also observed using a stroboscope. With the present arrangement, it was possible to provide frequency information about the initial disturbances before the waves are transformed from the dominantly

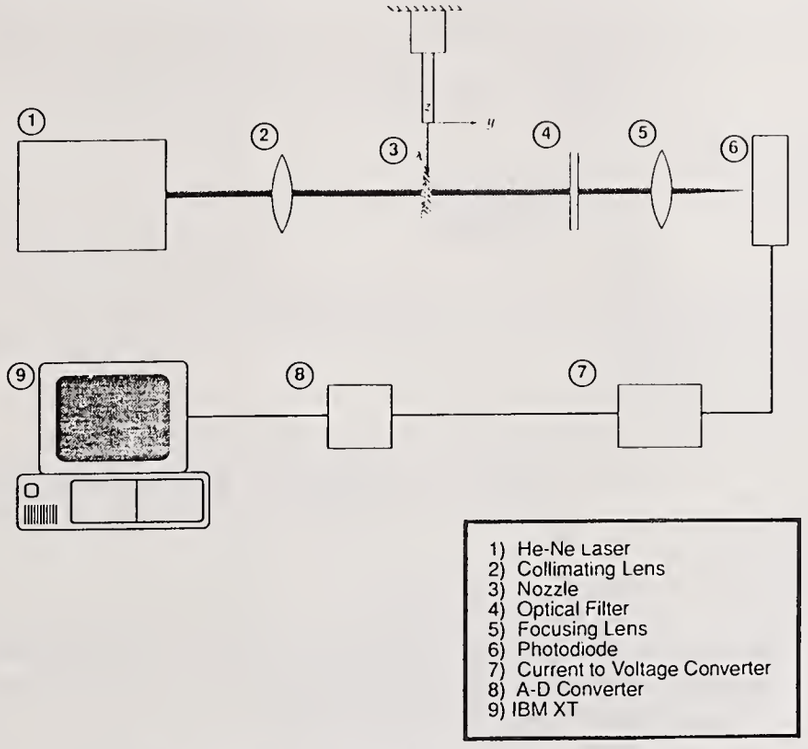

Fig. 2 Frequency measurement system

dilational to the sinuous mode. This information is particularly important for the computational analysis of liquid jet instability.

RESULTS AND DISCUSSION

Wave characteristics of liquid jets issuing from airblast coaxial atomizers were investigated in terms of wavelengths and frequencies. Jet surface wavelengths were measured from the photographs over the liquid jet velocity range 1.1 - 18.2 m/s and for the gas jet velocities 45.8, 56.12, 64.8 and 91.64 m/s. Liquid jet surface wave frequencies were measured using a laser beam attenuation technique.

Wavelengths

A careful investigation of the photographs shows that, in general, two types of waves are encountered as the liquid jet velocity is varied while keeping the air velocity constant. The dilational wave develops on the jet surface and may or may not be symmetrical with respect to the jet axis. The sinuous wave has an assymetric, snakelike shape whose centerline deviates from the nozzle axis. At low liquid jet velocities, the waves are predominantly sinuous, however, at high liquid velocities, the dilational waves are formed on the liquid jet surface.

Figure 3 shows the wave development of the liquid jet for the liquid and air velocities of 4.5 m/s and 56.12 m/s respectively. At such an intermediate liquid jet velocity, the initial disturbances are of the dilational type. Sinuous wave formation starts further downstream. Dilational waves are superimposed on the sinuous waves. Due to the aerodynamic action, dilational waves lead to the formation of ligaments mostly at the crests of the sinuous waves. These ligaments further

Fig. 3 Liquid Jet at V_{air} = 56.12 m/s, V_j = 4.5 m/s

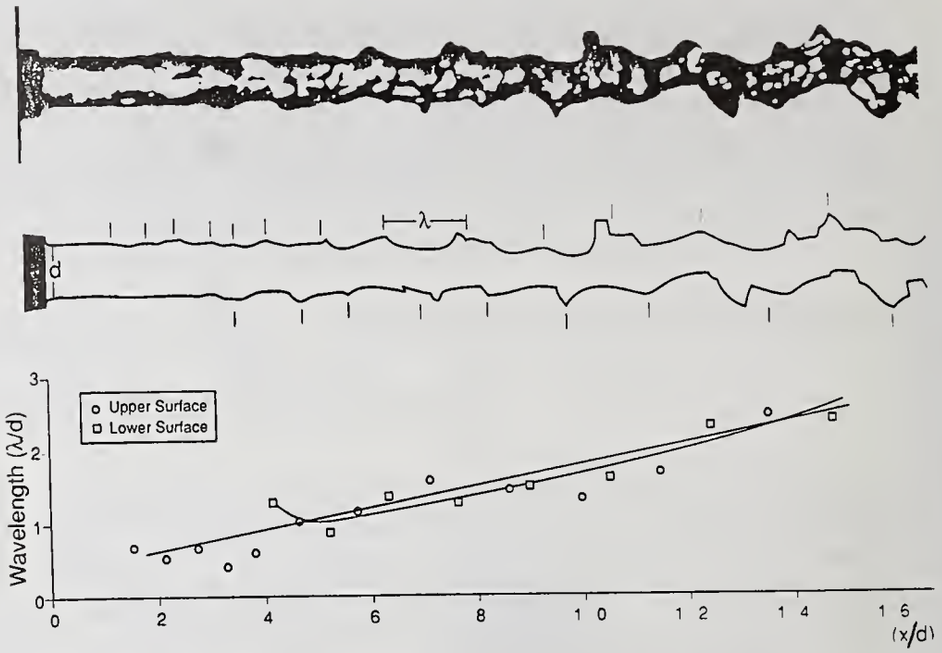

Fig. 4 Variation of wavelength along the jet axis (V_{air} = 56.12 m/s, V_j = 9.56 m/s)

disintegrate by the shear of the surrounding air as shown in Fig. 3. This figure also shows that the entire jet breaks up in a similar manner to that of liquid sheets where the half waves are torn off the liquid sheet when the wave amplitude reaches a critical value.

Figure 4 shows the wave formation on the liquid jet at liquid and gas velocities of 9.56 m/s and 56.12 m/s respectively. The upper figure was obtained by scanning the photograph of the liquid jet at 100% and 300 dots per inch using an HP scanner and Applescan software. The outline of the scanned image shown in the lower figure was then generated. The locations of wave crests were marked on the same figure, and the distances between the marks were measured. These distances were accepted as the wavelengths. The bottom figure shows the variation of the normalized wavelength (λ/d) in the axial direction (x/d) for both the upper and the lower surfaces. The wavelengths increase almost linearly in the downstream direction. The magnitudes of the wavelengths are very close to each other for the upper and the lower surfaces at the same axial location. Although the waves of Fig. 4 are predominantly of the dilational type, the initiation of sinuous wave formation can also be observed.

Since the wavelengths vary in the axial direction, average wavelengths were calculated for the dilational surface waves before the transition to sinuous mode takes place. These were normalized with respect to the jet diameter at the nozzle exit and plotted as a function of liquid jet velocity for four different gas velocities. Figure 5 shows this plot. In general, the wavelengths decrease with increase in liquid jet velocity and gas velocity. This decrease is more pronounced for the liquid jet velocities at which the transition from laminar to turbulent flow occurs. After transition to turbulence has been completed, the wavelengths seem to be insensitive to the increase in the liquid jet velocity. This may be due to the predominant effect of the small-scale turbulent structures inside the liquid jet controlling the initial phase of the wave development.

Figures 4 and 5 show that the dilational waves have lengths shorter than the perimeter of the liquid jet ($\lambda < \pi d$). It appears that the aerodynamic influence is the major destabilizing force for the wave development rather than the surface tension force within the investigated range of flow

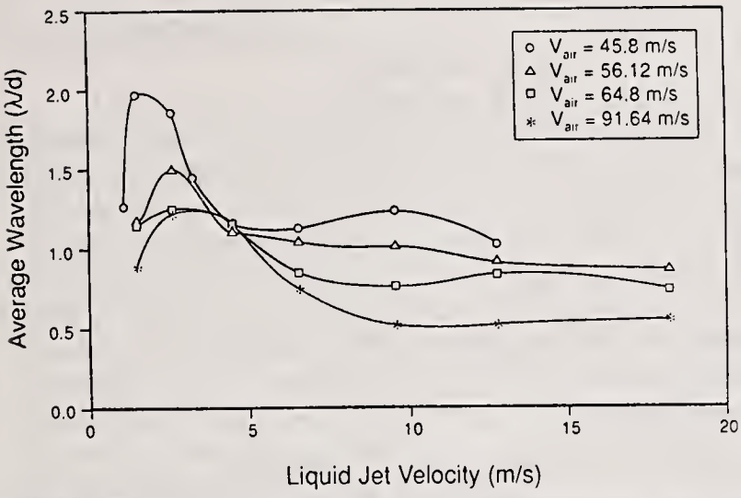

Fig. 5 Variation of average wavelength with liquid and gas jet velocities

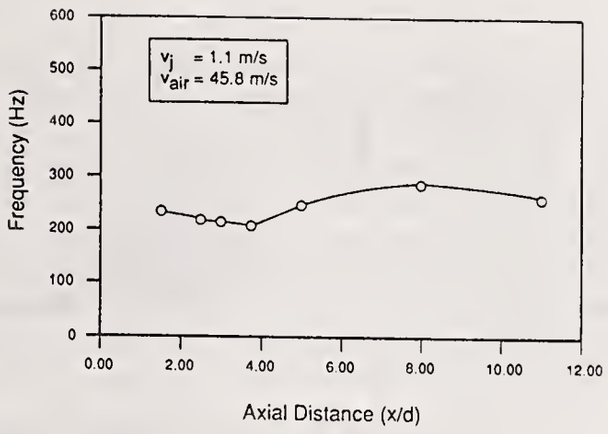

Fig. 6 Variation of average frequency along the jet axis (V_{air} = 45.8 m/s, V_j = 1.1 m/s)

conditions. It also seems that the turbulence in the liquid jet is responsible for the formation of initial disturbances as shown in Fig. 4 at higher liquid jet velocities.

Frequencies

The primary interest in this paper is to provide information on the initial disturbances close to the nozzle exit. The detection of the disturbances has less uncertainty, however, at downstream axial locations (x/d) because of the more pronounced waves. The effect of axial measurement location on the measured wave frequencies was investigated in an effort to determine the optimum measurement location before the waves are transformed into the sinuous mode. Figure 6 shows the result of this investigation for the liquid and gas jet velocities of 1.1 m/s and 45.8 m/s. Frequency is shown to be rather insensitive to the axial measurement location as long as the type of the wave remains the same.

Figures 7 and 8 show the power spectral densities of the liquid jet surface oscillations for an air velocity of 56.12 m/s and the water velocities of 1.5 m/s and 12.76 m/s, respectively. Figure 7 shows a dominant oscillation frequency at the lower liquid jet velocity. However, at higher liquid velocities (Fig. 8) several modes of oscillation appear, and the band width of oscillations increases considerably. The liquid jet turbulence is probably the major cause for this widening of the frequency band width. The measured frequencies also increase with the liquid jet velocity. Because of the difficulty in determining the dominant modes of oscillation at high liquid jet velocities, single representative frequencies were obtained at each pair of flow conditions by

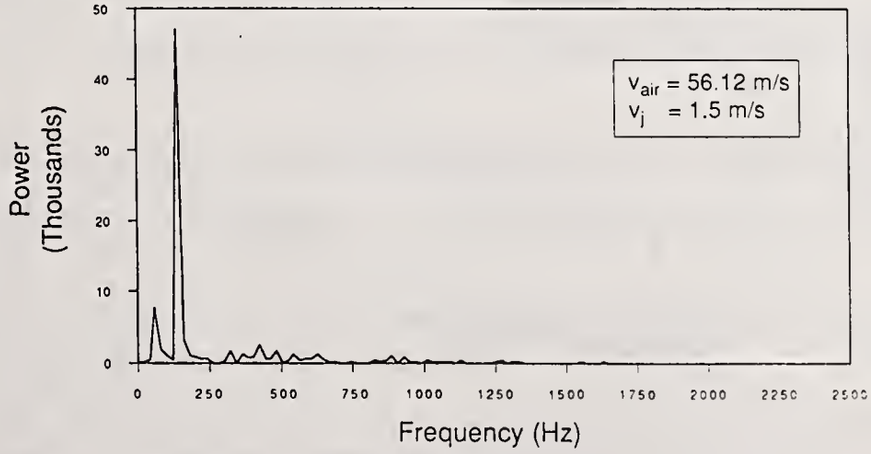

Fig. 7 Power spectral density at V_{air} = 56.12 m/s, V_j = 1.5 m/s

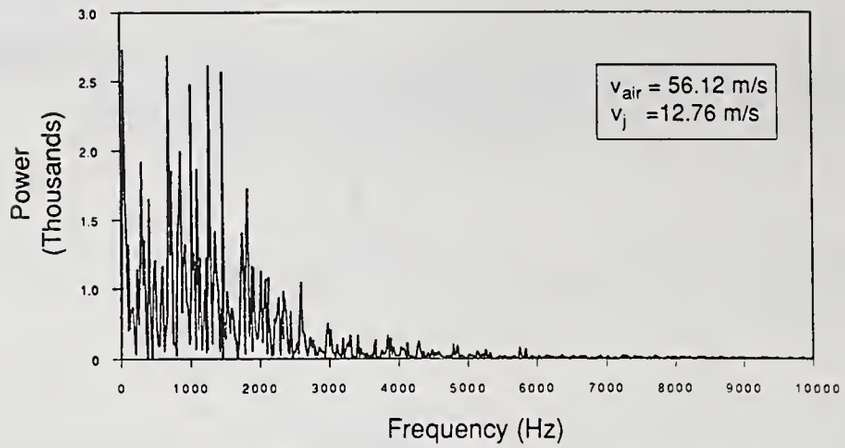

Fig. 8 Power spectral density at V_{air} = 56.12 m/s, V_j = 12.76 m/s

weighting the frequency values with corresponding power densities and averaging over the whole power range. The repeatability of the measurements was found to be poor (15% uncertainty) at high liquid jet velocities for which the frequency band widths widen considerably. Therefore, each experiment was repeated four to five times, and the calculated average frequencies were further averaged in order to increase the confidence in the data.

The variation of average frequencies as a function of nozzle exit liquid and gas jet velocities is shown in Fig. 9. The average frequencies increase both with the liquid and the gas jet velocities. This behavior is consistent with the results of Arai and Hashimoto [8] and Mansour and Chigier [9] on the liquid sheet instability with co-current air flow. The frequency jumps separating the regions for different modes of oscillation were also reported by Mansour and Chigier [9]. These jumps, however, were not observed for the coaxial liquid jet of this study. This was probably due to an insufficient number of variations of experimental conditions to identify this phenomenon.

Wave Propagation Speed

The wave propagation speeds were obtained by taking the product of average frequencies and wavelengths over the range of velocities 1.1 - 18.2 m/s for water, and 45.8 - 91.64 m/s for air. They were found to be in the order of 1 - 2 m/s and do not seem to be sensitive to the water and the air velocity variations. This behavior is consistent with the wavelength decrease in Fig. 5 and the corresponding frequency increase in Fig. 9 with increasing liquid and gas jet velocities.

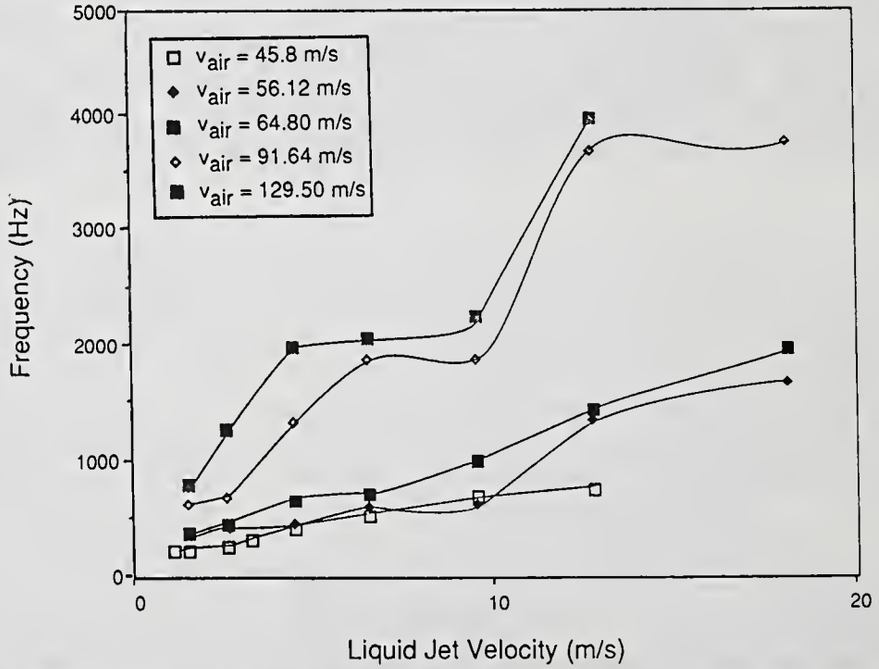

Fig. 9 Variation of average frequency with liquid and gas jet velocities

CONCLUSIONS

The wave characteristics of liquid jets issuing from airblast coaxial atomizers were investigated. Two types of waves were encountered. The dominant wave type was sinuous at low liquid jet velocities, and dilational at high liquid jet velocities. The wavelengths generally increased in the downstream axial direction. Average wavelengths decreased with liquid and gas jet velocities. The dilational waves of this study were found to have shorter lengths than the perimeter of the liquid jet. The major destabilizing force is the aerodynamic interaction at the liquid/gas interphase. The turbulence in the liquid jet is important in initiating the surface disturbances at high liquid jet velocities. The average oscillation frequencies at the liquid jet surface appear to be insensitive to the axial measurement location. The frequency band of the jet surface oscillations increased with the liquid jet velocity. Average frequencies were found to increase with both the liquid and the gas jet velocities. Wave propagation speed seems to be rather insensitive to the liquid and the gas velocity variations.

NOMENCLATURE

d	jet diameter
phi	circumferential direction of the atomizer
r	radial direction of the atomizer
V_{air}	air jet velocity
V_j	liquid jet velocity
x	axial direction of the jet
y	transverse direction of the jet
z	vertical direction of the jet; axial direction of the nozzle
λ	wavelength

ACKNOWLEDGEMENT

The authors wish to acknowledge financial support from NASA Marshall Space Center, grant number NAG8-126.

REFERENCES

1. McCarthy, M.J. and Molloy, N.A., "Review of Stability of Liquid Jets and the Influence of Nozzle Design", Chemical Engineering Journal, Vol. 7, pp. 1 - 20, 1974.

2. Reitz, R.D. and Bracco, F.V., "Mechanism of Atomization of a Liquid Jet", Physics of Fluids, Vol. 25, No. 2, pp. 1730 - 1741, 1982.

3. Lefebvre, A.H., Atomization and Sprays, Hemisphere Publishing Company, New York, 1989.

4. Levich, V.G., Physicochemical Hydrodynamics, Prentice-Hall, New Jersey, 1962.

5. Lin, S.P. and Lian, Z.W., "Mechanisms of the Breakup of Liquid Jets", AIAA Journal, Vol. 28, No. 1, pp. 120 - 126, 1990.

6. Przekwas, A.J., Chuech, S.G. and Singhal, A.K., "Numerical Modeling for Primary Atomization of Liquid Jets", AIAA Paper No. 89 - 0163, 1989.

7. Rangel, R.H. and Sirignano, W.A., "Nonlinear Growth of Kelvin-Helmholtz Instability: Effect of Surface Tension and Density Ratio", Physics of Fluids, Vol. 31, No. 7, pp. 1845 - 1855, 1988.

8. Arai, T. and Hashimoto, H., "Disintegration of a Thin Liquid Sheet in a Cocurrent Gas Stream", Proceedings of the 3rd International Conference on Liquid Atomization and Spray Systems, pp. VIB/1/1-7, 1985.

9. Mansour, A. and Chigier, N., "Dynamic Similarity Between Liquid Sheets and Hard Spring Systems", Physics of Fluids A, 1991.

10. Farago, Z. and Chigier, N., "Parametric Experiments on Coaxial Liquid Jet Atomization", ASME Paper No. 90-GT-81, 1990.

EFFICIENT SPRAY MODELING ON VARIOUS APPLICATIONS USING THE GROUP APPROACH

Q. Zhou and S.C. Yao

Department of Mechanical Engineering
Carnegie Mellon University
Pittsburgh, PA, U.S.A.

ABSTRACT

A "Group" approach for the modeling of sprays has been well established and applied to various problems, e.g. particle laden jets, impacting sprays and spray heat transfer. In the group model, a droplet group is considered to have a dimension which grows during its motion due to the turbulent dispersion of droplets. The droplet dispersion within a group is described by a probability density distribution function. All the applications have shown that the group model is very efficient in the computational time, can give very realistic descriptions, and have very wide applications.

INTRODUCTION

Turbulent sprays have been widely applied to various industrial processes, such as spray combustion, spray cooling, spray painting, spray drying etc. Computer modeling of turbulent sprays is becoming an increasingly viable part of the design process with the objective to reduce the time and cost of process development. In the efforts for developing spray models, the major focus is on the turbulent interaction between gas phase and dispersed phase. Several approaches have been employed to model the turbulent droplet dispersion in sprays [1]. However, because of their excessive computational requirements, the spray models are still not feasible for general industrial applications.

Among the existing models, a rather advanced one is the Stochastic Separated Flow (SSF) model which has been widely accepted for the modeling of turbulent sprays [1, 2]. The SSF model uses droplet clusters to represent a spray and simulate the turbulent dispersion directly by considering the interaction between pseudo-random turbulent eddies and droplets in a Lagrangian computation of cluster motion. In the SSF approach, however, all the droplets within the cluster are assumed to be concentrated at one point during the flight. A droplet cluster is essentially a computational droplet. Therefore, in order to obtain a statistically meaningful distribution, a significant number of computational droplets, and consequently, very long computation times are needed.

A new group approach has been well established by the authors of this paper [3, 4, 5]. The group model uses droplet groups to represent a spray and takes into account the turbulent droplet dispersion within each group. It considers that each group has a dimension which grows during the flight. This growth is due to the turbulent dispersion of droplets as the group travels in the Lagrangian coordinates. The droplet dispersion within the group is described by a probability density function which is a Gaussian

distribution. Due to the growth of the group, only a small number of groups must be traced to provide statistically reasonable results. Furthermore, the group approach closely simulates a real flow, because in a real flow the droplets within a group are dispersed by turbulence instead of staying at one point.

The intent of this paper is not to elaborate the details of the group model, but to provide various examples of its applications, the effectiveness of the model, and the efficiency of the computations using this approach. The implementation of this model to different problems, such as particle laden jets, impacting sprays, and spray heat transfer, has shown its generalized application to sprays. The concept of this group approach can be incorporated into any computational program which presently employs the Lagrangian approach to trace the dispersed phase, and widely applied to various sprays in industry. This new modeling concept is expected to have more advantages when the geometrical scale is large, where its higher computational efficiency becomes indispensable.

GROUP APPROACH

In the present study, a standard Eulerian approach is applied to the gas phase transport. The SSF analysis (Lagrangian formulation) is used to trace the motion of the center of each group which is assumed to behave like a single droplet interacting with a succession of random distributed turbulent eddies [1]. The major assumption in the modeling of droplet dispersion within a group is that the turbulent flow is assumed to be locally isotropic and homogeneous within each group. It is also assumed that all the droplets in a group move together in an absolute coordinate and the droplet dispersion is a relative motion to the center of the group. Therefore, the droplet group grows from its center, and the dispersion of droplets is observed from the center of the group. The relative droplet position within a group in respect to the group center at any time is random because of the turbulent gas velocity field. This kind of droplet dispersion can be closely represented by a normal Gaussian distribution [6]. The typical probability density function for this distribution can be given for a 2-D field as:

$$f(x,y,t) = \frac{N}{\sqrt{2\pi\bar{X^2}}\sqrt{2\pi\bar{Y^2}}} exp(-\frac{x^2}{2\bar{X^2}} - \frac{y^2}{2\bar{Y^2}}) \quad (1)$$

where N is the total droplet number in this group, and $\bar{X^2}$ and $\bar{Y^2}$ are the overall mean square distances in x and y directions. Further details of this group approach can be found in Ref. [3, 4, and 5].

APPLICATION OF GROUP APPROACH

Particle Laden Jets

In order to validate the new approach, the group modeling was applied to the analysis of a particle-laden jet containing fly ash particles. The preliminary results of this study were compared with the results of the SSF method and the experimental data. The experimental results were reported by Yuu et al. in reference [7]. Their experimental set-up contained a jet nozzle which could provide uniform exit properties. The nozzle diameter is 8mm. The particles are nearly monodisperse having a mass mean diameter of 20 μm. The flow is dilute with particle mass loadings of 0.1-0.4%. These loadings are sufficiently small, so that the particles have a negligible effect on the mean and turbulent gas phase properties.

The distributions of particle concentrations along the center line of the jet are shown in Figure 1 for the present method, the SSF approach, and the experimental results. The SSF results are presented for two different particle cluster numbers (20 and 500). For the smaller particle cluster number, the particle concentration distribution is not smooth due to statistically insufficient data. In order to obtain a reasonable agreement with the experimental results, 500 particle clusters were required as shown in the figure. Unlike the results of the SSF method, the results of the present approach are in sound agreement

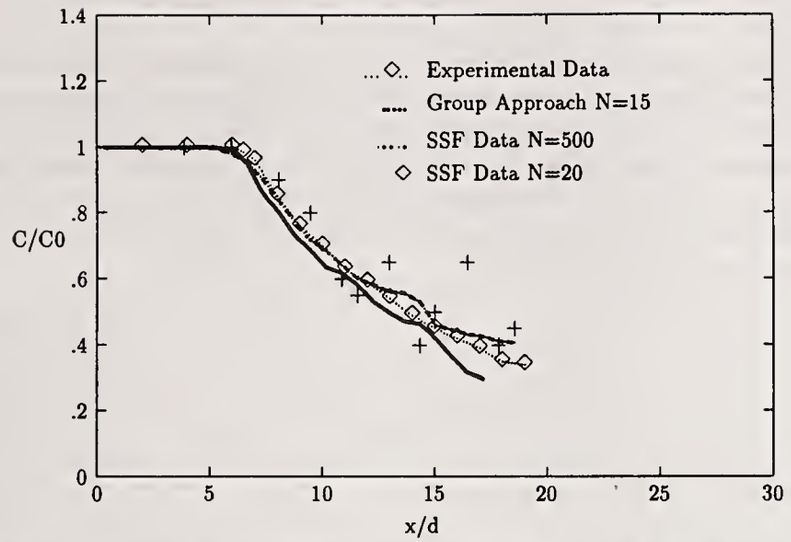

Figure 1: Axial Particle Concentration Distributions at the center line

with the experimental results with only 15 groups. At x/d more than 15, slightly larger deviation is observed.

Figure 2 compares the radial distributions of particle concentration for the present approach and the SSF method. Both methods have very similar results along radial direction also. Since the corresponding experimental data of radial distribution and radial initial conditions are not clearly reported in reference [7], the comparison was made only with the results of the SSF method.

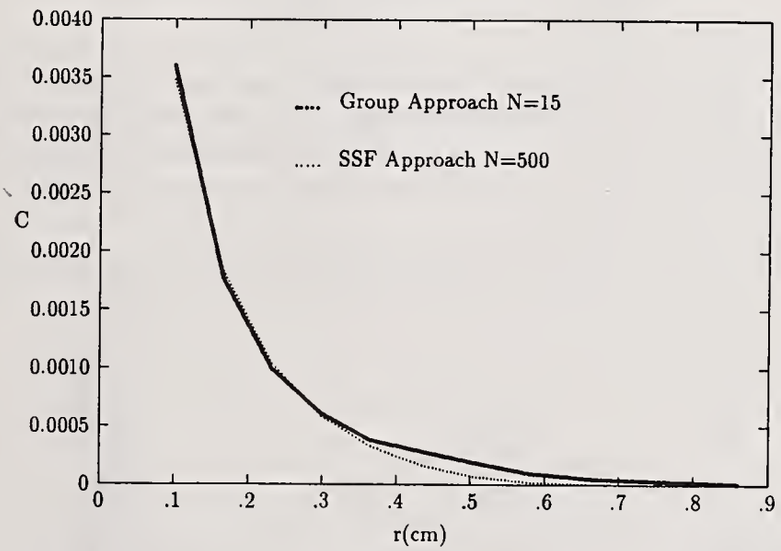

Figure 2: Radial Particle Concentration Distributions at x/d=20

A 32 × 29 grid was used in the calculations. The calculations were performed on a Sun 386i/250 computer(5 MIPS, 25 MHz). For the dispersed phase calculation, the computational time using SSF approach with 500 groups was 509 seconds, while the present study only took 53 seconds for a similar agreement with the experimental data. The computation time using the group model is about a factor of 10 times less than the corresponding calculation using the SSF approach. This major reduction in the computation time in the present approach is because of the significant decrease in the number of droplet groups required for realistic predictions.

Impacting Sprays

Impacting sprays were selected as an example to illustrate the capability of this group model. This selection was chosen because impacting sprays contain droplets of various sizes under severe flow conditions, and there are not many detailed investigations reported in literature despite its wide applications. Impingement of axisymmetric water sprays from a 9.5 mm diameter nozzle normally on a flat plate was studied using the group approach. The distance between the plate and the exit of the injector is 30.5 cm. The droplets are assumed to be monodisperse. The spray flow is considered to be dilute with an initial liquid volume flow rate fraction of 10^{-5}.

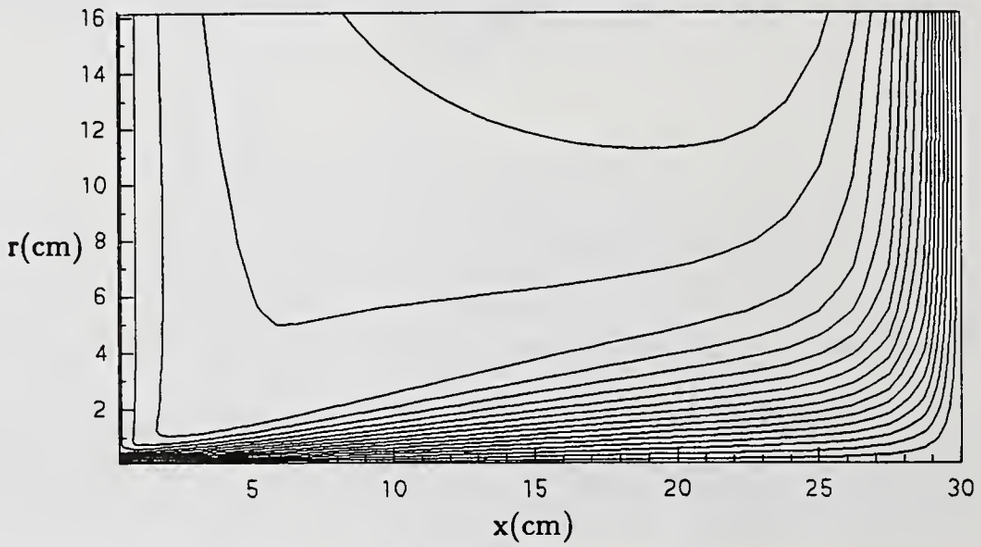

Figure 3: Gas Flow Streamlines

The gas phase mean flow field is shown in Figure 3. The mean flow streamlines demonstrate three flow regimes which were defined in reference [8]. The free jet regime is upstream of jet impingement. The strong interaction of the jet with the impingement surface produces a change in flow direction in the impingement regime. The wall jet regime consists of radial flow along the surface beyond the point at which the strong impingement to the wall occurs.

Figure 4 shows the trajectories of droplet group centers for the droplet diameter of 20 μm. It indicates

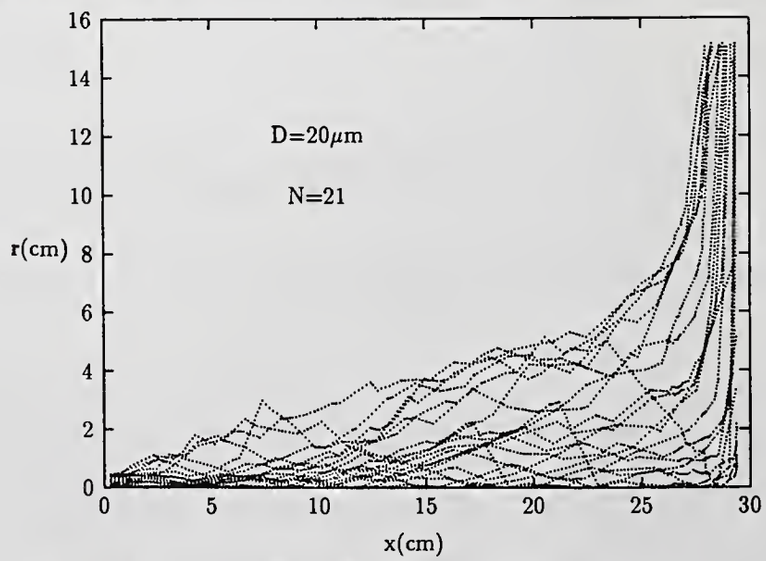

Figure 4: The Trajectories of Group Centers, D=20 μm

that the droplets follow the mean gas flow very closely and the spread of the trajectories is similar to that of the gas flow streamlines because of the small momenta of droplets. The irregularity of trajectories and the significant dispersion of droplets reveal that the interaction between the turbulent eddies and the droplets is very effective. The computations for the droplet diameters of 150 and 50 μm have also been performed. It was found that larger diameter droplets, such as those with a 150μm diameter, tend to continue in their initial direction with less influence by the gas flow field. As the droplet diameter decreases, the momenta of droplets decreases. Therefore, the droplets follow the mean gas flow more closely, the trajectories are more affected by the flow turbulence, and the droplets are spread more widely.

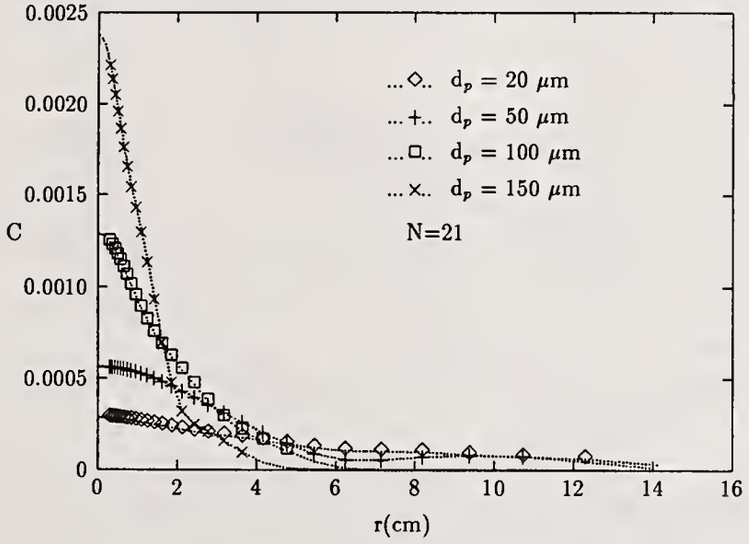

Figure 5: Radial Distributions of Droplet Deposition Flux

The radial distributions of the droplet deposition flux on the wall are shown in Figure 5 for the droplet diameters 20, 50, 100, and 150μm respectively. This droplet deposition flux is defined as the volume of total droplet deposition per unit wall area per unit time. A deposition is assumed to occur when a droplet approaches the wall surface within a distance of 0.01 cm. The figure demonstrates that the smaller diameter droplets spread wider and impinge over all the wall surface which is consistent with the implication of the trajectories. With increasing droplet diameters, the deposition flux distribution increases at the central locations, and the radial extent of impingements decreases.

A comparison of the group approach with the SSF approach was also made in the present study. Figure 6 shows that the present group approach with 21 groups yields results similar to the SSF approach with 980 clusters; however, the SSF distribution is not as smooth. Therefore, much less group number is needed for the group model to get more realistic results as compared to the SSF method.

The radial distributions of locally averaged impact angles for the four different droplet diameters are shown in Figure 7. The impact angle, α, is defined as the angle between the drop trajectory and the direction normal to the wall. The impact angle in general increases with distance from the symmetry axis. In the area near the symmetry axis, the impact angle increases as the droplet diameter decreases because the smaller droplets follow the gas flow more closely. The 150 μm diameter droplets have the smallest impact angles due to their high momentum. The impact angles of 20 and 50 μm droplets are smaller than expected in the area between 2 cm and 10 cm wall radii. It is noted that much of these small diameter droplets do not impact the surface of the plate and go out following the gas flow. For the droplets impacting the surface, they may impact at small angles due to the effect of gas flow turbulence. The average impact angles obtained from these few impacts, therefore, gives lower impacting angles within the 2 cm to 10 cm wall radius range as shown in Figure 7. The information of radial distributions of overall droplet impingement velocities for different droplet diameters was also provided in the computations. It also showed that the larger the droplets, the less influenced by the gas

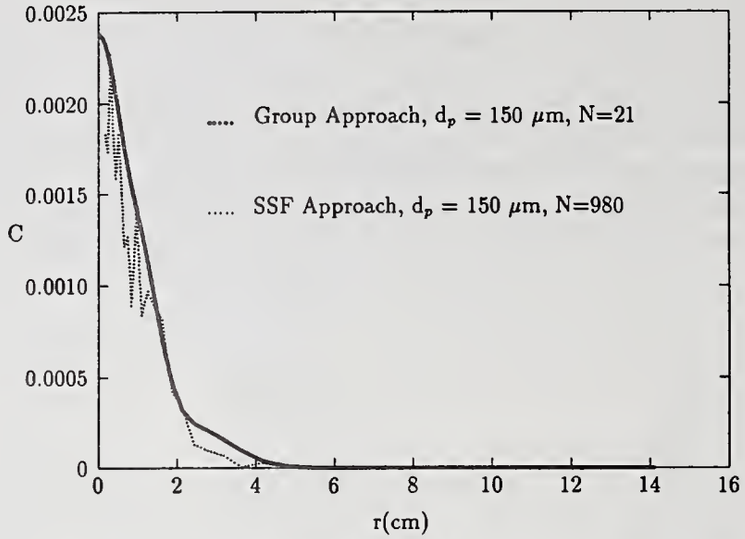

Figure 6: Radial Distributions of Droplet Deposition Flux

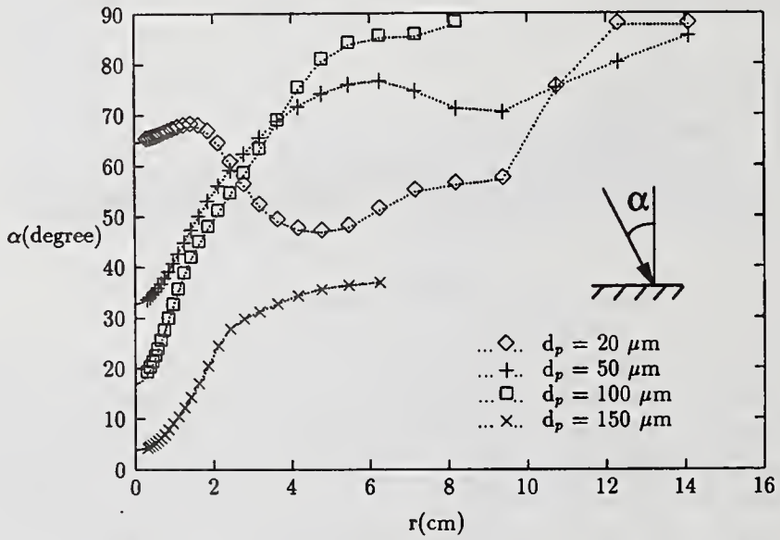

Figure 7: Impact Angle Distributions on the Wall

velocity distribution.

A 36 × 35 grid was used in the calculations. For the liquid phase calculation of 150μm diameter droplets, the SSF approach took about 900 seconds with 980 groups, while the group approach only took about 46 seconds for similar results. The computation time using the group approach is about a factor of 20 times less than the corresponding calculation using the SSF method. As expected, the reduction of computation time is more significant when the geometrical scale is large. Using the group approach, the information on spray trajectories, droplet deposition flux, impact velocity, and impact angle etc. can be obtained easily. This understanding allows for advances on various impacting spray applications.

Spray Heat Transfer

The heat transfer to particles in a spray was also investigated using the group approach. It is found that the group approach allows for very effective modeling of this heat transfer process in a very straightforward manner. The results are presented in Figure 8. The geometry and the initial kinematic conditions were kept similar to that in reference [7]. However, the cold particles with initial temperature 300K were

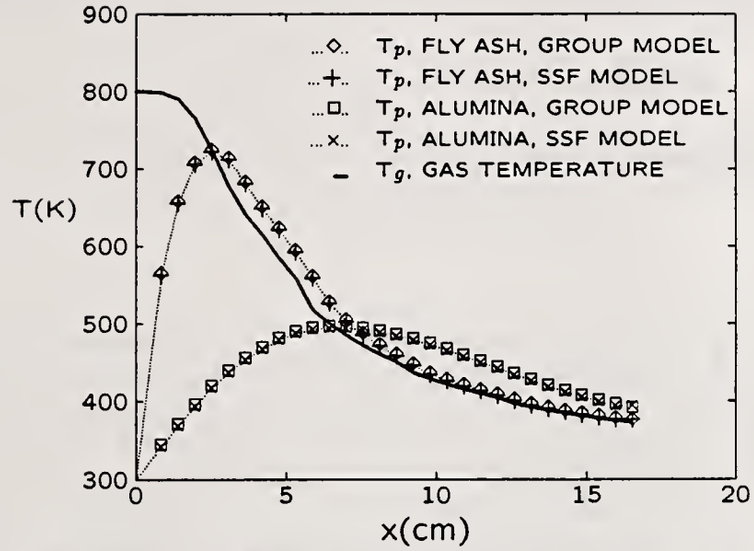

Figure 8: Axial Temperature Distributions at the center line

injected into hot air stream with initial temperature 800K, and were heated up by the surrounding gas due to mixing. The temperatures of gas and particles are solved by energy conservation equations. The calculations were performed for fly ash and alumina particles of the same size (20 μm). The density, ρ, and specific heat, C_p, for fly ash are 2.0 gm/cm^3 and 1.214 j/(kgK), respectively. These properties are 3.9 gm/cm^3 and 1.5 j/(kgK) for alumina particles.

Figure 8 shows the axial variation of gas and particle temperatures. The gas temperature decreases rapidly up to about 8 cm distance from the nozzle exit. Its decrease is more gradual further downstream. The average particle temperatures increase steeply for both particle materials immediately downstream of the nozzle. These temperatures show a peak for both materials, and gradually decrease. The calculated results of the group model which used 15 groups for both materials are in very good agreement with the results using the SSF method with 500 particle clusters.

A comparison of the average axial temperature distribution for the fly ash and alumina particles has shown that the product of density and specific heat have a strong influence on the magnitude of particle temperature. Alumina particles heat-up and cool down more slowly than fly ash due to their higher thermal inertia. This results in a lower peak and higher downstream temperatures for alumina particles.

CONCLUSIONS

A group approach has been well established. All the applications have shown that:

- The group approach is "efficient" in the computational time because of very small number of droplet group required.
- The group approach is "realistic", since it considers the turbulent droplet dispersion within each group.
- The group approach can be "generalized", and has very wide applications.

NOMENCLATURE

C	droplet concentration
f(x,y,t)	probability density distribution
N	number of droplets in a group
r	radial coordinate
t	time
T	temprature
x	axial coordinate
$\bar{X^2}, \bar{Y^2}$	mean square distances
y	vertical distance

Subscripts

d	droplet property

References

[1] G. M. Faeth. *Mixing, Transport and Combustion in Sprays,* Prog. Energy Combust. Sci. Vol.13, 293, 1987.

[2] A. D. Gosman. *Aspects of Computer Simulation of Liquid-Fueled Combustors,* AIAA Paper No. 81-0323, 1981.

[3] Q. Zhou, and S. C. Yao. *An Efficient Modeling of Turbulent Sprays,* Eastern States Section of the Combustion Institute, Clean Water Beach, Florida, 1988.

[4] Q. Zhou and S. C. Yao. *A Model of Particle Dispersion for Turbulent Sprays,* presented at Symposium on Heat and Mass Transfer in Fire and Combustion Systems, ASME Winter Annual Meeting, Dallas, Texas, Nov. 1990.

[5] Q. Zhou and S. C. Yao. *Group Modeling of Impacting Spray Dynamics*, accepted by International Journal of Heat and Mass Transfer.

[6] N. A. Fuchs *The Mechanics of Aerosols,* Macmillan Company, New York, 1964.

[7] S. Yuu, N. Yasukouchi, Y. Hirosawa and T. Jotaki. *Particle Turbulent Diffusion in a Dust Laden Round Jet,* AIChE Journal 24, 509, 1978.

[8] C.D. Donaldson and R.S. Snedeker. *A study of free jet impingement. Part 1. Mean properties of free and impinging jets,* J. Fluid Mech., vol. 45, part 2 pp281-319, 1971.

AXISYMMETRIC CALCULATIONS OF THREE-DROPLET INTERACTIONS

C.H. Chiang and W. A. Sirignano

Department of Mechanical and Aerospace Engineering
University of California
Irvine, CA, U.S.A.

ABSTRACT

The present study extends the previous droplet models [1, 2] to investigate numerically the system of three droplets which are moving in tandem with respect to the free flow. The purposes of this study are to study the wake effect of the lead droplet on the downstream droplets and to examine the effects of initial spacing on the total system. The effects of variable thermophysical properties, transient heating and internal circulation of liquid, deceleration of the flow due to the drag of the droplet, boundary-layer blowing, and moving interface due to surface regression as well as relative droplet motion are included. The results are compared with those of an isolated droplet [1] as well as those of the two-droplet system [2] to investigate the effect of the presence of the third droplet. The interaction effects from the downstream or upstream droplet are identified. The transport rates of droplets are reduced from the values for an isolated droplet, and values for the downstream droplets are profoundly less than those for the lead droplet. The difference in transport rates is large between the first two droplets; however, it becomes insignificant between the second and the third droplets since both downstream droplets are situated in a very low convective environment. The modifications to the transfer correlations for an isolated droplet needed to account for the interaction effects are determined.

INTRODUCTION

In realistic spray situations, the fuel is usually introduced into the combustor as a stream of liquid that breaks into droplets. The droplets subsequently vaporize in the convective gas stream to form the air-fuel mixture. Typically, the fuel is of sufficiently low volatility that vaporization is an important controlling factor in the estimation of combustion rates. Usually, in the dense-spray regions such as regions near the fuel nozzle, the droplet spacing is so small that the interaction effects would modify the droplet behavior significantly. In order to obtain the qualitative modification of the transfer coefficients in the practical dense spray calculation, it is then necessary to consider the interactions among a stream of multiple moving droplets. However, a detailed and accurate simulation of hundreds of droplets will be very time consuming and very difficult to perform. In fact, the behavior of trailing droplets, which follow the first two or three droplets, can be estimated from that of the first two or three droplets on account of the periodical nature of linear droplet arrangements. This research addresses the interaction of three vaporizing droplets moving collinearly which represents a model of an injected stream of fuel droplets.

There is a lack of a detailed investigation of multiple-droplet-interactions involving variable properties, transient heating and internal circulation of droplets in the literature. Even the simplified numerical computations of three-droplet dynamics are rarely found. Tal et al. [4] used a multisphere cylindrical cell model to study hydrodynamics and heat transfer in assemblages of spheres. They found the hydrodynamic solution and Nusselt number, defined by using average bulk temperature of the cell unit inlet, to be perodic. Tong and Chen [5] have included vaporization in Tal's model to investigate the effects of droplet spacing on heat and mass transfer of droplets in a liquid droplet array. A three-droplet array in a cylindrical duct has been used to obtain correlations between Nusselt number and local ambient properties for each droplet. The cylindrical cell model is somewhat idealized and some assumptions must be imposed on the cell boundaries. Hence, their results must be verified by calculations from an advanced model. Kleinstreuer et al. [6] used a finite-element microscale analysis to find the drag coefficients of interacting spheres in a linear array and a boundary-layer analysis for vaporizing droplets to simulate coupled transfer processes for three interacting droplets in a

one-dimensional trajectory. Their solution is basically the combination of three single-droplet-solutions with an "effective approach stream temperature" to account for interactions.

In the present study, the momentum, heat and mass transfer of three interacting, vaporizing droplets are taken into account and the relative motion due to different drag forces that the droplets have experienced is included. We aim to understand the wake effects on the transport rates of the downstream droplets. The primary emphasis will be placed upon the interaction effects due to different initial spacings.

The schematic flow configuration is presented in Figure 1 where the flow passing over three vaporizing droplets moving in tandem is shown. The flow is laminar and axisymmetric with initially uniform ambient conditions specified by $U'_\infty, T'_\infty, \rho'_{g,\infty}, p'_\infty$, and $Y_{f,\infty} = 0$. The initial droplet spacing is also prescribed. Dij is the non-dimensional droplet spacing (with respect to the initial radius of the first droplet) between the i^{th} droplet and the j^{th} droplet. The frame of reference is fixed to the center of the lead droplet. The problem can be viewed as an impulsively-started flow over a fixed droplet and two moving downstream droplets aligned in tandem.

The full consideration of forced convection of the gas phase, transient deceleration of the flowfield due to the drag force, internal circulation and transient heating of the liquid phase, variable properties, and transport processes occurring at the vaporizing droplet interface required to solve the Navier-Stokes equations, energy and species equations, combined with appropriate boundary conditions simultaneously. Also, in order to consider the moving boundaries due to surface regression and relative droplet motion, a general method of generating boundary-fitted coordinate systems is required.

The axisymmetric governing-equations in cylindrical coordinates and their corresponding finite-difference equations, and numerical procedures are given in Chiang [3]. The computer codes employed in our previous research [1, 2] have been modified to deal with the present three-droplet arrangement The modification involves the grid generation routine as well as the routines which handle the relative motion and spacings between droplets. The calling sequence and parameter transfer among subroutines have been adapted to accommodate new variables and the increase in memory size.

Unless otherwise stated, the nomenclature remain the same as employed in previous papers [1, 2, 3].

RESULTS AND DISCUSSION

Six production runs simulating three droplets, with the same droplet size but with different initial droplet spacings, moving collinearly have been performed. The values of physical parameters employed in each case are the same as the base case of the two interacting droplet-study [2]. The values of initial spacings in each case are given in legends of the figures.

The computations are performed on a CRAY Y-MP supercomputer. Figure 1 also shows the typical grid distributions at the beginning and at the final computational time for the case of droplet coalescence. It is noted that the computation is stopped when the droplet spacing is reduced below 2.6 or whenever the downstream droplet approaches the outer computational boundary, since the grid generation routine may generate overskewed grid system under these conditions. Often the computation terminated at a very early stage of the droplet lifetime during which most of heat flux to the droplet surface would be transferred to the interior of the droplet. Hence, the effective transfer number ($B_H = C'_{p_{g,film}}(T'_\infty - T'_s)(1 - \frac{Q'_l}{Q'_g})/L'_s$) is quite small. The amount of mass due to the evaporation is insignificant, as a result the evaporation rates of droplets are not reported here. The time scale used in the following discussion is the gas-phase hydrodynamic diffusion time scale.

The representative results to characterize the droplet behavior are summarized below.

The global contours of results from Case 1 (with D12=D23=12) and Case 4 (D12=D23=6) are compared in order to study the effect of initial spacing on the flow field. The vorticity distributions and isotherms for the gas and liquid phases are presented in the top and bottom portions of each plot of Figure 2, respectively. The results of Case 1 at two different times are portrayed in the upper two plots. At the early time, droplets experience the convective effect such that high vorticity gradients occur at the front portion of the droplet, and an asymmetric distribution is developed. The flow field surrounding each droplet resembles that surrounding an isolated droplet [1]. At five gas-phase diffusion times, the D12 is reduced from 12 to 2.96. The vorticity convected downstream from the first droplet has directly touched the second droplet and shifted the vortex center to the equatorial plane. The second droplet is well protected by the vorticity wake of the lead droplet, while the third droplet, spaced 9.5 droplet radii away from the second droplet, behaves

qualitatively as an isolated droplet.

For the case of small initial droplet spacing (Case 4), the interaction effects are expected to be strong. The velocities approaching the second and the third droplets are more or less similar but are considerably smaller than that approaching the lead droplet. As a result, the convective effect on transport is subdued. In both cases, the vorticity distribution for the lead droplet is distorted by the approaching of the second droplet.

The isotherms demonstrate thermal-transport interactions among three droplets and the gas phase. The three droplets show the same isolated-droplet-isothermal-pattern at the early time. The third trailing droplet always exhibits the same temperature contour as that of an isolated droplet, even though the approaching temperature and velocity have decreased from the values upstream of the lead droplet. The case with small initial spacing shows quite different thermal transport mechanisms. The temperature gradients for the downstream droplets are smaller than those for the lead droplet due to the action of the thermal wake. The thermal boundary layer thickness increases in the downstream direction along the surface for the lead droplet. This behavior is opposite for the third trailing droplet in the close spacing case.

The variations of Nusselt number along the gas/liquid interface of the droplets for Case 1 and Case 4 are shown in Figure 3. In Case 1, the decrease of Nusselt number at the front stagnation portions of the trailing droplets are caused by the cold fuel/air mixture convected downstream from the upstream droplets. The qualitative variations of Nusselt numbers of the second droplet and the third droplet in Case 4 are totally different from those in Case 1. The details have been discussed in Chiang[3]. The third droplet shows the same Nusselt number distribution as for the second droplet except at the separation region, where the third droplet possesses a higher value of Nusselt number due to the angular diffusion of heat flux from the free stream. Similar behavior for Sherwood numbers are observed for the three droplets.

Figures 4 and 5 present the time variations of drag coefficients and Nusselt numbers, respectively. As we expect, the transport rates of droplets are reduced from the values for an isolated droplet, and values for the downstream droplets are profoundly less than those for the lead droplet. The transport rates for the third droplet are lower than those for the second droplet, except when the lead droplet's interaction with the second droplet becomes very strong. The results of Case 4 show that the second and third droplets exhibit almost identical behaviors. The interaction between the downstream droplet and the lead droplet becomes very significant for the small initial spacing case.

The variations of trajectory with time and drag coefficients vs. instantaneous Reynolds number for the cases of different initial spacings are illustrated in Figure 6 (Cases 1, 2, and 3) and Figure 7 (Cases 4, 5, and 6), respectively. Results of Case 1 with large initial spacing (D12=D23=12) indicate that the drag coefficient is smaller for the second droplet than for the lead droplet and still smaller for the third droplet. The major decrease in drag occurs in the first two droplets. In Case 2, the drag coefficients of the lead and the second droplets are significantly reduced (comparing curves 7 and 10, and 8 and 11, respectively) due to the strong interactions when the first two droplets are spaced only two diameters away. Similar trends occur for the downstream droplet pairs of Case 3 (comparing curves 8 and 14,and 9 and 15, respectively). The third droplet in Case 2 has a higher drag coefficient than that of the second droplet since the second droplet is better shielded by the droplet before it. The D23 thus increases with time. Also, note that the drag coefficient of the third droplet, which is spaced far away from the second droplet, seems to be independent of D12 as indicated in curves 9 and 12. However, it strongly depends upon D23 as illustrated in curves 9, 12 and 15.

The comparison between results of Figures 6 and 7 leads to the clear conclusion that as initial spacings decrease, the transport rates decrease correspondingly. The drag coefficients for the downstream droplets are all collapsed together. However, at the final calculations when three droplets interact extensively with neighbors, the second droplet experiences not only downstream interactions from the lead droplet but also upstream interactions from the third droplet. As a result, the second droplet possesses the lowest drag coefficient. Note the interaction from the upstream droplet is considerably larger than that from the downstream droplet. The lead droplet in Case 2 has the lowest drag coefficient (curve 10) among the lead droplets of three cases since the interaction from the second droplet is the strongest (spacing D12 is the smallest). The behavior of the spacing variation is qualitatively similar to that of large initial spacing case. The variation of D23, for the cases of approaching droplets, is always negligible except during the final calculation period.

In order to investigate the effect of D23 on the first and the second droplets with a given D12, the comparisons of drag coefficients for the first two droplets with variable D23s are presented in Figures 8

and 9. The comparisons of results with the same D12 in the two-droplet-only arrangement are also presented. For the cases of small initial-D12, the main droplet interactions occur between the first two droplets. The presence of the third droplet does not affect the lead droplet but it reduces the Sherwood and Nusselt numbers of the lead droplet by less than 5 % in magnitude. The drag coefficients and Sherwood numbers for the second droplet decrease as the D23 decreases, though the percent change is small. For the cases of large initial D12, the behavior of the first droplet becomes insensitive to the presence of the third droplet. An interesting observation is that the presence of the third droplet at a sufficient distance from the second droplet, with insignificant hydrodynamic interaction between the second and the third droplet, may increase the drag coefficient of the second droplet (comparing curves 4 and 5 in Figures 9). The second droplet in the two-droplet-only arrangement receives the interaction of recirculating-thermal-entrainment from the free stream; as a result, the transfer number is high. Therefore, the surface blowing is enhanced and the friction drag is reduced. The addition of the third droplet to the system moves this thermal effect to the third droplet; hence, the transport rates of the second droplet are recovered. However, for the case of a small D23, the strong interaction from the third droplet reduces the transport rates of the second droplet by a large magnitude (curve 6).

A nonlinear regression model using least squares has been employed to find the correlations between the transport rates of an interacting droplet and the corresponding transport rates when droplet is isolated. The generalized form of numerical correlations for drag coefficient and Nusselt number of each droplet can be expressed as

$$\frac{C_{Di}}{C_{Diso}} \left(\text{or} \frac{Nu_{film_i}}{Nu_{film_{iso}}} \right) = 1. - aD12^{b}\ D23^{c} \qquad (1)$$

where the constants are given in the Table 1.

The correlations are valid for droplet spacing ranged from 2.7 to 12 and for Reynolds number ranged from 90 to 130. Some correction factors, with different combinations of D12s and D23s, computed from above correlations are presented in Table 2. The correlations basically predict the right trends of interacting effects on droplet transport rates. The influence of D12 on the third droplet is insignificant as indicated by the small exponents of D12.

CONCLUSIONS

The detailed behaviors of three vaporizing, interacting droplets for the cases of different initial spacings have been investigated carefully. The results indicate that the interacting effects are strongly dependent upon the initial droplet spacings. The general qualitative conclusions drawn from the two-droplet study [2] can be applied to two neighboring droplets in the three-droplet analysis.

Results for the cases of sufficiently large spacing (above approximately 6 droplet diameters) show that the flow field of each droplet is qualitatively similar to that of an isolated droplet, although the transport rates are reduced along the downstream direction due to the cascade effect of the wake. The major drops in transport rates occur in the first two droplets. For the cases of small droplet spacings (less than approximately 3 droplet diameters), the flow field of downstream droplets can be significantly altered due to the interaction effects from the upstream droplets. Usually, the second droplet has the lowest drag coefficient since it receives interactions from both neighboring droplets. However, the difference in transport rates between the second and the third droplets is not significant since both droplets are fully protected by the wake of the first droplet. The effect of D23 on the behavior of the first droplet is insignificant. However, depending upon the values of D12 as well as D23, the effect of D23 on the behavior of the second droplet may become significant. The correlations for heat transfer and droplet dynamics have been developed and are applicable in a one-dimensional droplet spray calculation.

ACKNOWLEDGEMENTS

This work has been supported by the Air Force Office of Scientific Research under grant No. 90-0064 with Dr. Julian Tishkoff acting as the technical monitor. The support of the San Diego Supercomputing Center under a Block Grant of the Office of Academic Computing at UCI is greatly appreciated.

REFERENCES

[1] Chiang, C. H., Raju, M. S. and Sirignano, W. A. "Numerical Analysis of Convecting, Vaporizing Fuel Droplet with Variable Properties", *AIAA Aerospace Sciences Meeting*, Paper 89-0834. (1989). Also to appear in Int. J. Heat Mass Transfer (1991).

[2] Chiang, C. H. and Sirignano, W. A., "Numerical Analysis of Interacting, Convecting, Vaporizing Fuel Droplet with Variable Properties", *AIAA Aerospace Sciences Meeting*, Paper 90-0357 (1990). Also to be submitted to Int. J. Heat Mass Transfer.

[3] Chiang, C. H., "Isolated And Interacting, Vaporizing Fuel Droplets: Field Calculation With Variable Properties", Ph.D. Dissertation, University of California, Irvine, Dept. of Mechanical Engineering (1990).

[4] Tal (Thau), R., Lee, D. N.and Sirignano, W. A. "Hydrodynamics and Heat Transfer in Sphere of Particle Assemblages - Cylindrical Cell Models", Int. J. Heat Mass Transfer, Vol 26 , , No. 9, pp. 1265-1273 (1983).

[5] Tong, A. Y. and Chen, S. J., "Heat Transfer Correlations for Vaporizing Liquid Droplet Arrays in A High-Temperature Gas at Intermediate Reynolds Number", Int. J. Heat & Fluid Flow, Vol 9, No. 2, pp. 118-130 (1988)

[6] Kleinstreuer, C., Chiang, H. and Wang, Y.-Y., "Mathematical Modelling of Interacting Vaporizing Fuel Droplets", HTD-Vol. 106, Heat Transfer Phenomena in Radiation, Combustion and Fire, pp. 469-477 (1989)

Table 1: Constants for Cd and Nu Correlations

	a	b	c
$\frac{C_{D1}}{C_{D_{iso}}}$	2.092	−1.575	−0.393
$\frac{C_{D2}}{C_{D_{iso}}}$	2.084	−0.482	−0.351
$\frac{C_{D3}}{C_{D_{iso}}}$	0.798	0.012	−0.320
$\frac{Nu_1}{Nu_{iso}}$	0.324	−0.266	−0.098
$\frac{Nu_2}{Nu_{iso}}$	1.218	−0.175	−0.398
$\frac{Nu_3}{Nu_{iso}}$	0.811	−0.093	−0.277

Table 2: Correction Factors for Cd and Nu with Different Combinations of D12 and D23

$D12$	$D23$	$\frac{C_{D1}}{C_{Diso}}$	$\frac{C_{D2}}{C_{Diso}}$	$\frac{C_{D3}}{C_{Diso}}$	$\frac{Nu_1}{Nu_{iso}}$	$\frac{Nu_2}{Nu_{iso}}$	$\frac{Nu_3}{Nu_{iso}}$
12.00	12.00	0.984	0.737	0.629	0.869	0.706	0.676
12.00	6.00	0.979	0.665	0.537	0.860	0.613	0.608
12.00	4.00	0.976	0.614	0.473	0.854	0.545	0.561
6.00	12.00	0.953	0.633	0.632	0.842	0.668	0.655
6.00	6.00	0.938	0.532	0.541	0.831	0.563	0.582
6.00	4.00	0.928	0.460	0.477	0.824	0.487	0.532
4.00	12.00	0.911	0.554	0.634	0.824	0.644	0.642
4.00	6.00	0.883	0.431	0.543	0.812	0.531	0.566
4.00	4.00	0.863	0.344	0.480	0.804	0.449	0.514
2.70	12.00	0.835	0.461	0.636	0.805	0.619	0.628
2.70	6.00	0.784	0.312	0.545	0.791	0.498	0.550
2.70	4.00	0.746	0.207	0.482	0.783	0.410	0.496

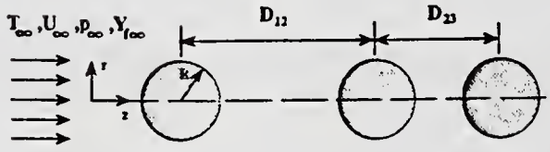

FLOW CONFIGURATION - SCHEMATIC

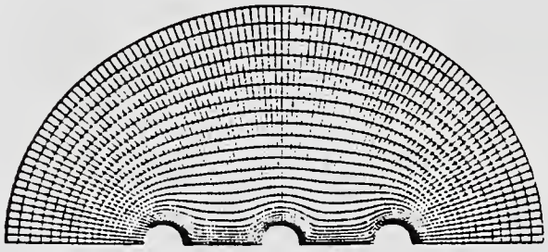

Time = 0.00
R1 = 1.00 , R2 = 1.00 , R3 = 1.00
Spacing12 = 6.00 , Spacing23 = 6.00

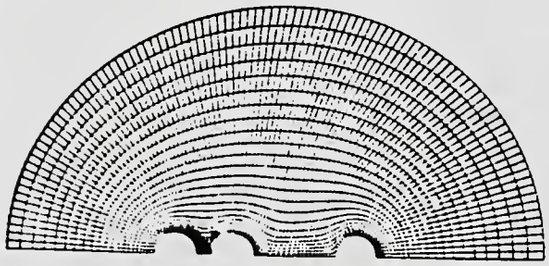

Time = 2.40
R1 = 1.00 , R2 = 1.00 , R3 = 1.00
Spacing12 = 2.78 , Spacing23 = 6.02

Fig. 1: Flow field configuration and grid distribution at two different times.

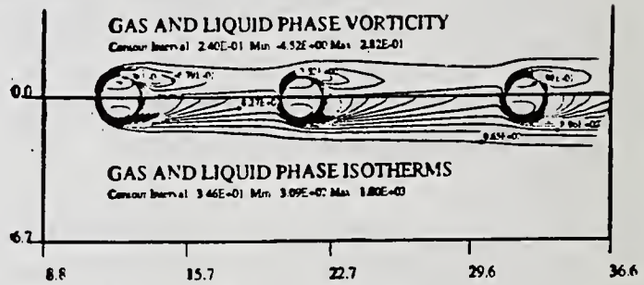

Time = 3.00
Re(1) = 79.93 , Re(2) = 84.50 , Re(3) = 85.90
R1 = 1.00 , R2 = 1.00 , R3 = 1.00 , Spacing12 = 8.73 , Spacing23 = 11.34

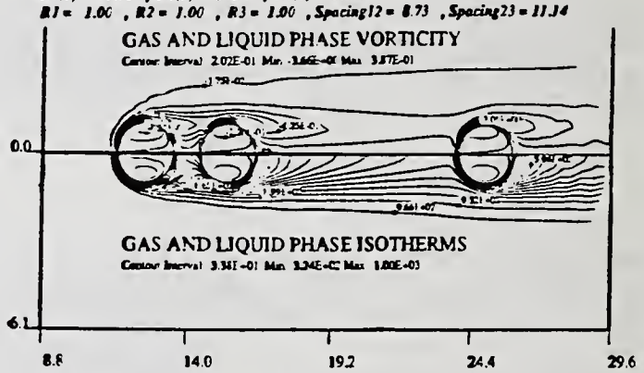

Time = 5.00
Re(1) = 70.55 , Re(2) = 77.52 , Re(3) = 79.11
R1 = 1.00 , R2 = 1.00 , R3 = 1.00 , Spacing12 = 2.96 , Spacing23 = 9.50
Initial R1=1, R2=1, R3=1, Spacing12=12, Spacing23=12

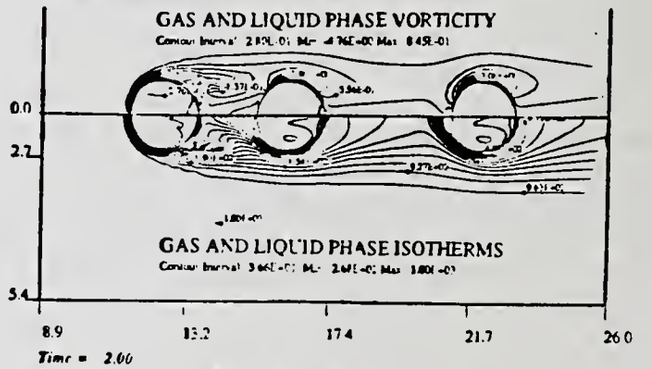

Time = 2.00
Re(1) = 86.53 , Re(2) = 91.29 , Re(3) = 91.26
R1 = 1.00 , R2 = 1.00 , R3 = 1.00 , Spacing12 = 3.74 , Spacing23 = 5.93
Initial R1=1, R2=1, R3=1, Spacing12=6, Spacing23=6

Fig. 2: Vorticity and isotherm contour plot of gas and liquid phases with different initial droplet spacings.

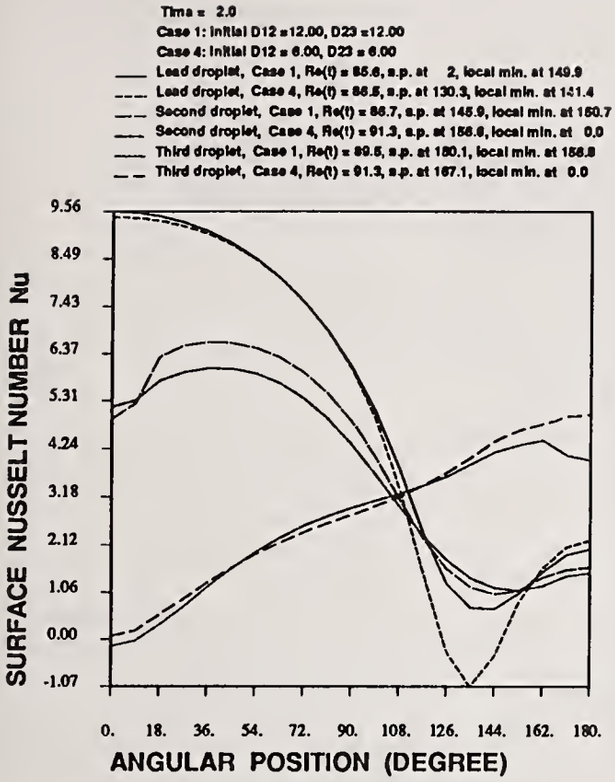

Figure 3: Surface Nusselt number distribution of the three droplets with different initial droplet spacings.

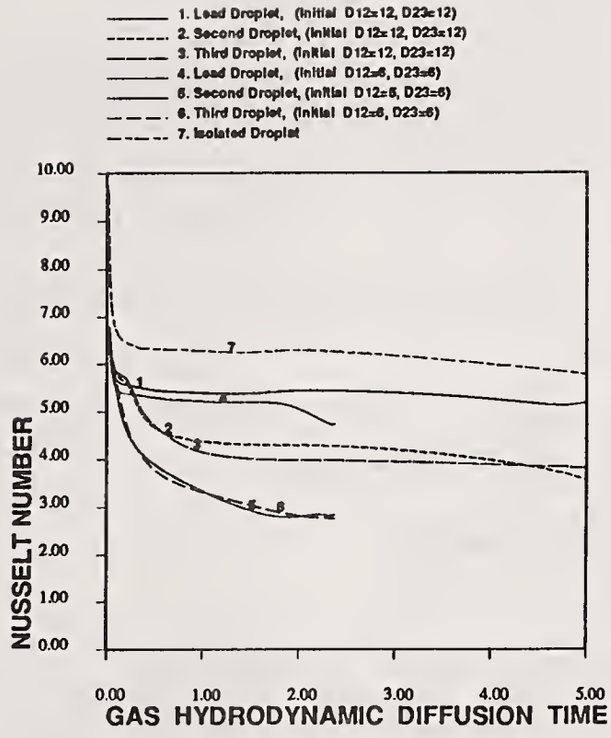

Figure 5 Time variation of Nusselt numbers of the three droplets with different initial droplet spacings.

Legends:
Case 1: Initial R1=1, R2=1, R3=1, D12=12, D23=12, Re=100
Case 2: Initial R1=1, R2=1, R3=1, D12=4, D23=12, Re=100
Case 3: Initial R1=1, R2=1, R3=1, D12=12, D23=4, Re=100
1. D12, Case 1; 2. D23, Case 1; 3. D12, Case 2;
4. D23, Case 2; 5. D12, Case 3; 6. D23, Case 3;
7. C_D for the Lead Droplet, Case 1; 8. G for the Second Droplet, Case 1;
9. C_D for the Third Droplet, Case 1; 10. G for the Lead Droplet, Case 2;
11. C_D for the Second Droplet, Case 2; 12. G for the Third Droplet, Case 2;
13. C_D for the Lead Droplet, Case 3; 14. G for the Second Droplet, Case 3;
15. C_D for the Third Droplet, Case 3; 16. G for an Isolated Droplet;

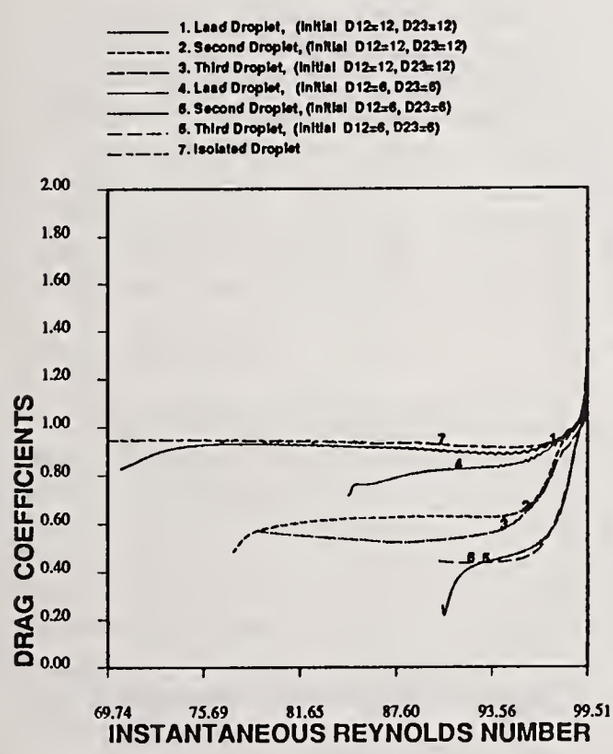

Figure 4 Time variation of drag coefficients of the three droplets with different initial droplet spacings.

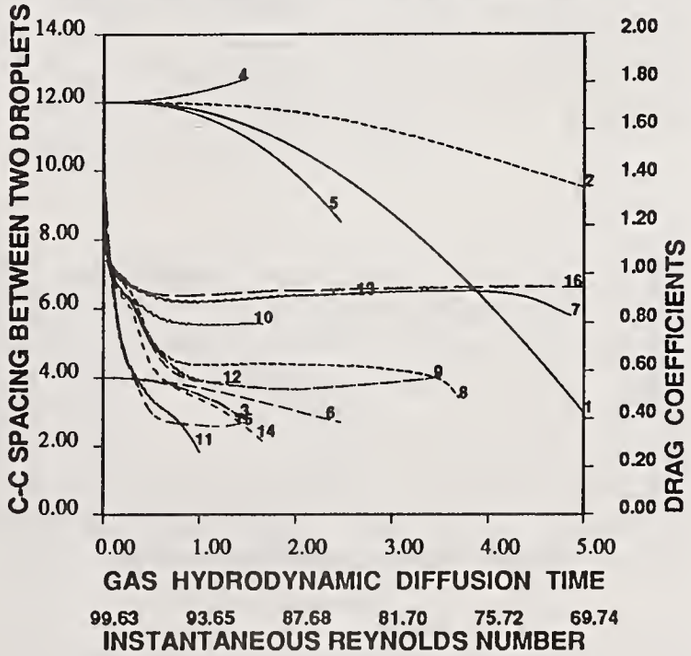

Figure 6: Time variation of droplet drag coefficients and droplet spacings for the cases of large initial droplet spacings (Cases 1, 2 and 3).

Legends:
Case 4: Initial R1=1, R2=1, R3=1, D12=6, D23=6, Re=100
Case 5: Initial R1=1, R2=1, R3=1, D12=4, D23=6, Re=100
Case 6: Initial R1=1, R2=1, R3=1, D12=6, D23=4, Re=100
1. D12, Case 4; 2. D23, Case 4; 3. D12, Case 5;
4. D23, Case 5; 5. D12, Case 6; 6. D23, Case 6;
7. C_D for the Lead Droplet, Case 4; 8. G for the Second Droplet, Case 4;
9. C_D for the Third Droplet, Case 4; 10. G for the Lead Droplet, Case 5;
11. C_D for the Second Droplet, Case 5; 12. G for the Third Droplet, Case 5;
13. C_D for the Lead Droplet, Case 6; 14. G for the Second Droplet, Case 6;
15. C_D for the Third Droplet, Case 6; 16. G for an Isolated Droplet;

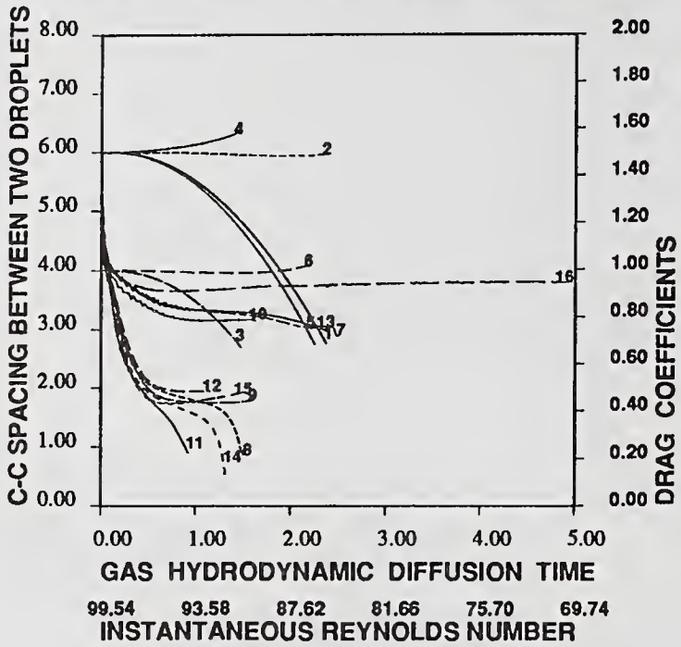

Figure 7: Time variation of droplet drag coefficients and droplet spacings for the cases of small initial droplet spacings (Cases 4, 5 and 6).

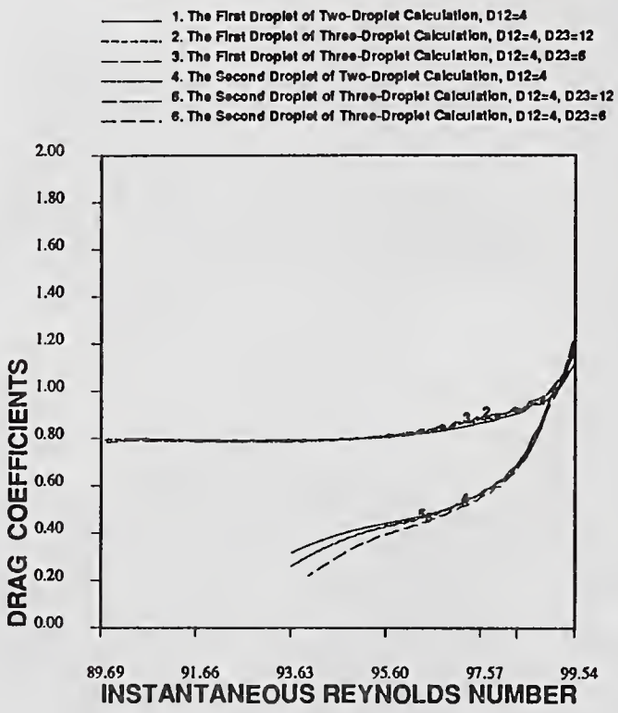

Figure 8 Time variation of drag coefficients of the first two droplets for D12 = 4 and variable D23s.

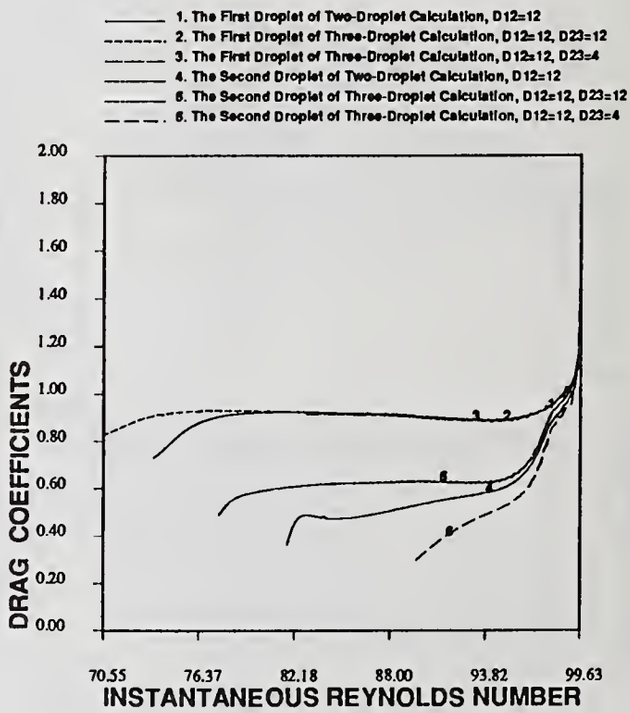

Figure 9 Time variation of drag coefficients of the first two droplets for D12 = 4 and variable D23s.

SOLUTIONS OF POLYDISPERSE SPRAY SECTIONAL-EQUATIONS VIA A MULTIPLE-SCALE APPROACH: AN ANALYSIS OF A PREMIXED POLYDISPERSE SPRAY FLAME

I. Silverman, J.B. Greenberg and Y. Tambour

Faculty of Aerospace Engineering
Technion - Israel Institute of Technology
Haifa, Israel

ABSTRACT

New solutions are presented for polydisperse spray sectional-equations. Simultaneous evaporation and coalescence processes of the spray droplets are considered. The mathematical procedure takes advantage of a multiple-scale approach in which different scales are applied to the different physical processes (convection and evaporation). Two small spray parameters are identified and used for expansion purposes. A special zonal density model is developed, thus enabling approximate analytic solutions to be extracted from the governing equations for the entire system. The method is employed to analyze adiabatic premixed polydisperse spray flames in a one-dimensional flow field. Computed results are presented for flame location versus flame velocity, the influence of droplet evaporation rate (with and without coalescence) on flame location, and the axial variation in temperature and chemical species profiles. As to the fuel spray, the evolution in droplet size distributions, for the various size sections, along the axial direction, is analyzed. Finally, all analytical results are compared with numerical solutions for the governing equations which are obtained here using standard finite difference methods. The good agreement between the analytical solutions and the numerical ones indicates that a multiple-scale approach may be an important satisfactory tool for the analysis of **polydisperse** sprays which undergo **simultaneous** evaporation and coalescence processes.

INTRODUCTION

The theoretical modelling of the behavior of a spray flame is of considerable importance in the analysis, design, and improvement of combustion equipment. In most industrial systems, the fuel spray is of a wide range of droplet sizes, i.e. it is polydisperse. The combustion processes are controlled by a 'cloud' or 'group' behavior of the spray rather then single droplet behavior [1-15]. The analysis of the evolution in local droplet size distributions, enables one to determine the amounts of fuel vapor which are locally released via the evaporation process of the 'cloud' as a whole, whereas the combustion chemical reactions are controlled by the local fuel vapor/oxygen concentration ratios and the local temperature and pressure. Thus, the theoretical modelling involves solutions of polydisperse intercoupled spray equations, which are coupled also to the flow field, energy, and chemical species conservation equations.

A representation of the polydisperse spray by a set of sectional-conservation equations [16-21] enables one to deal with a fairly small number of conservation equations. However, in relatively dense sprays coalescence may play an important role [20-22]. The equations describing dense sprays are nonlinear due to the coalescence terms, and therefore difficult to solve. Thus, the purpose of the present study is to present a mathematical procedure which takes advantage of a multiple-scale approach in which different scales are applied to the different physical processes: convection and evaporation,

enabling approximate analytic solutions to be extracted from the governing equations for the entire system.

The problem to be analyzed in the present study is a one-dimensional adiabatic laminar premixed polydisperse spray flame. For this geometrically straightforward type of combustion wave, a wide range of phenomena have already been investigated, including effects of transport properties, detailed chemical kinetics, etc. on such parameters as flame speed, temperature, ignition and extinction limits, to name but a few (see for example, the review paper by Clarke [23] and relevant material in Dixon-Lewis [24], Williams [25], Buckmaster and Ludford [26]). However, in all these studies a **gaseous** combustible premixture was assumed.

In fact, within the context of the 1-D premixed type flame a few attempts **have** been made to accommodate additional effects induced by the presence of fuel droplets [13, 27-30]. These analyses have usually dealt with single evaporating droplets and use was made of an average droplet size. Quite recently, Lin et al. [31] have proposed a theory of laminar flame propagation in dilute sprays. However, they have considered only monodisperse sprays, with no droplet-droplet interaction allowable.

A study of a premixed **polydisperse** spray flame in which droplet-droplet interactions within the spray were considered, was recently presented by the authors [32]. Using an **asymptotic analysis**, the influence of the spray on the burning velocity and on the flame temperature was examined. In the present study, however, **a multiple-scale analysis** will be exploited to provide tractable solutions for the major variables of the problem, such as the axial variation in temperature, chemical species profiles and the evolution in droplet size distributions for the various size sections along the axial direction. The influence of droplet evaporation rate, with and without coalescence, on flame location will also be examined.

CALCULATED RESULTS

The theory and the solution procedure have been presented elsewhere [37]. In order to provide some measure of the predictive capability of the aforedescribed solution a few computed results are presented in Figs 2-10. In the figures the solid lines represent the results of the analytical solution whilst the broken lines are for profiles obtained by solving the governing equations numerically using standard finite-difference methods. As can be seen for the problem at hand the agreement is very good.

In Fig. 2, the variation of temperature, chemical species concentrations and liquid-fuel integral-mass concentration along the axial direction are shown. (The evolution in droplet concentrations in **each size section** due to vaporization is presented in Figs. 3a,b, and will be discussed later.) As one approaches the flame front, the integral-mass concentration of the fuel-droplets decreases due to vaporization (see Fig. 2), while the concentration of fuel vapors increases in the beginning (defined as zone I in Fig. 1), and then decreases in zone II due to diffusion and consumption of fuel vapors by the combustion process. At the flame front the oxidant concentration approaches zero whereas the concentration of CO_2 reaches its maximum value. Since the flame is fuel-rich, fuel droplets that pass the flame front continue to vaporize in the "post-reaction zone" (zone III) and the concentration of fuel vapors starts to build-up again, since no more oxidant is left to react with.

The results presented in Fig. 2, which were discussed above, were computed for a vaporizing spray without coalescence, i.e. for $\theta=0$. The effects of coalescence are demonstrated in Figs. 4 and 5a,b and are discussed next. Since coalescence hinders vaporization, the flame front is found to be further downstream at $x_f=10.1$, in Fig. 4 (computed for $\theta=0.867$), whereas for $\theta=0$, i.e. without coalescence,

x_f=7.8 (see Fig. 2).

The droplet concentration in **each size section** decreases with the distance x due to vaporization of droplets, as shown in Figs. 3a and 3b, which were computed without coalescence (i.e. for θ=0). When coalescence is considered (θ=0.867) **an initial increase** in the concentrations of section VI, VII and VIII is observed (see Fig. 5b). This is due to coalescence of droplets in lower sections resulting in the production of larger droplets, i.e. causing a shift to the "right" of the size spectrum of droplets. Such behavior is as anticipated, having been observed experimentally and verified theoretically [20, 33]. This is also consistent with the steep drop in droplet concentrations in the lower sections I, II, III and IV (see Fig. 5a) whereas a rather gradual decrease in droplet concentrations in these sections is noticeable when only vaporization is considered (Fig. 3a).

As to the comparison of: (i) the effects of vaporization only with (ii) the effects of combined vaporization and coalescence, on flame location, these are shown in Figs. 6 and 7, respectively. The larger the evaporation rate, i.e. the larger the value of ε, the shorter the distance x_f which is required to build-up conditions so that a flame front will be located at $x=x_f$. For a given vaporization rate of ε=0.125, at low coalescence rates for which θ is smaller than unity (θ<1), coalescence causes a very slight shift of the flame downstream (see Fig. 7). This is due to the fact that coalescence hinders vaporization. For $\theta\approx$1 and for higher values of θ, the change in flame location is significantly noticed.

In Fig. 8, we illustrate the way that the flame location, x_f, behaves as a function of the flame velocity. This curve is drawn for a fixed **total equivalence ratio**, i.e., the ratio of the initial fluxes of **fuel (liquid + vapor)** and oxygen. However, the **effective equivalence ratio**, i.e., the ratio of the fluxes of fuel vapors only and oxygen varies along x and governs the flame. It is interesting to note that unlike the case of the steady premixed **gaseous** flame in which the **total** equivalence ratio uniquely determines the flame velocity and location, for the steady premixed **spray** flame this same **ratio** leads to a band of permitted flame velocities to each of which corresponds a single flame location. It is precisely this band of values that is shown in Fig. 8. For a **steady** flame, the flame velocity is equal to the upstream velocity at x=0. Thus, for each permitted upstream velocity at x=0, with a fixed **total** equivalence ratio, the downstream production of fuel vapors (for a given spray, it's size distribution, and ε and θ) will build-up conditions in terms of the **effective** equivalence ratio, at a single downstream distance $x=x_f$ at which the flame will be located.

Next, the comparison between analytical solutions and numerical results is discussed. As far as evolution in droplet concentrations in each size section is concerned, the agreement is excellent for the process of droplet evaporation (see Figs. 3a,b). For simultaneous vaporization and coalescence, the deviation of the analytical solutions from the numerical ones grows as the rate of coalescence increases, i.e. as θ increases. These quantitative differences can be attributed to the order of approximation assumed in the analytical calculation. For example, since we assumed $\theta<<\varepsilon<<1$, it is not surprising that analytical results calculated for a "large" value of θ, such as θ=0.867 deviate from the numerical solutions (see Figs. 5a,b). Better agreement is obtained for smaller values of θ, although still larger than ε, such as θ=0.347; (compare the axial downstream evolution of pointwise spray histograms for θ=0.347, Fig. 9 with those of θ=0.867, Fig. 10). Nevertheless, a comparison between the numerical and analytical solutions demonstrates that even for relatively "large" values of θ, the analytical solutions remain qualitatively satisfactory (see for example Fig. 4).

CONCLUSIONS

To summarize, the multiple-scale analysis that has been presented here has proven to be a satisfactory tool for the study of one-dimensional premixed **polydisperse spray** flames. All analytical results have been compared with numerical solutions of the governing equations and show good agreement with them. This was found for the variation with distance of many physical properties such as temperature, chemical species concentrations, and in the analysis of the effects of vaporization and coalescence on flame location.

REFERENCES

1. Chigier, N.A., *Energy Combustion and Environment*, McGraw-Hill, 1981.
2. Chigier, N.E., "Group Combustion Models and Laser Diagnostic Methods in Sprays (A Review), Combustion & Flame, 51, pp. 127-139 (1983).
3. Chigier, N.A., Ungut, A. and Yule, A.J.,*Particle Size and Velocity Measurements in Flames by Laser Anemometer*, Seventeenth Symposium (International) on Combustion, The Combustion Institute, Pittsburgh, pp. 315-324 (1979).
4. Chiu, H.H. and Liu, T.M.,"Group Combustion of Liquid Droplets", Combustion Science and Technology, 17, pp. 127-142 (1977).
5. Chiu, H.H., Kim, H.Y. and Croke, E.J.,*Internal Group Combustion of Liquid Droplets*, Nineteenth Symposium (International) on Combustion, The Combustion Institute, pp. 971-980 (1982).
6. Labowsky, M. and Rosner, D.E., "Group Combustion of Droplets in Fuel Clouds: Quasi-Steady Predictions", Evaporation-Combustion of Fuels, American Chemical Society, (1978), pp. 63-79 (1978).
7. Labowsky, M., "Calculation of the Burning Rates of Interacting Fuel Droplets", Combustion Science and Technology, 22, pp. 217-226 (1980).
8. Levebvre, A.H., *Gas Turbine Combustion*, McGraw-Hill (1983).
9. Twardus, E.M. and Brzustowski, T.A.,"An Experimental Study of Flame Spread and Burning in Arrays of Monosize Hydrocarbon Droplets", Combustion Science and Technology, 17, pp. 215-225 (1978).
10. Presser, C., Gupta, A.K., Santoro, R.J. and Semerjian, H.G., *Droplet Size Measurements in a Swirling Kerosene Spray Flame by Laser Light Scattering*, ICLASS-85 Meeting, 2 (1985).
11. Presser, C., Gupta, A.K., Santoro, R.J. and Semerjian, H.G., *Velocity and Droplet Size Measurements in a Fuel Spray*, AIAA-86-0297, AIAA 24th Aerospace Sciences Meeting, January 6-9, (1986), Reno, Nevada.
12. Beretta, F., Covaliere, A. and D'Alessio, A., "Drop Size and Concentration in a Spray by Sideward Laser Light Scattering Measurements", Combustion Science and Technology, 36, pp. 19-37 (1984).
13. Aggarwal, S.K. and Sirignano, W.A., "Unsteady Spray Flame Propagation in a Closed Volume", Combustion & Flame, 62, pp. 69-84 (1985).
14. Correa, S.M. and Sichel, M., *The Group Combustion of a Spherical Cloud of Monodisperse Fuel Droplets*, Nineteenth Symposium (International) on Combustion, The Combustion Institute, pp. 981-991 (1982).
15. Choudhury, P.R. and Gerstein, M., *Analysis of a Fuel Spray Subjected to Coupled Evaporation and Decomposition*, Nineteenth Symposium (International) on Combustion, The Combustion Institute, Pittsburgh, pp. 993-997 (1982).
16. Tambour, Y., "A Sectional Model for Evaporation and Combustion of Sprays of Liquid Fuels", Israel J. of Technology, 18, pp. 47-56 (1980).
17. Tambour, Y., "Transient Mass and Heat Transfer From a Cloud of Vaporizing Droplets of Various Size Distributions: A Sectional Approach", Chem. Eng. Commun. 44, pp. 183-196 (1986).
18. Tambour, Y., "Vaporization of Polydisperse Fuel Sprays in a Laminar Boundary Layer: *A Sectional* Approach", Combustion & Flame, 58, pp. 103-114 (1984).

19. Tambour, Y., "A Langrangian Sectional Approach for Simulating Droplet Size Di*stribution of* Vaporizing Fuel Sprays in a Turbulent Jet", Combustion & Flame, 60, pp. 15-28 (1985).
20. Tambour, Y., "Coalescence of Vaporizing Kerosene Fuel Sprays in a Turbulent Jet", Atomisation and Spray Technology, 1, pp. 125-146 (1985). See also: "Simulation of Coalescence and Vaporization of Kerosene Fuel Sprays in a Turbulent Jet: A Sectional Approach", AIAA/ASME/ASEE 21st Joint Propulsion Conference, Monterey, 1985. AIAA Paper No. 85-1315.
21. Greenberg, J.B. and Tambour, Y.,"Far-Field Coalescence Effects in Polydisperse Spray Jet Diffusion Flames", Twenty-First Symposium (International) on Combustion, The Combustion Institute, pp. 655-663 (1986).
22. O'Rourke, P.J. and Bracco, F.V., *Modelling of Drop Interaction in Thick Sprays and a Comparison with Experiments*, Conference on Stratified Charge Automotive Engines, The Institute of Mechanical Engineers, London (1980).
23. Clarke, J.F., "Parameter Perturbations in Flame Theory", Prog. Aerospace Sci., 16, pp. 3-29 (1975).
24. Dixon-Lewis, G., *Computer Modeling of Combustion Reactions in Flowing Systems with Transport*, Combustion Chemistry, ed. W.C. Gardiner, Jr., Springer-Verlag, New York, pp. 21-125 (1984).
25. Williams, F.A., *Combustion Theory*, 2nd Edition, The Benjamin/Cummings Publishing Co., Menlo Park, California (1985).
26. Buckmaster, J. and Ludford, G.S.S., *Theory of Laminar Flames*, University Press, Cambridge (1982).
27. Williams, F.A., *Monodisperse Spray Deflagration*, Liquid Rockets and Propellants, ed. L.E. Bollinger, M. Goldsmith and A.W. Lemmon, Jr., Academic Press, London, pp. 229-263 (1960).
28. Seth, B., Aggarwal, S.K. and Sirignano, W.A., "Flame Propagation Through an Air-Fuel *Spray Mixture* with Transient Droplet Vaporization", Combustion & Flame, 39 pp. 149-168 (1980).
29. Polymeropoulos, C.E., "Flame Propagation in a One-Dimensional Liquid Fuel Spray", Combustion Science and Technology, 9, pp. 197-207 (1974).
30. Satil, P.B., Sichel, M. and Nicolls, J.A., "Analysis of Spray Combustion in a Research Gas Turbine Combustor", Combustion Science and Technology, 18, pp. 21-31 (1978).
31. Lin, T.H., Law, C.K. and Chung, S.H., "Theory of Laminar Flame Propagation in Off-Stoichiometric Dilute Sprays", International Journal of Heat and Mass Transfer, 31, pp. 1023-1034 (1988).
32. Silverman, I., Greenberg, J.B. and Tambour, Y., "Asymptotic analysis of a Premixed Polydisperse Spray Flame", SIAM Journal on Applied Mathematics (1990), in press.
33. Yule, A.J., Ereat, P.R. and Ungut, A., "Droplet Sizes and Velocities in Vaporizing Sprays", Combustion & Flame, 54, pp. 15-22 (1983).
34. Law, C.K. and Sirignano, W.A., "Unsteady Droplet Combustion with Droplet Heating - II: Conduction Limit", Combustion & Flame, 28, pp. 175-186 (1977).
35. Law, C.K., "Adiabatic Spray Vaporization with Droplet Temperature Transient", Combustion Science and Technology, 15, pp. 65-74 (1977).
36. Yule, A.J., Seng, C.Ah., Felton, P.G., Ungut, A. and Chigier, N.A., "A Study of Vaporizing Fuel Sprays by Laser Techniques", Combustion & Flame, 44, pp. 71-84 (1982).
37. Silverman, I., Greenberg, J.B. and Tambour, Y., "Solutions of Polydisperse Spray Sectional-Equations via a Multiple-Scale Approach: An Analysis of a Premixed Polydisperse Spray Flame", submitted to Atomization and Sprays.

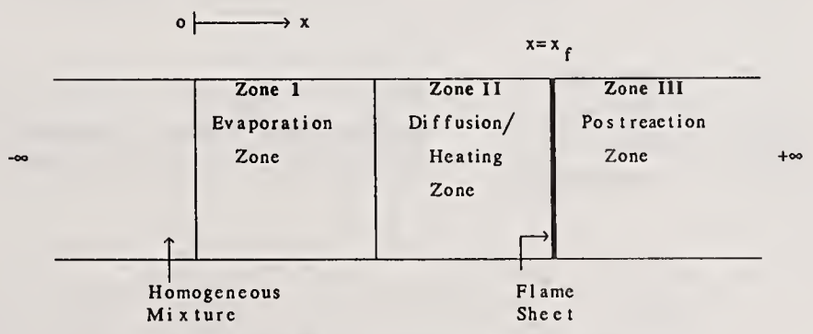

Fig. 1. Zonal subdomains of density model.

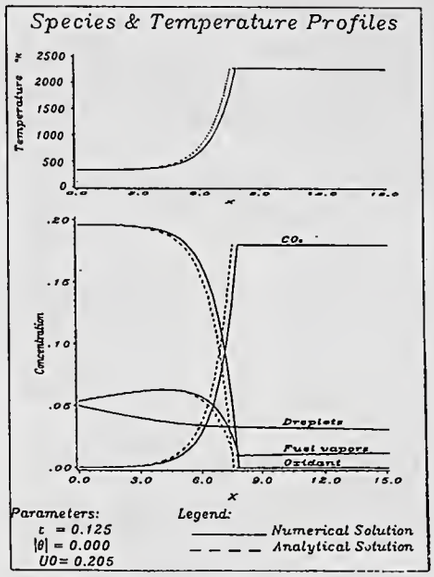

Fig. 2. Variation of temperature, chemical species concentrations, and liquid-fuel integral-mass concentration, along the axial direction; **no coalescence.**

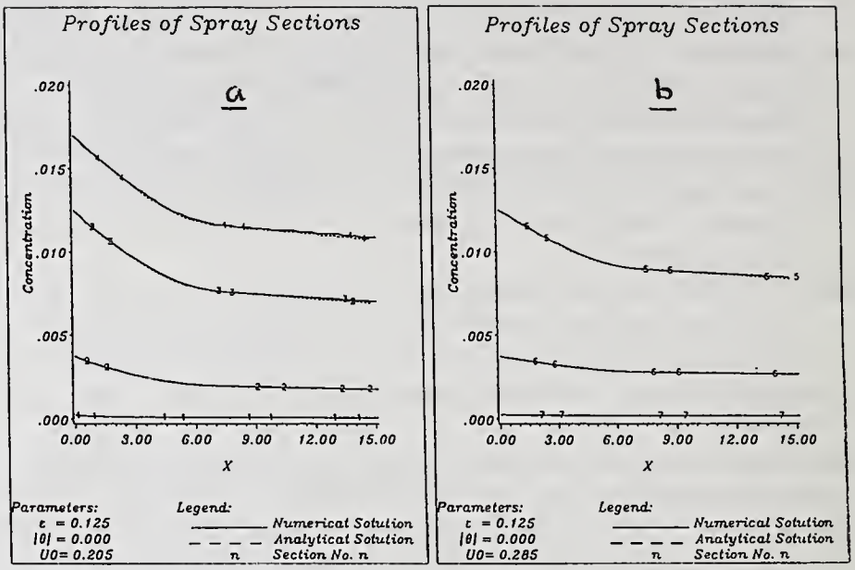

Fig. 3. Evolution in droplet concentrations in each size section; **no coalescence** (a) Sections I to IV, (b) Sections V to X.

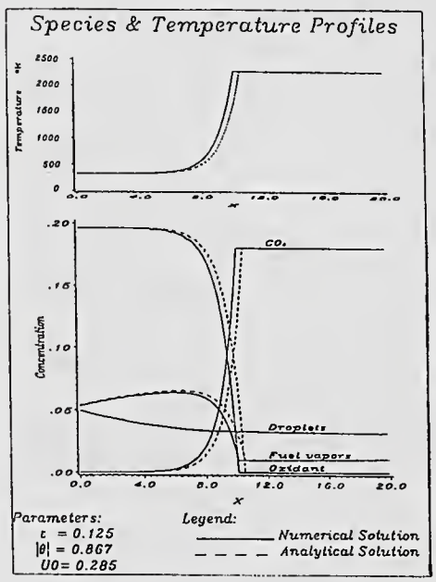

Fig. 4. Variation of temperature, chemical species concentrations and liquid-fuel integral-mass concentration, along the axial direction; **including coalescence.**

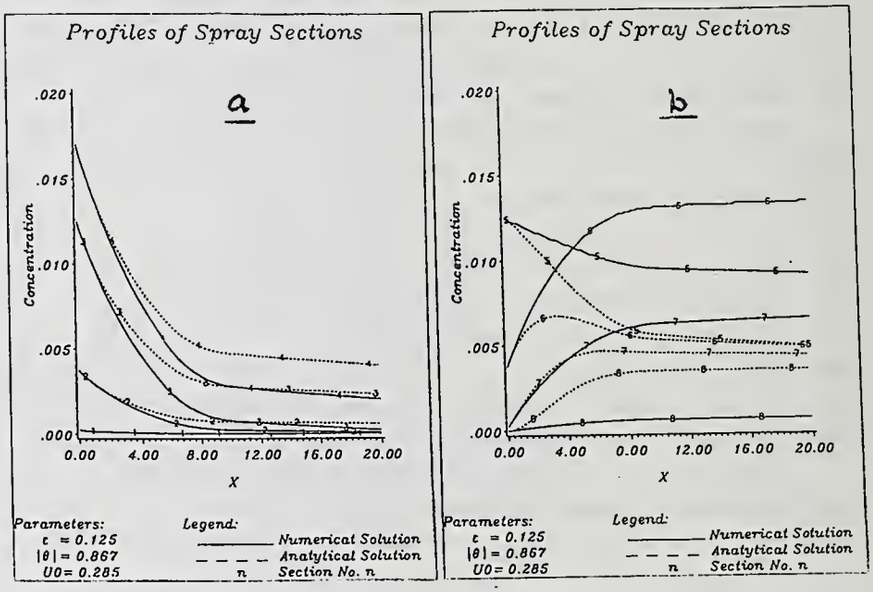

Fig. 5. Evolution in droplet concentrations in each size section; **including coalescence** (a) Sections I to IV, (b) Sections V to X.

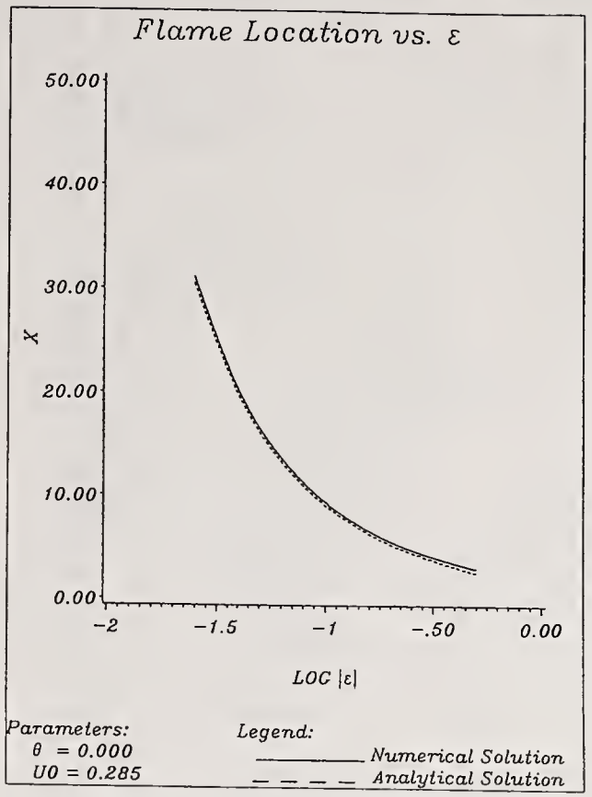

Fig. 6. Effect of evaporation rate on flame location; no coalescence.

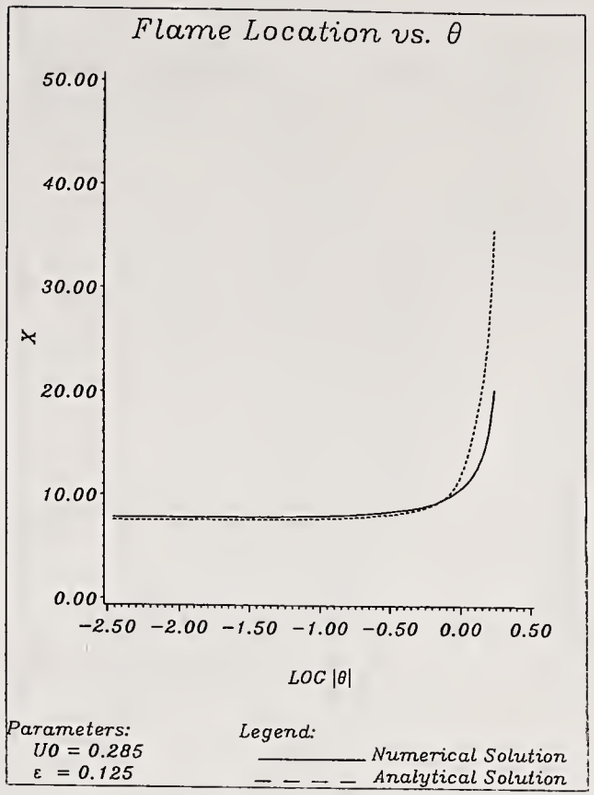

Fig. 7. Effect of coalescence rate on flame location.

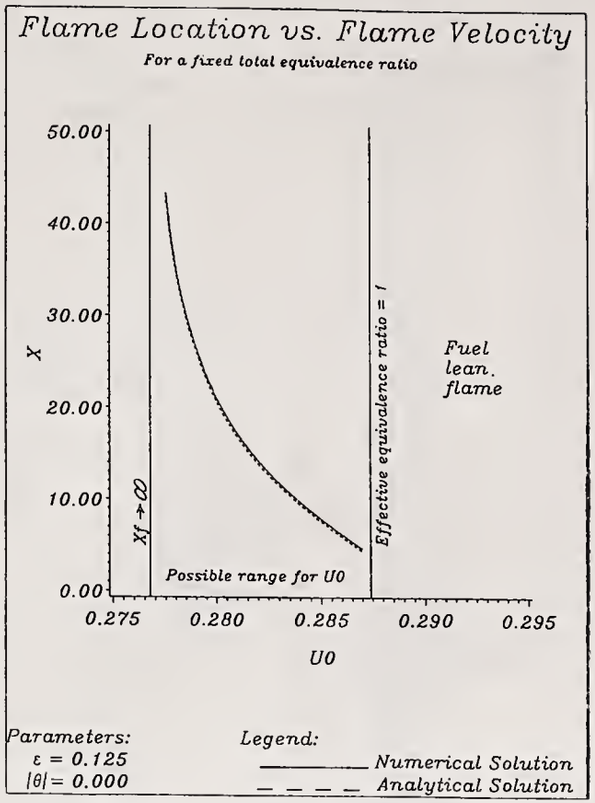

Fig. 8. Flame location vs flame velocity for a fixed total equivalence ratio.

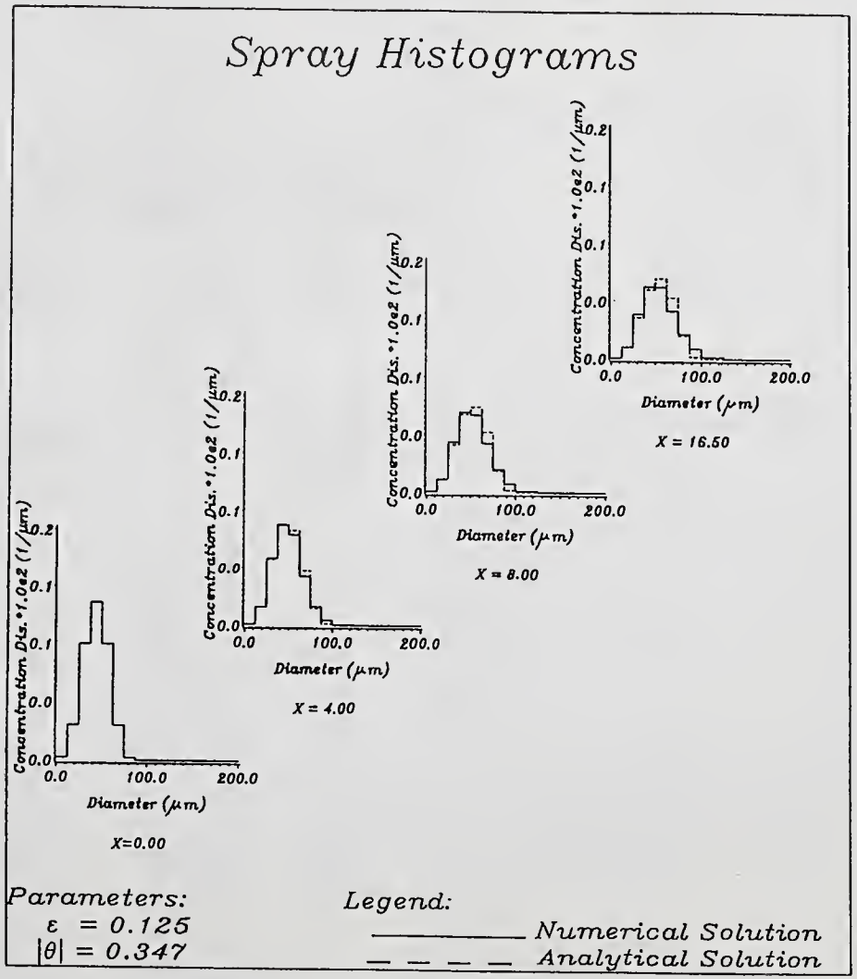

Fig. 9. Downstream evolution of pointwise spray histograms; θ=0.347.

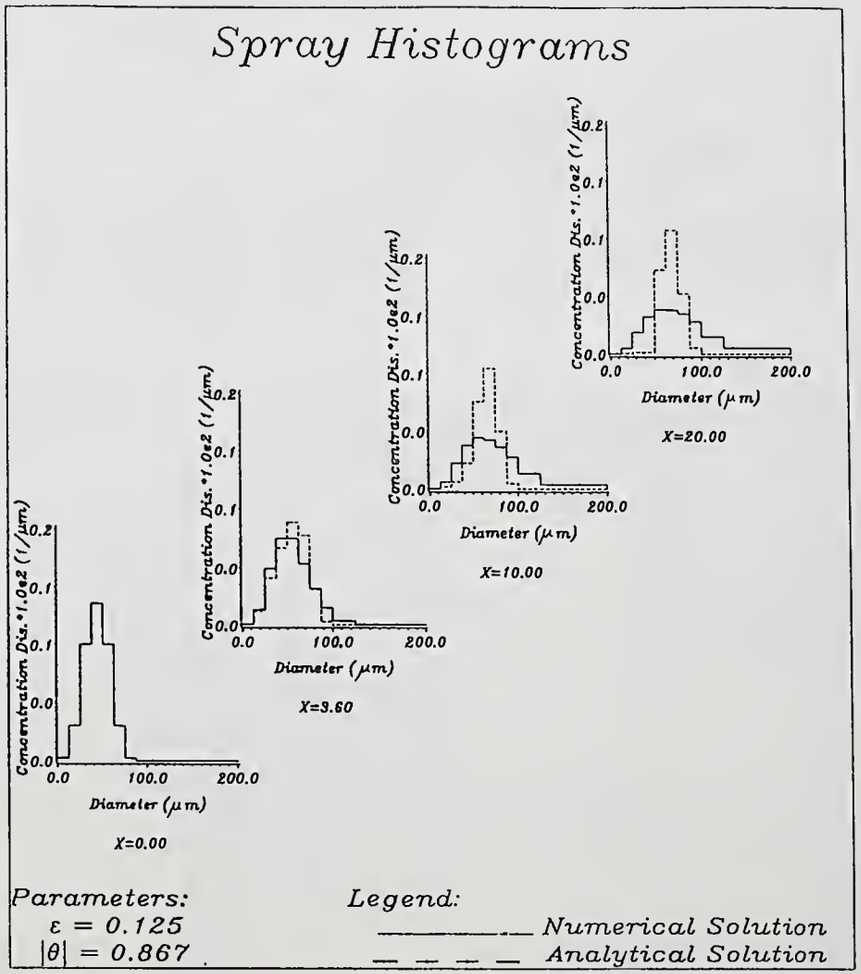

Fig. 10. Downstream evolution of pointwise spray histograms; θ=0.867.

ICLASS-91 *Gaithersburg, MD, U.S.A. July 1991* *Paper 82*

ON THE EVAPORATION OF BINARY-FUEL CLUSTERS OF DROPS HAVING A LARGE VOLATILITY DIFFERENTIAL

K. Harstad and J. Bellan

Jet Propulsion Laboratory
California Institute of Technology
Pasadena, CA, U.S.A.

ABSTRACT

A formulation has been developed to describe the evaporation of binary-fuel, dense or dilute clusters of drops. The binary fuel is assumed to be made of a solute and a solvent whose volatility is much lower than that of the solute. Convective flow effects, inducing a circulatory motion inside the drops, are taken into account, as well as turbulence external to the cluster volume.

Results obtained with this model show that, similar to the conclusions obtained for single, isolated drops, the evaporation of the volatile is controlled by liquid mass diffusion when the cluster is dilute. In contrast, when the cluster is dense, the evaporation of the volatile is controlled by surface layer stripping, that is by the regression rate of the drop which is in fact controlled by the evaporation rate of the solvent. These conclusions are in agreement with existing experimental observations. Parametric studies show that the above conclusions remain valid with changes in ambient temperature, initial slip velocity between drops and gas and initial cluster size.

I. INTRODUCTION

Most of the liquid fuels used to provide power through combustion are mixtures of several pure fuels. For this reason there has always been interest in the study of the combustion of multicomponent liquid fuels. This interest was hightened by the realization that, due to fuel scarcity, the next generation of fuels will have to contain more of the lower end of the distillation batch. The behavior of these heavier and more viscous compounds mixed with small quantities of more volatile compounds (left from the distillation process) became immediately the focus of many studies.

Since in most situations these fuels are introduced into the combustion chamber in the form of a spray, the focus of initial studies was on the evaporation and combustion of single, isolated multicomponent fuel drops. For example, the early study of Wood et al.[1] identified batch distillation, which

is a process relying entirely on volatility differentials, as the main controlling parameter for changing the internal composition of the drops. Landis and Mills [2] were among the first to identify the internal diffusional resistance as another possible controlling process for multicomponent fuel drop evaporation. Their numerical results show that at short time scales, batch distillation models fail to predict the rate of evaporation because they neglect thermal resistance, and for the bulk of the drop lifetime the distillation model fails because it neglects species diffusional resistance. Landis and Mills[2] acknowledge that they do not take into account the effect of circulation inside the drop, which would have the effect of bringing the results of the conduction/diffusion model closer to the batch distillation model. Subsequent investigators[3,4,5] who took into account convective transport through internal circulation found this assertion correct. More precisely, it was found[5] that internal circulation reduces the characteristic length of diffusion by about one-third, which has the effect of reducing the diffusion characteristic time by about an order of magnitude. The excellent review of Law[6] discusses in detail various situations and the relative importance of liquid phase mass diffusion with respect to batch distillation effects.

The importance of liquid phase mass diffusion was also investigated by Randolph et al.[7] whose experimental results revealed that the effectiveness of mass diffusion decreases with increasing volatility differentials of the mixture; the conclusion was that the gasification mechanism is intermediate between batch distillation and a steady state controlled by diffusion.

The results obtained from the studies of isolated, single, multicomponent fuel drops have been used directly in presently-existing calculations[8,9,10] dealing with multicomponent fuel sprays, which have thus all ignored effects due to drop interactions. The problem with this procedure is that in all these calculations the dense spray effects observed near the injector have been ignored. Existing evidence based upon numerical results obtained from calculations performed for single component fuel drops shows that these effects are important and do not have merely a quantitative effect because the controlling parameters might be totally different for dense and dilute collections of drops[11,12].

The focus of the present study is on the behavior of dense and dilute clusters of drops composed of a binary fuel which has one component that is considerably less volatile than the other. This conceptual model depicts the situation of the alternate fuels discussed above. Under the assumption of one fuel being much more volatile than the other, it will be shown that for dilute clusters of drops, similar to the results obtained for single drops, evaporation of the volatile is controlled by mass diffusion. However, in contrast to the dilute and single drop case, evaporation of the volatile is controlled by surface layer stripping of the less volatile component when the cluster of drops is dense.

II. MATHEMATICAL MODEL

The model describes clusters which are spherical and are composed of identical spherical drops, uniformly distributed within the cluster. The solvent is assumed to have a relatively low volatility with respect to the solute; practically the solute's volatility is infinite with respect to the solvent.

The formulation assumes that the drop is composed of a liquid core and a thin boundary layer at the drop surface as shown in Figure 1. In the liquid core

the motion of the liquid is described by a Hill vortex solution

$$u_r = AR^2 \, (1-r^2/R^2) \cos\theta \qquad (1)$$

$$u_\theta = - \, AR^2 \, (1-2r^2/R^2) \sin\theta$$

and the mass fraction of the high volatility component is uniform. The boundary layer is considered to be quasi-steady because it is assumed that the circulation time of the Hill vortex is much smaller than the regression time of the drop. A parameter, Be, representing the ratio of the mass regression rate to a characteristic volatile diffusion rate appears naturally in the analysis as follows:

$$Be \equiv - \, [R/D_m u_\ell]^{1/2} \, dR/dt, \; u_\ell \equiv AR^2 \qquad (2)$$

Thus, when Be<<1, diffusion into the boundary layer governs the rate of species transfer from the liquid core to the drop surface with subsequent transfer from the drop surface to the gas phase (evaporation) governed by the Langmuir-Knudsen evaporation law. Note that the overall rate of solute evaporation is governed by the slowest rate between the diffusion rate and the evaporation rate because these are sequential processes. When Be>>1, the transfer of the high volatility fuel from the liquid core to the gas phase is no longer controlled by diffusion into the boundary layer, but instead by boundary layer stripping, that is by the regression rate of the drop.

Note additionally that transfer of volatile to the drop surface is controlled by the fastest between the diffusion rate and the drop regression rate because these are competitive processes. It should also be pointed that the quasi-steady boundary layer assumption is consistent with Be<<1, when diffusion is important, and inconsistent with Be>>1, when diffusion is not important. As mentioned above, it is further assumed in this model that the volatile kinetic evaporation rate is much larger than the sum of the rates of mass diffusion through the drop boundary layer and of loss through surface regression. This assumption is checked continuously in the calculation using a relative activity coefficient of unity, thereby providing a conservative estimate of this ratio. It turns out that this is a very good assumption throughout the calculations. This assumption means that a batch distillation-like evaporation is totally excluded by this formulation.

In order to calculate the circulation velocity of the Hill vortex represented by u_ℓ one needs to relate it to the incoming flow velocity, u_g. This is done by relating u_ℓ and u_g through

$$K_s \equiv 2u_\ell/(3u_g) \qquad (3)$$

and finding the functional form for K_s. In the present model

$$K_s = \mu_g \, F_c \, (Re, \, Re_v)/(3\mu_\ell) \qquad (4)$$

where $Re \equiv 2\rho_g \, u_g \, R/\mu_g$, $Re_v \equiv \rho_\ell \, R|dR/dt|/\mu_g$, $F_c \, (Re, \, Re_v) = 1/16 \; Re \; C_F \; f(Re_v)$, and $C_F = 2C_D \, / \, [3(1 + 0.0045 \; Re^{0.86})]$. C_D is calculated using the numerical results of Cliffe and Lever[13] for drag on a drop with blowing effects from the drop. The function f is found from a curve fit and behaves approximately as $\exp(-0.1 \; Re_v)$. This insures that F_c goes to previously found limits[14,15] when $Re \to 0$ or $Re_v \to 0$. Thus the equations describing the evolution of drop are:

1) Conservation of mass

$$\dot{m} = - 4\pi R^2 \rho_\ell \, dR/dt \tag{5}$$

The evaporation rate for the drop is the sum of the evaporation rate of the solvent according to the Langmuir-Knudsen law, the diffusion rate of the volatile through the boundary layer and the rate of boundary layer stripping loss of the volatile.

2) The Langmuir-Knudsen kinetic evaporation law for the solvent

$$\dot{m}_{SOLV} = 4\pi R^2 \alpha_e \, [w_{SOLV}/(2\pi R_g T_{ds})]^{1/2} [X^\ell_{SOLV} P_{sat,s} (T_{ds}) - X^g_{SOLV} P_\infty] \tag{6}$$

3) Conservation of species

$$Y_{SOLV} = 1 - Y_{HV} \tag{7}$$

4) The average rate of volatile diffusion through the boundary layer is calculated by integrating the diffusion velocity over the surface of the drop as follows:

$$\overline{u_D} = 0.5 \int_o^\pi u_D \sin\theta \, d\theta = (D_m u_\ell/R)^{1/2} \quad Y_{HV,c} \, f_u \, (Be, W_r) \tag{8}$$

In Eq. (8), u_D is found from the boundary layer solution and W_r is a parameter much smaller than unity which describes the diffusion of volatile from the drop core into the return region of the boundary layer, located near the drop centerline. The dependence of f_u upon W_r is very weak and thus is further ignored.

5) The global conservation equation describing diffusion of volatile mass out of the core into the boundary layer

$$dY_{HV,c}/dt = - 3(D_m u_\ell/R)^{1/2}/R \, f_u \, (Be) \, Y_{HV,c} \tag{9}$$

6) The rate of boundary layer stripping is found by estimating the thickness of the boundary using a subsurface streamline flow time. By definition

$$\text{The mass carried away by the evaporating solvent} \equiv - 4\pi R^2 \rho_\ell \overline{Y_s} \, dR/dt = 4\pi R^2 \rho_\ell \, (D_m u_\ell/R)^{1/2} \overline{Y_s} \, Be \tag{10}$$

where

$$\overline{Y_s} \equiv 1/2\Delta\eta \int_o^{\Delta\eta} d\eta \int_o^\pi Y_{HV} \sin\theta \, d\theta, \quad \eta \equiv (u_\ell \, R/D_m)^{1/2} (1 - r/R) \tag{11}$$

The boundary layer thickness is estimated by $\Delta\eta = Be \oint \frac{u}{R} \, dt \equiv Be \, \tau$, and numerical calculations for subsurface streamlines give $\tau \simeq 5$. Thus $\overline{Y_s}$ can be written as $\overline{Y_s} = Y_{HV,c} \, f_y \, (Be)$.

Note then that the mass loss of volatile from the drop is

$$4\pi R^2 \rho_\ell \, (D_m \, u_\ell/R)^{1/2} \, Y_{HV,c} \, [f_u \, (Be) + Be \, f_y \, (Be)] \tag{12}$$

where functions f_u and f_y are shown in Fig. 2 for small Be.

Thus the rate of mass loss of the volatile from the drop is parameterized by Be. The time dependent parameter Be which changes the mass loss rate is calculated at each time step as it depends upon the solution of the global conservation equations for the entire cluster. These global conservation equations are similar to those previously used for single components fuels[11,12].

7) Conservation of energy inside the drop. The effect of circulation on heat transfer was investigated in detail by Abramzon and Sirignano[15] who performed detailed as well as approximate calculations. The results of that study show that circulation effects can be ignored if the conduction model for heat transfer inside the liquid uses an effective heat transfer coefficient. This effective liquid heat transfer coefficient is obtained by multiplying the conductivity by a factor depending upon the drop Peclet number. Numerically, it was shown[15] that this factor increases from 1 to 2.72 as the circulation strength increases. The advantage of this approximate model is that the global effect of circulation obtained with the more detailed calculations is retained[15] while the calculations are less cumbersome. This approach was adopted here as well and coupled to the previously developed model[11-12,16].

III. RESULTS

Baseline results were obtained for a two component fuel where the solvent is No 2-GT (light diesel) and the solute is n-decane. The calculations were performed at atmospheric pressure with the following parameters: $T^o_{ga} = 1000K$, $T^o_{gs} = 350K$, $Y^o_{Fva} = 0$, $\tilde{R}^o = 3cm$, $R^o = 2x10^{-3}cm$, $u^o_d = 200cm/sec$, $Y^o_{HV,c} = 2x10^{-2}$. Both in these calculations and the parametric studies discussed below, the gas is initially at rest and thus u^o_d represents also the initial value of the slip velocity between drops and gas. Table I shows the values of the thermophysical properties used in the calculations for all the fuels considered here.

Figure 3 depicts the evaporation time versus the initial air/fuel mass ratio for two turbulence models. In the first model, called the weak turbulence model[11], turbulence is not initially present in the surroundings of the cluster, but rather develops with time as the cluster becomes less "porous" to the ambient air[11]. In contrast, in the second model, called the strong turbulence model[11], turbulence is initially present in the surroundings of the cluster.

Similar to the results of previous work[11] it is found here that the evaporation time is insensitive to turbulence in the surroundings of the cluster in the dilute cluster regime, and very sensitive to turbulence in the surroundings of the cluster in the dense cluster regime. As can be seen in Fig. 3, with weak turbulence it is possible to obtain saturation before complete evaporation in the dense regime at initial air/fuel mass ratios for which complete evaporation occurs if the turbulence is strong. Another important feature of these plots is the fact that they show a considerable reduction in the evaporation time in the dense regime due to turbulence effects. This is due to the turbulent transport of hot air from the surroundings to inside the cluster thus replenishing the source of heat for the liquid phase and thereby promoting evaporation. When turbulence is weak, the liquid phase depletes the heat content of the gas phase without the possibility of hot air from the surroundings penetrating the cluster.

Most important, the plots of Be versus the residual drop radius presented

in Fig. 4 show that mass diffusion is a controlling parameter for dilute sprays (initial drop number density of the order of 10^3 cm^{-3} or less for drops having $R^\circ = 2x10^{-3}$ cm), but it is not controlling for dense clusters of drops where instead volatile loss is dominated by surface layer stripping. Basically, in the dense regime the slip velocity between drops and gas relaxes very fast because the cluster exposes a large area to the gas[12] and circulation in the drop ceases when the residual radius is still very large. In the absence of circulation, mass diffusion is too slow to be controlling evaporation, and evaporation proceeds at a basically frozen drop composition. This finding is in total qualitative agreement with the experimental observation of Law and Law[17] who minimized internal circulatory motion by conducting experiments with suspended drops in low pressure environments so as to minimize buoyancy effects.

The fact that the evaporation of the volatile is controlled by surface layer stripping is also clearly seen in Fig. 5 where $Y_{HV,c}$ is plotted versus R_1. The curves show that after an initial decrease in $Y_{HV,c}$ this quantity stays constant during the entire life time of the drops proving that the drops evaporate at constant composition.

Since control of the evaporation by surface layer stripping occur in the dense regime due to the fact that the slip velocity relaxes very fast with respect to the drop lifetime, parametric studies were performed to investigate the possibility that these two characteristic times might be of comparable value under realistic practical conditions. Thus, either T°_{ga} was increased or $\tilde{R}^\circ$ was decreased to reduce the evaporation time, or u°_d was increased to augment the relaxation time of the slip velocity. The value of T°_{ga} was increased in steps of 200°K from 1000°K to 1600°K and the same trends were observed. When the value of u°_d was increased from 200 cm/sec to 1000 cm/sec the results show that dense clusters of drops cannot sustain large slip velocities for any substantial amount of time and the trends of the baseline case were recovered again. This was also the case when $\tilde{R}^\circ$ was decreased from 3 cm to 1 cm.

IV. CONCLUSIONS

A model has been presented for use in the description of the evaporation of dense and dilute clusters of two-component fuel drops. The model assumes that the volatility of the solute is much higher than that of the solvent.

Results obtained with this model show that, similar to previously established results, the evaporation of the volatile in a dilute cluster is partially controlled by liquid mass diffusion. In contrast, results obtained for dense clusters of drops show that the evaporation of the volatile is controlled by surface layer stripping of the solvent; this is an entirely new result which is not totally surprising when one considers that the slip velocity between phases relaxes extremely fast in the case of dense clusters[12], and that it is the drop circulation induced by this slip velocity which enhances liquid mass diffusion which is otherwise an extremely slow process. This is also consistent with the experimental evidence of Randolph et al.[7] for fuels of increasing volatility differentials. In the present case, internal circulation is not effective both because there is negligible slip velocity and because one of the components is much more volatile than the other.

Parametric studies performed by varying the ambient temperature, the initial slip velocity, and the initial radius of the cluster show that surface layer stripping controls volatile evaporation for dense clusters of drops. In fact, it was also shown that dense clusters of drops cannot sustain finite slip

velocities for any substantial amount of time.

AKNOWLEDGEMENTS

The research described in this paper was performed by the Jet Propulsion Laboratory, California Institute of Technology, and was supported by the U.S. Department of Energy, Office of Energy Utilization Research, Energy Conversion and Utilization Technologies Program, Mr. Marvin Gunn, Jr., Program Manager, through an interagency agreement with the National Aeronautics and Space Administration.

REFERENCES

1. Wood, B. J., Wise, H. and Inami, S. H., "Heterogenous Combustion of Multicomponent Fuels", Combustion and Flame, 4, 235-242, 1960.
2. Landis, R. B. and Mills, A. F., "Effect of Internal Diffusional Resistance on the Evaporation of Binary Droplets", Paper B7.9, The 5th International Heat Transfer Conference, 4, 345-349, 1974.
3. Law, C. K., Prakash, S. and Sirignano, W. A., "Theory of Convective, Transient, Multicomponent Droplet Vaporization", 16th Symp. (Int.) on Combustion, 605-617, 1977.
4. Sirignano, W. A. and Law, C. K., "Transient Heating and Liquid-Phase Mass Diffusion in Fuel Droplet Vaporization", Advances in Chemistry Series 166, Zung, J. T. (Editor), 3-26, 1978.
5. Lara-Urbaneja, P., and Sirignano, W. A., "Theory of Transient Multicomponent Droplet Vaporization in a Convective Field", 18th Symp. (Int.) on Combustion, 1365-1374, 1981.
6. Law, C. K., "Recent Advances in Multicomponent and Propellant Droplet Vaporization and Combustion", Paper 86-WA/HT-14 presented at the Winter Annual Meeting, ASME, 1986.
7. Randolph, A. L., Makino, A. and Law, C. K., "Liquid-Phase Diffusional Resistance in Multicomponent Droplet Gasification", 21st Symp. (Int.) on Combustion, 601-608, 1986.
8. Continillo, G., and Sirignano, W. A., "A Numerical Study of Multicomponent Fuel Spray Flame Propagation in a Spherical Closed Volume", 21st Symp. (Int.) on Combustion, 1941-1949, 1988.
9. Aggarwal, S. K., "Ignition Behavior of a Multicomponent Fuel Spray", Combustion and Flame, 76, 5-15, 1989.
10. Raju, M. S. and Sirignano, W. A., "Multicomponent Spray Calculations in a Modified Centerbody Combustor", Paper AIAA-88-0638 presented at the 26th Aerospace Sciences Meeting, January 11-14, Reno, Nevada, 1988.
11. Bellan, J., and Harstad, K., "Turbulence Effects During Evaporation of Drops in Clusters", Int. J. Heat Mass Transfer, 31, 8, 1655-1668, 1988.
12. Bellan, J. and Harstad, K., "The Details of the Convective Evaporation of Dense and Dilute Clusters of Drops", Int. J. Heat Mass Transfer, 30, 6, 1083-1093, 1987.
13. Cliffe, K. A. and Lever, D. A., "Isothermal Flow Past a Blowing Sphere", Int. J. Numer. Meth. Fluids, 5, 709-725, 1985.
14. Sadhal, S. S. and Ayyaswamy, P. S., "Flow Past a Liquid Drop with a Large non-Uniform Radial Velocity, J. Fluid Mech. 133, 65-81, 1983.
15. Abramzon, B. and Sirignano, W. A., "Droplet Vaporization Model for Spray Combustion Calculations" Paper AIAA-88-0636 presented at the 26th

Aerospace Sciences Meeting, January 11-16, Reno, Nevada, 1988.
16. Bellan, J. and Harstad, K., "Evaporation, Ignition and Combustion of Nondilute Clusters of Drops", Combustion and Flame, 79, 272-286, 1990.
17. Law, C. K. and Law, H. K., "A d^2-Law for Multicomponent Droplet Vaporization and Combustion", AIAA Journal, 20, 4, 522-527, 1982.

NOMENCLATURE

A	-	vortex strength
Be	-	defined by Eq. (2)
C_D	-	drag coefficient
C_F	-	friction coefficient
C_p	-	heat capacity at constant pressure for the gas
C_ℓ	-	heat capacity at constant pressure for the liquid
D_m	-	coefficient of mass diffusion in the liquid
F_c	-	function of Re and Re_v
k	-	thermal conductivity
K_s	-	defined by Eq. (4)
L	-	latent heat of vaporization
$\dot{m}$	-	evaporation rate
p	-	pressure
Pr	-	Prandtl number
r	-	radial coordinate within the drop
R	-	radius of the drop
$\hat{R}$	-	radius of the cluster
Re	-	Reynolds number
Re_v	-	evaporation Reynolds number
R_g	-	universal gas constant
R_1	-	R/R^o
T	-	temperature
t	-	time
u_D	-	diffusion velocity
u_ℓ	-	velocity of the vortex motion inside the drop
u_r	-	radial velocity
u_θ	-	velocity in θ direction
W_r	-	parameter much smaller than unity
w	-	molecular weight
X	-	mole fraction
Y	-	mass fraction

GREEK SYMBOLS

μ	-	viscosity
ϕ	-	air/fuel mass ratio
ρ	-	density
η	-	boundary layer variable
τ	-	nondimensional
θ	-	angular coordinate within the drop

SUPERSCRIPTS

o	-	initial condition

SUBSCRIPTS

a	-	ambient
b	-	back
boil	-	boiling point
c	-	core
d	-	drop
f	-	forward stagnation point
g	-	gas
HV	-	high volatility
ℓ	-	liquid
s	-	drop surface
sat	-	saturation
SOLV	-	solvent
st	-	stoichiometric
∞	-	in the air field

TABLE I

THERMOPHYSICAL PROPERTIES OF FUELS

	n-decane	No.2-GT (Light Diesel)
w (g/mole)	142	170
C_p (cal/g K)	0.400	0.40
C_ℓ (cal/g h)	0.523	0.45
L_{boil} (cal/g)	73.92	56.72
T_{boil} (K)	447.7	498
k_ℓ(cal/cm s K)	3.25×10^{-4}	$\sim3.4\times10^{-4}$
ρ_ℓ (g/cm^3)	0.734	0.876
μ_ℓ (g/cm s)	9.2×10^{-3}	$\sim2.6\times10^{-2}$
D_m (cm^2/s)	4.4×10^{-5}(est)	4×10^{-5}(est)
ϕ_∞	14.97	15.0
Pr_ℓ	14.4	~34

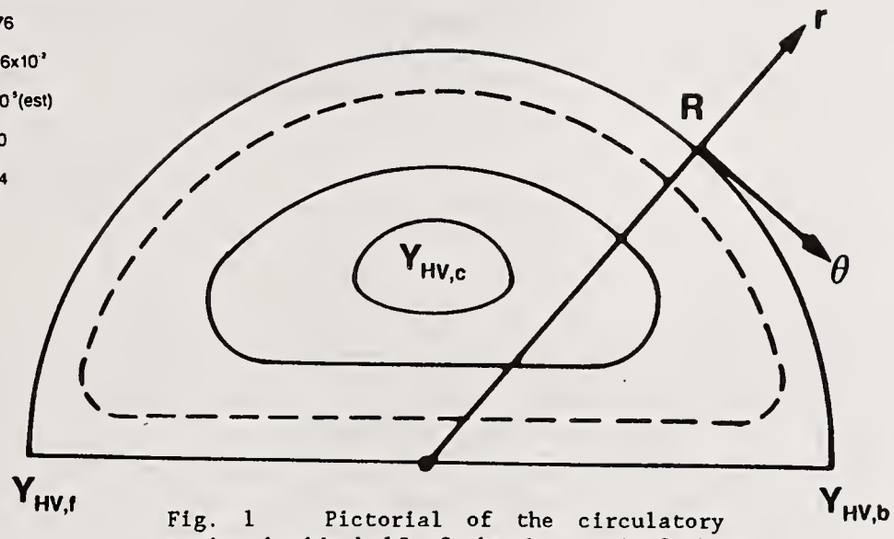

Fig. 1 Pictorial of the circulatory motion inside half of the drop and of the system of coordinates within the drop.

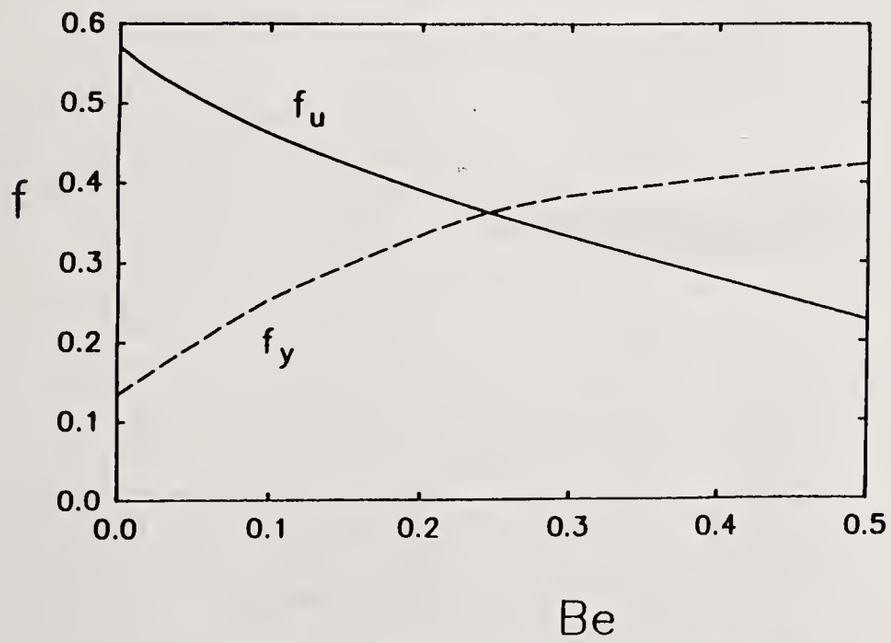

Fig. 2 Variation of functions f_u and f_y with Be.

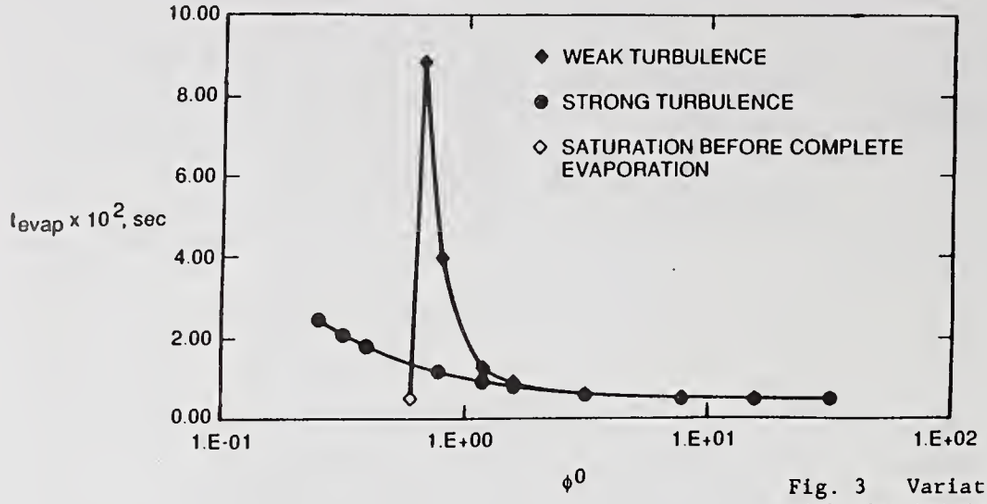

Fig. 3 Variation of the evaporation time with the initial air/fuel mass ratio; T^o_{ga} = 1000K, T^o_{gs} = 350K, $Y^o_{HV,c}$ = 0.02, u^o_d = 200cm/sec, $\hat{R}^o$ = 3cm, R^o = 2×10^{-3}cm, Y^o_{Fva}=0

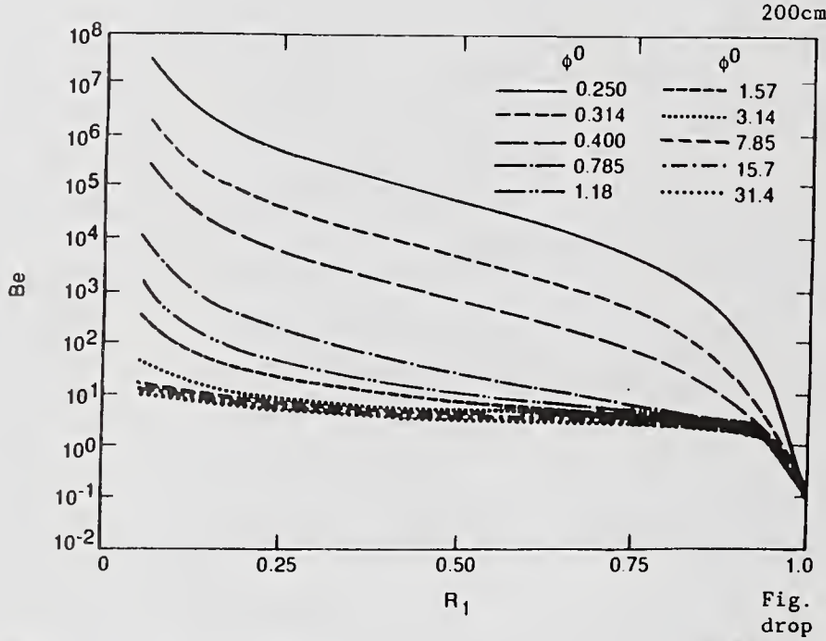

Fig. 4 Variation of Be with the residual drop radius for several initial air/fuel mass ratios for the strong turbulence case; T^o_{ga} = 1000K, T^o_{gs} = 350K, $Y^o_{HV,c}$ = 0.02, u^o_d = 200cm/sec, $\hat{R}^o$ = 3cm, R^o = 2×10^{-3}cm, Y^o_{Fva}=0

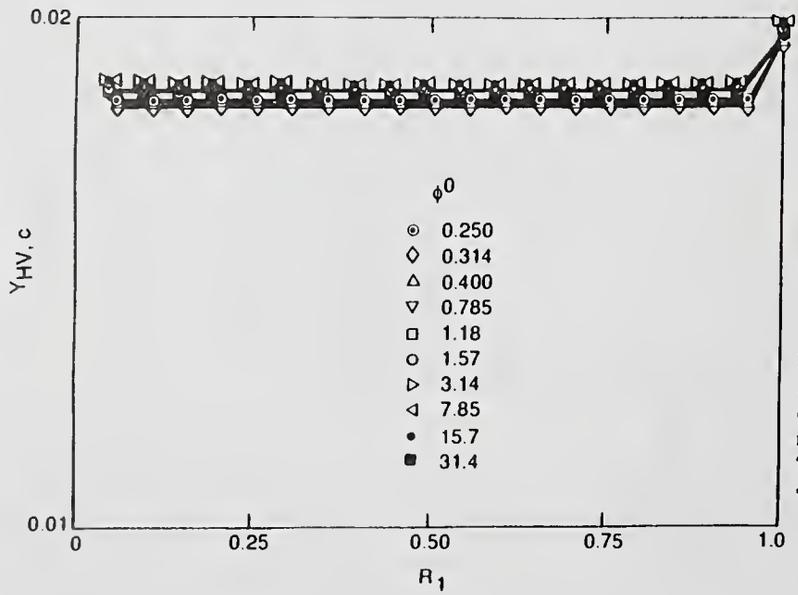

Fig. 5 Variation of the liquid mass fraction of the volatile with the residual drop radius for several initial air/fuel mass ratios for the stong turbulence case; T^o_{ga} = 1000K, T^o_{gs} = 350K, $Y^o_{HV,c}$ = 0.02, u^o_d = 200cm/sec, $\hat{R}^o$ = 3cm, R^o = 2×10^{-3}cm, Y^o_{Fva}=0

MODELLING OF ELECTRO-AEROSOL DEPOSITION IN HUMAN AIRWAYS

W. Balachandran, C.N. Ahmad and S.A. Barton

Department of Electronic and Electrical Engineering
University of Surrey
Guilford, United Kingdom

ABSTRACT

A mathematical model has been developed for the deposition of electro-aerosols in the human respiratory system. In this model an integrated approach is used which takes into account inertial impaction, gravitational sedimentation, Brownian diffusion, interception and electrostatic forces. The model has been realised using a personal computer. This model is capable of handling both homogeneous and inhomogeneous distributions of drop size and charge .

INTRODUCTION

In aerosol therapy the primary aim is to deliver the drug directly to the required site of action, and therefore the therapeutic effect is expected to be more rapid than that of the oral dose.The devices used at present for drug delivery into the human airways include nebulisers, metered-dose inhalers (MDI) and dry particle inhalers (DPI). The basic mechanisms involved in the deposition at specific sites are the same in all three cases, except the overall efficiency will depend on the nature of drug aerosol generated by the respective devices. The deposition of inhaled drug aerosol in the respiratory system is governed by inertial impaction, gravitational sedimentation, Brownian diffusion, interception and electrostatic forces.

Yu (1) and Hashish (2) have made a significant contribution in terms of theoretical studies on various lung deposition mechanisms of inhaled drug aerosols. Both groups have shown that deposition is dominated by electrostatic forces particularly in the alveolar region. Various simplifying assumptions were made in developing these models. It is desirable to re-examine these basic assumptions with a view to improving the model and achieving more realistic and better estimates of deposition efficiencies. We have developed an integrated deposition model for inhalation only, and tested it for consistency with work done by other researchers. The model assumes the airway structure to be tubular and does not include alveolar sacs. In this paper, the theoretical background and the evaluation of the model for various particle size ranges and charge levels is reported.

There are four main elements of the model - an anatomical model of the lung, a model of the act of breathing, a description of the aerosol and models of the mechanisms of deposition of aerosol particles. None of the

elements give a strictly true picture of the processes and structures represented. Indeed a true picture would not be desirable as it would be analytically incalculable. In each case an approximate model has been used, and in each case there are known means by which to refine the model should the extra complexity be justified by extra accuracy of descriptive or predictive performance.

The anatomical model of the lung used is based on Weibel's symmetrical model A (4). The morphometric data for the human lung, cited by Weibel and Yu has been modified in the light of more recent published data of Horsfield et.al.(5). Each airway generation is represented by a cylinder whose total length increases and diameter decreases with penetration into the lung.When using the Weibel lung model it is a natural step to assume that during an inspiration air flow divides symmetrically at branching points. We further assume that the flow rate during inspiration is constant, as are the conditions of the inspired aerosol. The properties of the aerosol used in this model can be either homogeneous or inhomogeneous, in terms of drop size and charge per drop, whereas the other parameters such as density and numerical concentration remain the same.

DEPOSITION EFFICIENCIES

We define deposition efficiencies η here in a simplified manner, valid as long as the total deposition efficiency is small, as the number of droplets deposited in a section of airway divided by the number entering the section. The expressions for the efficiencies due to different deposition mechanisms have been derived by various authors. For an airway distinguished here by its generation j the deposition efficiency components are as follows:-

Inertial Impaction: η_{Ij}

An empirical relation derived from the experimental data of Schlesinger et. al (6) and given by Yu (1) yields:

$$\eta_{Ij} = 0.768^{*} (St_j)\theta_j \qquad (1)$$

where St is the Stanton number and θ_j the assumed branching angle given by

$$S_{tj} = \frac{\rho d_p^2 u_j}{q\mu d_j} \text{ and } \theta_j = \frac{L_j}{4 d_j}$$

where ρ = droplet mass density, dp = droplet diameter, L_j = length of the airway (jth generation), u_j = air velocity in the airway, d_j = diameter of the airway, μ = air viscosity

Gravitational Sedimentation: η_{sj}

Pich (7), for a parabolic flow, give the expression:

$$\eta_{Sj.} = \frac{2}{\pi}\left\{\left(1-\varepsilon_j^{\frac{2}{3}}\right)^{\frac{1}{2}}\left(2\varepsilon_j - \varepsilon_j^{\frac{1}{3}}\right) + \sin^{-1}\left(\varepsilon_j^{\frac{1}{3}}\right)\right\} \qquad (2)$$

$$\varepsilon = \frac{3U_g L_j}{4U_j d_j}\sin\phi$$

where Ug = droplet settling velocity

The angle of inclination of the airway to the vertical, ϕ is assumed to be given by sin $\phi = \pi/4$ which corresponds to the case of a system of randomly oriented airways, Heyder (8).

Diffusion.

Two kinds of diffusion processes are considered in this study:

i) The expression for deposition efficiency due to diffusion in a *turbulent* flow is given empirically by Landahl (9):

$$\eta_{Dtj} = 4\Delta^{\frac{1}{2}}\left(1 - 0.44\Delta^{\frac{1}{2}} + \text{-------}\right) \tag{3}$$

ii) For *laminar* flow , Ingham (10) gives as an empirical result:

$$\eta_{Dlj} = 1 - 0.819\exp(-14.63\Delta) - 0.0976\exp(-89.22\Delta) - 0.0325\exp(-228\Delta) - 0.0509\exp\left(-125.9\Delta^{\frac{2}{3}}\right) \tag{4}$$

where in each case i and ii:

$$\Delta = \frac{DL_j}{d_j^2 U_j}$$

in which: D = The Brownian diffusion coefficient of an aerosol particle.

In the upper respiratory tract the Reynolds number is high. This together with the non-straight nature of the URT suggests that turbulent flow will prevail high up in the URT. However, as one penetrates deeper into the lung Reynolds number falls very rapidly, so inertial effects in the air flow become negligible and the flow will within any generation rapidly become established as fully-developed laminar flow. For this paper we have used to calculate the composite deposition efficiency a mean of the two values down to 13th generation beyond which we have used the expression for laminar flow.

Electrostatic Deposition: η_{Spj} and η_{Imj}

Two effects of electrostatic forces are considered in this study. These are the effects of forces on charged particles due to a space charge and those due to the perceived image of a charge in the proximity of a conducting surface.

(i) *The space charge force* is due to the mutual repulsion of aerosol particles of like charge. The deposition efficiency due to the space charge, was derived by Yu (1977) and is given by:

$$\eta_{Spj} = \frac{C_0 R_j^3 \tau_j}{1 + C_0 R_j^3 \tau_j} \quad \text{where} \quad \tau_j = \frac{Bq^2 L_j}{4\pi\varepsilon_0 R_j^3 U_j} \tag{5}$$

in which C_o = concentration of particles at the entrance of the airway.R_j, radius of the airway (jth generation), τ_j = a dimensionless residence time. μ = particle mobility, q = charge per particle ε_0 = permitivity of air.

(ii) *The image force* is due to the interaction of charged particles with the conducting respiratory walls. For a unipolar aerosol, under slug flow

conditions, Yu (11) derived analytically the following expression:

$$\eta_{Imj} = 1 - \left(\frac{r_c}{R_j}\right)^2$$

where rc , the 'critical radius vector' is related to τ as :-

$$\tau = 4\left(\frac{R_j}{r_c} + 2\ln\left(\frac{r_c}{R_j}\right) - \frac{r_c}{R_j}\right) \qquad (6)$$

The above set of equations is algebraically convoluted, to an extent not necessarily justified by the purpose of the model or by the resolution of any conceivable technique for testing or applying the model. A result of the algebraic complexity is that it is impossible with the equations in that form to have a feel of what the equations imply in a general manner. Any well-behaved (smooth, continuous) mathematical function can be expressed as an infinite polynomial, or approximated by a finite polynomial. Such approximations to the above equations were derived, using series expansions with just sufficient terms to leave in each equation a single (if composite) variable term. We then checked these simplified equations for accuracy within the range of deposition efficiencies suggested by the model using the full equations.

General constant.	Global parameter.	Generation parameters.	
$\eta_{Ij} \approx \{1.5*10^{6}\}$	$\{d_p^2 Q\}$	$\left\{\frac{L_j}{N_j d_j^4}\right\}$	----------Impaction.
$\eta_{Sj} \approx \{3*10^{7}\}$	$\left\{\frac{d_p^2}{Q}\right\}$	$\{L_j N_j d_j\}$	------- Sedimentation.
$\eta_{Dtj} \approx \{1.9*10^{-8}\}$	$\{d_p Q\}^{-\frac{1}{2}}$	$\{L_j N_j\}^{\frac{1}{2}}$	-Turbulent diffusion.
$\eta_{Dlj} \approx \{5.18*10^{-11}\}$	$\{d_p Q\}^{-\frac{2}{3}}$	$\{L_j N_j\}^{\frac{2}{3}}$	-- Laminar diffusion.
$\eta_{spj} \approx \{1.2*10^{-24}\}$	$\left\{\frac{q^2}{Q d_p}\right\}$	$\{L_j d_j^2 N_j C_{0j}\}$	----- Space charge.
$\eta_{imj} \approx \{3.9*10^{-8}\}$	$\left\{\frac{q^2}{Q d_p}\right\}^{\frac{1}{3}}$	$\left\{\frac{N_j L_j}{d_p}\right\}^{\frac{1}{3}}$	------Image force.

N_j = number of airways in the jth generation ,Q = air flow rate

Logarithmic differentiation of the single term gives an instant indication of the sensitivity of the solution either to variations of a controlled parameter (such as the size of the aerosol particles or the inspiratory flow rate) or to errors in assumed parameter values. Collecting global constants, general constants and global variables together,the resulting simplified equations were as listed above.

REALISATION OF THE MODEL AND RESULTS

The model was evaluated for both homogeneous and inhomogeneous distributions of droplet size and charge. Main features of the results are that the deposition efficiency due to impaction is extremely small throughout the lung for the drop size(0.5-7.0 μm) and drop charge levels (5.0 -300 charges per particle) used in this study. The deposition efficiencies due to sedimentation and diffusion, though generally higher than impaction, are still small compared to those due to electrostatic forces which in fact dominate the deposition throughout the lung. The total deposition, at this stage, is considered to be a simple addition of the individual deposition efficiencies.Fig . 1 indicates the effect of drop size on the amount of the aerosol deposited in different parts of the lung. The area under the curve between any two generations give the proportion of the original aerosol deposited between those two generations. This figure also indicates that, under the assumed parameters values, there is almost a constant deposition of 4 % throughout the lung. The figures within the square brackets represents the proportion of the aerosol which is left undeposited after 23rd generation.It is assumed that this amount, because of their small droplet size, high charge and laminar flow conditions, would be deposited in the alveolar sacs. As the droplet size is increased to 3 μm the deposition in

Table 1

Homogeneous Model							
Curve a	dp	1	1	1	1	1	1
	q	100	100	100	100	100	100
In-homogeneous Model							
Proportion	%	2	15	34	29	12	8
Curve b	dp	0.2	0.5	0.8	1.0	1.2	1.4
	q	100	100	100	100	100	100
Proportion	%	2	15	34	29	12	8
Curve c	dp	0.2	0.5	0.8	1.0	1.2	1.4
	q	20	30	40	60	80	100

the upper airways (0-12 generations) decreases due to the decreased charge effect on coarser droplets. This gives a peak deposition around 20th generation and minimal amount (1.7 %) penetrates the alveolar sacs. With 7 μm

droplets , due to increased impaction and sedimentation, the deposition in the upper airways is increased considerably The deposition peak also shifted from 20th to 14th generation with the result that nothing is left to be deposited in the alveolar sacs.Fig.(2) shows the effect of droplet charge on deposition. A small proportion of droplets is deposited up to 10th generation when charge level of 5 electronic charges per droplet were considered. The deposition increases slowly with the penetration into the lung attaining a peak deposition at 23rd generation and about 50% of the aerosol enters the alveolar sacs. As the charge is increased to 100 electronic charges per droplet the deposition throughout the lung is increased resulting in a peak deposition around 20th generation. When the charge level is further increased to 300 charges per droplet the situation is entirely changed. The deposition decreases exponentially from a maximum (13%) at zero generation to almost zero at 23rd generation with the consequence that only 0.4% is left for deposition in the alveolar sacs.

Fig 1. Drop size effect on deposition (homogeneous)

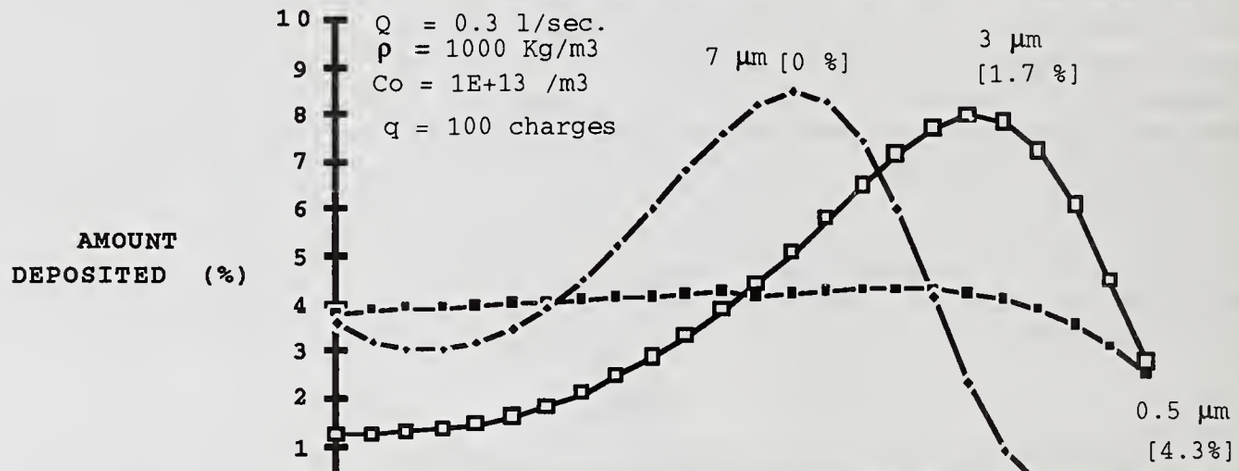

All the results uptill now were based on the assumption that the aerosol consists of collection of monosize droplets having equal amount of charge. In practice this is hardly the case and the aerosol not only has a narrow size distribution but also has a specific charge distribution. The results of the model, when these distributions were considered, are shown in fig.3. Curve (a) indicates the deposition pattern in the lung when all the droplets of the aerosol are considered to be of equal size and carrying same charge (homogeneous case) as in fig.1. Curves (b) and (c) are the results of the solution of the inhomogeneous model under an arbitrary set of parameters shown in table 1.

Curve (b) shows the effect of assumed narrow size distribution of inhaled droplets, each carrying 100 electronic charges. Since the size distribution taken for this model evaluation has a VMD of 1µm and the spread is narrow, the effect is not significant. However when both inhomogeneous distribution of size and corresponding charge distribution are used the model predicts a significant deviation in comparison with the homogeneous model. In this case the upper airway deposition decreases to about 1% and after 10th generation, the deposition efficiency increases significantly attaining a peak value

around 22nd generation. Although the amount entering into the alveolar sacs increases to 21%, it is believed that due to laminar flow conditions in the alveolar sacs , the image charge force will be strong to deposit almost all of these small droplets carrying high specific charge.

Fig 2. The effect of droplet charge on deposition (Homogeneous Model)

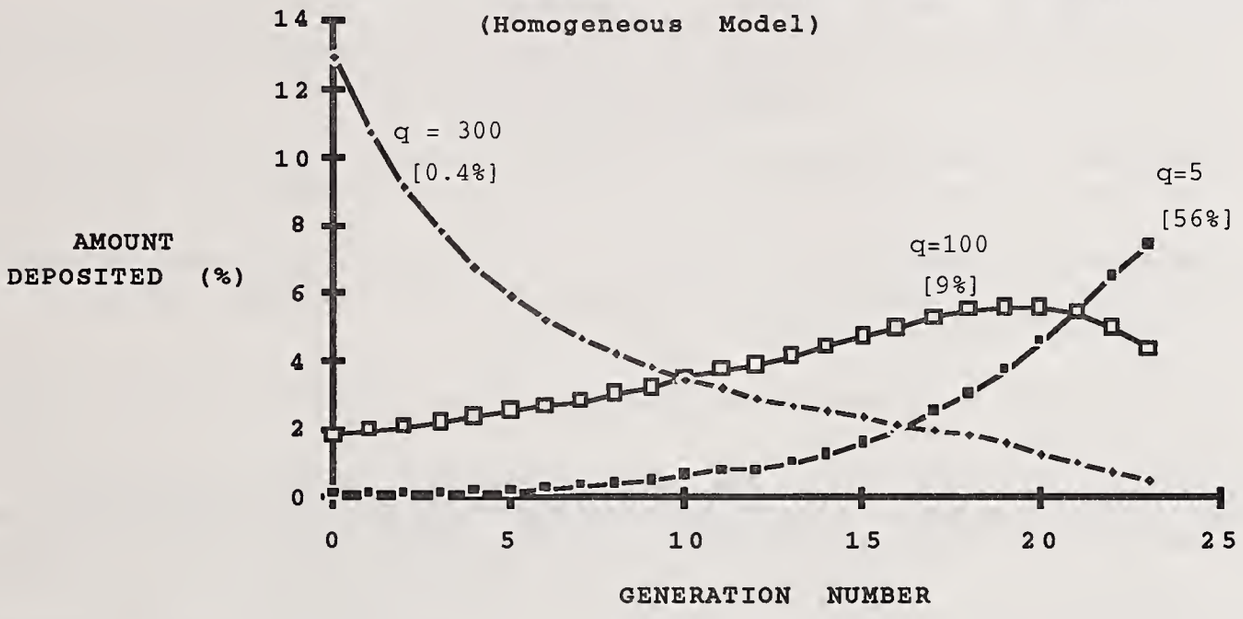

Fig.3 COMPARISON OF PARTICLE DEPOSITION IN HOMOGENEOUS AND INHOMOGENEOUS MODELS

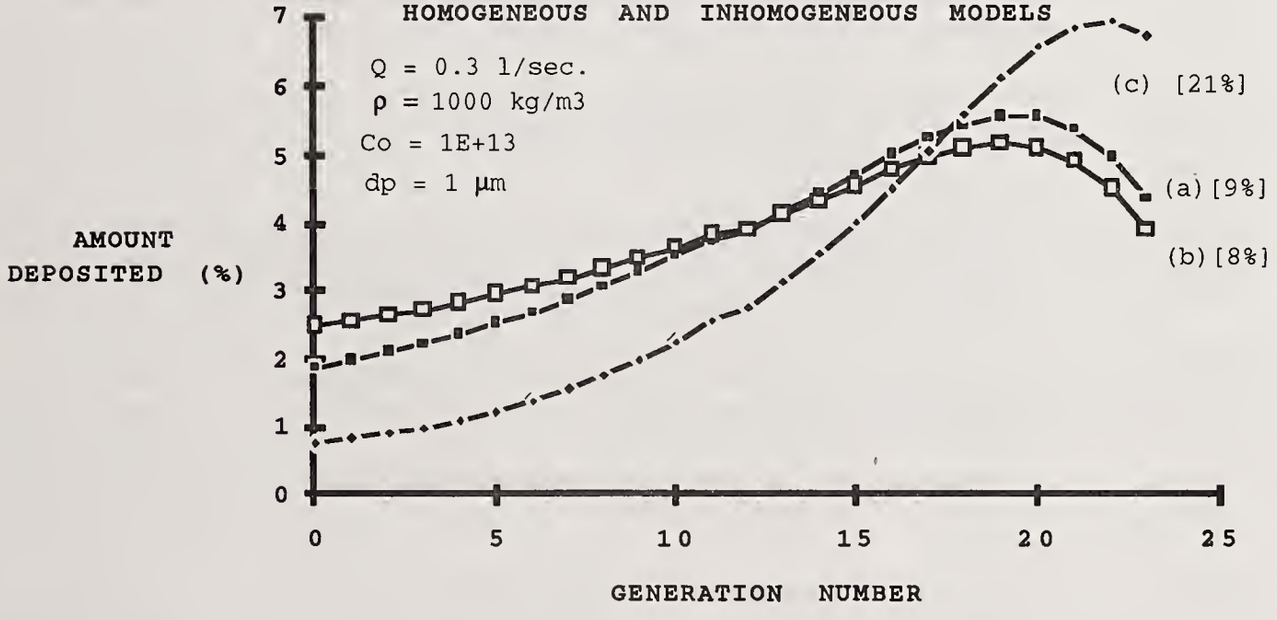

CONCLUSIONS.

A flexible integrated lung deposition model incorporating the effect of all five different mechanisms has been developed and realised. The analysis of the model indicates the approximate sensitivity of each deposition efficiency to variations in each parameter. With control over appropriate parameters, it is possible to predict or determine the primary target of an inhaled aerosol in the bronchial tree.

ACKNOWLEDGEMENT

.

The authors wish to acknowledge BESPAK Plc. for the financial support provided for the study.

REFERENCES:-

1. Yu C.P.and Diu C.K, "A comparative study of aerosol deposition different lung models", Am. Ind. Hyg. Assoc. J., 43, pp. 54 - 65 (1982).

2. Hashish A.," The influence of electrostatic charge on the deposition of therapeutic aerosols." PhD thesis University of Southampton UK (1988).

3. Melandri,C., Tarroni G., Prodi, V., De Zalacomo T., Formignani M., and Lombardi C.C." Deposition of charged particles in the human airways", J. Aerosol Sci., 14, pp. 657 - 669, (1983).

4. Weibel E.R., " Morphometry of the human lung", Academic Press New York , pp.136 -140, (1963).

5. Horsfield, K. et. al.," Models of human bronchial tree", Journal of applied physiology, vol.31 No. 2, pp. 207 - 217,(1971).

6. Schlesinger R.B., Bohning D.E., Chan T.L., and Lippmann M.,"Particle deposition in a hollow cast of the human tracheobronchial tree" J.Aerosol Sci., 8 , pp. 429 - 445 (1977).

7. Pich J., " Theory of gravitational deposition of particles from laminar flows in channels", J. Aerosol Sci., 3, pp. 351 - 361, (1972).

8 . Heyder J., " Gravitational deposition of aerosol particles within a system of randomly oriented tubes", J. Aerosol Sci. 6, pp. 133 - 137, (1975).

9. Landahl H. D., "Particle removal by the respiratory system" Notes on the removal of airborne particulates by the human respiratory tract with reference to the role of diffusion', Bull. Math.Biophys,25 pp. 29 - 39.

10. Ingham D.B.,"Diffusion of aerosols from a stream flowing through a cylindrical tube", J. Aerosol Sci.6, pp. 125-132,(1975).

11. Yu C.P.," Precipitation of unipolar charged particles in cylindrical & spherical vessels", J. Aerosol Sci., 8 , pp. 237 - 241,(1977).

DROPLET INTERACTION IN SPRAY MODELLING

M.M. Elkotb*, O.M.F. Elbahar*, T.I. Sabry† and S.A. Wilson†

*Cairo University, Cairo, Egypt
†Menoufia University, Egypt

ABSTRACT

A mathematical model with more advanced concept about the spray droplets interaction with the surrounding air is suggested in this work. Using the model, a parametric study has been carried out to analyse the effect of different operating conditions on the spray behaviour. A comparison of the theoretical results with available experimental data shows a fair agreement.

INTRODUCTION

Reviewing the theoretical models in literature, one can classify them to three different categories. The first category [1-5] is mainly based on correlations of experimental results to obtain the spray penetration length, and spray tip velocity. Such technique cannot give any information about the spray droplets and its behaviour and the interaction between spray droplets and the gas phase. The second is based on continuum mechanics [6,7,8]. These models enable the calculation of spray penetration , mean velocity and mean concentration distribution. The entrained air and the interaction between the air field and the droplets are not considered. The lateral velocity, droplet size distribution and consequently the local concentration cannot be calculated with this technique. The third category of spray modeling is based on discrete droplet model in which the spray droplets are divided into groups of certain size and number [9-14]. The classical differential equations of motion and energy are applied on each group to define the velocity, temperature, size and the location of each one.

Various modifications have been suggested such as variation of drag force and heat transfer with Reynolds number, droplet size distribution and stochastic behaviour of droplets. However, complete interaction between the two phases has not been satisfied. A trial has been performed in the present work to inrtoduce several modifications for the interaction between the two phases to improve the accuracy of the discrete droplet model.

MATHEMATICAL MODEL

In the present work the conservation equations of momentum, continuity and energy in 3D form have been used together with the two equations simulating the turbulence in the gas phase 'k-ε' . The constants of the turbulence model have been modified to fit the transient flow inside the cylindrical combustion chamber of a Diesel engine. The conservation equations representing the gas phase flow are Eularian and solved using the iteratively SIMPLEC technique, while the differential equations of droplets motion, which are in Lagrangian form, are solved for each group of droplet to obtain the droplets trajectory, velocity, size and temperature.

An interaction mechanism between the gas phase and the spray droplets are proposed as follows:
- Momentum transfer from the droplets to the gas phase and mutual interaction of droplets and its effect on drag force.

- Energy transfer to the gas phase due to fuel evaporation.
- Random motion of droplets and its effect on gas phase turbulence represented by the Pseudo-turbulence equation.

Governing Equations And Interaction Scheme

The general form of the conservation equations and the two equations of turbulence can be written with an arbitrary variable ϕ as follows:

$$\partial/\partial\tau\,(\rho\phi) + \partial/\partial x\,[\,\rho v\phi - \Gamma_\phi\,(\partial\phi/\partial x)] + 1/r\;\partial/\partial r\,[r\rho v\phi - \Gamma_\phi\, r\,(\partial\phi/\partial r)] + 1/r^2\;\partial/\partial\theta\,[r\rho w\phi - \Gamma_\phi\,\partial\phi/\partial\theta)]$$

$$= S_\phi + S_{\phi\,\ell} \qquad (1)$$

Where Values of S_ϕ , $S_{\phi\,\ell}$, Γ_ϕ and turbulence model constants are given in [20]. Shear stress, generated from the turbulence motion of droplets, appears in the source term of the momentum equation of gas phase as follows.

$$\tau_{ij\,ps} = \mu_{ps}\;[(\partial u_i / \partial x_j) + (\partial u_j / \partial x_i)] \qquad (2)$$

$$\text{Where } \mu_{ps} = 1.3\;\rho_\ell \alpha\, R\,(v_\ell - u_g) \qquad (3)$$

The Lagrangian conservation equations of the droplets can be written as follows:

$$d\,m_\ell/d\,\tau = - C_D\,A_\ell \rho_g\,V^2_{rel}/2 \qquad (4)$$

$$m_\ell\,C_{p\ell}\,(dT_\ell/d\tau) = A_\ell\,H\,(T_a - T_\ell) + L\,(dm_\ell/d\tau) \qquad (5)$$

$$-(dm_\ell/d\tau) = 4\,\pi\,R^2\,(Sh\,D_c/2R)\;(\rho_s - \rho_\infty) = 4\,\pi\,R^2\,\rho_\ell\,(dR_\ell/d\tau) \qquad (6)$$

diffusion coefficient,
$D_c = D_o\,(T_s/T_o)\;(P/P_a)$

Sherwood number,
$Sh = 2 + 0.6\;Re^{1/2}\;Sc^{1/3}$ [16]

And consequently the rate of change of droplet diameter becomes as follows.

$$dR/d\tau = -\,(Sh\;D_c/2R\rho_\ell)\,(P_s/R_v T_s) \qquad (7)$$

Where,

$P_s = 2.39 \times 10^9\;\; e^{-6065/Ts}$

$T_s = 462\,P_a^{0.043} + 0.06\,(T_a - 673)$, $350 < T_a < 600$ [14]

and the rate of temperature increase :

$$dT/d\tau = (3/R\,C_{p\ell})\,[\,h/\rho\,(T_a - T_\ell) - (L\,Sh\,D_c/2R\rho_\ell)\,(P_s/R_v\,T_s) \qquad (8)$$

Where h can be calculated from,

$Nu = ß\;0.54\;Re$ for $100 < Re < 1000$ [15,17]

$Nu = ß\;(2+0.6\,Re\,Pr)$ for $Re < 100$

Where ß is a correction factor to consider the effect of mass transfer;

$ß = Z / Exp(z) - 1$ [18]

and,

$$Z = -\,[C_{pv}\,(dm_\ell/d\tau)]/\pi\,d\,K\,Nu$$

The modified drag coefficient used in the momentum equation is that proposed by ELKOTB[19] in the following form.

$$C_D = (28/Re^{0.79})\ [1/\beta\ (2.5/Re^{0.233})]\ \frac{C_{pg}(T_\infty - T_s) + (Q\ AF/AF_{st})}{L} \quad (9)$$

The spray is considered initially formed of droplets distributed in size groups according to the following distribution function[14]:

$$1/n_t\ [dn/d\ (D/D_{32})] = 10\ (D/D_{32})^{2.4}\ e^{-2.4(D/D32)} \quad (10)$$

The Sauter mean diameter can be calculated from the following formula[14]:

$$D_{32}/d_n = 107\ Re^{-0.183}\ We^{-0.442}\ C_D^{-0.422}\ (\rho_f/\rho_a)^{-0.05} \quad (11)$$

Each group is treated as a single droplet according to the discrete droplet theory.

The traditional approach mentioned before, to modeling droplet dispersion in turbulent flow is based on that the diffusional mass flux is proportional to diffusion coefficient and concentration gradient. Such approach is not sufficient to predict droplet motion in case unequal turbulent velocity of air and droplets especially in a highly turbulent swirling air. In this case the air velocity fluctuation, which has a random behaviour, affects the droplet velocity through a fluctuating drag force. Thus, the air field transfers a random velocity component to the droplet motion, and a random droplet dispersion is obtained. The instantaneous turbulent velocity of air field is represented with a random number generator as follows:

$$u` = \sqrt{2 \ln (1/Rn)}\quad \sqrt{(2/3)K} \quad (12)$$

Where, Rn = random number (0.001 to 1)

Solution Procedure

The two systems of equations (the gas phase and liquid phase) are solved together numerically in iterative procedure method. The SIMPLEC algorithm is used to solve the finite difference form of the gas phase governing equations. The combustion chamber is divided into four cells u,v,w and scalar quantity cells covering the domain under consideration. The values of the dependent variables are calculated at the pole of each cell. The grid used is represented in ref [1].

The diffusional equations representing the droplets behaviour are solved using RK-4 steps technique taking into consideration the strong coupling between the two phases which is the interaction mechanism.

RESULTS AND DISCUSSION

The theoretical model was used to determine the trajectory of the droplets and its velocity as well as penetration, fuel concentration and spray geometry. The following operating conditions were used.

- Fuel type : Light diesel fuel
- Fuel density : 850 Kg/m^3
- Specific heat : 2.299 Kj/Kg K
- Cylinder bore : 87.5 mm.
- Nozzle diameter : 0.33 mm.
- Pump speed : 750 rpm.

The instantaneous and rate of injected fuel during the injection period were calculated using the following correlations[18].

$$Q^* = 0.9\ \emptyset^* + 1.3\ \emptyset^{*2} - 1.2\ \emptyset^{*3} \quad (13)$$

$$dQ^*/d\tau = 0.9 + 2.6\ \emptyset^* - 3.6\ \emptyset^{*2} \quad (14)$$

The generation and development of spray droplets and air field with time, according to the spray penetration had been calculated and the vector diagram of the gas phase and its variation with time are illustrated in Fig(1&2). From these figures it is clear that, the generated air velocity takes its maximum value along the spray center line. The higest value of the entrained air velocity in the spray zone lies near the injector and reaches its maximum value at the spray tip. This may be attributed to the small momentum exchange. It is noticed also that the entrained air is directed to the lower spray zone and outside in the upper part of the spray. Therefore, dispersion of droplet increases in this zone. Regarding the injection pressure, the droplet velocity increases with its increase due to the increase of momentum exchange. Thus the dispersion of droplets increases with the increasing of the injection pressure, causing dilution of the fuel concentration along the spray zone especially at the spray tip.

Parametric study had been carried with different drag force correlations to validate the model against the published experimental work[1]. The resulting turbulence from the spray droplets has been included also to define its effect on the accuracy of results. Figure(3) illustrates the effect of drag force represented by different correlations on the fuel concentration decay along the spray center line at stagnant medium condition. The results show that the concentration decay in the case of Ingebo correlation is less in magnitude than that in the case of modified drag correlation. The reason may be attributed to the small drag force value calculated by Ingebo drag correlation compared with that obtained by modified drag correlation. Introducing the Pseudo-turbulence the decay of the fuel concentration decreases. This may be attributed to the increase in gas phase turbulence level represented by the turbulence kinetic energy K, which increases the fluctuation gas velocity component u'. This leads to the increase of the random droplet's motion and consequently the droplet dispersion and decrease of the fuel concentration.

The same conclusion appears in Fig(4) which illustrates the effect of various drag correlations on the fuel concentration decay along the spray in the case of swirling flow.

The effect of various factors on the spray formation and penetration as well as the air field are represented in Figs(5&6). From these figures it is clear that a great deformation of the air field has been resulted in the spray zone especialy behined the injector where the momentum transfer is maximum.

The effect of gas temperature on the spray behaviour is studied also. Figures(7&8) represents the radial and axial concentration decay with increasing the gas temperature. This may be attributed to the increase of mass transfer rate by increasing the gas temperature.

CONCLUSION

The proposed mathematical model in the present work has more advanced mathematical approach to achieve better simulation for the spray droplets behaviour. The effect of Pseudo-turbulence generated from the spray droplets motion on the gas phase is considered. The results show that this factor decreases the fuel concentration along the spray center line due to the resulting droplets dispersion. Another important parameter which is the drag force was taken into consideration, so a modified drag correlations[19] as well as other different correlations are tested to clear its effect on the spray droplets. The results show that the use of modified drag correlation in the mathematical model gives a best agreement with experimental results. This can be attributed to the realestic conditions used in deriving this correlation. The effect of gas phase turbulence on the droplets motion is considered. This gives the spray droplets their random motion. So statistical approach is used to simulate the turbulence nature based on the turbulence kinetic energy of the gas phase, probability distribution function and random number generator.

Parametric study has been carried out to clear the effect of spray behaviour in side the open combustion chamber of Diesel engines . The spray inside a stagnant medium as well as the swirl air were studied. The effect of fuel evaporation process was considered also.

REFERENCES

1. SAAD M.A.,"Spray Formation and Entrainment Characteristics in Liquid Fuel Sprays of Diesel Engines. M.Sc. Thesis, Supervised by Prof. M.M. ELKOTB, Cairo University, (1985).

2. DENT, J.C.,"A Basis For The Comparison of Various Experimental Methods For Studying Spray Penetration." SAE paper No: 716571 , (1971).

3. HAY, N. and JONES, P.L.,"Comparison of Various Correlations For Spray Penetration" SAE paper No: 720776 , (1972).

4. SHAHED, S.M., CHIV, W.S. and LYN, W.T."A Transient Spray Mixing Model For Diesel Combustion." SAE . Trans. Vol. 85 , pp. 502-512, (1976).

5. HIROYASU, H. and KADOTA, T., " Models For Combustion AndFormation Of Nitric Oxide And Soot In Direct Injection Diesel Engines." SAE paper No:760129 , (1976).

6. ADLER, D. and LYN, W.T." The Steady Evaporation And Mixing Of A Spray In Gaseous Swirl." Int. J. Heat Mass Transfer, Vol (14), pp. 793, (1971).

7. WAKURI, Y. FUJII, M. AMITANI, T. and TSUNEYA, R. " Studies On The Penetration Of Fuel Spray In Diesel Engines." JSME. Bull., pp. 123-130 , (1960).

8. CATTON, I. , HILL, D.E. and McRAE, R.P., " Study Of Liquid Jet" AIAA Vol. 6, pp. 2084-2089 , (1968).

9. WESTBROOK, C.K., "Three Dimensional Numerical Modeling Of Liquid Fuel Sprays." California University, Livermore, Cal.94550.

10. CLIFFE, et. al,"A Finite Difference Calculation Of Spray Combustion In Turbulent Swirling Flow." Int. Conf. on Numerical Methods, SWANSEA, U.K. (1979).

11. BRACCO, et. al.," Theoretical Analysis of Stratified Two-Phase Wankel Engines Combustion." AIAA Vol. 16 , No. 10 , pp. 1053-1061, (1978).

12. ELKOTB, M.M. and RAFAT,N.M.,"Fuel Spray Trajectory In Diesel Engines." ASME, J. of Engr. for power, No.77 DGP-1, Oct., (1977).

13. ELKOTB, M.M., ELSABILIGI, M. and DIAB, R.," Spray Behaviour Inside a Swirl Chamber Of A Diesel Engine." Proc. of the 1st. Conf. of Mech. Power Eng., Cairo.,(1977).

14. ELKOTB,M.M., "Fuel Atomization For Spray Modeling." Progress in Energy and Combustion Science, vol.8,(1982).

15. RANZ, W.E. and MARSHALL, W.R.,"Evaporation From Drops." Chem. Eng. Prog. 48, 141, Part I & II, (1952).

16. BIRDS, R.B. , STEWART, E.W. and LIGHTFOOT, E.N. "Transport Phenomena." John Wiley, New York, (1960).

17. VIROPOFF, D.N.,"Evaporation Of Fuel Drops." Bull. of the central Scientific Aviation Institute, (1939).

18. ELWAKIL, M.M., UYEHARA, D.A. and MYERS, P.S.A,"Theoretical Investigation Of The Heating Up Period Of Injected Fuel Droplets Vaporizing In Air." NACA T.N. 3179, (1954).

19. ELSALMAWY H.A. "Evaporation And Drag Characteristics Of Multicomponent Hydrocarbon Droplets." M.Sc Thesis , Supervised by Prof. M.M.ELKOTB, Cairo University, (1986).

20. WILSON S.A. " Investigation of Spray Behaviour in Diesel Engiues". Ph. D. Thesis, Supervised by Prof. M.M. ELKOTB, Menoufia University, Egypt, (1990).

NOMENCLATURE

A	Cross section area, m^2 .
AF	Air to fuel mass ratio.
AF_{st}	Stochiometric air to fuel ratio.
C_d	Coefficient of discharge.
C_p	Specific heat at constant pressure, j / kg K.
D	Droplet diameter, m.
D_{sz}	Sauter mean diameter, m.
H	Coefficient of heat transfer, w / m^2 hr k·
L	Latent heat of fuel, j / kg
Nu	Nusselt number.
n	Number of droplets in each group.
n_t	Total number of fuel droplets injected during certain period.
P	Pressure, N / m^2.
Pr	Prandtl number.
Q	Heat of combustion per unit mass of fuel reacted, j / kg.
Q^*	Normalized comulative quantity of injected fuel.
R	Droplet radius, m.
Rn	Random number (0 - 1).
R_f	Richardson number.
R_v	Vapor gas constant.
Sc	Schmidt number.
Sh	Sherwood number.
S_R	Swirl ratio, ω / ω_e.
S_ϕ	Source term of the conservation equations.
T	Temperature, K.
U	Velocity component in angular direction, m / s.
V	Velocity component in radial direction, m / s.
W	Velocity component in axial direction, m / s.
We	Weber number.
α	Void fraction.
Γ_ϕ	Effective diffusivity coefficient for variable ϕ .
θ	Augular distance coordinate, degree.
K	Turbulence kinetic energy, m^2 / s^2.
μ	Viscosity, kg / m s.
ρ	Density, kg / m^3.
σ	Surface tension, N / m.
τ	Time, S.
τ_{ij}	Shear stress, N / m^2.
ϕ	Arbitrary dependant variable (ϕ = U, V, W, h, K and ε).
ϕ^*	Normalized crank angle degree.

SUBSCRIPT

a	Air.
e	Effective.
ℓ	Liquid.
P_s	Pseudo turbulence.

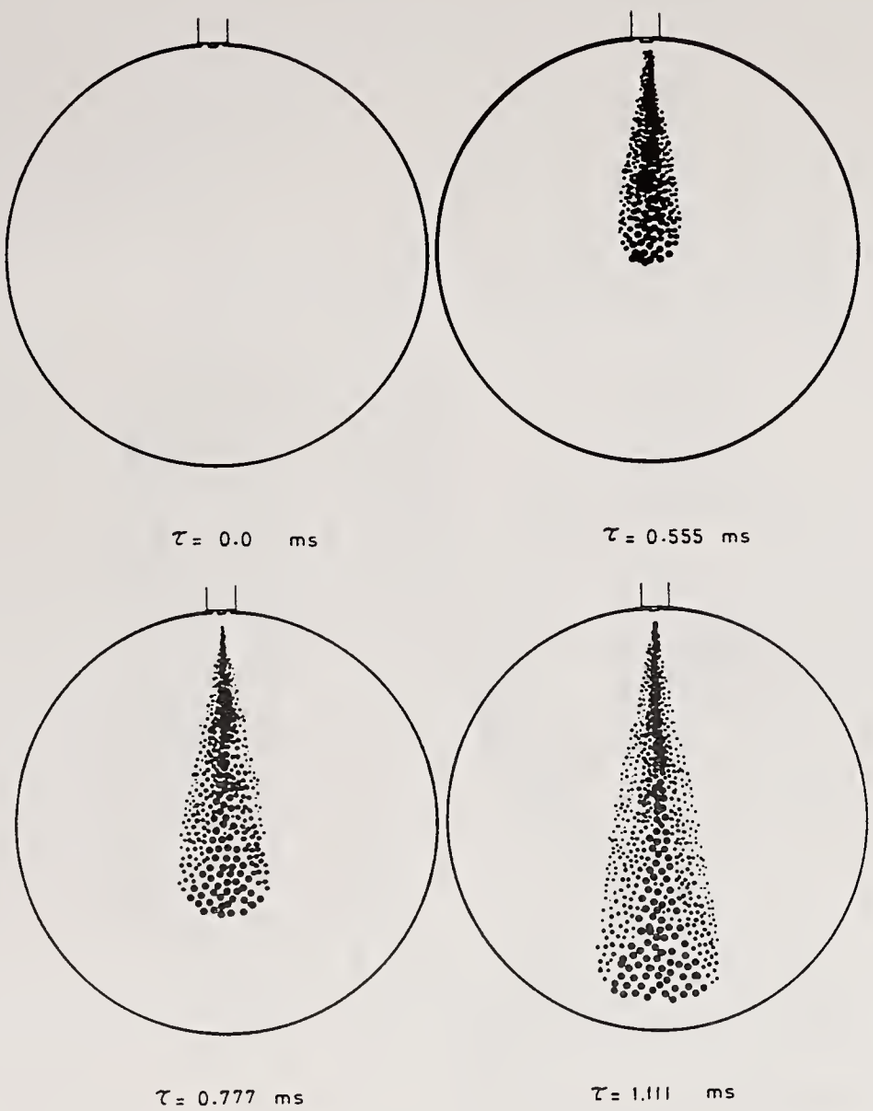

Fig. 1 Droplets size distribution at P_{inj}=120 bar & P_b=5 bar

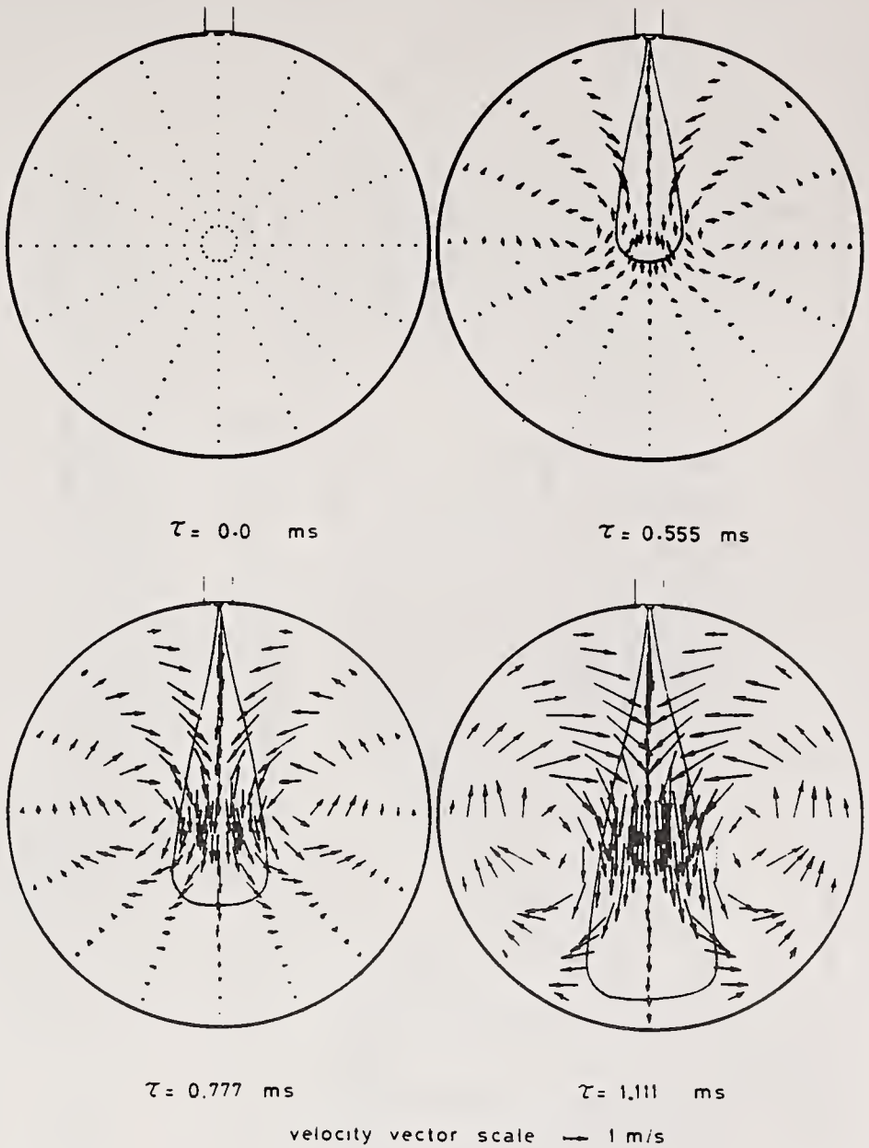

Fig. 2 Velocity distribution inside the chamber at P_{inj}=120 bar and P_b=5 bar

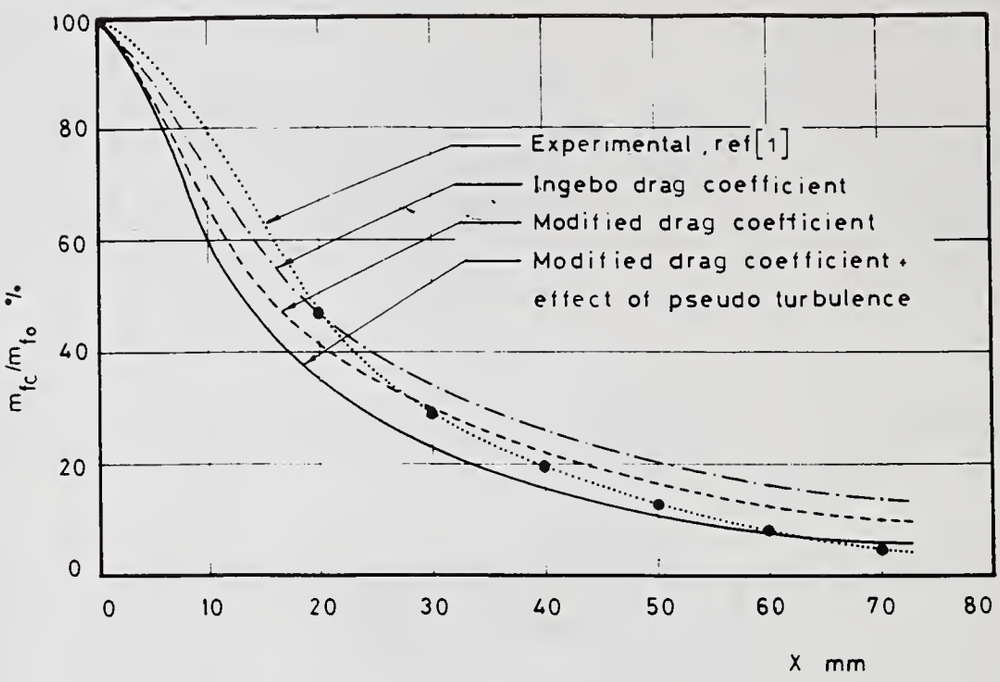

Fig . 3 Effect of various values of drag force on the fuel concentration along the spray centerline, at P_{inj}=120 bar and P_b=5 bar

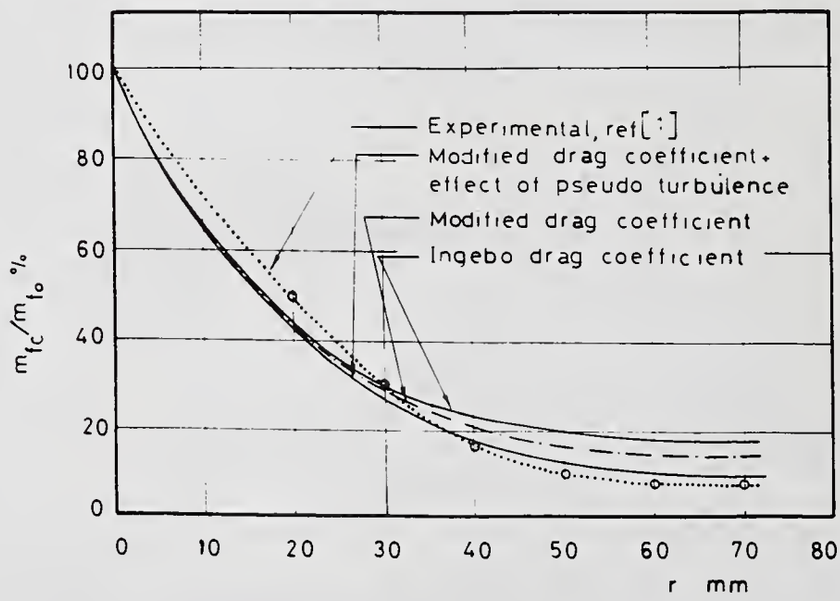

Fig. 4 Effect of various values of drag force on the spray concentration aloing centerline at ω =749 rad/s and P_{inj}= 40 bar

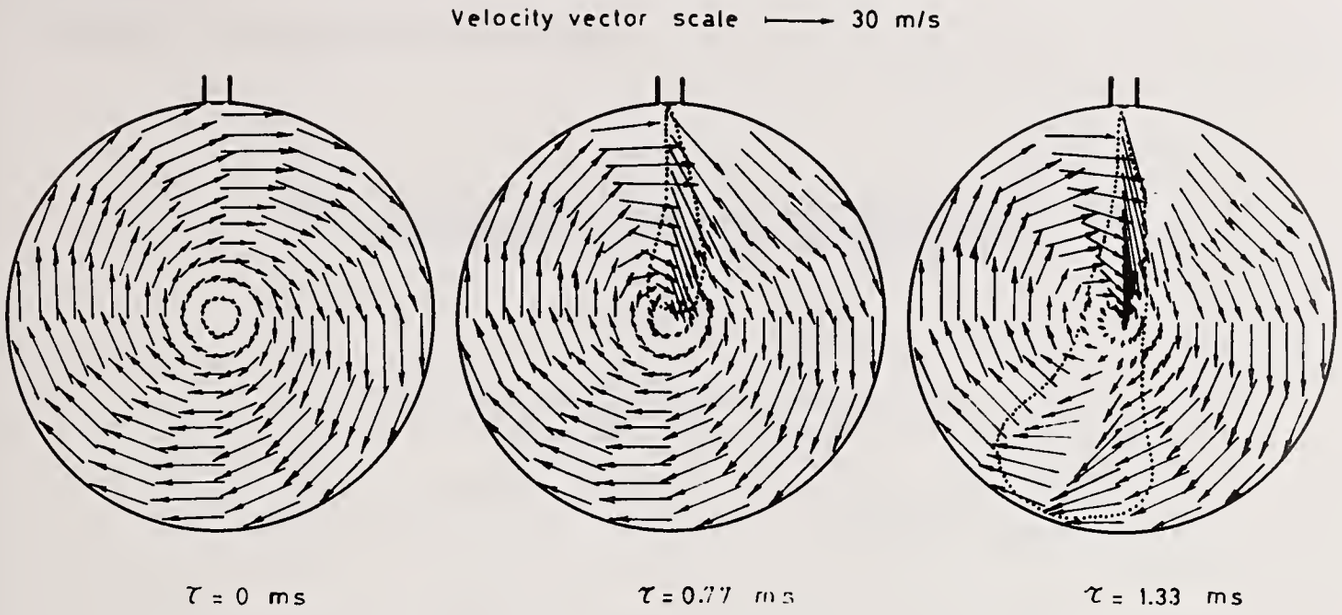

Fig. 5 Effect of spray penteration on the air field, ω = 1135 rad/s and P_{inj} = 40 bar

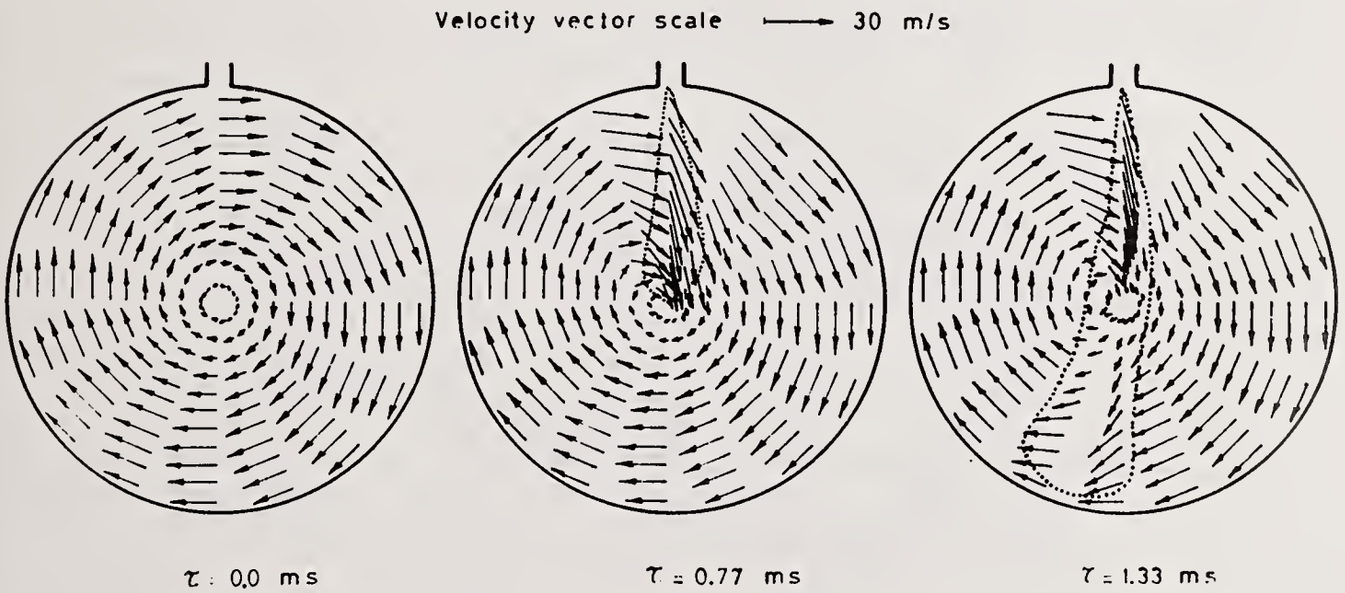

Fig. 6 Effect of spray penetration on the air field, ω = 749 rad/s and P_{inj} = 40 bar

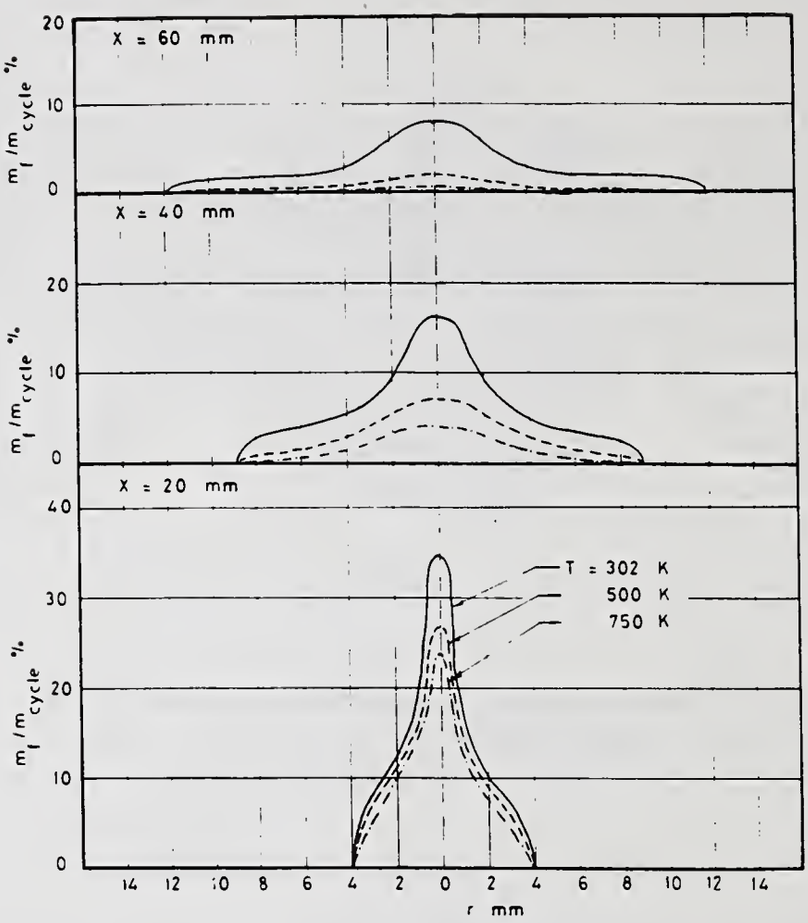

Fig. 7 Effect of ambient temperature on the fuel concentration at different cross section, P_{inj}= 120 bar and P_b= 5 bar

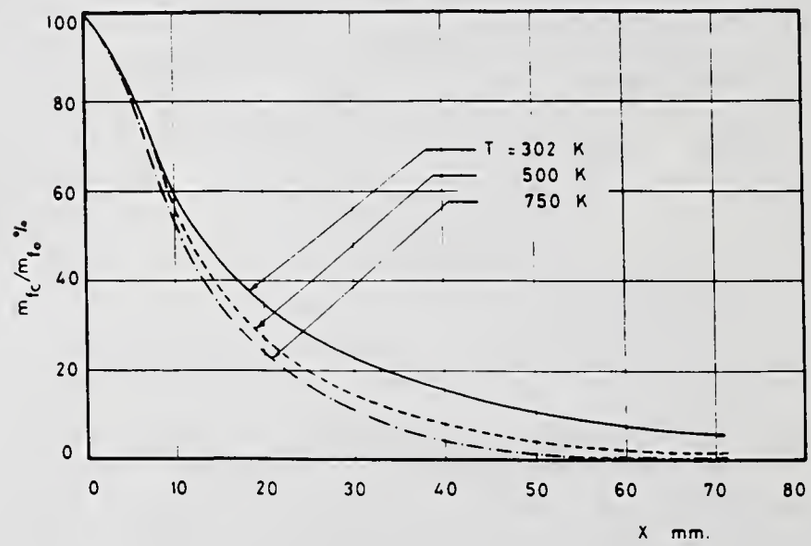

Fig. 8 Effect of ambient temperature on the spray concentration along the spray centerline, P_{inj}= 120 bar and P_b= 5 bar

STUDY OF AN AIR BLAST COAXIAL ATOMIZER EXPERIMENTS AND MODELISATION

I. Care and M. Ledoux

URA CNRS 230/CORIA - University of Rouen
Mont Saint Aignan, France

ABSTRACT

A coaxial air blast atomizer as used in rocket cryogenic engines has been experimentally and theoretically studied. Structure of the spray, map of spray sizes, evolution of air velocities and liquid have been investigated. A model is given to predict drop sizes (SMD), spray angles, and skimming kinetics (atomisation). This model is assessed by present experiments and datas from previous Diesel sprays studies.

INTRODUCTION

Air blast atomization is widely used. In cryogenic rocket engines (like HM7 engine of european rocket Ariane) atomization of a liquid (or supposed so) jet of oxygen is achieved by a gaseous coflowing hydrogen flow. Structure of such a pulverisation is studied here through experiments and modelisation.

In such pulverisation devices great relative velocities between gas and liquid lead to a skimming of the surface : an attempt will be done here to calculate both size and number (skimming kinetics) of drops formed. The problem presents many similar features with Diesel injection. Present results should then find an application in this field.

EXPERIMENTS

Apparatus

The atomization of a liquid cylindrical flow of initial radius a_o by a surrounding annular air flow of lateral dimension h has been achieved through a device described on figure 1. Particular attention has been paid to axisymmetry (non swirling) of both flows. Three configurations have been studied (A to C). Table on fig.1 give details.

Water and kerosene have been used as substitutes to O_2. Velocity of liquids U_L was 1.4m/s. Air was used as atomizing fluid. Velocities U_G were varied from 100 to 220m/s at the nozzle exit.

Photographic (short time -10μs- and long time exposure) investigation

were achieved as well as LDV (for air), and Malvern spray sizing.

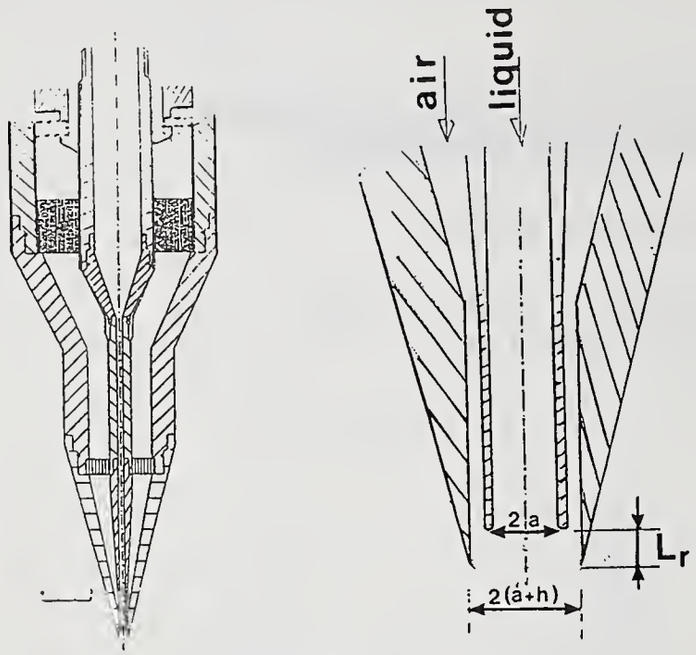

Atomizer	a (mm)	h (mm)	L_R (mm)
A	1.95	0.53	0.
B	1.95	0.53	2.5
C	1.95	0.93	0.

Figure 1
The atomizer

Different procedures of enlightening of the spray may show the liquid core or the fine (scattering) spray.

Dimensions of the experimental set-up are representative as well as relative velocities of those encountered on real rocket engines.

Structure of the spray is shown on scheme (Fig.1)

Near the nozzle an atomization zone (fine spray) takes place. The radius a(x) of the liquid is then decreasing downstream. The skimming of this surface is not sufficient to atomize completely the liquid, then a second zone of coarse pulverisation is found. All present study will be confined to first atomization zone.

Short time exposures show presence of large (order of a/2) structures in the atomization zones. Owing to the very small structures of instability leading to drop formation ($\Lambda/2$) long exposure time photographs have been used for determination of a time-mean decrease of liquid core

Experimental results

Following parameters have been measured :

-Radial profiles of drop sizes (given in terms of SMD values) at different abcissas x.Malvern 2600 particle sizer was used. Due to axisymetric structure an inversion process, similar to that of Gomi [2] has been employed [1].

-Mean air velocity fields around a solid cone simulating the liquid cone.

-Photographic investigation of liquid cone shape (measurement of a(x).

Injection parameters are U_G, σ, h, L_R

Some results are shown on figures 2,3 and 4.

Similar to Gomi's results [2] one can observe a radial increase of SMD's from surface to external part of spray. This can be explained by inertial effects of drops : greater droplets have greater response time

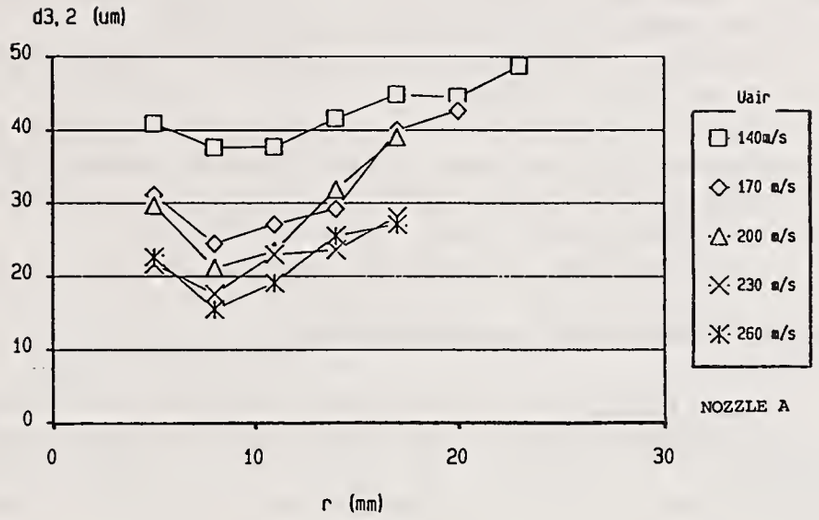

Figure 2 :
The radial evolution of SMD at x=30mm from the nozzle

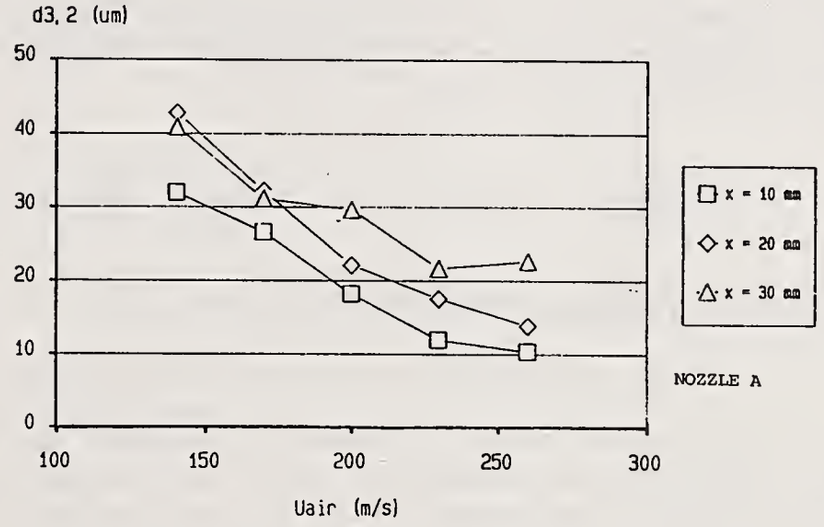

Figure 3
Influence of air velocity U_G on drop sizes at different downstream positions

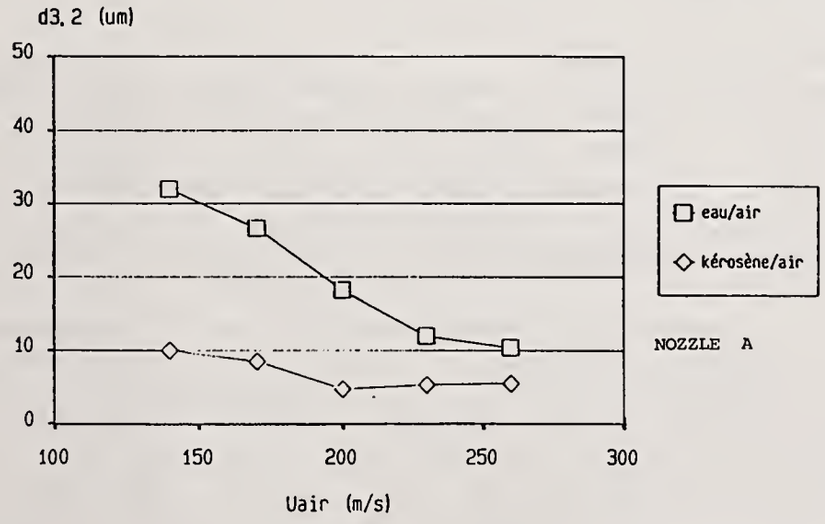

Figure 4
Influence of surface tension

$\tau \propto d^2$) and keep their radial velocity on a greater distance. Smaller drops are immediatly entrained by the gas.

A smaller surface tension leads to smaller drops (reduction of the stabilizing effect of σ).

According to following atomization theory, increase of ΔU leads to smaller droplets (increase of the destabilizing effect of ΔU).

Comparison between configuration A and B shows that an increase of L_R leads to higher drop sizes. (not shown here).

A complete set of results will be found in [1].

MODELISATION OF THE ATOMIZING ZONE

Drop size away from the surface ($r > 5mm$) can be influenced by several factors : 1) Aerodynamical effects quoted above. 2) Secondary atomization (breakup of drops by high velocity air stream). So calculations will be attempted here only for measurement made near the surface.

The authors developed previously a complete linear model of the instability of a (swirling) liquid jet in a (swirling) coflowing air current [1]. Due to high relative liquid-air velocities this model is in fact asymptotic to the classical Kelvin-Helmholtz theory for capillary waves at a simple interface. The dominant wavelength Λ of maximum growth Ω is then found [1].

$$\Lambda = \frac{3\pi\sigma}{\rho_G \Delta U^2} \qquad (3.1) \qquad \Omega = \frac{2\rho_G \Delta U^3}{3\sqrt{3}\,\sigma} \left[\frac{\rho_G}{\rho_L}\right]^{1/2} \qquad (3.2)$$

and the propagation velocity of the wave c is :

$$c = (\rho_G U_G + \rho_L U_L)/\rho_L \sim U_L \text{ according to } \rho_G/\rho_L = 0(10^{-3}) \qquad (3.3)$$

From Λ and Ω one can deduce different parameters of the atomizing zone : SMD, (initial) angle of spray cone, skimming kinetics. Here we have to deal with two aspects of pulverisation : non linearity at breakup and polydispersion. This can be achieved in a simplified way.

Drop diameters : determination of SMD

The wave is sinusoidal only in its initial part. Then the perturbation has the form : $\eta = \eta_o \exp \Omega t \exp i(Kx - \omega_r t)$ where $\omega_r = kc$. The velocity of the crest is $d\eta/dt = \Omega\eta$ where d/dt is a Lagrangian derivative. One assumes that, at breakup, the wave has the form of a cylindrical ligament of diameter $\Lambda/2$ (non linear theory of Nayfeh [3] gives an insight of this) and amplitude $A\Lambda$ where A is an unknown constant.

In reality atomization results in a spectrum of drops of diameters d_i-N_i being the number of drops of diameter d_i formed, one can write the conservation of mass for a ligament

$$\sum N_i\, d_i^3 = 3A\,\Lambda^3/8 \qquad (3.4)$$

One can also conserve surface tension energy $\Sigma\, N_i d_i^2 = A\Lambda^2$ (3.5)

SMD is defined as : $d_{32} = \sum N_i d_i^3 / \sum N_i d_i^2$ (3.6) Unknown constant A is then eliminated, and some effect of polydispersion is included in definition of d'_{32} : $d_{32} = 3/4\Lambda$ (3.7)

Mean number of drops formed by ligament is then of order A : $N=(8/9)/A$ (3.8)

Skimming kinetics

An important parameter, not yet found at our knowledge in the litterature, is the mass flow rate of drops teared off by unit surface. This is needed to predict the evolution of the diameter of the liquid cone.

The number dN_G of drops formed on a length dx of liquid cone during dt can be written :

$$d^2N_G = C_1 \frac{64\ \pi\ A\ a}{9\ t_r\ \Lambda^2}\ dx\ dt \qquad (3.9)$$

where a(x) is the local diameter of the cone and t_r the lifetime of a ligament. C_1 is an unknown constant (or assumed so).

Many authors write [8] : $t_r = C_2/\Omega$ (which is equivalent to : $\eta_{rupture}/\eta_o = \exp C_2$).

$$\text{Then } d^2N_G = \frac{64}{9}\frac{\pi_a}{\Lambda^2}\frac{C_1 A}{C_2}\Omega\ dr\ dt \qquad (3.10)$$

From a mass balance in the liquid core, assuming that the liquid velocity U_L is constant :

$$\rho_L\ \pi\ U_L\ 2a\ \frac{da}{dx}\ dx\ dt = \rho_L\ \frac{\pi}{\sigma}\ d_{32}^3\ d^2N_G \qquad (3.11)$$

So : $da/dx = -C\ \Omega\Lambda/U_L$ (3.12)

Here constant C, found equal to $0.78\ \frac{AC_1}{C_2}$ is introduced to summarize all unknowns A, C_1, C_2...).

In case of total atomization, a length cone L_c could be calculated :

$$L_c = \left\{2\sqrt{3}\ a_o U_L / 9\pi c \Delta U\right\}\ (\rho_L/\rho_g)^{1/2} \qquad (3.13)$$

This expression can be compared to expressions obtained by Cheroudi [6] and Arai [7] , in the case of Diesel sprays : $L/d = c'\ [\rho_L/\rho_g]^{1/2}$ (3.14)

Initial spray angle

Following an idea proposed by Reitz [4] and Chigier [5] the initial spray angle θ can be deduced from the velocity vector $\vec{V}$ of drops teared off from the surface. The axial component of V is U_L and the radial component can be identified with $d\eta/dt$.

Using relations (3.1) and (3.2) one finds :

$$\operatorname{tg}\frac{\theta}{2} = \frac{2\pi A \Delta U}{\sqrt{3}\ U_L}\left(\frac{\rho_G}{\rho_L}\right)^{1/2} = A\,\frac{\Lambda\Omega}{U_L} \qquad (3.15)$$

Some comparisons can be made with studies of Diesel sprays found in the litterature.

Reitz [9] found a relation of the form : $tg\theta/2 = 0.188\ \Lambda\ \Omega/U_L$ leading to A = 0.188.

Reitz and Diwakar [10] found experimentally : $\operatorname{tg}\frac{\theta}{2} = 0{,}7\left(\frac{\rho_G}{\rho_L}\right)^{1/2}$

Also can be quoted similar expression by O'Rourke and Amsden [11] and Ranz [12].

Taking A = 0.188 (Reitz) one founds : 0.68 instead of 0.7 four our atomizer. In the case of Diesel sprays $\Delta U \sim U_L$ and the result is consistent with the constant 0.7 of Reitz and Diwakar.

ASSESSMENT OF THE MODEL

Determination of SMD

Calculating SMD was possible only for the vicinity of the surface (owing to secondary atomization and aerodynamic effects at r > 5mm). A comparison is shown on fig.6 between experimental and calculated values for water and kerosene. A pretty good agreement is found.

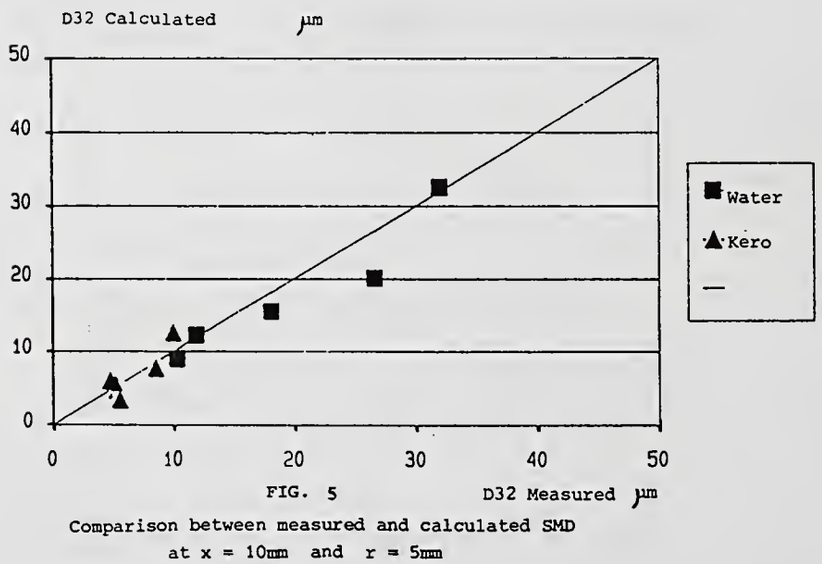

FIG. 5
Comparison between measured and calculated SMD
at x = 10mm and r = 5mm

U_G m/s	$-\frac{da}{dx}$	C	$-\frac{da}{dx}$	C
1 23	0.35	0.022	0.53	0.029
1 47	0.27	0.014	0.50	0.023
1 70	0.41	0.018	0.36	0.014
1 95	0.38	0.015	0.50	0.017
2 20	0.44	0.015	0.50	0.015

TABLE 1

Determination of C

From (3.12) C can be deduced from measurement of da/dx. As the liquid core is not too far from a cone (U_L, Ω and Λ varying too fast) da/dx can be deduced from photographs. Results are shown on table 1 -for water and kerosene jets-. More extended experiments should be needed to assess C as a constant, but if assumed so (which is not too unrealistic) C is found here equal to $1.8.10^{-2}$ with a standard deviation of $0.5.10^{-2}$.

Let's remark that with A = 0.188 and C_2 of order 10 (as assumed by

many authors [8] C_1 is of order 0.5 - 1.

We did not succeded to determine accurately initial angle from photographs (fine spray limits are difficult to appreciate) but an order of 0.15 for A could be deduced from some views.

CONCLUSION

The experimental study of a coaxial air blast atomizer showed a complex structure. Particular attention was paid to atomization zone (fine spray). A model of atomization in this zone presented here allows the determination of the particle sizes (SMD) near the surfaces, the length of the liquid cone (or the evolution of radius of this zone when atomization is not completed), the skimming kinetics and the initial spray angle.

A more complete determination of the spray should involve : 1)Aerodynamic in the fine spray zone as well as the secondary atomization. 2)The dynamical behaviour of the non-atomized liquid core and its break-up, which in practical cases, may lead to coarse pulverisation and a bad combustion quality.

Nomenclature

a	radius of the liquid jet
C	skimming kinetics constant
k	wave-number = $2\pi/\lambda$
r	radial coordinate
U_G	velocity of gas (air)
U_L	velocity of liquid
x	axial coordinate
η	instability
σ	surface tension
Λ	dominant instability wavelength
Ω	dominant instability growth coefficient

BIBLIOGRAPHY

[1] CARE I. - Etude d'un injecteur coaxial assisté. Ph.D Thesis Rouen. Dec.1990

[2] GOMI H. - Pneumatic atomization with coaxial injectors. Ph.D Thesis Sheffield. 1984.

[3] NAYFEH A.H. - Phys. Fluids 1970, 1970, vol.13 (4), p.841-847.

[4] REITZ R.D., BRACCO F.V. - Phys. Fluids 1982, vol.25 (10), p.1730-1742.

[5] RUIZ F., CHIGIER N. - The mechanics of high speed atomization Iclass 1985 proceedings.

[6] CHEROUDI B., CHEN S.H., BRACCO F.V., ONUMA Y. - SAE Paper 850 126. 1985.

[7] ARAI M., TABATA M., HIROYASU H., SHIMIZU M. - SAE Paper 840 275. 1984.

[8] DOMBROWSKI N., HOOPER P.C. - Chemical engineering Science, Vol.17, 1962, p. 291-305.

[9] REITZ R.D. - Atomization and spray technology 1987, Vol.3, p.309-337.
[10] REITZ R.D., DIWAKAR R.- SAE Paper 870 598, 1987.
[11] O'ROURKE P.J., AMSDON A.A. - SAE Paper 872 089, 1987.
[12] RANZ W.E. - Canadian J. of Chem. Engineering, 1958, p.175-181.

CHARACTERIZATION OF A LOW FLOW RATE/HIGH CHARGE DENSITY ELECTROSPRAY

A. Gomez and K. Tang

Department of Mechanical Engineering
Yale University
New Haven, CT, U.S.A.

ABSTRACT

Detailed measurements of droplet size and velocity distributions by phase Doppler anemometry were performed in a low-flow-rate/high-charge-density electrospray of methanol, producing micron-size droplets. Complementary information was also obtained by pulsed shadowgraph imaging of the spray break-up. When the spray was operated in the so-called rainbow mode, characterized by the emission of high order Tyndall spectra under white light illumination, small droplets were generated with average diameter of the order of 2 μm and narrow size and velocity distributions. Both velocity and electric field monotonically decrease as function of the distance from the thin jet formed at the liquid meniscus, where the field is most intense. Electric fields as high as 10^6 V/m were achieved in this spray. Velocity-diameter correlations showed that the charge to volume ratio varies approximately with the inverse of the square of the droplet diameter. Coulomb explosion is unlikely to play any role in the formation of this spray.

INTRODUCTION

One of the simplest implementation of an electrospray consists of a small metal tube maintained at several kilovolts relative to a ground electrode few centimeters away. If a liquid of sufficient electric conductivity is fed into the tube, its meniscus at the outlet of the capillary takes a conical shape under the action of the electric field, with a thin jet emerging from the cone tip. This jet breaks up a short distance downstream into a fine spray of charged droplets, which, under certain conditions, may have a possibly narrow droplet size distribution. In fact, almost forty years ago some observations of High Order Tyndall Spectra were reported in the scattering of white light by "smokes" produced in electric dispersion of liquids (1,2). This optical phenomenon is indicative of droplet formation of narrow size distribution in the size range 0.1-2 μm (3). Whereas studies, both experimental and theoretical, of the electrohydrodynamic phenomena leading to the formation of the liquid conical meniscus have been reported (4-9), no quantitative measurements of droplets sizes in this regime have been reported to date, with the exception of some recent work of Fernandez de la Mora et al. (10) on the generation of submicron monodisperse aerosols in

electrosprays of glycerol. Consequently, it is in the area of the spray formation that we have concentrated the initial efforts discussed here.

The selection of the spray was motivated by the following consideration: electrosprays of water/methanol solutions operated in the same conditions as in the present study are used to ionize very effectively large macromolecules of biological interest, which are subsequently introduced in a mass-spectrometer. This approach is bringing about a revolution in the field of mass-spectrometry, as documented by the pioneering work of Fenn's research group at Yale (11), and has resulted in probably the only *practical* application of this type of electrospray to date. A preliminary account of part of this work was presented elsewhere (12).

EXPERIMENTAL METHODS

Methanol at a flow rate of 0.003 cc/min was fed into a stainless steel metal capillary (I.D.≅0.20 mm) by a syringe pump. The tube was maintained at a voltage of about 3 kilovolts relative to a ground electrode positioned 3 cm away. In a typical experiment, while methanol was pumped through the system, the voltage applied to the capillary was progressively increased until a diffuse spray of very fine droplets was formed, which under white light illumination exhibited the characteristic Tyndall Spectra. At these operating conditions, hereafter referred to as *rainbow* mode, detailed single point measurements were taken throughout the spray by a commercial Phase Doppler Anemometer (Dantec Electronics), which yielded simultaneous inference of droplet size and axial velocity distribution, as well as size-velocity correlation. Some pulsed shadowgraph imaging of the spray break-up was also attempted. The total magnification of the system (≅ 800X) did not permit a quantitative use of the images; nevertheless, some qualitative features of the break-up were observed. Further details on the imaging technique are given by Gomez and Tang (13). The system electrical behavior was monitored by connecting the virtual ground plate to an oscilloscope, thereby recording the current collected by the electrode. All experiments were performed at ambient temperature and atmospheric pressure.

RESULTS AND DISCUSSION

Characteristic size and velocity distributions of the methanol spray operated in the rainbow mode are shown in Fig. 1. The size distribution appear roughly symmetric, with a remarkably small ratio of standard deviationover mean diameter of 0.13. This result already shows the electrospray capability to generate narrowly disperse droplets with a size two orders of magnitude smaller than the diameter of the spray orifice. Clogging problems that characteristically prevent monodisperse aerosol generators from operating in this size range can be circumvented by following this approach. The velocity distribution is even narrower than the size distribution, suggesting that at a given location the velocity is essentially independent of particle size; this finding can be exploited to infer information on droplet charge density, as shown below.

The spray evolution was probed in both axial and radial scans. As a validation of the Phase Doppler Anemometer measurements, total mass conservation was verified within about 14% by integrating droplet average size and velocity over the spray radius, at a fixed axial coordinate, and comparing the result with the metered liquid flow rate.

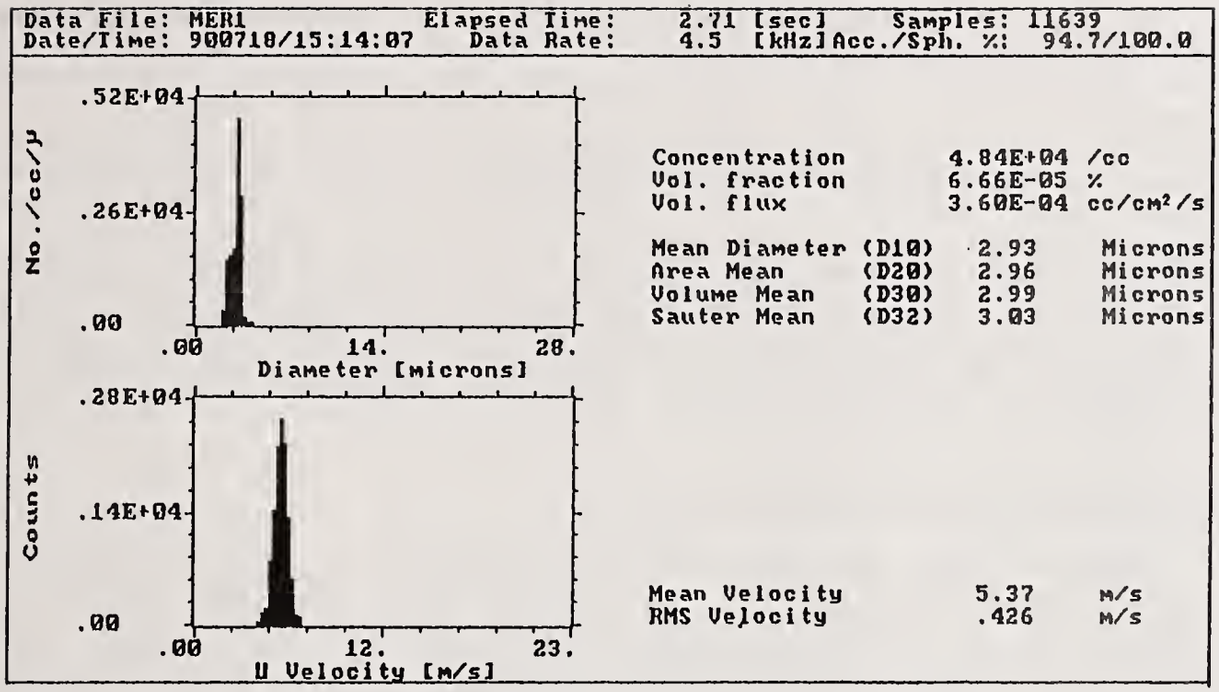

Fig. 1: Representative size and velocity distribution

Jet break up

Qualitative aspects of the spray break-up were investigated by pulsed shadowgraph. It was observed that under the rainbow mode of operation: i) the liquid exits the cone formed at the outlet of the charged capillary as a thin, stable thread that persists for a short distance; ii) this ligament then breaks up into an array of droplets; iii) droplets move downstream and are displaced radially because of coulombic repulsion from neighboring droplets, thereby leaving a wavy "signature" under pulsed illumination; iv) once displaced radially, droplets tend to follow diverging lines of field because of both relatively small inertia and high charge to mass ratio, as shown below. They eventually form a fan which coincides with the visible electrospray. Figure 2 is a digitized picture showing some details of the break up, as discussed in ii) and iii). Because of limitations in the resolution of both imaging system and PDA no further probing was possible to see if satellite droplets were generated at break-up as observed in sprays of larger droplets (13). However, a rough comparison is still possible, at least on the basis of average quantities. In particular, it is interesting to address the question of Coulomb explosion which occurs when the so-called Rayleigh limit is attained and electrostatic repulsive forces overcome surface tension forces.

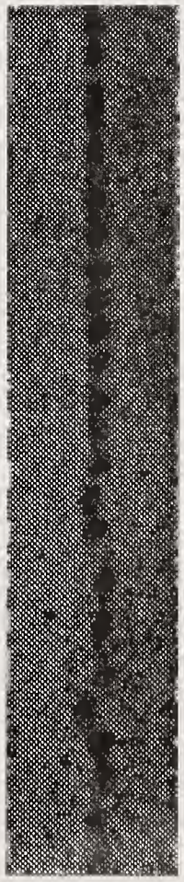

Fig.2

This process inevitably takes place at some point during the droplet evaporation, since there is experimental evidence that charge remains attached to the droplet while it is evaporating (14). The question is if this mechanism determines or, at least, contributes to the droplet dispersion and the resulting spray formation. In a related study on electrostatic sprays of heptane quite similar to the one examined here, except for the fact that they produced larger droplets (13), we showed that there is no evidence of Rayleigh disruption in this type of electrospray if the average charge to mass ratio is below about 60% of the Rayleigh limit. This methanol electrospray has a high charge density of 6.2 10^{-4} C/cc, which however corresponds to only about 35% of the Rayleigh limit based on an average diameter. This observation and the similarity of the break up patterns observed in the two studies suggest that, in analogy with the heptane sprays, Coulomb explosion is not occurring in the probed region of the spray.

Velocity and Electric Field Evolution

Figure 3 shows the average droplet diameter and average axial velocity component measured along the axis of the jet, with the origin of the coordinate system taken at the capillary outlet. The spray shows a diameter monotonically decreasing as function of the axial coordinate, as a result of evaporation effects. Monotonically decreasing diameters are also observed when scanning the spray in the radial direction. These observations are consistent with the visual observation of Tyndall spectra, which are typically attributed to monodisperse aerosols in the (0.1-2 μm size range) (3). The velocity also monotonically decreases along the axis, from around 26 m/s to about 4 m/s in the scanned region. Thus, the liquid is first rapidly accelerated in the conical meniscus into a thin jet, that breaks up into a stream of droplets, which in turn rapidly decelerate to the measured velocities.

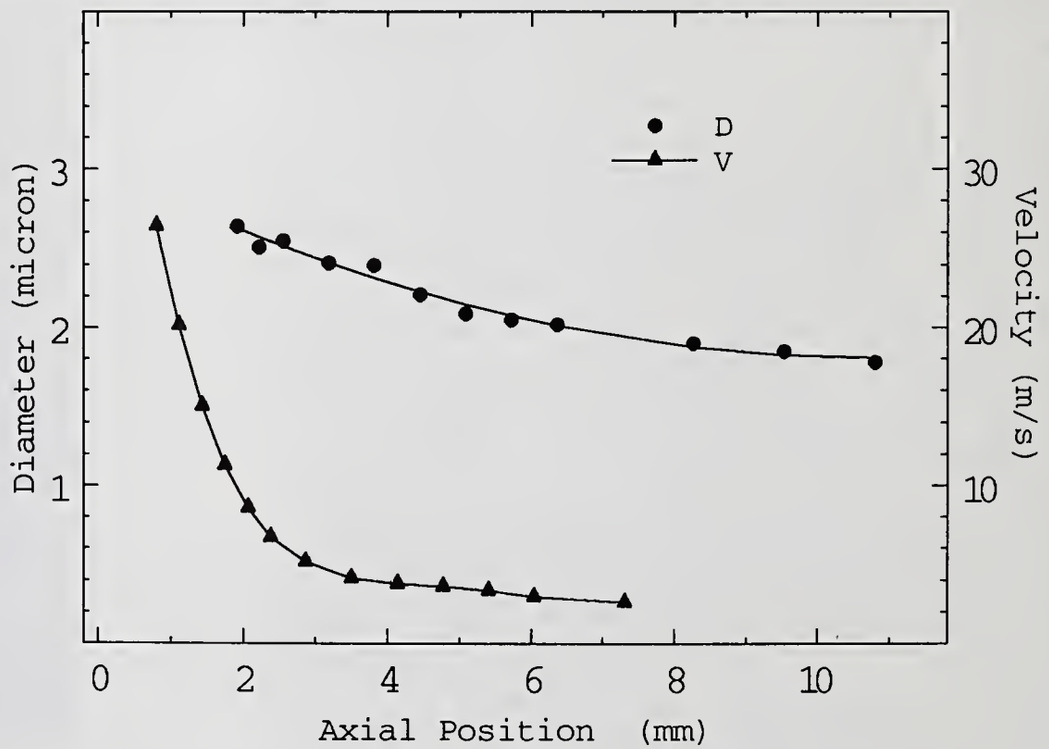

Fig. 3: Average diameter and axial velocity component versus axial coordinate

To understand this behavior, let us consider the equation of motion of an isolated droplet under the action of electrostatic, gravitational and drag forces:

$$\rho_d \frac{\pi d^3}{6} \frac{d\vec{V}}{dt} = \frac{\pi d^3}{6} (\rho_d - \rho_g)\vec{g} + n_e e\vec{E} - c_D \frac{Re}{24} (1+0.158Re^{2/3})\, 3\pi\mu d(\vec{V} - \vec{V_g}) \tag{1}$$

where at the left hand side of the equation is the inertia term with a lagrangian derivative, and the right hand side terms are the gravitational term, the electrostatic force and the droplet drag, respectively. Here, V is the velocity, d, the droplet diameter, n_e denotes the number of charges per droplets, e is the elementary charge, E is the electric field, Re is the Reynolds number, C_D is the drag coefficient and $V-V_g$ is the relative velocity between the droplet and the surrounding gas. Under steady state condition, the time derivative equals the convective derivative, which, evaluated on the centerline of the spray, is given by $V_z \partial V_z/\partial z$. An order of magnitude analysis yields negligibility of the gravitational term. Since the Reynolds number is O(1), the drag force can be approximated to the Stokes formula by setting $c_D=24/Re$. We will also assume negligible gas velocity, i.e. $V_g \cong 0$, which amounts to neglecting the gaseous entrainment in the otherwise stagnant atmosphere were the spray discharges. Thus, the axial component of the equation above reduces to

$$\rho_d \frac{\pi d^3}{6} V_z \frac{\partial V_z}{\partial z} \cong n_e e E_z - (1+0.158Re^{2/3})\, 3\pi\mu d V_z \tag{2}$$

Since size and velocity are known, from eq. 2 we can try to infer the local electric field, which is very important for the determination of limits of operation of the electrospray, for spray modelling and can also help future analyses of the complex electrohydrodynamics in the liquid meniscus. To this end, a value for n_e can be obtained from

$$n_e e = \frac{I}{Q} \frac{\pi d_0^3}{6} \tag{3}$$

where I is the total measured current, Q is the volume flow rate and d_0 is the volume average droplet diameter as measured at the very beginning of the spray. Substituting eq. (3) into eq. (2) and solving for E_z, we obtain

$$E_z(z) = \frac{Q\,6}{I\pi d_0^3} \cdot \left[\rho_d \frac{\pi d^3}{6} V_z \frac{\partial V_z}{\partial z} + (1+0.158Re^{2/3})\, 3\pi\mu d V_z \right] \tag{4}$$

The resulting electric field is plotted in Fig. 3. Electric fields of the order of 10^6 V/m are generated, with the strongest field near the breakup region of the spray, as expected since the liquid ligament can be regarded as a "sharp point", which, as is well known, is surrounded by very intense fields when charged at a high potential. The velocity profile is also superimposed on the same plot. Notice that when the inertia term in eq. 4 can be neglected, which holds true everywhere in the spray except in the initial

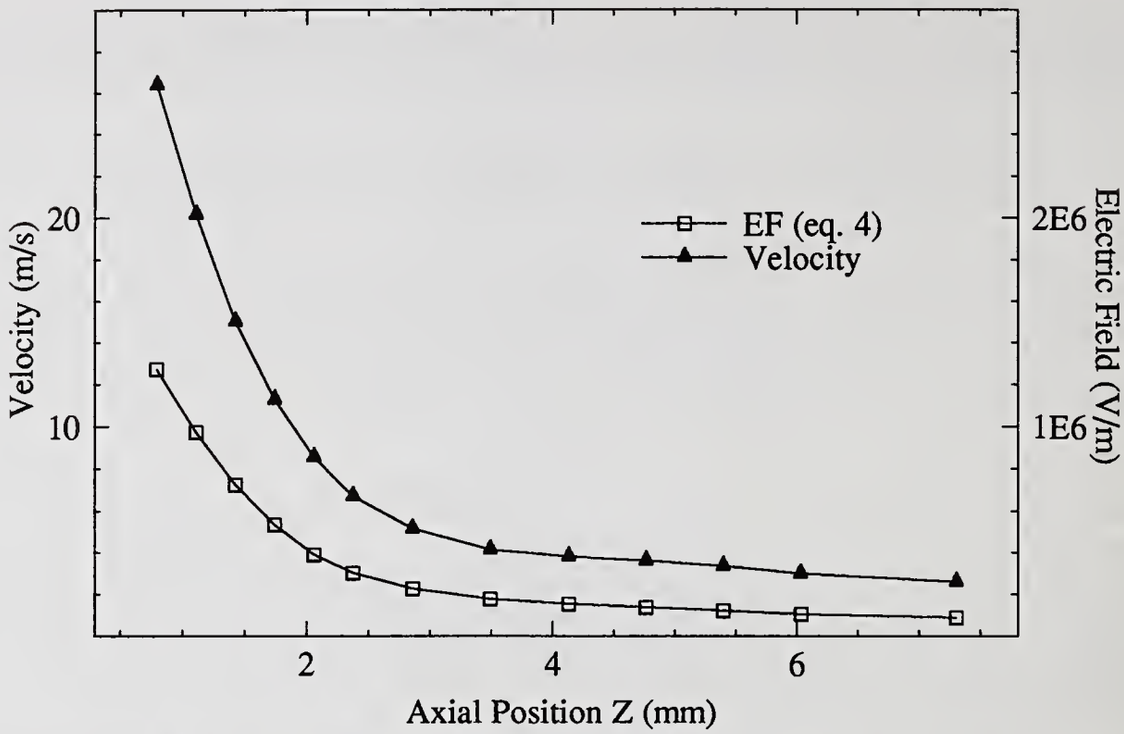

Fig. 4: Average droplet velocity and electric field along the spray axis.

region where the deceleration is most rapid and the velocity gradient high[2], eq. 2 reduces to a balance between electrostatic force and drag. Consequently, the reason why droplets rapidly decelerate is that once generated at the jet break-up they relax within a short distance to the local terminal velocity which roughly decreases as the electrostatic field. The field calculated by this procedure is the total field acting on the droplet and accounts for both the external field applied between capillary and ground electrode as well as the "internal" field due to the coulomb interaction between charged droplets.

Charge Density

From local simultaneous measurements of size and velocity distribution, we can also gather information about charge density. Figure 5 shows the size/velocity correlation as obtained with the PDA at a typical location along the spray axis, where both the inertia term and the Reynolds number correction to the drag term in eq. 2 are negligible. The velocity is essentially uniform, regardless of particle size. Eq. 2 reduces her to

$$n_e e E_z \cong 3\pi\mu d V_z \qquad (5)$$

[2]Estimates of the Stokes number, defined as the ratio of a droplet relaxation time over characteristic flow time (15), yielded values between 10^{-1} and 10^{-4}, indicating the negligibility of inertia over most of the spray region.

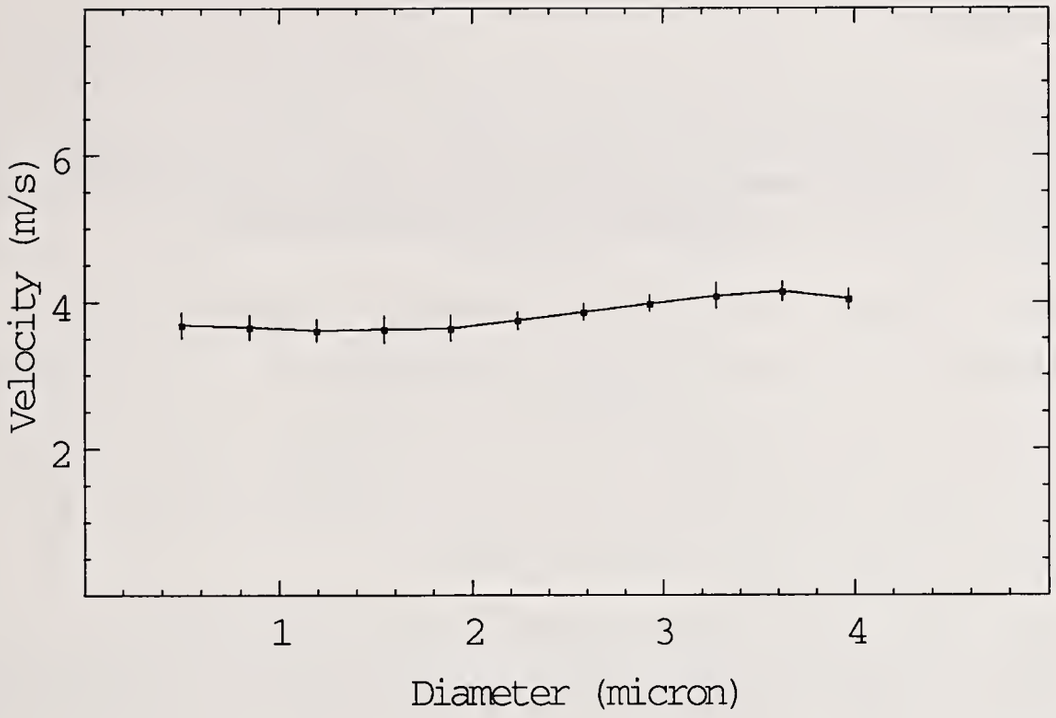

Fig. 5: Typical velocity-size correlation.

At a given location, the electric field is constant and the velocity is essentially independent of droplet size, as per Fig. 5. Consequently, $n_e \propto d$ and the charge to volume ratio should scale as the inverse of the square of the diameter.[3]

CONCLUSIONS

Detailed measurements of droplet size and velocity distributions were performed along the axis of a low flow rate/ high charge density electrospray of methanol, producing micron-size droplets. The following conclusions can be drawn from these measurements:

1) When the spray is operated in the rainbow mode, corresponding to the emission of Tyndall spectra under white light illumination, small droplets are generated with average diameter of the order of 2 μm and narrow size and velocity distributions;

2) Both velocity and electric field monotonically decrease as function of the distance from the thin jet formed at the liquid meniscus, where the field is most intense. Electric fields as high as 10^6 V/m were determined;

3) Velocity-size correlation showed that charge to mass ratio varies approximately with the inverse of the square of the droplet diameter.

4) Coulomb explosion is unlikely to play any role in the formation of this spray.

---

[3]This dependence was independently confirmed by deconvolving the total current measurement, as well as size and velocity measurements obtained in a radial scan. This approach also confirmed that the charge to mass ratios are substantially below the Rayleigh limit in the probed region.

ACKNOWLEDGMENTS

We are indebted to Profs. J. B. Fenn and J. Fernandez de la Mora, for many stimulating discussions and helpful comments. Thanks are also due to Dantec Electronics for allowing us to use their particle measurement systems in extensive laboratory demonstrations. This research was in part supported by an NSF Equipment Grant #CBT-8806608 and a NASA Grant #NAG3-1259.

REFERENCES

1. Vonnegut, B. and Neubauer, R.L., *J. Colloid Sci.*, **7**, p.616 (1952).

2. Vonnegut, B. and Neubauer, R.L., *J. Colloid. Sci.*, **8**, p.551 (1953).

3. van de Hulst, Light Scattering by Small Particles, Wiley, 1957.

4. Zeleny, J., *Phys. Rev.*, **10**, p.1 (1917).

5. Taylor, G.I., *Proc. Roy Soc. Lond. A*, **313**, p.453 (1969).

6. Hayati, I., Bailey, A.I. and Tadros, Th. F., *J. Colloid. Interface. Sci.*, **117**, p.205 (1987a).

7. Hayati, I., Bailey, A.I. and Tadros, Th. F., *J. Colloid. Interface. Sci.*, **117**, p.222 (1987b).

8. Smith, P.H., *IEEE Trans. Industr. Appl.*, **IA-22**, p.527 (1986).

9. Turnbull, R.J., *IEEE Trans. Industr. Appl.*, **IA-25**, p.699 (1989).

10. Fernandez de la Mora, J., Navascues, J., Fernandez, F. and Rosell-Llompart, J., *J. Aerosol Sci.*, **21**, Suppl. 1, p. 673 (1990).

11. Fenn, J.B., Mann, M., Meng C.K., Wong, S.F. and Whitehouse, C.M., *Science*, **246**, p.64 (1989).

12. Gomez, A. and Tang, K.,"*Characterization of Liquid Fuel Electrostatic Sprays*", Paper presented at the Western States Section/The Combustion Institute 1990 Fall Meeting, La Jolla CA.

13. Gomez, A. and Tang, K., "*Atomization and Dispersion of Quasi-monodisperse Electrostatic Sprays of Heptane*", Proceedings of the Fifth International Conference on Liquid Atomization and Spray Systems, ICLASS-91, Gaithersburg, MD, U.S.A., 1991.

14. Abbas, M.A. and Latham, J., *J. Fluid Mech.*, **30**, p.663 (1967).

15. Fuchs, N.A., The Mechanics of Aerosols, Dover, 1964.

CHARACTERIZATION OF THE SPRAY STRUCTURE OF A LARGE SCALE H.F.O. ATOMIZER

G. De Michele, M. Graziadio, F. Morelli and G. Novelli

ENEL-C.R.T.N., Pisa, Italy

ABSTRACT

The spray produced by a large scale h.f.o. Y-jet nozzle has been characterized in cold conditions using simulating fluids and two different laser instruments (diffraction and phase-doppler techniques). The study has been carried out to obtain a detailed spray description to be utilized in the prevision of combustion performances.

It has been found that some important variations of the spray structure cannot be completely described using only mean spray parameters, such as mean drop diameter and velocity. For this reason, in addition with the mentioned values, the analysis has also regarded the spray angle and the position of the largest drops in the cross section.

All variations of spray structure have been interpreted with reference to different fluidynamic regimes inside the nozzle. General relationships have been obtained which allow the spray quality to be predicted, as well as the spatial position of larger drops in the spray cone.

INTRODUCTION

Y-jet atomizers are widely employed in power stations due to the versatility of operation and reliability. Notwithstanding their extensive use, the number of published works on this class of atomizers are relatively few [1-4].

An extensive work on burner development, at the Nuclear and Thermal Research Center (C.R.T.N.) of ENEL (the Italian Electricity Generating Board), has included research carried out to characterize a Y-jet nozzle in many different operating conditions. The work has allowed the definition of correlations between input parameters and spray characteristics.

EXPERIMENTAL APPARATUS

Test rig and atomizer

The atomization rig "I.S.A." employed during the tests has been described elsewhere [4]. The rig is operated by using a mineral oil which at 30°C has the same physical and rheological properties as h.f.o. in industrial burners. Compressed air is used to simulate the atomizing steam.

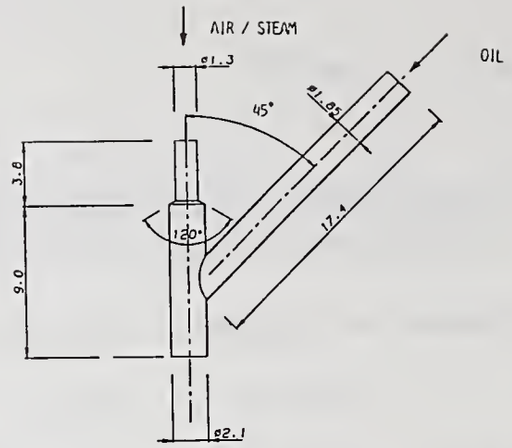

Fig. 1 Geometry of the atomizer 1Y-45-55-49.

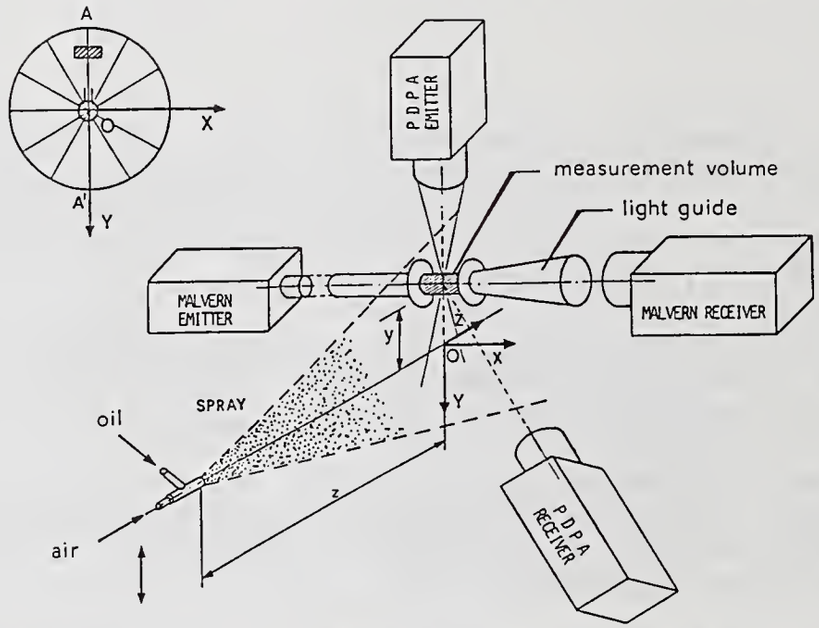

Fig. 2 Relative position of the laser instruments and the atomizer.

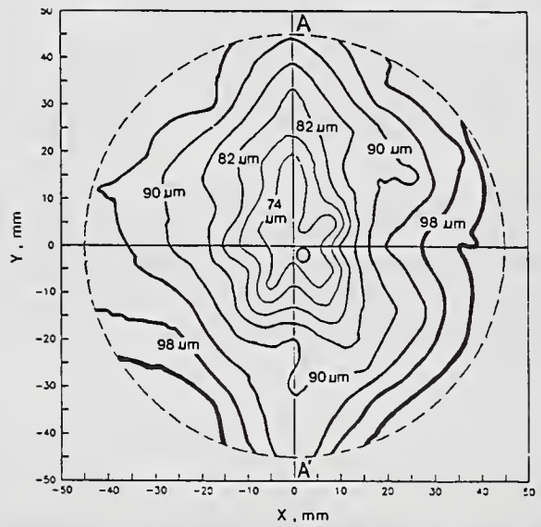

Fig. 3a Interpolation maps of Dv0.5 on the spray cross-section.

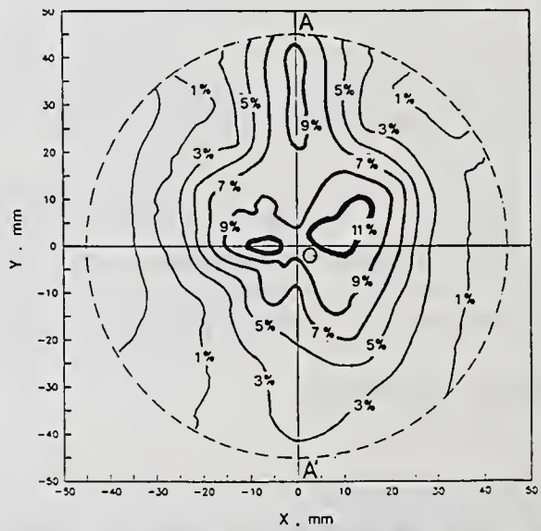

Fig. 3b Interpolation maps of the percentage of drops larger than 225 μm.

The trials have been carried out with a single port Y-jet atomizer labelled 1Y-45-55-49. The Y-duct geometry, shown in Fig. 1, is the same characterizing an industrial multi-hole nozzle used with the following conditions (for each Y-duct):

Wo = 0.050 Kg/s Po = 1.4 MPa Ps = 1.15 MPa

Measurement technique

The spray quality is measured using a Malvern 2600 D particle sizer, while the drop velocity is obtained with an Aerometrics PDPA. The optical arrangement of the instruments is shown in Fig. 2. To reduce the obscuration during the trials with the Malvern analyzer, two light guides are employed.

A reference X-Y-Z coordinate system is defined with the Z axis orthogonal to the laser beam and coincident with the axis of the outlet port. The oil port lies in the Z-Y plane on the negative Y side. All trials are carried out with Z = 250 mm, by moving the nozzle while the laser instruments are fixed.

EXPERIMENTAL RESULTS

Evaluation of mean spray characteristics

The evaluation of mean spray characteristics on a fixed cross-section requires the measure of local diameters and velocities followed by an integration based on droplet concentrations. This procedure is time consuming, except when the spray is axisymmetric [5].

To verify this possibility, the present investigation has started with the complete spray mapping at nominal conditions Wo=0.050 Kg/s and Pa = 1.15 MPa. Granulometric measurements have been obtained with the Malvern on six equispaced diameters on the cross-section (Fig. 2) and, using these data, drop size maps have been calculated.

Figure 3a shows the map of mass median diameters. The dropsize isocontours are slightly asymmetric around 0 (Z axis). This result is confirmed by the map of the percentage of drops larger than 225 μm, shown in Fig. 3b.

The asymmetric structure of the spray is in agreement with other results obtained by ENEL with Y-jet nozzles of different geometry [4]. Due to the lack of spray axisymmetry, the study of Y-jet nozzles at different operating conditions is prohibitive if the above-mentioned mapping is used.

Figures 3a and 3b however suggest that a simplified calculation of mean spray quantities can be obtained by evaluating the means only on A-A′. The highest values of drop size distribution, in fact, are often found near diameter A-A′ as a consequence of its position in the plane Y-Z of the oil and outlet ports [4]. For this reason A-A′ can be utilized to detect the main spray asymmetries and to evaluate rapidly mean diameters which never underestimate the spray quality all over the cross-section. This simplified approach has been adopted in the spray characterization described in the following section.

Spray characterization

The spray characterization has been carried out with Wo = 0.050, 0.047, 0.041, 0.036, 0.030, 0.025, 0.019 Kg/s; at each flowrate the nozzle has been operated with Pa = 1.15, 1.0, 0.9 and 0.8 MPa. In this way, 28 different operating conditions have been studied by measuring the spray quality over A-A′

The Dv0.5 profiles at different oil flowrates and the same air pressure are shown in Fig. 4. The variation of volume concentration C with Y has the same trend. Both profiles demonstrate that, at a fixed air pressure, the liquid

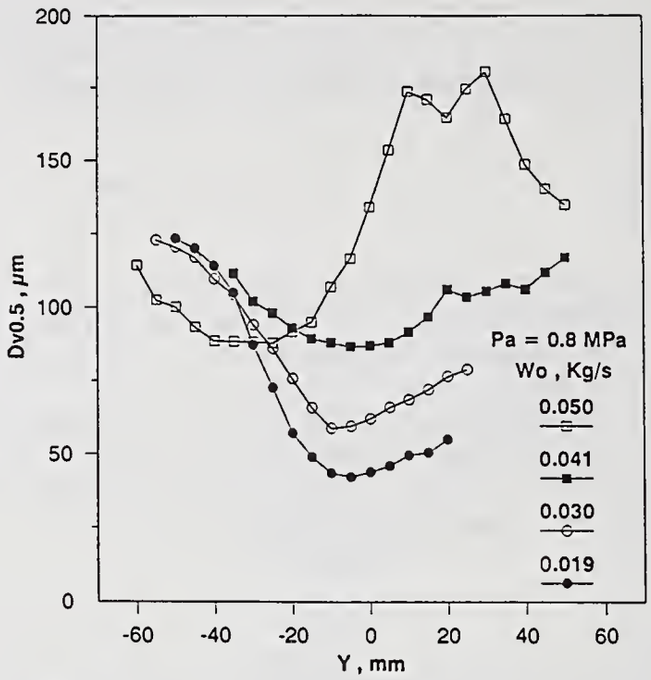

Fig. 4 Dropsize profiles along Y-direction at different oil flowrates.

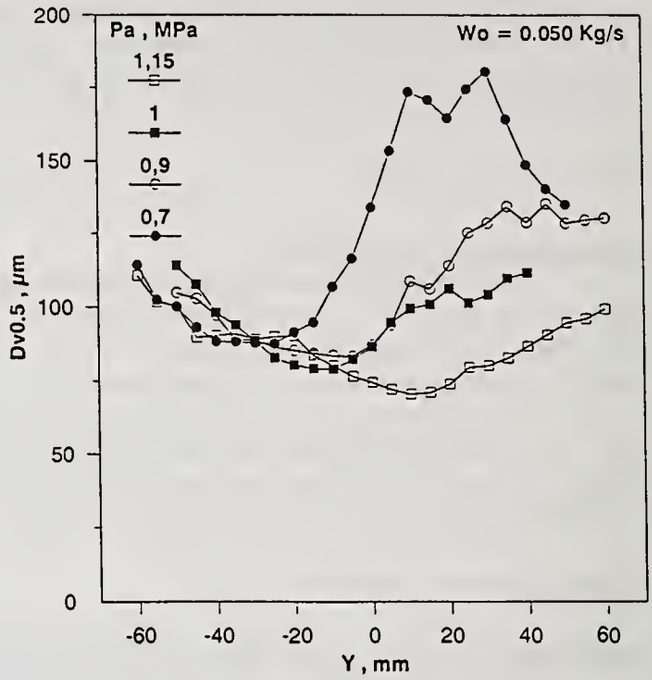

Fig. 5 Dropsize profiles along Y-direction at different air pressures.

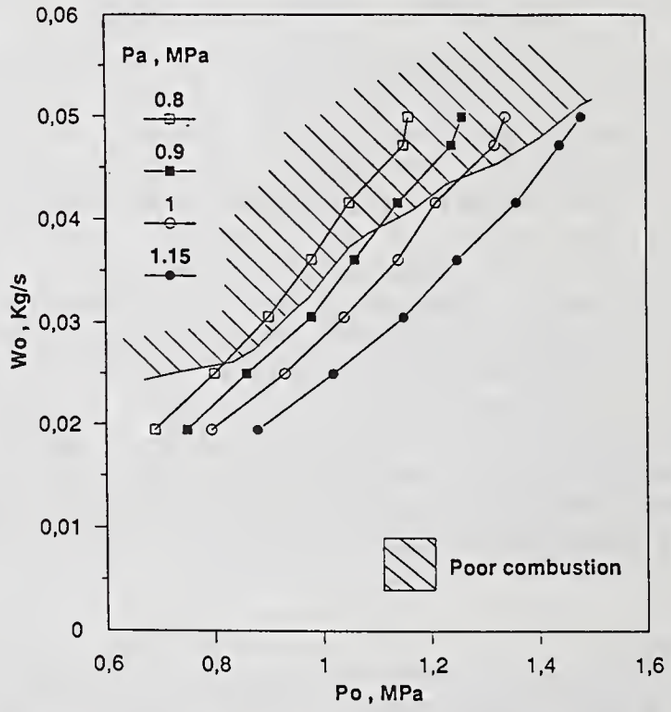

Fig. 6 Optimum operating range of atomizer 1Y-45-55-49.

flowrate strongly influences the spatial position of the largest drops in the cross section and consequently the liquid mass spatial distribution.

Using the Aerometrics PDPA, it has been found that the velocity profile varies with Wo, but there are no pronounced asymmetries as those existing in the case of drop diameters.

When the liquid flowrate is fixed, the atomizing air pressure influences the spray structure, as shown in Fig. 5. In this case the velocity profiles are slightly asymmetric.

ANALYSIS OF THE EXPERIMENTAL RESULTS

Definition of the nozzle operating range

The atomizer operating range has been examined in order to define a zone of good performance in real combustion trials.

For this scope a mean spray diameter Dv0.5 M has been calculated in each condition and compared to that of nominal operation (Wo = 0.050 Kg/s, Pa = 1.15 MPa). By the exclusion of the conditions corresponding to diameters higher than the reference, an optimum combustion zone has been defined, Fig. 6.

However, the mean drop diameter is not the only factor determining good combustion performance, and other spray parameters (such as liquid fluxes and spray momentum) must be considered.

Figure 7 shows, for instance, the shapes of opposing sprays in the case of a multi-port atomizer with several Y-ducts similar to the one studied. Each spray angle has been drawn in accordance with the dropsize profiles found for the 1Y-45-55-49 nozzle, assuming no interaction between adjacent sprays and no deflection induced by combustion air. Two operating conditions are shown in Fig. 7, each corresponding to an acceptable mean spray diameter. Notwithstanding that, the inner and outer spray angles and the location of drops larger than 225 μm are strongly influenced by input conditions, thus probably giving different combustion performance for the two cases.

Prevision of spray characteristics

An attempt has been made to correlate input data with the mean spray quality and the spatial location of the largest drops in the cross section.

The values of Dv0.5 M have been related with flow conditions using the relationship proposed by Lefebvre [6]:

$$Dv0.5\ M/D = A \cdot We^{-0.5} + B \cdot Zo \qquad (1)$$

The coefficients A and B of (1) can be evaluated only if the atomizing air mass flowrate Ga and the mean pressure Pm in the Y-duct are known, thus allowing the calculation of We.

In the present case Ga has been measured while Pm has been evaluated using the relationship:

$$\frac{G_A^2}{K} \ln \frac{P_1}{P_2} + \frac{K}{K+1} \frac{P_1}{v_1} \left[\left(\frac{P_2}{P_1} \right)^{\frac{(K+1)}{K}} - 1 \right] + \frac{F}{2} G_A^2 = 0 \qquad (2)$$

which has successfully proved to describe the pressure losses in the exit port of Y-jet nozzles [7]. Using this approach the following relationship has been obtained:

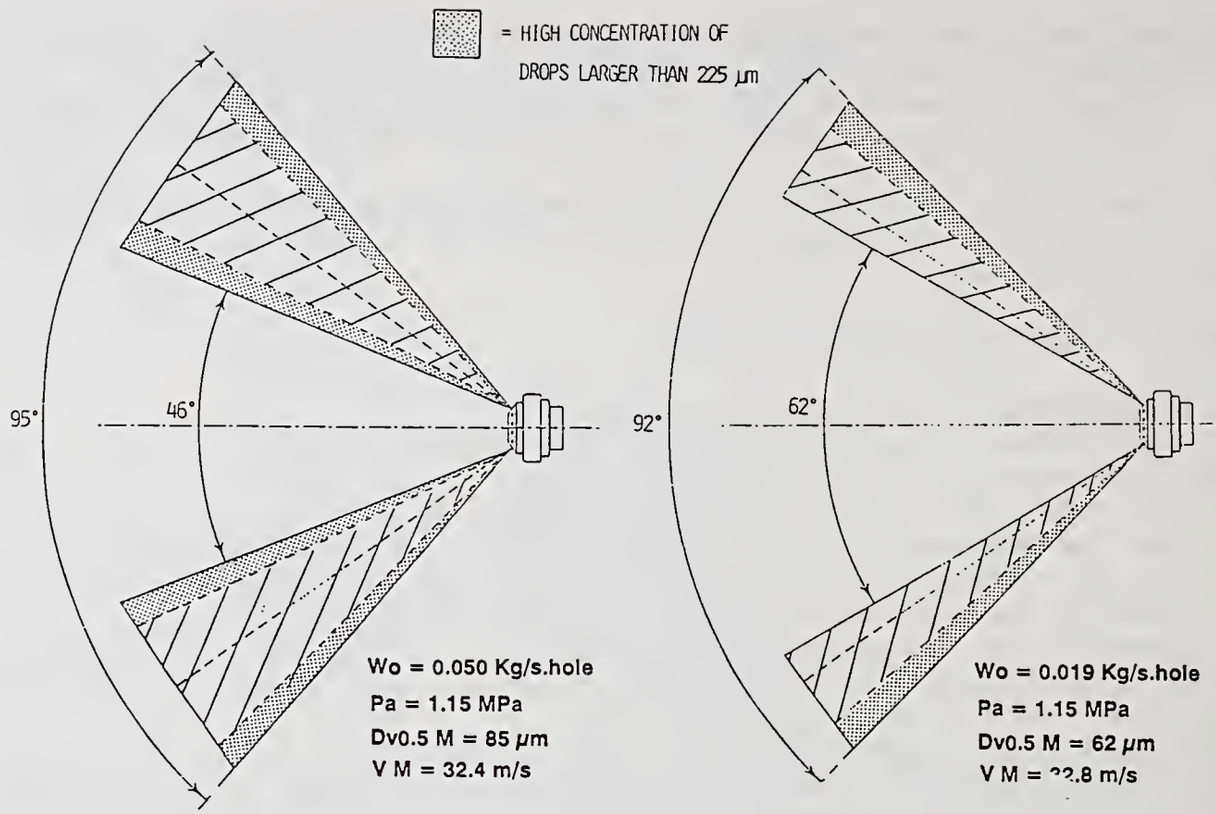

Fig. 7 Variation of spray structure with oil flowrate.

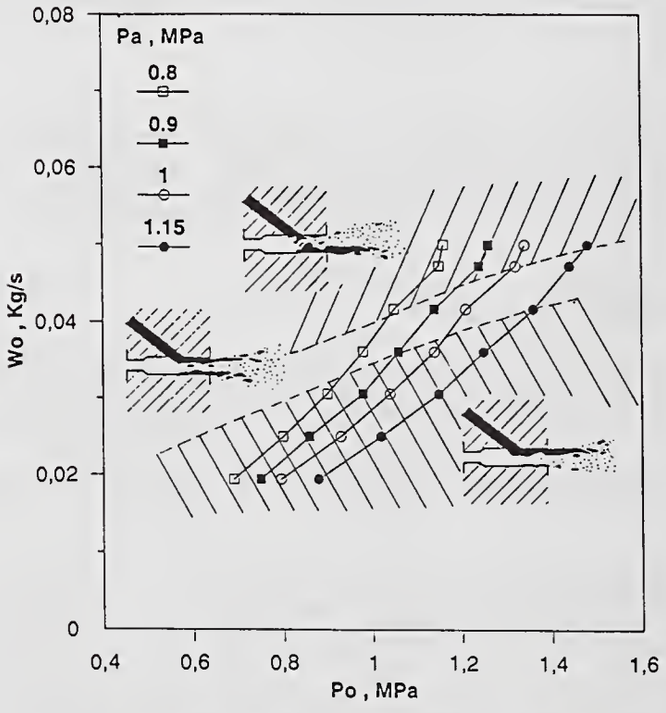

Fig. 8 Relationship between the flow regime in the nozzle and input conditions.

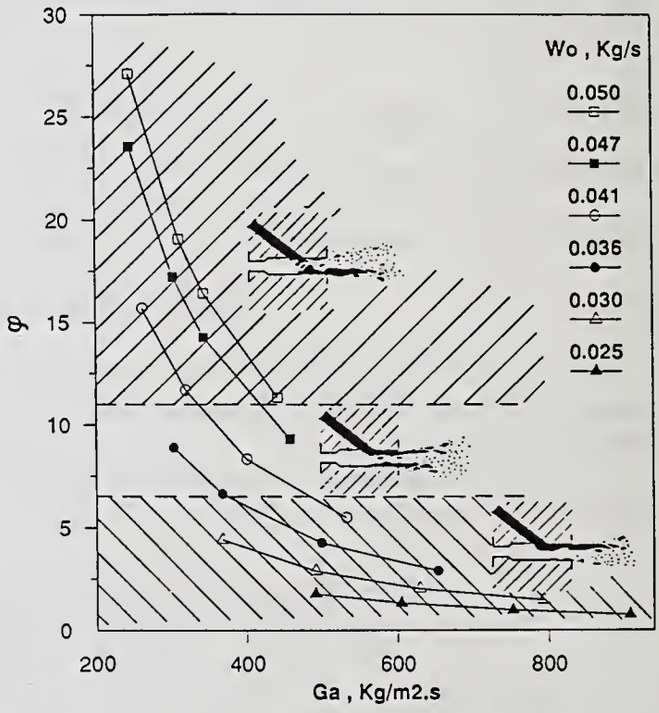

Fig. 9 Liquid jet lateral momentum, normalized with respect to the gas axial momentum, plotted versus the gas mass velocity.

$$Dv0.5\ M/D = 0.75 \cdot We^{-0.5} + 0.34 \cdot Z_o \qquad (3)$$

The values of coefficients (A = 0.75 and B = 0.34) are slightly different from those calculated in [7]. The differences could derive from scaling effects and/or from inadequacies in the evaluation of Pm.

The spatial position of the largest drops in the cross section mainly depends on the presence of liquid films in the atomizer exit port [4]. Figure 8 shows that this approach allows, in the test case, the determination of three different operating zones.

An interpretation of the spray regimes can be done by considering the ratio between the liquid momentum and the atomizing air axial momentum [4]:

$$\varphi = \frac{G_O^2\ D_O^2}{G_A^2\ D_A^2}\ \frac{\rho_A}{\rho_O}\ \sin\vartheta \qquad (4)$$

The dimensionless parameter has been evaluated by estimating Pm as shown before. Figure 9 shows as a function of Ga for all input conditions. It can be noticed that, when Ga is constant, varies with Go due to the different lateral momentum of the liquid and the different of air.

If each operating point is related to the corresponding liquid film regime, as reported in Fig. 8, it appears that the parameter can be usefully employed to predict both the liquid film position and the spatial drop distribution.

CONCLUSIONS

The following conclusions can be made:

- The atomizer 1Y-45-55-49 can be operated at oil flowrates that are different from the nominal ones, provided that the operating conditions remain within the range of Fig. 6. This optimum zone has been defined solely by the comparison of dropsize data with those of nominal operation.

- The input variables influence not only the mean spray quality but also the spray angle and the location of the largest drops in the spray cross section. As these parameters can be important for combustion performance, the influence of input data on the total spray structure must always be considered in order to predict the operating region of full scale nozzles.

- Predictive correlations have been obtained for the drop diameter and the location of largest drops in the spray. These correlations will be systematically tested in future developments using different Y-jet geometries and conditions.

NOMENCLATURE

A, B	Coefficients
C	Volumetric concentration
D	Diameter of the mixing duct
Do	Diameter of the oil port
Dv0.5	Mass median diameter
F	Frictional loss coefficient
G	Mass velocity
k	Coefficient of polytropic expansion
P	Pressure
V	Velocity
v	Specific volume
W	Mass flowrate
We	Weber number
X,Y,Z	Cartesian coordinates
Zo	Ohnesorge number
ϑ	Angle between fuel and mixing duct
ρ	Density
φ	Ratio between liquid and gas momentum
a	Air
o	Oil
s	Steam
m	Mean
M	Mean on A-A', Fig. 2
1,2	Inlet and outlet sections

REFERENCES

1. Mullinger, P.J., Chigier, N., Jour. Inst. Fuel, Vol. 47, pp. 251-261 (1974).
2. Bryce, W.B., Cox, N.W., Joyce, W.I., ICLASS '78, paper 10-4, Tokyo (1978).
3. Prasad, K.S.L., ICLASS '82, paper 4-3, Madison (1982).
4. De Michele, G., Graziadio, M., Novelii, C. Giacomelli, A., Andreussi, P., 9th IFRF Members Conf., Noordwijkerhout (1989).
5. Andreussi, P. Tognotti, L. Graziadio, M. De Michele, G. Aerosol Sci. and Techn., Vol. 13, pp. 35-46 (1990).
6. Lefebvre, A.H., Prog. En. Comb. Sci. Vol. 6, pp. 233-261 (1980).
7. Andreussi, P., Graziadio, M., Novelli, G., Tognotti, L., ICIASS Europe '90 Meet, pp. 115-124 (1990).

CHARACTERIZATION AND PERFORMANCE OF SPRAY NOZZLES FOR WATER DISTRIBUTION IN COOLING TOWERS

L. Tognotti*, S. Zanelli*, B. Bellagamba†, F. Mattachini† and G. Lotti†

*Dipartimento Ingegneria Chimica, Universita' di Pisa, Pisa, Italy
†ENEL-CRTN, Pisa, Italy

ABSTRACT

An experimental study has been carried out on the water distribution system of a pilot cooling tower of 160 m^3/hr . The performances of different industrial water distributors have been evaluated by changing the operative conditions of the pilot tower. In particular, the efficiency and the uniformity of the water distribution have been investigated and compared with the results obtained in a small-scale loop, in which the single nozzles were tested. Measurements in both systems, pilot tower and small scale loop, included the geometric characteristics of the jet umbrella by ensemble photography, the wetted zone by measuring the specific flowrate, the drop-size distribution and liquid concentration by high-speed photography. The results show that correlations exist between the nozzle behaviour in single and pilot tower configuration. The uniformity of water distribution in the pilot tower is strongly related to the nozzle installation pattern and to the operative conditions. Coalescence plays an important role on the drop size distribution in the pilot-tower. Comments upon the influence of these parameters on tower behaviour are also included.

INTRODUCTION

The distribution of water to the top of counterflow fill of cooling towers is a key aspect for the performance of the whole cooling system. It is a function of nozzle design and installation, height of the spray zone and the structural cleanliness of the spray chamber. The impact of water distribution on performance is a combination of uniformity of water distribution, air-side pressure drops, and heat transfer in the spray zone (1).

As the matter of fact, simulation of cooling tower behaviour by means of a two-dimensional code (2) showed that drop size distribution in spray zone plays an important role in tower performances.

In spite of its practical importance, the water distribution process has not been studied enough. In this work different nozzles were studied in a pilot tower of 160 m^3/hr and in a single-nozzle small-scale loop in order to find out the parameters to be measured in evaluating the water distribution performances. On the basis of the results, some performance parameters have been defined and evaluated, which can be related to heat transfer and pressure drops in the spray zone of a cooling tower.

EXPERIMENTAL

Two different experimental loops were used in this work. A small scale circuit was employed in order to study the behaviour of each single nozzle, while the effect of nozzle installation pattern on tower performance has been

tested in a pilot-tower of 160 m^3/hr potentiality (3). In the small-scale loop, a single nozzle was studied by measuring the liquid specific flowrate and the drop size distribution (4,5).
In the small scale circuit, a single nozzle was mounted under a reservoir with controlled and adjustable head, and measurements were carried out on the jets or sheets produced by the single nozzle. Measurements included the geometric characteristics of the jet umbrella by photographing the whole jet, the wetted zone by measuring the liquid specific flowrate, the drop-size distribution and liquid concentration by high-speed photography (fig.1)

The pilot tower has been described in (2). The liquid flowrates tested were: 220, 160 and 100 m^3/hr, maximum, nominal and minimum loading, respectively. The air mean velocities through the tower were 1, 2.5 and 3.5 m/s, in order to consider the typical conditions of natural and forced draught towers

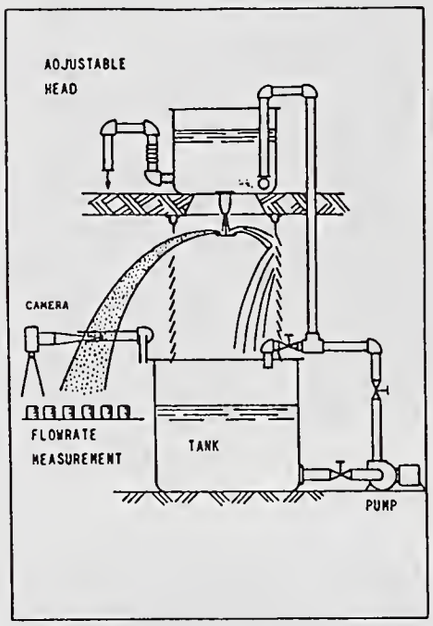

Fig.1: Small scale experimental loop

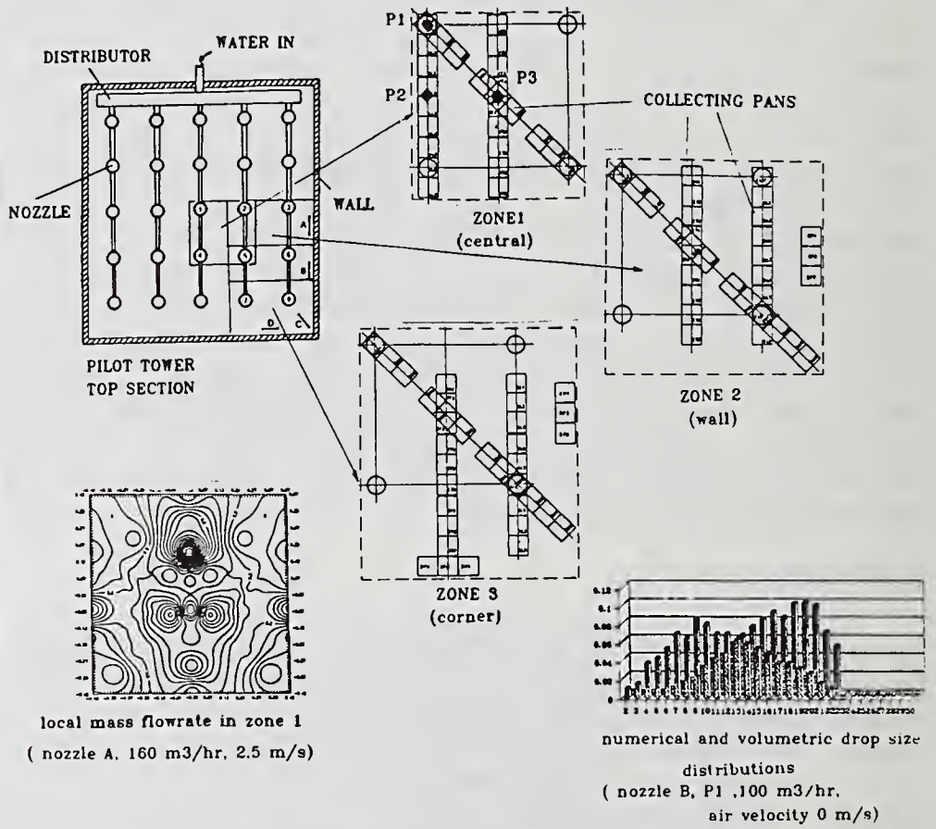

Fig.2: Measurement stations in pilot-tower and examples of local flowrate and drop size results

Figure 2 shows the configuration of the local flowrate measurement stations on the top of the packing. They have been chosen in order to completely characterize three different configurations of water distribution: central zone, wall zone and corner zone (1,2 and 3 in Fig.2). The liquid flowrate has been measured collecting the water in small vessels placed as described in Fig.2. The spray characterization has been performed, by means of high-speed photography, in three points (P_1, P_2 and P_3 in Fig.2) inside the zone 1, at the centre of the packing. A 50 mm macro lens has been used, which gave a magnification of 0.475 and a distance of 23.5 cm from the lens to the best focus zone, with a depth of field of about 5 cm. About 500 drops have been classified and counted for each flow configuration, in order to evaluate

statistically representative parameters of drop size distribution.

Four commercial nozzles were tested. Table I reports the main characteristics of the nozzles. In small-scale experiments the adjustable head (Fig.1) was chosen in order to provide the pilot-tower nominal loading for each nozzle (1.77 Kg/s) Nozzle D was tested, in the single configuration, with an half of the nominal flowrate, since it needed a hydraulic head not feasible in the small-scale loop.

TABLE I

Single nozzle characteristics

NOZZLE	CHARACTERISTICS	NOZZLE DIAMETER (cm)	STANDARD HEAD (cm)	SPECIFIC MASS FLOWRATE (kg/s)
A	plate cone with carves	3	50	1.77
B	three cones	3.2	50	1.6
C	plate with edges	2.6	100	1.72
D	elicoydal structure	4.8	100	0.75

RESULTS AND DISCUSSION

Small scale experiments

Visual and photographic observation of the jet, as well as the measurement of the specific mass flow rate, allow the complete characterization of the jet from a macroscopic point of view. It is possible to evaluate:

- size of the umbrella produced by the nozzle;
- the wetted zone under the nozzle at a certain distance from the nozzle (in this case 1.8 m);
- the zones of the jet formed by coherent liquid (as ligaments or sheets), the breakup zone and the spray zone.

Figure 3 shows some ensemble photographs of the jets produced, while Fig.4 shows the results of the macroscopic characterization for nozzles A and B.

Nozzle A produces single cylindrical jets with different initial angle respect to the horizontal. These jets are produced by carves of different geometry in the nozzle plate. The jet breakup takes place in the initial zone, due to the initial perturbations produced by nozzle vibrations. The specific flowrate changes with 0 (see Fig.4).

Nozzle B produces three paraboloidal umbrellas of different size. The size of each sheet decreases as the umbrella enlarges, forming ligaments and then drops, of size of the same order of magnitude of the ligament size (6), as shown in Fig.5. Figure 4 shows the geometry of the jet and the specific flowrate q at 1,3 m as a function of the distance from the nozzle axis

Nozzle C produces single jets, but narrower than those produced by nozzle A.

Nozzle D forms a swirling paraboloidal sheet, breaking up immediately outside the nozzle (fig.3).

As already pointed out, two different breakup mechanisms are recognizable for the jets investigated. Nozzles A and C present cylindrical jets which produces

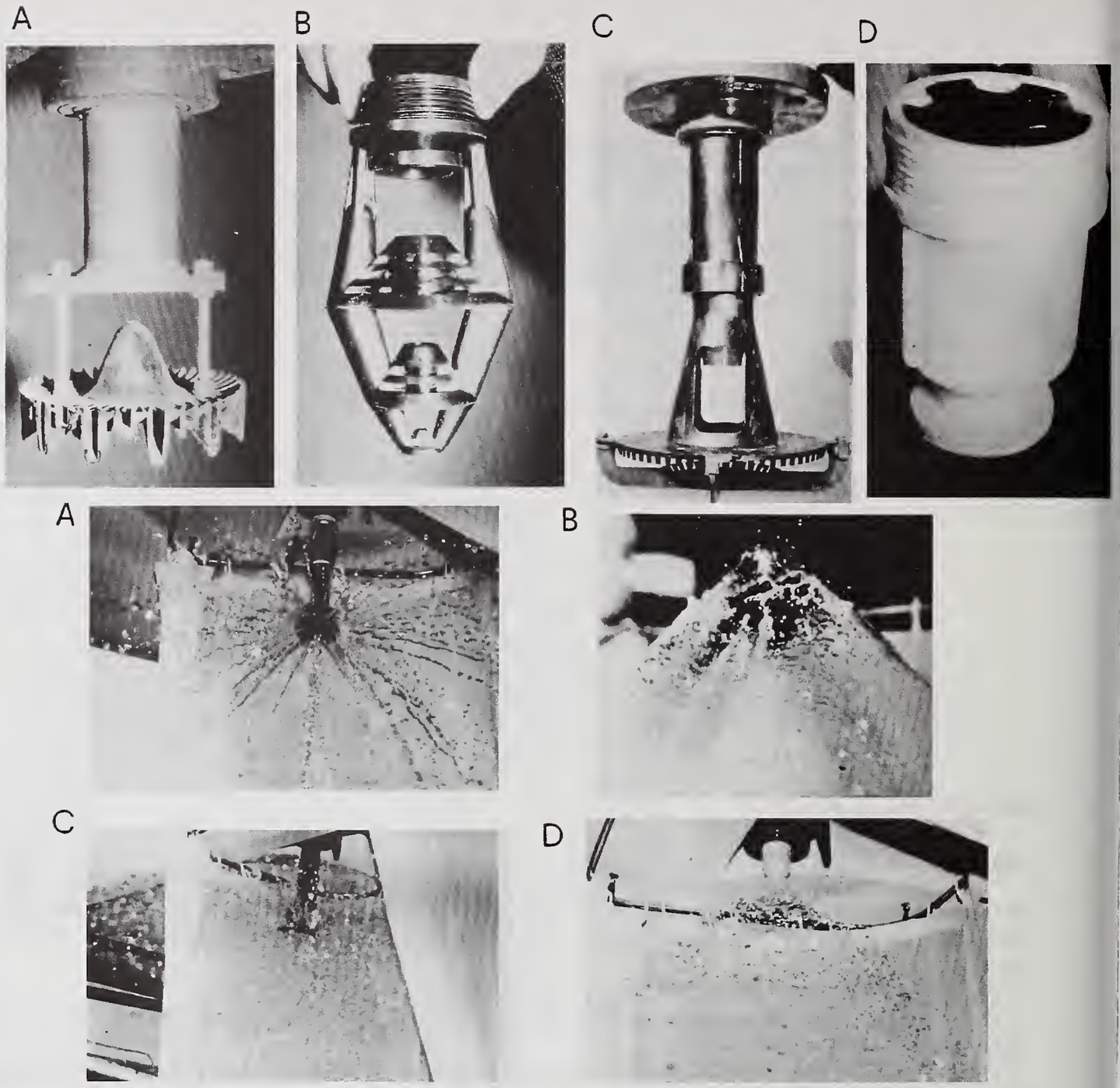

Fig.3: Ensemble photographs of the jets produced by the nozzles

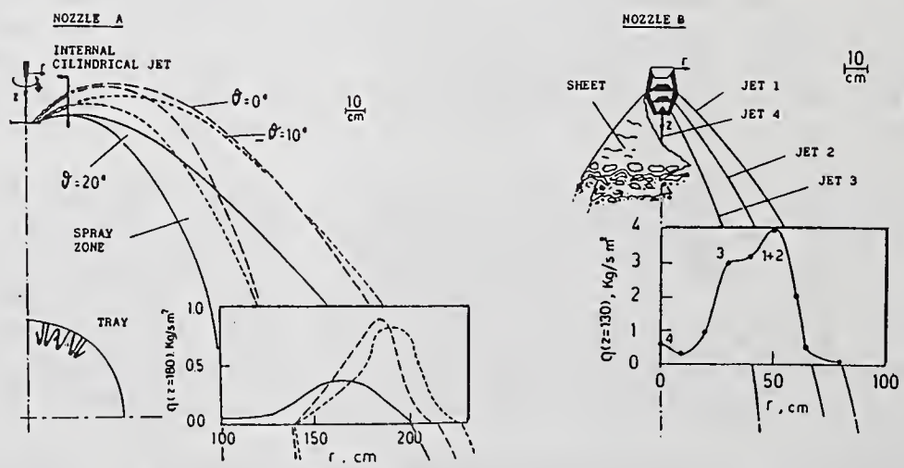

Fig.4: Results of the macroscopic characterization for nozzles A and B

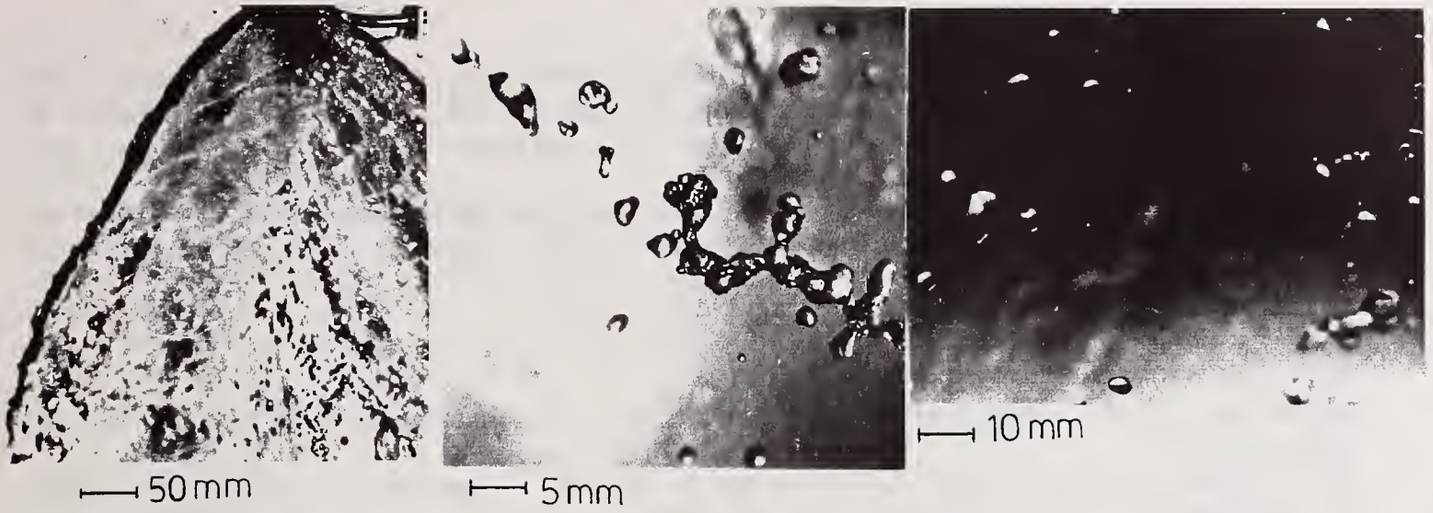

Fig.5: Example of breakup of a paraboloidal sheet (nozzle B): the sheet; ligament produced by the sheet breakup; drops produced by the ligament breakup

drops of range dependent on the breakup regime (7). For nozzle B and D breakup takes place by means of the growing disturbances on the sheet, coupled with the reduction of sheet size.

From the photographic analysis of the spray zone it is possible to evaluate the drop size distribution and drop concentration for the spray zone produced by each nozzle. Table II reports, together with other parameters that will be defined later on, the diameter of the wetted zone at a distance 1.8 m under the nozzle and two different mean drop sizes D_{pq} (8) for the four nozzles.

It is worthwhile to note that this characterization is important either to verify the goodness of nozzle installation pattern suggested by nozzle manufacturers for cooling towers, or to measure quantities needed to evaluate some nozzle performance parameters as described in the following section.

Definition and evaluation of performance parameters for water distribution

From the characterization on single nozzles, it is interesting to define and to evaluate some parameters related to the behavior of water distribution system in cooling towers. In particular, these parameters should provide a first estimate of the heat transfer and pressure drops in the spray zone, as well as on the uniformity of water distribution on the tower packing.

As "performance" parameters, one might define:

1) the ratio S_b between the surface of the drops and their volume, which is related to the heat transfer in the spray zone.

$$S_b = 6 \frac{\Sigma N_j (d_j)^2}{\Sigma N_j (d_j)^3} = 6/ D_{32} \qquad [1]$$

2) the ratio η_w between the wetted surface at $z=z^*$ and the total surface under the nozzle.

3) the uniformity of liquid distribution σ_w, defined as

$$\sigma_w = [\ \Sigma (q_i - \overline{q})^2 / (n-1)]^{1/2} \qquad [2]$$

where q_i is the local flowrate and $\overline{q}$ is the mean liquid flowrate.

Parameters 2) and 3) give a first idea on the efficiency and uniformity of the

water distribution produced by each nozzle. However, many nozzles operate in practical systems so that these parameters may not be directly extrapolated to battery configuration, but they suggest the optimum configuration to be used in practical systems.

4) the mean liquid hold-up in the spray zone. This parameter gives indication on the reduction of the net section for air flow due to the presence of the drops.

$$H_L = N_v \ (D_{30})^3 \ / \ 6 \qquad [3]$$

where Nv is the number of drops per unit volume and D_{30} the volume median diameter

5)the velocity heads lost per unit length of spray zone. This parameter is related to the air pressure drops in the spray zone and can be evaluated by means of the relation (9):

$$N/L_s = (2g/v_o) \ (q_L/q_g) \ / \ v_o \ (v_r - v_o) \qquad [4]$$

where N is the number of velocity heads lost for a length L_s, q_L and q_g the specific flow rates of the liquid and gas, respectively, v_o is the mean air velocity and v_r the terminal velocity of the drops. Assuming v_o=3m/s as reference air-side velocity, and evaluating v_r for drops of size D_{32}, the values of N/L_s reported in Table II are obtained. In the calculation it has also been assumed that q_L is equal to the mean specific flowrate of the liquid phase and q_g is given by the product of v_o and the air density.

Table II gives an interesting set of results on which it is possible to make comparison among the behavior of the four nozzle in single configuration.

TABLE II

Single nozzle behaviour: performance parameters

NOZZLE	DIAMETER OF THE WETTED ZONE (m) at H = 1.8 m	D_{32} (mm)	D_{30}	η_w	σ_w	q .Kg/sm^2	H_L x10^4	S_b m^2/m^3	v_r m/s	N/L_s m^{-1}
A	4	6.5	6.0	0.35	1.5	0.14	6-7	923	13	0.012
B	1.5	4.2	2.5	0.7	0.7	1.00	4-5	1428	11.2	0.11
C	5	4	2.7	0.9	0.09	0.093	.2	1500	11	0.01
D	3	4.1	2.8	0.85	0.2	0.25	2-6	1463	11.1	0.028

Nozzle C and D present a good wetting uniformity and efficiency even in single configuration, suggesting a slight dependence of these parameters on the nozzle installation pattern in practical application. Nozzle A gives the worst behavior, since it presents the largest mean drop size (that is to say the lowest S_b), together with the lowest wetting efficiency coupled with a high σ_w

As regards the air flow in the spray zone, the values of H_L are so low, as expected, that the reduction of the net section for air flow is negligible. It is more important to consider that the presence of a coherent paraboloidal sheet (for nozzles B and D) produces a reduction ot the net section for air flow up to a value of 7% (nozzle C). Finally,
the values of N/L_s indicates that the lowest air-side pressure drops are to be expected for the nozzle producing the largest umbrella, being the mean

specific liquid flowrate the minimum and the D_{32} quite similar for the four nozzle in the single configuration.

Pilot-tower experiments

Figure 6 shows an example of the results on local flowrates measurements for the four nozzles in the central zone, in a three-dimensional representation. These figures, obtained by interpolation (spline smoothing) of the measured values, give an idea on the uniformity of water distribution by the different nozzles. Nozzle A presents the worst behaviour in these conditions, since the local flowrate is strongly oscillating inside the examined area. In order to compare the behaviour in single and battery configurations, a pilot-tower "ensemble" standard deviation for the liquid flowrate can be evaluated by Eq.[2] by using different weights for the mean values obtained in the three zones of Fig.2. Figure 7 reports the values of σ_w as a function of pilot-tower operating conditions. The standard deviations are generally greater than those for the single configuration, but it should be noted that the same nozzle spacing was employed for the nozzles (Fig.2) and a different geometrical arrangement for each nozzle type should probably result in a smaller σ_w. However, information about the influence of operating condition can still be obtained. The standard deviation does not seem to be affected by air velocity. The effect of liquid flowrate is generally to enhance σ_w .

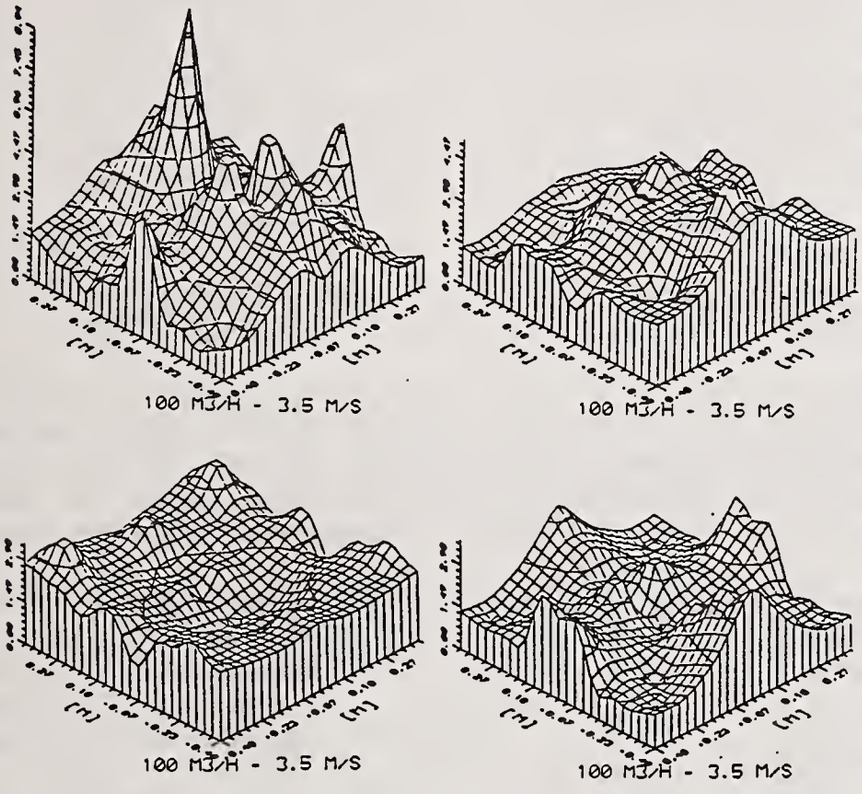

Fig. 6: Three-dimensional representation of local flowrate for the four nozzles (liquid flowrate 100 m^3/hr, air velocity 3,5 m/s).

Table III shows the values of the Sauter mean diameter of the water drops as a function of measurement position and air velocity. The position P_1 generally gives the greatest value of D_{32} and the smallest drop concentration for nozzles A and B, because of the big drops produced by the dripping immediately under the nozzle and the poor cooperative effect of the overlapping jets for these nozzle configurations. The "mean" D_{32} on the whole section has been calculated by weighing the measured values on the basis of suitable geometric coefficients. The values are generally greater than those measured in the single nozzle configuration. The nozzle D "single" D_{32} was measured with a liquid flowrate about an half than the pilot tower case and it is not directly comparable. This increase of mean drop diameter is the result of the coalescence of small drops occurring when two or more jets, produced by

contiguous nozzles, impact during the fall. This fact is confirmed by the

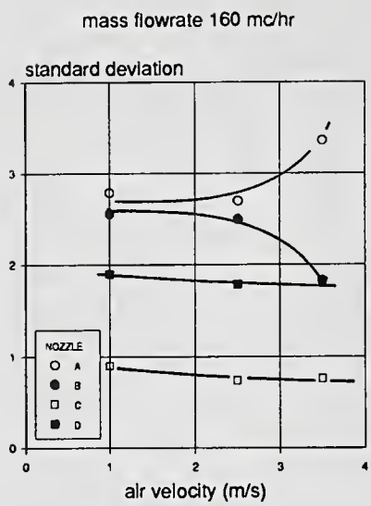

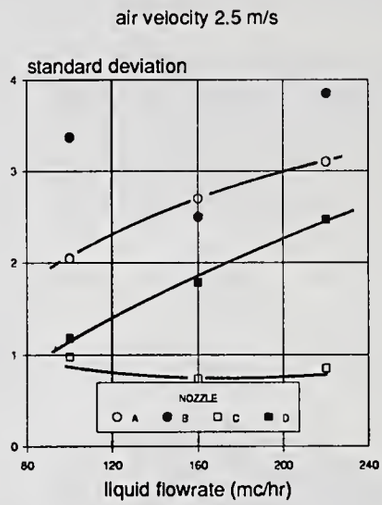

Fig.7: Effect of operating conditions on the uniformity parameter σ_w

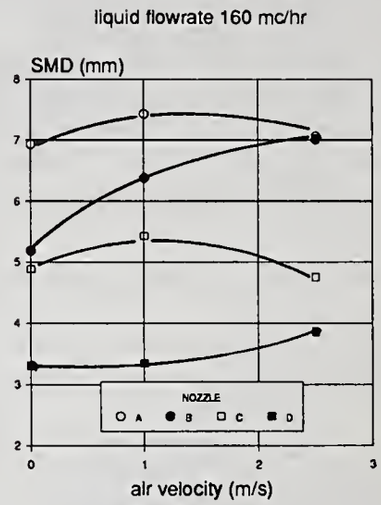

Fig.8: Effect of air velocity on SMD

increase of D_{32} values, shown in Fig.8, for the nozzle for which is greater the deformation of the umbrella with air velocity (nozzle B). In other words, nozzle B produces a paraboloidal coherent sheet (Figs.3,4) that is wider as air velocity increases; thus the overlapping of two contiguous sheets is more pronounced and the probability of drop collisions increases as well. The mean drop size is also important for the amount of drifting.

These results suggest some concluding remarks about the behaviour of these nozzles. The best performing nozzle should give the higher wetting efficiency with the lowest standard deviation, and a relatively low Sauter mean diameter in order to improve the heat transfer efficiency in the spray zone (3), and these characteristics should be relatively insensitive to changes in operating conditions. Among the four nozzles employed in this work, nozzle D seems to present the most satisfactory behaviour.

As regards the air-side pressure drops, the calculated values of N/L_s are very similar ($\simeq$0.23), since the mean liquid specific flowrate and terminal velocity of the drops are the same for the four nozzle ensembles.

TABLE III

Sauter mean diameter (mm) of the drops produced by the nozzles: effect of position and operative conditions

W_L (m^3/h)	160				160				160			
V_a (m/s)	0				1				2.5			
NOZZLE	D_{32} P_1	D_{32} P_2	D_{32} P_3	D_{32} mean	D_{32} P_1	D_{32} P_2	D_{32} P_3	D_{32} mean	D_{32} P_1	D_{32} P_2	D_{32} P_3	D_{32} mean
A	8.9	6.9	5.3	6.93	9.1	7.2	7.1	7.43	9.2	6.6	6.7	7.01
B	7.9	3.3	6.4	5.19	8.0	5.3	7.0	6.38	7.2	7.0	7.1	7.06
C	4.7	4.0	6.0	4.89	4.6	5.3	5.9	5.43	4.3	3.9	5.9	4.75
D	3.7	2.7	3.9	3.31	4.0	3.2	3.3	3.35	4.7	3.7	3.75	3.86

CONCLUSIONS

Careful experimental characterization of water distribution nozzles is needed in order to evaluate the performances of water distribution systems in cooling towers. On the basis of the results, some performance parameters have been defined and evaluated, which can be related to heat transfer and pressure drops in the spray zone of a cooling tower.

Measurements in two configurations, pilot tower and small scale loop, included the geometric characteristics of the jet umbrella by ensemble photography, the wetted zone by measuring the specific flowrate, the drop-size distribution and liquid concentration by high-speed photography. The results show that correlations exist between the nozzle behaviour in single and pilot tower configuration. The uniformity of water distribution in the pilot tower is strongly related to the nozzle installation pattern and to the operative conditions. Coalescence plays an important role on the drop size distribution in the spray zone of the pilot-tower.

REFERENCES

1. Berman, L.D., "Evaporative Cooling of Circulating Water", Pergamon Press 1961.

2. B.Bellagamba, G.Dinelli, F.Macchi, M.Ceccanti, C.Scali, S.Zanelli "A study on the performance of evaporative cooling towers with natural draft", 5th International Association on Hydraulic Research Cooling Tower Workshop, Monterey, Cal, (1986).

3. B.Bellagamba, G.Dinelli, F.Macchi "Physical and engineering aspects of a cooling tower performance test programme" 5th IAHR Coolin. Tower. Workshop, Monterey (1986).

4. B.Bellagamba, G.Dinelli, L.Tognotti, S.Zanelli "Water distribution in cooling towers: characterization of industrial spray nozzles" 6th IAHR Cooling Tower Workshop, Pisa, Italy, (1988).

5. F.Macchi, B.Bellagamba, S.Baldacci, L.Tognotti, 42nd Associazione Termotecnica Italiana National Congress, Genova , Edited by CLEUP, Padova, Italy (1987).

6. Dombrowski,H., Hopper,P.C. ; Chem.Eng.Sc., 17, 1962,291-305

7. Reitz, R.D., Bracco,F.V.; Mechanism of atomization of a liquid jet, Phys.Fluids, Vol.25, 1730-1742, (1982).

8. Mugele, R.A., Evans, H.D.; Ind.Eng.Chem., 43 (1951)

9. Lowe,H.S., Christie, D.J. : "Heat Transfer and Pressure Drop Data on Cooling Tower Packings, and Model Studies of the Resistence of National Draught Towers to Air Flow" Conference on Heat Transfer, (1961)

SUPPRESSION OF SMOKE PARTICLES USING ELECTROSTATIC SPRAYING

C.N. Ahmad and W. Balachandran

Department of Electronic and Electrical Engineering
University of Surrey
Guilford, United Kingdom

ABSTRACT

Experimental investigation has been undertaken to study the efficiency of precipitating smoke particles using electrically charged water spray . A laser attenuation measurement system was employed to study the precipitation rate of cigarette smoke particles using charged and uncharged water spray . The negatively charged water spray cleared the test chamber three times faster than the uncharged spray . Based on the test results , a realistic time for complete clearance of the test chamber independent of source was estimated to be 60 seconds .

INTRODUCTION

A spray of fine water droplets is a well known means of airborne dust removal . Many of the commercially available fog devices for fugitive emission control are not very efficient . One method of improving the effectiveness of water spray is by applying electrical charge to the spray that is opposite in polarity to the charge on the dust to be suppressed . It has been found that most industrial pollutants and naturally occurring fugitive dust acquire an electrostatic charge , well above the Boltzman equilibrium , as they are dispersed in the air . If this charge of airborne material is exposed to an oppositely charged water spray , contact between the particulate matter and the water droplets is enhanced . After contact is made , the wetted particulate matter agglomerates rapidly and falls out of the atmosphere . The use of technology to suppress smoke particulates in controlling indoor air quality has not been studied extensively.

There are mainly four methods that are commonly used to control the effects of indoor smoke contamination . They are ventilation , filtration, electrostatic precipitation and odour masking . In our study electrostatic precipitation technique is the only method that was considered . Suppression of smoke particles by electrostatic precipitation involves drawing smoke and air into an ionisation chamber in which the particles acquire an electric charge . The mixture of air and smoke particles passes through two or more plates between which electrical fields are maintained . The charged particles accelerate in the field and are deposited onto the

plates . Such devices can be even more effective by incorporating an adsorptive filter , such as activated charcoal . A simpler device than an electrostatic precipitator is an air ioniser ,which generates an abundance of small ions , which due to its high mobility , bombards onto the smoke particles and accelerates their precipitation . Although there is no doubt that these devices are efficient in removing particulate matter , several studies have failed to show that the devices do alter the concentration of the gas phase contaminants and therefore have limited value in removing the odour .

There is at present no alternative technology available for eliminating smoke or controlling it to acceptable limits , other than the ventilation which must be adjusted to cope with any practical situation . In many instances the volumes of ventilation required to control odour and irritant effects are unrealistically high , it is therefore necessary to investigate alternative methods of suppressing both smoke particulate matter as well as the odour . In the work reported in the literature regarding the use of charge and water sprays for the suppression of smoke particles , there have been some limitations in achieving efficient precipitation due to low specific charge levels and lack of understanding of the optimum droplet size required for such applications . It is believed that the effectiveness of these charged sprays can be improved by controlling the spray drop size distribution and specific charge .

In this paper a brief theoretical background and some results of the preliminary empirical studies carried out will be presented .

THEORETICAL BACKGROUND.

The collection of an aerosol particle by charged droplet is the result of a number of simultaneous mechanisms of interaction between them such as inertial impaction , direct interception , Brownian diffusion and electrostatic diffusiophoretic and thermophoretic forces . The particle collection efficiency of uncharged water sprays where inertial impaction is the major collection mechanism is given by Cheng (1) as

$$E = 1 - EXP\left[-\frac{3}{2} * \frac{Q_l}{Q_a} * \frac{L}{d} * \eta\right] \quad \ldots\ldots(1)$$

where E is the overall collection efficiency , η single droplet collection efficiency , Q_l volumetric flowrate of water, Q_a volumetric flowrate of air, L characteristic length of the total capture process , d mean droplet diameter.

When the droplets and particles are electrically charged, η is given by Prem et. al. (4)

$$\eta = -\frac{C q_p q_d}{6\pi^2 \varepsilon_0 r_p r_d^2 \mu U_0} \quad \ldots\ldots(2)$$

where q_p is the charge on the particle., q_d the charge on the droplet. C the Cunningham slip correction factor, ε_0 permitivity of free space, μ viscosity of the liquid, U_o droplet free stream velocity

For a given particle size distribution , electrostatic forces are proportional to the magnitude of the charge and inversely proportional to the droplet's size and its free stream velocity. When charged droplets are sprayed into the air they will evaporate unless the air is saturated with water vapour. The droplet lifetime determines the effective contact time

between the droplet and particles and thus strongly influences the overall particle control efficiency of the system . The lifetime of water droplets depends upon the temperature and relative humidity of the medium into which it is introduced . To obtain the best collection efficiency , the droplet must be small enough to provide both an adequate spray rate per volume of gas treated and sufficient contact time yet large enough so as not to evaporate too quickly .

Equations (1) and (2) show that the addition of electrical charge onto the droplets yields values of E which are 5 to 10 times higher in certain ranges for uncharged spray , the overall collecting efficiency of an operating system may not be that high. Pilat (3) observed that an increase in collection efficiencies of about 15% for 1 μm particles to over 45% for 0.3 μm particles . Hoenig (2) reported values of 10 - 40% with charged water droplets under controlled experimental conditions. He also demonstrated that the greatest effectiveness is obtained when water droplets are of a size similar to that of the particulates .

EXPERIMENTAL ARRANGEMENT.

The experimental setup used in this study consisted of the three parts as (a) the chamber (b) smoke generator (c) spray nozzle.

The Chamber

A cubical chamber (0.5 * 0.5 * 0.5 m^3) was constructed of 5 mm thick perspex (as shown in fig 1). Two optical windows are incorporated on the opposite sides of the chamber . A smoke generator and the spray nozzle are mounted on top of the chamber . A recirculator fan mounted on the side near the top provides a link between the top and bottom of the chamber to achieve uniform density of smoke within the chamber . The chamber is fixed on an optical bench along with a He-Ne (2 milliwatt) laser and a polariser on one side and a pin photodiode detector on the other side of the chamber A drain plug is also provided at the bottom of the chamber to empty the contents after the experiment . The floor of the chamber is covered with fine wire wool to eliminate the spray bounce back which tends to interfere with the laser beam and give erroneous measurements during the experiment . Two cases were considered in the series of experiments to be described here One with insulating walls and the other with conducting walls to the chamber . The latter was achieved by sticking aluminium foil on all sides inside the chamber. This case is more representative of the real situation since in a room the walls and the floor are always at or near ground potential compared to the charged spray and ions . The photodiode detector output was connected to a Keithley (610C) electrometer . The analogue output of the electrometer was fed to a chart recorder via a 10 K resister. After initial tests the charged spray in the chamber fouled the optical windows inspite of using anti-fog spray,thus making measurements impossible The problem was overcome by mounting two circular metallic ring electrodes around the windows . These rings when maintained at potential of the same polarity as the spray, repelled the charged spray away from the window.

The Smoke Generator .

The smoke generator consists of a bell shaped glass chamber with one inlet and two outlets. A cigarette is held on a flat circular glass plate with a hole in the centre . The main glass tube sits on this plate and a good seal is obtained at the bottom . The air blown through the inlet is forced through the cigarette, generating smoke into the test chamber by controlling the outlets with an on-off solenoid to simulate human 2-second duration puffs.

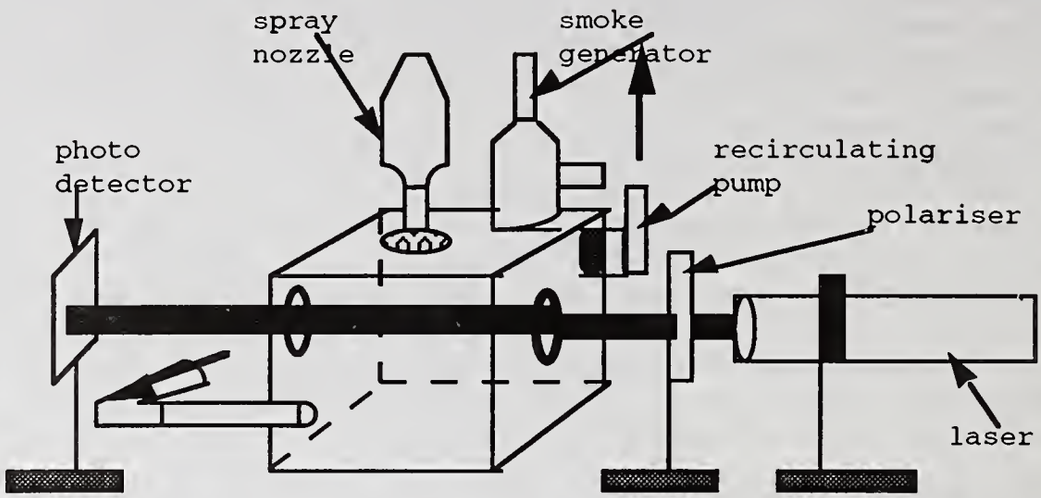

Fig 1 SCEMATIC OF THE TEST CHAMBER

Spray Nozzle

The spray nozzle used in these experiments is the standard spraying systems air atomising (1/4 JAU) nozzle . The metallic air cap has been replaced by a PVC air cap incorporating an embedded ring electrode to charge the spray by induction . When the nozzle is in operation a sheet of high velocity air flows between the liquid film and the electrode so that the gap between the electrode could be kept very small (1mm) without any electrical breakdown . Moreover since this gap is small , hence high charging efficiency is obtained with relatively low applied potential (<1KV) . Both air supplies to the nozzle as well as to the piston were controlled by two on - off solenoid valves so that the duration of the spraying could be controlled precisely. The spray nozzle is characterised in terms of the droplet size distribution and the charging efficiency . In these tests the nozzle was operated at a liquid flow rate of 75ml/min. and air pressure of 20 and 40 psi to the piston and to the nozzle respectively giving a typical droplet size VMD (volume median diameter) of 20 µm . The spray size distribution was measured using a Malvern Particle Size Analyser and typical results are shown in fig 2 . The corresponding charge to mass ratio was found to be 2mC/Kg . Fig 3 shows the specific charge values (q/m) obtained for different operating conditions of the nozzle .

Fig. 2 Droplet size distribution

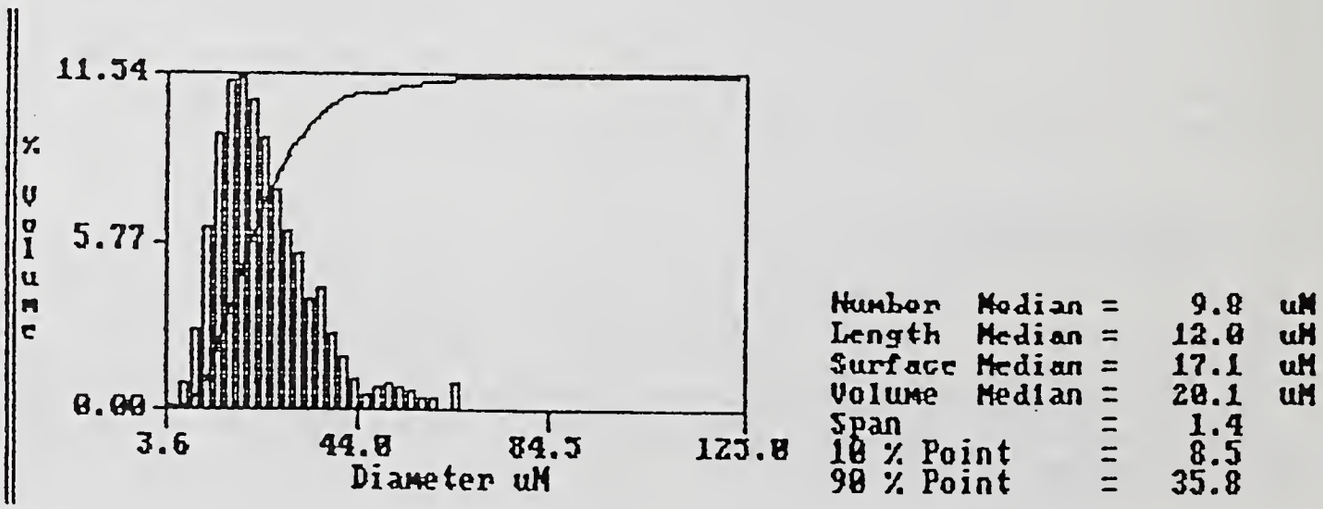

Fig. 3 Charge to mass ratio Measurements for 1/4 JAU nozzle.

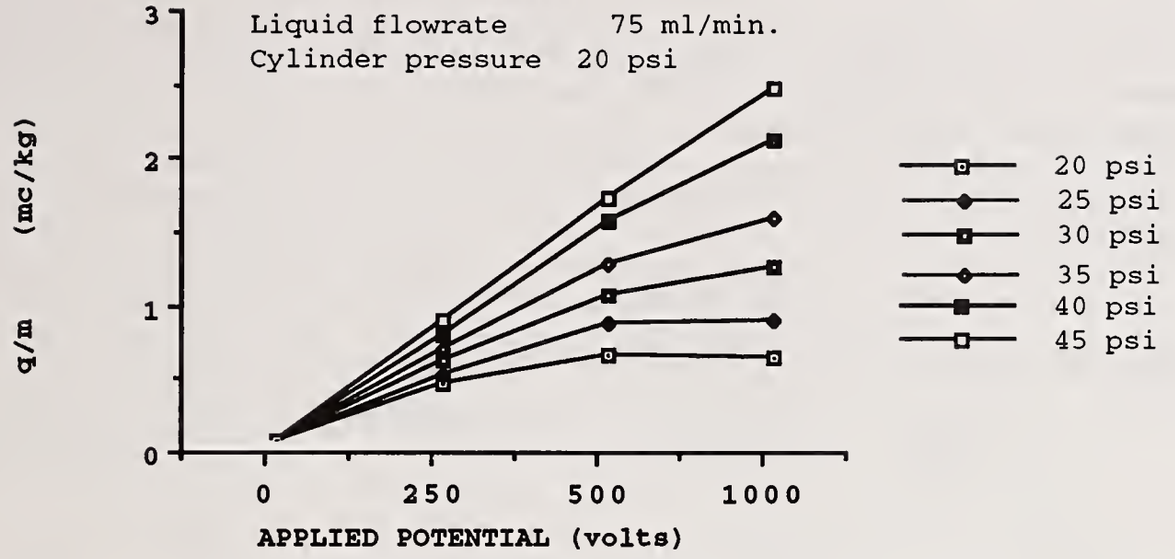

LASER MEASUREMENTS

Before each set of measurements the chamber , laser and the detection system was properly aligned to get a maximum signal output . The chamber was then filled with smoke through the smoke generator . In these experiments only 1/4 of the Marlboro cigarette was used each time, to simulate a realistic situation . The recirculating fan was kept on until a uniform density of smoke was achieved throughout the chamber and then it was switched off . The smoke was then exposed to an appropriate treatment i.e.exposed to the ioniser, (positive or negative) charged spray or uncharged spray . The treatment duration was fixed throughout these experiments , to 30 seconds only and the signal output was recorded for upto six minutes . Once the measurements were completed the chamber was cleared of the residual smoke by starting the recirculating fan and by disconnecting the bottom end of the link.

RESULTS AND DISCUSSIONS

From the experimental recordings , the signal was monitored upto 2 minutes from the start of the treatment . In each case the signal was normalised to the level of signal at the start of the treatment and then plotted against time to get the rate of smoke clearance from the chamber . These results are shown in Figures 4 and 5 for conducting and non - conducting walls of the chamber respectively . From these results , the times for complete clearance of the chamber could be easily projected and are given in table 1 The laser measurement system used in these experiments relies on the level of attenuation of the beam intensity due to light scattering . When the laser beam propagates through a cloud of smoke particles , light is scattered by the particles , and therefore only the transmitted beam will reach the detector . The intensity I of a plane electromagnetic wave of wavelength I and intensity I_o after traversing a distance L through the smoke particles is given by Bouguer's (Lambert-Beer's) Law , namely

$$I(\lambda) = I_o(\lambda)\exp[-\tau(\lambda)] \quad \ldots\ldots(3)$$

where the optical depth $\tau(\lambda)$ is given by $\tau(\lambda) = \int_o^L \beta_{ext}(\lambda)\,dl$

$$= \int_{r_1}^{r_2} \int_0^L Q_{ext}(x,m)\, \pi r^2 n(r)\, dr dl \quad \ldots\ldots(4)$$

where β_{ext} (cm^{-1}) is the volume extinction coefficient, Qext (x,m) the extinction efficiency, $x = 2\pi r/\lambda$ the size parameter, m = m' - i m" the aerosol complex refractive index, r_1 and r_2 are the upper and lower limits of the aerosol radii.

If we assume that n (r) remains constant along the path of the laser beam, then

$$\tau(\lambda) = \pi L \int_{r_1}^{r_2} Q_{ext}(x,m)\, r^2 n(r)\, dr \quad \ldots\ldots(5)$$

Hence the transmission coefficient can be written as:-

$$T = \frac{I(\lambda)}{I_0(\lambda)} = \exp - \left[\left(\frac{3}{4} CL \right) \left\{ \frac{\int_{r_1}^{r_2} r^2 n(r) Q_{ext}(x,m)}{\int_{r_1}^{r_2} r^3 n(r) dr} \right\} \right] \quad \ldots\ldots(6)$$

where C is the volume concentration of the aerosol.

In practice , due to the detector's finite field of view , some forward scattered light invariably enters into the detector's view cone along with the direct beam . This effect can be minimised using a pin hole appropriately placed in front of the detector and further correction factors can be added to equation (6) . However , for this study , such effects are assumed to be negligible .For a mono dispersed aerosol of mean radius r:

$$T = \exp - \left[\left(\frac{3}{4} C^* L \right) * \frac{Q_{ext}(x,m)}{\bar{r}} \right] \quad \ldots\ldots(7)$$

The above equation indicates that the transmission coefficient is a function of volume concentration and the size distribution of the aerosol cloud. In our experiments , as indicated initially the attenuation of the laser beam was due to the smoke particles . When the spray was introduced , the attenuation further increased as expected from equation (7) . This lasted as long as the spray was in the field of view and therefore , when the spraying ceased , it was possible to then relate the rate of clearance of the chamber to the increase in detected signal . This way it was possible to quantify and compare the operation of the system under different conditions . These tests were repeated several times and the repeatability was good .With ionisers , additional attenuation of the laser light was not observed, because the small ions are submicron in size and hence do not have any influence on the measurement system .

The results shown in table 1 clearly indicate that the suppression of smoke particles with the conducting chamber , in general is better than the non - conducting chamber . This is not surprising , as the conducting walls are at ground potential , therefore the precipitating charge agglomerates are strongly attracted to the ground surfaces . In the case of non - conducting chamber , based on the level and nature of surface charge on the surface of the walls , the precipitation rate varied . Although the net charge on smoke particles appears to be neutral (equal amount of positive and negative) , the projected results for positive and negative ioniser are significantly different . The mechanisms involved in suppressing smoke particles appears to be complex and has not been studied in depth in this

preliminary investigation . However , it is clear in both cases that the presence of positive ions clears the chamber much faster than either negative ions or negatively charged water spray . There is no doubt that the negatively charged water spray clears the chamber three times faster than the uncharged spray . With the conducting chamber , the clearance rate of smoke particles with negatively charged spray is 1.5 times faster than the presence of negative ions . These results clearly indicate that negatively charged water spray significantly increases the suppression of smoke particles . Another observation that was made was that the use of positive spray did not significantly improve the precipitation rate compared to the negative spray . This obviously contradicts the observations made with positive ions , and therefore needs further investigation .

Fig. 4 Rate of smoke clearance from a conducting chamber.

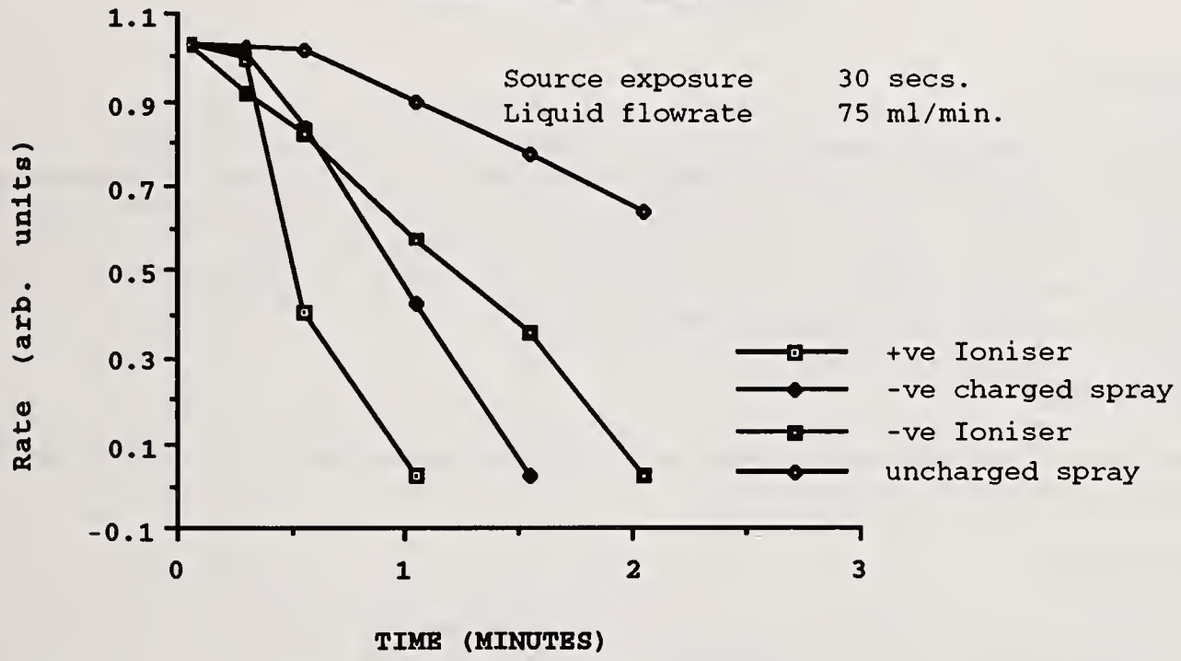

Table 1 Projected Time for Complete Clearance of the Chamber.

Source	Non-conducting Chamber	Conducting Chamber
Negative Ioniser	6.5 minutes	2.2 minutes
Positive Ioniser	1.4 minutes	0.61 minutes
Uncharged Spray	6.4 minutes	4.5 minutes
Charged Spray(-ve)	2.1 minutes	1.5 minutes

Fig. 5 Rate of smoke clearance in non-conducting chamber.

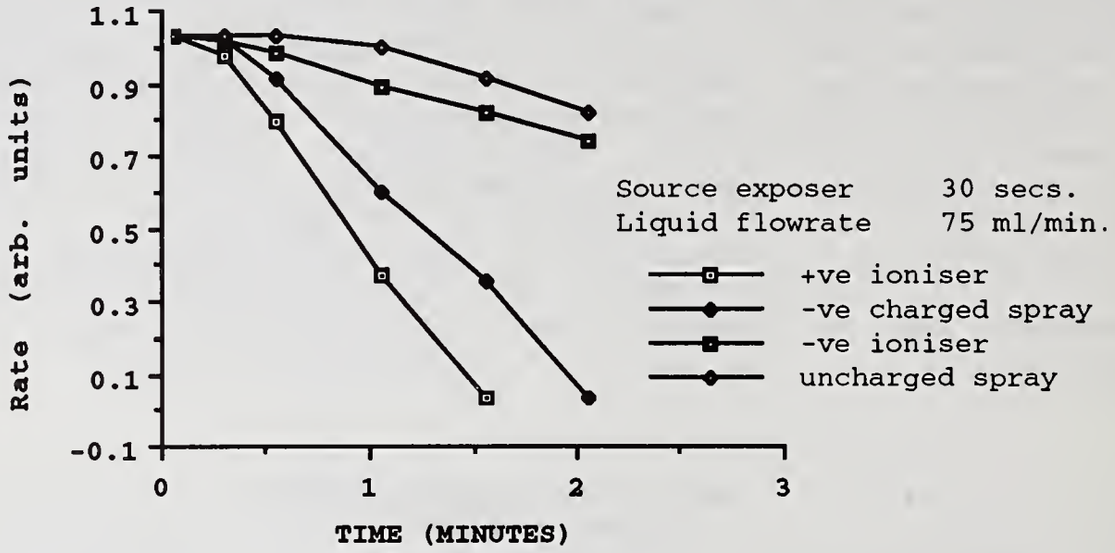

CONCLUSION

Electrically charged water spray can be used successfully to suppress smoke particles . Typical specific charge necessary for efficient precipitation is about 2mC/Kg . The rate of precipitation of smoke particles by negative ions is about 50% less than charged water spray of VMD 20μm. The realistic time of complete clearance of an enclosed room is estimated to be three times faster than an uncharged water spray.

Acknowledgement.

The authors wish to acknowledge S.C Johnson & son Inc. for the financial support provided for this study.

REFERENCES

1. CHENG L ,"Collection of airborne Dust by water sprays " Ind. Eng. Chem.Process Des. Development , 12 pp 221-225 (1973).

2 HOENIG S A ,"Control of Industrial fugitive dust with electrostatically charged fog devices " , A Status report , Conf. Record , IEEE - IAS , pp 982- 986 (1982).

3. PILAT M J , "Collection of Aerosol particles by electrostatic droplet spray scrubbers "JAPCA ,25 pp 176-178.(1975).

4 PREM A and PILAT M J, " Calculated particle collection efficiencies by single droplets considering inertial impaction, Brownian diffusion and electrostatics " 12 , pp 1981-1990 (1978).

ATOMIZATION AND DISPERSION OF QUASI-MONODISPERSE ELECTROSTATIC SPRAYS OF HEPTANE

A. Gomez and K. Tang

Department of Mechanical Engineering
Yale University
New Haven, CT, U.S.A.

ABSTRACT

Detailed measurements by digital imaging techniques and phase Doppler anemometry were performed to study the atomization and evolution of liquid fuel electrostatic sprays. The electrospray was chosen to assess its potential as a research tool for laboratory scale combustion experiments under conditions much better defined than in practical sprays. Experiments were carried out on heptane doped with an antistatic additive to enhance its electric conductivity. Stable electrosprays with droplets characterized by a remarkably quasi-monodisperse size distribution were generated over a wide range of experimental conditions. Average droplet diameters anywhere from 1 to over a 100 μm were obtained depending on liquid flow rate and electric field intensity. A phenomenological picture of the atomization and dispersion processes leading to these results is formulated. Images of the jet break-up showed that, when narrow size distributions are generated, the spray is formed from a thin, stable jet that breaks up into a stream of droplets. The resulting size distribution is typically bimodal with two peaks corresponding to primary droplets and satellite droplets, respectively. The smaller droplets at the breakup are electrostatically/inertially separated from the larger ones. Therefore, farther downstream, the size distributions is locally quasi-monodisperse. Spray dispersion is determined by both coulombic repulsion between droplets and diverging lines of field. No Coulomb explosion of the droplets was observed in the region where the electrospray is formed.

INTRODUCTION

Fuel atomization processes typically involve a two-phase flow of a polydisperse distribution of droplets in a turbulent gaseous environment: a formidable challenge to both experimentalists and theoreticians. It would then be extremely useful in sorting out the roles played by different aspects of the process to use an experimental arrangement that allow a systematic study of spray evolution and burning in configurations of gradually increasing levels of complexity, in both laminar and fully turbulent flows. An electrostatic spray of charged droplets seems to lend itself admirably to combustion experiments under well-defined conditions. In its simplest implementation, which is also the one we adopted in this study, a liquid is fed into a small metal tube maintained at several kilovolts relative to a ground electrode few centimeters away. If the liquid has sufficient electric

conductivity, its meniscus at the outlet of the capillary takes a conical shape under the action of the electric field, with a thin jet emerging from the cone tip. This jet breaks up farther downstream into a fine spray of charged droplets. Distinctive advantages of the electrospray over alternative atomization techniques are: the self-dispersion property of the spray due to coulombic repulsion; the absence of droplet coalescence; and the opportunity of manipulating the trajectories of charged droplets by suitable disposition of electrostatic fields. Furthermore, in contrast to aerodynamic atomization processes, the electrospray relies on charging to atomize the liquid fuel, so that atomization and gas flow processes are relatively uncoupled. This last feature provides an additional degree of freedom and may in principle allow a systematic study of the spray evolution and burning starting from laminar sprays to fully turbulent ones.

A well-defined spray combustion experiment requires control on droplet size distribution which should ideally be monodisperse to simplify the experiment interpretation. The electrospray appears also promising in this respect, on the basis of fragmentary data reported in the literature that indicated the generation of narrow droplet size distribution under disparate experimental conditions. Almost forty years ago some observations of High Order Tyndall Spectra were reported in the scattering of white light by "smokes" produced in electric dispersion of liquids (1,2). This optical phenomenon is indicative of droplet formation of narrow size distribution in the size range 0.1-2 μm (3). At the other end of the size spectrum, Thong and Weinberg (4) showed that a kerosene electrospray, in a very narrow range of operating conditions, could generate monodisperse droplets varying in size from 50 to 120 μm. These authors also demonstrated the feasibility of burning the electrostatically atomized fuel.

The application of liquid fuel electrostatic spraying to more practical situations, involving high flow rates, has been studied by Kelly (5) at atmospheric pressure and, more recently, by Kwack et al. (6) at Diesel engine pressures. Spraying involves a charge injection technique based on the use of a patented "triode" (7). The distinctive advantages of handling large flow rates is unfortunately partially offset by the polydispersion of the droplet size distribution. We chose the simpler configuration described above, which, even though limited to relatively small flow rates, appears more promising for the controllability of spray combustion experiments.

Detailed studies, both experimental and theoretical, of the electrohydrodynamic phenomena leading to the formation of the liquid conical meniscus have been reported (8-12). With regard to the details of the jet and its break up, the most relevant contributions, from our perspective, are the work of Thong and Weinberg (4), briefly discussed above, and the study of Mutoh et al. (13) who investigated the break up of charged liquid jets of xylene. Observations on the spray formation, including both jet break up and droplet dispersion, are more difficult and information available is rather scanty; it is therefore in this area that we have concentrated the initial efforts discussed here. This experimental study focuses primarily on the characterization of the atomization process and subsequent spray evolution in heptane electrosprays, with the ultimate goal of identifying the mechanism governing the generation of narrowly disperse particles over a wide size range. A preliminary account of part of this work was presented elsewhere (14).

EXPERIMENTAL

Heptane, whose flow rate was controlled and metered by a syringe pump, was fed into a stainless steel metal capillary (I.D.≅0.20 mm) maintained at a fixed voltage within the 3-5 kV range relative to a ground electrode positioned 3 cm away. The spray break-up was observed by using an optical

system consisting of: a (25 ns) pulsed flashlamp, as illumination source, which was focused on the electrospray by a quartz lens; a stereozoom microscope, positioned in a shadowgraph configuration; and a digital camera mounted on the microscope. The camera signal was recorded by a VCR and digitized, off-line, by a frame grabber installed on a personal computer. The quantitative use of this optical arrangement was restricted to experimental conditions yielding droplet diameters larger than 10 μm because of limitations in the resolution of the microscope. The overall magnification on the computer monitor was ≅800 X. Detailed single point measurements taken throughout the spray by commercial Phase Doppler Anemometers (PDA) allowed simultaneous inference of droplet size and axial velocity distribution, as well as size-velocity correlation. In a typical experiment, for a given flow rate, the voltage was operated in a range corresponding to the generation of a narrow size distribution, as monitored on line by the PDA along the spray axis. Heptane was doped with an antistatic additive (Stadus 450, Dupont; 0.3% by weight) to enhance its electric conductivity. The total current collected by the ground electrode was measured by an oscilloscope. All experiments were performed at ambient temperature and atmospheric pressure.

RESULTS AND DISCUSSION

Stable jets with droplets characterized by a locally quasi-monodisperse size distribution were generated over a broad range of experimental conditions. Average droplet diameters anywhere from 1 to over a 100 μm were obtained depending on: liquid flow rate; shape and intensity of the electric field; and, although not investigated in the present study, liquid physical properties. Four sample distributions are shown in Fig. 1, corresponding to the following flow rates: 0.0067 cc/min (Fig. 1a), 0.017 cc/min (Fig. 1b), 0.17 cc/min (Fig. 1c) and 0.34 cc/min (Fig. 1d), respectively. Size distributions appear roughly symmetric, with a remarkably small ratio of standard deviation over mean diameter of 0.10, 0.07, 0.04 and 0.06, respectively. It should be particularly emphasized that narrowly dispersed micron-size droplets where generated from a relatively large tube, thereby circumventing all clogging problems that characteristically plague alternative, monodisperse aerosol generators.

Figure 2 shows the dependence of droplet diameter on applied voltage, for selected flow rates; all measurements were taken in conditions yielding quasi-monodisperse size distributions. We observe that: i) droplet size is primarily dependent on liquid flow rate and increases monotonically with it; ii) at fixed flow rate, an increase in voltage, on the other hand, causes a decrease in size anywhere between 10 and 30%; and iii) for each flow rate, there is a fairly wide (1, 1.5 kV) range of voltages over which quasi-monodispersity prevails.

In an effort to investigate the mechanism determining the quasi-monodispersity of the generated sprays, details of the dynamics of the jet break-up were examined in imaging experiments. Typically, a sequence of events shown in Figure 3, in this particular case obtained for a 0.17 cc/min heptane spray, was observed:

1) the liquid exits the cone formed at the outlet of the charged capillary as a thin, stable, thread that persists for a short distance, here of roughly 2 mm (Fig. 3 a);
2) this ligament then breaks up into droplets, which typically, as in the present case, exhibit a bimodal distribution(Fig. 3 b);
3) the smaller (satellite) droplets at the break up are rapidly displaced radially with respect to the larger, primary particles generated (Fig. 3 c);
4) the primary droplets left behind are quasi-monodisperse. They move downstream, are gradually displaced radially and leave a "wavy" signature under instantaneous illumination (Fig. 3 d).

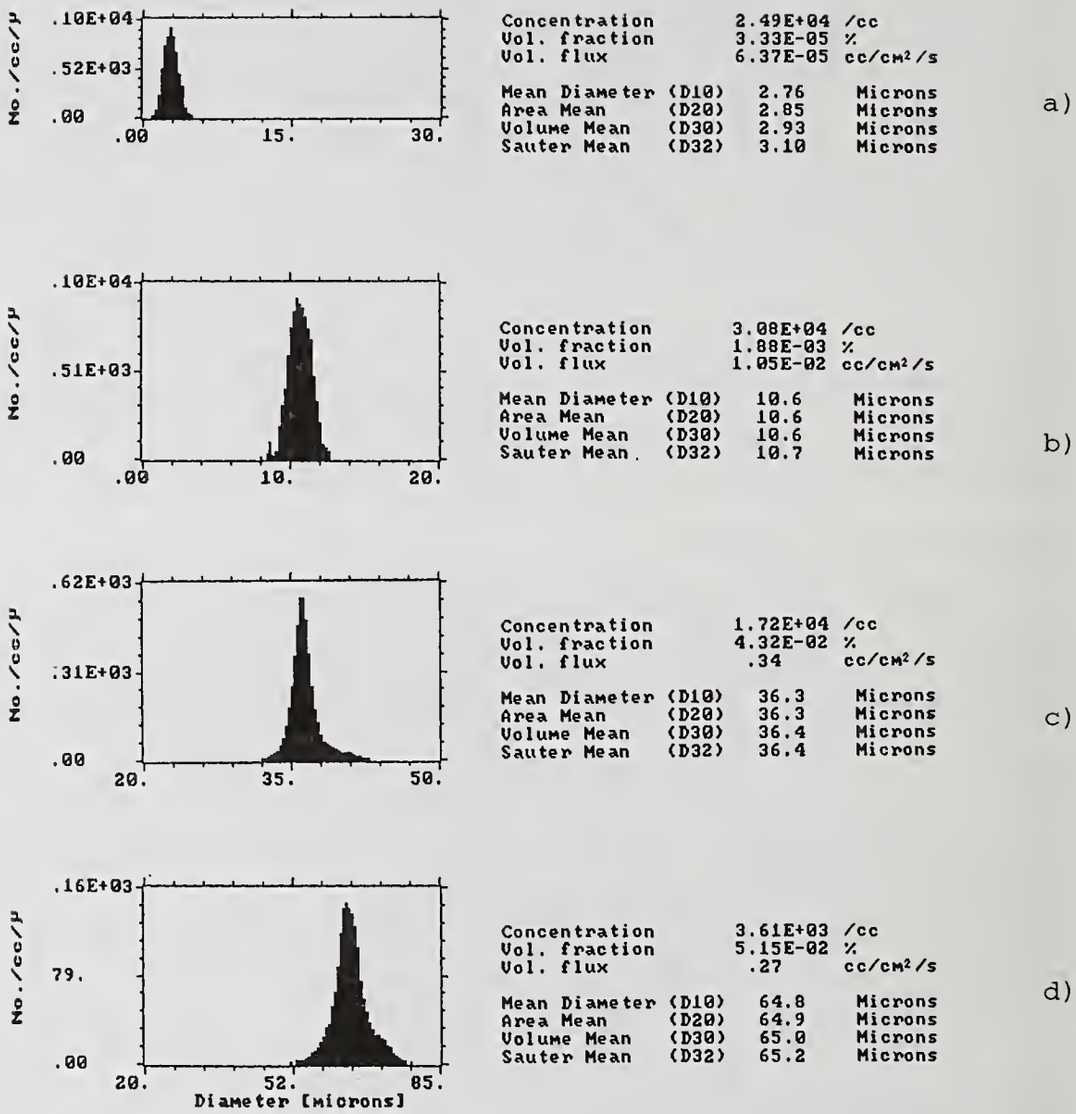

Fig. 1: Droplet size distribution for sprays with different mean diameters.

It can be clearly seen from Fig. 3b that, before break-up occurs, varicose waves propagate along the ligament. The ratio of primary droplet to ligament diameter was measured at about 1.9, in good agreement with the classic theory of Rayleigh on the stability of capillary jets (15). Extension of Rayleigh theory to account for electrification effects, worked out by Schneider (16) and corrected to second order terms by Neukermans (17), showed that, even at relatively large charge levels, the predictions of Rayleigh theory, at least in so far as dominant propagating wavelength is concerned, are not significantly altered. Our findings are consistent with the theoretical predictions. Experimental confirmation was also provided by a study on the break up of charged xylene jets (13). We conclude that electrification is controlling droplet size through electrohydrodynamic processes in the cone determining the formation and diameter of the jet.

The satellite droplets generated at break up are first displaced radially by a small disturbance and the Coulomb interaction with neighboring droplets; subsequently, they tend to follow the diverging lines of field

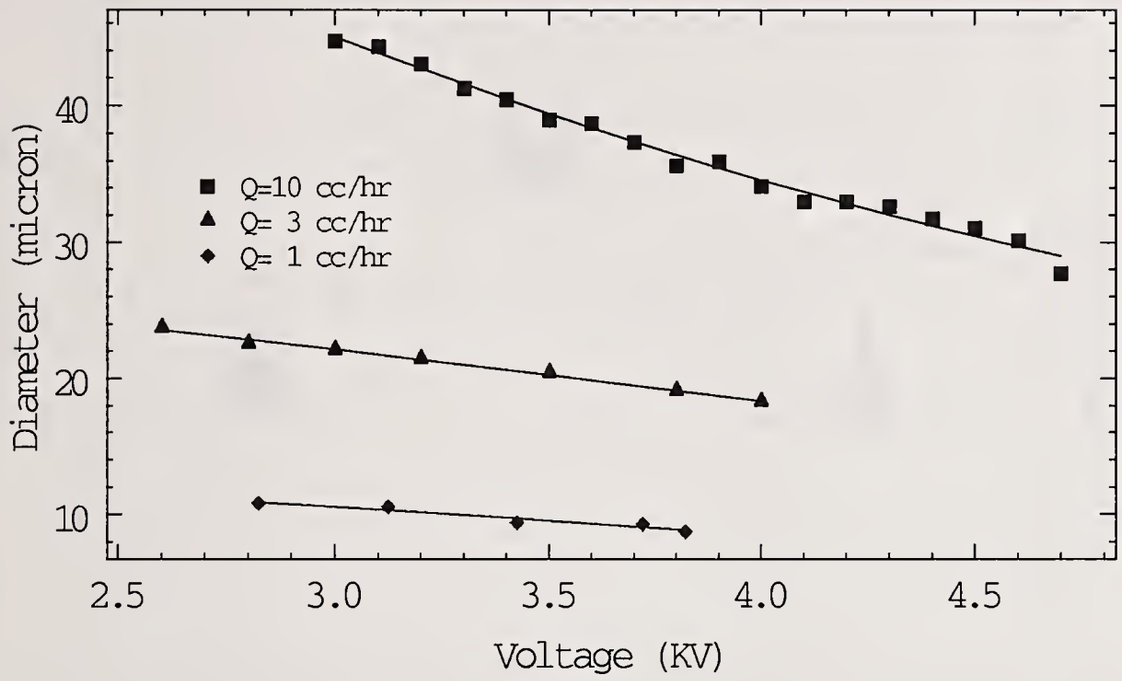

Fig. 2: Average droplet diameter versus applied voltage at different flow rates.

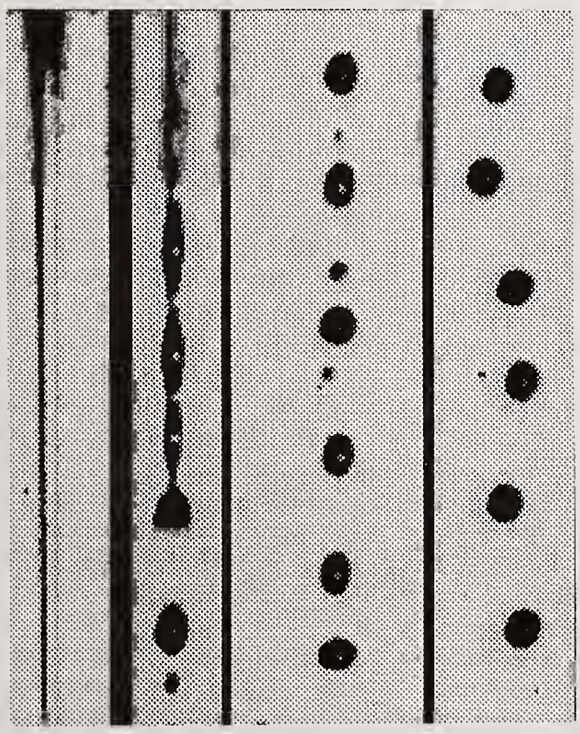

a) b) c) d)

Fig. 3: Jet breakup images obtained at increasing distance from the capillary (a→d).

because of both relatively small inertia and, possibly, higher charge to mass (18). Thus, they are removed from the core of the spray by electrostatic/inertial separation. The establishment of the sinuous pattern in the array of primary droplets in Fig. 3d can also be attributed to the coulombic interaction among droplets: it can be readily shown that if a droplet in a linear array is displaced radially by a small disturbance, the vector summation of the resulting electrostatic repulsive forces inevitably leads to the observed wavy pattern. Notice that this is not to be confused with a droplet trajectory.

Figure 4 shows the variation of the droplet average diameter as a function of radial coordinate, at fixed axial position, for the same 0.17 cc/min heptane spray. Superimposed on the plot are histograms of the size distribution at

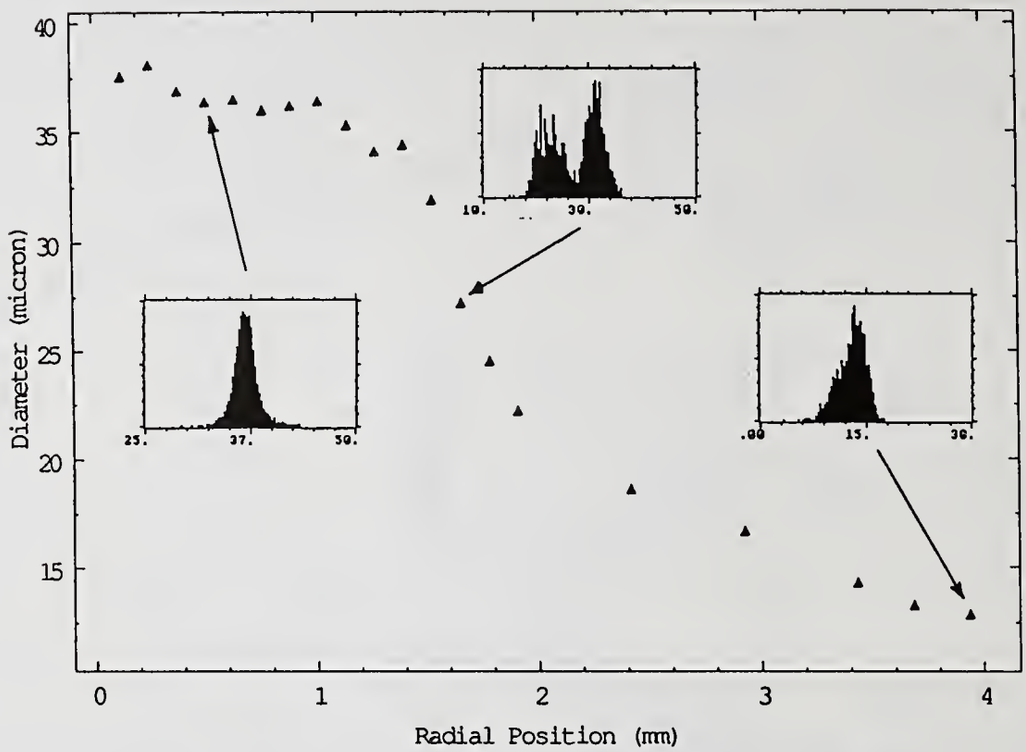

Fig. 4: Average droplet diameter versus radial position at a fixed axial coordinate.

three radial positions. It is evident that the average droplet size monotonically decreases as a function of the radial position. This is not a consequence of different evaporation rates, which have negligible effects under the present experimental conditions, but it is consistent with the interpretation of Fig. 3c in terms of electrostatic/inertial separation. At intermediate radial positions, we observe the existence of a bimodal size distribution in correspondence with the region between the spray core, characterized by the primary droplets, and the outer shroud of satellite droplets formed at the jet break up.

We also looked for evidence of Coulomb explosion which occurs near the so-called Rayleigh limit, when electrostatic repulsive forces overcome surface tension forces and the droplet disrupt into smaller droplets. This process inevitably occurs at some point during the droplet evaporation, since there is experimental evidence that charge remains attached to the droplet while it is evaporating (19). The question is if it determines or, at least, contributes to, the droplet dispersion and therefore the spray formation. A detailed examination of the shape and evolution of the size distribution along and around the axis of the 0.17 cc/min spray provided no evidence of the occurrence of droplet disruption in the probed region.

We can now attempt to generalize these observations to other flow rates or experimental conditions. At all flow rates, the break-up region showed a stable ligament, as in Fig. 3a, which would disrupt into a stream of droplets leaving the wavy "signature" as in Fig. 3d. However, for the smallest flow rates, and correspondingly smallest average droplet diameter, no observation of satellite droplets, nor bimodal size distribution, was possible, possibly because the limits of resolution of both imaging system and PDA were reached. Figure 5 shows the average charge to mass ratio (C/M) versus the applied voltage for different flow rates for the same conditions as in Fig. 2; the C/M's are normalized with respect to the Rayleigh limit calculated for the

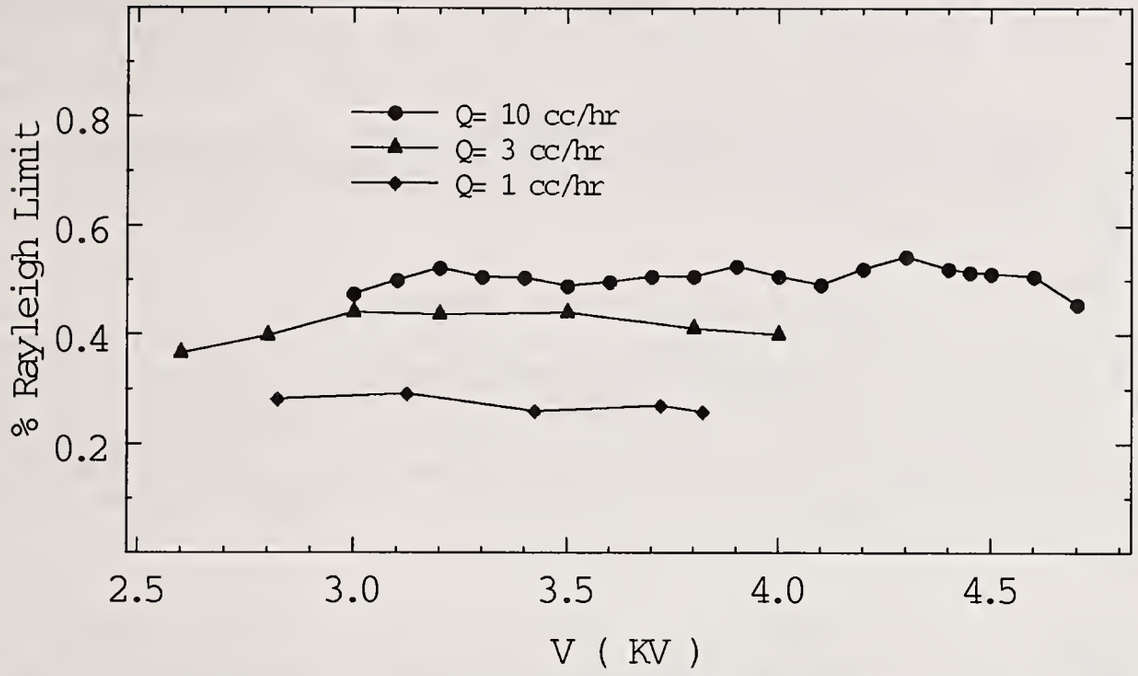

Fig. 5: Average charge to mass ratio, normalized with respect to the Rayleigh limit, versus applied voltage.

average droplet size of each spray. Since the normalized C/M's of the other two sprays tested are lower than the values of the 0.17 cc/min spray for which Coulomb explosion was ruled out, we expect that no droplet disruption is occurring in any of the sprays examined.

Our observations indicate that only when a stable, thin jet is formed at the outlet of the metal capillary quasi-monodisperse size distribution are generated. For a given flow rate, if the voltage was lowered below a lower threshold the jet would be unsteady and pulsating; if, on the other hand, it was raised above an upper threshold, whip-like lateral instabilities would ensue, as also theoretically predicted in similar geometries and at high charging levels (20) and experimentally verified by others (9,13). In this case the break-up mechanism appears qualitatively unchanged in the imaging experiments; however, the whipping of the ligament causes unsteadiness in the local electric field and mixing of the droplets generated. Consequently, the droplets are no longer spatially separated by electrostatic-inertial effects and locally the size distribution is broadened to encompass the whole size spectrum generated at break-up. Under this condition, monodispersity can still prevail if utmost care is taken towards the elimination of satellite droplets at break-up, as Thong and Weinberg (4) reported.

CONCLUSIONS

1) Stable electrosprays with droplets characterized by a locally quasi-monodisperse size distribution can be generated over a wide range of experimental conditions. Average droplet diameters anywhere from 1 to over a 100 μm were produced depending on liquid flow rate, shape and intensity of the electric field. Size distribution is typically symmetric, with a ratio of standard deviation over average diameter of approximately 0.1;

2) Liquid flow rate is the primary variable influencing droplet size, with the average diameter increasing monotonically with it; at fixed flow rate, an increase in voltage, on the other hand, causes a decrease in size anywhere between 10 and 30%. For each flow rate, there is a fairly wide (1, 1.5 kV) voltage range over which quasi-monodispersity prevails;

3) Images of the jet break-up, showed that, *when narrow size distributions are generated*, the spray is formed from a thin jet that breaks up into droplets with a bimodal distribution. After break-up, electrostatic/inertia separation of the smaller droplets from the larger ones yields *locally* quasi-monodisperse droplet size distributions;
4) No Coulomb explosion was observed in the region where the electrospray is formed. Coulombic repulsion between droplets and diverging line of fields cause the spray dispersion.

ACKNOWLEDGMENTS

We are indebted to Profs. J. B. Fenn, J. Fernandez de la Mora and D.E. Rosner for many stimulating discussions and helpful comments. Thanks are also due to both Dantec Electronics and Aerometrics for allowing us to use their particle measurement systems in extensive laboratory demonstrations, during which some of the data of this work was gathered. This research was in part supported by an NSF Equipment Grant #CBT-8806608 and a NASA Grant #NAG3-1259.

REFERENCES

1. Vonnegut, B. and Neubauer, R.L., *J. Colloid Sci.*, **7**, p.616 (1952).
2. Vonnegut, B. and Neubauer, R.L., *J. Colloid. Sci.*, **8**, p.551 (1953).
3 van de Hulst, Light Scattering by Small Particles, Wiley, 1957.
4. Thong, K.C. and Weinberg, F.J., *Proc. Roy. Soc. Lond. A*, **324**, p.201 (1971).
5. Kelly, A.J., *The Electrostatic Atimization of Hydrocarbons*, Second International Conference on Liquid Atomization and Spray Systems, ICLASS-82, Madison, Wisconsin (1982).
6. Kwack, E. Y., Back, L.H. and Bankston, C.P., *Electrostatic Dispersion of Diesel Fuel Jets at High Back Pressure*, Fall Technical Meeting, Western States Section, The Combustion Institute, Dana Point, Ca, 1988.
7. Kelly, A.J., *Electrostatic Atomization Device*, U.S. Patent No. 4, 255, 777, March 10 1981.
8. Zeleny, J., *Phys. Rev.*, **10**, p.1 (1917).
9. Taylor, G.I., *Proc. Roy Soc. Lond. A*, **313**, p.453 (1969).
10. Hayati, I., Bailey, A.I. and Tadros, Th. F., *J. Colloid. Interface. Sci.*, **117**, p.205 (1987a).
11. Hayati, I., Bailey, A.I. and Tadros, Th. F., *J. Colloid. Interface. Sci.*, **117**, p.222 (1987b).
12. Turnbull, R.J., *IEEE Trans. Industr. Appl.*, **IA-25**, p.699 (1989).
13. Mutoh, M., Kaieda, S., Kamimura, K., *J. Appl. Phys.*, **50**, p.3174 (1979).
14. Gomez, A. and Tang, K.,"*Characterization of Liquid Fuel Electrostatic Sprays*", Paper presented at the Western States Section/The Combustion Institute 1990 Fall Meeting, La Jolla CA.
15. Rayleigh, Lord, *Proc. Roy. Soc.*, **29**, p.71 (1879).
16. Schneider, J.M., Lindblad, N.R., Hendricks, C.D. and Crowley, J.M., *J. Appl. Phys.*, **38**, p. 2599 (1967).
17. Neukermans A., *J. Appl. Phys.*, **44**, p. 4769 (1973).
18. Gomez, A. and Tang, K., "*Characterization of a High Charge Density Electrospray of Methanol*"", Proceedings of the Fifth International Conference on Liquid Atomization and Spray Systems, ICLASS-91, Gaithersburg, MD, U.S.A., 1991.
19. Abbas, M.A. and Latham, J., *J. Fluid Mech.*, **30**, p.663 (1967).
20. Melcher J., *Field Coupled Surface Waves*, Chap.6, M.I.T. Press, Cambridge, Mass. (1963).

EVALUATING THE INFLUENCE OF FUEL PREPARATION ON THE PERFORMANCE OF A SPARK-IGNITED ENGINE

C.H. Daniels, L.W. Evers and Z. Han

Michigan Technological University
Houghton, MI, U.S.A.

ABSTRACT

An experimental technique has been developed for evaluating the influence of mixture preparation on the performance of a spark-ignited engine. The preparation components studied were fuel vapor, droplets, and liquid streams. These components were created and physically measured in a specially designed mixture preparation channel. Their effects on in-cylinder pressure performance and exhaust gas concentrations were investigated for a 1.9 L Ford engine operating at a speed of 1500 rpm and an absolute manifold pressure of 49.1 kPa (14.5 in Hg).

Results from this investigation showed that the performance of the engine was, in general, diminished by increasing the amount of fuel in liquid stream form. In addition, an "equivalent" mixture resulting from the engine's conventional port injection system was identified in relation to engine performance.

INTRODUCTION

The degree of fuel atomization and vaporization in the intake port of a spark-ignited engine is generally thought to influence engine performance. Many investigators have performed tests with a variety of engines in the hopes of determining the effects of air/fuel mixture preparation on engine performance [1-4]. In almost all cases, however, no physical measurements of the degree of fuel vaporization and atomization were made. Because of this, the results of these studies tended to be qualitative in nature. In general, the results of these studies showed an extension of the lean limit, a reduction in hydrocarbon and carbon monoxide emissions, an increase in nitrogen oxide emissions, and greater stability with increased mixture homogeneity.

The purpose of our work is first to develop a testing procedure for evaluating quantitatively the influence of mixture preparation in the intake port on engine performance. Second, to show how the results obtained can be used to evaluate the operation of a conventional port injector.

The fuel in the intake port appears in three distinct physical forms. These are vapor, droplets, and streams. Figure 1 shows these fuel forms produced from the spray of a port injector.

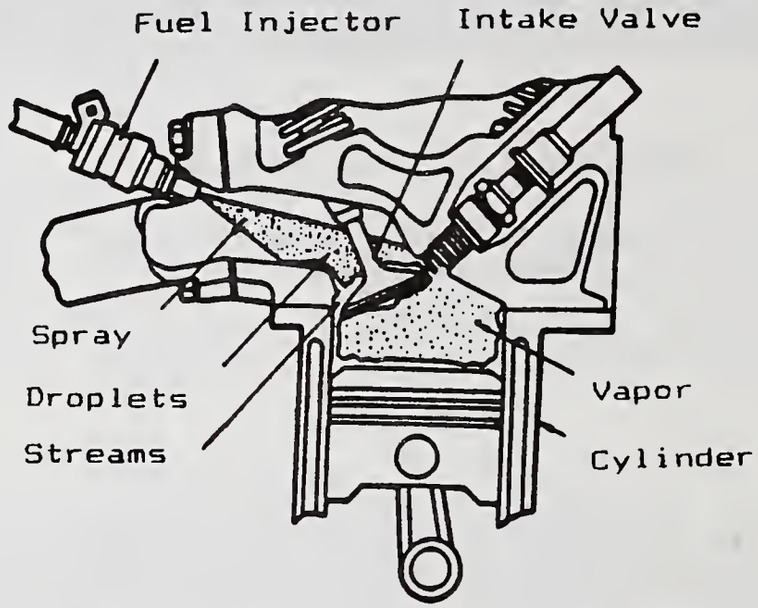

Figure 1: Mixture Components in the Intake Port

Droplets are formed from the atomization of the fuel spray. Some of the droplets, especially the larger ones, impinge on the passage walls and form liquid streams. Vaporization of the droplets and streams occurs throughout the intake process and is limited by the fuel's vapor pressure, time, and surface temperatures. It is these components and their effects on engine performance that is investigated in this study.

The engine performance parameters are obtained from in-cylinder pressure and exhaust gas measurements. The in-cylinder pressure parameters studied are the gross indicated mean effective pressure (IMEP), the coefficient of variation in the IMEP (COV), and the 10-90% burn time (BT). The exhaust gas parameters studied are the concentrations of carbon monoxide (CO), carbon dioxide (CO_2), oxygen (O_2), hydrocarbons (HC), nitric oxide (NO), and nitrogen oxides (NOx).

TEST EQUIPMENT

Engine

The engine used is a Ford 1.9 L EFI HO. The EGR system of the engine is removed. In addition, the intake manifold is modified such that one cylinder (the test cylinder) of the engine receives air and fuel via a special mixture preparation channel.

Fuel Preparation Channel

The mixture preparation channel, shown in Figure 2, contains devices for the creation and measurement of the different mixture preparation components: fuel vapor, droplets, and liquid streams.

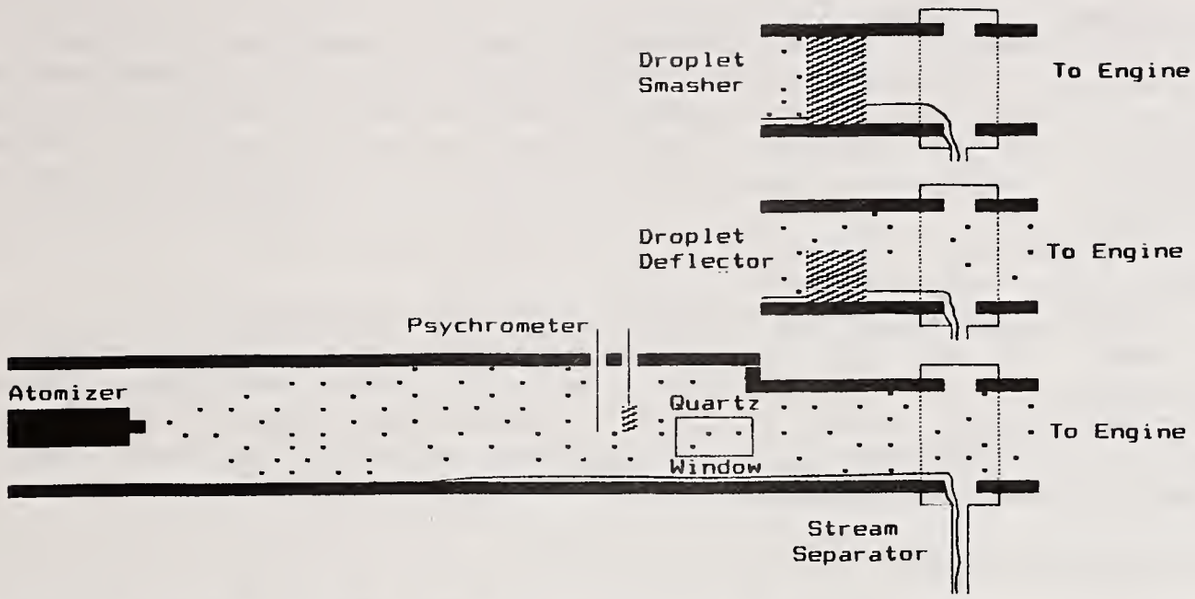

Figure 2: Mixture Preparation Channel

Atomizer. A pneumatic atomizer introduces fuel into the preparation channel. The atomizer produces droplets small enough so that some of droplets can traverse the channel length and avoid impingment on the channel walls.

Psychrometer. A psychrometer is used in the preparation channel to determine mixture equilibrium. Mixture equilibrium insures that the vaporization is completed. The "wet-bulb" probe consists of a thermocouple with its junction wrapped in a gauze wick. This probe is wetted by the droplets of the mixture. The "dry-bulb" probe consists of a thermocouple with its junction coated in a non-wetting, teflon wax. A temperature difference indicated between these probes is the result of evaporative cooling. Hence, equilibrium is demonstrated by the same temperature being indicated by both probes.

Stream Separator. The stream separator is a device used to measure the liquid streams. When the separator is in the "open" position, the streams are diverted to a buret for measurement.

Droplet Smasher. The droplet smasher is a device consisting of fine-grade steel wool. When it is placed in the channel, the fuel droplets collect on it and are converted to liquid streams.

Droplet Deflector. The droplet deflector is another device consisting of fine-grade steel wool. When it is placed in the channel (of which it occupies part of the cross-section), some of the droplets are converted to liquid streams.

Laser Droplet-sizer

A Malvern 2600 Particle-sizer is used to measure droplet sizes and distributions in the preparation channel. This instrument uses the principle of light diffraction in its determination of droplet sizes and distributions.

In-cylinder Pressure Measurement

The pressure in the test cylinder is measured through a Kistler pressure transducer (type 6123) located in the head of the engine. The signal from this transducer is recorded and analyzed using Ford Motor Company's Combustion Pressure Analysis System (COMPAS). IMEP, COV, and BT are obtained directly from the COMPAS program.

Exhaust Gas Measurement

The exhaust gas is sampled from the exhaust pipe of the test cylinder. CO and CO_2 are measured by Beckman 315A infrared analyzers. O_2 is measured by a Beckman 715 O_2 monitor. HC is measured by the "flame ionization detection" method using a Beckman 402 analyzer. NO and NOx are measured by the "chemiluminescence" method using a Beckman 955 analyzer.

EXPERIMENTAL PROCEDURE

The engine is allowed sufficient time to reach a steady-state operation. By changing the source air temperature, the equilibrium mixture temperature is adjusted until it reaches a prescribed value. The performance measurements are then taken. After this, the streams are measured via the stream separator.

When the above is completed, the droplet deflector is inserted into the preparation channel to convert some of the droplets to liquid streams, and the above testing is repeated. Next the droplet smasher is inserted into the channel to convert all of the droplets to liquid streams, and the above testing is again repeated. In this manner, various percentages of vapor, droplets, and streams can be evaluated.

The air-to-fuel ratio (A/F) is determined from the measured exhaust gas concentrations and from an oxygen senser located in the test cylinder exhaust. Variations in A/F are kept within 3% of the stoichiometric ratio. Although these variations may seem small, the performance variables are quite sensitive to the overall A/F. For this reason, the variation of the overall A/F ratio is included in the analysis of results.

DROPLET SIZE

From experimentation, the droplet size at the outlet of the preparation channel is found to be nearly constant under the equilibrium temperature range studied. The Sauter mean diameter was measured between 4 and 5 μm with 10% of the droplets under 3.5 μm and 90% under 8.0 μm. This is probably the result of the smaller droplets being able to traverse the channel length, while the larger ones impinge on the channel walls.

REGRESSION MODELING OF DATA

Variable Analysis

The performance values (IMEP, COV, BT, CO, CO_2, O_2, HC, NO, and NO_x) obtained from the above procedure are treated as functions of the percentage of fuel in two forms (vapor and

streams) and the equivalence ratio (Φ). Since the sum of the percentages of fuel in vapor, droplet, and stream form must equal 100%, they are not independent of each other, and only two of the three are required. The equivalence ratio is defined as the actual A/F divided by the stoichiometric A/F.

Regression Analysis

The data obtained is fitted to a linear regression model presented below. "Y" corresponds to the dependent variables (IMEP,

$$Y = A + B(\text{vapor \%}) + C(\text{streams \%}) + D(\Phi)$$

COV, ect.). "A", "B", "C", and "D" are constants determined through a least-squares regression fit. With the regression relations obtained, "performance maps" can be constructed for a range of independent variables. This is done later on.

ENGINE PERFORMANCE WITH THE MIXTURE PREPARATION CHANNEL

The 1.9 L engine was operated at a speed of 1500 rpm and a manifold absolute pressure (MAP) of 49.1 kPa (14.5 in Hg). The test fuel was Amoco Silver (93 octane, summer grade). Table 1 presents regression results obtained using this procedure.

	IMEP		COV	BT	CO_2	CO	O_2	HC	NO	NOx
	psi	kPa	%	deg	%	%	%	ppm	ppm	ppm
A	80.0	551	4.92	-29.4	19.3	-16.3	5.50	-25540	-242	-11.0
B	0.46	3.2	-0.021	0.463	-0.037	-0.008	0.046	232	3.20	5.28
C	-0.13	-0.9	0.049	0.503	-0.052	-0.037	0.043	285	-27.0	-21.8
D	-60.9	-420	-1.18	13.5	-2.28	17.6	-9.03	5699	968	578
R^2	87.1%		93.9%	77.2%	21.7%	60.0%	88.0%	92.0%	76.3%	64.5%
σ	0.570	3.93	0.047	0.46	0.14	0.13	0.042	127	39.6	45.9

Table 1: Results from Linear Regression Model for the 1.9 L Engine Operating at 1500 rpm and 49.1 kPa (14.5 in Hg) (MAP)

Figures 3 and 4 show contour plots of the best correlated performance parameters. The contour plots are presented on triangular graphs with the investigated region outlined. The results generally show that performance is significantly affected by the mixture preparation.

By increasing the percentage of fuel in stream form; CO, NO, and NOx are shown to be decreased, as indicated by the slopes in Table 1. COV, BT, O_2, and HC are shown to be increased. These trends are generally indicative of less desirable combustion. This is probably the result of a less homogeneous mixture present in the cylinder. NO, NOx, CO, and COV seem more strongly

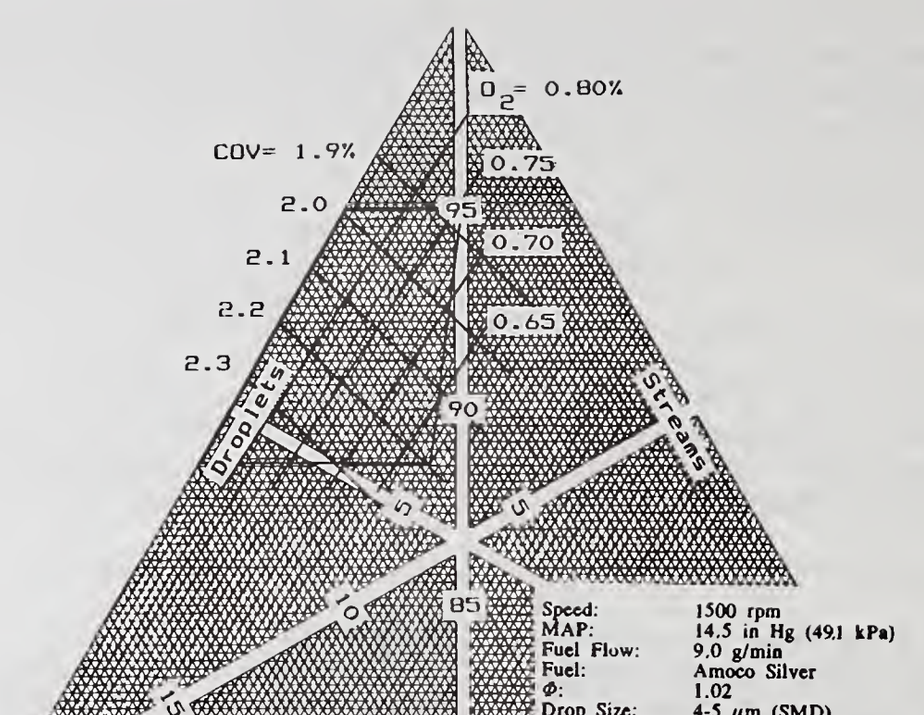

Figure 3: Performance Contours of COV and O_2

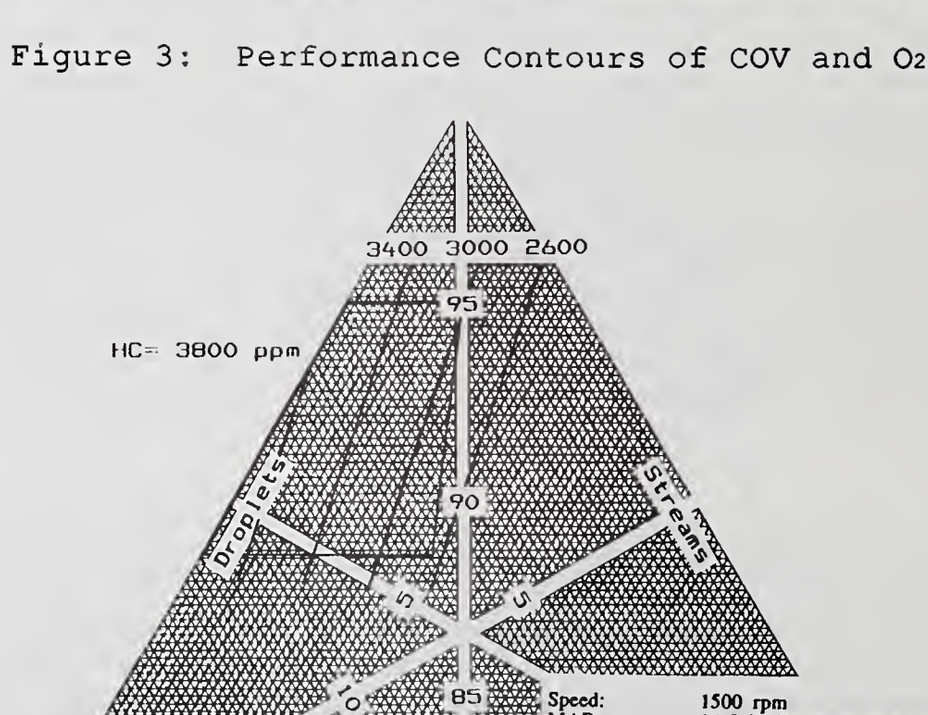

Figure 4: Performance Contours of HC

influenced by streams, as indicated by their greater slopes.

By increasing the percentage of fuel in vapor form; IMEP, NO, and NO_x are shown to be increased. COV is shown to be reduced. These trends are generally indicative of more desirable combustion. This is probably the result of a more homogeneous mixture present in the cylinder. IMEP seems to be more strongly influenced by vapor.

By increasing the percentage of fuel in droplet form; BT, O_2, and HC are shown to be reduced. CO is shown to be increased. These trends are generally indicative of desirable combustion. BT, O_2, and HC seem to be more strongly influenced by droplets.

EQUIVALENT PORT INJECTOR OPERATION

An equivalent fuel preparation (percentage of fuel in vapor, droplet, and stream form) produced by the port injector can be deduced from the above regression relations. In theory, all nine regression relations may be used. Ideally, only three of the nine relations are required for a solution. But because of the existence of variation in data measurements, the solutions from different combinations may not be the same. The accuracy of the deduction depends upon the fit of the regression relations and upon the magnitude of error in the data. The fit of the data with the regression relations is indicated by the coefficients of correlation (R^2). Large R^2 values are indicative of a "good" fit. Therefore when deducing an "equivalent" fuel form, regression relations with relatively high R^2 values should be used.

Figure 5 shows the "equivalent" fuel form produced from the port injector. This deducted fuel form may not represent the actual fuel form but the "equivalent" fuel form with respect to engine performance. In other words, the fuel form produced by the injector burns in the same manner as an "equivalent" fuel form prepared in the channel. Figure 5 also shows the gradients corresponding to the various performance parameters. The arrows show the direction of maximum increase in performance. The length of the arrows is proportional to the degree of performance change. From Figure 5, the direction of improvement, in relation to mixture preparation, in the existing port injection system can be readily seen.

CONCLUSIONS

(1) The testing procedure can be used to evaluate the relative effects of mixture preparation on engine performance.

(2) The testing procedure offers a means of evaluating an equivalent mixture preparation introduced by a port fuel injector with regards to engine performance.

The following conclusions are valid for the Ford 1.9 L EFI HO engine operating at a speed of 1500 rpm and an absolute manifold pressure of 49.1 kPa (14.5 in Hg):

(3) By increasing the amount of fuel in stream form; CO, NO, and NO_x are decreased. COV, BT, O_2, and HC are increased. NO, NOx, CO, and COV seem more strongly influenced by streams.

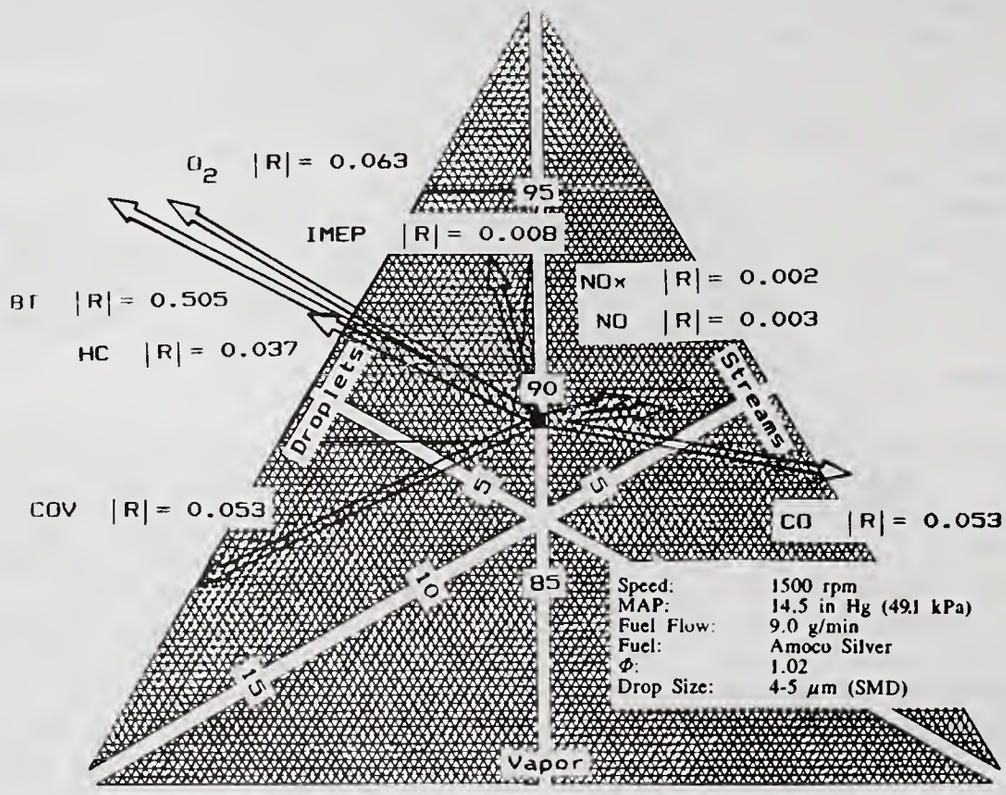

Figure 5: "Equivalent" Fuel Form and Performance Gradients

(4) By increasing the amount of fuel in vapor form; IMEP, O_2, NO, and NO_x are increased. COV is decreased. IMEP seem more strongly influenced by vapor.

(5) By increasing the amount of fuel in droplet form; BT, O_2, and HC are decreased. CO is increased. BT, O_2, and HC seem more strongly influenced by droplets.

(6) In general, engine performance is diminished by increases in the amount of fuel in liquid stream form.

REFERENCES

1. Robison, J. A. and Brehob, W. M., "The Influence of Improved Mixture Quality on Engine Exhaust Emissions and Performance," Journal of the Air Pollution Control Association, Vol. 17, No. 7 (July 1967).

2. Matthes, W. R. and McGill, R. N., "Effects of the Degree of Fuel Atomization on Single-Cylinder Engine Performance," Society of Automotive Engineers Transactions, No. 760117 (1976).

3. Nogi, T., Ohyama, Y., Yamauchi, T., and Kuroiwa H., "Mixture Formation of Fuel Injection Systems in Gasoline Engines," Society of Automotive Engineers Transactions, No. 880558 (1988).

4. Namiyama, K., Nakamura, H., Kokubo, K., and Hosogal, D., "Development of Ultrasonic Atomizer and Its Application to S. I. Engines," Society of Automotive Engineers Transactions, No. 890430 (1989).

EFFECT OF FLOW RATE ON THE SPRAY CHARACTERISTICS OF IMPINGING WATER JETS

P. Vassallo and N. Ashgriz

Department of Mechanical and Aerospace Engineering
State University of New York
Buffalo, NY, U.S.A.

ABSTRACT

The effect of flow rate and injector type on the spray characteristics of impinging, turbulent, water jets for jet Reynold's number in the range of 3,000 < Re < 7,500 is investigated. These characteristics are obtained using a Phase Doppler Particle Analyzer, and include diameter, velocity, number density and volume flux. For two impinging jets at a 45° angle the shattering improves (i.e. drop sizes reduce) as the jet velocities increase. For four impinging jets (two 45° jets with two straight jets in the middle) there exists a critical straight jet velocity for any given 45° jet velocities. The shattering at the edges of the spray improves above this critical condition and worsens below it. The shattering in the center of the spray constantly worsens as the straight jets are added.

1. INTRODUCTION

The performance of liquid propellant rocket engines is intimately related to the spray characteristics generated by the fuel injectors. In rocket engines the fuel injectors are typically of impinging jet type. Two or more jets of liquid fuel and oxidizer are impinged on each other at high velocities, the outcome of which is shattering of the liquid into small drops and mixing of the fuel and oxidizer. The spray characteristic of these injectors were extensively studied in late 1950's and early 1960's [1], and some information their overall behavior was obtained. The basic characters of these injectors are discussed next.

When two liquid jets impinge, they form a liquid sheet (also called a fan) perpendicular to the plane of the two jets. The liquid sheet disintegrates intermittently to form groups of drops, which appear to propagate as waves from the point of impingement. Heidmann and Humphrey [2] measured the frequency of this wave formation using a photoelectric technique over a finite time interval under constant operating conditions. Later, Heidmann, et al. [3] extended their previous results to cover the effects of liquid viscosity and surface tension. They discovered that the wavelike pattern was more pronounced with higher viscosity liquids. Also, they identified four regimes of spray pattern as a function of jet velocity: Closed rim, Periodic drop, Open rim, and Fully developed impinging spray. Each of the aforementioned regimes is encountered in the order shown as the velocity is increased. Continuing their investigations, Heidmann and Foster [4] studied the effect of the impingement angle on drop size distributions for a range of velocities. They obtained drop counts from shadowgraphs using a particle analyzer, and concluded that all distributions showed bimodal characteristics. Overall volume-number mean and mass median drop

diameters were observed to increase with a decrease in velocity and a decrease in impingement angle, with impingement angle having the most pronounced effect.

In all of the above studies, simple photographic techniques were used to obtain drop sizes and liquid sampling technique was the main measuring method for the distribution of the volumetric flow rate. Due to the recent advances in the spray diagnostic systems it is now possible to obtain detailed information throughout the whole spray. In this paper, the effect of flow rate on the spray characteristics of a two-jet and four-jet rocket injector is described.

2. EXPERIMENTAL SET-UP

An actual rocket injector of a 22N thruster manufactured by Atlantic Research Corporation is used in these studies. The injector contains four orifices so that liquid fuel and liquid oxidizer may impinge on each other to provide for the mixing necessary for the combustion process. The diameter of the two fuel orifices are 0.3 mm, and are set to impinge at a 90° angle. The oxidizer streams are 0.356 mm in diameter, 1.27 mm apart from each other, and emanate straight down into the fuel streams, resulting in a 45° impact angle between each fuel-oxidizer pair. Figure 1 shows a schematic diagram of the impingement. Although water is used in place of fuel and oxidizer for testing purposes, we will still refer to the liquid jets using the terms fuel and oxidizer to distinguish between the two.

A Phase Doppler Particle Analyzer (PDPA), designed and manufactured by Aerometrics Inc. [5-7] is used for simultaneous measurements of diameter, velocity, number density, and volume flux throughout the complete spray field. A 3-D traversing system is designed and built in order to map the spray field. The injector is mounted on the traversing system, and the PDPA is kept stationary. The traversing system is mounted on the top of a 90 cm x 90 cm x 152 cm stand. The traversing system moves by a leadscrew-stepping motor arrangement on linear motion ball bushing bearings. The range of motion is approximately 46 cm in each direction and the stepping motors provide accurate steps for motion as small as 1 mm. A conical liquid catcher collects the spray and channels it into a drain. Besides the traversing stand, another stand was built to hold two 30 liter water storage tanks (one for the fuel line and the other for the oxidizer line), and to house the control valves and pressure gages that were used to monitor the flow. The flow rate is measured by an orifice flow meter.

3. VARIATION OF SPRAY PROPERTIES WITH FLOW RATE

For this particular injector the drops are not spherical up to 5 cm downstream of the injector. At this location a 4 cm x 4 cm zone encompasses the whole spray region. Therefore, detailed measurements of the spray character are confined to this zone. The spray distribution throughout a 4 cm x 4 cm region at an axial distance from the face of the injector of 5 cm is obtained for several different flow rates and jet orientation. Figure 1 shows the reference axes used throughout this report. For example, $y = 0$ corresponds to a centerline perpendicular to the plane of the impinging jets, and $x = 0$ corresponds to a centerline parallel to the plane of impinging jets. The z coordinate is kept constant at 5 cm.

In order to see the effect of the flow rate on the spray character several critical points in the spray are examined to determine how each spray parameter changes with changing flow rate. These points are (0,0), (±2,0), and (0,±2). It is observed that the results at (2,0) corresponded well with those at (-2,0) and

the results at (0,-2) corresponded well with those at (0,2), indicating fair symmetry. The results for (0,0), (0,-2) and (2,0) are shown in Figs. 2-4.

Figure 2 shows the variation in parameters as a function of flow rate at the center of the spray (0,0). This figure is divided into two regions. In the first region, only the fuel jets are flowing and the spray character of two impinging jets are investigated. In the second region all four jets are flowing. However, the flow rate of two fuel jets is kept constant at 3.18 ml/s, while the oxidizer jet flow rate is changed. It can be seen that for fuel only injection, the diameter decreases, the velocity increases, the number density increases, and the volume flux decreases with increasing flow rate. The diameter decrease and number density increase follow from increased shattering, and the velocity increase follows from increased flow rate. The volume flux decreases because at higher impingement velocities (higher flow rates), flow deflects more to the sides. As the oxidizer is added at a constant fuel flow rate of 3.18 ml/s, the diameter and volume flux constantly increase. This is due to the added mass in the center of the spray. At first the velocity feels little change, then it too increases as the oxidizer is increased. Note that the oxidizer flow rate where the velocity begins to increase is 2.72 ml/s. This implies below 2.72 ml/s, the added oxidizer stream does not significantly effect the drop velocity in the center, but after 2.72 ml/s it does. The number density is seen to constantly decrease. The increase in drop size and decrease in number density indicates that the efficiency of shattering at the center of the spray constantly reduces with adding the oxidizer jets.

Figure 3 shows how diameter, velocity, number density and volume flux vary as a function of flow rate at (0,-2). Again the diameter decreases, velocity increases, number density increases as fuel flow rate increases. However, the volume flux increases in this section of the spray with increasing flow rate where in the center it decreases. This is due to the fact that the number density increases at a faster rate at (0,-2) than it does at (0,0), since more flow is deflected toward the sides. As the oxidizer streams are added to the nominal fuel streams, an interesting pattern is observed. For oxidizer flow rates less than 2.72 ml/s, increasing oxidizer flow increases diameter and velocity while for oxidizer flow rates greater than 2.72 ml/s, increasing oxidizer flow rate decreases diameter and velocity. This implies a critical oxidizer flow rate exists for a particular fuel flow rate. The reason such a critical value exists is that at relatively low oxidizer flow rates the added oxidizer stream reduces the effective impact velocity of the fuel jets, and also causes the impingement angle to decrease. This results in an increase in diameter and a decrease in number density due to less efficient shattering. This effect continues up to the critical flow rate. As the oxidizer flow rate is increased further than critical, the impingement angle decreases even further such that a smaller fraction of the spray reaches (0, ±2). This small fraction contains small drops. The decrease in impingement angle may be observed by comparing Fig. 5a, Fig. 6a, and Fig. 7a. Note that the point of impingement is pushed further downstream with higher oxidizer flow, thereby decreasing the mass of fluid that travels to (0,-2). It is also observed that both number density and volume flux constantly decrease.

Figure 4 shows variation in spray parameters at (2,0) as a function of flow rate. As before, for fuel only injection, the diameter decreases, and velocity and number density increases as fuel flow rate increases. However, the volume flux is nearly constant indicating that the spray becomes more dispersed in the vicinity of this point as the flow rate increases. As the oxidizer is added, the critical peak at 2.72 ml/s is again observed. Here again, diameter and velocity increase, with increase in oxidizer flow rate up to 2.72 ml/s. This effect in the direction of $y = 0$ is due to the splitting of the relatively low

speed oxidizer stream impacting the high velocity fuel jets. Figure 6b shows a photograph of this case. As the oxidizer impinges on the fuel jet, it splits in the x direction at an angle dependant on its flow rate. As the flow rate increases, the split angle goes down. The split flow passes through point (2,0) at the critical flow condition. Below the critical flow rate the split flow is outside of point (2,0), therefore smaller mass of liquid reaches that point. After the critical flow condition, the oxidizer-fuel jet impingement results in a better shattering, reducing the splitting effect. This explains the observed increase of the volume flux up to the critical point, and then its decrease, along with diameter and velocity, after the critical value. Since the number density increases in the primary shattering direction (fan direction) for fully developed impingement it increases after the flow rate of 2.72 ml/s.

4. FULL SPRAY CHARACTERIZATION

Although the variation in spray parameters as a function of flow rate has been discussed for several important points in the spray, it is difficult to gain a global perspective without looking at entire spray cross section. In the next section, the complete contours of the spray parameters for a four jet injector is given. The flow rate of the fuel jets is set at 3.18 ml/s and the flow rate of the oxidizer jets is set at 4.08 ml/s.

4.1 Four-Jet Injector

The spray contours of diameter, velocity, number density and volume flux for the four-jet case are shown in Figs. 8-11, respectively. The diameter contour of Fig. 8 shows that the largest diameters are bunched about the center of the spray. This is a result of the addition of the heavy flow of oxidizer stream straight down into the fuel jets. If the oxidizer jets were not flowing, the diameters at the center of the spray would be among the smallest present, since the fuel jets would be shattering with full impact at that location. Also, for two-jet impingement, the magnitudes of the diameters in the fan direction (x-direction) would be relatively the same, but for the four-jet injector, this is no longer the case. In fact, the pattern that exists is for the diameter to decrease in every direction away from the center.

The number density contour is shown in Fig. 9. As this figure shows, the largest number density occurs in the area of (±2,0), a medium number density occurs in the center, and the smallest number density occurs in the area of (0,±2). The reason the number density is highest at (±2,0) is that this is the primary shattering direction for the fan which is formed by each pair of fuel-oxidizer streams. The number density is lowest at (0,±2) because the oxidizer stream issues straight down and tends to inhibit any spray from reaching the edges in the y direction. There is no simple relationship between diameter and number density, as there is for the two-jet case. There the number density is seen to be inversely proportional to the diameter raised to a power, but here the largest drops in the center have a higher number density than the smaller drops in the region of (0,±2).

The volume flux is shown in Fig. 10. It is observed that a symmetric heavy band of flux occurs about y = 0, and that the flux falls off sharply with increasing y. The largest flux occurs in the center, and the flux decreases slightly as the x position is increased. The heavy band of volume flux coincides with the fan, which can be observed by referring to the pictures in Fig. 7, which show perpendicular and parallel views of the four-jet case.

The velocity contour of Fig. 11 has a similar pattern to the diameter

contour. This is a result of the general size-velocity correlation present in sprays where the largest diameters also have the largest velocities. The reason this correlation exists is that in the presence of air resistance, small drops initially moving at the same velocity as large drops will lose their velocity faster than the large drops. Thus, by the time the drops reach the z = 5 measurement plane, the smaller drops are moving slower than the larger drops. It is seen in Figs. 8 and 11 that both diameter and velocity plots lose a portion of their symmetry in the region near (-1,-1), and the magnitudes are both slightly larger than would be expected for a perfectly symmetric case.

5. CONCLUSIONS

Spray characterization of two and four impinging water jets is undertaken to investigate the effect of flow rate on different spray parameters. For 45° impinging water jets (referred to as fuel jets) the flow rates in the range of 1.81 ml/s to 3.63 ml/s are examined. The x and y directions are defined as the directions perpendicular and parallel to the impinging plane. In all spatial positions, increasing flow rate decreases diameter, increases number density and increases velocity. The volume flux decreases in the center, increases along y, and remains relatively the same along x for increasing flow rate. A four impinging jet injector composed of two jets at 45° with two straight jets in the middle (referred to as oxidizer jets) is also investigated. The flow rates of the straight jets are varied in the range of 1.81 ml/s to 4.08 ml/s, while the 45° jets are kept constant at 3.18 ml/s. For this type of injector, for any given fuel flow rate, a critical oxidizer flow rate exists for which the shattering behavior changes. Drop diameters and velocities increase as the oxidizer flow rate increases up to the critical condition, after which they reduce (except at the spray center). This effect is shown to be a result of the splitting of the fluid in the x direction, and the suppression of impact angle in the y direction. At high flow rates for both the fuel (3.18 ml/s) and the oxidizer (4.08 ml/s) jets it is obtained that the largest diameters are in the center, and that in all directions from the center the diameter decreases. The number density is largest at the edges of the x axis, medium in the center, and smallest at the edges of the y axis. The volume flux is heavy about y = 0, decreasing substantially as y increases. The velocity is largest in the center, and is similar in pattern to the diameter contour.

6. REFERENCES

1. Harrje, D.T., "Liquid Propellant Rocket Combustion Instability", NASA SP-194 (1972).

2. Heidmann, M.F., and Humphrey, J.C., "Fluctuations in a Spray Formed by Two Impinging Jets", NACA TN 2349 (1951).

3. Heidmann, M.F., Priem, R.J., and Humphrey, J.C., "A study of Sprays Formed by Two Impinging Jets", NACA TN 3835 (1957).

4. Heidmann, M.F., and Foster, H.H., "Effect of Impingement Angle on Drop-Size Distribution and Spray Pattern of Two Impinging Water Jets", NASA TN D-872 (1961).

5. Bachalo, W.D., and Houser, M.J., "Development of the Phase Doppler Spray Analyzer for Liquid Drop Size and Velocity Characterizations", 20th Joint

Propulsion Conference, AIAA-84-1199 (1984).

6. Bachalo, W.D., and Houser M.J., "Phase/Doppler Spray Analyzer for Simultaneous Measurements of Drop Size and Velocity Distributions", Opt. Engr., Vol. 23, No. 5, pp. 583 (1984).

7. Bachalo, W.D., Rudoff, R.C., and Brena de la Rosa, A., "Mass Flux Measurements of a High Number Density Spray System using the Phase Doppler Particle Analyzer", AIAA 26th Aerospace Sciences Meeting, AIAA-88-0236 (1988).

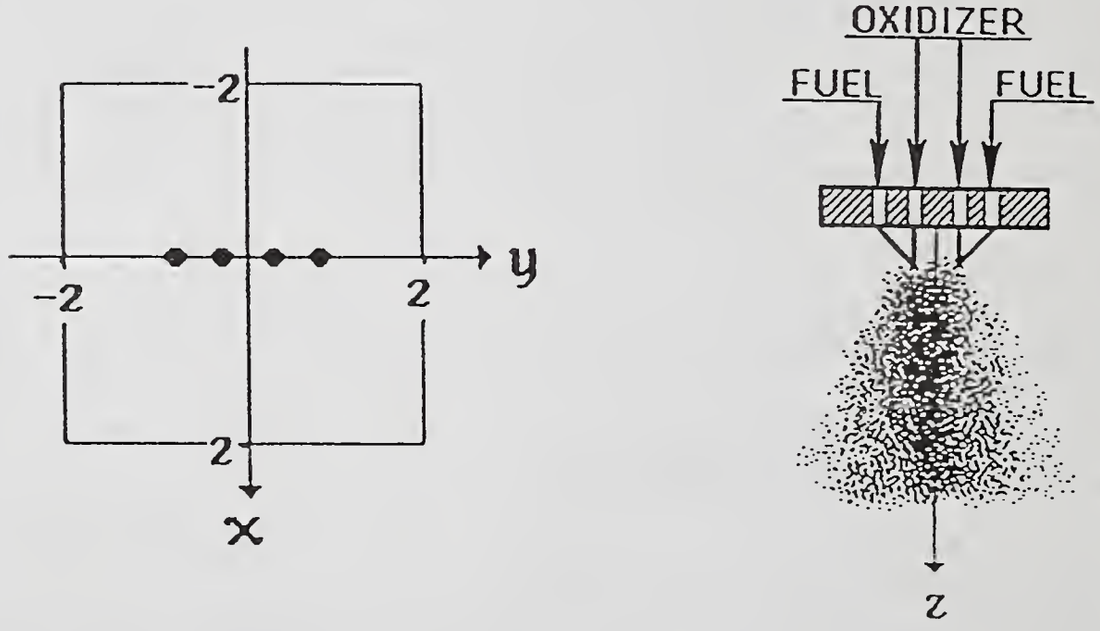

Fig. 1 Schematic of Impingement and Axes of Reference

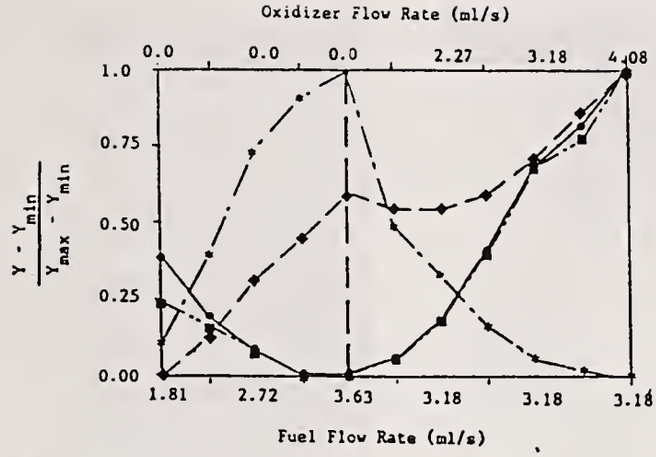

Fig. 2 Parameter Variation at (0,0): Mean Velocity (◆) Y_{min}=7.126, Y_{max}=15.987 m/s; Number Density (✱) Y_{min}=780, Y_{max}=2800 /cc; Volume Flux (■) Y_{min}=.36, Y_{max}=3.6 cc/sec/cm^2; Diameter (●) Y_{min}=23.377, Y_{max}=84.387 um

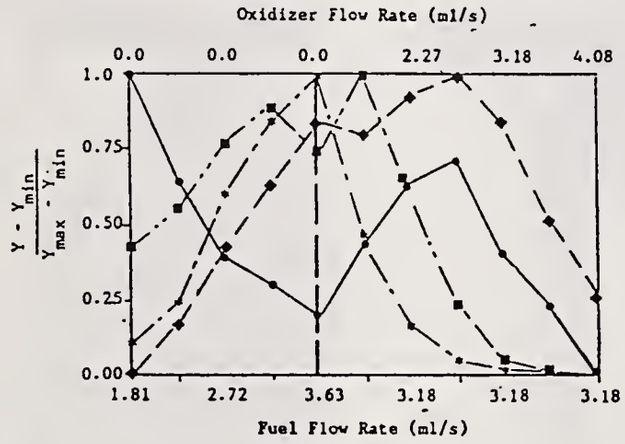

Fig. 3 Parameter Variation at (0,2): Mean Velocity (◆) Y_{min}=5.441, Y_{max}=9.195 m/s; Number Density (✱) Y_{min}=5.7, Y_{max}=380 /cc; Volume Flux (■) Y_{min}=.0011, Y_{max}=.19 cc/sec/cm^2; Diameter (●) Y_{min}=36.489, Y_{max}=97.526 um

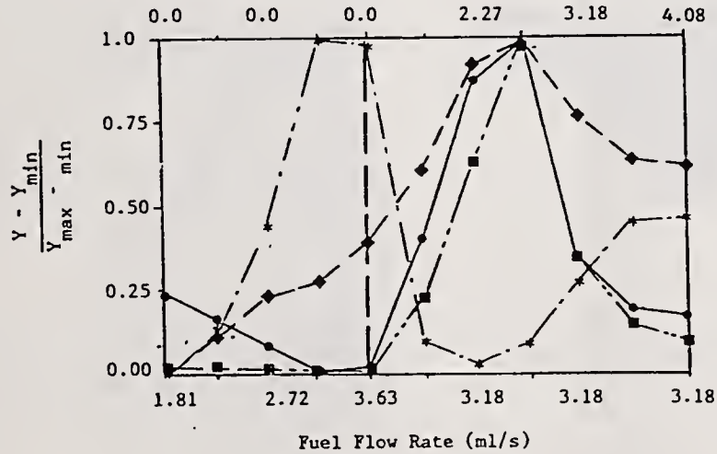

Fig. 4 Parameter Variation at (2,0): Mean Velocity (◆) Y_{min}=3.924, Y_{max}=9.142 m/s; Number Density (✱) Y_{min}=550, Y_{max}=2400 /cc; Volume Flux (■) Y_{min}=.11, Y_{max}=2.7 cc/sec/cm^2; Diameter (●) Y_{min}=24.343, Y_{max}=84.395 um

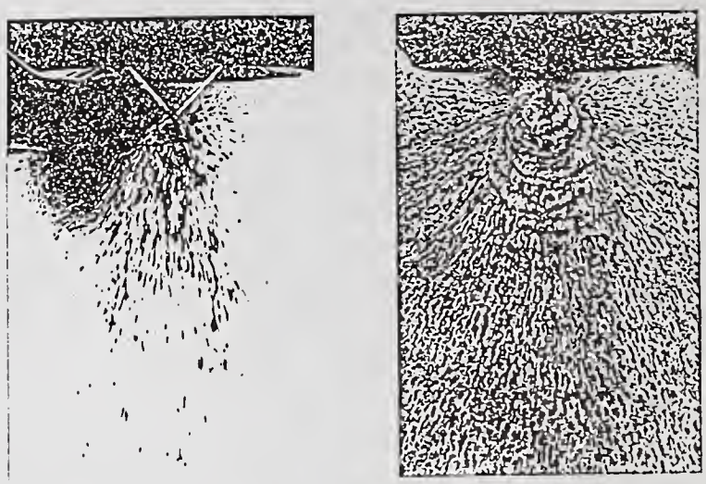

Fig. 5 Parallel and Perpendicular Views of Two-Jet Impingement with Fuel Flow = 3.18 ml/s; Oxidizer = 0.0 ml/s

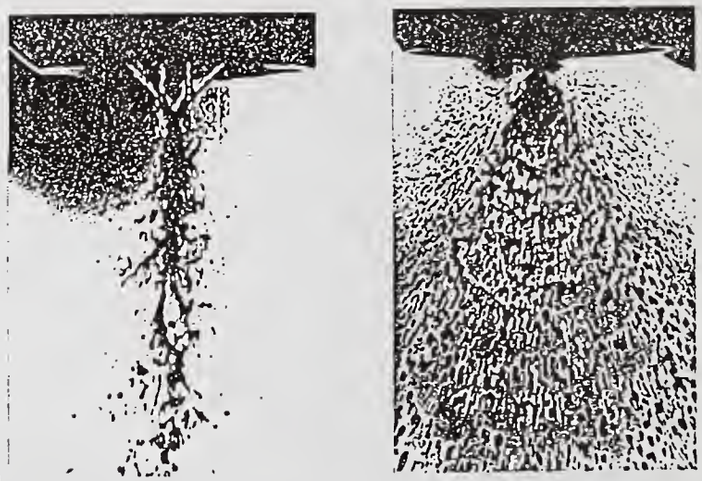

Fig. 6 Parallel and Perpendicular Views of Four-Jet Impingement with Fuel Flow = 3.18 ml/s; Oxidizer = 2.72 ml/s

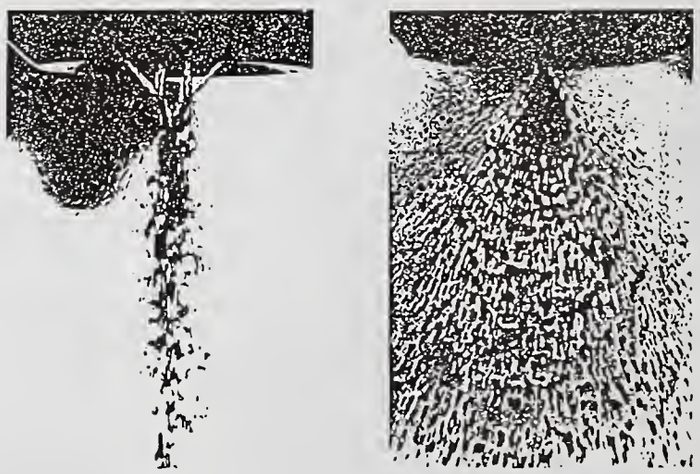

Fig. 7 Parallel and Perpendicular Views of Four-Jet Impingement with Fuel Flow = 3.18 ml/s; Oxidizer = 4.08 ml/s

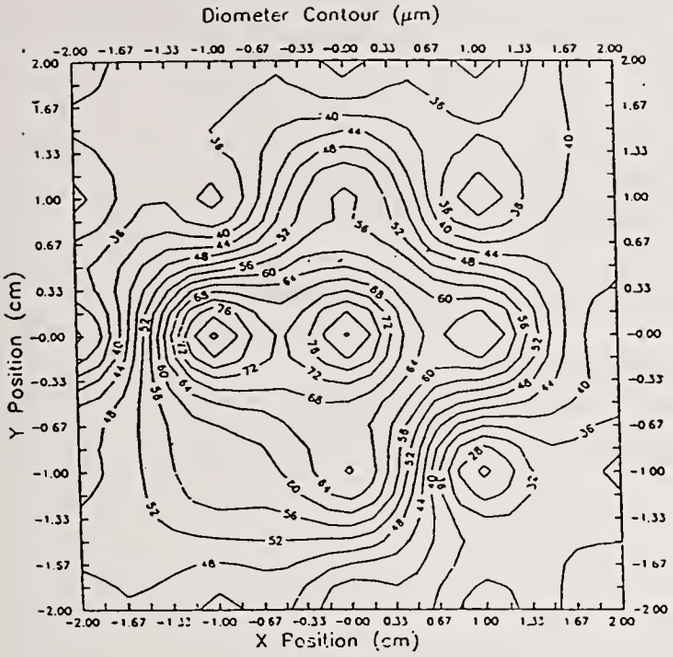

Fig. 8 Diameter Contour
Fuel=3.18 ml/s
Oxidizer=4.08 ml/s

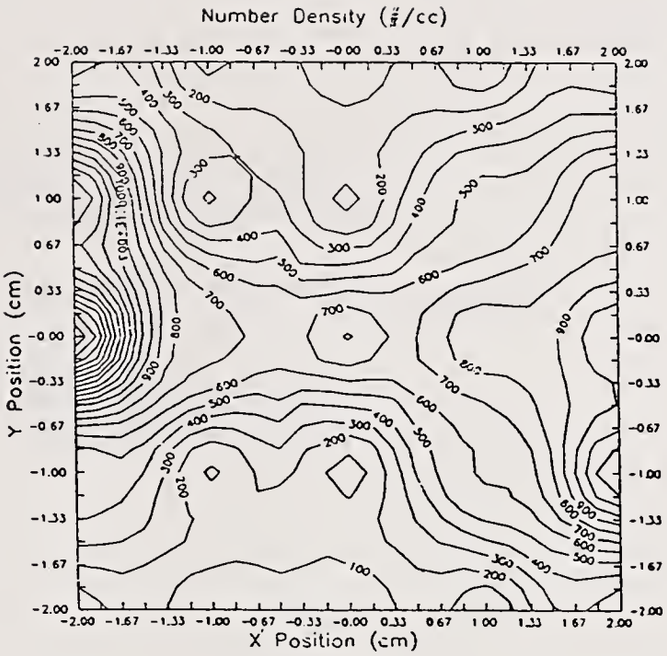

Fig. 9 Number Density Contour
Fuel=3.18 ml/s
Oxidizer=4.08 ml/s

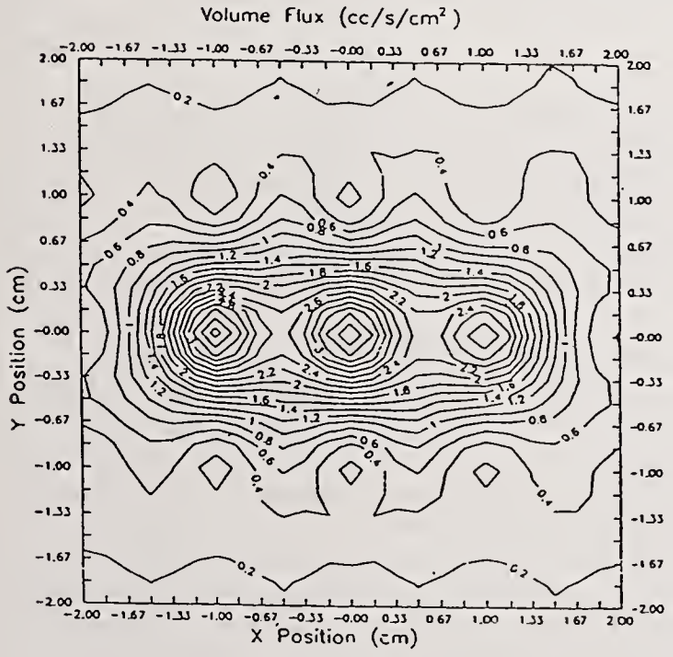

Fig. 10 Volume Flux Contour
Fuel=3.18 ml/s
Oxidizer=4.08 ml/s

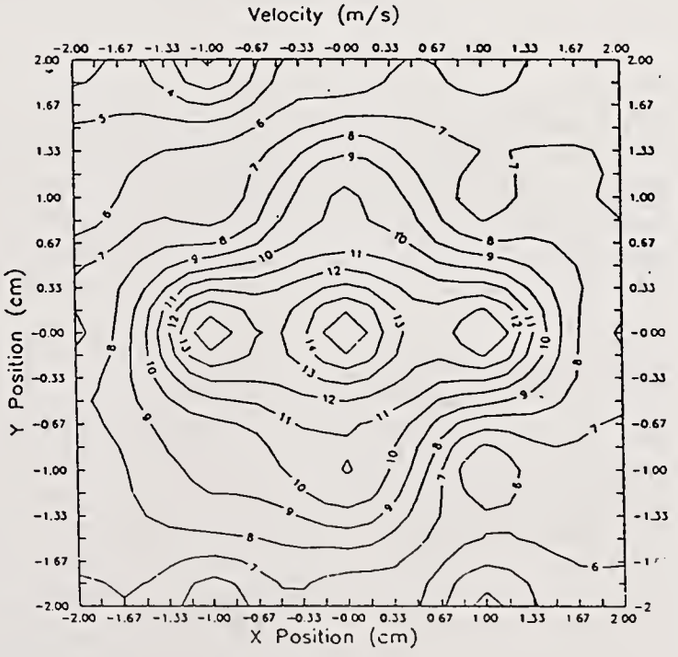

Fig. 11 Velocity Contour
Fuel=3.18 ml/s
Oxidizer=4.08 ml/s

ANALYTICAL AND EXPERIMENTAL STUDY OF PRIMARY ATOMIZATION OF WATER JETS

A.J. Przekwas*, J.-G. Lee*, K.W. Gross†, N.A. Chigier‡ and H. Eroglu‡

*CFD Research Corporation, Huntsville, AL, U.S.A.
†NASA Marshall Space Flight Center, Huntsville, AL, U.S.A.
‡Dept. of Mechanical Engineering, Carnegie Mellon University, Pittsburgh, PA, U.S.A.

ABSTRACT

The objectives of the present investigation are to predict primary atomization of liquid jets employing the jet embedding technique coupled with jet instability analysis, and to compare the prediction with experimental measurements. A novel jet breakup model is proposed, which reduces the computation time by an order of magnitude as compared to the previously reported breakup model. Experiments were performed to measure liquid jet core intact length and droplet size distribution. Results of the validation study show that the predictions agree favorably with the experimental measurements on liquid jet intact length and drop sizes at different flow conditions.

INTRODUCTION

Gas-liquid two-phase flow is common to practical combustion systems [1]. Primary atomization of liquid jets has been studied for over a century, which includes classical works such as Rayleigh [2] and Weber [3], and recent studies such as Reitz and Bracco [4], Meyer and Weihs [5], Lefebvre [1] and Lee and Chen [6]. It has been recognized that the relative velocity between the gas and liquid is the cause of the primary atomization resulting in small droplets detaching from the liquid surfaces. The present investigation focuses on the numerical prediction of atomization of liquid jets with high speed air flows.

Przekwas, *et al.* [7] studied the primary breakup of liquid oxygen jets with high speed gaseous hydrogen annular jets. Predicted results were in favorable agreement with Sutton, *et al.* [8] (CICM formula) and Liang, *et al.* [9]. The frequency scanning approach used in the original atomization model [7] required long computational time. In the present paper, instead of scanning the entire wavelength spectrum, the maximum growth rate is computed by analytic differentiation of the dispersion equation. The breakup mass and drop sizes are calculated based on the local wavelength. An order of magnitude gain in computational time was achieved with minor change in accuracy of the results. The breakup of the surface into small droplets is assumed to occur when the local amplitude of the disturbance exceeds one half the wavelength of the disturbance at the maximum growth rate.

The results of the calculated jet intact length and droplet size are compared with the complementary experimental measurements recently conducted by Chigier and Eroglu [10] for liquid jet atomization under the influence of surrounding gas flows. Atomization characteristics such as liquid core intact lengths and droplet sizes were measured. The core intact length was determined from photographs, while drop size was measured using the Phase Doppler Particle Analyzer (PDPA).

JET EMBEDDING TECHNIQUE

In the Jet Embedding (JE) technique, Przekwas [11], the liquid sheet is described in a one-dimensional form with a computational grid conforming to the liquid jet shape. At present, the gravitational force and internal viscous effects are neglected. The friction between the liquid and gas is accounted for at the jet interface. The basic conservation equations of mass, axial- and cross-stream momentum are expressed as follows:

$$\frac{\partial \rho_f}{\partial t} + \frac{\partial \rho_f U_f}{\partial s} = \dot{m}_B \tag{1}$$

$$\frac{\partial \rho_f U_f}{\partial t} + \frac{\partial \rho_f U^2_f}{\partial s} = -\frac{\partial p_f}{\partial s} - \dot{m}_B (U_f - U^o_d) - \xi_s'' \rho_f (U_f - U_g)^2 \tag{2}$$

$$\frac{\partial \rho_f V_f}{\partial t} + \frac{\partial \rho_f U_f V_f}{\partial s} = - \dot{m}_B (V_f - V^o_d) - \xi_n'' \rho_f (V_f - V_g)^2 \tag{3}$$

where m_B is the droplet breakup rate, U_f and V_f are liquid velocities, U^o_d and V^o_d are initial droplet velocities leaving the jet surface, ρ_f is the liquid density, and ξ''_s and ξ''_n are the gas-liquid friction coefficients for the coaxial and cross flow directions, respectively.

The three conservation equations are approximated by the finite volume method on a one-dimensional adaptive, surface conforming grid (*i.e.*, see Figure 1). A space marching technique is employed to integrate the governing equations along the liquid surface trajectory from the nozzle exit until the liquid jet mass is completely atomized. A schematic of an imbedded jet and its interaction with the gas phase is shown in Figure 1.

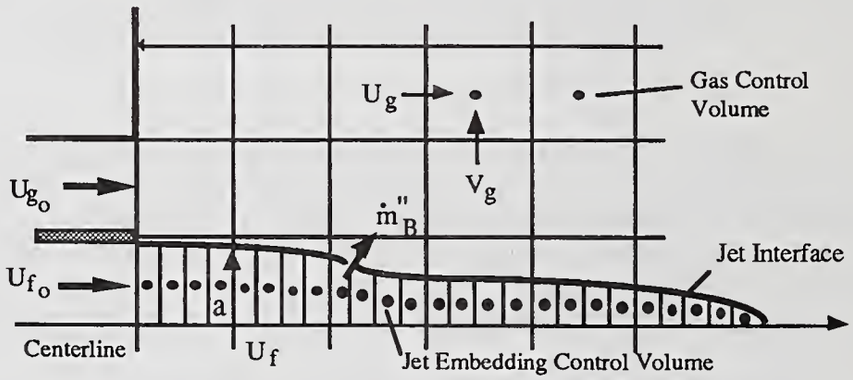

Fig. 1 Schematic representation of the liquid jet breakup using an Eulerian Computational grid for the gas phase equations.

LINEAR STABILITY ANALYSIS OF LIQUID JETS WITH HIGH SPEED AMBIENT GAS FLOWS

As a liquid jet issues from a nozzle, its surface is subjected to various disturbances, caused by vibrations of the nozzle, shape of the jet, gas motion surrounding the jet, turbulence in the liquid, and roughness of the wall surface. Disturbances can be represented by the superposition of Fourier components. A Fourier component is expressed in the following form:

$$\zeta = \zeta_o e^{ikz+\alpha t} \tag{4}$$

where ζ_o is the initial amplitude of an infinitesimal axisymmetric displacement (disturbance) at the interface. k is the wave number, and α is the growth rate of disturbances.

After algebraic manipulation (*e.g.*, Levich [12] and Chuech, *et al.* [13]), a governing wave dispersion equation is obtained in the general form:

$$\alpha^2 + 2\nu_f k^2 \left[\frac{I'_1(ka)}{I_0(ka)} - \frac{2kl}{k^2+l^2}\frac{I_1(ka)I'_1(la)}{I_0(ka)I_0(la)}\right]\alpha$$

$$= \frac{\sigma k}{\rho_f a^2}(1-k^2a^2)\left(\frac{l^2-k^2}{l^2+k^2}\right)\frac{I_1(ka)}{I_0(ka)} + \frac{\rho_g U_r^2 k^2}{\rho_f}\left(\frac{l^2-k^2}{l^2+k^2}\right)\frac{I_1(ka)}{I_0(ka)}\frac{K_0(ka)}{K_1(ka)} \qquad (5)$$

where a is the jet radius, σ is surface tension, ρ_f is liquid density, ν_f is liquid kinematic viscosity, $l^2 = k^2 + a^2$, and $I_n(x)$ and $K_n(x)$ are Bessel functions of the first and second kinds of order n, respectively. The two terms on the LHS represent liquid inertia and viscosity, while the two RHS terms represent the surface tension and gas-liquid relative velocity effects. Numerical solutions of the full dispersion equation were obtained by Chuech, *et al.* [13]. However, considerable useful information can also be obtained by analyzing the solutions of the simplified limiting forms from the full dispersion equation. In the following, two such limiting forms are discussed.

<u>High-speed Ambient Gas Jets With Long Wavelength Disturbances ($\lambda > a$ or $ka < 1$)</u>

For long wavelength disturbances, $\frac{K_0(ka)}{K_1(ka)} \approx -ka \ln\left(\frac{ka}{2}\right)$, the dispersion equation can be approximated as:

$$\alpha^2 + \nu_f k^2 \alpha = \frac{\sigma k^2}{2a\rho_f}(1-k^2a^2) - \frac{\rho_g U_r^2 k^4 a^2}{2\rho_f}\ln\left(\frac{ka}{2}\right) \qquad (6)$$

<u>High-speed Ambient Gas Jets With Short Wavelength Disturbances ($\lambda < a$ or $ka > 1$)</u>

For short wavelength disturbances, $I_1(ka) \approx I_0(ka)$, $I_1(la) \approx I_0(la)$, $I_1'(ka) \approx I_1(ka)$, and $K_0(ka) \approx K_1(ka)$, the simplified equation is expressed as:

$$\alpha^2 + 2\nu_f k^2 \alpha = -\frac{\sigma k^3}{\rho_f} - \frac{\rho_g U_r^2 k^2}{\rho_f} \qquad (7)$$

It is noted that for high-speed gas flows, for both cases, the dispersion equations reduced to quadratic form which admits real and imaginary solutions. If the real part of the solution, $\alpha_r > 0$, the disturbances grow exponentially in time, otherwise, the disturbances will be damped out.

MODEL OF PRIMARY ATOMIZATION

To improve the computational efficiency of the atomization model by Przekwas [7], an alternative breakup model was postulated. In the original Jet Embedding model, the entire wavelength spectrum, λ, was employed. Here the wave dispersion equation is differentiated and the maximum growth rate wave length, λ_{max}, is directly computed. Based on the local wave amplitude ξ, and the maximum wavelength λ_{max}, a surface breakup mechanism is invoked to calculate liquid breakup rate. Since finding the wavelength at the maximum growth rate can be done much faster than scanning the entire wave spectrum, much less time is required to obtain the results. Assuming λ_{max} as the characteristic length of the atomization process, *i.e.*, $\lambda_{max} = 2D_{drop}$, where D_{drop} is the diameter

of the liquid droplets detaching from the liquid surface, the breakup rate per unit circumferential area (mass leaving the liquid surface due to breakup) is therefore calculated as:

$$\dot{m}''_B = \frac{n\ V}{A^S\ T} = \frac{\pi\ \lambda_{max}\ \alpha_{max}}{16\ \ln\ (\lambda_{max}\ /\ 2\xi_o)} \tag{8}$$

where $n = \frac{\Delta\ x}{\lambda_{max}}$ is the number of wavelets per unit length,

$V = \pi\ D\ (\frac{\pi\lambda_{max}^2}{16})$ is the volume of the liquid ring generated by a single wavelet, and

$T = \frac{1}{\alpha_{max}} \ln\ (\frac{\lambda_{max}}{2\xi_o})$ is the characteristic time for a wavelet growing into a liquid ring.

COUPLING PROCEDURE

The main steps of the coupling procedure between the Jet Embedding technique and the proposed primary breakup model in the present computation are summarized below:

1) Calculate the jet velocity and diameter at a given axial location using the Jet Embedding technique (see Figure 1).
2) Update the coefficients in the dispersion equation (7) and solve the equation for the wavelength corresponding to the maximum growth rate.
3) Calculate the mass breakup rate (Eq. 8) and the droplet size at the same location.
4) Move to the next axial position along the jet axis, and go back to Step 1 with the updated mass breakup rate.

EXPERIMENTAL TEST CONDITIONS

In order to validate the proposed atomization model, experimental measurements were performed for the liquid jet atomization in coflowing air streams. Details of the experimental study were reported by Chigier and Eroglu [10]. Two different nozzle geometries, namely, plane and round jets, were investigated. For the round jet, two different central tube designs were tested to assess the influence of nozzle geometry on the atomization process. The working fluids are air (in the annulus) and water (in the central tube). Atomization characteristics such as liquid intact lengths and droplet sizes were measured, the former was determined from photographs, while the latter was obtained using the Phase Doppler Particle Analyzer (PDPA). Chigier and Eroglu [10] also reported the non-axisymmetric breakup of liquid jet, and its theoretical analysis has been performed by Yang [14]. Since only the round jet case is relevant to our study, the following discussion is limited to the round jet results. The dimensions of the nozzle are given in Figure 3, and the test conditions are summarized in Table 1.

The following empirical correlation was formulated from the photographs by Chigier:

$$\frac{L}{D_o} = 0.5\ We^{-0.4}\ Re^{0.6} \tag{9}$$

where L is jet intact length, D_o is the diameter of the central jet, $We = \frac{\rho_L D_o (u_L - u_g)^2}{2\sigma}$ and $Re = \frac{\rho_L\ u_L\ D_o}{\mu_L}$, and σ is surface tension, ρ_g, u_g and ρ_L, u_L are densities and velocities of air and water, respectively. The correlation implies that the intact length is not only controlled by the relative velocity (*i.e.*, Weber number), but also by the momentum of the liquid jet (*i.e.*, Reynolds number). Experimental results also show that intact lengths are independent of the nozzle shape, but it does have an impact on the droplet sizes.

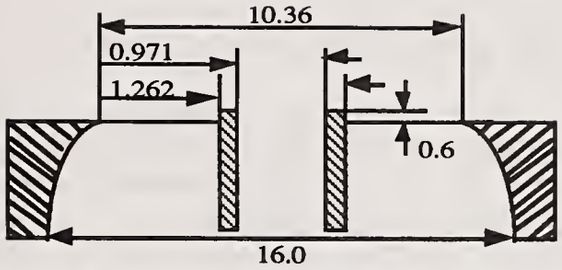

Fig. 2 Nozzle geometry for coaxial atomizer (dimensions in mm), Chigier and Eroglu [10].

Table 1 Experimental conditions of air-water jets by Chigier [10].

Water Velocity (m/s)	Reynolds Number	Air Velocity (m/s)	Weber Number
1.51	1456	36.7 - 159.0	50 - 200
4.52	4370	39.8 - 162.0	50 - 200
9.65	9328	44.9 - 167.0	50 - 200

RESULTS AND COMPARISON

Computations were made by employing the Jet Embedding technique, Equation (7), (8), and the coupling procedure. Air and water properties at standard conditions were used, and the test conditions are given by Table 1. The calculated liquid jet lengths are shown in Figure 3 for Re=1456 and We=10-200. It is obvious that the jet length is decreased as Weber number increases. Increase of Weber number means increase of relative velocity between the air and liquid, assuming fluid properties remain constant. A higher relative velocity results in a higher breakup rate, *i.e.*, a shorter jet. It should be noted that the steps on the jet surfaces in Figure 3 are due to the resolution of the graphics software. Jet velocities as a function of axial distance are plotted in Figure 4, which shows that higher gas velocity reduces jet lengths and results in a higher jet velocity as the jet diameter approaches zero. Figure 6 depicts the droplet size variation under the same flow conditions. It appears that the droplet size decreases significantly as Weber number number increases, particularly when Weber number is changed from 10 to 50. The droplet sizes are under 50 μm for Weber number =50 to 200. The size of the droplets at the separation increases along the jet direction axial direction (Figure 5), as the relative velocity between gas and liquid gradually diminished.

Calculations were also performed for Reynolds numbers 3270 and 9328, and Weber numbers ranging from 10 to 200. Results with similar trends were obtained. Figure 6 shows the calculated jet intact lengths under different flow conditions, including Reynolds numbers equal to 3270 and 9328. The experimental observations of the jet intact length by Chigier are included for comparison. Comparison shows good agreement at low Reynolds number, and is less satisfactory as Reynolds number is increased. It is noted that the empirical correlation shown above for the measured breakup lengths was obtained from the scattered experimental data (*i.e.*, see Figure 6). Figure 7 shows the comparison between the experimental correlation and the prediction from the CICM code [8]. It is seen that the present prediction compares favorably with the jet intact length calculated from the CICM code for Reynolds numbers 1456 and 3270. For Re=9328, the present prediction shows better prediction in the low Weber number regime, and less satisfactory in the high Weber number regime than CICM prediction. However, it is noted that an empirical constant has to be determined in the CICM mass breakup rate correlation:

$$\text{Mass breakup rate } \dot{m}_B = C_A \left[\frac{\mu_l (\rho_g u_r^2)^2}{\sigma/\rho_l}\right]^{1/3} \tag{9}$$

where Liang, *et al.* (1986) use C_A = 0.0378 in the injector element cup region, and 0.14 in the main chamber. The constant has to be estimated from experimental measurements. The present CICM results shown in Figure 8 use C_A = 0.14 in the mass breakup rate equation (9), and it is also noted that previous

CICM results from the SSME LOX jet calculation (Chuech and Przekwas, 1988) used C_A = 0.0378. The present prediction, however, using the proposed breakup model performs faster and without adjusting the constants.

The predicted drop sizes and measured Sauter Mean Diameter (SMD) are presented in Figure 8. It should be noted that the measured drop sizes are obtained approximately 2 mm downstream of the jet's tip location, and SMD variation in the radial direction was recorded. Since the present numerical analysis predicts droplet sizes leaving the liquid surface, but not beyond the jet tip, a direct comparison is not possible. To circumvent the difficulty, we assume that all droplets leaving the jet surface reach the downstream location with negligible coalescence. The predicted droplet size along the jet axis remains relatively unchanged (*e.g.*, see Figure 5), and only the averaged droplet sizes are plotted in Figure 8. The measured droplet sizes show variation in the radial direction, and only the minimum and maximum droplet sizes in the radial direction are shown in Figure 8. It appears that the present prediction agrees reasonably well with the measured droplet size for low Weber numbers, and underestimates the droplet size as Weber number increases.

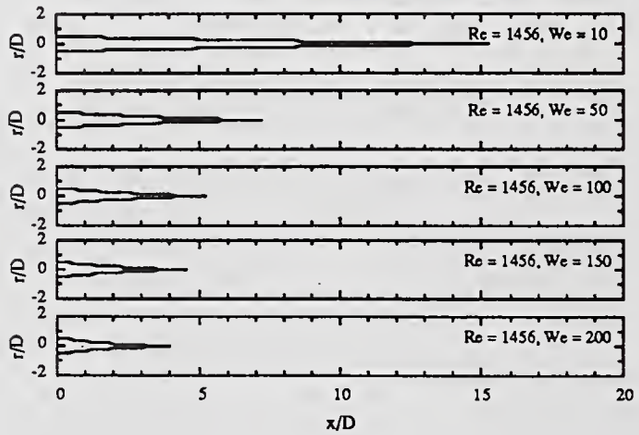

Fig. 3 Liquid jet profiles for Re=1456 and We=10-200.

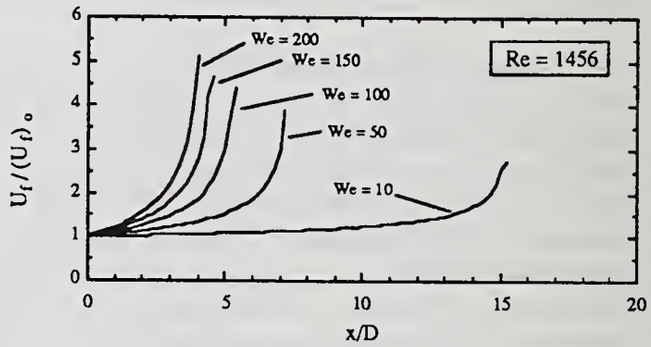

Fig. 4 Axial liquid jet velocities for Re=1456 and We=10-200.

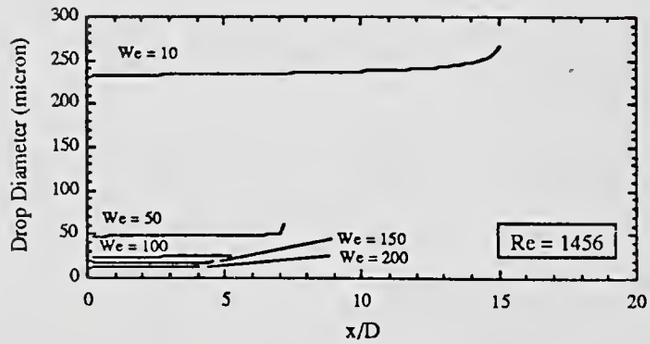

Fig. 5 Estimated droplet diameters in the axial direction for Re=1456 and We=10-200.

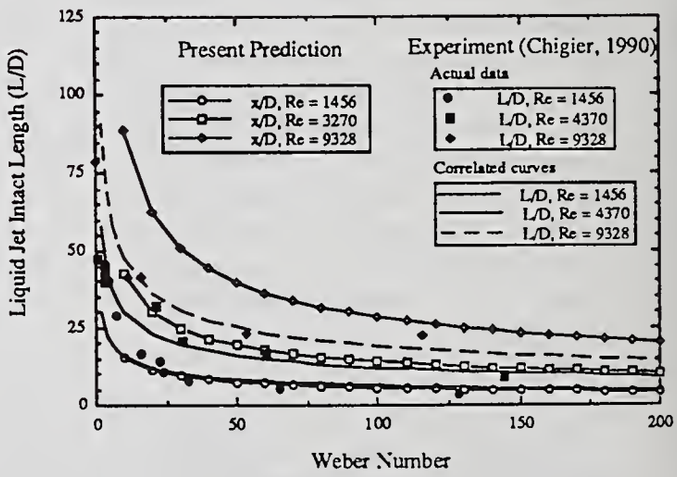

Fig. 6 Comparison of liquid jet intact lengths between present prediction and experiments by Chigier [10].

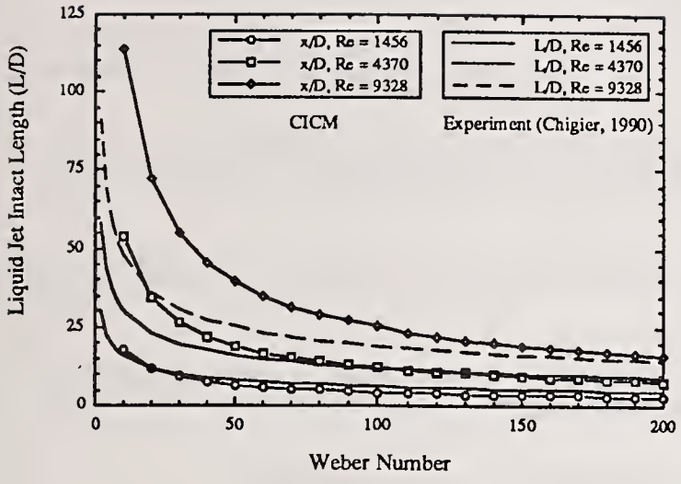

Fig. 7 Comparison of liquid jet intact lengths between CICM prediction and experiments by Chigier [10].

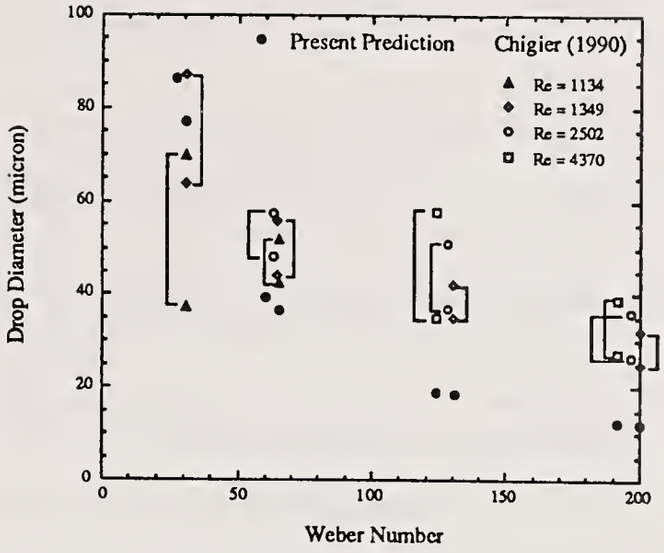

Fig. 8 Comparison of predicted and measured droplet sizes.

CONCLUSIONS

A novel breakup model is proposed and implemented in the present numerical analysis exploiting the Jet Embedding technique. Complementary experimental measurements of water jet atomization were performed. The comparison shows favorable agreement between numerical data and experimental measurements of liquid jet intact lengths and droplet sizes for water jets with ambient air flows. The computation time has been improved by an order of magnitude compared to the previous prediction method by the authors. The model will be further validated for the SSME LOX jet flow conditions.

ACKNOWLEDGEMENT

The present work was performed under an SBIR study for NASA MSFC (Contract NAS8-38425). The authors express their gratitude to Dr. A. K. Singhal, President and Technical Director of CFD Research Corp. for his active participation and valuable guidance.

REFERENCES

1. Lefebvre, A. H., Atomization and Sprays, Hemisphere (1989).

2. Rayleigh, L., Theory of Sound, Dover, Vol 2, pp. 351-365 (1941).

3. Weber, C., "Disintegration of Liquid Jets", Z. Angew. Math. Mech., Vol 11, No. 2, pp. 136-159 (1931).

4. Reitz, R. D. & Bracco, F. V., "Mechanisms of Breakup of Round Liquid Jets" in Encyclopedia of Fluid Mechanics (N. P. Cheremisinoff, Ed.), Vol 3, Gulf, pp. 233-249 (1986).

5. Meyer, J. and Weihs, D., "Capillary Instability of an Annular Liquid Jet", J. Fluid Mech., Vol 179, pp. 531-545 (1987).

6. Lee, J.-G. and Chen, L.-D., "A Linear Stability Analysis of Gas-Liquid Interface", AIAA J. (in press) (1991).

7. Przekwas, A. J., Chuech, S. G. and Singhal, A. K., "Numerical Modeling for Primary Atomization of Liquid Jets", AIAA J. of Propulsion and Power (1991).

8. Sutton, R. D., Schuman, M. D. and Chadwick, W. D., "Operating Manual for Coaxial Injection Combustion Model", NASA CR-129031 (1974).

9. Liang, P. Y., Jensen, R. J. and Chang, Y. M., "Numerical Analysis of SSME Preburner Injector Atomization and Combustion process", AIAA-86-0454 (1986).

10. Chigier, N. and Eroglu, H., "Atomization of Liquid jets from Injection Elements in Liquid Rocket Combustion Chambers", NASA NAG8-126 (1990).

11. Przekwas, A. J., "Spray Formulation in Liquid Propellant Atomization Systems", IANNAF Workshop on Atomization, NASA MSFC, Huntsville, AL (1987).

12. Levich, V. G., Physicochemical Hydrodynamics, Prentice-Hall, pp. 591-668 (1962).

13. Cheuch, S. G., Przekwas, A. J. and Singhal, A. K., "A Computer Code for Liquid Jet Atomization in Rocket Thrust Chambers", Appendix C, NASA NAS8-37620 (1988).

14. Yang, H. Q., "Non-axisymmetric Breakup of a Liquid Jet during Atomization", AIAA 91-0693, 29th Aerospace Sciences meeting, Reno, Nevada (1991).

DISINTEGRATION PHENOMENA OF METALIZED SLURRY FUEL JETS IN HIGH SPEED AIR STREAM

T. Inamura, N. Nagai, T. Hirai and H. Asano

Faculty of Engineering
Tohoku University
Sendai, Japan

ABSTRACT

The metalized slurry fuels are anticipated to enhance the combustion efficiency and the specific thrust of a ramjet and a scramjet engine. The disintegration mechanism of slurry fuel is expected to differ from that of single phase liquid, such as water. Because the slurry fuel is generally non-Newtonian liquid and it has rheological nature. Consequently it is difficult to apply the experimental results obtained for the single phase liquid to slurry fuels. This study aims to clarify the disintegration mechanism and spray characteristics of slurry fuels in high speed air flow. In this report, the empirical equations of the jet penetration and the jet width for water and slurry fuels were deduced. Furthermore, break-up lengths of liquid jets and mass flux of water spray drops were measured. And compared the experimental results of slurry fuels to those of water, it was clarified that the measuring results of slurry fuels slightly differ from those of water.

INTRODUCTION

As the fuel of the air breathing engine such as ramjet and scramjet engine, metalized slurry fuels have the advantages of high density and volumetric heating value, they contribute to the compactness of the fuel storage [1]. Yatsuyanagi [2] showed experimentally that the kerosene fuel including aluminum powder has a good combustion efficiency for a rocket engine. And highly metalized slurry fuels are expected to enhance the combustion efficiency and the specific thrust of the ramjet and scramjet engine.

In order to ignite the fuel spray stably, to hold the flame in a high speed air stream and to complete the combustion in a combustion chamber, improvement of the spray characteristics and the control of the mixing between fuel sprays and combustion air are required. To accomplish these purposes, it is needed to clarify the disintegration mechanism of liquid jet and the behavior of the fuel spray in a high speed air stream.

On the other hand, high metalized slurry fuel is generally non-Newtonian liquid. And its disintegration mechanism seems to differ from that of single phase liquid fuel [3]. For example the viscosity of slurry fuel depends on the shear velocity, this fact contributes to different disintegration mechanism.

There are many studies on the disintegration of single phase liquid jet in high speed air stream [4,5], however concerning to the slurry fuel jet there are few studies [6]. The present study aims to clarify the disintegration mechanism of metalized slurry fuel jet in a high speed air stream, the spray characteristics and the mixing characteristics between fuel sprays and air stream. In this report the empirical equations of the jet penetration and the jet width for metalized slurry fuel and water were deduced. Furthermore, jet breakup lengths of liquid jets and the mass flux of water spray drops were measured.

APPARATUS AND PROCEDURES

The subsonic air flow was selected in order to observe the disintegration mechanisms and to measure the atomization characteristics easily. Liquid jet was injected transverse to a subsonic air crossflow.

Water was used to simulate hydrocarbon fuels and a mixture of water and aluminum particles was used as a slurry fuel. The aluminum particles have a density of 2.67 g/ml and of irregular shapes. Their average diameter is 3.1 μm, and the surfactant was included to prohibit the deposition of aluminum particles.

Figure 1 shows the experimental apparatus. The air blown off from a blower 1 is supplied to the test section 4 passed through a settling chamber 2 and a nozzle 3. The air/liquid two phase flow is decelerated by diffusor and then exhausted. The slurry particles are eliminated by cyclone separator 5, before they are exhausted. The blower is driven by a motor 6, and the rotational speed of the motor is controlled by a inverter 7. The pressure vessel 8 for water supply and 9 for slurry supply are pressurized by the air from a screw compressor 10. The concentration of the water/aluminum slurry was kept constant during the experiments by a stirrer in the pressure vessel. The water is metered by orifice flow meter 11, and the metalized slurry is metered by electro-magnetic flow meter 13 through a trap 12 for a verification of density.

The disintegration phenomena were observed by back-lighted instantaneous photograph. The microflash 15, exposure time is less than 1 μs was used as a light source in this case. The jet penetration and jet width were measured by side-lighted streak photograph, exposure time is 1/30 s to obtain the time-averaged contour of the unsteady spray flow.

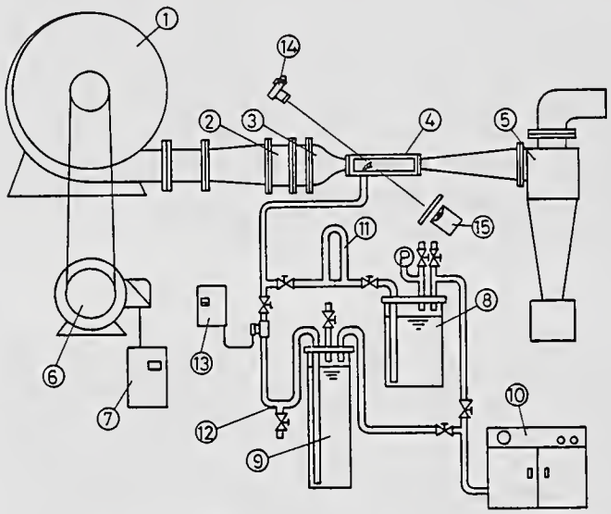

Fig.1 Experimental apparatus

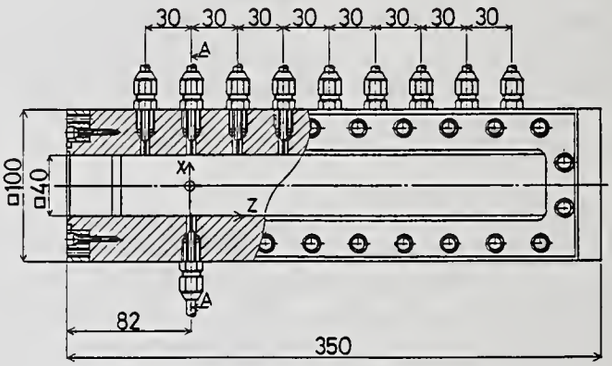

Fig.2 Details of test section

Figure 2 shows the details of the test section. This is 40 × 40 mm subsonic blowdown wind tunnel up to 140 m/s. Its length is 350 mm. The pressure taps are installed at the top wall of wind tunnel every 30 mm to measure a static pressure on the wall surface. The Pyrex plates are attached to both sides of wind tunnel to take a picture. The liquid injection nozzle, directed perpendicularly to air stream is located at 82 mm downstream of the entrance of wind tunnel. And liquid nozzle edge is in same plane with the bottom wall surface. Three sizes of liquid nozzle, inner diameter is 0.5, 1.0, 2.0 mm were used. Coordinate system is right-hand system. X coordinate is in a direction of liquid jet at liquid nozzle exit, Y coordinate is in a direction of width of wind tunnel and Z coordinate is in a direction of a air stream. And the origin of coordinate system is placed on the upstream edge of liquid nozzle exit.

Figure 3 shows the contact needle probe to measure the breakup length of liquid jet by the electrical resistance method. Needle probe is movable up and down and back and forth by micrometer head 3 and precisely movable stage 4. A direct current voltage, which amplitude is 15 v was applied between the liquid nozzle and the needle probes. If the liquid jet contacts to the

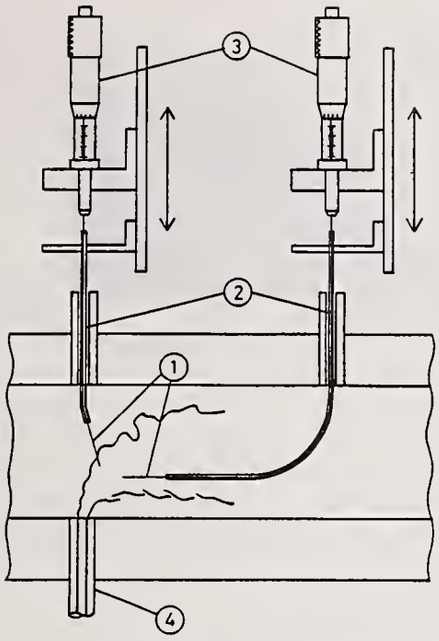

Fig.3 Details of contact needle probe

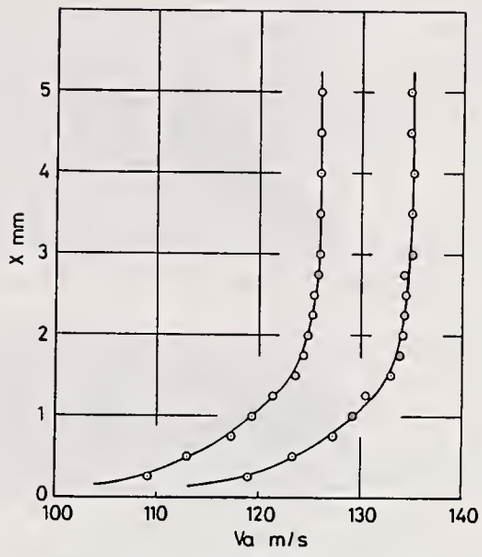

Fig.4 Air velocity distribution in the vicinity of liquid nozzle exit

needle probe, then circuit is closed and the output is obtained. The needle probe 1 was used to measure the breakup length of downstream side of liquid jet, and the probe 2 upstream side.

The local mass flux of droplets was measured by the iso-kinetic sampling probe, which inner diameter is 0.7 mm and outer diameter 2.5 mm.

Tap water and water/aluminum slurry fuels, 20 wt% and 40 wt% were used as a injectant. The range of injection velocity of the injectant is 7 $\sim$ 26 m/s and air velocity 55 $\sim$ 140 m/s. The viscosity of 20 wt% slurry at low shear velocity is 2.1×10^{-3} Pa·s. And the surface tension is 62.5×10^{-3} N/m.

RESULTS AND DISCUSSIONS

Air Velocity Distribution

Figure 4 shows the air velocity profiles in the vicinity of the liquid nozzle exit measured by hot wire anemometer. Boundary layer thickness is about 2 mm under these operating conditions. The turbulent component of the air flow is less than 2 % of the average air velocity.

Disintegration Phenomena of Liquid Jet

Typical pictures of disintegration phenomena of water and slurry jet are shown in Fig.5. Figure 5(a) and 5(b) are the side view photographs and Fig.5(c) is the top view photograph. In the case of water jet (Fig.5(a)), near the bottom wall liquid jet moves perpendicularly and then is bent downstream rapidly. The cross section of liquid jet is circular at the nozzle exit, then it is transformed into kidney shape and the drag by the air stream increases rapidly. This increase of the drag results in the rapid downstream bend of liquid jet. On the upstream surface of liquid column, the wave originated at liquid nozzle exit grows rapidly and the small particles are produced from the side surface and downstream surface of liquid column. On the other hand, the large liquid lump detaches at the trough of surface wave from the liquid column. Then it is atomized into finer particles further downstream. The location where the liquid lump detaches from the liquid column is about three times of nozzle diameter downstream of the origin of the coordinate system. At this location the fine spray particles are torn off by the shear force of air stream at the surface wave crest.

In the case of slurry jet(Fig.5(b)), the disintegration phenomena are almost similar to those of water jet. But the surface waves are slightly smaller than those of water jet. This seems to be due to the viscosity increase of the slurry or the rheological nature of slurry jet.

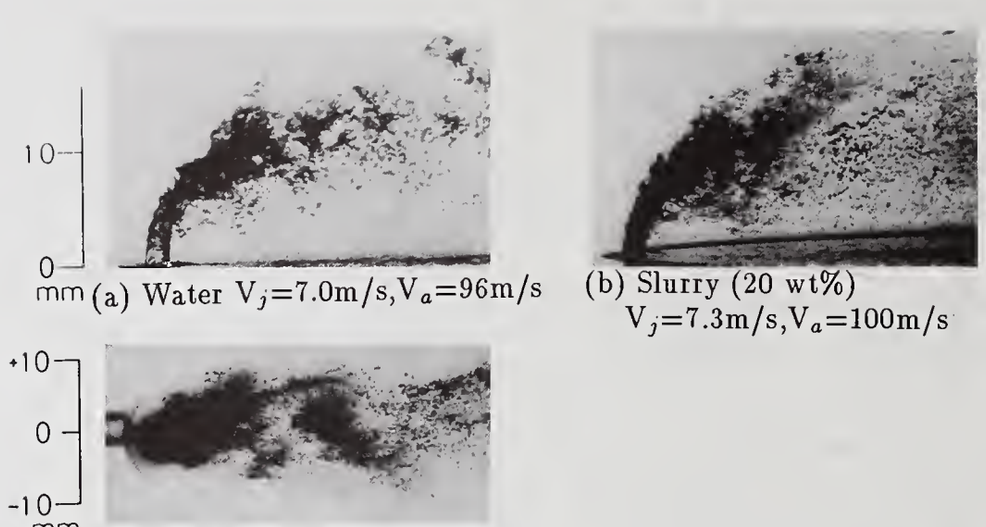

Fig.5 Disintegration phenomena

Fig.6 Magnified picture of disintegration phenomena

For both of liquid jets the penetrations of the spray increase as the liquid injection velocity increases, as the air velocity decreases and as the the nozzle diameter increases. And under same liquid injection velocity, the penetrations increase with increasing the loading of aluminum particles, that is the increase in the liquid density.

To take the top view photograph(Fig.5(c)) the bottom wall of test section was changed to the grass plate and the picture was taken back-lighted by the microflash. This picture is in the case of large injection velocity of the liquid jet. The large liquid lumps detach alternatively from the both sides of liquid column such as Kármán's vortex streets.

Figure 6(a) shows the magnified picture of water jet at nozzle exit. Taking notice of the surface waves, near the nozzle exit the waves incline downstream. And then they incline upstream. These

phenomena mean that the relative velocity of liquid surface to surrounding air directs downstream first and then it directs upstream. This point where the shapes of surface waves change leaves from the nozzle exit with increasing injection velocity.

Figure 6(b) shows the magnified picture of slurry jet. The surface waves are obviously smaller than those of water jet (Fig.6(a)). This is caused by the stability of the slurry jet due to high viscosity [6].

Jet Penetration

The jet penetration and the jet width are very important for the design of combustor. The combustor dimensions are also affected by the jet penetration and the jet width. Furthermore, combustion characteristics are affected by those.

In this report the jet penetration and jet width were measured by side-lighted streak photographs and the empirical equations of those were deduced.

The jet penetration and jet width were defined as shown in Fig.7. The jet penetration was defined as the length from the spray axis to the contour of side view photograph of spray(Fig.7(a)). And the jet width was defined as that of top view photograph(Fig.7(b)).

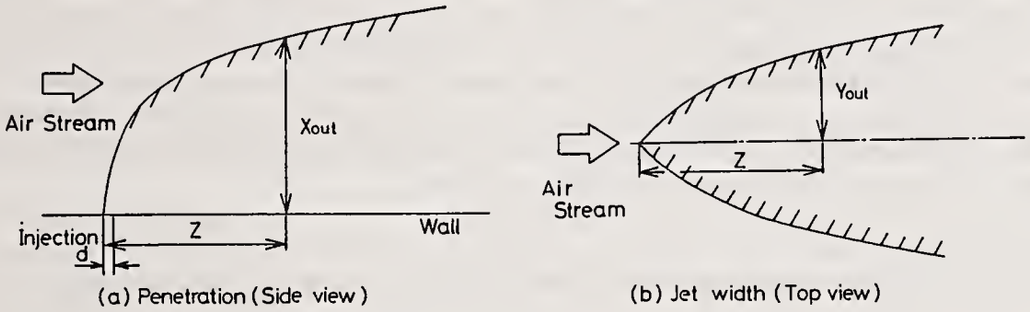

Fig.7 Definitions of the jet penetration and the jet width

By the observations of streak photographs the jet penetration increases with increasing the injection velocity of liquid jet and with decreasing air velocity. And the penetration increases as liquid density increases due to the momentum increase of liquid jet. Therefore the jet penetration seems to be the function of momentum ratio, nozzle diameter and the streamwise distance from the liquid nozzle [7]. From these considerations and the preparatory experiments the jet penetration was assumed as follows:

$$\frac{X_{out}}{d} = A(d)\,\overline{q}^{\alpha} \ln\left\{1 + B(d)\,\frac{Z}{d}\right\} \tag{1}$$

where α is constant and $A(d)$, $B(d)$ are function of liquid nozzle diameter, d.

α, $A(d)$ and $B(d)$ were determined by least square method as follows:

for water jet;

$$\frac{X_{out}}{d} = (1.18 + 0.24\,d)\,\overline{q}^{0.36} \ln\left\{1 + (1.56 + 0.48\,d)\,\frac{Z}{d}\right\} \tag{2}$$

for both of slurry jets;

$$\frac{X_{out}}{d} = (1.17 + 0.16\,d)\,\overline{q}^{0.43} \ln\left\{1 + (0.75 + 0.95\,d)\,\frac{Z}{d}\right\} \tag{3}$$

Figure 8 shows the variation of the jet penetration curve with liquid nozzle diameters. Under same momentum ratio the larger the nozzle diameter the larger the jet penetration is. Figure 9 shows the variation of the jet penetration curve with various kinds of liquids. Under large

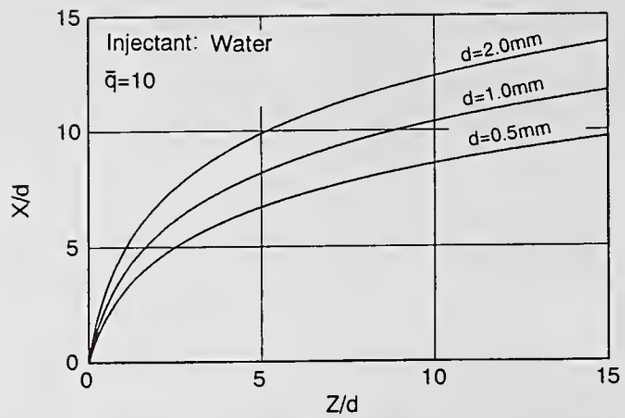

Fig.8 Variation of jet penetration curve with liquid nozzle diameters

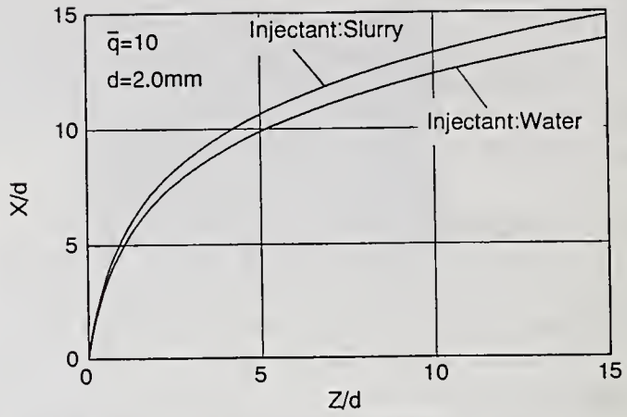

Fig.9 Variation of jet penetration curve with various kinds of liquids

momentum ratio ($\overline{q}$ = 10.0), the jet penetration of slurry jet is larger than that of water. This trend is different from the results obtained by Less and Schetz [6]. They observed the phase separation, and they concluded that the separation of the phases results in reduced penetration of liquid portion of the injectant as the loading is increased. However, in our studies phase separation was never observed. This is due to the differences of air velocity. They used the supersonic air flow, and in our case the subsonic air flow was used. In our case the large jet penetration of slurry jet is caused by the stability of slurry jet due to high viscosity.

Jet Width

The empirical equation of the jet width was assumed as follows from the preparatory experiments.

$$\frac{Y_{out}}{d} = C\,\overline{q}^{\beta}\left(\frac{Z}{d}\right)^{\gamma} \tag{4}$$

where C, β, γ is constant.

C, β, γ were determined by least square method as follows:

for water jet (for all nozzle diameters);

$$\frac{Y_{out}}{d} = 1.4\,\overline{q}^{0.18}\left(\frac{Z}{d}\right)^{0.49} \tag{5}$$

for slurry jet (for 20 wt %, d=1.0 mm);

$$\frac{Y_{out}}{d} = 3.1\,\overline{q}^{0.06}\left(\frac{Z}{d}\right)^{0.32} \tag{6}$$

For the water jet, the nozzle diameters donot influence on the jet width, and this trend is contrastive with that of the jet penetration (Fig.8).

Break-up Location of Liquid Jet

The examples of break-up length of liquid jets measured by the contact needle probes are shown in Fig.10. The values in percent in the figure indicate the rate of the period in which the probe detaches from the liquid column. Here 5% break-up location is defined as the break-up location of liquid jet.

The break-up location in X-direction moves downstream as the momentum ratio increases, whereas that in Z-direction is almost constant in spite of the momentum ratios and $Z/d = 3 \sim 3.5$. This break-up location is almost coincident with the point at which the large liquid lumps detach from the liquid column.

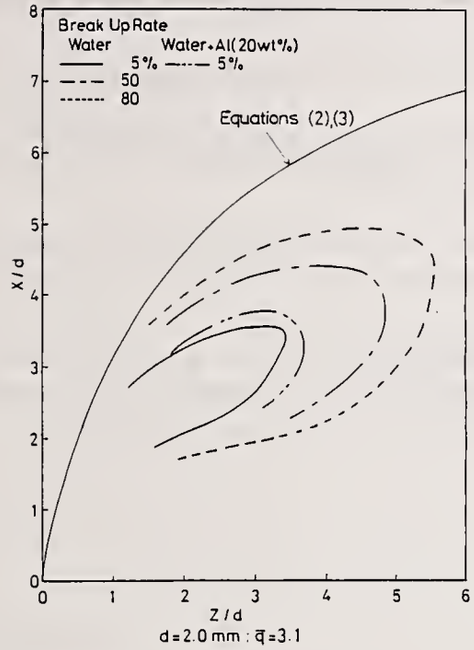

Fig.10 Break-up length of liquid jet

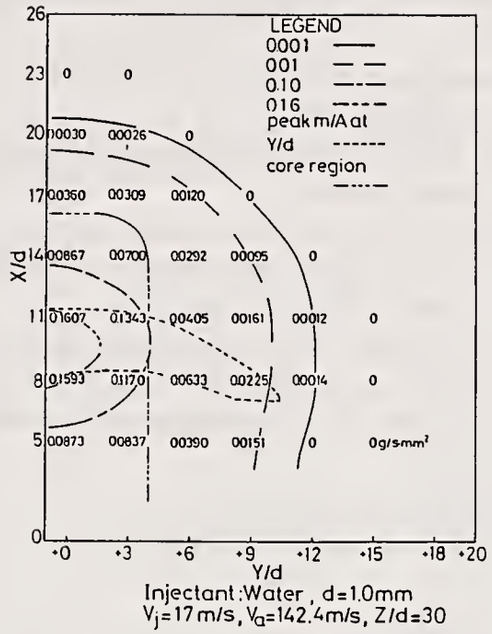

Fig.11 Mass flux of spray drops

In the figure the break-up location of slurry jet is shown compared to that of water jet. And the momentum ratio of water jet and slurry jet is kept constant. The break-up location of slurry jet slightly moves downstream compared to that of water in the case of same momentum ratio. This seems to be caused by the stability due to the viscosity increase of slurry jet and further researches on the disintegration mechanism of slurry jets are required.

Mass Flux of Spray Drops

Figure 11 shows the mass flux of spray drops measured by the iso-kinetic sampling probe at $Z/d = 30$. Defining the contour of spray as the location of 0.001 g/s·mm^2, X_{out}/d is equal to 20 and Y_{out}/d is equal to 12. Compared this values to the values measured by the photograph, the penetration measured by the photographs is underestimated about 20 %. And the width measured by the photographs is underestimated about 5 %.

In the region of $X/d = 5 \sim 14$ and $Y/d = 0 \sim 3$, the mass flux is almost constant and this region is seemed to form the core region of the spray. Furthermore by the measurements of the mass flux variation in Z-direction, the contour line of 0.001 g/s·mm^2 spreads and that of 0.1 g/s·mm^2 narrows further downstream. By the comparison of the mass flux measurements to the break-up location measurements, the large liquid lumps detached from the liquid column form the core region of the spray after those are atomized into spray drops, whereas the fine drops atomized from the spray lumps in the core region and torn off from the liquid surface by the shear force of air stream form the surrounding of the core region. Consequently mean diameter of spray drops in the core region seems to be larger than that in the surrounding of the spray.

CONCLUSIONS

In order to clarify the disintegration mechanism of metalized slurry fuel jet in a high speed air stream, the jet penetration and the jet width of metalized slurry fuel and water are measured and the break-up location of liquid jets and the mass flux of water spray drops were measured. Consequently the following results were obtained.

1. The waves on the liquid surface are amplified rapidly as they move downstream and the large liquid lumps detach from the liquid jet at the trough of surface wave. These liquid lumps

are atomized again into further fine spray and then form the core region of the spray further downstream.

2. The jet penetration and the jet width can be represented by the empirical equations (2), (3) and (5), (6) respectively.
3. The slurry jets are more stable than the water jet, and it results in larger penetrations and longer break-up lengths.
4. The distance from the liquid nozzle exit to the point where the liquid lumps detach from liquid jet in a direction of the air stream is almost constant over the whole momentum ratios for both of slurry jets and water jet.
5. The spray consists of core region in which mass flux of spray drops is constant and the surrounding region in which the mass flux is smaller than that in core region. The core region becomes small and the surrounding region becomes large as one moves downstream.

NOMENCLATURE

d	:	liquid nozzle inner diameter
$\bar{q}$	:	momentum ratio$(= \rho_j V_j^2 / \rho_a V_a^2)$
V	:	velocity
X,Y,Z	:	coordinates
X_{out}	:	jet penetration
Y_{out}	:	jet width
ρ	:	density

Subscripts

a	:	air
j	:	liquid

ACKNOWLEDGEMENTS

The authors would like to thank Dr. N. Yatsuyanagi and Mr. A. Kumakawa of National Aerospace Laboratory for their valuable advice. They also acknowledge the help in the experiments with Mr. N. Fukuda, Mr. M. Kuroda and Mr. M. Tomita of Tohoku University.

REFERENCES

1. Northam, G. B., "Combustion in Supersonic Flow", Proc. 21st JANNAF Combust. Meeting, pp.399-410, JPL,Pasadena,CA (1985).
2. Yatsuyanagi, N., "Combustion Characteristics of Metalized Hydrocarbon Fuels",Journal J.S.A.S.S., Vol.37, No.427, pp.393-399 (1989) (in Japanese).
3. Inamura, T., Nagai, N. and Inagaki, H., "A Study on the Twin-Fluid Atomization of a Highly Concentrated Coal-Water Mixture", Trans. J.S.M.E., Ser.B, Vol.53, No.490, pp.1846-1851 (1987) (in Japanese).
4. Catton, I., Hill, D. E. and McRae, R. P., "Study of Liquid Jet Penetration in a Hypersonic Stream", AIAA Journal, Vol.6, No.11, pp.2084-2089 (1968).
5. Kush Jr., E. A. and Schetz, J. A., "Liquid Jet Injection into a Supersonic Flow", AIAA Journal, Vol.11, No.9, pp.1223-2114 (1973).
6. Less, D. M. and Schetz, J. A., "Penetration and Breakup of Slurry Jets in a Supersonic Stream", AIAA Journal, Vol.21, No.7, pp.1045-1046 (1983).
7. Thomas, R. H. and Schetz, J. A., "Distributions Across the Plume of Transverse Liquid and Slurry Jets in Supersonic Airflow", AIAA Journal, Vol.23, No.12, pp.1892-1901 (1985).

THERMODYNAMICS AND APPLICATIONS OF A SPRAY INTERACTING WITH A COMPRESSIBLE FLOW

F. Ruiz

Department of Mechanical and Aerospace Engineering
Illinois Institute of Technology
Chicago, IL, U.S.A.

ABSTRACT

The final state of the interaction of a compressible flow with a spray (or solid particle dispersion) is analyzed, using elementary fluid mechanics and a control-volume approach, in order to detect variations of the flow Mach number at low values of the liquid volume fraction. It was found that the flow can be choked by effect of the spray in a way analogous to that of a heat addition into the flow. The effects of downstream pressure changes are discussed. Two applications are presented: as a flow control device, and as the basis of a ramjet engine.

INTRODUCTION

It is well known that the addition of a solid or liquid phase to a gas can lower the speed of sound of the resulting two-phase mixture to very low values [1]. This phenomenon has been used to generate underexpanded air-liquid jets which diverge on contact with the lower ambient pressure, and cause the liquid phase to be finely atomized [2]. Critical flow effects are also encountered in flash-boiling systems, where the separation of vapor bubbles from a liquid flow can lead to choking of the flow [1]. Ramjet engines rely on the injection of a liquid fuel into a high subsonic or supersonic flow. In the latter case, unlike the others, the volume occupied by the liquid is negligible (although its mass is not) compared with that of the gas phase. In most cases analyzed in the literature, however, the liquid volume fraction is considered to be significantly larger than that of the gas. This paper intends to present an analysis for the opposite case, where the liquid volume fraction is much smaller than that of the gas, which is the situation encountered in spray systems. We will see how a spray interacting with a high speed flow can change its Mach number, and open the possibility of some interesting applications.

DISPERSION OF A SPRAY IN A COMPRESSIBLE STREAM

A gas flows at an initial velocity V_1 (and Mach number M_1) through a constant-area duct. From the initial section (section 1) to the final section 2, liquid particles are added to the flow, so that at section 2 both phases have reached the same velocity V_2. Solid particles would have the same effect; the name "spray" used throughout the paper is understood to mean also a dispersion of solid particles. Now, the addition of particles to the gas alters the speed of sound, since the particles add to the inertia of the two-phase mixture, but leave its compressibility untouched, if the liquid volume fraction is much

smaller than that of the gas. For this limit, and assuming that the particles are small enough to instantly follow the velocity variations of the gas flow, Wallis [1] gives the following expression for the speed of sound of the two-phase mixture:

$$C_2 = \sqrt{\frac{k\,Rg\,T_2}{1+ms}} \tag{1}$$

where Rg is the original ideal gas constant and ms is the liquid mass flow rate divided by the gas mass flow rate. Equation (1) is based on the assumption that the only effect of the liquid particles is to increment the inertia of the mixture.

When the injecting liquid velocity, V_L, is other than V_1, there will be momentum transfer between the phases, and perhaps some mass and heat transfer. To simplify the problem, it will be assumed that there is no mass nor heat transfer between the phases, no heat nor momentum transfer with the duct walls. If a solution involving these processes is desired, it can be obtained by adding them at a section after section 2, using the classical control volume solutions [3]. In other words, it will be assumed that the two-phase liquid addition and momentum transfer between the phases proceeds at a much faster rate than the other processes. The final pressure, velocity, and temperature must be determined by the conservation laws between sections 1 and 2:

Continuity in the gas phase:

$$\rho_1 V_1 = \rho_2 V_2 \tag{2}$$

Momentum, with friction allowed only between phases:

$$(P_1 - P_2)\,A = \dot{m}l\,(V_2 - V_L) + \rho_1 A\,V_1\,(V_2 - V_1) \tag{3}$$

Energy, assuming no heat transfer between phases:

$$\rho_1 A\,V_1\,(Cp\,T_2 + \frac{1}{2}V_2^2 - Cp\,T_1 - \frac{1}{2}V_1^2) - \dot{m}l\,(\frac{1}{2}V_L^2 - \frac{1}{2}V_2^2) = 0 \tag{4}$$

Equations (2) to (4) can be put in dimensionless terms using the Mach numbers M_L and M_1, and the relative temperature τ, defined by:

$$M_L = \frac{V_L}{C_1} = \frac{V_L}{\sqrt{k\,Rg\,T_1}} \tag{5}$$

$$M_2 = \frac{V_2}{C_2} = \frac{V_2}{\sqrt{\frac{k\,Rg\,T_2}{1+ms}}} \tag{6}$$

$$\tau = \frac{T_2}{T_1} \tag{7}$$

The equations, in dimensionless terms, and substituting continuity into the other equations, become:

Momentum:

$$\tau\,(k\,M_2 + \frac{1}{M_2})^2(1 + ms) = (k\,M_L\,ms + k\,M_1 + \frac{1}{M_1})^2 \qquad (8)$$

Energy:

$$\tau\,(\frac{2}{k-1} + M_2^2) = \frac{2}{k-1} + M_1^2 + M_L^2\,ms \qquad (9)$$

These equations are of second degree in ms and M_L (M_1 is a fixed parameter, in all that follows). For each value of ms and M_2 there will be two (or none) values of M_L. The same can be said of ms.

Let us first determine the conditions that lead to a final sonic state ($M_2 = 1$). Substituting into equations (8) and (9) the following relationship is obtained:

$$(1+k)\,(2 + (k-1)\,(M_1^2 + M_L^2\,ms))\,(1 + ms) = (k\,M_L\,ms + k\,M_1 + \frac{1}{M_1})^2 \qquad (10)$$

Equation (10) is plotted in Fig. 1 for $M_1 = 0.8$ and physically meaningful values of ms ($ms > 0$). There is no solution for an injection Mach number M_L between M_1 and another high value of M_L, normally in the hypersonic region. It seems paradoxical that it is possible to reach sonic conditions by injecting liquid at a velocity V_1 (and rate $ms = 1/M_1^2 - 1$ or less), but not at a higher speed (which would tend to increase the final velocity V_2), nor at a higher rate (which would tend to lower the speed of sound to an even lower value). For these values of M_L, the increase of the speed of sound caused by the heat generated by friction between the phases is larger than the drop due to the increased inertia of the mixture (eq. (1)). The paradox can be better understood by replacing M_2 in the equations. Given certain values of ms and M_L, the final Mach number M_2 is given by the following equation (from eqs. (5) and (6)):

$$\frac{(k\,M_2 + \frac{1}{M_2})^2}{\frac{2}{k-1} + M_2^2} = \frac{(k\,M_L\,ms + k\,M_1 + \frac{1}{M_1})^2}{(1 + ms)\,(\frac{2}{k-1} + M_1^2 + M_L^2\,ms)} \qquad (11)$$

Equation (11) is of fourth degree in M_2; for each pair of values of ms and M_L there are two real values of M_2 (one subsonic and one supersonic, the other two solutions are not real) or none. Regions II and IV in Fig. 1 allow two values of M_2, while regions I and III do not allow any real solution. The two solutions in regions II and IV, M_2 and M_2', are related by:

$$\frac{(k M_2 + \frac{1}{M_2})^2}{1 + \frac{k-1}{2} M_2^2} = \frac{(k M_{2'} + \frac{1}{M_{2'}})^2}{1 + \frac{k-1}{2} M_{2'}^2} \tag{12}$$

yielding:

$$M_{2'} = \sqrt{\frac{M_2^2 + \frac{2}{k-1}}{\frac{2k}{k-1} M_2^2 - 1}} \tag{13}$$

which binds the different values of the Mach number across a normal shock wave. If one solution is subsonic, then the other is supersonic. Normally the only physically possible solution is the subsonic one, because the supersonic solution would involve a spontaneous decrease of entropy, against the second law, as we shall see later.

In regions I and III there is no solution for M_2. It seems, however, that since *ms* and M_L are independent variables, there should be at least one value of M_2, if there is any flow at all. The problem is similar to that of arbitrary heat addition or flow contraction: a point is reached in which any further variation in a certain direction does not change the Mach number, which continues at its sonic value, but will cause the initial conditions to be changed. In the case of this study, any attempt to inject a liquid with a combination of the parameters *ms* and M_L within regions I and III will result in a choked exit flow, with $M_2 = 1$, and a decrease of M_1 below the original value, if M_1 was subsonic, or the upstream propagation of a shock wave that brings M_1 to a subsonic value, if it was originally supersonic.

It is interesting to see how the choking state will evolve as *ms* is increased, at a constant $M_L < M_1$ (M_1 subsonic). First M_2 will increase with *ms*, until $M_2 = 1$ is reached (point "a" in Fig. 2). A further increase of *ms* will continue choking the flow and M_1 will be decreased. Physically, this represents a sonic compression wave travelling upstream. The change in M_1 will continue until the higher choking point ("b" in Fig. 2) is reached and $M_1 = M_L$. Another increase of *ms* will maintain $M_1 = M_L$, but the final state will be supersonic, and the phase interaction frictionless (point "c" in the figure). The final pressure will be adjusted by an expansion wave or a system of oblique shock waves, like in a supersonic nozzle.

If M_1 is subsonic and $M_L > M_1$, the exit Mach number will never reach unity: it will start decreasing as *ms* increases, after an initial increase. If M_1 is supersonic and $M_L > M_{1'}$, the exit Mach number will stay supersonic, as long as the outside pressure is low enough to prevent the formation of a normal shock wave.

ENTROPY VARIATION IN ADIABATIC SPRAY MIXING

Another way to look at the choking problem is to consider the change in entropy of the air, before and after it interacts with the spray, and acquires the same velocity. The variation of entropy of the gas (the thermodynamic state of the liquid does not change) from 1 to 2, after substituting the

appropriate equations, is given by:

$$\frac{S_2 - S_1}{Rg} = \frac{\Delta S}{Rg} = \frac{k+1}{2(k-1)} \ln \frac{T_2}{T_1} - \ln \frac{M_1}{M_2} - \frac{1}{2} \ln (1 + ms) \tag{14}$$

Substituting sample values for ms, M_L, and the two corresponding solutions of M_2, one can see that the subsonic M_2 normally corresponds to a positive ΔS, while the supersonic M_2 solution normally gives a negative ΔS and is, therefore, impossible by the second law of thermodynamics. Obviously, when $M_L = M_1$, the phase interaction is frictionless and we obtain, from equations (8) and (9):

$$M_2 = M_1 (1 + ms)^{1/2} \tag{15}$$

$$T_2 = T_1 \tag{16}$$

and, therefore:

$$\frac{\Delta S}{Rg} = 0 \tag{17}$$

Thus, it is physically understandable how the flow will be able to pass from subsonic to supersonic by adding spray droplets, if these are injected at the same speed as that of the gas flow.

Following a constant M_2 line, the entropy variation looks as shown in Fig. 3. For a subsonic M_2 value, the entropy change has a zero and a local minimum at $M_L = M_1$, on the left side of the higher choking point ("b" in Fig. 2). The conjugated supersonic Mach number, M_2', which gives the same line in the ms-M_L plane, gives a local maximum of the entropy at the crossing with $M_L = M_1$, this time on the right side of the higher choking point. Both curves are separated by a constant offset of value:

$$\frac{\Delta S_{sub} - \Delta S_{super}}{Rg} = \frac{k}{k-1} \ln \left[\frac{M_2'}{M_2} \sqrt{\frac{1 + \frac{k-1}{2} M_2^2}{1 + \frac{k-1}{2} M_2'^2}} \left(\frac{1 + k M_2^2}{1 + k M_2'^2} \right) \right] - \ln \left[\frac{1 + k M2^2}{1 + k M_2'^2} \right] \tag{18}$$

which is the entropy generated by a normal shock wave, lowering the Mach number from an initial $M_2' > 1$, to its conjugated $M_2 < 1$, given by eq. (13). It appears, thus, that the solutions in the subsonic sheet are equivalent to those in the supersonic sheet, followed by a normal shock wave. It makes sense, since the assumptions made for the phase interaction process (adiabatic, conservation of mass and momentum) can also give a normal shock wave as a possible solution. The subsonic solutions physically correspond to a supersonic solution followed by a shock wave, but with both processes (mixing and entropy generation) occurring simultaneously.

Many supersonic M_2 cases would yield $\Delta S < 0$, in violation of the second law of thermodynamics. If the second law is to be preserved, then ΔS will need to be greater or equal than zero: $M_2 > 1$ can only be possible on the line $\Delta S = 0$ when $M_1 < 1$. For this to occur (given that M_L and ms are arbitrarily chosen, and the downstream pressure can be lowered to whatever value is required) the

upstream conditions must change, as in the cases of choking. In other words, M_1 will remain locked to the value M_L.

Which solution for M_2 appears in a real case will be determined by the downstream pressure. If the pressure is high enough to support a normal shock wave, then the exit flow will be subsonic. If, on the contrary, the downstream pressure is low enough, then the shock cannot be supported, and M_2 will be larger than one. Between these, other cases can appear in which the mixing is followed by an oblique shock wave. In the subsonic M_2 cases, a variation in the exit pressure will automatically induce a change in M_1, whether $M_L < M_1$ or not. When M_2 reaches unity, variations in the exit pressure will still be transmitted upstream, so that the choking condition is maintained. Only when M_1 has reached the value $M_1 = M_L$ will M_2 become supersonic. Physically, this can be viewed as the separation of the shock component of the two-phase interaction, which is decomposed into an isentropic spray dispersion, followed by a normal shock wave. If the exit pressure falls below the value required for a normal shock, the isentropic interaction with $M_1 = M_L$ will be maintained, but followed by a system of oblique shock or expansion waves, to reach the appropriate external pressure.

In the supersonic M_1 and M_2 cases, the two-phase interaction will be fully supersonic, followed by oblique shock or expansion waves. If the downstream pressure reaches the level that would produce a normal shock wave, this shock wave will propagate upstream until the whole flow is subsonic. A further increase in the downstream pressure will lower M_1 accordingly.

The temperature-entropy locus (τ, $\Delta S/Rg$) of the final state of the interaction, as the relative liquid flow, *ms,* is increased from zero, for constant values of M_L, is plotted in Fig. 4, for $M_1 = 0.8$, and $M_L = 0.5, 0.6,$ and 0.7. The exit Mach number, M_2, is subsonic in the upper branches of the curves, and supersonic in the lower branches. The analogy with the Fanno line (of flow with friction) or the Rayleigh line (of flow with heat addition) can be seen easily [3]. The choking condition corresponds to the maximum of the entropy generation. Unlike in those classic cases, however, choking is not always reached as *ms* increases. For a subsonic M_L slightly larger than M_1, the flow will always remain subsonic, M_2 reaching a maximum for a certain value of *ms* and decreasing as *ms* increases beyond this value. For $M_L = M_1$, the flow will be able to pass from subsonic to supersonic, as *ms* increases, since the interaction would be isentropic.

APPLICATIONS

The choking effect can be used for flow control in exhaust ducts. Water (or other fluid) can be injected at low speed ($M_L \sim 0$) into the duct. The relative flow of water, *ms*, necessary to choke the flow of gas is given by:

$$ms = \frac{(\frac{1}{M_1} - M_1)^2}{(1+k)(2+(k-1)M_1^2)} \qquad (19)$$

The liquid flow can control a much larger gas flow (given by M_1) with great accuracy. The relative spray flow required to control a given gas flow is represented in Fig. 5. This device could by particularly

suitable for discharge of hot gases, which could damage other control systems, such as dampers, venturis, or critical flow orifices.

Another practical application results from this analysis. A spray-driven ramjet engine would be composed of a diffuser, a spray-mixing area, and a nozzle (optional) as represented in Fig. 6. The increment of the flow Mach number caused by the spray would be equivalent to that caused by combustion, which is the method universally applied to generate thrust in ramjet engines. If the Mach number is increased between the diffuser and the nozzle (not necessarily by heat addition), the engine will deliver a thrust. An analysis has been performed which shows that the thrust comes from the kinetic energy of the liquid stored in the structure, with energy conversion efficiencies potentially higher than 60%. This kind of engine would be advantageous in those situations where a cool exhaust, without any infrared emissions, would be desirable.

CONCLUSIONS

1. There is an analogy between the interaction of a spray with a compressible gas flow, and heat addition into a gas flow: Mach number changes leading to eventual choking are predicted.

2. Unlike in the case of heat addition, a point will be reached where the interaction would be isentropic, leading to a continuous change of the Mach number from subsonic to supersonic.

3. Applications of this phenomenon to control a subsonic or supersonic exhaust flow and as the basis of a spray-driven ramjet engine are envisioned.

REFERENCES

1. Wallis, "One-Dimensional Two-Phase Flow", p. 209, McGraw-Hill. 1964.

2. Chawla, J.M., "Atomisation of Liquids Employing the Low Sonic Velocity in Liquid/Gas Mixtures", Proceedings of ICLASS-85. p. LP/1A/5/1. 1985.

3. Shapiro, A.H., "The Dynamics and Thermodynamics of Compressible Fluid Flow". Ronald, 1953.

NOMENCLATURE

A	local section area	T	gas temperature
C	speed of sound	V	velocity
Cp	specific heat at constant pressure	ρ	density
k	adiabatic exponent	τ	temperature ratio T2/T1
M	Mach number		
M'	conjugated Mach number	subscripts:	
ms	relative liquid/air flow ratio	1	before phase interaction
$\dot{m}$	mass flow rate	2	after complete phase interaction
P	pressure	g	of the gas
Rg	ideal gas constant	L	of the liquid
S	gas entropy	'	conjugated (across a shock wave)

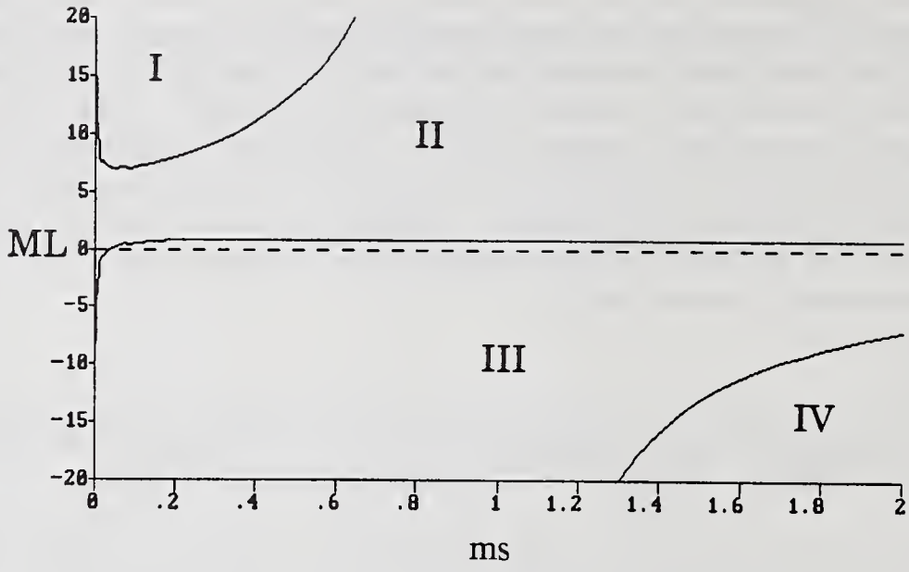

Fig. 1 Regions in the ms M_L plane of possible solution for M_2

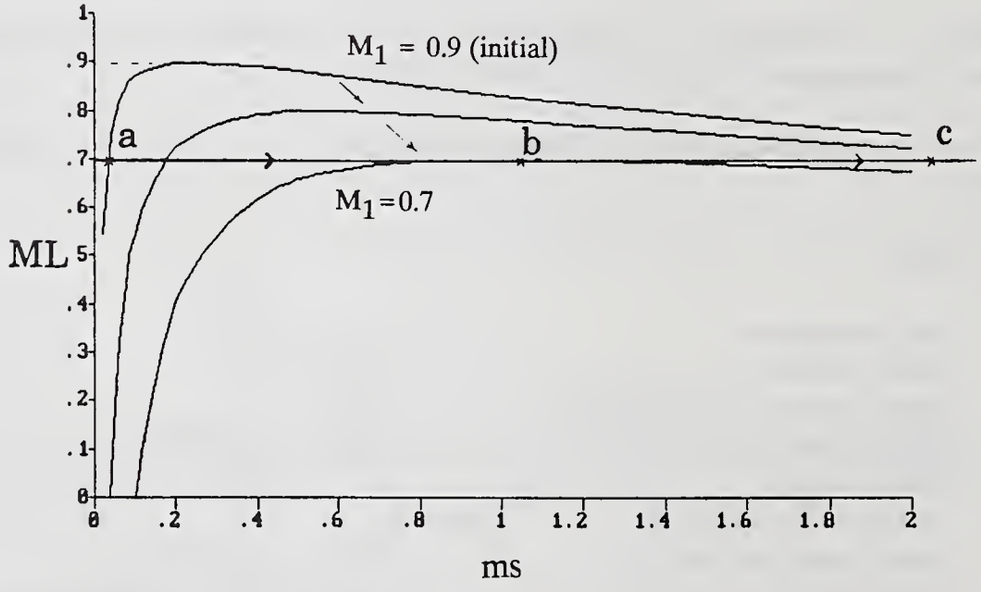

Fig. 2 Change of M_1 as ms is increased in choking conditions

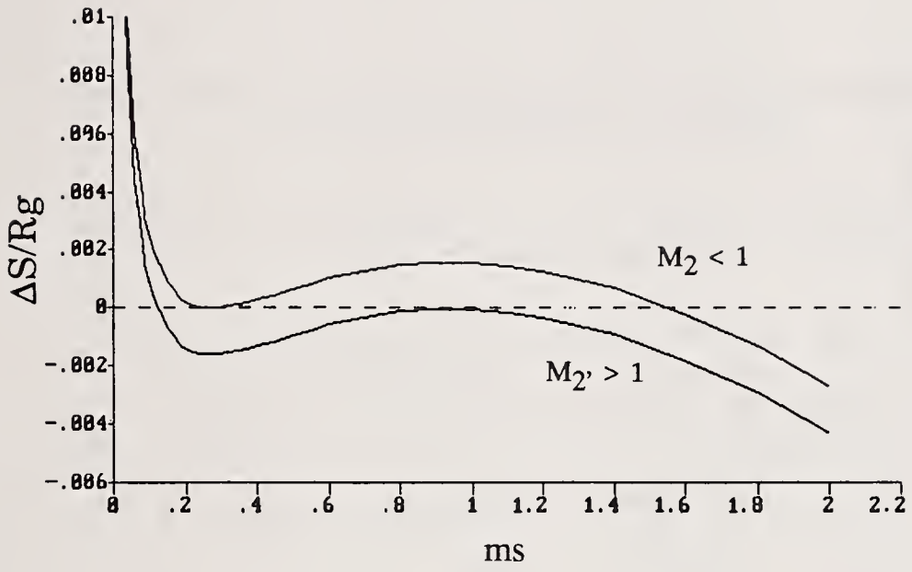

Fig. 3 Entropy increase along a constant M_2 line: subsonic and its conjugated supersonic M_2,

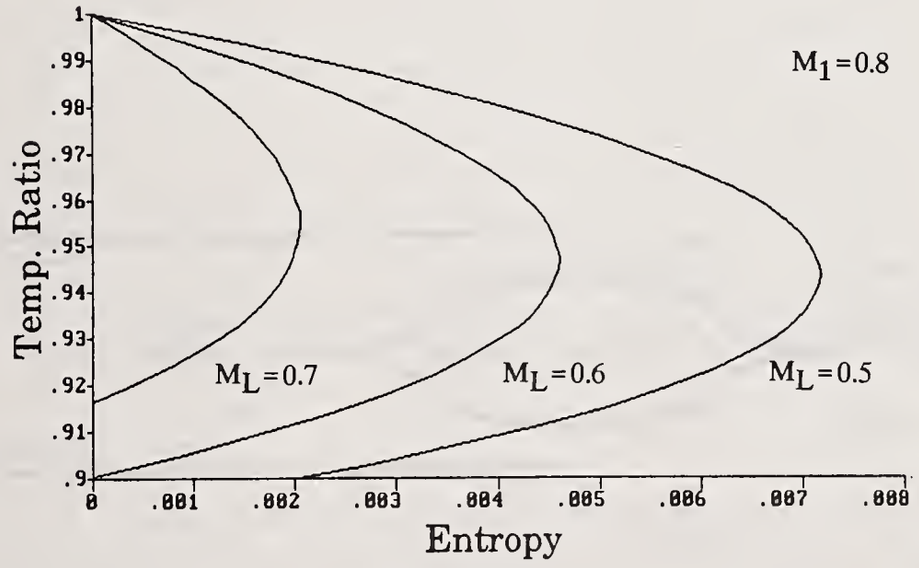

Fig. 4 Lines of constant M_L in the T-S diagram

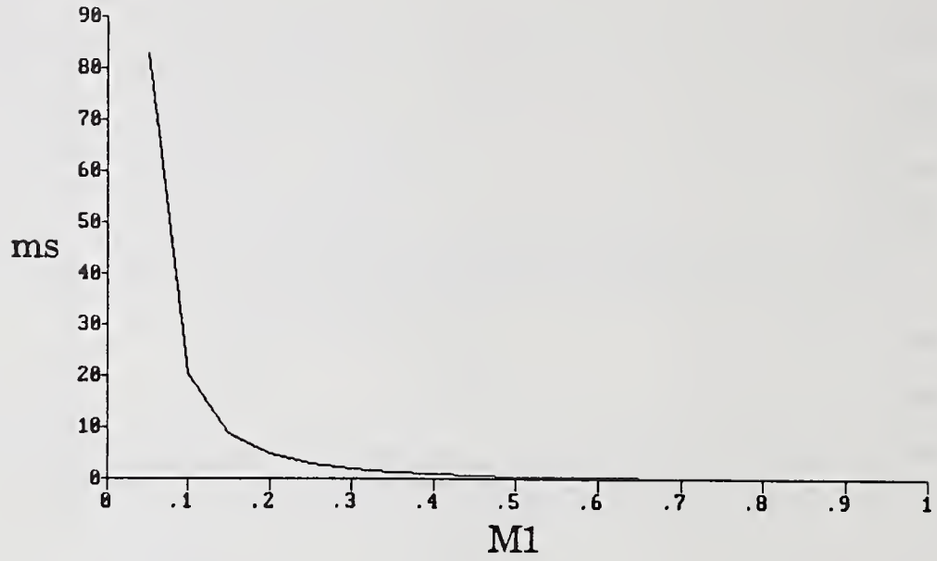

Fig.5 Relative liquid flow required to choke the gas flow, vs. inlet Mach number M_1

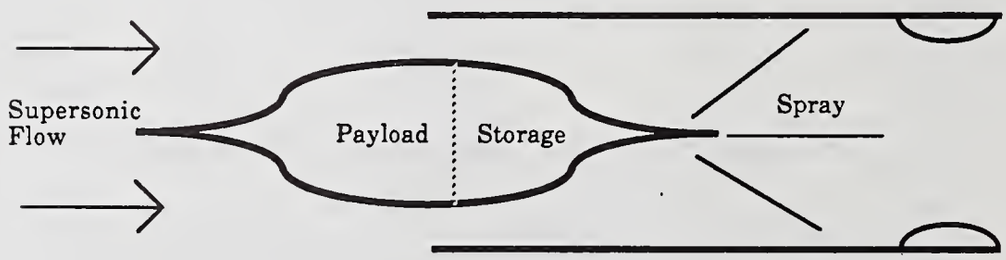

Fig.6 Schematic diagram of the spray-driven ramjet engine

SPRAY CHARACTERISTICS OF PINTLE TYPE INJECTOR UNDER LOW-PRESSURE FIELD

J. Senda*, M. Yamaguchi*, T. Wakashiro†, T. Tsukamoto‡, K. Hojyo§ and H. Fujimoto*

*Dept. of Mechanical Engineering, Doshisha University, Kyoto, Japan
†HONDA R&D Co., Ltd, Tochigi, Japan
‡HORIBA Ltd., Automotive Analysis Dept., Kyoto, Japan
§Dept. of Mechanical Engineering, Osaka Institute of Technology, Osaka, Japan

ABSTRACT

The purposes of this study are to clarify the atomization mechanism of the spray injected into low-pressure field through a pintle type electronic control injector, especially the change in spray characteristics dependent on the surrounding back pressure. In the experiments, the fuel oil is injected with the relative low-pressure into the quiescent gaseous atmosphere under the atmospheric pressure. The spray is observed by taking photographs at an arbitrary time varying the back pressure, using 35mm camera and CCD camera system. The results show that the back pressure has a great influence on the spray characteristics. In particular, the saturated vapor pressure of the fuel oil is the most significant factor. Spray pattern such as the spray angle, and the atomization characteristics such as Sauter mean diameter of breakup droplets are almost constant in the range of back pressure from atmospheric pressure to the vapor pressure. As the back pressure reaches to the vapor pressure, the vapor bubbles start to grow due to flash boiling. Further decreasing the back pressure below the vapor pressure results in an increase in the spray angle and in a decrease in Sauter mean diameter markedly, since rapid expansion of the vapor phase may them atomize the fuel jet. Consequently, in the case of back pressure below the vapor pressure, the characteristics can be explained in terms of the growth rate of vapor bubbles corresponding with the pressure difference between the back pressure and the vapor pressure.

INTRODUCTION

In SI Engines, a multi-point injection system, which is controlled electrically, is predominant at present, owing to high responsibility and high control quality of fuel flow. However, in some operating conditions, a great deal of unburnt hydrocarbon is emitted, because of low quality of the spray atomization. Therefore, it is necessary to reveal spray formation and atomization processes . Particularly, spray characteristics under the low-pressure field is attractive with reference to the reduced pressure state in an actual suction manifold.

Conventional studies on fuel injection system for gasoline engines have dealt with the mixture formation process considering the droplet deposition

against the wall in order to improve fuel economy and emission characteristics [1]. And in some cases, fuel flow analysis and the droplet size distribution for the spray have been reported [2] as to engine performance. However, no investigations have been attempted to clarify the characteristics of the spray, injected into lower ambient pressure field than the saturated vapor pressure of the fuel, where it is necessary to consider the effect of flash boiling.

When liquid fuel is injected into an ambient pressure lower than the equilibrium pressure, so-called vapor pressure for the liquid temperature, the liquid spray disintegrates into fine droplets by partial evolution of vapor. This flash boiling phenomena occurs when a liquid is rapidly depressed to a pressure below saturated vapor pressure to initiate a rapid boiling process. And then, in connection with flash boiling fuel injection, superheated liquid jets generally have been researched. Brown et al. [3] have described the relation between the droplet mean size and the growth rate constant of the bubbles, and Lienhard et al. [4] have presented the breakup length of the flashing superheated liquid jet. Further, the effects of the nuclei number and the idle time of bubble growth rate on the atomization process [5], and research on analytical bubble growth rate for practical injectors [6] have been reported also.

EXPERIMENTAL APPARATUS AND PROCEDURE

Figure 1 shows a schematic diagram of experimental apparatus. A constant volume vessel① (170mm x 210mm x 350mm width) has reinforced glass windows ② on both sides to photograph the spray by transmitted light. Fuel was injected vertically through an electromagnetic pintle type injector ③ (0.798mm in pintle diameter and 0.931mm in inside diameter of a hole) installed in the top of the vessel. A pressure inside the vessel, that is an ambient back pressure P_b, could be regulated arbitrarily reducing the pressure by using a vacuum pump④. This back pressure was measured by a vacuum pressure sensor⑤. Pressure was applied to a fuel tank⑥ by an air bomb⑦, and this fuel injection pressure P_f was picked up with a pressure gage⑧. And fuel was injected through the injector, operated with a control circuit⑨, during valve opening period t_i= 4 ms. at constant.

The photographs of the spray were taken by CCD Camera system ⑩ using the transmitted light of a micro-flash ⑪. Thereafter, images obtained with CCD Camera were recorded on a image memory ⑫, and the spray characteristics, that is spray pattern and droplet mean diameter and so on, were analyzed with an image analyzer equipment ⑬ via a micro-computer ⑭.

In this study, a pressure drop for injection ΔP ($\Delta P=P_f-P_b$) was held constant at 250 kPa. And we introduce a new parameter defined by the pressure difference ΔP_{bv} between back pressure P_b and saturated vapor pressure P_v ($\Delta P_{bv}=P_b-P_v$) to express the intensity of flash boiling phenomena. Experiments were conducted at room temperature under the back pressure P_b ranged from atmospheric pressure to the pressure less than the vapor pressure P_v.

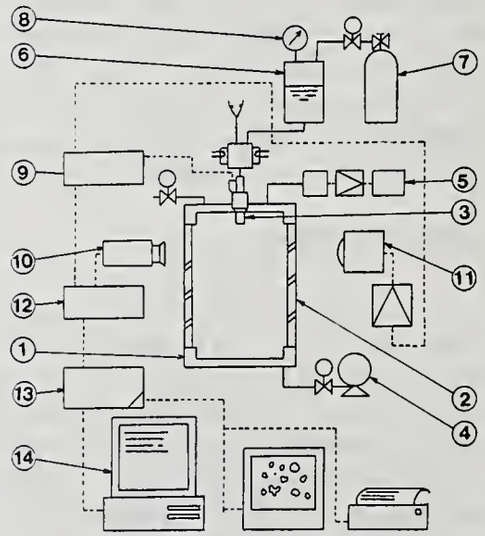

Fig.1 Schematic diagram of experimental apparatus

Shell-LAWS, n-pentane and n-hexane were used for test fuel at room temperature, T_f=20 °C. Fuel properties for each oil were shown in Table 1, respectively.

Table 1 Fuel properties

	Shell-LAWS	n-pentane	n-hexane
Specific gravity ρ_l (kg/m^3)	793	626	662
Surface tension σ x 10^3 (N/m)	25.1	16.05	18.4
Viscosity μ x 10^6 (Pa s)	121	236	320
Saturated vapor pressure P_v (kPa)		62.5	20.5

RESULTS AND CONSIDERATION

Spray Pattern

Injected fuel from an injector appears in the form of a liquid film with conical shape near the injector and the breakup of the film flow into droplets is not completed immediately. In fact, aerodynamic forces and the instability of fuel film cause unstable wave growth leading to the disruption of the film flow, resulting to liquid ligaments and to droplets.

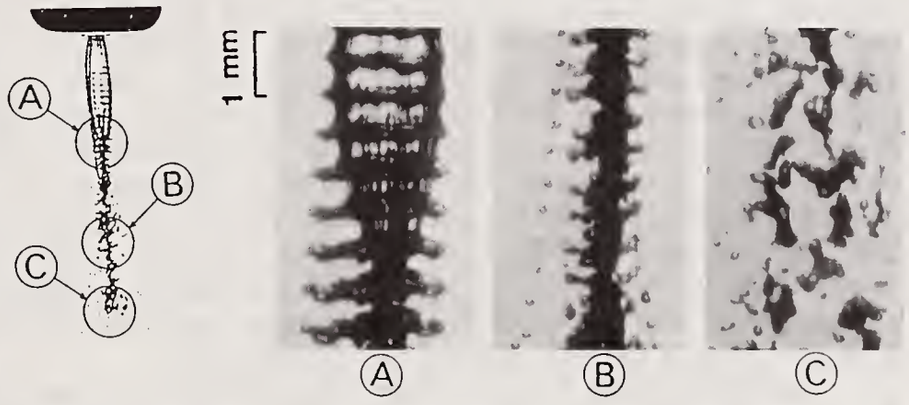

Fig.2 Atomization process for Shell-LAWS spray (ΔP=150kPa, P_b=101kPa, t=2.0ms.)

Figure 2 shows a unique atomization process for Shell-LAWS spray, under the conditions of ΔP=150 kPa, P_b=101 kPa and t=2.0 ms. Injected fuel forms a conical shaped liquid film, and thereafter they contract gradually in progress. Then, the wavy hollow cone jet is formed by the collision of the film, and it eventually breaks up into relative large droplets from the circumference of the wavy jet. Finally, in the down stream region, the wavy flow disrupts leading to large droplets near the spray axis with increasing disturbance as time passes. In this case, the atomization is suppressed by the spray contraction.

Figure 3 shows the change in spray pattern with the back pressure P_b for n-pentane, at the time from injection t=3.0 ms. In n-pentane spray, distinct changes in spray patterns are not observed in the back pressure range 101 to 61 kPa. At P_b=48 kPa, which is below the vapor pressure P_v, the spray atomization is little promoted with contracting spray expanse slightly. Also, the vapor bubbles start to grow due to the flash boiling inside the liquid film, and this film length becomes longer a little. On the contrary, as the back pressure is reduced to 35 kPa, the spray starts to expand in radial direction again markedly and high atomization quality is revealed, activated by flash boiling. In this condition, a large number of bubbles are observed inside the liquid film near the injector. With a further decrease in

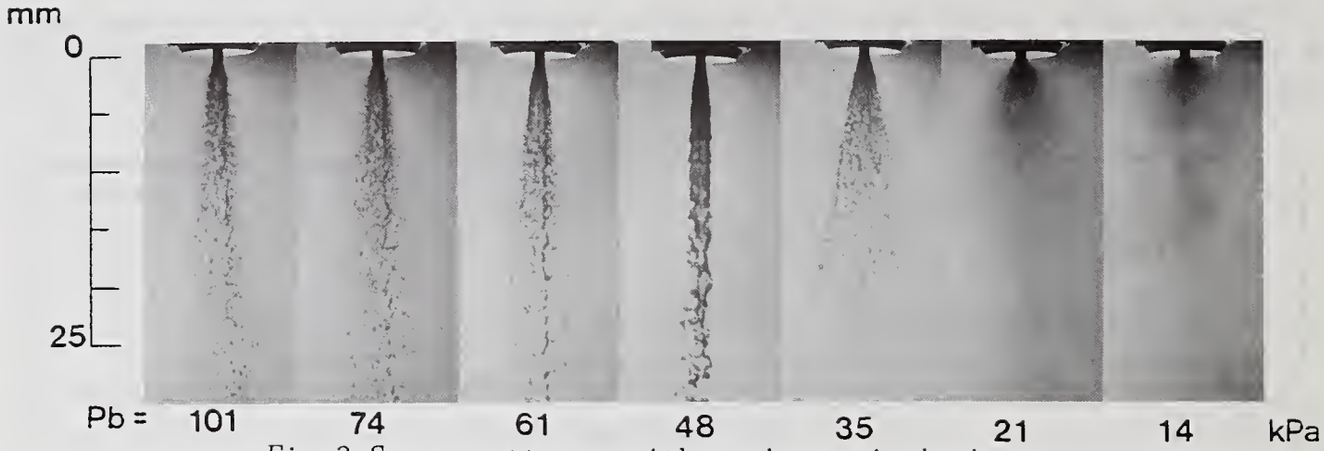

Fig.3 Spray patterns with a change in back pressure P_b (n-pentane, t=3.0ms.)

the back pressure, the spray angle increases to a greater extent, and it is found that the liquid spray breaks up promptly into small droplets since the fuel is flash boiled vigorously at the hole exit of the injector. And then, the spray vanishes near the injector because of an rapid evaporation of the small droplets and the film. Thus, it seems to suggest that the spray characteristics may be assessed in relation to the bubble growth rate, due to flash boiling, corresponding with the pressure difference ΔP_{bv} in the case of the back pressure P_b below the vapor pressure P_v.

In n-hexane spray, spray patterns are almost similar in its properties to the n-pentane spray, considering the pressure difference ΔP_{bv}. Accordingly, flash boiling phenomena has a remarkable effect on the spray pattern and the atomization mechanism such as the spray injected into low-pressure field nearby the vapor pressure.

In Shell-LAWS spray, with decreasing the back pressure P_b, the liquid film length along the spray axis increases and the atomization becomes low quality. This result appears to be due to the decrease in ambient density. The film intact length is longer apparently than that of the sprays of n-pentane over the range of the back pressure independent of the flash boiling.

Spray Angle and Breakup Length

In the following, spray characteristics is described for n-pentane and n-hexane. In this study, a spray angle θ and a breakup length l_b are defined as shown in Fig.4. The spray angle θ indicates the cone angle of the liquid film at the edge of the pintle, and the breakup length l_b presents the distance of the film intact length from the injector.

Figure 5 shows the dependence of spray angle θ and the breakup length l_b on pressure difference ΔP_{bv} under the condition of ΔP=250 kPa and t=3.0 ms. For each fuel, θ becomes almost constant in the region of $\Delta P_{bv}>0$, and has a minimum value near $\Delta P_{bv}=0$, then θ increases markedly with a further decrease in ΔP_{bv} attributed to violent flash boiling in the spray, also shown in Fig.3. Here, the minimum value of θ near $\Delta P_{bv}=0$ appears to be a transitional region with the spray contraction owing to the bubble initiation in the film. Therefore, it seems that the atomization mechanism transits from the process corresponding to aerodynamical instability to the process controlled by flash boiling in the case of $\Delta P_{bv}=0$. And the value of θ over the range of ΔP_{bv} is depend on the fuel own properties.

The breakup length l_b shows a symmetrical tendency with the spray angle θ against ΔP_{bv}. Accordingly, in the region of $\Delta P_{bv}<0$, l_b decreases promptly

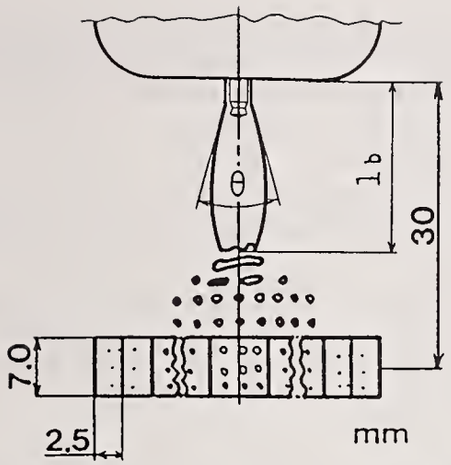

Fig.4 Measuring region of fuel spray

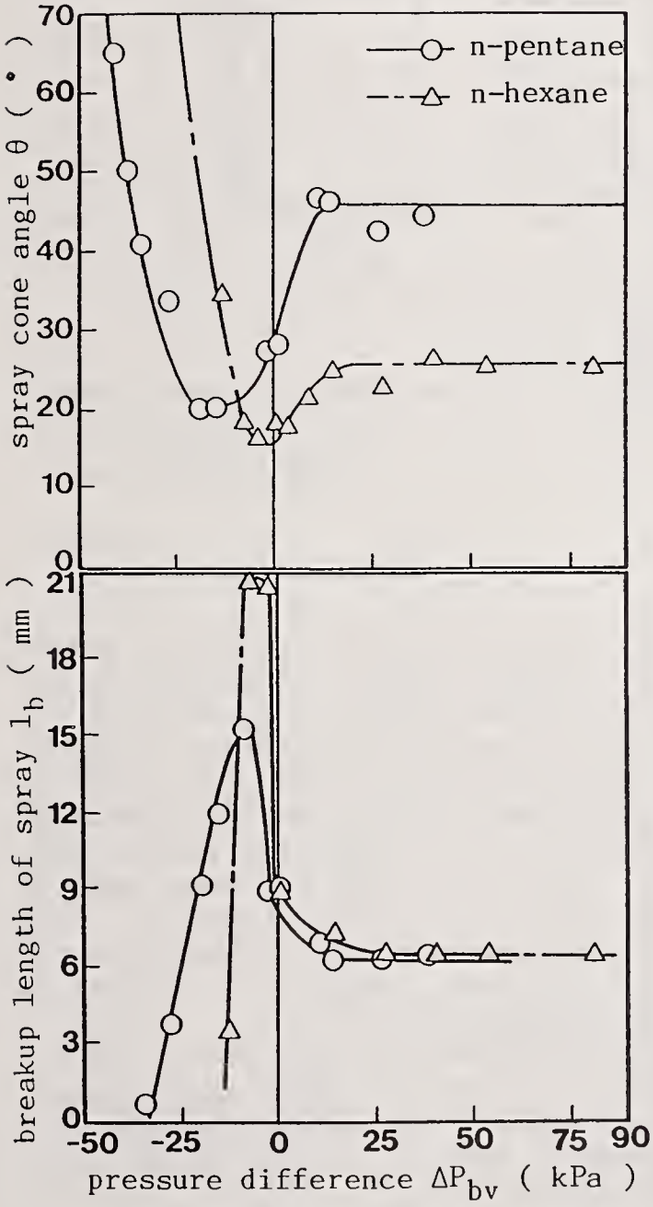

Fig.5 Dependence of spray angle θ and breakup length l_b on pressure difference ΔP_{bv} (t=3.0ms.)

by the effect of flash boiling, corresponding with an increase in the spray angle θ. And then it appears that the bubble growth rate exerts a great influence on the rapid decrease in θ in the ΔP_{bv} range of less than 0 kPa.

Atomization Characteristics

Here, as the atomization characteristics, droplet size distribution and the meandiameter of breakup droplets are took up for n-pentane and n-hexane sprays. Figure 4 illustrates the measuring region of fuel droplets.

Figure 6 shows the dependence of Sauter mean diameter d_{32} of breakup droplets on the pressure difference ΔP_{bv} under the condition of ΔP=250 kPa and t=3.0 ms. In this figure, the region drawn with hatched line indicates the range of impossible measurement of mean droplet diameter in presence of very large liquid with irregular massive state for n-pentane spray. The results of Sauter mean diameter d_{32} are similar in its properties to the breakup length l_b over the range of ΔP_{bv}.

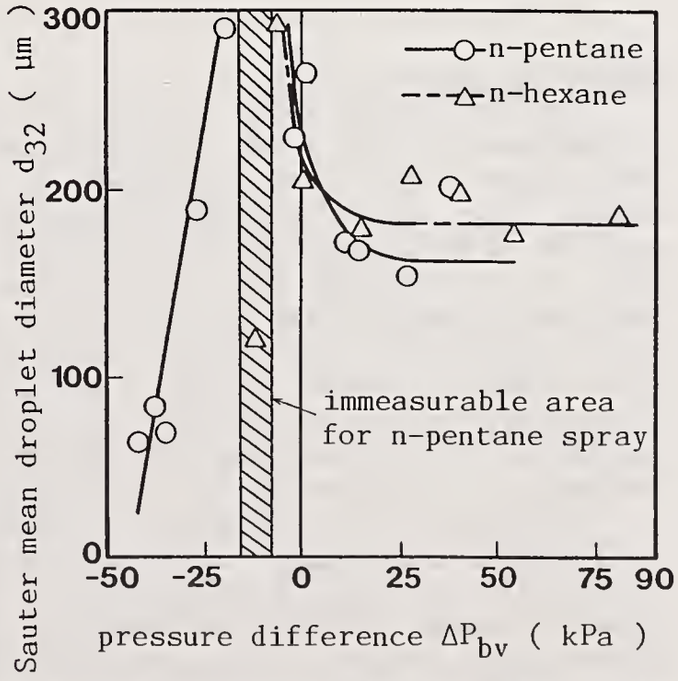

Fig.6 Dependence of Sauter mean droplet diameter, d_{32} on pressure difference ΔP_{bv} (t=3.0ms.)

The variation in droplet size distribution for n-pentane spray with pressure difference ΔP_{bv} is revealed in Fig.7. The results indicated that the distribution was relatively non-uniform having large droplets up to 200 μm in diameter in ΔP_{bv} range from 38.5 to -1.5 kPa. With a decrease in ΔP_{bv}, the large droplets reduced gradually the number. Further, in the case of -48.5 kPa in ΔP_{bv}, it became uniform obviously due to flash boiling, showing the shape of high frequency of small droplets less than 80 μm in diameter and the narrow range of the distribution.

Thus, with a further decrease in back pressure P_b less than the vapor pressure P_v, rapid flashing of grown up cavitation bubbles provides the uniform droplet size distribution as shown in Fig.7 and the uniform distribution of d_{32} in radial direction in the spray.

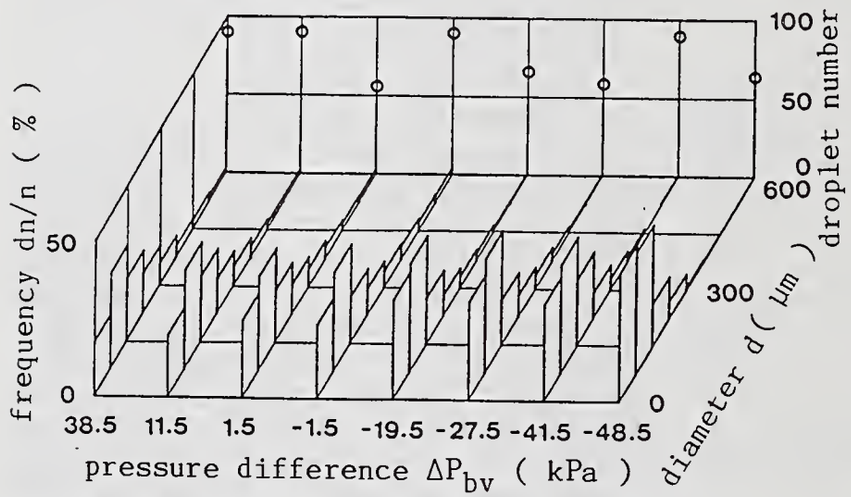

Fig.7 Variation in droplet size distribution for n-pentane spray with pressure difference ΔP_{bv}

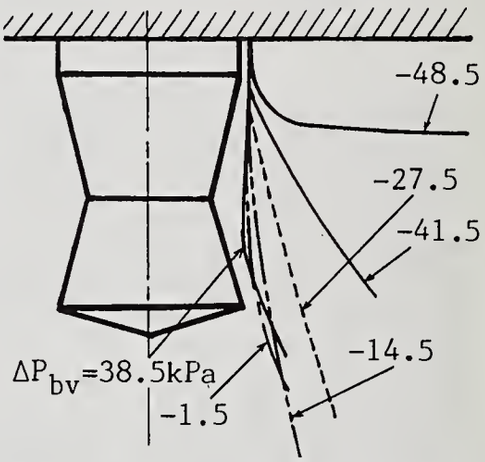

Fig.8 Spray outside shape near the pintle for n-pentane spray (t=3.0ms.)

Effect of Flash Boiling

The outline of spray outside near the pintle obtained by the micrographs illustrated in Fig.8 for n-pentane spray. In the pressure difference ΔP_{bv} range above 0 kPa, the disturbance in liquid film, which is produced at the pintle edge, has a marked influence in the spray atomization since the outline of spray outside flows along the pintle shape. With a decrease in ΔP_{bv} in the range of $\Delta P_{bv}<0$, the spray expansion, that is the spray angle θ, decreases gradually due to the spray contraction, not along the pintle edge. With further decreasing ΔP_{bv}, the spray angle θ markedly increases and the start point of spray expansion approaches gradually to the injector. From these results, it seems that the spray atomization is attributed to the intensity of flash boiling, that is the bubble growth rate and so on, not to the shape of injector outlet in the range of $\Delta P_{bv}<0$ kPa.

Therefore, the behavior of a cavitation bubble growth due to flash boiling was investigated in this section. The bubble is assumed to grow spherically, and the Rayleigh-Plesset equation [7] is used to indicate the growth process. The growth rate of cavitation bubbles is controlled by the hydrodynamic forces as shown following equation.

$$R\ddot{R}+\frac{2}{3}\dot{R}^2=\frac{1}{\rho_l}(P_w-P_r) \qquad (1)$$

where, R is the bubble radius, ρ_l the liquid density, P_w the pressure in liquid at the bubble wall and P_r is the pressure of liquid surrounding the bubble. The pressure P_w is defined by the following equation in this study.

$$P_w = P_v + P_{go}\left(\frac{R_0}{R}\right)^{3\kappa} - \frac{2\sigma}{R} - 4\mu\frac{\dot{R}}{R} \qquad (2)$$

where, P_v is the saturated vapor pressure, P_{go} the initial pressure of noncondensable gas inside the bubble, R_o the initial radius of bubble, κ the ratio of specific heat of gas, σ the surface tension and μ is the liquid viscosity.

For applying the bubble growth analysis to flash boiling injection, it is necessary to estimate the pressure profile inside the injector. In this study, pressures and velocities in steady state were assessed using the Bernoulli equation with loss terms, considering the cross sectional area at each point inside the injector.

Figure 9 shows the temporal change in the bubble radius R with each pressure difference ΔP_{bv} calculated from equations (1) and (2) for n-pentane spray, in the case of R_o=15 μm. The bubble radius R increases abruptly with decreasing ΔP_{bv}. In particular, in the conditions of ΔP_{bv}=-41.5 and -48.5 kPa, the bubble nuclei starts to grow inside the orifice of the injector. In this calculation, we can obtain the bubble growth rate $\dot{R}$ which appears to be controlling the spray atomization. Here, the growth rate $\dot{R}_{t=tb}$ at the breakup time t_b corresponding with the breakup length l_b was considered as a typical rate.

Figure 10 shows the relation between the bubble growth rate $\dot{R}_{t=tb}$ at t_b and the pressure difference ΔP_{bv} assessed with bubble growth analysis. The bubble grow rate $\dot{R}_{t=tb}$ increases gradually with decreasing the pressure difference ΔP_{bv}. Therefore it is found that vigorous flash boiling phenomena

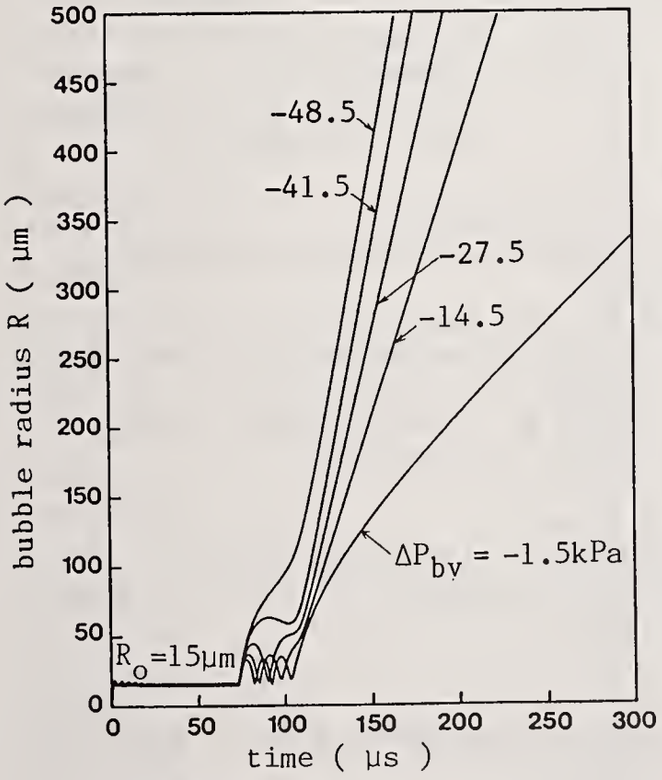

Fig.9 Bubble growth calculation for n-pentane spray

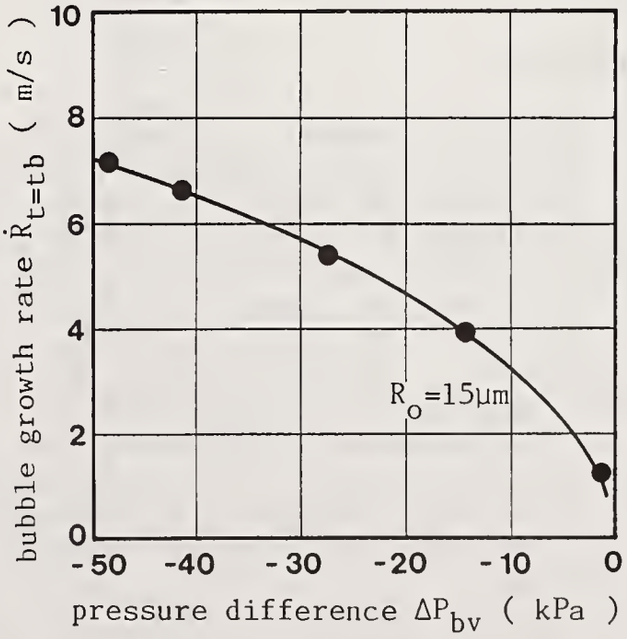

Fig.10 Relation between bubble growth rate $\dot{R}$ and pressure difference ΔP_{bv} for n-pentane spray

occurs with a decrease in ΔP_{bv} from this bubble growth analysis. And we could convert the experimental parameter such as the pressure difference ΔP_{bv} into the physical quantities such as the growth rate $\dot{R}$ in connection with a description of spray characteristics with flash boiling.

Finally, several spray characteristics mentioned above are arranged qualitatively with the bubble growth rate. Thus, spray characteristics, such as the spray angle θ, the breakup length l_b and the droplets mean diameter d_{32}, were plotted against the growth rate as shown in Fig.11. With increasing the rate $\dot{R}_{t=tb}$, the spray angle increases rapidly, and the breakup length l_b and Sauter mean diameter d_{32} decrease rapidly, respectively. Therefore, it seems to suggest that the spray characteristics in the back pressure range of less than the vapor pressure P_v can be described qualitatively by the bubble growth rate in terms of flash boiling phenomena. However, it is necessary to consider the distribution of the bubble nuclei and the nucleation process to perform quantitatively this flash boiling analysis.

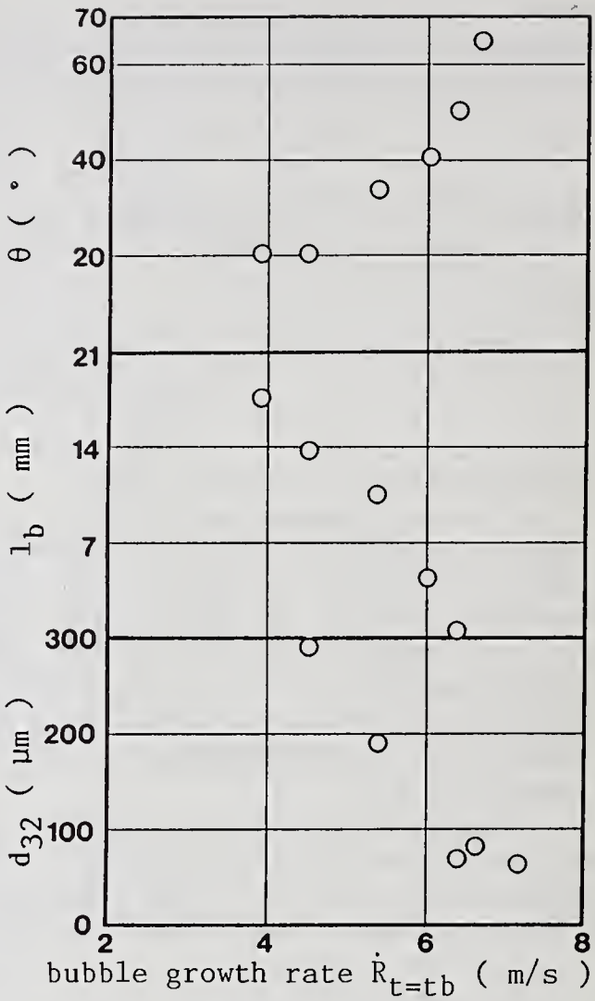

Fig.11 Dependence of spray characteristics on bubble growth rate $\dot{R}$ for n-pentane spray (t=3.0ms.)

REFERENCES

[1] Nogi,T., Ohyama,Y., Yamauchi,T. and Kuroiwa,H., "Mixture Formation of Fuel Injection Systems in Gasoline Engines", SAE Technical Paper, No. 880558 (1988).

[2] Kashiwaya,M., Kosuge,T., Nakagawa,K. and Okamoto,Y., "The Effect of Atomization of Fuel Injectors on Engine Performance", SAE Technical Paper, No. 900261 (1990).

[3] Brown,R. and York,J.L., "Spray Formed by Flashing Liquid Jets", A.I.Ch.E. Journal, Vol.8, No.2 (1962), pp.149-153.

[4] Lienhard,J.H. and James,B.D., "The Breakup of Surperheated Liquid Jets", Trans.of ASME, J. of Basic Engineering, (1970), pp.515-522

[5] Suzuki,M., Yamamoto,T., Futagami,N. and Maeda,S., "Atomization of Superheated Liquid Jet", ICLASS '78, 2-2 (1978), pp.37-43

[6] Oza,R.D. and Sinnamon,J.F., "An Experimental and Analytical study of Flash-Boiling Fuel Injection", SAE Technical Paper, No. 830590 (1983).

[7] Plesset,M.S., "Cavitation in Real Liquids", Amer. Elsevrer Pub. Co., (1964), p.1.

ICLASS-91
INDEX OF AUTHORS
(Numbers refer to paper numbers)

☆ U.S. GOVERNMENT PRINTING OFFICE: 1991-261-616/42749

NIST-114A
(REV. 3-89)

U.S. DEPARTMENT OF COMMERCE
NATIONAL INSTITUTE OF STANDARDS AND TECHNOLOGY

BIBLIOGRAPHIC DATA SHEET

1. PUBLICATION OR REPORT NUMBER
NIST/SP-813

2. PERFORMING ORGANIZATION REPORT NUMBER

3. PUBLICATION DATE
July 1991

4. TITLE AND SUBTITLE
Proceedings of the Fifth International Conference on Liquid Atomization and Spray Systems (ICLASS-91)

5. AUTHOR(S)
Hratch G. Semerjian (Editor)

6. PERFORMING ORGANIZATION (IF JOINT OR OTHER THAN NIST, SEE INSTRUCTIONS)
U.S. DEPARTMENT OF COMMERCE
NATIONAL INSTITUTE OF STANDARDS AND TECHNOLOGY
GAITHERSBURG, MD 20899

7. CONTRACT/GRANT NUMBER

8. TYPE OF REPORT AND PERIOD COVERED
Final

9. SPONSORING ORGANIZATION NAME AND COMPLETE ADDRESS (STREET, CITY, STATE, ZIP)
Institute for Liquid Atomization and Spray Systems (ILASS-Americas)
and
National Institute of Standards and Technology

10. SUPPLEMENTARY NOTES

[ ] DOCUMENT DESCRIBES A COMPUTER PROGRAM; SF-185, FIPS SOFTWARE SUMMARY, IS ATTACHED.

11. ABSTRACT (A 200-WORD OR LESS FACTUAL SUMMARY OF MOST SIGNIFICANT INFORMATION. IF DOCUMENT INCLUDES A SIGNIFICANT BIBLIOGRAPHY OR LITERATURE SURVEY, MENTION IT HERE.)

This NIST Special Publication contains the Proceedings of the Fifth International Conference on Liquid Atomization and Spray Systems, sponsored and organized by the Institute for Liquid Atomization and Spray Systems (ILASS-Americas) and the National Institute of Standards and Technology (NIST), held at NIST, in Gaithersburg, Maryland on July 15-18, 1991. One hundred papers were presented at the Conference, including four keynote lectures on "Physics of Atomization", "Experimental and Theoretical Studies on the Structure of Fuel Sprays in Diesel Engines", "Atomization of Liquid Metals for the Manufacture of Metal Powder and for Spray Forming", and "Twin Fluid Atomization: Factors Influencing Mean Drop Size". Technical sessions were organized on Evaporation and Mass Transfer in Sprays, Spray Coating, Basic Atomization Processes, Pressure Atomizers, Diesel Sprays, Drop Size Distribution of Sprays, Novel Atomizers, Diagnostics, Atomization of Special Liquids, Spray Combustion, Twin Fluid Atomization, Spray Modeling, Airblast and Electrostatic Atomization, and Airbreathing and Rocket Engines.

12. KEY WORDS (6 TO 12 ENTRIES; ALPHABETICAL ORDER; CAPITALIZE ONLY PROPER NAMES; AND SEPARATE KEY WORDS BY SEMICOLONS)
Atomization, Atomization of Special Liquids, Diagnostics, Drop Size Distribution, Electrostatic Atomization, Fuel Atomization, Pressure Atomizers, Spray Combustion, Spray Modeling, Sprays, Twin Fluid Atomizers.

13. AVAILABILITY

[X] UNLIMITED

[ ] FOR OFFICIAL DISTRIBUTION. DO NOT RELEASE TO NATIONAL TECHNICAL INFORMATION SERVICE (NTIS).

[X] ORDER FROM SUPERINTENDENT OF DOCUMENTS, U.S. GOVERNMENT PRINTING OFFICE, WASHINGTON, DC 20402.

[X] ORDER FROM NATIONAL TECHNICAL INFORMATION SERVICE (NTIS), SPRINGFIELD, VA 22161.

14. NUMBER OF PRINTED PAGES
869

15. PRICE

ELECTRONIC FORM

NIST Technical Publications

Periodical

Journal of Research of the National Institute of Standards and Technology—Reports NIST research and development in those disciplines of the physical and engineering sciences in which the Institute is active. These include physics, chemistry, engineering, mathematics, and computer sciences. Papers cover a broad range of subjects, with major emphasis on measurement methodology and the basic technology underlying standardization. Also included from time to time are survey articles on topics closely related to the Institute's technical and scientific programs. Issued six times a year.

Nonperiodicals

Monographs—Major contributions to the technical literature on various subjects related to the Institute's scientific and technical activities.

Handbooks—Recommended codes of engineering and industrial practice (including safety codes) developed in cooperation with interested industries, professional organizations, and regulatory bodies.

Special Publications—Include proceedings of conferences sponsored by NIST, NIST annual reports, and other special publications appropriate to this grouping such as wall charts, pocket cards, and bibliographies.

Applied Mathematics Series—Mathematical tables, manuals, and studies of special interest to physicists, engineers, chemists, biologists, mathematicians, computer programmers, and others engaged in scientific and technical work.

National Standard Reference Data Series—Provides quantitative data on the physical and chemical properties of materials, compiled from the world's literature and critically evaluated. Developed under a worldwide program coordinated by NIST under the authority of the National Standard Data Act (Public Law 90-396). NOTE: The Journal of Physical and Chemical Reference Data (JPCRD) is published quarterly for NIST by the American Chemical Society (ACS) and the American Institute of Physics (AIP). Subscriptions, reprints, and supplements are available from ACS, 1155 Sixteenth St., NW., Washington, DC 20056.

Building Science Series—Disseminates technical information developed at the Institute on building materials, components, systems, and whole structures. The series presents research results, test methods, and performance criteria related to the structural and environmental functions and the durability and safety characteristics of building elements and systems.

Technical Notes—Studies or reports which are complete in themselves but restrictive in their treatment of a subject. Analogous to monographs but not so comprehensive in scope or definitive in treatment of the subject area. Often serve as a vehicle for final reports of work performed at NIST under the sponsorship of other government agencies.

Voluntary Product Standards—Developed under procedures published by the Department of Commerce in Part 10, Title 15, of the Code of Federal Regulations. The standards establish nationally recognized requirements for products, and provide all concerned interests with a basis for common understanding of the characteristics of the products. NIST administers this program as a supplement to the activities of the private sector standardizing organizations.

Consumer Information Series—Practical information, based on NIST research and experience, covering areas of interest to the consumer. Easily understandable language and illustrations provide useful background knowledge for shopping in today's technological marketplace.

Order the **above** *NIST publications from: Superintendent of Documents, Government Printing Office, Washington, DC 20402.*

Order the **following** *NIST publications—FIPS and NISTIRs—from the National Technical Information Service, Springfield, VA 22161.*

Federal Information Processing Standards Publications (FIPS PUB)—Publications in this series collectively constitute the Federal Information Processing Standards Register. The Register serves as the official source of information in the Federal Government regarding standards issued by NIST pursuant to the Federal Property and Administrative Services Act of 1949 as amended, Public Law 89-306 (79 Stat. 1127), and as implemented by Executive Order 11717 (38 FR 12315, dated May 11, 1973) and Part 6 of Title 15 CFR (Code of Federal Regulations).

NIST Interagency Reports (NISTIR)—A special series of interim or final reports on work performed by NIST for outside sponsors (both government and non-government). In general, initial distribution is handled by the sponsor; public distribution is by the National Technical Information Service, Springfield, VA 22161, in paper copy or microfiche form.

U.S. Department of Commerce
National Institute of Standards and Technology
(formerly National Bureau of Standards)
Gaithersburg, MD 20899